

274

AD 6 30

USAAVLABS TECHNICAL REPORT 68-65

**ADVANCEMENT OF HIGH-TEMPERATURE TURBINE
TECHNOLOGY FOR SMALL GAS TURBINE ENGINES**

FLUID-COOLED AXIAL FLOW TURBINE

By

Ronald M. Gabel

Arthur J. Tabbey

January 1969

**U. S. ARMY AVIATION MATERIEL LABORATORIES
FORT EUSTIS, VIRGINIA**

CONTRACT DA 44-177-AMC-184(T)

**CONTINENTAL AVIATION AND ENGINEERING CORPORATION
DETROIT, MICHIGAN**

TECHNICAL LIBRARY
REFERENCE COPY

*This document has been approved
for public release and sale; its
distribution is unlimited.*



20030108046

~~20020729246~~

Disclaimers

The findings in this report are not to be construed as an official Department of the Army position unless so designated by other authorized documents.

When Government drawings, specifications, or other data are used for any purpose other than in connection with a definitely related Government procurement operation, the United States Government thereby incurs no responsibility nor any obligation whatsoever; and the fact that the Government may have formulated, furnished, or in any way supplied the said drawings, specifications, or other data is not to be regarded by implication or otherwise as in any manner licensing the holder or any other person or corporation, or conveying any rights or permission, to manufacture, use, or sell any patented invention that may in any way be related thereto.

Trade names cited in this report do not constitute an official endorsement or approval of the use of such commercial hardware or software.

Disposition Instructions

Destroy this report when no longer needed. Do not return it to the originator.



DEPARTMENT OF THE ARMY
U. S. ARMY AVIATION MATERIEL LABORATORIES
FORT EUSTIS, VIRGINIA 23604

USAAVLABS technical personnel have reviewed this report and concur in the conclusions contained herein.

The findings and recommendations outlined herein have been and will be taken into consideration in the planning of future programs for turbines and turbine engines.

Task 1G121401D14413
Contract DA 44-177-AMC-184 (T)
USAAVLABS Technical Report 68-65
January 1969

ADVANCEMENT OF HIGH-TEMPERATURE TURBINE
TECHNOLOGY FOR SMALL GAS TURBINE ENGINES

FLUID-COOLED AXIAL FLOW TURBINE

Continental Report No. 1094

By

Ronald M. Gabel
Arthur J. Tabbey

Prepared by

Continental Aviation and Engineering Corporation
Detroit, Michigan

for

U.S. ARMY AVIATION MATERIEL LABORATORIES
FORT EUSTIS, VIRGINIA

This document has been approved
for public release and sale; its
distribution is unlimited.

SUMMARY

The overall contract objective was to advance and demonstrate high turbine inlet temperature technology for small gas turbine engines to the level that will provide a potential for doubling the specific horsepower (horsepower per pound of airflow per second) relative to current small aircraft propulsion engines. A fluid-cooled, single-stage axial flow turbine concept is being investigated with the following design point performance goals:

2300°F	TIT
85.0	percent adiabatic turbine efficiency
5.0	lb/sec airflow
$\frac{\Delta H}{\Theta_{cr}}$	= 26.0 Btu/lb air

The objective is the demonstration of a capability for 213 BHP/lb of air/sec, assuming that this gas generator turbine is coupled to a 9.2 pressure ratio, 79.5-percent efficient compressor in a turboshaft engine with 11.5-percent total cycle pressure drop, and using a power turbine with an efficiency of 92 percent.

The turbine uses a closed-loop fluid (steam) thermosiphon cooling system to cool the rotor blades and to transfer the heat to the fuel. As this heat is put into the fuel, it is not lost to the cycle. Combustor primary airflow is used to cool the turbine inlet nozzles; virtually no bleed air is used in the system.

Phase I covers the design of the turbine rotor, nozzle, and combustor with their test rig. Experimental verification of turbine performance by cold test and turbine nozzle cooling effectiveness by a hot cascade test is included. The feasibility of turbine rotor blade fabrication is also demonstrated by fabrication and proof testing of actual blades.

Phase II covers the experimental evaluation, through hot testing, of the thermosiphon fluid-cooled turbine. An actual specific horsepower demonstration of 171 hp/lb/sec was run at a turbine inlet temperature of 2344°F. A maximum temperature of 2450°F was achieved, and a total of 21 hours' running time above 2100°F was achieved. No problems were encountered with the cooling system, and with additional work the turbine efficiency could be improved. Also, no catastrophic structural failures occurred during the test program.

FOREWORD

This report, prepared by Continental Aviation and Engineering Corporation, presents Phase I and Phase II of a fluid-cooled turbine program for the advancement of small gas turbine component technology. The program was sponsored by the U. S. Army Aviation Materiel Laboratories, Fort Eustis, Virginia under contract DA 44-177-AMC-184 (T).

Acknowledgement is given to the following Continental Aviation and Engineering personnel who were the prime contributors to the accomplishment of this program and the preparation of this report:

E. Dellert

C. Rogo

J. Gaff

R. Trauth

J. Lenkay

R. Vaughan

R. Marshall

T. Weidig

R. Phebus

TABLE OF CONTENTS

	<u>Page</u>
SUMMARY	iii
FOREWORD	v
LIST OF ILLUSTRATIONS	xvi
LIST OF TABLES	xxxxxi
LIST OF ABBREVIATIONS	xxxiv
LIST OF SYMBOLS	xxxvii
FLUID-COOLED TURBINE DESIGN CONCEPTS, HARDWARE PROCUREMENT, AND DESIGN OPTIMIZATION	1
INTRODUCTION	1
TEST RIG	1
AERODYNAMIC DESIGN AND COLD FLOW TEST	1
BLADE MANUFACTURING TECHNOLOGY	4
BLADE/DISC DESIGN STUDIES	7
Pinned Attachment	7
Cast-Cored Wheel	10
Electron Beam Welding	10
Selection of Rotor Cooling System Design	12
NOZZLE/COMBUSTOR DESIGN STUDIES	12
NOZZLE VANE CASCADE DESIGN, FABRICATION AND TEST	13
FLUID-COOLED TURBINE TEST RIG	16
COOLED TURBINE RIG	16
Shaft	16
Rotor Shaft	16

TABLE OF CONTENTS (Continued)

	<u>Page</u>
Fuel Slinger Shaft	23
Shaft Bearings	24
Air Inlet Plenum	24
Exhaust Diffuser	24
Fuel Pressurizing Valve	25
RIG INSTALLATION	25
Dynamometer	28
Gear Reduction Unit	28
INSTRUMENTATION	32
Rig Airflow	32
Rig Fuel Flow	32
Slip Ring	32
Dynamometer Rig Speed and Torque	33
Rig Main Stream Gas Temperatures	33
Rig Main Stream Pressures	36
Effect of Instrument Inaccuracies on Calculated Turbine Efficiency	40
Rig Metal Temperatures	41
Stresses	42
Adhesives	44
Fuel Temperatures	44
TURBINE AEROTHERMODYNAMIC DESIGN AND COLD TEST . .	45
AEROTHERMODYNAMIC DESIGN	45
Overall Design	45
Nozzle	52
Rotor	54

TABLE OF CONTENTS (Continued)

	<u>Page</u>
Efficiency Considerations at Design Point	69
Stewart's Method - Reference 12	69
Ainley and Mathieson Method	70
Continental Method	72
COLD FLOW TESTING	75
Summary	75
Nominal Design	83
Rotor Solidity Tests	90
Nozzle Solidity Tests	90
Nozzle Trailing Edge Effects	90
Rotor Trailing Edge Effects	102
PROCESS FEASIBILITY STUDIES FOR FLUID-COOLED TURBINE BLADES	107
INTRODUCTION	107
PRECISION CASTING TECHNIQUES	107
Preliminary Rectangular Test Blocks	107
Airfoil Castings	117
Blade Tip Closure	125
Blade Closure (Stem)	153
Electron Beam Welding	158
Welding Unfilled Passages	164
Unfilled Passages and Heat Sinks	169
Welding With Filled Passages	176
DIFFUSION BONDING	190
TESTING	200
Testing Rectangular Samples	200

TABLE OF CONTENTS (Continued)

	<u>Page</u>
Nondestructive	201
Destructive	201
Testing Airfoil Blades	214
Tensile Testing	215
Fatigue Testing	215
Thermal Shock Tests	217
BLADE AND DISC DESIGN STUDIES	225
BLADE COOLING SYSTEMS	225
FUEL THERMAL STABILITY	236
ANALYSIS OF TURBINE ROTOR METAL TEMPERATURES	238
Disc Temperature Distribution	238
Disc Rim Temperature	238
Heat Transfer Coefficient to Disc Rim h_{pl}	240
Disc External Heat Transfer Coefficients	241
Internal Heat Transfer Coefficient	241
Results and Discussion	241
External Heat Transfer Coefficients	244
Internal Heat Transfer Coefficients	244
Blade Attachment Temperature Distribution	249
STRUCTURAL DESIGN	257
Rotor Disc	257
Pinned Blade - Heat Exchanger Concept Analysis	257
Welded Blade - Heat Exchanger Attachment Analysis	266
Full Cast Integral Blade and Disc With Heat Exchanger in the Shaft Analysis	276
Rotor Blade and Attachment	283

TABLE OF CONTENTS (Continued)

	<u>Page</u>
Blade Attachment Analysis.	284
Stresses and Growth.	288
Blade	289
Conclusions	298
Attachment	300
Rotor Life	300
Disc Weight	300
LABORATORY EVALUATION OF FUEL SEALS AND PINNED ATTACHMENTS	300
Seal Testing	303
Conclusions and Recommendations	317
SELECTION OF ROTOR COOLING SYSTEM DESIGN	317
TURBINE NOZZLE/COMBUSTOR DESIGN STUDIES	321
NOZZLE DESIGNS CONSIDERED	321
Segmented Configurations	321
Continuous Ring Nozzle Configurations	331
TURBINE NOZZLE ASSEMBLY	333
Temperature Distribution	333
Vane	333
External Heat Transfer Coefficients	337
Internal Heat Transfer Coefficient	342
Convection Cooling Design No. 1	342
Convection Cooling Design No. 2	342
TURBINE NOZZLE SHROUDS	344

TABLE OF CONTENTS (Continued)

	<u>Page</u>
TURBINE NOZZLE STRUCTURAL DESIGN	349
Conclusions	349
Segmented Versus Continuous Shrouds	349
Separate Rotor Shroud Versus Integral Rotor Shroud	349
NOZZLE VANES	352
COMBUSTOR.	358
Design Analysis	358
TURBINE INLET NOZZLE CASCADE DESIGN.	368
HOT CASCADE RIG	368
TEST SECTION	368
INSTRUMENTATION.	373
TEST PROGRAM	373
DISCUSSION OF TEST RESULTS	385
INTRODUCTION TO PHASE II	401
AEROTHERMODYNAMIC PERFORMANCE	406
TURBINE	406
Correction Factor Analysis	411
Turbine Analysis	414
Test Results	421
COMBUSTOR	426
Combustor Development	429

TABLE OF CONTENTS (Continued)

	<u>Page</u>
Combustor Development During Rotor Testing	462
HEAT TRANSFER	493
Discussion	494
MECHANICAL-STRUCTURAL INTEGRITY	521
SUMMARY	521
MECHANICAL ASSEMBLY	523
Turbine Rotor	523
Gearbox - Assembly	526
TEST AND FAILURE ANALYSIS	530
Test Plan	530
Test Runs 15-22	533
Test Runs 23 Through 27	538
Test Runs 28 Through 31	548
Test Runs 32 - 50	551
Test Runs 51 - 59	557
Test Run 60	564
Test Runs 61 and 62	565
Component Testing	570
VERIFICATION OF DESIGN	579
Turbine Blades	579
Airfoil Stress Analysis	580
Blade-to-Disc Pin Attachment	582
Blade-to-Disc Seal	582
Disc Stress Analysis	582
Fuel Circuit	583

TABLE OF CONTENTS (Continued)

	<u>Page</u>
Fuel Deposits	583
Bearings.	583
Turbine Shroud	584
Exhaust Duct.	584
Turbine Nozzle and Combustor Assemblies	584
MANUFACTURING TECHNOLOGY	585
BACKGROUND	585
DISCUSSION	585
Turbine Disc	585
Turbine Blade	593
Nondestructive Testing (NDT)	603
Turbine Shaft Assembly	607
Pin	609
Subcomponents	611
CONCLUSIONS AND RESULTS	617
RECOMMENDATIONS	619
REFERENCES	620
APPENDIXES	
I RESEARCH AND DEVELOPMENT QUALITY CONTROL SPECIFICATION NO. 51 BLADE CASTING AND MACHINING	625
II HEAT TRANSFER IN A COOLED TURBINE BLADE CONTINENTAL IBM PROGRAM 25-007	652
III DESIGN OF FLUID-COOLED TURBINE FUEL-TO- STEAM HEAT EXCHANGER	665

TABLE OF CONTENTS (Continued)

	<u>Page</u>
IV GENERAL THREE-DIMENSIONAL TRANSIENT TEMPERATURE DISTRIBUTION	683
V TURBINE PERFORMANCE DATA REDUCTION PROGRAM - 08.079	687
VI TURBINE PERFORMANCE DATA REDUCTION PROGRAM - INPUT COMPUTER PROGRAM 08.079 TURBINE TEST 62	695
VII TURBINE PERFORMANCE DATA REDUCTION PROGRAM - READOUT COMPUTER PROGRAM 08.079 TURBINE TEST 62	697
VIII TURBINE RIG INSTRUMENTATION	698
IX ELECTRON BEAM WELDING AND SEALING FLUID-COOLED BLADE, PART NO. 709627 CONTINENTAL PROCESS 402	709
X WELDING OF TURBINE SHAFT (FUEL VALVE HOUSING, PART NO. 711008)	713
DISTRIBUTION	716

LIST OF ILLUSTRATIONS

<u>Figure No.</u>		<u>Page</u>
1	Test Cell Layout	2
2	Turbine Test Rig Cross Section	3
3	Effect of Turbine Inlet Temperature and Turbine Efficiency on Specific Horsepower.	5
4	Fluid-Cooled Blade Containing Water-Welded Cap and Plug	6
5	Blade-to-Disc Pinned Attachment	8
6	Cooling System for Fluid-Cooled Turbine Blade . . .	9
7	Cast-Cored Wheel With Heat Exchanger in Engine Shaft	11
8	Cast-Segmented and Continuous-Ring Turbine Inlet Nozzle	14
9	Fluid-Cooled Turbine Rig Metal Temperatures - Regenerative Running	17
10	Fluid-Cooled Turbine Rig Metal Temperatures - Nonregenerative Running	18
11	Fluid-Cooled Turbine Rig Component Materials . . .	19
12	Liquid-Cooled Turbine Critical Speed Versus Spring Rate of Rear (Turbine) Bearing for Various Values of Front Bearing Support Spring Rate	20
13	Characteristic Shaft Motion at First, Second, and Third Critical Speeds.	21
14	Typical Spring Cage-Type Shaft Support Bearing. . .	22
15	Double-Walled Exhaust Diffuser Cooling Airflow Path and Metal Temperature	26
16	Fuel Pressurizing Valve	27
17	Fluid-Cooled Turbine Rig Test Envelope	29
18	Reduction Gearbox for Fluid-Cooled Turbine	30
19	Bean VHS-F6 Slip Ring	33

LIST OF ILLUSTRATIONS (Continued)

<u>Figure No.</u>		<u>Page</u>
20	Double-Shielded Traversing Turbine Inlet Thermocouple	34
21	Turbine Inlet Total-Temperature Probe Location . .	35
22	Turbine Discharge Total Temperature	37
23	Turbine Inlet Pressure	38
24	Turbine Discharge Pressures	39
25	Anticipated Thermocouple Locations	43
26	Fuel Temperature Rotor Exit	44
27	Fluid-Cooled Turbine Flow Path for Cold Flow Rig Testing, 23 Nozzle Vanes	46
28	Turbine Velocity Diagram Station and Sign Notation	48
29	Velocity Diagrams - Fluid-Cooled Turbine	49
30	Effect of Meridional Constriction on Losses of a Nozzle	53
31	Fluid-Cooled Turbine Nozzle Coordinate Designations	55
32	Velocity Distribution - Nozzle Hub Section - 12.5 Percent Blade Height	56
33	Velocity Distribution - Nozzle Mean Section - 50 Percent Blade Height	57
34	Velocity Distribution - Nozzle Tip Section - 87.5 Percent Blade Height	58
35	Flow Path for Cold Flow Rig Testing With Second Design Nozzle	59
36	Nozzle Area Distribution	60
37	Nozzle Velocity Distribution - 50 Percent Blade Height	61
38	Rotor Hub Section - 12.5 Percent Blade Height - 34 Blades	63
39	Rotor Mean Section - 50 Percent Blade Height - 34 Blades	64

LIST OF ILLUSTRATIONS (Continued)

<u>Figure No.</u>		<u>Page</u>
40	Rotor Tip Section - 87.5 Percent Blade Height	65
41	Fluid-Cooled Rotor - 34 Blades	66
42	Rotor Stagger Variation With Solidity and Number of Blades	67
43	Comparison of Fluid-Cooled Turbine With Scaled J69-T-39 First-Stage Turbine	71
44	Comparison of CAE Predicted and Experimental Turbine Efficiencies	73
45	Front View of Turbine Test Stand	77
46	Rear View of Turbine Test Stand	78
47	Cold Flow Turbine Test Assembly Installation Turbine Test Stand	79
48	Turbine Test Stand Instrumentation Diagram	81
49	Turbine Test Stand Circumferential Instrumentation Diagram	82
50	Effect of Turbine Inlet Temperature and Turbine Efficiency on Specific Horsepower	84
51	Cold Flow Turbine Inlet Nozzle Assembly - View Looking Downstream	85
52	Cold Flow Turbine Rotor Assembly - View Looking Downstream	86
53	Fluid-Cooled Turbine - Test Stand Performance . .	87
54	Rotor Exit Characteristics - 23 Vanes, 34 Blades . .	88
55	Nozzle Pressure Characteristics - 23 Vanes Set Nominally	89
56	Fluid-Cooled Turbine - Test Stand Performance . .	91
57	Fluid-Cooled Turbine Performance - 23 Nozzle Vanes and 40 Rotor Blades	92
58	Fluid-Cooled Turbine Performance - 23 Nozzle Vanes and 28 Rotor Blades	93
59	Fluid-Cooled Turbine Performance - 23 Nozzle Vanes and 22 Rotor Blades	94

LIST OF ILLUSTRATIONS (Continued)

<u>Figure No.</u>		<u>Page</u>
60	Turbine Efficiency Versus Solidity	95
61	Fluid-Cooled Turbine Performance - 17 Nozzle Vaness and 34 Rotor Blades	96
62	Nozzle Pressure Distribution - 17 Vanes	97
63	Nozzle Pressure Distribution - Taps Along Outer Wall	98
64	Turbine Inlet Nozzle Vanes Before and After Trailing Edge Thinning	99
65	Fluid-Cooled Turbine - Test Stand Performance . . .	100
66	Modified Fluid-Cooled Blade Sections	103
67	Fluid-Cooled Turbine Rotor Blades Before and After Trailing Edge Thinning	104
68	Fluid-Cooled Turbine - Test Stand Performance . . .	105
69	Preliminary Rectangular Blade With Electron Beam Welded Cap.	108
70	Cross Section of Preliminary Rectangular Blade . . .	109
71	Cross Section of Cast Preliminary Rectangular Blade	110
72	Rectangular Blade Ceramic Core, Wax Pattern and Wax Injection Dies	110
73	Wax Pattern for Rectangular Blade	111
74	Radiograph of Ceramic Core for Rectangular Blade	111
75	Rectangular Blade Casting	112
76	Radiograph of Rectangular Blade Casting	113
77	Representative Surface Condition of Rectangular Blade Casting	114
78	Macro-Etched Cross Section Showing Grain Structure	115

LIST OF ILLUSTRATIONS (Continued)

<u>Figure No.</u>		<u>Page</u>
79	Typical Microstructure of Cast Rectangular Blade	116
80	Typical Example of Leaching Defect	117
81	Machined, Welded Airfoil Blade and Tip-Cap	118
82	Cooled Turbine Blade Casting, Part No. 709627 . . .	118
83	(Left and Right) - Ceramic Setter Block Halves (Middle) - Two-Piece Ceramic Core	119
84	(Right) - Two-Piece Baked Ceramic Core (Left) - Green Ceramic Core and Setter Block Half .	120
85	Cavitron Machining of Cores for Cooled Blade.	121
86	Injection Mold for Making Wax Pattern.	123
87	Wax Pattern Gating.	124
88	Cast Cooled Blade Etched to Show Equiaxed Surface Grain and Columnar Internal Grain Where Ingate Was Cut Off	126
89	Blacklight Photo Showing Zyglo Indications on Cast Blade Surface	127
90	Cross Sections of Cooled Turbine Blade	128
91	Cross Section of Cooled Turbine Blade Showing Typical Microstructure of Cast U-700 Alloy	129
92	Heat Exchanger Shank Cross Section Showing Shrink Defect Location	130
93	Shrink Defects in Heat Exchanger	131
94	Rectangular Casting With EDM Cap From Carbon Tool	133
95	Rectangular Blade Used as EDM Tool to Machine Tip-Cap	134
96	Rectangular Blade Used as Finishing Tool for EDM Tip-Caps	135
97	Cap Design for EDM Tip-Cap - Rectangular Blade Block.	135
98	Design for EDM Tip-Cap - Airfoil Casting	136

LIST OF ILLUSTRATIONS (Continued)

<u>Figure No.</u>		<u>Page</u>
99	Preliminary Welds With EDM Tip-Caps	137
100	Rectangular Castings With EDM Tip-Caps	139
101	Internal Passage After Tip-Cap Welding	140
102	Cross Section of Tip-Cap Weld	141
103	Cross Section of Tip-Cap Weld - Beam Focus at Cap Edge	142
104	Cross Section of Tip-Cap - Beam Focus 0.030 Inch From Cap Edge	143
105	Blade and Cap With 15° Notch	146
106	EDM Cap With Wrought Cap Inserted Into Blade Casting	146
107	Cross Section of Cap Weld	148
108	Cast Cooled Blade, Part No. 709627, With Tip-Cap - EDM With Carbon Roughing Tool	149
109	EDM Operation on Cooled Turbine Blade	150
110	Beam Welded Airfoil Cap	152
111	Plug Designs	154
112	TIG Welded Heat Plug in Airfoil Blade	155
113	Electron Beam Welded Heat Exchanger Plug	156
114	Tooling Print for EDM Machining Test Blocks	159
115	Tooling Print for EDM Machining Test Blocks	160
116	Tooling Print for EDM Machining Test Blocks	161
117	Finished EDM Wrought Blade Half	162
118	Parameter Test Block, Sciaky Welder	165
119	Parameter Test Block, Hamilton Standard Welder	166
120	Welding Between Grooves, Sciaky Welder	167
121	Welding Between Grooves, Hamilton Standard Welder	168
122	Welding Between Grooves With Lands Visible	170

LIST OF ILLUSTRATIONS (Continued)

<u>Figure No.</u>		<u>Page</u>
123	Welding in Grooves Over Lands	171
124	Penetration Variation When Welding Over Copper Bars	172
125	Transverse Section Through Adjacent Welds	173
126	Welds Made Using Copper Replica of Internal Passages	174
127	Penetration Variation When Welding Over Copper Mask	175
128	Welding Using Tungsten Mask	177
129	Cross Section of Welds Made Using Tungsten Mask	178
130	Nickel Filled Test Blocks (As Plated)	179
131	Electroplated U-700 Blocks Ground for Weld Test	180
132	Electron Beam Weld Over Electroplated Nickel Before Nickel Removal	181
133	Electron Beam Weld Over Electroplated Nickel After Nickel Removal	182
134	Compacted Nickel-Filled U-700 Blocks Ground for Weld Test	184
135	Electron Beam Weld After Removal of Compacted Nickel	185
136	Weld With Ceramic-Filled U-700 Blocks After Ceramic Removal (Direction of Weld - Parallel to Interface)	186
137	Weld With Ceramic-Filled U-700 Blocks After Ceramic Removal (Direction of Weld - Normal to Interface)	187
138	Welding Over Various Fillers in 304 Stainless Before Filler Removal	188
139	Welding Over Various Fillers in 304 Stainless After Filler Removal	189

LIST OF ILLUSTRATIONS (Continued)

<u>Figure No.</u>		<u>Page</u>
140	Tooling for Pressure Bonding of U-700 Grooved Blocks	191
141	Resistance Heating Setup for Pressure Bonding	192
142	First Diffusion Bond at 1890°F and 0.0005-Inch Nickel Plate	193
143	First Diffusion Bond at 1890°F (No Nickel Plate) . . .	194
144	Second Diffusion Bond at 1850°F and 0.0005-Inch Nickel Plate	195
145	Photomicrograph After Pressing 4 Hours at 1850°F	196
146	Photomicrograph of Sample Pressed 4 Hours at 1850°F Followed by 2 Hours at 2150°F	197
147	Induction Heating Diffusion Bond Setup	198
148	Overheated Diffusion Bond Trial With Induction Heating	199
149	Induction Heated Bond Trial - 2100°F for 1 Hour - Showing Separation on Machining	199
150	Fluid-Cooled Blade - Electron Beam Welded	202
151	Leak Test Equipment - Veeco Model MS-9A Mass Spectrometer for Testing Cooled Hardware	203
152	Leak Testing - Cooled Turbine Blade, Welded Tip	204
153	Pull Test Fixture - To Measure Strength of Blade	207
154	Welded Blade Tip	208
155	Tensile Testing of Rectangular Blades	209
156	Pull Test on Blade Caps	210
157	Fatigue Test Setup	211
158	Typical Fatigue Fracture of Rectangular Blade	212
159	Fatigue Curves - Wrought U-700	213

LIST OF ILLUSTRATIONS (Continued)

<u>Figure No.</u>		<u>Page</u>
160	Typical Tensile Airfoil Fractures	215
161	Interference Diagram - Turbine Blade	217
162	Thermal Shock Rig Out of Chamber Showing Rotating Specimen Holder in Line With Gas Burner and Air Blast	218
163	Mechanical Fatigue Results for IN-100 at 1700°F. . .	220
164	IN-100 - Thermal Fatigue Cycles to Initial Cracking	221
165	IN-100 - Thermal Fatigue Cycles to Failure	222
166	Thermal Shock Blade Specimen	223
167	Effect of Cooled Blade Surface Temperature on Fuel Temperature Rise at Design Point	227
168	Fluid-Cooled Turbine Blade - Spiral-Fin Heat Exchanger	229
169	Fin Steam to Fuel Heat Exchanger	232
170	Fluid-Cooled Turbine Configuration II Heat Exchanger in Engine Shaft	234
171	Effect of Part-Power Operation on Fuel Temperature Rise	237
172	Turbine Rotor Disc Radial Temperature Distribution	242
173	Turbine Rotor Shaft Radial Temperature Distribution	243
174	Critical Velocity Ratio, Rotor Mean - 50 Percent Blade Height, 34 Blades	245
175	Variations of Nusselt Number With Reynolds Number	246
176	Turbine Rotor Blade Heat Transfer Coefficient Distribution	247
177	Turbine Rotor Blade Temperature Distribution - °F, Mid-Span Section	248
178	Blade Attachment Sectioning for Heat Transfer	250

LIST OF ILLUSTRATIONS (Continued)

<u>Figure No.</u>		<u>Page</u>
179	Perfect Thermal Contact Temperature Distribution - Cross-Sectional Side Views	251
180	Perfect Thermal Contact Temperature Distribution - Cross-Sectional Top Views, J-J, L-L, and N-N.	252
181	Twenty Percent Thermal Contact Temperature Distribution - Cross-Sectional Side Views	253
182	Twenty Percent Perfect Thermal Contact Temperature Distribution - Cross-Sectional Top Views, J-J- L-L, and N-N	254
183	Insulated Boundary Temperature Distribution - Cross-Sectional Views	255
184	Insulated Boundary Temperature Distribution - Cross-Sectional Top Views, J-J, L-L, and N-N . . .	256
185	Turbine Rotor Disc - Heat Exchanger In-Disc	258
186	Pinned Attachment Loading Directions	259
187	Rotor Temperature Gradient - Pinned Attachment	261
188	Turbine Rotor Disc With Pinned Attachment - Radial Stress at 50, 000 RPM	262
189	Turbine Rotor Disc With Pinned Attachment - Tangential Stresses at 50, 000 RPM	263
190	Turbine Rotor Disc With Pinned Attachment - Equivalent Stresses at 50, 000 RPM	264
191	Turbine Rotor Disc With Pinned Attachment - Thermal Stresses at Shutdown (RPM = 0)	265
192	Mechanical Properties of Wrought U-700 and Inco 713 LC Low Fe	267
193	Temperature Gradient Welded Attachment	268
194	Welded Attachment Loads	269
195	Disc With Welded Rim Attachment	270
196	Turbine Rotor Disc With Welded Attachment - Tangential Stresses at 50, 000 RPM	271

LIST OF ILLUSTRATIONS (Continued)

<u>Figure No.</u>		<u>Page</u>
197	Turbine Rotor Disc With Welded Attachment - Radial Stresses at 50, 000 RPM	272
198	Turbine Rotor Disc With Welded Attachment - Equivalent Stresses at 50, 000 RPM	273
199	Turbine Rotor Disc With Welded Attachment - Thermal Stresses at Shutdown (RPM = 0)	274
200	Integral Cast Turbine and Rotor Disc	277
201	Temperature Gradient - Cast Disc	278
202	Integral Cast Turbine Rotor Disc - Radial Stresses at 50, 000 RPM	279
203	Integral Cast Turbine Rotor Disc - Tangential Stresses at 50, 000 RPM	280
204	Integral Cast Turbine Rotor Disc - Equivalent Stresses at 50, 000 RPM	281
205	Integral Cast Turbine Rotor Disc - Thermal Stresses at Shutdown (RPM - 0)	282
206	Pinned Attachment Load Identification	285
207	Turbine Rotor Blade Temperature Distribution - °F, Mid-Span Section	287
208	Blade Stresses Due to Centrifugal Loading Only - Unmodified Blade Core	290
209	Bending Stresses Due to Steam Pressure	291
210	Fluid-Cooled Turbine Rotor Blade Thermal Stress Distribution, Mid-Span Section	292
211	Stress-Rupture Properties - Cast U-700	294
212	Turbine Rotor Blade - Radial Blade Growth	296
213	Pin Detail	297
214	Blade Stresses Due to Centrifugal Loading Only - Modified Blade Core	299
215	Blade-to-Disc Pinned Attachment and Fuel Seal Test Specimen	301

LIST OF ILLUSTRATIONS (Continued)

<u>Figure No.</u>		<u>Page</u>
216	Blade-to-Disc Pinned Attachment Test Fixture With Radial Displacement Indicator	302
217	Blade-to-Disc Pinned Attachment Test Fixture With Hydraulic Loading Mechanisms and Dial Indicators	304
218	Metal "W" Seal	305
219	Metal "K" Seal	306
220	Metal "V" Seal	307
221	"V" Seal - Load Versus Response	309
222	Blade Attachment - Test Specimen	310
223	Fluid-Cooled Rotor Hub - Test Specimen	311
224	Left Pin - Fluid-Cooled Turbine Blade - Test Specimen	312
225	Right Pin - Fluid-Cooled Turbine Blade - Test Specimen	313
226	Metal "V" Seal - Revised	314
227	Fuel Seal Test Specimen	316
228	Segmented Nozzle Design - Configuration 1	322
229	Segmented Nozzle Design - Configuration 2	323
230	Segmented Nozzle Design - Configuration 3	323
231	Segmented Nozzle Design - Configuration 4	324
232	Continuous Ring Nozzle Design - Configuration 5 ..	325
233	Continuous Ring Nozzle Design - Configuration 6 ..	326
234	Continuous Ring Nozzle Design - Configuration 7 ..	327
235	Continuous Ring Nozzle Design - Configuration 8 ..	328
236	Cast Turbine Inlet Nozzle - 24-Vane Design	329
237	Continuous Ring Nozzle Design - Configuration 9 ..	332

LIST OF ILLUSTRATIONS (Continued)

<u>Figure No.</u>		<u>Page</u>
238	Fluid-Cooled Turbine Inlet Nozzle Blade Profile - Angular Orientation of Film-Cooling Slots	334
239	Fluid-Cooled Turbine Inlet Nozzle Blade Profile - Location of Film-Cooling Slots	335
240	Fluid-Cooled Turbine Inlet Nozzle Vane Proposed Film-Cooling Arrangement	336
241	Nozzle Vane Temperature Versus Percent Total Airflow Film-Cooling	338
242	Velocity Distribution Along Turbine Nozzle Vane - 50-Percent	339
243	Variation of Nusselt Number With Reynolds Number	340
244	Turbine Inlet Nozzle Vane - External Heat Characteristics	341
245	Turbine Inlet Nozzle Vane - Metal Temperature Distribution (Design #1)	343
246	Vane Temperature Distribution - Nonregenerative Case	345
247	Vane Temperature Distribution - Regenerative Case	346
248	Shroud Temperature - Nonregenerative Case	347
249	Shroud Temperature - Regenerative Case	348
250	Nozzle Vane Radial Temperature Distribution - Nonregenerative Case	350
251	Nozzle Vane Radial Temperature Distribution - Regenerative Case	351
252	Vane Temperatures (From Reduced Test Data) - Nonregenerative	353
253	Vane Temperatures (From Reduced Test Data) - Regenerative	356
254	René 41 High Temperature Properties	357
255	Nonregenerative Cycle - Combustor Airflow and Port Area Distribution	360

LIST OF ILLUSTRATIONS (Continued)

<u>Figure No.</u>		<u>Page</u>
256	Regenerative Cycle - Combustor Airflow and Port Area Distribution	361
257	Turbine Inlet Nozzle Hot Cascade Rig	369
258	Turbine Inlet Nozzle Hot Cascade Rig	371
259	Turbine Inlet Nozzle Test Cascade	374
260	Detail of TD Nickel Nozzle Vane	375
261	View of Test Section Inlet	376
262	Rear View of Test Section	377
263	Close-Up of Vanes and Outer Shroud Showing Finned Internal Surface of Vanes	378
264	Profile of Finned Surface (26 x Size)	379
265	View of Inner Shroud Showing Vane and Shroud Instrumentation	380
266	View of Outer Shroud Showing Vane and Shroud Instrumentation	381
267	Vane Instrumentation	382
268	Inner Shroud Instrumentation	383
269	Outer Shroud Instrumentation	383
270	Vane Metal Temperature - Reading No. 1	386
271	Vane Metal Temperature - Reading No. 2	386
272	Vane Metal Temperature - Reading No. 4	387
273	Vane Metal Temperature - Reading No. 5	387
274	Vane Metal Temperature - Reading No. 6	388
275	Vane Metal Temperature - Reading No. 7	388
276	Vane Metal Temperature - Reading No. 8	389
277	Vane Metal Temperature - Reading No. 9	389
278	Vane Metal Temperature - Reading No. 10	390
279	Vane Metal Temperature - Reading No. 11	390
280	Vane Metal Temperature Reduced to $T_g = 2636^\circ\text{F}$ From $T_g = 2374^\circ\text{F}$ Test Data	391

LIST OF ILLUSTRATIONS (Continued)

<u>Figure No.</u>		<u>Page</u>
281	Comparison of Measured (Reduced) and Calculated Temperatures	392
282	Inner Shroud Metal Temperatures - Reading No. 8	393
283	Outer Shroud Metal Temperatures - Reading No. 8	394
284	Inner Shroud Metal Temperatures - Reading No. 9	394
285	Outer Shroud Metal Temperatures - Reading No. 9	395
286	Inner Shroud Metal Temperatures - Reading No. 10	395
287	Outer Shroud Metal Temperatures - Reading No. 10	396
288	Inner Shroud Metal Temperatures - Reading No. 11	396
289	Outer Shroud Metal Temperatures - Reading No. 11	397
290	Turbine Inlet Nozzle Cascade After Test - View of Outer Shroud	398
291	Turbine Inlet Nozzle Cascade After Test - View of Inner Shroud	399
292	Fluid-Cooled Turbine Rotor Assembly and Gas Generator	402
293	Turbine Test Rig Cross Section	405
294	Fluid-Cooled Turbine - Test Stand Performance . . .	407
295	Power Turbine Horsepower at Various Gas Generator Efficiencies	410
296	Fluid-Cooled Turbine Nozzle Coordinate Designations	411

LIST OF ILLUSTRATIONS (Continued)

<u>Figure No.</u>		<u>Page</u>
297	Fluid-Cooled Rotor - 34 Blades	412
298	Nozzle/Turbine Dimensional Variation Due to Thermal and Stress Compensation	413
299	Gearbox Coast-Down Parameter	414
300	Gearbox and Windage Losses - Horsepower Versus Turbine Shaft Speed	415
301	Exhaust Gas Temperature - Corrected	417
302	Shroud Cooling Flow and Leakage	418
303	Shroud Inlet Referred Flow Versus Pressure Ratio	419
304	Fluid-Cooled Turbine Performance Map.	424
305	Fluid-Cooled Turbine Performance - 23 Nozzle Vanes and 28 Rotor Blades	425
306	Mean Wheel Speed Versus Turbine Efficiency	427
307	Cooling System and Design Features - Fluid-Cooled Turbine	429
308	Three-Quarter View of Outer Combustor and Swirl Vane Assembly Showing Swirl Vane Louvers.	431
309	Combustion Efficiency Versus Fuel-Air Ratio - Combustor Build 2	432
310	Temperature Distribution Factor Versus Temperature Rise - Combustor Build 2	433
311	Combustor Exit Radial Temperature Profile	435
312	Combustor Exit Radial Temperature Profile	436
313	Combustor Exit Radial Temperature Profile	437
314	Rigimesh Swirl Plate	438
315	Combustion Efficiency Versus Fuel-Air Ratio	439
316	Temperature Distribution Factor Versus Temperature Rise - Combustor Build 3	439
317	Combustor Exit Radial Temperature Profile	441
318	Combustor Exit Radial Temperature Profile	442

LIST OF ILLUSTRATIONS (Continued)

<u>Figure No.</u>		<u>Page</u>
319	Combustor Exit Radial Temperature Profile	443
320	Temperature Distribution Factor Versus Temperature Rise - Combustor Build 4	444
321	Combustion Efficiency Versus Fuel-Air Ratio - Combustor Build 4	444
322	Combustor Exit Radial Temperature Profile	445
323	Combustor Exit Radial Temperature Profile	446
324	Combustor Exit Radial Temperature Profile	447
325	Pressure Drop Corrected Versus Fuel-Air Ratio - Combustor Build 4	448
326	Combustion Efficiency Versus Fuel-Air Ratio - Combustor Build 5	449
327	Temperature Distribution Factor Versus Temperature Rise - Combustor Build 5	450
328	Combustor Exit Radial Temperature Profile	450
329	Combustor Exit Radial Temperature Profile	451
330	Combustor Exit Radial Temperature Profile	452
331	Combustor Exit Radial Temperature Profile	453
332	Combustion Efficiency Versus Fuel-Air Ratio - Combustor Builds 5 and 6	454
333	Temperature Distribution Factor Versus Temperature Rise - Combustor Builds 5 and 6	454
334	Combustor Exit Radial Temperature Profile Builds 5 and 6	455
335	Combustor Exit Radial Temperature Profile	456
336	Turbine Inlet Temperature at Various Circumferential Positions	457
337	Turbine Inlet Temperature at Various Circumferential Positions	457
338	Pressure Drop Corrected Versus Fuel-Air Ratio - Combustor Builds 5 and 6	458

LIST OF ILLUSTRATIONS (Continued)

<u>Figure No.</u>		<u>Page</u>
339	Nozzle Vane Assembly Trailing Edge	459
340	Nozzle Vane Assembly Leading Edge	460
341	Combustor Assembly	461
342	Swirl Plate - Forward	462
343	Swirl Plate - Rear	463
344	Turbine Rig and Combustor Rig Comparison of Combustion Efficiency Versus Fuel-Air Ratio	464
345	Outer Combustor After Test.	465
346	Combustion Efficiency Versus Fuel-Air Ratio, Builds 1 and 2 - Turbine	466
347	Comparison of Circumferential Temperature Profile - Turbine Build	467
348	Combustor Circumferential Airflow Distribution Through Axial Inlet	468
349	Schematic of Inner Combustor and Shaft Eccentricity	469
350	Combustion Efficiency Versus Fuel-Air Ratio - Turbine Rig Build	471
351	Combustion Efficiency Based on Calculated Turbine Inlet Temperatures - Turbine Rig Build	471
352	Combustion Efficiency Versus Fuel-Air Ratio, Build 5 - Turbine Rig	473
353	Exhaust Gas Temperature Versus Circumferential Location of Probes - Turbine Rig Build 5	474
354	Redesigned Swirl Plate	475
355	Film-Cooled Swirl Plate Assembled to Outer Combustor Shell	476
356	Inner Combustor Modification	477
357	Shroud, Outer Combustor Labyrinth Seal	478
358	Combustor Assembly	479
359	Temperature Distribution Factor, Builds 5 and 6 - Turbine Rig	480

LIST OF ILLUSTRATIONS (Continued)

<u>Figure No.</u>		<u>Page</u>
360	Combustion Efficiency, Build 6 - Turbine Rig	480
361	Exhaust Gas Circumferential Temperature Profile - Build 6	481
362	Carbon Buildup on Swirl Plate After Build 6 Testing - Turbine Rig	482
363	Inner Combustor and Nozzle Assembly After Build 6 Testing - Turbine Rig	483
364	Modified Inner Combustor Shell	484
365	Combustion Efficiency Versus Fuel-Air Ratio, Build 6 - Turbine Rig	485
366	Temperature Distribution Factor Versus Combustor Temperature Rise - Turbine Rig	485
367	Local Temperature Distribution Factor, Build 7 With Preheat - Turbine Rig	487
368	Local Temperature Distribution Factor, Build 7 Without Preheat - Turbine Rig	488
369	Exhaust Gas Circumferential Temperature Profile, Build 7 - Turbine Rig	489
370	Outer Combustor Shell and Swirl Plate Assembly at Completion of Build 7 Testing - Turbine Rig	489
371	Outer Combustor Shell and Swirl Plate Assembly at Completion of Build 7 Testing - Turbine Rig	490
372	Inner Combustor and Turbine Inlet Nozzle Assembly at Completion of Build 7 Testing - Turbine Rig	491
373	Combustion Efficiency Versus Fuel-Air Ratio - Builds 7 and 8	492
374	Circumferential Temperature Gradient	493
375	Schematic of Closed-Loop Thermosyphon System . .	495
376	Fuel Flow Through Rotor	496
377	Measured Fuel Temperature Rise Versus Relative Gas Temperature	497

LIST OF ILLUSTRATIONS (Continued)

<u>Figure No.</u>		<u>Page</u>
378	Calculated Fuel Temperature Rise Due to Blade Cooling	498
379	Normalized Measured Fuel Temperature Rise	499
380	Normalized Calculated Fuel Temperature Rise Due to Blade Cooling.	499
381	Heat Rejected to Fuel	501
382	Measured Fuel Flow	502
383	Comparison of Measured Fuel Flow Requirements for Rotors I and II	502
384	Comparison of Calculated and Measured Fuel Temperature Rise	503
385	Rotor Disc Temperature Instrumentation	504
386	Measured Disc Temperatures.	504
387	Heat Flow Through the Disc	506
388	Comparison of Calculated and Measured Fuel Temperature Rise	509
389	Calculated Turbine Blade Temperature	510
390	Calculated Turbine Blade Temperature With Adjusted Fuel Flow	511
391	Air-Cooled Nozzle Vane Assembly	512
392	Trailing-Edge Slots, Air-Cooled Nozzle	513
393	Interior Cooling Fins, Air-Cooled Nozzle	514
394	Measured Temperatures Corrected for Conduction Errors	515
395	Exhaust Diffuser Cooling	517
396	Double-Walled Exhaust Diffuser Cooling Airflow Path and Metal Temperature	518
397	Thermocouple Locations for Exhaust Diffuser Wall	519
398	Exhaust Diffuser Wall Temperature for Several Coolant Flow Rates	520

LIST OF ILLUSTRATIONS (Continued)

<u>Figure No.</u>		<u>Page</u>
399	Turbine Rotor Assembly	524
400	Nickel Plating of Blade	525
401	Cross Section of Plating	525
402	Gearbox Housing - Forward	527
403	Gearbox Housing - Aft	528
404	Gearbox Pinon Gear Assembly	529
405	Test Cell Layout	531
406	Combustor Development Slinger Shaft	532
407	Turbine Rotor I Build History	534
408	Turbine Rotor II Build History	535
409	Fuel Face Seal	536
410	Fuel Wiper	537
411	Turbine Rotor Tip-Cap Failures - Nos. 25, 37, and 51	539
412	Nozzle Vane Assembly After Test 27 - Damaged Vane	540
413	Turbine Shroud and Nozzle Vane Assembly	541
414	Forward Thrust Bearing	542
415	Fluid-Cooled Turbine Blade No. 51	543
416	Fluid-Cooled Turbine Blade Nos. 25 and 37	544
417	Blade 37 Fracture	546
418	Airfoil Section Between Leading-Edge Blade 49 and Trailing Edge	547
419	Blades 44 and 76 After Testing	549
420	Blade 44 - Welding	550
421	Blades 76 and 44 Microstructural at Weld	551
422	Blade 27	552
423	Blade Seal Rupture	554

LIST OF ILLUSTRATIONS (Continued)

<u>Figure No.</u>		<u>Page</u>
424	Blade 110 - Oxide Inclusion in Wall, Magnification 500 X	555
425	Blade-to-Disc "V" Seal	556
426	Turbine Rotor II - Tip-Cap Failure	558
427	Blade 9A	559
428	Turbine Rotor II After Testing - Rear View	560
429	Turbine Rotor II After Testing - Rear View	560
430	Blade 35A - Airfoil Tearing and Distortion.	561
431	Blade 35A - Airfoil Surface Necking	562
432	Blade 8 - Break Through Airfoil	566
433	Turbine Rotor Assembly - After Run No. 62	567
434	Exhaust Duct Oil Scavenging Port	568
435	Blade 86 - Fracture	569
436	Blade 86 - Cross Section of Fluid Channel	570
437	Pinned Blade Attachment Test Specimen	571
438	Load Versus Deflection Udimet 700 Pins (4)	573
439	Load Versus Deflection Inconel 718 Pins	574
440	Load Versus Deflection Rene 41 Pins	575
441	Pin Deformation	576
442	Blade/Disc Pin Attachment	577
443	Blade/Disc Pin Attachment Yield Comparison	578
444	Stress-Temperature Relationship of Udimet 700	581
445	Turbine Blade Fabrication - Tip-Cap Grooved by EDM, Using Blade as a Tool	586
446	Experimental Manufacturing of Joining Methods for Tip-Caps	587
447	Sample EDM Drilling of Blade-to-Disc Materials	589
448	Blade Root Machining of Pinholes	590
449	Disc - Fuel Passage	591

LIST OF ILLUSTRATIONS (Continued)

<u>Figure No.</u>		<u>Page</u>
450	Turbine Disc and Blade Pin Attachment - Rough Machining	592
451	Turbine Disc and Blade Pin Attachment - Finish Machining	592
452	Rotor Pinhole Blade Attachment Sample, Fluid-Cooled Turbine	594
453	Pinhole Broaching Setup - Fluid-Cooled Turbine . .	595
454	Fluid-Cooled Blade, Welded Assembly	596
455	Finish Machined Blade	598
456	Wax Pattern and Core for Blade	598
457	Photograph of Blade Microscopic Showing Area of Oxide Inclusions and Shrinkage	599
458	Blade Showing Thin Wall at Trailing Edge Caused by Core Mismatch	600
459	Surface Condition Found on Castings	601
460	Blade - Shuttle Fixture for Locating Prior to Machining	602
461	Blade - Grinding Wheels and Dressing Templates . .	602
462	Blade - Pinhole Grinding Templates	604
463	Turbine Blade - Machining Construction, Airfoil Template	604
464	Turbine Blade Platform	605
465	Turbine Blade Platform	606
466	Combustor Development Slinger Shaft	608
467	Turbine Rotor I Shaft Assembly	608
468	Pins - Blade-to-Disc Attachment	609
469	Microstructure - Attachment Pin Surfaces	610
470	Air-Cooled Turbine Inlet Nozzle	611
471	Air-Cooled Turbine Shroud	612

LIST OF ILLUSTRATIONS (Continued)

<u>Figure No.</u>		<u>Page</u>
472	Nozzle - Shroud Assembly	613
473	Outer Combustor Assembly	614
474	Exhaust Diffuser Assembly - Aft	615
475	Exhaust Diffuser Assembly - Forward	616

APPENDIX I

476	Turbine Blade - Cast	627
477	Blade Machining Operations 1 Through 5	631
478	Blade Machining Operation 6	633
479	Blade Machining Operation 7	634
480	Blade Machining Operation 8 - Plug	635
481	Tip-Cap Machining Operation 9	636
482	Tip-Cap Machining Operation 10	637
483	Tip-Cap Machining Operation 11	638
484	Tip-Cap Operations 13, 15, and 16	639
485	Plug Weld - Operation 14	640
486	Heat Exchanger Machining Operation 19	641
487	Heat Exchanger Machining Operation 20	642
488	Blade Platform Machining - Operation 21	645
489	Blade Platform Machining - Operation 22	646
490	Blade Platform Machining - Operation 23	647
491	Blade Platform Machining - Operations 24 and 25 . .	648
492	Final Machine Tip-Cap - Operations 26, 27, and 28 .	649
493	Sealing Heat Exchanger - Operations 29, 30, 31, 32, and 33	650

LIST OF ILLUSTRATIONS (Continued)

<u>Figure No.</u>		<u>Page</u>
APPENDIX II		
494	Schematic of Closed-Loop Thermosyphon System . .	652
APPENDIX III		
495	Fluid-Cooled Turbine Blade Flow Areas	667
496	Heat Exchanger Fuel Wetted Area	670
497	Cooling Volume of Heat Exchanger Manifold	675
APPENDIX VIII		
498	Instrumentation Schematic Test Rig Fluid-Cooled Turbine Thermocouple Locations	701
499	Instrumentation Schematic Test Rig Fluid-Cooled Turbine Thermocouple Locations	702
500	Test Rig Instrumentation	703
501	Test Rig Assembly	704
502	Rig Lubricating Assembly	705
503	Lube Oil System	706
504	Fuel System	707

LIST OF TABLES

<u>Table No.</u>		<u>Page</u>
I	TURBINE DESIGN POINT SUMMARY	68
II	DESIGN POINT EFFICIENCY INPUT.....	74
III	INTERNAL LOSS BREAKDOWN OF GAS GENERATOR TURBINE	76
IV	SUMMARY OF COLD FLOW TURBINE AERODYNAMICS	80
V	JOINT DETAILS OF TIP-CAP WELDS	144
VI	JOINT DETAILS OF MODIFIED TIP-CAP WELDS ..	144
VII	PRESSURE TEST TREATMENTS	145
VIII	LEAK TEST OF BEAM WELDED AIRFOIL CAPS ..	151
IX	PLUGGED HEAT EXCHANGER WEIGHT MEASUREMENTS	157
X	TYPICAL SETTINGS FOR EDM	163
XI	STRESS-RUPTURE TESTS AT 1400°F OF U-700 ELECTRON BEAM WELDS.....	205
XII	TENSILE STRENGTHS OF CAPPED BLADES	209
XIII	FATIGUE TESTS OF CAPPED BLADES	211
XIV	HARDWARE AND TESTS CONDUCTED	214
XV	TENSILE RESULTS	215
XVI	THERMAL FATIGUE DATA INCO 713C AND HS 31	219

LIST OF TABLES (Continued)

<u>Table No.</u>		<u>Page</u>
XVII	THERMAL SHOCK RESULTS	224
XVIII	SUMMARY OF COOLED TURBINE DESIGN POINT PARAMETERS	226
XIX	FLUID-COOLED TURBINE DESIGN POINT PARAMETERS	233
XX	FLUID-COOLED TURBINE SIMULATED ALTITUDE PARAMETERS	235
XXI	AIRFOIL GAS LOADS AND MOMENTS	286
XXII	BLADE ROOT PINNED ATTACHMENT	288
XXIII	TANG PINNED ATTACHMENT	289
XXIV	SEAL TEST DATA	318
XXV	TURBINE INLET NOZZLE VANE STRESS ANALYSIS - NONREGENERATIVE CASE	354
XXVI	TURBINE INLET NOZZLE VANE STRESS ANALYSIS - REGENERATIVE CASE	355
XXVII	COMBUSTOR ANALYSIS SUMMARY	367
XXVIII	CASCADE RIG - OFF-DESIGN CONDITIONS	384
XXIX	COMPARISON OF PERFORMANCE TESTS TO OBJECTIVE	409
XXX	FLUID-COOLED TURBINE PERFORMANCE	422
XXXI	COMBUSTOR PERFORMANCE	428

LIST OF TABLES (Continued)

<u>Table No.</u>		<u>Page</u>
XXXII	COMPONENT RUNNING TIME	521
XXXIII	DATA ACQUISITION RUNNING TIME	521
XXXIV	HARDWARE STATUS AFTER TESTING	522
XXXV	COMPONENT MATERIALS AND SPECIFICATIONS .	588
XXXVI	COMPONENT MATERIALS AND SPECIFICATIONS .	596
APPENDIX I		
XXXVII	X-RAY QUALITY STANDARDS	629

ABBREVIATIONS

A/F	airfoil
AVG	average
BAR	barometric
B/P	blueprint
C/A	chrome alumel
$^{\circ}\text{C}$	degrees, centigrade
CAE	Continental Aviation and Engineering
cc	cubic centimeter
C/L	center-line
Circum.	circumference
Comb.	combustor
Comp	compressor
Const	constant
DYN	dynamometer
E/B	electron beam
ECM	electro-chemical machining
EDM	electro-discharge machining
EGT	exhaust gas temperature
EMF	electromotive force
F/A	fuel air ratio
f	function
HE	heat exchanger

ABBREVIATIONS (Continued)

HS	Haynes Stellite
I. D.	inside diameter
I/C	iron constantan
INCO	Inconel
Insp	inspection
Instr	instrumentation
KV	kilovolts
LER	leading edge radius
LKG	leakage
MA	miliamps
MAX	maximum
MIN	minutes
NDT	non-destructive testing
No. (s)	number(s)
O. D.	outside diameter
Pcs	pieces
P/N	part number
PTS	points
PR	pressure ratio
Rel	relative
RMS	root mean square
rpm	revolutions per minute

ABBREVIATIONS (Continued)

rpm	revolutions per second
TDF	temperature distribution factor
Temp	temperature
TER	trailing edge radius
TIG	tungsten inert gas
SFC	specific fuel consumption
sec	seconds
Surf.	surface
SHP	shaft horsepower
tot.	total
U	wheel speed
Vel	velocity
W/O	without
Wg	weight, gas
X-Ray	radiographic

SYMBOLS

A	area square inches
BAR	barometric
Btu	British thermal unit
Co	isentropic velocity corresponding to total head, feet per second
CPS	cycles per second
DIA.	diameter, inches
Deg.	degree
γ	ratio of specific heats
ft	feet
$^{\circ}\text{F}$	degrees Fahrenheit
fps	feet per second
g	gravity, ft/sec^2
ΔH	enthalpy change, work Btu/lb
hr	time, hour
H_2O	water
HP	horsepower
Hg	pressure, inches of mercury
in. (s)	inch(s)
J	heat equivalent, ft-lb/Btu
δ	pressure ratio
lb(s)	pound(s)

SYMBOLS (Continued)

N_2	nitrogen
N	revolution per minute, rpm
n	number of stages
η_c	combustion efficiency, percent
η_t	turbine efficiency, percent
θ	temperature ratio
P_t	total pressure, psia
P_s	stagnation pressure, psia
psi	pressure, pounds per square inch - gage
psia	pressure, pounds per square inch - absolute
psig	pressure, pounds per square inch - gage
ΔP	pressure change
P_{up}	pressure upstream, psia
P_{BAR}	pressure barometric, psia
PPH	flow, pounds per hour
q	flow, Btu/lb
$^{\circ}R$	temperature, degrees Rankine
R	radius, inches
sq	square
sec	time, seconds
W	weight, lbs
ΔT_c	combustion temperature rise, $^{\circ}F$

SYMBOLS (Continued)

T_{up}	temperature upstream, $^{\circ}F$
T_t	temperature total
U	tip speed, fps
U-700	Udimet 700
UP	upstream
V_{θ}	tangential velocity, fps
V_x	axial velocity, fps
V_v	radial velocity, fps

SUBSCRIPTS

a	air
b	blade
c	combustor
f	function
cr	critical
h	hub
t	turbine
s	span
m	mean

FLUID-COOLED TURBINE DESIGN CONCEPTS, HARDWARE PROCUREMENT, AND DESIGN OPTIMIZATION

INTRODUCTION

With the program objectives in mind, a number of design concepts were studied, hardware procured, and testing conducted to optimize the designs.

Test cell layouts were made and the hardware required to support the testing was outlined for procurement. Cold flow tests were conducted on the turbine blades. A hot cascade rig test was performed on the nozzle vanes. Manufacturing technology of the turbine blade and the blade/disc pin attachment was established.

TEST RIG

The test cell layout for the fluid-cooled turbine rig installation is shown in Figure 1. Shop air is provided to the rig and permits operation of the turbine at design speed above 10,000 feet, and down to sea level at below 80 percent speed. The air is heated in a combustion preheater to compressor or regenerator outlet temperature and is delivered to the test combustor/turbine combination (Figure 2) through an annular plenum. Turbine exhaust gas passes through an air-cooled exhaust diffuser to a duct which delivers it to the test cell exhaust system. The 50,000-rpm test turbine is coupled through a reduction gearbox to a Taylor water brake dynamometer for load and torque measurement.

Instrumentation is provided for turbine performance measurement, for evaluation of the turbine rotor and nozzle cooling system operation, and for monitoring temperatures important to the structural design of the turbine and rig. Performance is measured by fuel and airflow meters, a Taylor water brake dynamometer, traversing turbine inlet temperature thermocouples, turbine outlet temperature thermocouple rakes, turbine inlet and outlet total, and static pressure probes. Thermocouples provide metal temperatures, and a slip ring permits temperature measurements on the rotor.

AERODYNAMIC DESIGN AND COLD FLOW TEST

This covers the aerodynamic design of the turbine and cold tests to establish turbine performance.

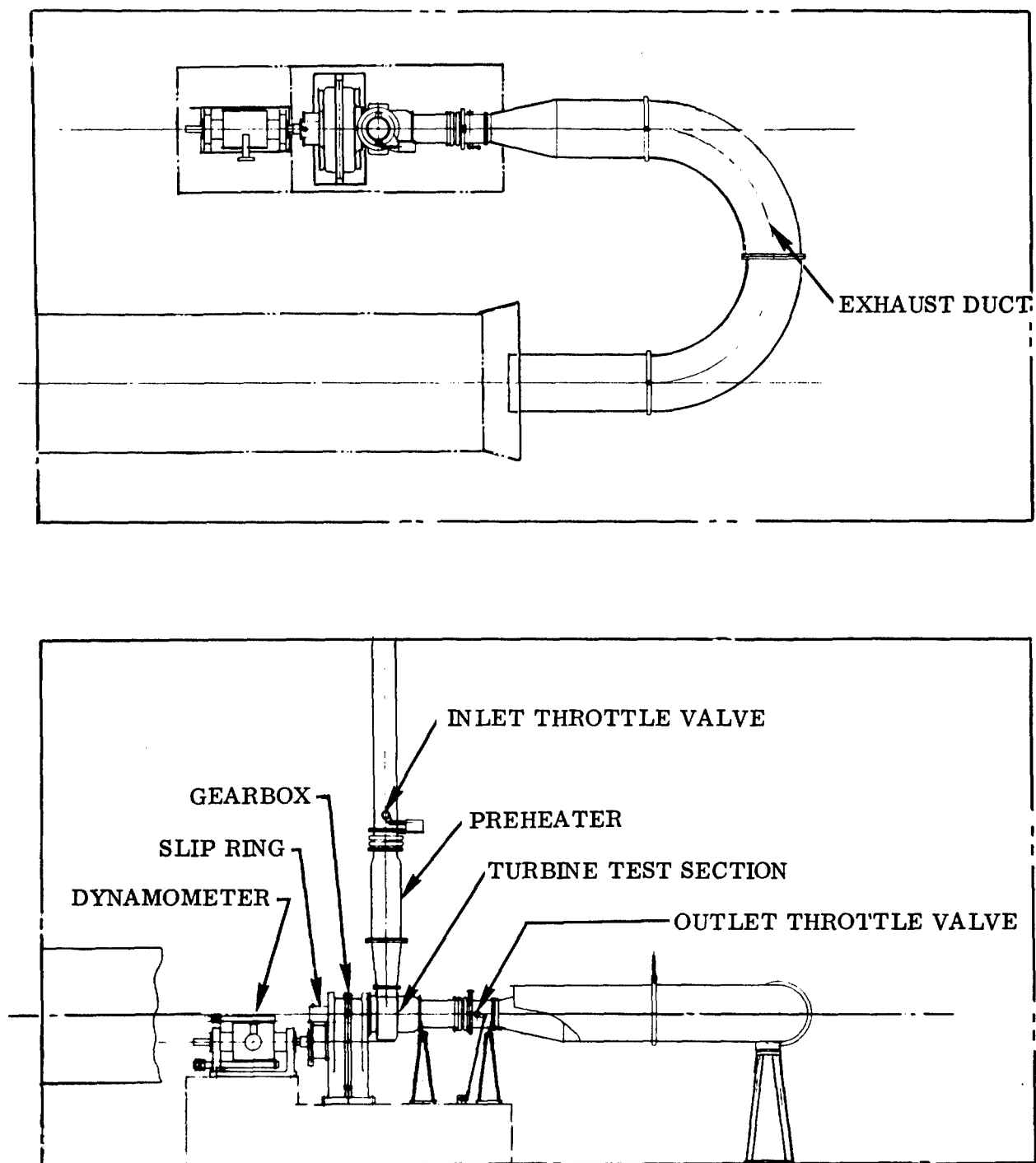


Figure 1. Test Cell Layout.

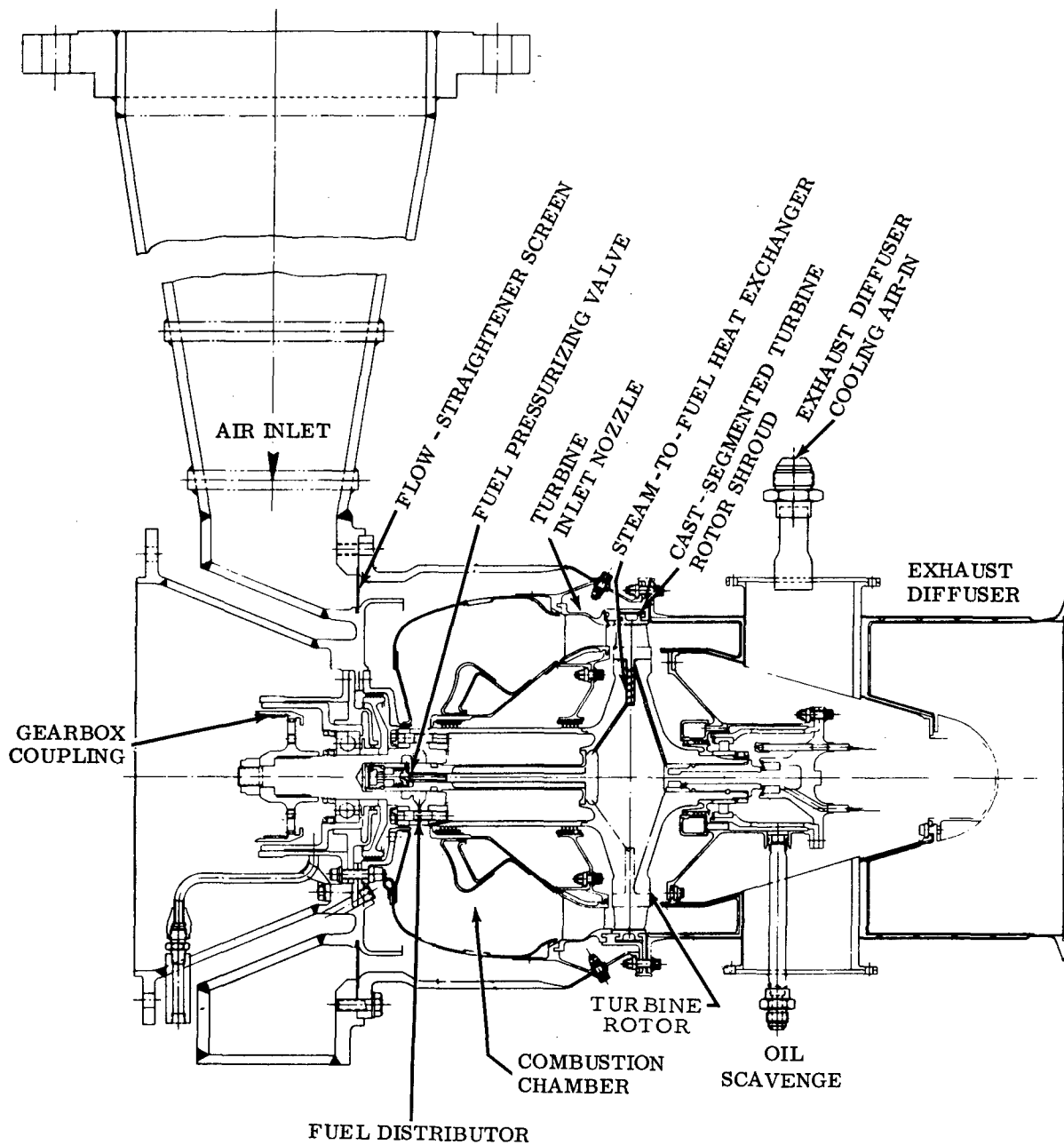


Figure 2. Turbine Test Rig Cross Section.

The turbine aerodynamic design is a trade-off between heat transfer and aerodynamic and stress requirements. The nozzle has a thick, long chord blade to provide passages for the inner combustor air; this selection entails high secondary losses. The rotor blade is also thick and has a relatively long chord to accommodate the cooling holes. The selected nominal design has 34 rotor blades and 23 nozzle vanes with a design point efficiency objective of 86.5 percent. Six design point efficiency analyses representing methods of Stewart (basic plus two variations), Ainley, and Continental were used. The analysis gave efficiencies of 86.1 (90, 87.5), 86.5, and 79, respectively, and tended to confirm the original proposal estimates.

Hardware was designed and procured, and cold tests were run to establish the effect of rotor solidity using 22, 28, 34, and 40 blades, the effect of nozzle solidity using 17 and 23 vanes, and the effect of rotor and stator trailing edge thickness for incorporation into heat transfer and structural designs. The design selection of 34 rotor blades with 23 nozzle vanes proved to be the optimum, with a peak efficiency island at 82 percent and a design point value of 81 percent. The agreement of measured data with the Continental prediction, in contrast with the other predictions, is attributed to the secondary losses associated with the very short blade heights; these losses are considered only in the Continental method.

Analysis of the effect of decreased efficiency on the target cycle shows that the objective of 213 BHP/lb of air/sec can be met by running at a turbine inlet temperature 50°F higher than design, that is, at 2350°F, as shown in Figure 3.

The use of 31 blades, selected prior to completion of cold flow tests for stress and cooling considerations, costs 2.8 percent in measured efficiency. An increase in the number of blades will be considered for the final Phase II test turbine.

BLADE MANUFACTURING TECHNOLOGY

Internally cooled blades of the small size required were manufactured and tested to prove manufacturing feasibility.

It was necessary to determine whether turbine rotor blades of this size could be made and whether coolant could be sealed in them. Three processes - precision casting, electron beam welding, and diffusion bonding - were tried in rectangular test blocks. Precision casting with subsequent welding of tip caps and root plugs was selected, because the blade halves were not successfully joined in usable condition by electron beam welding or diffusion bonding.

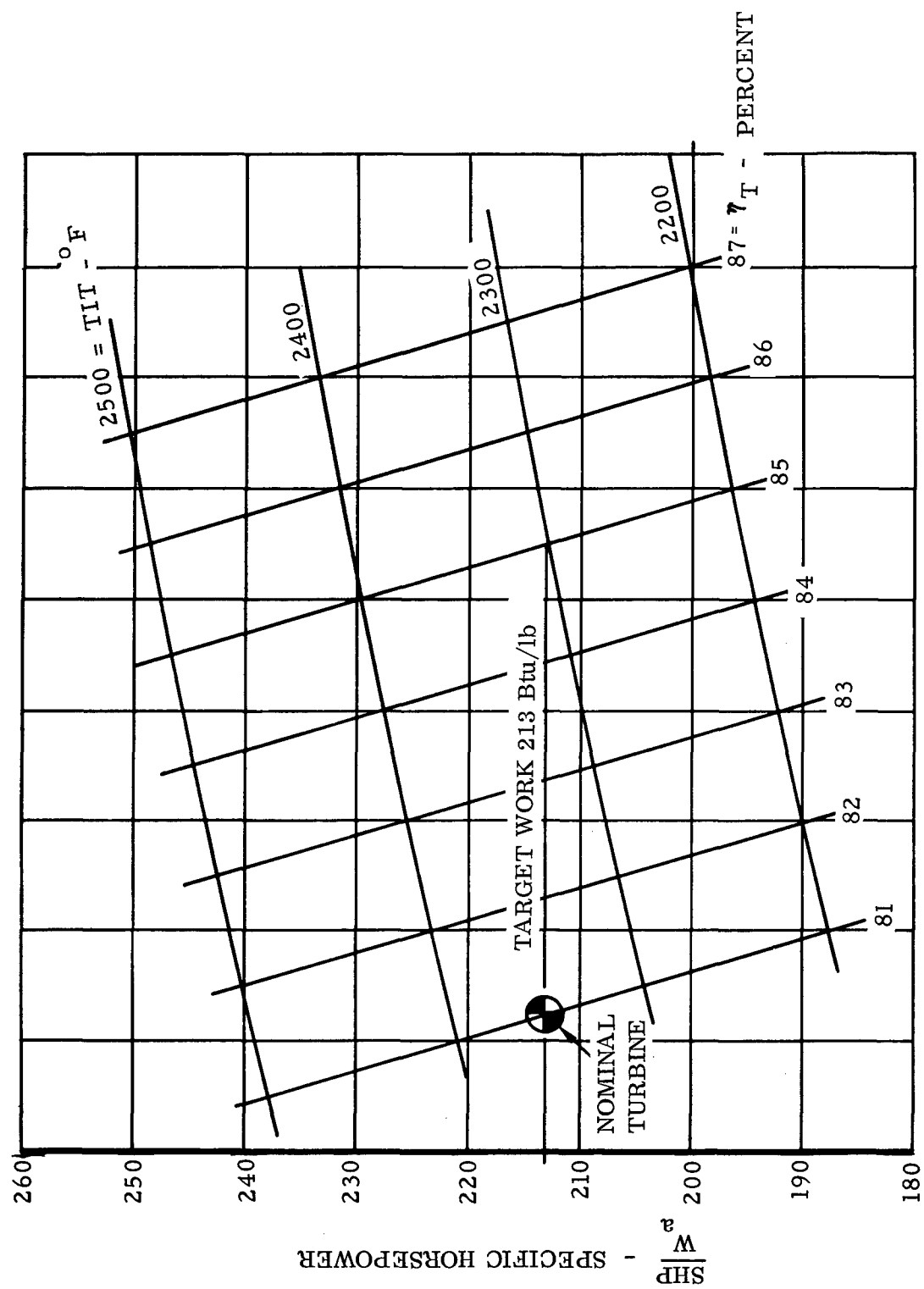


Figure 3. Effect of Turbine Inlet Temperature and Turbine Efficiency on Specific Horsepower.

Casting with welded tip and root coolant closure was used successfully to make actual blades of the design required for a pinned attachment configuration. A precision cast blade with finned heat exchanger and water sealed in is shown in Figure 4.

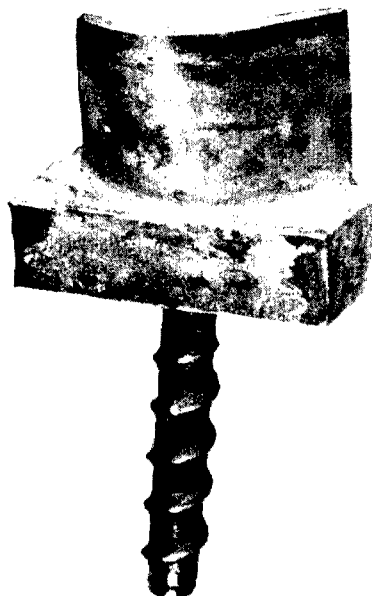


Figure 4. Fluid-Cooled Blade Containing Water-Welded Cap and Plug.

Blades were individually X-rayed, Zygloed, and submitted to micro and macro examination. Tensile tests on capped turbine blades were conducted at both room and elevated temperatures. The tests were successful, and results obtained confirmed that this blade will adequately meet design conditions.

Stress rupture tests at high temperature were run on simulated blade-to-cap joints and confirmed that this blade will successfully fulfill the design requirements.

Pressure tests were successfully conducted on capped blades at room temperature to confirm that the blades are leak-proof.

A 500-cycle thermal shock test to 1700°F was completed. The three blades tested appeared to be similar before and after testing. Two of the three blades had water seals welded in prior to testing. The unsealed blade passed a 1500-psi leak test after the thermal shock test, but the two sealed blades leaked at the tip caps after thermal shock. Additional blades with tip caps welded by an improved method will be thermal shock tested.

Vibration tests have indicated that vibratory fatigue is not a problem in this design.

BLADE/DISC DESIGN STUDIES

The activity included the rotor cooling system design, the disc-to-blade and attachment temperature distribution analysis, the rotor structural design, and tests of a mechanical fuel seal and pinned attachment.

Seven rotor blade fluid cooling systems were initially considered, and two were selected for detailed analysis; both use fuel as the heat sink. A secondary coolant system isolates the fuel from the small passages and from the high metal temperatures encountered in the blades. One configuration has an individual, sealed steam secondary coolant circuit in each blade, with a coolant-to-fuel heat exchanger extending radially into the disc; the second has a common steam circuit for all blades, with a steam-to-fuel heat exchanger in the shaft.

Three structural designs were considered:

1. A forged disc with individually cooled cast blades and coolant-to-fuel heat exchangers in the disc. A pinned attachment allows radial insertion of the heat exchangers and mechanical fuel seals between each blade and the disc.
2. A cast-cored wheel, with blades having a common steam cooling system, and a steam-to-fuel heat exchanger in the shaft.
3. An electron-beam-welded blade attachment applicable to either the disc or the shaft heat exchanger secondary coolant system.

Pinned Attachment

The pinned attachment and cooling system are shown in Figures 5 and 6. Blade, disc, and attachment temperatures were computed for use in the structural design. Udimet 700 was selected because of its high strength and availability in both cast and wrought form. The disc has a burst margin of 1.396 at 50,000 rpm and a maximum web radial stress of 82,300 psi, which is below the allowable 87,500 psi, and, thus, is an acceptable design. The combined stress, including inertia, internal pressure, and thermal effects, has been examined at points throughout the airfoil. The present design, as based on analytically obtained temperatures, is predicted to have a life of 300 hours.

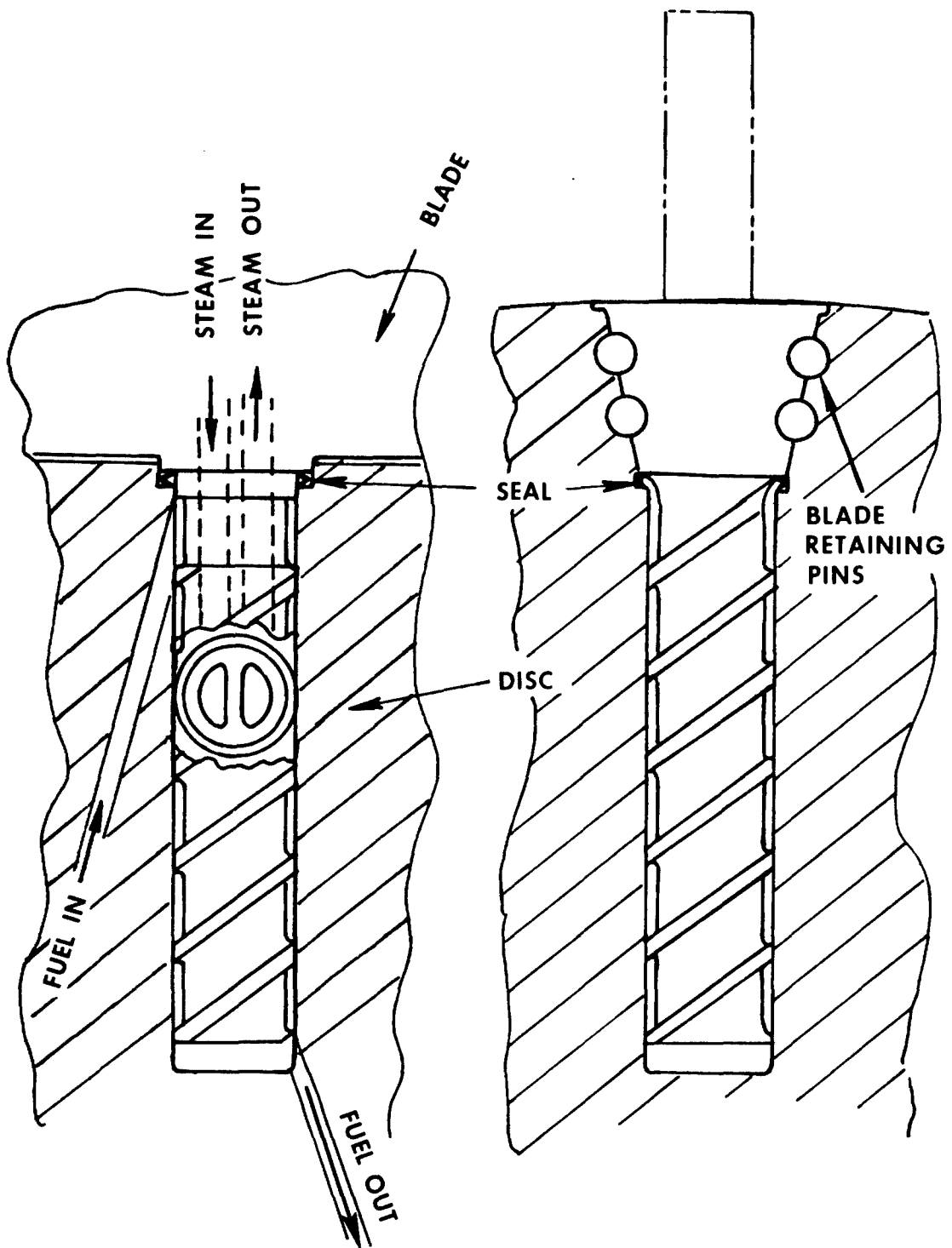


Figure 5. Blade-to-Disc Pinned Attachment.

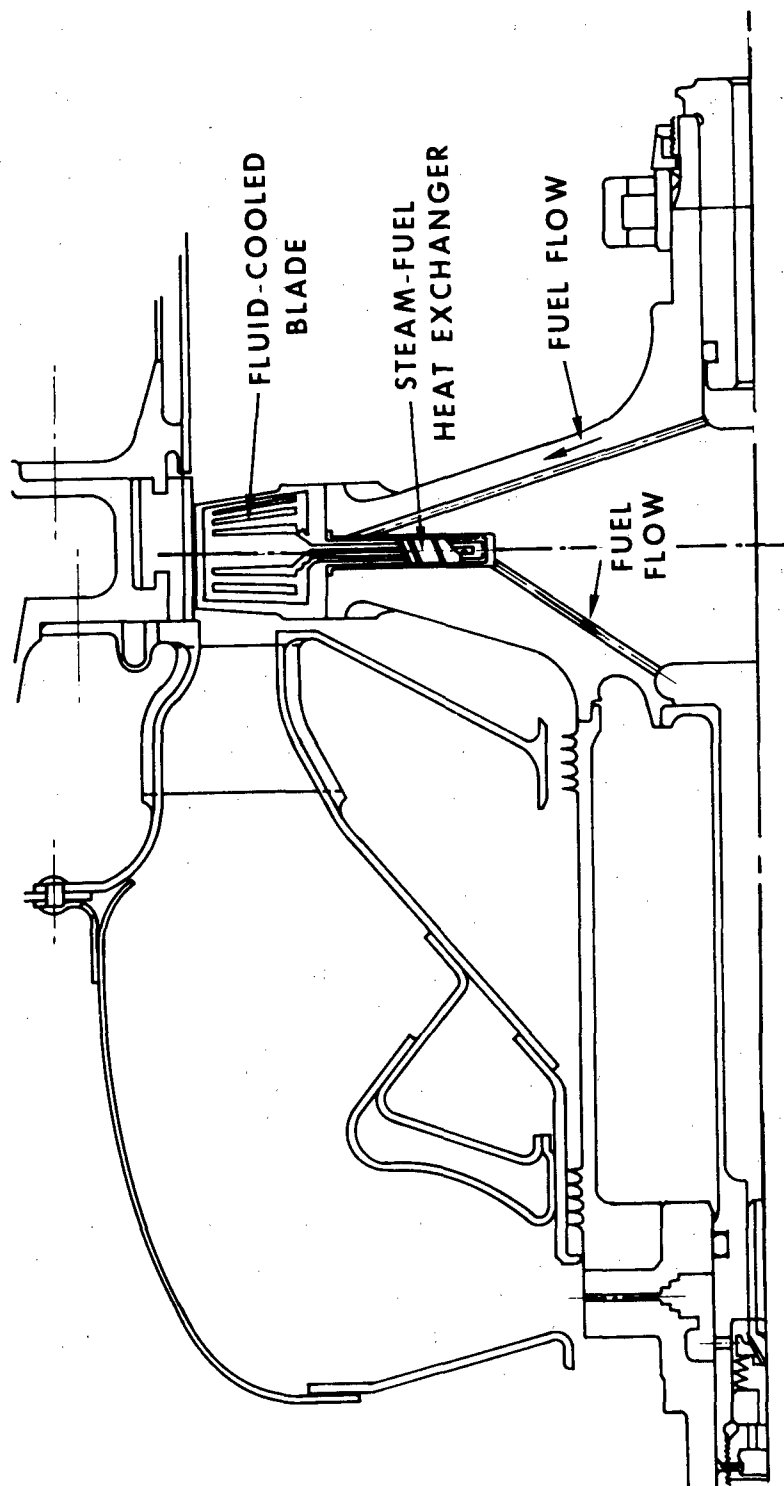


Figure 6. Cooling System for Fluid-Cooled Turbine Blade.

The pinned attachment was designed to balance blade root and disc tang stresses and pin loading. The highest computed load is a 59,000-psi shear stress in the outer pins; this stress is acceptable. The attachment is cool enough that it will not be submitted to creep rupture.

To establish that a mechanical fuel seal is feasible in this location, and to confirm the adequacy of the pinned attachment, a single-attachment test rig was constructed and subjected to simulated fuel pressure and inertia loads. The first seals tested did not have enough elastic recovery to maintain a seal with the attachment deflection under load. Subsequently, a double "V" seal sealed successfully under the design pressure and simulated inertia load at the expected temperature of 1100°F adjacent to the seal.

Cast-Cored Wheel

The cast-cored wheel with shaft heat exchanger is shown in Figure 7. The temperature distribution has been computed, and the stress analysis has been completed. The disc burst margin is 1.36 and the maximum web radial stress is 65,600 psi; these are acceptable. The cast wheel has a problem of ductility at the hub. If selected at some later date, ductility test bars would be taken in this region, and each wheel would be subjected to a cold spin test before use. This approach was not selected primarily because there is no assurance that an acceptable casting could be made. Parallel Continental contract effort is expected to supply some of this assurance.

Electron Beam Welding

Electron beam welding techniques have been established for individual blade blocks simulating the attachment. For the heat exchanger in disc configuration, the temperature gradient causes an unacceptable rim crushing load. For the heat exchanger in the shaft, welding might be considered as a blade attachment technique or as a low-ductility cast hub replacement.

Electron beam welding was not selected because consistent reproducible welding of over 30 blades into a disc in these materials is not considered to be feasible at present, and because experienced shrinkage in 30 to 60 welds around the periphery of a disc is considered to be a problem not amenable to ready solution.

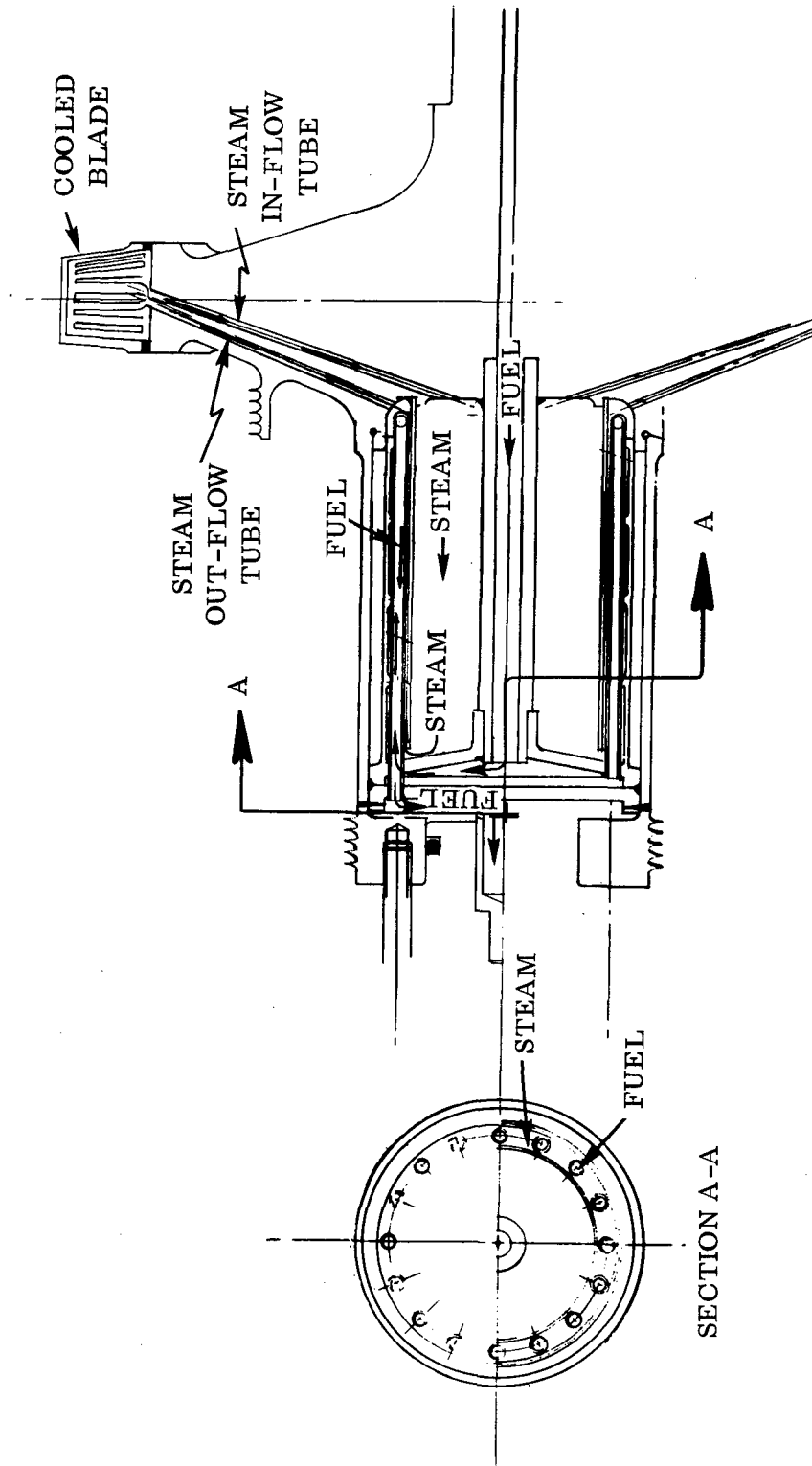


Figure 7. Cast-Cored Wheel With Heat Exchanger in Engine Shaft.

Selection of Rotor Cooling System Design

The pinned attachment with mechanical fuel seal using individual coolant-to-fuel heat exchangers in the disc for each blade has been selected for the following reasons:

1. Structural design analysis shows that it is acceptable. (See Structural Design Section.)
2. Tests of the blade attachment method show that it will withstand design loads at temperature.
3. An acceptable mechanical fuel seal has been developed in testing.
4. This configuration allows replacement of individual blades.
5. The complete fuel system is accessible for examination and mechanical cleaning, if necessary, in the event of inadvertent fuel overheating.

NOZZLE/COMBUSTOR DESIGN STUDIES

The turbine inlet nozzle serves to turn and accelerate the hot gas entering the turbine, to support the inner combustor and shaft seals, and to provide a duct for the primary combustor air. While ducting the primary combustor air restricts the nozzle aerodynamic shape, it provides a simple means of cooling the nozzle vanes.

The test combustor uses the basic outer and inner shell shape of the Continental T65-T-1 turboshaft engine with enlarged air holes and with additional cooling of the aft end for the higher temperature operation. This selection permits utilization of existing tooling to reduce cost and to expedite fabrication.

Several turbine inlet nozzle cooling schemes were considered. Both film cooling and convection cooling were investigated. Results showed that film cooling would require an excessive amount of cooling air and that a convection cooling configuration would be adequate. Convection cooling in this design concept is advantageous. The cooling air required is not lost to the engine cycle, as would be the case with film cooling. In convection cooling the air passes through the hollow nozzle vanes into the combustion chamber.

A number of turbine inlet nozzle mechanical designs were considered, including segmented and continuous-ring configurations using cast or wrought construction. Selection was narrowed to the simplest two designs with development flexibility: a cast-segmented configuration and a welded sheet metal configuration, Figure 8; both are used in conjunction with a cast-segmented turbine rotor shroud.

The nozzle mechanical and aerodynamic stresses are quite low, while the thermal stresses are the largest contributor to the total stress.

A convection-cooled design with fins on the inside of the vanes and trailing edge cooling slots was selected for testing in the cascade rig. This test confirmed the effectiveness of the fins and cooling slots and showed acceptable low shroud temperatures. While measured temperature levels were of the same order as the predicted values, the measured temperature levels were more uniform.

The experimental temperatures have been used to refine the nozzle and shroud temperature analysis and to calculate thermal stresses.

The measured temperatures were adjusted to the regenerative case, and the results showed that some additional cooling will be required for this condition.

A fabricated René 41 design with vane internal cooling fins and trailing-edge cooling slots using welded construction has been selected for the following reasons:

1. The design is adequate for the nonregenerative case.
2. A sheet metal design is more "flexible" if aerodynamic adjustment is required. Retooling for modification is less expensive.
3. Tooling procured for the cascade can be used for the full ring rig design.
4. Supplementary cooling can be added for regenerative operation.

NOZZLE VANE CASCADE DESIGN, FABRICATION AND TEST

A turbine inlet nozzle cascade was designed, built, and tested on an existing hot cascade rig to establish manufacturing techniques and to prove the adequacy of the nozzle cooling arrangement.

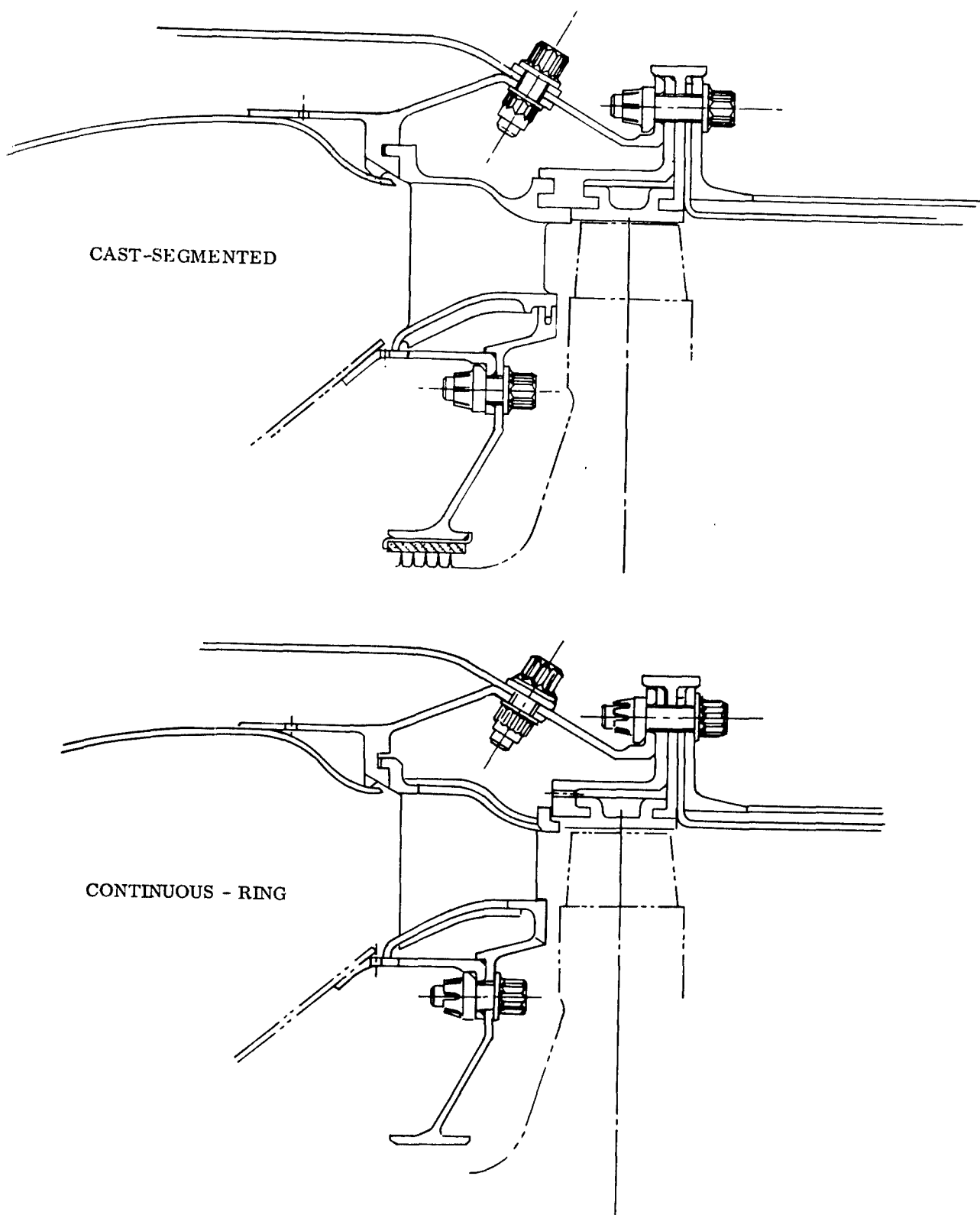


Figure 8. Cast-Segmented and Continuous-Ring Turbine Inlet Nozzle.

The internal finned vane with trailing-edge cooling slots was selected and built into a cascade test specimen. The specimen was instrumented to measure metal temperatures and flow conditions and was tested at nonregenerative conditions for 17.5 hours; 3.5 were at over 2000°F turbine inlet gas temperature.

The highest vane temperature measured was 1470°F at a mean turbine inlet temperature of 2403°F. Results confirm the general level of vane temperatures computed, with measured vane temperature distribution being more uniform than predicted. Shroud temperatures were found to be lower than predicted.

The measured vane and shroud temperatures validate the adequacy of the convective cooling system. Measured temperatures were used in the nozzle structural analysis.

FLUID-COOLED TURBINE TEST RIG

This section covers the test rig with its components, the rig installation, and the rig instrumentation.

COOLED TURBINE RIG

The fluid-cooled turbine is to be demonstrated and its performance is to be evaluated by testing or tests in a turbine test rig (reference Figure 2). This figure shows the test turbine rotor, cooling system, combustor, and turbine inlet nozzle described in other sections of this report. The rig air inlet plenum, the shaft and bearings, the fuel pressurizing valve, and the exhaust diffuser are discussed below.

Metal temperatures for the rig components have been predicted for regenerative and nonregenerative running, as shown in Figures 9 and 10. Material selections for rig components not discussed in later sections of this report are shown in Figure 11. These temperatures, along with manufacturing tolerances, established the stacking limit of the test rig.

Shaft

Two shafts are used in this rig. The turbine shaft carries the rotor for normal turbine testing, and an alternative fuel distributor shaft is required to drive the fuel distributor during combustor and inlet nozzle development. This second shaft includes a spacer for the turbine wheel.

The principal source of mechanical vibration in any high-speed rotating system is imbalance in the rotor. This imbalance may excite critical speeds of the rotor itself and/or induce resonance in any combination of structural elements that may be tuned to the running frequency of the rotor. The fluid-cooled turbine has been designed to minimize the effects of rotor imbalance and critical speeds through the proper combination of rotor and supporting structure compliances.

Rotor Shaft

The rotor suspension system of the turbine is based on the concept of a relatively rigid rotor shaft assembly mounted on flexible, hydrodynamically damped bearing supports. Critical speeds are controlled by regulating the spring rates and damping constants of these bearing supports. The flexible mounting also serves to isolate rotor imbalance from the bearings and outer structure.

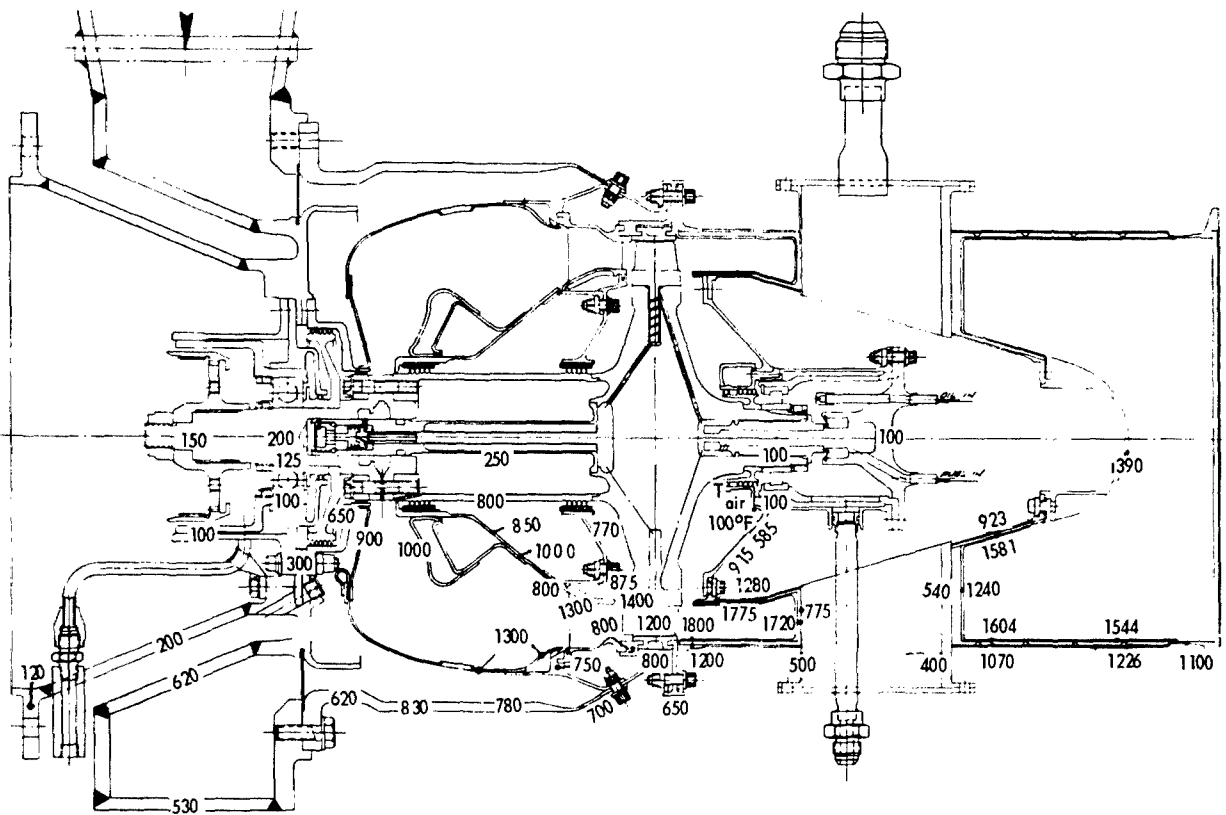


Figure 10. Fluid-Cooled Turbine Rig Metal Temperatures - Nonregenerative Running.

Design values of bearing support flexibility are determined from a series of curves covering the complete spectrum of possible critical speeds over the turbine operating range, Figure 12. The curves are developed through the use of a digital computer programmed to determine the flexural resonant frequencies of a variable cross-sectional shaft rotating on elastic supports. Gyroscopic stiffening effects of large disc inertias are included in the calculations. Three modes of vibration are illustrated in Figure 13.

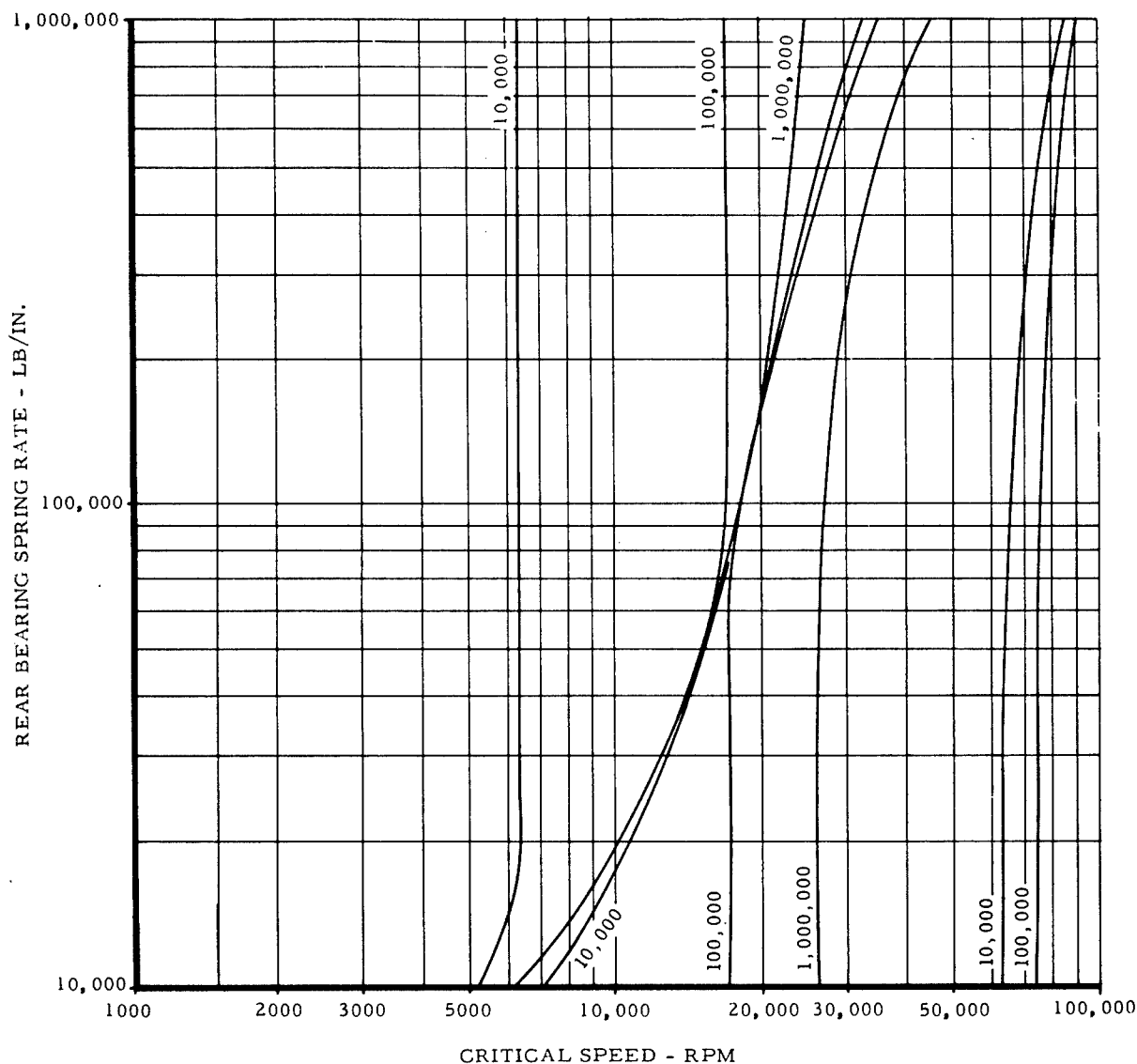


Figure 12. Liquid-Cooled Turbine Critical Speed Versus Spring Rate of Rear (Turbine) Bearing for Various Values of Front Bearing Support Spring Rate.

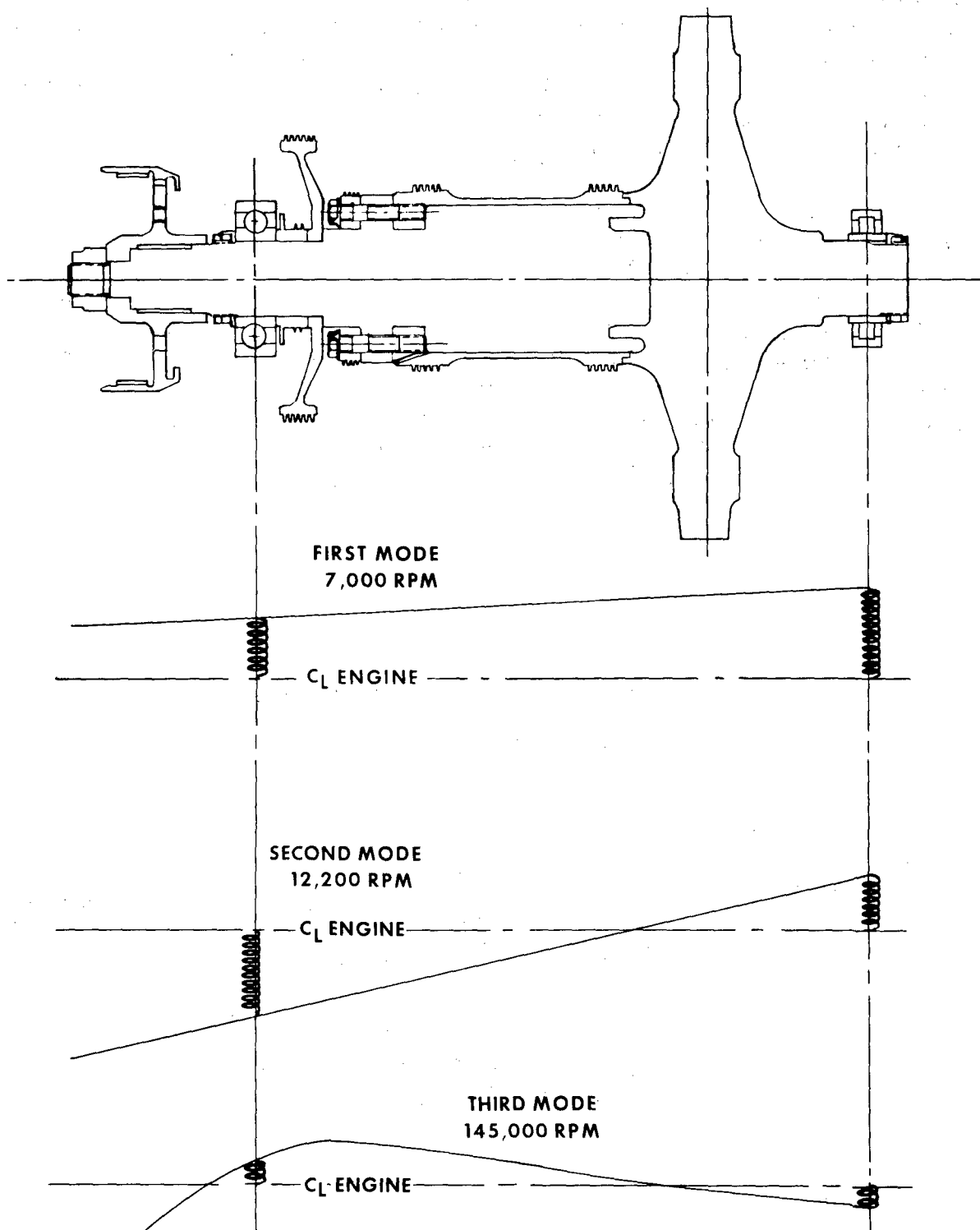


Figure 13. Characteristic Shaft Motion at First, Second, and Third Critical Speeds.

Spring rates are selected to place the first two critical speeds below the normal operating range. These modes will occur at 7,000 and 12,200 rpm for front and rear bearing spring rates of 15,000 pounds per inch. Shaft deflection in these two modes is almost completely described by the bearing displacements. The third mode, which involves considerable shaft bending as well as bearing displacement, occurs over 175 percent above maximum turbine speed.

Required bearing support compliance is provided by a flexible retainer consisting of a cylindrical member containing a number of longitudinal slots. The slot dimensions determine the radial spring rate of the bearing cage, while maximum deflection is controlled by an oil-fed snubber surface. The deflection snubber limits the maximum stringer bending stresses at resonance to 45,000 psi. The effect of main structural compliance on the overall system is negligible compared to the relatively low spring rate of the cage, and critical speeds can be accurately established. Figure 14 illustrates the application of this feature in one of Continental's line of turboshaft gas turbine engines.

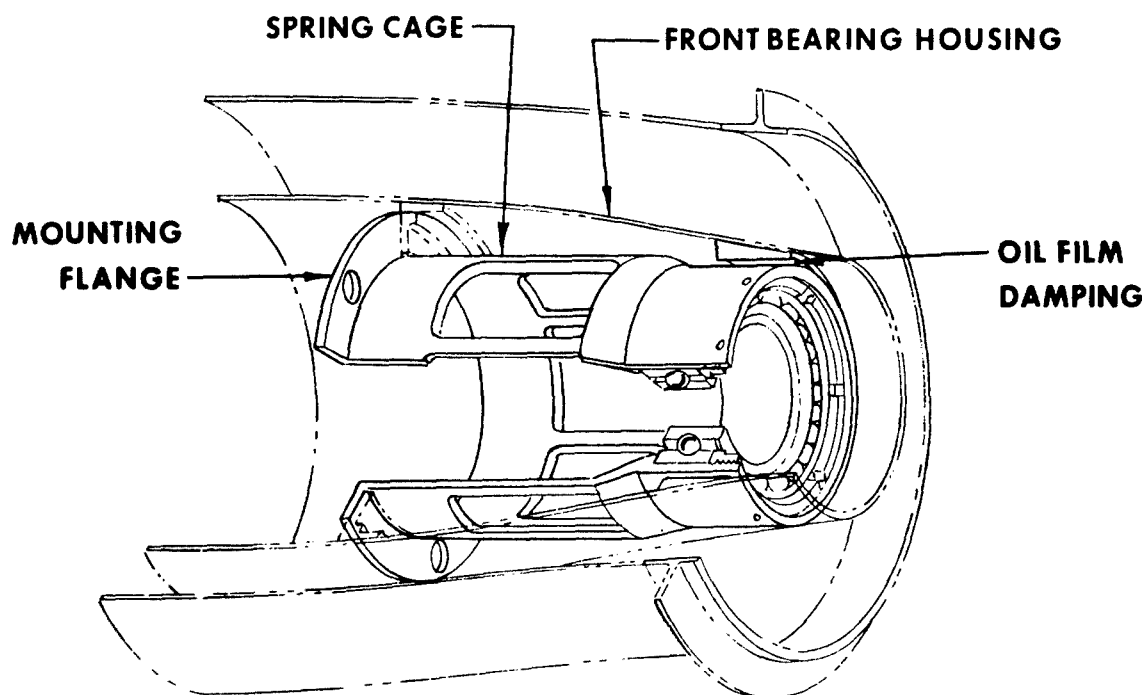


Figure 14. Typical Spring Cage-Type Shaft Support Bearing.

Operation in the region far above resonance causes the shaft to seek a rotational centerline about its mass center of gravity. The effect of imbalance is merely to displace this center of gravity slightly from the geometric centerline. The only force experienced by the bearings and the stator system is then equal to the product of the displacement and the spring rate of the bearing cage. An eccentricity of 0.001 inch and a spring rate of 15,000 pounds per inch would result in a rotating force of only 15 pounds, although this amount of eccentricity would amount to an imbalance of 0.25 ounce-inch or about 1240 pounds at maximum turbine speed, if mounted on rigid supports.

The capability of this system to accommodate large imbalance has been demonstrated experimentally in similarly suspended full-scale gas turbine engines by introducing massive imbalances into the rotors and by running at full speed with very little increase in external vibration levels.

The stiff construction of the turbine shaft minimizes its tendency to go out of balance at high speeds. If sufficient flexibility exists in a rotor system, locked-in bending moments caused by the uneven distribution of imbalance along the length of the rotor will cause the shaft to deflect at high speeds, destroying the balance that was obtained statically or at a fairly low speed. In some cases it is necessary to balance such flexible rotors at high speeds and in three or more planes to attain satisfactory running balance.

Bearing support deflection is limited at resonance by two concentric, oil-fed snubbing surfaces. The clearance, width, and diameter of these surfaces are closely controlled parameters of a viscous damping system, in which the hydrodynamic force vector generated by rotating oil film squeeze action varies in both magnitude and direction with speed and imbalance. There is an optimum combination of values for which the damper is adequate to provide low-frequency vibration absorption without increasing transmissibility at high speeds to such an extent that the bearing support spring no longer functions as an effective mass isolator.

Fuel Slinger Shaft

The flexible rotor suspension system designed for the full-scale fluid-cooled turbine will also function satisfactorily for the combustion test rig. The replacement of the turbine rotor by a fairly light dummy shaft has the effect of shifting the first two critical modes upward somewhat while lowering the third mode. The decrease in the third mode is due to the loss of the mass moment of inertia of the turbine rotor, which has a stiffening effect on the slope of the shaft at higher speeds.

The first three critical speeds of the dummy shaft test rig occur at 9,700, 16,300, and 107,000 rpm, respectively. These speeds are outside the rig operating range.

Shaft Bearings

The rotor shaft is supported by a ball bearing at the front end and a roller bearing at the turbine end. The front bearing, which absorbs the residual rotor thrust, is a Class 5, deep-groove conrad type with internal construction designed to accommodate the load and high speed involved. The retainer will be made from forged silicon iron bronze and will be silver plated to prevent corrosion and to improve frictional characteristics.

In high-speed ball bearings, a differential contact angle between inner and outer races results from centrifugal force on the balls, and a certain amount of ball skidding occurs. The extent of skidding depends upon the number and size of the balls, the initial contact angle, the retainer velocity, and the applied thrust load. The ball complement and contact angle contemplated result in an axial load requirement of at least 75 pounds at maximum turbine speed to prevent excessive ball skidding. The rotor shaft incorporates a pressure balancing disc designed to provide a net forward thrust of 200 pounds. The resulting B10 bearing life is 1500 hours.

The rear roller bearing provides for differential thermal axial expansion between the shaft and stator assemblies. It will have a silver-plated forged silicon iron bronze retainer. The races and rollers will be manufactured from M-50 tool steel to obtain the high-temperature properties characteristic of this material. Vacuum remelting will be specified to ensure the cleanliness of the steel. This bearing will also conform to Class 5 tolerances.

Air Inlet Plenum

The air inlet plenum directs the main rig air into the combustor. This plenum is sized to give low Mach numbers around its entire circumference to minimize the pressure or flow profiles in the rig combustor. There are provisions for the use of a flow-straightener screen if required. The rig combustor inlet is designed to simulate normal compressor discharge flows.

Exhaust Diffuser

The turbine exhaust diffuser is exposed to main stream temperatures up to 1830°F during rig running and up to 2300°F during combustor

development without the rotor. These temperatures require the cooling of diffuser metal components. Proper cooling is achieved through the use of the "double-wall" design shown in Figure 2. This type of construction provides two important advantages:

1. Cooling airflow required is minimized since air is directed along the parts to be cooled.
2. Structural components are shielded from the hot main stream. This provides greater strength because of lower temperatures and reduced thermal gradients.

Cooling air bathes the bearing housing before being directed along the inner duct wall, out through the vanes, and along the outer duct wall to be dumped into the main stream at the front and rear through circumferential orifices as shown.

Thermal analysis of the entire diffuser showed that a cooling airflow of 0.132 pound per second at 500°F was sufficient to provide good cooling. During turbine rig testing, a lower flow is permissible because of lower supply temperatures. Metal temperatures are shown in Figure 15.

Fuel Pressurizing Valve

A fuel pressurizing valve, as shown in Figure 16, provides back pressure to prevent fuel vaporization and to ensure that the fuel pumping action of the turbine rotor does not cavitate the fuel supply line. The fuel pressure rise through the rotor is caused by the high "g" field acting on different density columns of fuel. Blade cooling causes a temperature rise in the fuel that creates this density change. The valve is designed to supply the proper fuel pressure over the rig operating range.

RIG INSTALLATION

The fluid-cooled turbine rig will be located at the Continental Component Test Laboratory at Toledo, Ohio. The test cell layout showing the location of auxiliary components is shown in Figure 1. The rig test section of Figure 2, the air supply and combustion preheater, the reduction gearbox, and the slip ring are shown.

The required high-pressure airflow for rig running will be provided from the shop air supply at the test facility. This air supply is limited to 3.5 pounds per second at the required pressures, and it will, therefore, be necessary for the testing to be conducted at simulated

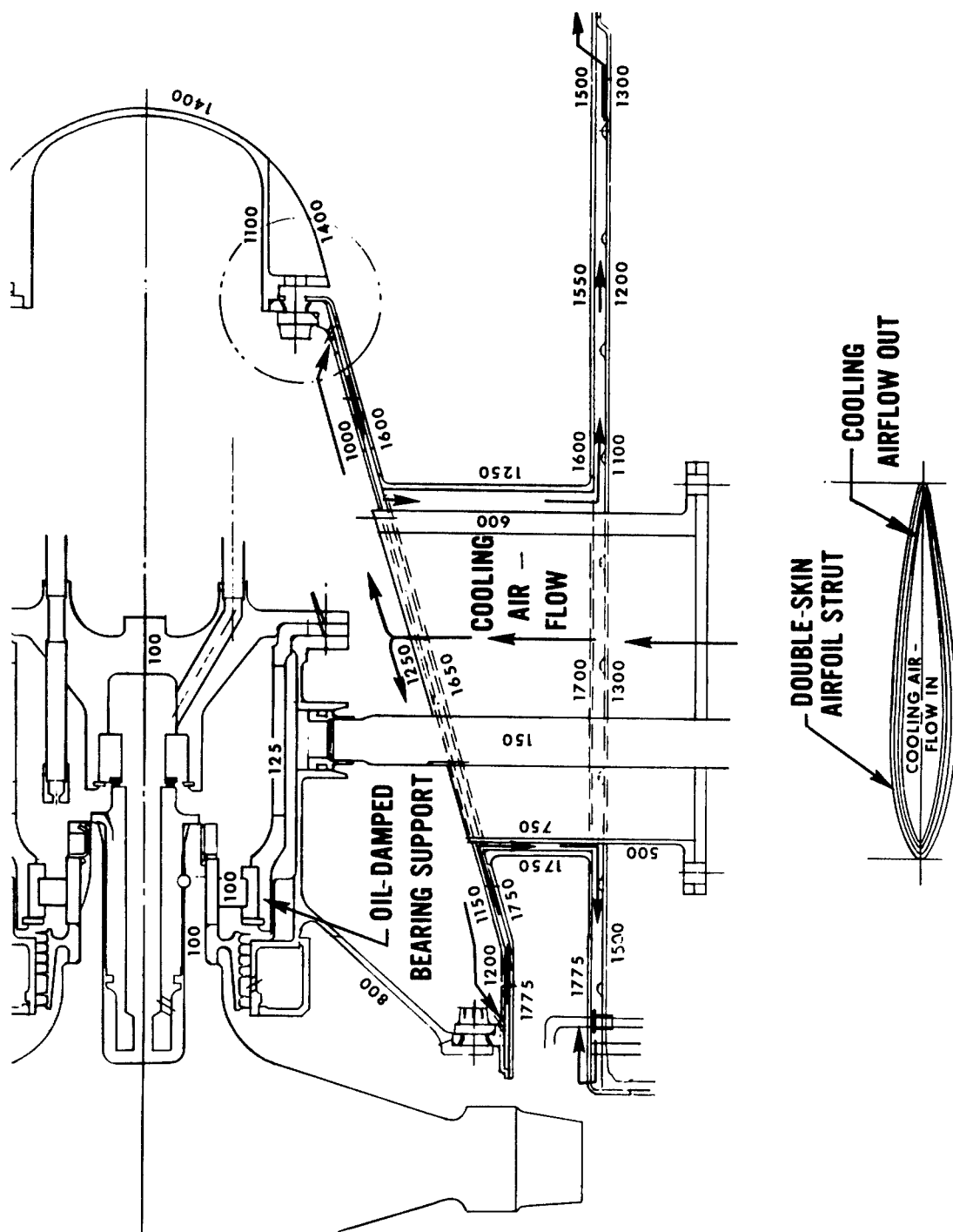


Figure 15. Double-Walled Exhaust Diffuser Cooling Airflow Path and Metal Temperature.

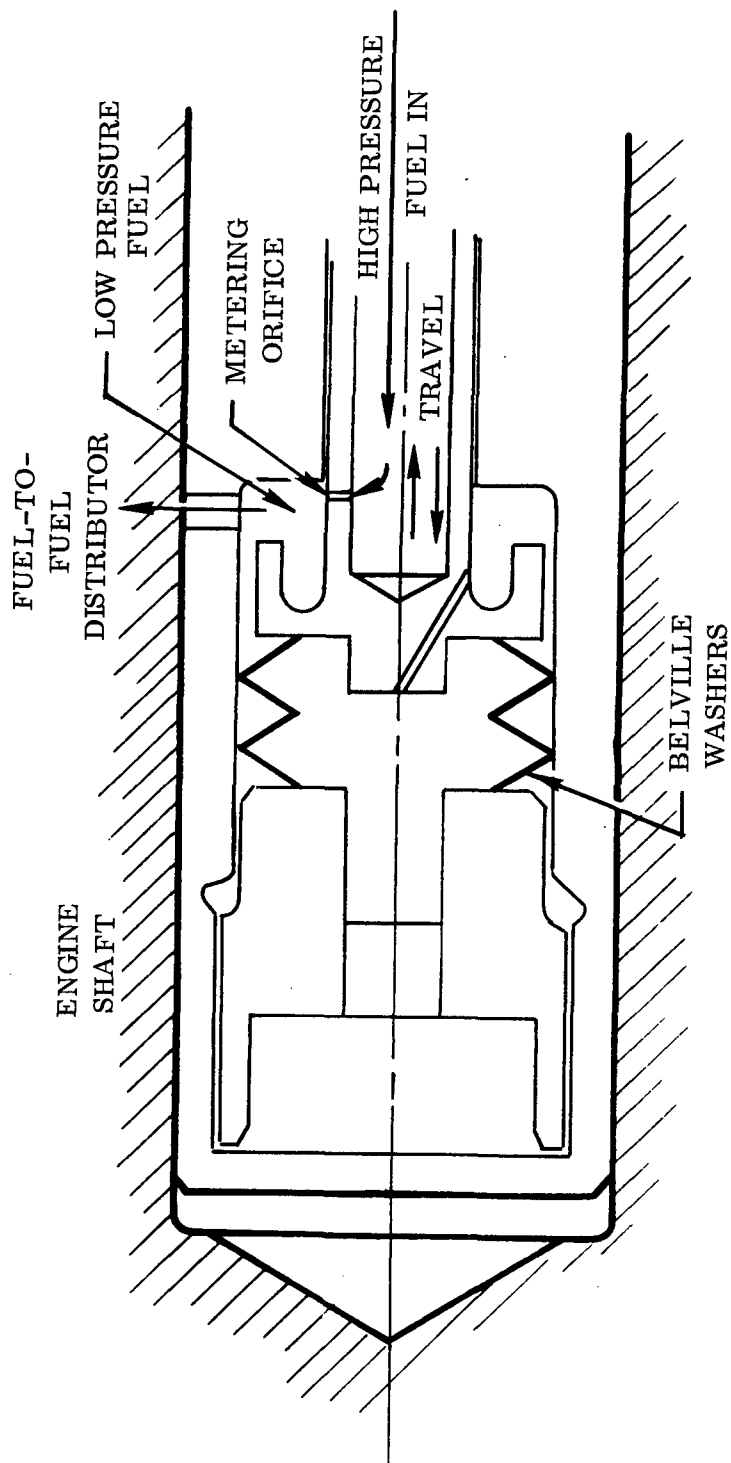


Figure 16. Fuel Pressurizing Valve.

altitude or reduced speed conditions. Figure 17 shows the test envelope using available shop air.

Rig running at design rpm (50,000) and design turbine inlet temperature (2300°F) will be conducted at a simulated altitude of approximately 10,000 feet. At this condition, engine fuel flow is reduced along with airflow. The effect of this reduced airflow on rotor and blade stresses is negligible. The effect of reduced fuel flow on blade cooling is shown to be small.

	<u>Design Point</u>	<u>Test Point</u>
Rig Airflow (lb/sec)	5.0	3.5
Rig Fuel Flow (lb/hr)	343	233
Turbine rpm	50,000	50,000
Turbine Inlet Temperature, °F	2300	2300
Fuel Temperature Rise, °F	244	284
Average Blade Metal Temperature, °F	1452	1433

Supply air will be heated to simulate compressor discharge temperatures by the combustion preheater, which is vertically mounted just upstream of the rig air inlet plenum.

Dynamometer

The rig dynamometer serves a dual purpose: loading the turbine and measuring torque. The dynamometer is a Taylor D-20-9 water brake capable of absorbing 1100 hp at 6500 rpm. Load absorption is adjusted by turning off water flow from one to seven of the nine separate elements. Water to the two end elements cools the bearings and is not turned off. Torque and speed measurement capabilities of the dynamometer are covered under "Instrumentation".

Gear Reduction Unit

The basic configuration of the gear reduction unit, Figure 18, for decreasing the speed of the fluid-cooled turbine to normal dynamometer input speed consists of a straddle-mounted helical input pinion running at 52,500 rpm maximum speed, driving an output gear at 6510 rpm. The input gear is supported radially on two roller bearings that are incapable of resisting axial loads. Pinion thrust is absorbed by a ball bearing, which is mounted with sufficient housing clearance to avoid any radial load. The output gear is also straddle-mounted and depends on a roller

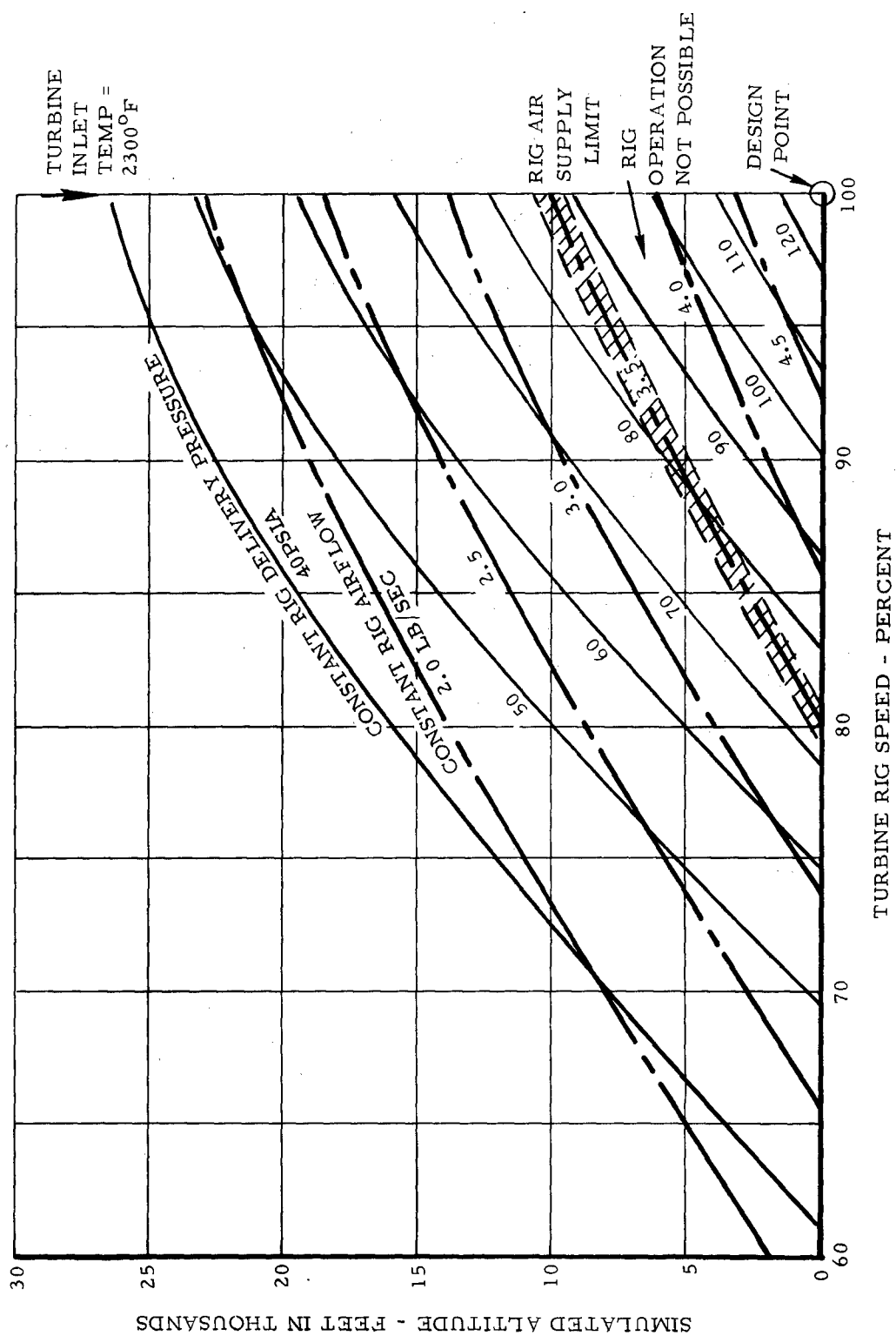


Figure 17. Fluid-Cooled Turbine Rig Test Envelope.

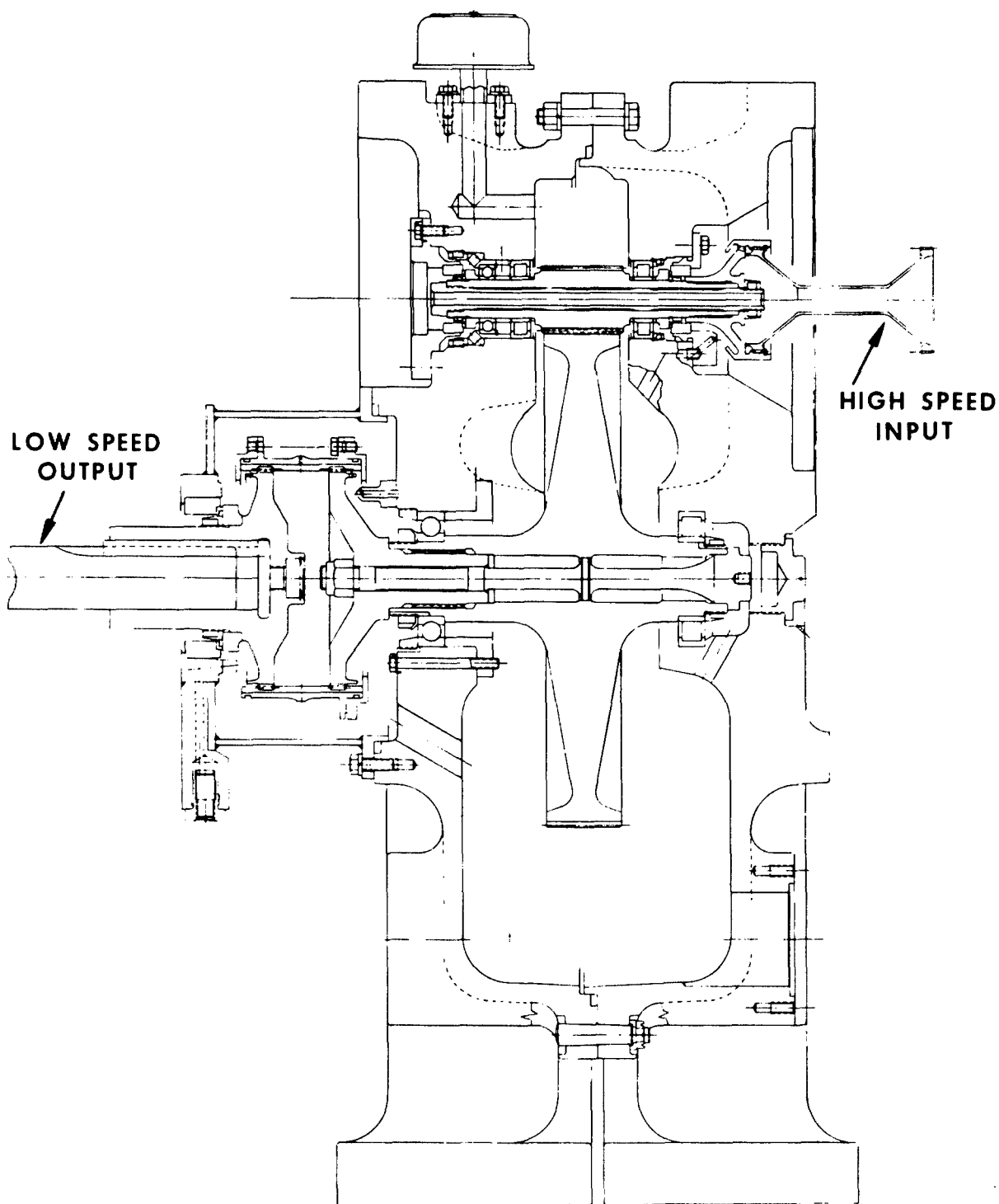


Figure 18. Reduction Gearbox for Fluid-Cooled Turbine.

bearing mounted fairly close to the plane of mesh to absorb most of the normal gear force; a stabilizing ball bearing mounted on the opposite side of the mesh plane absorbs the gear thrust and the residual portion of the normal tooth load.

The gear mesh has a contact ratio greater than three by virtue of the overlapping action of the helical teeth. The resulting smooth flow of power is beneficial in reducing dynamic tooth engagement loads and in lowering turbine blade excitation forces that might cause fatigue failures. The gear mesh is isolated from the turbine inertia by a flexible connecting quill, which ensures a low level of tooth error inertia forces. Similarly, the turbine blades are isolated from high-frequency tooth meshing vibrations.

The gear teeth have been analyzed and designed against the three general types of gear failure: pitting, bending or tooth breakage, and scoring. The first two types are essentially fatigue in character and are functions of the total number of stress cycles as well as the magnitude of dynamic load. Scoring is almost always caused by local friction welding and is independent of length of operation of the gears. If scoring does not occur on the first application of maximum speed and torque, it is not likely to occur at all.

The gears have a pressure angle of 20 degrees, which was selected as the best compromise between the higher bearing loads and the lower contact ratios obtained with higher pressure angles and the higher Hertz stress and scoring factors resulting from lower pressure angles.

The normal diametral pitch of 16 was determined from beam stress and scoring factor considerations. In general, the finest pitch compatible with adequate tooth bending strength will provide the most satisfactory results for high-speed gearing because of the higher contact ratios and lower scoring factors obtained.

Tooth proportions have been modified to obtain equal scoring factors between the drive pinion and the driven output gear. In addition, tip relief has been specified to avoid premature tooth contact due to bending deflections and tooth spacing errors. High stress concentrations at the edges of the teeth are also avoided by slightly crowning the ends of the teeth.

The helix angle of 6.5 degrees is sufficient to ensure a contact angle of over three to one, but it is not large enough to result in excessive thrust bearing loads or gear hub deflections.

All bearings in the gearbox have minimum calculated lives of over 500 hours under maximum speed and power conditions. The vacuum-degassed steel specified for the bearings will increase their lives three-fold.

INSTRUMENTATION

Turbine test rig instrumentation to establish turbine performance, turbine rotor and nozzle cooling system design data, and turbine and test rig structural integrity is described below. The use of instrumentation is listed, followed by a description of specific instruments to be used.

Rig Airflow

Inlet airflow is to be measured by a sharp-edged orifice per ASME specifications given in Reference 1.

This report predicts an accuracy of ± 1 percent for this type of airflow measurement.

Rig Fuel Flow

Fuel flow is to be measured using the standard Potter or Cox variable area flow meter. This type of flow meter consists of a tapered metering tube and a float that is free to move up and down inside the tube meter. The fluid entering the bottom of the meter raises the float because of the fluid's dynamic head. As the float rises, the tube area increases, and a balance is achieved between the weight of the float and the hydraulic forces. Flow rate is indicated by the position of the float in the tube. An accuracy of ± 1 percent is achieved after the flow exceeds 8 percent of the total meter capacity (50-500 lb/hr).

Slip Ring

The Bean VHS-F6 slip ring is to be used to transmit rotating instrumentation emf's to the test cell. This slip ring, Figure 19, is designed for operation to 65,000 rpm with low noise levels.

The slip ring is air-cooled to maintain brushes and rings at the same temperature, so that extraneous emf's are not generated. There are six rotating rings of coined silver with two brushes per ring of silver graphite, which gives the low and very stable value of contact resistance. Brushes maintain a pressure of 10 to 15 psi on the slip rings. A matched pair of precision, high-speed bearings is used to maintain ring centers.

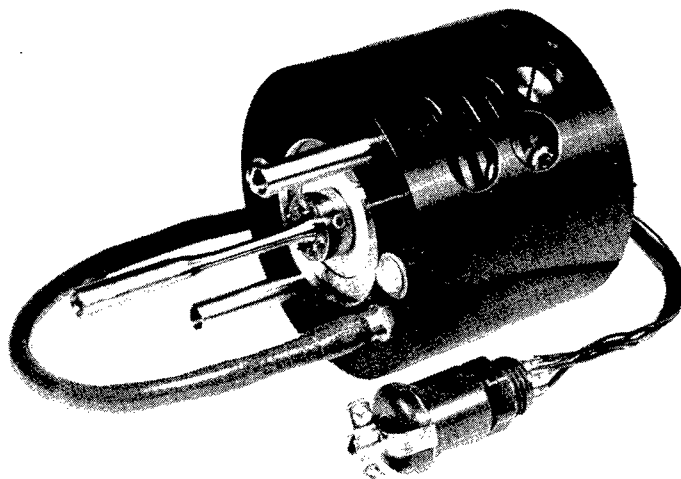


Figure 19. Bean VHS-F6 Slip Ring.

Six rings give the capability of three ungrounded or five grounded readings. Two VHS-F6 rings may be mounted on the same shaft to double readable instrumentation.

Continental has developed the T65-T-1 turboshaft engine through FAA certification using the Bean VHS-F6 slip ring. The T65-T-1 has a gas generator rpm of 55,250, and this slip ring was effectively used at this speed.

Dynamometer Rig Speed and Torque

Turbine rig speed and torque will be measured by a Taylor D-20-9 water brake dynamometer, as explained with other test installation components. This dynamometer provides rig rpm measurements within ± 0.25 percent and rig torque outputs within ± 0.5 percent.

Rig Main Stream Gas Temperatures

Turbine Inlet Total Temperature. Seven double-shielded, aspirating probes are to be used. These probes have water-cooled shanks and may be traversed to any radial location. Probe tips are 90-percent platinum and 10-percent rhodium with insert and shields per Reference 2, probe No. 8. Figure 20 shows a sketch of this probe.

The seven total-temperature probes are to be located midway between the turbine inlet nozzles, flush with the leading edge, Figure 21.

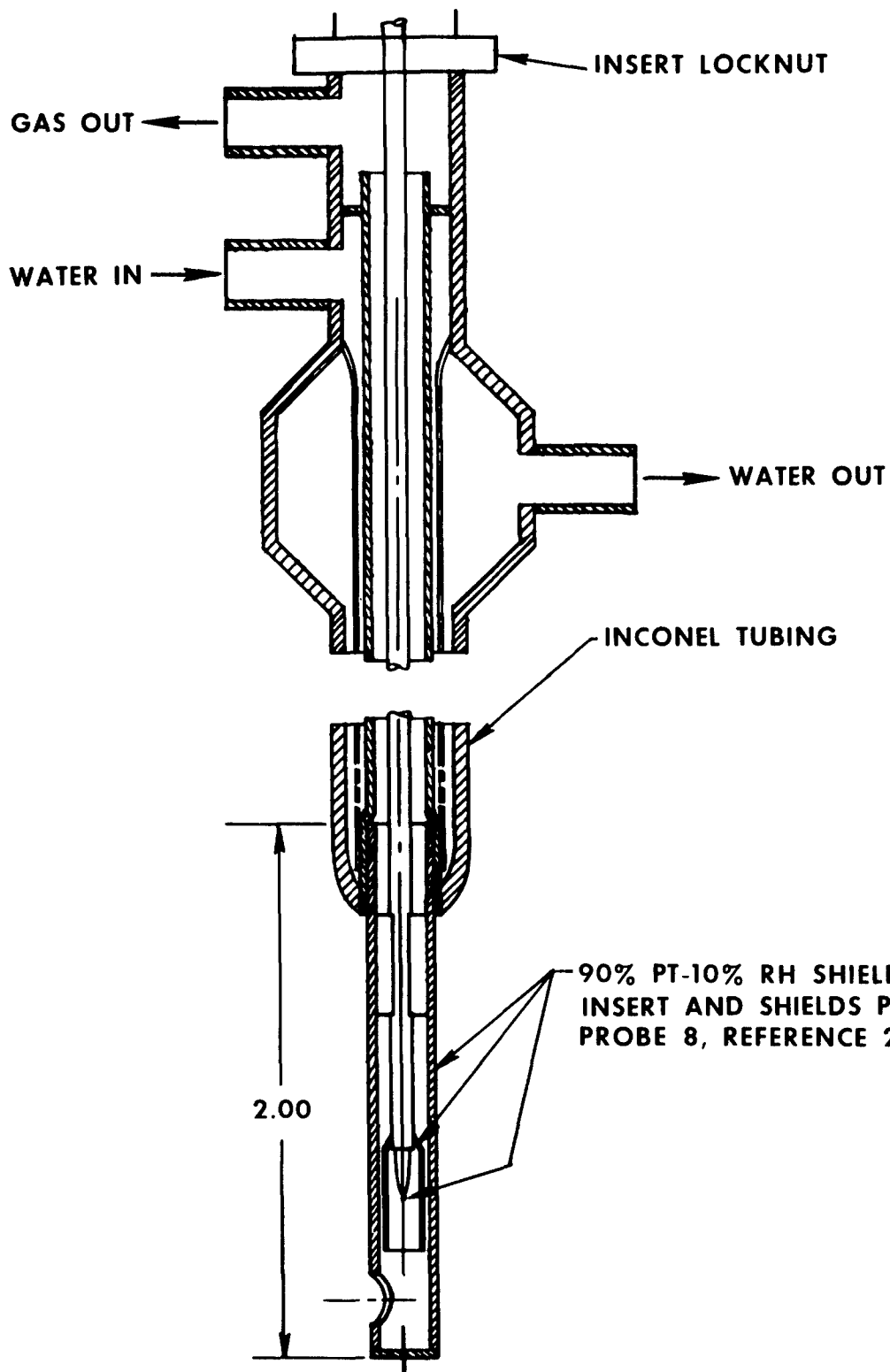


Figure 20. Double-Shielded Traversing Turbine Inlet Thermocouple.

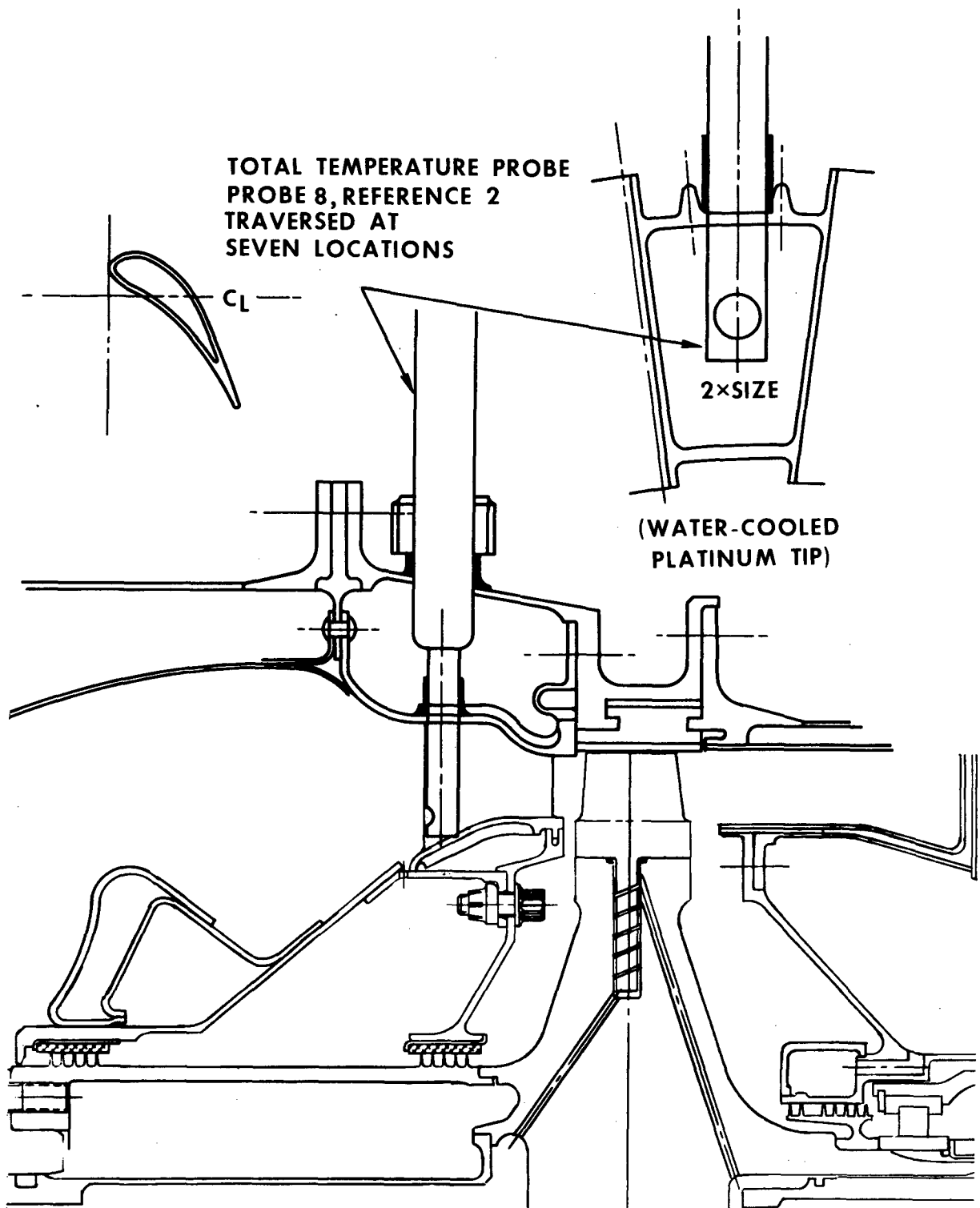


Figure 21. Turbine Inlet Total-Temperature Probe Location.

Measured inlet temperature will be used to calibrate the combustor efficiency; thereafter, combustion efficiency will be used on routine tests for calculation of turbine inlet temperature. Temperature traversing will be used as a check, when required.

Turbine Discharge Total Temperatures. Turbine discharge total temperature is to be measured at the turbine exhaust diffuser outlet, Figure 22, with the use of a multiple-thermocouple survey ring. This survey ring will contain six rakes with three probes per rake located on centers of equal areas.

Probe Selection Considerations. Care must be taken in the design of gas-measuring thermocouples to eliminate errors due to conduction and radiation in low-velocity gas streams, while in higher velocity flows the recovery factor must be considered. Calculation of correction factors for several probe designs is discussed in Reference 2. Correction for radiation and conduction errors is given by equation (5) of Reference 2 for the probes investigated.

Turbine inlet total temperature is to be measured using probe No. 8, and turbine exhaust temperature is to be measured using probe No. 3 of Reference 2. Calculation of probe radiation and conduction errors shows a possible 10 degrees on turbine inlet temperature and 9 degrees on turbine exhaust temperatures. The low Mach numbers in these areas require no additional recovery factor correction. Consideration of thermocouple wire calibration tolerances and potentiometer error gives a possible couple error of ± 0.7 percent of the total reading.

Rig Main Stream Pressures

Turbine Inlet Total Pressure. Six total-pressure probes per References 3 and 4 are to be placed in the leading edge of the inlet nozzles, as shown in Figure 23. Three radial locations are to be examined, with probes at the same radius 180 degrees opposed.

Turbine Inlet Static Pressure. Three static-pressure probes are to be affixed to the inlet nozzle outer shroud, and three are to be affixed to the inner shroud, as shown in Figure 23.

Turbine Discharge Total Pressure. Turbine discharge total pressure is to be measured at eight circumferential locations, using the total pressure probe of References 3 and 4. Figure 24 shows the installation of these probes.

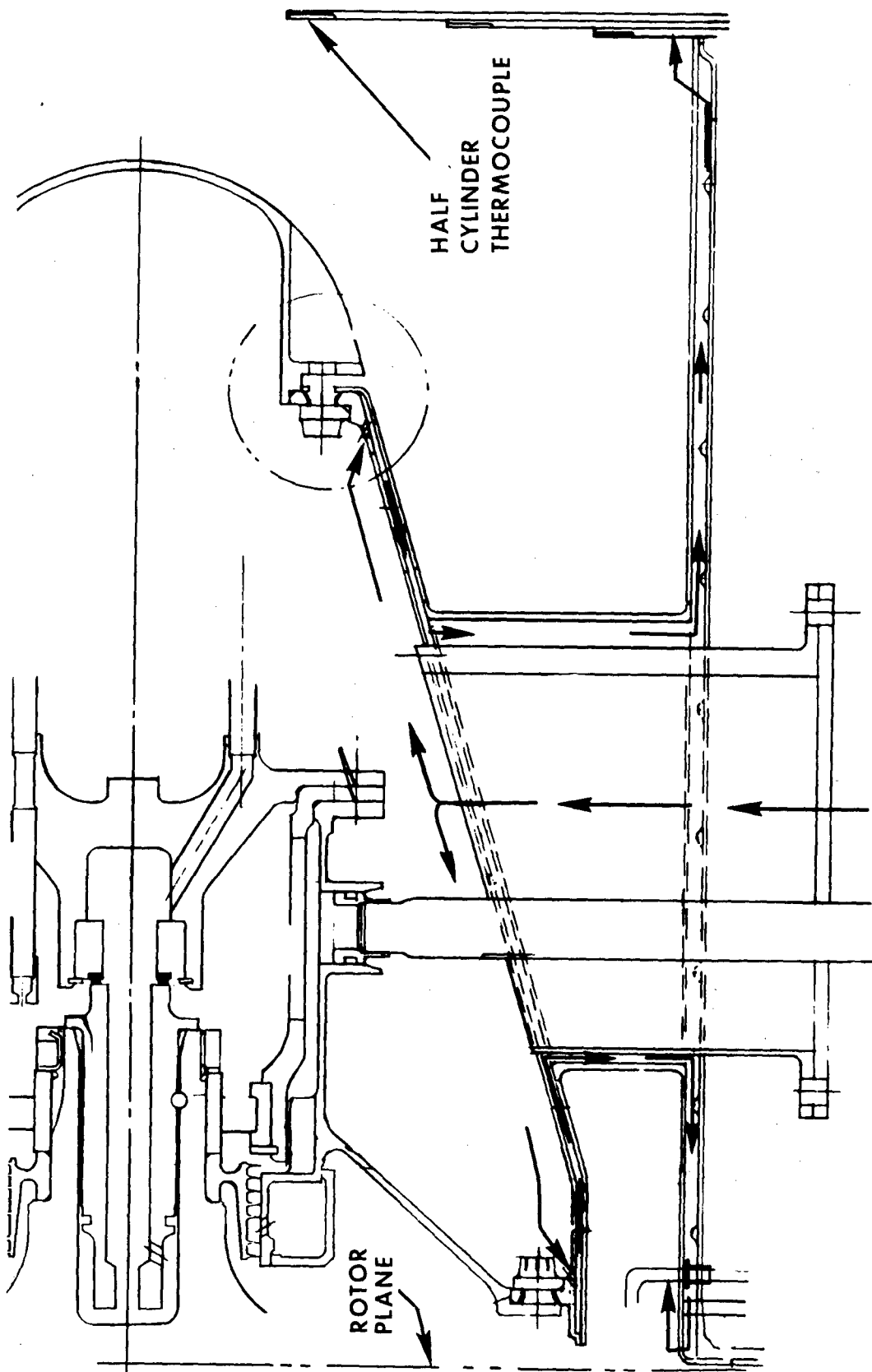


Figure 22. Turbine Discharge Total Temperature.

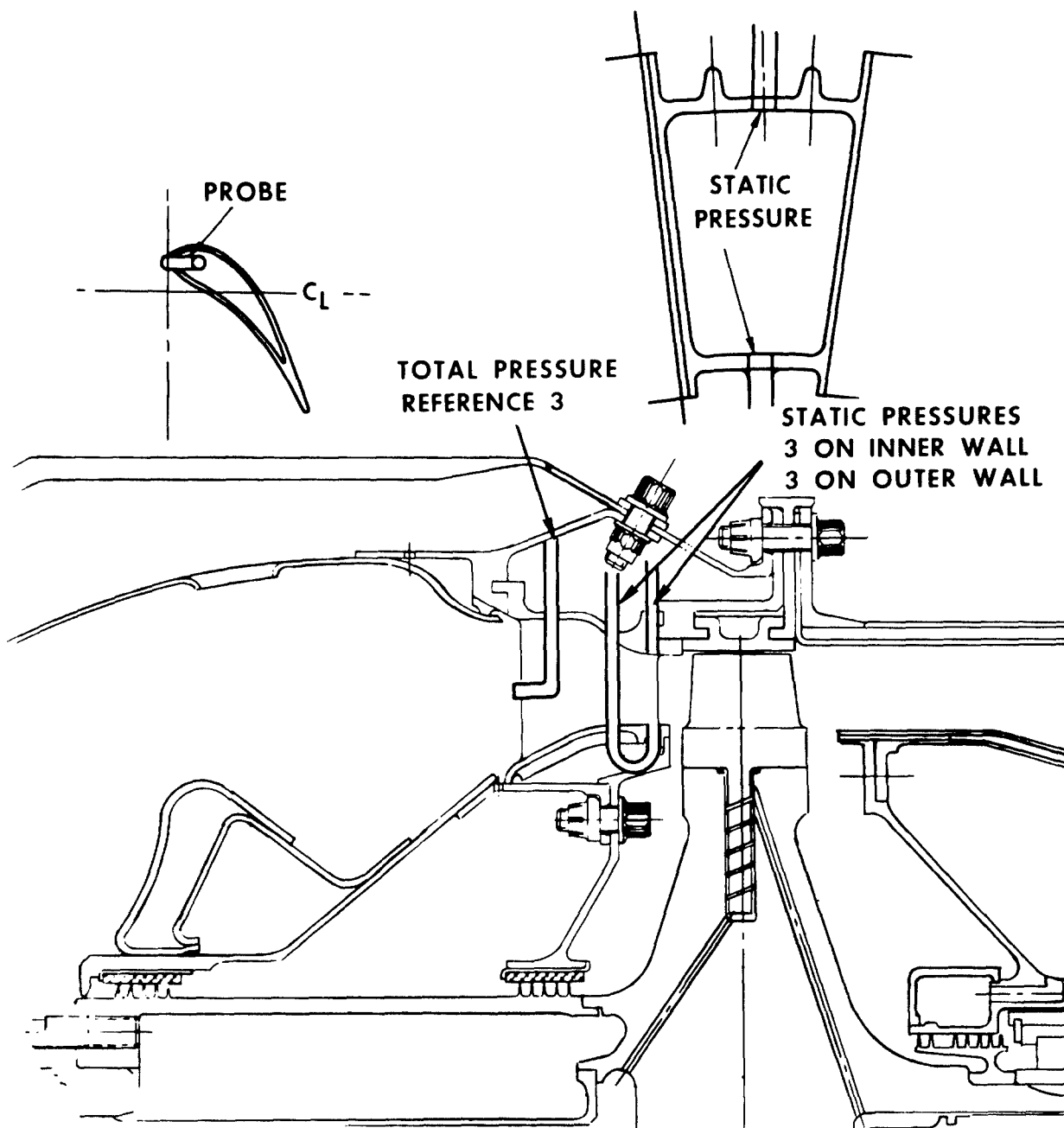


Figure 23. Turbine Inlet Pressure.

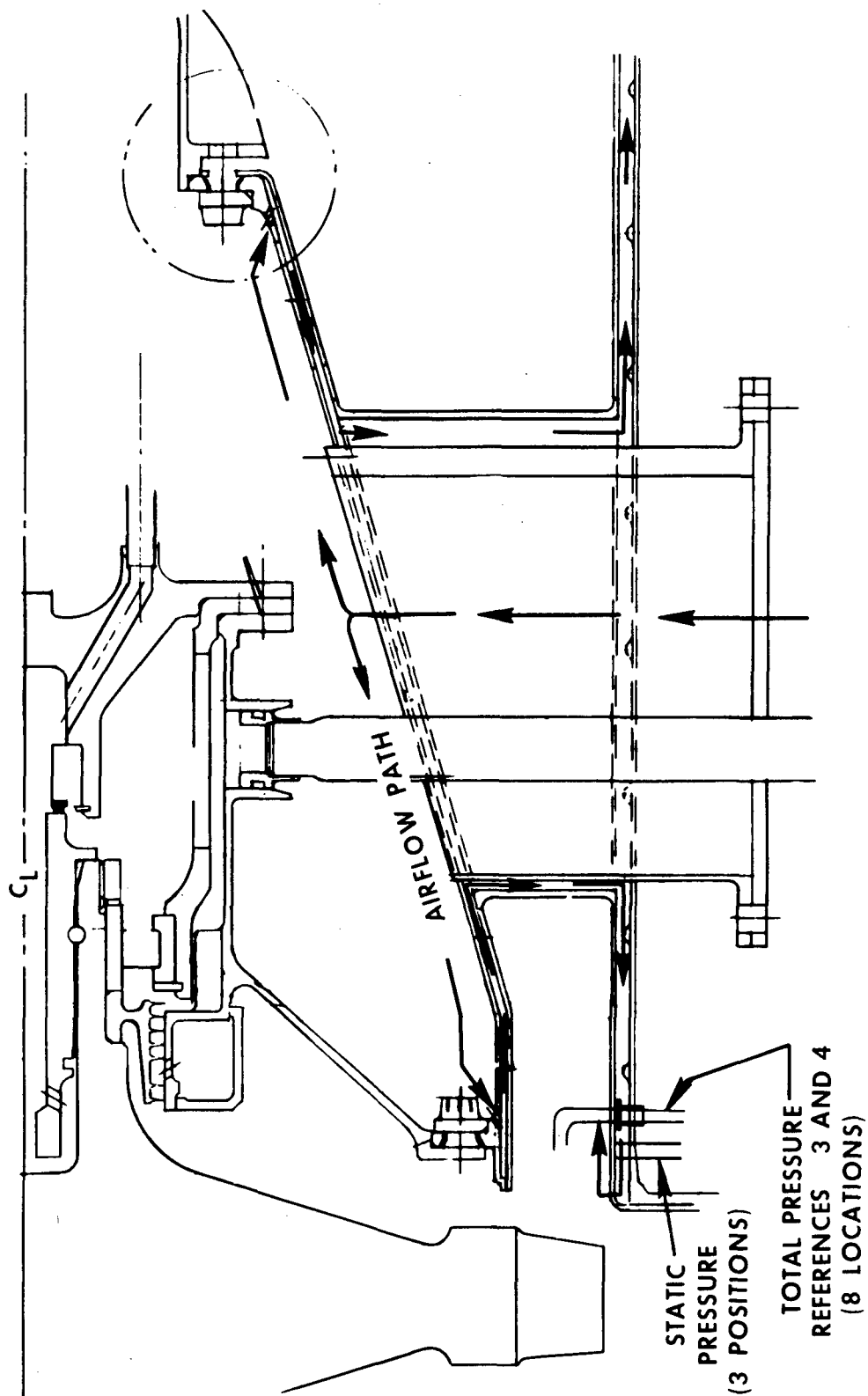


Figure 24. Turbine Discharge Pressures.

Turbine Discharge Static Pressure. Turbine discharge static pressure is to be measured at three positions on the inner exhaust diffuser wall and at three positions on the outer wall, Figure 24.

Probe Selection Considerations - Total Pressure. The selection of a probe design to measure total pressure in subsonic flow requires the consideration of probe insensitivity to various main-stream angles of attack. Thirty-nine total-pressure tubes were examined in Reference 4 with respect to external shape, internal shape, and configuration of the total-pressure entry.

Probe No. A-7 of Reference 4, which is to be used, gave total-pressure readings within 0.2 percent of the actual total head over a range of ± 20 degrees on angle of attack. The probe has an internal cone angle of 15 degrees with a sharp metal edge at the inlet.

Probe Selection Considerations - Static Pressure. The static-pressure reading of a static wall tap is affected by the tap diameter and the inclination to the stream flow. Various tap configurations are discussed in Section 3.3.3 of Reference 5. Reference 5 shows that taps of 0.020 to 0.040 inch in diameter, counter sunk $1/2$ tap diameter, substantially eliminate tap errors.

Effect of Instrument Inaccuracies on Calculated Turbine Efficiency

The effect of instrument inaccuracies given in the preceding sections upon calculated turbine efficiency was established from the root-mean-square of the individual reading accuracies. Instrument measurement inaccuracies were given as

		<u>Percent of Total Reading</u>	<u>Possible Error at Design Point - P</u>
Torque	T	$\pm 1/2$	± 0.52 ft/lb
Speed	N	$\pm 1/4$	± 125.0 rpm
Airflow	W_a	± 1	± 0.05 lb/sec
TIT		± 1	± 24.8 deg
Pressure Ratio	λ	$\pm 1/2$	± 0.0018
Function	f		

Turbine efficiency is calculated as

$$\eta = f (T, N, W_a, TIT, \lambda)$$

The possible error in efficiency (P_η) is given by the root-mean-square of the possible errors due to each instrument alone:

$$P_\eta^2 = \left[\frac{\partial f}{\partial T} \cdot P_T \right]^2 + \left[\frac{\partial f}{\partial N} \cdot P_N \right]^2 + \left[\frac{\partial f}{\partial W_a} \cdot P_{W_a} \right]^2 + \left[\frac{f}{\partial TIT} \cdot P_{TIT} \right]^2 + \left[\frac{\partial f}{\partial \lambda} \cdot P_\lambda \right]^2 \quad (1)$$

where the error in efficiency at design point due only to

Torque	= ±0.41 percent In η
Speed	= ±0.203 percent In η
Airflow	= ±0.81 percent In η
TIT	= ±0.73 percent In η
Pressure Ratio	= ±0.34 percent In η

The root-mean-square of these individual errors showed turbine efficiency to be calculable within ±2 percent of the actual value.

Rig Metal Temperatures

During shakedown running, critical areas will be examined to locate hot spots, using temperature-sensitive paints. Examined areas will be

1. Turbine inlet nozzles
 - a. Nozzle
 - b. Inner shroud
 - c. Outer shroud
2. Rotor shroud
3. Rotor

4. Exhaust diffuser

- a. Inner and outer aerodynamic wall at inlet
- b. Airflow support strut

High metal temperature locations will be further examined with the use of chromel-alumel thermocouples with Inconel sheathing. Anticipated locations are shown in Figure 25.

The chromel-alumel thermocouples are to be fabricated per specifications listed in Section 1.4 of Reference 5. The bimetallic or hot junction will be tack-welded to the instrumented component and covered with cement to eliminate convective and radiation errors. Extension wires will be affixed to the metal components with cement. Lead-out wires will be alumel with a high-temperature insulation.

Stresses

Rotor stress patterns will be established during cold spin test with the use of strain gages. Thermal stresses, calculated from measured temperatures during initial running, will be added to the mechanical stresses previously established to determine operational stress levels. Critical stress areas, thus located, will be subsequently instrumented.

Component stresses are to be measured with the use of high-temperature metalfilm strain gages. These gages are manufactured from extremely thin precision foil, which permits the production of a gage that is conformable to curved surfaces, gives low errors in measurement of bending strains, and produces very little interference with the aerodynamics of the structure. The strain gage alloy is Nichrome-V, approximately 80-percent nickel and 20-percent chromium, and possesses greater stability at these high temperatures than most alloys.

Electrical resistance of gage material is affected both by changes in its physical dimensions (strain) and by temperatures. In order to measure strain at elevated temperatures, it is therefore necessary to make a temperature correction to establish the actual or static strain. Above 600°F, corrections become a large percentage of the total reading, and it is possible to read only the sharp variations in strain (dynamic strain). The gage used gives good dynamic readings to temperatures of 1800°F.

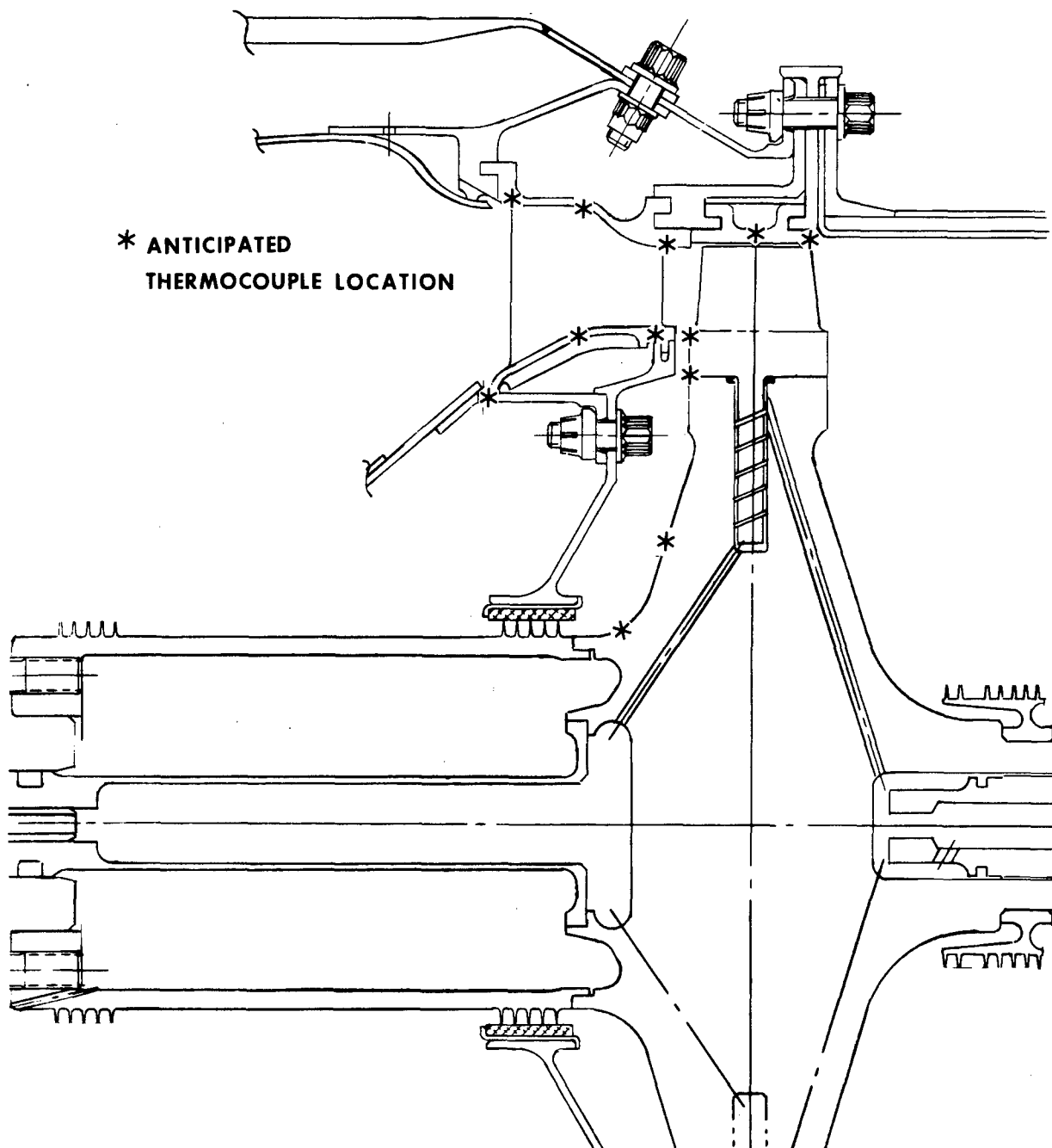


Figure 25. Anticipated Thermocouple Locations.

Adhesives

A strong, high-temperature cement is required to affix thermocouple and strain gage extension wires to hot, rotating components. Since the same cement is to be used to attach strain gage elements, a composition that does not thermally induce electrical currents or inhibit compatible growths is required. Adhesives that can be easily mixed, shelf-stored, and cured at a low temperature are desirable.

A family of adhesives, designated "H" adhesives, which meets these requirements has been commercially developed and shows good performance up to metal temperatures of 1600°F. These cements, and others, have been tested, and results have been reported in Reference 7.

Continental has successfully used one of these cements on metals at temperatures above 1600°F and in "g" fields of 4.6×10^7 pound force per pound mass. The cement cures at a low temperature, accurately transmits strains, and is opaque.

Fuel Temperatures

Fuel temperature rise through the steam-to-fuel heat exchanger will be used to calculate heat flow from rotor blade cooling. Fuel temperature will be measured at the engine inlet and just upstream of the pressurizing valve.

Two wells will be drilled in the shaft as shown in Figure 26. Silver solder will be used to support the bead in the well. Since this area is bathed by fuel, the possible conduction error is negligible.

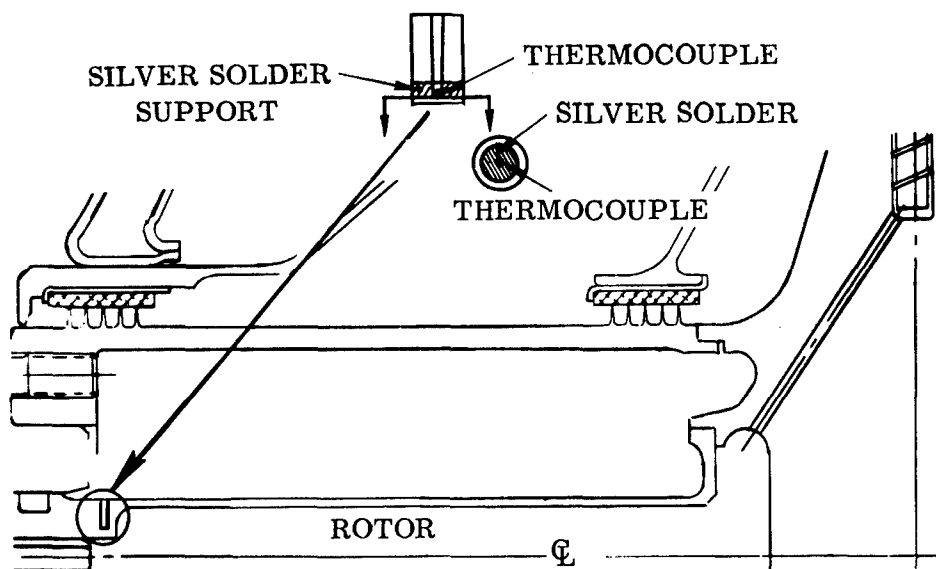


Figure 26. Fuel Temperature Rotor Exit.

TURBINE AEROTHERMODYNAMIC DESIGN AND COLD TEST

AEROTHERMODYNAMIC DESIGN

The objective of the fluid-cooled turbine program is the demonstration of a high-temperature, single-stage axial turbine capable of doubling the specific horsepower of current small aircraft propulsion engines. The performance specified to meet the objective is:

2300°F TIT

85.0-percent adiabatic turbine efficiency

5-lb/sec airflow

$$\frac{\Delta H}{\theta_{cr}} = 26.0 \text{ Btu/lb of air}$$

The Phase I effort to accomplish this goal consisted of aerothermodynamic design and cold flow testing of the evolved geometry.

Overall Design

The high-temperature turbine is assumed to be driving a two-stage centrifugal compressor, developing a pressure ratio of 9.2 at an efficiency of 79.5 percent. As determined during preliminary design, the compressor aerodynamics of a practical machine would demand a rotative speed of about 50,000 rpm. Fixing the speed, work, and flow requirements greatly narrows the choice of parameters affecting the efficiency of a single-stage turbine. Further restrictions are imposed by considerations of stress, degree of reaction, Mach number levels, blade turning angles, blade solidities, and physical geometry. The effects of parameter variation were investigated by means of semiempirical techniques on an IBM 1620 digital computer. The flow path evolved from this study is shown in Figure 27.

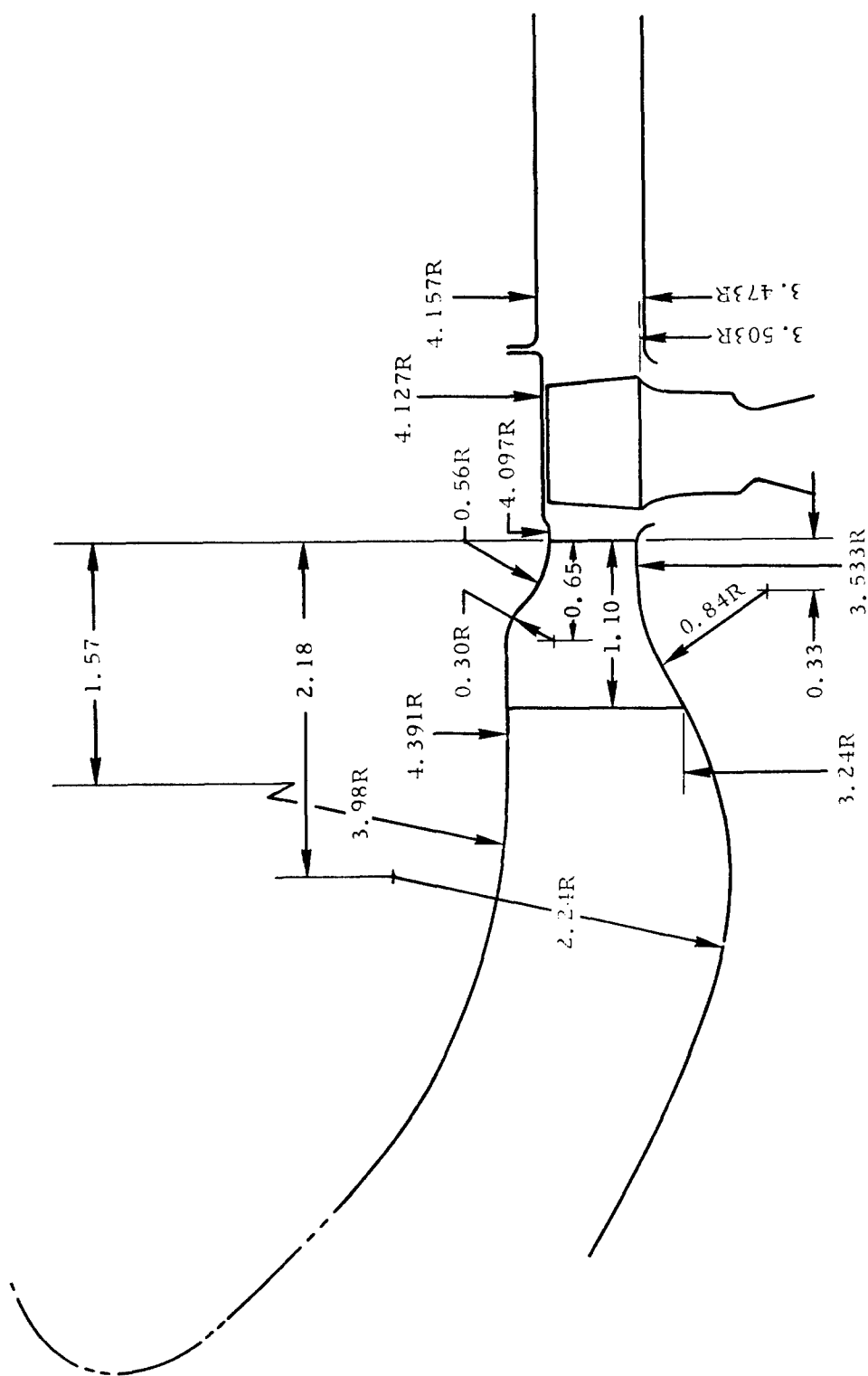


Figure 27. Fluid-Cooled Turbine Flow Path for Cold Flow Rig Testing,
23 Nozzle Vanes.

The turbine velocity triangles were calculated from the basic compressible flow relations. The simplified equations for axisymmetric flow may be stated as

(2)

$$\text{(radial equilibrium equation)} \quad gJ \quad C_p \quad \frac{\partial T}{\partial r} = gJT \quad \frac{\partial S}{\partial r} +$$

$$\frac{V_\theta}{r} \frac{\partial V_\theta}{\partial r} + \frac{V_\theta^2}{r} + V_x \frac{\partial V_x}{\partial r} - V_x \frac{\partial V_r}{\partial x}$$

(3)

$$\text{(continuity equation)} \quad W = 2\pi g \int_{r_h}^{r_t} \rho V_x r \, dr = \text{const}$$

(4)

$$\text{(energy equation along a steamtube)} \quad gJ \quad \Delta H = \Delta (UV_\theta) = gJ \quad C_p \quad \Delta T$$

When the notation of Figure 28 is used, the application of all the specified variables results in the velocity diagrams given in Figure 29.

Once the reaction, annulus geometry, and cycle conditions in terms of velocity diagrams are satisfied, the blade numbers and shapes are then specified. This is inherently a lengthy trial-and-error process, balancing the aerodynamic blade loadings against practical blade size and shape. A typical analysis for a blade at a given radial station is as follows.

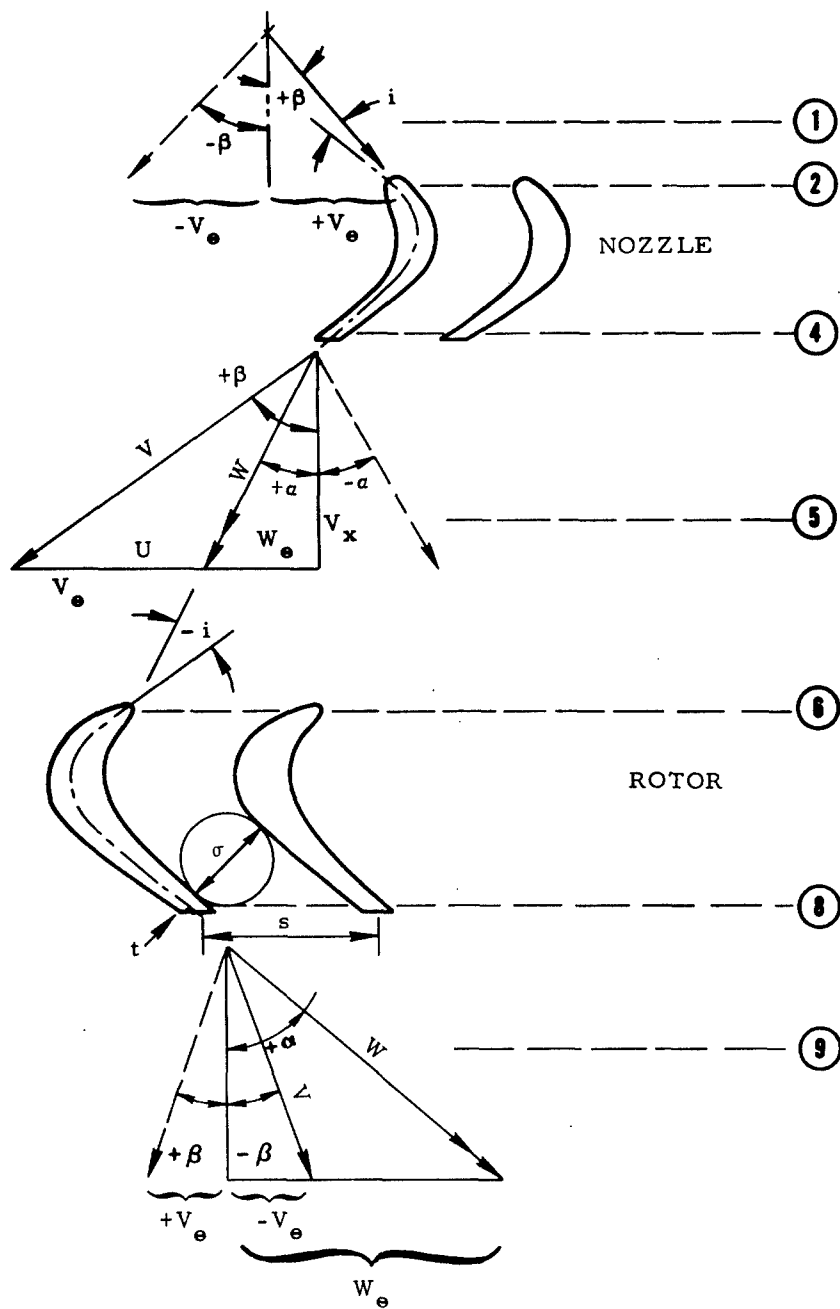


Figure 28. Turbine Velocity Diagram Station and Sign Notation.

$N = 50,000 \text{ rpm}$
 $W_g = 5.09525 \text{ lb/sec}$
 $T_o = 2760^\circ\text{R}$
 $\Delta H = 138.39 \text{ Btu/lb}$
 $P_o = 124.25 \text{ psi}$

$U = \text{Wheel Speed, fps}$
 $V = \text{Velocity, fps}$
 $W = \text{Angular Velocity, fps}$

$\theta = \text{Tangential Velocity, fps}$
 $x = \text{Axial Velocity, fps}$
 $\alpha = \text{Absolute Flow Angle, deg}$
 $\beta = \text{Relative Flow Angle, deg}$
 $cr = \text{Critical Velocity}$

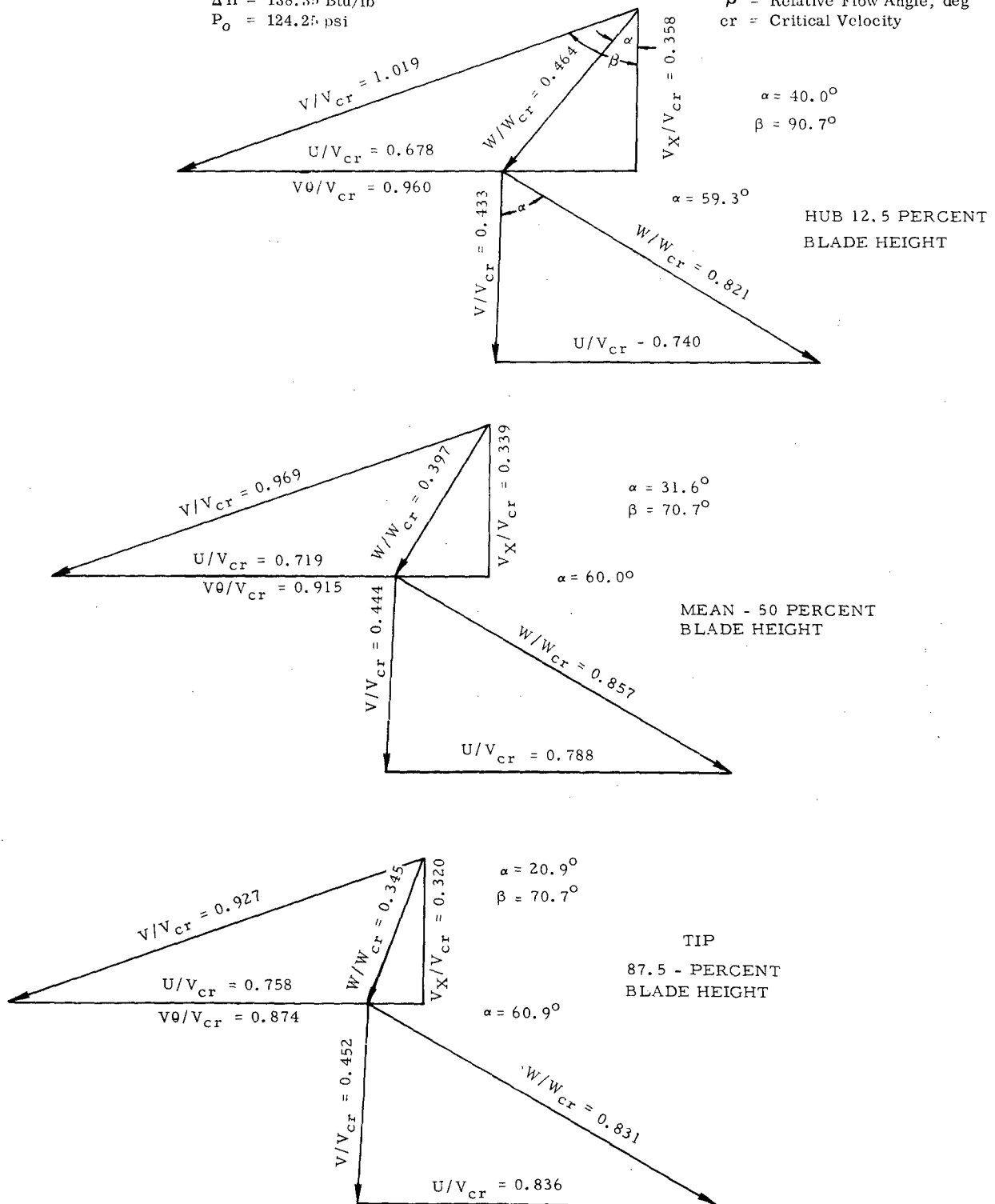


Figure 29. Velocity Diagrams - Fluid-Cooled Turbine.

An initial estimate of a pitch/chord value is made by the use of a Zweifel coefficient (\emptyset) (Reference 8), defined by (5)

$$\emptyset = \frac{4 \pi r_{m9} h_r V_{x9}}{z S W_9^2} (r_{m9} V_{\theta g} - r_{m5} V_{\theta 5})$$

where

- z = number of blades
- s = meridional blade surface area times radius to center of gravity
- h_r = blade height
- r_{m9} = outlet mean radius
- r_{m5} = inlet mean radius
- V_{θ}, W, V_x = velocity components as obtained from velocity diagrams (Reference Figure 28)

Specification of the hub-tip ratio, tip diameter, and aspect ratio, along with the Zweifel coefficient, gives a first approximation of the required number of blades. The local throat area required is calculated from the equation of continuity, and the requirements imposed by the velocity diagrams are evolved from the general radial equilibrium equations. A thickness-chord ratio is selected consistent with blade cooling and stress requirements. Incidence and deviation considerations fix the inlet and outlet blade angles. Additional conditions specified during the initial phases of the design are

1. The use of a parabolic or hyperbolic mean line.
2. The selection of one of the following blade thickness distributions, or a combination thereof:
 - a. British T-6
 - b. NACA 65 series
 - c. NACA 63 series
 - d. NACA primary series
 - e. NACA secondary series

A computer program is used to wrap the thickness distribution about the mean line and to iterate until throat requirements are met. The blade coordinates thus given are then refined to satisfy diffusion loading requirements.

Velocity distributions around the blading are obtained using simplified NACA stream filament techniques (Reference 9). A linear variation of total pressure is assumed through the channel, and mean line flow conditions are established from the equation of continuity. Suction and pressure surface local velocities V_s and V_p are then obtained from the local mean line value V_m from

$$\frac{V_s}{V_m} = e^{m_1} \quad \text{and} \quad \frac{V_p}{V_m} = e^{m_2} \quad (6)$$

where

$$m_1 = \left[\frac{C_s l_o}{2} \left\{ 1 + \frac{(C_p - C_s)}{4 C_s} \right\} \right]$$

$$m_2 = \left[\frac{-C_s l_o}{2} \left\{ 1 + 3 \frac{(C_p - C_s)}{4 C_s} \right\} \right]$$

l_o = distance from the blades along an equipotential line

The local suction and pressure surface curvatures C_s and C_p are calculated from the blade coordinates. The equipotential flow network required for this calculation is calculated by computer relaxation procedures.

The blade surface velocities thus calculated are examined to find if they fall within prescribed limits. Modifications are made to the blade shape, and the velocities are recalculated. If warranted, solidity and incidence changes are made. The trial-and-error procedure is repeated until aerodynamic loading requirements are satisfied.

Blade loading limits were estimated by the use of diffusion factors defined as

Pressure surface diffusion parameter

$$D_p = \frac{\text{Blade Inlet Rel Vel} - \text{Minimum Blade Surf. Rel Vel}}{\text{Blade Inlet Rel Vel}}$$

Suction surface diffusion parameter

$$D_s = \frac{\text{Max Blade Surf. Rel Vel} - \text{Blade Outlet Rel Vel}}{\text{Max Blade Surf. Rel Vel}}$$

$$D_{\text{tot.}} = \text{Ave of hub mean and tip}$$

$$D_{\text{tot.}} = D_p + D_s$$

Reference 10, Figure 40, shows how the boundary layer thickness increases with the surface diffusion parameter.

In general, a high efficiency is designed for

$$(1) D_s \leq 0.10$$

$$(2) D_{\text{tot.}} \leq 0.5$$

Nozzle

The nozzle performs the dual function of accelerating the gases to produce turbine work and of providing a flow path for combustor primary air. A total flow cross-sectional area of 4.5 square inches was required for the combustor. An area this large could be provided only by long axial chords and high thickness-chord ratio blading. The nozzle height, fixed from continuity and deflection, is small, giving a very low aspect ratio. This type of blading inherently has high secondary losses. The nozzle shrouds were, therefore, profiled to minimize this effect.

Figure 30 (taken from Reference 11) shows the improvements that can be made with various wall shapes. The best performance gains were obtained from unsymmetrical constriction on the outer wall near the nozzle throat.

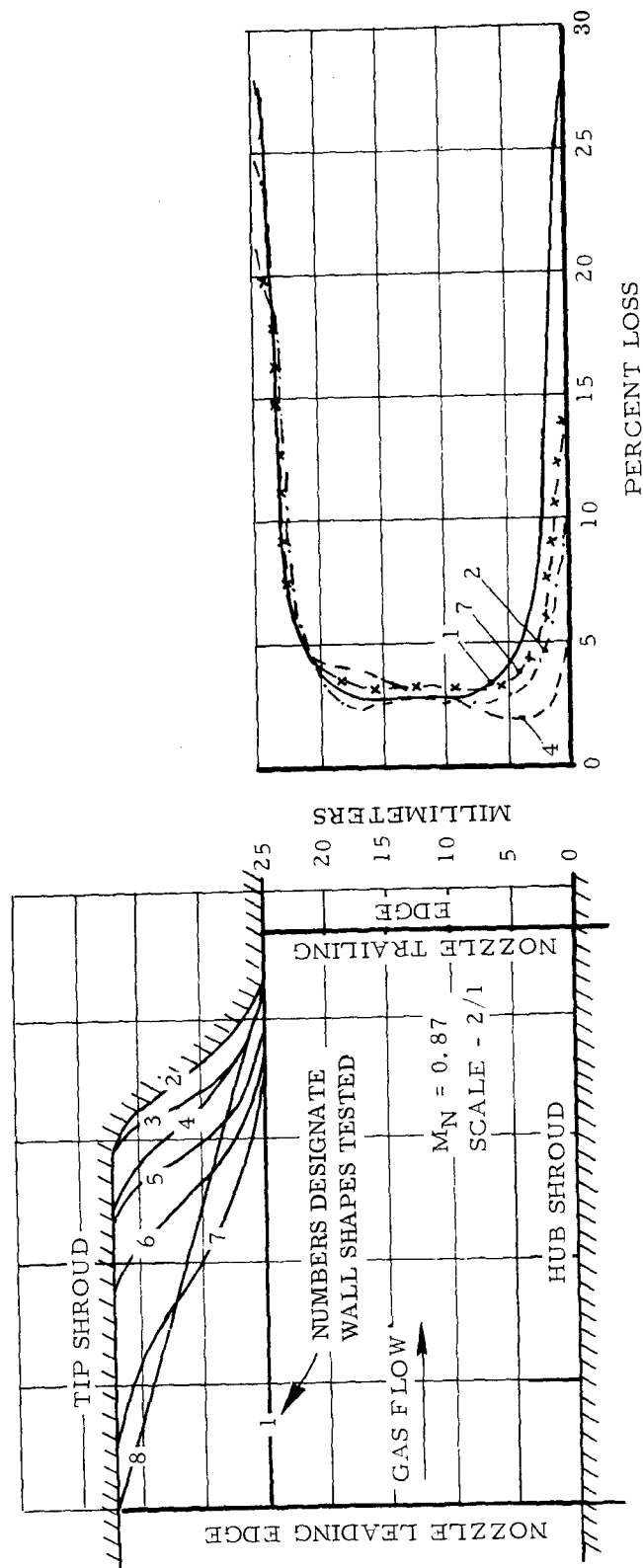


Figure 30. Effect of Meridional Constriction on Losses of a Nozzle.

This unsymmetrical type of constriction was introduced into the design, and blade shapes were varied until satisfactory velocity distributions were attained. Figure 31 describes the nozzle profile; Figures 32 through 34 describe the blade loading diagrams for a 23-vane nozzle version. Provision of trailing edge cooling and the combustor air supply necessitated a high thickness-chord ratio of 20 percent and a thick trailing edge of 0.050 inch.

A second nozzle assembly was also designed with a lower vane solidity. The essential differences from the first design are as follows:

1. The number of vanes was reduced from 23 to 17.
2. The outer meridional wall constriction profile was moved upstream.
3. The vane profile was rotated about its trailing edge and closed 2.8 degrees.

Figure 35 describes the flow paths.

The purpose of this solidity reduction is the same as that for the rotor; that is, to end up with as small a number of vanes as possible without deteriorating turbine performance. Changes 2 and 3 above were necessary to obtain a nozzle throat identical to the first design. The area distribution as a function of turning angle for several meridional wall shapes is given in Figure 36. The second distribution is nearly the same as the first. In order to minimize secondary losses, it is desirable to do most of the gas turning at low velocities or at high local-to-throat area ratios. Both nozzle designs have this feature.

Figure 37 shows a comparison of velocity distributions around the nozzle vane at the mean section for the two nozzles. The major difference is an increase in the suction surface velocity of the second design over the first. This occurs as a result of the increased aerodynamic load carried by 17 vanes, as compared to that carried by 23 vanes. The suction surface diffusion rate, however, has been held at zero, and acceleration of the gases occurs throughout the passage (diffusion is avoided whenever possible as it is inherently a less efficient process than acceleration).

Rotor

Aerodynamic design of the rotor follows the same principles as previously outlined. A fairly large blade cross section was required for the cooling holes, resulting in large axial chords for a low-flow turbine. A mean camber line method of trial and error along with stream filament theory was used to derive profiles that would satisfy the design velocity

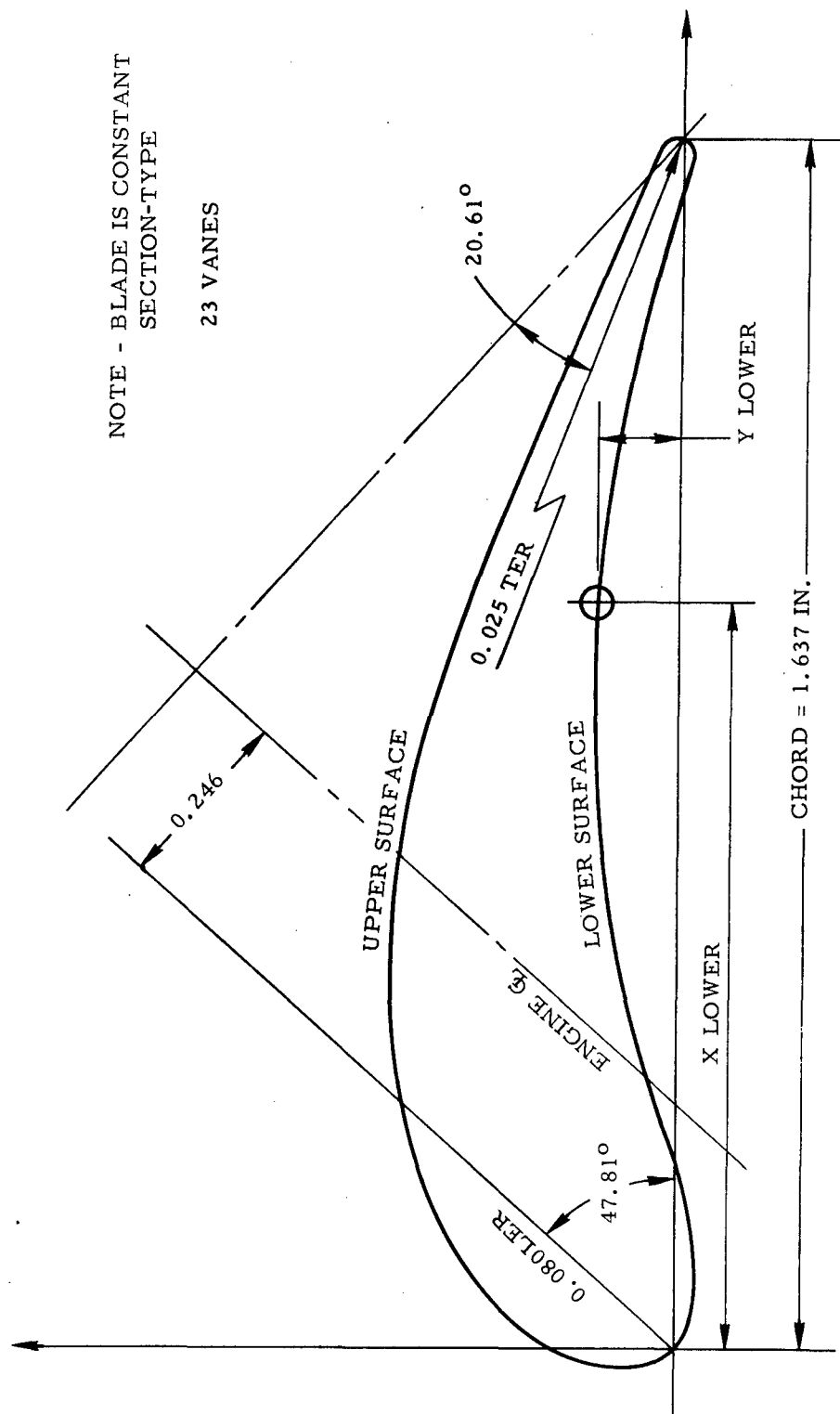


Figure 31. Fluid-Cooled Turbine Nozzle Coordinate Designations.

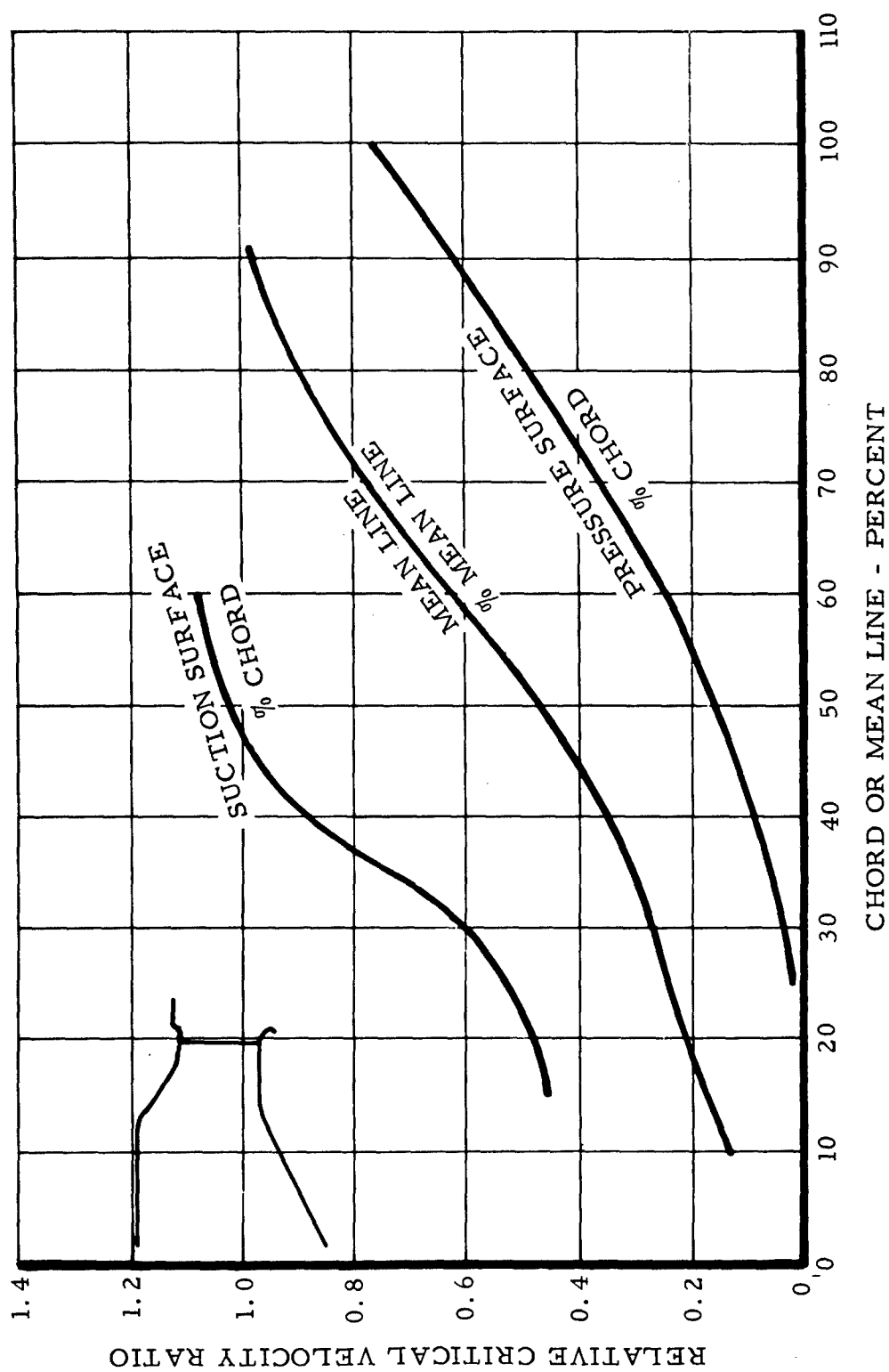


Figure 32. Velocity Distribution - Nozzle Hub Section - 12.5 Percent Blade Height.

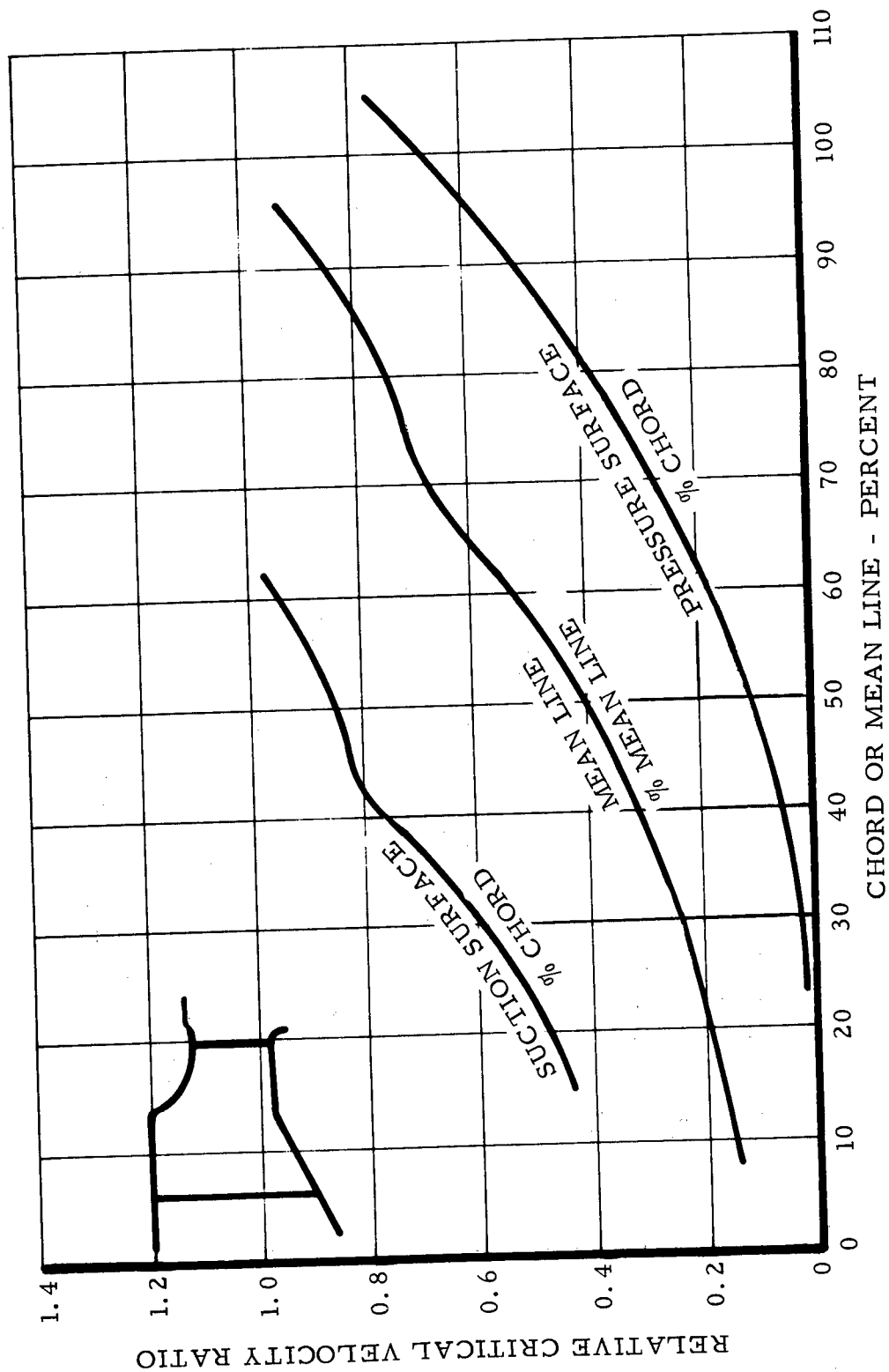


Figure 33. Velocity Distribution - Nozzle Mean Section - 50 Percent Blade Height.

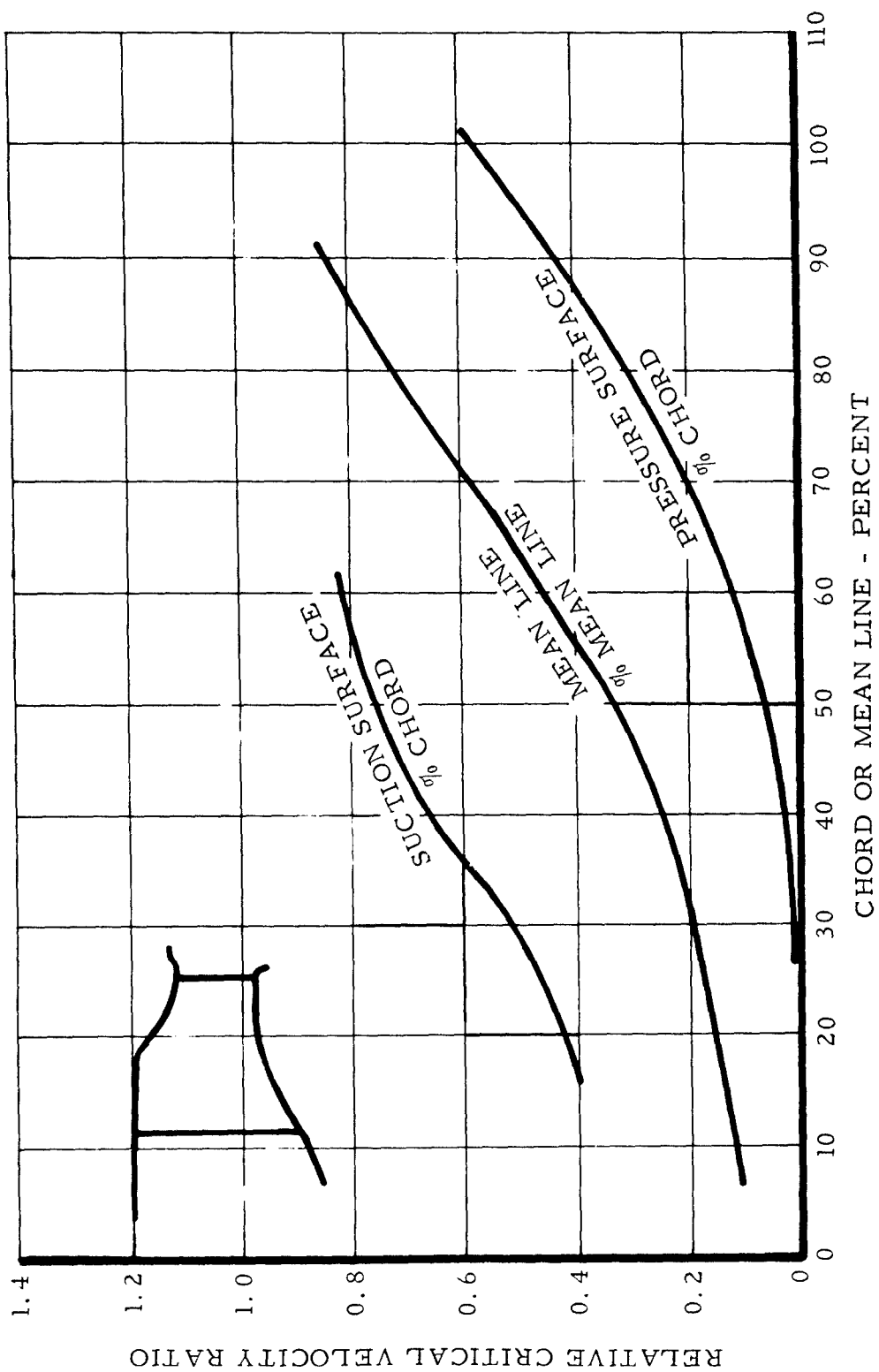


Figure 34. Velocity Distribution - Nozzle Tip Section - 87.5 Percent Blade Height.

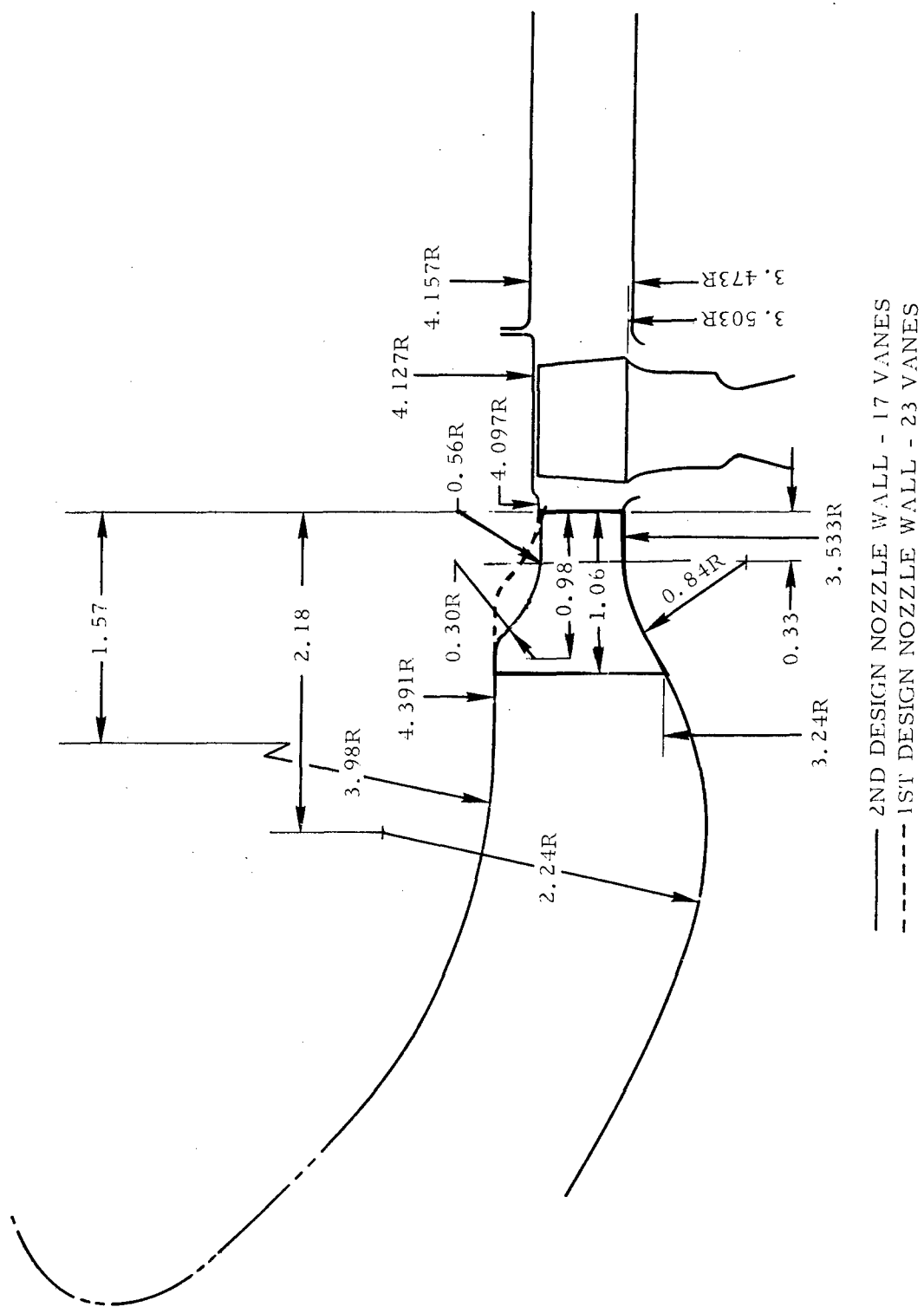


Figure 35. Flow Path for Cold Flow Rig Testing With Second Design Nozzle.

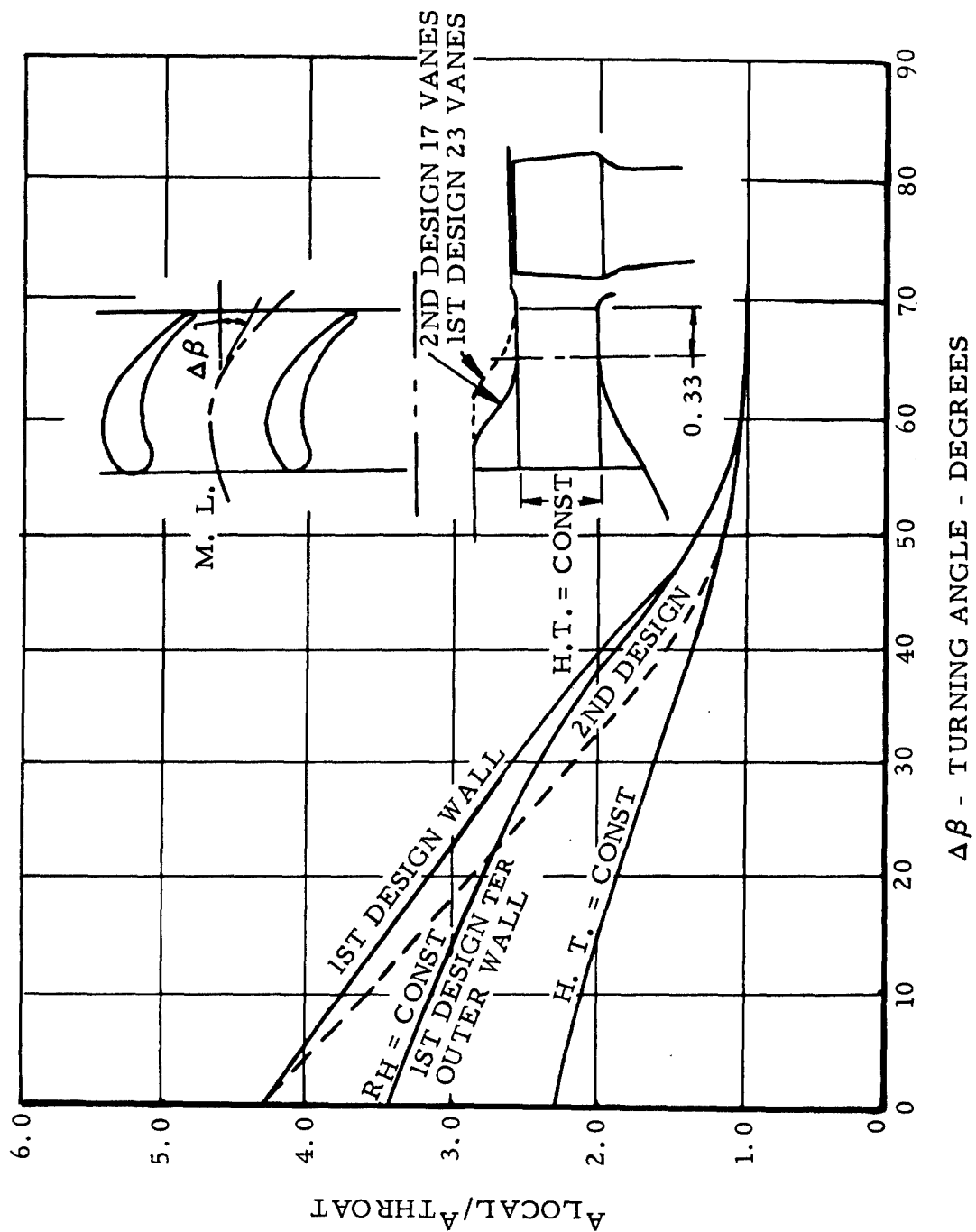


Figure 36. Nozzle Area Distribution.

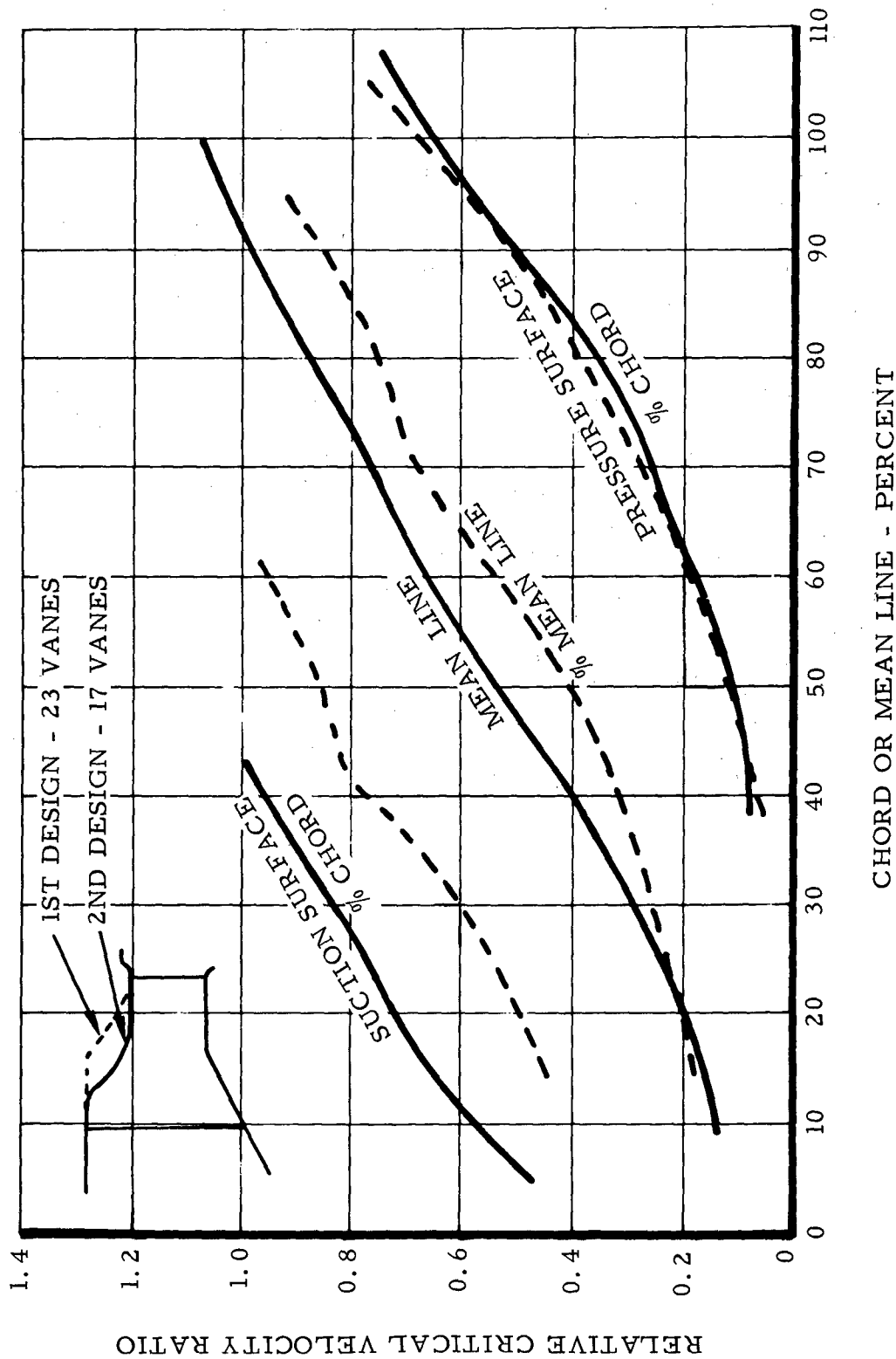


Figure 37. Nozzle Velocity Distribution - 50 Percent Blade Height.

triangles. The blade was designed to result in near straight-line fairing from hub to tip to simplify cooling-hole geometry. To attain this goal, a small amount of turbine efficiency was lost. The amount of loss, however, was believed to be within the boundaries of horsepower-per-pound realization.

Figures 38 through 40 give the velocity distributions about the blade at three radial sections, and Figure 41 presents a scale drawing of the principal sections stacked in their relative positions. As indicated by the velocity curves, $D_{tot.}]_{ave} = 0.794$ and the maximum $D_S = 0.247$. These values are high, but they have been attained successfully in previous high turbine efficiency designs at Continental and are, therefore, believed to be adequate.

The initial number of rotor blades was selected as 34. This value was established as a near-optimum pitch-chord ratio from aerodynamic considerations. Obviously, the cooling requirements can be simplified if a fewer number of blades can do the same job. To evaluate the performance penalties associated with the reduction of blades, a series of solidity tests was conducted (solidity defined as the ratio of chord to pitch distance between blades). To maintain optimum aerodynamic loading on the blades, each solidity change requires a separate airfoil design. A much simpler attack was chosen by restaggering the rotor for ideal loading. This condition is approximated by maintaining the nozzle-to-throat area ratio constant. Figure 42 presents a rotor-solidity-versus-stagger-angle curve to produce this effect. On this basis, rotor spacer rings were designed for 40, 34, 28, and 22 blades, respectively.

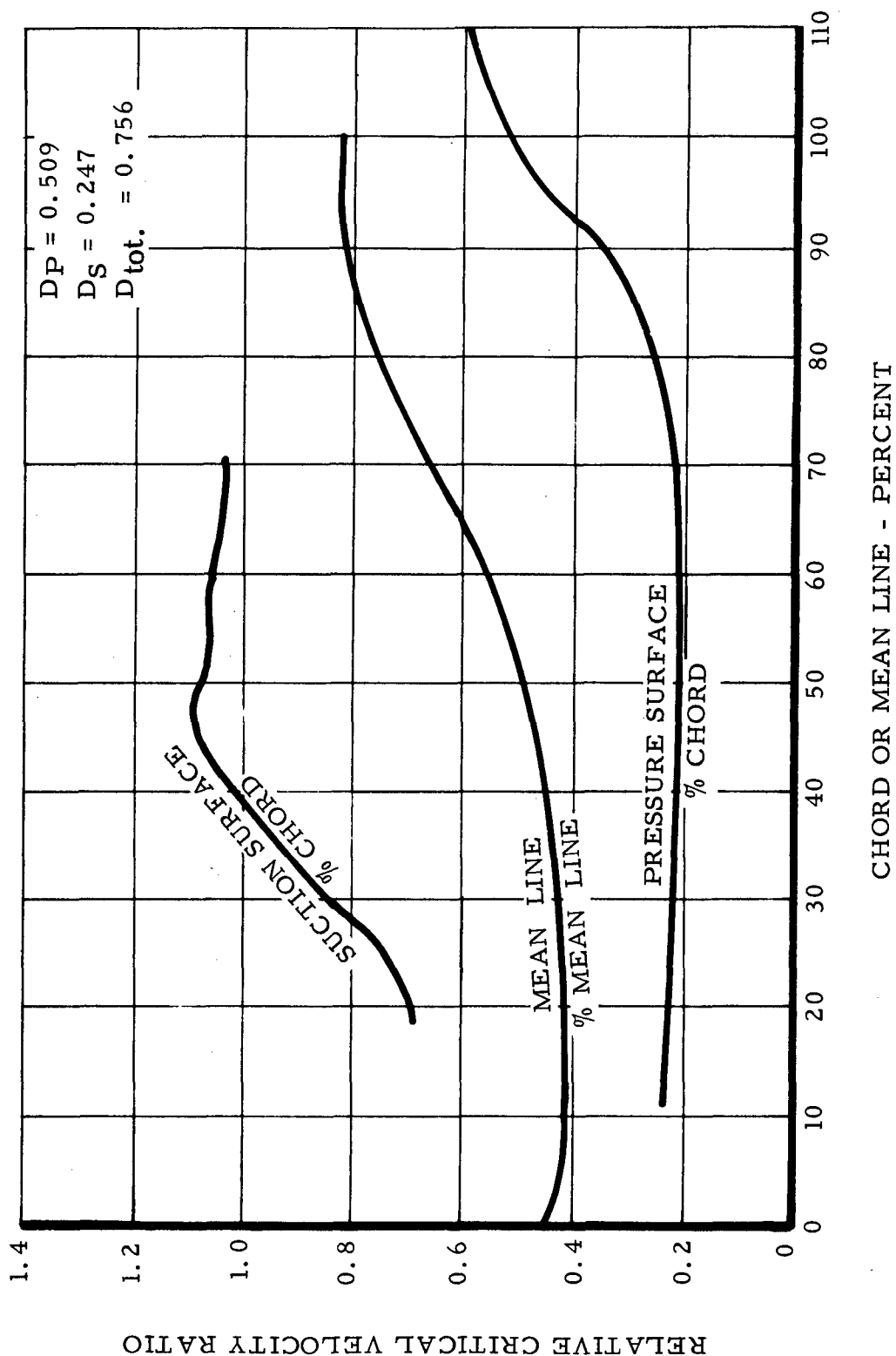


Figure 38. Rotor Hub Section - 12.5 Percent Blade Height - 34 Blades.

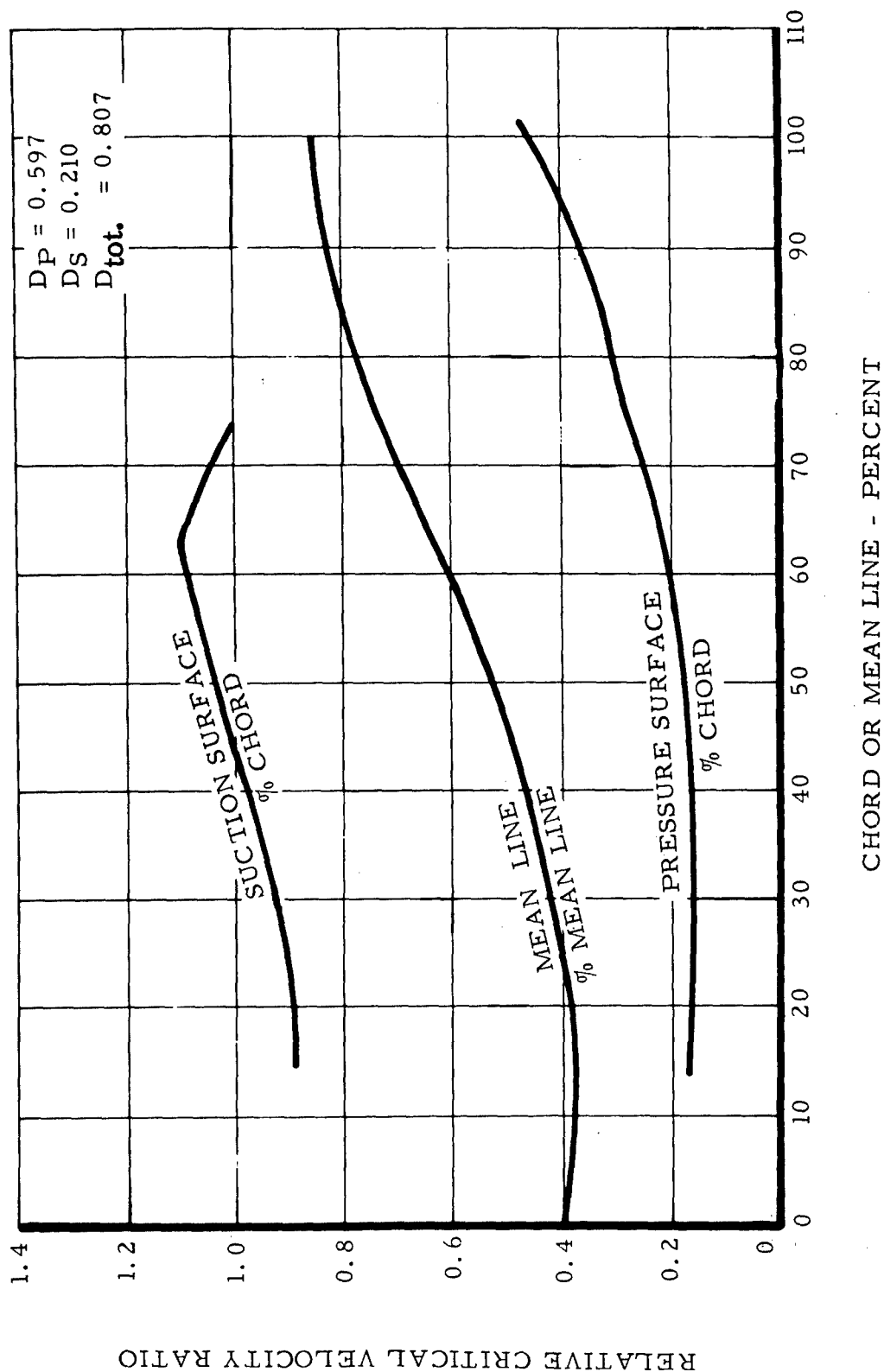


Figure 39. Rotor Mean Section - 50 Percent Blade Height - 34 Blades.

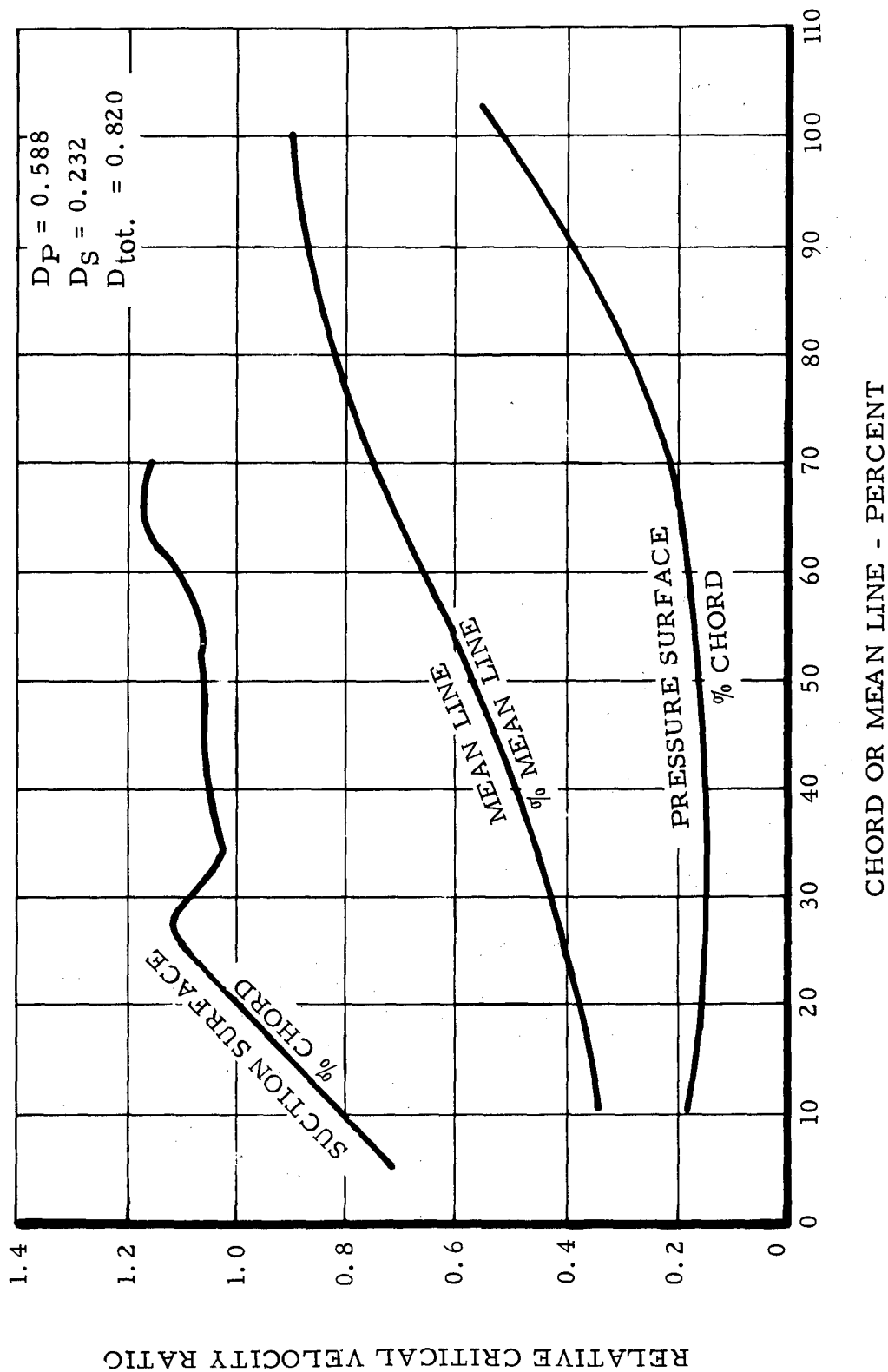


Figure 40. Rotor Tip Section - 87.5 Percent Blade Height.

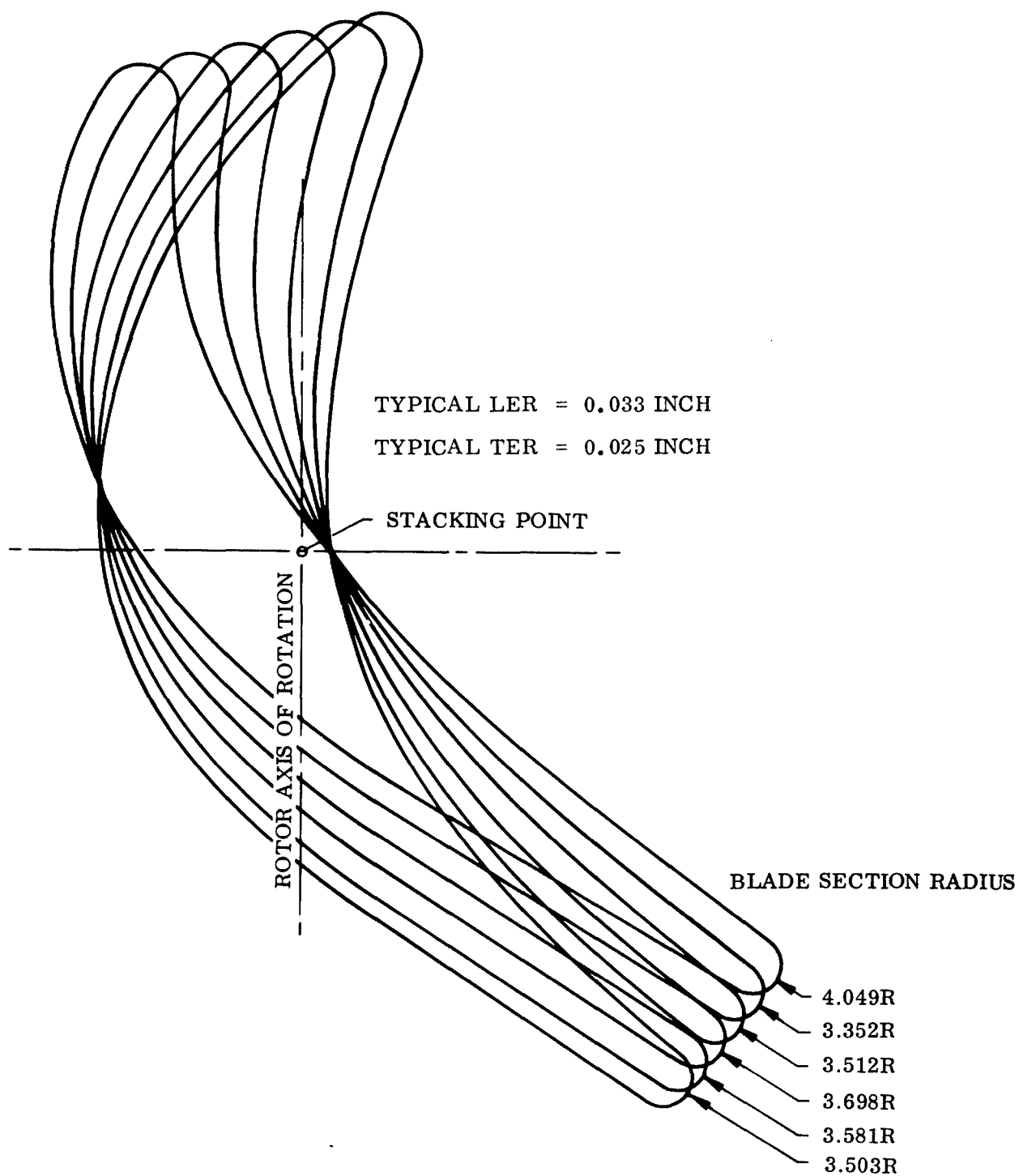


Figure 41. Fluid-Cooled Rotor - 34 Blades.

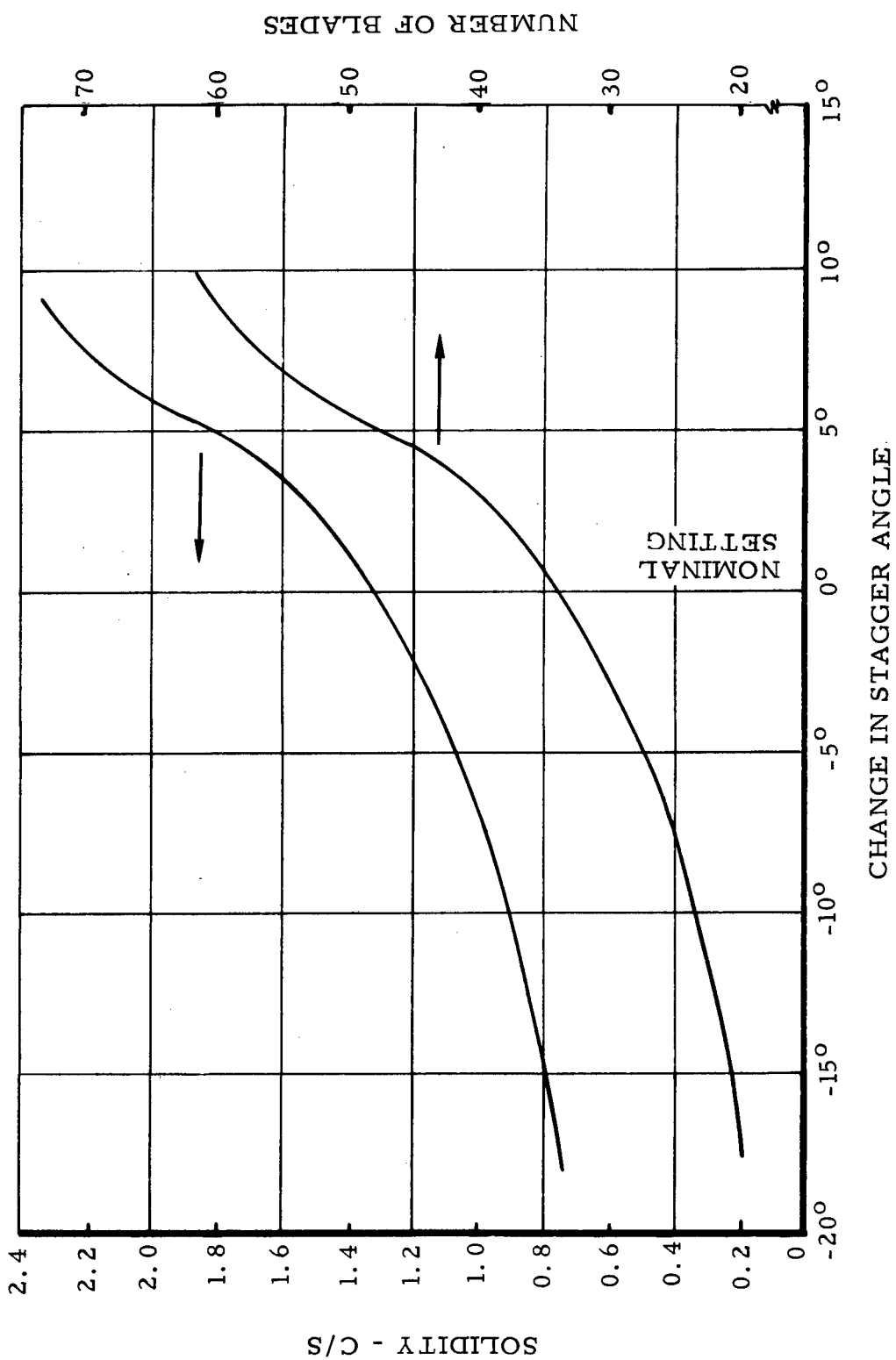


Figure 42. Rotor Stagger Variation With Solidity and Number of Blades.

Table I summarizes the design point data for the nominal turbine; that is, 23 nozzle vanes and 34 rotor blades. The wheel was sized for the regenerated version, since this would constitute the most severe cooling case (lowest fuel flow).

TABLE I TURBINE DESIGN POINT SUMMARY			
	Nonregenerated Version		Regenerated Version
Airflow, lb/sec	5.0		5.0
Compressor Pressure Ratio	9.2:1		9.2:1
Turbine Inlet Temp, °F	2300		2300
Rotative Speed, rpm	50,000		50,000
Corrected Speed, $\frac{N}{\sqrt{\theta_{cr}}}$, rpm	22,060		22,040
Corrected Flow, $\frac{W N}{60} \epsilon$, $\frac{\text{lb} \cdot \text{rev}}{\text{sec}^2}$	513		525
Turbine Work, ΔH , Btu/lb	138.39		138.39
Specific Work, $\frac{\Delta H}{\theta_{cr}}$, Btu/lb	26.94		26.89
Efficiency, total-to-total, percent	86.5		
	Hub	Mean	Tip
Rotor Speed, fps	1529	1665	1800
Reaction, percent	25.6	35.7	43.6
Nozzle Diffusion Factor, Pressure Side, D_p	0.684	0.737	0.789
Nozzle Diffusion Factor, Suction Side, D_s	0.065	0	0
Nozzle Diffusion Factor, Total, D_t	0.749	0.737	0.789
Rotor Diffusion Factor, Pressure Side, D_p	0.509	0.597	0.588
Rotor Diffusion Factor, Suction Side, D_s	0.247	0.210	0.232
Rotor Diffusion Factor, Total, D_{tot}	0.756	0.807	0.820
Rotor Hub-Tip Ratio, $\frac{r_h}{r_t} = 0.850$			
Mean Work Speed Parameter			
$\Omega = \frac{2 g J \Delta H}{U_m^2} = 2.50$			
Mean Rotor Aspect Ratio = 0.67			
Mean Nozzle Aspect Ratio = 0.34			

Efficiency Considerations at Design Point

The predicted total-to-total adiabatic efficiency level of the fluid-cooled turbine by conventional means is about 86.5 percent. Rig testing showed a design efficiency of only 81 percent, indicating inadequacy of the prediction for this application. At the time of the Turbine Proposal, five different efficiency-estimating methods were applied; four of these gave a performance over 86 percent. A Continental computer program yielded a value just under 80 percent. This program, however, used limited extrapolated data that accounted for short-blade secondary losses. In view of the lack of supporting data of the secondary losses and the results of the four calculations, 86.5 percent was taken to be a valid estimate at that time.

The prediction techniques are briefly discussed below along with the Continental method, which gave the best agreement with test data.

Stewart's Method - Reference 12

This technique was developed at NASA to provide a simple, rapid estimate of efficiency from a given set of design parameters. Blade-loss characteristics were related to the turbine mean-section velocity diagrams. The only required inputs to make an efficiency calculation are simply

1. Mean-section velocity triangles
2. Number of stages, n
3. Mean radius, r_m
4. Mass flow, W , and inlet gas viscosity
5. Mean speed-work parameter, $\lambda = \frac{U_m^2}{gJ\Delta H_t}$

where U_m = mean wheel speed, fps

ΔH_t = total-to-total turbine enthalpy drop

6. Empirical constant, K

NASA has found that a value of $K = 0.4$ shows close agreement between experimental and analytical efficiencies on a large number of turbines. The efficiency prediction is considered valid only if the turbine has

"reasonably good surface velocity distributions with a resulting near-optimum solidity, close running and tip clearances, and small trailing edge blockages." Using these assumptions on the design point gives a predicted efficiency of 86.1 percent. Two other unpublished procedures similar to Stewart's yielded predicted efficiencies of 90 and 87.5 percent.

The major shortcoming of this type of analysis is that it is limited to only a given family of turbines having similar geometries. The uniqueness of the size, geometry, and cooling requirements of the fluid-cooled turbine puts this machine in a separate category. The departure from conventional geometry is illustrated in Figure 43. Here, the fluid-cooled turbine is compared to a scaled-down Continental J69-T-39 first-stage gas generator turbine. The two machines have nearly identical mean

speed-work parameters, $\lambda = \frac{U_m^2}{gJ\Delta H_t}$, corrected wheel speeds, $\frac{U_m}{\sqrt{\theta_{cr}}}$,

and flow parameters, $\frac{WN}{860} \epsilon$. The comparatively long blade chords and thick blading for cooling result in high wake, profile, annulus, and secondary losses. A more elaborate efficiency prediction technique is, therefore, necessary to compensate for these factors. A more general approach is that of Ainley (Reference 13).

Ainley and Mathieson Method

The much more cumbersome method of Ainley takes into consideration the effects of a large number of factors on blade rows, such as

1. Profile losses
2. Secondary losses
3. Tip clearance
4. Annulus loss
5. Trailing edge loss
6. Reynolds number
7. Incidence losses
8. Solidity

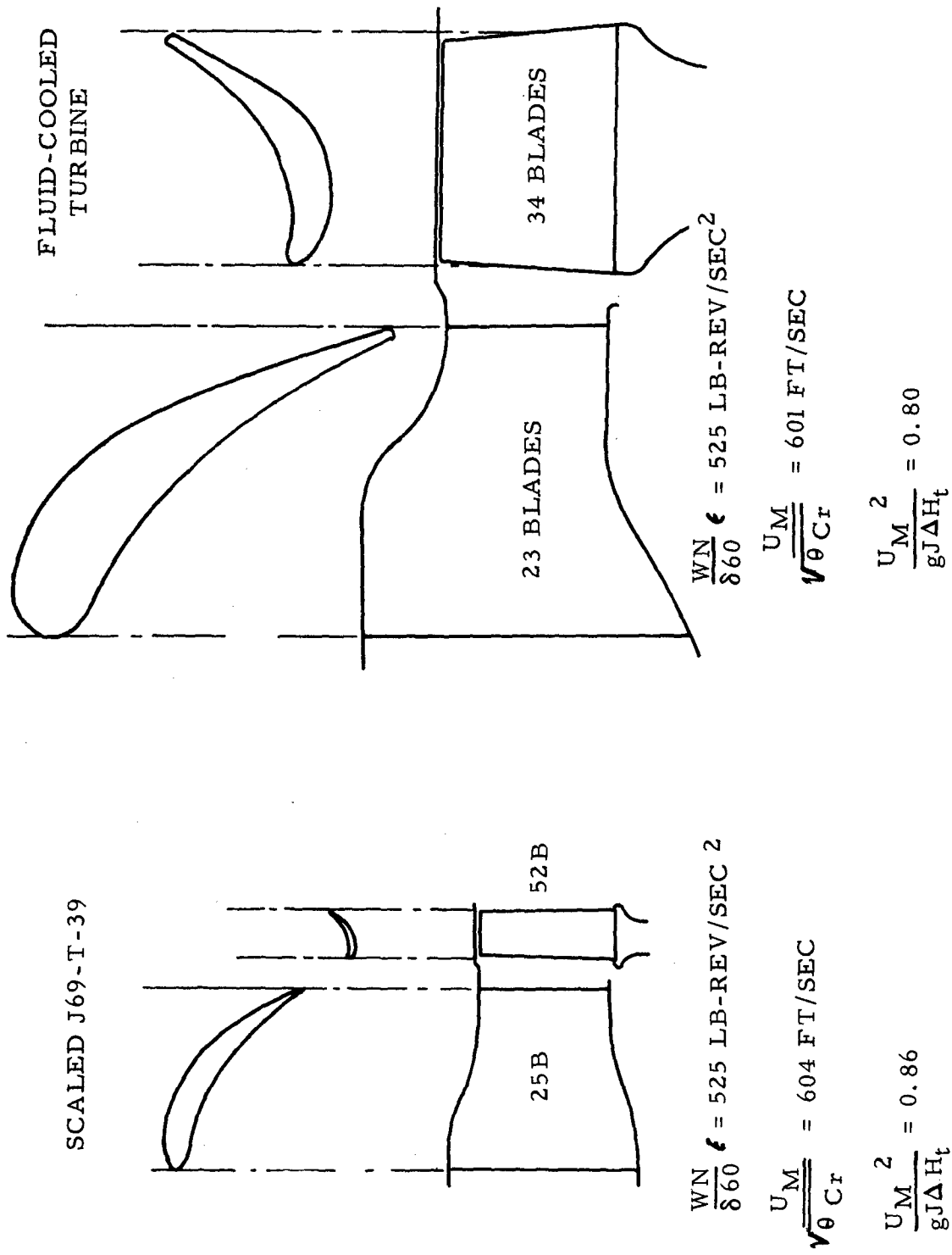


Figure 43. Comparison of Fluid-Cooled Turbine With Scaled J69-T-39 First-Stage Turbine.

The loss data are generalized in the form of a number of semiempirical equations and curves. An accuracy of ± 2 percent on efficiency is attained on the type of blading surveyed in the Ainley analysis.

Using these loss data on the cooled turbine gives an efficiency of 86.5 percent. Several other Continental and NASA turbines were also found to be outside the accuracy band, indicating that further variables must be introduced.

Continental Method

The computerized Continental design point program is essentially an outgrowth and modification of the Ainley blade-loss treatment. Numerous additions and changes have been made to reflect the most recent turbine performance data.

One of the more important modifications that allows a better agreement of predicted to experimental efficiency on short-blade turbines is that of secondary loss treatment. Secondary losses comprise the difference between the total loss and the sum of incidence, profile, clearance trailing edge, and disc losses. Data were accumulated on a number of recent turbine stages, covering a broad range of blade geometries. The information was then correlated as a function of mean deflection angle, pitch opening, blade height, and blade chord. Figure 44 shows a comparison of Continental predicted and experimental efficiencies of 18 different turbines. The range of geometry covered by the analysis is demonstrated by the following parameters:

Blade height	h	= 0.1 to 3.5 in.
Solidity	σ	= 0.97 to 2.6
Aspect ratio	$\frac{h}{c}$	= 0.34 to 3.3
Blade height-to-throat opening ratio	$\frac{h}{o}$	= 1.1 to 5.3
Wheel tip diameter	d	= 4.0 to 22 in.
Flow parameter	$\frac{WN}{860} \epsilon$	= 54 to 3700 $\frac{\text{lb-rev}}{\text{sec}^2}$
Single-stage specific work	$\frac{\Delta H}{\theta_{cr}}$	= 8.8 to 29 $\frac{\text{Btu}}{\text{lb}}$

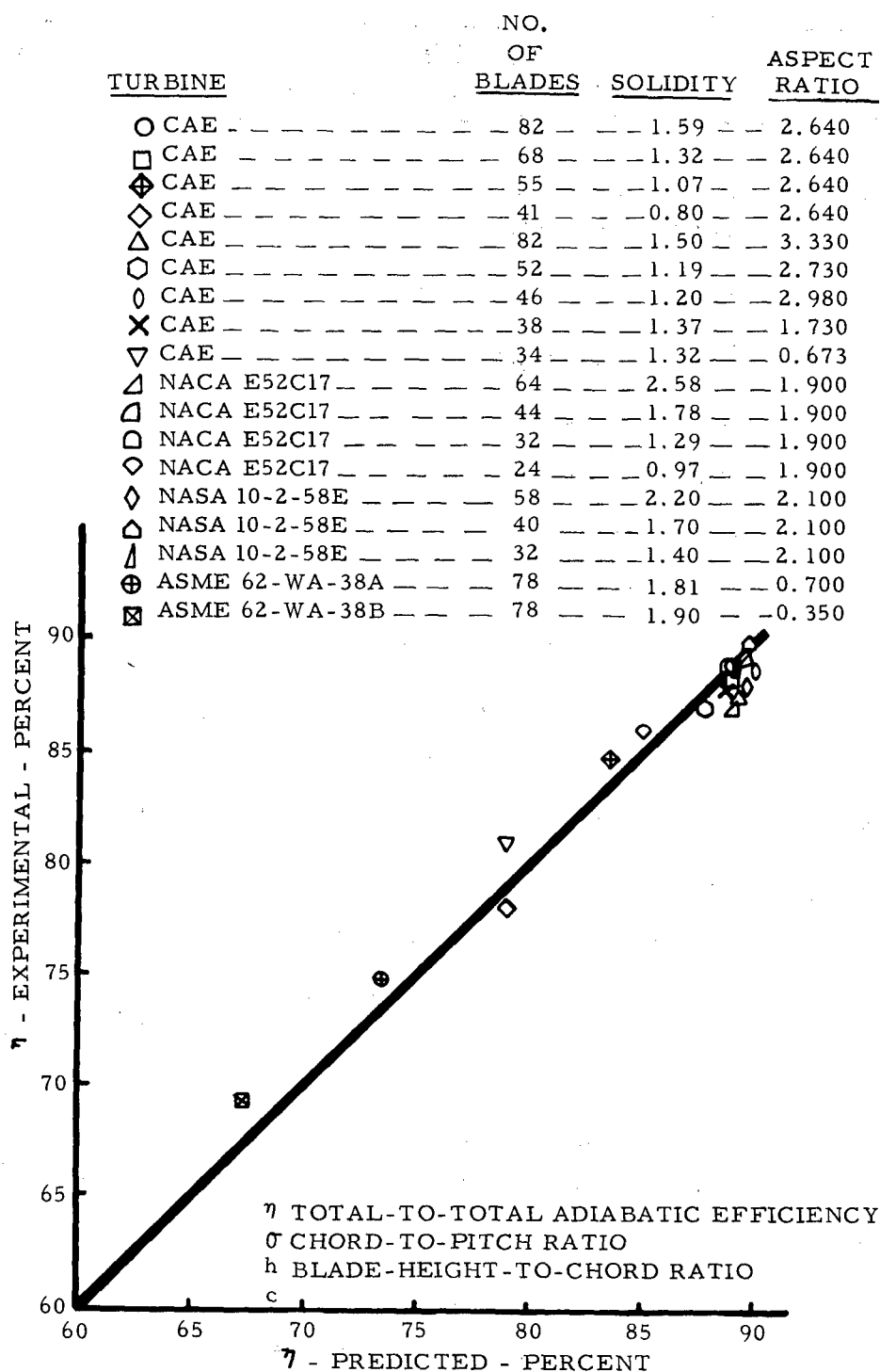


Figure 44. Comparison of CAE Predicted and Experimental Turbine Efficiencies.

The predicted design point efficiency is calculated from the data in Table II.

TABLE II DESIGN POINT EFFICIENCY INPUT		
		Design Point
ω	= Rotation speed, rpm	50,000
ΔH	= Total-to-total enthalpy drop, $\frac{\text{Btu}}{\text{lb}}$	138.4
T_1	= Inlet total temperature, $^{\circ}\text{R}$	2760
P_1	= Nozzle inlet total pressure, psia	124.2
r_m	= Mean rotor radius, in.	3.815
i_n	= Mean nozzle incidence angle, deg	0.0
i_r	= Mean rotor incidence angle, deg	0.0
A_1	= Inlet nozzle annulus area, in. ²	27.594
A_5	= Exit nozzle annulus area, in. ²	13.519
A_9	= Exit rotor annulus area, in. ²	14.958
f/a	= Fuel-air ratio	0.030
W_g	= Gas flow, lb/sec	5.095
β_1	= Nozzle inlet gas angle at mean, deg	0.0
$V_{\theta 9}$	= Tangential velocity at rotor discharge mean, fps/sec	0.0
b_n	= Nozzle cascade axial width, in.	1.10
b_r	= Rotor cascade axial width, in.	0.820
t_{en}	= Nozzle trailing edge thickness, in.	0.050
t_{er}	= Rotor trailing edge thickness, in.	0.050
n_n	= Number of nozzle vanes	23
n_r	= Number of rotor blades	34
$(t/c)_n$	= Mean thickness-chord ratio of nozzle vane	0.20
$(t/c)_r$	= Mean thickness-chord ratio of rotor blade	0.174
k_n	= Nozzle tip and/or hub clearance, in.	0.0
k_r	= Rotor tip clearance, in.	0.010

A blade internal loss breakdown at 100 percent and 50 percent engine power operating conditions is given in Table III. Losses are given in terms of pressure coefficients defined as

$$Y = \frac{P_i - P_o}{P_o - p_o} \quad (7)$$

where

P_i = Inlet blade relative stagnation pressure

P_o = Outlet blade relative stagnation pressure

p_o = Outlet blade static pressure

The loss distribution at 100 percent and 50 percent power is essentially unchanged. This occurs because of nearly identical operating points on the gas generator turbine map. Whereas the gas generator mechanical speed is reduced to 88 percent and actual work drops 22 percent, the referred speed remains at 97.5 percent, and specific work drops only 3.1 percent of design. The net effect is that the gas generator turbine operates very close to its design point and performance is not sacrificed. The operating conditions at 50 percent power are based on a fixed geometry machine operating along a minimum specific fuel consumption line.

COLD FLOW TESTING

Several versions of the turbine were cold flow tested to substantiate design and to evaluate the effects of nozzle and rotor solidity and trailing edge thickness. The turbine test stand used for this purpose is pictured in Figures 45 through 47. Eight different turbine configurations were evaluated. The geometries are given in Table IV. Rotor blading was mounted on a split disc with spacer rings to change solidity and stagger angle. Inlet and exhaust valves to the rig control the flow and pressure conditions, and power is absorbed via a water dynamometer. Instrumentation diagrams are given in Figures 48 and 49.

Summary

The base line design, that is, 23 nozzle vanes and 34 rotor blades, demonstrated the best performance with a peak efficiency island of 82 percent. Solidity tests on nozzle and rotor verified that the optimum number of blades was used in both rotor and nozzle. Indicated performance

TABLE III
INTERNAL LOSS BREAKDOWN OF GAS GENERATOR TURBINE

Engine Power Rating, Percent	100	50		
Specific Work, $\Delta H/\theta_{cr}$, Btu/lb	26.9	26.1		
Actual Work, ΔH , Btu/lb	138.4	108.1		
Referred Speed, $N/\sqrt{\theta_{cr}}$, rpm	22,040	21,500		
Mechanical Speed, N, rpm	50,000	43,796		
Turbine Inlet Temperature, $^{\circ}\text{R}$	2760	2225		
Total-to-Total Efficiency, N_t	0.81	0.81		
Blade Type	<u>Nozzle</u>	<u>Rotor</u>	<u>Nozzle</u>	<u>Rotor</u>
Blade Outlet Angle	69.4	54.8	69.4	54.8
Blade Camber	69.4	85.2	69.4	85.2
Pitch Chord Ratio	0.636	0.761	0.636	0.761
Profile Loss Coefficient, Y_p	0.043	0.040	0.043	0.040
Secondary Loss Coefficient, Y_s	0.084	0.266	0.084	0.266
Clearance Loss Coefficient, Y_k	0	0.038	0	0.038
Trailing Edge Loss Coefficient, Y_{TE}	0.047	0.061	0.046	0.061
Total Loss Coefficient, $Y_{tot.}$	0.174	0.41	0.173	0.41

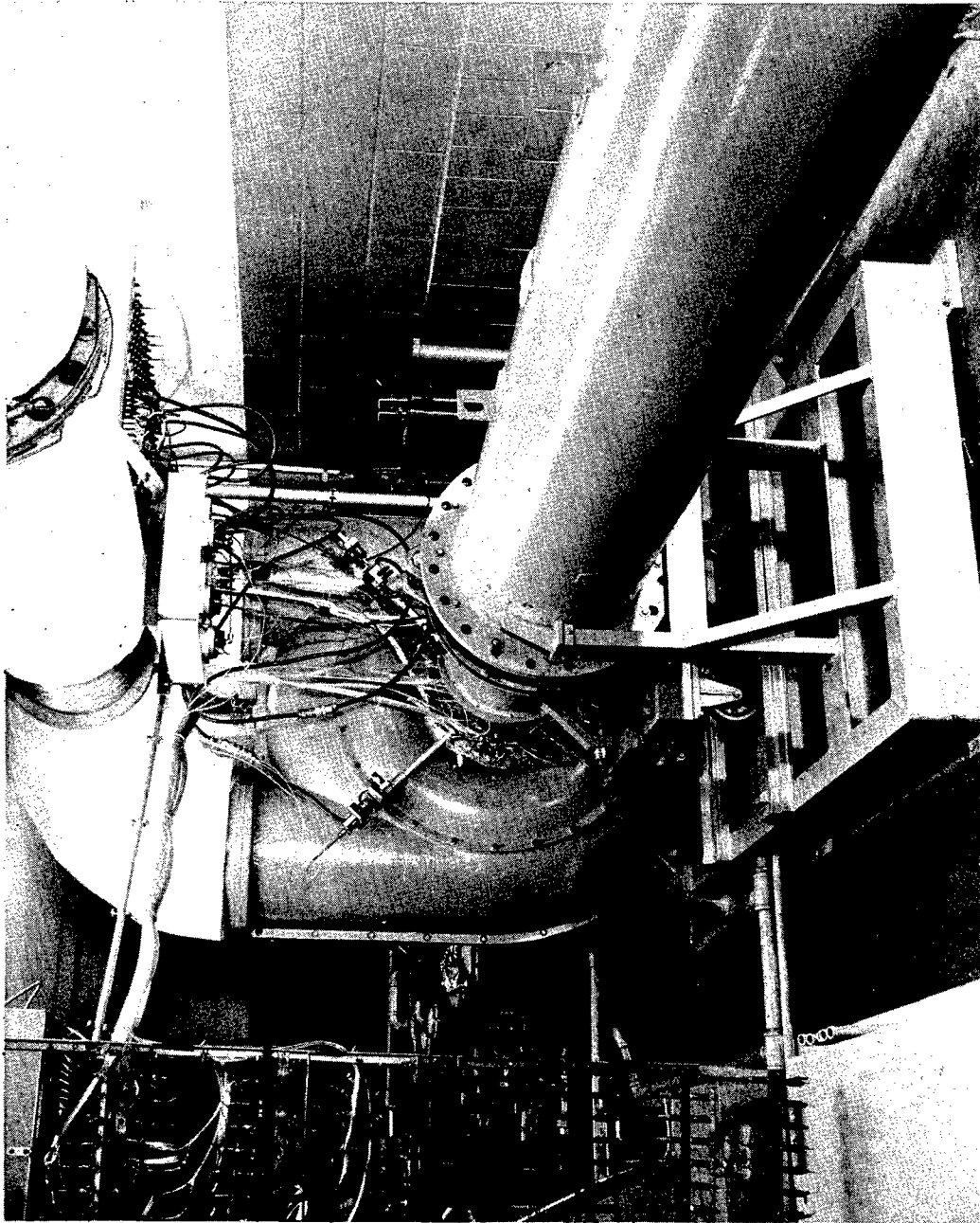


Figure 45. Front View of Turbine Test Stand.

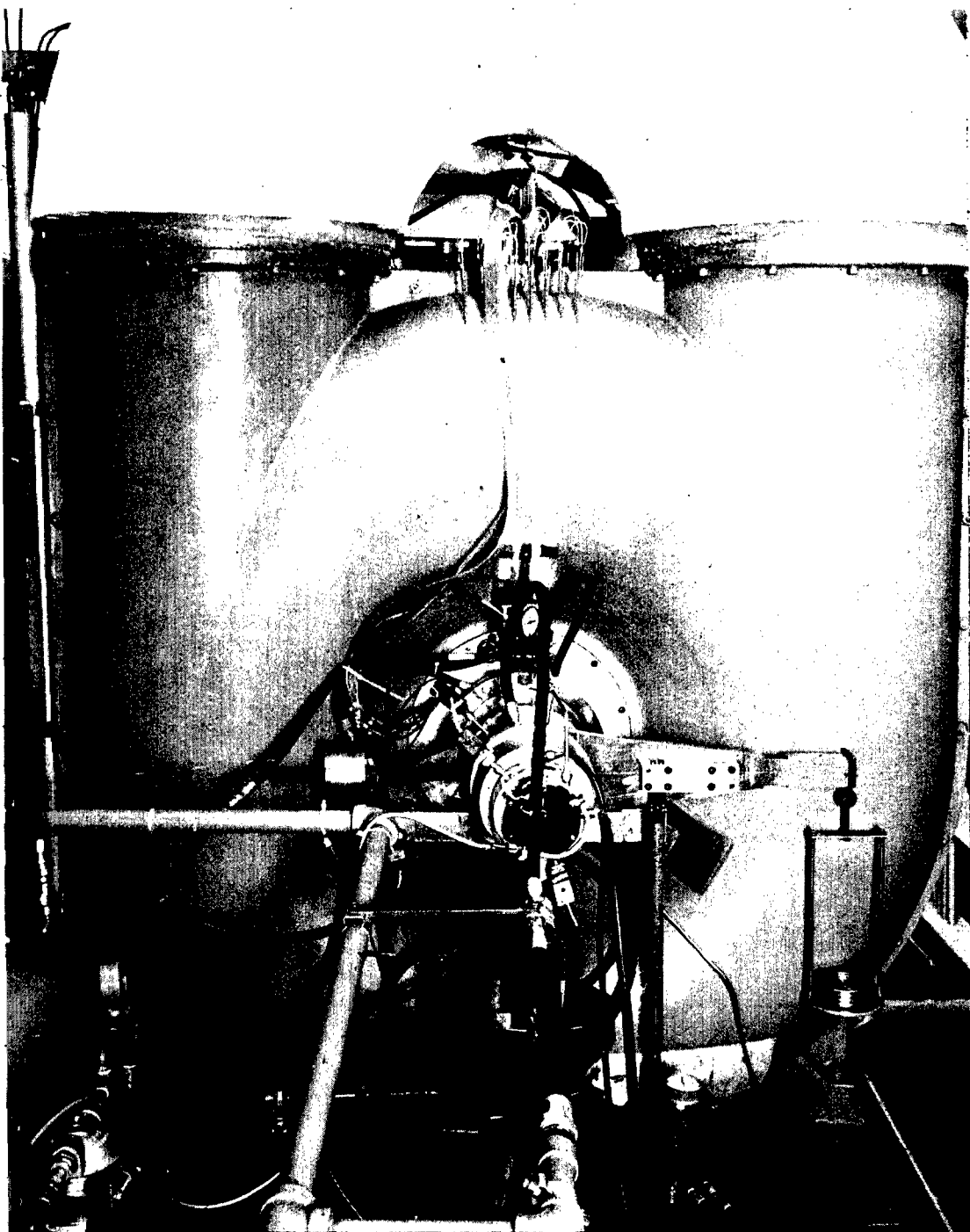
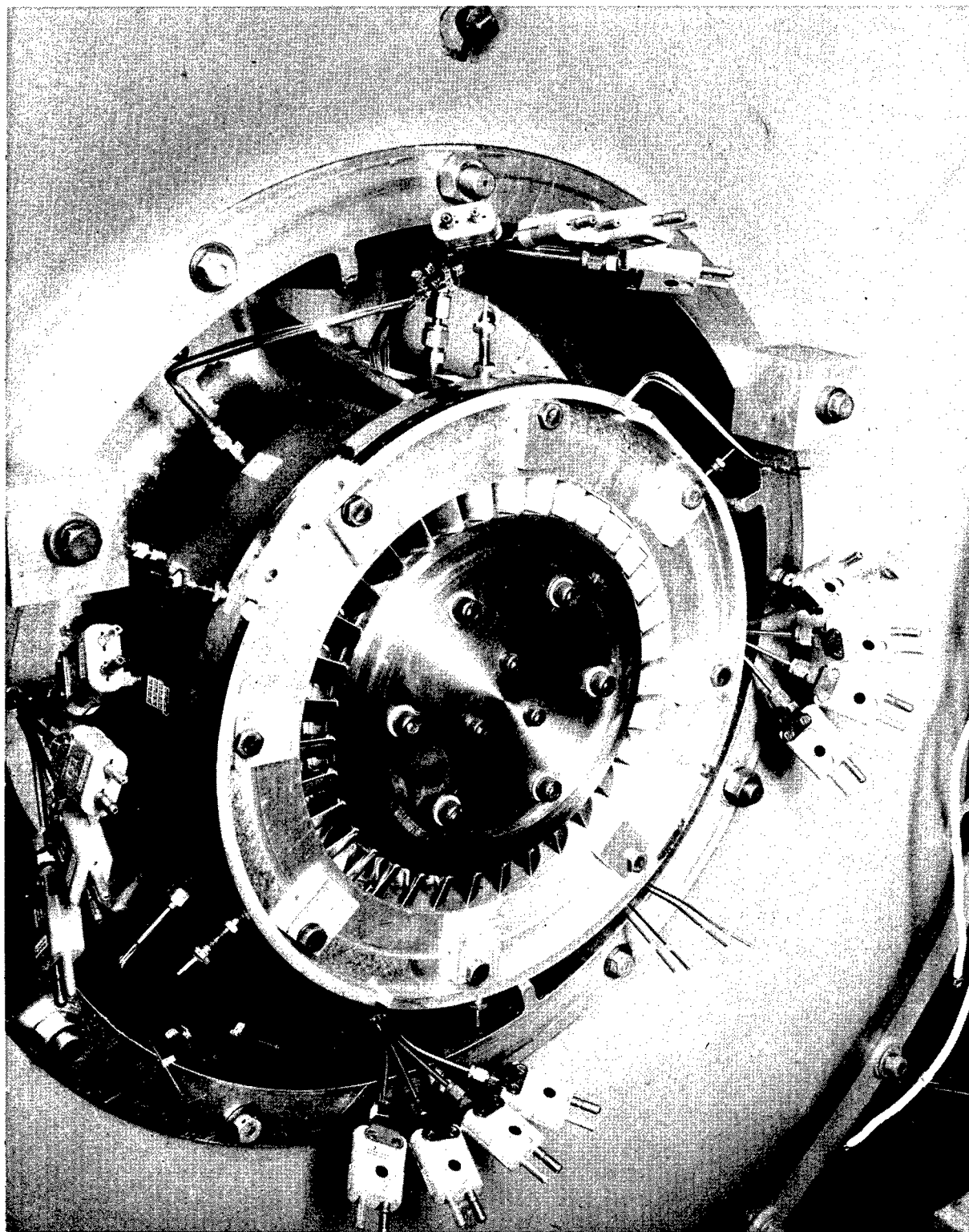


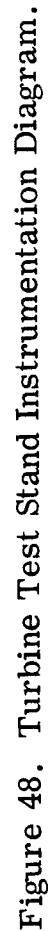
Figure 46. Rear View of Turbine Test Stand.



**Figure 47. Cold Flow Turbine Test Assembly Installation
Turbine Test Stand.**

TABLE IV
SUMMARY OF COLD FLOW TURBINE AERODYNAMICS

Configuration	No. of Nozzle Vanes	Nozzle Stagger Angle	No. of Rotor Blades	Rotor Stagger Angle	Nozzle Trailing Edge Thickness	Rotor Trailing Edge Thickness
1	23	Nominal	40	3° Open	Nominal 0.050	Nominal 0.050
2	23	Nominal	34	Nominal	Nominal 0.050	Nominal 0.050
3	23	Nominal	28	5° Closed	Nominal 0.050	Nominal 0.050
4	23	Nominal	22	12° Closed	Nominal 0.050	Nominal 0.050
5	23	Nominal	34	Nominal	Nominal 0.050	0.020
6	23	2° Closed	34	Nominal	Nominal 0.050	Nominal 0.050
7	17	2.8° Closed	34	Nominal	Nominal 0.050	Nominal 0.050
8	17	2.8° Closed	34	3° Open	0.020	Nominal 0.050



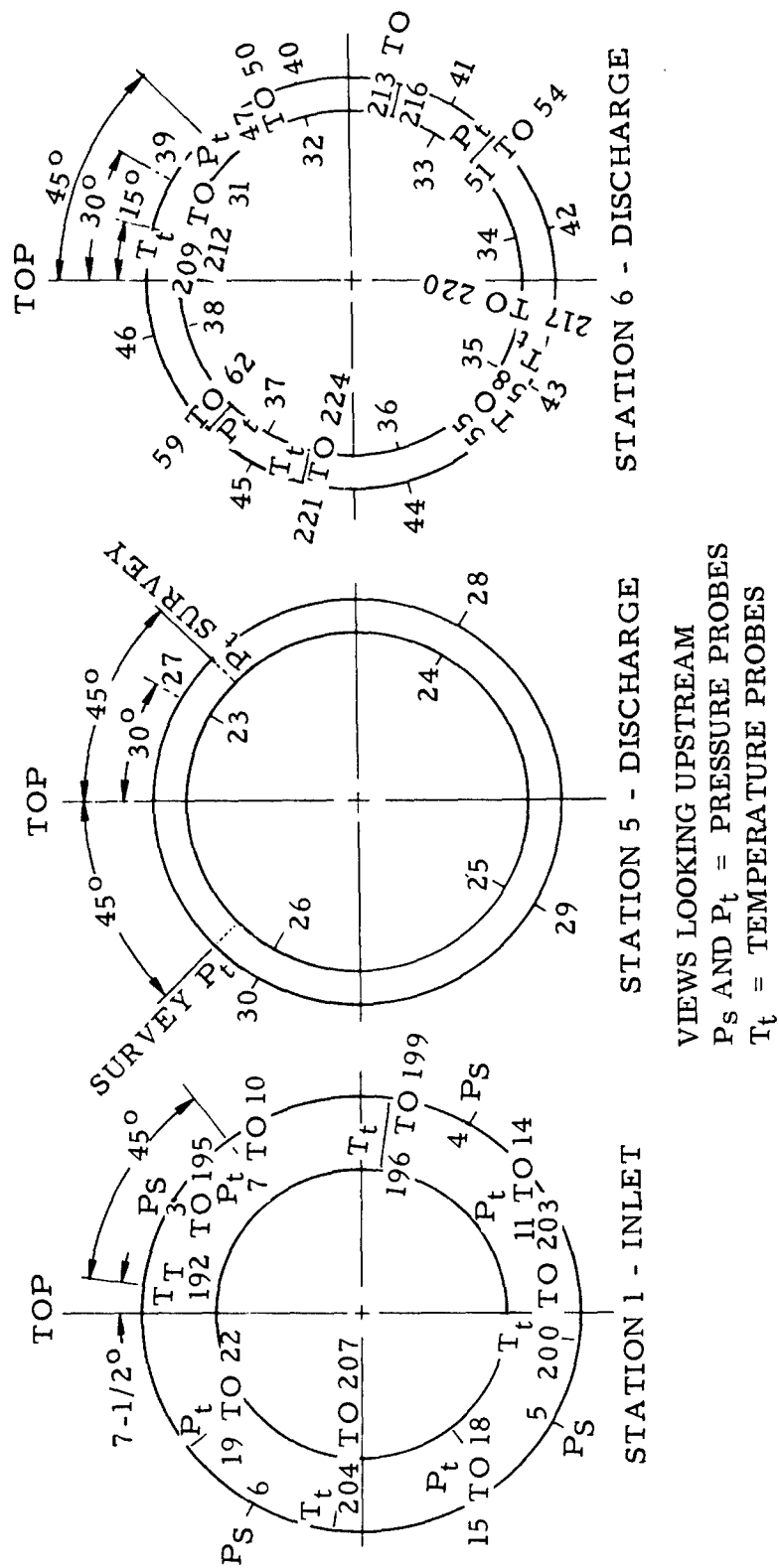


Figure 49. Turbine Test Stand Circumferential Instrumentation Diagram.

gain due to thin nozzle trailing edges is 0.5 percent for a decrease to 0.020 inch from 0.050 inch. No improvement was shown on the rotor because of increased diffusion rates resulting from the simplified method of thinning the trailing edges. Redesign of profiles is necessary to realize gains for thinner rotor blades.

Design objective efficiency was not met on the nominal geometry. A review of efficiency prediction techniques shows inadequacies for short-blade turbines (see Efficiency Considerations at Design Point, page 70). It is concluded that the design objective of 86.5 percent was optimistic for this type of short-blade turbine. Examination of the trade-off between efficiency and temperature, Figure 50, shows that the objective of 213 BHP/lb air/sec can be met by running at a turbine inlet temperature 50°F higher, or at 2350°F.

Nominal Design

The base line design consists of the 23-vane nozzle assembly and 34 rotor blades. The two components are shown in Figures 51 and 52. The overall performance map is given in Figure 53. A peak efficiency of 82 percent was attained at design referred speed of 22,040 rpm. Lines of average discharge whirl are also superposed on the map.

The objective of axial discharge was attained at the design work and referred speed point. Figure 54 presents the spanwise distribution of exit whirl and total pressure surveyed nearest this point. Pressure and angle gradients were found to be small except in the tips where rotor clearance effects predominate.

The inner and outer walls of the nozzles were instrumented to verify that no separation was taking place. Figure 55 substantiates the design. A sharp increase in static pressure is evidenced on the inner wall on the next to last data point. This occurred because the last static tap was located just downstream of the trailing edge where the flow area increases suddenly.

Flow capacity of this turbine geometry was found to be higher than design. Reexamination of inspection reports and drawings revealed the following factors, which account for the flow capacity increase:

1. Nozzle stagger angle was found to be open about one-half of a degree - accounting for 3.5 percent flow increase.
2. Six of nine rotor blades inspected were found to be an average of 0.008 inch too thin in the trailing edge of the upper third of the blade. This results in larger throat areas.

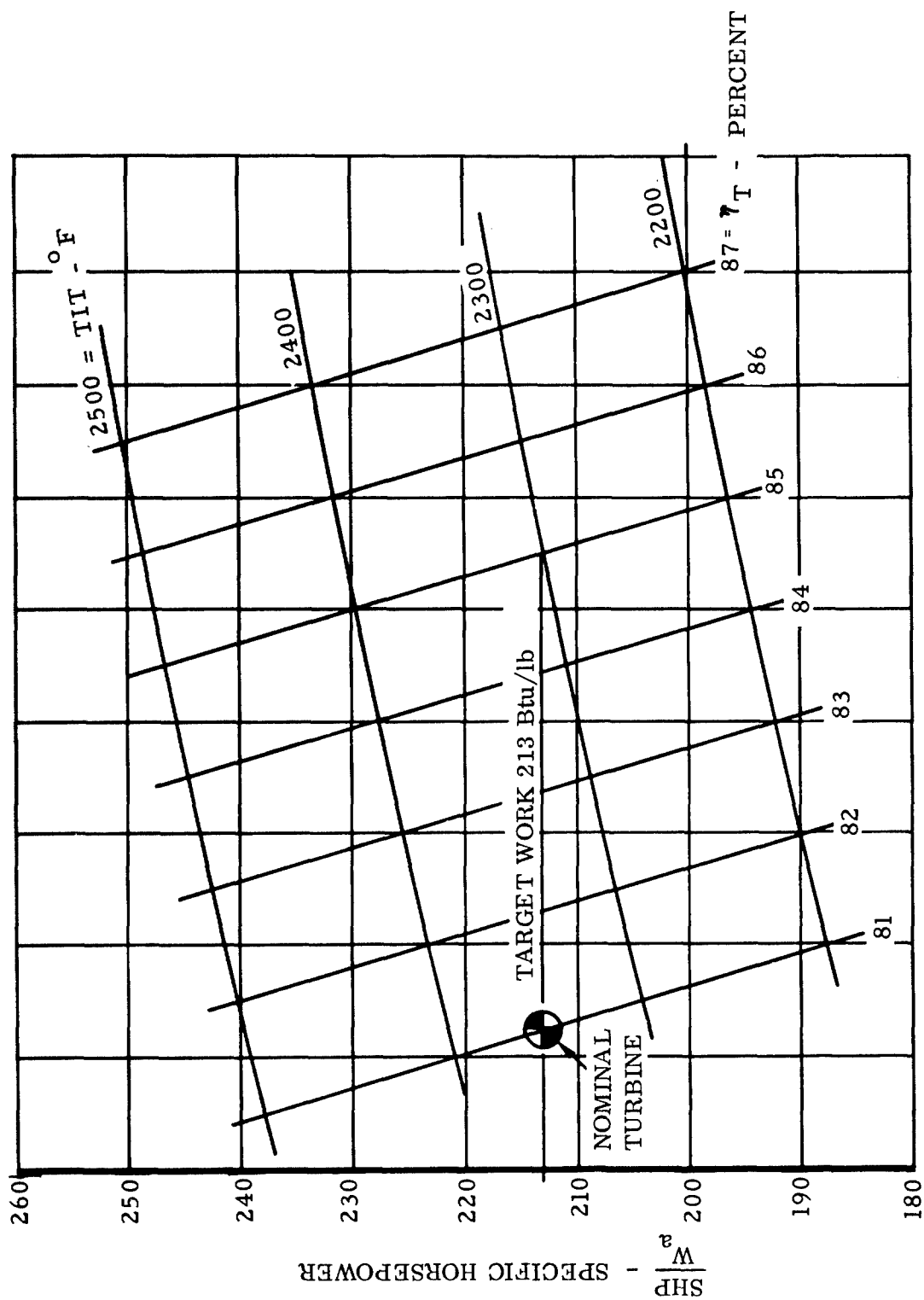


Figure 50. Effect of Turbine Inlet Temperature and Turbine Efficiency on Specific Horsepower.

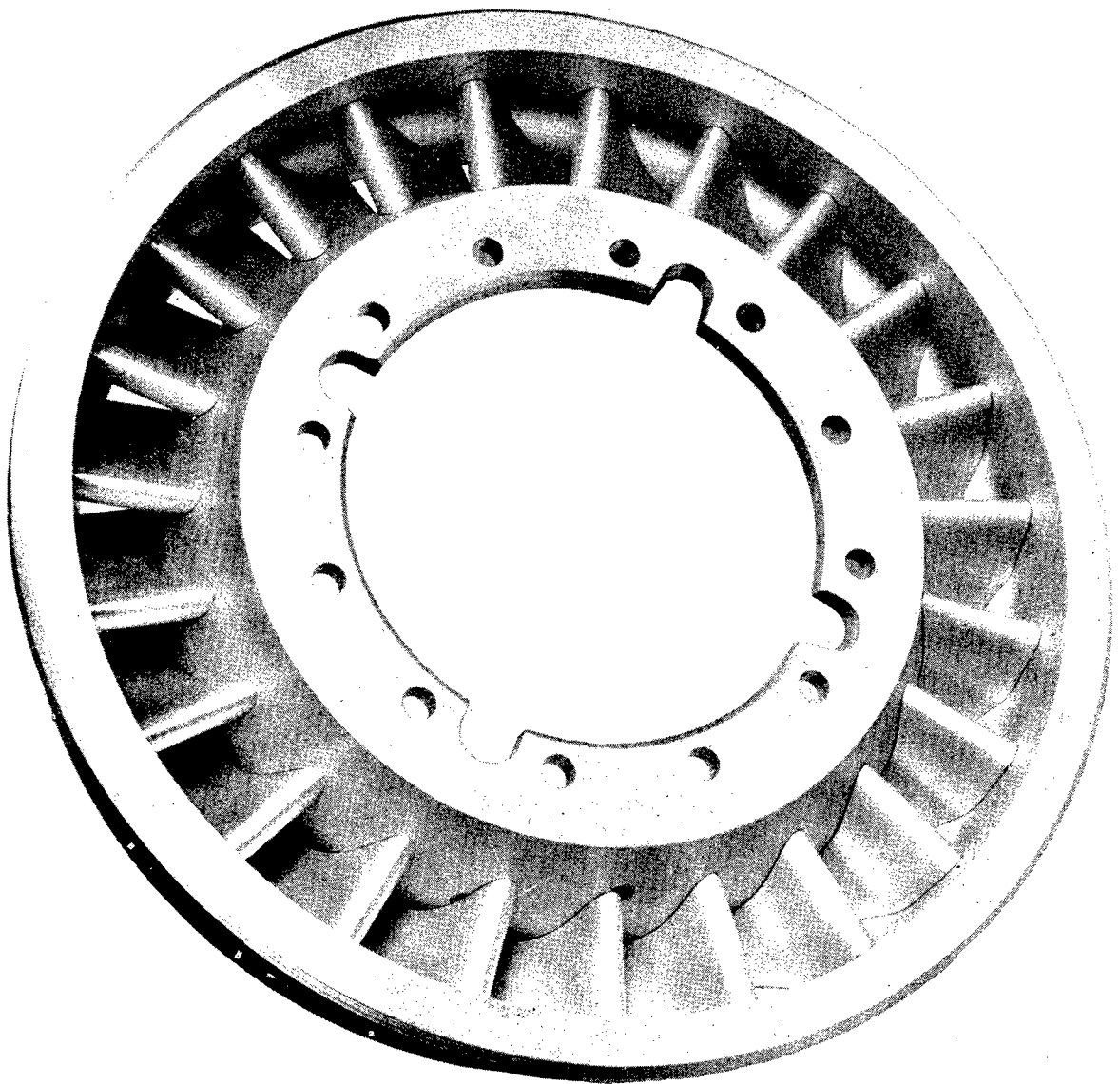
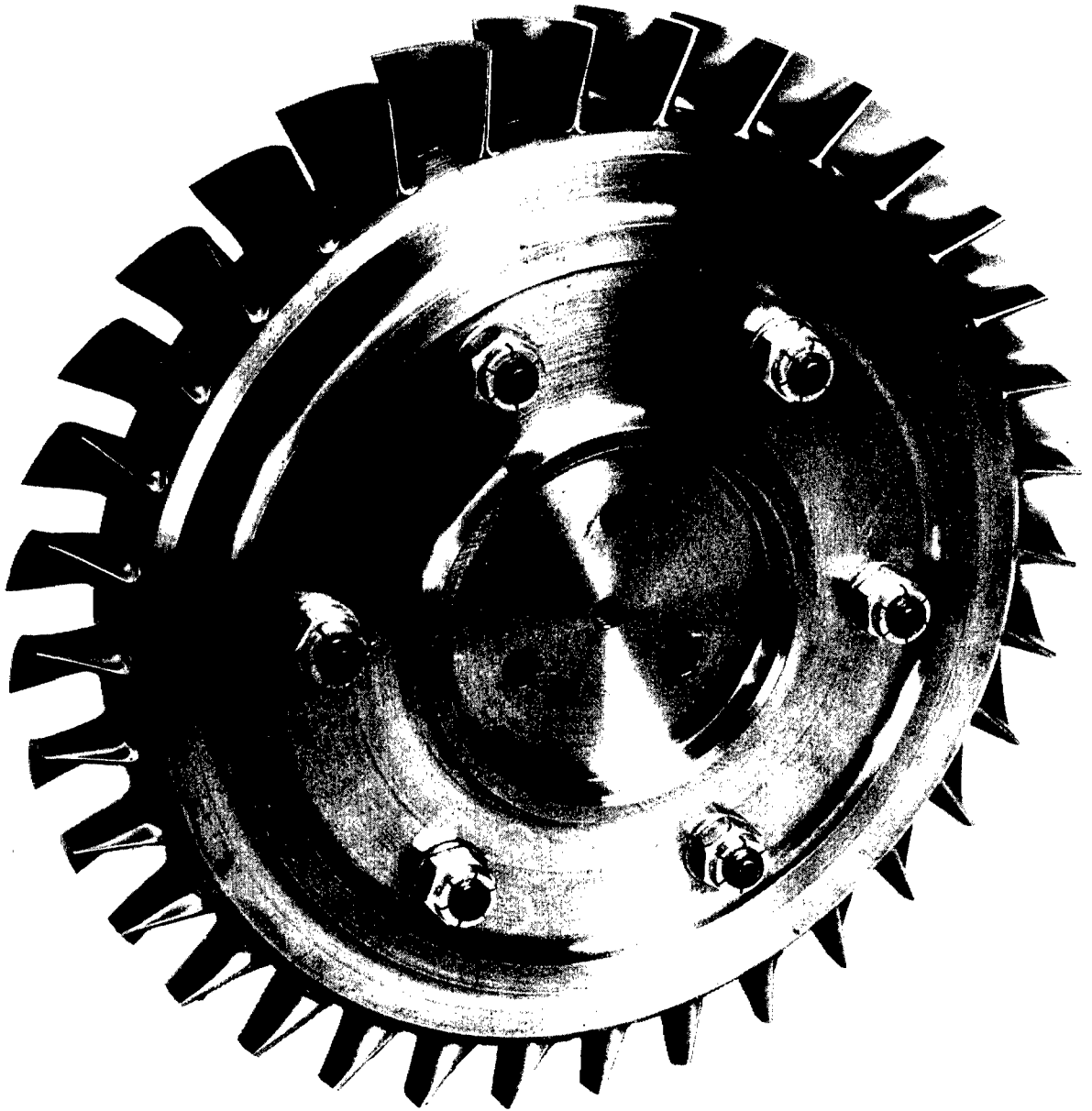
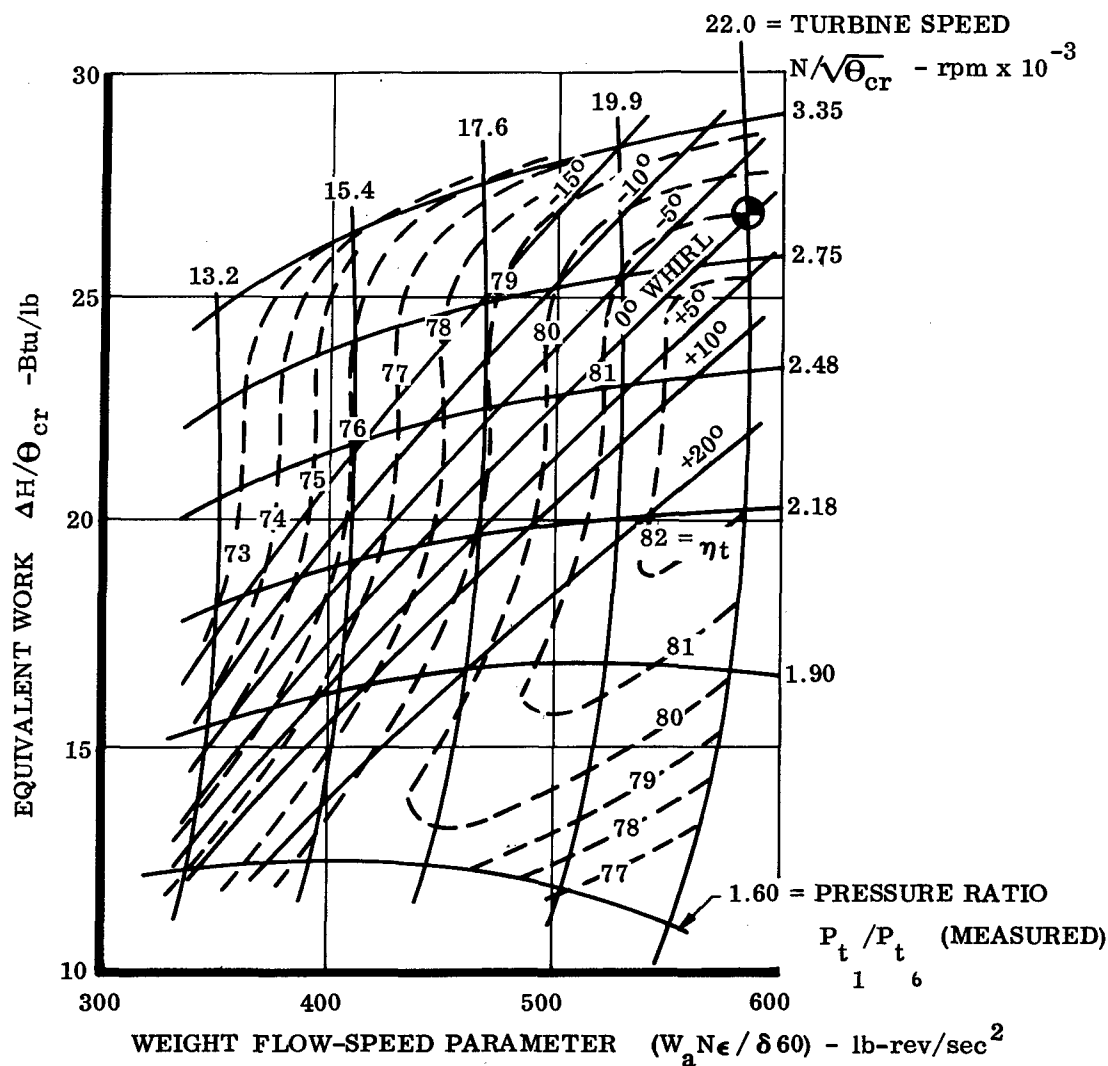


Figure 51. Cold Flow Turbine Inlet Nozzle Assembly - View Looking Downstream.



**Figure 52. Cold Flow Turbine Rotor Assembly -
View Looking Downstream.**



⊕ DESIGN WORK $\frac{\Delta H}{\theta_{cr}} = 26.9$ Btu/lb

DESIGN SPEED $N/\sqrt{\theta_{cr}} = 22,040$ rpm

CONFIGURATION

34 ROTOR BLADES, P/N 2490-20-0089
 SET AT NOMINAL STAGGER ANGLE.
 23 TURBINE INLET NOZZLE VANES
 P/N 249020-0086, SET AT 46° 50'
 DIAL SETTING

Figure 53. Fluid-Cooled Turbine - Test Stand Performance.

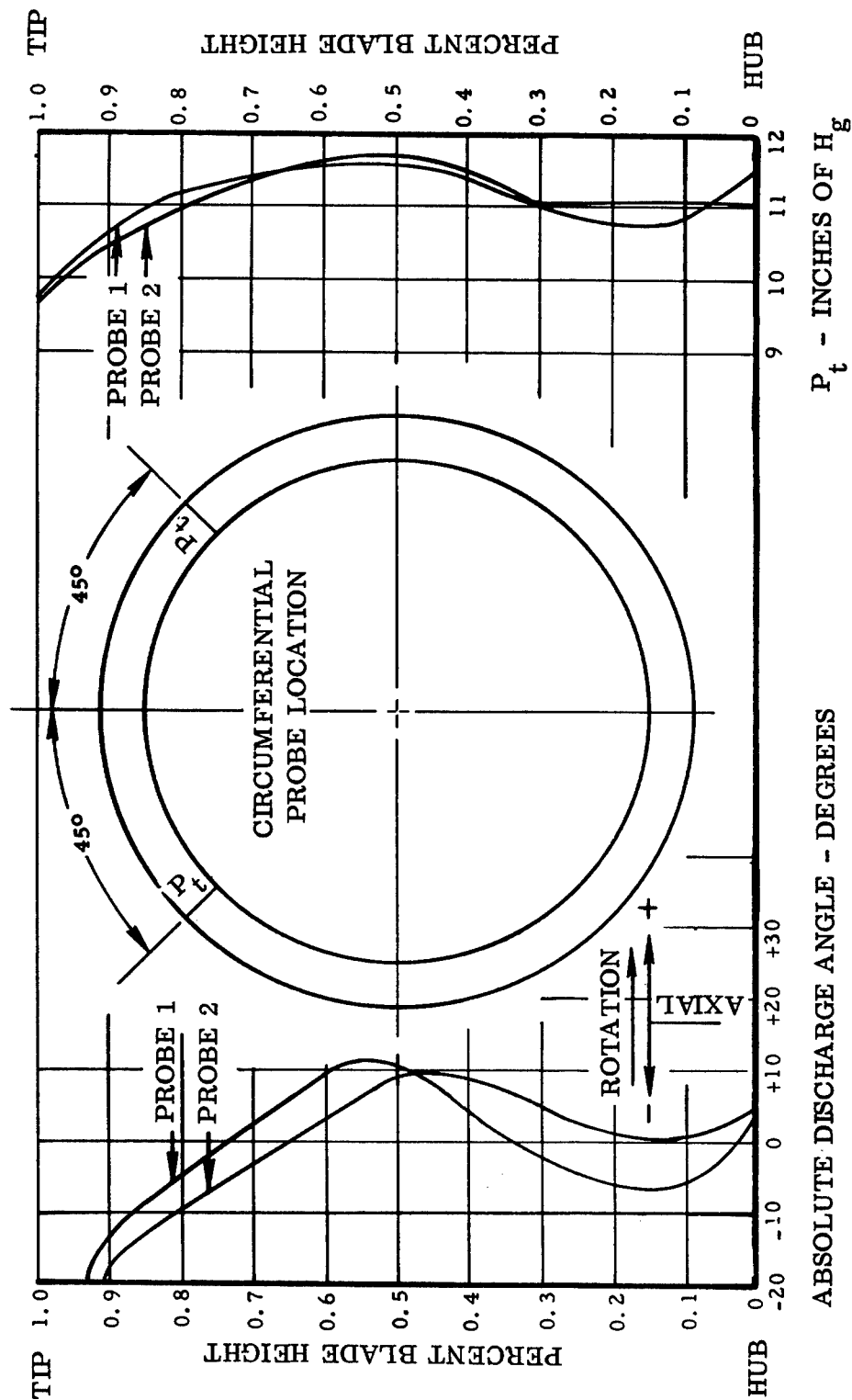


Figure 54. Rotor Exit Characteristics - 23 Vanes, 34 Blades.

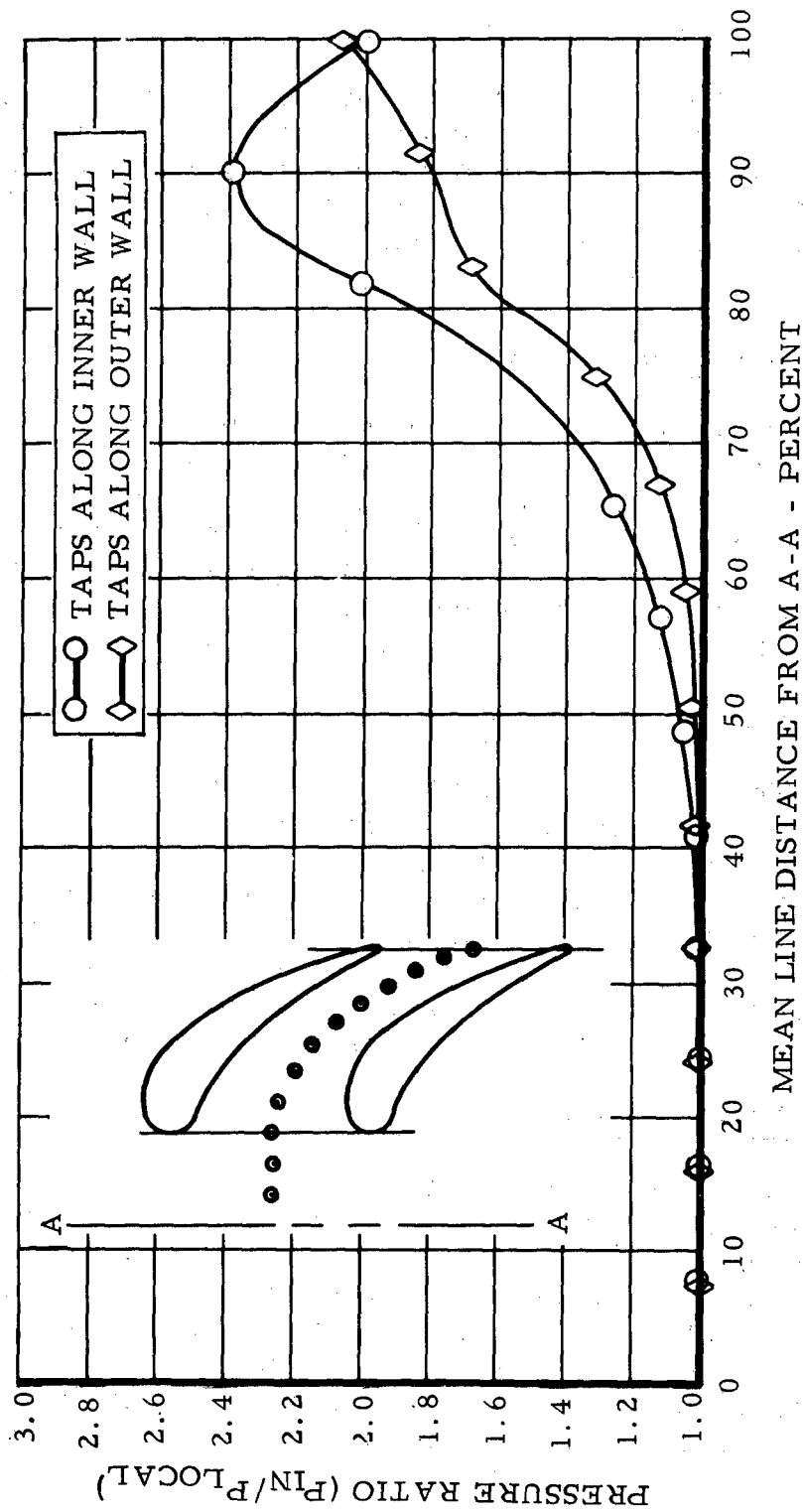


Figure 55. Nozzle Pressure Characteristics - 23 Vanes Set Nominally.

3. There was a step of 0.030 inch on the rotor disc to allow assembly of the spherical variable geometry blading. This allows a leakage path in the rotor hubs which increases flow capacity and decreases performance.

To account for some of these factors, the 23-vane nozzle assembly was restaggered, closed 2 degrees, and the rotor hubs were filled in with epoxy. Figure 56 gives the performance and shows that design flow was attained but at a reduced efficiency level of 77 percent. Efficiency deterioration is due to nozzle and rotor mismatch and would not be expected in the turbine made to print.

Rotor Solidity Tests

The rotor was tested with the nominal nozzle at four solidities corresponding to 40, 34, 28, and 22 blades. Overall performance maps are given in Figures 53 and 57 through 59. The effects of the design work and speed are summarized in Figure 60. Peak performance is attained with the nominal design. A loss of 2.6 percent occurs if the blade number is reduced to 31. If the number of blades is reduced to less than 28, design work cannot be attained because of rotor limit loading.

Nozzle Solidity Tests

The number of blades in the nozzle was reduced from a nominal 23 to 17 and was tested with the nominal rotor. At the design work and speed, efficiency dropped 1-1/2 points (see Figure 61). Wall static tap data on the nozzle, Figure 62, show a uniform decrease of static pressure with no separation evident. A comparison of static-pressure decrease on the outer wall of 17- and 23-vane nozzles is given in Figure 63. In view of the similarities of the two configurations, the loss increase is directly attributable to increased vane loadings arising from lower solidity.

Nozzle Trailing Edge Effects

Nozzle and rotor trailing edge effects were evaluated separately. To accomplish this with minimal effort and expenditure, the existing blading was reworked. Blade loadings and velocity levels were kept similar by maintaining the nozzle-to-throat area ratio constant. Figure 64 describes the modified blading of the nozzle. By referring to Table IV, configuration No. 8 was tested for nozzle trailing edge effect. The trailing edge thickness was reduced from 0.050 to 0.020 inch. Overall performance is given in Figure 65. At design work and speed conditions, the performance was essentially unchanged.

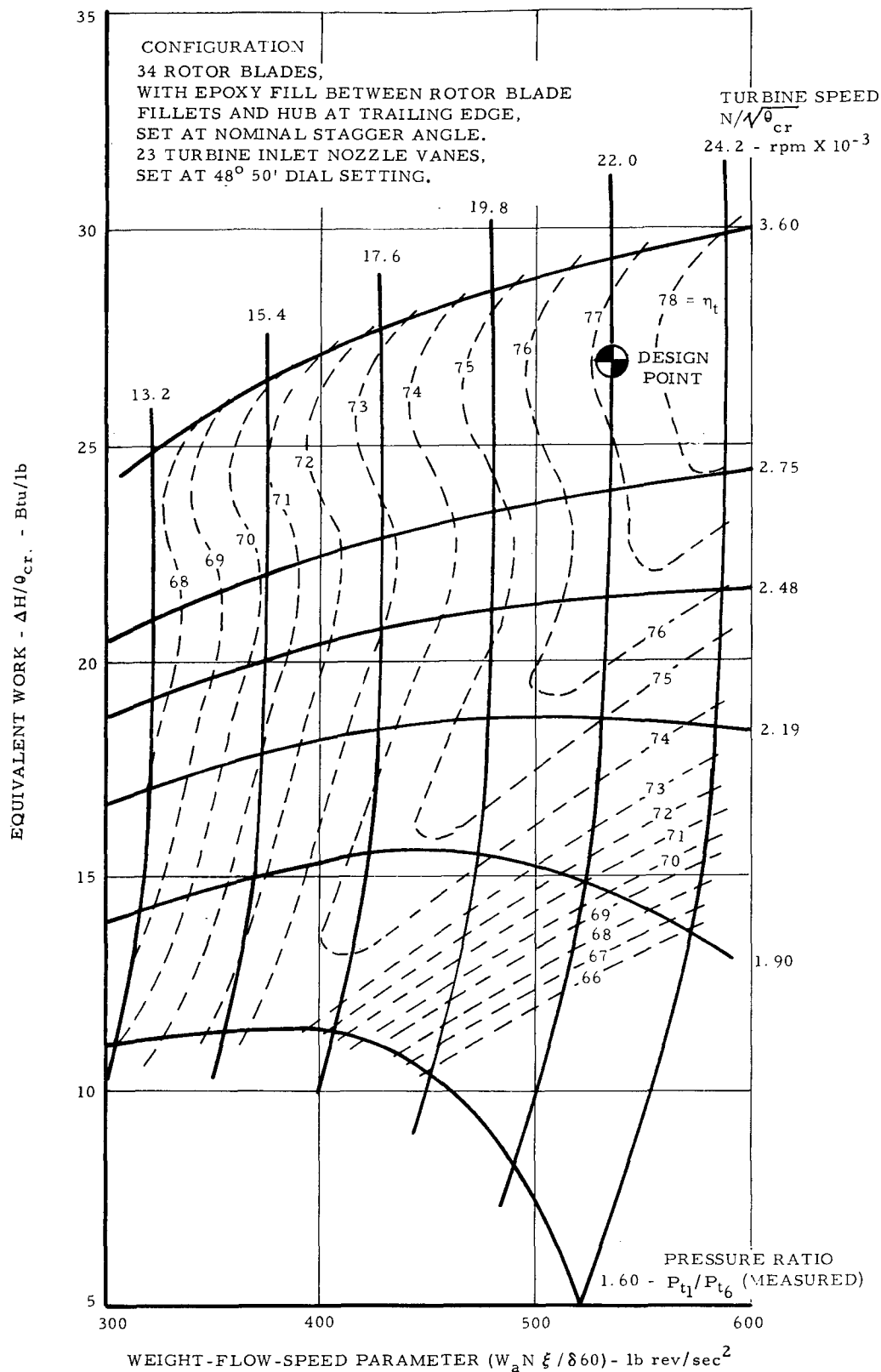


Figure 56. Fluid-Cooled Turbine - Test Stand Performance.

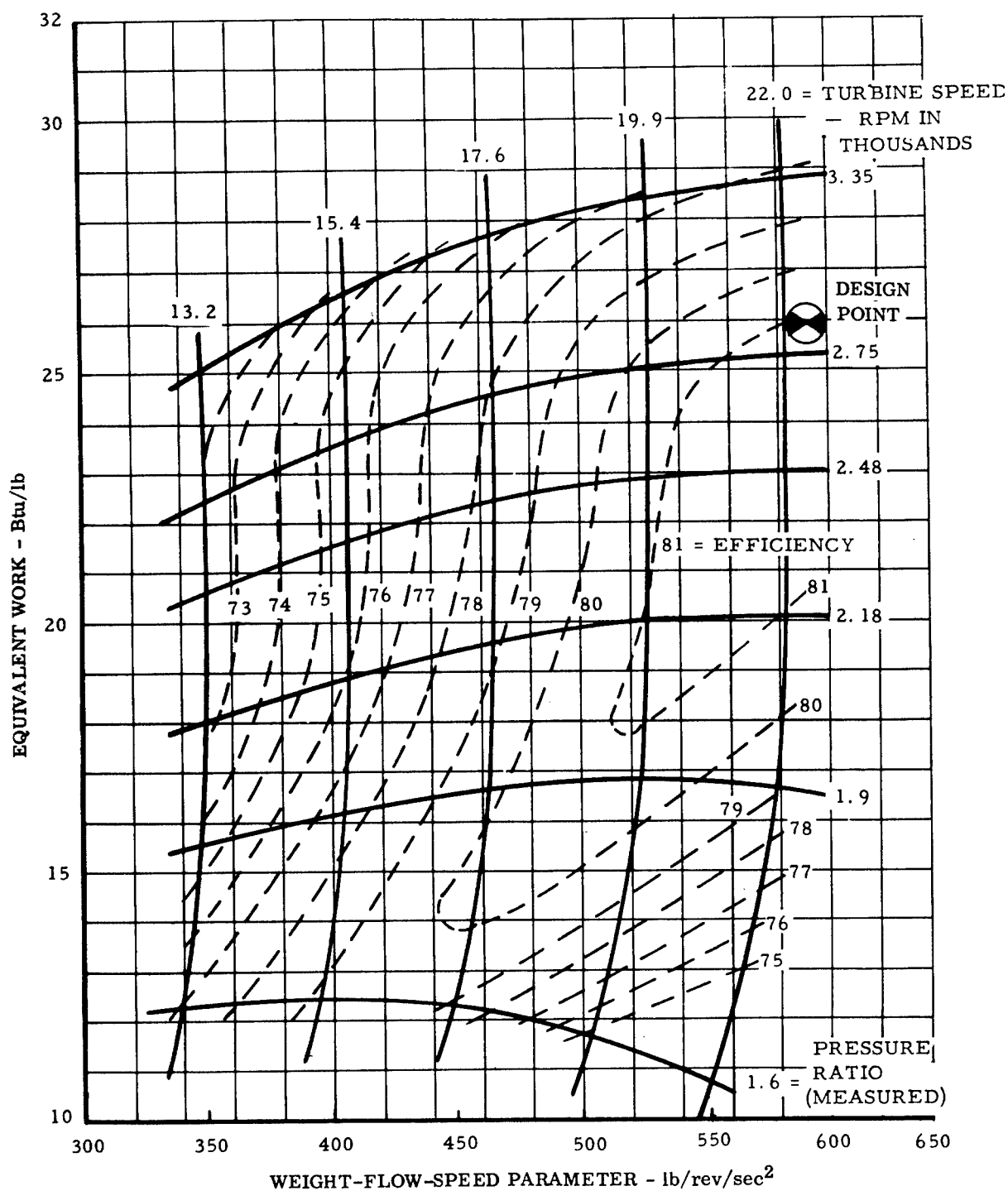


Figure 57. Fluid-Cooled Turbine Performance - 23 Nozzle Vanes and 40 Rotor Blades.

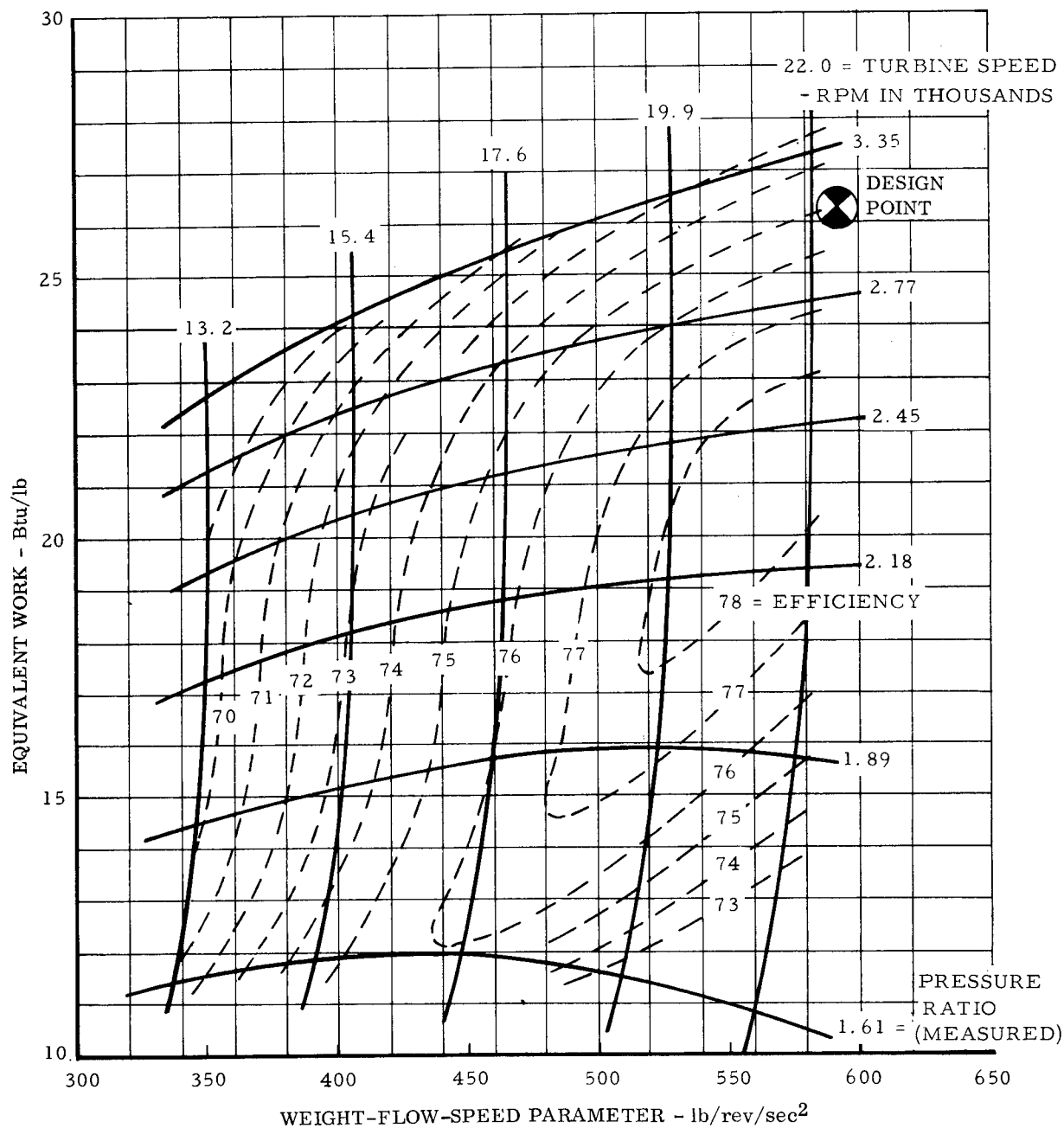


Figure 58. Fluid-Cooled Turbine Performance - 23 Nozzle Vanes and 28 Rotor Blades.

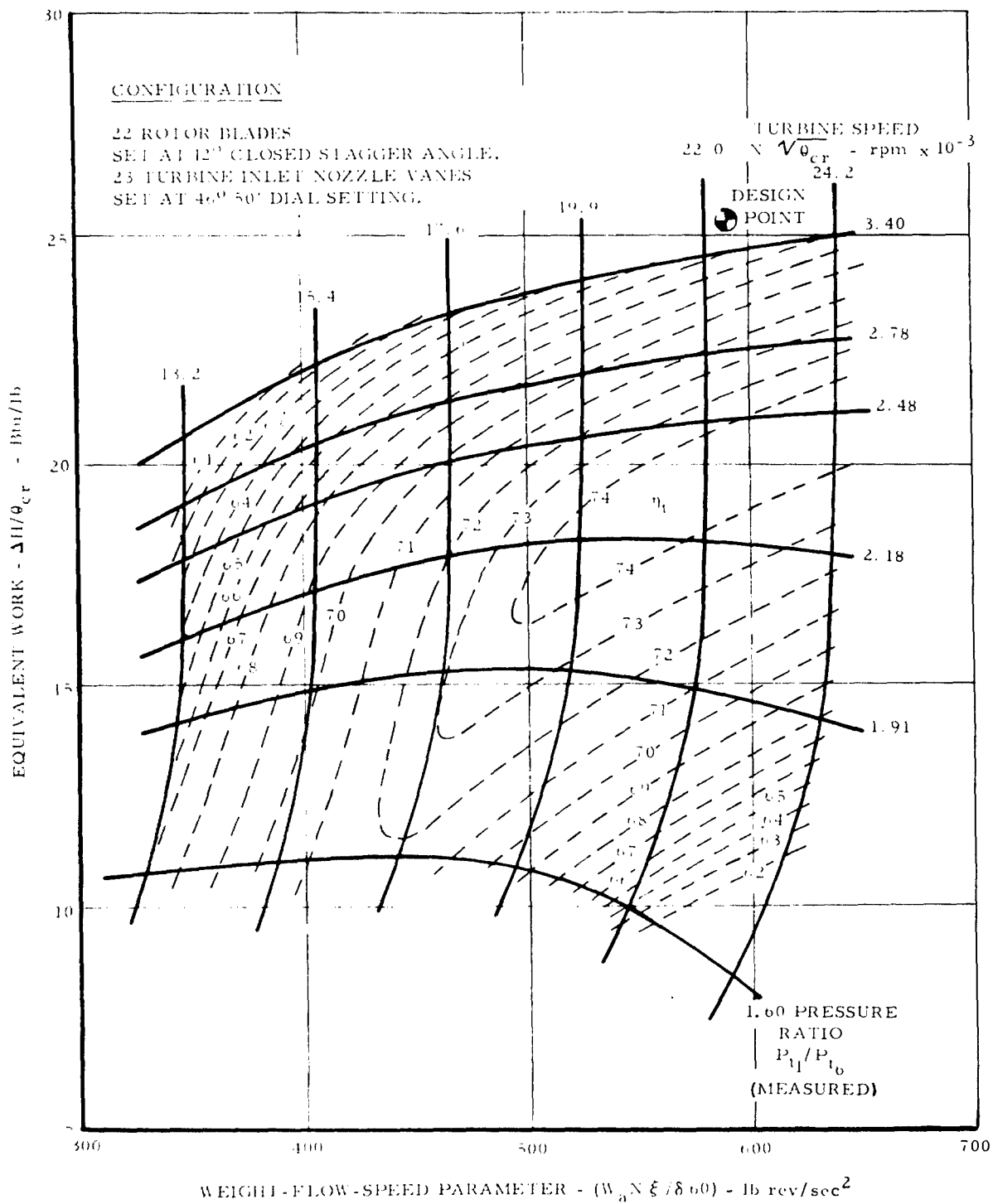


Figure 59. Fluid-Cooled Turbine Performance - 23 Nozzle Vanes and 22 Rotor Blades.

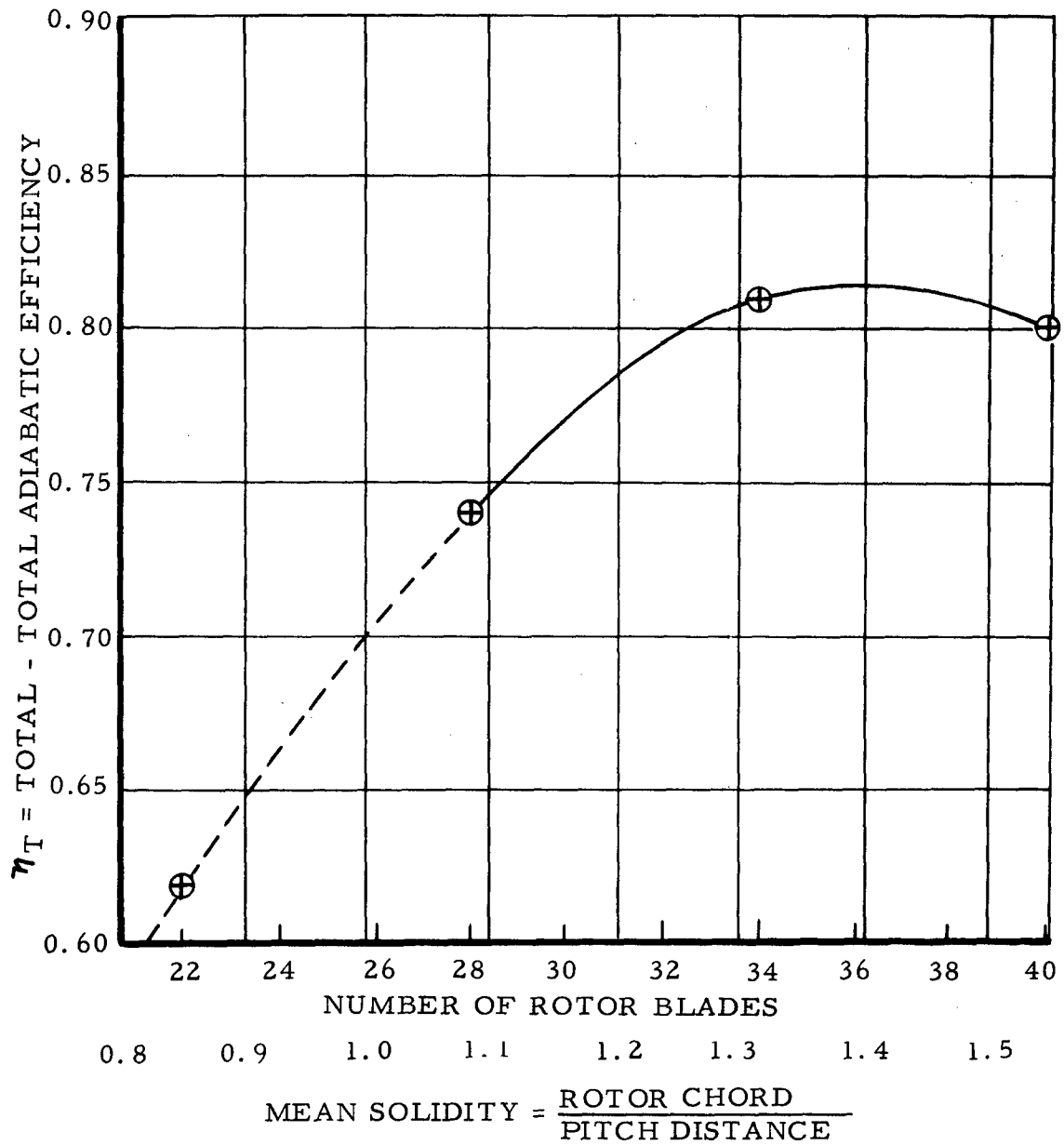


Figure 60. Turbine Efficiency Versus Solidity.

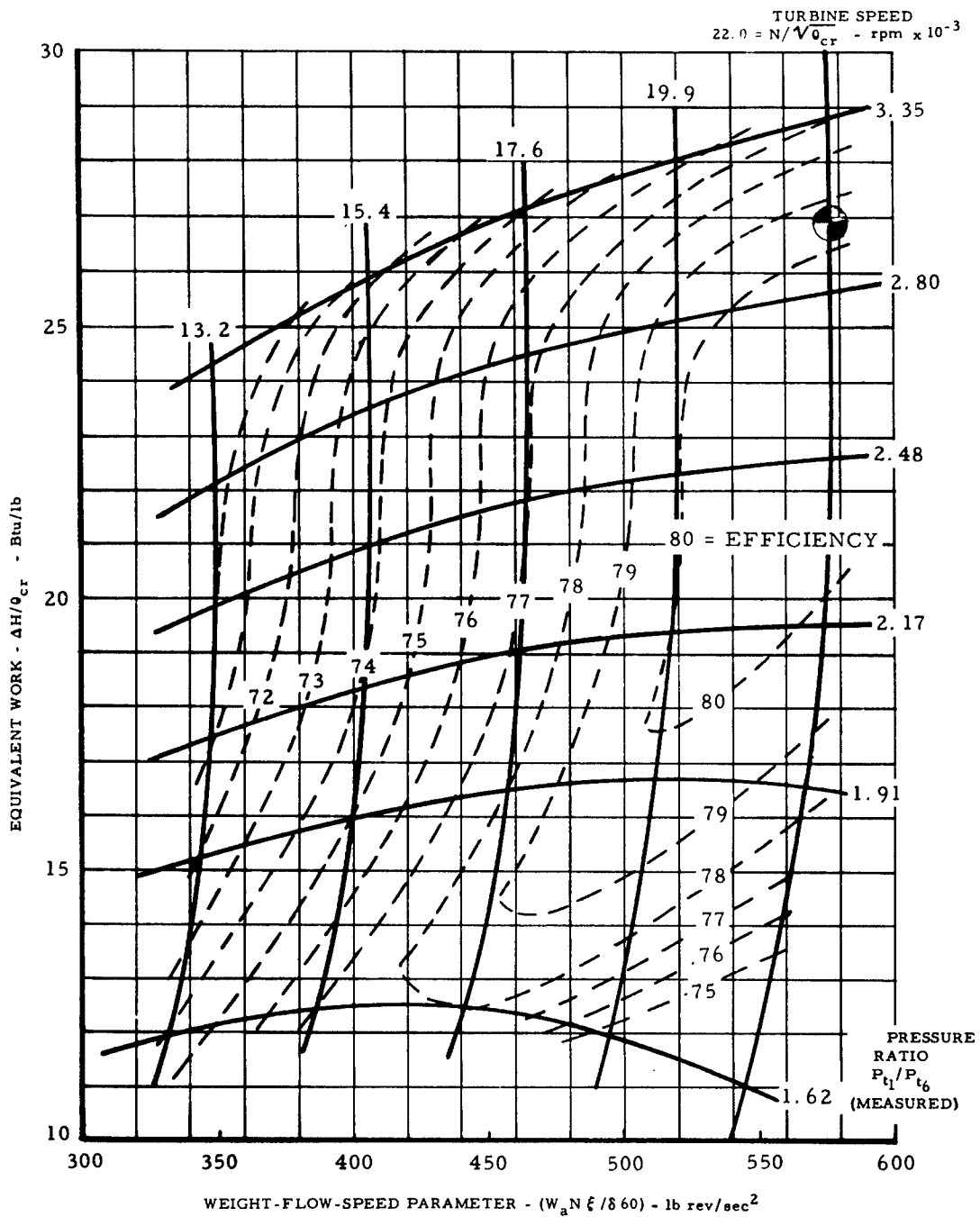


Figure 61. Fluid-Cooled Turbine Performance - 17 Nozzle Vanes and 34 Rotor Blades.

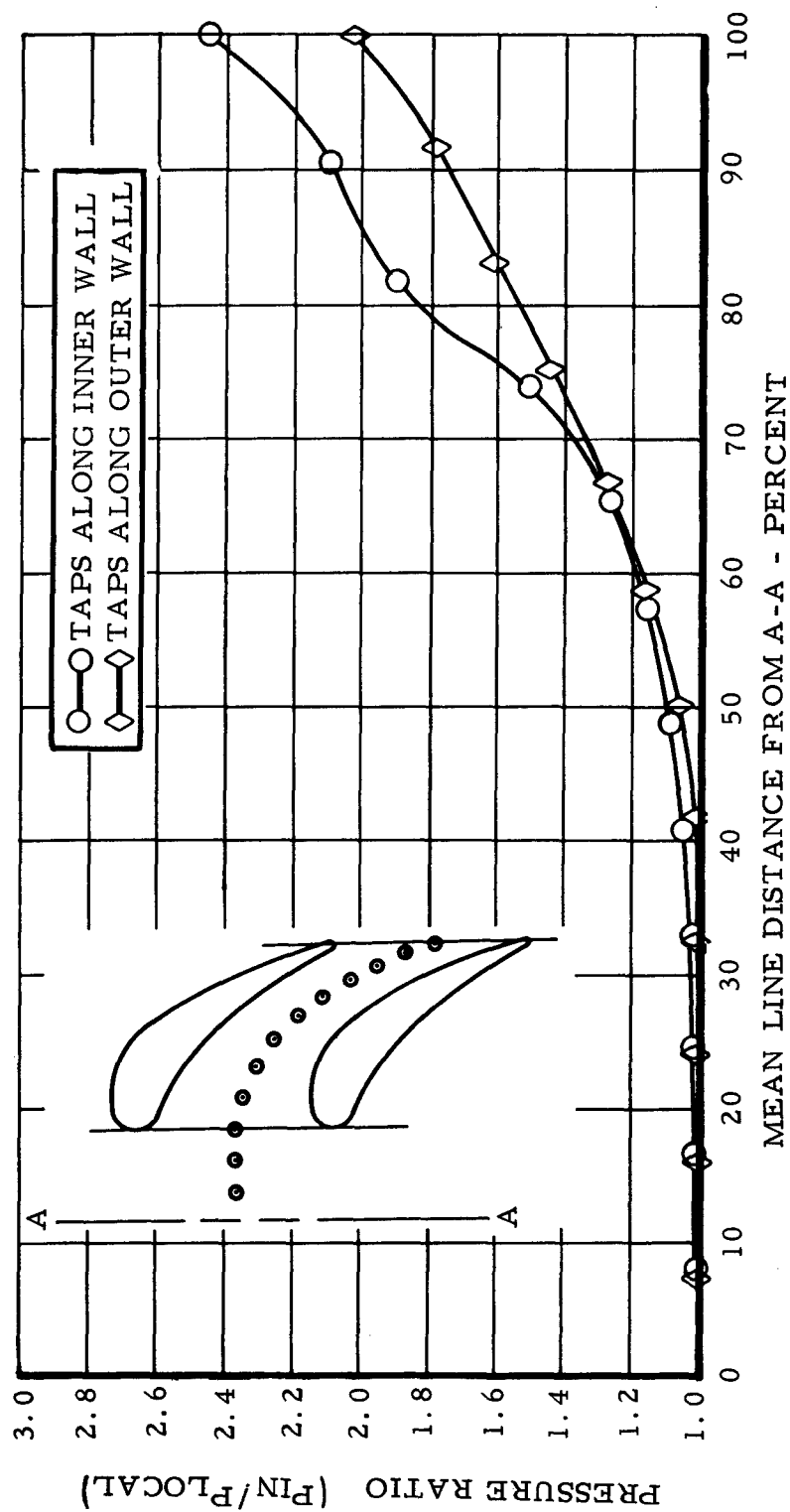


Figure 62. Nozzle Pressure Distribution - 17 Vanes.

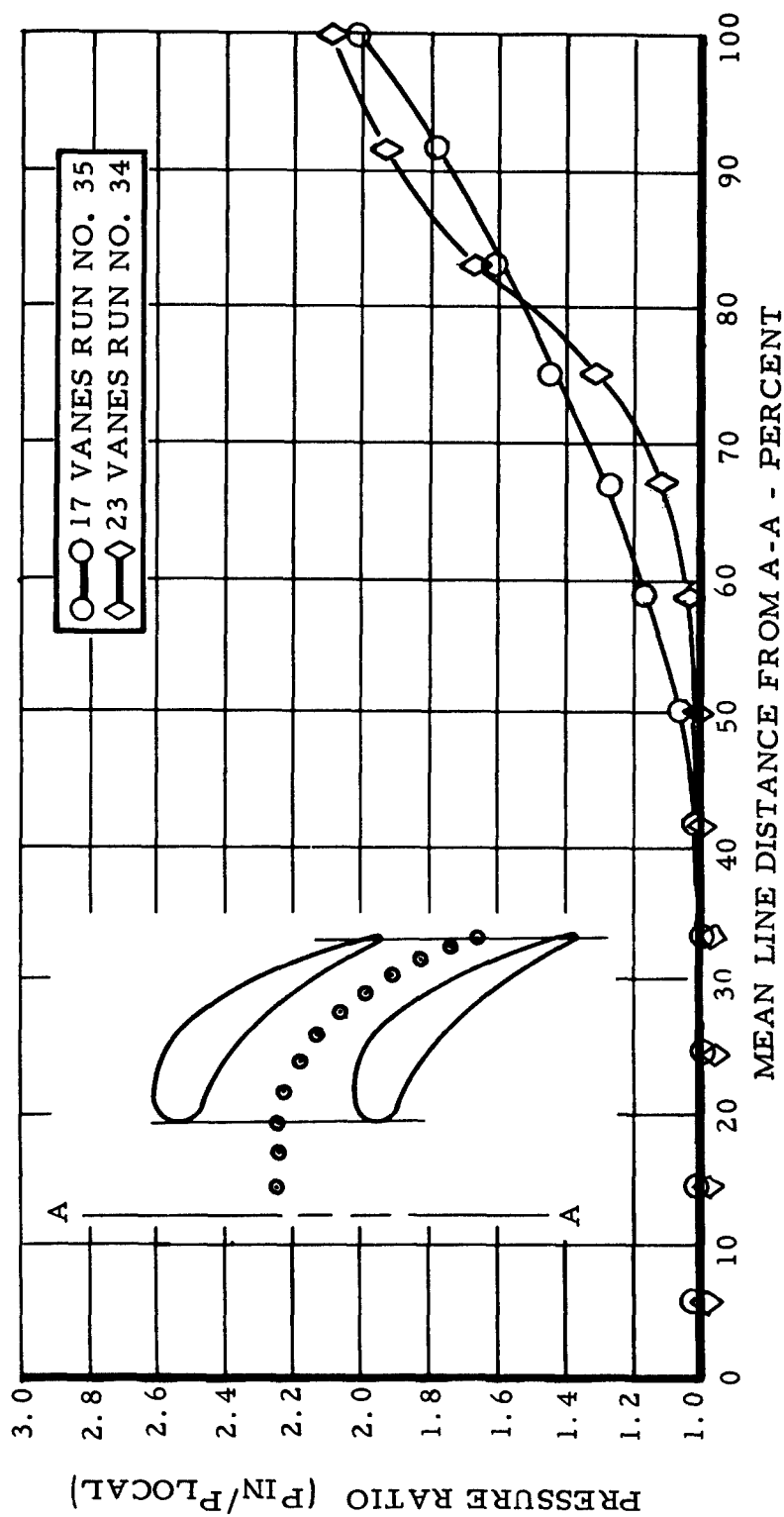


Figure 63. Nozzle Pressure Distribution - Taps Along Outer Wall.

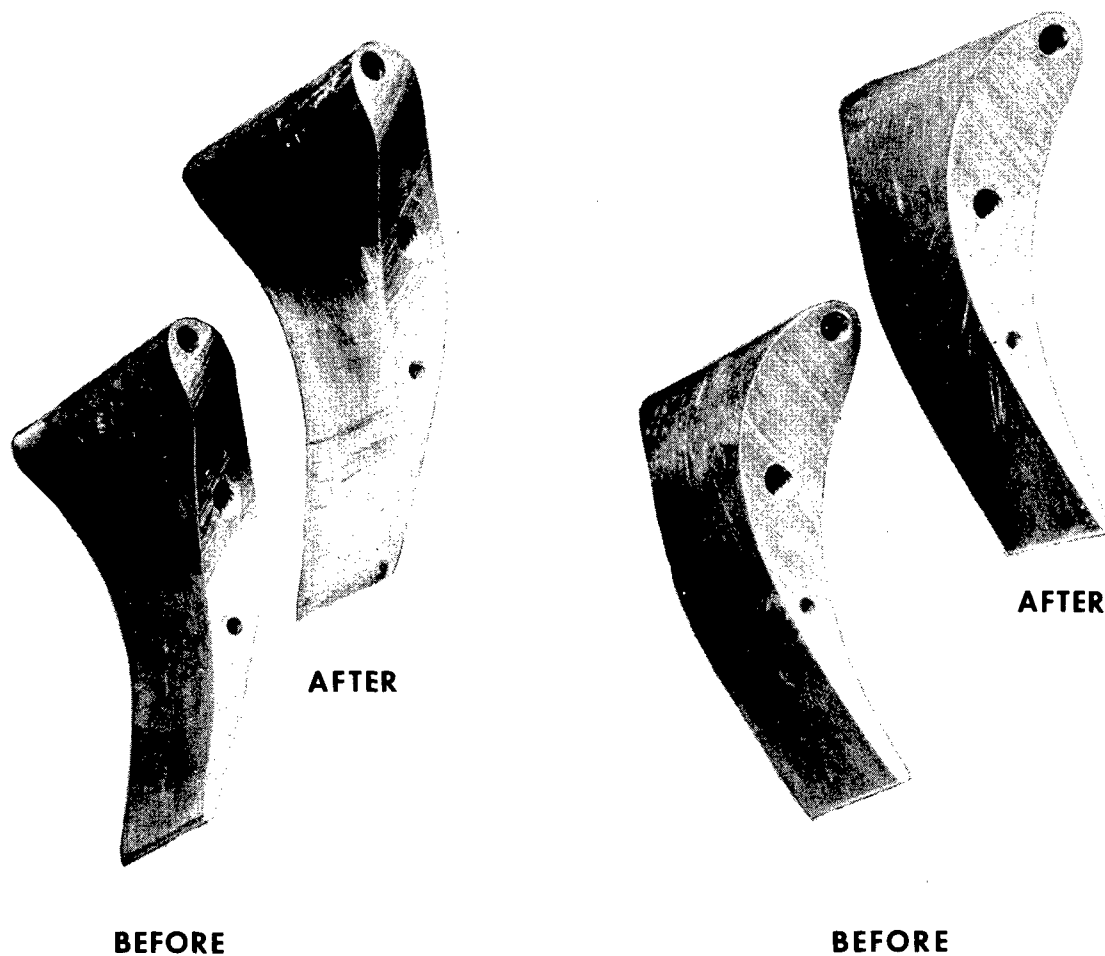


Figure 64. Turbine Inlet Nozzle Vanes Before and After Trailing Edge Thinning.

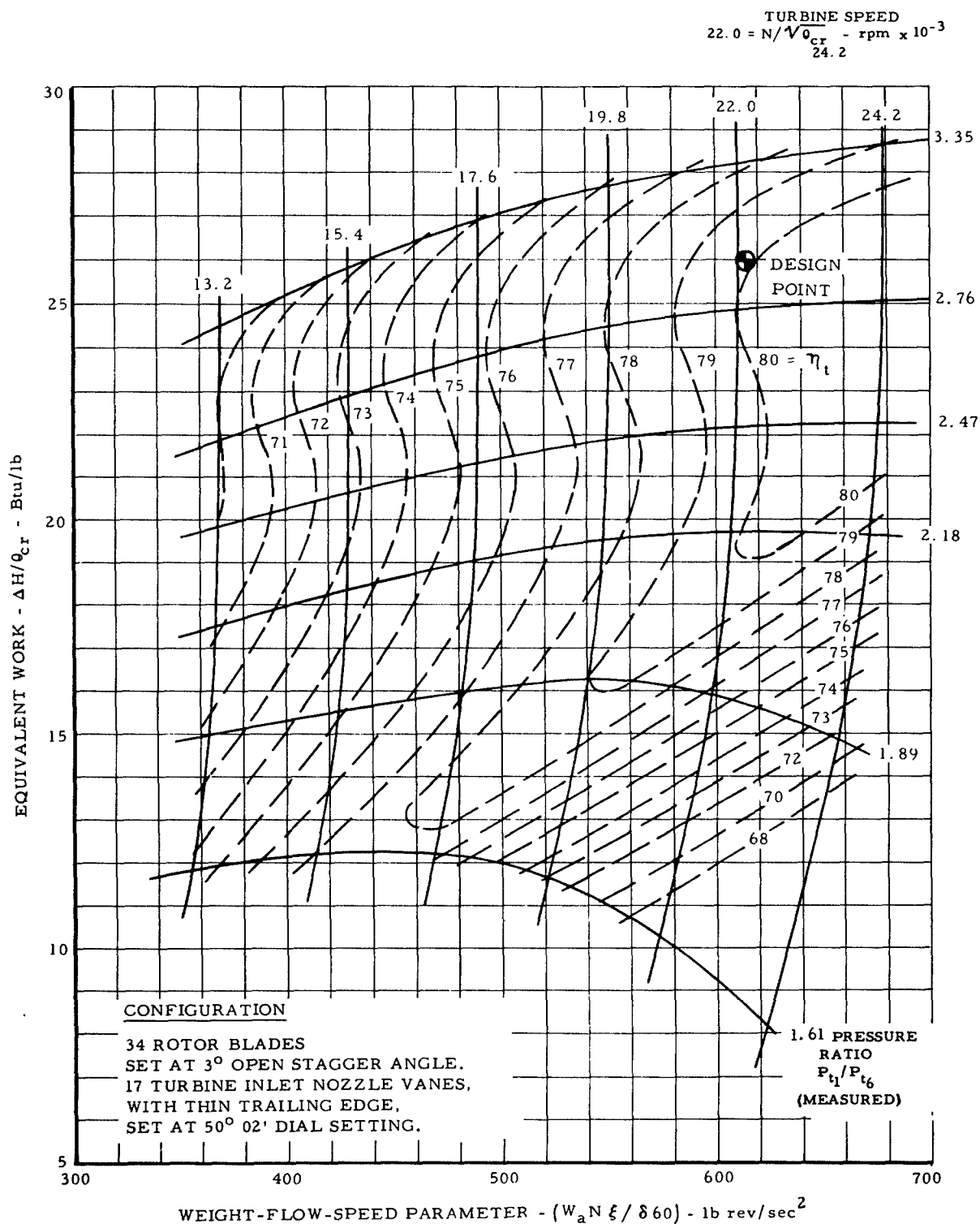


Figure 65. Fluid-Cooled Turbine - Test Stand Performance.

The nozzle trailing edge-to-pitch ratio was changed from 0.048 to 0.019. This corresponds to a reduction of total loss coefficient of $\Delta Y = 0.030$. It may be shown that the total-to-total adiabatic efficiency is given in terms of loss coefficients as:

(8)

$$\eta = \frac{T_1 - T_9}{T_1 - T_9 \left\{ \left[\frac{1}{Y_{5\text{tot.}} \left(1 - \frac{P_5}{P_5} \right) + 1} \right] \left[\frac{1}{Y_{9\text{tot.}} \left(1 - \left[\frac{t_9}{T_{9r}} \right]^{\frac{\gamma}{\gamma-1}} \right) + 1} \right] \right\}^{\frac{\gamma-1}{\gamma}}}$$

where

- T_1 = nozzle inlet stagnation temperature, $^{\circ}\text{R}$
- T_9 = rotor exit stagnation temperature, $^{\circ}\text{R}$
- T_{9r} = rotor exit relative stagnation temperature, $^{\circ}\text{R}$
- t_9 = rotor exit static temperature
- p_5 = nozzle exit static pressure
- P_5 = nozzle exit total pressure
- $Y_{5\text{tot.}}$ = nozzle total loss coefficient
- $Y_{9\text{tot.}}$ = rotor total loss coefficient
- γ = ratio of specific heats

At the design point, a ΔY of 0.030 translates into a $\Delta \eta$ of only 0.5 per-cent. This is within the measuring accuracy of the rig instrumentation, and improvements of this magnitude are difficult to pick up.

Rotor Trailing Edge Effects

Rotor trailing edges were also thinned from 0.050 to 0.020 inch, Figures 66 and 67. Again, for expediency, the existing hardware was modified. For ease of machining, all the material was taken from the suction side of the blade back from the throat to the trailing edge. Thinning the blade in this region, however, increases the diffusion factors. Since the "D" factors were already very high (see Table I), an increase could easily nullify any gains from the thin edges.

Configuration No. 5, Table IV, was tested for trailing edge effects. Overall performance is given in Figure 68. A comparison with the nominal map of Figure 53 shows that efficiency dropped 1 percent. This loss is attributable to the increased loading, causing separation on the suction side of the blade. If a thinner trailing edge is found to be practical, a new airfoil shape must be designed to avoid the high rotor diffusion factors. Only in this manner can the baseline design performance be improved by thinner trailing edges.

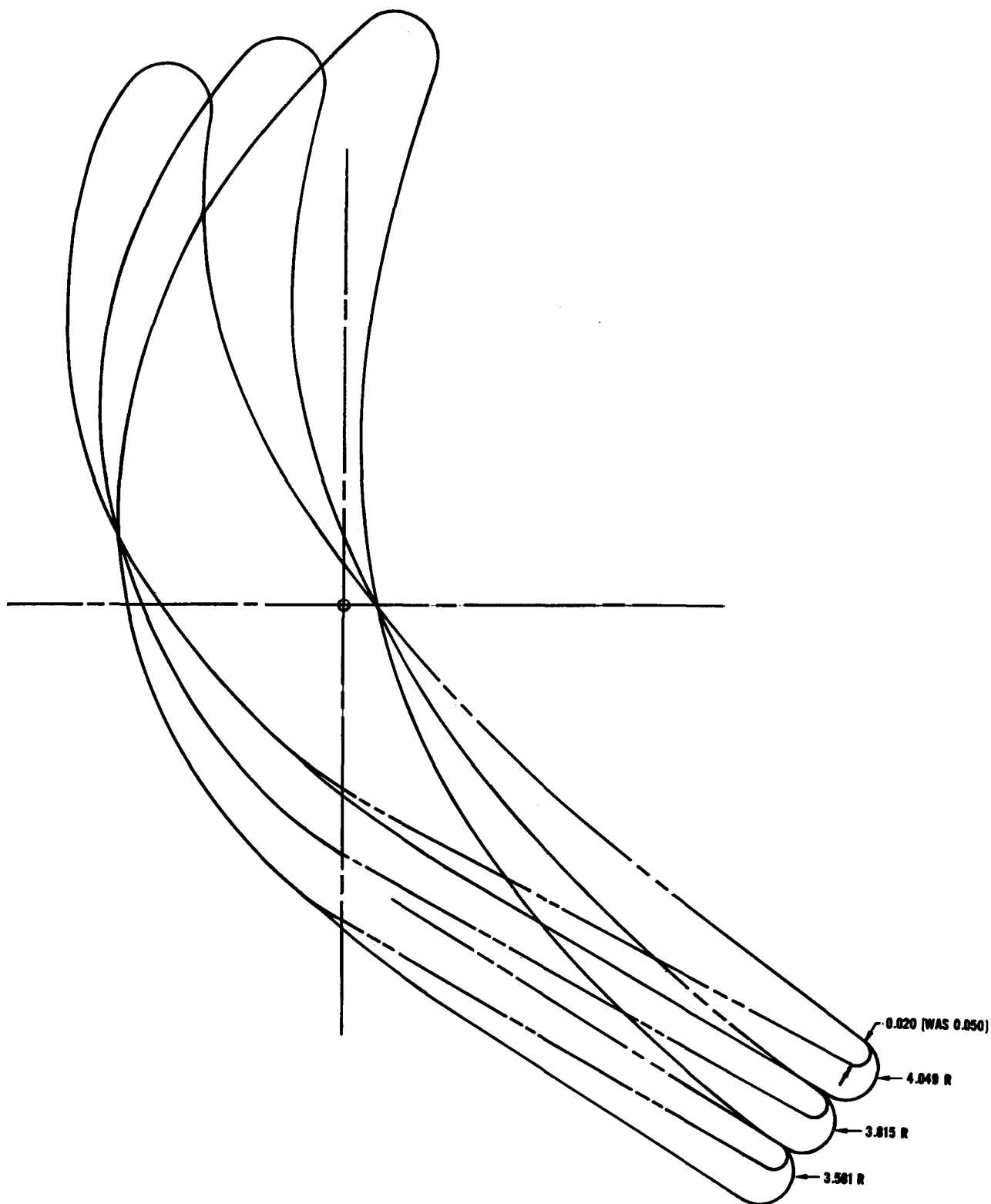


Figure 66. Modified Fluid-Cooled Blade Sections.



ORIGINAL



REWORKED

Figure 67. Fluid-Cooled Turbine Rotor Blades Before and After Trailing Edge Thinning.

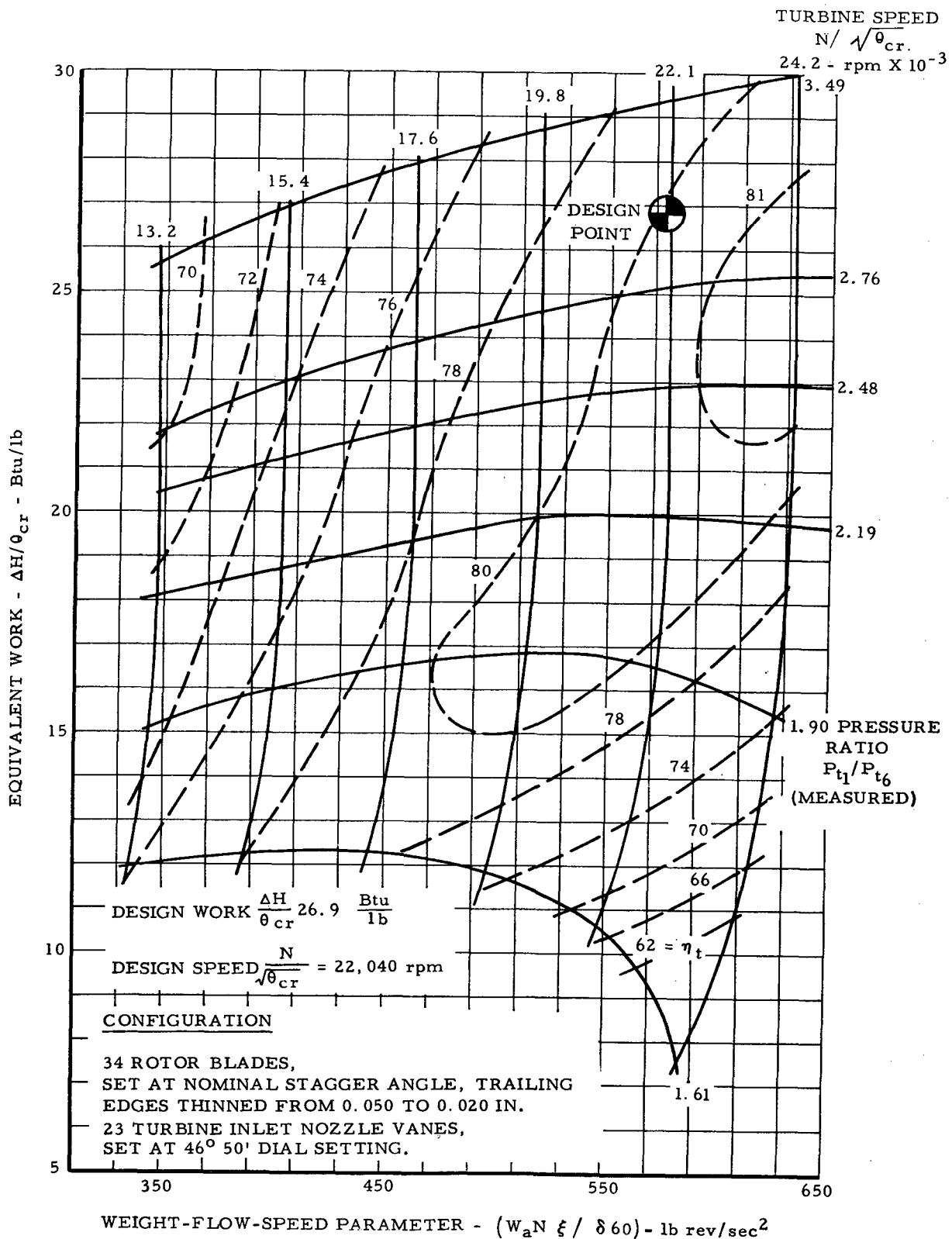


Figure 68. Fluid-Cooled Turbine - Test Stand Performance.

PROCESS FEASIBILITY STUDIES FOR FLUID-COOLED TURBINE BLADES

INTRODUCTION

The preliminary survey of fabricating techniques at the beginning of the program produced six possible methods for feasibility studies of manufacturing techniques for fluid-cooled turbine blades.

The methods were:

1. Composite castings
2. Diffusion bonding
3. Electron beam welding
4. Explosive welding
5. Integral precision castings
6. Machining from solid blanks

This list was narrowed to the three most likely to meet the requirements of the contract on the basis of a Continental survey of the respective industry technical experience and projected time and cost estimates required to obtain a satisfactory result.

The three methods chosen for actual procurement of hardware and related studies were diffusion bonding, electron beam welding, and integral precision casting. Each of these techniques will be discussed in more detail in this report.

PRECISION CASTING TECHNIQUES

Preliminary Rectangular Test Blocks

The most favorable technique to date for fabricating simulated fluid-cooled blades has been as follows: a precision cast blade, open at the tip, is fitted with a wrought tip-cap precisely fitted by the EDM process and sealed by electron beam welding. A typical test specimen fabricated by this technique is shown in Figure 69.

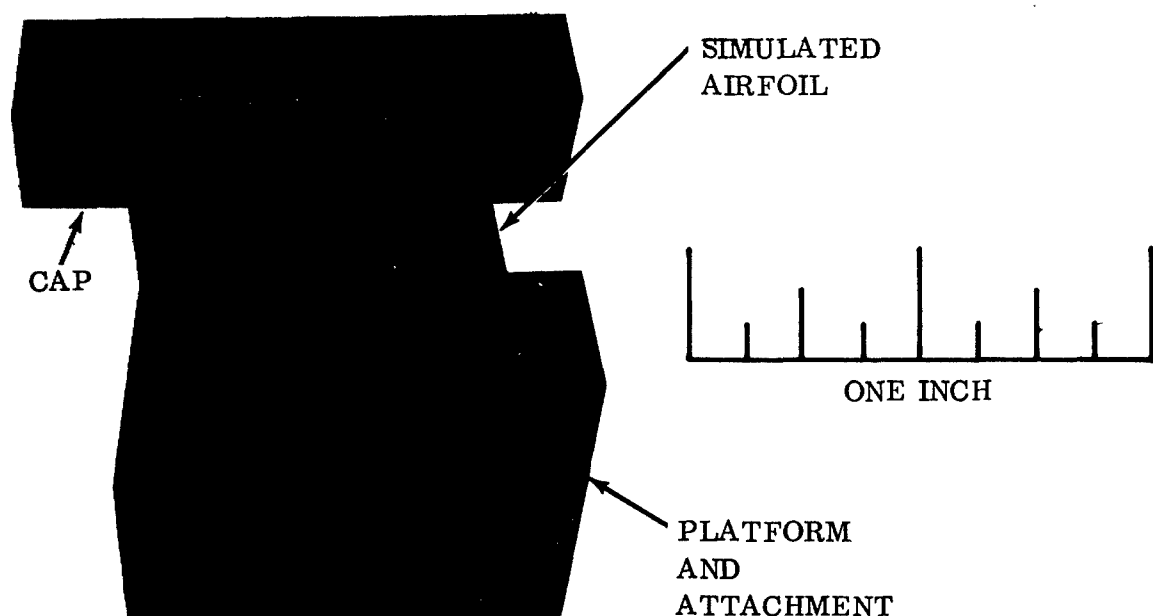


Figure 69. Preliminary Rectangular Blade With Electron Beam Welded Cap.

A simulated blade design, Figure 70, was produced by Continental to provide process feasibility results at a lesser cost than an actual airfoil contour blade. Requests for quotes were sent out to the precision casting foundries to supply parts to this design.

Continental chose the Martin Metals Company on the basis of experience, extent of guaranteed results, cost, delivery time, and promptness of quotes. For casting, it was necessary to modify the design to allow core print openings at each end of the blade block as shown by the sectioned casting (Figure 71).

The casting process of Martin Metals, as with all foundries, is proprietary in many details; however, the general procedure is not. The U-700 metal was vacuum furnace melted into a master heat. Smaller heats of the master melt were vacuum melted to pour the casting. The wax patterns were cast around the machined ceramic cores in the metal pattern dies. The necessary mold riggings, such as down sprues, ingates, heads, and risers, were added to the wax pattern by fusion. The entire wax pattern was then dip coated with successive layers of ceramic slurries to form the ceramic mold. The initial coating of wax was made with zircon slurries followed by alumina slurries for backup and greater mold thickness. The ceramic mold was then fired to a temperature above 1900°F that melted the wax out of the mold cavity and preheated the mold for receiving the metal. The casting temperature of the U-700 metal was 200°F over its melting temperature.

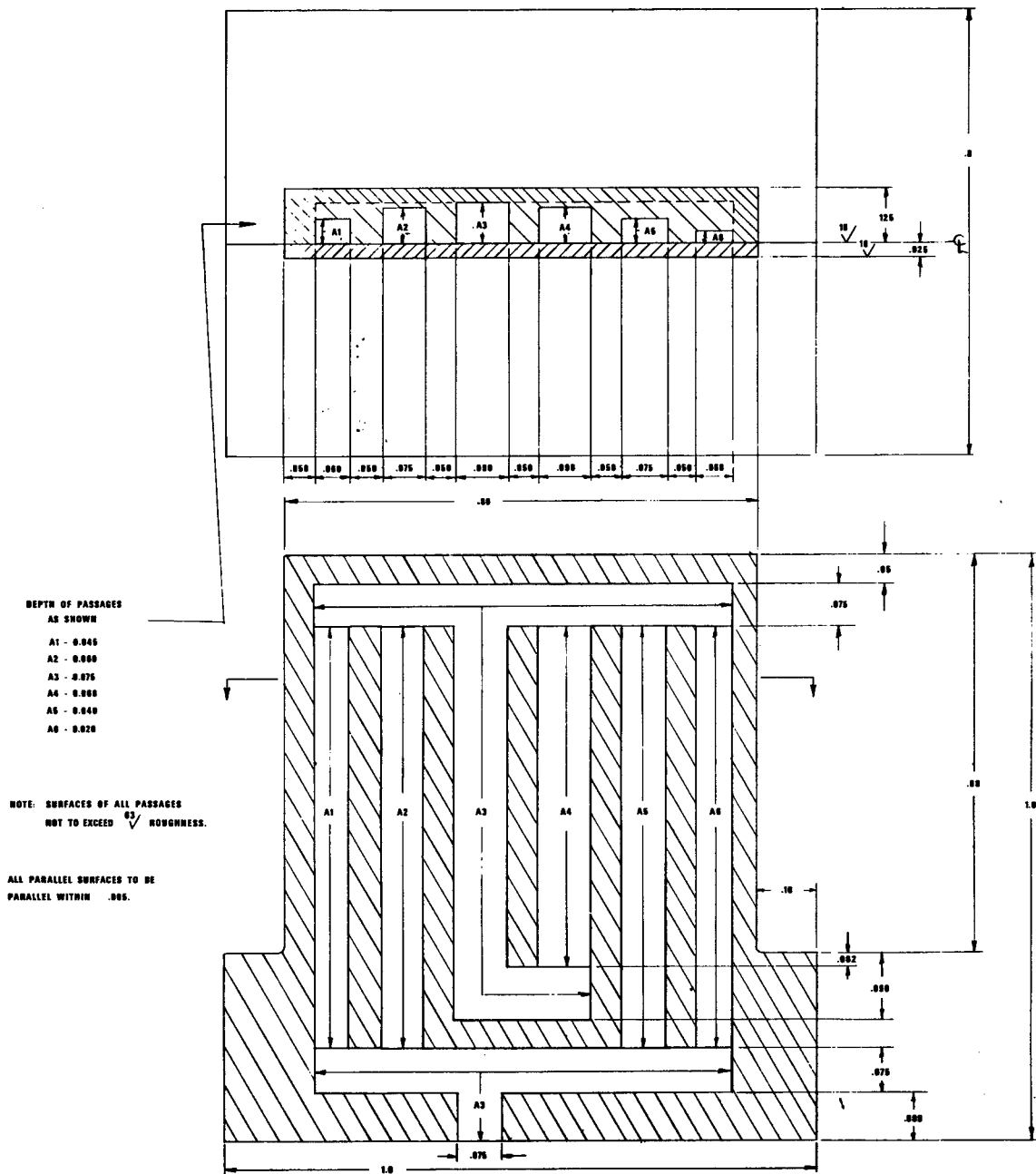
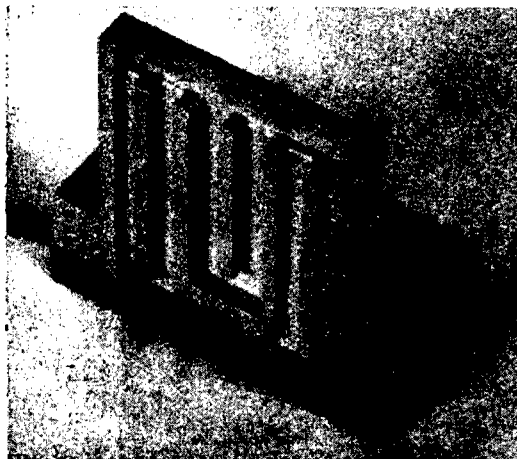


Figure 70. Cross Section of Preliminary Rectangular Blade.

Figure 71. Cross Section of Cast Preliminary Rectangular Blade.



Tooling drawings for the wax patterns were prepared by the Martin Metals Company and approved by Continental. The tooling, Figure 72, and the wax patterns, Figure 73, were procured. Ceramic cores were machined from solid blanks rather than by tooling up with the core molds because of the small quantity involved. A radiograph of one of these cores is shown in Figure 74.

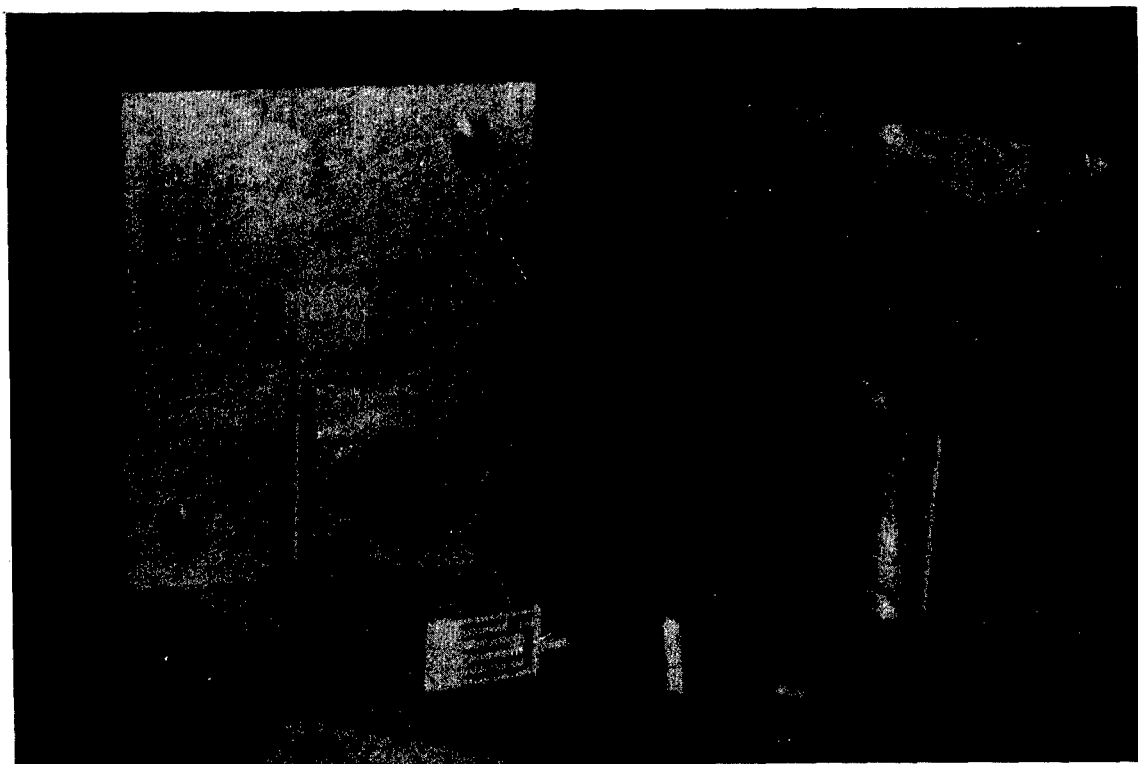


Figure 72. Rectangular Blade Ceramic Core, Wax Pattern and Wax Injection Dies.

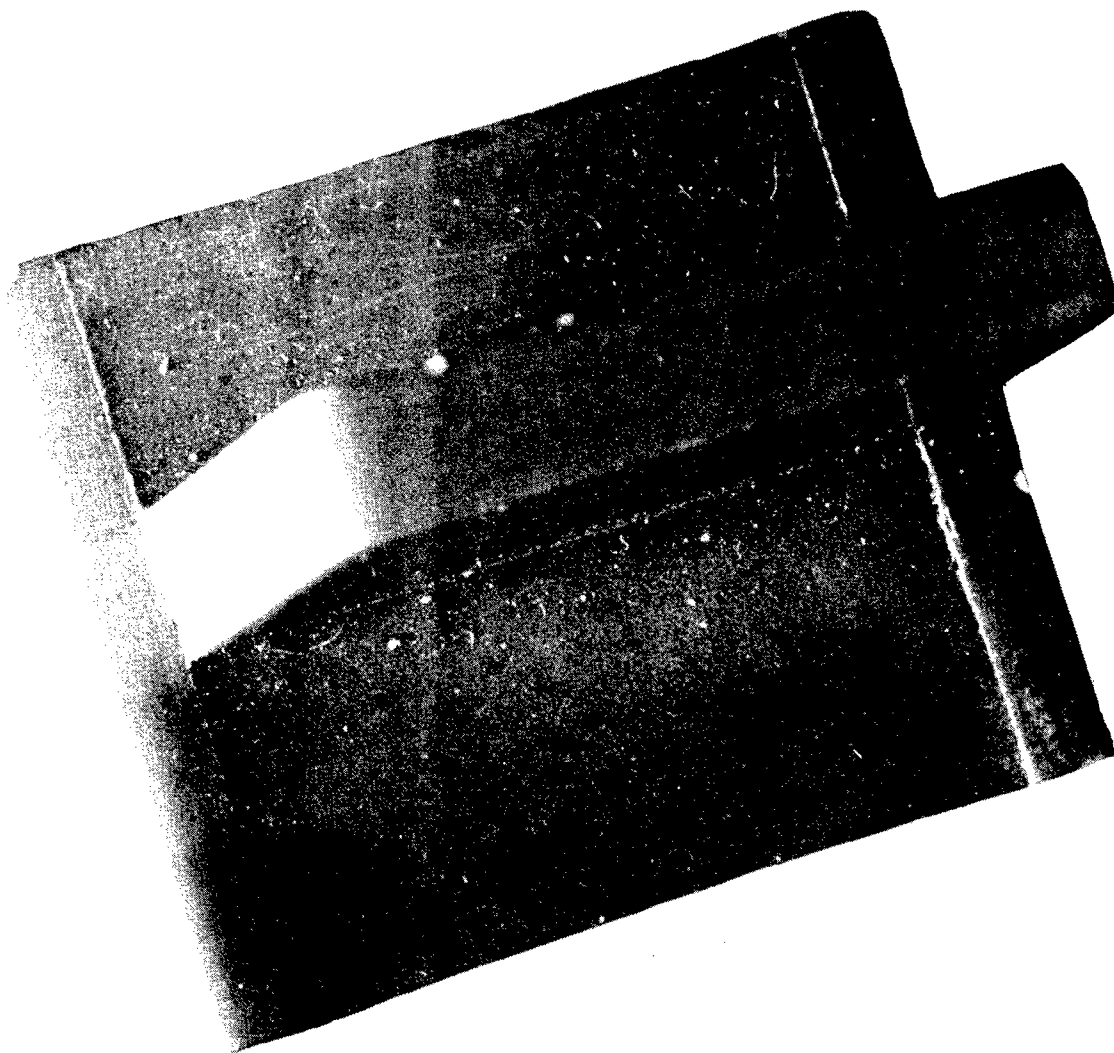


Figure 73. Wax Pattern for Rectangular Blade.

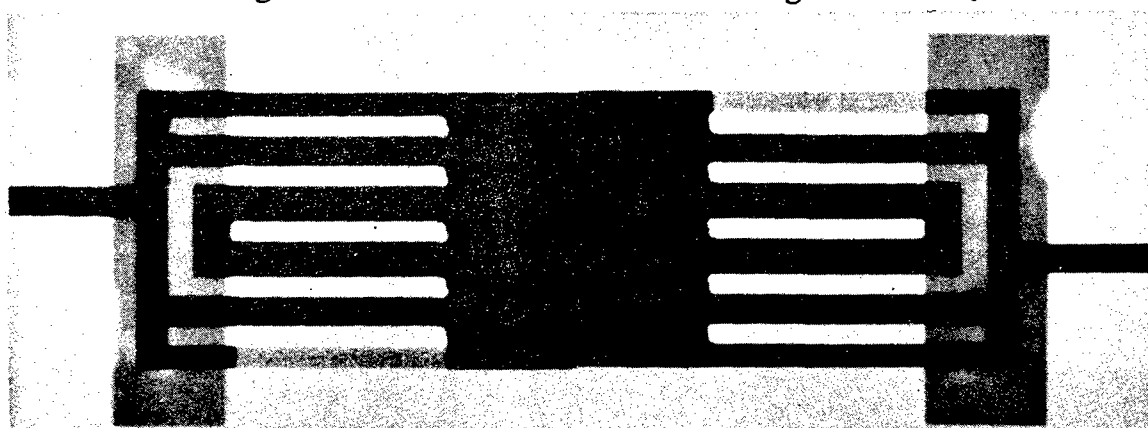


Figure 74. Radiograph of Ceramic Core for Rectangular Blade.

Initial proof castings were made to check out the wax pattern and tooling using a solid core rather than the expensive channeled cores. This casting, Figure 75, was checked for dimensional accuracy and metallurgical quality and minor corrections were made to the tooling. A radiograph of this casting, Figure 76, depicts a reasonably sound casting.

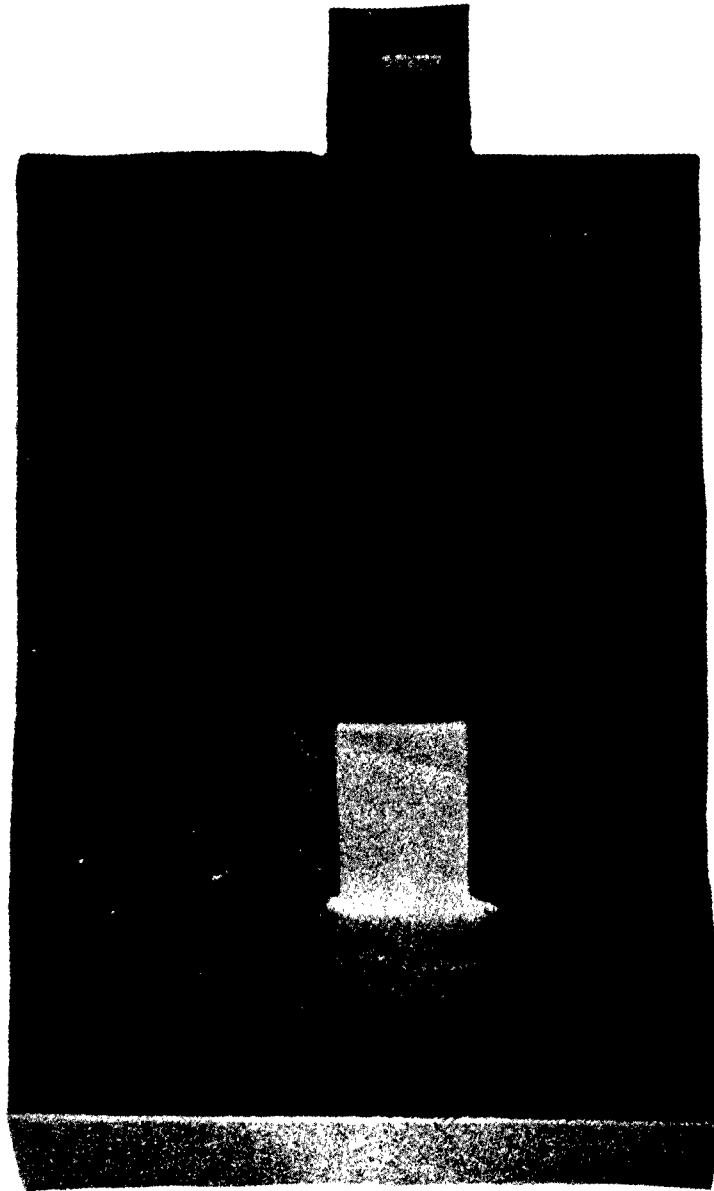


Figure 75. Rectangular Blade Casting.

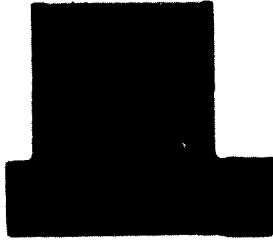


Figure 76. Radiograph of Rectangular Blade Casting.

Minor corrective action was taken to improve the dimensional integrity of the initial proof castings. Wall thickness control was excellent with variations within 0.001 to 0.003 inch. Core channel dimensions were in most cases within 0.001 inch of blueprint, with some variations of 0.005 inch.

The "as cast" surface was considered satisfactory; measurements indicated a finish in the range of 40 to 50 rms microinches. Figure 77 shows the average cast surface.

In addition to surface requirements, certain metallurgical quality standards were imposed; namely, grain size ($1/16$ to $3/16$ inch with no columnar grains in the simulated airfoil) and no internal shrinkage or porosity. Figures 78 and 79 show that these conditions were obtained in the sample sections shown.

Removal of the ceramic cores required further development. The leaching process used by Martin Metals, a hot liquid salt bath, failed to remove all the ceramic material from the smaller (0.020-inch-wide) channel in one out of seven blades. Also associated with the core leaching process were areas of the casting exhibiting a rough etched appearance with a 180-220 rms finish (Figure 80). This condition was found only on one casting but indicated the possible effects of an improper core leaching procedure.

Satisfactory castings suitable for further blade fabrication studies were obtained.

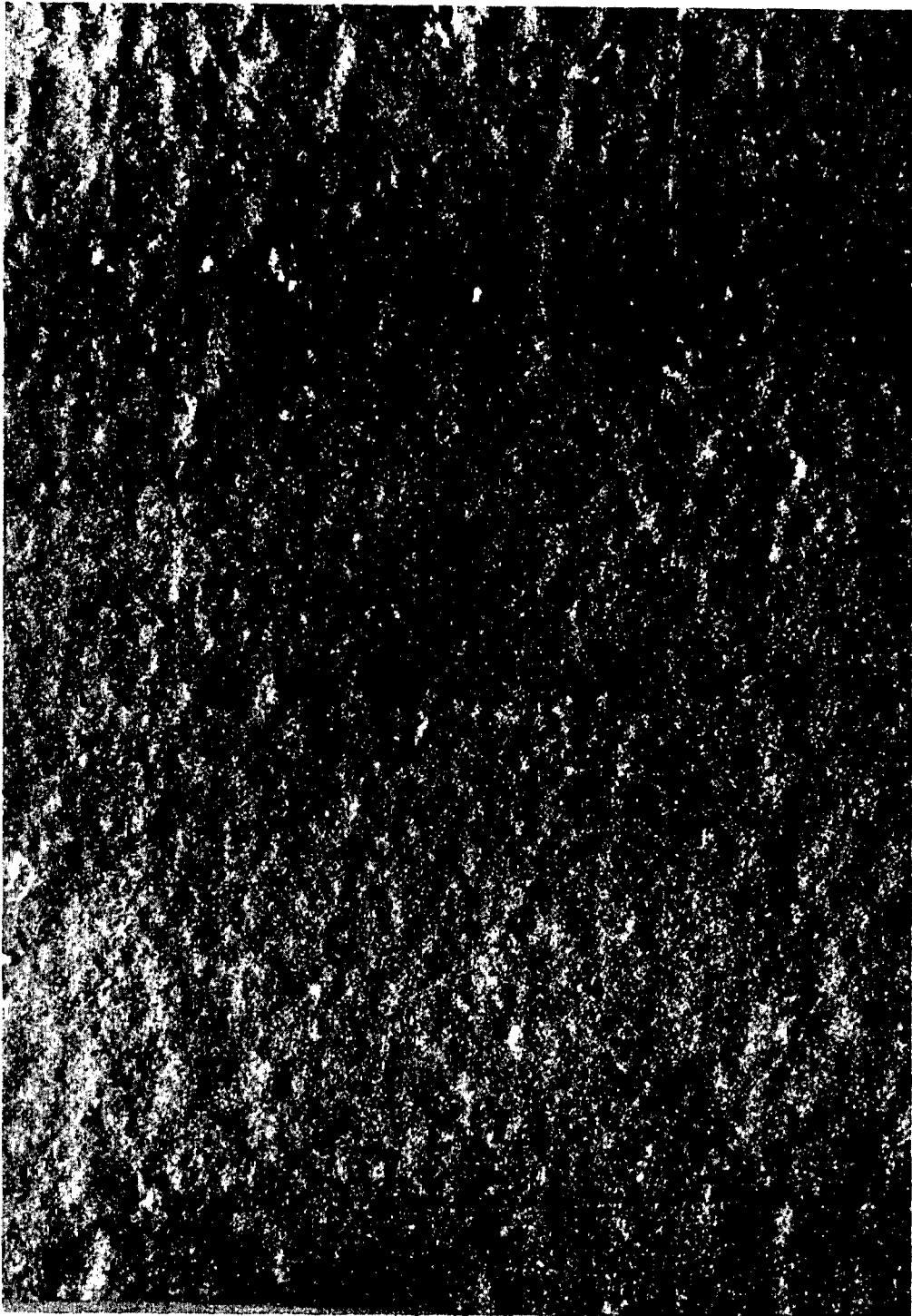


Figure 77. Representative Surface Condition of Rectangular Blade Casting.

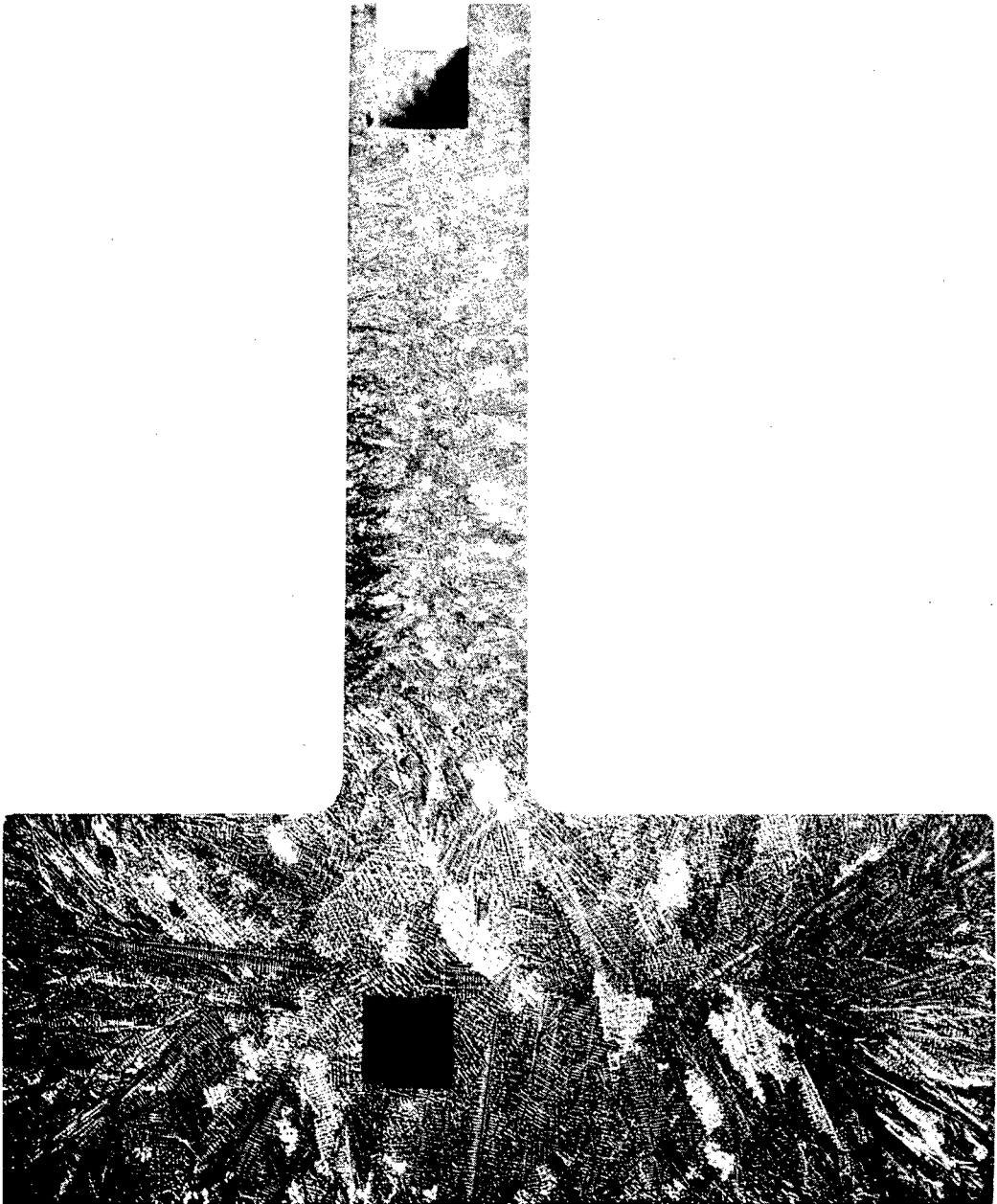


Figure 78. Macro-Etched Cross Section Showing Grain Structure.



Figure 79. Typical Microstructure of Cast Rectangular Blade.

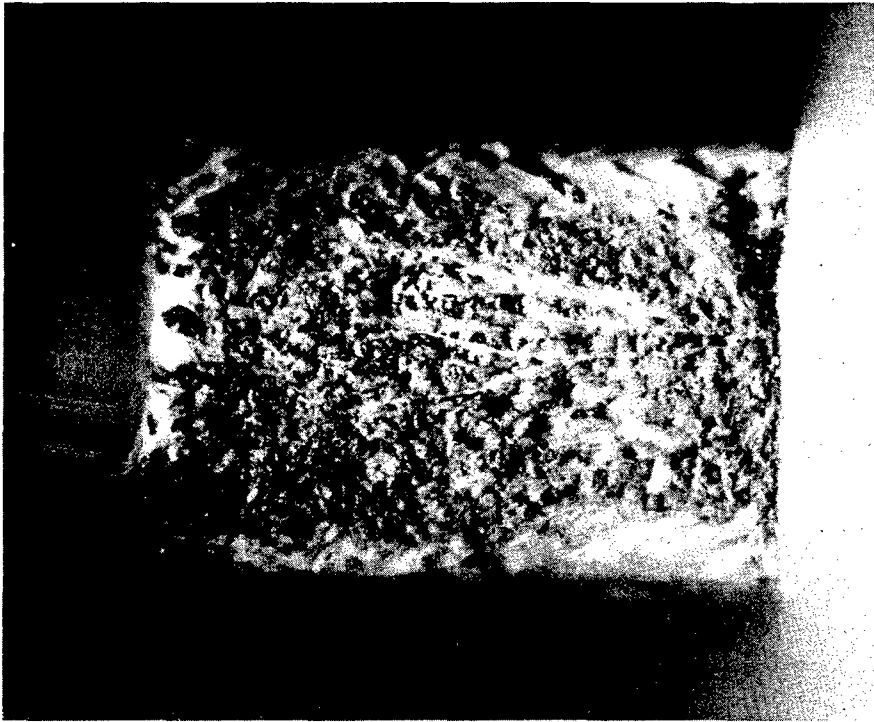


Figure 80. Typical Example of Leaching Defect.

Airfoil Castings

On the basis of satisfactory results obtained with the preliminary rectangular blade blocks, airfoil castings complete with heat exchanger and disc attachment area were obtained. A finished casting with welded tip-cap and heat exchanger plug is shown in Figure 81.

Based on competitive bidding and delivery of quality castings, Austenal was selected to produce the fluid-cooled turbine blade casting, part No. 709627 (Figure 82).

The tooling for these castings was engineered in the following three stages:

1. Cores

The ceramic cores were made in two separate pieces using injection molding techniques followed by cementing the two pieces together, as shown in Figures 83 and 84. The cores were slotted by the Cavitron process (ultrasonic machining) to produce the internal channel dividers (Figure 85).

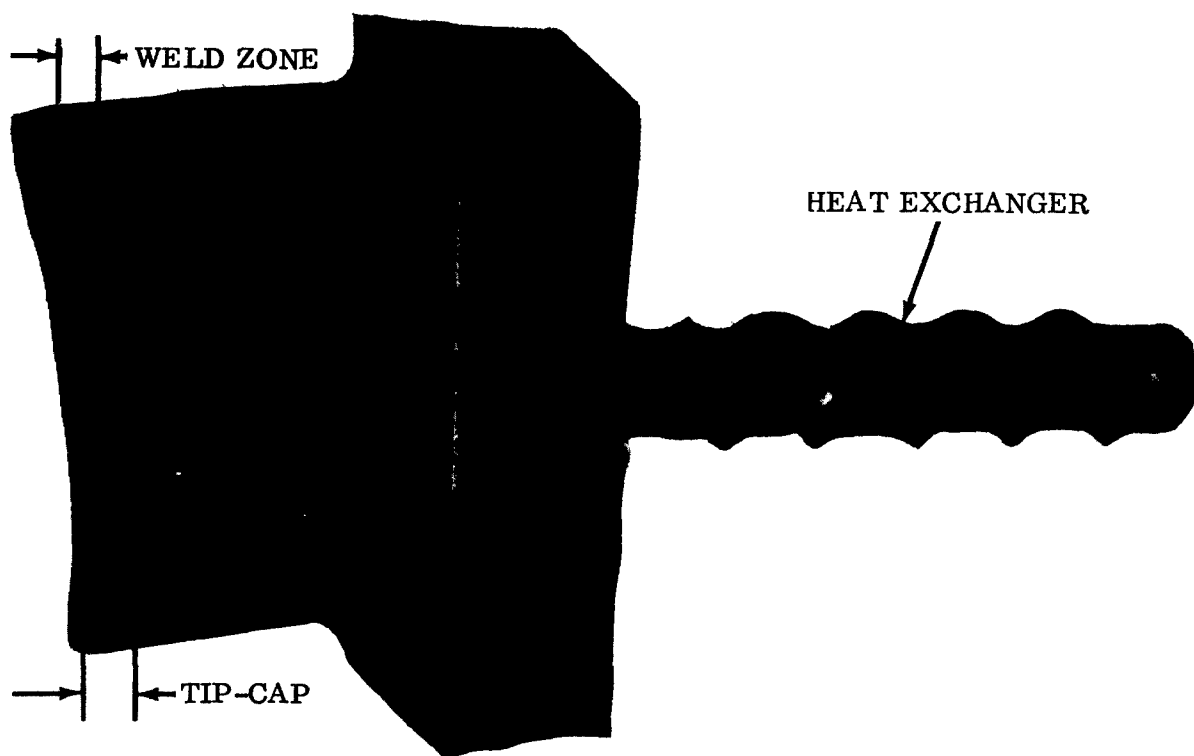


Figure 81. Machined, Welded Airfoil Blade and Tip-Cap.

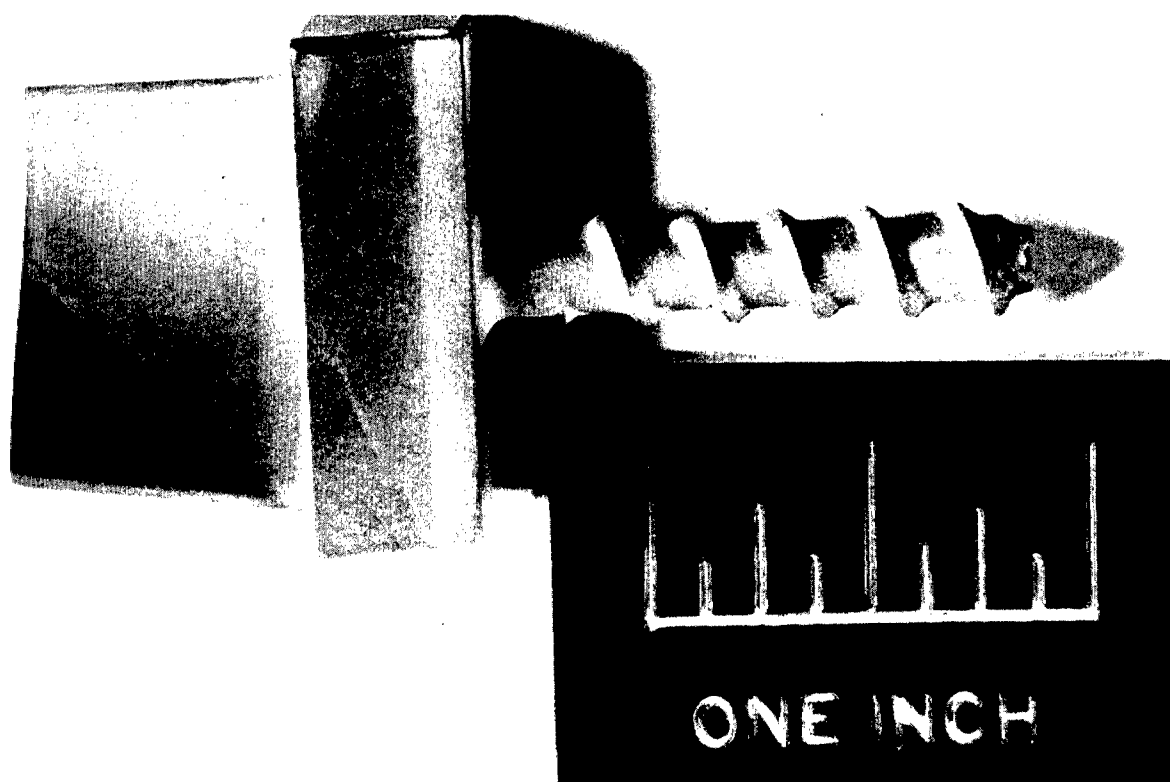


Figure 82. Cooled Turbine Blade Casting, Part No. 709627.

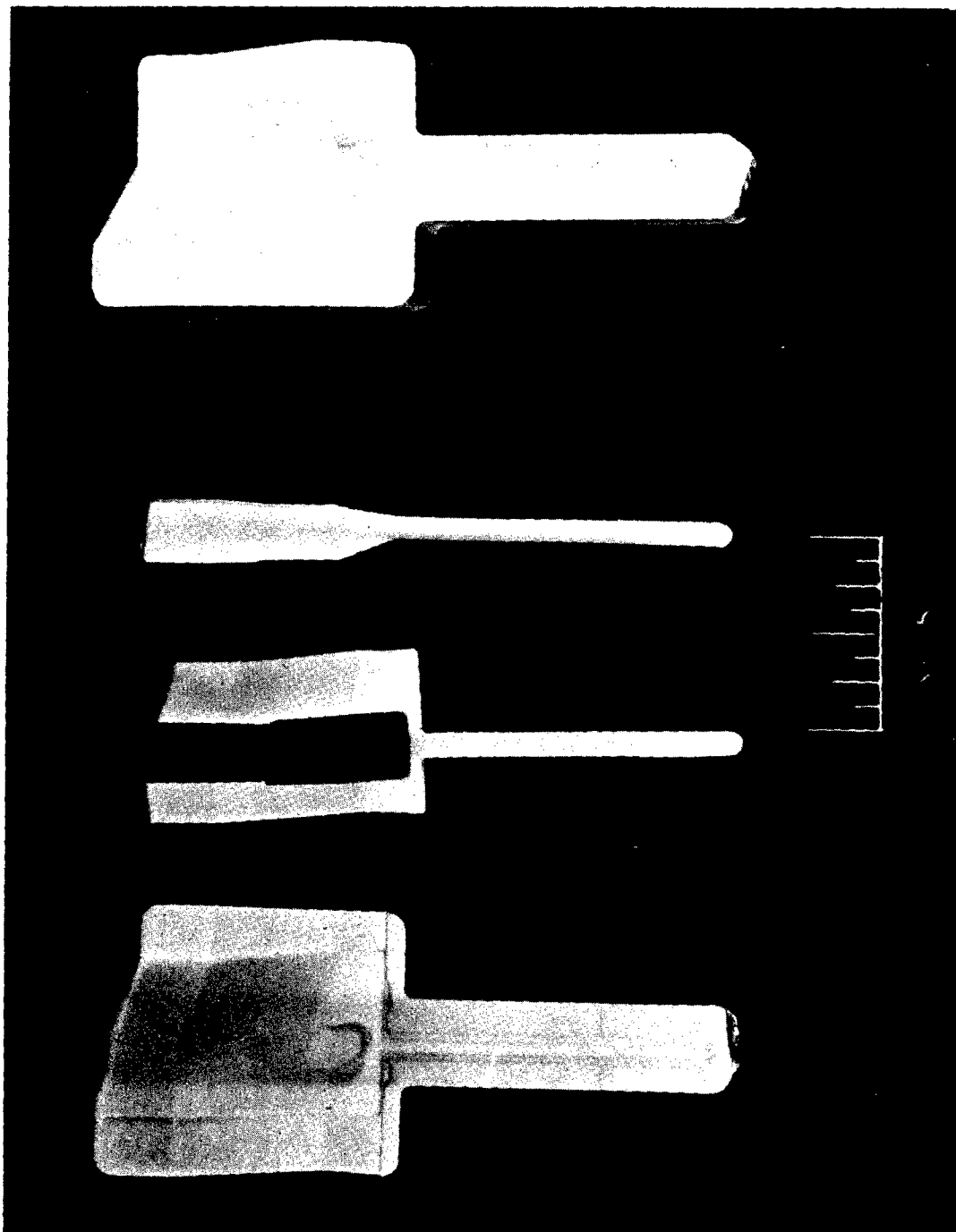


Figure 83. (Left and Right) - Ceramic Setter Block Halves.
(Middle) - Two-Piece Ceramic Core.

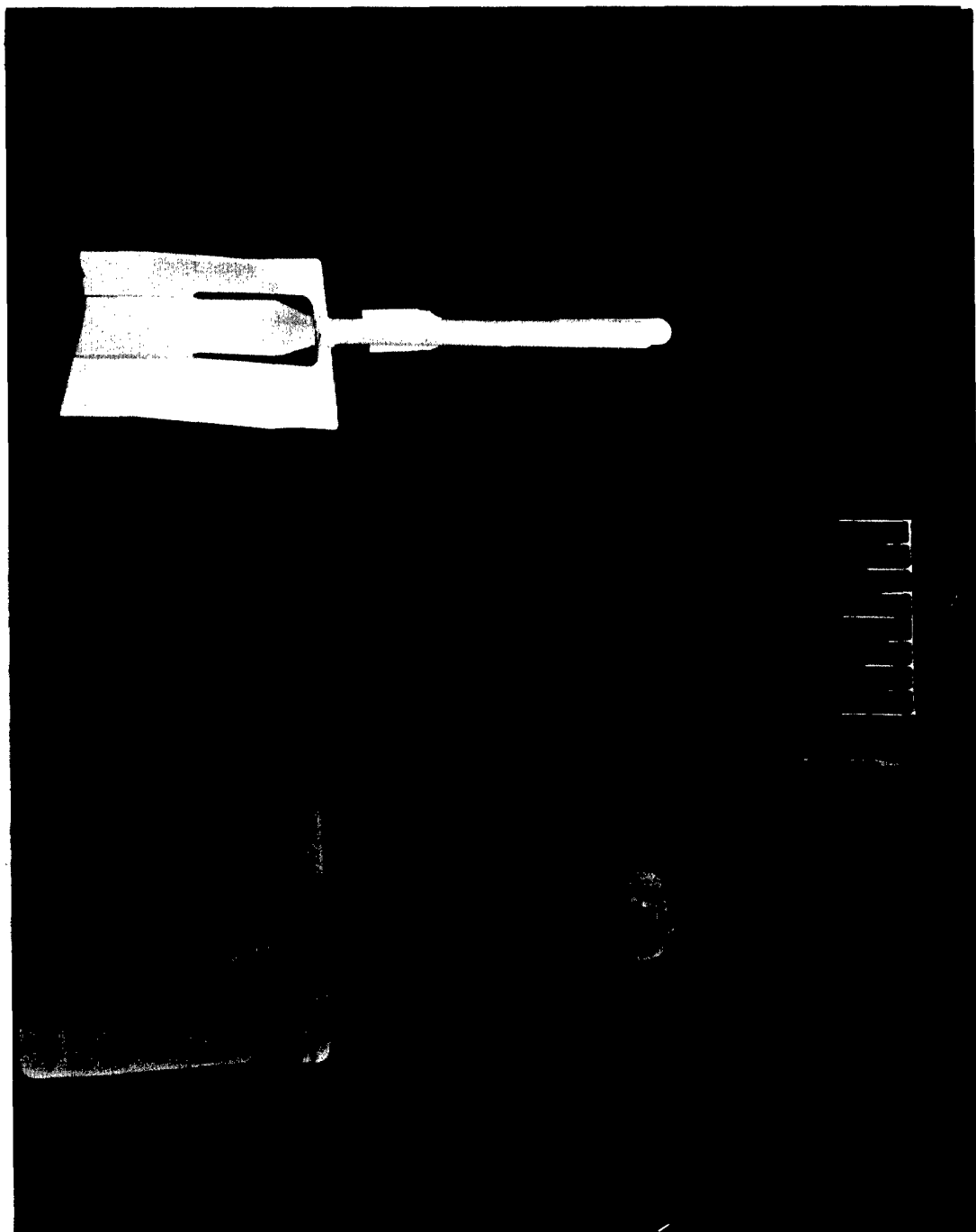
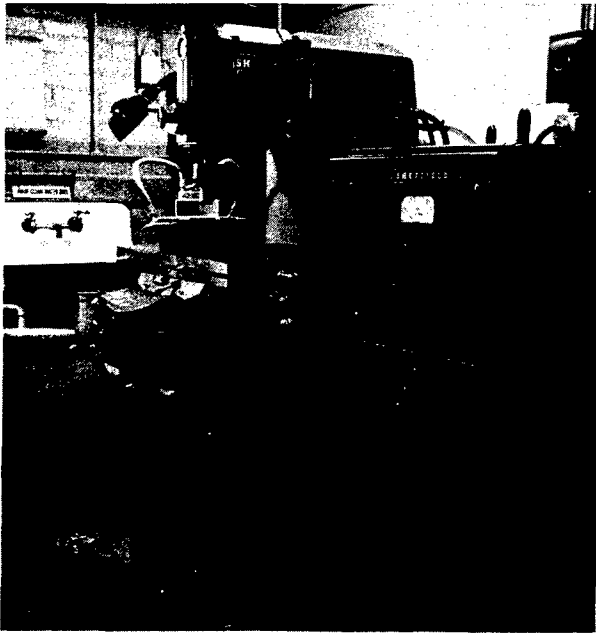
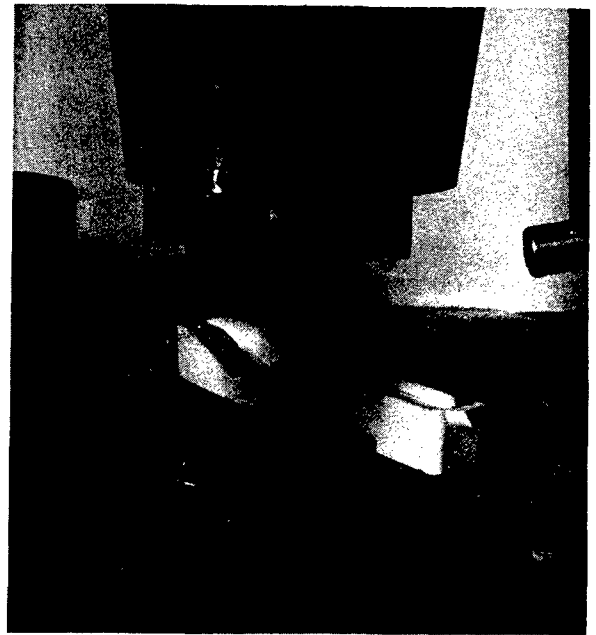


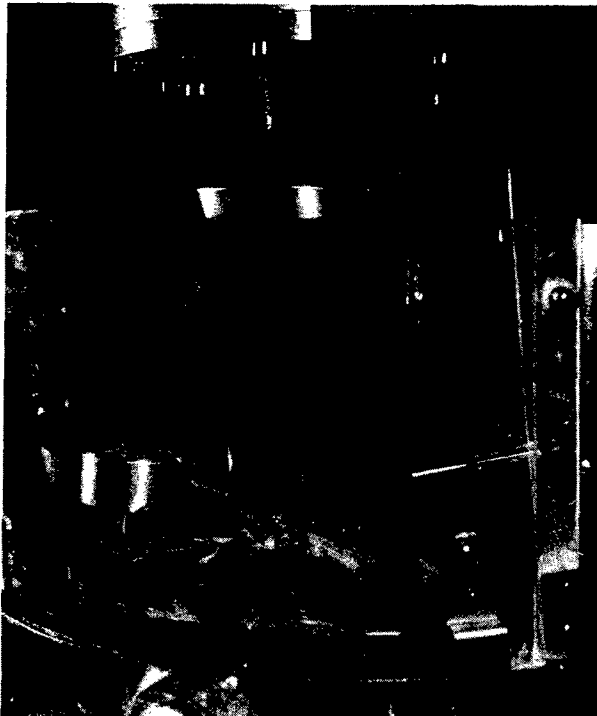
Figure 84. (Right) - Two-Piece Baked Ceramic Core.
(Left) - Green Ceramic Core and Setter Block Half.



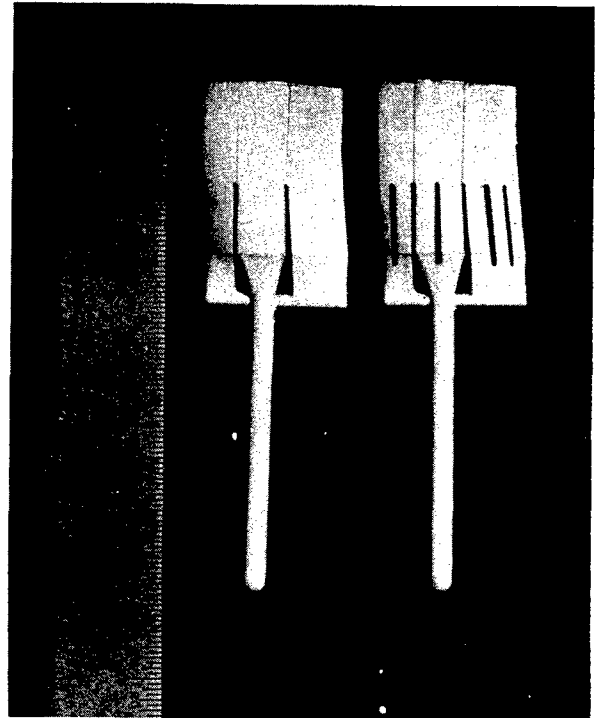
CAVITRON MACHINE



FIRED CORE IN PLACE TO MACHINE



FIRED CORE BEING MACHINED



FIRED CORES BEFORE AND AFTER
CAVITRON MACHINING

Figure 85. Cavitron Machining of Cores for Cooled Blade.

2. Core Dryers (Setter Blocks)

These ceramic blocks (Figure 83) were made by the injection molding techniques and were used to support the green cores during baking and to maintain contour and dimensions of the cores.

3. Blade Wax Pattern

Injection molding methods were used to make wax patterns of the blade contour. Core prints were added to the blade tip and the heat exchanger to support the ceramic core during the casting operation.

During processing of the castings, the core channel shape was changed to permit Cavitron machining.

Several additional changes were agreed to at this time:

1. The blade length would be increased 0.030 inch to allow for casting defect removal at the tip and for metal loss during EDM machining of the blade cap.
2. The spiral portion of the heat exchanger would cast as an integral part with excess stock to eliminate "back draft".
3. Castings were to be on a "best efforts" basis, using Continental Specification No. 51, Appendix I.

The preparation of wax patterns and core tooling proceeded without any major difficulties. Figure 86 is a photograph of a wax pattern used in making the precision casting mold.

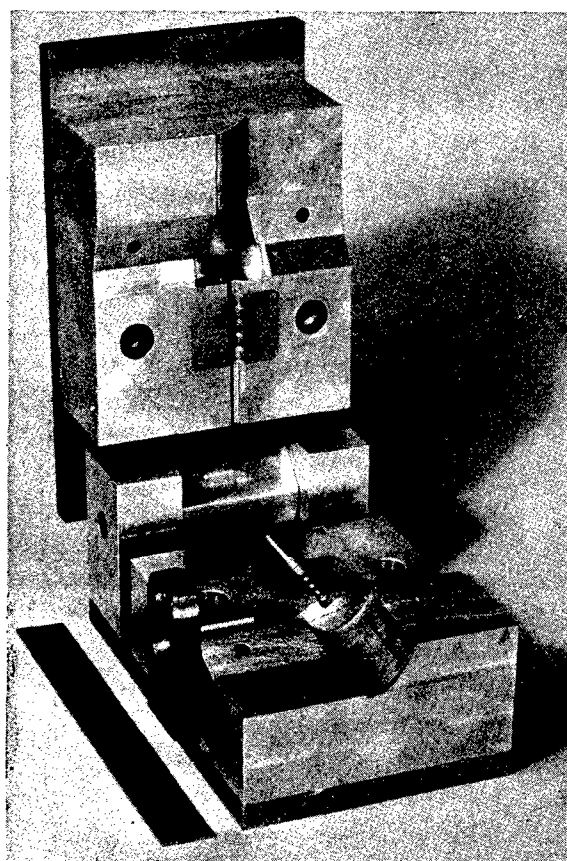
Figures 83 and 84 are examples of component parts required to assemble the ceramic core used to cast the hollow blade. These figures show the core prior to Cavitron machining the core slots.

Cavitron machining is one of the more advanced machining techniques used in the machining of ceramics and other brittle materials. The small size of this casting and core resulted in a very fragile core with a possible high breakage rate requiring the use of more advanced machining techniques. Such a fragile core is shown in Figure 85.

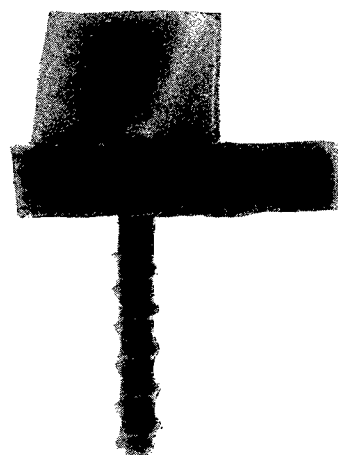
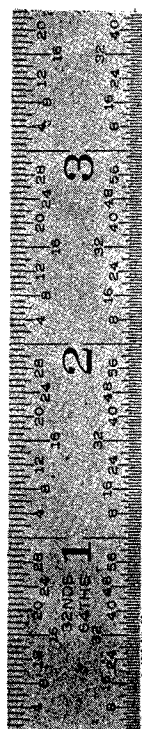
In anticipating some of the casting process problems which would be encountered and the reporting material that would be needed, check

lists were prepared to record the manufacturing process and quality level obtained on the castings, covering the following major areas:

1. Material certifications
2. Inspection requirements and standards
3. Routing and operation sheets
4. Inspection method sheets - dimensional
5. X-ray technique card
6. Tool inspection report form



INJECTION MOLD



WAX PATTERN

Figure 86. Injection Mold for Making Wax Pattern.

Casting requires care in rigging and gating to ensure an adequate yield. Figure 87 illustrates the technique necessary to achieve the successful gating of this blade configuration.

An initial lot of castings, containing both solid and slotted cores, was poured to evaluate several process variations. Additional lots were poured utilizing the best techniques obtained from the first lot.

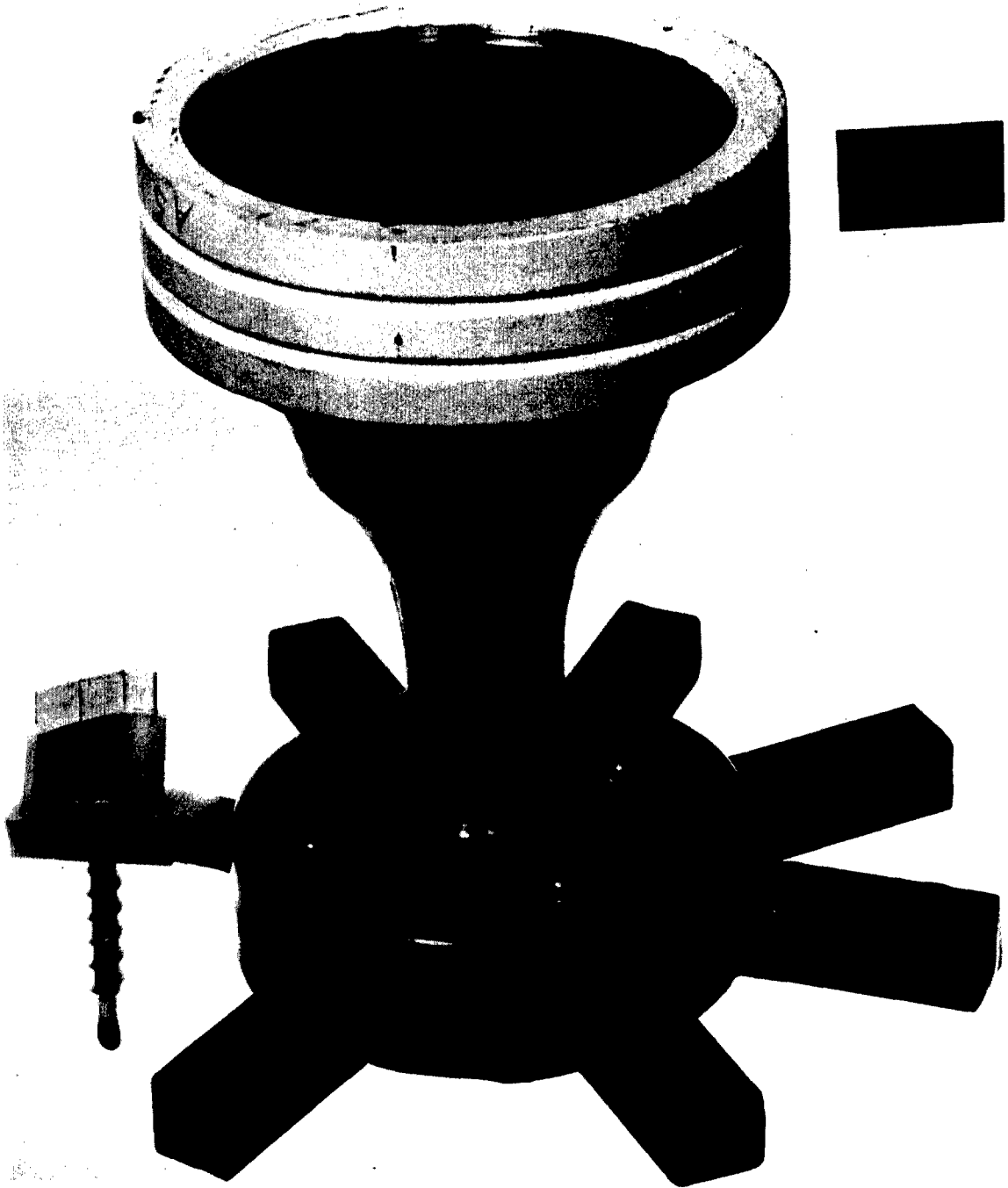


Figure 87. Wax Pattern Gating.

Inspection of a typical casting indicated that these castings were within the state-of-the-art-airfoil contour falling within the +0.005- to 0.003-inch tolerance band.

A metallurgical examination was made of casting serial No. 56 for comparison with Appendix I. The following results were obtained.

The surface of the cast blade revealed an equiaxed grain structure having a grain size less than 1/8-inch diameter maximum with an average of less than 1/16-inch diameter. The internal grain structure examined at the junction of the ingate and the blade root was found to be columnar, as shown in Figure 88. This examination indicated that the grain size requirement was met.

Surface indications, as determined by zyglo, were reviewed and found to be acceptable to specification in all areas. The largest indications were measured at 0.012-inch diameter and were separated by 1/8 inch (see Figure 89).

The casting was sectioned in several areas to examine the general internal microstructure and for evidence of microporosity. These sections are shown in Figures 90 through 93. A porous shrink condition shown in Figures 92 and 93 was found in the heat exchanger shank. This type of defect could interfere with welding operations and general strength requirements and is prohibited by the X-ray requirements of the specification. However, the defect is not readily detected in the radiograph so that a destructive spot check must be relied upon, together with casting process improvements, to eliminate the defect.

In view of the findings mentioned and considering the size and intricacies of the internal passages, this casting represents a major advancement in the state of the art. The small amount of shrink observed in the heat exchanger shank can be reduced with minor variations in technique. The production of cast fluid-cooled blades of this design is considered practicable.

Blade Tip Closure

Results of feasibility studies of the three methods of blade manufacture indicated that casting techniques would at this time produce the most satisfactory hollow blade for this application.

With this method of blade manufacture, one technique remained to be established; namely, closing of the blade opening left for core supports. This operation has been referred to as tip capping.



Figure 88. Cast Cooled Blade Etched to Show Equiaxed Surface Grain and Columnar Internal Grain Where Ingate Was Cut Off.



Figure 89. Blacklight Photo Showing Zyglo Indications on Cast Blade Surface.

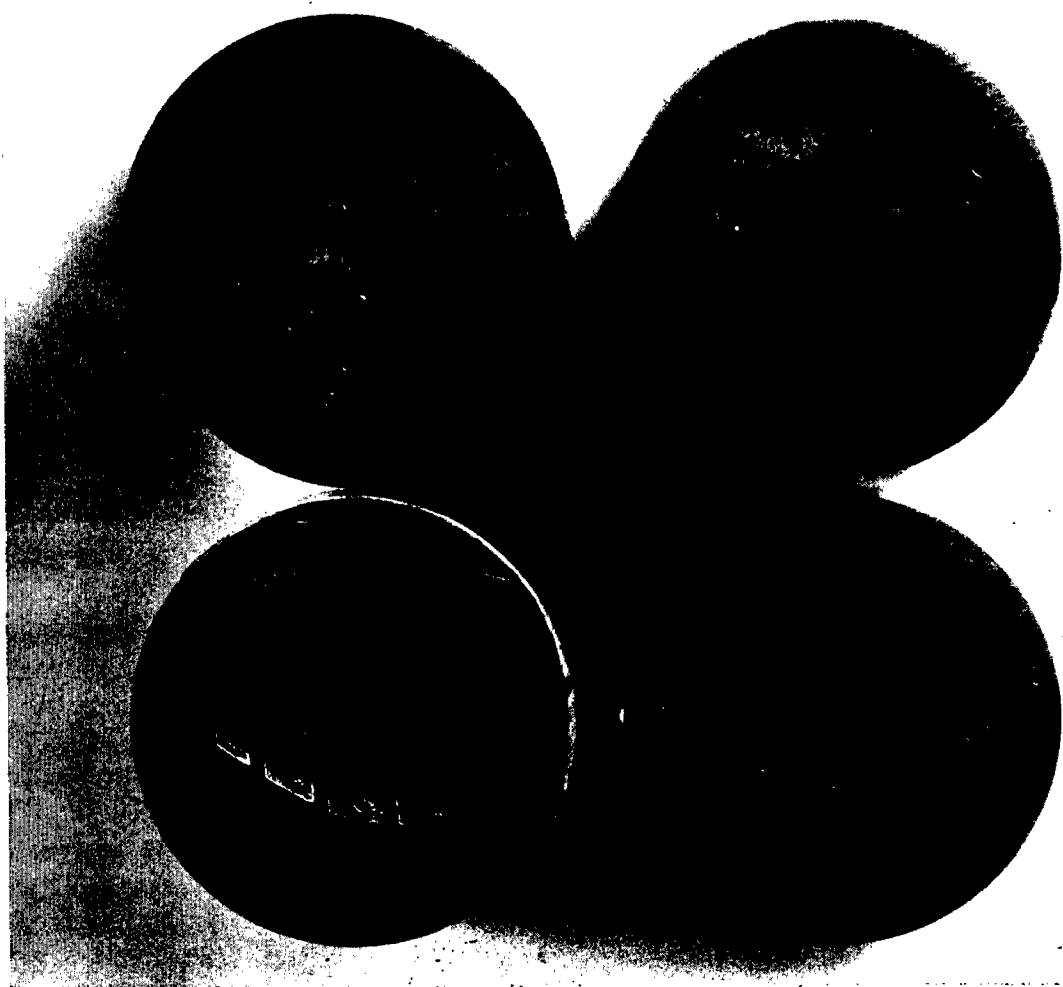


Figure 90. Cross Sections of Cooled Turbine Blade.

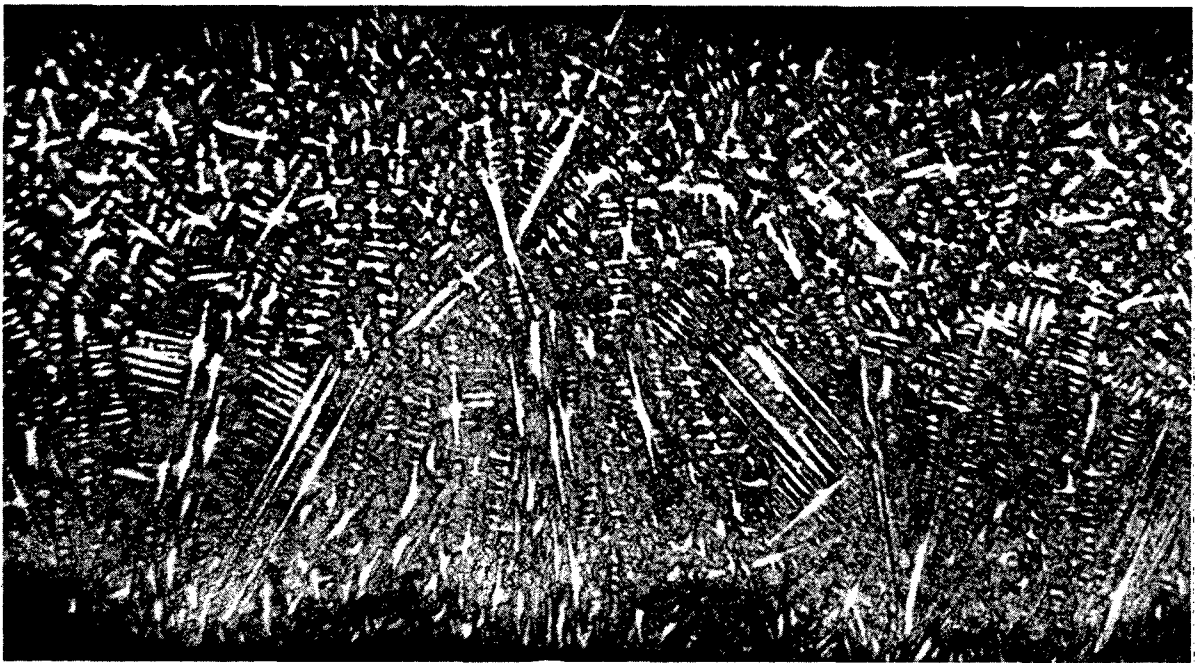
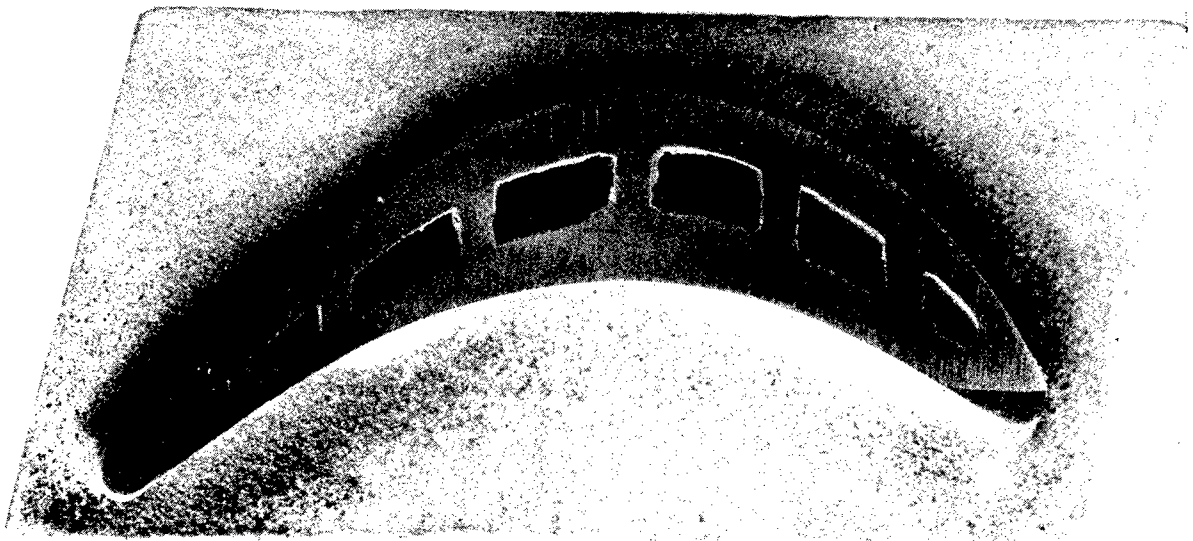


Figure 91. Cross Section of Cooled Turbine Blade Showing Typical Microstructure of Cast U-700 Alloy.

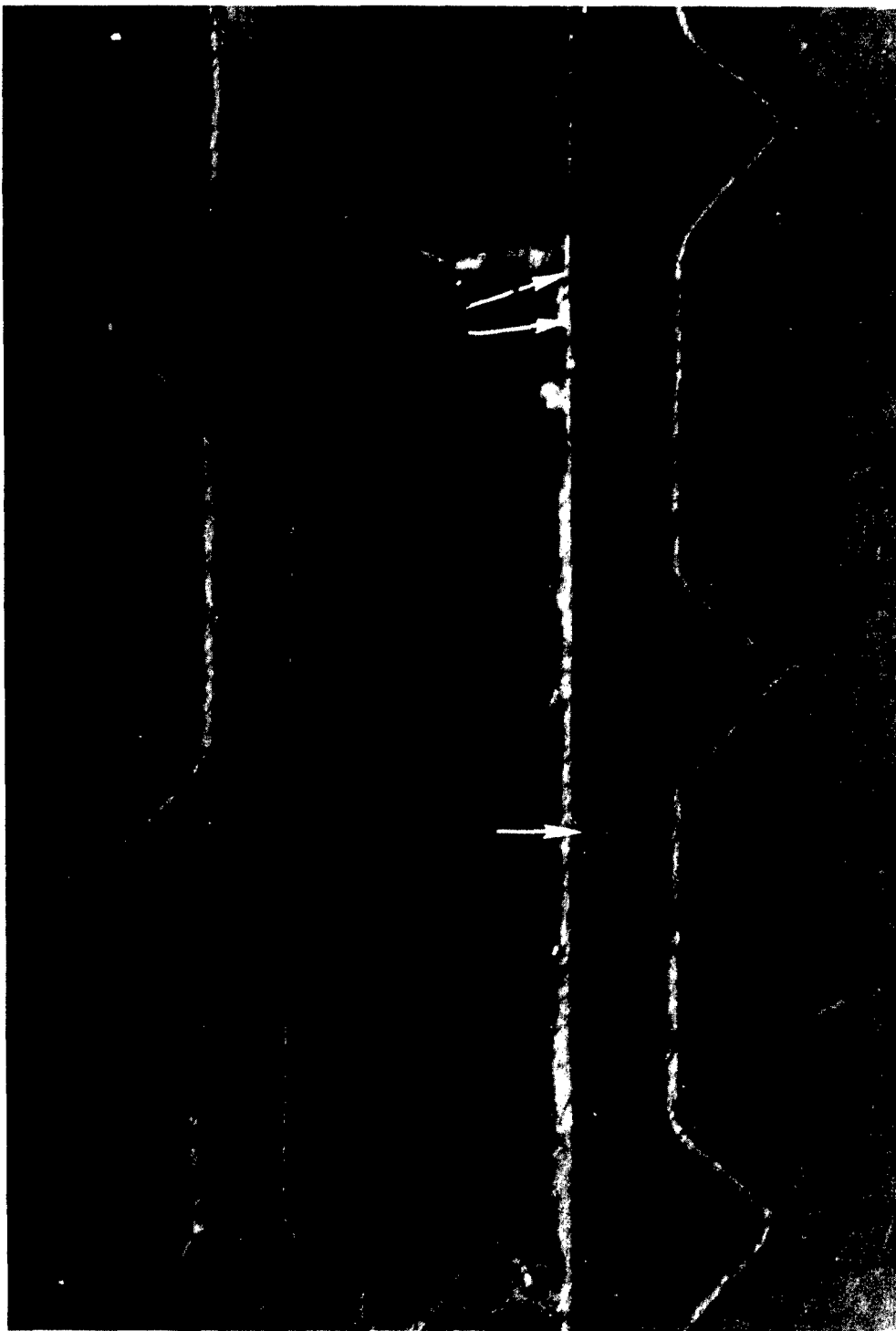


Figure 92. Heat Exchanger Shank Cross Section Showing Shrink Defect Location.

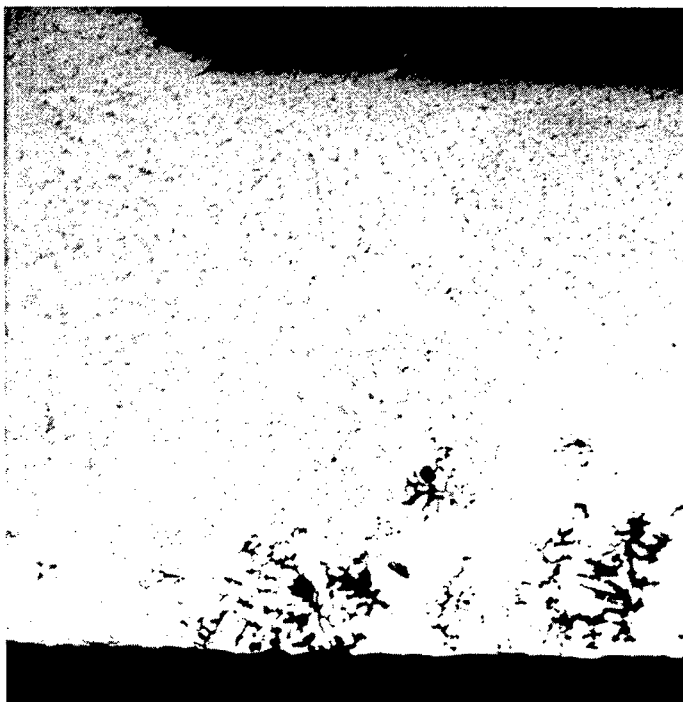


Figure 93. Shrink Defects in Heat Exchanger.

Related experience in this area indicated that butting a plate to the airfoil end and electron beam welding it on required further development. The success with EDM machining of intricate passages in wrought blocks indicated that the airfoil shape could be EDM machined into a rectangular cap to provide a good fit between the surfaces to be welded. This technique would also greatly facilitate the fixturing and welding operation.

The feasibility of this process was first demonstrated by Thompson Ramo Wooldridge (TRW), as shown in Figure 94.

The electron beam welding process, which had been selected to seal the blade and tip-cap, requires a very tight fit-up. Each blade casting will contain some irregularity peculiar to itself. Therefore, to obtain the desired fit-up, it is considered advantageous to use each casting as an EDM tool. Preliminary tests, as shown in Figure 95, showed an 8:1 tool loss, indicating the need for an alternate approach. This approach was a two-step process, and consisted of using a 0.001-inch undersize carbon roughing tool and the blade casting for the finish tool. This technique was considered successful, and a typical example is shown in Figure 96.

From the preliminary drawings of the airfoil, a tip-cap design as shown in Figures 97 and 98 was selected for this operation. The dimensions of this initial cap were as follows:

1. 0.375 inch deep to accommodate airfoil section.
2. 1.250 inch wide to accommodate airfoil section.
3. 0.125 inch thick - an arbitrary selection.
4. 0.06 inch penetration of the blade - an arbitrary selection.

Preliminary test welds simulating a blade-to-cap joint had indicated that the following was necessary to minimize weld cracking on heat treatment: welding at the point at which the blade enters the cap and, with a single pass of the beam, encompassing the entire penetration of the blade into the cap.

Several of these initial trial welds are shown in Figure 99.

The next series of tests was conducted with sample cast blades and EDM wrought caps having various blade penetrations and cap dimensions as follows:

- | | |
|-------------------|-------------------|
| 1. 0.125-inch cap | 0.060-inch cavity |
| 2. 0.095-inch cap | 0.030-inch cavity |
| 3. 0.250-inch cap | 0.060-inch cavity |

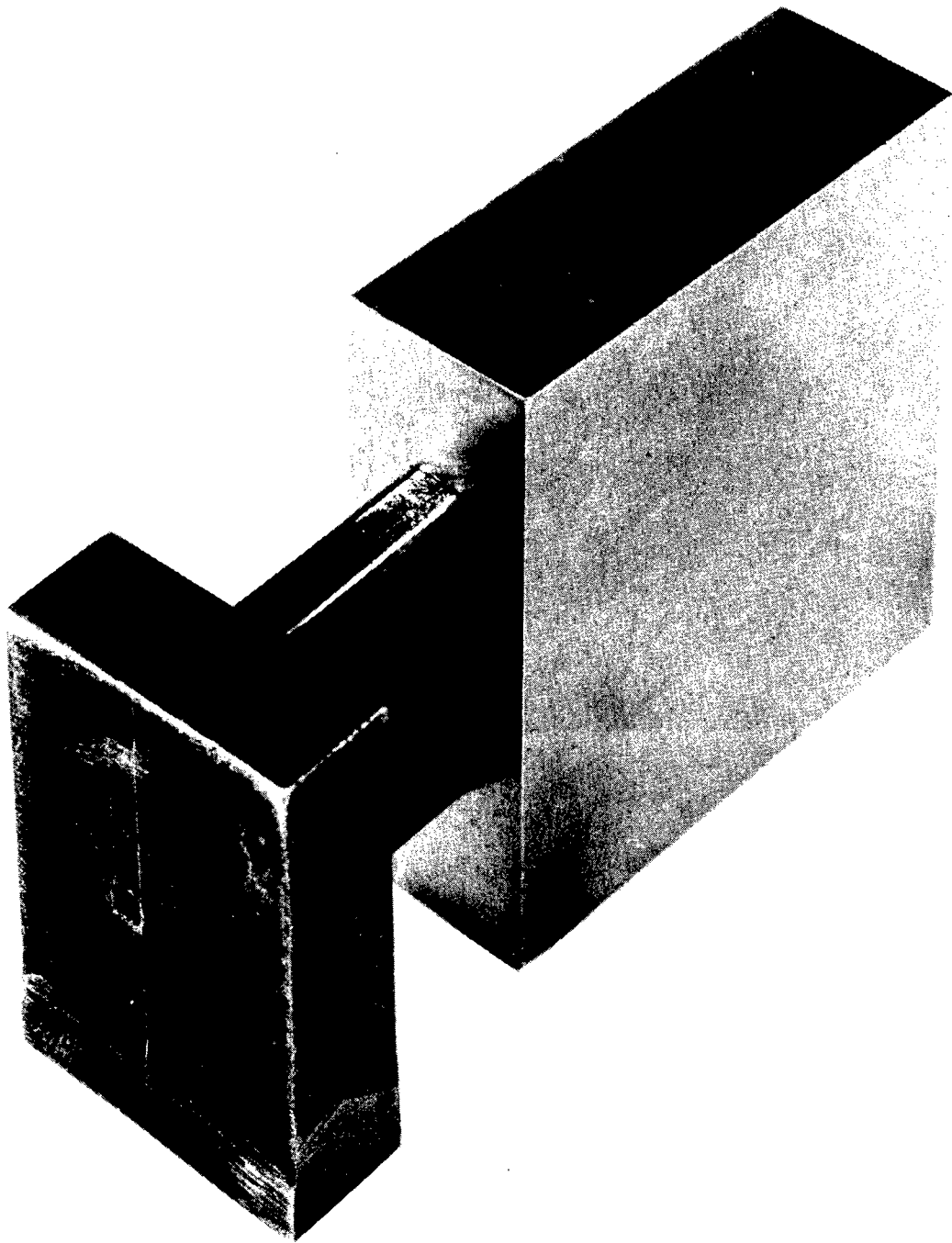


Figure 94. Rectangular Casting With EDM Cap From Carbon Tool.

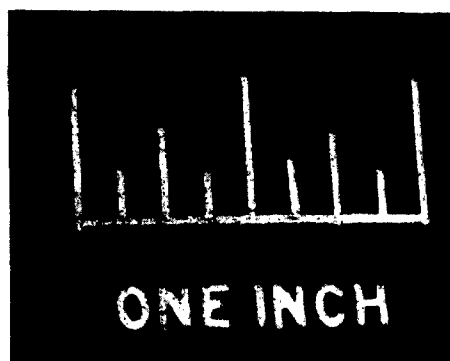
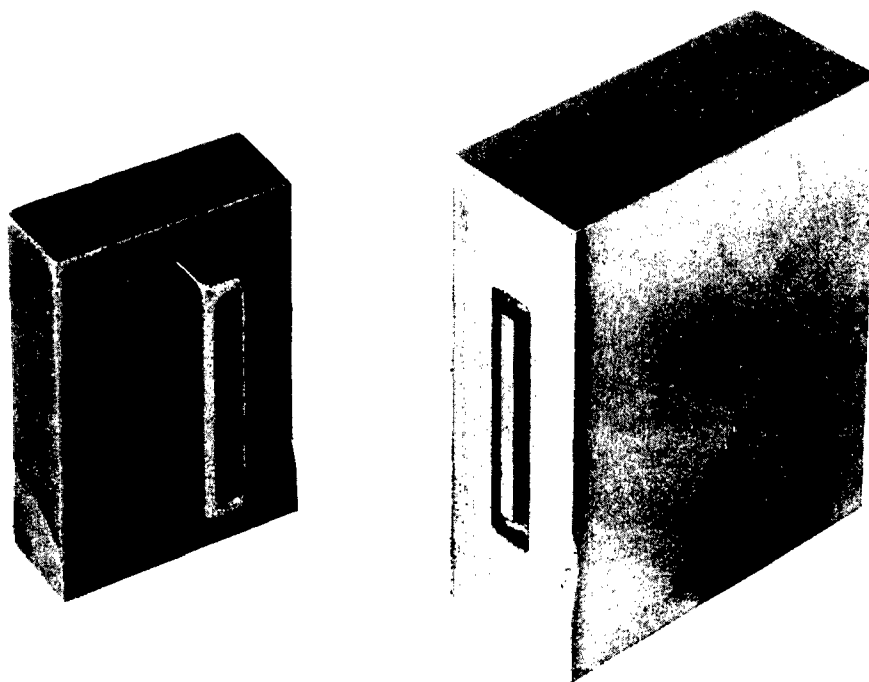


Figure 95. Rectangular Blade Used as EDM Tool to Machine Tip-Cap.

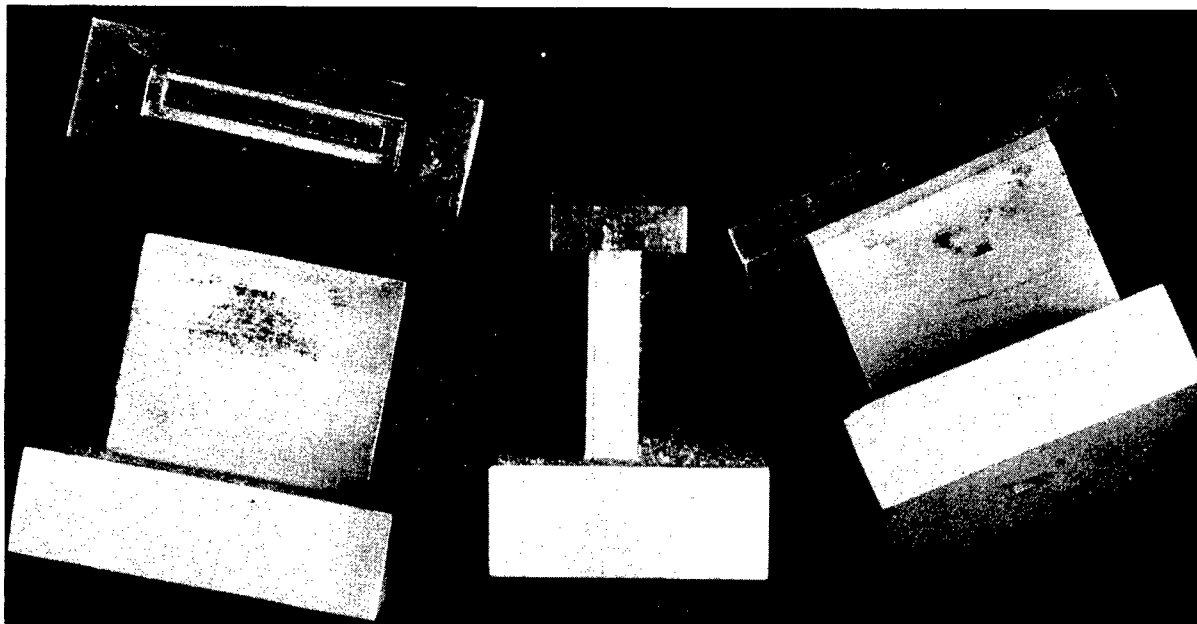


Figure 96. Rectangular Blade Used as Finishing Tool for EDM Tip-Caps.

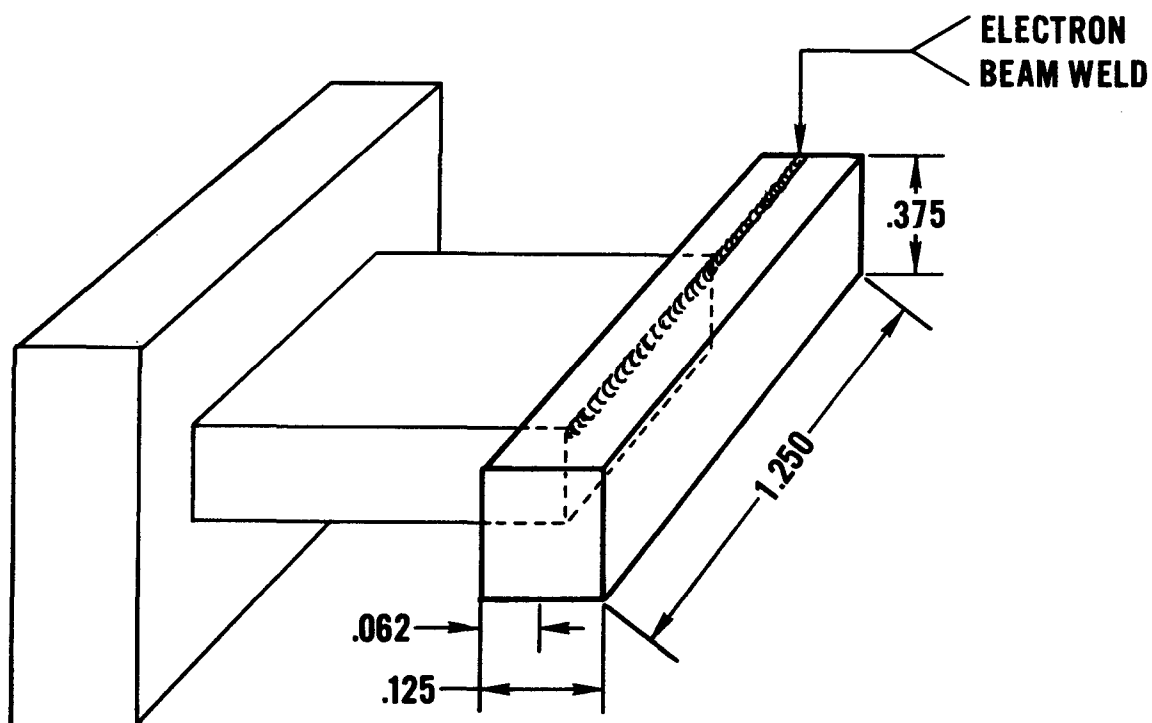


Figure 97. Cap Design for EDM Tip-Cap - Rectangular Blade Block.

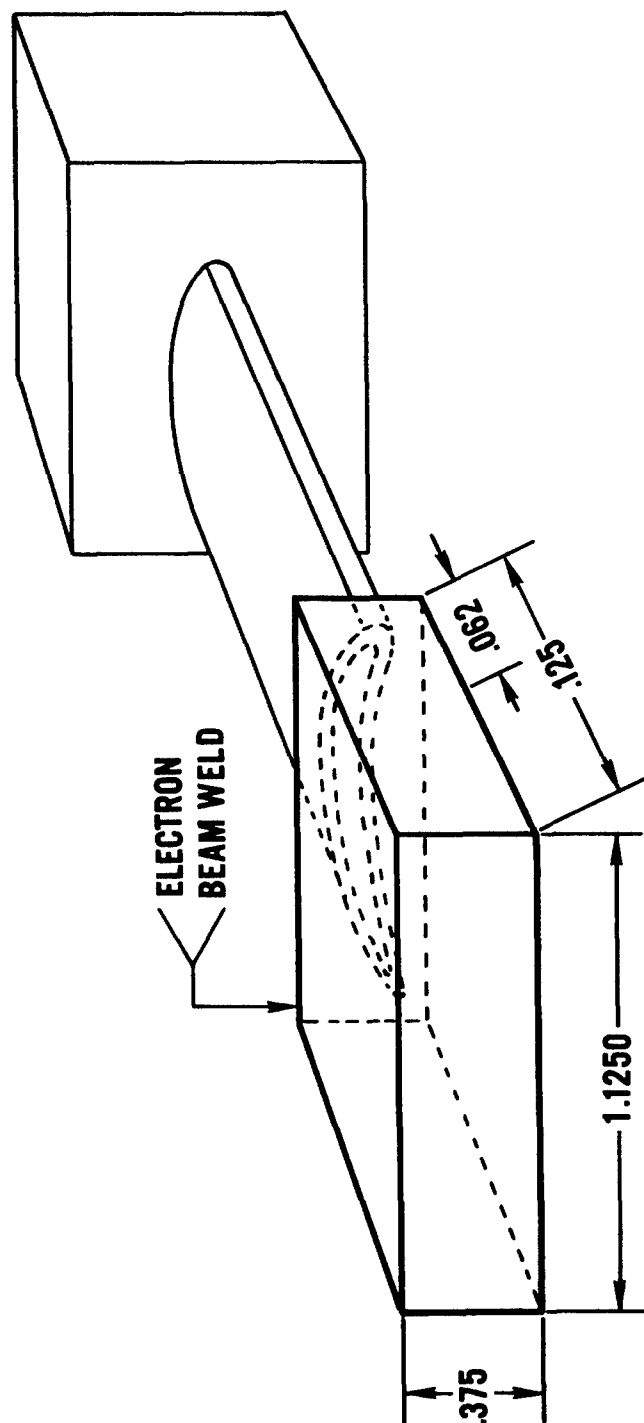
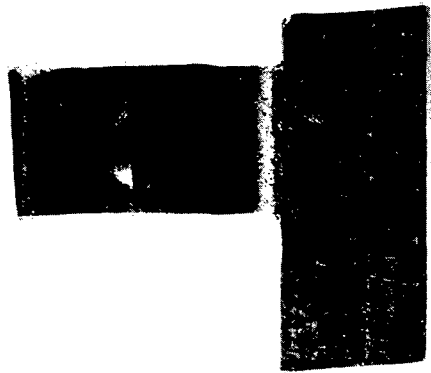
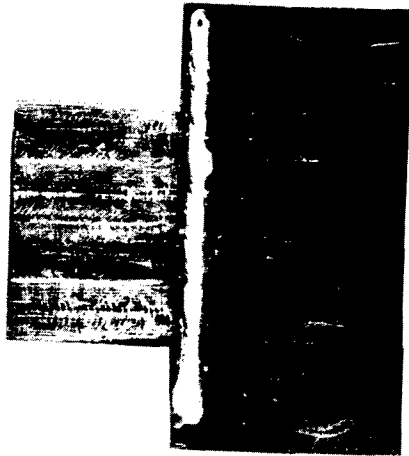


Figure 98. Design for EDM Tip-Cap - Airfoil Casting.



0.250 INCH CAP
0.060 INCH CAVITY



0.095 INCH CAP
0.030 INCH CAVITY



0.125 INCH CAP
0.060 INCH CAVITY

Figure 99. Preliminary Welds With EDM Tip-Caps.

The location of the electron beam with reference to the point at which the blade enters the cap was found to be important for two reasons: to control the amount of spill into the top cooling manifold and to encompass the entire joint.

Samples of these welds are shown in Figures 100 through 102.

These test welds indicated that two dimensions of the cap should be revised as follows:

1. Reduce the penetration of the blade into the cap to 0.030 inch to ensure encompassing the entire joint.
2. Increase the thickness of the cap to 0.250 inch for heat sink and better control of the electron beam alignment.

These test welds also indicated that location of the electron beam was an important factor in successfully closing this blade. The location of this beam was established to be 0.020 to 0.030 inch from the point at which the blade enters the cap.

The above results are demonstrated, using 140 KV, 16.5 MA at a rate of 45 inches per minute (see Figures 103 and 104).

Four additional blade samples having caps and dimensions shown in Table V were welded to verify preliminary results.

Later in the program, additional rectangular blades were capped using modified tip caps as shown in Figures 99 and 100. The joint details are shown in Table VI.

These test welds were submitted to the Continental-Toledo facility for leak testing and X-ray prior to heat treatment.

All of these castings and closure welds successfully passed a 1850 psig N₂ leak test. The X-rays of the joints were satisfactory, but supplemental nondestructive tests are considered necessary.

Following this proof testing the samples were heat-treated as follows:

Recommendation for Cast U-700

1975° F	4 hours' air cooling followed by
1400° F	16 hours' air cooling

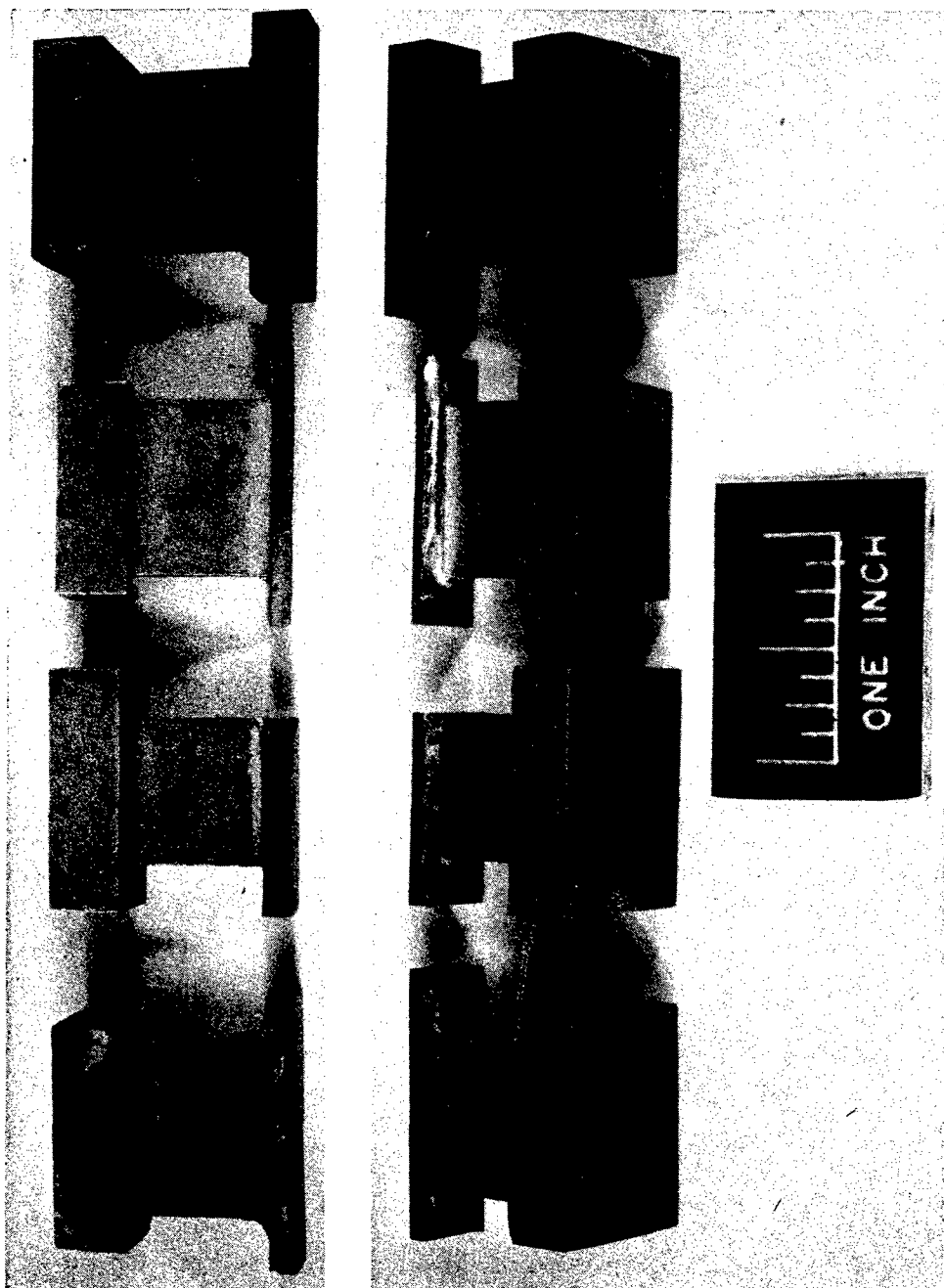


Figure 100. Rectangular Castings With EDM Tip-Caps.

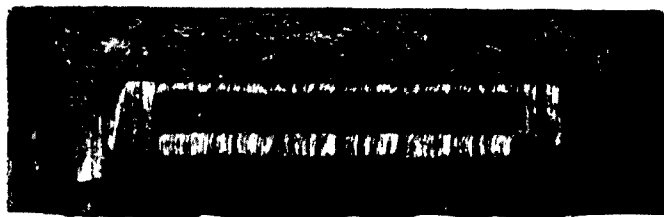
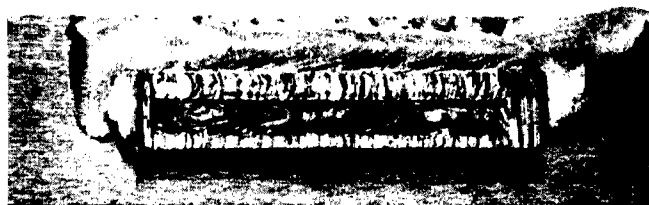
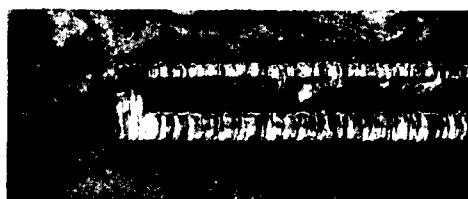
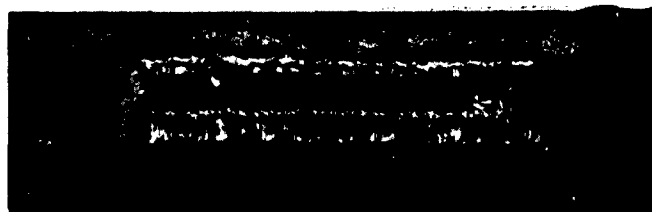


Figure 101. Internal Passage After Tip-Cap Welding.

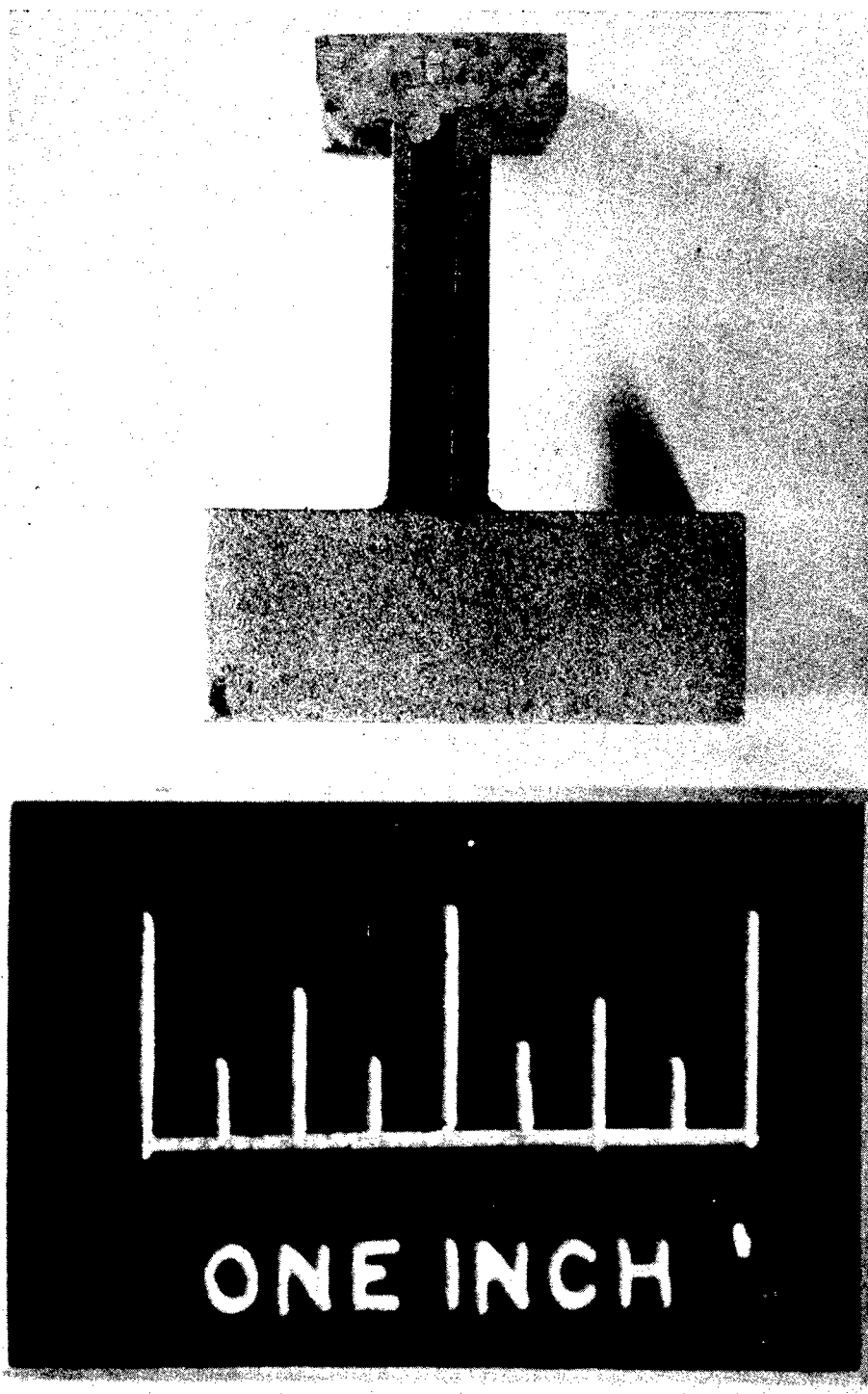


Figure 102. Cross Section of Tip-Cap Weld.



Figure 103. Cross Section of Tip-Cap Weld - Beam Focus at Cap Edge.



Figure 104. Cross Section of Tip-Cap - Beam Focus 0.030
Inch From Cap Edge.

TABLE V
JOINT DETAILS OF TIP-CAP WELDS

Casting No.	Blade Ltr.	Cap Mat.	Thick Cap (in.)	Depth Cap (in.)	Depth Cavity (in.)	Beam Location (in. from edge)
39412	E-2	U-700	0.225	0.375	0.030	0.030
6830	A-2	U-700	0.225	0.375	0.030	0.030
69791	D-2	Inco 718	0.225	0.375	0.030	0.030
69803	F-2	Inco 718	0.225	0.375	0.030	0.030

TABLE VI
JOINT DETAILS OF MODIFIED TIP-CAP WELDS

Casting No.	Cap Mat.	Thick Cap (in.)	Depth Cap (in.)	Depth Cavity (in.)	Beam Location (in. from edge)
*6556	U-700	0.250	0.375	0.030	0.030
8394-2	U-700	0.250	0.375	0.030	0.030
8395-1	U-700	0.250	0.375	0.030	0.030
8393	U-700	0.250	0.375	0.030	0.030
8396-5	U-700	0.250	0.375	0.030	0.030
8395-9	U-700	0.250	0.375	0.030	0.00
8396-12	U-700	0.250	0.375	0.030	0.00

* Sample contains cored passages

Inco 718 Welds

1325° F 16 hours' air cooling

Upon completion of the above heat treatment, these welds were examined as shown in Table VII.

TABLE VII
PRESSURE TEST TREATMENTS

Casting No.	Ltr. No.	Cap Material	Remarks
39412	E-2	U-700	Weld leaked at 50 psig N ₂
6830	A-2	U-700	Passed 2000 psig N ₂ leak test
69791	D-2	Inco 718	Macro section of weld joint free from cracks
69803	F-2	Inco 718	Passed 2000 psig N ₂ leak test
* 6556		U-700	Passed 2000 psig N ₂ leak test
8394-2		U-700	Passed 2000 psig N ₂ leak test
8395-1		U-700	Passed 2000 psig N ₂ leak test
** 8393		U-700	Passed 2000 psig N ₂ leak test
***8396-12		U-700	Passed 2000 psig N ₂ leak test
* Sample contained cored passages			
** Sample modified per Figure 105			
*** Sample modified per Figure 106			

On the basis of the above leak test results, it is concluded that by the technique of using EDM tip-caps and electron beam welding, hollow turbine blades may be closed at the tip with a high degree of success.

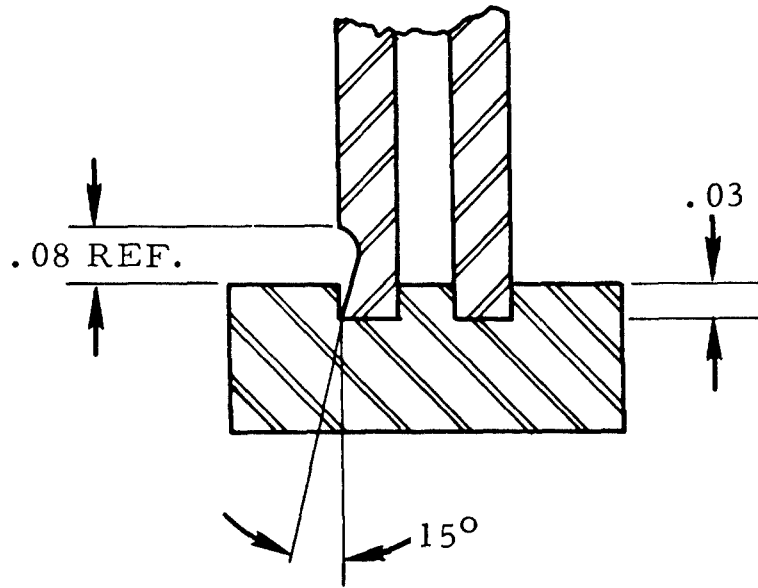


Figure 105. Blade and Cap With 15° Notch.

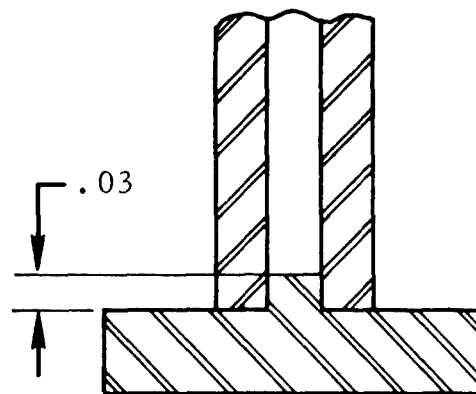


Figure 106. EDM Cap With Wrought Cap Inserted Into Blade Casting.

In anticipation of a transition to an airfoil contour and the possibility of a maximum 0.007 inch gap with an EDM cap, two rectangular blades were modified with a 15° notch after machining the EDM cap (Figure 105).

These samples were welded using the same techniques as above. As shown in Figure 107A, this gap did not hinder the welding operation.

A further modification of tip-cap was made to expose the joint between the cast blade and the wrought cap as shown in Figure 106.

These samples were welded and successfully leak tested as shown in Figure 107B.

Upon completion of the above capping and welding on rectangular castings, development work was begun on enclosing the airfoil castings.

The EDM preparation of airfoil tip-cap blocks was initiated at two vendors.

Vendor A produced the first airfoil cap, Figure 108, using a carbon tool for roughing and the cast blade for finishing in accordance with the sketch shown in Figure 109.

Vendor B produced a cap using the cast blade for the entire operation. Both types of tip-caps were processed through welding. Four additional castings were fitted with EDM caps, and 30 additional castings were shipped from the casting source.

The progress on tip-cap development was expedited by proceeding with roughing operations on the EDM slot in the tip-cap prior to obtaining castings of the blade. The cast blade will be used as a finishing tool during EDM and is needed for final dimensional adjustments in the carbon roughing tool.

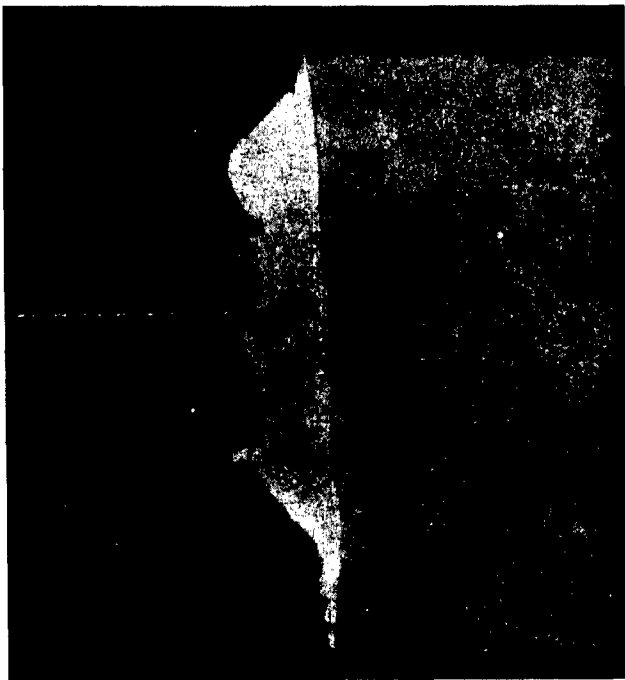
An initial lot of airfoil castings were fitted with both EDM type caps and flat butt caps for closure welding. These capped castings were pressure checked (2000 psig N₂), and the results are presented in Table VIII.

Continental has assembled 23 leak-tight airfoil castings with electron beam welded tip-caps.

From the above results and the photograph, Figure 110, Continental has demonstrated the ability to produce a cored cast blade having a leak-tight electron beam welded tip-cap.



(A) 15-DEGREE NOTCH



(B) EDM INSERT

Figure 107. Cross Section of Cap Weld.

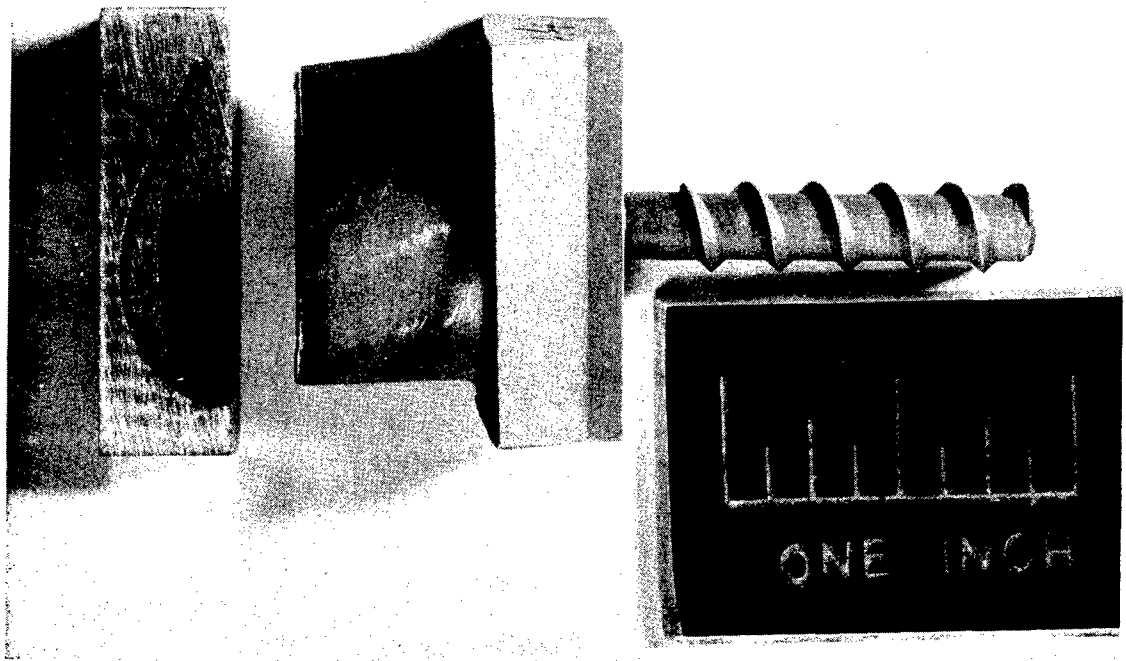


Figure 108. Cast Cooled Blade, Part No. 709627, With Tip-Cap - EDM With Carbon Roughing Tool.

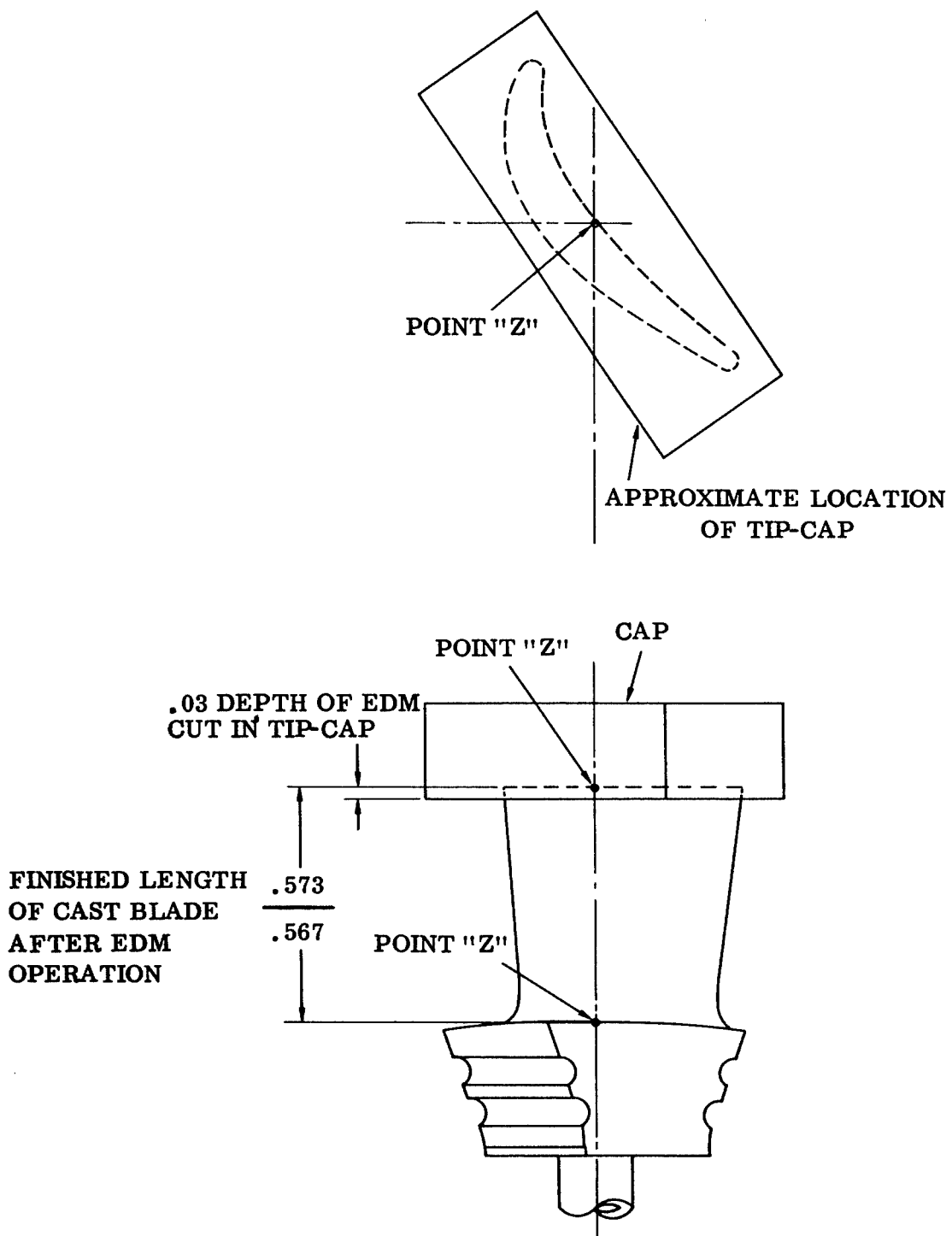


Figure 109. EDM Operation on Cooled Turbine Blade.

TABLE VIII
LEAK TEST OF BEAM WELDED AIRFOIL CAPS

Casting No.	Cap Type	Core Type	Casting Length	Remarks
A-3	EDM	Solid	-	Leak tight after weld repair
A-4	EDM	Solid	-	Passed leak test
A-5	Butt	Solid	Uncut	Passed leak test
A-6	Butt	Solid	Uncut	Passed leak test
A-13	EDM	Slotted	-	Passed leak test
A-21	EDM	Slotted	-	Passed leak test
A-30	Butt	Slotted	Cut to Length	Leak tight after weld repair
A-33	Butt	Slotted	Cut to Length	Leak tight after weld repair
A-34	Butt	Slotted	Cut to Length	Leak tight after weld repair
A-37	Butt	Slotted	Cut to Length	Leak tight after weld repair
A-42	Butt	Slotted	Cut to Length	Leak tight after weld repair
A-47	Butt	Slotted	Cut to Length	Leak tight after weld repair
A-50	Butt	Slotted	Cut to Length	Leak tight after weld repair
A-53	Butt	Slotted	Cut to Length	Passed leak test
A-60	Butt	Slotted	Cut to Length	Passed leak test

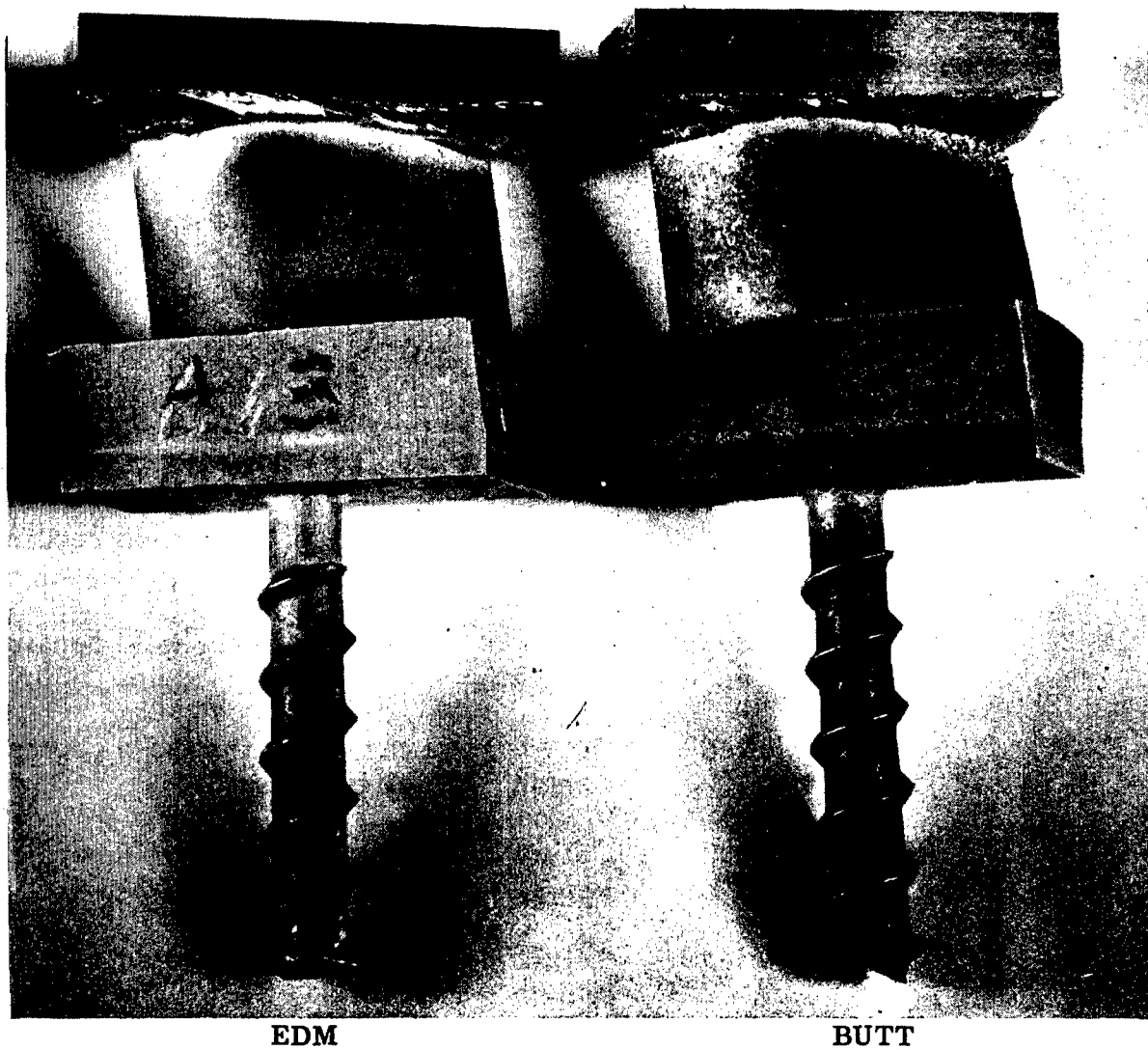


Figure 110. Beam Welded Airfoil Cap.

Blade Closure (Stem)

Preliminary tests were conducted to seal the heat exchanger stem after inserting a specific quantity of water. Electron beam welding was not considered for this application, as it was considered impractical to maintain water in this assembly during pump-down to 10^{-5} torr vacuum. Therefore, efforts were directed toward tungsten inert gas (TIG) welding of the plug.

Several plug designs were considered using a drilled cast block to contain the water.

Utilizing a simulated stem from a cast U-700 block containing a specific quantity of water and a plug design shown in Figure 111A, a partially satisfactorily TIG welded joint was obtained. This weld showed porosity which was attributed to the expansion of air in the tube causing blowout of the weld metal.

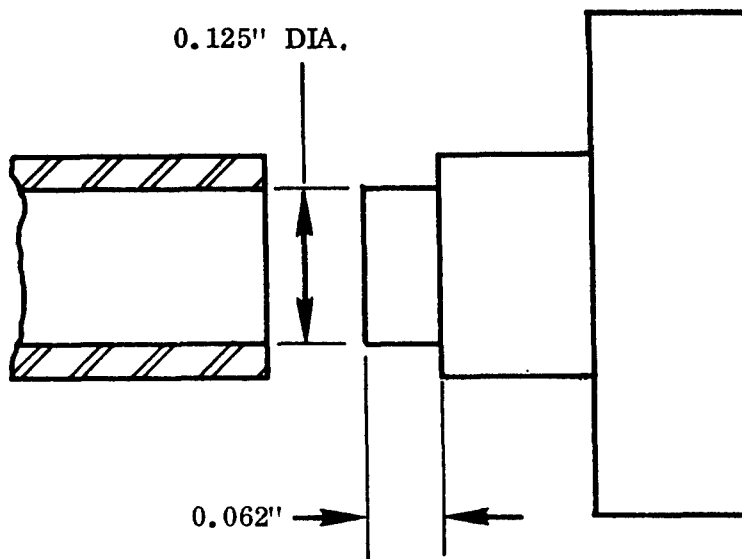
Using the plug design shown in Figure 111B, two simulated joints were successful and, on the basis of weight, water containment was considered feasible with this technique.

The successful plug design described above was applied to capped airfoil blades. The initial attempt resulted in an unsatisfactory TIG weld as evidenced by the collapse of the cast wall and the inability of the joint materials to flow properly. This was attributed to micro shrink of the cast blade stem as described in the preceding section.

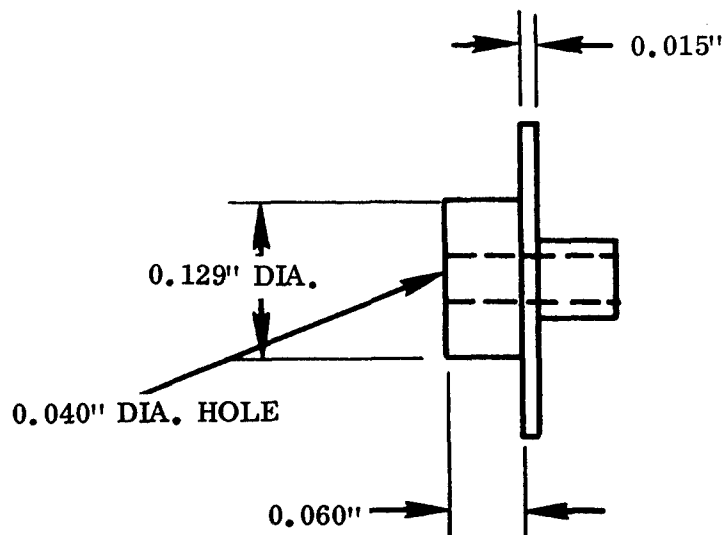
This technique was repeated with a second blade casting with similar results. Figure 112 shows the results of these efforts.

The unsuccessful TIG welded plug was removed from the first sample and a new plug was electron beam welded prior to water insertion. This joint satisfactorily passed a leak test. A specific quantity of water was inserted through the plug pin hole and the pin hole sealed by TIG welding. On the basis of weight, this blade contained water after welding. This was further verified by opening the stem and shaking out drops of water. This technique was repeated on a second blade shown in Figure 113; and on the basis of weight, successful containment of water was indicated. These data are shown in Table IX.

While the precise amount of contained water has not been determined, further test with radioactive tracers will determine this quantity.



A. INITIAL DESIGN



B. FINAL DESIGN

Figure 111. Plug Designs.



Figure 112. TIG Welded Heat Plug in Airfoil Blade.

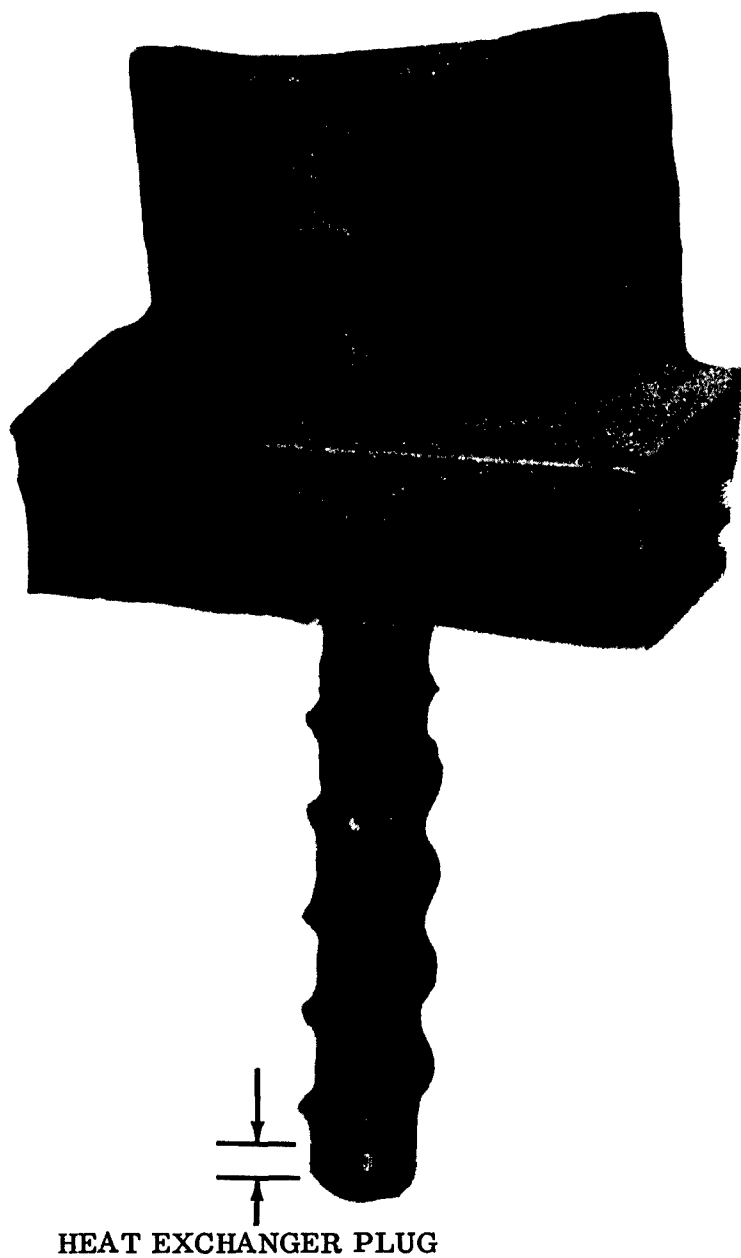


Figure 113. Electron Beam Welded Heat Exchanger Plug.

TABLE IX
PLUGGED HEAT EXCHANGER WEIGHT MEASUREMENTS

	Sample No. 1	Sample No. 2	Sample No. 3	Sample No. 4	Sample No. 5	Blade A-4	Blade No. 34	Blade No. 50	Blade No. 60	Blade No. 47	Blade No. 30
Weight of Part	8.0570g	18.1980g	21.9300g	11.5500g	11.5249g	46.8816g	45.0962g	45.0377g	44.8942g	44.8532g	44.7311g
Weight of Part Plus Water	8.0770g	18.2345g	21.9632g	11.5885g	11.6624g	46.9290g	45.1092g	45.0589g	44.9110g	44.8673g	44.7452g
Weight of Water Added	0.0200g	0.0365g	0.0332g	0.0385g	0.1375g	0.0474g	0.0130g	0.0212g	0.0168g	0.0141g	0.0141g
Remarks	Weld Contained Blow Hole	Sample Contained 0.0355g Water	Sample Contained 0.0331g Water	Sample Contained Water When Cut Open	Sample Contained Water When Cut Open	Initial Tip Weld Col- lapsed Casting. and Plug Redesigned	Plug De- sign No. 3 - By Weight Sam- ple Contains 0.0068g Water	Tip Welded Casting Collapsed Filler Metal Added	Weld Design No. 3 Slight oxide noted after tip weld	Weld Design No. 3	Weld Design No. 3

Continental has demonstrated the ability to contain a fluid in a fluid-cooled blade using the above technique for final closure.

The other methods investigated, for the manufacture of cooled turbine blades, are reported below.

Electron Beam Welding

The second process evaluated for blade fabrication was electron beam welding.

A wrought U-700 block 1.5 inches by 1.5 inches by 0.5 inch was grooved to simulate the internal passages of a hollow blade. Superimposed on this block was another ungrooved matching block of the same dimensions. The objective of this method was to join these two halves by electron beam techniques without closing the cooling passages. Two approaches to this problem were planned: welding with the passages unfilled and welding with the passages filled with nickel or a ceramic.

The following machining methods were considered for the production of the grooved test blocks: end milling, electro-chemical machining, and electrical discharge machining.

End milling of the intricate cooling passages was considered to be expensive, and experience with U-700 material indicated a high breakage rate and excessive tool wandering with resulting dimensional errors. Because of this, electro-chemical machining (ECM) and electrical discharge machining (EDM) were considered. EDM was selected over ECM because its advantage of better dimensional control outweighed the faster cutting rate and better surface finish obtainable by the ECM process.

Test blocks for both electron beam welding and diffusion bonding studies were made using carbon tooling. This tooling is shown in Figures 114 through 116. Two separate tools were required for each test block: one for the vertical channels, all of varying depths; the other cut the cross passageways, all of equal depth. Each electrode was reground twice on the cutting face to re-establish small corner radii and face trueness for each part.

The normal cycle time, including two tool redressings to produce a finished blade block, as shown in Figure 117, was less than 4 hours.

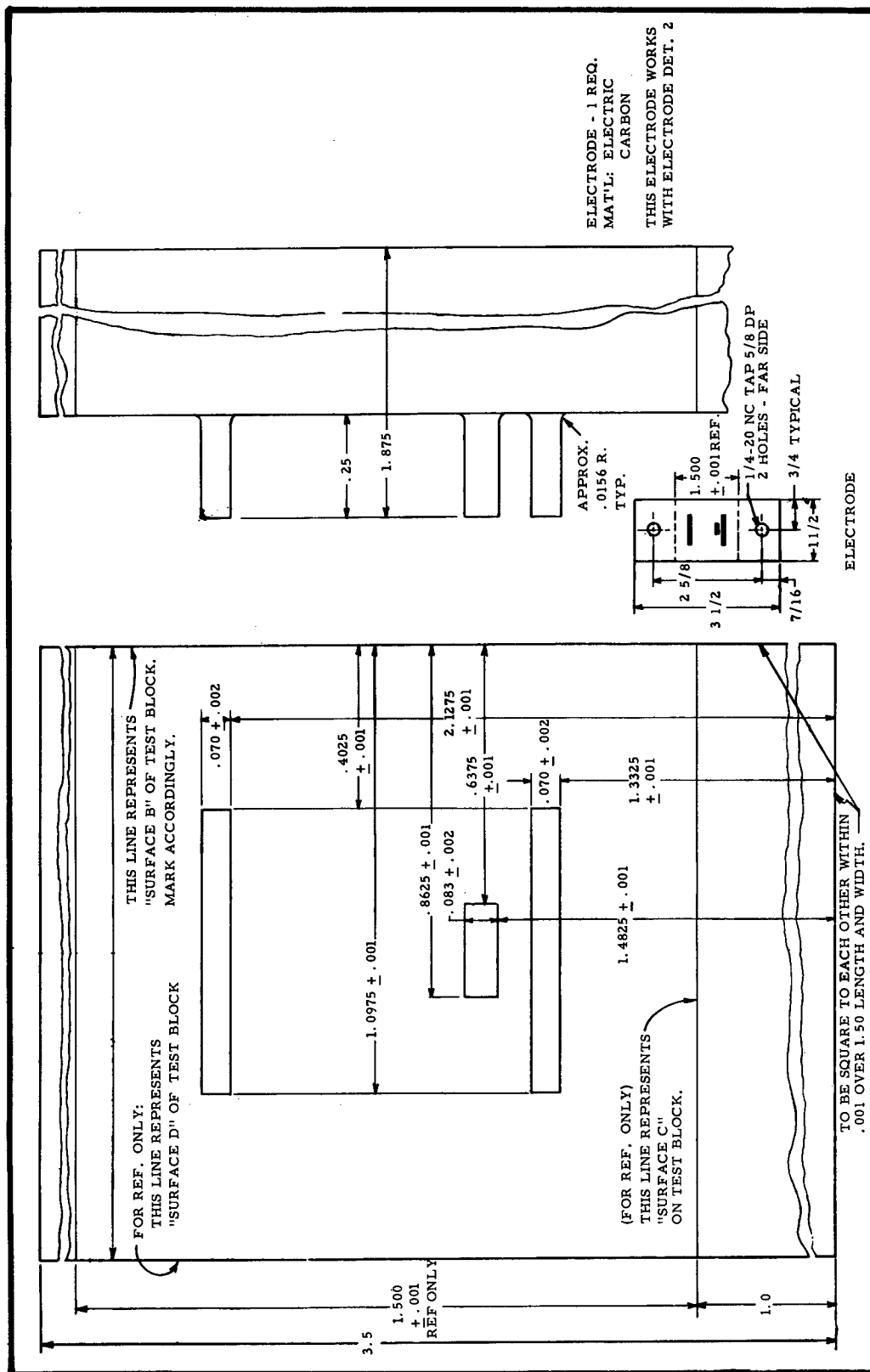


Figure 116. Tooling Print for EDM Machining Test Blocks.

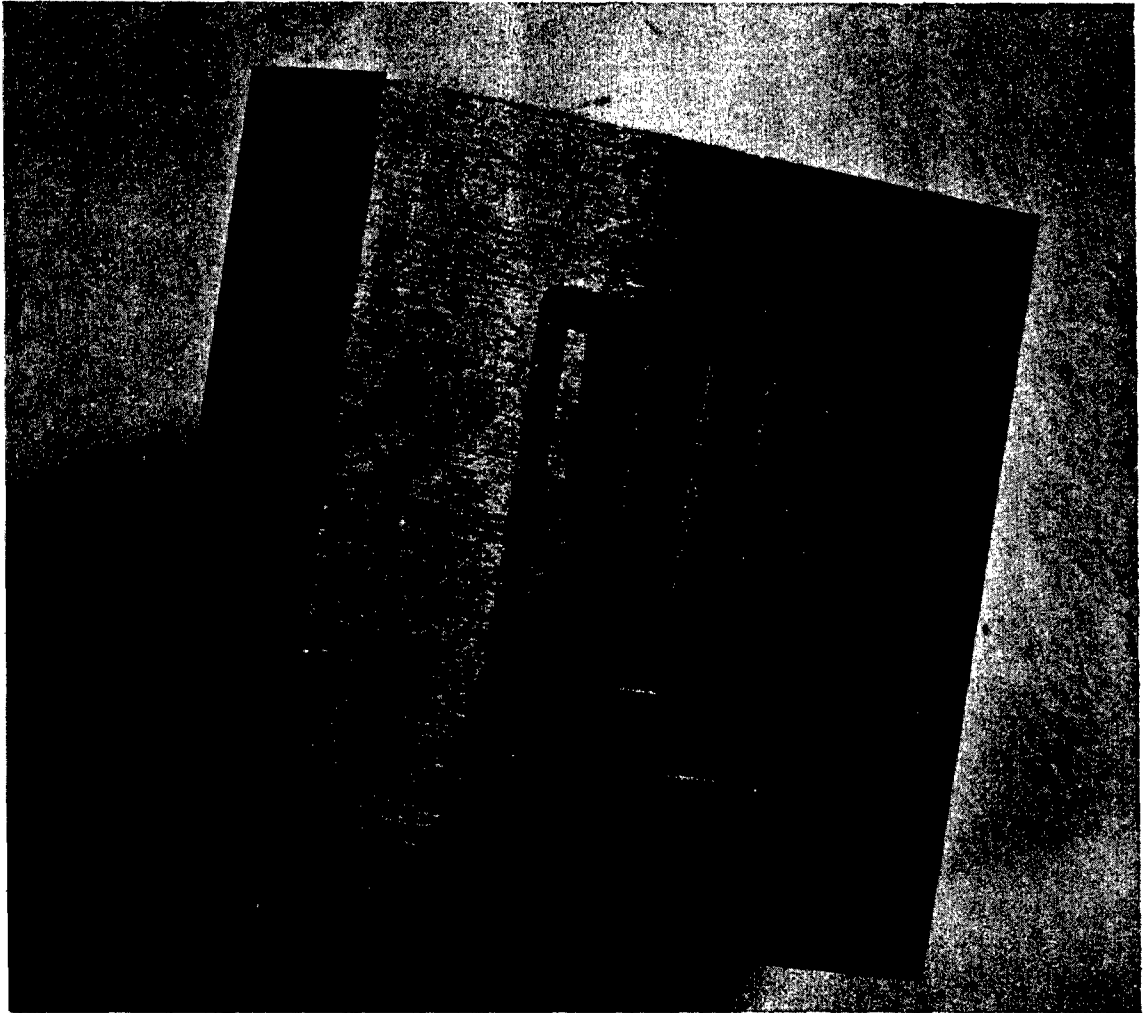


Figure 117. Finished EDM Wrought Blade Half.

A surface finish of 125 to 150 rms resulted from the conservative cutting practice of 130,000 cps and low power feeds. Table X gives a typical setting for the EDM machining of interval grooves.

TABLE X
TYPICAL SETTINGS FOR EDM

Type Machine	EASCO Sparktron
Power Setting	1 (Lowest)
Frequency, cps	130,000
Feed Rate, in/min	0.010-0.015
Polarity	Positive
Over Cut	0.0025 inch each side
Pressure	60 psi
Electrode	Carbon

Inspection of these grooved blocks indicated that the slot width and slot depth were maintained on the average within ± 0.001 inch of design values with a maximum variance in isolated areas of 0.005 inch.

The first effort in electron beam welding was to establish the desired welding parameters on sample test blocks.

The criteria upon which these weld parameters were to be established were selected from the basic block design as follows:

Width at interface	- 0.045 to 0.050 inch
Penetration past interface	- 0.035 to 0.045 inch
Total penetration	- 0.585 to 0.595 inch

Figure 118 is typical of the test block welded by one vendor using a Sciaky electron beam welder to establish these conditions. Typical settings are as follows with Sciaky equipment:

	<u>KV</u>	<u>MA</u>	<u>Speed in./min</u>	<u>Beam Width in.</u>	<u>Penetration in.</u>
1	35	260	69	0.048	0.105
2	35	260	67	0.036	0.050
3	35	260	68	0.042	0.058

Figure 119 is typical of the test block by another vendor to establish these conditions using Hamilton Standard equipment. Typical settings for this equipment are as follows:

	<u>KV</u>	<u>MA</u>	<u>Speed in./min</u>	<u>Beam Width in.</u>	<u>Penetration in.</u>
1	150	13	15	0.055	0.608
2	150	13	15	0.050	0.528
3	150	11	15	0.045	0.496

Welding Unfilled Passages

Figure 120 is typical of results obtained using a Sciaky welder in attempting to weld blocks with unfilled or open passages. Note that the heat input necessary to obtain the correct penetration is sufficient to collapse the passage dividers and thereby fill the cooling passages. Based on this evidence, the vendor directed their subsequent electron beam welding efforts to welding with filled passages.

Hamilton Standard equipment operates on the principle of higher voltages and lower currents. This equipment tends to produce a deeper and narrower weld at the same power level. Therefore, concurrent with the effort on the Sciaky machine, tests were made using Hamilton Standard equipment. A trial weld to join the areas between the grooves with Hamilton Standard equipment is shown in Figure 121. This test weld was made using scribe lines on the cover plate to align the beam. From this test, it was determined that these guides were inaccurate due to shrinkage of the cover plate during welding.

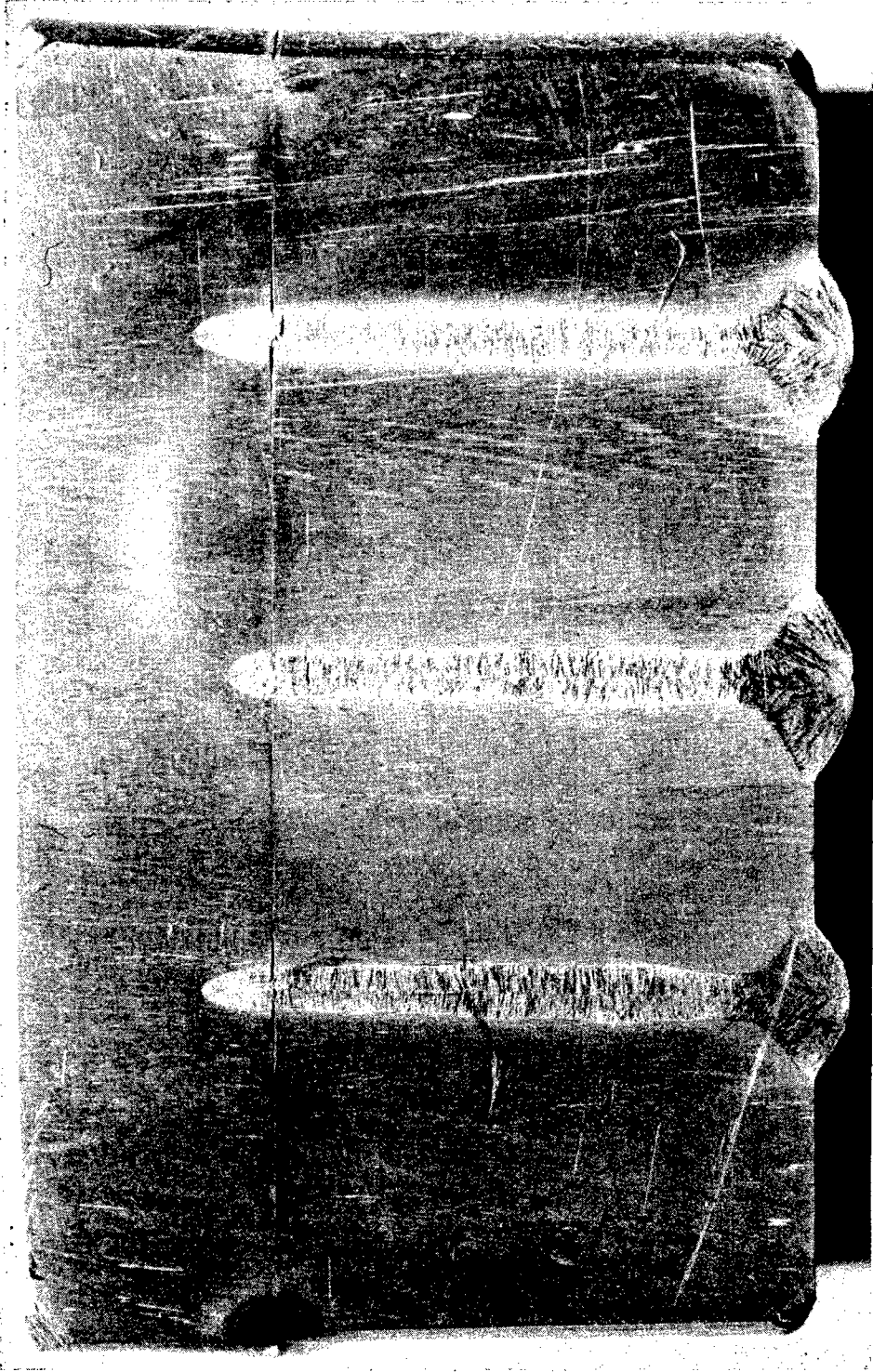


Figure 118. Parameter Test Block, Sciaky Welder.



Figure 119. Parameter Test Block, Hamilton Standard Welder.

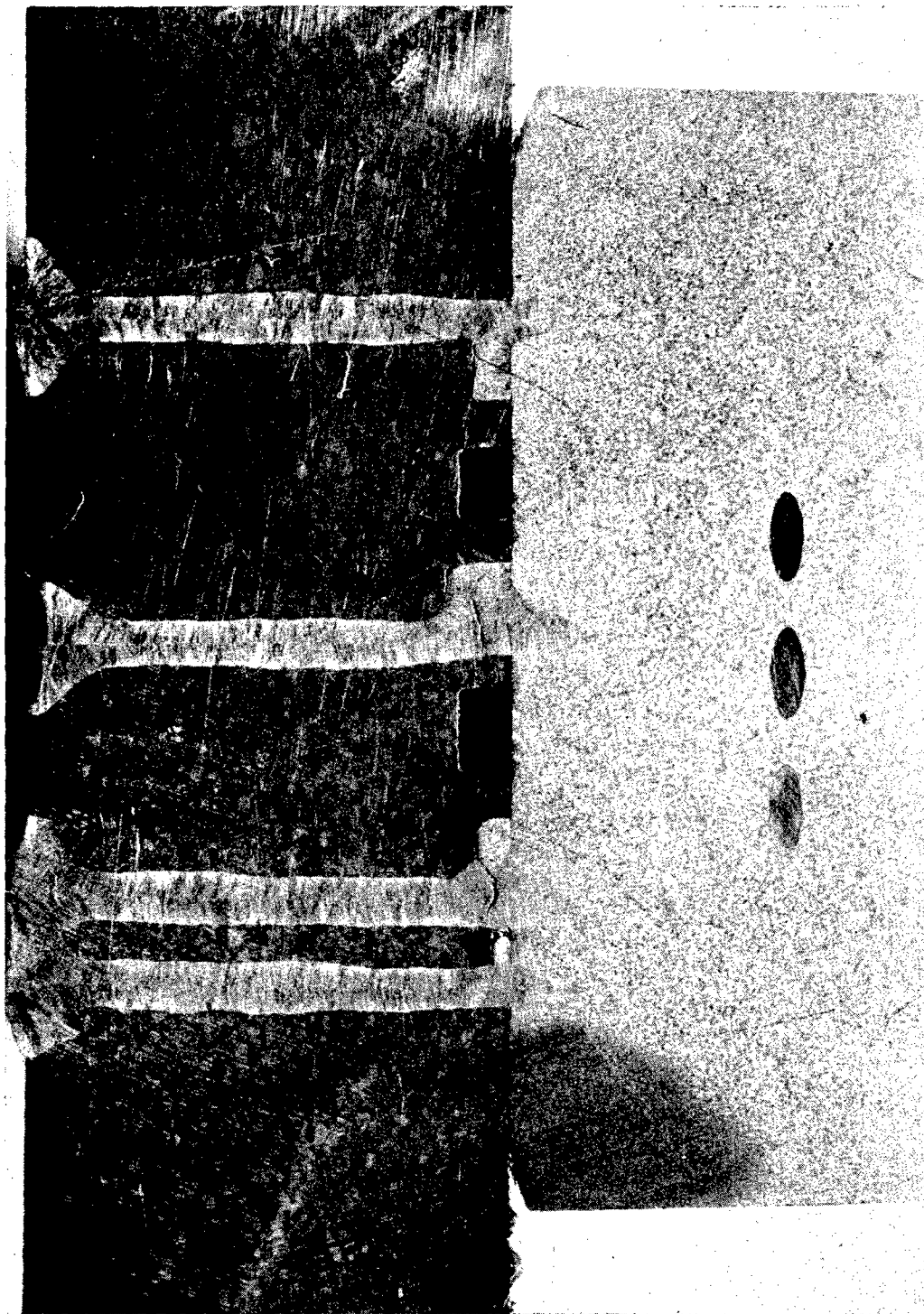


Figure 120. Welding Between Grooves, Sciaky Welder.

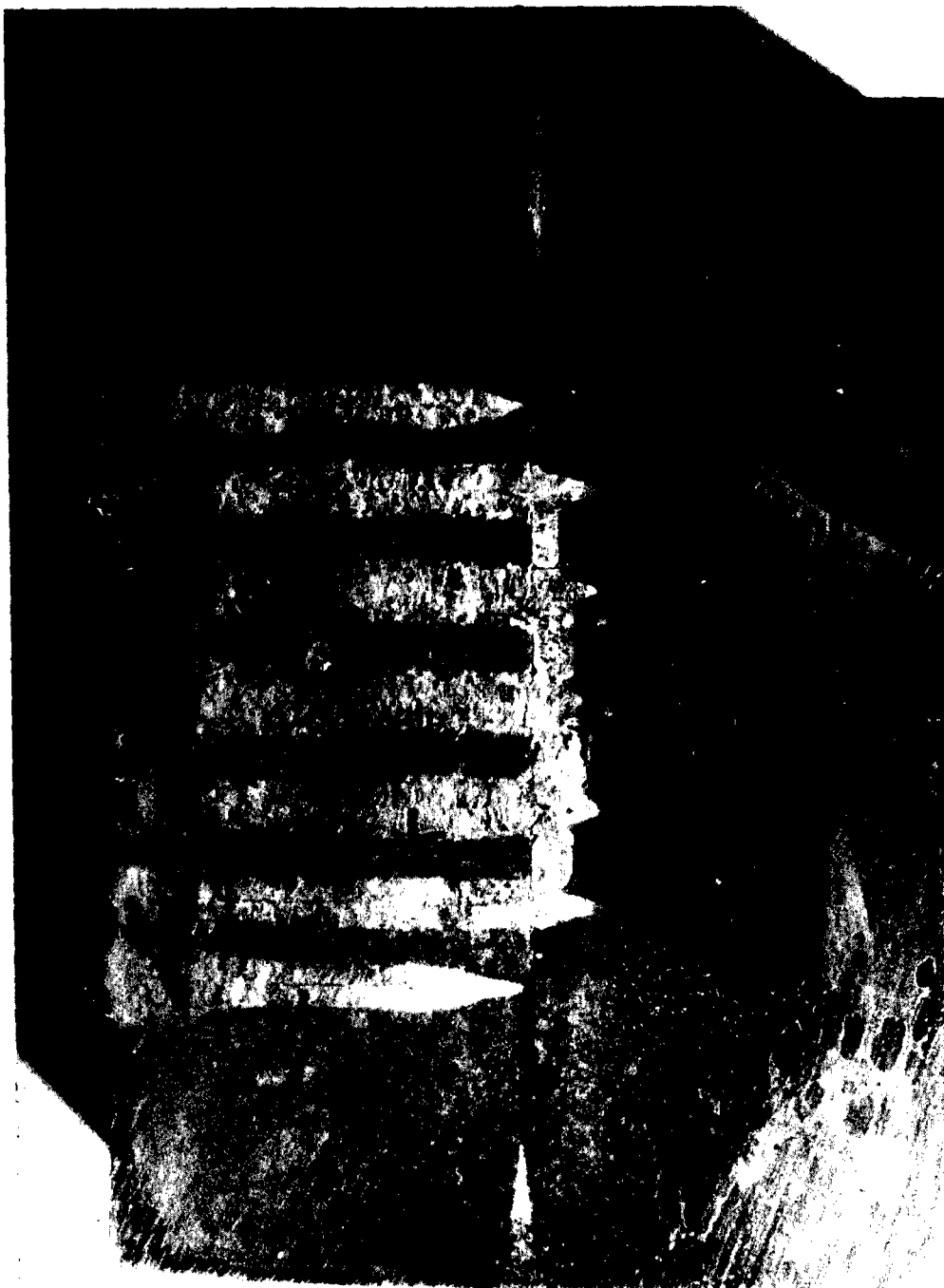


Figure 121. Welding Between Grooves, Hamilton Standard Welder.

Further efforts were conducted to establish the feasibility of welding over unfilled passages. The sample in Figure 122 was made from carbon steel with the grooved plate longer than the cover plate to permit alignment of each electron beam weld pass on the center of the passage divider. Note again that the location of the beam in the cover plate tends to shift slightly and the penetration appears to vary slightly, possibly as a result of preheat of the cover plate from succeeding weld passes.

Welding with the unfilled passages without the use of heat sinks proved to be unsuccessful for the following reasons:

1. Mass of the parts was such that for a specified set of weld parameters, the shape and penetration of the weld could not be controlled within the desired limits. This resulted in excessive penetration upon occasion and frequent closing of the cooling passages.
2. Power settings necessary to accomplish the bond were of such magnitude that excessive preheat and shrinkage in the part dictated an impractical welding sequence.

Unfilled Passages and Heat Sinks

In another test to weld unfilled passages using Hamilton Standard equipment, the sample was prepared by grooving the cover plate to correspond to the lands or passage dividers in the gas plate. In this test, two objectives were considered: (1) by welding in the grooves over the lands, a deeper and wider fusion zone at the interface would be obtained; and (2) the external ribs would tend to remove some of the excess heat of the welding process and tend to reduce transverse shrinkage. The results are shown in Figure 123. The tendency of the fusion zone to shift and the penetration to vary slightly can be seen in this figure.

Efforts at welding unfilled cooling passages were continued using various types of heat sinks or ribbed shields. The ribs interrupt the beam and reduce its penetration in the area of the slots in the blade block.

In Figure 124, a test sample was prepared from carbon steel and 1/8-inch-thick copper plate. This figure shows the variation in penetration where welding is normal to the ribs in the copper plate. Figure 125 shows the variation in penetration obtained when a series of adjacent welds is made.

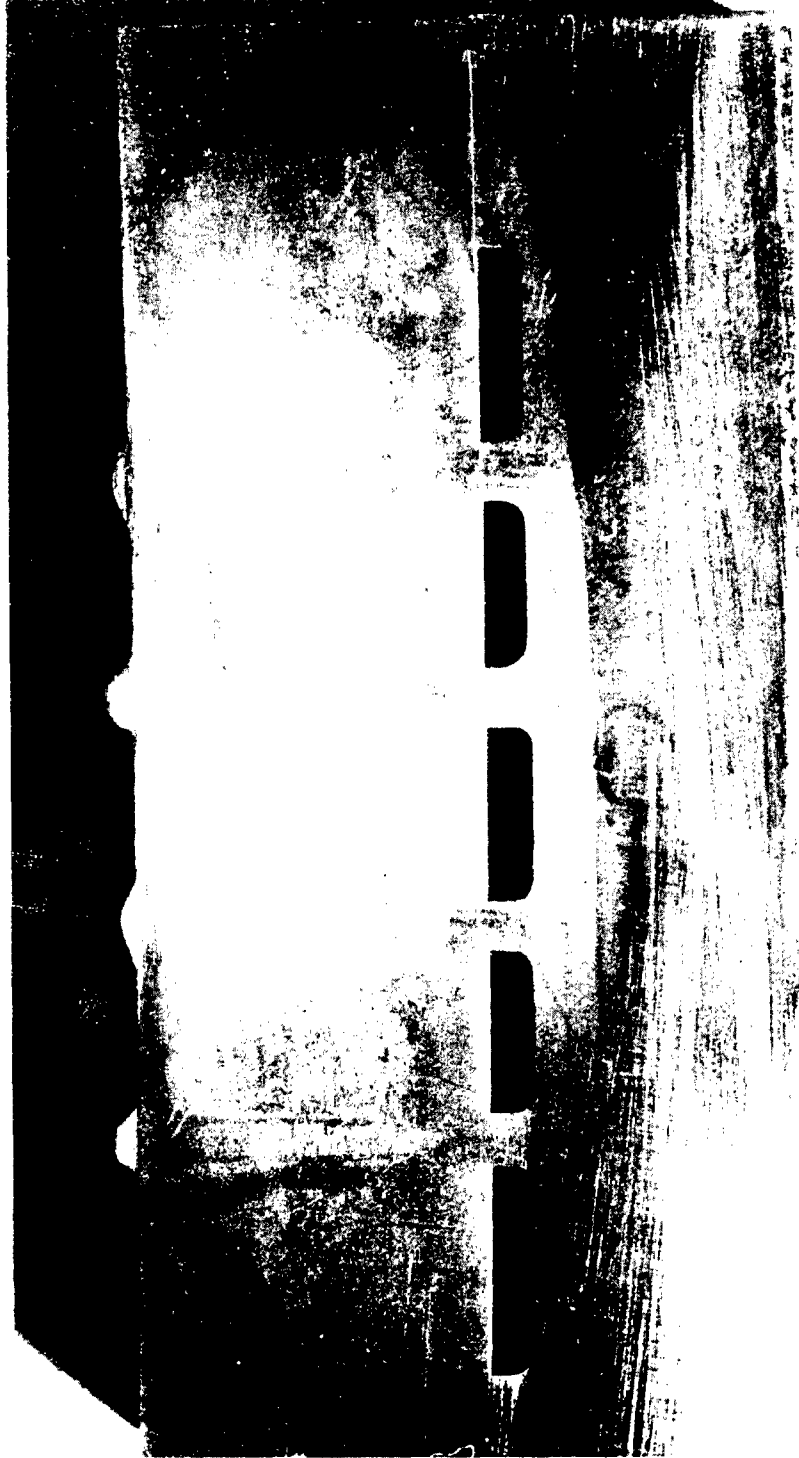


Figure 122. Welding Between Grooves With Lands Visible.

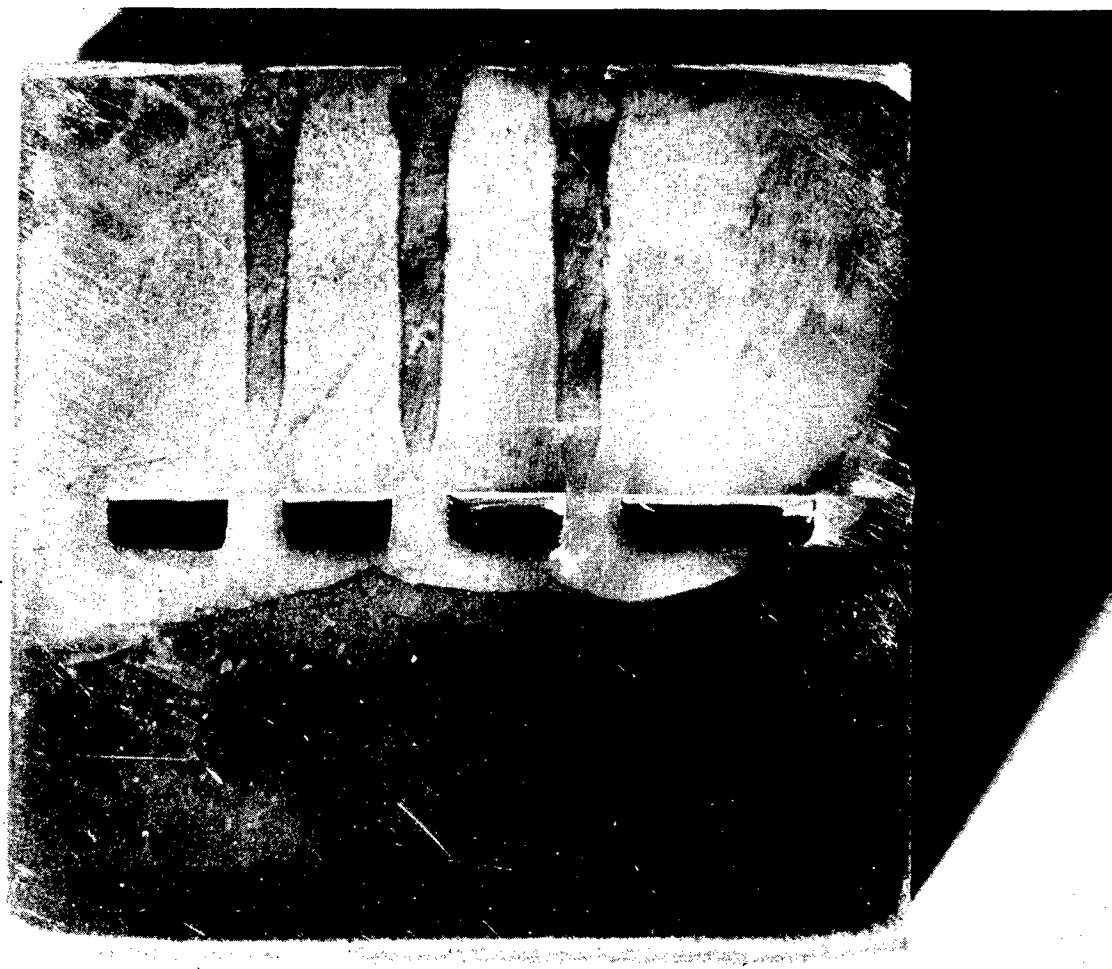


Figure 123. Welding in Grooves Over Lands.



Figure 124. Penetration Variation When Welding Over Copper Bars.

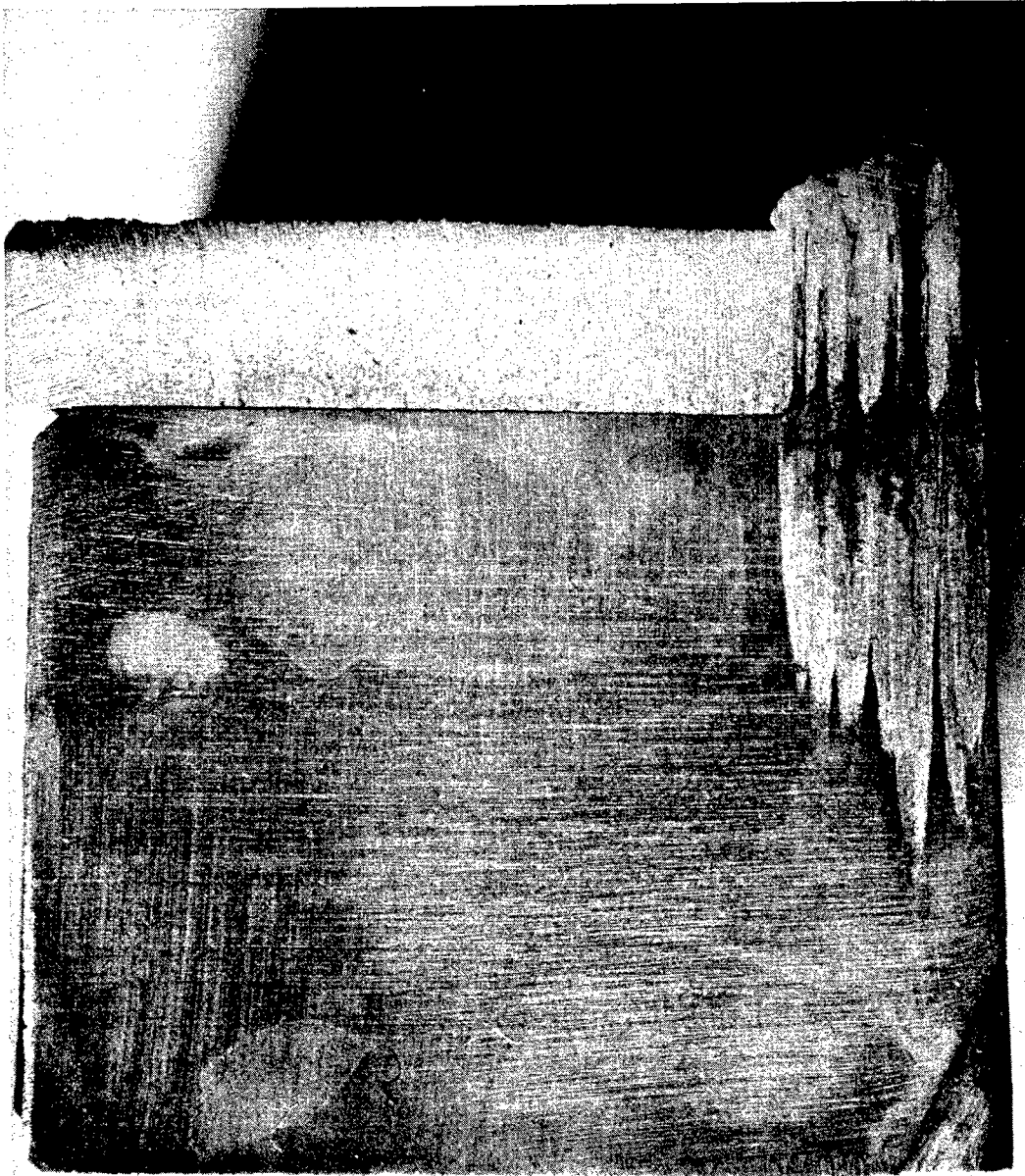


Figure 125. Transverse Section Through Adjacent Welds.

Weld tests using copper masks or heat sinks were continued using a replica of the cooling passages. Figures 126 and 127 show the effort in this direction. Figure 127 shows the effectiveness of the mask to reduce penetration when the beam crosses the copper lands. However, it will also be seen that a lead would be required for this technique to be effective.

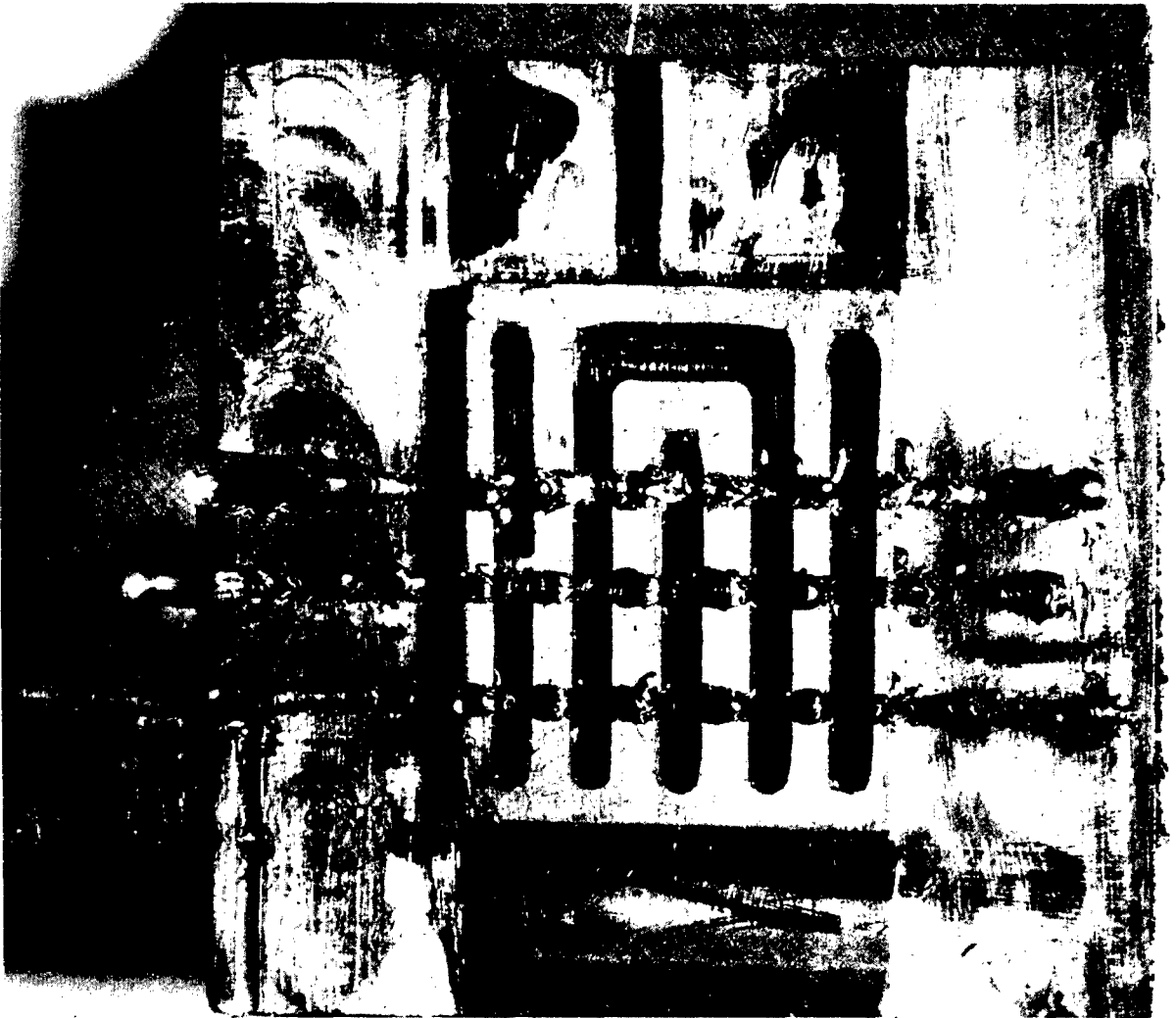


Figure 126. Welds Made Using Copper Replica of Internal Passages.

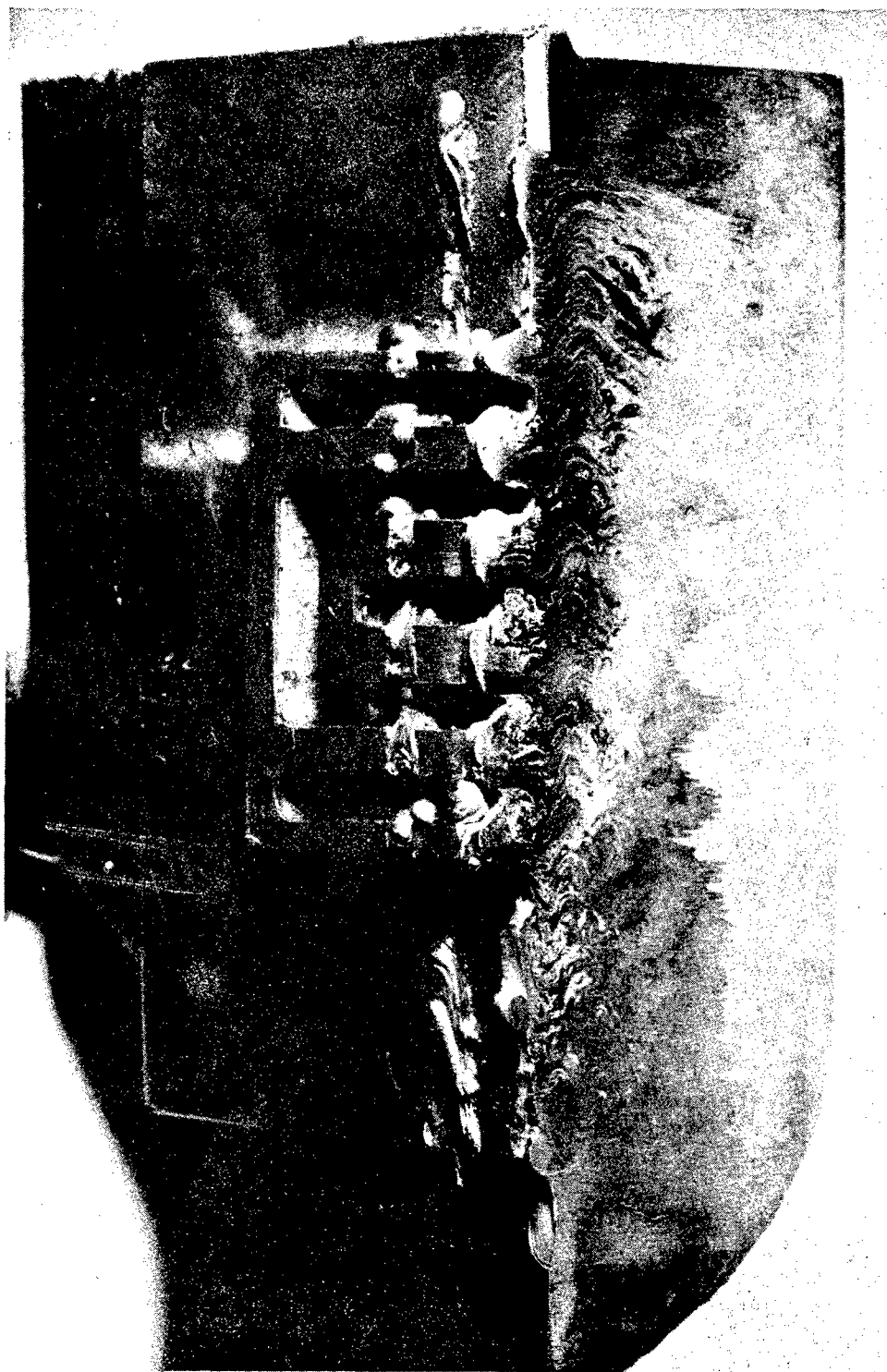


Figure 127. Penetration Variation When Welding Over Copper Mask.

Tungsten was considered to be more suitable than other materials for stopping off the electron beam; therefore, a test sample was made using an external fixture for aligning the beam and using tungsten blocks to block off the beam. Figure 128 is a photograph of this sample. In Figure 129 a cross section of this sample is shown. It is noted that the passages are again filled, the fusion zone is widened by preheat, and the penetration is deepened by preheat.

Weld tests using external copper masks machined opposite to the grooved block were also tried. This technique was found to be impracticable for the following reasons:

1. The spacing of the cooling passages was so small that the external mask had very little effect on controlling the penetration of the beam.
2. Location of the masks appeared to present difficulties, and the reproducibility factor also appeared to be unreliable.

Welding with Filled Passages

Additional electron beam welding tests were conducted with the grooves filled with a removable filler to prevent the collapse of the lands by the electron beam.

Filler metals were selected principally on the basis of their ease of removal and for their stability. Previous experience indicated that EDM machined holes could be filled with nickel and processed through a forming operation; then the nickel could be successfully removed.

Test welds were conducted using both electroplated nickel and compacted nickel.

A ceramic filler material was selected on the basis of removal of ceramic cores from castings, even though there was the possibility of the core material outgassing and resulting in a porous weld.

Figure 130 shows the surface of a grooved block electroplated to fill the grooves for subsequent welding. Figure 131 shows this block as ground prior to assembly in the test weld.

Figures 132 and 133 show the cross section of an electron beam weld over passages filled with electroplated nickel. These figures show that some degree of protection was obtained for the cooling passages; however, upon removal of the nickel, penetration was noticeably not con-

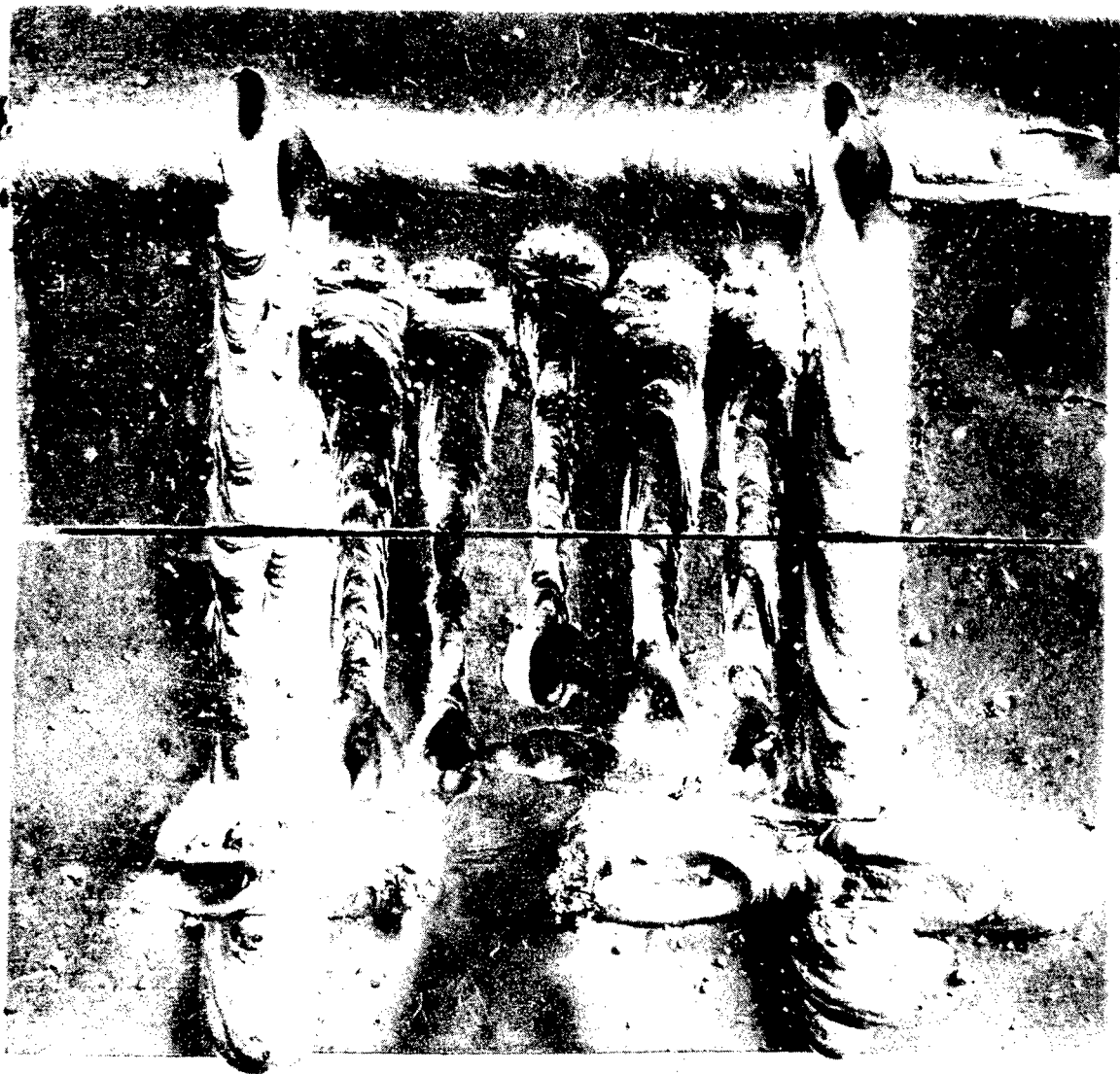


Figure 128. Welding Using Tungsten Mask.



Figure 129. Cross Section of Welds Made Using Tungsten Mask.

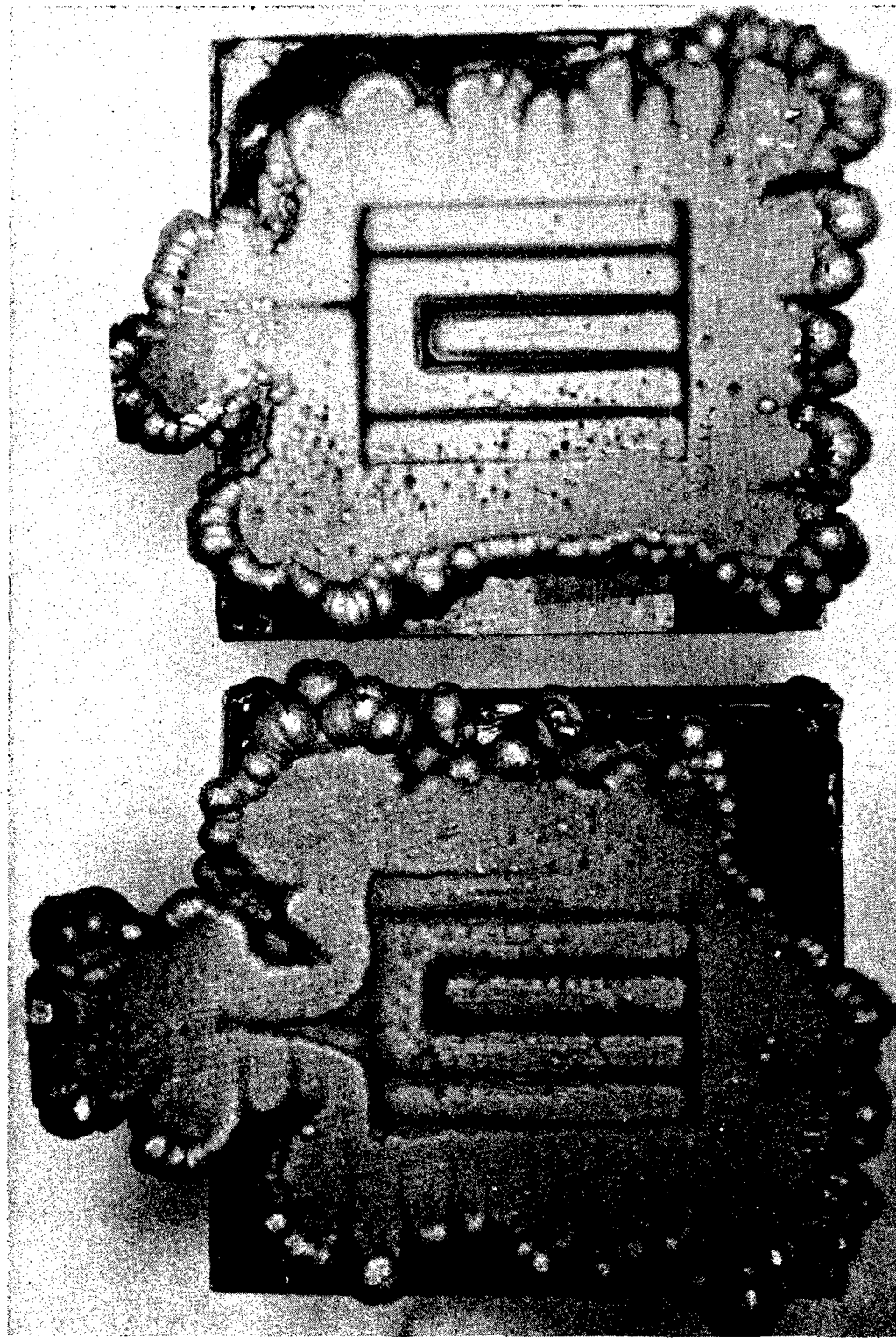


Figure 130. Nickel Filled Test Blocks (As Plated).

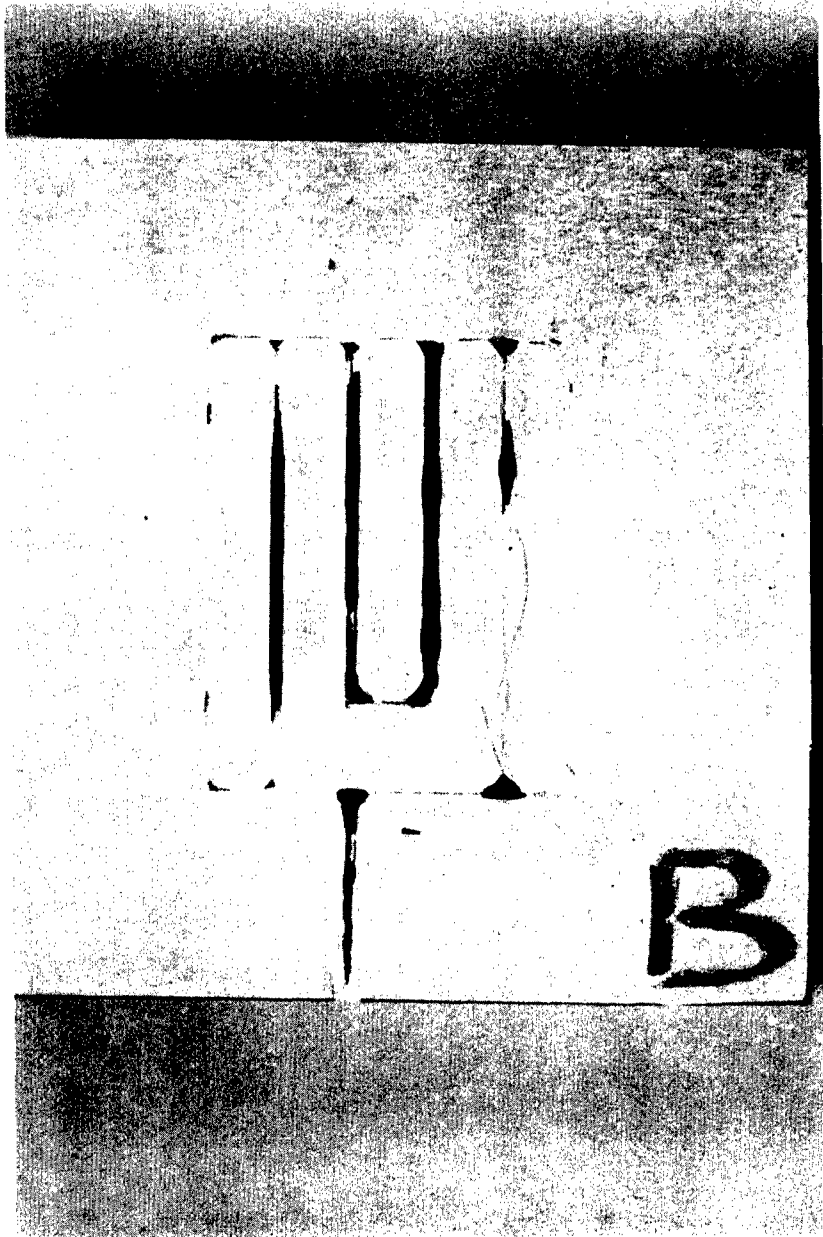


Figure 131. Electroplated U-700 Blocks Ground for Weld Test.

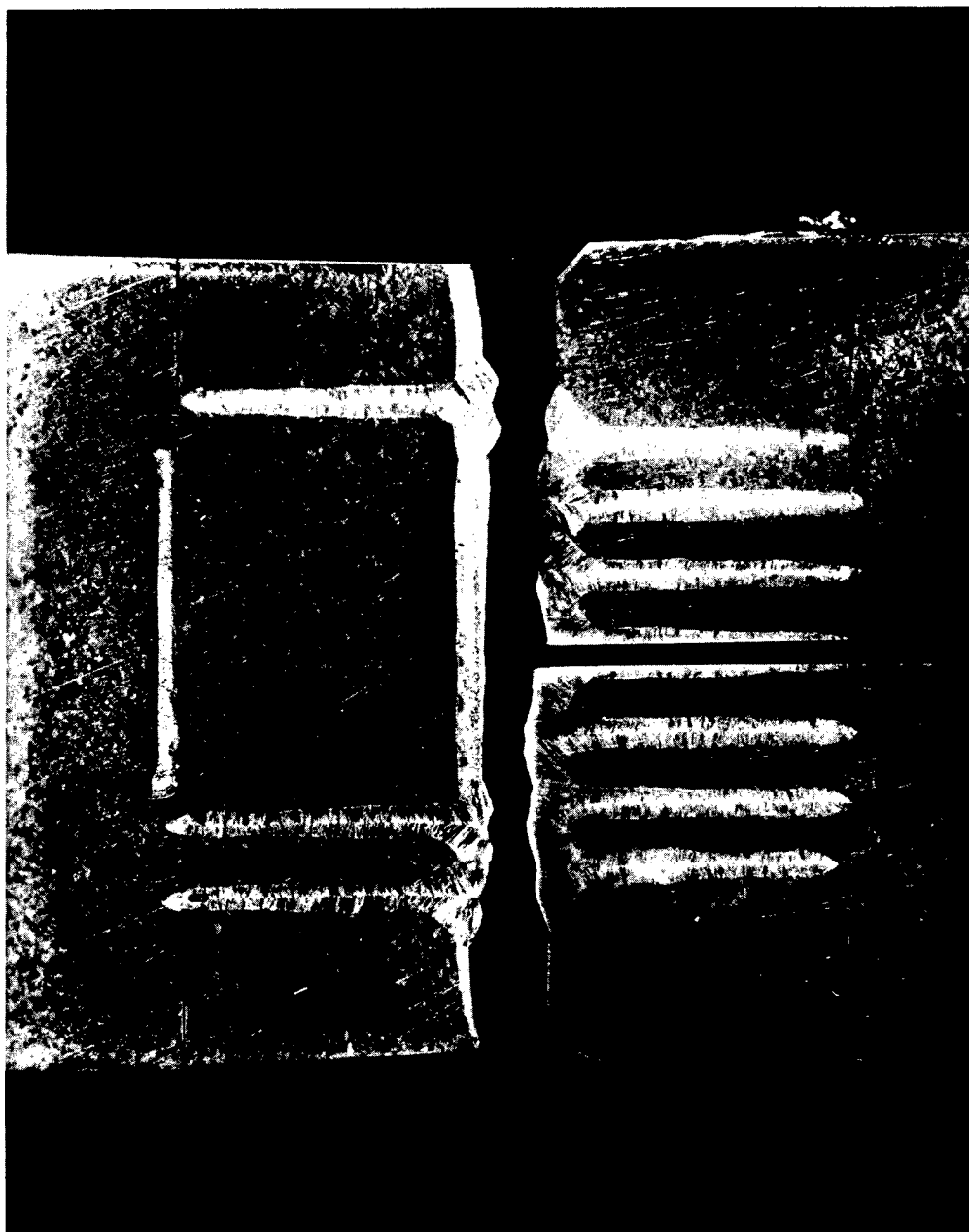
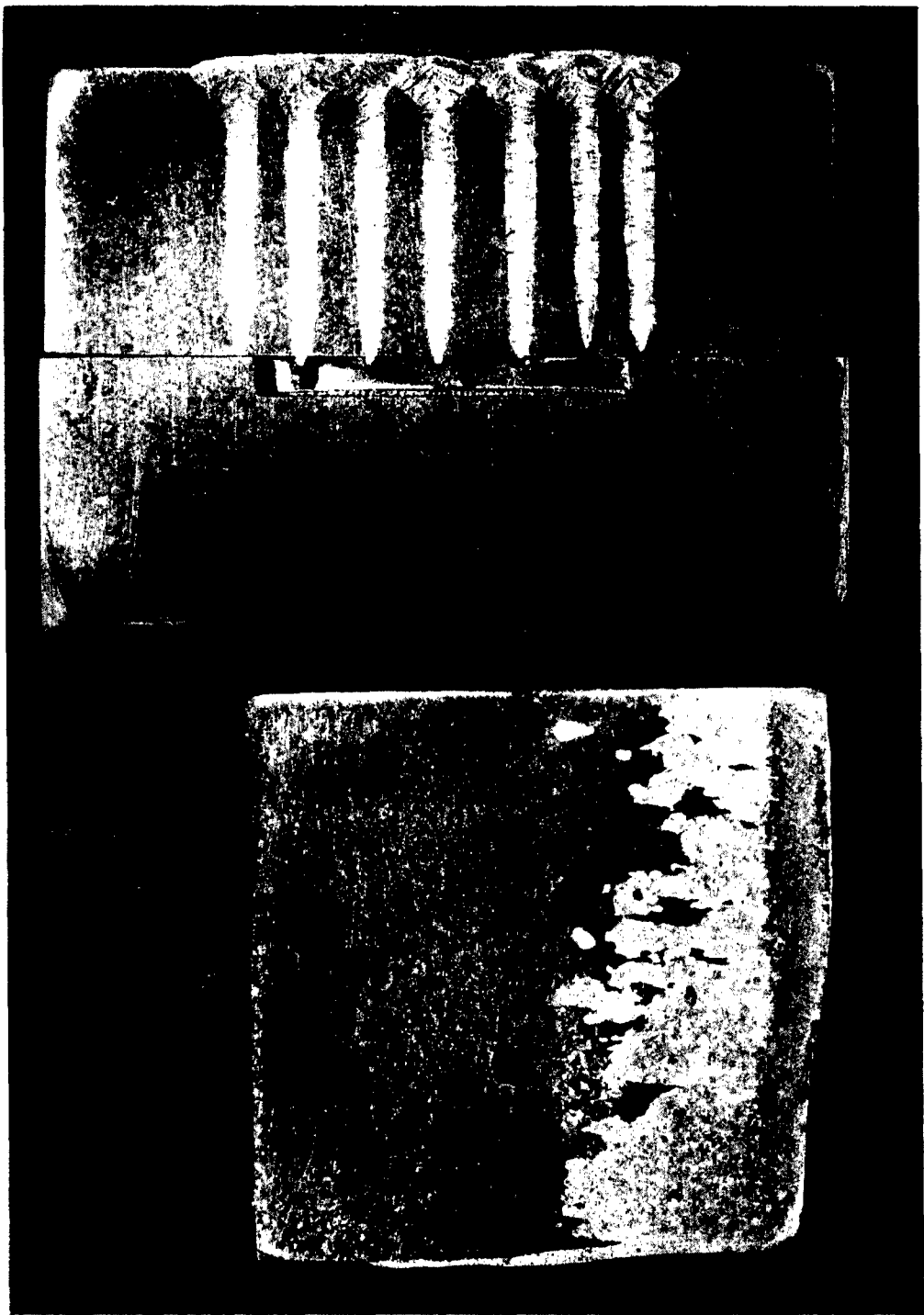


Figure 132. Electron Beam Weld Over Electroplated Nickel Before Nickel Removal.



**Figure 133. Electron Beam Weld Over Electroplated Nickel
After Nickel Removal.**

sistent and, in some instances, projection of the weld in the cooling passages was noted after core removal.

Compacted nickel powder was also used to fill the cooling passages. Figure 134 shows this block as ground prior to assembly into a test weld. In Figure 135, a cross section of this test weld is shown. Notice that a consistent weld penetration was not obtained and that some penetration of the weld into cooling passages was obtained.

The next trials were with ceramic cores. In this case, welding was to be attempted parallel and normal to the interface of the five U-700 blade blocks. Figure 136 shows the unsatisfactory results obtained after core removal when welding parallel to the interface. Figure 137 is a cross section of a ceramic filled weld, after core removal and welding normal to the interface. This sample again demonstrates the nonuniformity of penetration in addition to porous welds.

Trials using various filler materials, namely, nickel (plated and compacted) and ceramic, did not produce a satisfactory technique. The results with nickel showed some evidence of effectiveness; they also indicated some problems in the method of application and of surface preparation. The results of using a baked ceramic filler indicated that excessive porosity would be encountered with this method, probably due to the release of organic binder or moisture.

Following the performance of these tests, several small stainless steel blocks were drilled and filled with rods of materials such as brass, beryllium oxide, tungsten, and molybdenum. An electron beam was then passed over the blocks to study the effectiveness of these materials in stopping the electron beam and to study its ability to remove the materials. A cross section through these welds is shown in Figure 138. Compacted beryllium oxide did not appear to be effective in stopping the beam; after welding, the beryllium oxide was easily removed by probing. The remaining blocks were placed in a furnace for filler removal by oxidation. This core removal technique was successful for molybdenum, as shown in Figure 139.

While it was found that both tungsten and molybdenum were effective in stopping the electron beam, and that molybdenum could be removed by oxidation, it was concluded that the state of the art was such that removable filler metals and electron beam welding did not warrant the use of this technique at this time to fabricate hollow turbine blades.

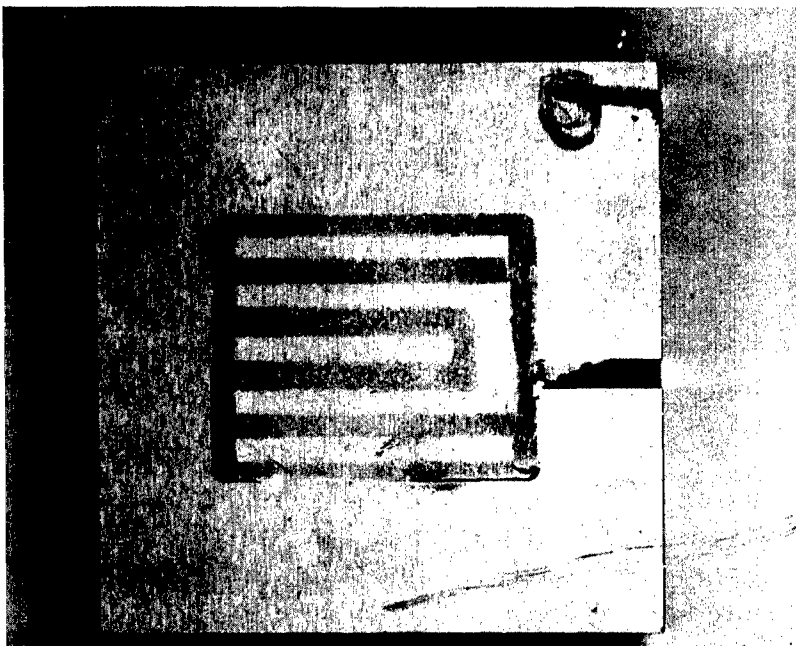
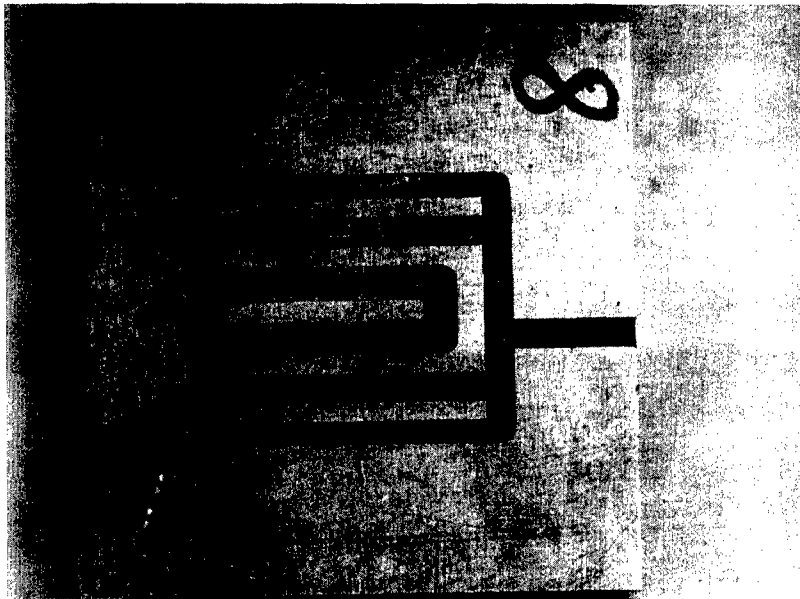


Figure 134. Compacted Nickel-Filled U-700 Blocks Ground for Weld Test.

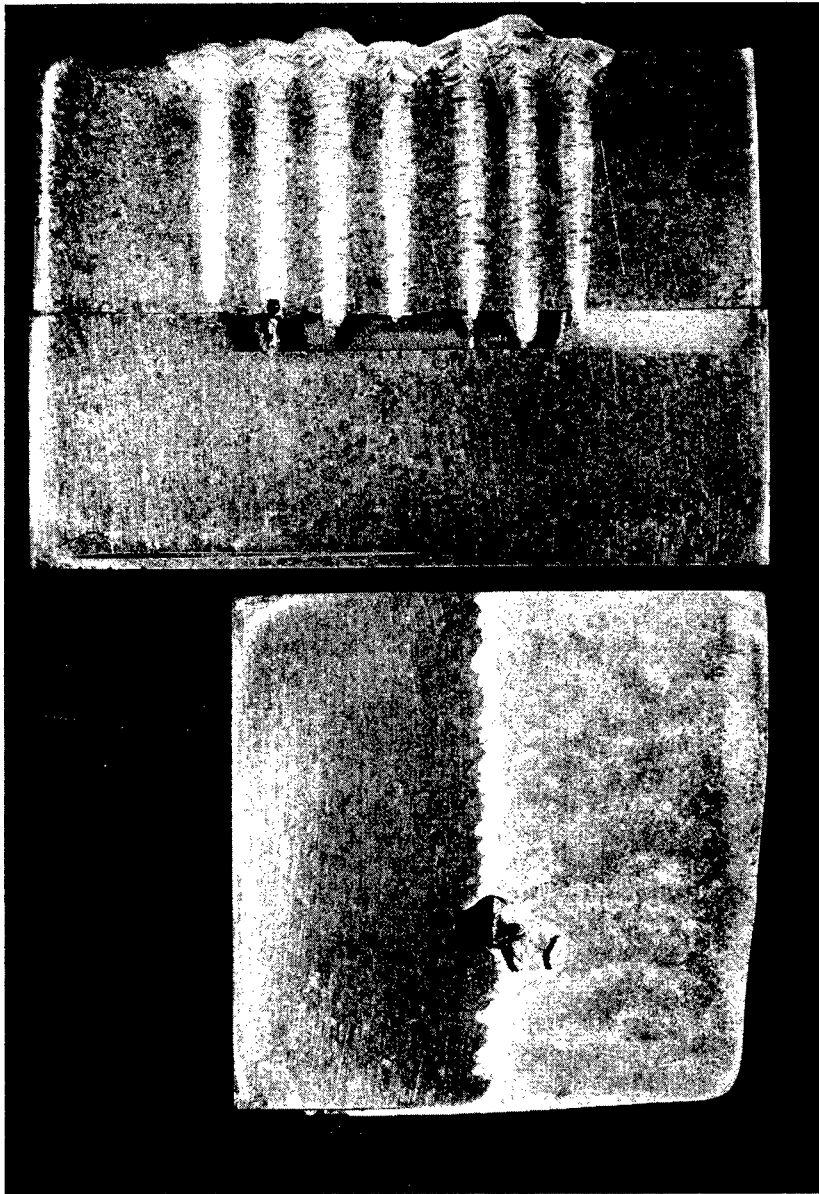


Figure 135. Electron Beam Weld After Removal of
Compacted Nickel.

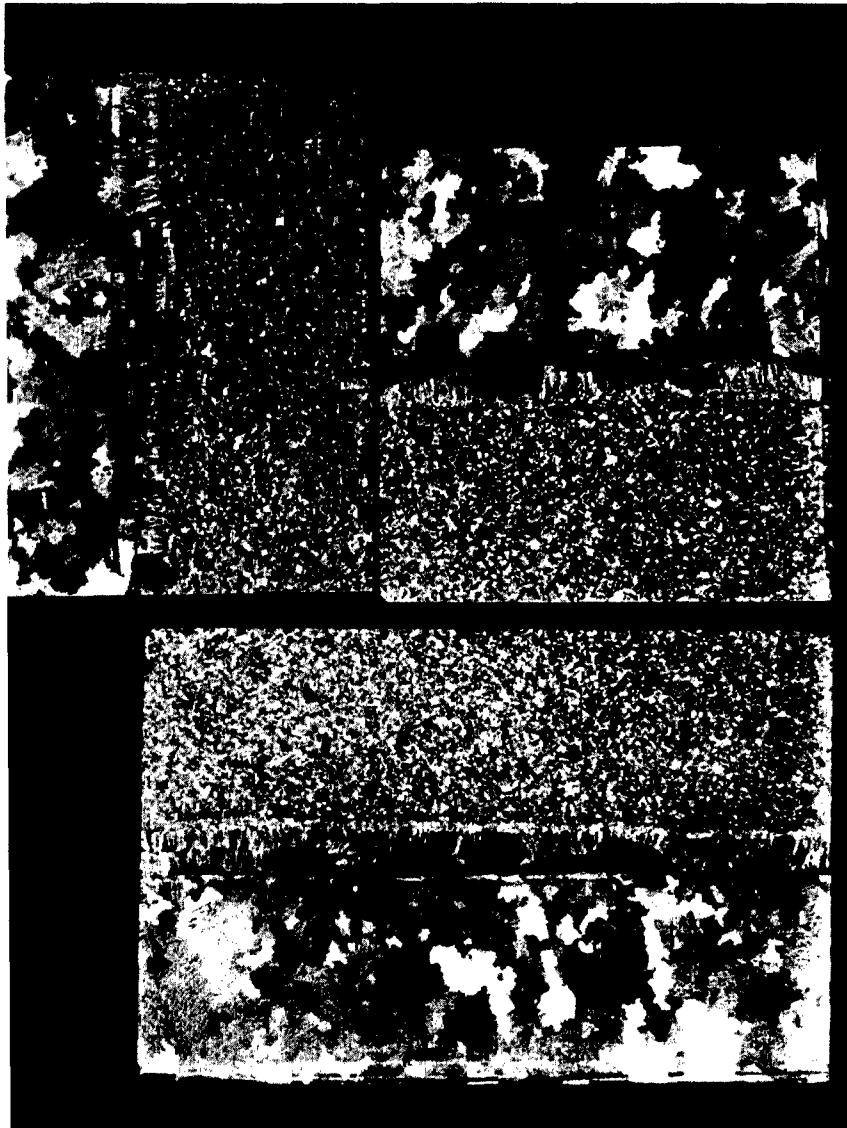


Figure 136. Weld With Ceramic-Filled U-700 Blocks After Ceramic Removal (Direction of Weld - Parallel to Interface).

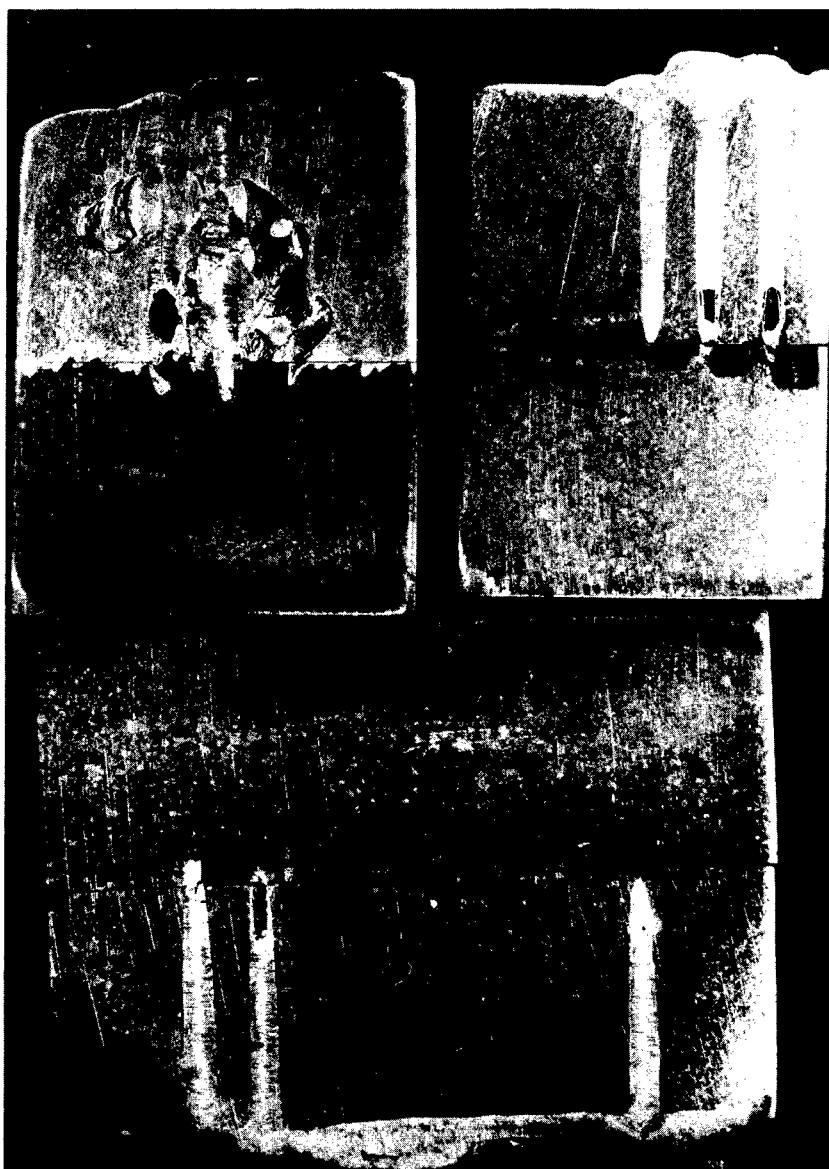
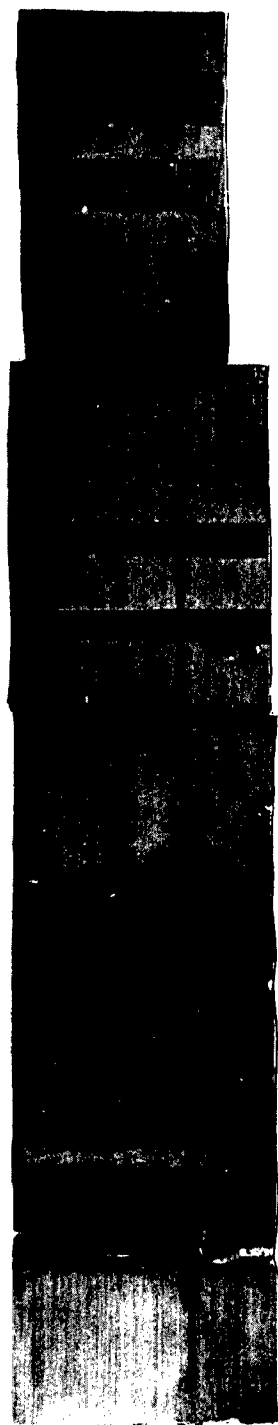


Figure 137. Weld With Ceramic-Filled U-700 Blocks After Ceramic Removal (Direction of Weld - Normal to Interface).



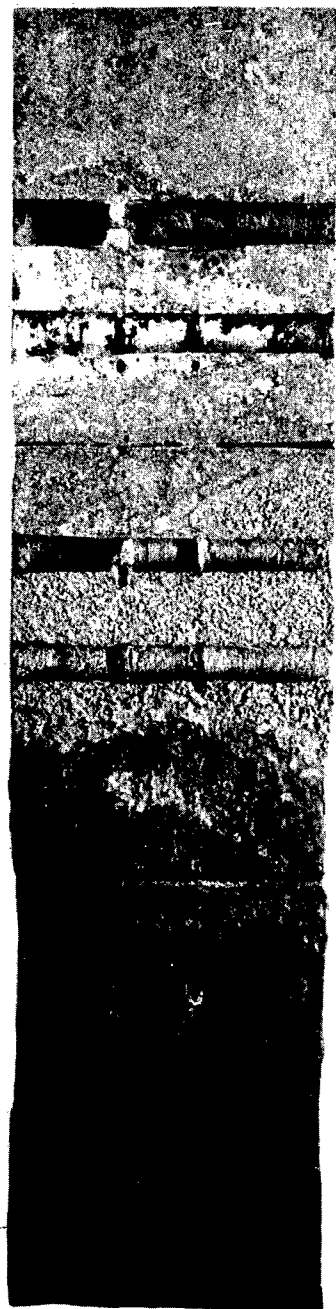
TUNGSTEN

MOLYBDENUM

BERYLLIUM OXIDE

BRASS

Figure 138. Welding Over Various Fillers in 304 Stainless Before Filler Removal.



MOLYBDENUM

BERYLLIUM OXIDE

BRASS

Figure 139. Welding Over Various Fillers in 304 Stainless After Filler Removal.

DIFFUSION BONDING

Wrought U-700 samples identical to those used in the electron beam trials were to be encapsulated in Inconel cans as shown in Figure 140. These trials were to be pressure bonded under the following conditions:

1. 1975°F 2 hours at 10,000-pound load
2. 2150°F 1 hour at 5,000-pound load
3. 2150°F 2 hours at 5,000-pound load

In reviewing the proposed plan, it was thought that Inconel 600 pushrods would not endure, and the pushrod material was changed to a molybdenum alloy encased in an Inconel sheath. Considerable manufacturing and scheduling difficulties were encountered in getting this work started.

The first trial in diffusion bonding at 1975°F, using resistance heating, is shown in Figure 141. It was unsuccessful because of equipment malfunction. In this trial the furnace reached a temperature of 1890°F; a 10,000-pound load was immediately applied and held for approximately 30 minutes, at which time the temperature had dropped to 1300°F. Upon removal of the samples from the capsule, one sample shown in Figure 142, which contained 0.005-inch nickel plate, showed some evidence of adherence. The other sample in the capsule contained no nickel plate and revealed lack of bonding, as shown in Figure 143.

A second attempt at diffusion bonding was made in which both samples were nickel plated. During this run the maximum temperature reached was 1850°F. This temperature was held for a period of 4 hours, maintaining a load of 10,000 pounds. Upon removal of the samples from the capsule, it was determined that some evidence of bonding was accomplished, as shown in Figure 144. In subsequent cutting of this sample, the two halves separated. A typical microstructure of this sample is seen in Figure 145.

One-half of this sample was heat-treated at 2150°F for 2 hours in vacuum and the microstructure was examined. This microstructure, Figure 146, shows some evidence of diffusion or grain boundary migration. Further heat treatment at 1976°F for 4 hours in vacuum failed to show any further diffusion.

Heat treatment of the second half of this sample at 1975°F for 4 hours in vacuum failed to show evidence of diffusion, indicating that after the pressing operation a solution heat treatment is required for these bonding conditions.

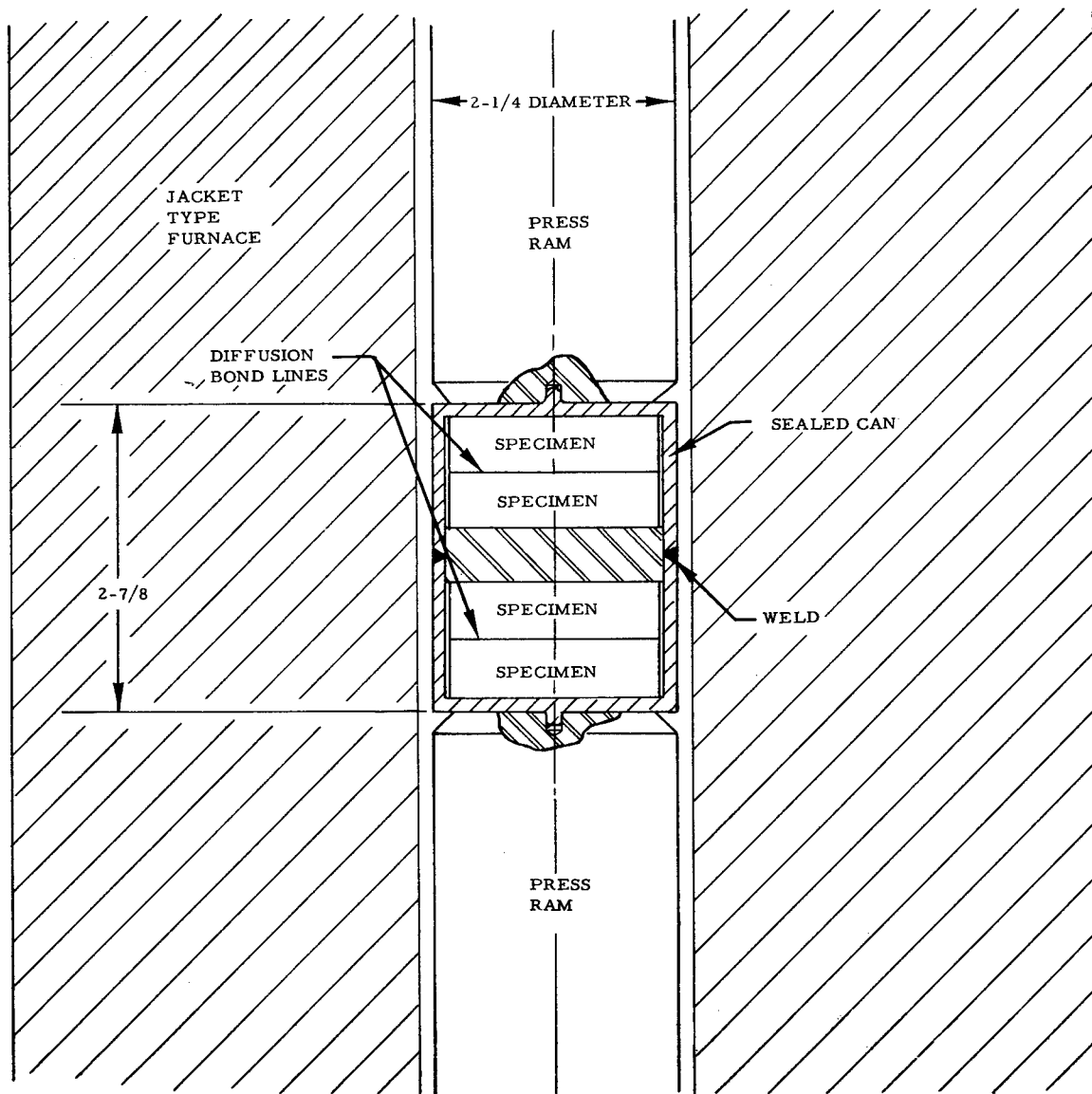


Figure 140. Tooling for Pressure Bonding of U-700 Grooved Blocks.

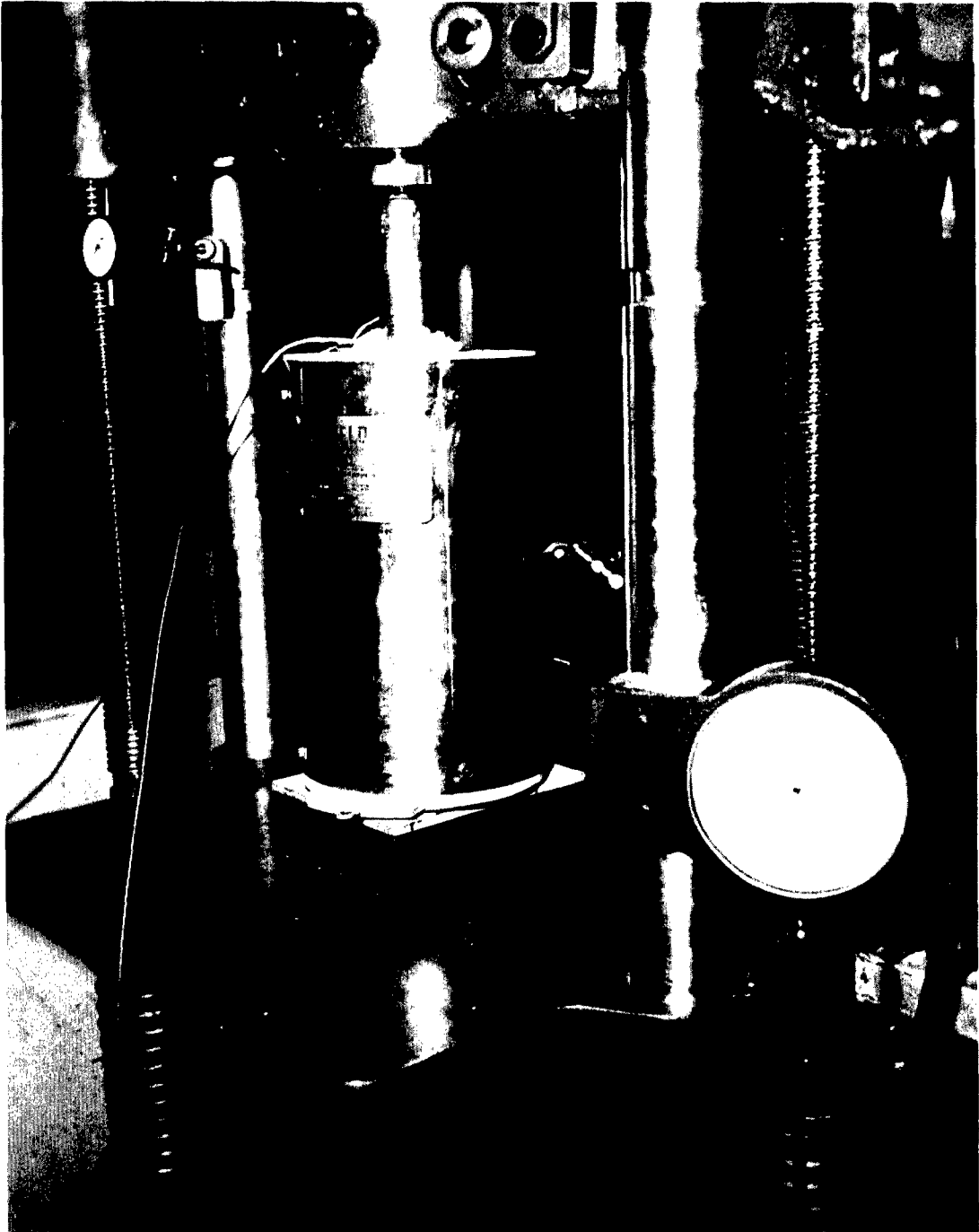


Figure 141. Resistance Heating Setup for Pressure Bonding.

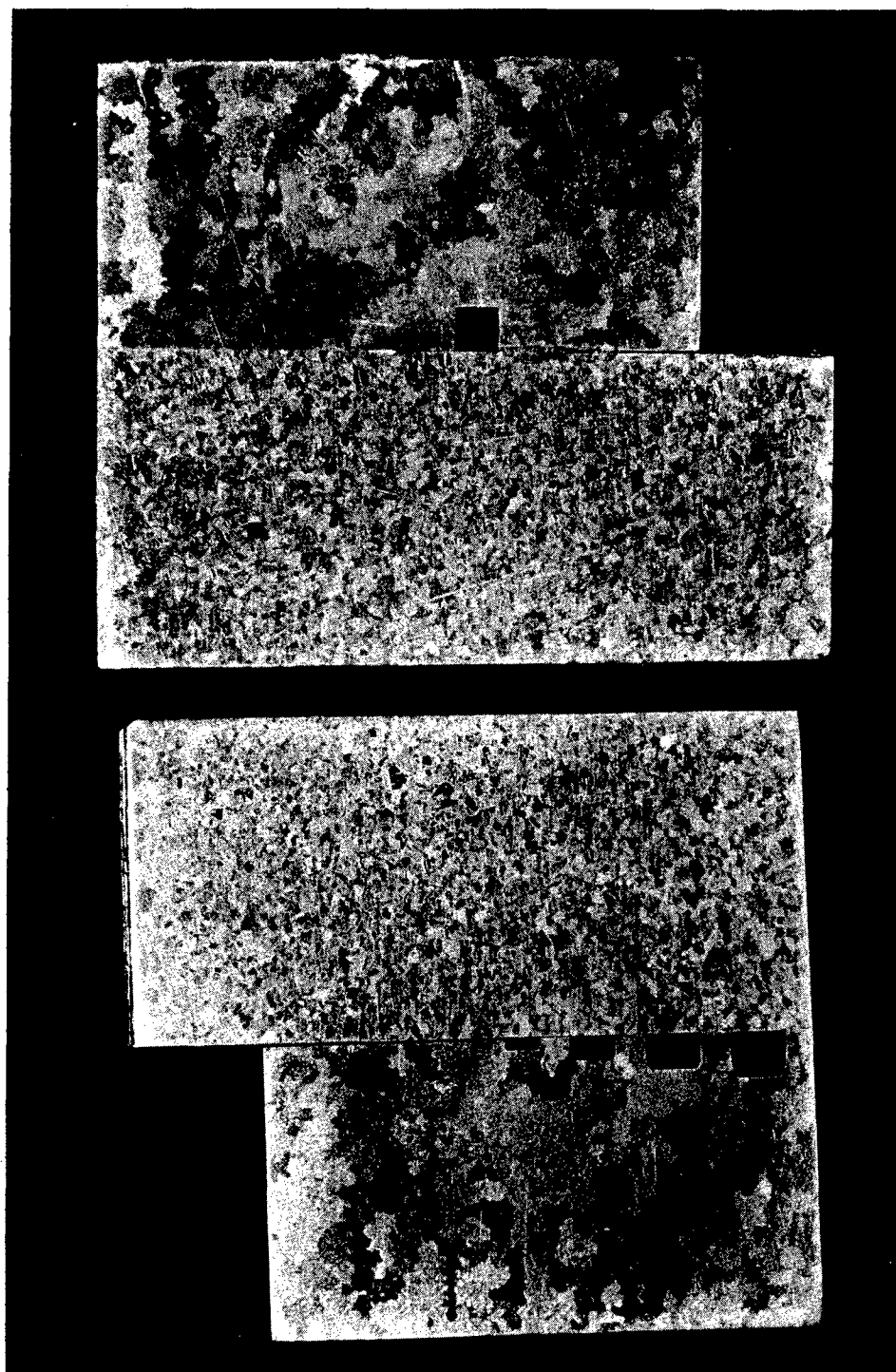


Figure 142. First Diffusion Bond at 1890° F and 0.0005-Inch Nickel Plate.

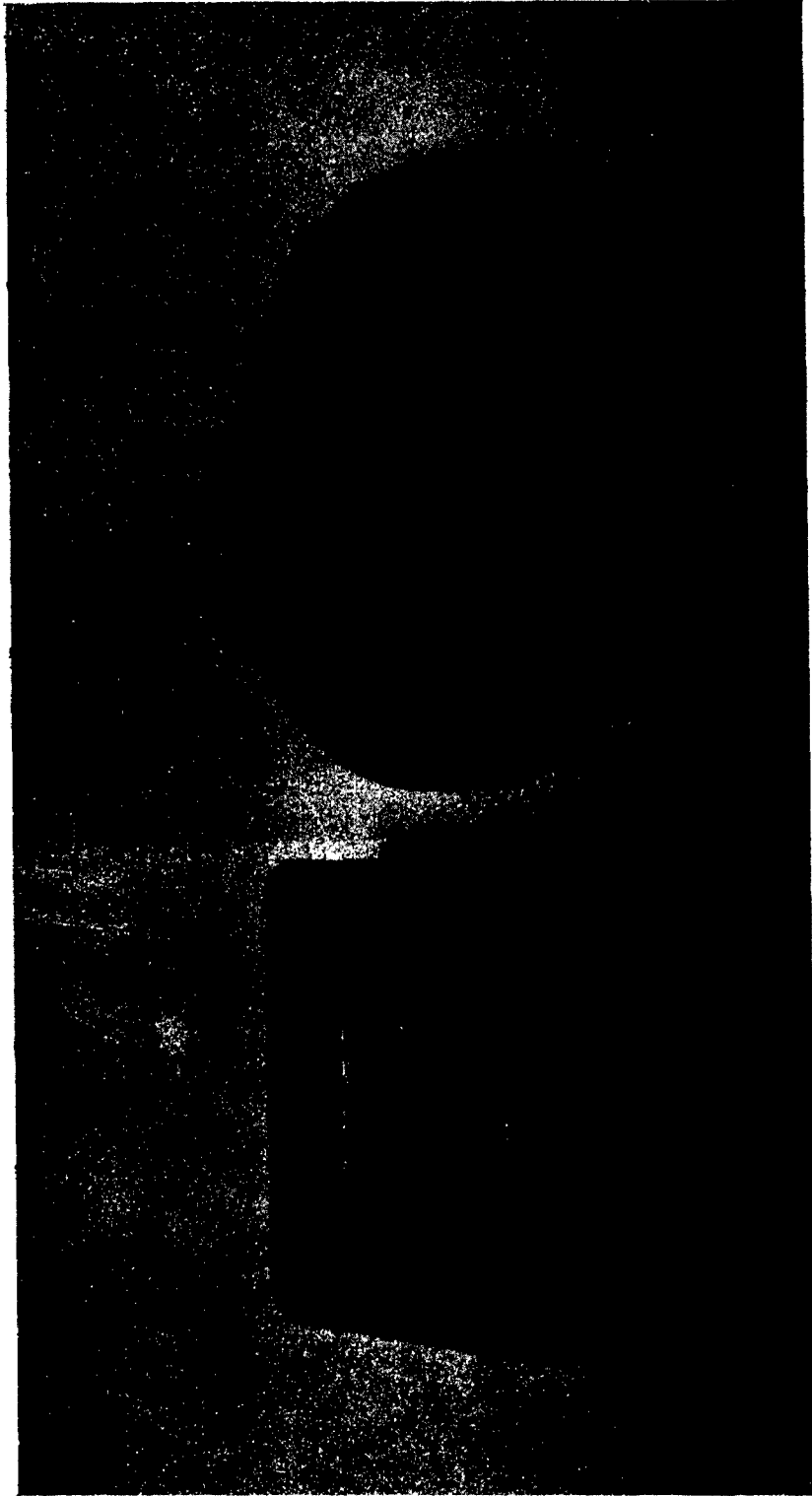


Figure 143. First Diffusion Bond at 1890° F (No Nickel Plate).

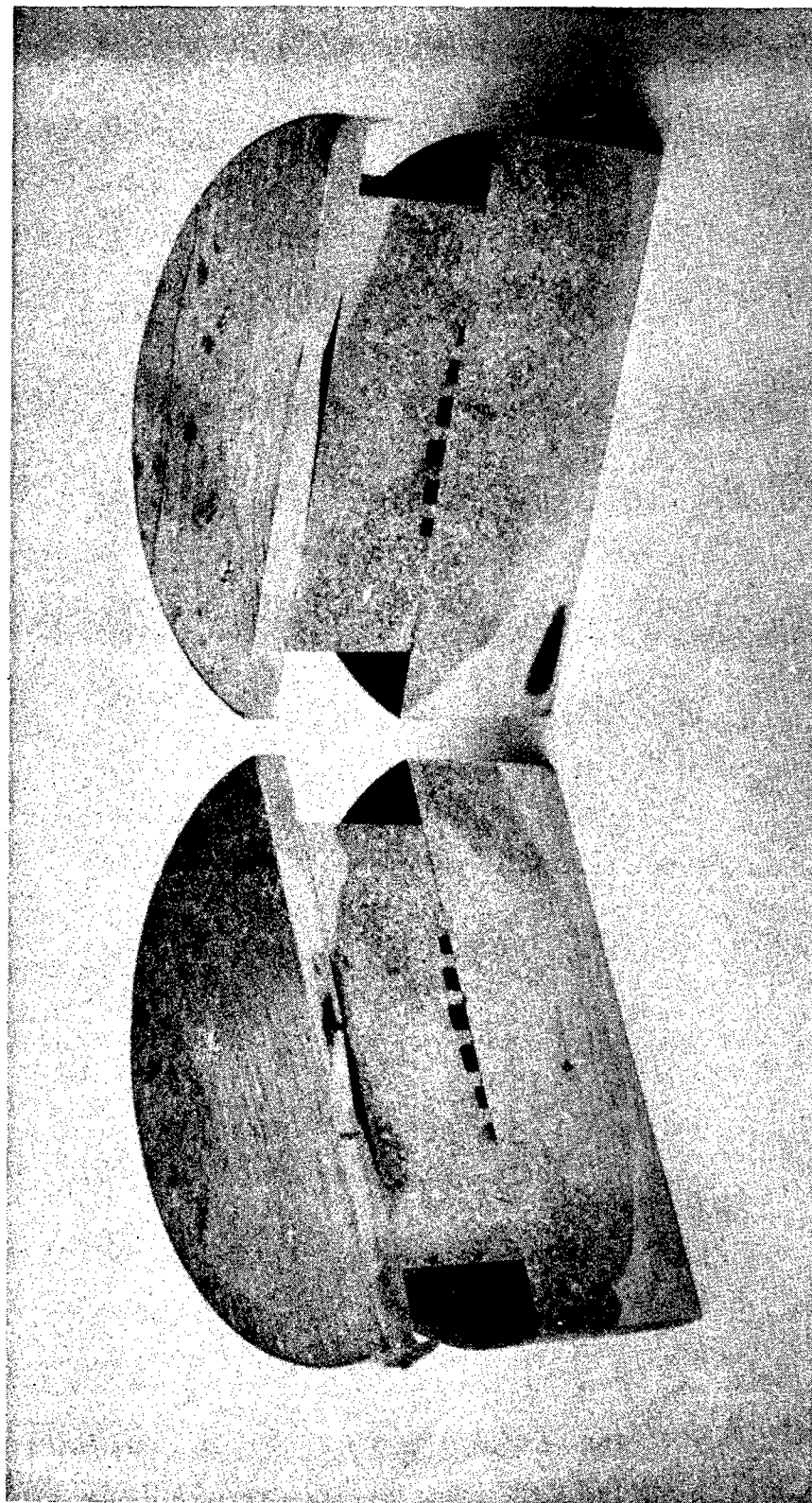


Figure 144. Second Diffusion Bond at 1850° F and 0.0005-Inch Nickel Plate.

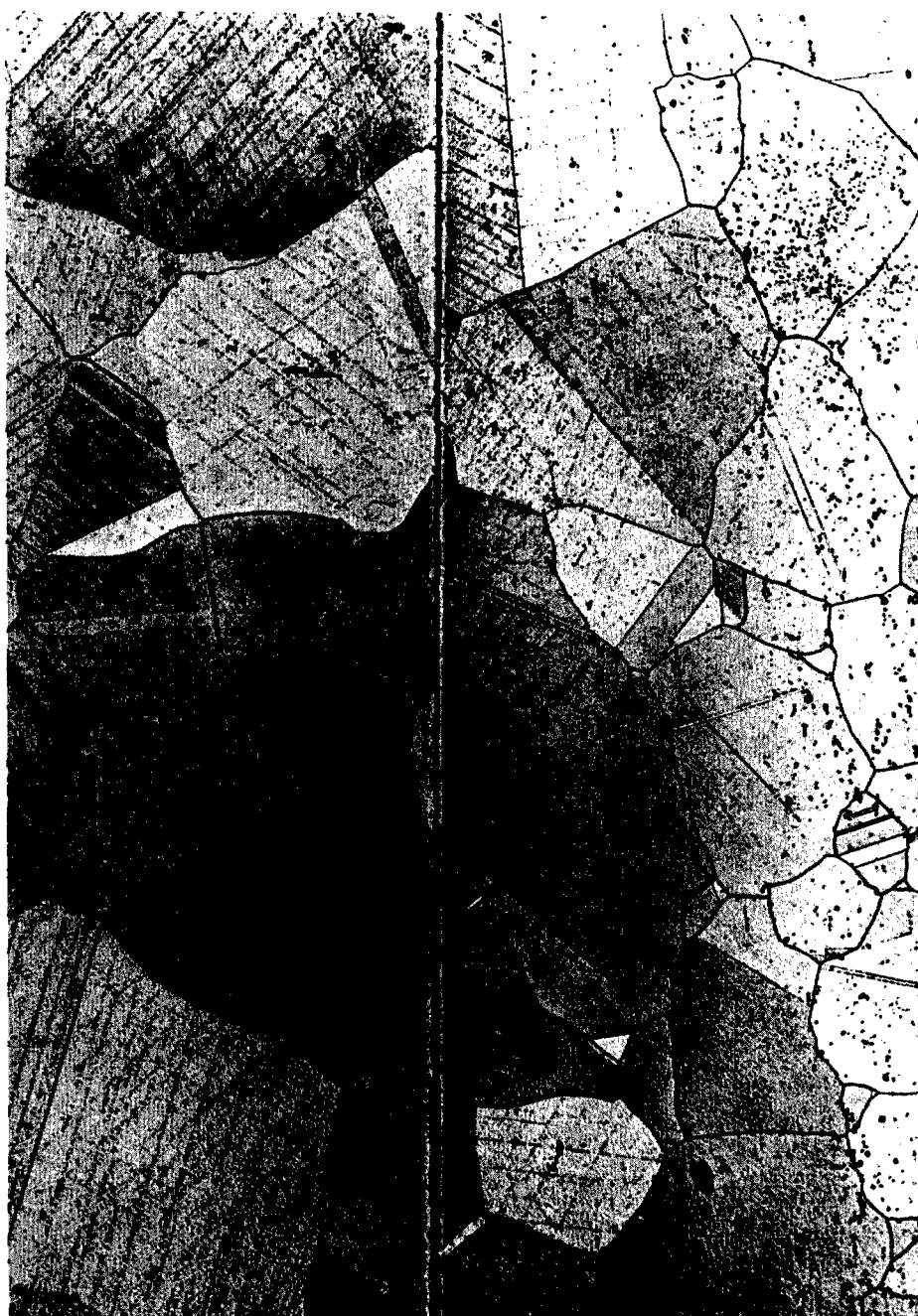


Figure 145. Photomicrograph After Pressing 4 Hours at 1850° F.



Figure 146. Photomicrograph of Sample Pressed 4 Hours at 1850° F Followed by 2 Hours at 2150° F.

It became apparent from the above tests that a new heating source would be required to conduct bonding operations at 2150°F. Therefore, an induction heating source was devised. In this procedure, new pushrods were required and Alloy TRW-1800 was used. A photograph of the procedure is shown in Figure 147.

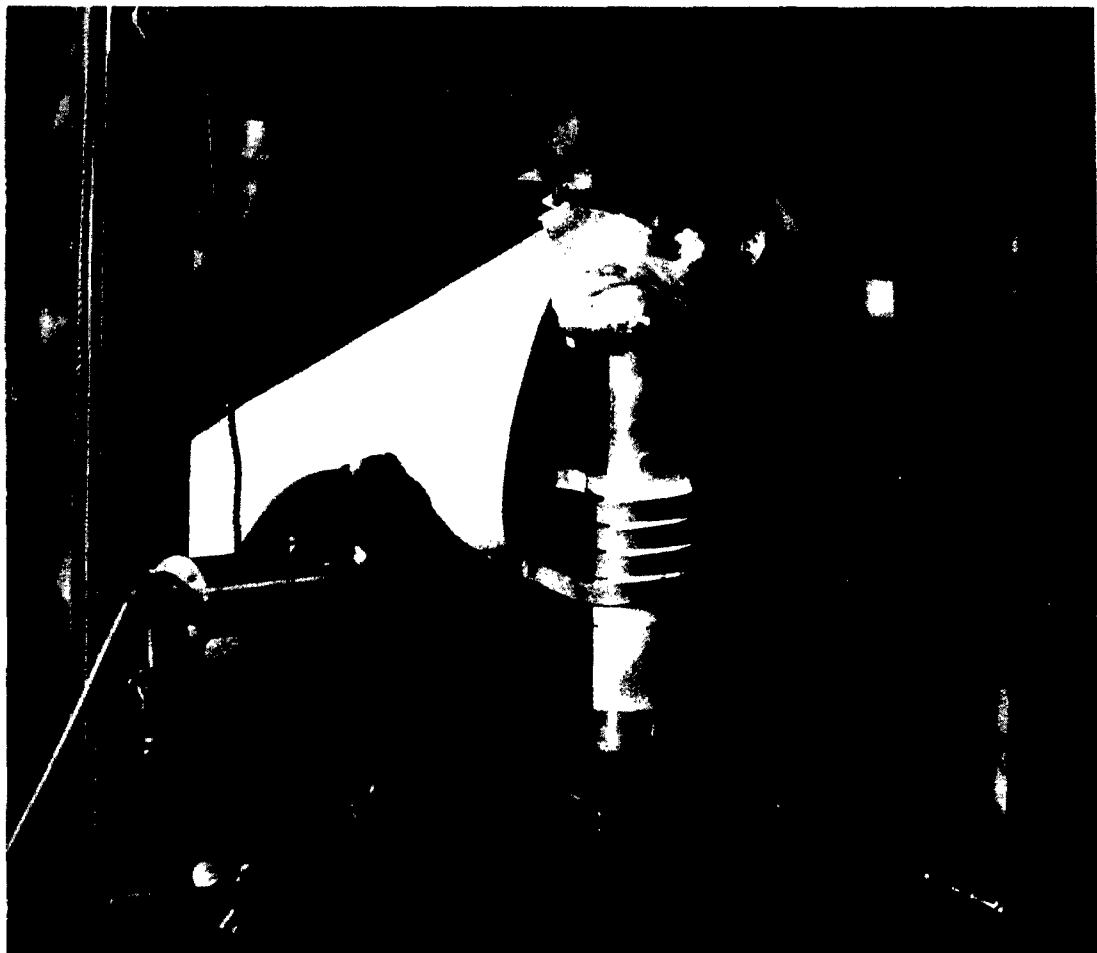
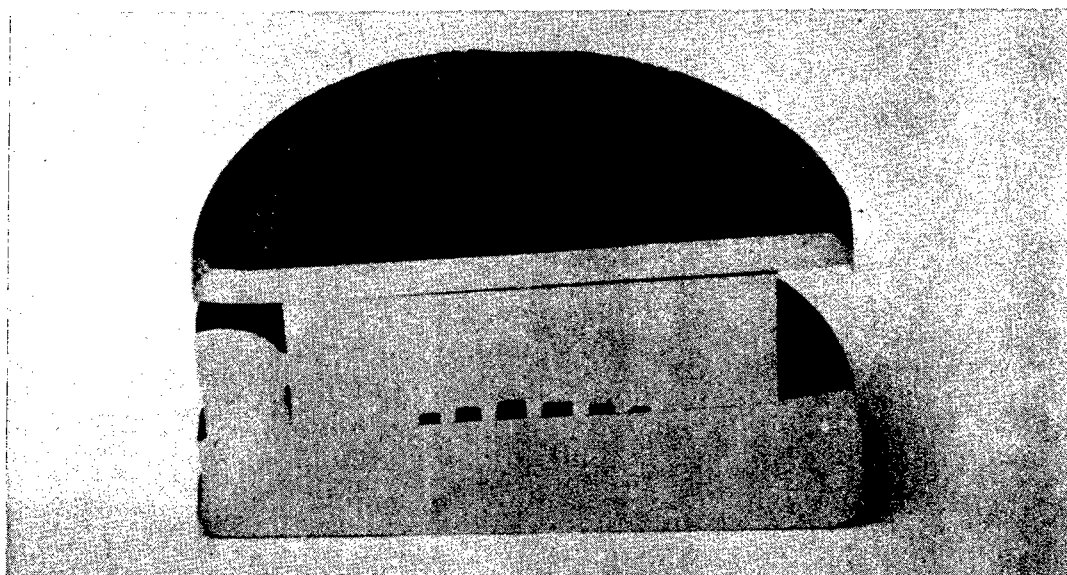


Figure 147. Induction Heating Diffusion Bond Setup.

During the first diffusion bonding test with this procedure, thermocouple failure was encountered and excessive temperature and deformation were observed with no evidence of bonding, as shown in Figure 148. The second run using this equipment appeared to be successful from the standpoint of temperature and pressure controls. A temperature of 2100°F was maintained for 1 hour at an initial load of 10,000 pounds, which slowly diminished to 5000 pounds at the end of the run.



**Figure 148. Overheated Diffusion Bond
Trial With Induction Heating.**

At the completion of this run, the capsule was heated in a salt bath at 2150°F for 1 hour. The capsule was then sectioned to remove one bond sample. This bond sample separated during machining of the capsule (Figure 149).

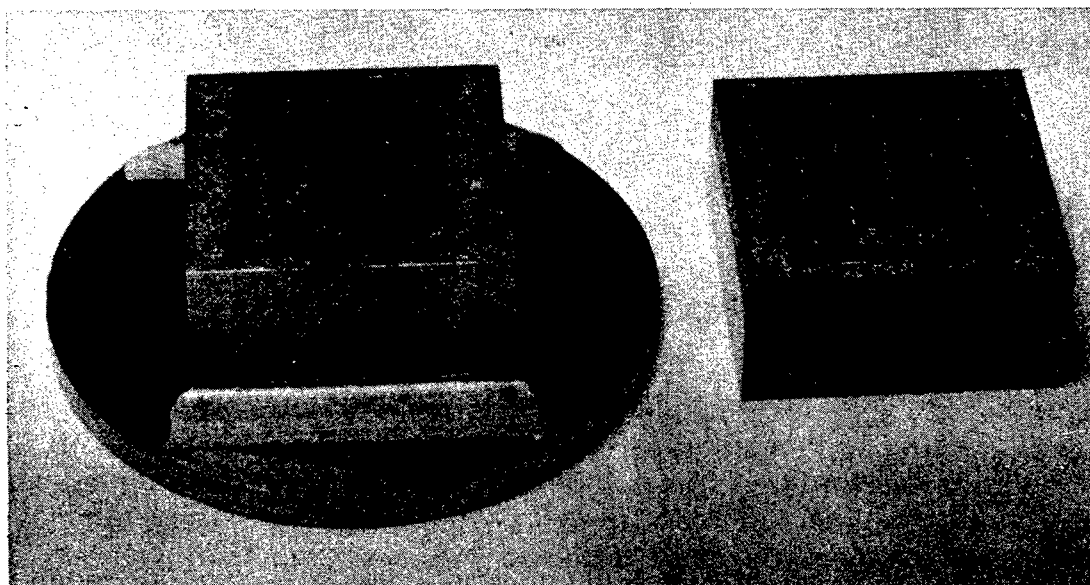


**Figure 149. Induction Heated Bond Trial - 2100°F for 1 Hour -
Showing Separation on Machining.**

The other half of the capsule was returned to heat treatment in a salt bath for the following times:

2150°F	2 Hours
1975°F	4 Hours
1550°F	24 Hours
1400°F	16 Hours

This sample also separated in the machining operation to remove the capsule.

It is probable that more satisfactory results at this temperature may be obtained with one or both of the following:

1. Longer holding time at this temperature and pressure
2. Higher pressure at this temperature

However, because of the lack of success, diffusion bonding as applied was not selected for the blade fabrication study.

TESTING

Testing Rectangular Samples

During the initial phases of this program, the following tests were to be used to evaluate the various techniques for fabricating the blade:

Nondestructive

1. X-ray
2. Penetrant
3. Ultrasonic
4. Leak Testing

Destructive

1. Microexamination
2. Macroexamination
3. Tensile
4. Stress-Rupture

Nondestructive

Cast blade samples were X-rayed and penetrant inspected after receipt from the foundry.

The inherent dendritic structure of castings has presented obstacles to the testing and interpretation of ultrasonic test results. The physical size of these castings also presents difficulties in obtaining a suitable size crystal.

Open ends of the raw castings require special seals and fixtures for the performance of pressure tests on the raw castings at meaningful pressure and temperature conditions.

While ultrasonic and pressure tests of the raw castings appear to be impractical, pressure tests of a cast blade capped by beam welding were considered to be very advantageous. Therefore, hollow blades from another program were used to investigate the possibility of using a helium leak-type test to determine the soundness of a finished blade. These preliminary tests were conducted under vacuum at both room temperature and at an elevated temperature. These preliminary tests are described below.

Fluid-cooled turbine blades, in order to function properly, must be leak tight, and a determination of this integrity becomes more critical when the blade is closed by welding. Experience gained from previous cooled blade fabrication studies led to the investigation of the mass spectrometer leak-type test for this application. Preliminary tests were conducted on the blade shown in Figure 150. These tests were conducted at room temperature at 1800 psi helium internally and under vacuum and failed to exhibit a leak rate greater than 1×10^{-10} cc/sec of helium, which is the sensitivity of the testing equipment. The vacuum test was repeated with the blade tip heated to 1600°F. This test failed to show a leak rate greater than 1×10^{-10} cc/sec helium. The apparatus used in this test is shown in Figures 151 and 152.

The results of these preliminary tests were successful; this type of test was conducted at room temperature prior to sealing the coolant in the finished blades.

Destructive

Destructive tests such as macro- and microexamination (as shown in the previous sections of this report) have shown the inability to achieve a satisfactory blade configuration from wrought U-700 by electron beam welding only, or by diffusion bonding.



Figure 150. Fluid-Cooled Blade - Electron Beam Welded.

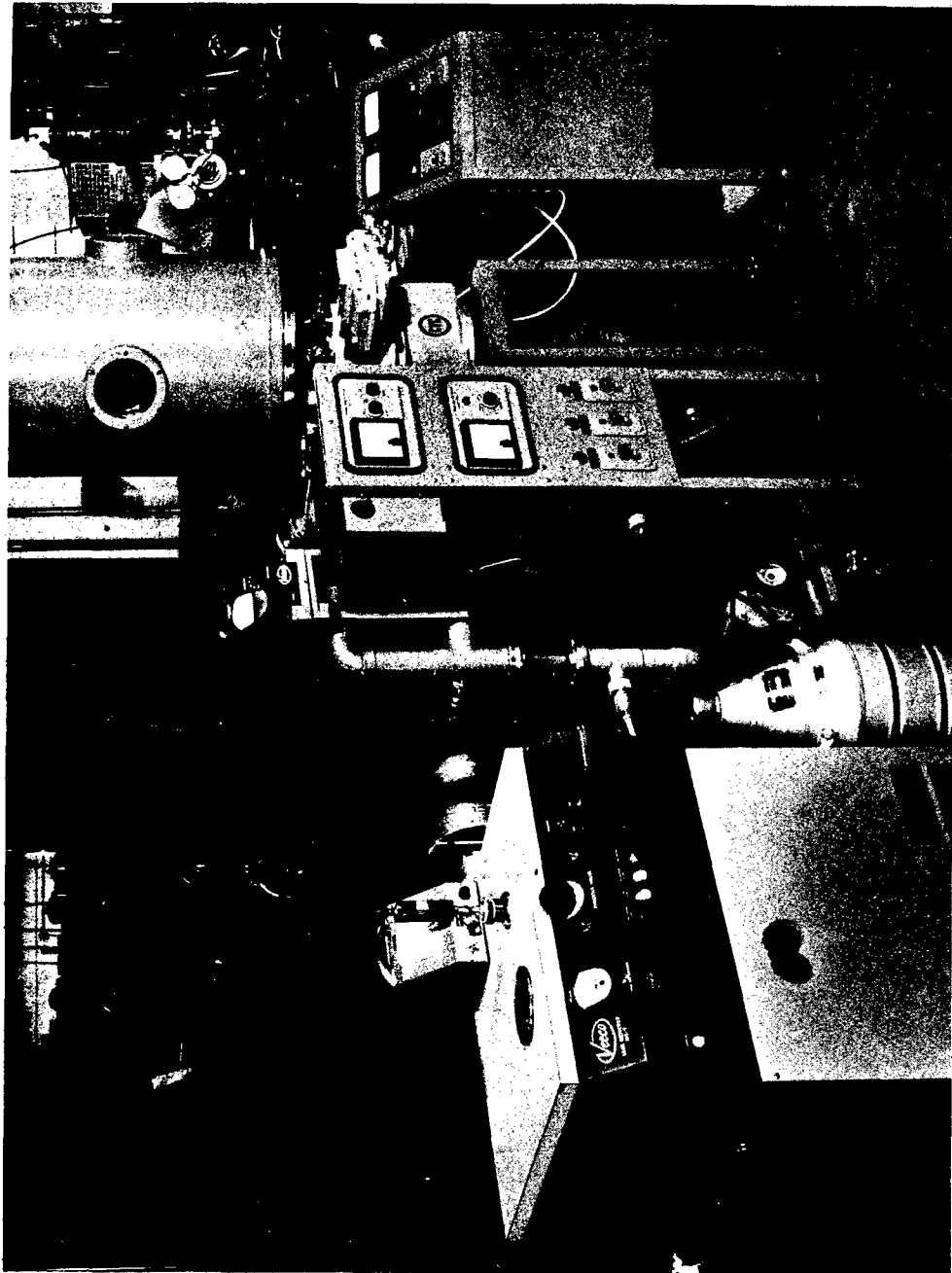


Figure 151. Leak Test Equipment - Veeco Model MS-9A Mass Spectrometer for Testing Cooled Hardware.



Figure 152. Leak Testing - Cooled Turbine Blade, Welded Tip.

Macro- and microexamination of integrally cast rectangular blades and blade tip closed by electron beam welding described in previous sections of this report show that a satisfactory blade configuration may be obtained.

Destructive tests, such as stress rupture, were conducted on butt joints to evaluate the blade capping operation. This test program is summarized in Table XI.

TABLE XI
STRESS-RUPTURE TESTS AT 1400°F OF U-700
ELECTRON BEAM WELDS

Condition	Loading				Total Time to Failure (Hrs.)
	Initial		Increased		
	Stress (psi)	Time (Hrs.)	Stress (psi)	Time (Hrs.)	
<u>As-Cast Block</u>					
Aged 16 Hours at 1400° F	65,000	72.1	75,000	16.6	85.7
After Welding	75,000	26.0	--	--	26.0
<u>Cast-to-Cast Weld</u>					
Aged 16 Hours at 1400° F					
After Welding	85,000	1.0	--	--	1.0
Casting Fully Heat Treated	65,000	0.0	--	--	0.0
After Weld, Heat Treat to 1975° F, 4 Hours, Plus 1400° F, 16 Hours, Air Cooled	50,000	67.6	60,000	25.6	93.2
<u>Cast-to-Wrought Weld</u>					
Casting Fully Heat Treated	65,000	67.5	75,000	38.6	106.2
	60,000	67.5	70,000	97.7	165.2
After Weld, Heat Treat to 1975° F, 4 Hours, Plus 1400° F, 16 Hours, Air Cooled	75,000	114.2	--	--	114.2
	65,000	90.0	75,000	67.3	157.3

From these data it is expected that electron beam welded joints between cast U-700 and wrought U-700 will safely operate at a stress level of 70,000 to 75,000 psi for 100 hours. This value is approximately 90 percent of that specified in Continental Material Specification 700 for wrought stock.

Fixtures were designed and procured to pull test a prototype blade having the blade tip closed by welding a wrought cap to the cast blade. The fixture shown in Figure 153 was designed to obtain the strength of the capped blade. The test specimen is shown in Figure 154. This test is to be performed before removing the excess cap material to facilitate the fixturing in the standard tensile machine. The same fixture and specimen may be used for both room temperature and elevated temperature testing, as shown in Figure 155.

Five electron beam welded rectangular blades were tested with this equipment at 1700° F. These results are given in Table XII. The stress values were calculated from a measurement of the cross section of the open end of the blade casting. Fractures are shown in Figure 156.

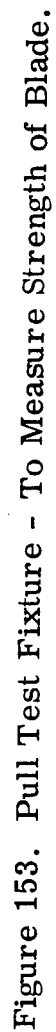
On the basis of past experience and other published data, fatigue failure generally occurs as a result of stress concentration near the root of the airfoil. Therefore, in considering fatigue testing, two factors will be evaluated:

1. Holding of the blade sample
2. Method of applying load

Background experience exists in testing rotating blades in bending fatigue with various methods of clamping fixtures. The fluid-cooled rectangular blade was clamped in a standard vise-type clamp and tested in alternating fatigue. This type of fixturing was adequate for determination of the room temperature fatigue properties.

A schematic sketch of the fatigue setup is shown in Figure 157.

Sample number 5 from the pull test described above was rebrazed and tested in alternating bending along with an electron beam welded specimen. The results of these room temperature tests are given in Table XIII.



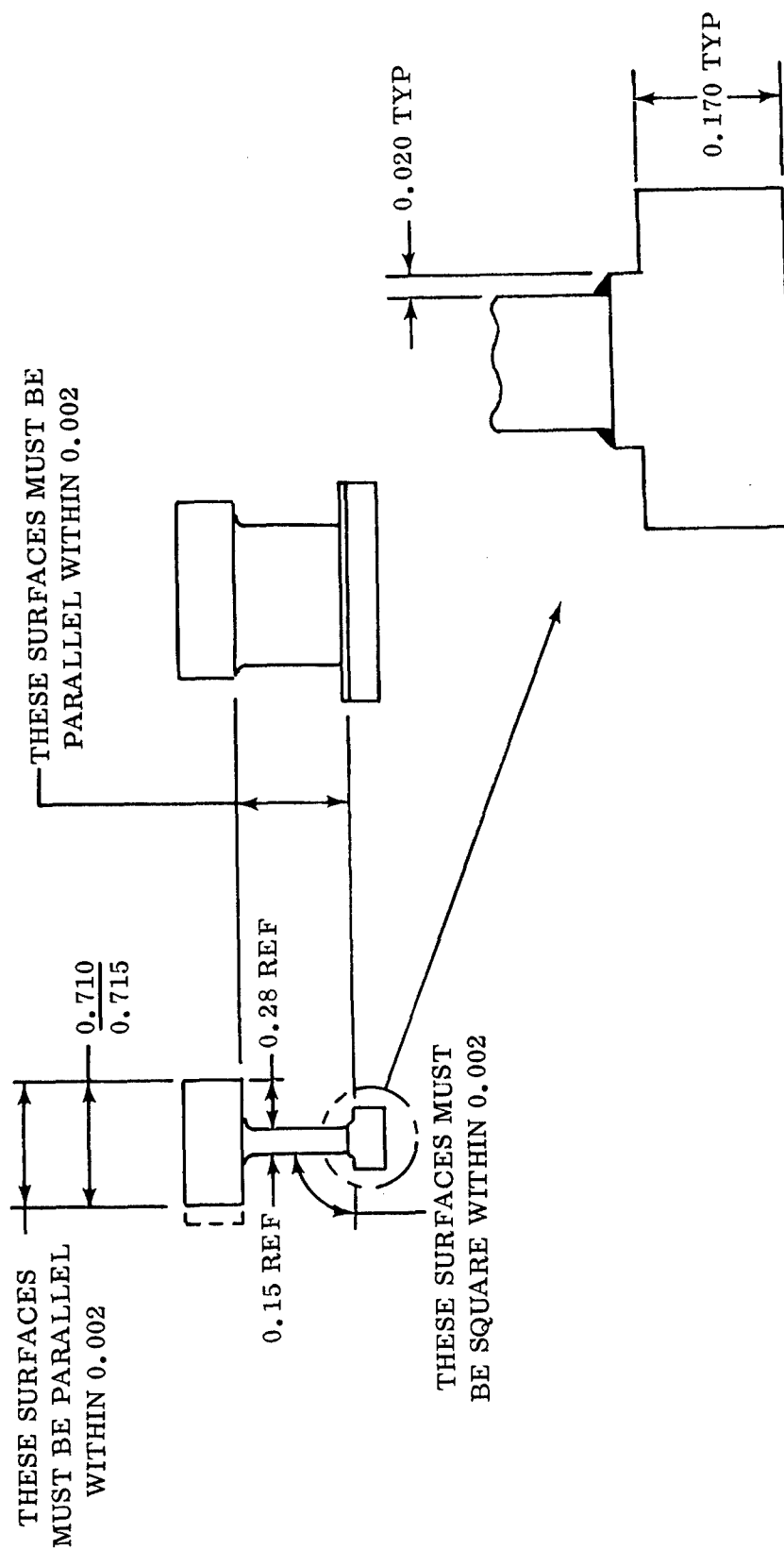


Figure 154. Welded Blade Tip.

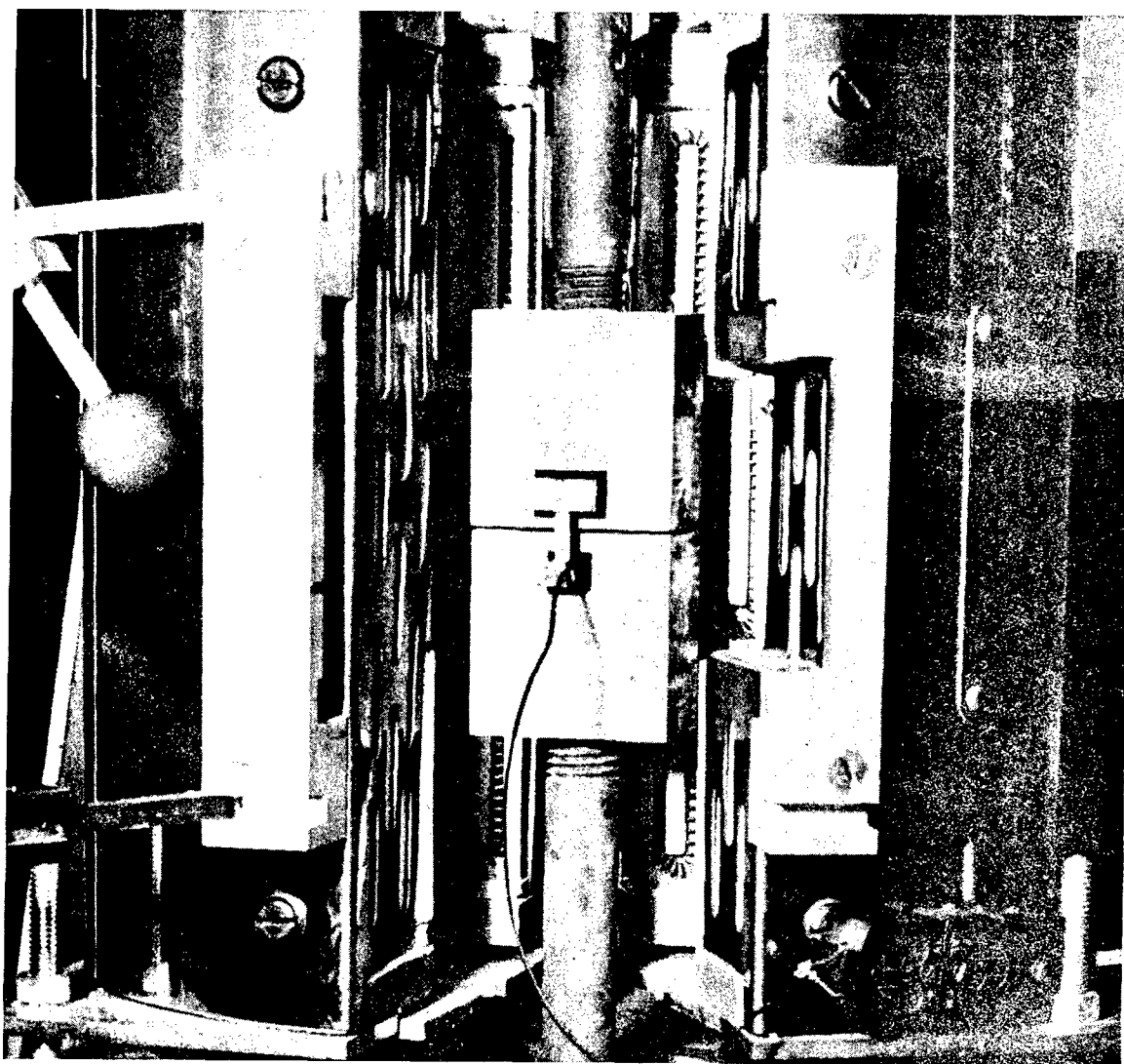
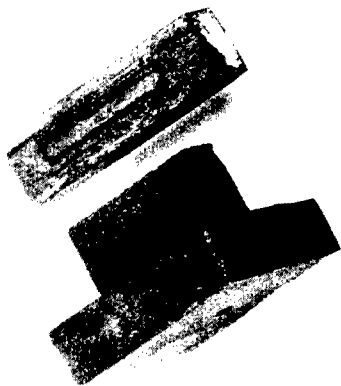


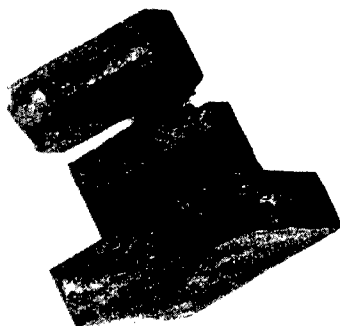
Figure 155. Tensile Testing of Rectangular Blades.

TABLE XII
TENSILE STRENGTHS OF CAPPED BLADES

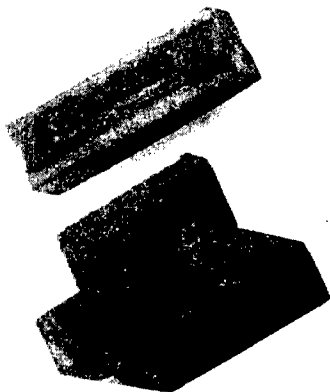
Casting No.	Cap Material	Tensile psi at 1700°F
1	U-700 (Weld)	67,300
2	Inco 718 (Weld)	54,600
3	Inco 718 (Weld)	57,300
4	U-700 (Weld)	40,300 (Leaked on Pressure Test)
5	U-700 (Brazed)	24,000



No. 1
CASTING NO. 6830
U-700
WELDED



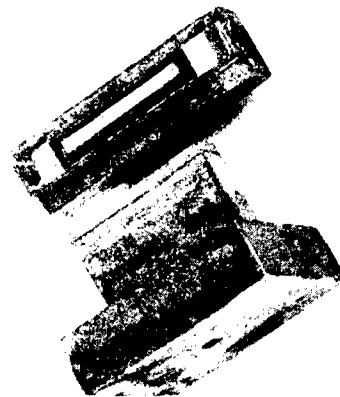
No. 2
CASTING NO. 69791
INCO 718
WELDED



No. 3
CASTING NO. 69803
INCO 718
WELDED



No. 4
CASTING NO. 39412
U-700
WELDED



No. 5
CASTING NO. 6831
U-700
BRAZED



Figure 156. Pull Test on Blade Caps.

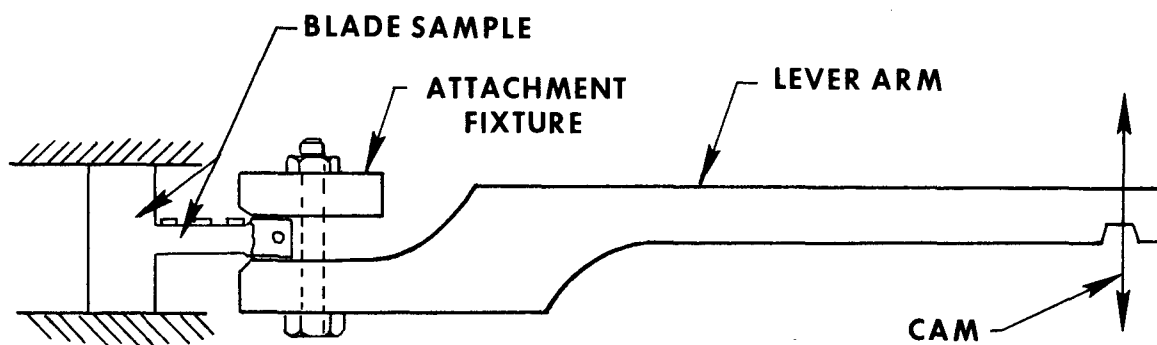


Figure 157. Fatigue Test Setup.

TABLE XIII
FATIGUE TESTS OF CAPPED BLADES

Sample	Stress at Blade Root (psi)	Stress at Blade Cap (psi)	Cycles to Failure	Location of Failure
Brazed	49,200	31,000	3×10^5	Cap
Welded	40,000	21,000	7×10^5	Cap

A typical fatigue fracture from this test is shown in Figure 158.

For purposes of comparison, Figure 159 shows typical fatigue curves for full heat-treated wrought U-700 at 1300 and 1500° F temperatures.

While these tests were preliminary, the loading and test duration exceeded calculated design values.



Figure 158. Typical Fatigue Fracture of Rectangular Blade.

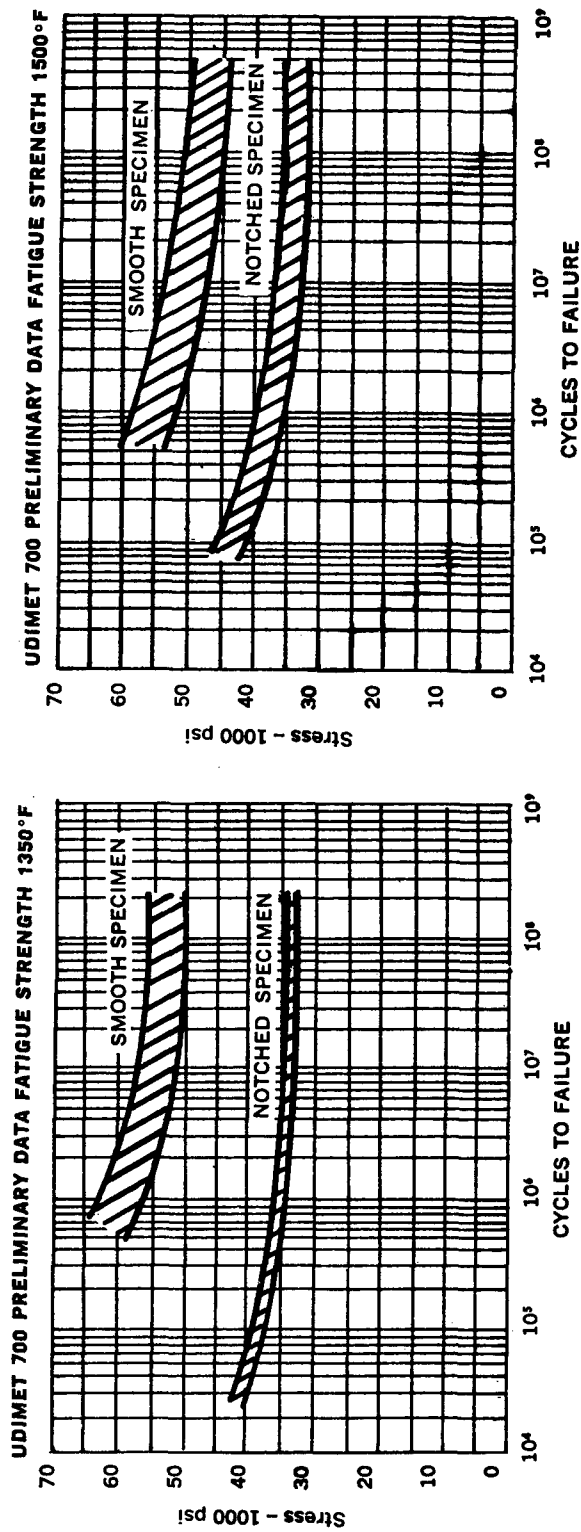


Figure 159. Fatigue Curves - Wrought U-700.

Testing Airfoil Blades

Testing of blades shall have two objectives; namely, sample quality assurance and design integrity type tests. Quality assurance tests will consist of standard type tests, such as

1. X-ray examination
2. Penetrant dye examination
3. Micro- and macroexamination

These tests have been performed and have been adequately described in a previous section of this report.

Design integrity tests will be both nondestructive and standard destructive type tests modified to produce test data related to design data. These tests are summarized in Table XIV.

**TABLE XIV
HARDWARE AND TESTS CONDUCTED**

Type of Test	No. Caps and Plugs	Blade Form	
		No. Unmachined Caps and Plugs	No. Machined Caps and Plugs
Pressure 2000 psig N ₂	-	12 pieces	-
Pressure Helium Leak	-	-	4 pieces
Liquid Filled by Weight	-	-	4
Thermal Shock 1700° F	-	-	4
Tensile R. T.	-	2	-
1700° F	-	2	-
Fatigue Resonant Freq.	1	-	1
Thermal Conduit No Liquid	1	1	1
Liquid Filler	-	-	1

Tensile Testing

The fixture shown in Figure 153 was modified to accommodate the airfoil casting with its electron beam welded cap. Both room temperature and elevated temperature tests were conducted; the results are given in Table XV. A typical fracture from this test is shown in Figure 160.

TABLE XV
TENSILE RESULTS

Blade No.	Ultimate Load (pounds)	Stress (psi)	Test Temp.
53	5,750	95,800	Room
49	6,125	102,000	Room
40	2,425	40,400	1700° F
41	3,500	58,300	1700° F

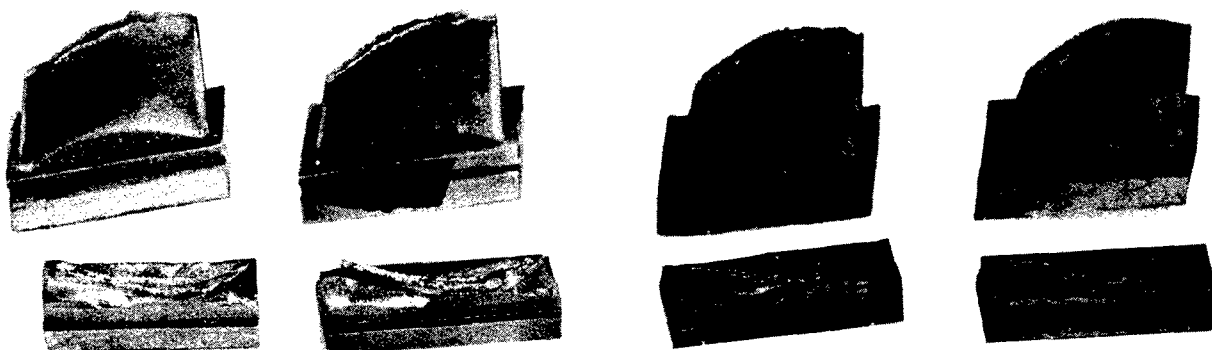


Figure 160. Typical Tensile Airfoil Fractures.

Fatigue Testing

The airfoil casting was considered too rigid to be tested in alternating bending on available company equipment; therefore, this type of fatigue test was not conducted.

Attempts to vibrate this blade casting on the company pulsed air rig indicated that this blade was too rigid to be tested with this equipment.

Continental determined the natural frequency of the turbine blade to be 12,350 cps clamped at the parallel base section and 13,800 cps clamped across the full base. This was done by pulsing air across the blade and measuring the frequency with a strain gage pickup. No other modes of vibration could be determined utilizing the equipment in the laboratory. The rigidity of the turbine blade did not permit the utilization of normal techniques of excitation.

A strain gage was installed on the blade convex trailing root to monitor blade response to pulsed air excitation. At resonance (13,800 cps), the maximum indication was ± 95 microstrain. To determine the area of maximum stress, resonance should be excited while monitoring a series of strain gages. However, this determination is not considered necessary at this time.

Sufficient force to excite blade resonant fatigue testing is not readily available within the laboratory. The extreme difficulty experienced in natural frequency determination indicates a very strong reluctance to excitation. Thus, engine or test rig operational excitation would probably require interference with a strong prime order disturbance; that is, nozzles, struts, and so forth. Figure 161 indicates the unlikelihood of resonance within the turbine operating range. Possible resonances may exist at transition speeds of 35,000 and 39,000 rpm. Note that the interference points may be slightly altered by a speed effect upon the resonant frequency according to the following relationship:

(9)

$$f_n^2 = f_o^2 + CN^2$$

where:

f_n, f_o = natural frequencies at speed and stationary, respectively, cps

N = speed, rps

C = blade constant

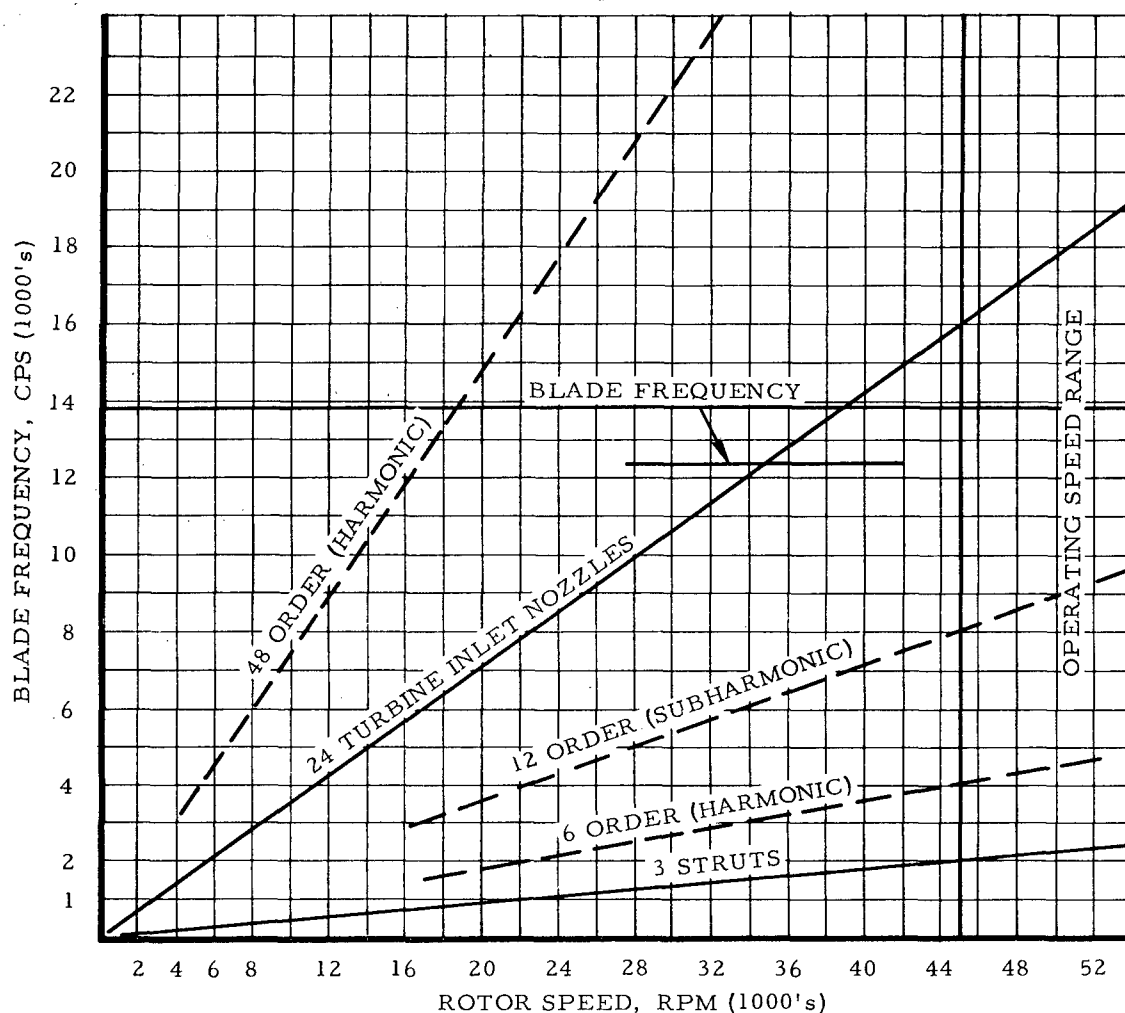


Figure 161. Interference Diagram - Turbine Blade.

Thermal Shock Tests

The thermal shock experienced by a turbine blade has been simulated for the Protective Coatings Program at Continental. In this test, blades are mounted on a rotating disc which passes through a gas flame of known temperature for a specific length of time. The blades are then removed from the flame and exposed to a cold air stream for a finite time interval. Testing on this rig (Figure 162) has been accomplished at temperatures up to 1900°F, and data for several turbine materials are available for up to 600 thermal cycles.

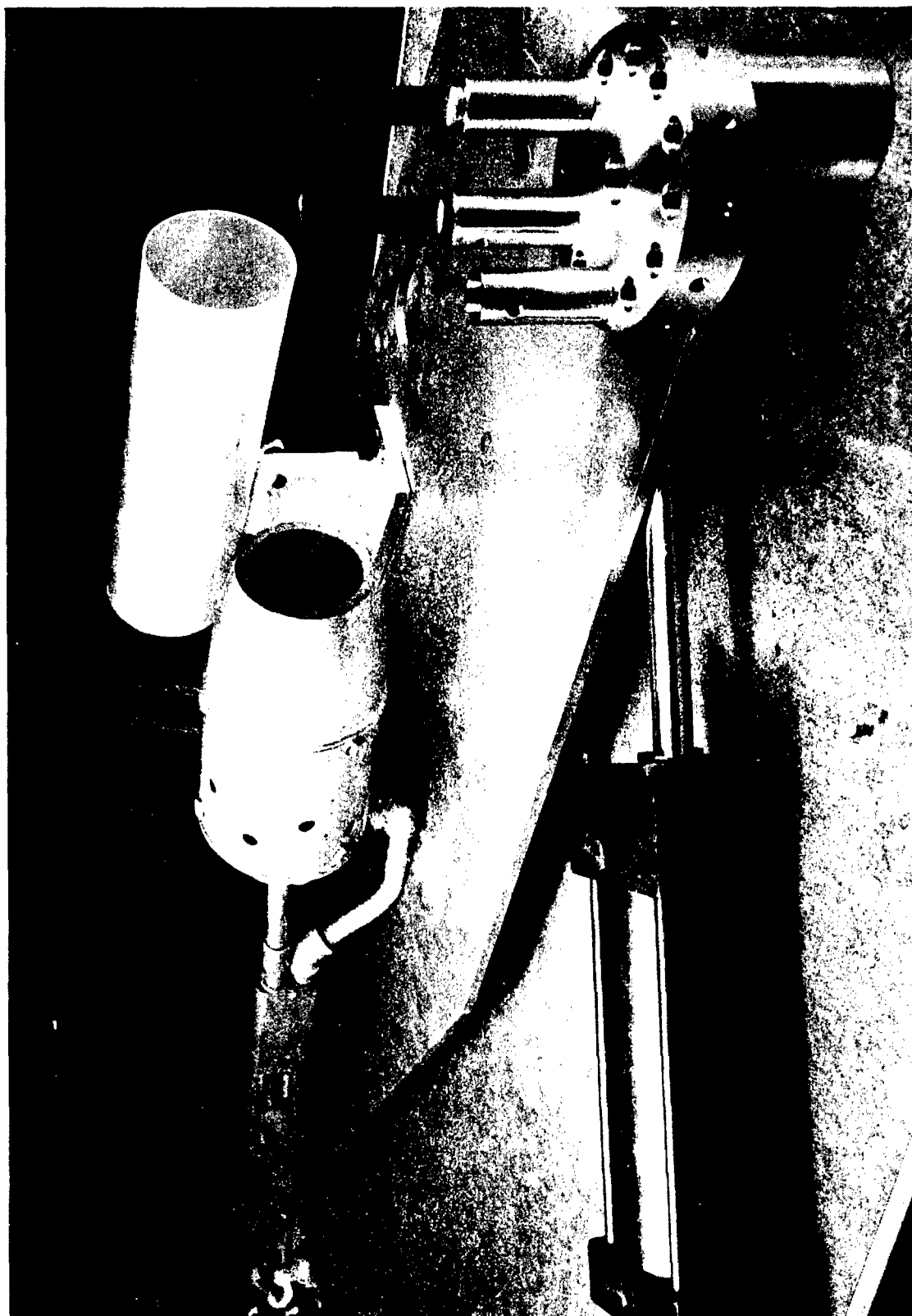


Figure 162. Thermal Shock Rig Out of Chamber Showing Rotating Specimen Holder
in Line With Gas Burner and Air Blast.

The test temperature of 1700°F, the number of cycles, and the duration of cycle were selected on the basis of available design data and on the basis of a review of thermal shock data for similar materials.

These data were used due to lack of concrete data on the U-700 material. Vendor specified that the properties of IN-100 were similar and the data were conservative.

Thermal fatigue data for these similar materials are given in Table XVI and Figures 163 through 165.

TABLE XVI THERMAL FATIGUE DATA INCO 713C AND HS 31			
Alloy	Temp. °F	Average Cycles to Initiate Cracking	Average Cycles to 1/8-inch-long Crack
713C	1700	813	2493
713C	1800	854	2521
713C	2000	164	947
AMS 5382B	1700	426	928
(HS 31)	1800	196	529

Thermal shock testing of the blade was accomplished on the Continental rig using both a standard wedge and Continental standard sample (Figure 166) as control samples. These data are recorded in Table XVII.

As seen in Table XVII, a 500-cycle thermal shock test to 1700°F was completed. The three blades tested appeared similar before and after test. Water was seal-welded in two of the blades prior to test. The unsealed blade passed a 1500 psi pressure leak test after the thermal shock test; the two sealed blades were found to contain no water and, in addition, leaks were found at the tip caps after thermal shock. Additional blades with tip caps welded, ground, and pressure checked before seal welding will be thermal shock tested.

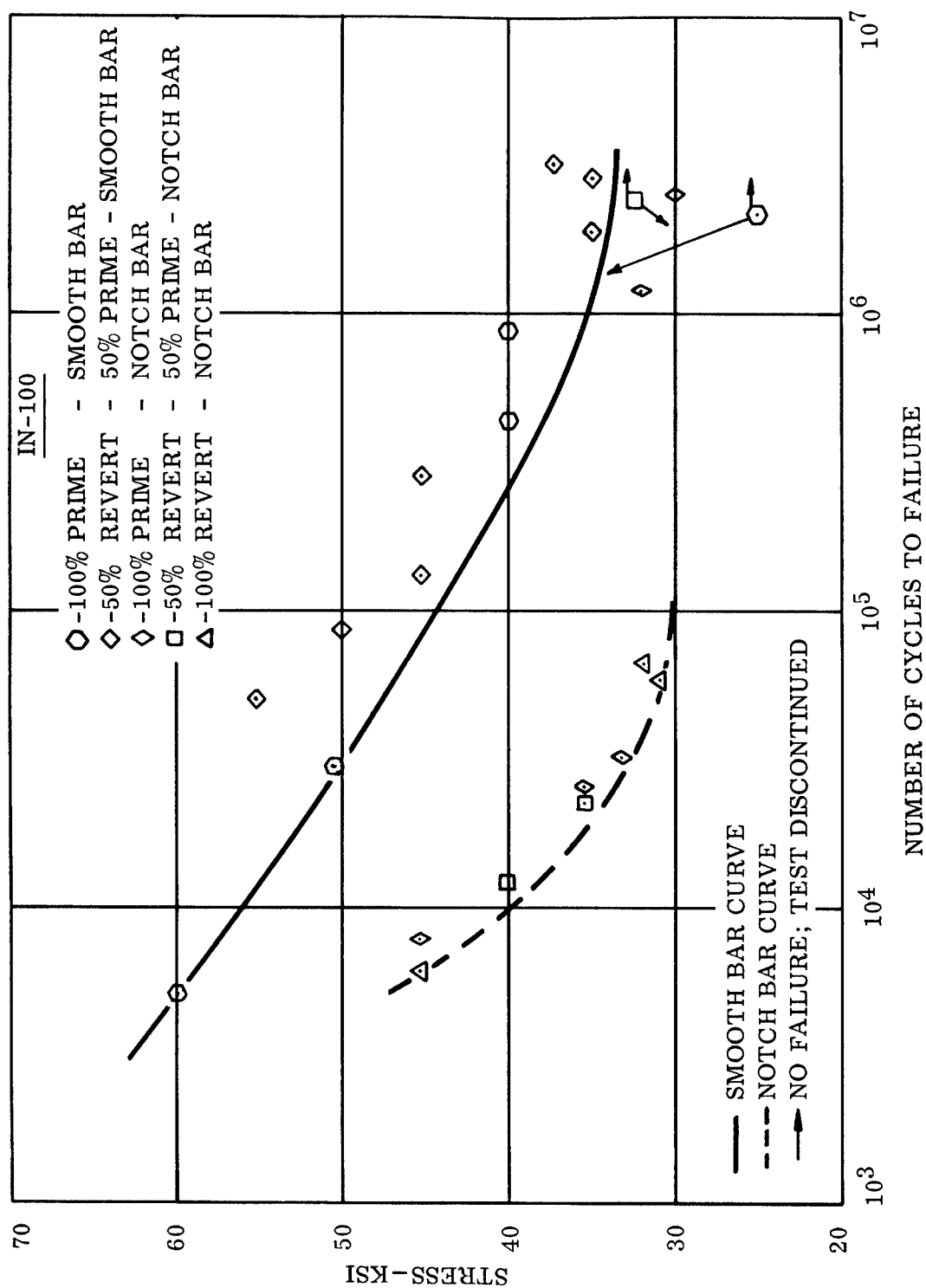


Figure 163. Mechanical Fatigue Results for IN-100 at 1700°F.

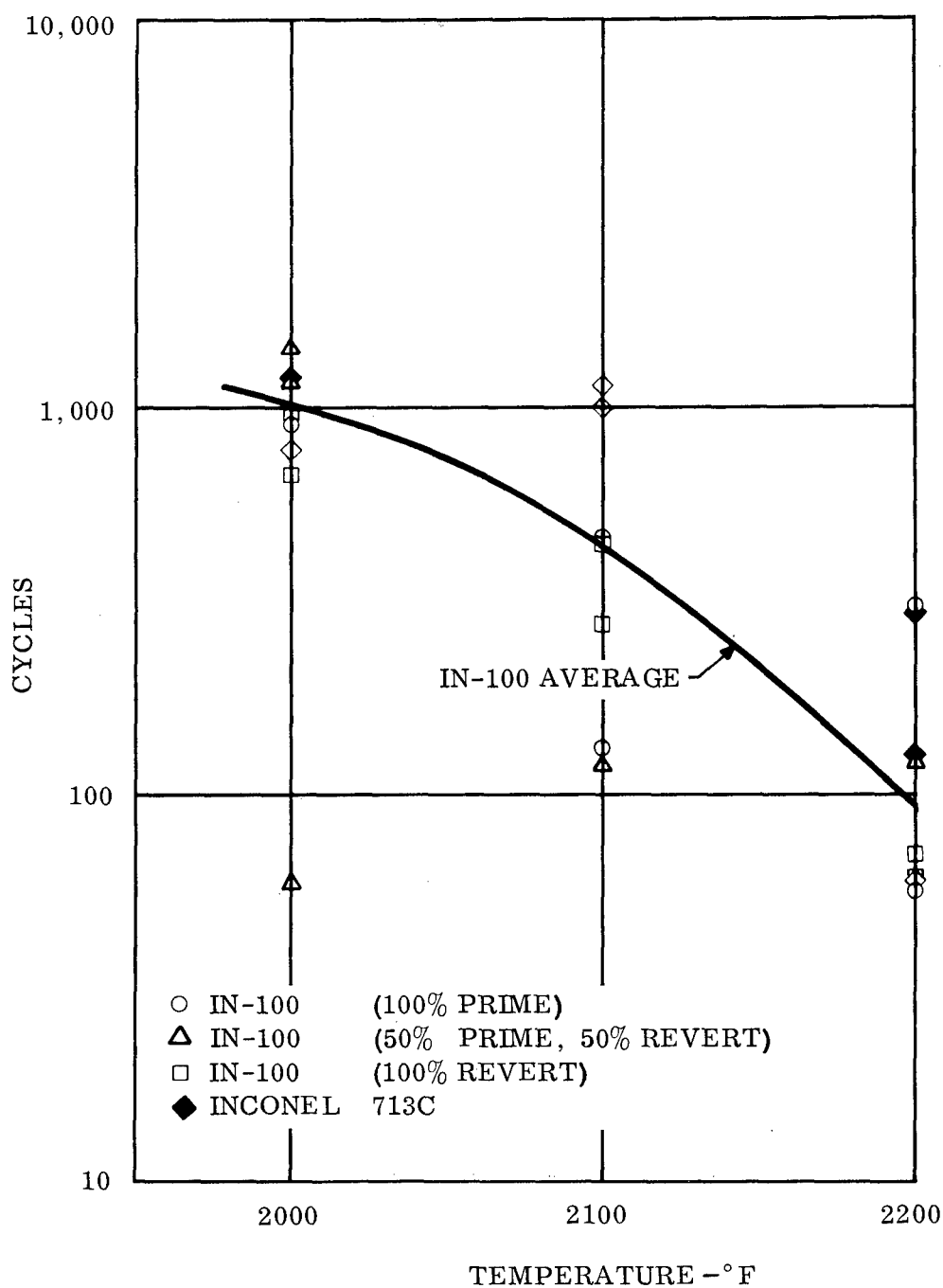


Figure 164. IN-100 - Thermal Fatigue Cycles to Initial Cracking.

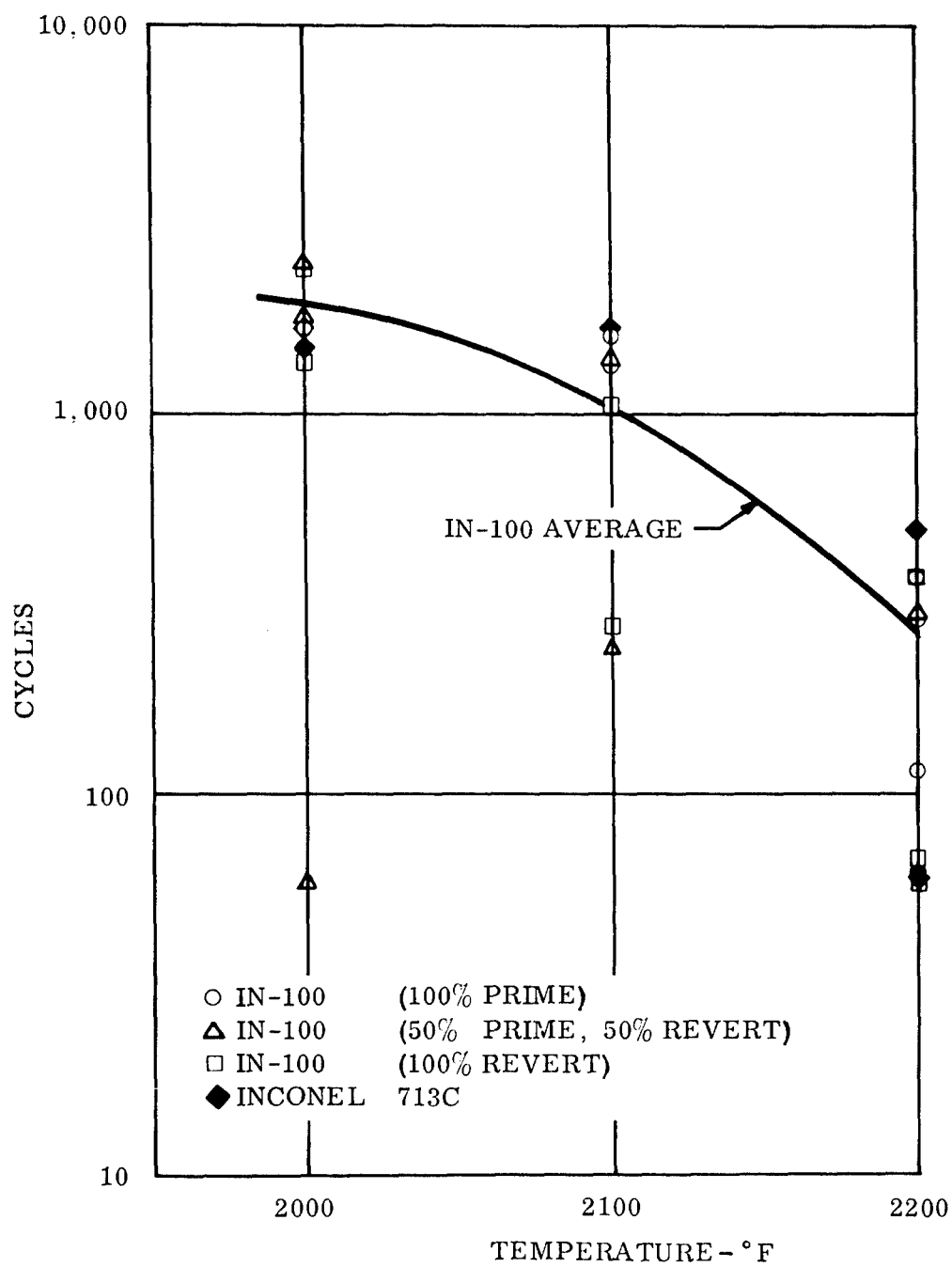


Figure 165. IN-100 - Thermal Fatigue Cycles to Failure.

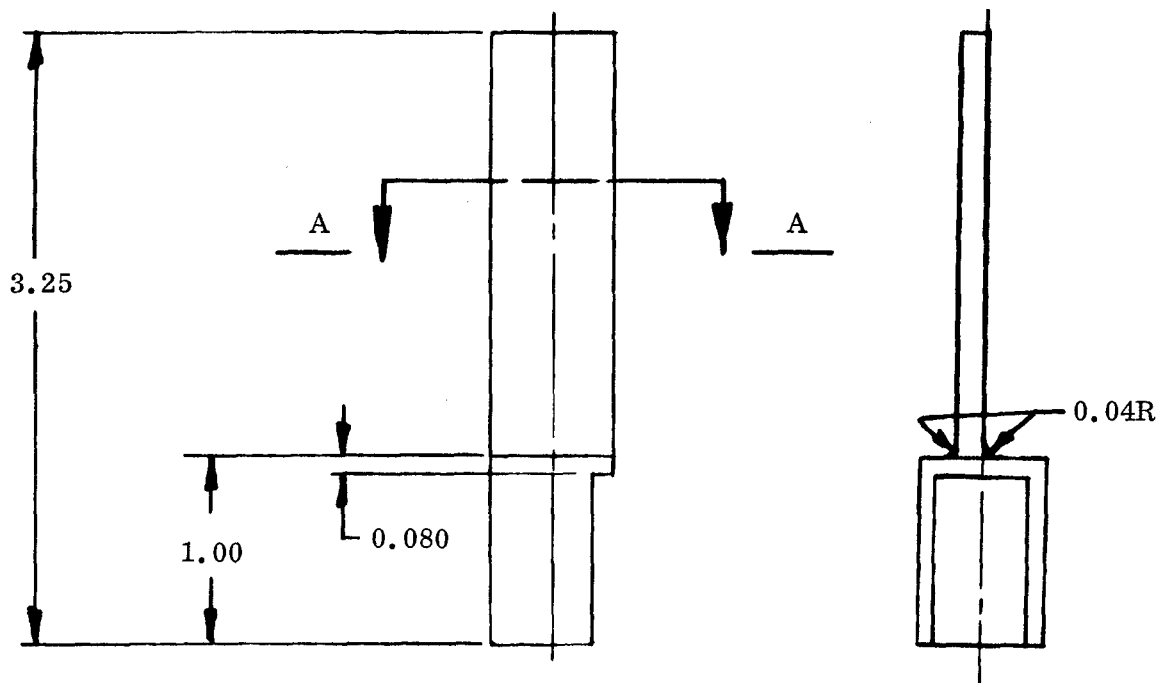
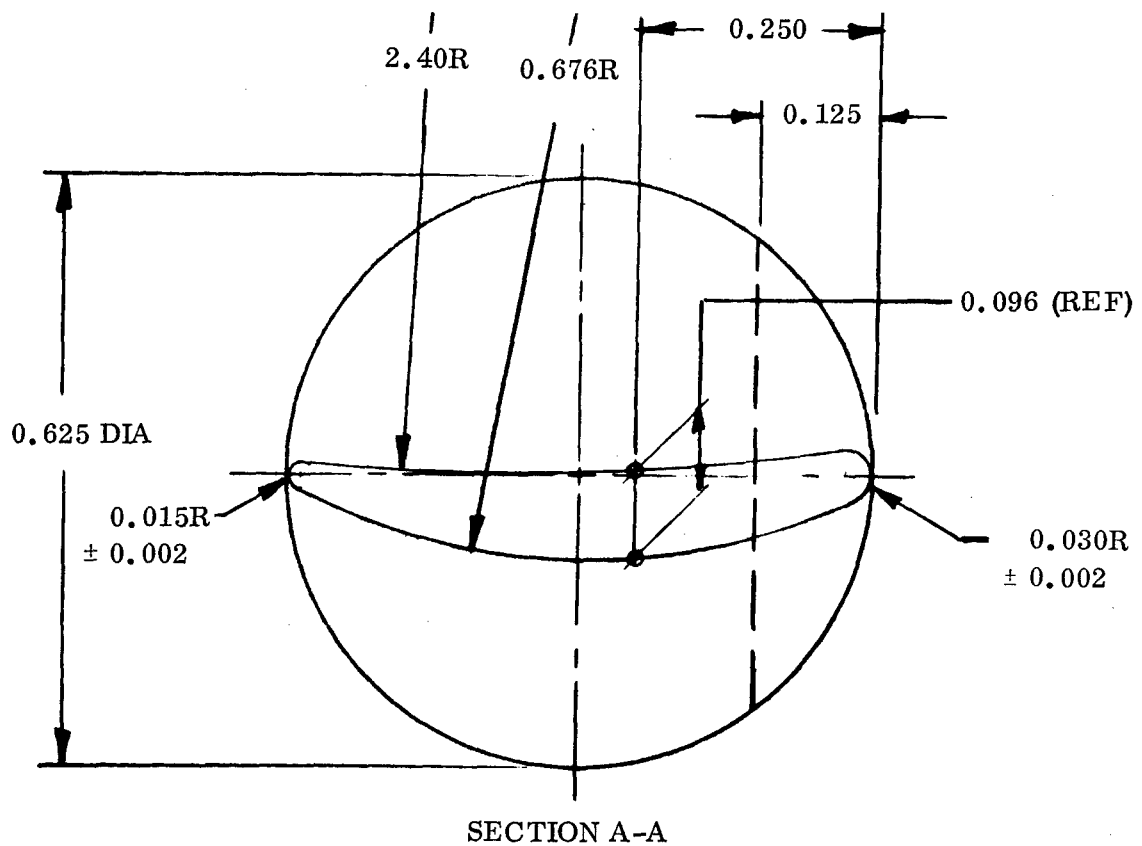


Figure 166. Thermal Shock Blade Specimen.

TABLE XVII
THERMAL SHOCK RESULTS

Test Type: Thermal Shock
Specimen Ident.: Blade, Fluid Cooled
Test Temp.: 1700° F (Optical Pyrometer)
Time in Flame: 30 Seconds - Temp. 1700° F
Cooling Period: 30 Seconds - Temp. 1000° F
Test Time: 500 Minutes
Total Test Time: 8.20 Hours

<u>Data:</u>	<u>Sample No. 30 - H₂O Filled and Plugged</u>				<u>Remarks</u>
Cycle No.	75	200	400	500	
Weight (Grams)	32.045	32.047	32.042	32.041	No H ₂ O found on opening plug after test. Leaks in airfoil at 1800 psig N ₂ .
Deformation	Crack indicated top concave side	Same	Same	Same	
No. of Cracks	1	1	1	1	
Length of Cracks (in.)	0.25	0.25	0.25	0.25	
Surface Condition	Spotty Oxidation	Spotty Oxidation	Spotty Oxidation	Spotty Oxidation	
<u>Data:</u>	<u>Sample No. 33 - Unfilled and Unplugged</u>				
Cycle No.	75	200	400	500	
Weight (Grams)	32.286	32.285	32.280	32.281	No leaks in airfoil at 1800 psig N ₂ after test.
Deformation	Crack indicated on weld edge	Possible cracks on weld junction	Still only crack indications	Same	
No. of Cracks	3	3	3	3	
Length of Cracks (in.)	0.25	0.25	0.25	0.25	
Surface Condition	Spotty Oxidation	Spotty Oxidation	Spotty Oxidation	Spotty Oxidation	
<u>Data:</u>	<u>Sample No. 47 - H₂O Filled and Plugged</u>				
Cycle No.	75	200	400	500	
Weight (Grams)	32.206	32.208	32.199	32.199	No H ₂ O found on opening after test. Plug pin hole leak in airfoil at 1800 psig.
Deformation	Spot upper left corner on concave side	Same	Same	Same and indication of galling on weld	
No. of Cracks	0	0	0	0	
Length of Cracks					
Surface Condition	Spotty Oxidation	Spotty Oxidation	Spotty Oxidation	Spotty Oxidation	

BLADE AND DISC DESIGN STUDIES

This section covers the analytical design of the blade cooling systems considered; discussion of fuel thermal stability; analytical determination of rotor metal temperature distribution; structural design of the disc, blades, and attachments; and results of tests of the fuel seal and pinned attachment.

BLADE COOLING SYSTEMS

The cooled turbine blade is designed to maintain a structurally acceptable metal temperature below the blade-relative temperature of the main gas stream. In supporting this temperature difference, the cooled blade absorbs a heat input from the main stream which is a function of the design parameters of the turbine.

The heat absorbed by the cooled blade is transferred to the engine fuel flow which is to be used as a thermal sink in this design. The thermal capacity of the fuel sink is limited by the engine fuel flow and by the thermal stability of the fuel. Fuel thermal stability limits are discussed later in this report.

Table XVIII summarizes the design point parameters for the cooled turbine.

The limits of possible cooled blade temperatures can be established with a knowledge of these engine parameters. Figure 167 shows the engine fuel temperature rise versus blade temperature for the regenerated and nonregenerated engine at design point.

Two heat transfer systems were considered in order to use the thermal sink capacity of the engine fuel flow to cool the turbine blades:

1. Direct fuel cooling of the blade.
2. A steam vapor secondary thermosyphon system to transfer heat from the blade to the fuel.

Direct fuel cooling of the turbine blades was rejected as posing difficult design and development problems. Fuel pressure in the blade, caused by the high "g" field, would complicate structural design and fuel sealing. High blade metal temperatures could cause fuel coking and shel-lacking of blade cooling passages. It would be difficult to limit fuel temperature rise while providing uniform blade cooling.

TABLE XVIII
SUMMARY OF COOLED TURBINE DESIGN POINT PARAMETERS

Turbine Inlet Pressure	126.8 psia
Turbine Inlet Total Temperature	2300° F
Turbine Relative Temperature	2021° F
Number of Turbine Blades	31
Turbine Blade Root Radius	3.503 inches
Turbine Blade Tip Radius	4.123 inches
Turbine Blade Gas Wetted Area	0.0105 sq ft/blade
Turbine rpm	50,000
Fuel Assumed	JP-4
Engine Airflow (lb/sec)	5.0
Heat Trans. Coeff., Gas to Blade	$\frac{(\text{Btu})}{(\text{hr-ft}^2-\text{°F})} \quad 270$
Engine Fuel Flow, Regenerated (lb/hr)	343
Engine Fuel Flow, Nonregenerated (lb/hr)	501

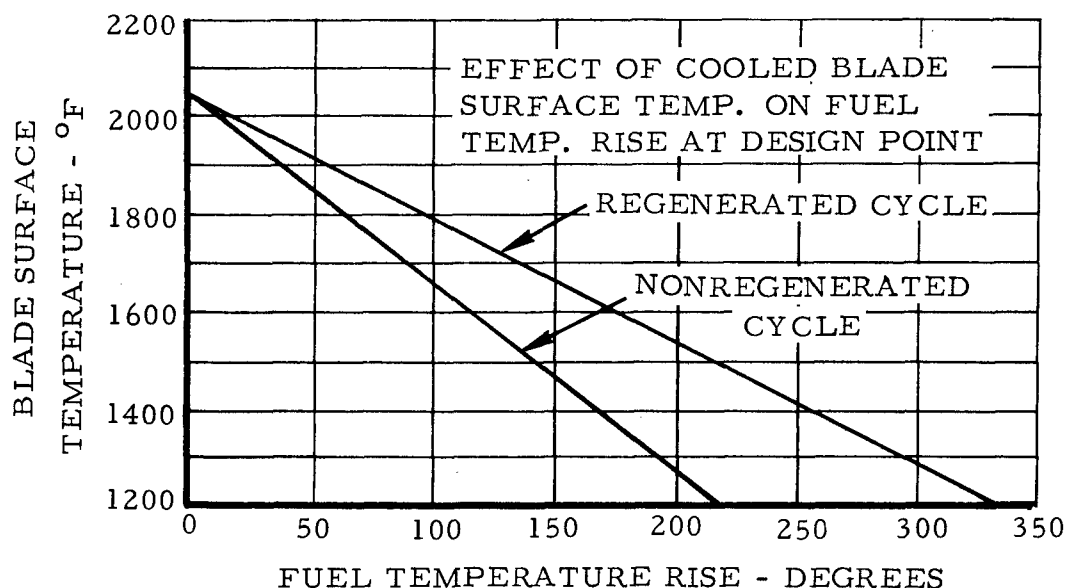
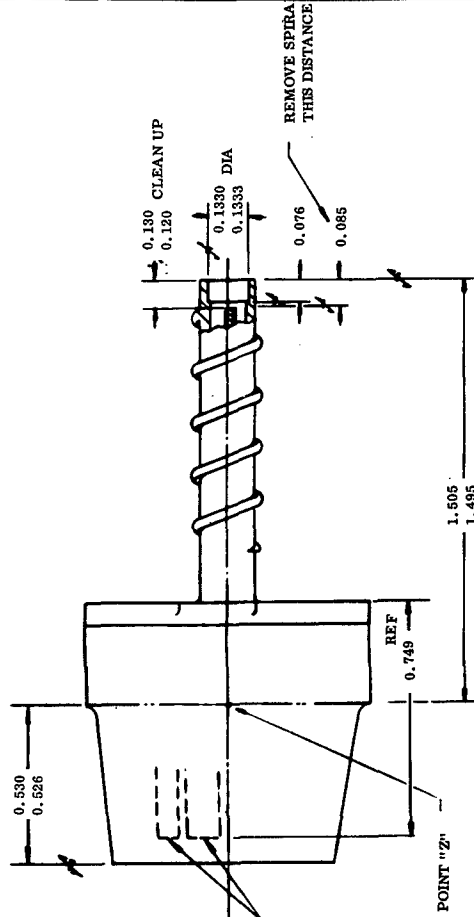


Figure 167. Effect of Cooled Blade Surface Temperature on Fuel Temperature Rise at Design Point.

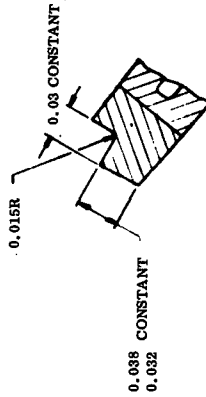
The use of a secondary steam vapor system to transfer heat from the blade to the fuel was found to offer thermal, structural, and manufacturing advantages.

The secondary vapor system, with superheated steam as the transfer medium, operates on the thermosyphon principle. The heat absorbed by the blade airfoil surface is transferred into the secondary fluid (superheated steam) flowing through the closed-circuit cooling passages inside the turbine blades, Figure 168. In cooling the blade, the steam vapor is heated, becoming less dense, and is forced radially inward by the cooler, more dense steam coming from the steam to fuel heat exchanger. Upon returning to the steam-fuel heat exchanger, the steam is again cooled, increasing in density, and is forced back to the rotor periphery by the high rotational "g" forces. It is this density gradient, acted on by the high "g" field, which creates the cooling flow.

Continental's IBM Program 25-007, Appendix II, was written to balance thermosyphon pumping forces, frictional pressure loss, and heat flows. The analytical methods used to calculate blade metal temperatures, heat flows, and fuel temperature rise in a thermosyphon system are explained by an examination of this program.

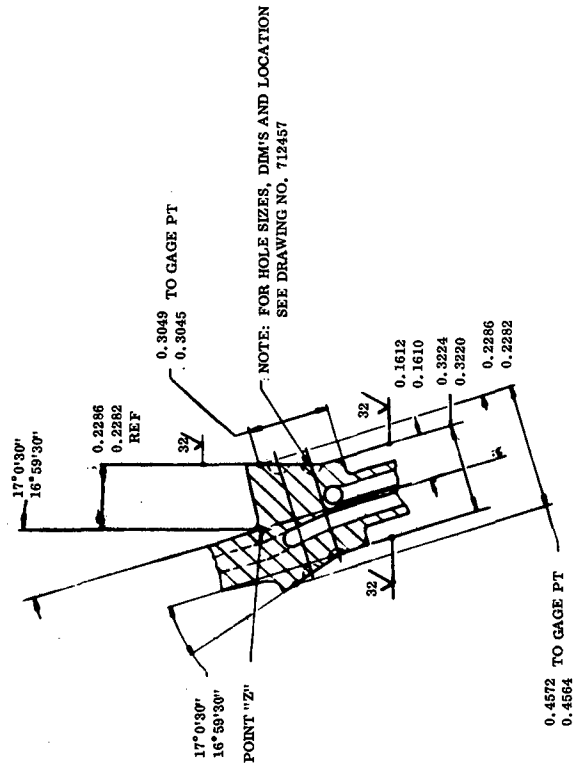
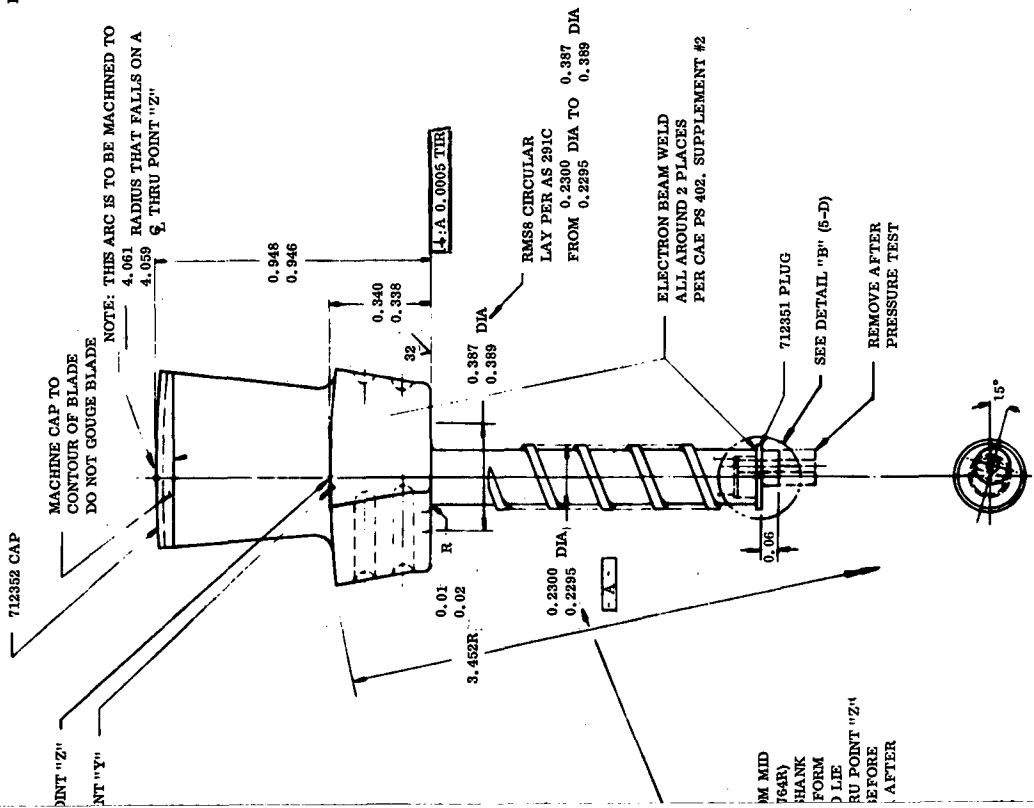


MACHINING BEFORE WELDING



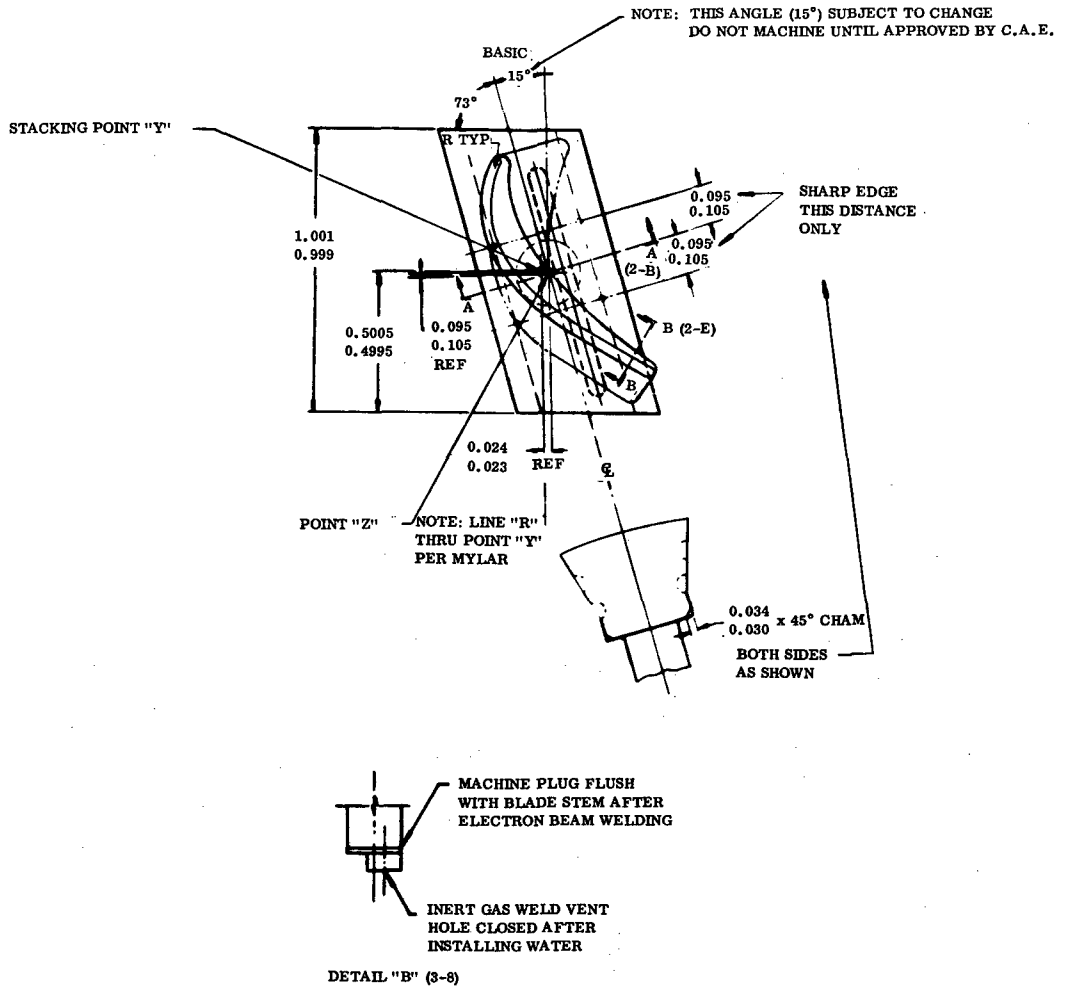
SECTION B-B (3-F)
SCALE 20:1

NOTE: THIS ARC IS TO BE MACHINED TO
4.061 RADIUS THAT FALLS ON A
4.059 ϕ THRU POINT "Z"



NOTE: FOR HOLE SIZES, DIM'S AND LOCATION
SEE DRAWING NO. 712457

SECTION "A-A" (3-G)



AFTER ELECTRON BEAM WELDING, PRESSURE TEST AT 1200 PSIG.
HEAT TREAT PER AMS 5662 PARAGRAPH 6.1.4.
AFTER HEAT TREAT PRESSURE TEST AT 1200 PSIG.
AFTER MACHINING CAP AND PLUG TO FINISHED CONTOUR,
PRESSURE TEST AT 1200 PSIG.
INJECT 0.015 CC OF WATER INTO BLADE CAVITY.
AFTER INERT GAS SHIELDED WELD CLOSURE OF VENT HOLE,
SUBJECT BLADE TO 1200 PSIG MINIMUM EXTERNAL GAS
PRESSURE AND CHECK FOR OUT-GASSING DURING ACETONE OR
ALCOHOL IMMERSION.

PARTS SHALL BE SUBJECT TO VISUAL FLUORESCENT
PENETRANT INSPECTION PER AMS 2654

FOR BLADE CONTOUR SEE DRAWING C 709627

THE NOMINAL STACKING LINE FOR ALL AIRFOILS IS A
STRAIGHT RADIAL LINE THRU POINT "Y"

LOCATE BLADE FROM
SECTION MYLAR (3).
AND MINOR DIA OF
ADJACENT TO PLUG
AND BEND SHANK TO
ON CENTERLINE THRU
"Z" IF NECESSARY
MACHINING THIS DIA
C.A.E. APPROVAL

Figure 168. Fluid-Cooled Turbine Blade - Spiral-Fin Heat Exchanger.

Two types of thermosyphon steam-fuel heat exchanger configurations were considered. In each configuration the blade cooling passages are of identical design (Figure 168). Blade passage sizes and shapes were dictated by structural and manufacturing considerations. Good thermal design requires maximum surface area exposed to the coolant. Preferential cooling of the leading and trailing edges may be obtained by adjusting cooling hole location. This will reduce thermal stress. This approach will be used to refine the second rotor blade design as required from temperature indications obtained on test of the present design. Blade passage inflow and outflow areas were held as near equal as possible to minimize any expansion losses.

The two exchanger configurations considered were:

1. An independently sealed cooling system in each blade with a coolant to fuel heat exchanger in the blade root.
2. A common secondary coolant circuit to all blades with a single coolant to fuel heat exchanger in the engine shaft.

The first configuration is illustrated in Figure 169. Fuel is routed to each blade root by supply tubes in the turbine disc. A single spiral is used on the fuel side of the steam-fuel exchanger to increase fuel velocity. This increases the total heat flow and thus reduces the average blade metal temperatures. Pertinent geometric and heat transfer parameters of this configuration used to input Continental Program 25-007 (Appendix II) are given in Appendix III. Important thermal parameters resulting from this design are given in Table XIX for design point operation.

The second configuration is illustrated in Figure 170. This design utilizes a single steam-fuel heat exchanger which is common to all blades. Engine fuel flow is manifolded into seven 1/8-inch O.D. tubes which spiral rearward 260 degrees and then turn back alongside themselves to spiral forward 260 degrees. This design provides a large steam-to-fuel heat transfer area while maintaining high fuel side velocities. The steam circuit is as shown with individual supply tubes to each blade. Pertinent geometric and heat transfer parameters of this configuration used to input Continental Program 25-007 (Appendix II) are given in Appendix III. Important thermal parameters resulting from this design are given in Table XIX for design point operation.

Testing of the fluid-cooled turbine will be conducted at design speed at simulated altitude conditions and at reduced rpm sea level conditions. Important thermal parameters of the two thermosyphon configurations at test rig operating conditions are given in Table XX.

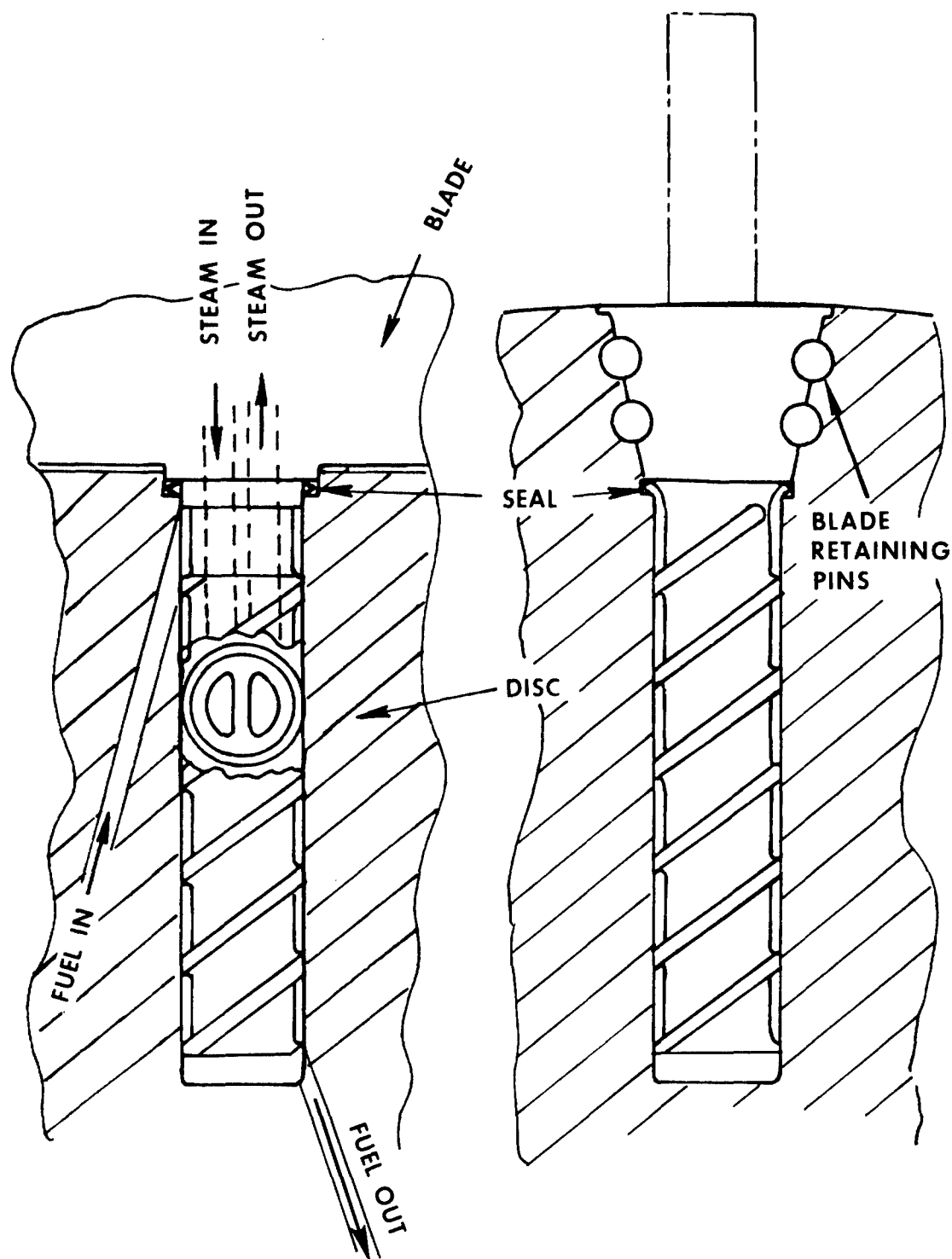


Figure 169. Fin Steam to Fuel Heat Exchanger.

TABLE XIX
FLUID-COOLED TURBINE DESIGN POINT PARAMETERS
(Sea Level Regenerated)

	Configuration I (Heat Exchanger in Blade Root)	Configuration II (Heat Exchanger in Engine Shaft)
Engine Speed, rpm	50,000	50,000
Engine Airflow, lb/sec	5.0	5.0
Engine Fuel Flow, lb/sec	343	343
Combustor Delivery Press., psia	126.8	126.8
Turbine Inlet Total Temp., °F	2300	2300
Blade Relative Temp., °F	2020	2020
Heat Trans. Coef., Gas to Blade, Btu/hr ft ² °F	266	268
Coolant Density (Steam), lb/cu ft	1.4	1.4
Velocity of Coolant in Blade, ft/sec	135	95.2
Coolant Mass Flow per Blade, lb/sec	0.0135	0.00964
Heat Trans. Coef., Blade to Coolant, Btu/hr ft ² °F	1008	766
Mean Temp. of Coolant, °F	1170	1182
Mean Press. of Coolant, psia	1317	1327
Temp. Rise of Coolant, °F	74	97
Heat Flow per Blade, Btu/hr	1583	1447
Velocity of Coolant in Heat Exchanger, ft/sec	263	186
Heat Trans. Coef., Steam to Heat Exchanger, Btu/hr ft ² °F	1681	1270
Velocity of Fuel in Heat Exchanger, ft/sec	3.4	11.96
Heat Trans. Coef., Heat Exchanger to Fuel, Btu/hr ft ² °F	451	1075
Fuel Temp. Rise, °F	244	225
Average Blade Metal Temp., °F	1453	1507
Fuel Pressure at Root Seal, psia	10,150	—

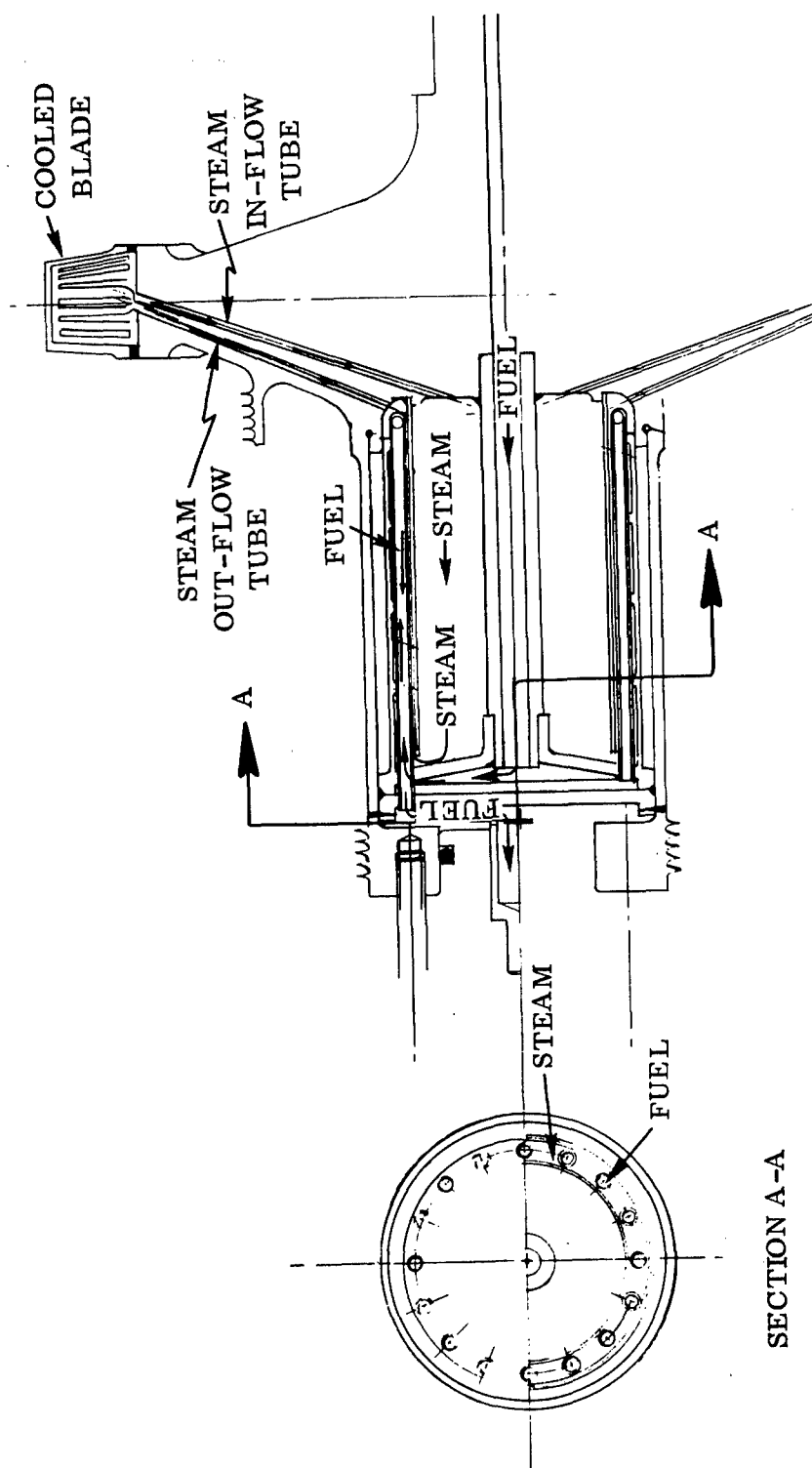


Figure 170. Fluid-Cooled Turbine Configuration II Heat Exchanger in Engine Shaft.

TABLE XX
FLUID-COOLED TURBINE SIMULATED ALTITUDE PARAMETERS
(Sea Level Nonregenerated)

	Configuration I (Heat Exchanger in Blade Root)	Configuration II (Heat Exchanger in Engine Shaft)
Engine Speed, rpm	50,000	50,000
Engine Airflow, lb/sec	3.5	3.5
Engine Fuel Flow, lb/sec	338	338
Combustor Delivery Press., psia	87.3	87.3
Turbine Inlet Total Temp., °F	2300	2300
Blade Relative Temp., °F	2020	2020
Heat Trans. Coef., Gas to Blade, Btu/hr ft ² °F	203	205
Coolant Density (Steam), lb/cu ft	1.4	1.4
Velocity of Coolant in Blade, ft/sec	133	94.7
Coolant Mass Flow per Blade, lb/sec	0.0135	0.0096
Heat Trans. Coef., Blade to Coolant, Btu/hr ft ² °F	972	742
Mean Temp. of Coolant, °F	1089	1107
Mean Press. of Coolant, psia	1253	1267
Temp. Rise of Coolant, °F	69	91
Heat Flow per Blade, Btu/hr	1422	1177
Velocity of Coolant in Heat Exchanger, ft/sec	259	183
Heat Trans. Coef., Steam to Heat Exchanger, Btu/hr ft ² °F	1623	1230
Velocity of Fuel in Exchanger, ft/sec	3.31	11.7
Heat Trans. Coef., Heat Exchanger to Fuel, Btu/hr ft ² °F	438	1050
Fuel Temp. Rise, °F	225	209
Average Blade Metal Temp., °F	1352	1411
Fuel Pressure at Root Seal, psia	10,500	

FUEL THERMAL STABILITY

When the fuel is to be used as a heat sink, the thermal stability limit of the fuel controls the heat flow or minimum blade metal temperature allowable. The available heat sink capacity of the fuel is determined by (1) the fuel flow rate and (2) the allowable fuel temperature rise. The fuel flow rate is determined by engine requirements, and the allowable fuel temperature is a function of the fuel thermal stability.

A survey of current literature (References 14 through 34) indicates that thermal stability measurements cannot be used to predict the performance of the fuel as a heat sink in a specific cooling configuration. Therefore, the maximum temperature which a fuel in a given system may be allowed to obtain without causing degradation of the cooling system performance must be determined experimentally.

The blade metal temperature gives a heat flow value from which a corresponding fuel temperature rise can be determined (Figure 167).

The maximum design point fuel temperatures for the cooling configurations considered are:

Regenerative Cycle	340° F
Nonregenerative Cycle	287° F

During part-power operation, fuel flow is reduced at a greater rate than blade relative temperature. Fuel temperature rise, therefore, increases with decreasing percent power. The effect of part-power operation on fuel temperature rise is shown in Figure 171. Therefore, operation of the rig at off-design, part-power conditions will result in fuel temperatures up to 20 percent higher than the design point values indicated above. Since these part-power fuel temperatures are near the thermal stability test temperature of JP-4 as called out in MIL-J-5624F, experience with similar applications must be relied upon to provide an insight into the possible effects on system performance of these fuel temperatures.

To evaluate the effect of hot fuel and a hot fuel distributor system on combustor and engine performance, Continental operated a modified J69-T-25 engine on heated JP-4 for approximately 11 hours. Almost 6 hours of this running time was conducted with fuel temperatures above 300° F, and 1 hour of operation was with a fuel temperature above 500° F.

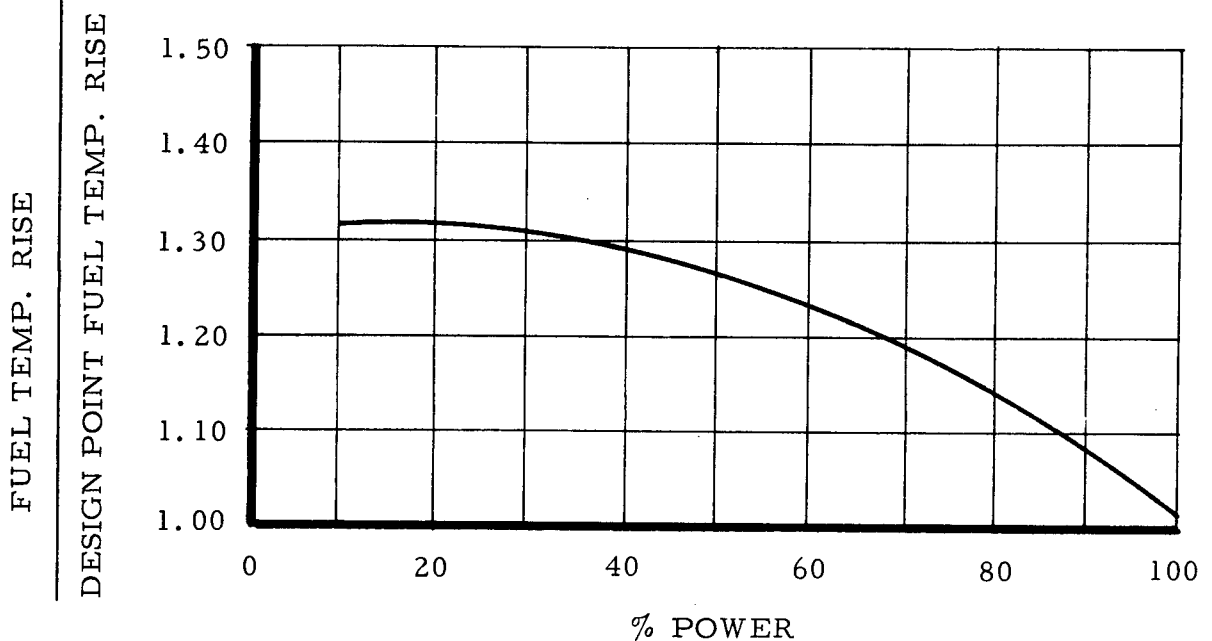


Figure 171. Effect of Part-Power Operation on Fuel Temperature Rise.

Similar tests were conducted with JP-6, accumulating an additional 11-3/4 hours of running time. Six hours of this test were with fuel temperatures above 300°F, four hours above 500°F, and one hour above 700°F.

The fuel system for these tests contained a fuel pressure control valve to prevent vaporization of the fuel before its introduction into the fuel distributor. This valve operated satisfactorily over the full range of the tests.

During these tests the fuel distributor and combustor showed no deterioration in performance that was attributable to the hot fuel.

In view of Continental's experience with the above tests, no adverse effects on the fuel distributor system are anticipated at the fuel temperatures to be encountered during operation of the hot turbine rig.

Also to be considered, however, is the reduction of heat flux due to fuel deposits on the heat transfer surface of the fuel-to-steam heat exchanger. The percent reduction in heat flow is a function of the deposits' thickness and thermal conductivity. As previously mentioned, it cannot be predicted in what amount deposits will occur, or even if they will occur, for a specific cooling configuration in which maximum fuel temperatures are near the threshold temperature of the fuel. It follows, then, that the

reduction in heat flux due to these deposits cannot be predicted. Formation of fuel deposits during test will become apparent by a reduction in fuel temperature rise and an increase in blade metal temperature. This process will be self-limiting; that is, the blade metal temperature will increase as fuel temperature rise decreases until the fuel temperature rise is no longer sufficient to cause formation of deposits. At this point, the cooling system will reach equilibrium between blade metal temperature and fuel temperature rise.

Upon experimental confirmation of the heat transfer parameters, the fuel-to-steam heat exchanger can be redesigned to obtain an optimum compromise between blade metal temperature and formation of fuel deposits.

The heat exchanger and fuel distributor system will be closely examined at the conclusion of each test series of Phase II. Should deposits occur, deposition rate versus fuel temperature will be determined and a cleaning method and schedule established if required.

ANALYSIS OF TURBINE ROTOR METAL TEMPERATURES

Disc Temperature Distribution

An analysis of the radial temperature distribution of the fluid-cooled turbine rotor disc has been completed. The disc was analyzed for the heat exchanger in-disc and for the heat exchanger in-shaft configurations. The foregoing analyses were done in cylindrical coordinates, taking into account the heat transfer from the disc to the steam, the fuel, and the external surroundings.

Disc Rim Temperature

It was necessary to establish the disc rim temperature because it is a boundary condition to the disc problem. A heat balance was therefore written for the disc rim. The conductivity of the blade to the rim was neglected, which is consistent with the assumptions made in the thermosyphon IBM program.

We have

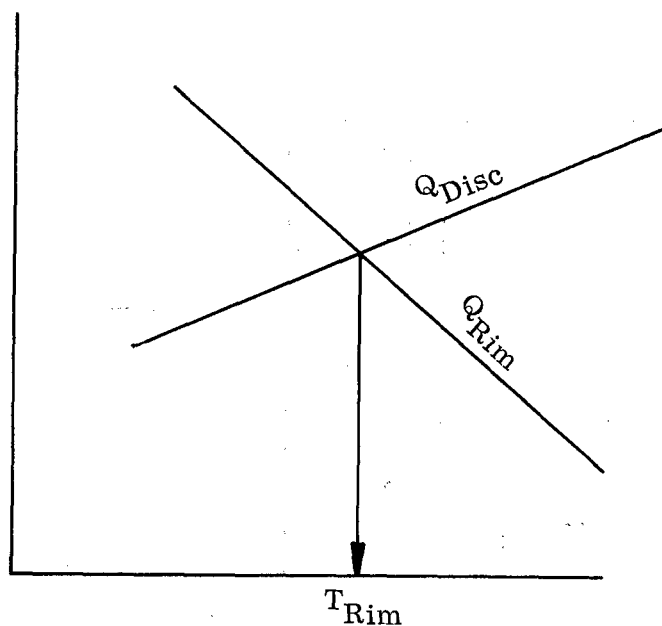
$$Q_{\text{Rim}} = Q_{\text{Disc}}$$

where

$$\begin{aligned} Q_{\text{Rim}} &= \text{Heat "In" given by convection from gas to rim} \\ &= h_{\text{pl}} A_{\text{pl}} (T_{\text{gas}} - T_{\text{pl}}) \end{aligned} \quad (10)$$

$$\begin{aligned} Q_{\text{Disc}} &= \text{Heat "Out" by conduction to the disc} \\ &= 4KA_{\text{Disc}} \frac{dT}{dR} \end{aligned} \quad (11)$$

By plotting Q_{Rim} and Q_{Disc} versus T_{Rim} , we can obtain the rim temperature.



Heat Transfer Coefficient to Disc Rim h_{pl}

The heat transfer coefficient from the gas to the disc rim was calculated from the empirical formula obtained for the turbulent boundary layer over a flat plate.

(12)

$$N_u = 0.029 R_e^{0.8} P_r^{0.33} = 0.029 (R_e)^{0.8} (P_r)^{0.33}$$

where

$$h = \frac{N_u K}{D}$$

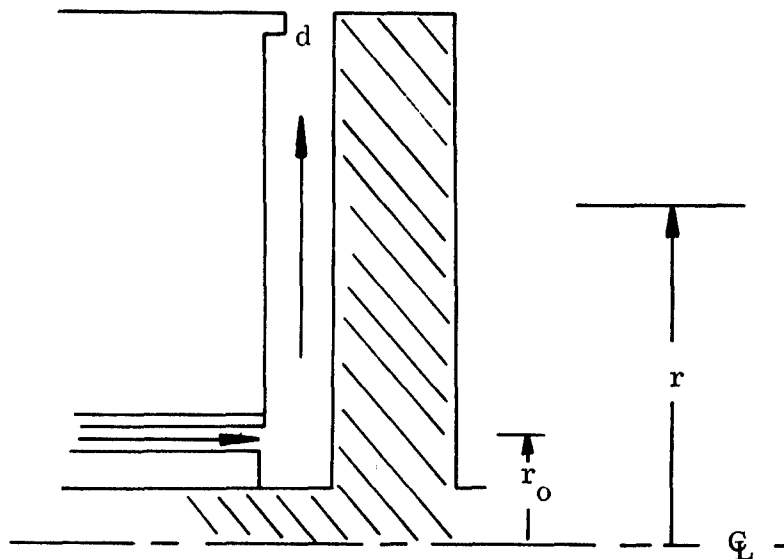
N_u = Nusselt Number

R_e = Reynolds Number

P_r = Prandtl Number

D = Hydraulic Diameter

k = Gas Thermal Conductivity



Disc External Heat Transfer Coefficients

The external heat transfer coefficients from the surroundings to the disc were calculated using the results from Petrick and Smith, Reference 35.

(13)

From impinging flow,

$$N_u = 0.20 R_e^{0.67} P_r^{0.4}$$

and for radially outward flow along the disc,

(14)

$$N_u = 0.10 R_e^{0.75} P_r^{0.4} \left[\frac{2 \frac{d}{r_0} \frac{r}{r_0}}{\left(\frac{r^2}{r_0^2} \right) - 1} \right]^{0.3}$$

Internal Heat Transfer Coefficient

The internal heat transfer coefficient was calculated by the thermosyphon IBM Program which evaluates the Nusselt number from

(15)

$$N_u = 0.23 R_e^{0.8} P_r^{0.33}$$

Results and Discussion

The results for the two different rotor configurations are shown in Figures 172 and 173 and they are representative of a radial mean temperature distribution. Heat transfer in the tangential and axial directions was neglected. However, it will be taken into account in the analysis of the pin blade attachment.

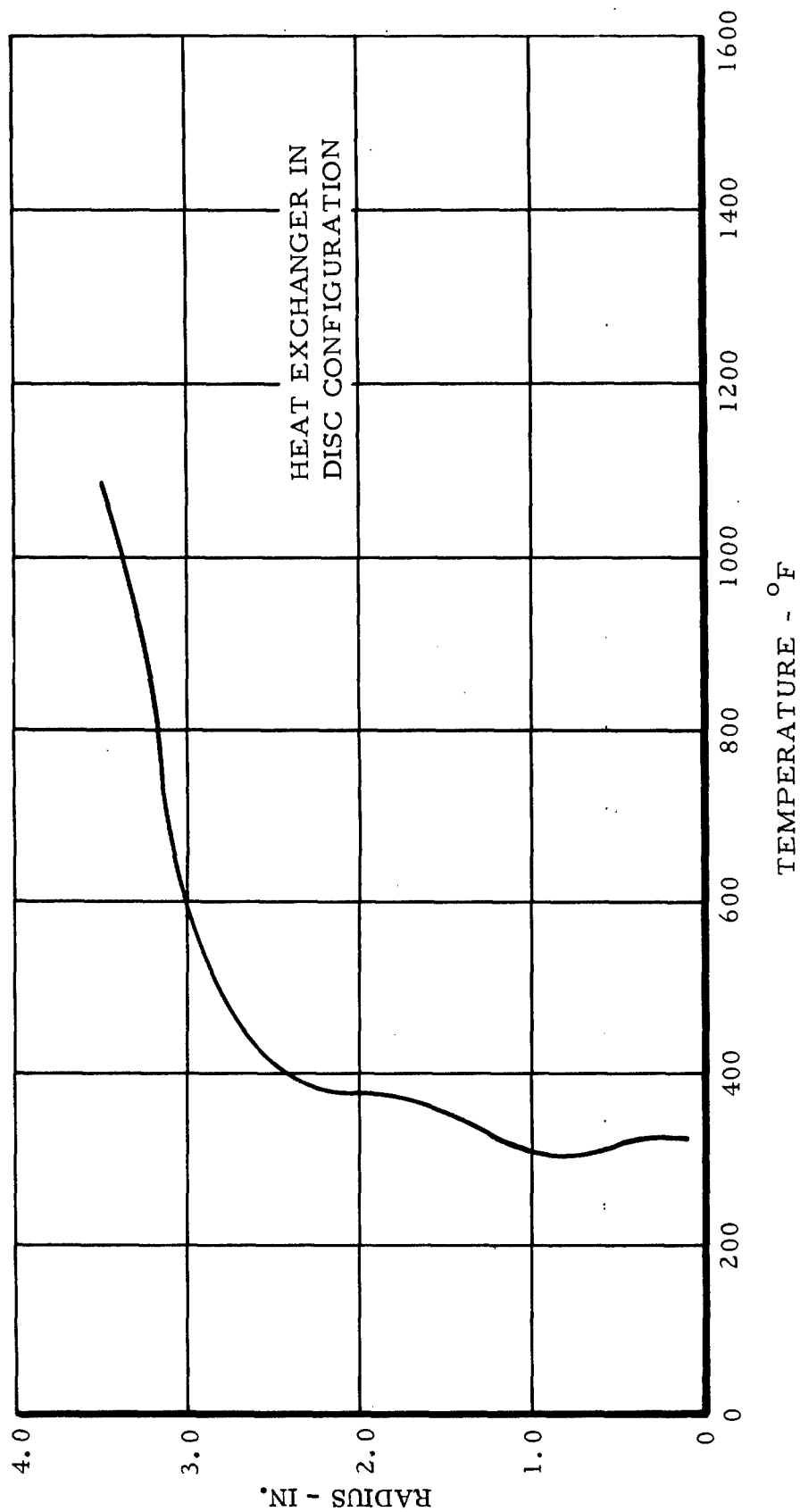


Figure 172. Turbine Rotor Disc Radial Temperature Distribution.

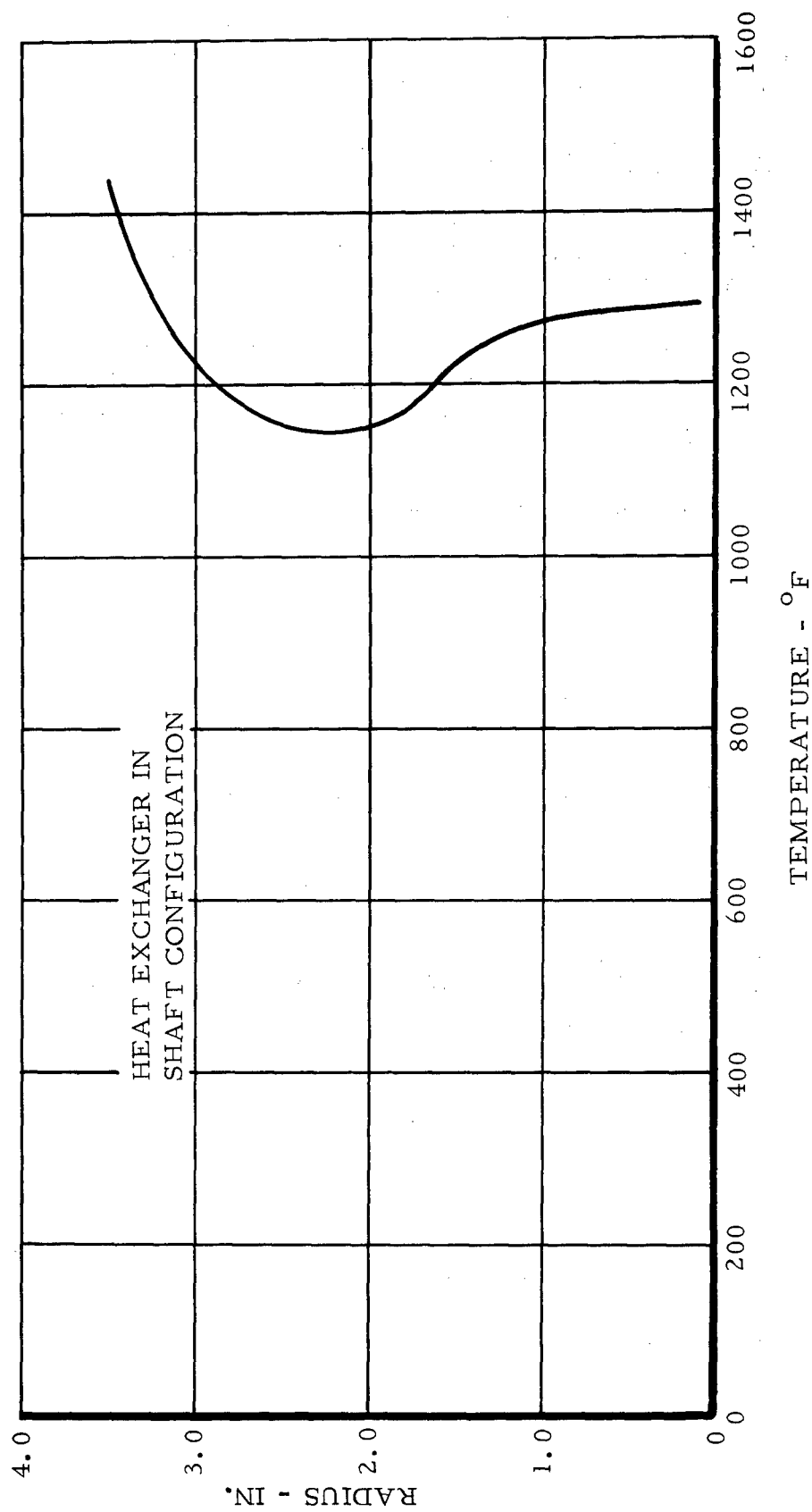


Figure 173. Turbine Rotor Shaft Radial Temperature Distribution.

The temperature distribution in the turbine rotor blade was analyzed. The radial conduction effects were found to be relatively small away from the hub. It was therefore decided to restrict the investigation to a two-dimensional temperature distribution.

External Heat Transfer Coefficients

The external heat transfer coefficient (gas-to-blade) calculation was based on the velocity distribution along the turbine rotor blade (mean radius section) shown in Figure 174.

1. The leading edge heat transfer coefficients were obtained from data measured for flow around circular cylinders. The data were obtained by J. Kestin and P. F. Maeder, Reference 36, and are summarized in Figure 175.
2. The other external heat transfer coefficients were calculated using Johnson and Rubesin formula for heat transfer in a turbulent boundary layer.

(16)

$$N_u = 0.0296 (P_r)^{1/3} (R_e)^{0.8}$$

The external heat transfer coefficient distribution along the turbine rotor blade is shown in Figure 176.

Internal Heat Transfer Coefficients

The internal heat transfer coefficients from the blade to the coolant were calculated in the thermosyphon program. The Nusselt numbers were calculated using the following relation:

(17)

$$N_u = 0.023 (R_e)^{0.8} (P_r)^{0.33}$$

The temperature distribution in the turbine rotor blade is shown in Figure 177, which indicates that the blade average temperature is between 1450°F and 1500°F and that the leading and trailing edge temperatures reach 1725°F locally.

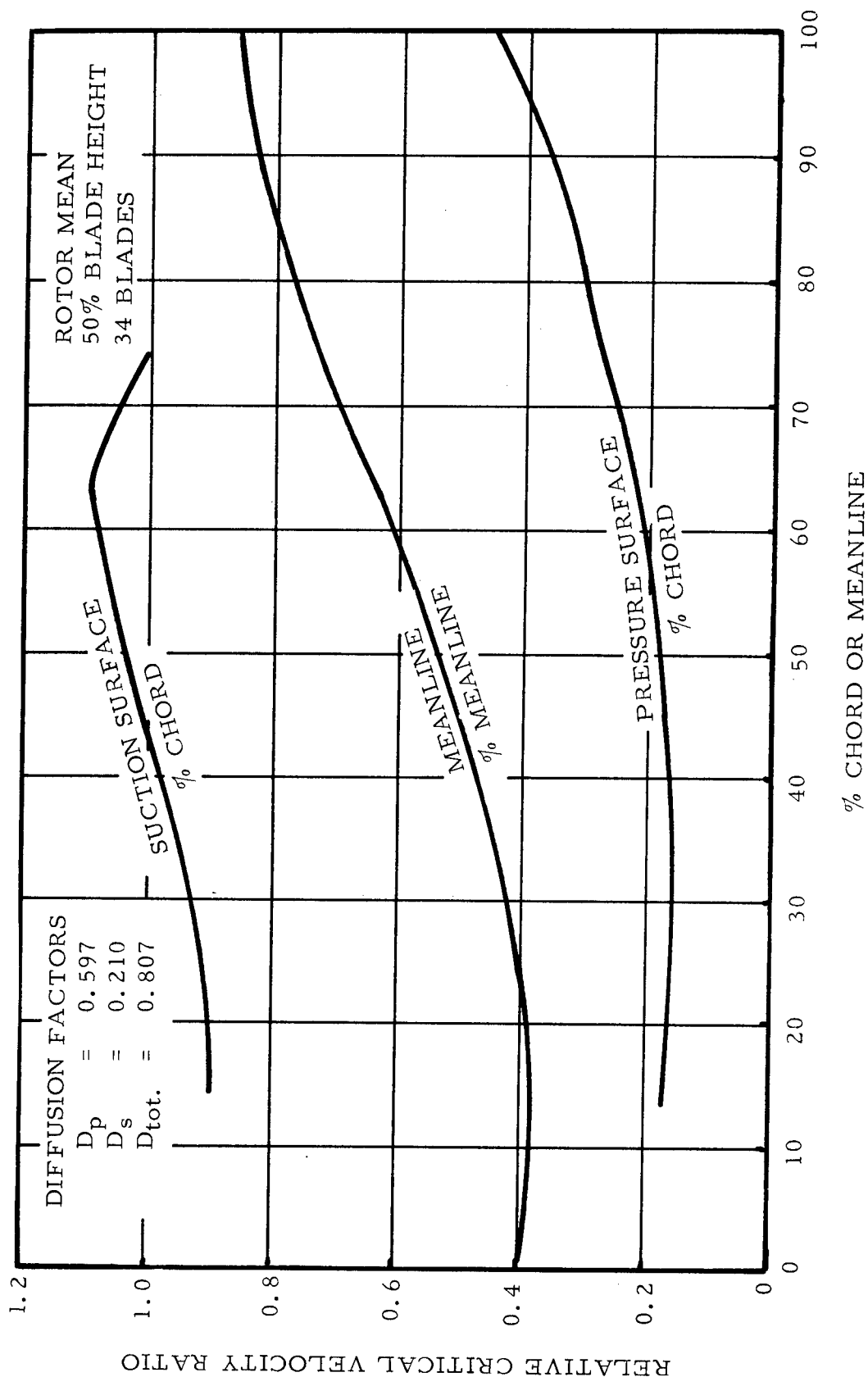


Figure 174. Critical Velocity Ratio, Rotor Mean - 50 Percent Blade Height, 34 Blades.

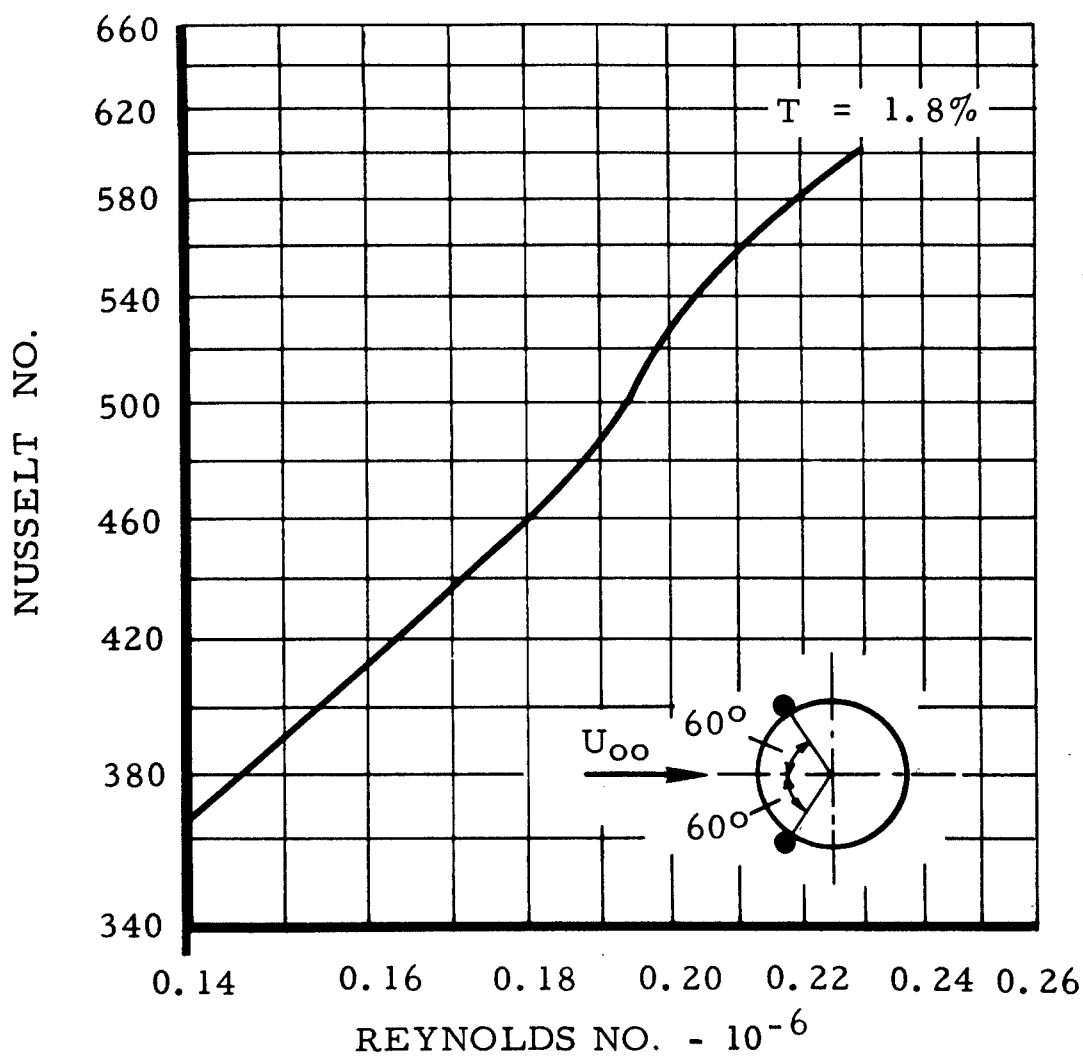


Figure 175. Variation of Nusselt Number With Reynolds Number.

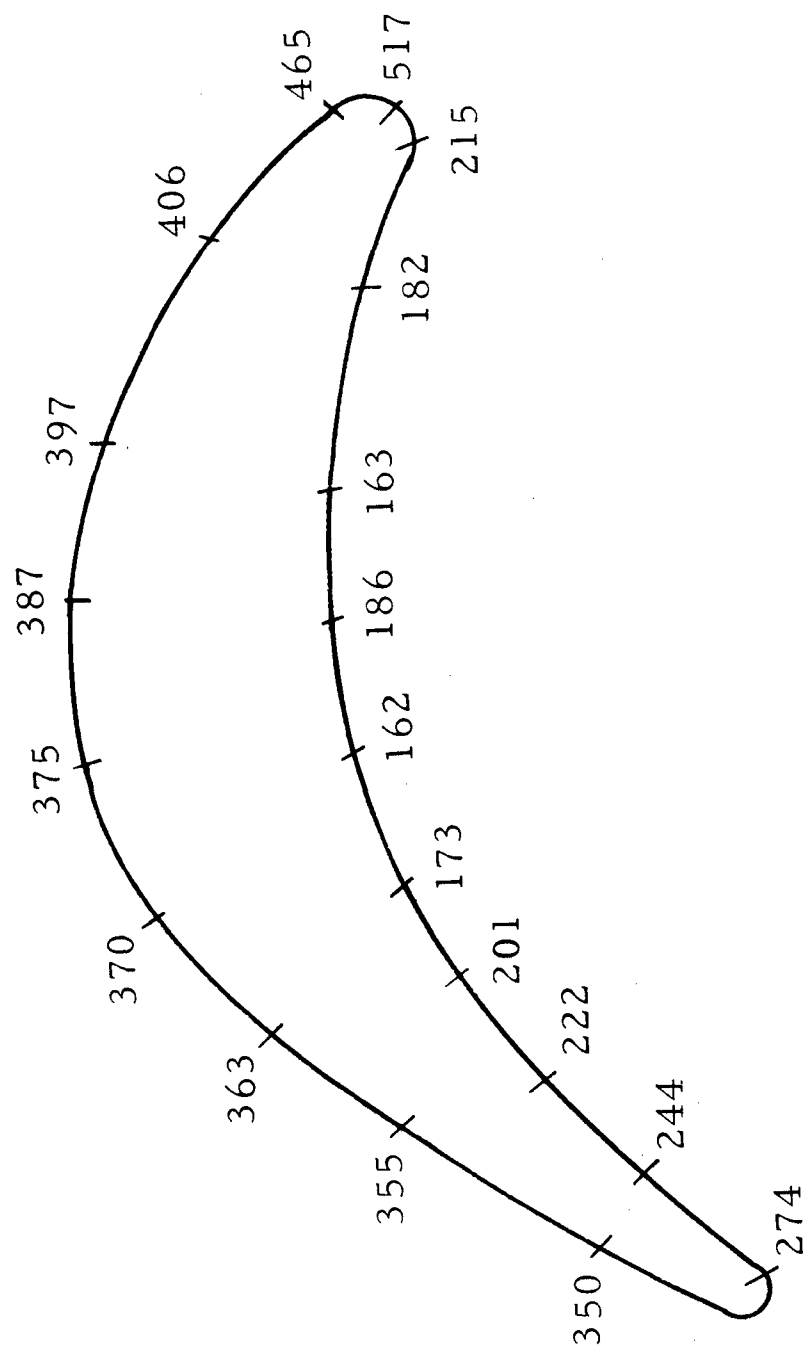


Figure 176. Turbine Rotor Blade Heat Transfer Coefficient Distribution.

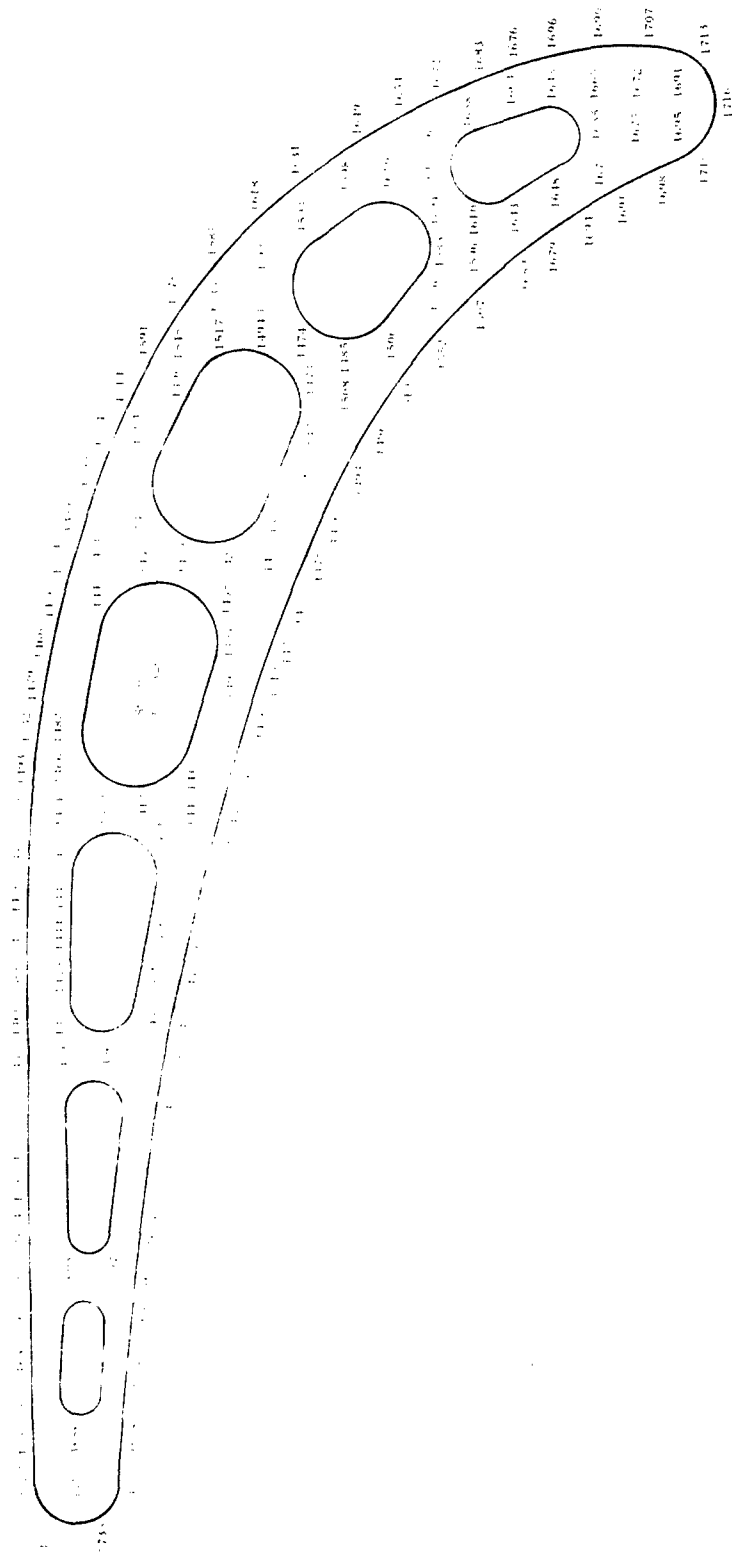


Figure 177. Turbine Rotor Blade Temperature Distribution - °F, Mid-Span Section.

The temperatures were calculated at the mean radius blade cross section. At different cross sections, the external velocities differ slightly. It was determined (using a flat radial combustor profile) that with a local change of velocity of 20 percent, the calculated temperatures would not change more than $\pm 12^{\circ}\text{F}$. With a combustor profile of $\pm 100^{\circ}\text{F}$, the temperature variation would be $\pm 28^{\circ}\text{F}$, which would give a total change of $\pm 40^{\circ}\text{F}$.

The coolant temperature rises by 74°F going through the blade. Calculation shows that this would change the metal temperature by $\pm 25^{\circ}\text{F}$.

The differences are not directly additive. The effect must be applied at particular points for assessment.

Blade Attachment Temperature Distribution

The evaluation of the temperature differentials across the pinned rotor blade attachment interfaces required a three-dimensional heat transfer analysis. This study was done using the general three-dimensional transient temperature distribution program described in Appendix IV. The heat transfer coefficients were the same as those used for the one-dimensional radial temperature distribution.

A general illustration of the heat transfer nodal system for the rotor blade attachment is presented in Figure 178.

The thermal contact resistance between the blade attachment and the rotor disc depends on the contact pressure in addition to the roughness. The pinned attachment interfaces with the rotor disc were investigated for the following three cases:

1. 100 percent perfect thermal contact.
2. 20 percent perfect thermal contact.
3. Zero (1 percent) thermal contact (insulated boundary).

The two extreme boundary conditions (perfect thermal contact and insulated) were investigated in order to establish the limits of the temperature differentials across these interfaces as well as from node to node.

The 20 percent perfect contact case was assumed for stress calculations. The insulated and perfect thermal contact limiting conditions are presented for comparative purposes.

The results for the three different cases are shown in Figures 179 through 184.

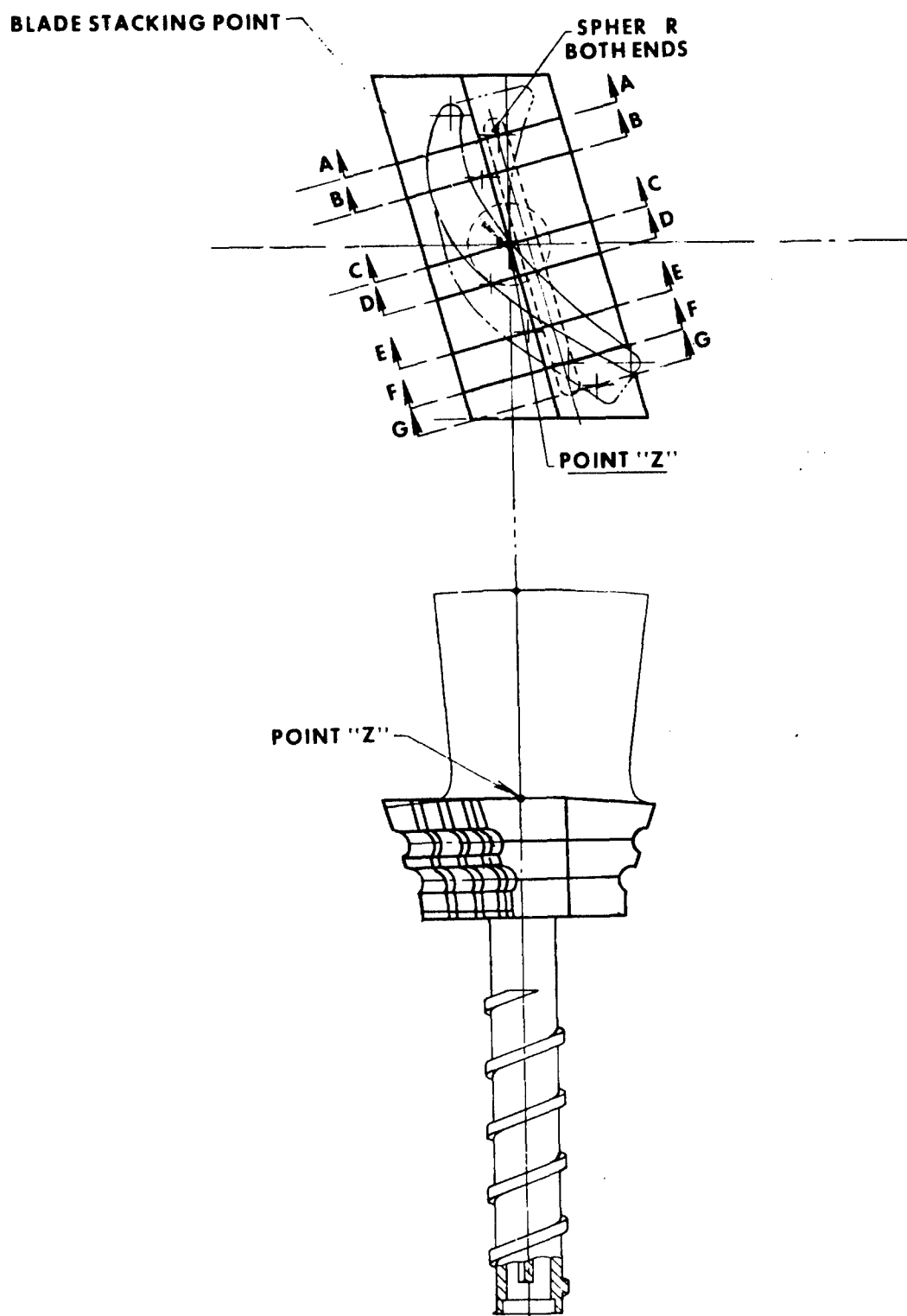


Figure 178. Blade Attachment Sectioning for Heat Transfer.

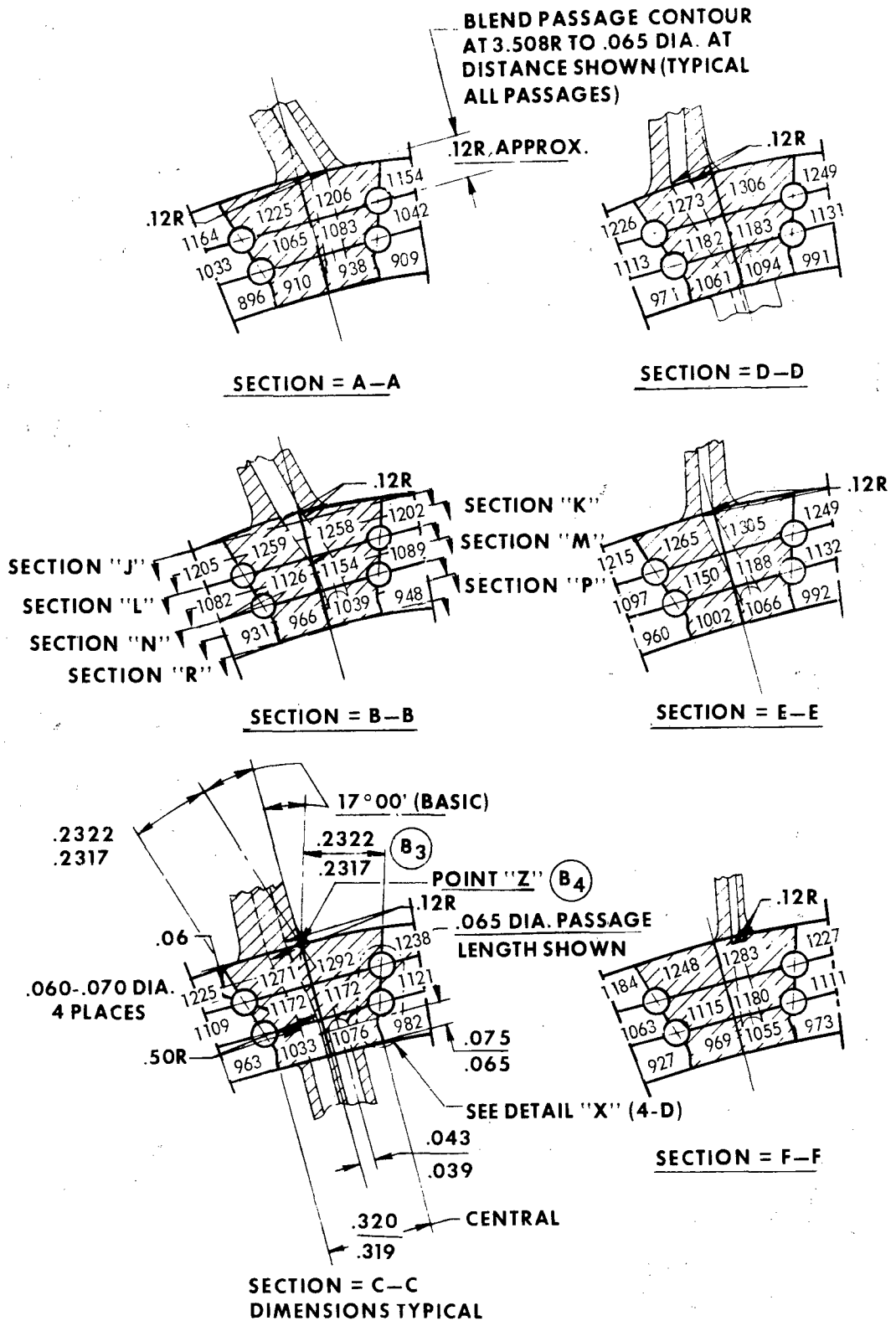
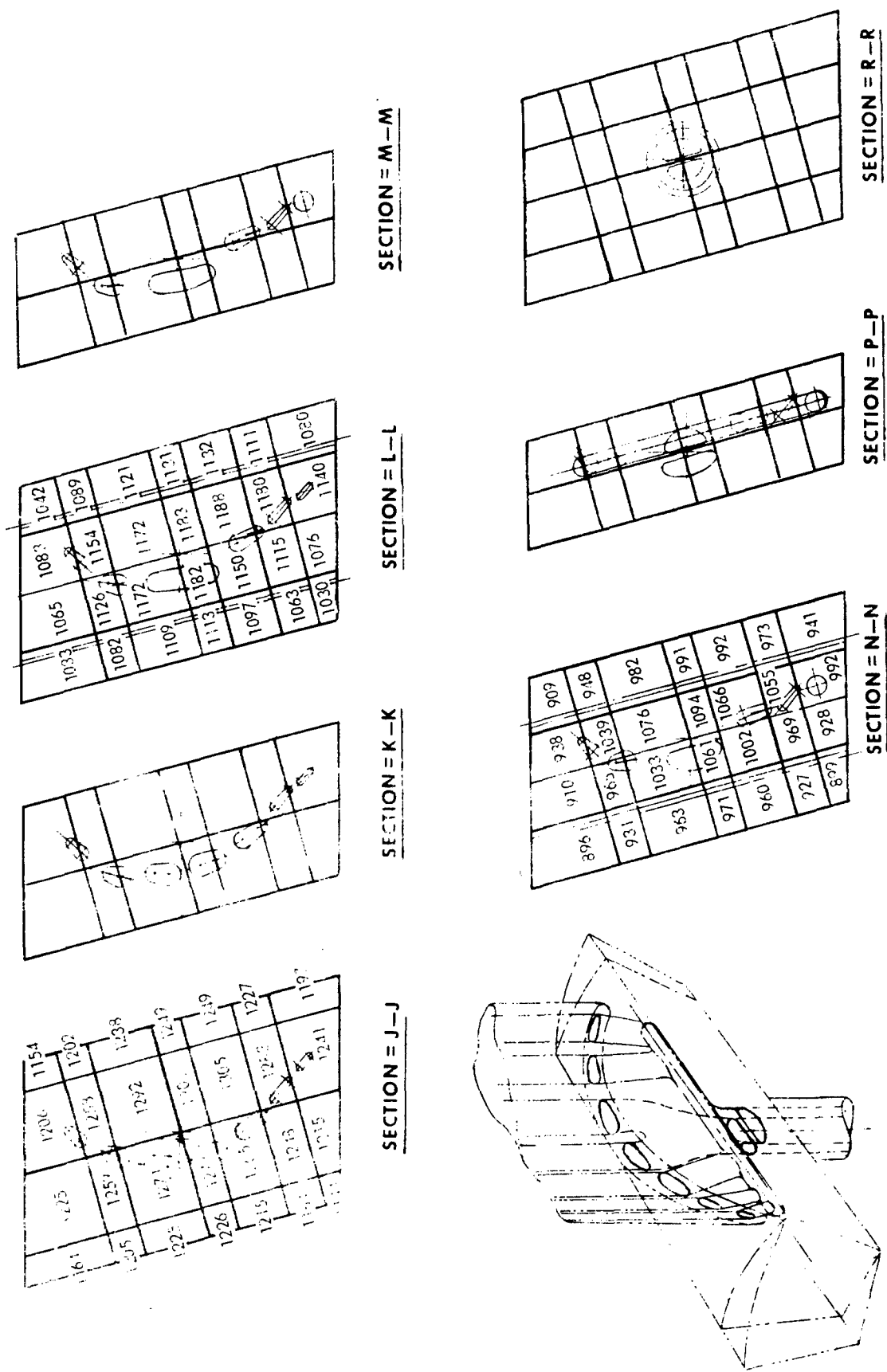


Figure 179. Perfect Thermal Contact Temperature Distribution - Cross-Sectional Side Views.



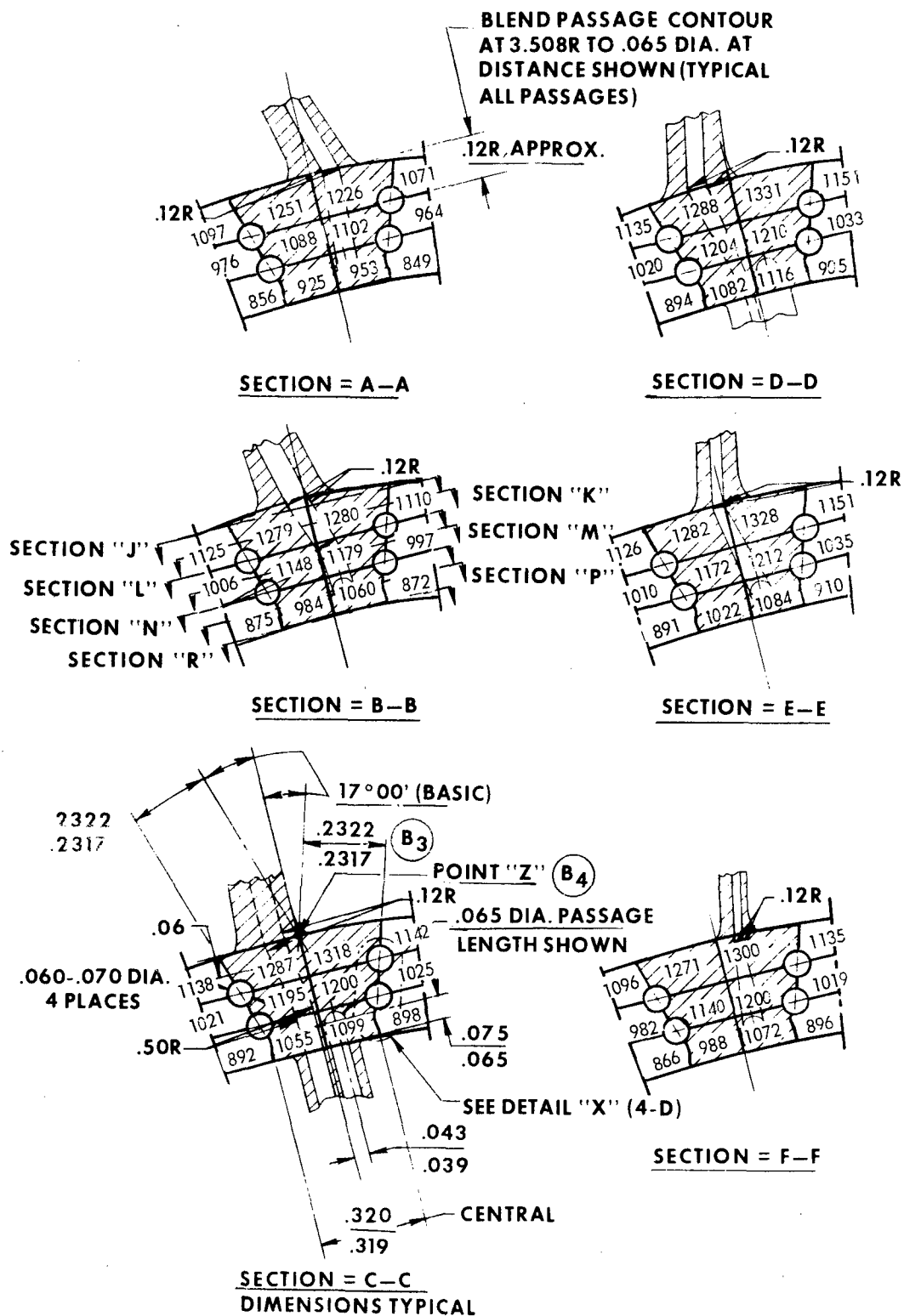


Figure 181. Twenty Percent Thermal Contact Temperature Distribution - Cross-Sectional Side Views.

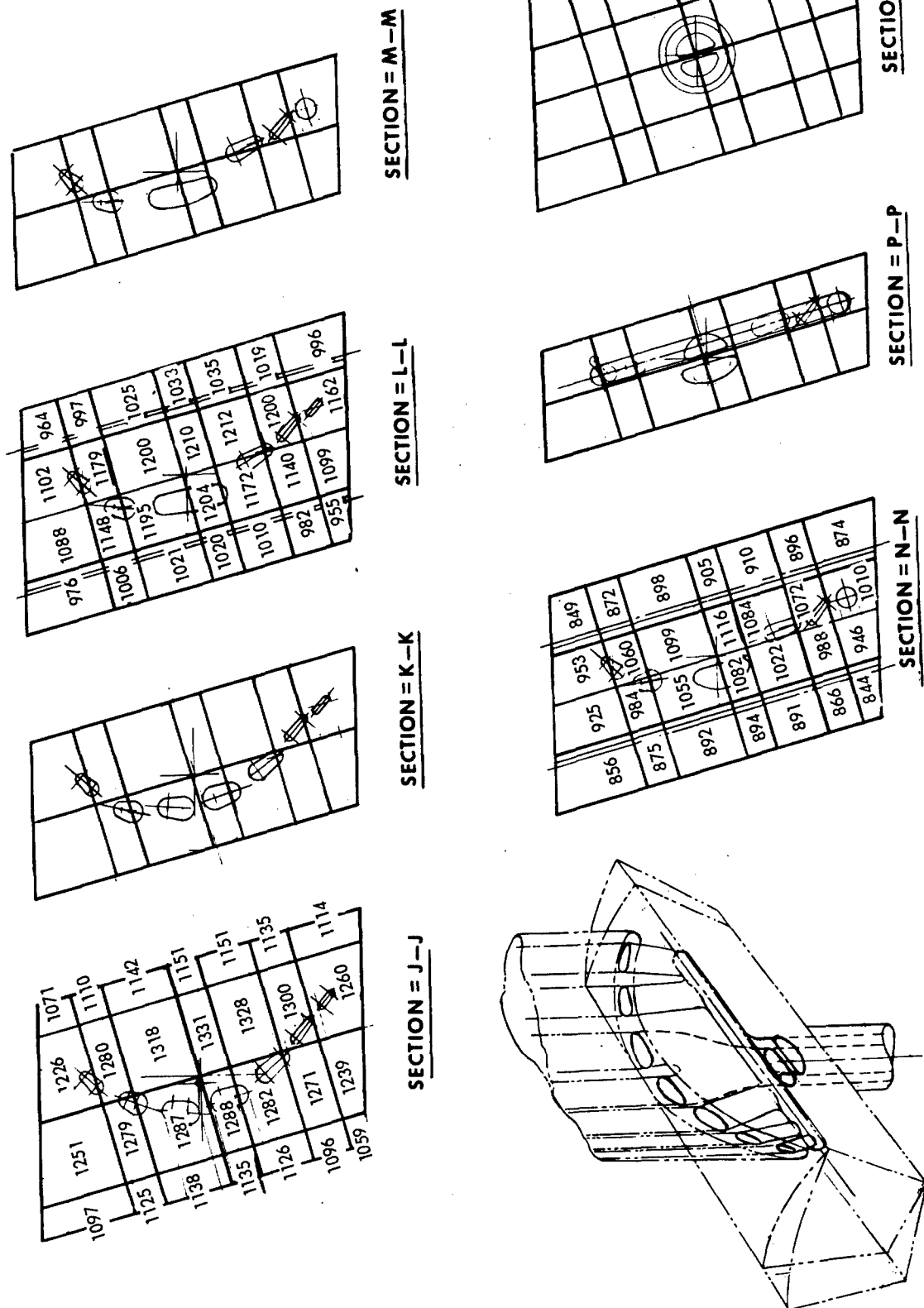


Figure 182. Twenty Percent Perfect Thermal Contact Temperature Distribution - Cross-Sectional Top Views, J-J, L-L, and N-N.

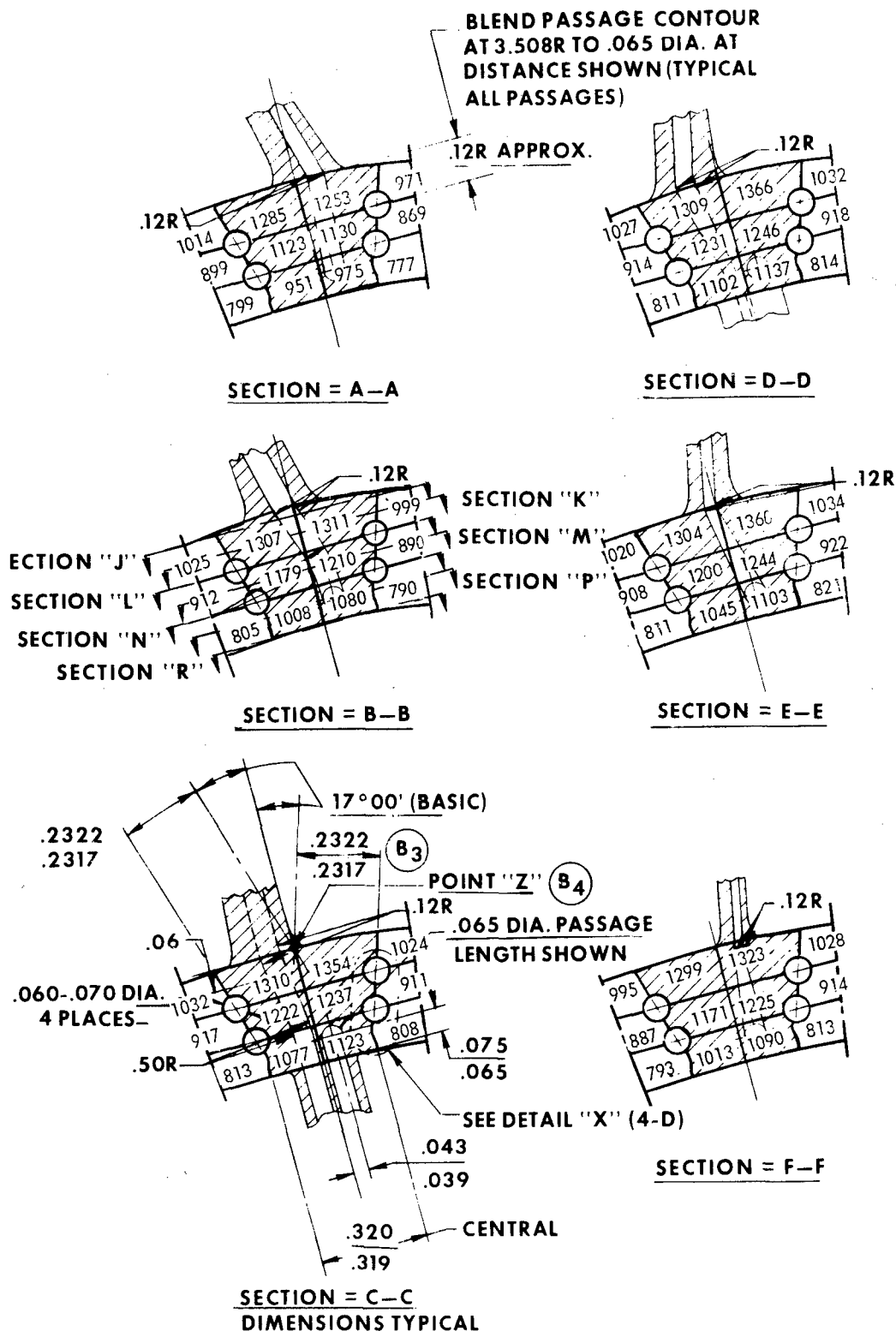
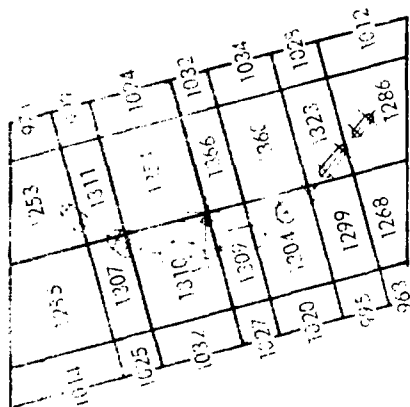
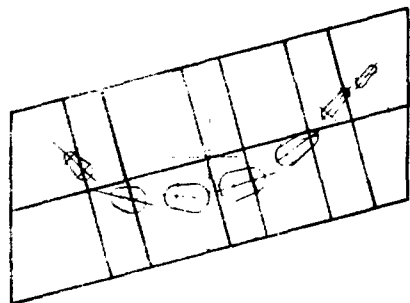


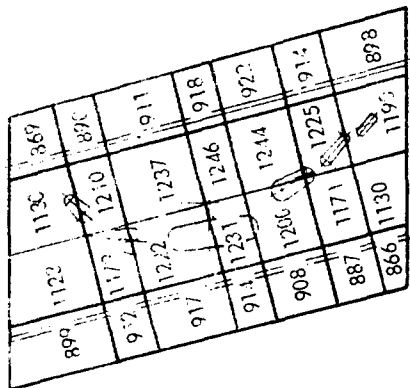
Figure 183. Insulated Boundary Temperature Distribution - Cross-Sectional Views.



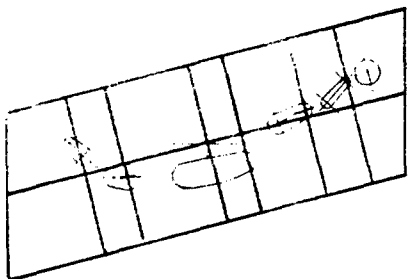
SECTION = J-J



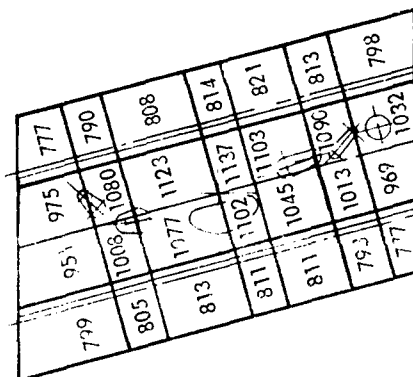
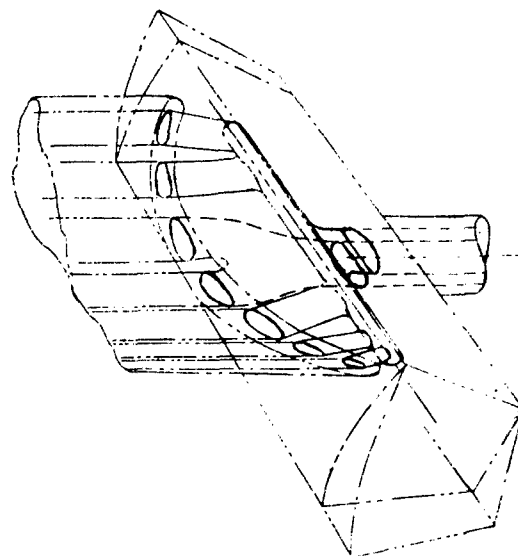
SECTION = K-K



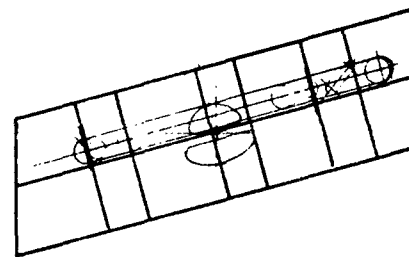
SECTION = L-L



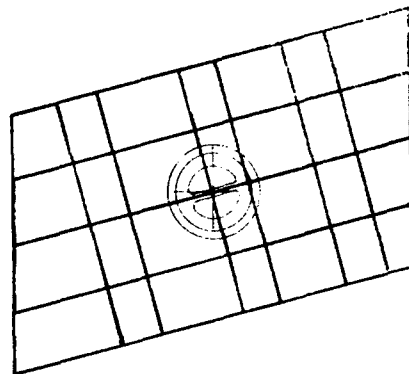
SECTION = M-M



SECTION = N-N



SECTION = P-P



SECTION = R-R

Figure 184. Insulated Boundary Temperature Distribution - Cross-Sectional Top Views, J-J, L-L, and N-N.

STRUCTURAL DESIGN

Rotor Disc

Three types of discs have been analyzed:

1. A wrought disc with mechanically attached blade heat exchanger units.
2. A wrought disc with the blade heat exchanger attached by electron beam welding.
3. Integrally cast disc and blades with heat exchanger not contained in disc.

The primary criterion against failure is the burst margin which is based on the average tangential stress of the disc and the ultimate tensile strength at temperature of the specific material. In addition, severe thermal gradients require the consideration of a rim crushing criterion.

For each design evaluated, the following data are presented:

1. Geometric structure
2. Applied loads
3. Method of analysis
4. Resulting stresses
5. Summary of criteria
6. Results
7. Conclusions

Pinned Blade - Heat Exchanger Concept Analysis

Structure. A meridional view of the structure is represented by Figure 185. No coring of the blade or root is shown - only the disc cross section is exposed. It is a solid (as opposed to annular) disc with 31 blade-heat exchanger units attached by means of four pins per unit. The disc and pins are made of forged U-700 and the blades are of cast U-700. The pinned attachment loading directions are depicted in Figure 186.

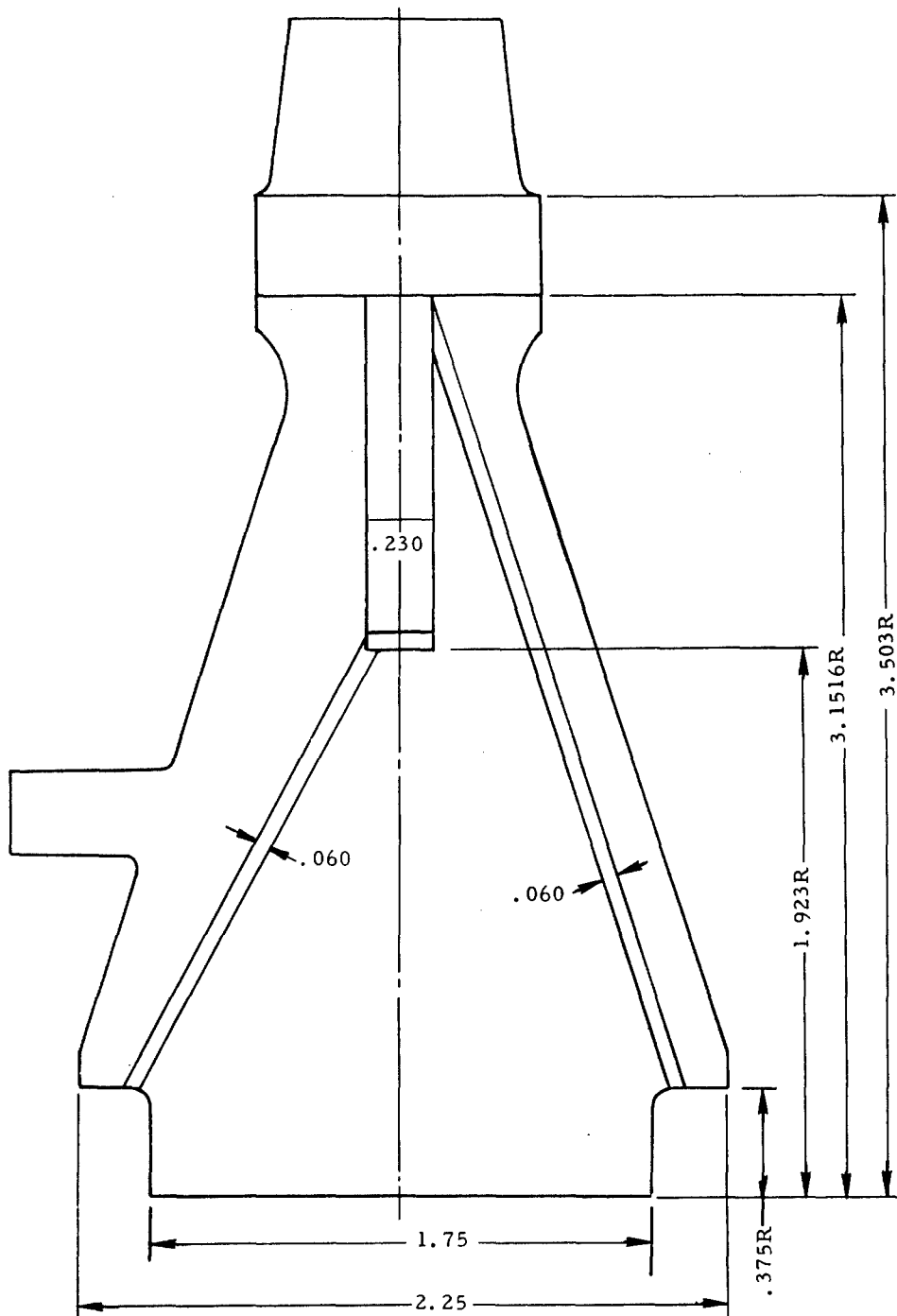
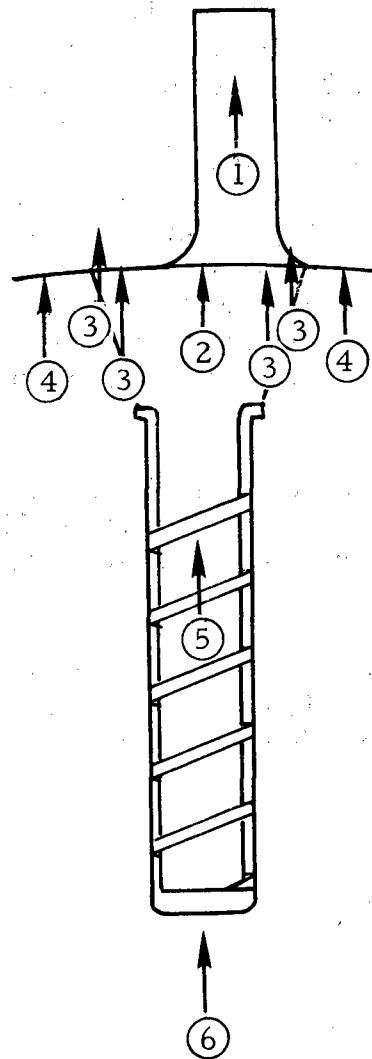


Figure 185. Turbine Rotor Disc - Heat Exchanger In-Disc.



- ① BLADE
- ② BLADE ROOT
- ③ PINS
- ④ TANG
- ⑤ HEAT EXCHANGER
- ⑥ FUEL LOAD

Figure 186. Pinned Attachment Loading Directions.

Loads. The loads assumed in the analysis are the inertia loads due to rpm and a radial thermal gradient. The rim load components are shown in Figure 186 and the temperature-radius curve in Figure 187.

Method of Analysis. Two methods were used to analyze the disc: Manson's method and the average tangential stress method. The average tangential stress method was used as a criterion against overloading the disc. Manson's method was derived in detail in Reference 37, and was programmed on Continental digital program. In Manson's method, a homogeneous disc was assumed with the density modified to account for the radial holes in the disc. The fuel and heat exchanger were considered to be part of the rim load. The average tangential stress, $\sigma_{T_{avg}}$, was calculated using the net disc cross section properties for A and I, where A is the area of the disc material exposed by a meridional view of the net solid section above the rotation axis and I is the moment of inertia of A about the same axis.

Disc Stresses. The results of the analysis by Manson's method are given in Figures 188 through 191. Figures 188, 189, and 190 are combined thermal and inertial stresses. The average tangential stress is 70,054 psi.

Criteria. Design criteria were based on the limitations imposed on the maximum radial stress in the web and the average tangential stress of the disc. The burst margin (BM) was used as the controlling parameter and was calculated by equation (18).

$$BM = \sqrt{\frac{0.75 \sigma_{ult}}{\sigma_{T_{avg}}}} \quad (18)$$

where

σ_{ult} = Ultimate tensile strength of the metal at the average disc temperature

$\sigma_{T_{avg}}$ = Average tangential stress

The desired maximum radial stress in the disc web should not be greater than $\sigma_{T_{avg}}$ as calculated by equation (18) with $BM = 1.25$.

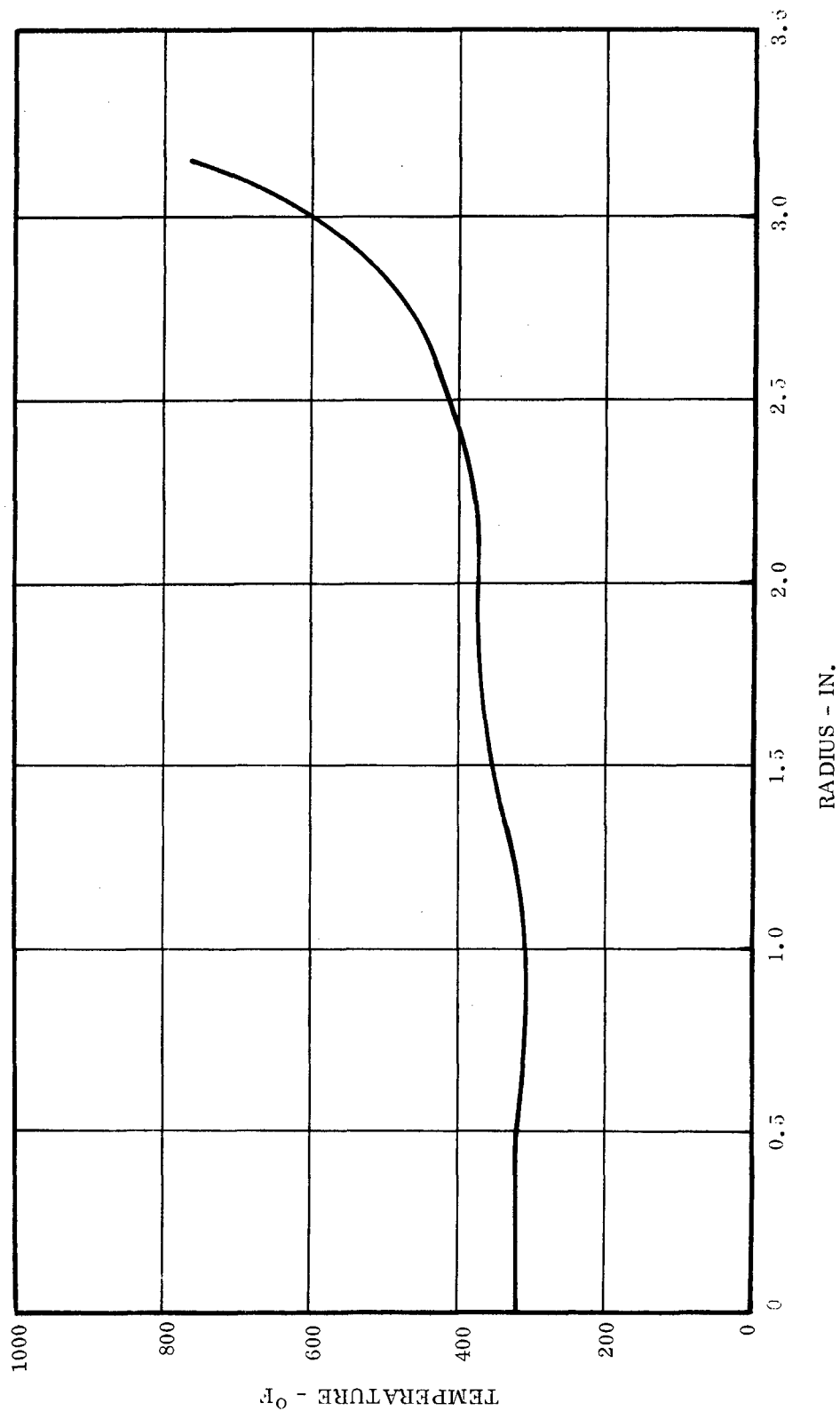


Figure 187. Rotor Temperature Gradient - Pinned Attachment.

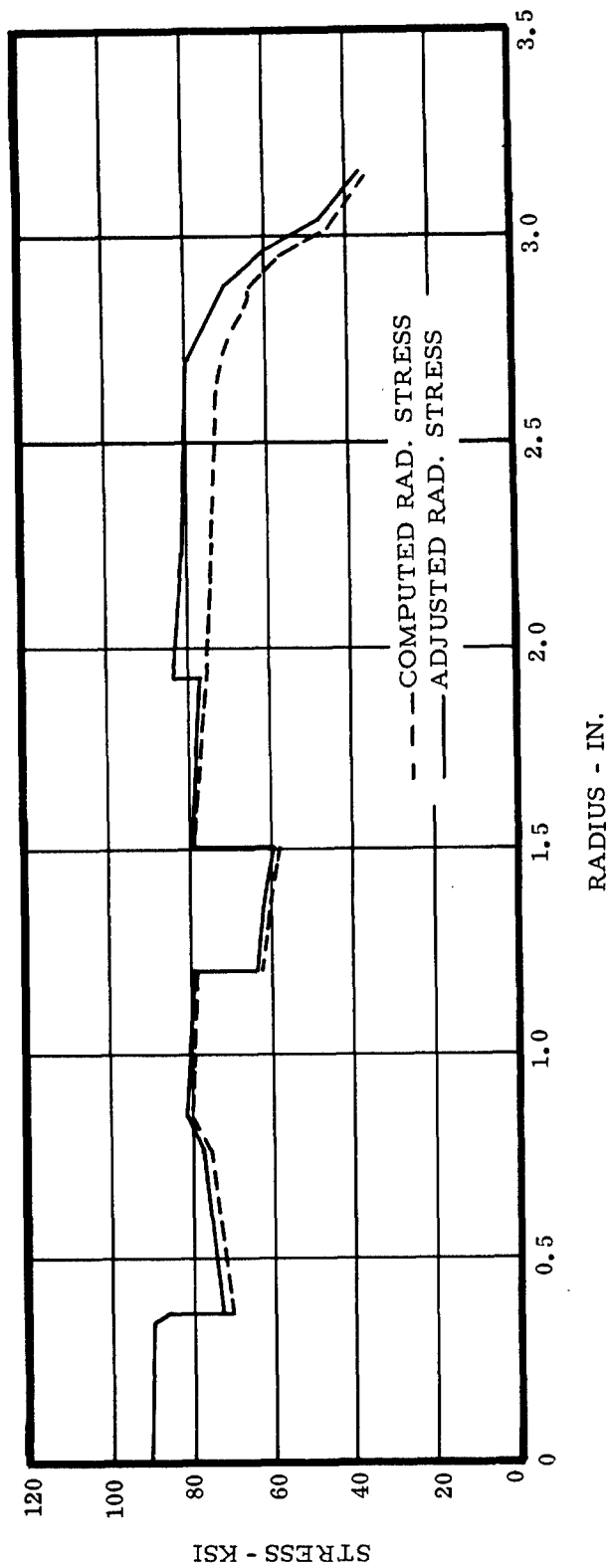


Figure 188. Turbine Rotor Disc With Pinned Attachment - Radial Stress at 50,000 RPM.

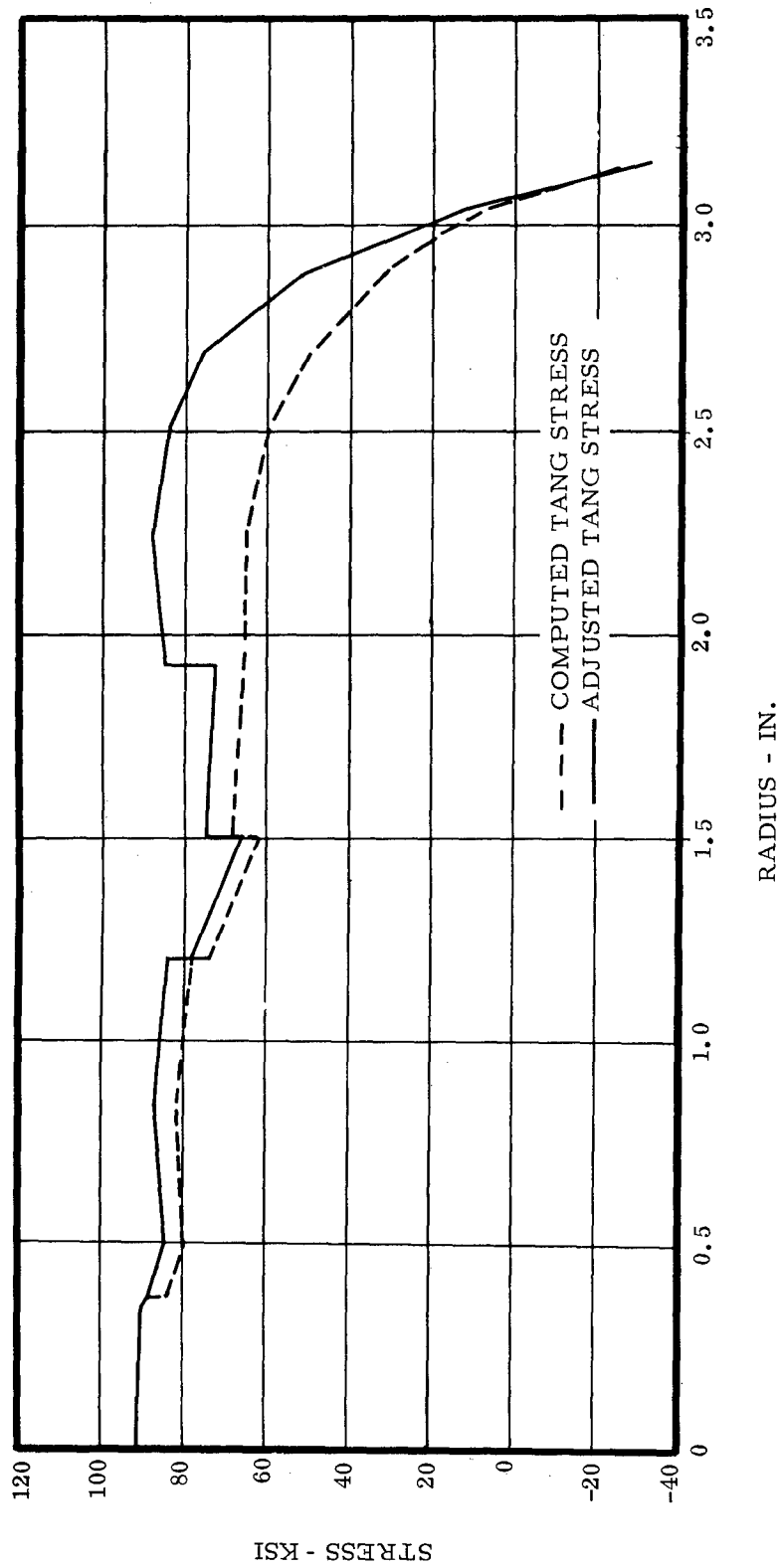


Figure 189. Turbine Rotor Disc With Pinned Attachment - Tangential Stresses at 50,000 RPM.

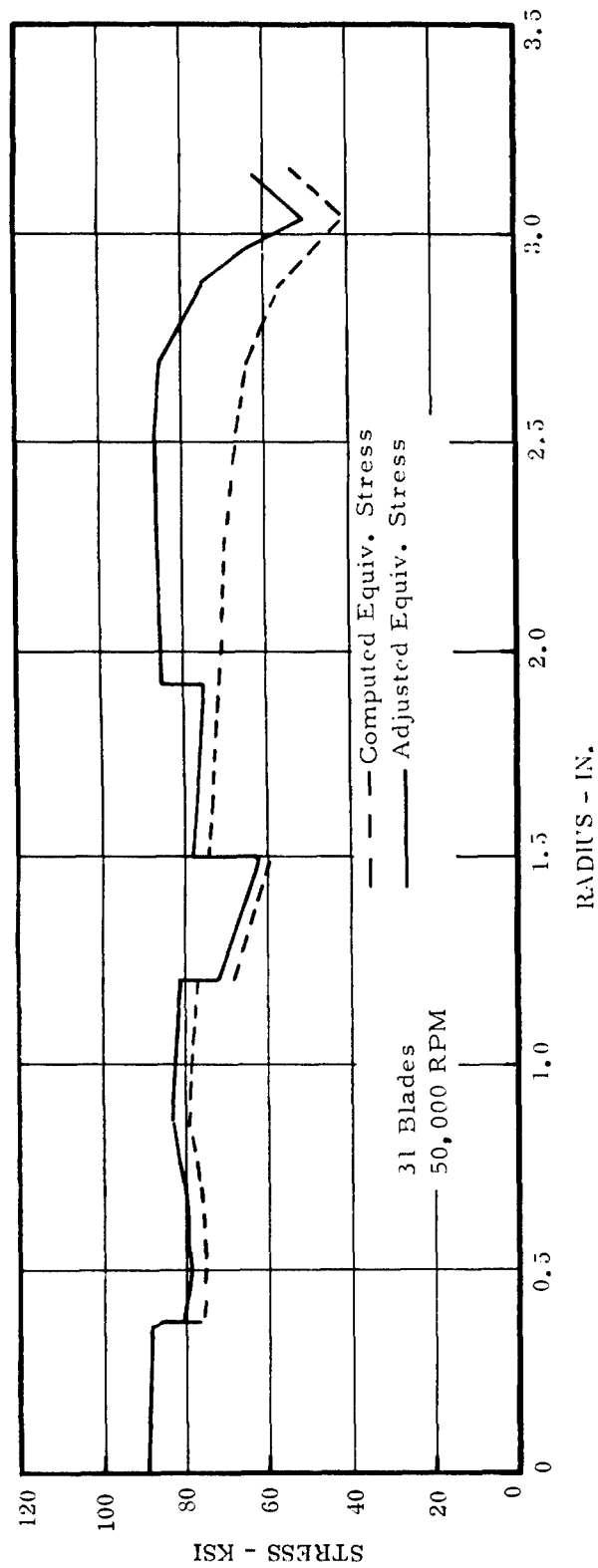


Figure 190. Turbine Rotor Disc With Pinned Attachment - Equivalent Stresses at 50,000 RPM.

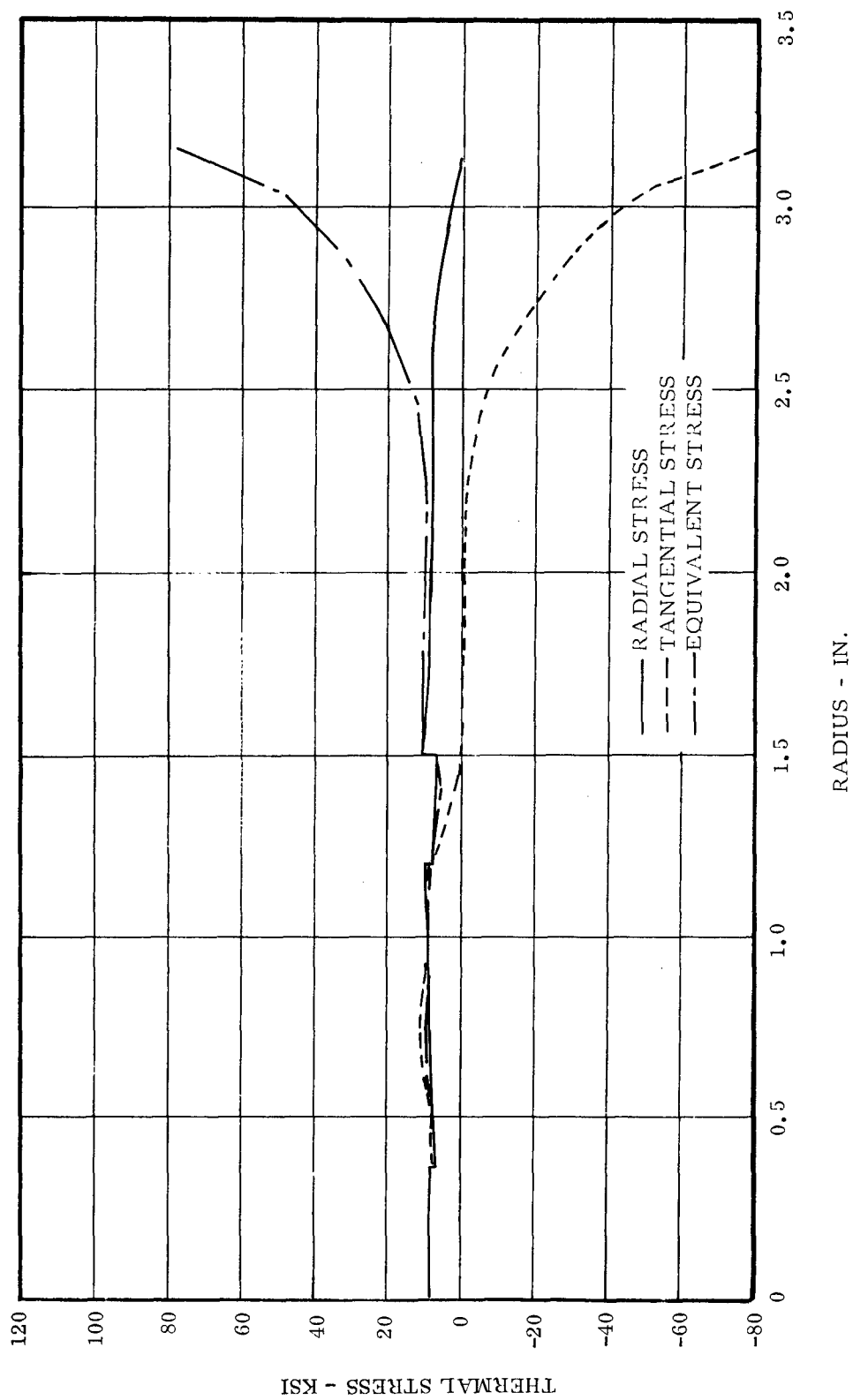


Figure 191. Turbine Rotor Disc With Pinned Attachment - Thermal Stresses at Shutdown (RPM = 0).

Results. The burst margin was calculated using the vendor guaranteed data (Figure 192). These strength properties are lower for U-700 than those published in Reference 38. It was comparable to INCO 713 material, Figure 192 ; therefore, the data below are conservative.

Disc Average Temperature	=	400° F
σ_{ult} for U-700 at 400° F	=	182,000 psi
Average Tangential Stress	=	70,100 psi
Maximum Web Radial Stress	=	82,300 psi

1. Tang Burst Margin

$$BM = \sqrt{\frac{.75 \times 182,000}{70,100}} = 1.396$$

2. Allowable Max. Web Radial Stress

$$\sigma_{allowable} = \frac{182,000 \times 0.75}{(1.25)^2} = 87,500 \text{ psi}$$

Conclusions. This approach is satisfactory with respect to burst margin and maximum web radial stress criteria. Consideration must be given to the fact that all the thermal stresses have been evaluated utilizing analytically obtained thermal gradient data. Initial testing to evaluate the thermalsyphon concept and confirm analytical-temperature conditions will substantiate the thermal stress values prior to full speed operation. Cold spin tests are also planned to confirm that stress concentration factors around the coolant and heat exchanger holes in the disc are not excessive.

Welded Blade-Heat Exchanger Attachment Analysis

Structure. The disc is basically the same as the pinned type shown in the cross section (Figure 185). However, the depth of weld is not equal to the depth of the pinned root.

Loads. The loads are assumed to be the inertia loads and thermal loads. The thermal profile is shown in Figure 193 and the rim loads in Figure 194. The heat exchanger and fuel loads are assumed to be intermediate applied loads - not at the rim but just inside it.

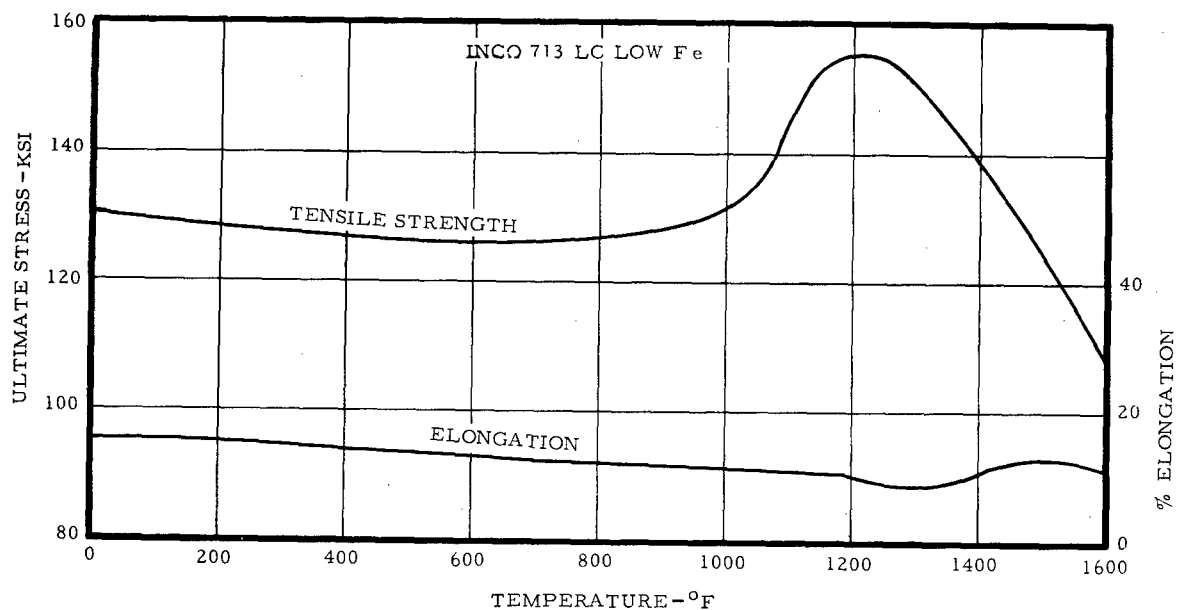
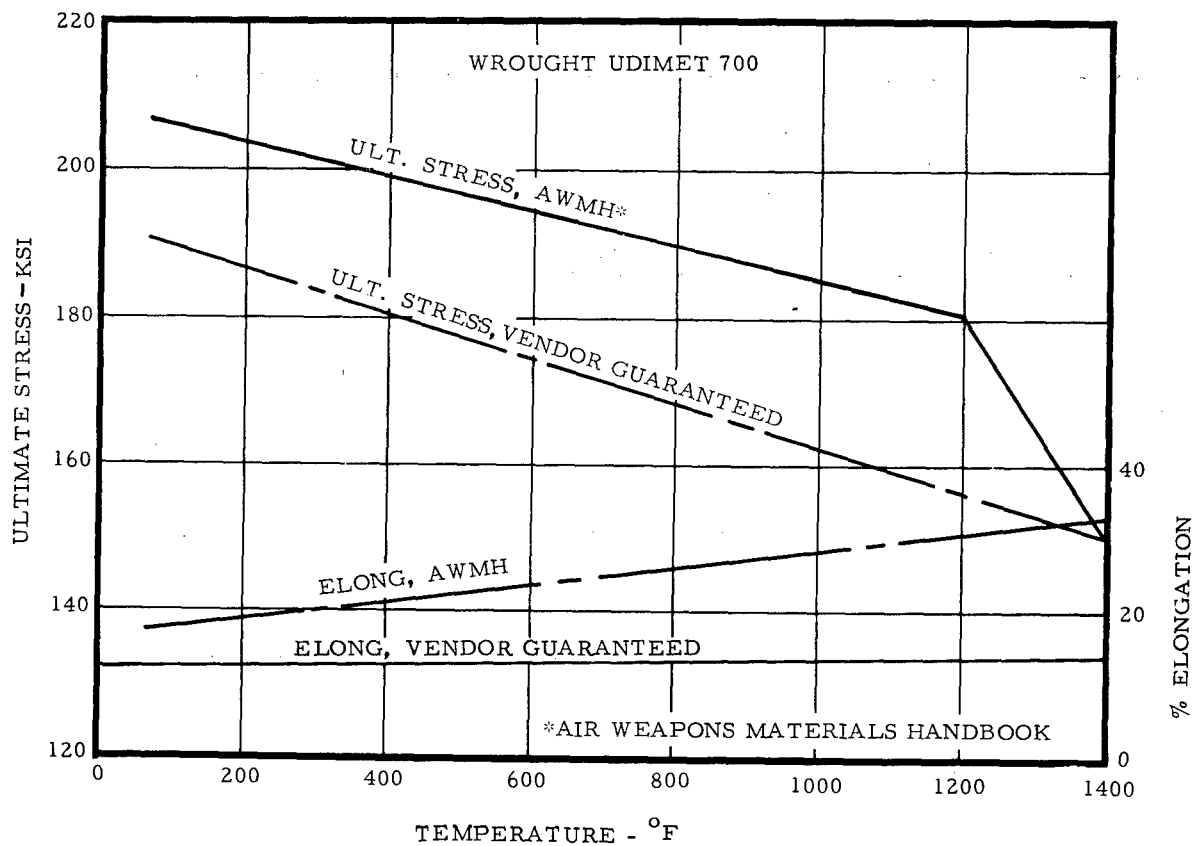


Figure 192. Mechanical Properties of Wrought U-700 and Inco 713 LC Low Fe.

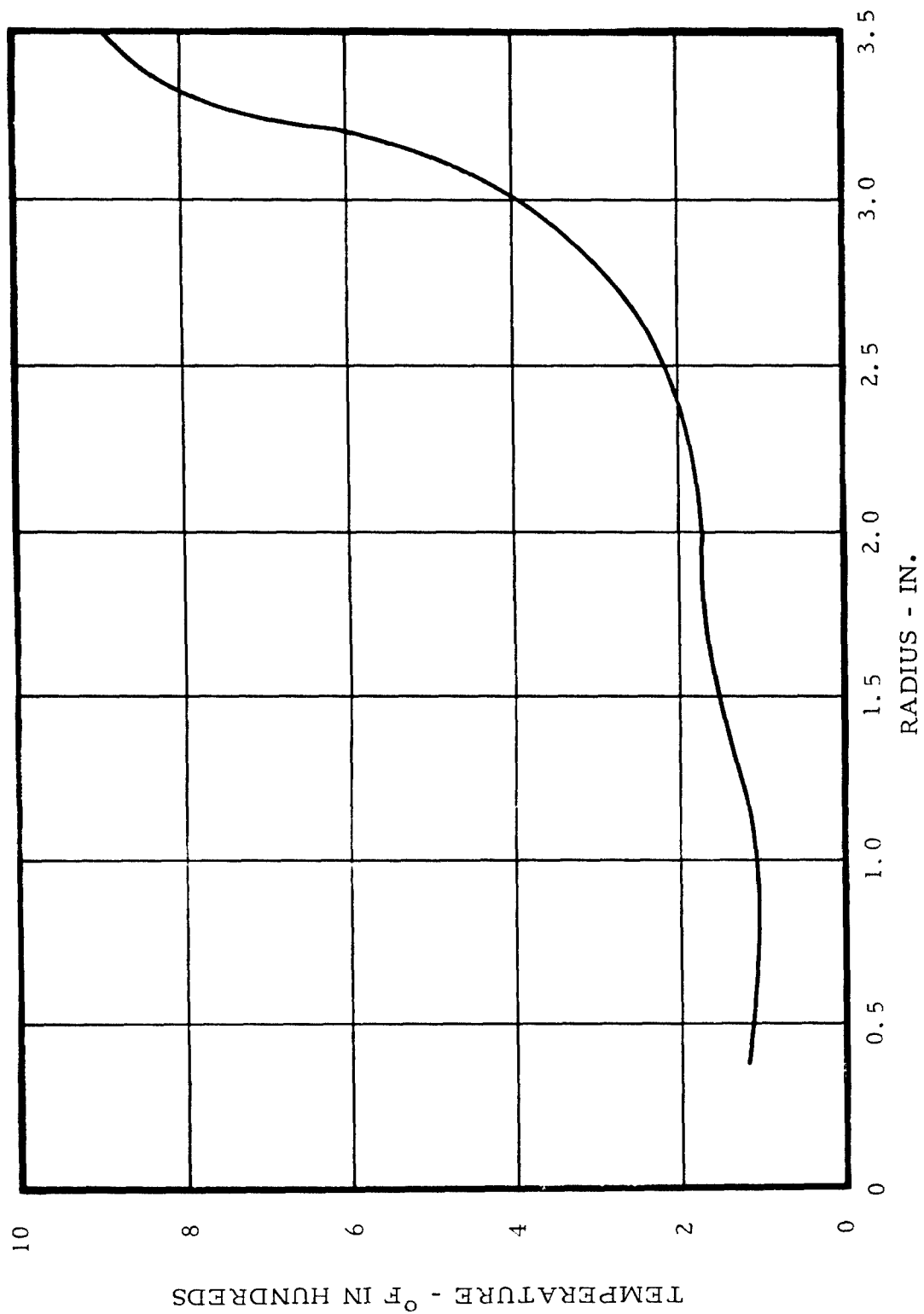


Figure 193. Temperature Gradient Welded Attachment.

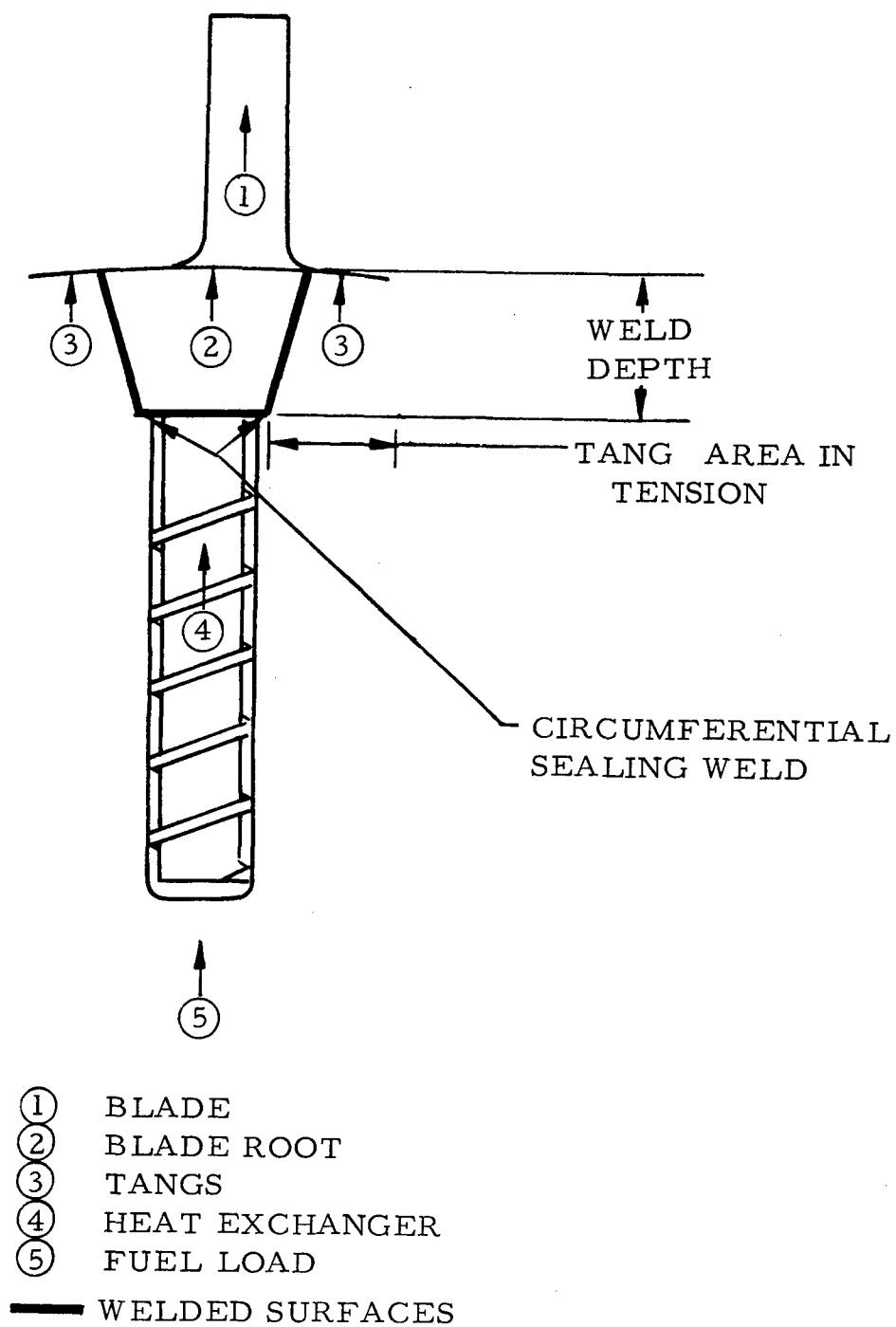


Figure 194. Welded Attachment Loads.

Attachment Stresses. The attachment stresses are weighed off as shear-out stresses versus radial stress over the connecting disc tang. No strength was assumed in the circumferential sealing weld (Figure 194). Figure 195 shows the effect of a shear-out load on the depth of weld versus the tensile stress at the bottom of the disc tang. Based on Figure 195, a depth of side weld of 0.25 inch is adequate from a stress standpoint.

Method of Analysis. Manson's method and the average tangential stress method are used to analyze the disc.

Disc Stresses. The results of Manson's method are shown in Figures 196 through 199. The average tangential stress is 60,087 psi.

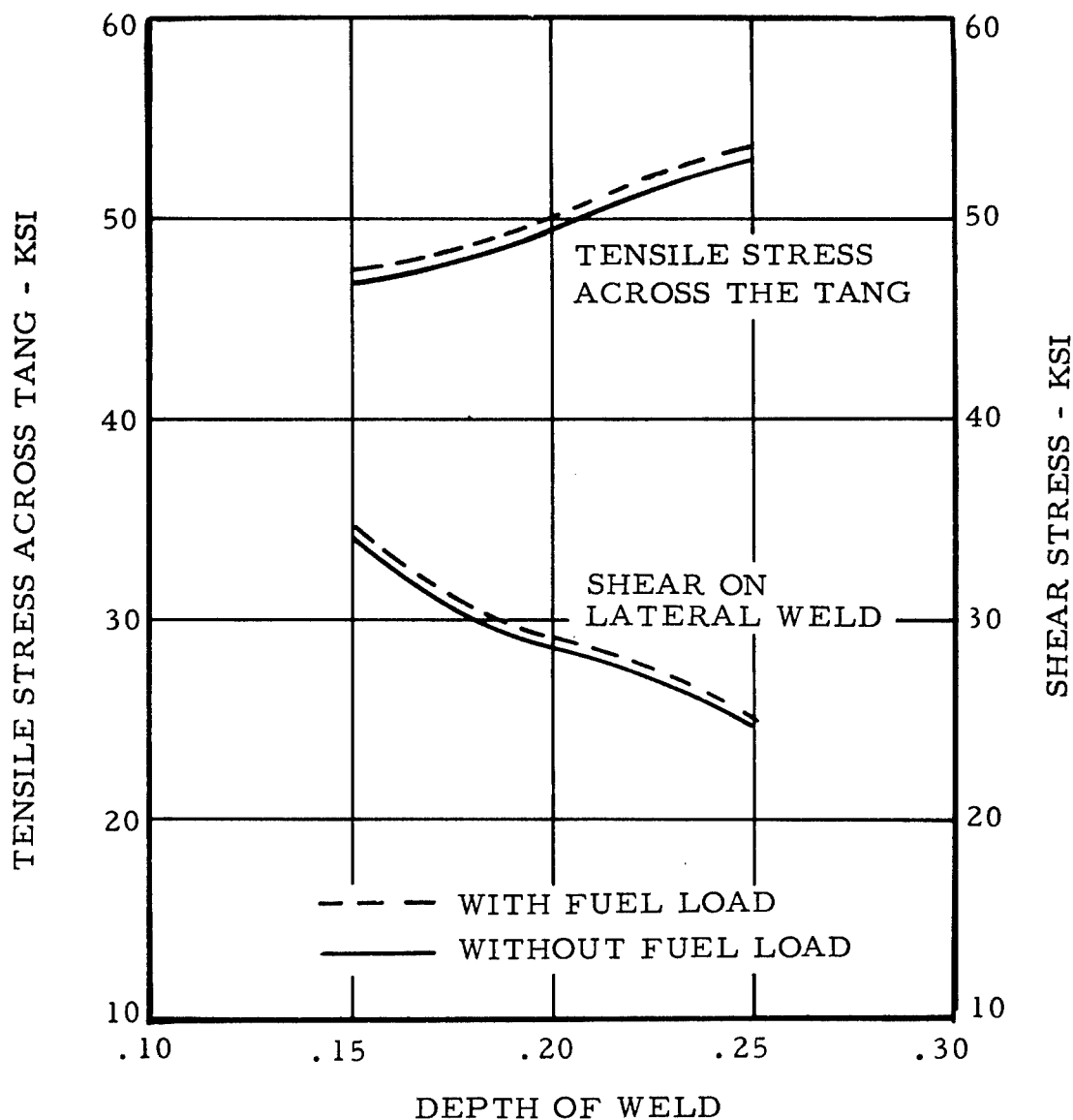


Figure 195. Disc With Welded Rim Attachment.

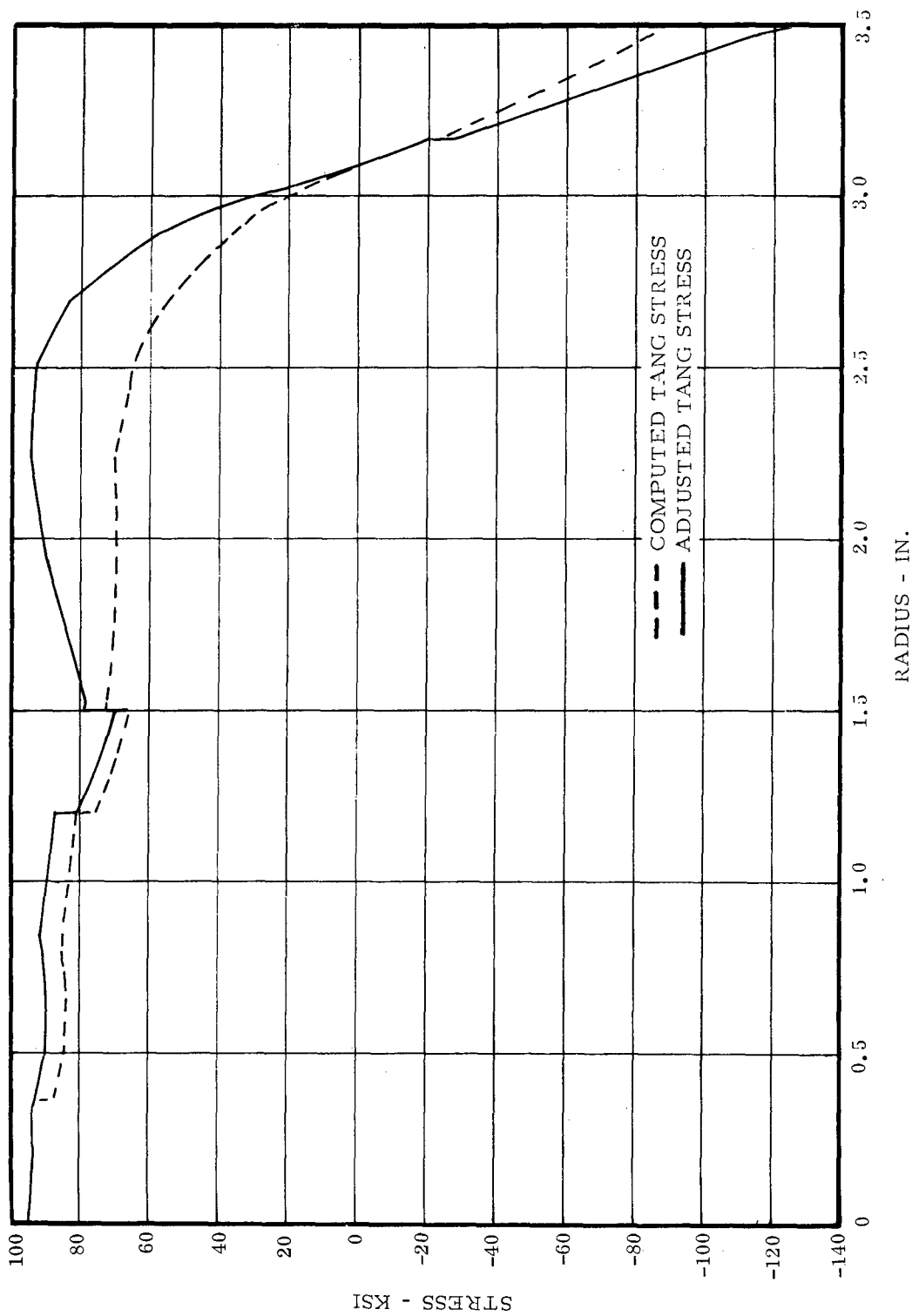


Figure 196. Turbine Rotor Disc With Welded Attachment - Tangential Stresses at 50,000 RPM.

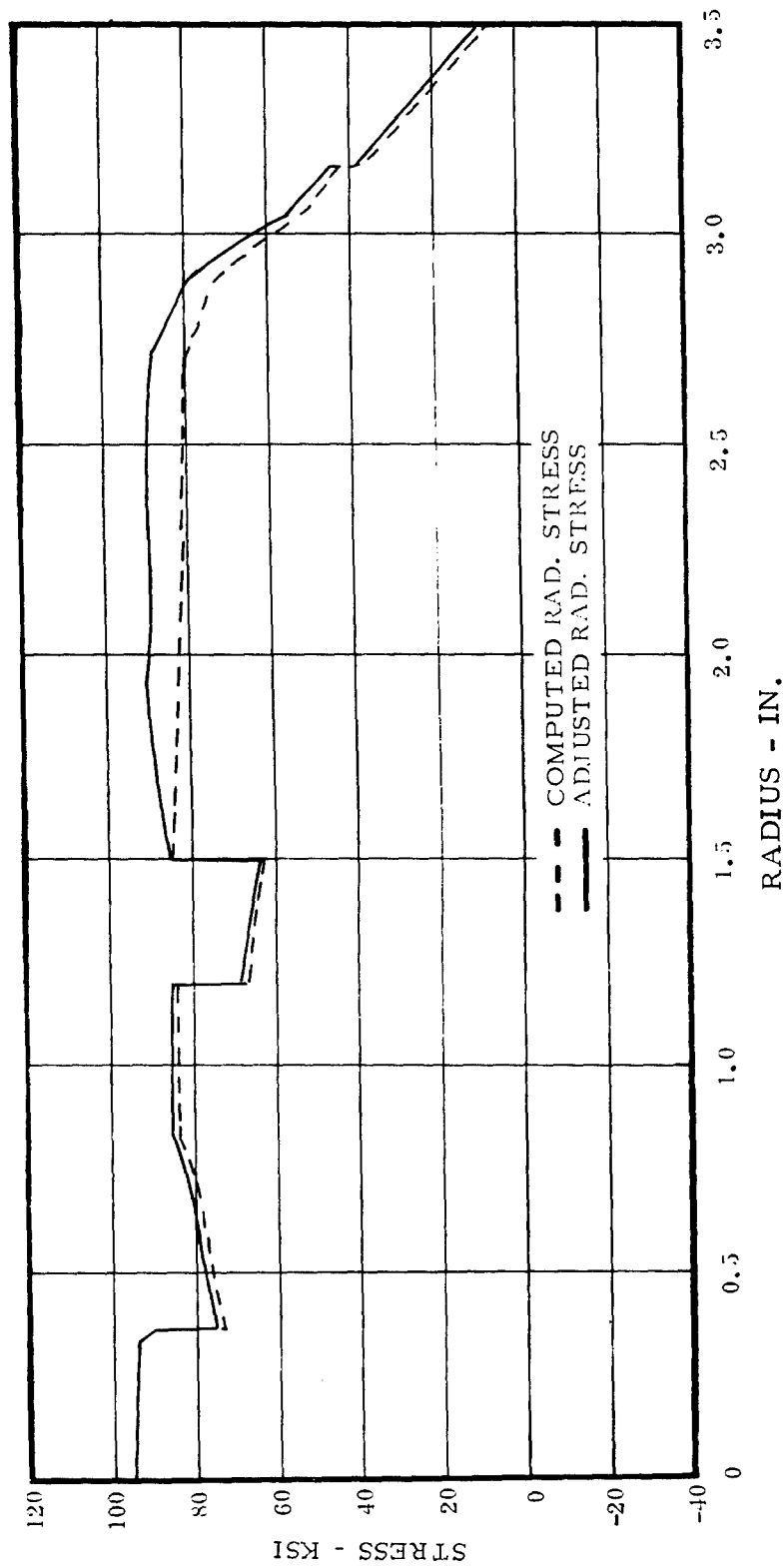


Figure 197. Turbine Rotor Disc With Welded Attachment - Radial Stresses at 50,000 RPM.

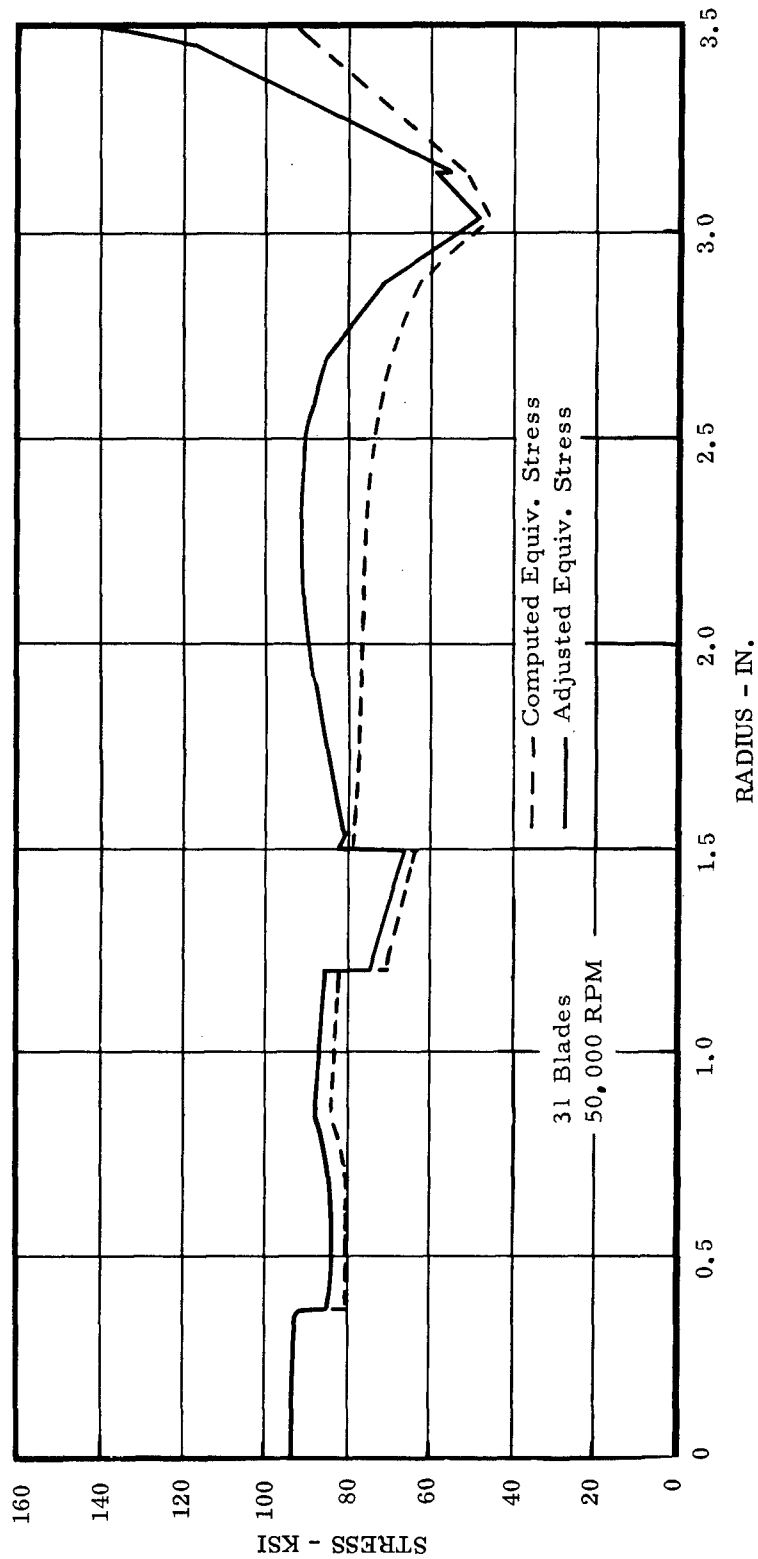


Figure 198. Turbine Rotor Disc With Welded Attachment - Equivalent Stresses at 50,000 RPM.

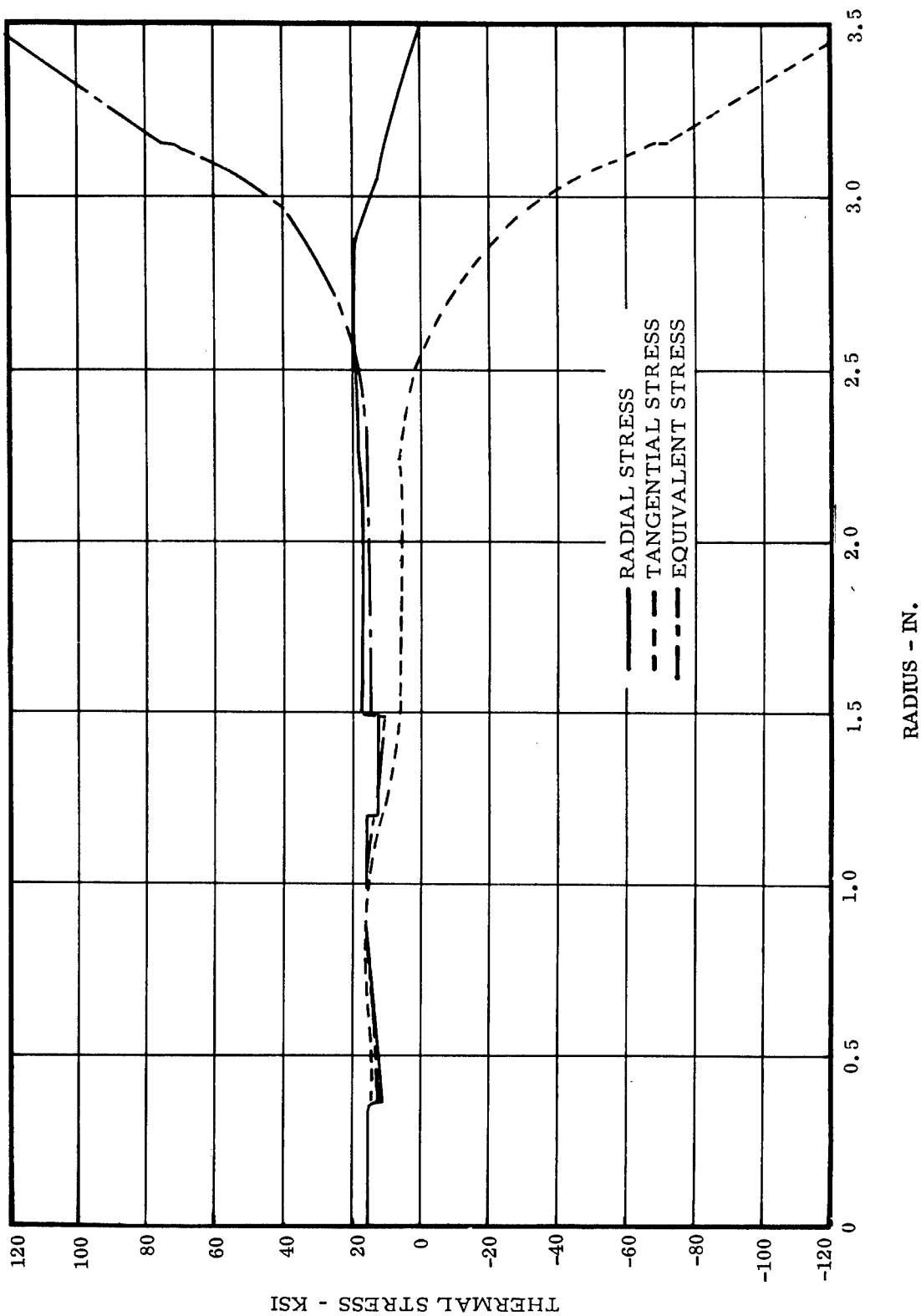


Figure 199. Turbine Rotor Disc With Welded Attachment - Thermal Stresses at Shutdown (RPM = 0).

Criteria. Besides the criteria specified for the pinned attachment concept, an additional control must be included for this disc. A thermal gradient of 680°F is imposed over the last 1 inch of the disc. This causes a high compression stress at the rim. Since cyclic yielding would not be acceptable with this design, it will be seen that rim crushing will control. The criterion to prevent rim crushing was to allow the maximum "elastic" tangential stress on a net section to be equal to $0.9 \sigma_{YP}$ in tension. In this report such a stress is assumed to be at the point of incipient yielding in compression.

Results. The results are shown below.

Disc Average Temperature	=	520°F
σ_{ult} for U-700 at 520°F	=	176,000 psi
Average Tangential Stress	=	60,080 psi
Maximum Web Radial Stress	=	89,500 psi
Maximum Rim Compressive Stress	=	140,000 psi

1. Tang Burst Margin

$$BM = \sqrt{\frac{0.75 \times 176,000}{60,080}} = 1.48$$

2. Allowable Max. Web Radial Stress

Web Temperature	=	380°F
σ_{ult} for U-700 at 380°F	=	182,000 psi
σ_{rad} Allowable	=	$\frac{182,000 \times 0.75}{(1.25)^2} = 87,500$ psi

3. Allowable Rim Compressive Stress

Rim Temperature	=	1,090°F
σ_{Yield} for U-700 at 1,090°F	=	115,000 psi
σ_{Yield} in Compression = $0.9 \sigma_{Yield}$	=	104,000 psi

4. Conclusion

Although the disc has a satisfying burst margin, the web radial and the rim compressive stresses exceed the allowable values. In this design concept, a more intensive cooling of the rim will have to be provided.

Residual stresses due to welding have not been analyzed. They would relieve the rim compression to a certain extent, but it would take an appreciable residual tension to remove the large compression at the rim.

The concept of a disc with welded blade attachments is unsatisfactory for a design incorporating a heat exchanger in the disc. The concept could be applied to a design with a heat exchanger in the shaft which has a much smaller disc thermal gradient.

Full Cast Integral Blade and Disc With Heat Exchanger in the Shaft Analysis

Structure. The disc configuration studied is the same basic profile as the pinned and welded versions with the heat exchanger excluded (Figure 200).

Loads. The loads assumed were the inertia loads due to rpm and the thermal loads due to a radial temperature gradient. A plot of the temperature versus radius profile is shown in Figure 201. The rim load is due to the blade pull plus steam pressure.

Method of Analysis. Manson's method and the average tangential stress method were used to analyze the disc.

Disc Stresses. The results of the analysis by Manson's method are given in Figures 202 through 205.

The average tangential stress is 62,358 psi. The maximum radial web stress is 65,541 psi.

Criteria. Design criteria are based on limitations imposed on the maximum radial stress in the web and the average tangential stress. The burst margin is used as the controlling parameter.

$BM = 1.25$ is the minimum desirable limit.

Rim crushing could occur at design and/or in transient.

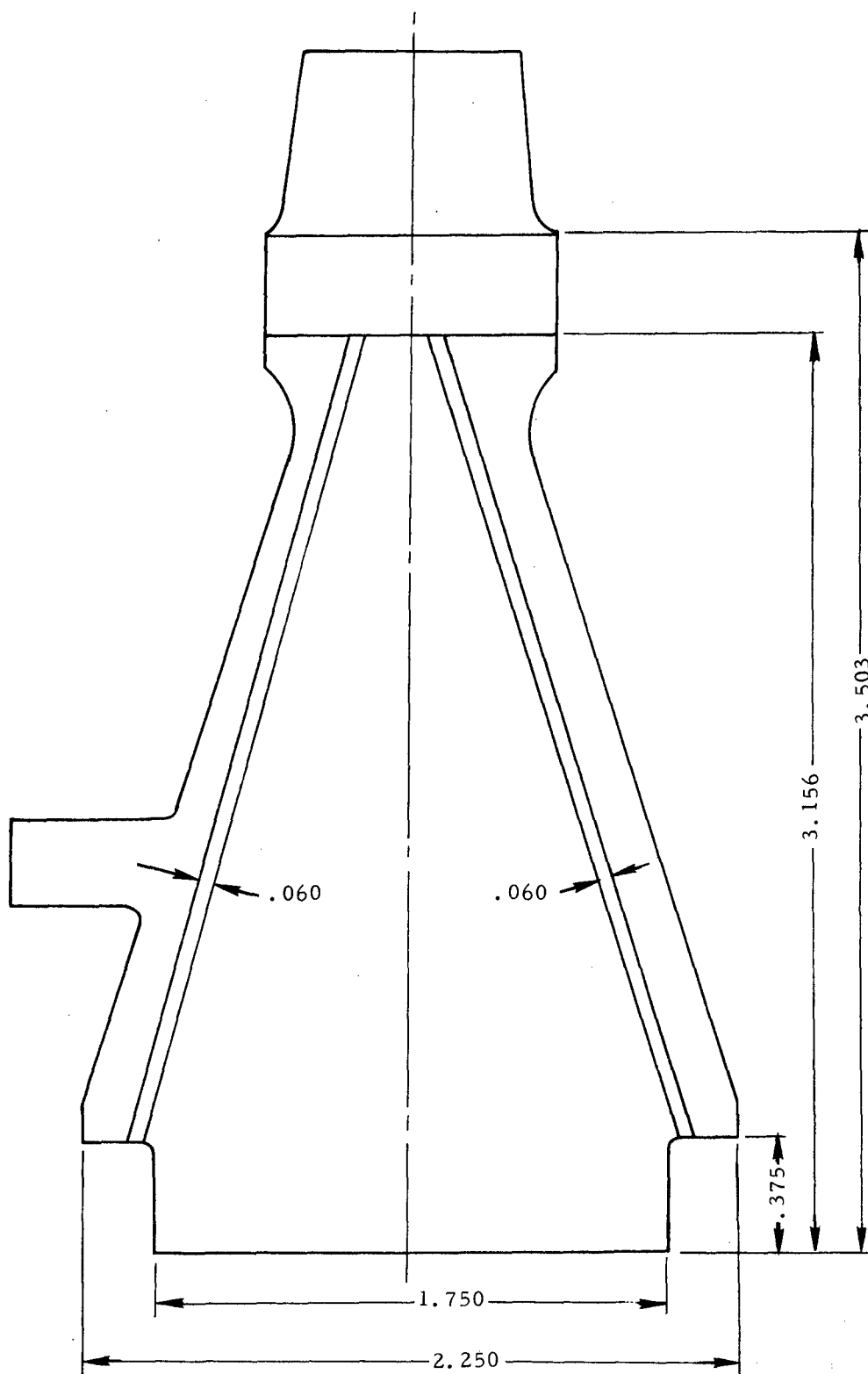


Figure 200. Integral Cast Turbine and Rotor Disc.

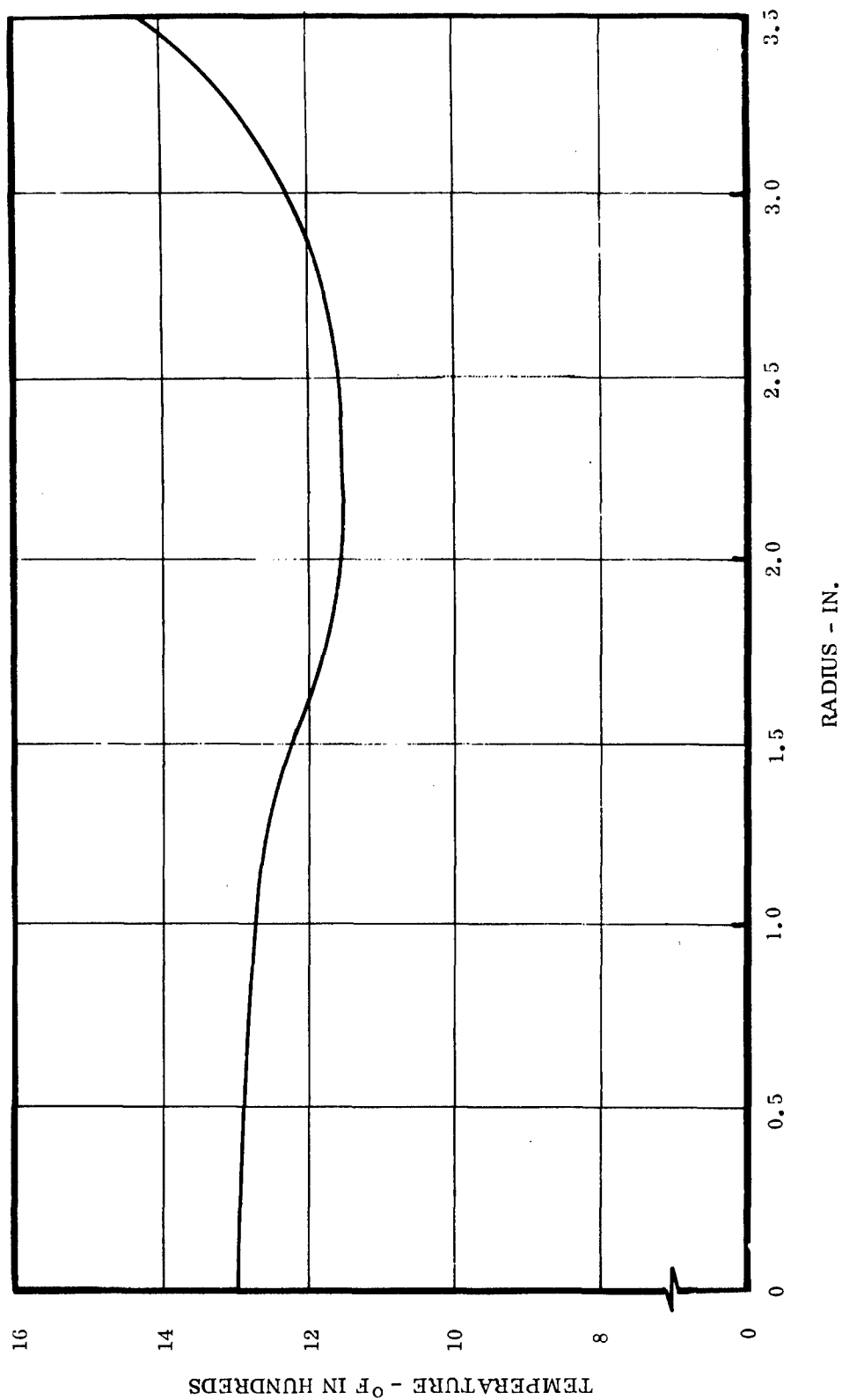


Figure 201. Temperature Gradient - Cast Disc.

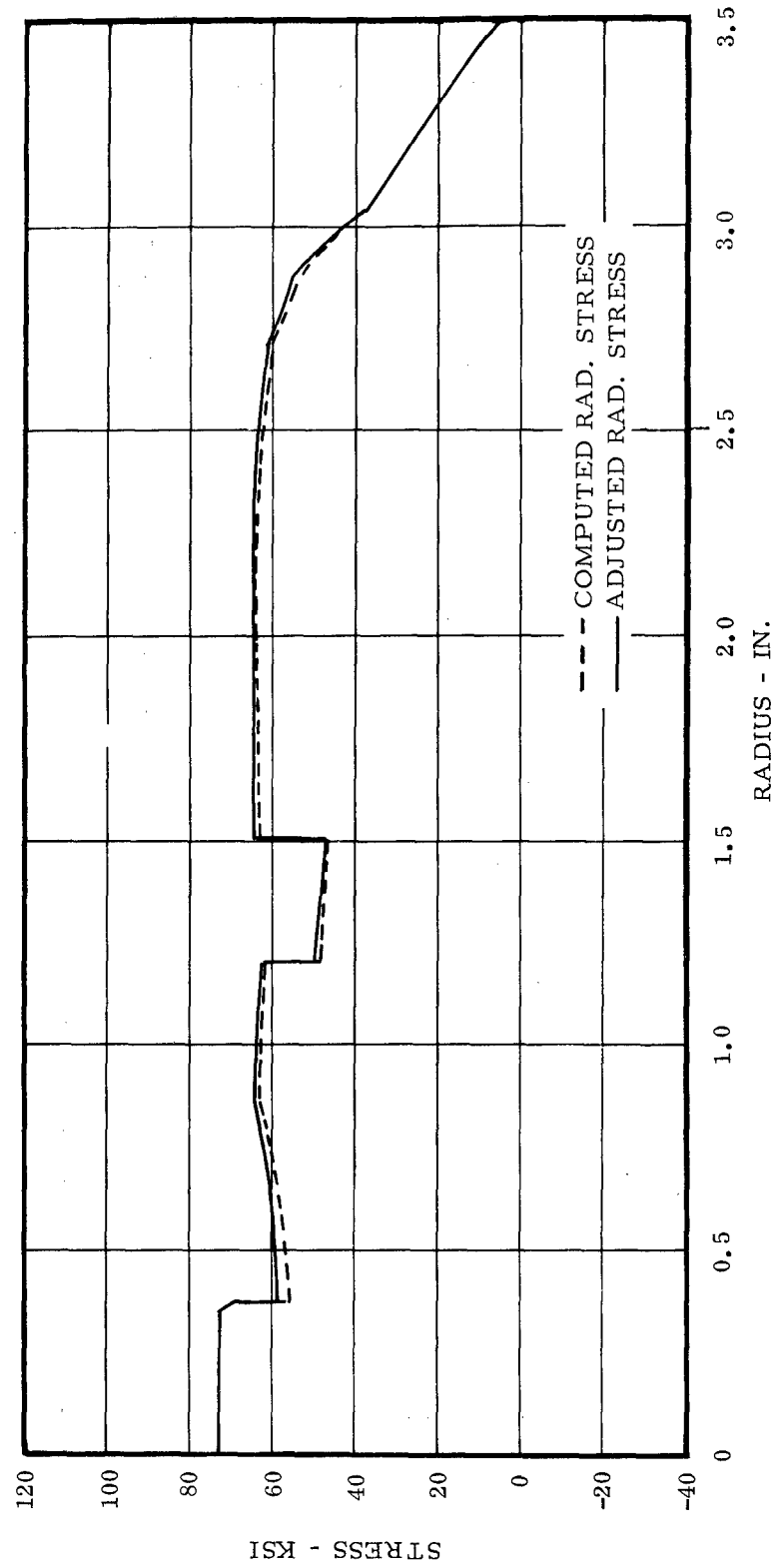


Figure 202. Integral Cast Turbine Rotor Disc - Radial Stresses at 50,000 RPM.

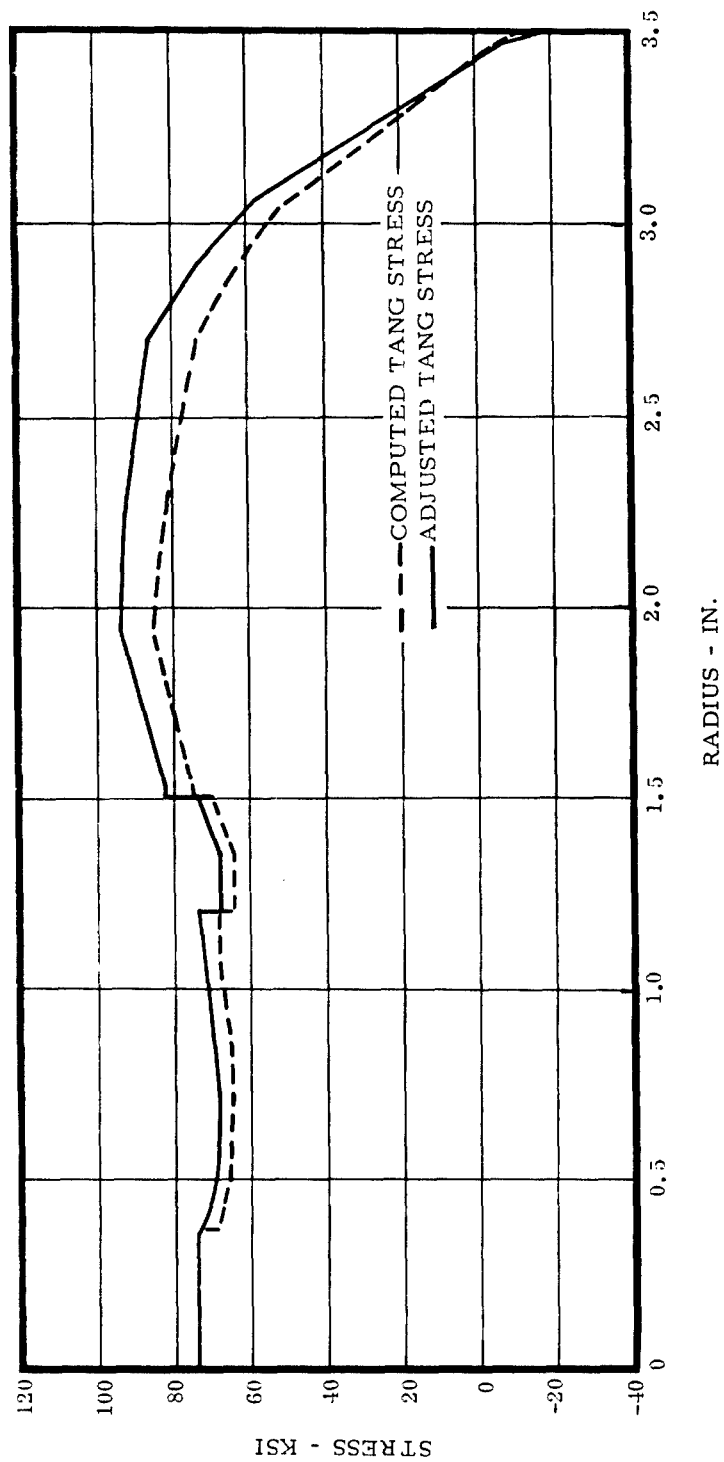


Figure 203. Integral Cast Turbine Rotor Disc - Tangential Stresses at 50,000 RPM.

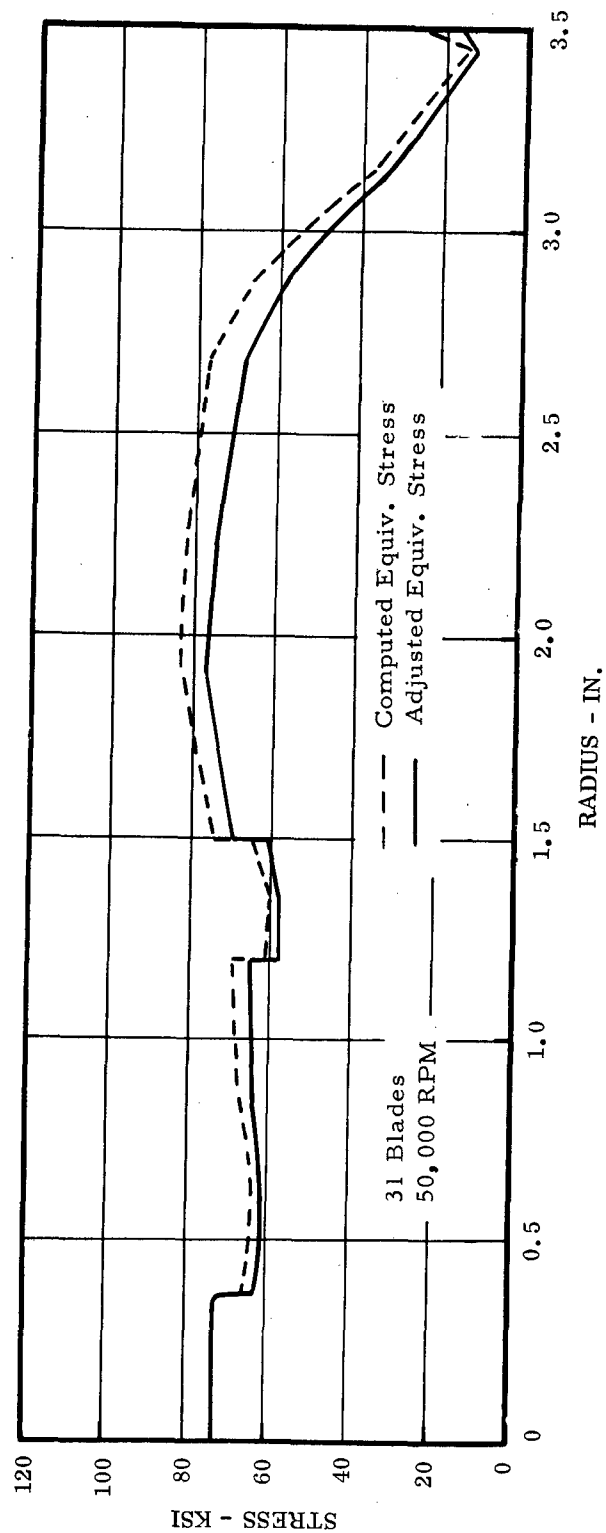


Figure 204. Integral Cast Turbine Rotor Disc - Equivalent Stresses at 50,000 RPM.

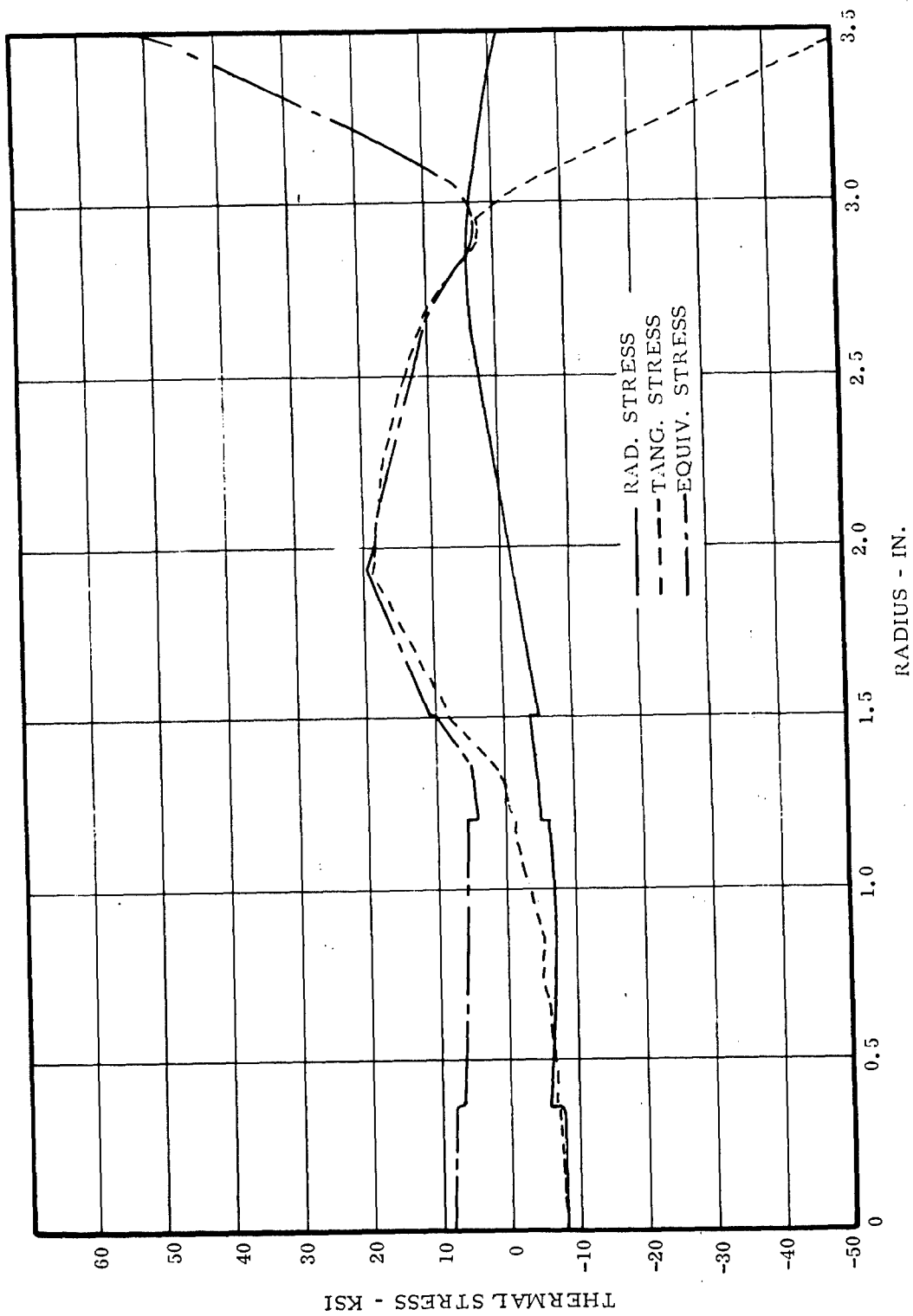


Figure 205. Integral Cast Turbine Rotor Disc - Thermal Stresses at Shutdown (RPM - 0).

Summarized below are the failure criteria calculations for this version of the disc.

Disc Average Temperature	=	1,244° F
σ_{ult} for Inco 713 LC at 1244° F	=	155,000 psi
Average Tangential Stress	=	62,360 psi
Maximum Web Radial Stress	=	65,540 psi
Maximum Rim Compressive Stress	=	83,500 psi

1. Tang Burst Margin

$$BM = \sqrt{\frac{0.75 \times 155,000}{62,360}} = 1.36$$

2. Allowable Max. Web Radial Stress

$$\sigma_R \text{ allowable} = 0.75 \times 155,000 / (1.25)^2 = 75,000 \text{ psi}$$

3. Allowable Rim Compressive Stress

$$\sigma \text{ at } 1440^\circ\text{F} = 105,000 \text{ psi}$$

$$\sigma \text{ Yield in Compression} = 0.9 \times \sigma \text{ Yield} = 94,500 \text{ psi}$$

The average tangential and the maximum web radial stress fall within the specified criteria.

Conclusions. A disc cast of Inco 713 LC Low Fe meets our design criteria. Castings frequently have a low ductility at the center of the pour. Should the casting respond as a brittle material, one can expect a failure in the disc.

Rotor Blade and Attachment

The analytical results of a U-700 pin attached blade-heat exchanger design are presented and conclusions reached based on the information available and degree of analysis conducted. Possible problem areas are identified.

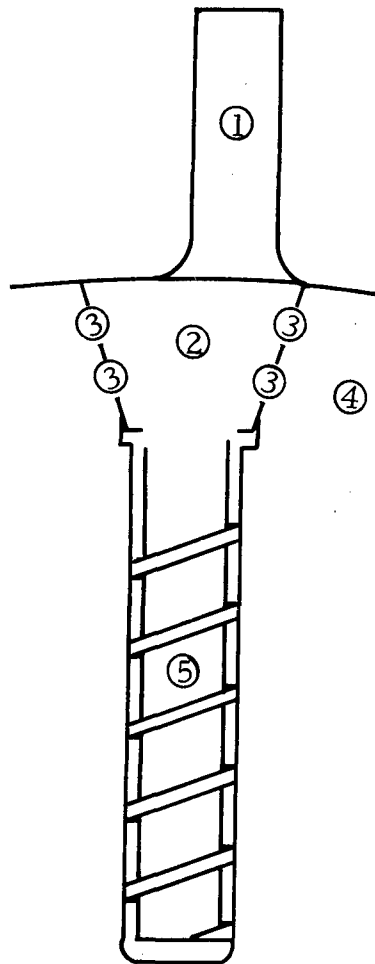
The following approach has been utilized:

1. Establishment of individual component loads on the attachment
2. Blade airfoil evaluation
 - a. Inertia
 - b. Steam pressure
 - c. Thermal
 - d. Gas bending
 - e. Maximums
 - f. Growth
3. Blade root - disc tang attachment
 - a. Root stresses - inertia
 - b. Tang stresses - inertia
 - c. Pin stresses - inertia
 - d. Thermal expansion
4. Conclusions
 - a. Recommendations
 - b. Problem areas

Blade Attachment Analysis

Loads. Load identification on each attachment is shown in Figure 206. The loads are calculated for a wheel rotation at 50,000 rpm.

<u>Part</u>	<u>Load (lb.)</u>
Blade	4, 170
Root	8, 064
Heat Exchanger and Fuel and Seal	1, 630
Top Pins (2)	714
Bottom Pins (2)	690
Tang	<u>6, 632</u>
Total	21, 900



- ① BLADE
- ② ROOT
- ③ PIN
- ④ DISC TANG
- ⑤ HEAT EXCHANGER AND FUEL

Figure 206. Pinned Attachment Load Identification.

The gas bending loads are very slight. They were computed by Continental Program No. 08.008 and are tabulated in Table XXI with the computed gas bending moments. The maximum gas bending stress is 380 psi, and is low compared to the accompanying centrifugal, thermal, and internal pressure stresses. The mean span temperature distribution for thermal stresses is shown in Figure 207. A uniform steam pressure of 1500 psi was assumed in the cooling passages. The load paths are easily traced by means of Figure 206. Loads 1, 2, 3, and 5 are transferred through 3 into 4, thence into the disc.

TABLE XXI
AIRFOIL GAS LOADS AND MOMENTS

Radius (in.)	Load (lb.)		Gas Bend. Mom. (in. -lb.)	
	Tangential	Axial	Tangential	Axial
3.503	20.645	3.400	102.494	72.994
3.581	40.116	20.873	78.496	57.150
3.659	41.211	22.606	57.617	42.919
3.737	41.233	24.554	39.962	30.451
3.815	41.231	26.518	25.708	20.032
3.893	41.205	28.510	14.341	11.438
3.971	41.163	30.511	6.434	5.258
4.049	41.104	32.530	1.573	1.326
4.127	20.427	17.233	0	0

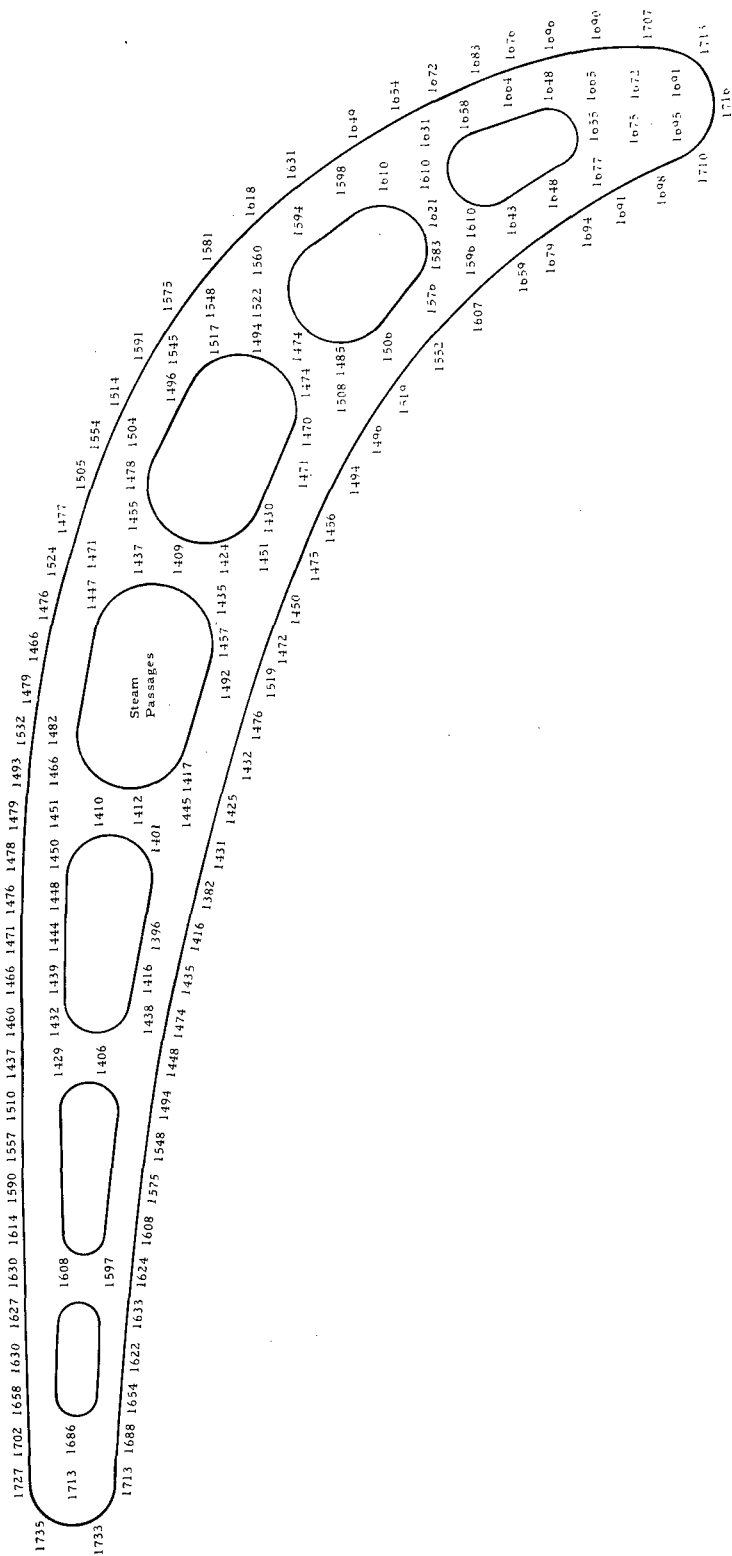


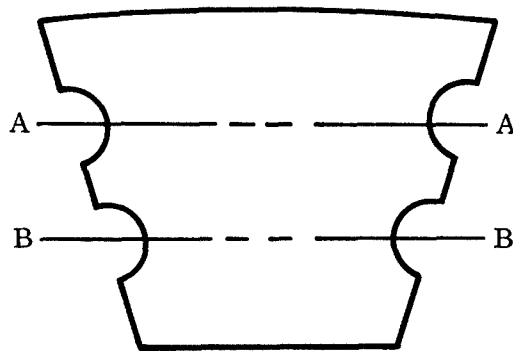
Figure 207. Turbine Rotor Blade Temperature Distribution - °F, Mid-Span Section.

Stresses and Growth

1. Root - Blade

The stress due to rpm through the root at each row of pins is given in Table XXII.

TABLE XXII
BLADE ROOT PINNED ATTACHMENT

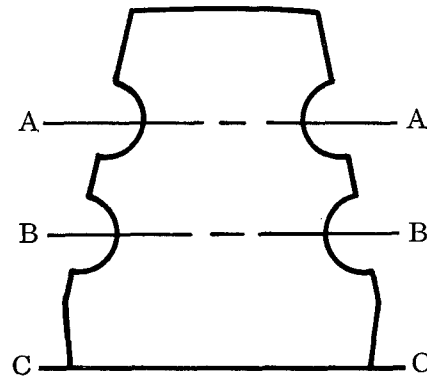


<u>Section</u>	<u>Load (lb.)</u>	<u>Area (in. ²)</u>	<u>Rad (psi)</u>
A-A	7405	.30615	23,422
B-B	2996	.20532	12,213

2. Tang - Disc

The stress across the tang at each row of pins is given in Table XXIII.

TABLE XXIII
TANG PINNED ATTACHMENT



<u>Section</u>	<u>Load (lb.)</u>	<u>Area (in. ²)</u>	<u>Rad (psi)</u>
A-A ¹	19, 500	0. 19665	48, 400
B-B	19, 321	0. 24840	77, 782
C-C	21, 661	0. 32706	66, 229

¹ 50 percent load distribution assumed

Blade

Inertia. A plot of the P/A stresses due to rotation only is shown in Figure 208. The maximum stress occurs at the root and is 37, 480 psi.

Steam Pressure. The steam pressure is assumed to react on the blade in three ways: (1) it adds to the centrifugal stress load, (2) it subjects the blade to a pressure vessel type of thrust load on the walls of the steam passages, and (3) it causes a bending load on the walls of the steam passages as though the walls are flat plates with the edges fixed.

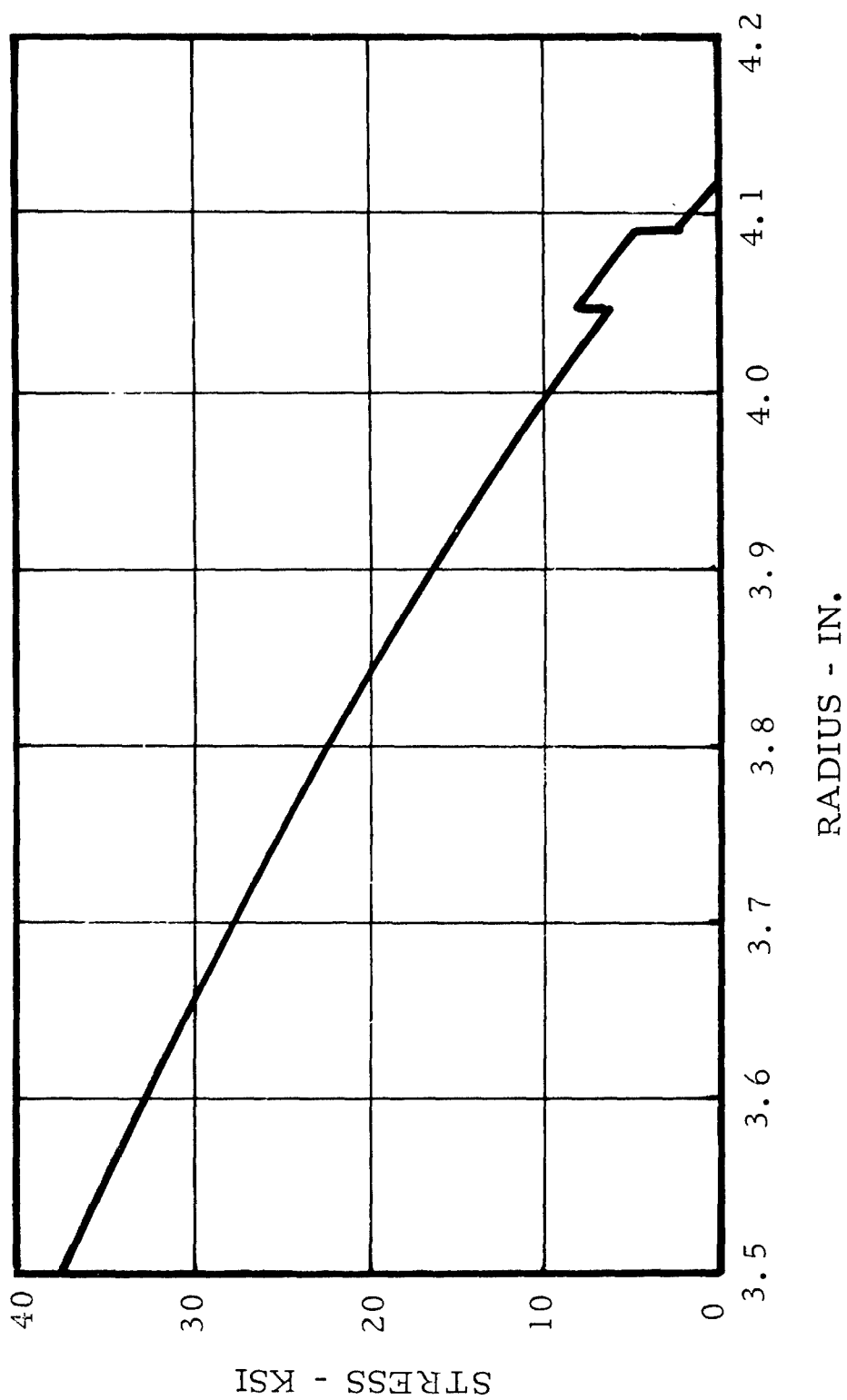
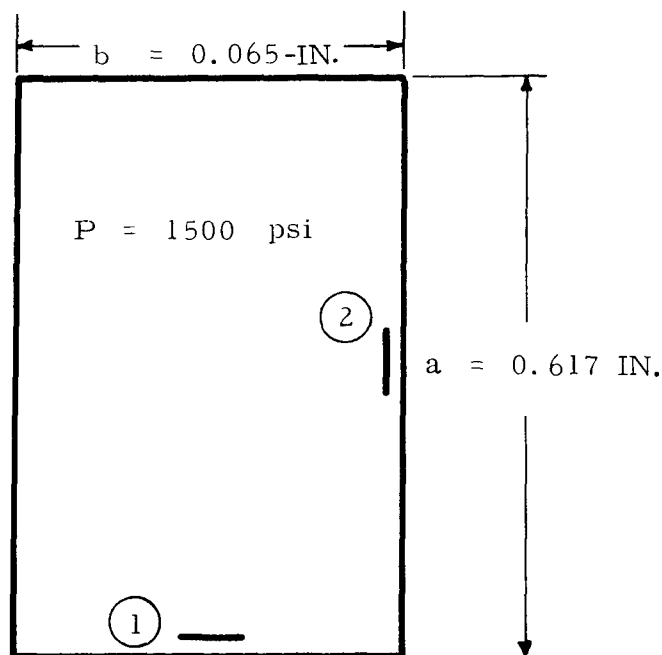


Figure 208. Blade Stresses Due to Centrifugal Loading Only - Unmodified Blade Core.

Only the latter is of any magnitude and causes localized flexural stresses. The highest bending stresses occur at the root and in the chordwise direction at the mid-span of the blade. The maximum flexural stresses due to internal pressures occur in the cooling passages of the trailing edge when assuming the minimum allowable thickness distribution resulting from fabrication tolerances. Figure 209 shows the points of maximum stress due to steam pressure based on nominal wall thickness and minimum allowable wall thickness due to fabrication techniques.



AT ②	$t_1 = 0.012\text{ IN.}$	$\sigma = \pm 21,680\text{ psi}$	CHORDWISE
AT ①	$t_1 = 0.012\text{ IN.}$	$\sigma = \pm 10,840\text{ psi}$	SPANWISE

Figure 209. Bending Stresses Due to Steam Pressure.

Thermal Stresses. The blade temperature stresses were computed by means of Continental Program No. 02.008. The mid-span temperature distribution is given in Figure 207, and the stresses in Figure 210. It should be pointed out that these stresses are approximate, since the span is very short compared to the chord length. The analysis used in the computer program assumes that end conditions do not affect the results (St. Venant's principle) and is only true when the section analyzed occurs at least one chord length away from the end. These blades have a span less than the chord, which invalidates the exactness of the results;

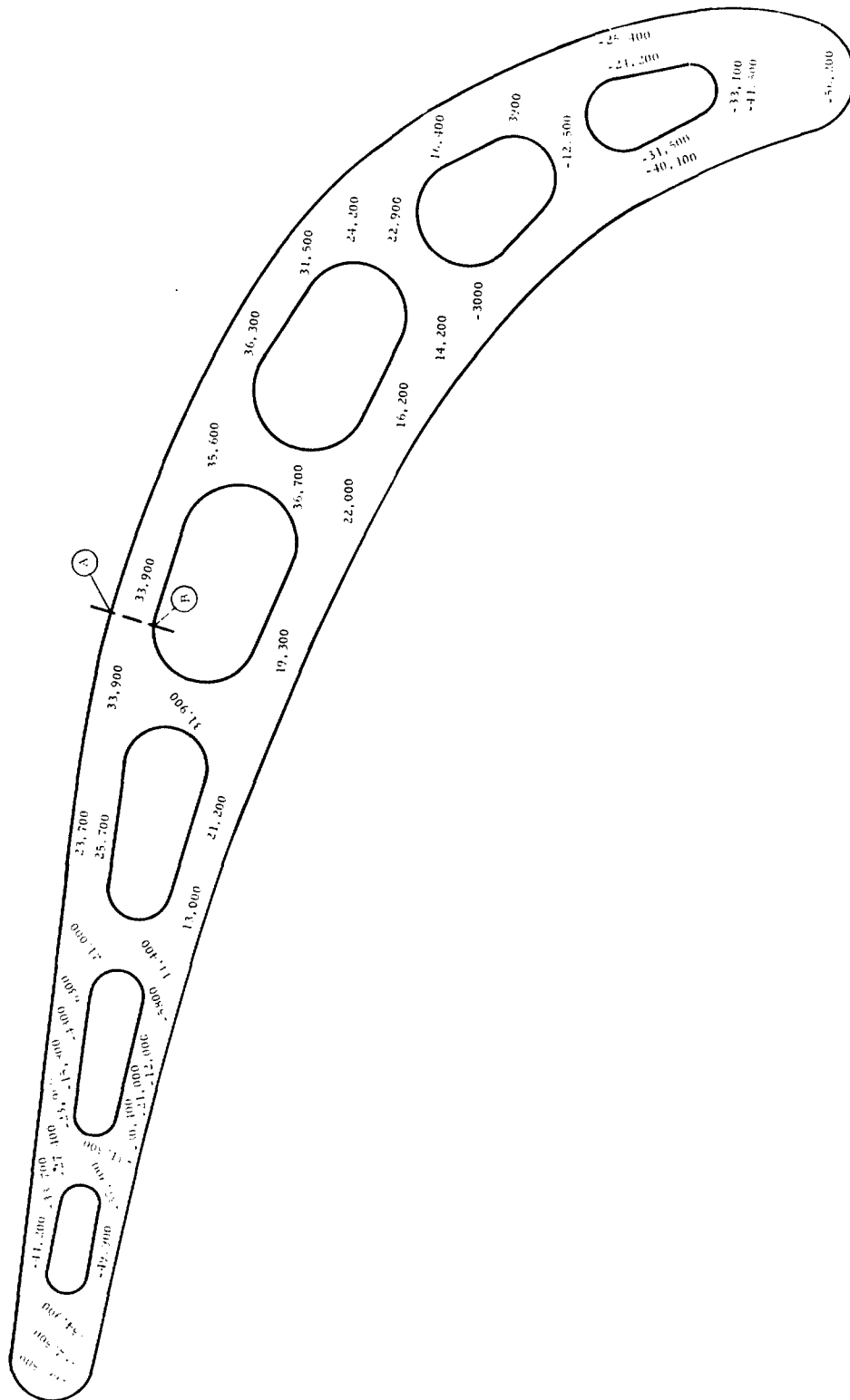


Figure 210. Fluid-Cooled Turbine Rotor Blade Thermal Stress Distribution, Mid-Span Section.

however, it would appear that the results do represent a maximum stress condition and can thus be useful in determining conservative level of stress occurring in mid-span and at the root. The thermal stresses in a thin flat plate with a similar temperature distribution have been analyzed in Reference 39. This reference shows that the thermal stresses in the leading and trailing edges would be appreciably reduced at the mid-span, which is only 1/4 chord from the tip.

Gas Bending. Stresses due to gas bending are very low, with the maximum unrestored stress being 380 psi. This is not of enough magnitude to consider when compared to the preceding stress levels. Cast U-700 material properties are shown in Figure 211.

Maximum Stress Location. Two basic spanwise locations are discussed:

1. Airfoil Root
 - a. Mid-chord
 - b. Trailing edge
2. Airfoil Mid-Span
 - a. Mid-chord
 - b. Trailing edge

1a. Airfoil Root at Mid-Chord. At this location the inertia, steam pressure, and thermal are additive. Mechanical stresses of 48,500 psi are expected. If the mid-span temperature distribution is utilized at the root section, a stress of 33,900 psi will result from the thermal gradient. The thermal gradient, however, is not as severe at the root due to the presence of the disc. An approximate calculation showed that the gradient was reduced by a factor of two. This gives a total radial stress of about 64,000 psi, so the blade is not rupture limited at the predicted temperature.

1b. Airfoil Root at Trailing Edge. At this location the mechanical tensile inertia and steam pressure stresses are counterbalanced by the compressive thermal stresses. During operation, the maximum stress point will occur at the inner surface of the trailing edge cooling duct. Resultant stress will be between 4300 psi and 25,000 psi at 1660° F, depending on wall thickness. Stress-rupture life in excess of 300 hours will be obtained.

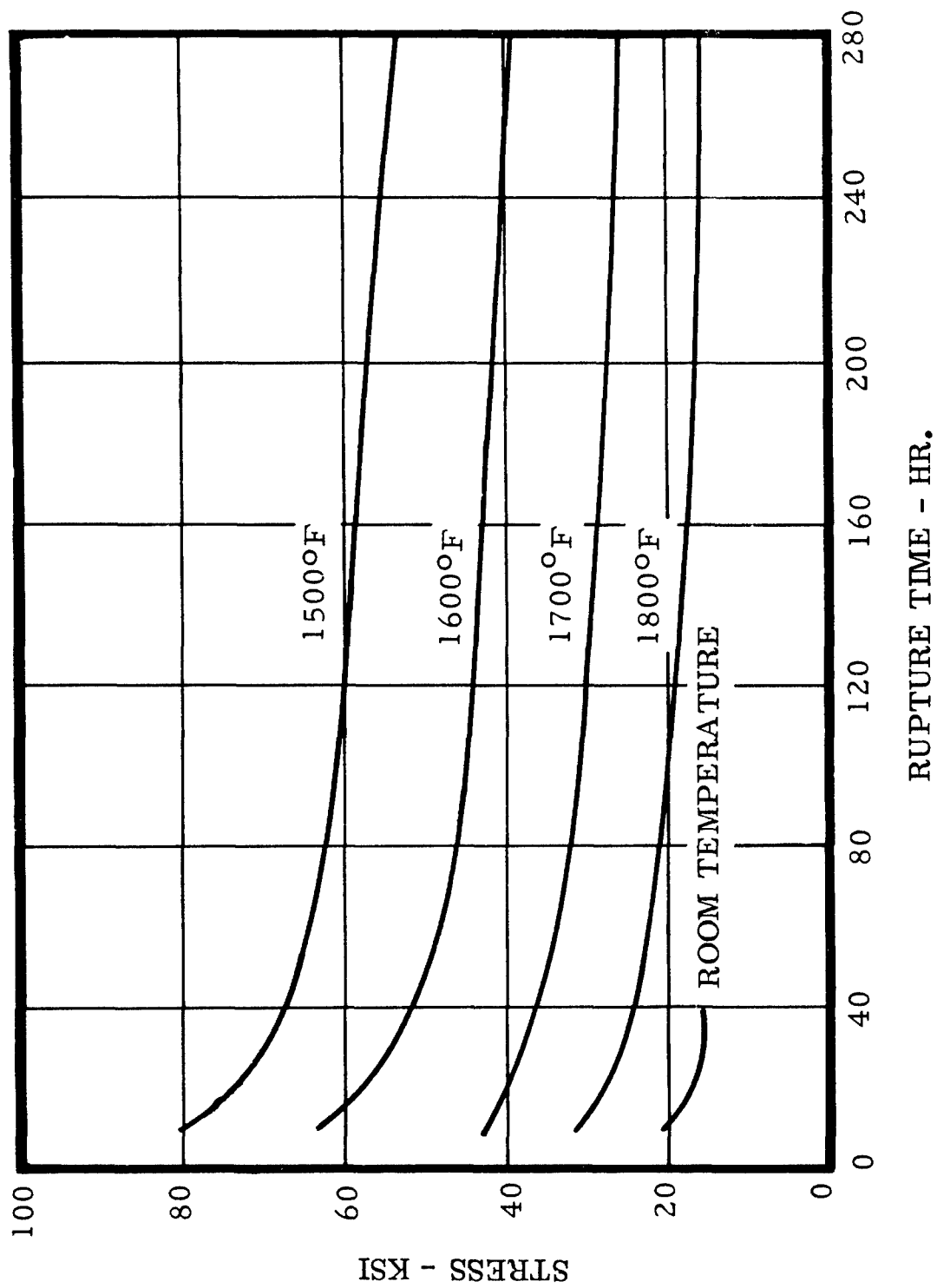


Figure 211. Stress-Rupture Properties - Cast U-700.

2a. Mid-Span, Mid-Chord. At this location the thermal and inertia stresses are additive, resulting in a radial stress of approximately 55,900 psi at 1500° F. A 200-hour stress rupture life could be expected under these conditions. At this location there is a 21,700 psi tensile stress applied at 90 degrees to the radial stress from internal steam pressure. This will result in an equivalent stress of 48,800 psi and approximately a 350-hour stress rupture life.

2b. Mid-Span, Trailing Edge. The compressive thermal stress has been evaluated to be 66,500 psi at the trailing edge for a blade of infinite span. This condition, however, is too conservative in our case. The results of the analysis of Reference 18 show that for a similar case, the thermal stresses in the leading and trailing edges at the mid-span (1/4 chord from the tip) would be reduced by a factor of 2.2. The resultant compressive thermal stress would be 30,000 psi. This stress will be counterbalanced by a 22,000 inertia stress. One will end up with a resultant compressive stress of 8000 psi at 1700° F (not rupture limited).

Blade Growth. Blade growth due to P/A and an average temperature of 1500° F has been plotted in Figure 212.

Root-Tang Connector Design. The root-tang connector has been designed to allow a free expansion to prevent rim crushing. A gap of not less than 0.002 inch between the root and tang faces will exist at fabrication so that the surfaces will not crush the root at design condition. Figure 206 demonstrates the proposed method and Figure 213 shows a detail of a cross section of the pin in place. The design assumes that the load is equally distributed to each pin. Two stress conditions are studied for possible criteria against failure.

1. Average Shearing Stress Method. Average shearing stresses are computed on two surfaces as follows:
 - a. The maximum average shear stress over a pin with a nominal diameter of 0.08 inch is 47,733 psi.
 - b. The average shearing stress over the root and tang areas between pins is 29,817 psi.
2. Average Pin Bearing Stress Method. The average crushing stress on a pin is 51,509 psi.

As a criterion against failure, the methods of 1 and 2 above were used. It was assumed that the shear yield is 0.577 of the tensile yield strength. (Actually, this is true only of the start of yielding; that is, the yield point.) Test results have shown that $T_{ult} = \sigma_{ult}$ at failure.

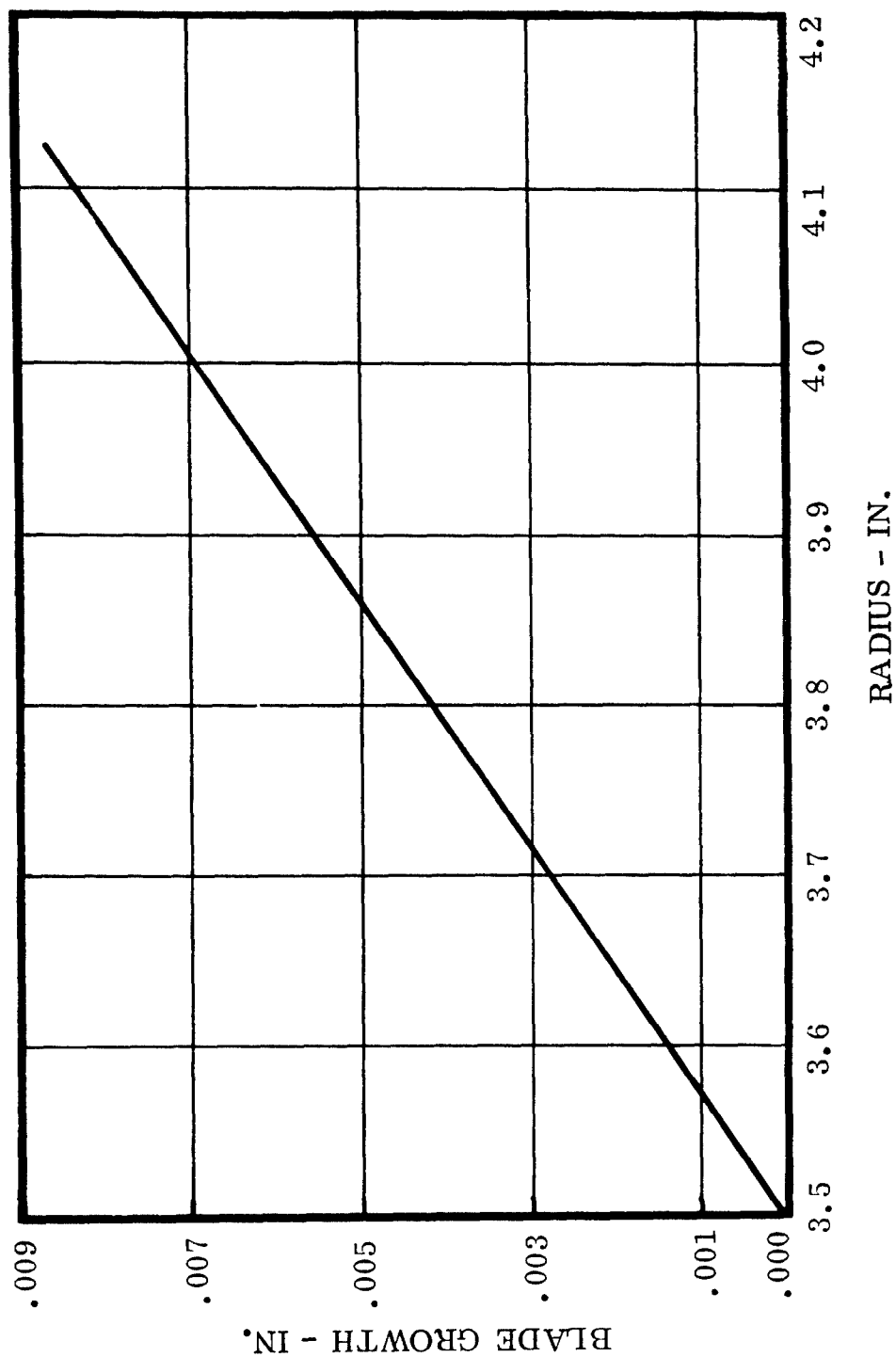


Figure 212. Turbine Rotor Blade - Radial Blade Growth.

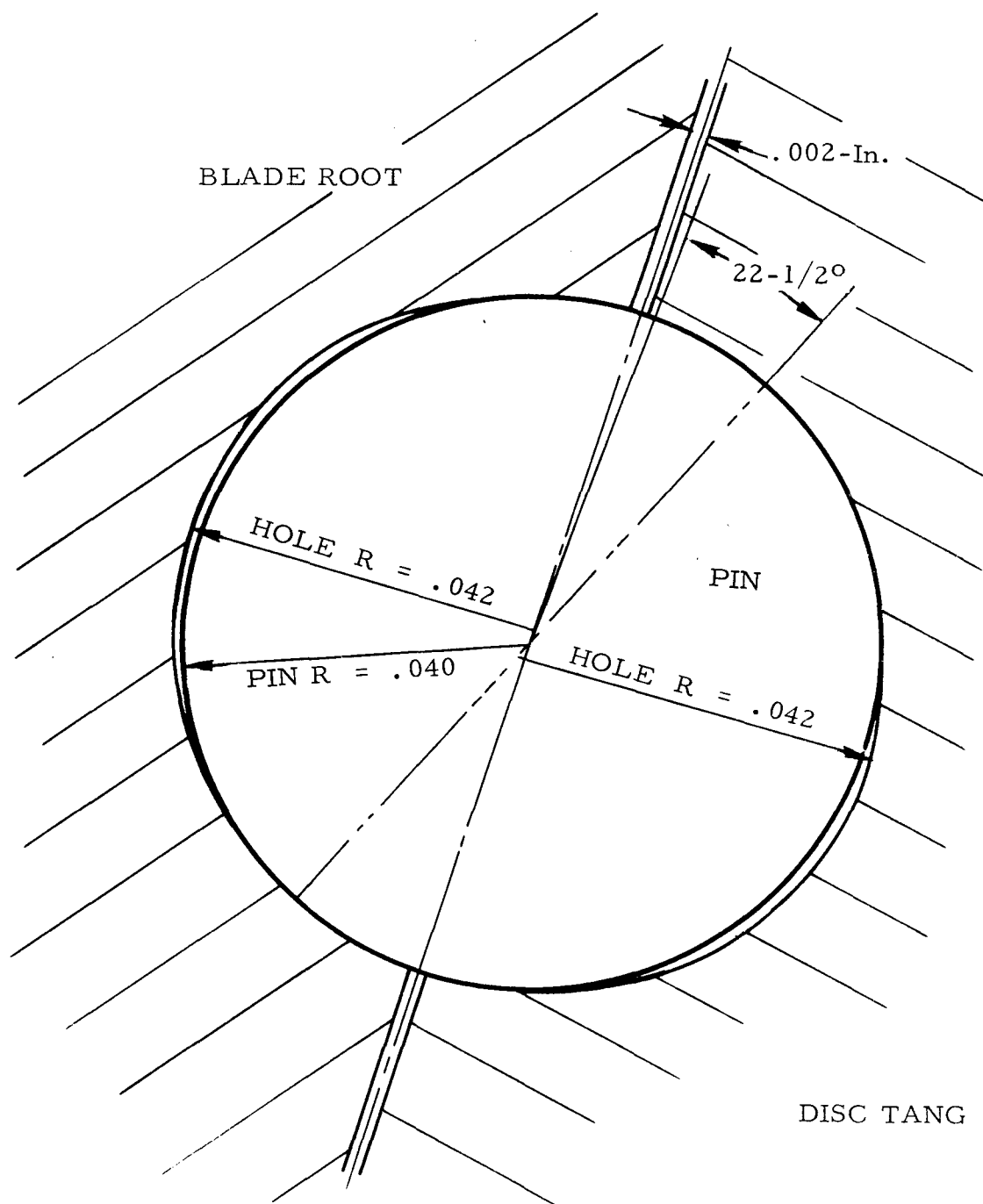


Figure 213. Pin Detail.

Cylinder and Groove Method. The maximum pin temperature will be about 1100°F. The 0.2-percent yield strength at that temperature is at least 113,000 psi; therefore, the shear yield would be 65,201 psi. The root stress is 73.2 percent of the yield under the assumed conditions. The average pin bearing or crushing stress is 44.8 percent of the yield strength.

Thermal Expansion of the Root. An analysis based on temperature computed for the assumption of 20-percent thermal contact between blade root and disc was made with due consideration of the spring values of the pins and shear members of the root and disc tang. It was found that a load of 2152 pounds will be transferred to the outer pin row which is additive to the inertia load. This causes the following changes in stresses at 50,000 rpm:

- | | | |
|---|---|------------|
| 1. Radial stress in disc tang, outer row | = | 64,860 psi |
| 2. Average shear-out stress on outer pins | = | 59,000 psi |
| 3. Average pin crushing stress | = | 72,050 psi |

Conclusions

Blade Airfoil. The gas bending stresses in the airfoil are of no significance in the design. Inertia stresses all have a maximum value of 42,700 psi at the root section (Figure 214). These, in themselves, are not too severe at the blade predicted temperatures.

Localized flexural stresses due to 1500 psi internal steam pressure occur in the cooling passages, with the trailing edge being the most critical point when the wall thickness is on the minimum side of the fabrication tolerance.

The thermal stresses due to the chordwise temperature distribution were calculated utilizing present Continental computer programs assuming an infinite span. A correction was then applied to the calculated stresses to take into account the end effects: namely, the short span and the effect of the disc on the blade root temperature.

It was shown that the remaining thermal stresses will be counterbalanced by the inertia and steam pressure stresses and that the life of the airfoil is about 300 hours.

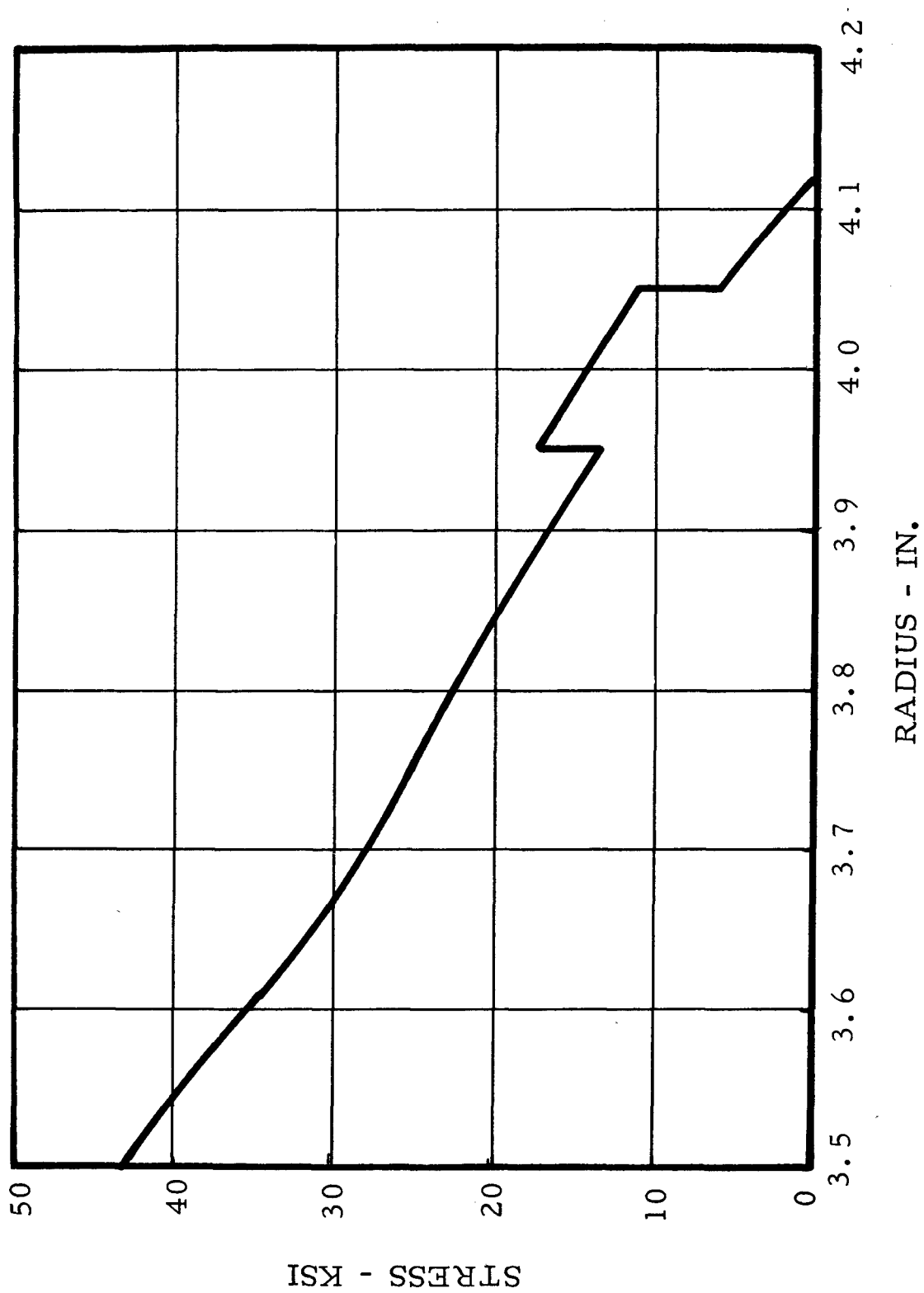


Figure 214. Blade Stresses Due to Centrifugal Loading Only - Modified Blade Core.

Attachment

To prevent failure through rim crushing of the manifold, a minimum 0.002 inch gap will be maintained during assembly between the root and tang surfaces.

The maximum average shear stress over the pin due to inertia loads is 47,700 psi. This value will reach 59,000 psi under the presently assumed thermal gradient between the blade root and disc tang. The maximum pin temperature is assumed to be 1100°F. The yield shear strength will be approximately 67,000 psi for U-700.

The blade attachment has an operating stress from inertia loads of 23,400 psi across the outer two pins. At 1200°F, no difficulty is expected.

Rotor Life

The turbine rotor disc stress analysis shows that the disc is not rupture limited. The turbine blade designed has over 300-hour stress rupture life. After the analytically obtained temperatures have been confirmed experimentally and stress analysis assumptions have been verified, the blade will be reexamined for a life in excess of 1000 hours.

Disc Weight

The weight of the bladed turbine rotor is 14.5 pounds. This figure compares favorably with the combined weight of two lower-pressure-ratio turbine stages, as in the current Continental Model 217 (6 lb/sec). In the Model 217 the weight of the two rotor wheels plus the additional turbine inlet nozzle is equal to approximately 21 pounds.

LABORATORY EVALUATION OF FUEL SEALS AND PINNED ATTACHMENTS

A test program was devised to evaluate the mechanical fuel seal necessary for the pinned design fluid-cooled turbine blade and to substantiate the theoretical stress analysis performed on the pinned design. The fabrication of the rig components, necessary to perform these seal evaluations, also allowed for a review of the manufacturing techniques necessary to make the design.

Testing was conducted at the Continental Research Laboratory, Detroit, Michigan. The rig components, Figures 215 and 216, were built

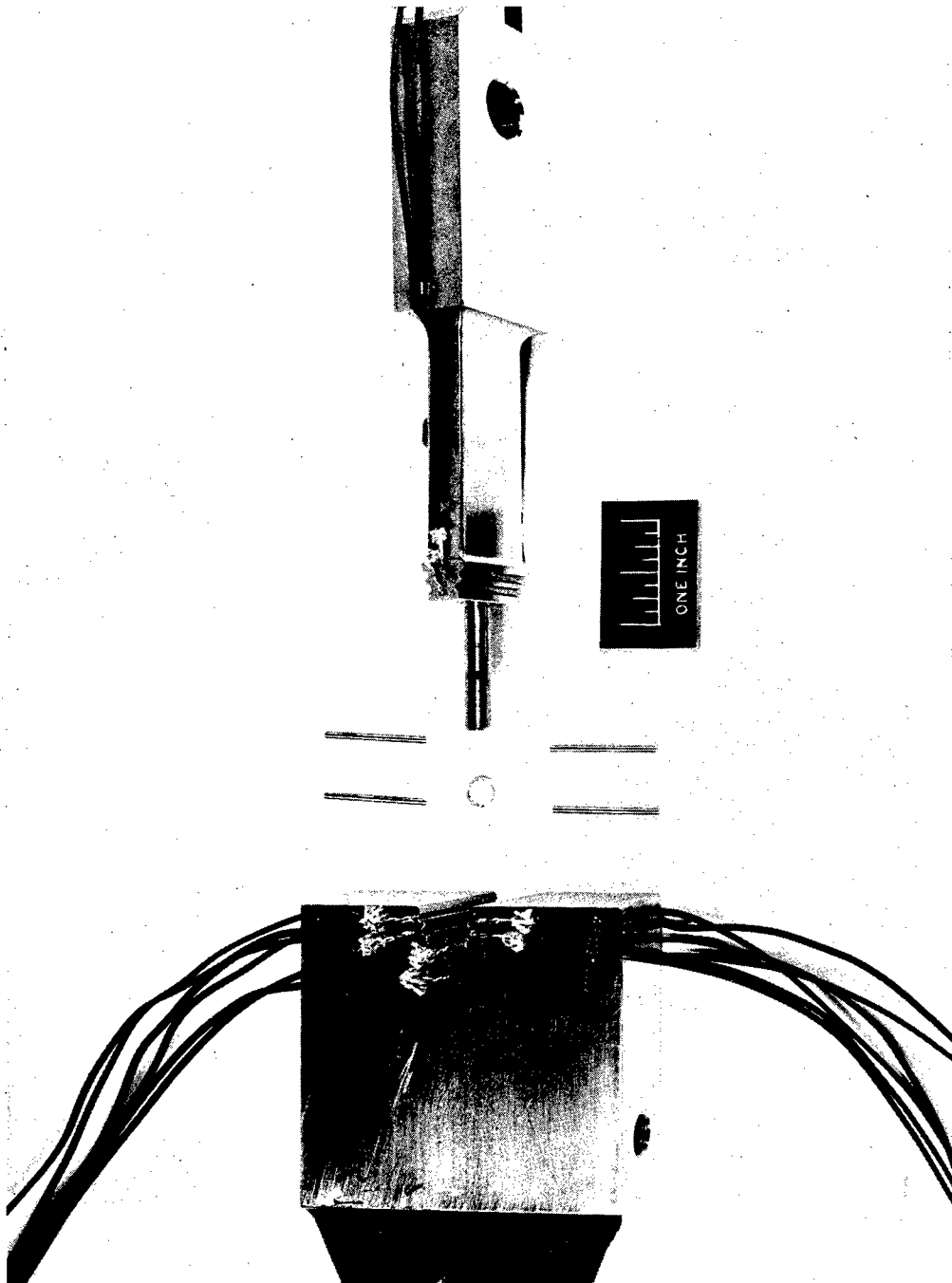


Figure 215. Blade-to-Disc Pinned Attachment and Fuel Seal Test Specimen.

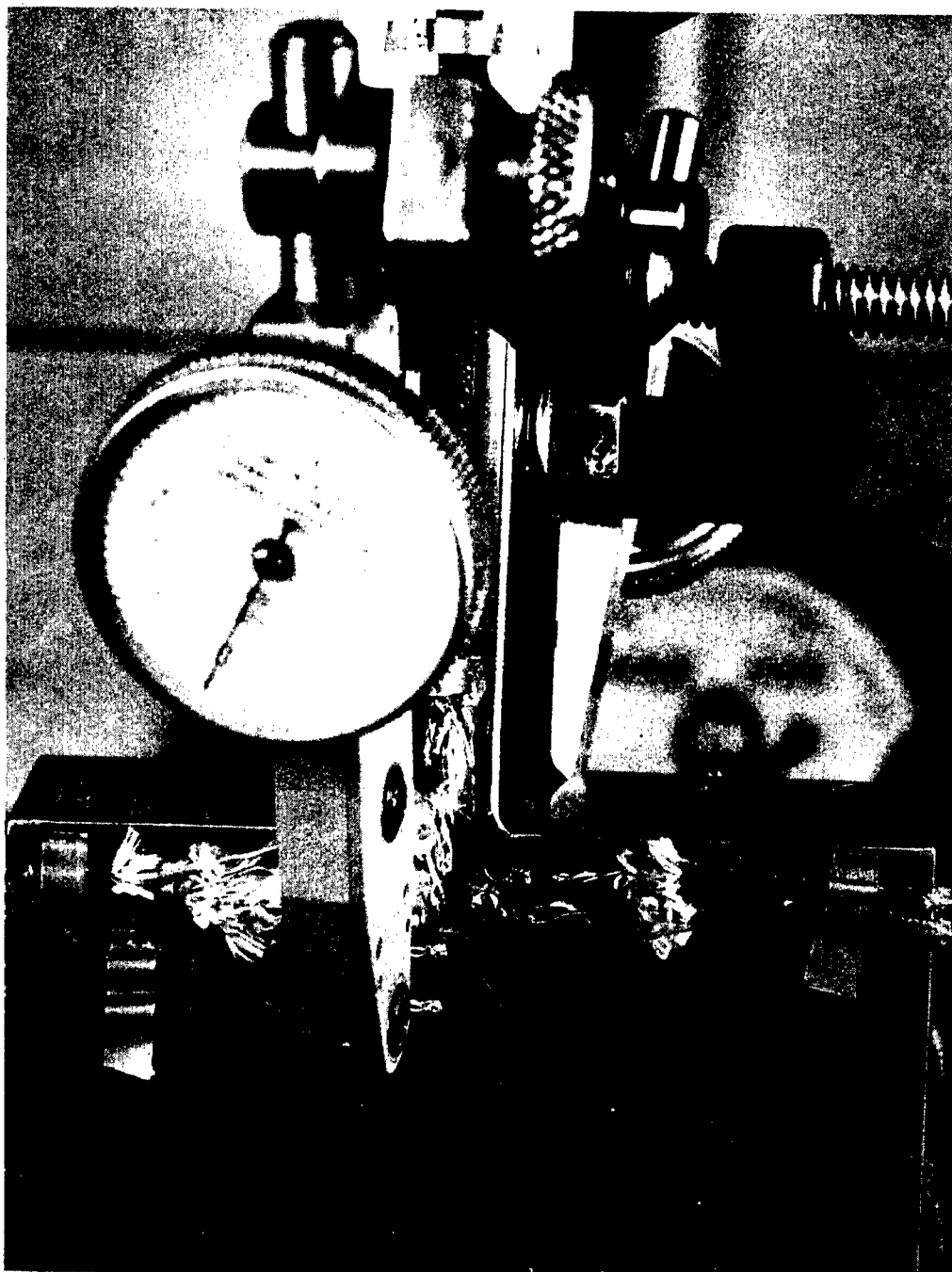


Figure 216. Blade-to-Disc Pinned Attachment Test Fixture With Radial Displacement Indicator.

which represented the pinned blade and turbine wheel hub. Both of these components were identical to the engine designed component in the critical sealing and blade/hub root areas. The blade was extended and was provided with a means of attachment to a hydraulic ram. The assembly was then mounted in a tensile testing stand shown in Figure 217. The fuel pressure on the seal was simulated by hydraulic pressure applied through the turbine rotor hub block.

In the fluid-cooled turbine design a mechanical seal is provided between the turbine rotor disc and turbine blade. This seal must contain the pressure generated by the heat exchanger fluid when it is subjected to high centrifugal loads. This sealing must be accomplished even though adverse thermal expansion, or manufacturing tolerances, plus the blade centrifugal loads imposed, allow the hub/blade sealing surfaces to move apart. Two mechanical seals have successfully fulfilled these sealing requirements. These seals shown in Figures 218 and 219 have demonstrated a 10,000 psi cyclic internal pressure capability. In order to seal against separation of the hub and blade sealing surfaces, the "K" seal was designed to have a response of 0.010 inch and the "W" seal 0.007 inch. Testing to date has shown that the maximum relative movement between the blade and the hub, at the seal, has been only 0.00315 inch.

Both seals were separately compressed, while pressurized to 10,000 psi, to 0.006 inch and then relaxed to 0.0015 inch with no adverse effects. This was a sealing response of 0.0045 inch - which is sufficient to overcome the hub/blade parting imposed by the blade centrifugal loads.

The "W" seal has been simultaneously tested under all three variable conditions of temperature, pressure, and centrifugal load. In this instance the blade temperature was increased until 1100°F was achieved at the blade root opposite the seal cavity. This temperature simulated the maximum calculated temperature expected in the seal area during the turbine wheel soak-down. While the blade was heated the seal was pressurized to 10,000 psi and a simulated centrifugal blade load of 13,000 pounds was imposed on the pins. This test was repeated five times to date with complete sealing in each test.

Seal Testing

Testing of the mechanical seal began with the metal "V" seal, shown in Figure 220. This seal was subjected, by 500 psi increments, to 8500 psi pressure, and under these conditions a positive seal was effected (no leakage) in the simulated blade attachment test fixture. The test rig was disassembled for inspection and the seal was found to have a free height after test of 0.030 inch. This was in effect a permanent set of 0.005 inch, based upon the seal's installed free height of 0.035 inch. A second

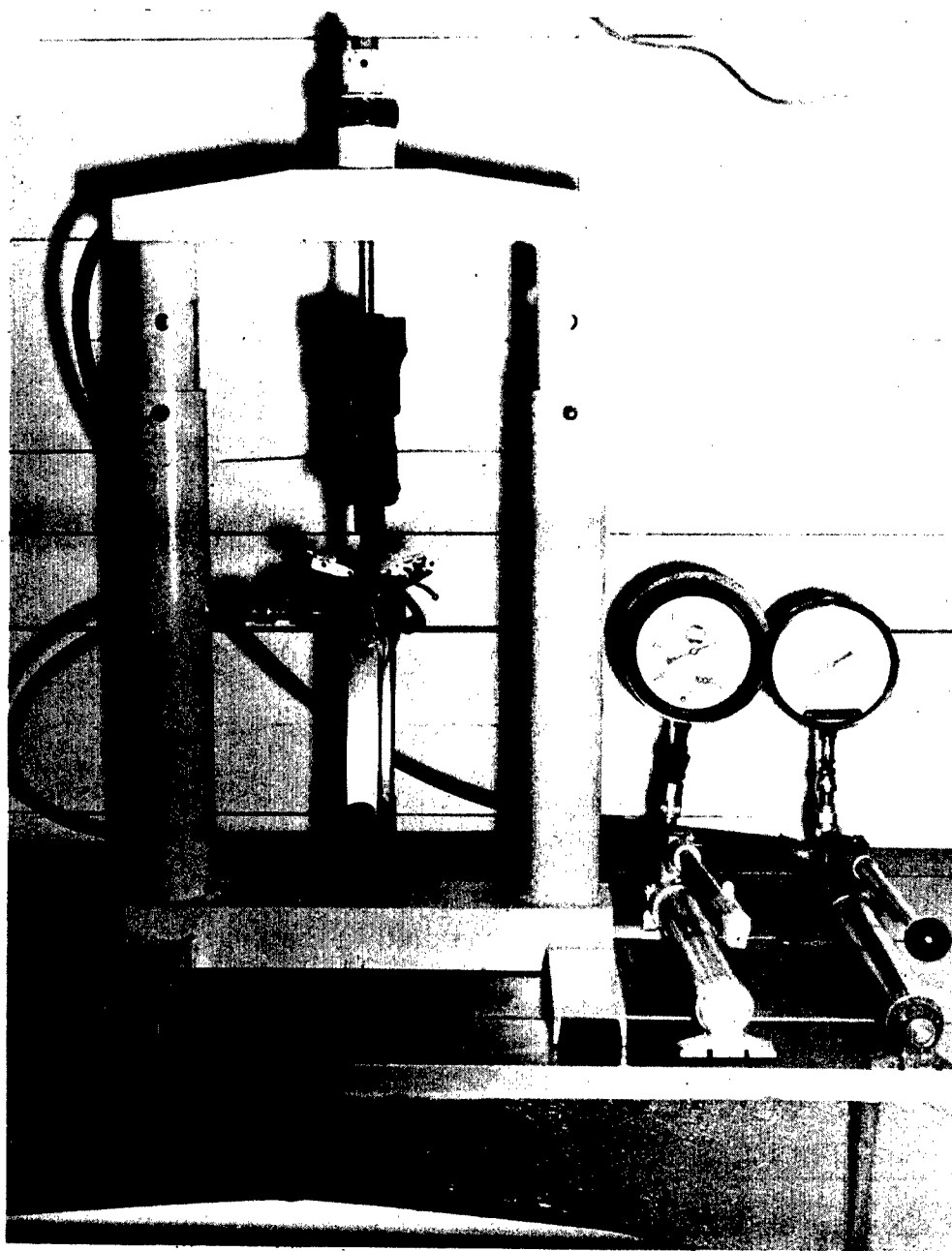
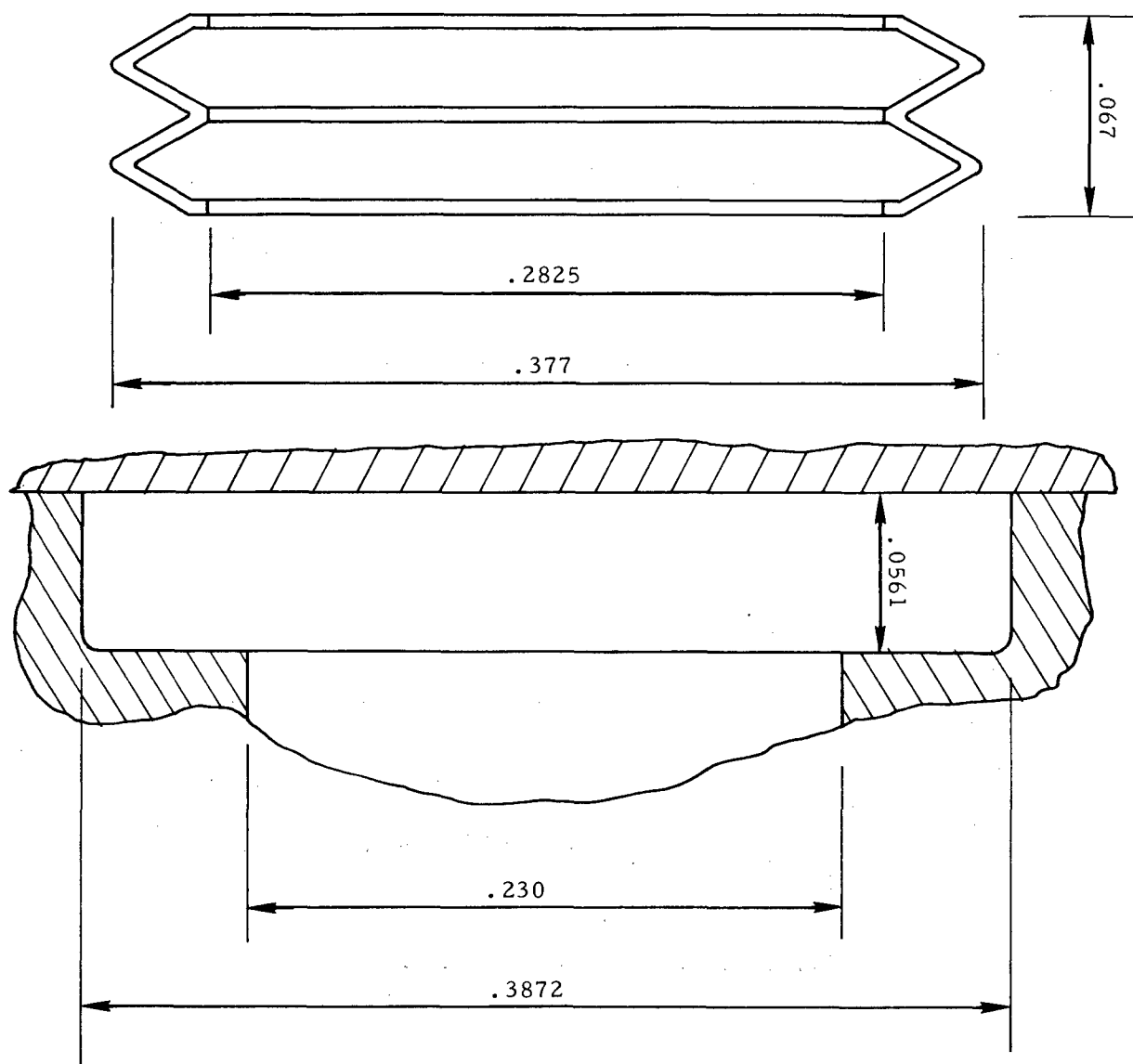


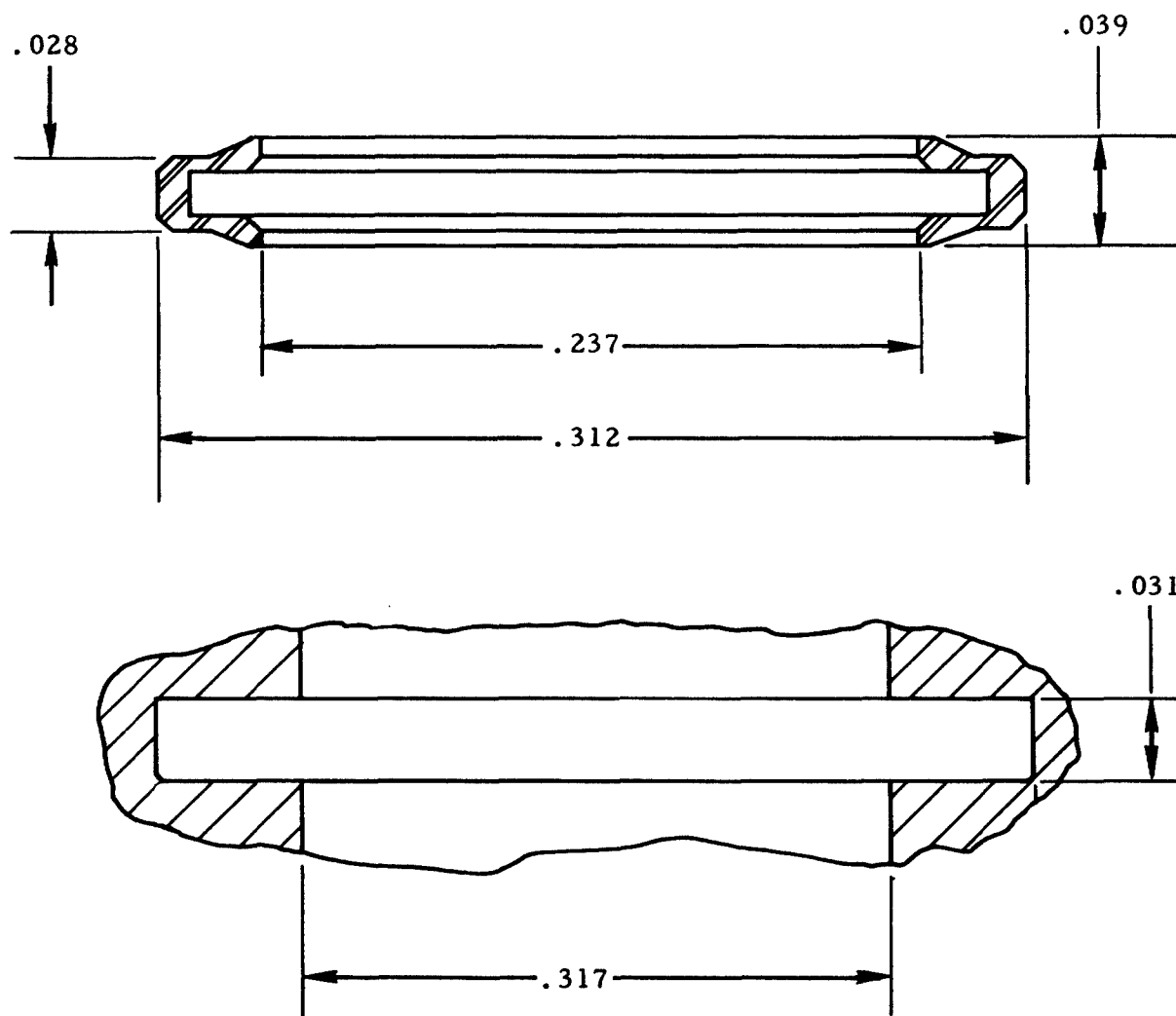
Figure 217. Blade-to-Disc Pinned Attachment Test Fixture With Hydraulic Loading Mechanisms and Dial Indicators.



MATERIAL: INCO X-750

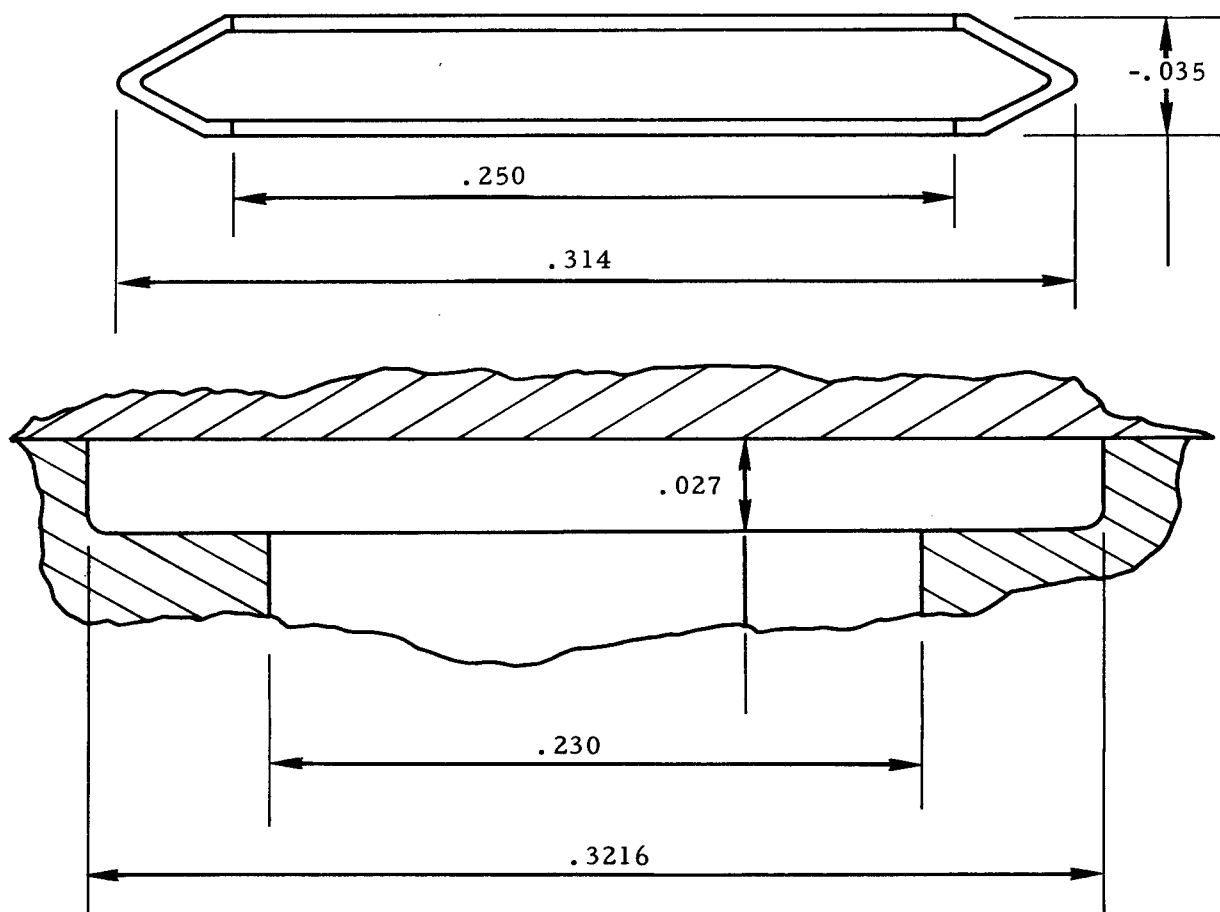
FINISH: GOLD PLATE PER MIL-G-45204-1

Figure 218. Metal "W" Seal.



MATERIAL: INCO X-750
FINISH: GOLD PLATE

Figure 219. Metal 'K' Seal.



MATERIAL: INCO X-750

FINISH: GOLD PLATE - MIL-G-45204-1

Figure 220. Metal "V" Seal.

"V" seal was tested and experienced the same permanent deformation. During the second test a simulated centrifugal load was applied to the blade via a hydraulic ram and the seal was pressurized to 10,000 psi. Under this pressure and a centrifugal load of 3380 pounds, the seal began to leak. It should be noted that the calculated total centrifugal load on all four pins is 13,100 pounds (6400 pounds bottom pins and 6700 pounds top pins). The original seal was reinstalled and again 10,000 psi was applied at the seal. With this pressure, leakage occurred at a centrifugal load of 4150 pounds. Dial gage measurements showed that the blade to hub relative movement, under a load of 7200 pounds, was 0.0026 inch. Data presented in Figure 221 indicate that this movement was more than could be tolerated by the "V" seal. In Figure 221 it can be seen that the seal has an effective response (recovery within elastic limit) of 0.0025 to 0.003 inch.

A fourth seal was tested with only the two upper pins installed in the test fixture. A centrifugal load, in increments of 1000 pounds, was applied and at the 14,000 - 15,000 pound load point, the pins sheared (see Figures 222 through 225). This was over twice the load that these pins would experience in operation, and it was concluded that an adequate safety factor had been designed into the system.

An additional test was conducted with the "V" seal where the diametral fit between cavity and seal was made line to line. In this instance, the sealing edge was found buckled after test, and a further examination and calculations based on geometrical considerations showed that the material loadings were as high as 1,500,000 psi (elastic), which resulted in seal buckling. From this group of tests on the "V" seal, it was concluded that a response of more than 0.0025 inch to 0.0030 inch would be needed to achieve positive sealing and that the seal did require a particular clearance between it and its housing to keep it from buckling.

In order to achieve greater seal response - where the seal would follow the movement between the hub and blade - a second type seal was used. This seal, shown in Figure 226, was designed to have a repeated response of 0.004 inch. The first test of this seal, using only the bottom two pins with the cavity/seal tolerances as recommended by the vendor and shown in Figure 226, allowed for 7200 psi fuel pressure and a centrifugal load of 4500 pounds. This seal also had a 10,000 psi capability; however, at centrifugal loads above 4500 pounds, leakage would occur. A movement of 0.0315 inch was measured between the hub and blade. This movement, too, was too large for proper sealing, even though the seal had a reported 0.004 inch capability. Additional tests were conducted with this type seal wherein the "fits" between seal and cavity were changed from the original line to a line of a 0.003 inch diametrical clearance. Leakage occurred at a load of 4500 pounds and at a pressure of 8000 psi.

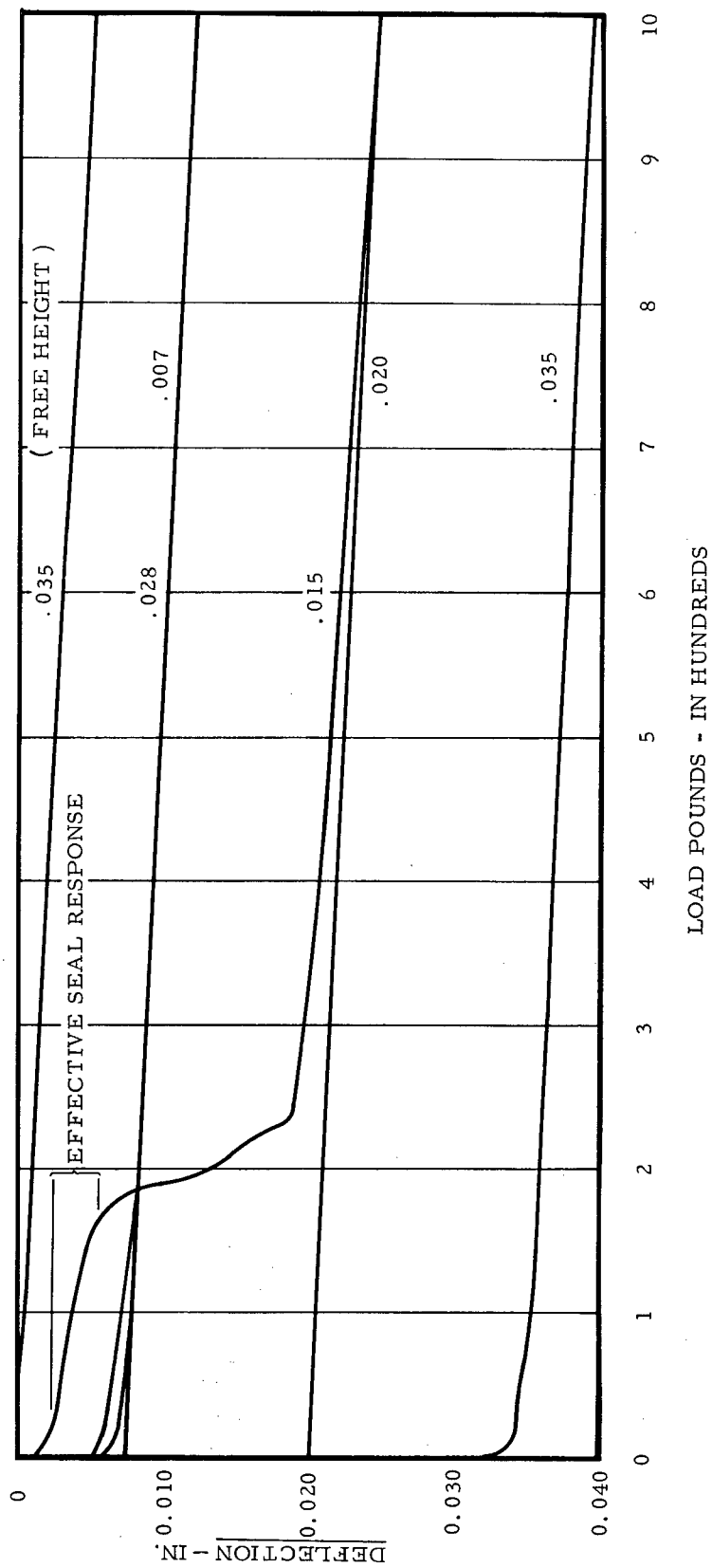


Figure 221. "V" Seal - Load Versus Response.



Figure 222. Blade Attachment - Test Specimen.

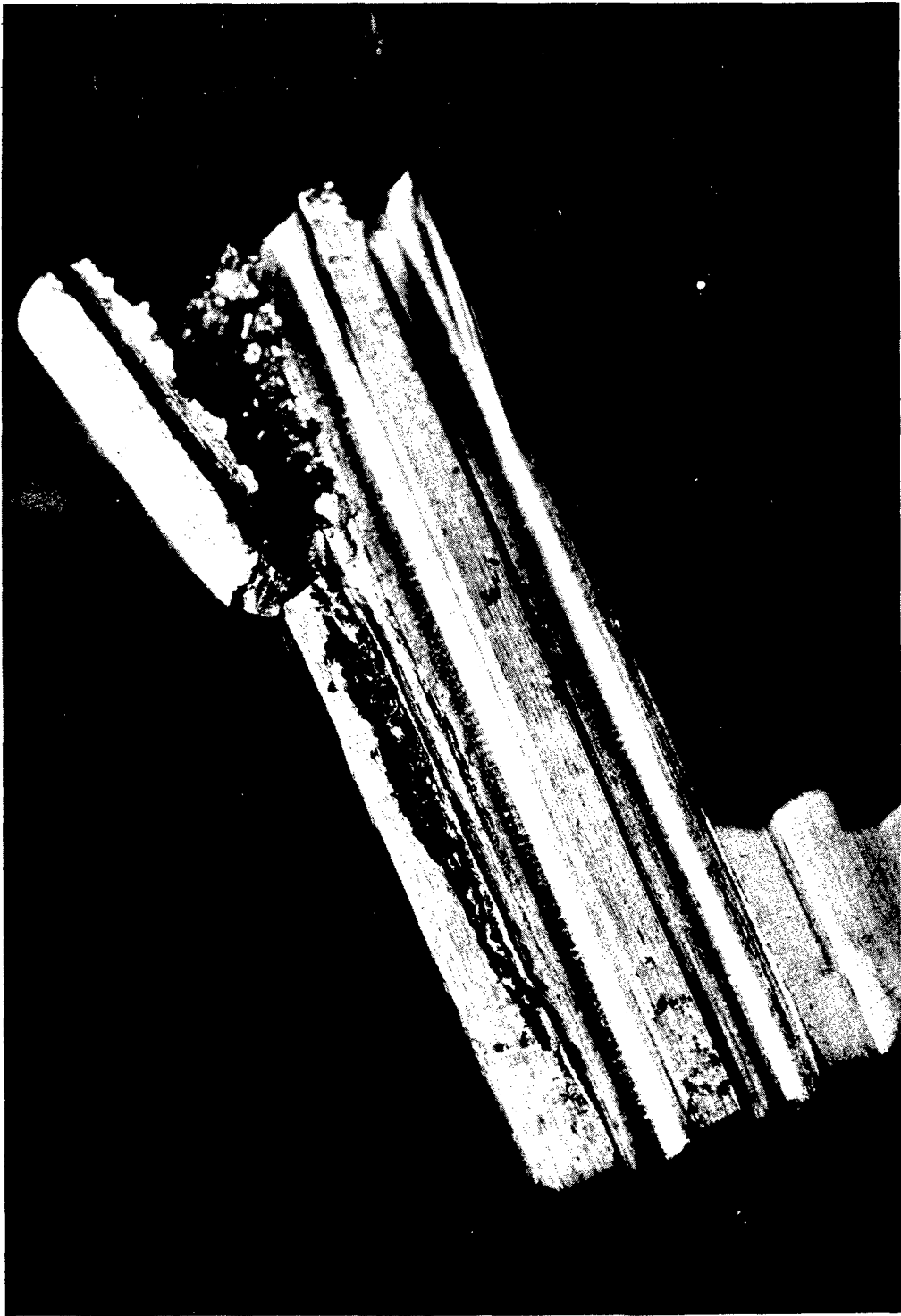


Figure 223. Fluid-Cooled Rotor Hub - Test Specimen.

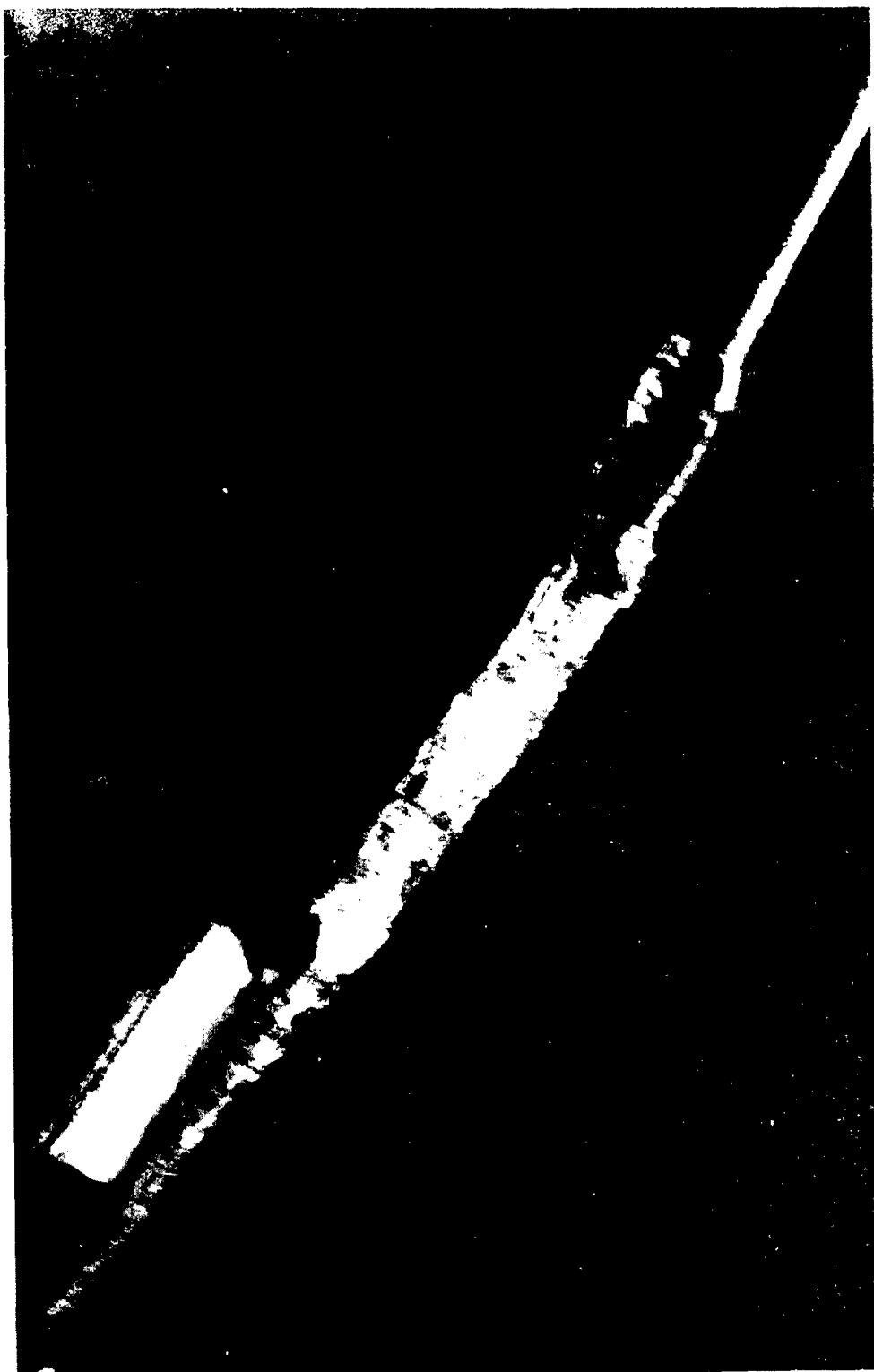


Figure 224. Left Pin - Fluid-Cooled Turbine Blade - Test Specimen.

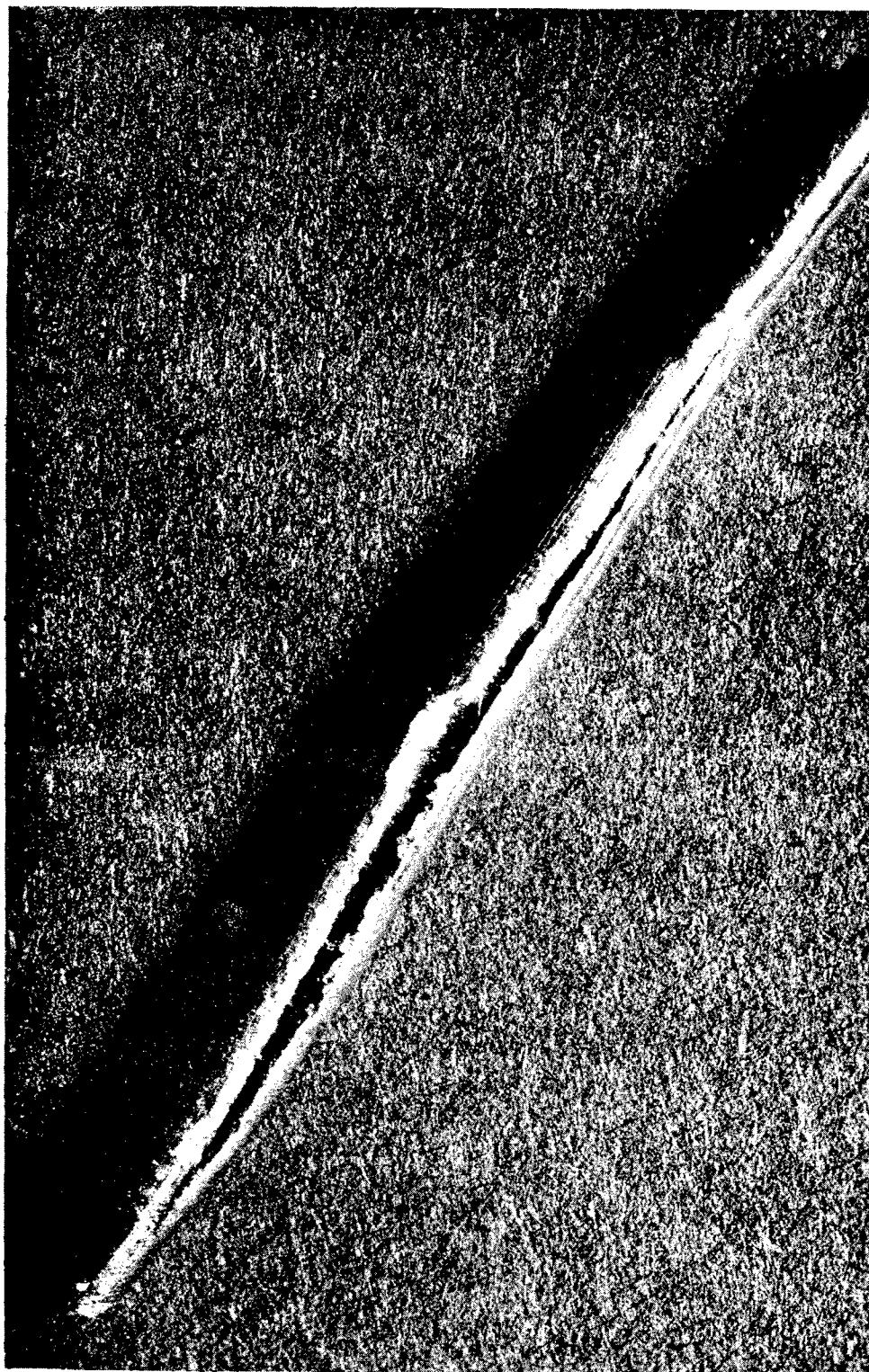


Figure 225. Right Pin - Fluid-Cooled Turbine Blade - Test Specimen.

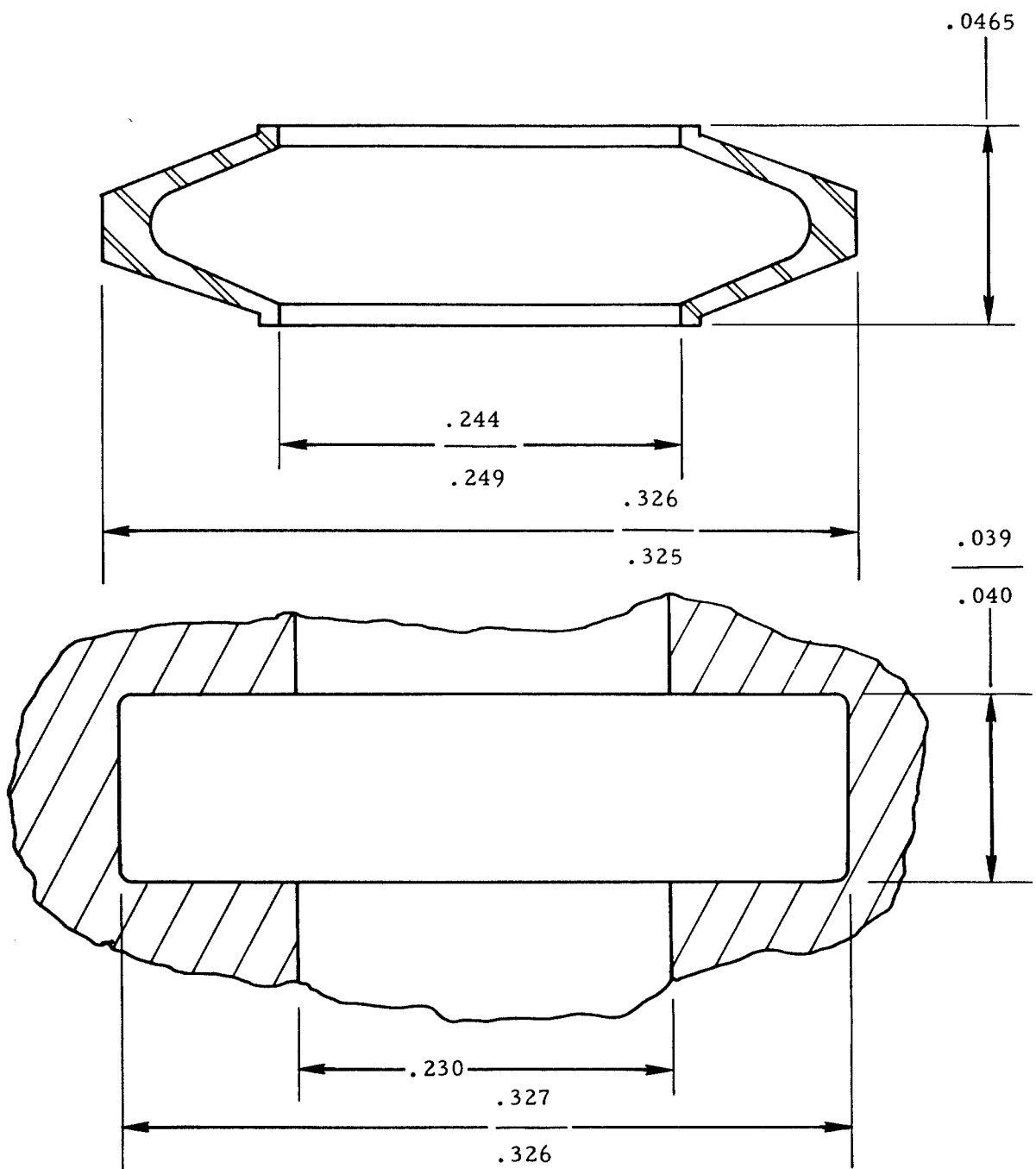


Figure 226. Metal "V" Seal - Revised.

The diametrical clearance was increased to 0.0085 inch, and with all four pins installed a pressure load of 10,000 psi and a centrifugal load of 9000 pounds was achieved before leakage occurred. The movement between hub and blade was measured as 0.0034 inch in this test. Again, it was concluded that the movement was too great to effect total sealing.

It was apparent that "off-the-shelf" seals, applicable to the pinned fluid-cooled turbine blade, did not have the required response. Therefore, a seal was designed and fabricated which could be continuously flexed 0.007 inch. This "W" seal, shown in Figure 218, had a free height of 0.067 inch and an O.D. of 0.377 inch. The seal I.D. was made in error to 0.2825 inch rather than the required 0.250 inch. In order to test this seal, a second test fixture, shown in Figure 227, was built. This fixture has an advantage over the simulated turbine blade/hub rig in that it allows for observation of the seal while it is being pressurized and has a screw mechanism which is capable of flexing the seal to known quantities.

The "W" seal was installed in this test fixture with a compression of 0.010 inch (this compression was recommended by the vendor in order to get a 0.007 inch response from the seal) and was pressurized to 10,000 psi. Upon relaxing, the seal began to leak immediately. The seal was examined and it was found that the gold overlay was separated from the parent Inconel X seal material. It was determined that the gold was applied to too great a thickness, and it was further concluded that this might not allow the seal to respond properly. A second "W" seal design without this gold overlay and with a sharp sealing edge was tested. This seal was compressed 0.006 inch and pressurized to 10,000 psi. The compression was relaxed (simulating the centrifugal action of the turbine blade on the seal) by 0.0045 inch until only 0.0015 inch compression remained and complete sealing was achieved. A second seal of this same configuration was tested where the compression was again 0.006 inch and again under a 10,000 psi pressure. In this test, however, the compression was relaxed; the total initial 0.006 inch compression and the sealing surfaces were moved an additional 0.004 inch apart. No leakage was observed.

This seal was then cycled 50 times in this manner:

1. A maximum compression of 0.006 inch was applied.
2. The seal was then pressurized to 10,000 psi.
3. The seal pressure was dropped to zero.
4. While the seal pressure was being dropped to zero, the compression was relaxed to 0.0015 inch.

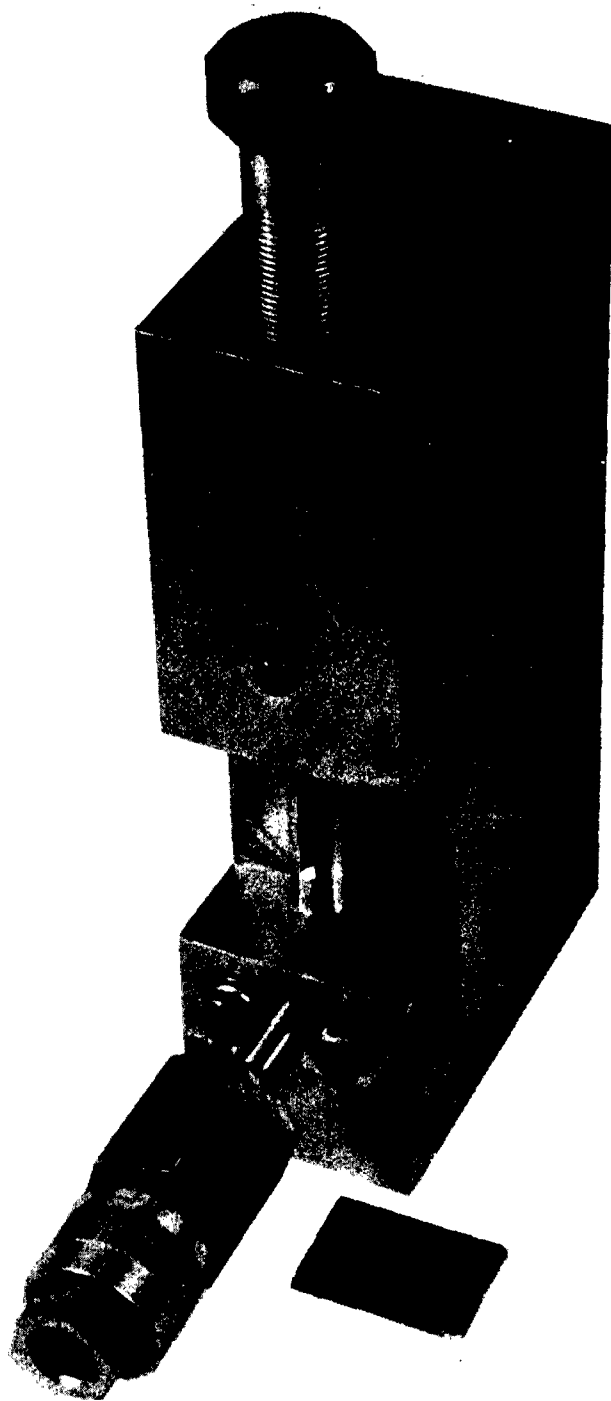


Figure 227. Fuel Seal Test Specimen.

5. With the 0.0015 inch compression, the seal was pressurized to 10,000 psi.
6. The seal pressure was dropped to zero.
7. While the pressure was being dropped to zero, the compression was increased to 0.006 inch.
8. Steps 1 through 7 were repeated 50 times.

A "K" seal shown in Figure 219 was also tested utilizing the same procedure as the last-mentioned "W" seal. The seal, however, was relaxed the total compression dimension of 1.006 inch and was still capable of sealing. After completing 26 cycles, failure occurred. A second "K" seal successfully completed 50 flexure/pressure cycles, as mentioned for the "W" seal with 0.045 inch cyclic deflection.

Conclusions and Recommendations

Table XXIV identifies all of the seal testing conducted to date. From these tests it has been concluded that the mechanical seal (as per the "W" unplated sharp edge seal or "K" seal) will work for the fluid-cooled turbine blade. Additional testing should be conducted on this sealing arrangement in the blade/hub rig and at temperature, in the event that a refinement of the seal is needed. Spin testing of the seal to subject it to actual "g" loads should also be undertaken.

SELECTION OF ROTOR COOLING SYSTEM DESIGN

The pinned attachment with mechanical fuel seal using individual coolant to fuel heat exchangers in the disc for each blade has been selected for the following reasons:

1. Structural design analysis shows that it is acceptable.
2. Tests of the attachment show that it will withstand design loads at temperature.
3. An acceptable mechanical fuel seal has been developed on test.
4. This configuration allows replacement of individual blades.
5. The complete fuel system is accessible for examination and mechanical cleaning if necessary in the event of inadvertent fuel overheating.

TABLE XXIV SEAL TEST DATA									
Test Date	Seal		Seal Cavity in.	Seal Cavity Depth in.	Relative Movement Hub/Blade in.	No. of Pins	Test Conditions		
	Free Height Before Test in.	Free Height After Test in.					Seal Pr. (psi)	Centri. Load (lb)	Seal ** Temp.
"W" Seal 3-20-65	N. R. *	.030	.314 ±.0005	.027	N. R.	4	10,000		Room
"W" Seal 3-29-65	.035	.030	.314 ±.0005	.027	N. R.	4	10,000	3,380	Room
"W" Seal	.030	.030	.314 ±.0005	.027	.0026	4	10,000	4,150	Room
"W" Seal 4-9-65	.035	.030	.314 ±.0005	.027	.00325	2 Bottom	5,000	4,500	Room
"W" Seal 4-9-65	.030	.030	.314 ±.0005	.027	.0022	2 Top	6,000	4,500	Room
"W" Seal 4-22-65	.035	.030	.314 ±.0005	.027	.0046	4	5,000	7,050	Room
"W" Seal 5-6-65	.035	.031	.314 ±.0005	.030	N. R.	2 Bottom	Zero	300	Room
"W" Seal 5-7-65	.035	.0319	.3125	.030	N. R.	2 Bottom	2,000	Zero	Room
"W" Seal	N. R.	.0319	.3130/ .3133	.030 .0009	N. R.	2 Bottom	7,000	Zero	Room
"V" Seal 5-25-65	.048	.0413/ .0420	.3252	.039	N. R.	2 Bottom	7,200	4,500	Room
"V" Seal	.0413/ .0420	.0413/ .0420	Mach to fit cavity	.039 ±.0005	N. R.	2 Bottom	1,000	600	Room
"V" Seal 5-26-65	.0475	.0425/ .043	Mach to fit cavity	.039 ±.0005	.0028	2 Bottom	8,000	4,500	Room
"V" Seal 6-2-65	.0455	.0420/ .0428	.3265	.0397/ .0386	.0016	2 Bottom	7,000	3,000	Room

* NOT RECORDED

TABLE XXIV - Continued

Test Date	Seal		Seal Cavity in.	Seal Cavity Depth in.	Relative Movement Hub/Blade in.	No. of Pins	Test Conditions		
	Free Height Before Test in.	Free Height After Test in.					Seal Pr. (psi)	Centri. Load (lb)	Seal ** Temp.
"V" Seal 6-3-65	.046	.0425/.0415	.326	.004 .0397/ .0386	.0018/ .0008	4	10,000	3,000	Room
"V" Seal 6-6-65	.0463	.0425/.0430	.326	.0085 .0397/ .0386	.0034/ .0024	4	10,000	9,000	Room
"W" Seal 6-10-65	.0672	N. R.	.3770	.0102 .0560	.00238/ .00176	2 Top	6,000	450	Room
"W" Seal 6-10-65	.0670	N. R.	.3760	.0112 .0560	N. R.	2 Top	Zero	1,500	Room
"W" Seal 6-17-65	.0670	.0593/.0546	.3770	-	.0014	-	8,000	-	Room
"W" Seal 6-17-65	.0671	N. R.	.3770	-	.0022	-	10,000	-	Room
"W" Seal 6-21-65	.0789	.077	.3754	-	.0044	-	10,000	-	Room
"W" Seal 6-21-65	.07861 .0789	.0783/ .0788	.3752	-	.010	-	10,000	-	Room
"W" Seal 6-22-65	.077	N. R.	.3752	-	.0045	-	10,000	-	Room
"W" Seal 6-22-65	.0667	N. R.	.3765	-	.002	-	10,000	-	Room
"K" Seal 6-28-65	.038	N. R.	.3132	-	.006	-	10,000	-	Room
"K" Seal	.0385	N. R.	.3132	-	.0045	-	10,000	-	Room
"W" Seal 7-1-65	.0657	N. R.	.3787	-	.002	-	10,000	-	Room

TABLE XXIV - Continued

Test Date	Seal		Seal Cavity in.	Seal Cavity Depth in.	Relative Movement Hub/Blade in.	No. of Pins	Test Conditions		
	Free Height Before Test in.	Free Height After Test in.	O.D. in.				Seal Pr. (psi)	Centri. Load (lb)	Seal ** Temp.
"W" Seal 7-6-65	.0646/ .0650	.057/ .058	.3784	.00661 .0070	.002	-	10,000	-	Room
"W" Seal 7-6-65	N.R.	N.R.	N.R.	N.R.	.002	-	10,000	-	Room
"W" Seal 7-6-65	.0736	.071	.3752	.007	.010	-	10,000	-	Room
"W" Seal 7-8-65	.077	N.R.	.3754	.0126	.0045	4	-	-	1000° F
"W" Seal 7-9-65	.077	N.R.	.3754	.0126	.0045	4	10,000	13,000	1000° F
"W" Seal 7-9-65	.077	.0733	.3754	.0126	.0045	4	10,000	13,000	1000° F
"W" Seal 7-14-65	.0733	N.R.	.3754	.0126	.004	4	10,000	13,000	1000° F

** MEASURED @ BLADE ROOT (SKIN)

TURBINE NOZZLE/COMBUSTOR DESIGN STUDIES

This section discusses the turbine inlet nozzle and combustor design studies.

A number of turbine inlet nozzle designs are described, nozzle and shroud metal temperature are computed, and the nozzle structural design based on experimentally determined nozzle and shroud temperatures is presented.

The combustor design is outlined with the computed port arrangement to give acceptable operation.

NOZZLE DESIGNS CONSIDERED

The turbine inlet nozzle designs considered are categorized as segmented (Figures 228 through 231) and full-ring designs (Figures 232 through 235) and are described below.

Segmented Configurations

The segmented nozzle designs consist of a ring of six four-vane nozzle segments supported at the outside by two rings engaging slots in nozzle shrouds. The segments in turn support the turbine diaphragm, seals, and inner combustor. A detail of a segment is shown in Figure 236. This is as shown in Configuration 1 (Figure 228).

Segments for Configurations 1, 2, 3, and 4 (Figures 228 through 231) are cast using high temperature casting alloys such as Inco 713C low carbon, low iron, or SM 302. Segments are not welded, so difficult-to-weld higher temperature materials can be used.

Configuration 4 (Figure 231) shows a segmented turbine nozzle. The segments are supported at the outside by two rings that engage slots in the front and rear of the shroud. The diameter of the nozzle is controlled by the two rings with thermal expansion of the segments taken up by "free" circumferential growth. The inner seals and turbine diaphragm are supported by a radial tongue and groove joint. This joint has minimal radial clearance on the pilot diameter while cold, closing up to essentially line-to-line while hot in order to maintain seal concentricity. As with the outer rings and slots, the inner joint allows free circumferential growth of the segments to minimize thermal stress. Improved sealing and vibration damping could be achieved by inserting a seal ring or packing in the

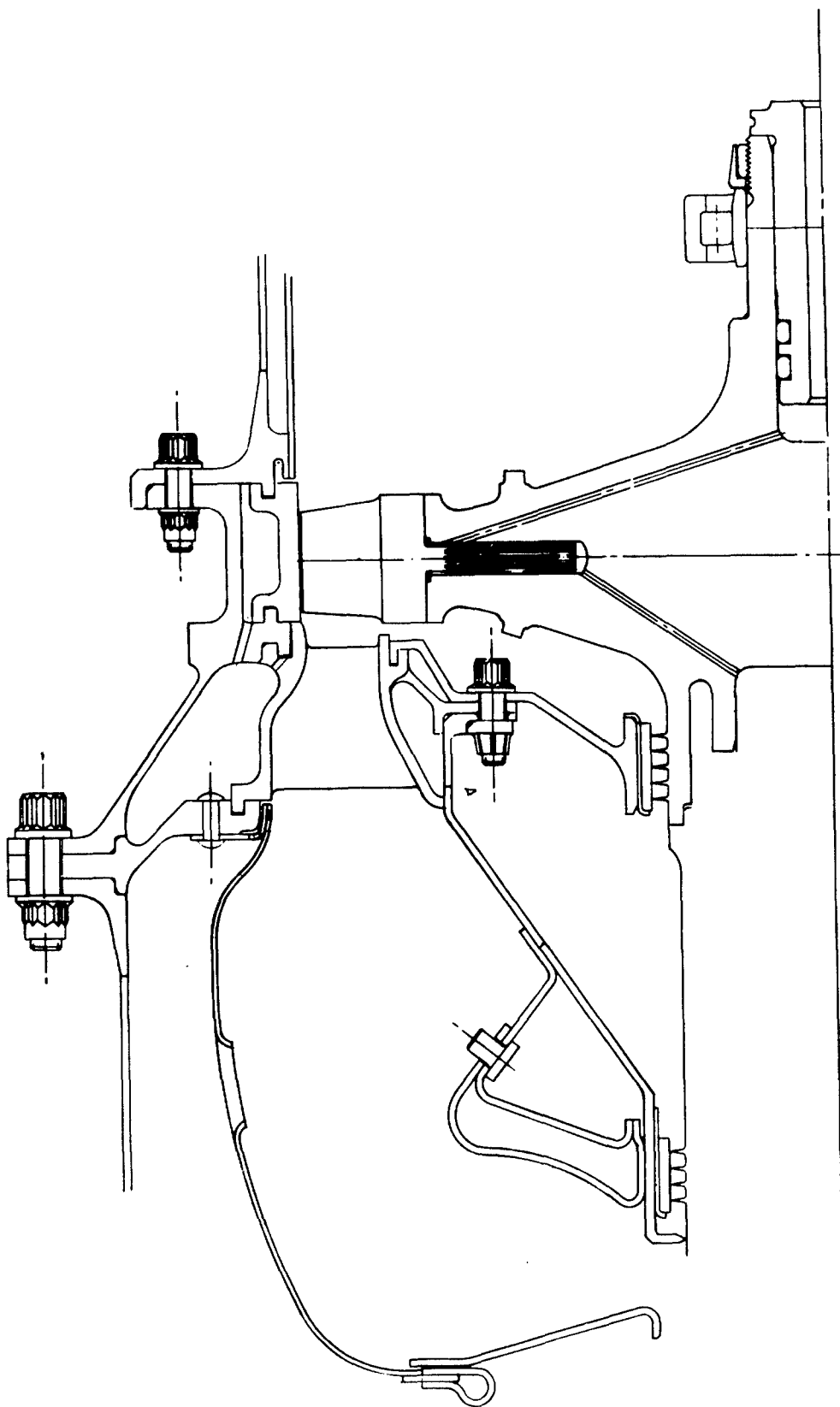


Figure 228. Segmented Nozzle Design - Configuration 1.

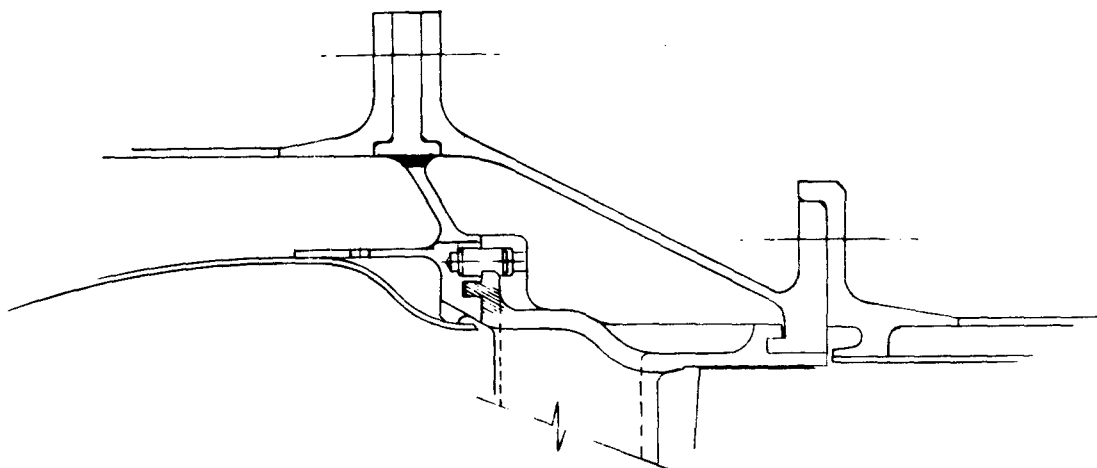


Figure 229. Segmented Nozzle Design - Configuration 2.

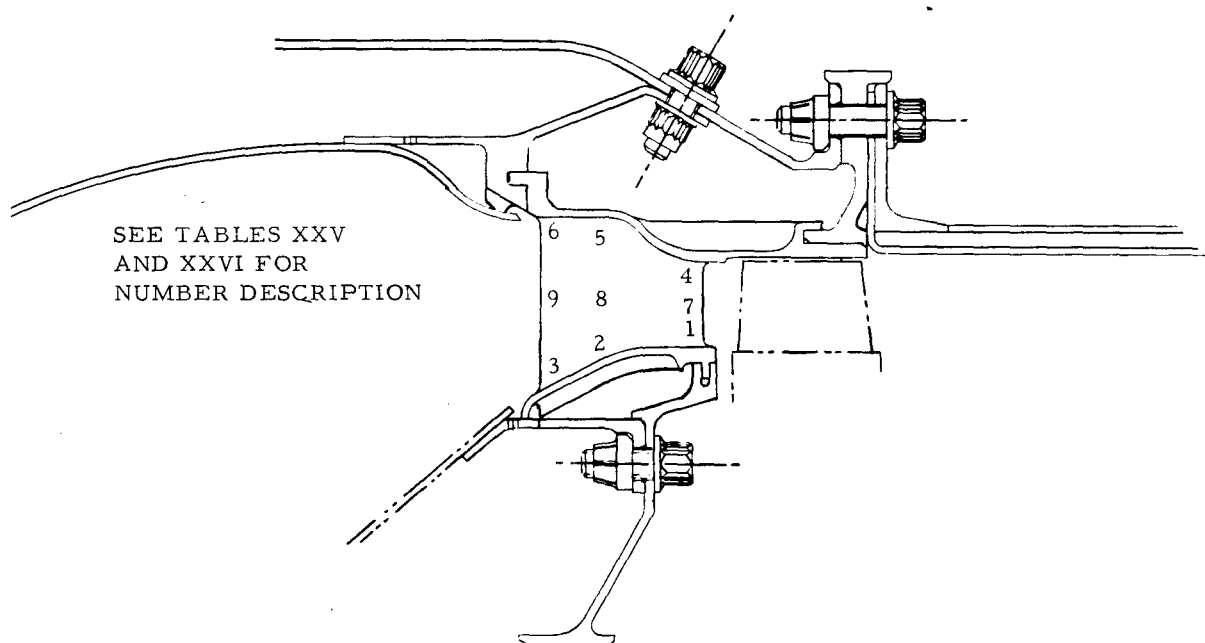


Figure 230. Segmented Nozzle Design - Configuration 3.

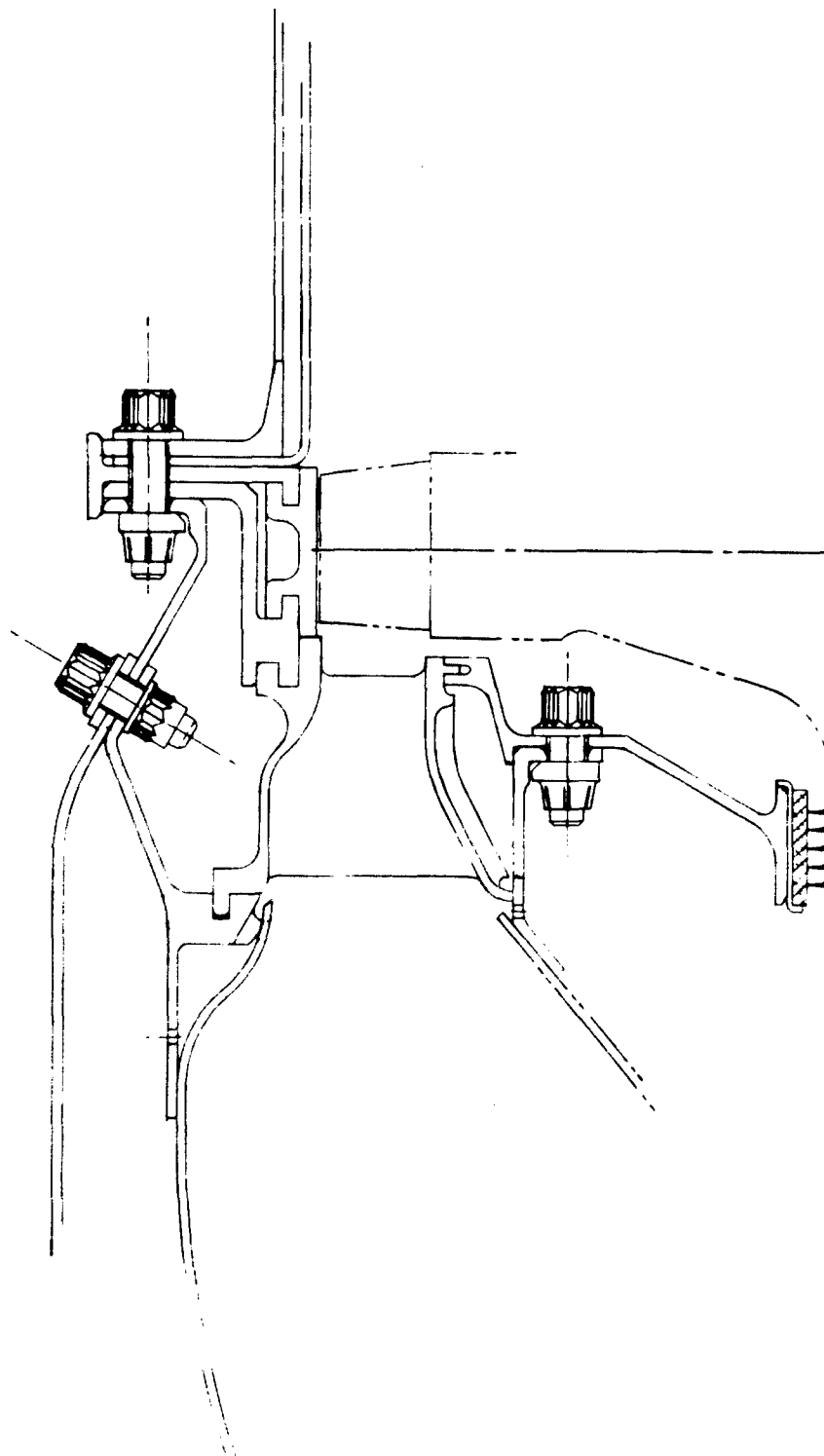


Figure 231. Segmented Nozzle Design - Configuration 4.

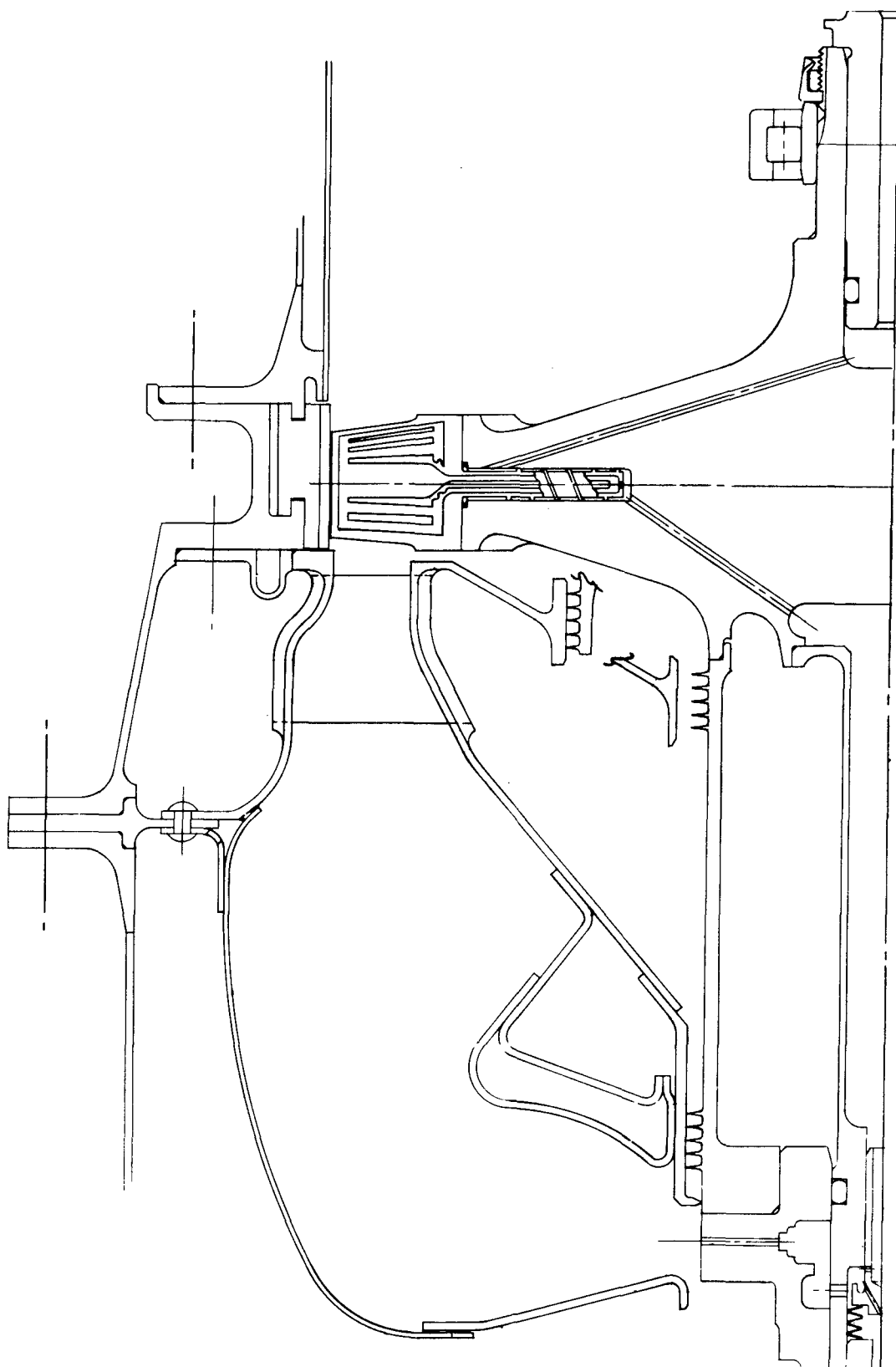


Figure 232. Continuous Ring Nozzle Design - Configuration 5.

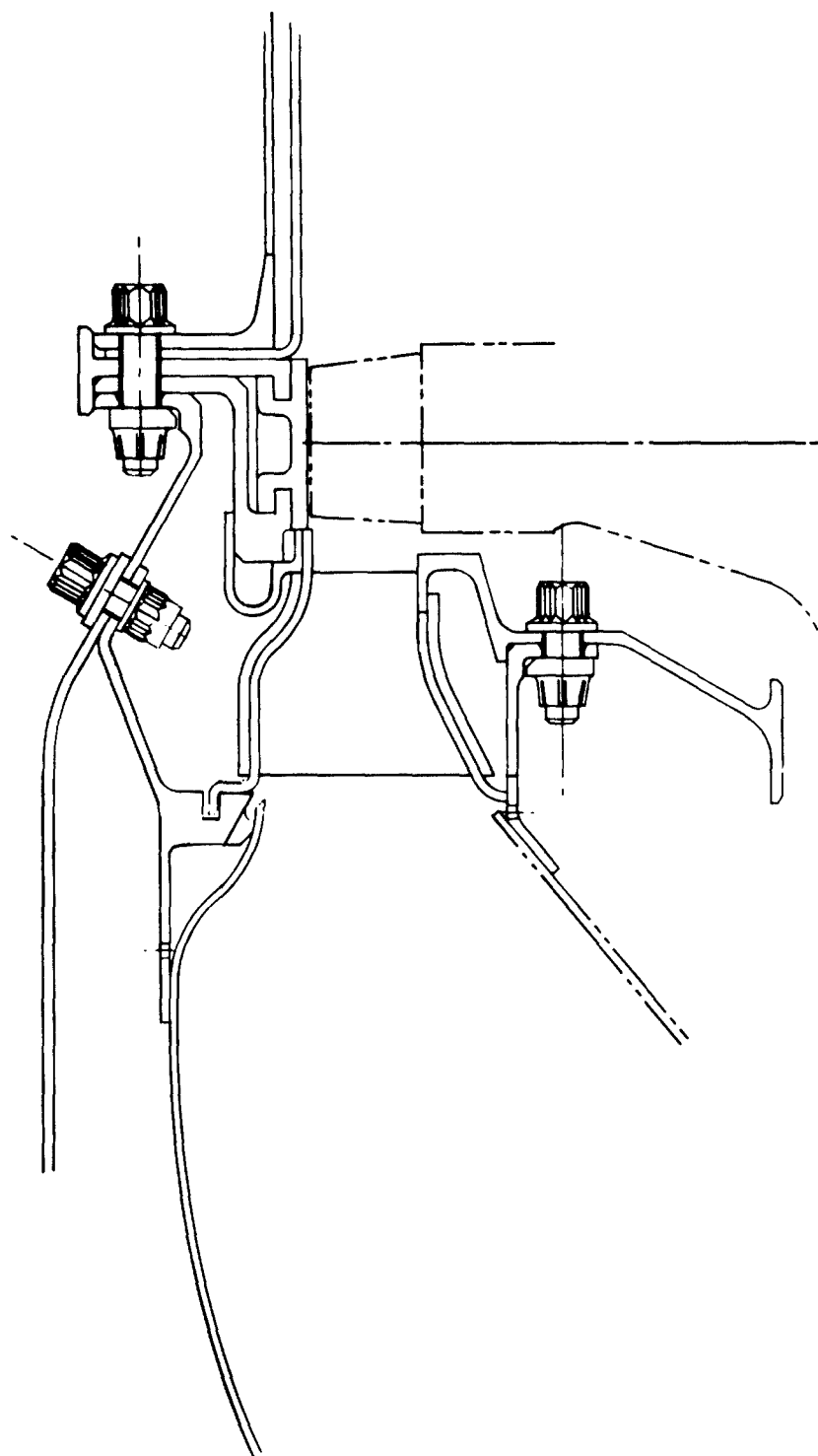


Figure 233. Continuous Ring Nozzle Design - Configuration 6.

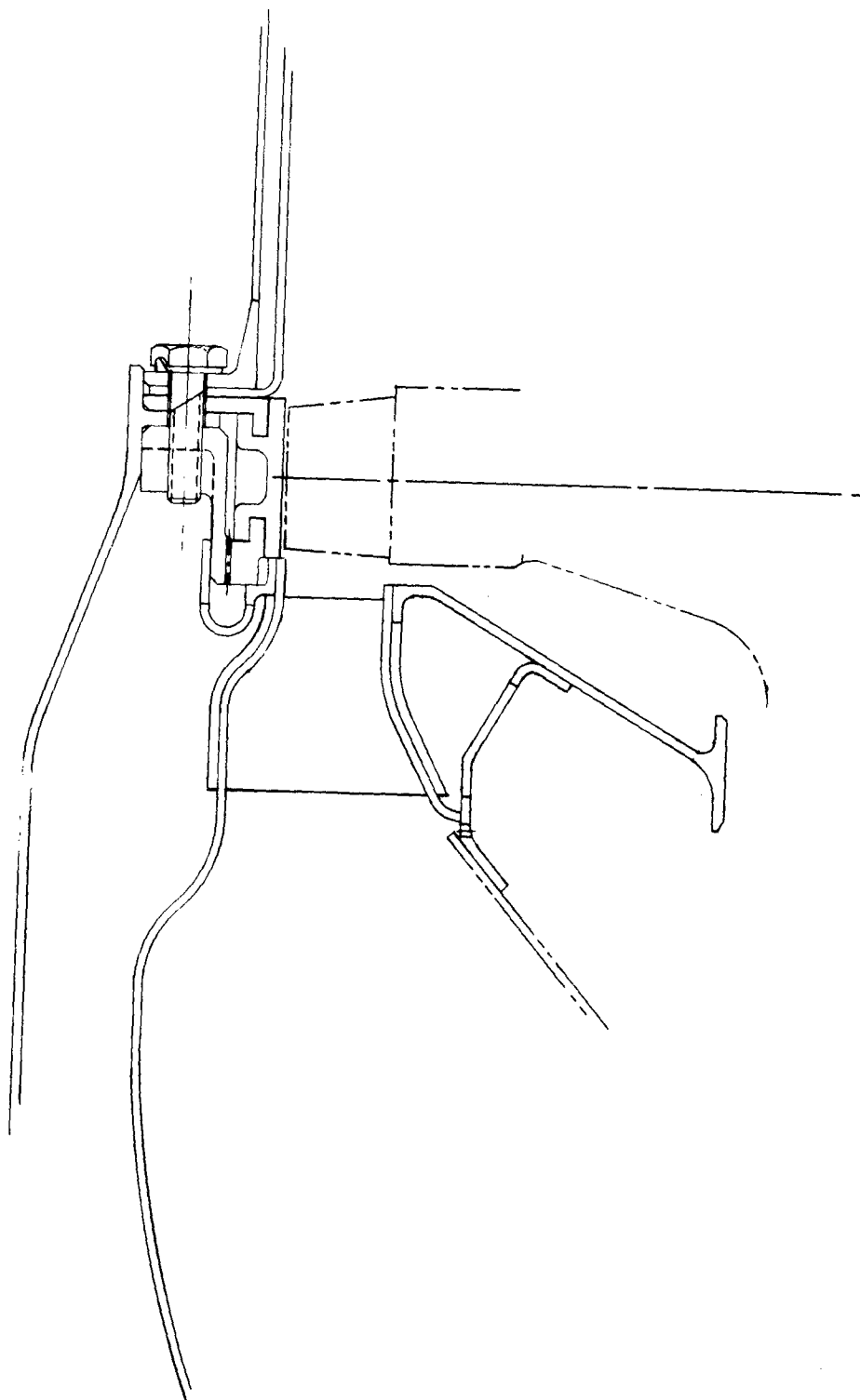


Figure 234. Continuous Ring Nozzle Design - Configuration 7.

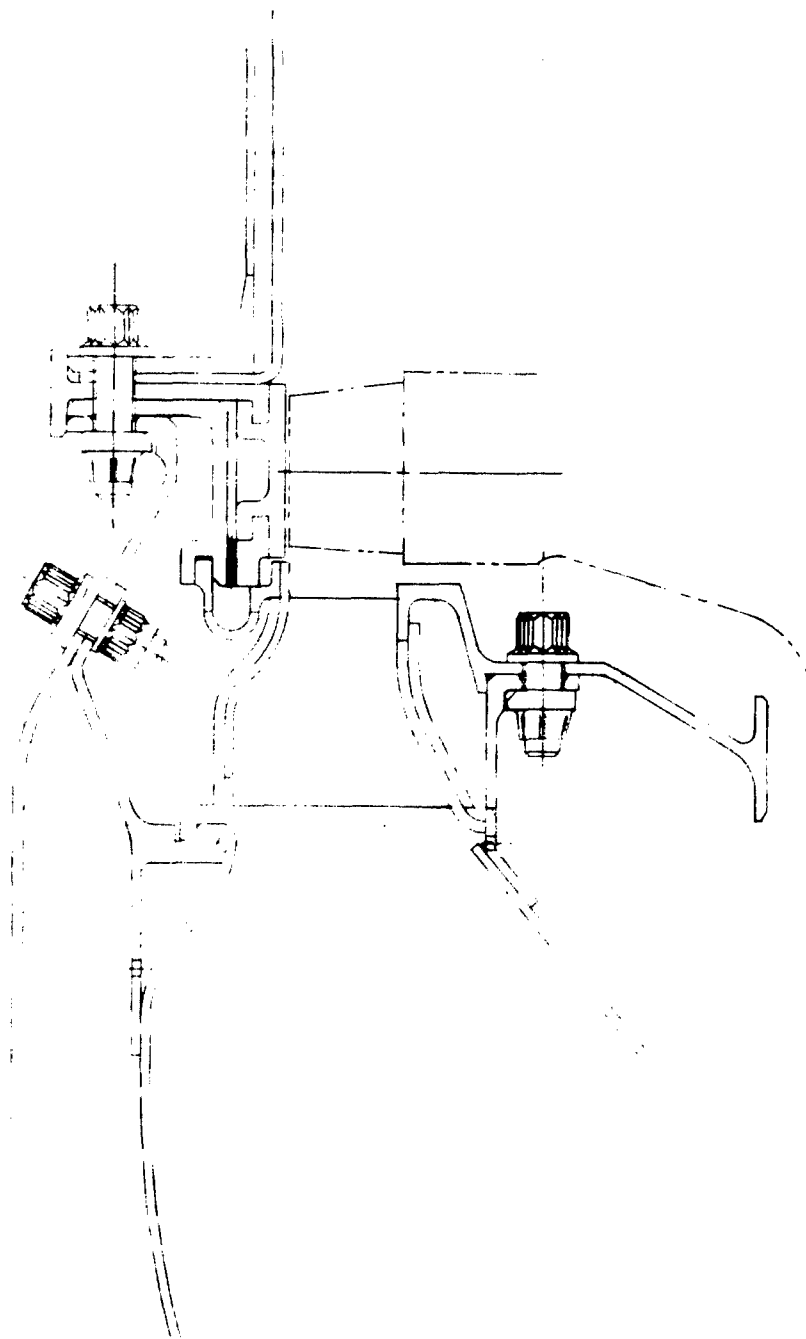


Figure 235. Continuous Ring Nozzle Design Configuration 8.

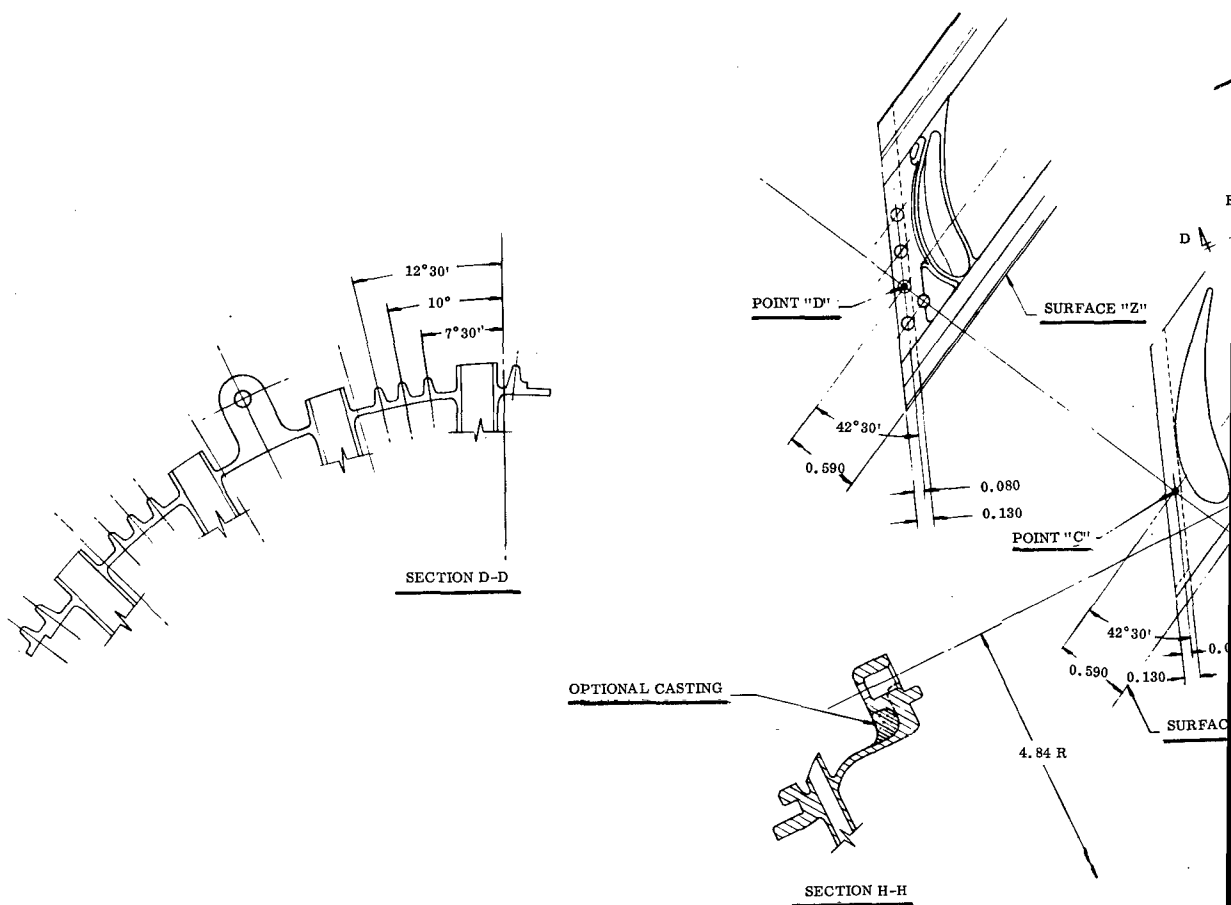
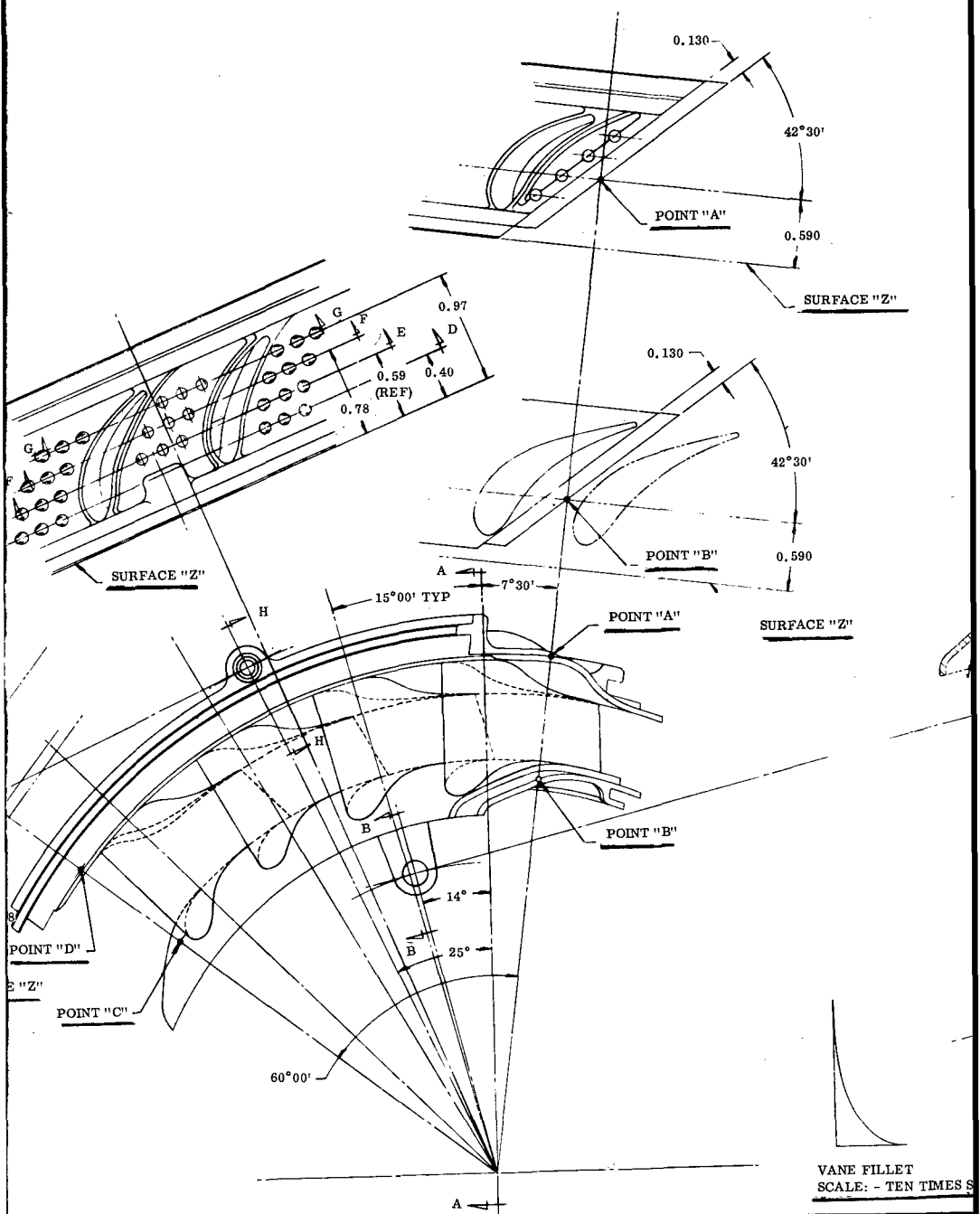
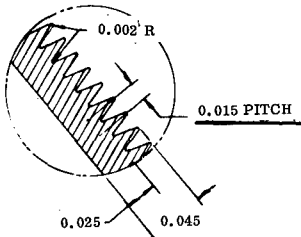
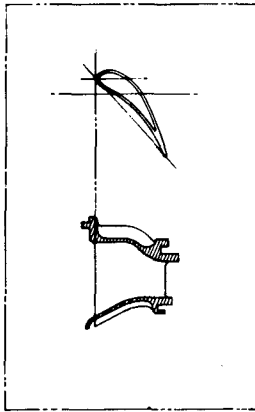
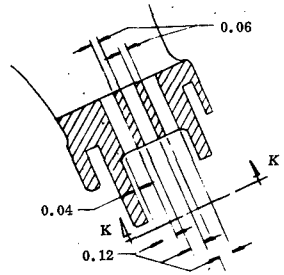


Figure 236. Cast Turbine Inlet Nozzle - 24-Vane Design.

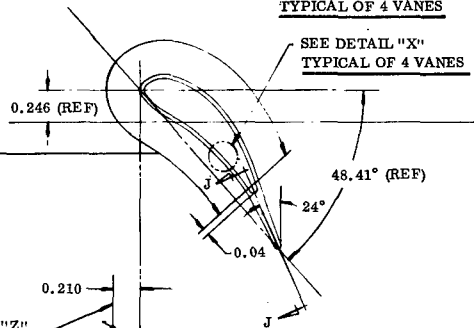




DETAIL "X"
SCALE: 20/1
CAST SERRATIONS THRU LENGTH
OF VANES FOR THIS DISTANCE

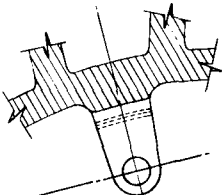


SECTION J-J
TYPICAL OF 4 VANES

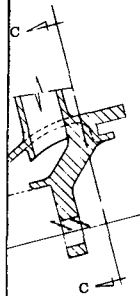


SEE DETAIL "X"
TYPICAL OF 4 VANES

0.210
SURFACE "Z"

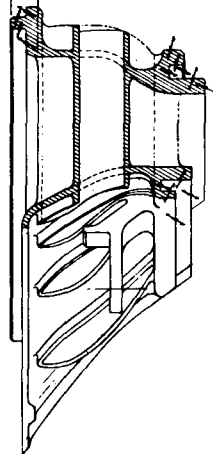


SECTION C-C

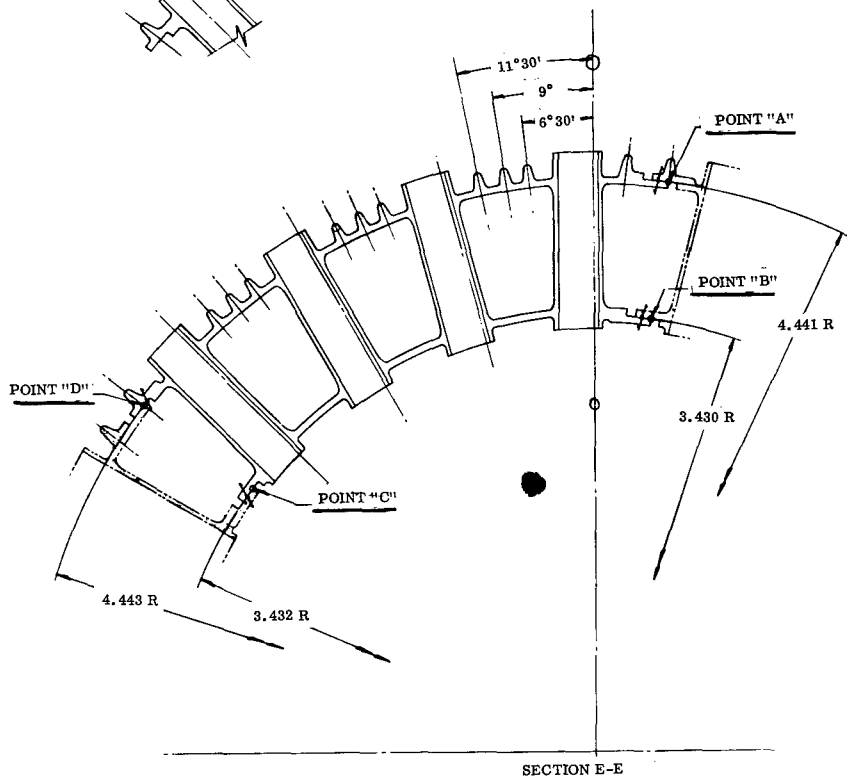
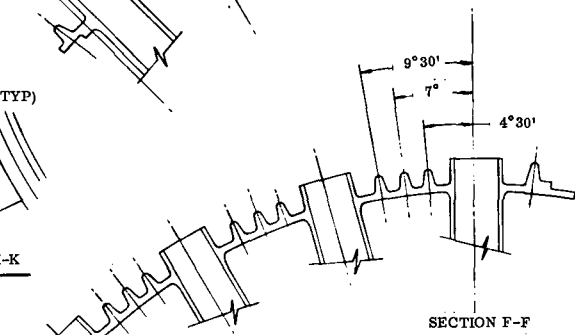
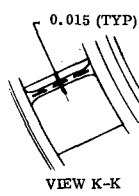
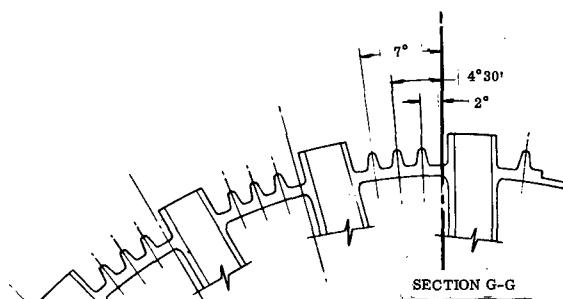


SECTION B-B

2.66 R



SECTION A-A



bottom of the diaphragm groove. The "axial" joints between segments are ground lap joints. Grinding will give a good fit to minimize leakage.

The turbine rotor shroud consists of separate segments supported by two tongue and groove joints, as is the nozzle. Using this design instead of a continuous ring shroud allows control of turbine hot tip clearance because the relatively cool support rings define the shroud diameter. This shroud is also used in Configurations 1, 5, 6, 7, and 8 (Figures 228 and 232 through 235).

Configuration 3 (Figure 230) consists of cast nozzle segments integral with turbine rotor shroud segments. This is a simplification of configuration 4 (Figure 231) in that a support ring with its leakage paths is eliminated. This configuration has the rear support ring relocated over the center of the turbine rotor so that thermal distortion of the segments will have a minimum effect on rotor tip clearance. Note that the segments are stiffened by cooling fins on the rotor shroud extending from the rear support slot to the stator shroud and vane trailing edges.

Configurations 1 and 2 (Figures 228 and 229) are similar to Configurations 3 and 4 (Figures 230 and 231) but have the inner diaphragm supported by bolted lugs on the segments. They have an extra external flange to support the front support ring of the nozzle.

Continuous Ring Nozzle Configurations

Configurations 5, 6, 7, and 8 (Figures 232 through 235) are sheet metal continuous ring nozzles with cast segmented rotor shrouds. The continuous ring nozzles may be fabricated using high temperature sheet alloys such as René 41, either brazed or welded, and might be fabricated using brazed TD nickel.

Configuration 5 (Figure 232) uses the flange support of Configuration 1 (Figure 228) at the front outer diameter. Configuration 6, 7, and 8 (Figures 233 through 235) eliminate this flange. The four configurations show various combinations of brazed, welded, or machined nozzle shrouds and attachments. It should be noted that the inner and outer combustor shells of Configurations 6 and 8 (Figures 233 and 235) are interchangeable with those of the cast segmented nozzle Configurations 3 and 4 (Figures 230 and 231).

The welded outer combustor of Configuration 7 (Figure 234) (cooling and air entry ports not shown) and the inner combustor of Configuration 5 or 7 (Figures 232 and 234) all use simplified welded constructions, which illustrates the potential simplicity of this design for future production.

The multiple sandwich flange construction of Configurations 6, 7, and 8 (Figures 233 through 235) and also Configurations 3 and 4 (Figures 230 and 231) can be simplified in production by combining parts. The construction shown was selected to maintain flexibility for modifications during initial testing.

Configuration 9 (Figure 237) is similar to Configuration 8 with the exception of the concentricity ring, which has been eliminated.

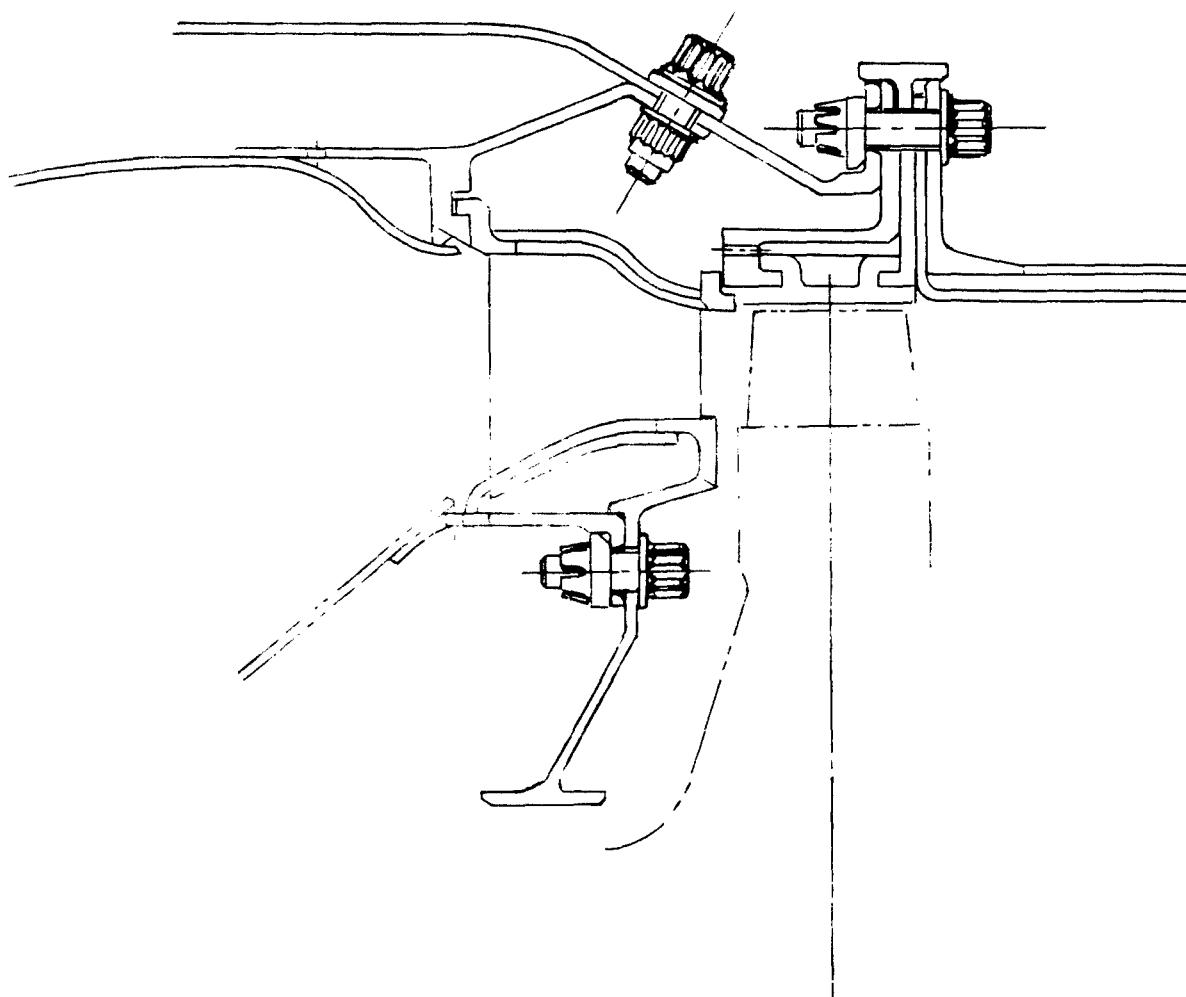


Figure 237. Continuous Ring Nozzle Design - Configuration 9.

TURBINE NOZZLE ASSEMBLY

Temperature Distribution

Vane

The turbine inlet nozzle vanes are subjected to gas at temperatures of 2300°F with peaks of 2640°F. They have to be extensively cooled. Different methods of cooling have been analyzed and evaluated.

1. Vane Film-Cooling. A film-cooling arrangement was designed and is shown in Figures 238 through 240. The film-cooling analysis was based on Wieghard's investigation reported by Eckert and Livingood, Reference 40.

Wieghard empirical results are summarized in the following equation:

$$\frac{T_w - T_{a,s}}{T_g - T_{a,s}} = 1 - 21.8 \left(\frac{S \rho_{a,s} V_{a,s}}{X \rho_g V_g} \right)^{0.8} \quad (19)$$

where:

T_w	=	Wall temperature, °F
T_g	=	Gas temperature, °F
$T_{a,s}$	=	Cooling air temperature, °F
$\rho_{a,s}$	=	Cooling air density, lb /ft ³
ρ_g	=	Gas density, lb/ft ³
$V_{a,s}$	=	Cooling air velocity, fps
V_g	=	Gas velocity, fps
X	=	Distance from cooling slot, ft
S	=	Cooling slot width, ft

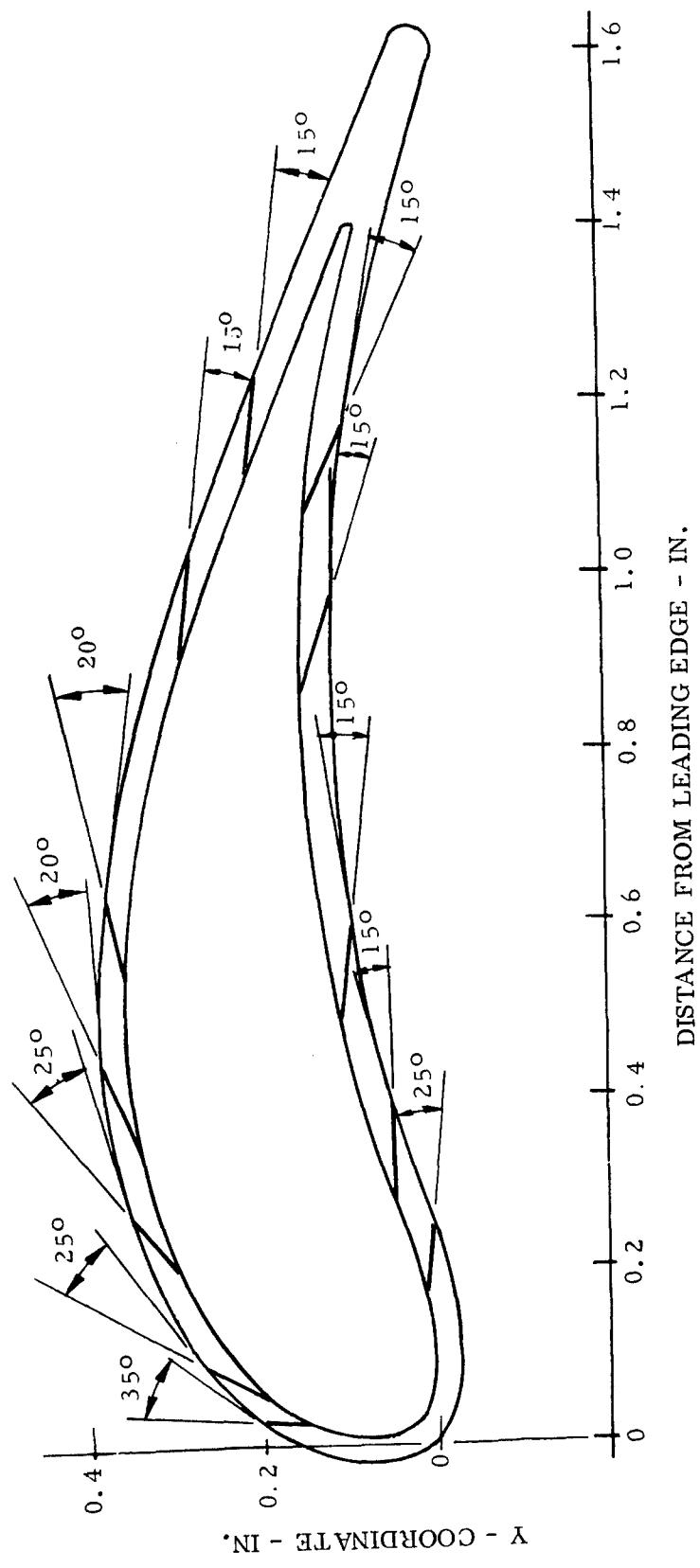


Figure 238. Fluid-Cooled Turbine Inlet Nozzle Blade Profile - Angular Orientation of Film-Cooling Slots.

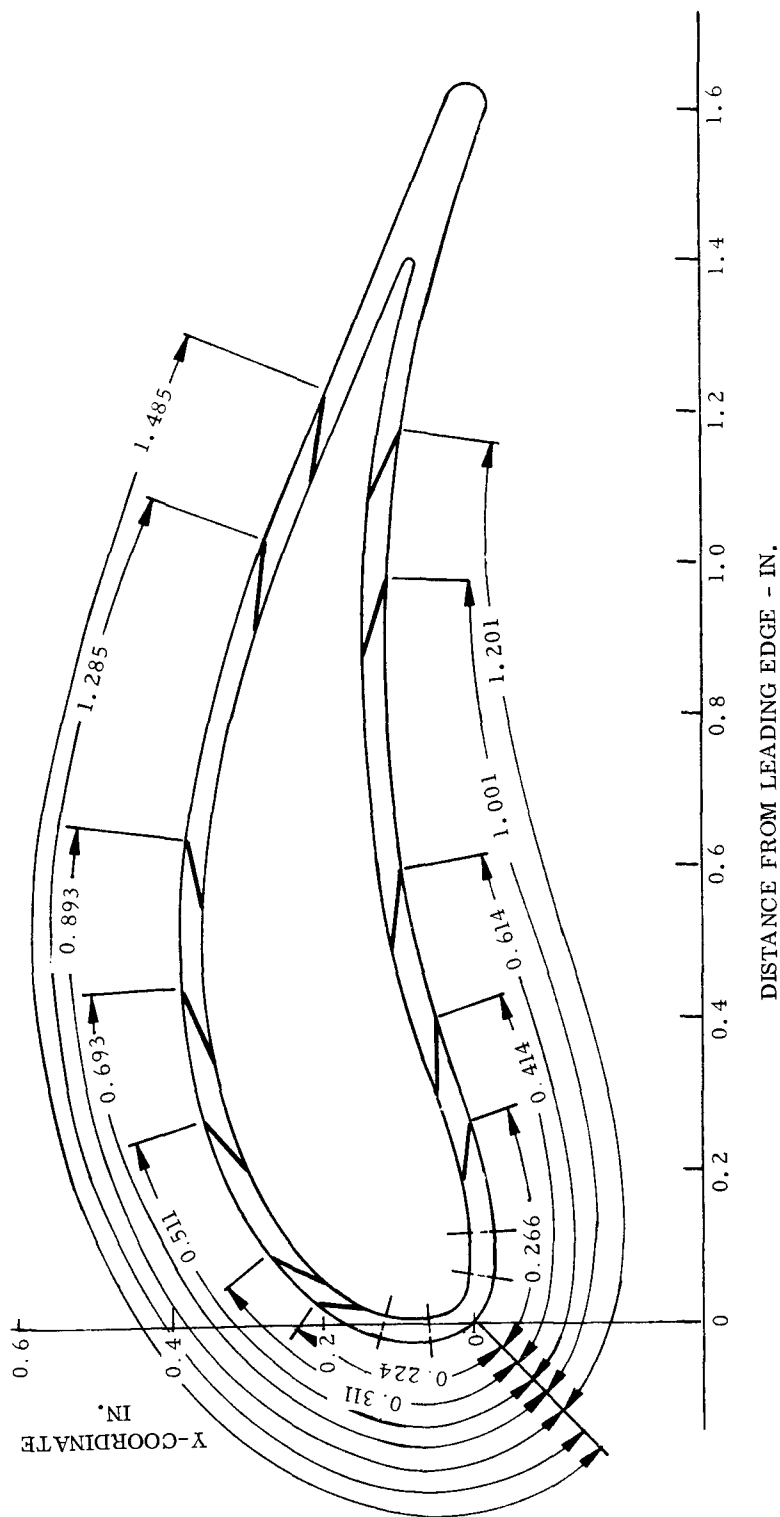


Figure 239. Fluid-Cooled Turbine Inlet Nozzle Blade Profile - Location of Film-Cooling Slots.

The regenerative and nonregenerative cases were investigated for different percentages of cooling air. The results are shown on Figure 241.

2. Convection Cooling. The Continental combustor requires that a substantial percent of the compressor delivery air go through the turbine nozzle vanes to the inner combustor. This air can be very efficiently used to convection cool the vanes.

The temperature distribution in the vanes was calculated for different designs.

External Heat Transfer Coefficients

The external heat transfer coefficients (from the gas to vane) calculation was based on the velocity distribution along the turbine nozzle vane (mean radius section) shown on Figure 242.

1. The leading edge heat transfer coefficients were obtained from data measured for flow around circular cylinders. The data were obtained by J. Kestin and P. F. Maeder (Reference 36) and are summarized in Figure 243.
2. The other external heat transfer coefficients were calculated as follows:

$$N_u = 0.0296 (P_r)^{1/3} (R_e)^{0.8} \quad (16)$$

where:

$$N_u = \text{Nusselt number}$$

$$P_r = \text{Prandtl number}$$

$$R_e = \text{Reynolds number}$$

and

$$h = \frac{N_u K}{D}$$

where:

$$K = \text{Gas conductivity}$$

The external heat transfer coefficients distribution along the turbine nozzle vane is shown on Figure 244.

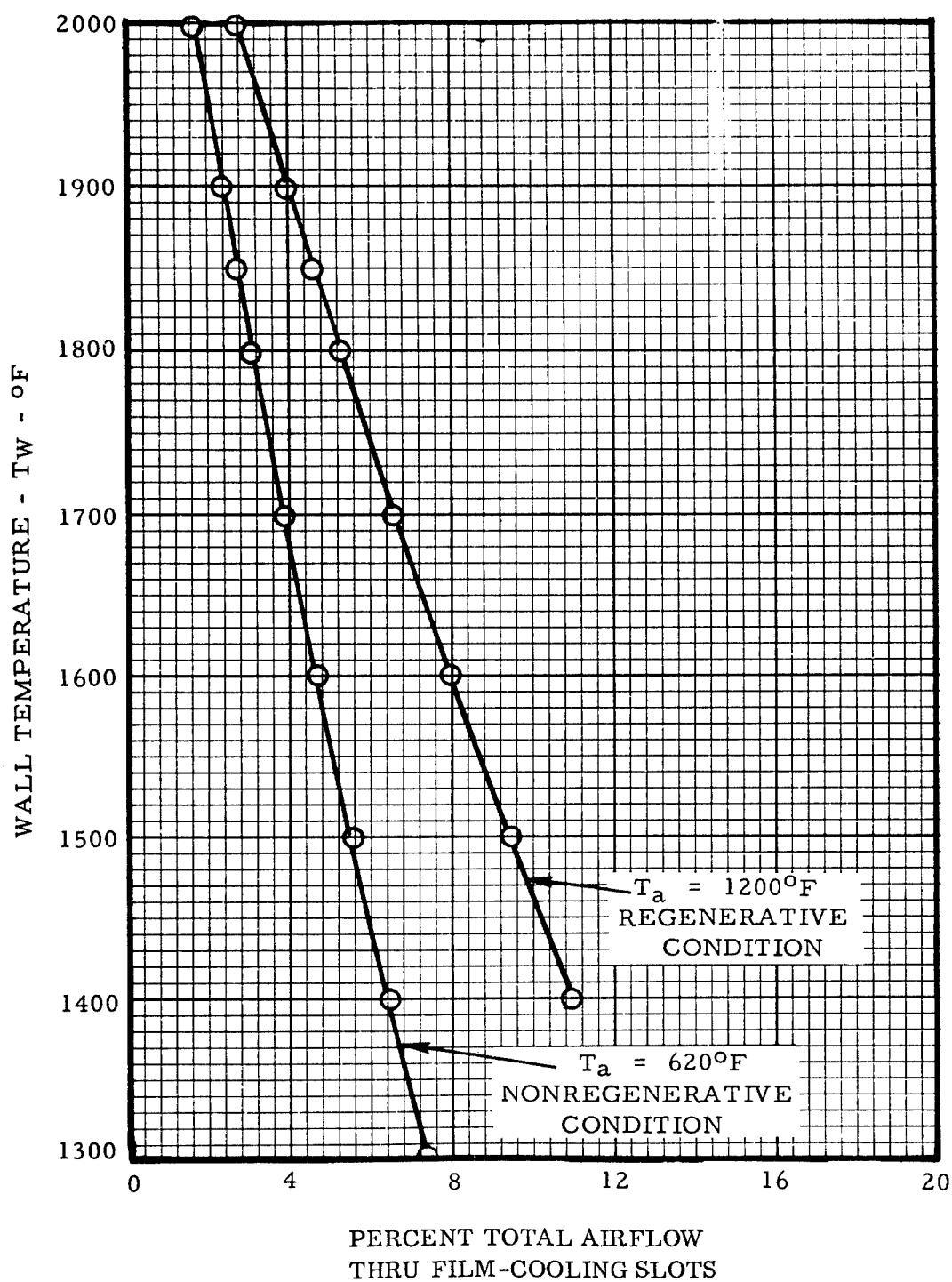


Figure 241. Nozzle Vane Temperature Versus Percent Total Airflow Film-Cooling.

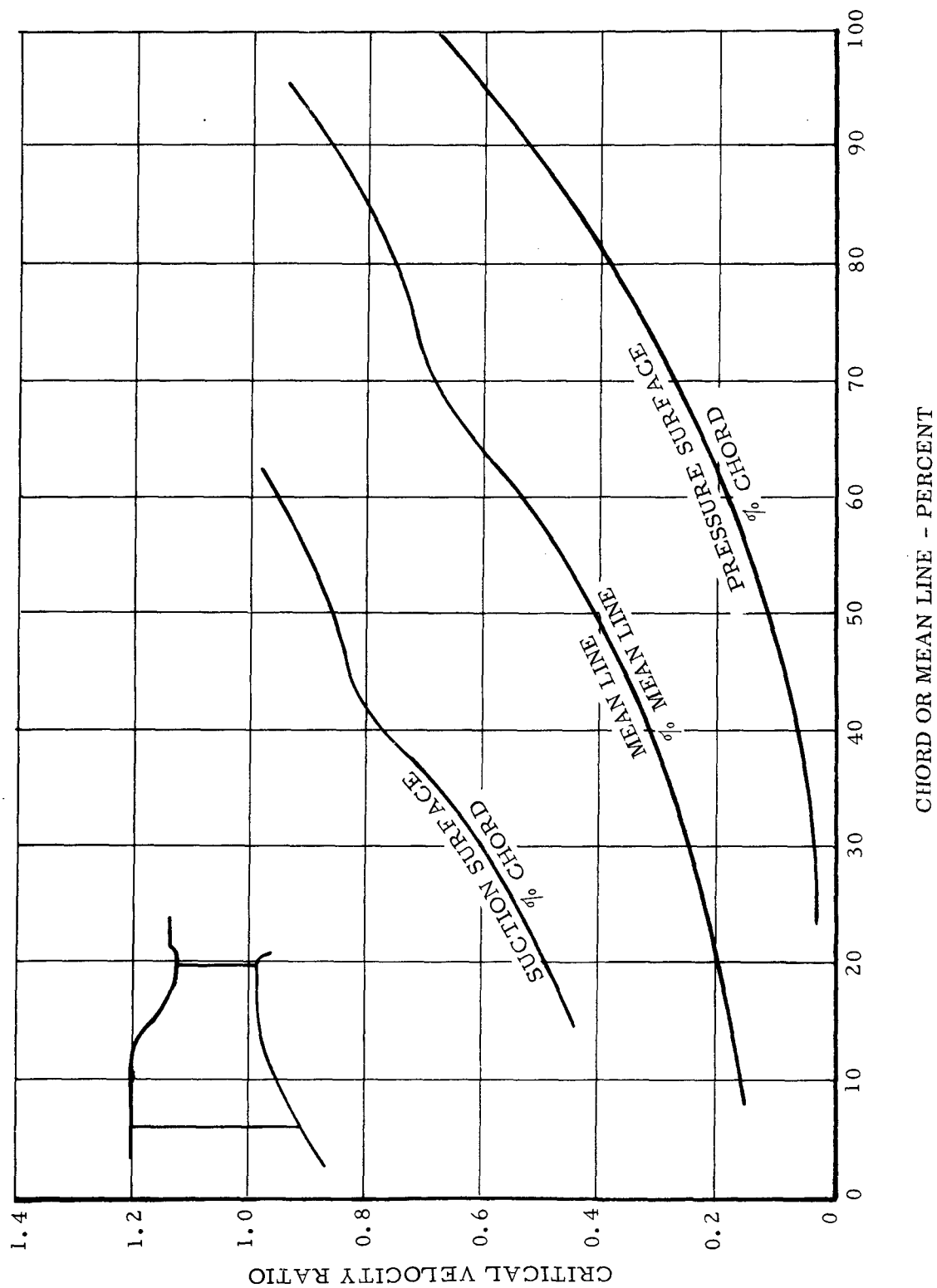


Figure 242. Velocity Distribution Along Turbine Nozzle Vane - 50 Percent.

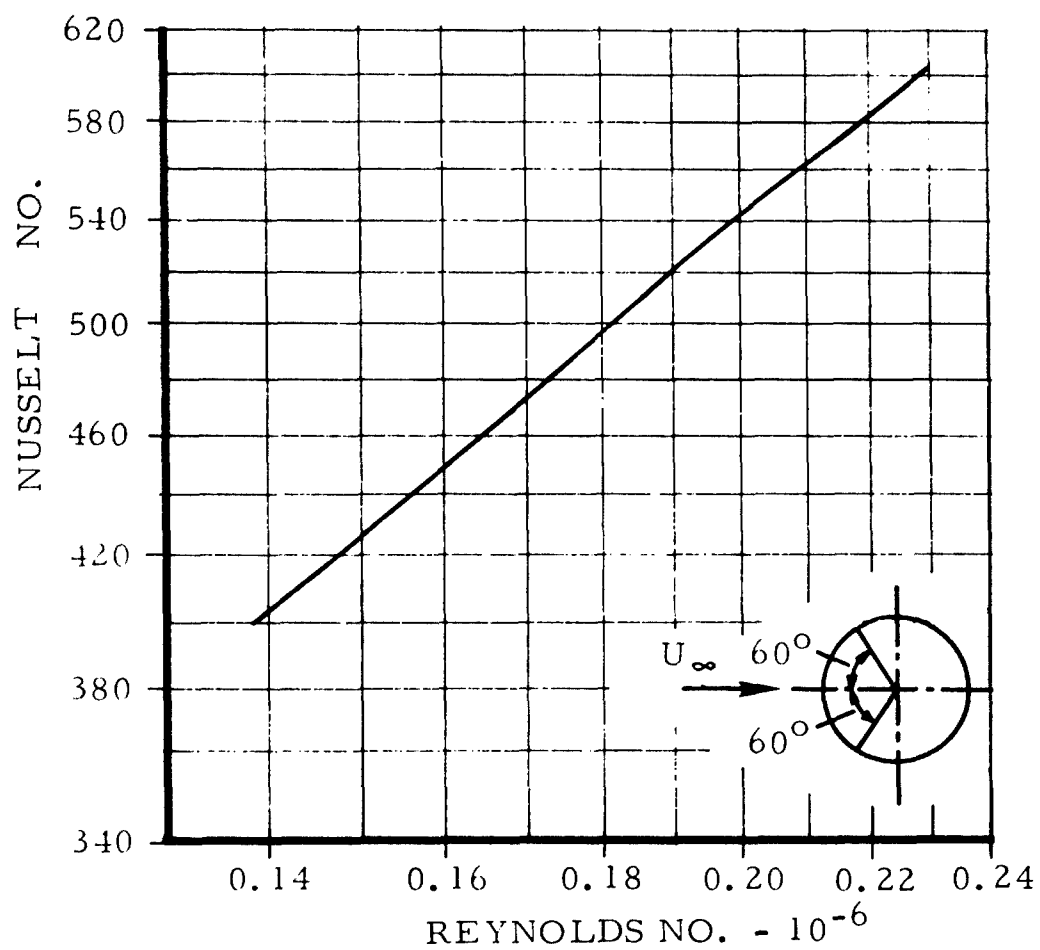


Figure 243. Variation of Nusselt Number With Reynolds Number.

Internal Heat Transfer Coefficient

The internal heat transfer coefficient was calculated using the expression for turbulent flow in tubes:

(17)

$$N_u = 0.023 (R_e)^{0.8} (P_r)^{0.33}$$

Convection Cooling Design No. 1

A first design consisting of a straight wall vane (no internal fins) was analyzed. The temperature distribution in the nozzle is shown in Figure 245 for the nonregenerative case.

The results were obtained using the assumptions of peak turbine inlet temperature and no metal conduction.

The results show fairly high metal temperatures, and the necessity of a more efficient convection concept becomes apparent.

Convection Cooling Design No. 2

It was decided to improve the convection cooling, and this was accomplished by putting internal fins in the vanes. The fins have increased the heat transfer area by a factor of three. The fin effectiveness is close to 100 percent.

The design incorporates trailing edge slots that will cool these edges with about 1 percent of air.

A two-dimensional analysis of the temperature distribution in a vane cross section was completed for the regenerative and nonregenerative cases. The analysis was based on a relaxation solution of the Laplace equation, and was programmed for the IBM computer.

Two vane materials of different conductivities (TD nickel, $K = 28.4$ Btu/hr - ft °F; SM 302, $K = 14.6$ Btu/hr - ft °F) were investigated.

TEMPERATURES - °F

EFFECTIVE GAS TEMPERATURE = 2636°F
EFFECTIVE AIR TEMPERATURE = 620°F
(NONREGENERATIVE CONDITION)

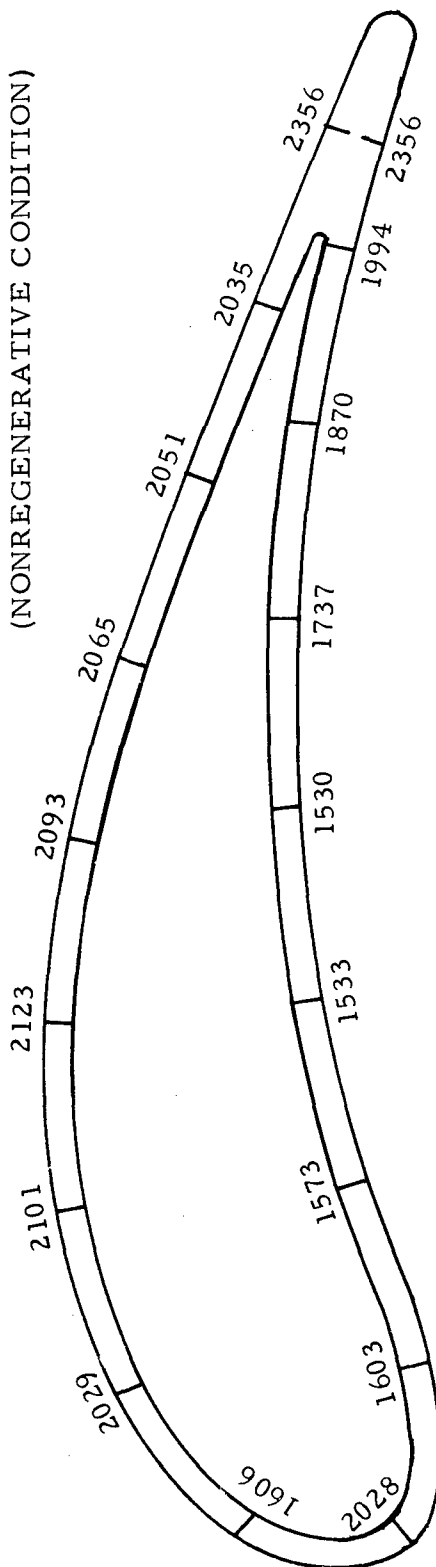


Figure 245. Turbine Inlet Nozzle Vane - Metal Temperature Distribution (Design #1).

Test results indicated that:

1. Conduction in the chordwise direction of the vane is very small. This could be expected in view of the small wall thickness ($t = 0.032$ inch). The thermal conductivity of the metal considered, therefore, does not have a major effect on the temperature distribution.
2. Augmentation of the internal surface area obtained by the use of fins improves the cooling considerably.
3. The trailing edge slots cool the trailing edges very efficiently.

Temperature distribution for the nonregenerative case (cooling air temperature = 620°F) and the regenerative case (cooling air temperature = 1185°F) is shown on Figures 246 and 247.

TURBINE NOZZLE SHROUDS

An analytical study was conducted to determine the effect of the presence of the shrouds on the vane radial temperature distribution. The analysis, which is discussed in Appendix II, took into account the cooling effect of a nozzle vane extended through the shroud into the relatively cool combustor inlet air as in Figure 494, Appendix II.

The results showed that:

1. Presence of the vane extension reduces the brazed joint temperature by 325°F in the nonregenerative case and by 138°F in the regenerative case.
2. Vane radial temperature distributions for the TD nickel and the SM 302 configurations are practically the same, so there is relatively little conduction effect on vane temperature due to the difference in metal conductivity.
3. Vane cooling effect of the fin is overridden by the heating from the shrouds, so the inner and outer shrouds must be cooled. It was therefore decided to film cool the shrouds by injecting cooling air along the wall at the vane leading edge.

Temperature distribution along the shroud walls for the nonregenerative and the regenerative cases is shown in Figures 248 and 249.

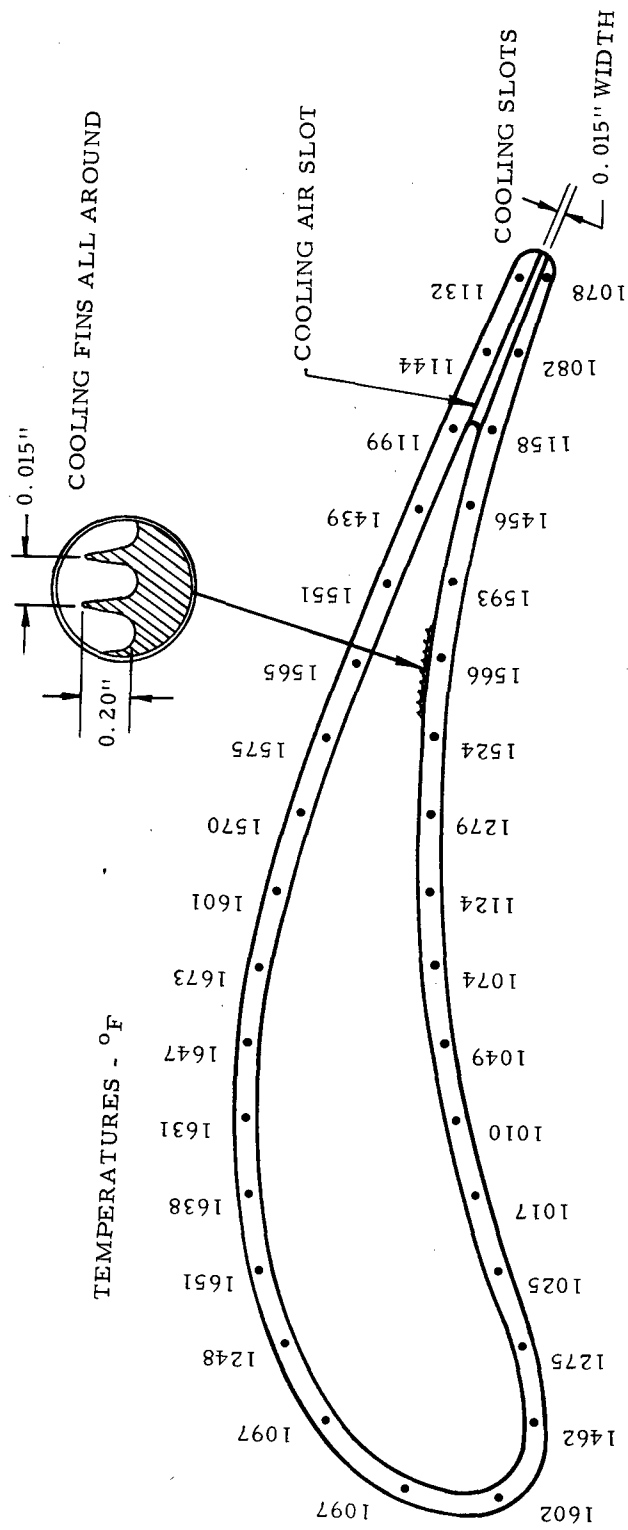


Figure 246. Vane Temperature Distribution - Nonregenerative Case.

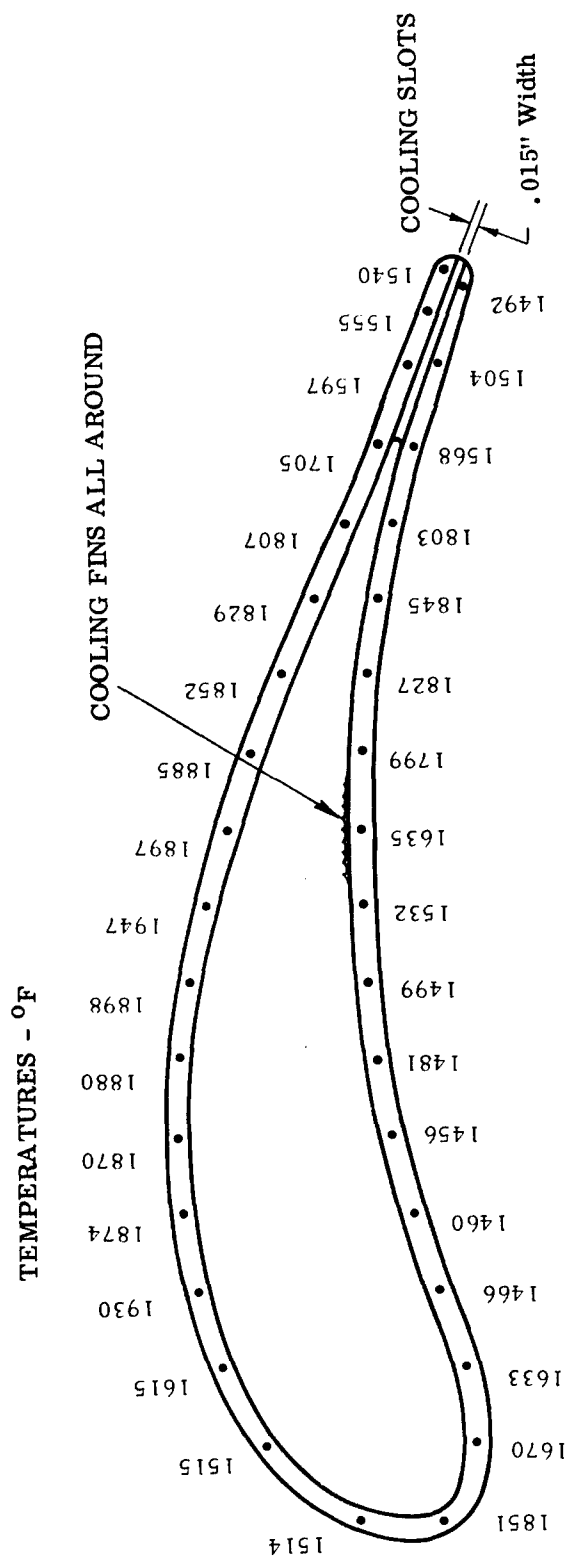


Figure 247. Vane Temperature Distribution - Regenerative Case.

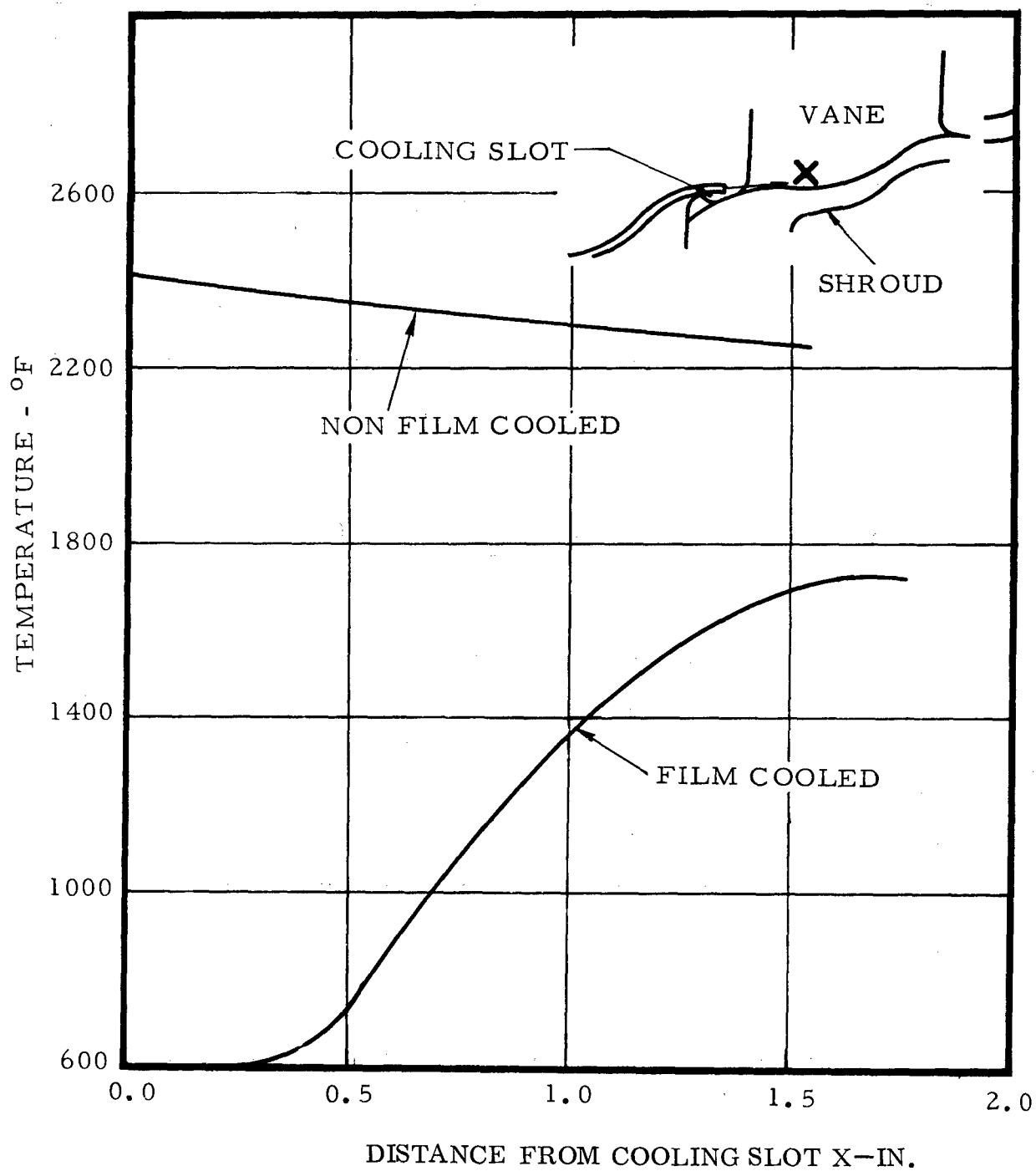


Figure 248. Shroud Temperature - Nonregenerative Case.

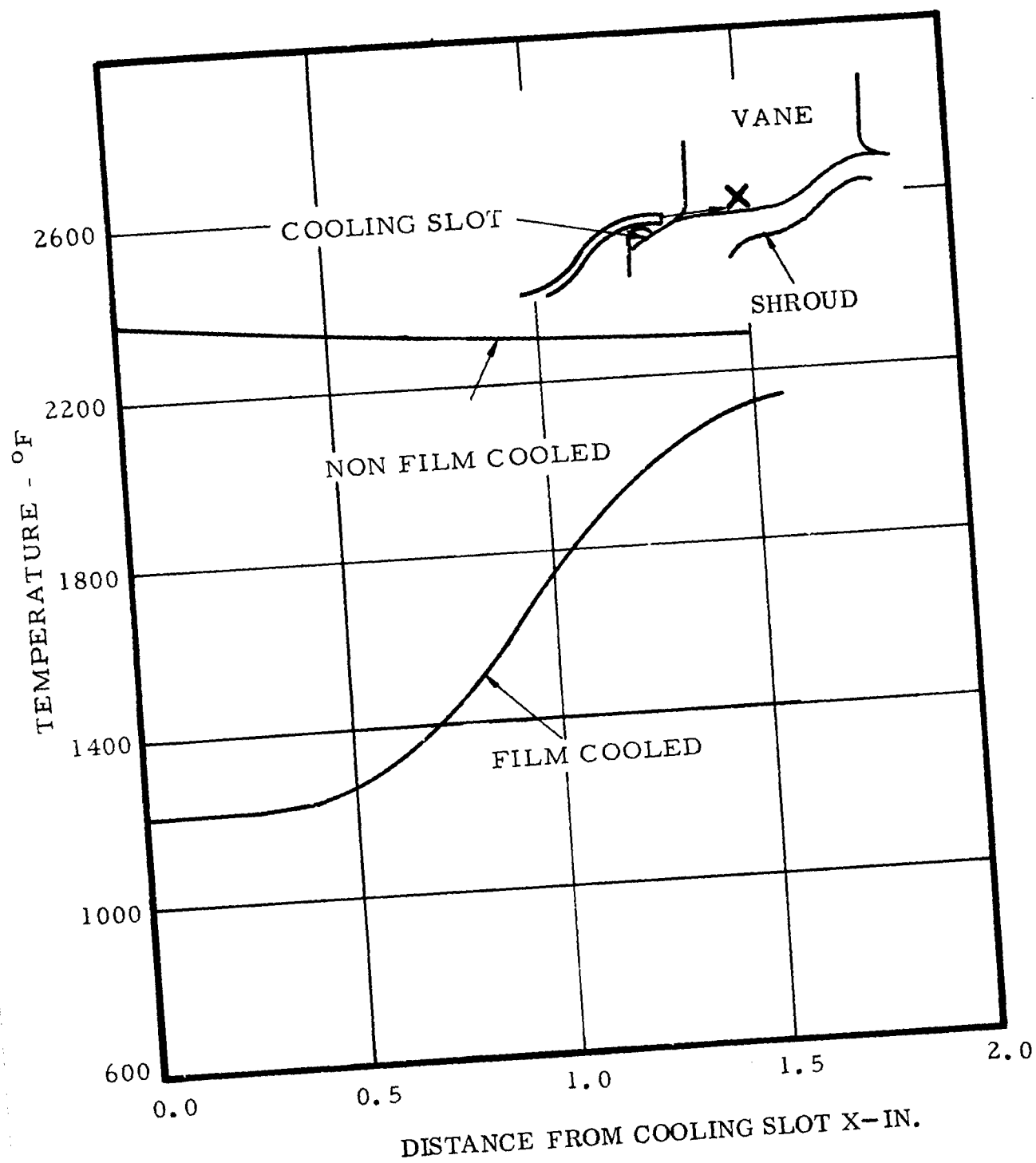


Figure 249. Shroud Temperature - Regenerative Case.

Radial temperature distributions in the vane at the leading edge, apex, and trailing edge for the nonregenerative and the regenerative cases using the above film-cooled shroud temperatures are shown in Figures 250 and 251. These figures show that the film-cooled shroud and the vane extension "fin" effectively cool the vane near the shroud by conduction.

TURBINE NOZZLE STRUCTURAL DESIGN

The study incorporated the design and analysis of several nozzle concepts:

1. Cast segmented nozzle, separate rotor shroud.
2. Cast segmented nozzle, integral rotor shroud.
3. Cast full nozzle ring, separate rotor shroud.
4. Cast full nozzle ring, integral rotor shroud.
5. Fabricated sheet metal, full ring, separate rotor shroud.

Configurations 1 and 5 were stressed in detail for the nonregenerative and regenerative cases. Design 3 was considered geometrically identical to design 5. Designs 2 and 4 were similar enough to 1 and 5, respectively, so that only the stresses in the integral shroud had to be considered. The materials analyzed were SM 302 for design 1 and both TD nickel and René 41 for design 5.

Conclusions

Segmented Versus Continuous Shrouds

The effect of continuous shrouds did not increase the vane stresses appreciably, and the shrouds did not present any structural problem. The rings are being designed to take into account the temperature discontinuities in the assembly. It was therefore decided (to keep the leakage to a minimum) to go to a full-ring design.

Separate Rotor Shroud Versus Integral Rotor Shroud

Both designs were found to be structurally adequate. The separate shroud was selected due to the fact that it permits holding a tighter rotor clearance under operating conditions and is adaptable to fabricated sheet metal or cast nozzles.

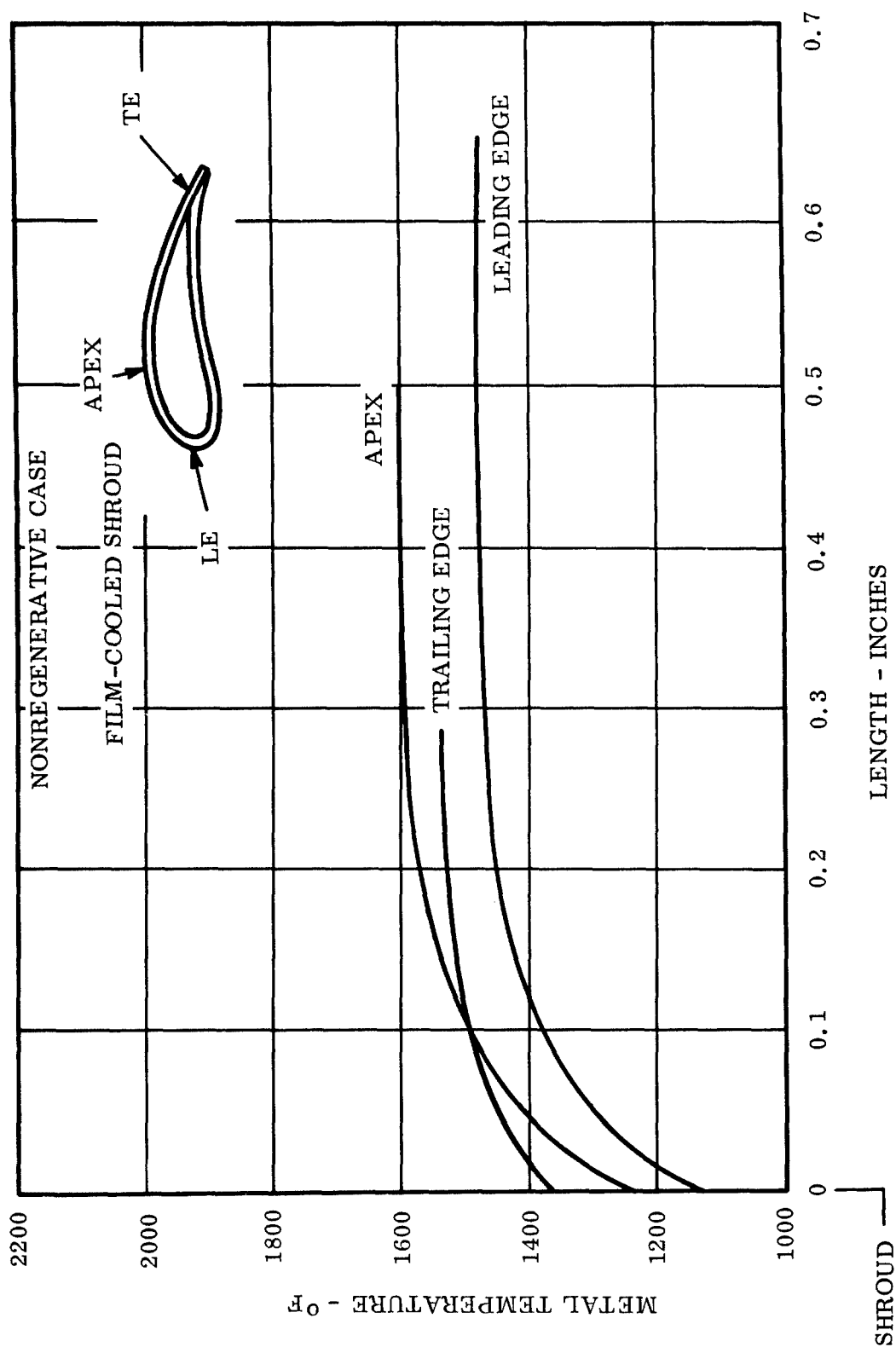


Figure 250. Nozzle Vane Radial Temperature Distribution - Nonregenerative Case.

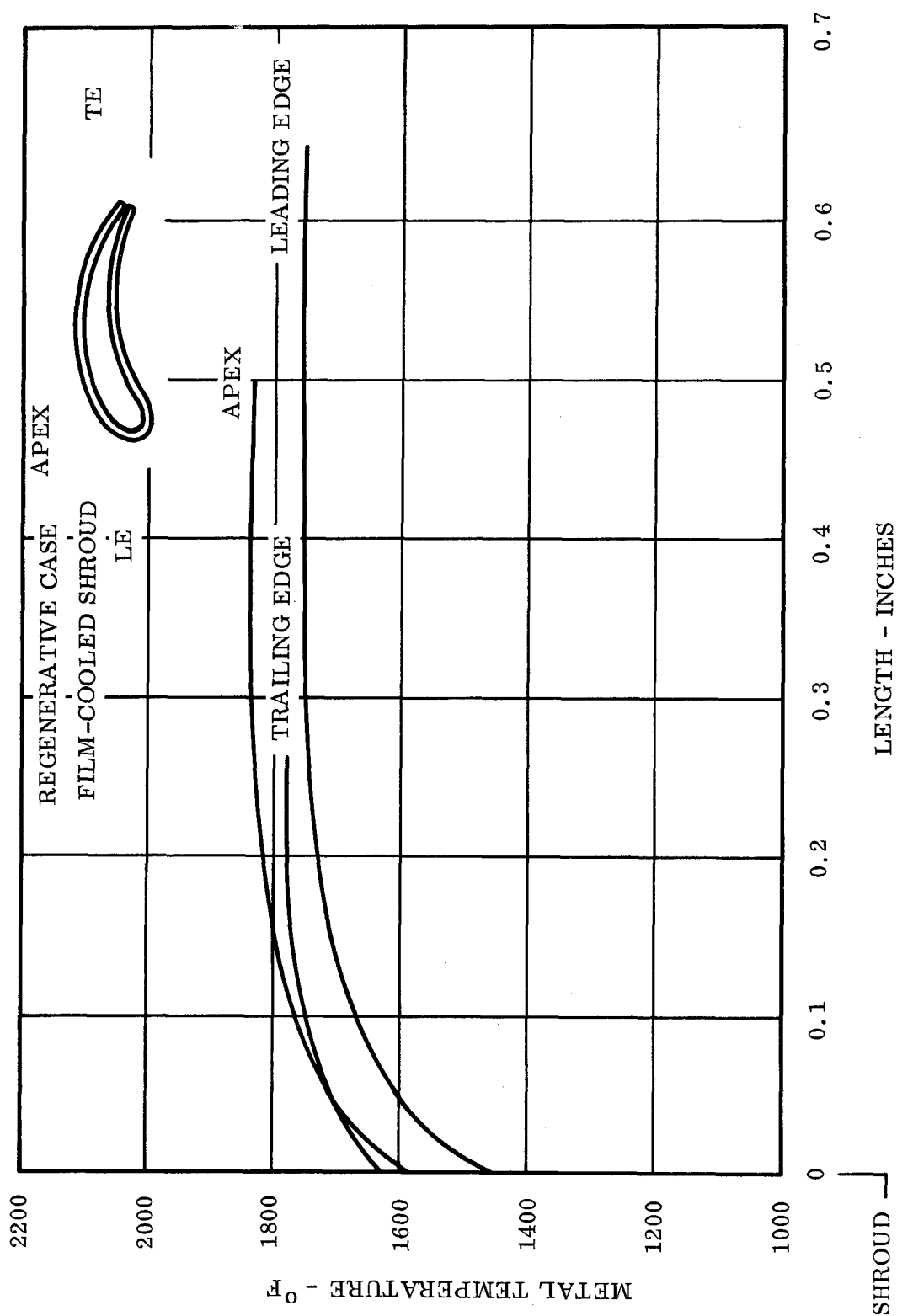


Figure 251. Nozzle Vane Radial Temperature Distribution - Regenerative Case.

NOZZLE VANES

The nozzle vanes are highly stressed areas in all designs. The combined stress in the vane is due to:

1. Vane gas bending.
2. Pressure differential across the vane wall.
3. Thermal stress.
4. Radial growth discontinuity between the vanes and the shrouds.

Important contributors to the total stress are the thermal stresses in the vane. These stresses were calculated using a temperature distribution obtained from the nozzle cascade test. The measured temperatures were reduced to match the design condition (turbine inlet temperature plus 20 percent of combustor temperature rise = 2636°F) and are shown on Figure 252. The corresponding thermal stresses for a René 41 sheet metal design (nonregenerative) are shown in Table XXV.

It was found that either a cast or a sheet metal design would be adequate for the nonregenerative case. A sheet metal configuration was selected due to cost and procurement-time considerations. René 41 was selected over TD nickel due to its better material properties at the operating conditions.

Tables XXV and XXVI show the stress results for a René 41 full-ring sheet metal design with separate rotor shrouds for the nonregenerative and the regenerative cases, respectively.

From Table XXV it can be noted that all the stresses are below the 0.2-percent yield. All points are practically below the 100-hour stress rupture. The two points (2 and 5) that do exceed this limit are under thermal load. The material will, in these cases, creep and relieve itself. These two points, therefore, do not present any particular problem. From Table XXVI one can see that several points do exceed the 0.2-percent yield strength. This is due to the lower material properties of René 41 at the now higher metal temperatures (Figures 253 and 254). For the regenerative case, two courses of action are therefore possible:

1. Provide some additional cooling (film-cooling) to bring the René 41 temperature down.
2. Go to a high-strength material (such as SM 200) at high temperatures. This would involve a cast design.

TURBINE INLET TEMPERATURE = 2636°F
INLET COOLING AIR TEMPERATURE = 620°F

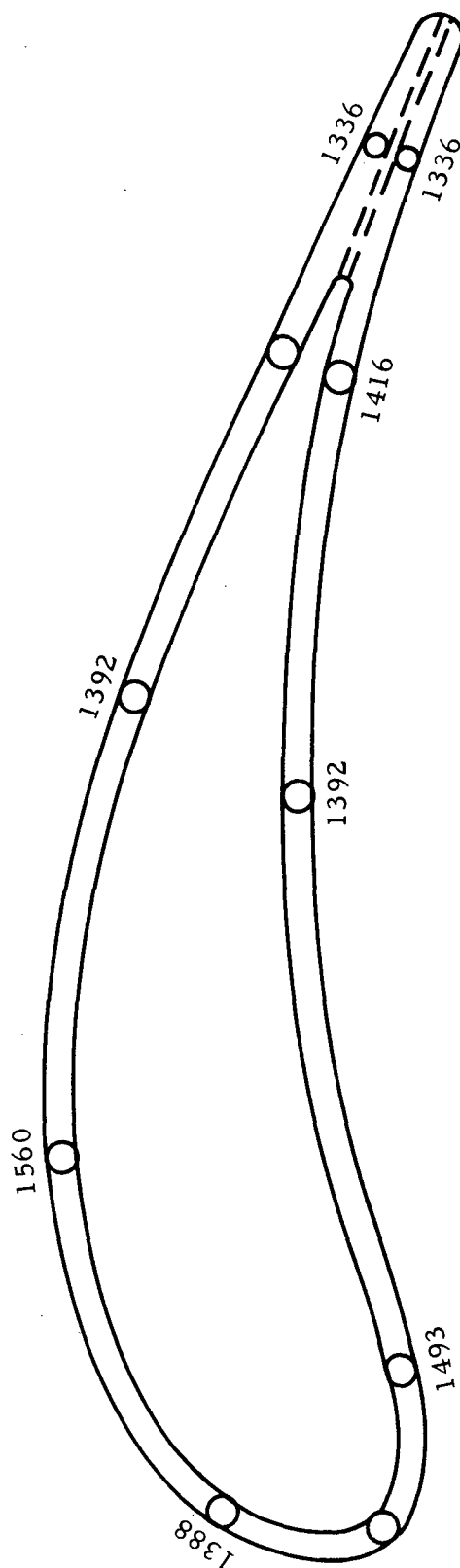


Figure 252. Vane Temperatures (From Reduced Test Data) - Nonregenerative.

TABLE XXV
TURBINE INLET NOZZLE VANE STRESS ANALYSIS -
NONREGENERATIVE CASE

Pos. **	Temp. (° F)	Stresses Due To	Stress (psi)	René 41 Matl. Prop.
1	1336	Vane bending	-2307	0.2% F _{ty} = 125,000
		Rad. discon.*	-906	10 hr. SR = 95,000
		Thermal	19,250	100 hr. SR = 74,500
2	1560	Vane bending	4680	0.2% F _{ty} = 91,000
		Int. press.	±20,230	10 hr. SR = 44,000
		Rad. discon.	-906	100 hr. SR = 31,500
		Thermal	-25,874	
3	1564	Vane bending	-5424	0.2% F _{ty} = 91,000
		Rad. discon.	-906	10 hr. SR = 44,000
		Thermal	-26,655	100 hr. SR = 31,500
4	1336	Vane bending	3045	0.2% F _{ty} = 125,000
		Rad. discon.	-906	10 hr. SR = 95,000
		Thermal	19,250	100 hr. SR = 74,500
5	1560	Vane bending	-6266	0.2% F _{ty} = 91,000
		Int. press.	±20,230	10 hr. SR = 44,000
		Rad. discon.	-906	100 hr. SR = 31,500
		Thermal	-25,874	
6	1564	Vane bending	7356	0.2% F _{ty} = 91,000
		Rad. discon.	-906	10 hr. SR = 44,000
		Thermal	-26,655	100 hr. SR = 31,500
7	1336	Int. press.	±12,867	0.2% F _{ty} = 125,000
		Rad. discon.	-906	10 hr. SR = 95,000
		Thermal	19,250	100 hr. SR = 74,500
8	1560	Int. press.	9836	0.2% F _{ty} = 91,000
		Rad. discon.	-906	10 hr. SR = 44,000
		Thermal	-25,874	100 hr. SR = 31,500
9	1564	Int. press.	3186	0.2% F _{ty} = 91,000
		Rad. discon.	-906	10 hr. SR = 44,000
		Thermal	-26,655	100 hr. SR = 31,500

* Radial Discontinuity

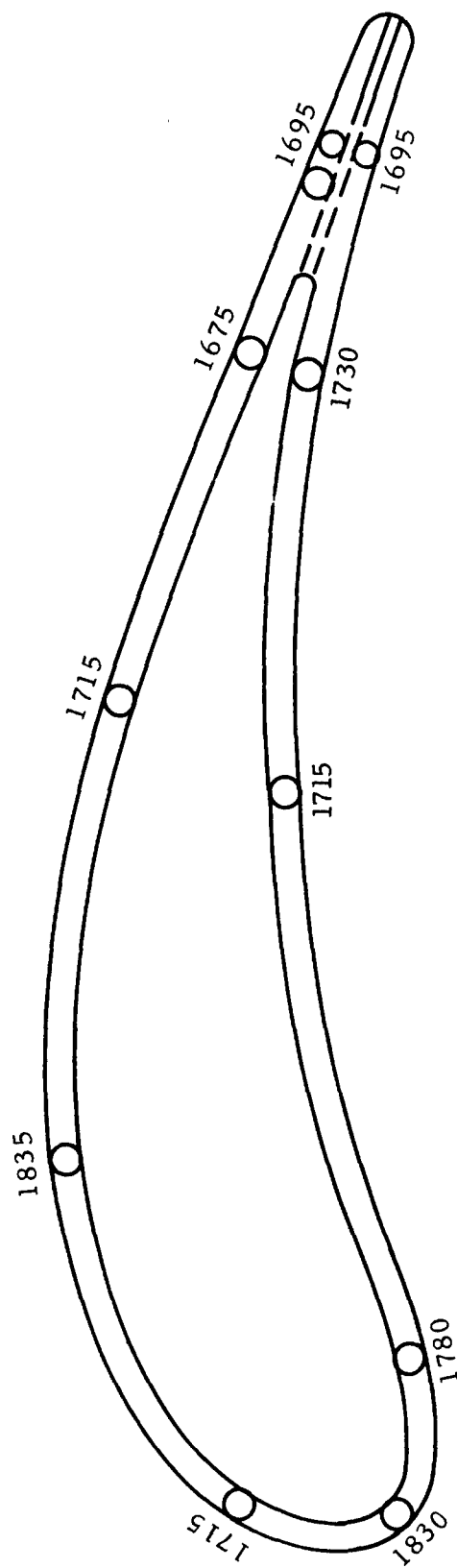
** Ref. Figure 230 for position

SR = stress-rupture

TABLE XXVI
TURBINE INLET NOZZLE VANE STRESS ANALYSIS -
REGENERATIVE CASE

Pos. *	Temp. (° F)	Stresses Due To	Stress (psi)	René 41 Matl. Prop.
1	1695	Vane bending	-2307	0.2% F _{ty} = 60,000
		Rad. discon.	-906	10 hr. SR = 26,300
		Thermal	8594	100 hr. SR = 16,300
2	1835	Vane bending	4680	0.2% F _{ty} = 28,000
		Rad. discon.	-906	10 hr. SR = 13,000
		Thermal	-17,566	100 hr. SR = 7,000
		Int. press.	±20,230	
3	1830	Vane bending	-5424	0.2% F _{ty} = 29,000
		Rad. discon.	-906	10 hr. SR = 13,500
		Thermal	-16,692	100 hr. SR = 7,400
4	1695	Vane bending	3045	0.2% F _{ty} = 60,000
		Rad. discon.	-906	10 hr. SR = 26,300
		Thermal	8594	100 hr. SR = 16,300
5	1835	Vane bending	-6266	0.2% F _{ty} = 28,000
		Int. press.	±20,230	10 hr. SR = 13,000
		Rad. discon.	-906	100 hr. SR = 7,000
		Thermal	-17,566	
6	1830	Vane bending	7356	0.2% F _{ty} = 29,000
		Rad. discon.	-906	10 hr. SR = 13,500
		Thermal	-16,692	100 hr. SR = 7,400
7	1695	Int. press.	±12,867	0.2% F _{ty} = 60,000
		Rad. discon.	-906	10 hr. SR = 26,300
		Thermal	8594	100 hr. SR = 16,300
8	1835	Int. press.	9836	0.2% F _{ty} = 28,000
		Rad. discon.	-906	10 hr. SR = 13,000
		Thermal	-17,566	100 hr. SR = 7,000
9	1830	Int. press.	3186	0.2% F _{ty} = 29,000
		Rad. discon.	-906	10 hr. SR = 13,500
		Thermal	-16,692	100 hr. SR = 7,400

* Ref. Figure 230 for position



TURBINE INLET TEMPERATURE = 2540°F
 INLET COOLING AIR TEMPERATURE = 1200°F

Figure 253. Vane Temperatures (From Reduced Test Data) - Regenerative.

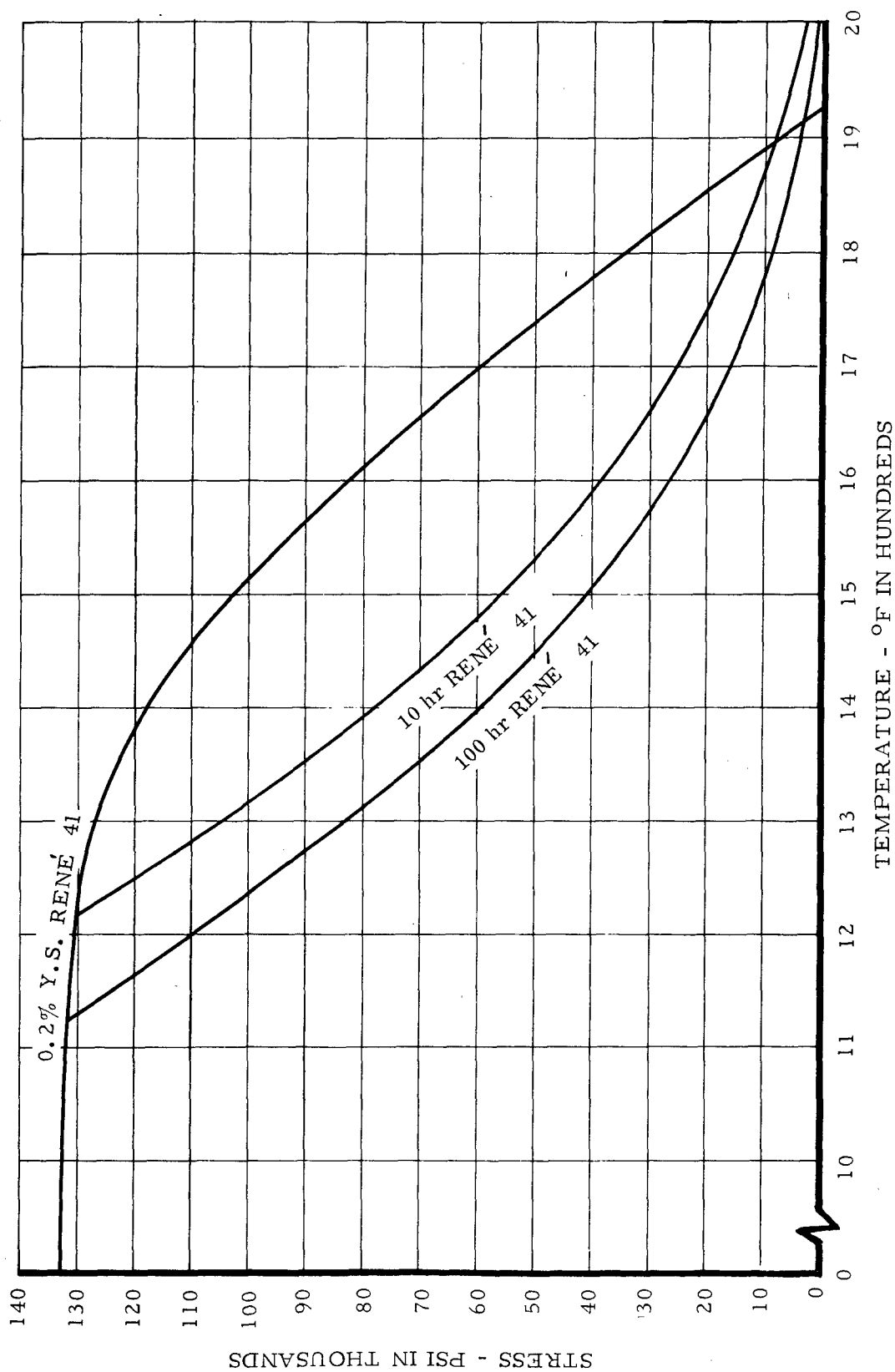


Figure 254. René 41 High Temperature Properties.

A fabricated René 41 design with vane internal cooling fins and trailing edge cooling slots using welded construction is selected for the following reasons:

1. The design is adequate for the nonregenerative case (Table XXV).
2. A sheet metal design is more "flexible" if aerodynamic adjustment is required. Retooling for modification is less expensive.
3. Tooling procured for the cascade can be used for the full-ring rig design.
4. Supplementary cooling could be added for regenerative operation.

COMBUSTOR

The combustor configuration is of annular design similar to the designs in operational Continental engines.

The combustor has been designed to operate efficiently under regenerative as well as nonregenerative cycle conditions.

The calculated cold combustor pressure losses of 4.8 percent and 6.8 percent for the nonregenerative and regenerative cycles, respectively, bracket the estimated cycle analysis combustor pressure loss of 5.8 percent.

Port areas and airflow distribution were determined to provide a stoichiometric fuel-air ratio in the primary zone for the nonregenerative cycle. The primary zone of the regenerative cycle is consequently somewhat less than stoichiometric (0.046).

Film-cooling louvers are provided for cooling the aft portions of the inner and outer combustor shells and the turbine inlet nozzle shrouds.

Design Analysis

This combustor is similar in size to the Continental T65-T-1 engine combustor. However, various changes in port areas and airflow distribution, as well as provision for cooling the inner and outer combustor shells, have been incorporated to allow for the higher turbine inlet temperature required.

The design point operating conditions of the combustor are:

Airflow - W_a	=	5 lb/sec
Fuel Flow - W_f	=	491 lb/hr (nonregenerative)
	=	336 lb/hr (regenerative)
Inlet Pressure - P_t	=	134.6 psia
Discharge Pressure - P_t	=	126.8 psia
Inlet Temperature - T_t	=	620° F (nonregenerative)
	=	1178° F (regenerative)
Turbine Inlet Temperature	=	2300° F
Combustor Pressure Drop - P	=	7.8 psi or 5.8 percent P_t

The requirement that the combustor operate efficiently under regenerative as well as nonregenerative cycle conditions has been considered in this design analysis. A single combustor configuration has been chosen for both conditions to provide as complete interchangeability of components between the two cycles as possible. This configuration has been designed to give a calculated cold combustor pressure loss of 4.8 percent for the nonregenerative cycle and 6.8 percent for the regenerative cycle. These pressure drops bracket the estimated cycle analysis combustor pressure drop of 5.8 percent and provide efficient operation of the combustor under regenerative and nonregenerative conditions.

The design is also capable of adaptation to provide the smallest pressure drop and the most efficient combustor for the regenerative or the nonregenerative cycle separately, should this be desirable.

Port areas and airflow distribution of the combustor were determined for the nonregenerative cycle conditions and then applied to the regenerative cycle conditions. The calculated combustor airflow distribution provides for a stoichiometric fuel-air ratio in the primary zone for the nonregenerative cycle. This is accomplished by a proper ratio of primary zone port areas (swirl vane plus inner combustor) to secondary, or mixing, zone port areas. This same primary-to-secondary flow area ratio provides a regenerative cycle primary fuel-air ratio of 0.0464. Airflow and port areas distribution are indicated on Figures 255 and 256 for the nonregenerative and regenerative cycles, respectively.

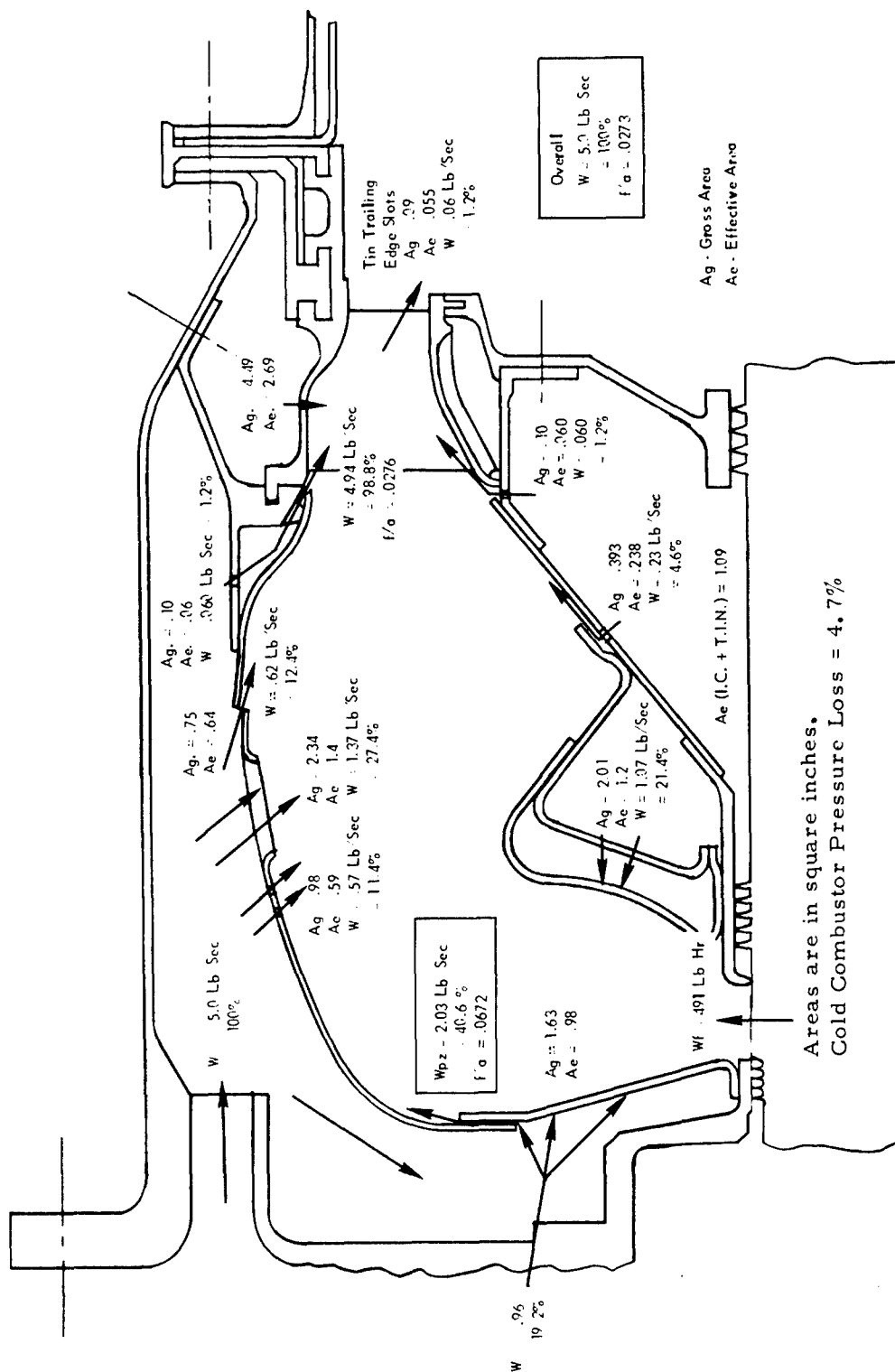


Figure 255. Nonregenerative Cycle - Combustor Airflow and Port Area Distribution.

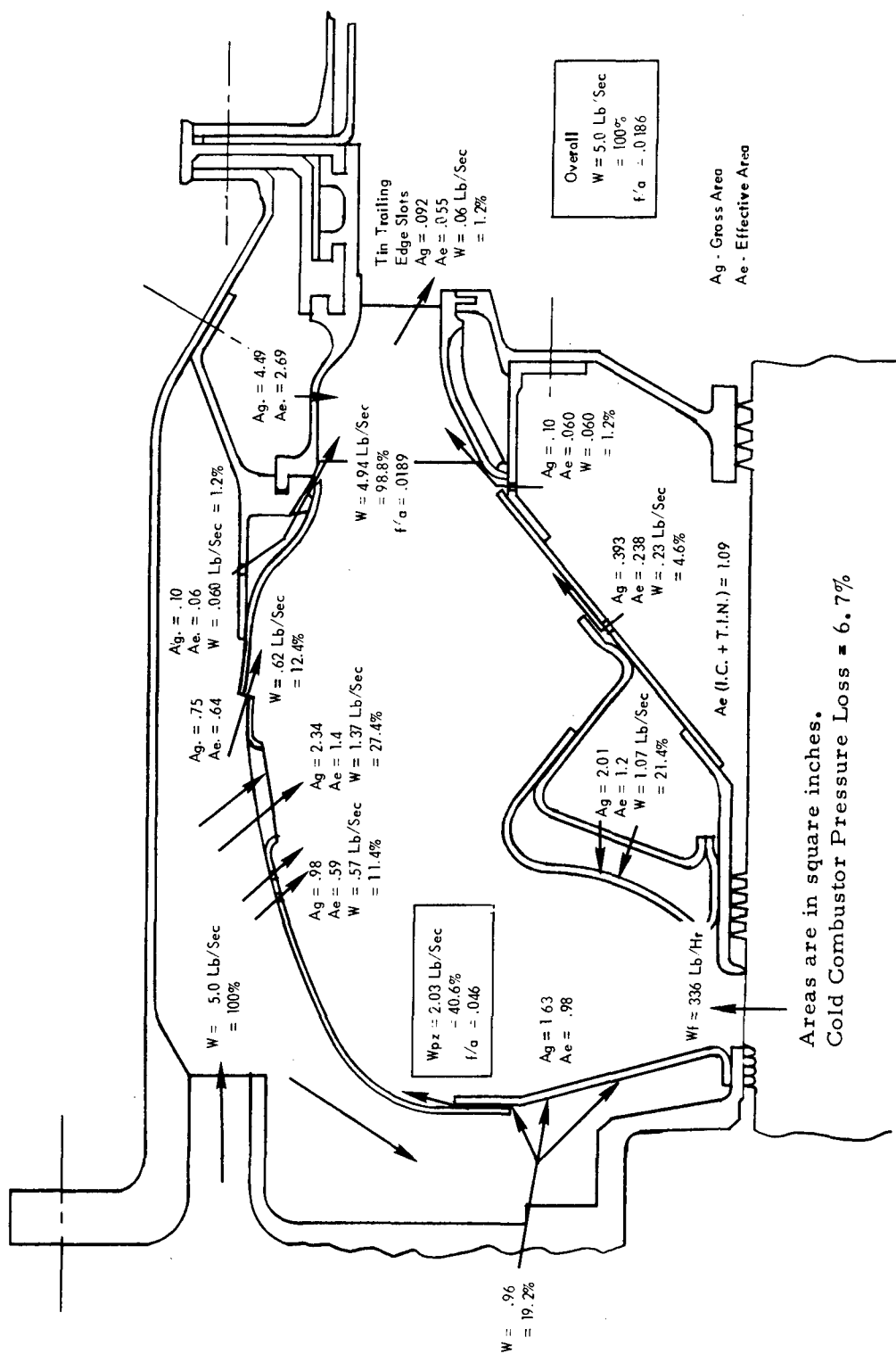


Figure 256. Regenerative Cycle - Combustor Airflow and Port Area Distribution.

For the required nonregenerative cycle fuel flow of 491 pounds per hour, approximately 40.1 percent of the combustor airflow is required in the primary zone for a stoichiometric fuel-air ratio. Therefore, 40.1 percent of the total combustor effective flow area must pass primary zone air. The total combustor effective flow area required for a given pressure drop may be approximated by the relation

$$\Delta P_c = \frac{1}{2g} \left(\frac{W_a^2}{\rho_a A_e^2} \right) \quad (20)$$

where:

ΔP_c = Combustor pressure drop, lb/ft²

ρ_a = Air density, lb/ft³, at combustor inlet

A_e = Total effective flow area of the combustor, ft²

For a 4.8-percent pressure drop,

$$\Delta P_c = 6.42 \text{ psi} = 924 \text{ lb/ft}^2$$

$$\rho_a = 0.337 \text{ lb/ft}^3$$

The required effective combustor flow area A_e is

$$A_e = 5.08 \text{ in.}^2$$

The primary zone effective flow area is then

$$P Z A_e = 0.401 (5.08) = 2.03 \text{ in.}^2$$

Good primary zone flow circulation is provided when the airflow from the inner combustor is approximately equal to the airflow from the swirl vane. Therefore, the effective port area of the swirl vane and inner combustor will be sized to allow for an equal flow split.

The swirl vane port area consists of the following:

1. Three rows of louvers, 36 louvers per row, with two 0.060-inch-diameter stress relief holes per louver.

Inner row - 0.34-x-0.020-inch opening

$$A_g = 0.354 \text{ in.}^2 \text{ (includes stress relief holes)}$$

Middle and outer rows - 0.34-x-0.040-inch opening

$$A_g = 1.007 \text{ in.}^2 \text{ (includes stress relief holes)}$$

2. Expansion slots - 0.060-inch-wide

$$A_g = 0.112 \text{ in.}^2$$

Total swirl vane gross area - $A_g = 1.47 \text{ in.}^2$

Total swirl vane effective area - $A_e = 0.945 \text{ in.}^2$

The inner combustor (IC) effective flow area must account for the added restriction caused by the internal flow path of the turbine inlet nozzles (TIN). This may be done by considering the flow areas of the turbine inlet nozzles and inner combustor face to be orifices in series. The circuit effective area may then be approximated by

$$SV A_e = \left(\frac{A_{IC}^2 \times A_{TIN}^2}{A_{IC}^2 + A_{TIN}^2} \right)^{1/2} \quad (21)$$

Since the internal flow area of the turbine inlet nozzles is fixed by aerodynamic requirements, the flow area of the inner combustor face must be sized to provide the proper circuit effective area. The desired circuit effective area is

$$\begin{aligned} \text{Circuit } A_e &= PZ A_e - SV A_e \\ &= 2.03 - 0.945 \\ &= 1.09 \text{ in.}^2 \end{aligned}$$

The effective flow area of the internal flow path of the turbine inlet nozzles for 23 vanes is

$$TIN A_e = 2.69 \text{ in.}^2$$

Therefore, the required inner combustor face effective flow area is

$$IC A_e = 1.2 \text{ in.}^2$$

and the inner combustor face flow area configuration is

1. Four rows of 24 holes each

Inner row - 0.100-inch-diameter holes

$$A_g = 0.188 \text{ in.}^2$$

Inner middle row - 0.125-inch-diameter holes

$$A_g = 0.294 \text{ in.}^2$$

Outer middle row - 0.125-inch-diameter holes

$$A_g = 0.294 \text{ in.}^2$$

Outer row - 0.125-inch-diameter holes

$$A_g = 0.294 \text{ in.}^2$$

2. Twenty-four expansion slots - 0.040-inch-wide

$$A_g = 0.935 \text{ in.}^2$$

Total gross area of inner combustor face

$$IC A_g = 2.01 \text{ in.}^2$$

Total inner combustor face effective flow area

$$IC A_e = 1.2 \text{ in.}^2$$

The secondary (mixing) port areas constitute the other 60 percent of the total combustor effective flow area. However, a portion of the secondary air must be utilized to cool the aft portions of the inner and outer combustor shells, the inner and outer turbine inlet nozzle shrouds, and the trailing edges of the turbine inlet nozzle vanes.

Analysis of the film-cooling process for the turbine inlet nozzle shrouds, Reference 41, indicates that approximately 1.2 percent of airflow is required for each of the inner and outer shrouds. Therefore, an effective area of

$$A_e = 0.060 \text{ in.}^2$$

will be required to film-cool each of the turbine inlet nozzle shrouds. This effective area will be provided by fifty 0.50-inch-diameter holes

discharging into a circumferential plenum that will distribute the flow and exhaust it aft approximately parallel to the main gas stream, through a circumferential slot.

The film-cooling analysis of the aft portions of the inner and outer combustor shells is based on Reference 42. This analysis indicates that film-cooling in this area is very effective for a short distance downstream of the film-cooling slot and then deteriorates rapidly. The analysis indicates that film-cooling louvers passing 12.5-percent airflow and located 1.85 inches forward of the shroud film cooling slots have a cooling effectiveness, η , defined as

$$\eta = \frac{T_{ad} - t_w}{T_{ad} - t_c} \quad (22)$$

equal to 1.0 for approximately 1.9 inches downstream of the louvers (this indicates a wall temperature equal to the coolant temperature, or $t_w = t_c = 620^\circ\text{F}$ for this distance). However, at a distance 2 inches downstream of the louvers, the calculated effectiveness is

$$\eta = 0.069,$$

giving a wall temperature of

$$t_w = 2184^\circ\text{F}$$

This large change in cooling effectiveness is probably caused by the large difference in velocity between the coolant and gas streams, resulting in rapid mixing of the two streams. Due to the extreme turbulence existing in this area of the combustor, the actual cooling effectiveness of these film-cooling louvers will be something less than 1.0 and will be determined during development testing of the combustor.

Similarly, the film-cooling slots for the inner combustor rear cone were sized to provide a cooling effectiveness, η , of

$$\eta = 1$$

over the length of the rear cone to be cooled. This requires 4.6 percent of the total airflow. As with the outer shell cooling, the cooling effectiveness of the inner combustor rear cone film-cooling will be determined during development testing.

The total amount of air utilized for cooling is 20.7 percent, leaving 39.2 percent for secondary mixing.

The secondary air effective flow area required to pass 39.2 percent of the airflow is 1.99 square inches. The secondary air ports consist of the following:

1. Eighty 0.125-inch-diameter holes
 $A_g = 0.981 \text{ in.}^2$
 $A_e = 0.588 \text{ in.}^2$
2. Twenty tubes, 0.286-inch-wide x 0.470-inch-long
 $A_g = 2.34 \text{ in.}^2$
 $A_e = 1.4 \text{ in.}^2$

Total secondary effective flow area is

$$A_e = 1.99 \text{ in.}^2$$

Port areas and airflow distribution are shown in detail in Figures 255 and 256. Table XXVII is a summary of the combustor analysis for the regenerative and nonregenerative cycles.

TABLE XXVII

COMBUSTOR ANALYSIS SUMMARY

Characteristic	Engine Units	Regenerative	Nonregenerative	Characteristic	Engine Units	Regenerative	Nonregenerative
Rated Speed	rpm	50,000	50,000	Ratio 25/13	—	1.59	1.59
Fuel Flow	lb/hr	336	491	Ratio 26/12	—	7.73	7.73
Airflow	lb/sec	5.0	5.0	Ratio 26/13	—	2.59	2.59
Comp. Pressure Ratio	—	9.2	9.2	Comb. Outlet Velocity	ft/sec	215	215
Overall Fuel-Air Ratio	—	0.0186	0.0273	Sec. Comb. Zone Mean Path Length	in.	2.7	2.7
Primary Airflow	lb/sec	2.03	2.03	Sec. Comb. Zone Dwell Time	Millisec	2.05	2.16
Primary Zone Out. Spec. Vol.	cu. ft/lb	11.65	12.7	Overall Comb. Dwell Time	Millisec	4.4	4.4
Comb. Outlet Spec. Vol.	cu. ft/lb	8.06	8.06	125 Percent Total Comb. Vol. Heat Rel. Rate	Btu/cu. ft/hr/Atm	4.41 x 10 ⁶	6.46 x 10 ⁶
Primary Comb. Zone Vol.	cu. in.	27.6	27.6	Comb. Out. Area	sq. in.	27.6	27.6
Prim. + Int. Comb. Zone Vol.	cu. in.	82.5	82.5	Swirl Plate Flow Area (Includes SV - OC Gap)	sq. in.	1.63	1.63
Ratio 13/12	—	2.99	2.99	Inner Comb. Hole Flow Area	sq. in.	2.01	2.01
Heat Rel. Rate-Prim. Zone	Btu/cu. ft/hr/Atm	42.7 x 10 ⁶	62.4 x 10 ⁶	Sec. Air Tube Flow Area	sq. in.	2.34	2.34
Heat Rel. Rate-Prim. + Int. Zone	Btu/cu. ft/hr/Atm	14.3 x 10 ⁶	20.9 x 10 ⁶	Sec. Air Total Flow Area	sq. in.	4.46	4.46
Prim. Comb. Zone Out. Flow Area	sq. in.	31.8	31.8	Ratio 37/36	—	1.23	1.23
Prim. Comb. Zone Out. Flow Vel.	ft/sec	106	117	Total Prim. Airflow Area	sq. in.	3.64	3.64
Int. Comb. Zone Out. Flow Area	sq. in.	40.6	40.6	Ratio 39/41	—	1.22	1.22
Int. Comb. Zone Out. Flow Vel.	ft/sec	112	123	Total Comb. Vol. Heat Release Rate	Btu/ft. 3/hr	5.52 x 10 ⁶	8.07 x 10 ⁶
Prim. Comb. Zone Mean Path Length	in.	1.16	1.16	Total Comb. Airflow Area	sq. in.	8.396	8.396
Prim. Comb. Zone Dwell Time (Comp. Comb.)	Millisec	0.983	1.00	Turbine Inlet Temp.	°F	2300	2300
Prim. + Int. Comb. Zone Mean Path Length	in.	3.03	3.03	Prim. Zone Fuel-Air Ratio	lb Fuel/lb Air	0.046	0.0672
Prim. + Int. Comb. Zone Dwell Time (Comp. Comb.)	Millisec	2.35	2.24	Comp. Disch. Temp.	°F	620	620
Sec. Comb. Zone Volume	cu. in.	130.9	130.9	Heat Exch. Disch. Temp.	°F	1178	—
Total Combustor Volume	cu. in.	213.4	213.4	Comb. Δp/p (Cold) (Calculated)	Percent	6.7	4.7
				Heat Exchange Effectiveness	ε	0.77	—

TURBINE INLET NOZZLE CASCADE DESIGN

This section describes the design details of a hot turbine inlet nozzle cascade and test of the nozzle cooling schemes on the hot cascade rig.

The turbine inlet nozzle cascade to be tested under this program was designed to be adaptable to the existing hot cascade rig shown in Figure 257.

HOT CASCADE RIG

The hot cascade rig, shown schematically in Figure 258, consists of the following basic elements:

1. A metered air supply.
2. One preheater to provide cooling air simulating compressor discharge temperature.
3. One preheater to provide hot gas at the desired turbine inlet temperature.
4. Inlet, exhaust, and bypass ducting as required.
5. A plenum on the exit of the high temperature preheater to provide a uniform temperature profile into the test section.
6. Valves to provide control of rig pressures and flow rates.
7. Orifices to meter the cooling airflow rates upstream and downstream of the test section.
8. Two actuated, double-shielded, aspirating, Pt 30 percent Rh/Pt 6 percent Rh thermocouples conforming to the configuration defined in Reference 2, Probe 8.

TEST SECTION

The cascade tested consisted of a brazed TD nickel turbine inlet nozzle segment of three vanes and four flow passages. This configuration was chosen to eliminate sidewall effects on the central, instrumented vane, thus closely simulating actual engine flow conditions.

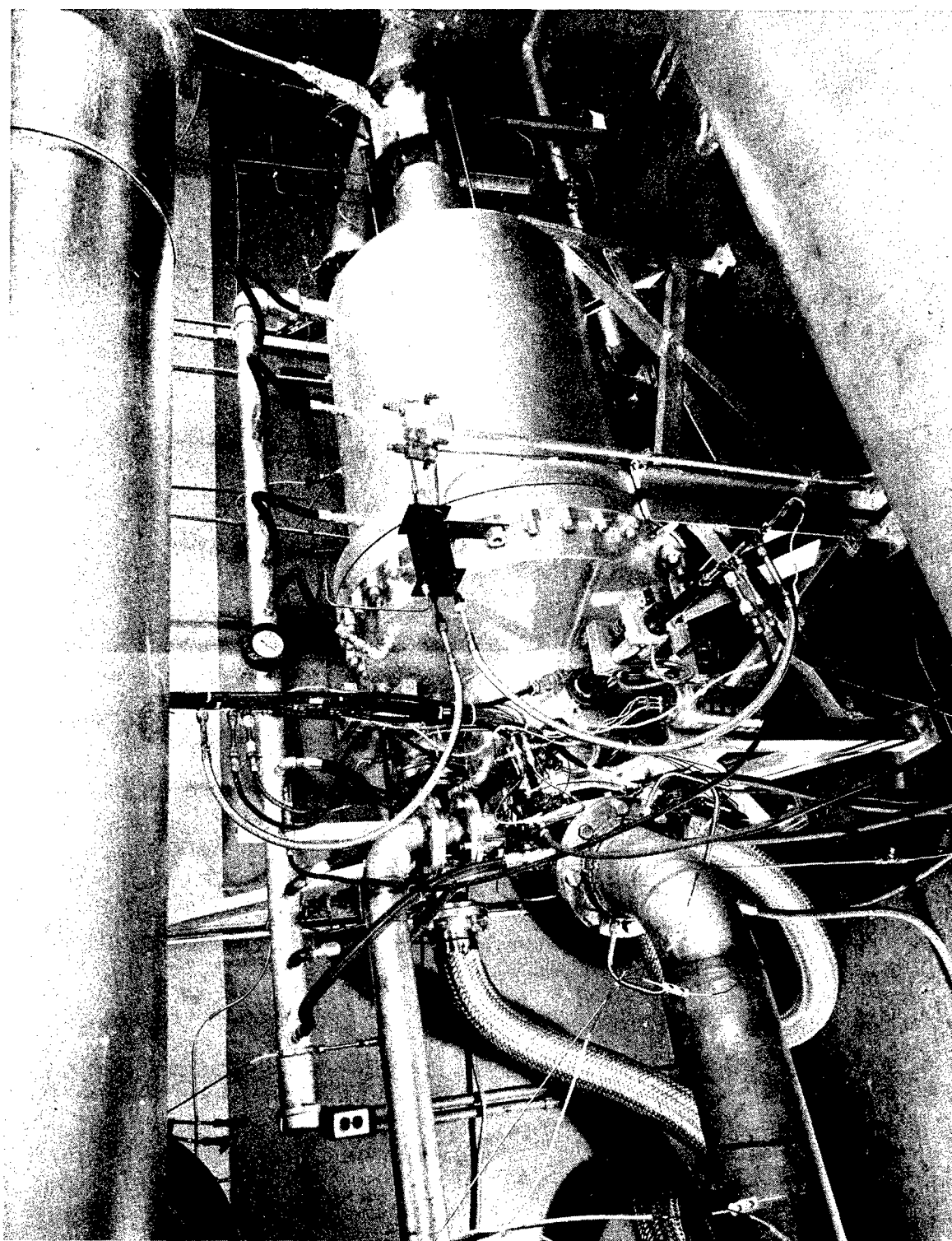


Figure 257. Turbine Inlet Nozzle Hot Cascade Rig.

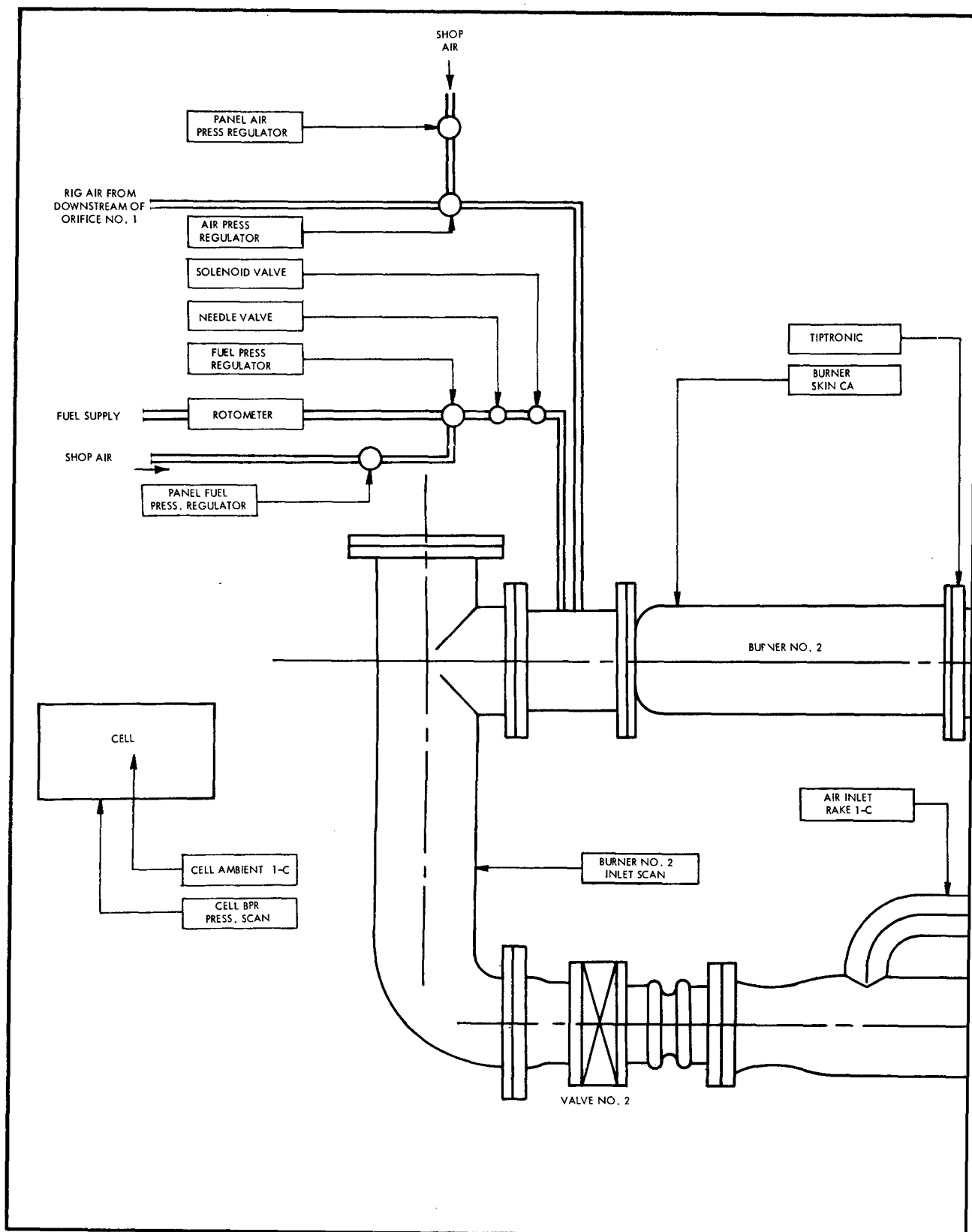
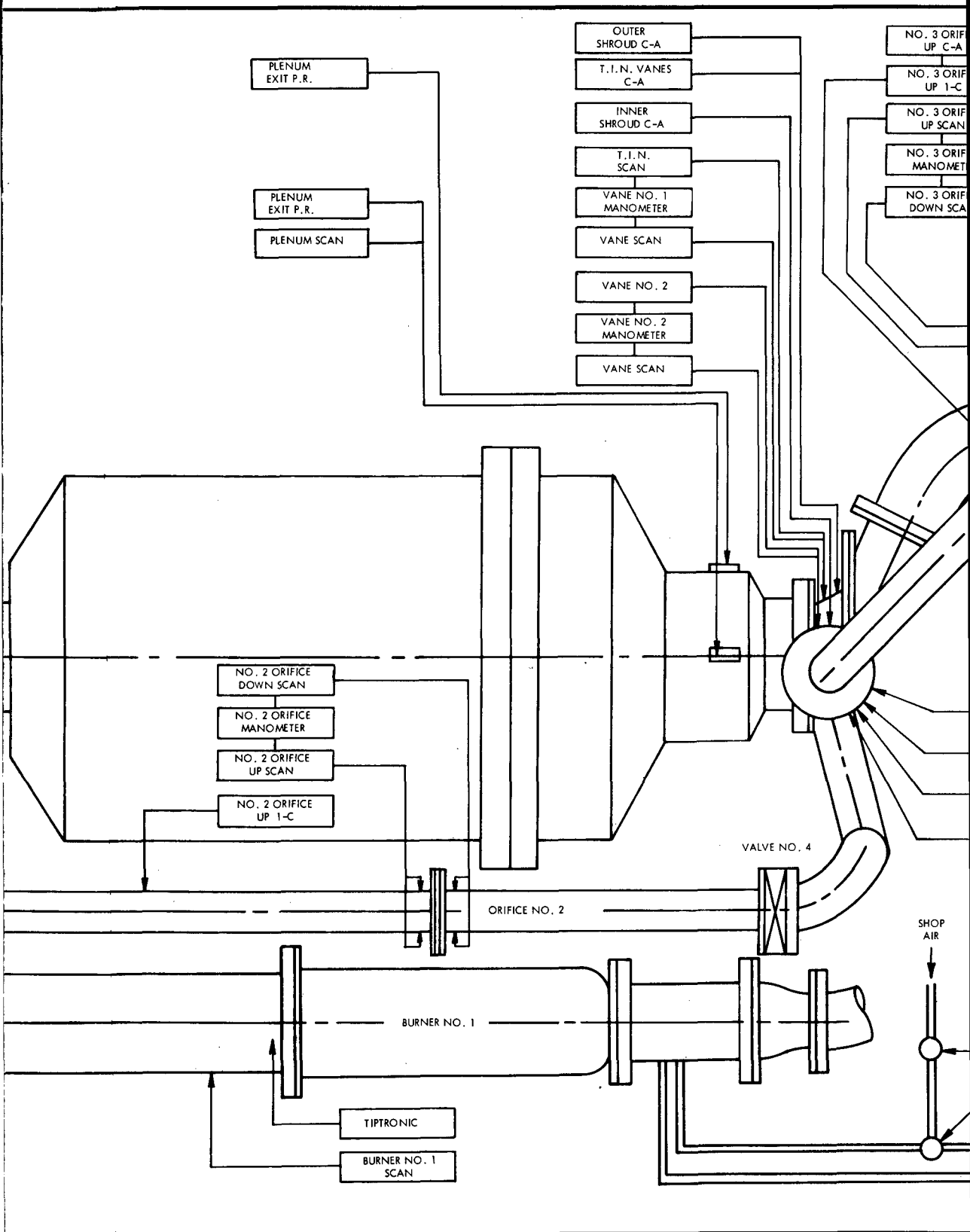
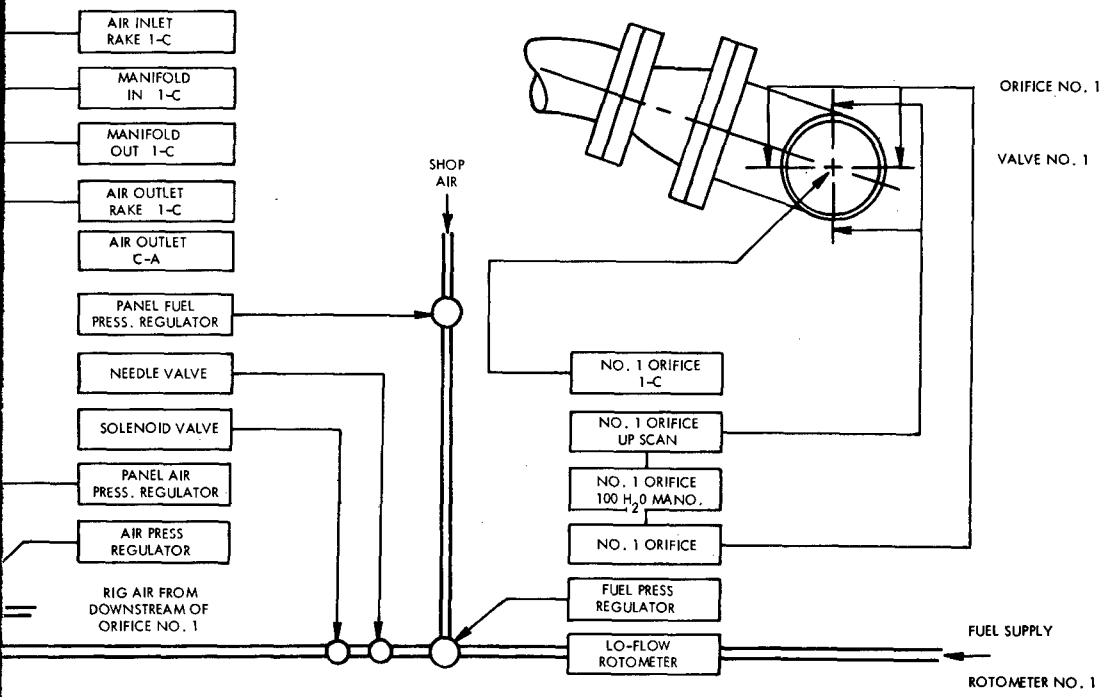
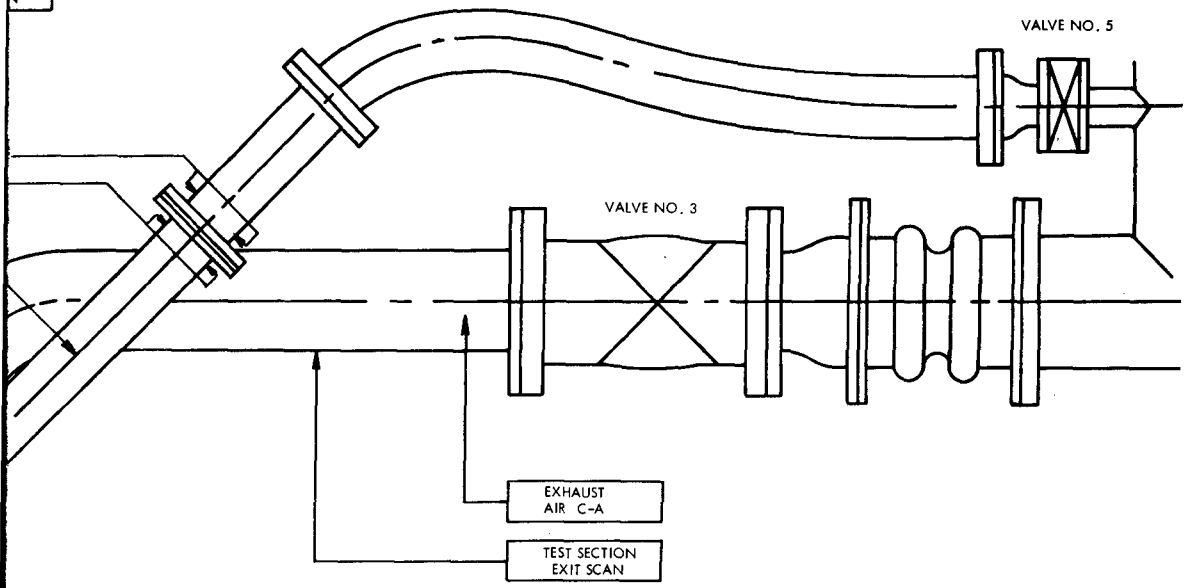


Figure 258. Turbine Inlet Nozzle Hot Cascade Rig.



CE
CE
CE
CE
ER
CE
N



A cross section of the cascade is shown in Figure 259, and the nozzle vane is detailed in Figure 260.

Figures 261 and 262 show the instrumented test section ready for assembly into the hot cascade rig. The trailing edges of two vanes are clearly visible through the viewing port opening in Figure 262.

The finned internal surface of the vanes is evident in the closeup of the outer shroud, Figure 263, prior to instrumentation. The uniformity of the finned surface is indicated in Figure 264.

INSTRUMENTATION

The vane and shroud metal temperatures were measured with Inconel sheathed, magnesium oxide insulated, chromel-alumel thermocouples welded in place and insulated with a ceramic cement. Figures 265 and 266 show this instrumentation installed; identification of the individual thermocouples is shown schematically on the vane profile and shroud sketches of Figures 267 through 269.

In addition to the metal temperature instrumentation mentioned above, four-element chromel-alumel thermocouple rakes were installed in the cooling air inlet and outlet ducts to monitor the cooling air temperature.

Total pressure of the hot gas entering the test section was measured by total pressure probes installed in the outer vanes of the test section. Static pressure of the cooling air passing through the vanes was measured by static pressure probes installed inside the outer vanes. The pressure probes are shown installed in Figures 261 and 266.

TEST PROGRAM

The test program was set up to provide heat transfer data which would permit verification of analytical design data.

Test points were selected to cover a range of part-power as well as design point engine operating conditions. Limitations in the available air supply required testing at a simulated altitude of 10,000 feet, and test point conditions were adjusted accordingly. Details of the test points chosen are given in Table XXVIII, which differ only in the amount of cooling air flow through the nozzle vanes (inner combustor flow). Although the

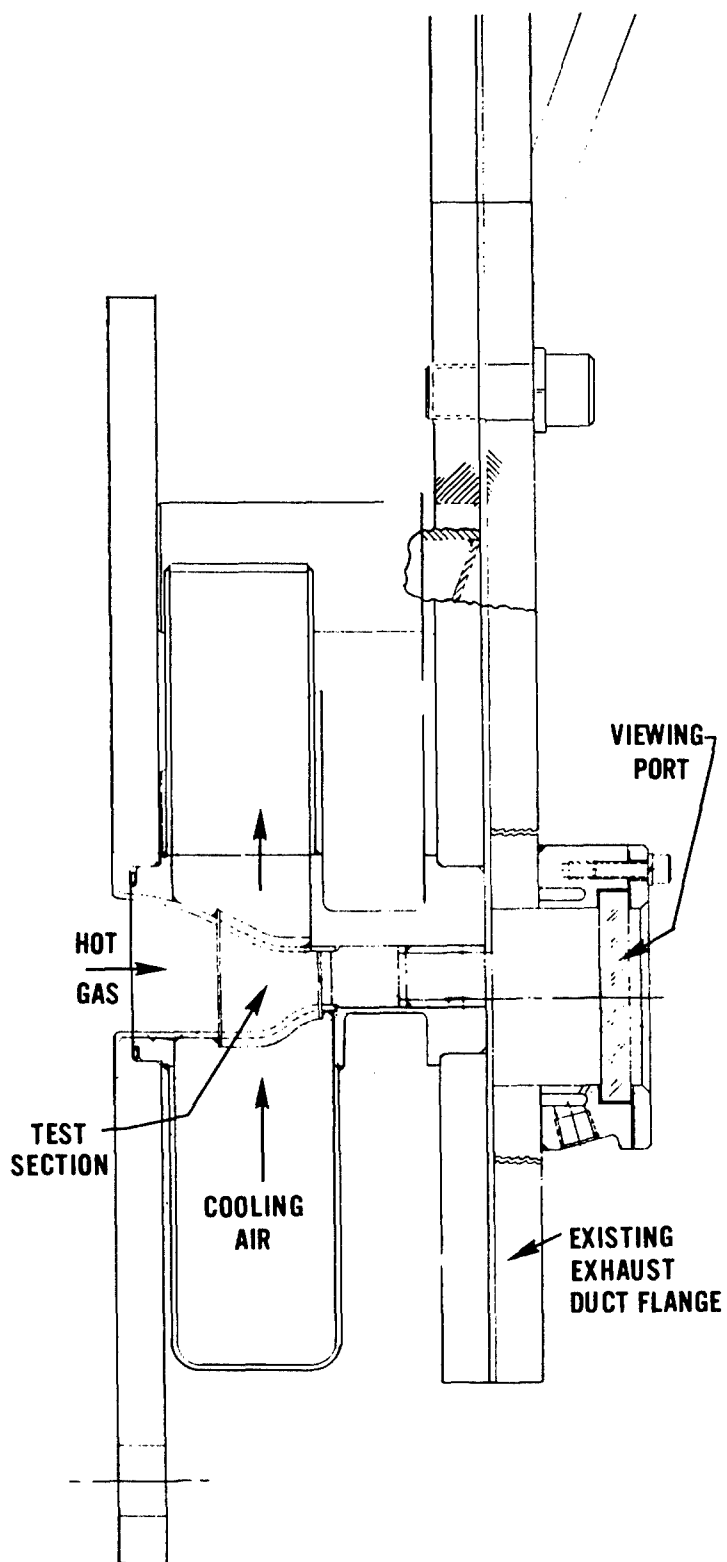


Figure 259. Turbine Inlet Nozzle Test Cascade.

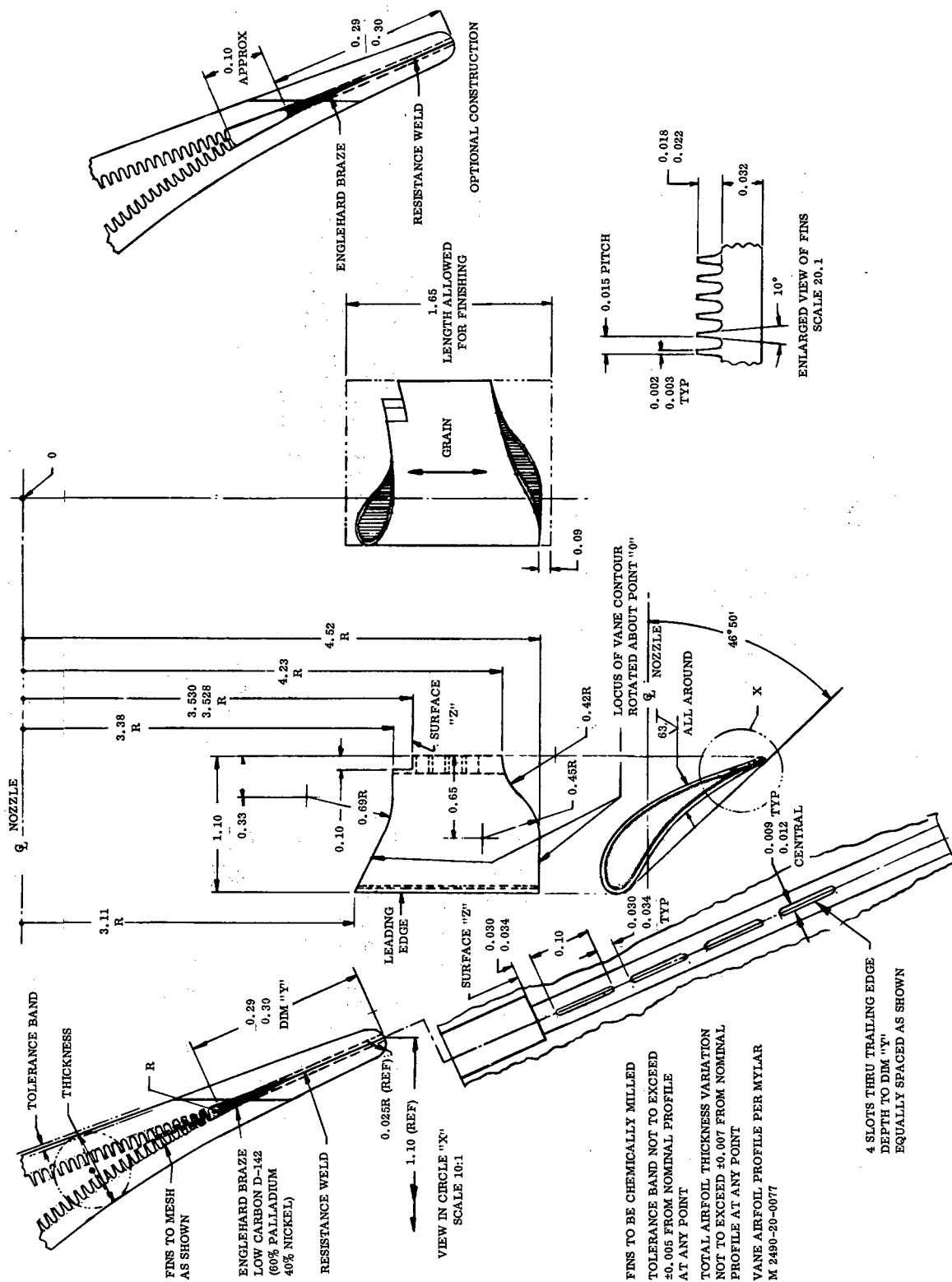


Figure 260. Detail of TD Nickel Nozzle Vane.

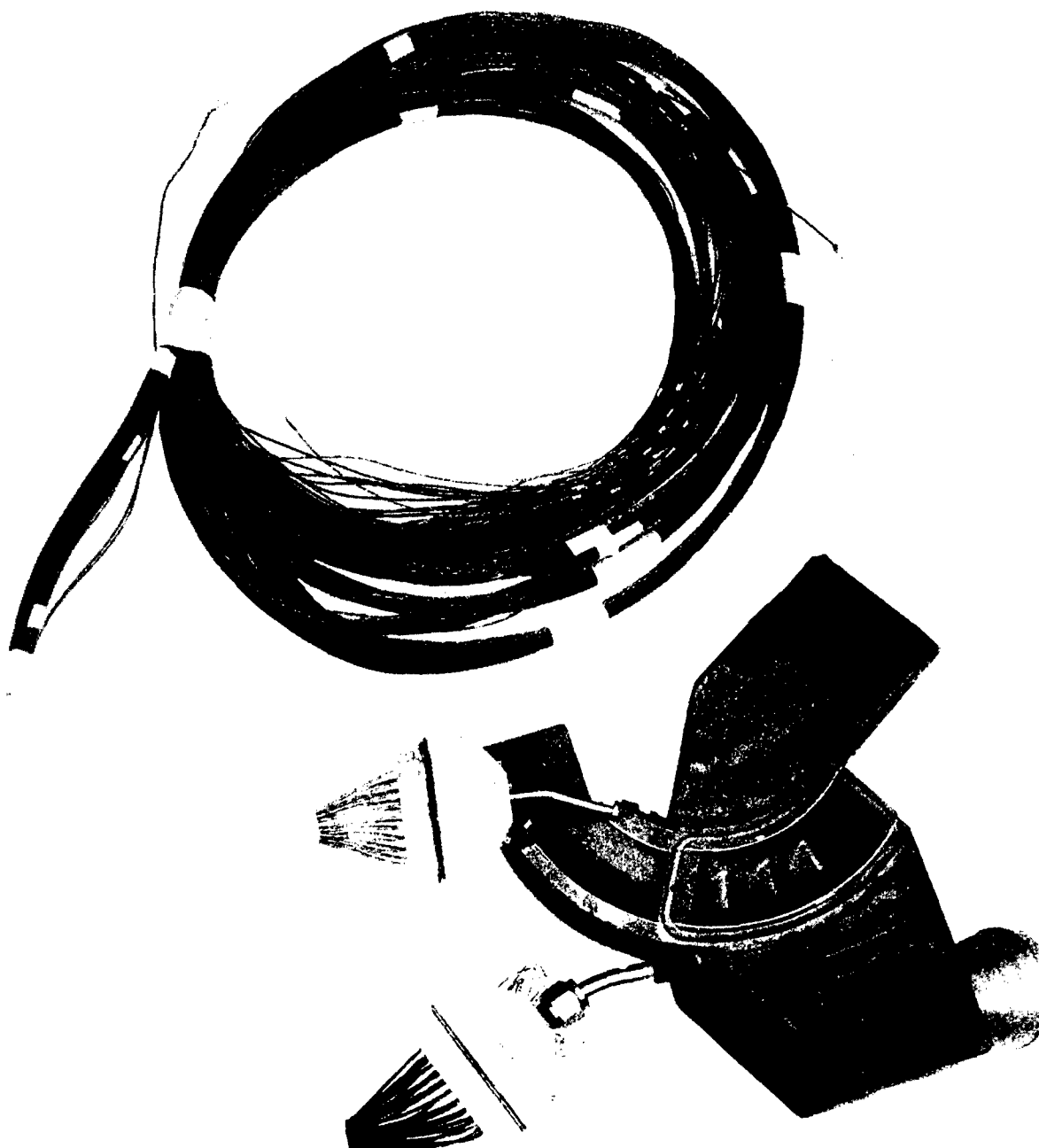


Figure 261. View of Test Section Inlet.

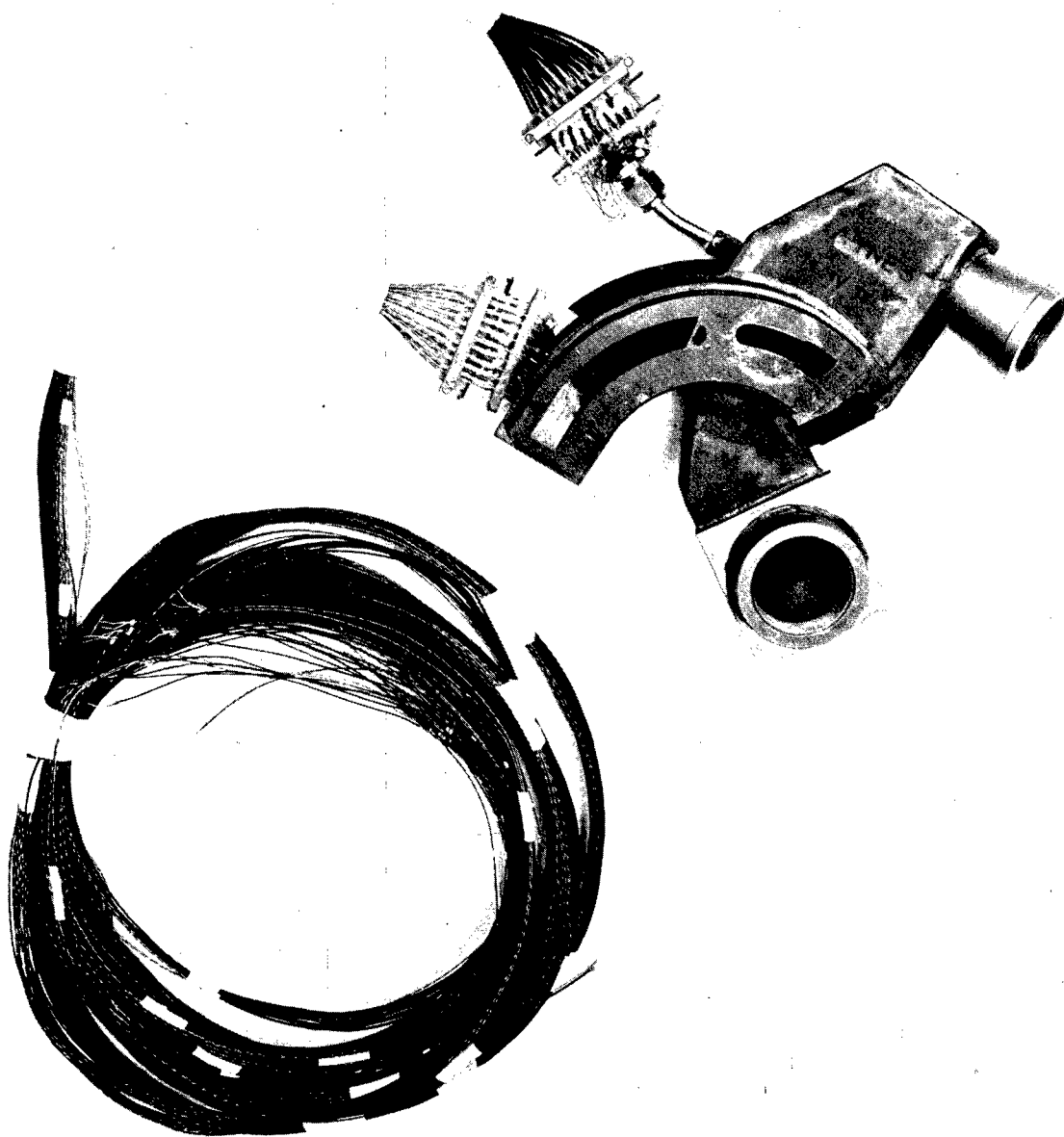


Figure 262. Rear View of Test Section.



Figure 263. Close-Up of Vanes and Outer Shroud Showing Finned Internal Surface of Vanes.

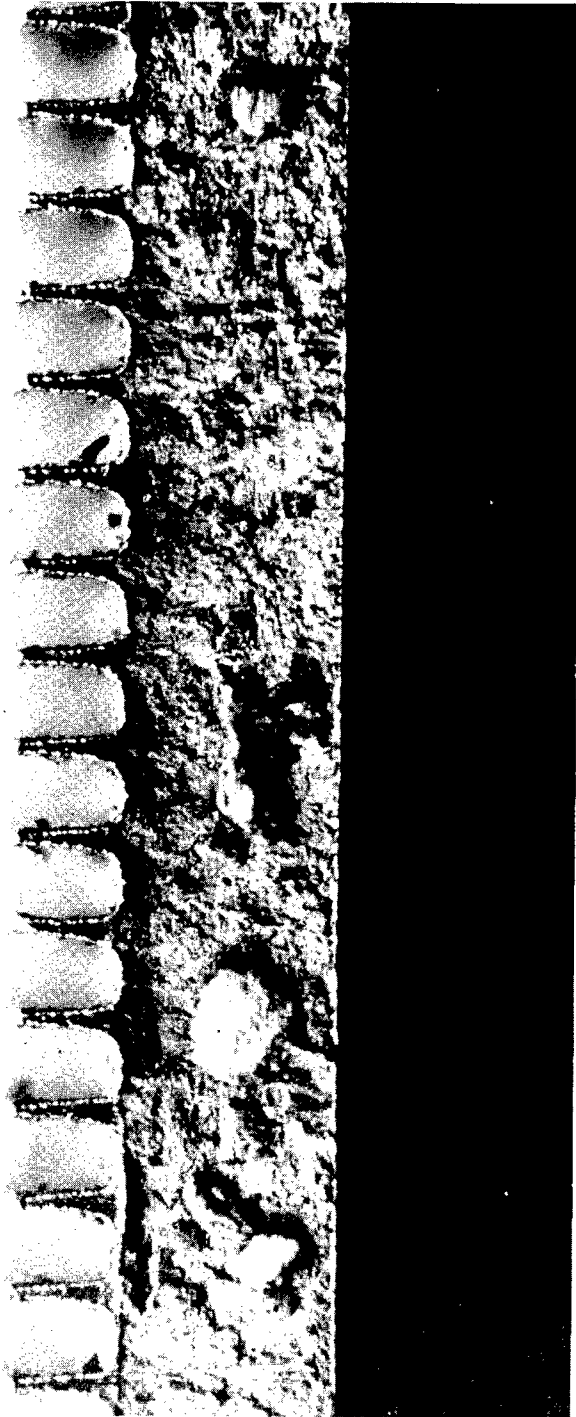


Figure 264. Profile of Finned Surface (26 x Size).



Figure 265. View of Inner Shroud Showing Vane and Shroud Instrumentation.



Figure 266. View of Outer Shroud Showing Vane and Shroud Instrumentation.

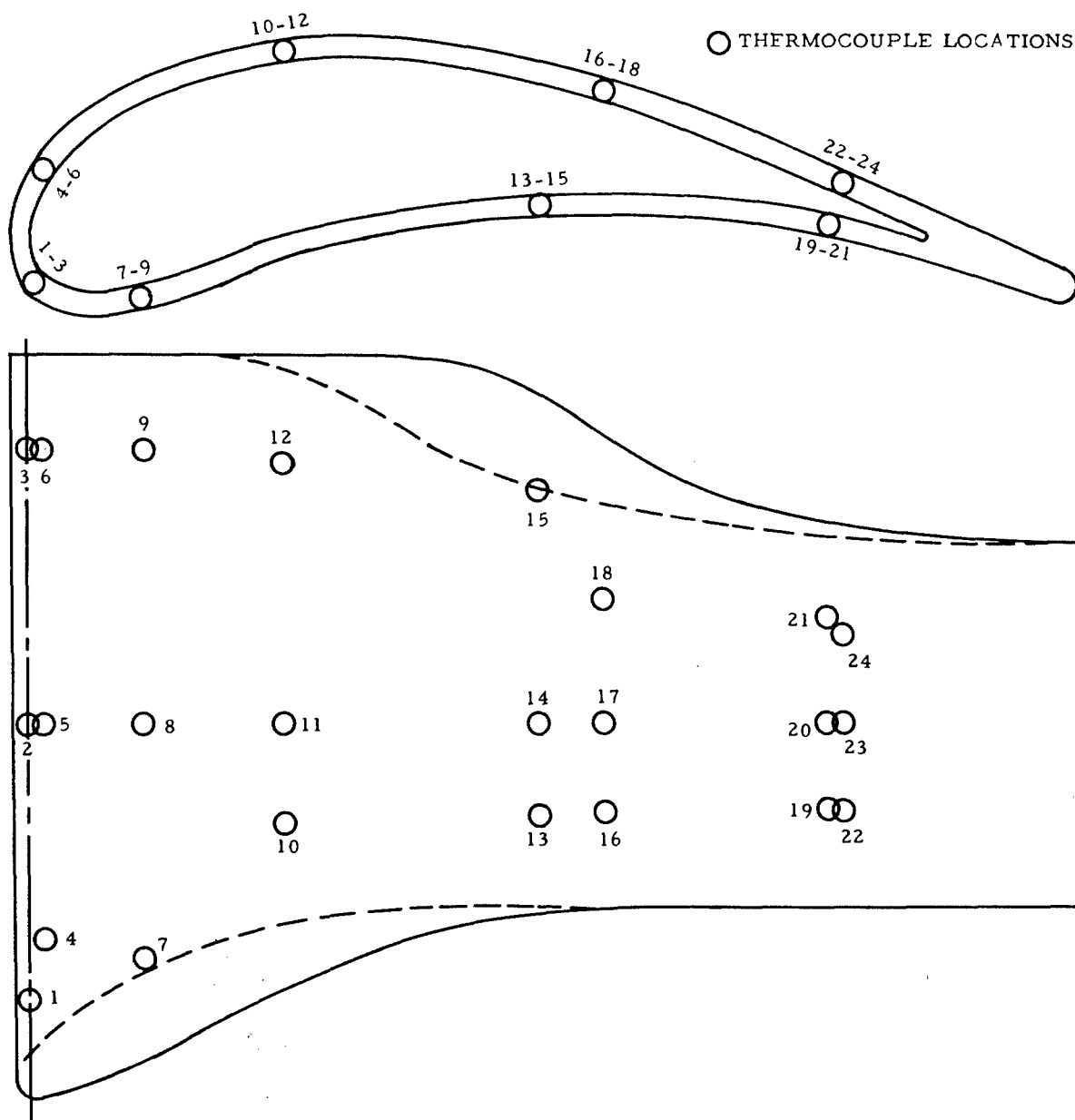


Figure 267. Vane Instrumentation.

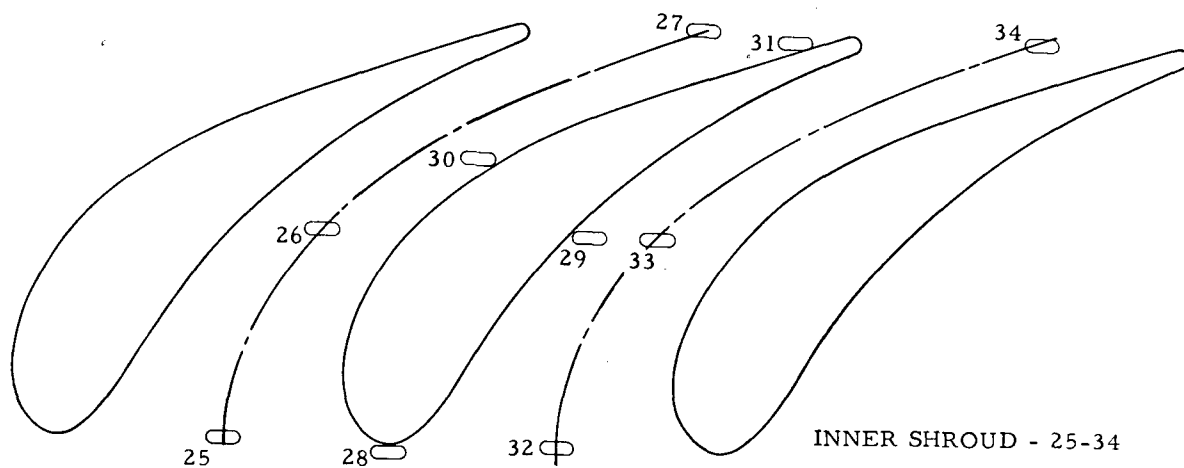


Figure 268. Inner Shroud Instrumentation.

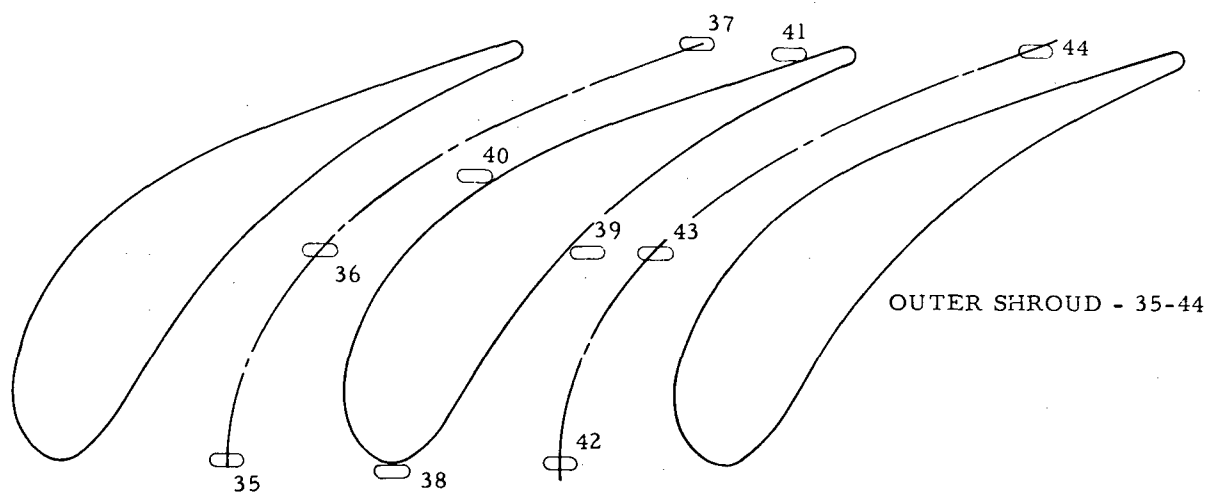


Figure 269. Outer Shroud Instrumentation.

TABLE XXVIII
CASCADE RIG - OFF-DESIGN CONDITIONS

RPM	Altitude (ft)	Burner No.	W _a (Lb /Sec)	P _{in} (PSIA)	T _{in} (°F)	t/a	W _f (Lb /Hr)	T _{out} (°F)	Test Section Inlet	
									P (PSIA)	T (°F)
Assumes 5 Percent Loss in P _T in each Preheater										
Inner Combustor Flow (IC) = 30 Percent W _a										
50,000	10,000	1	0.792	97.3	60	0.00777	22.2	611	—	—
47,500	↓		0.737	85.2	60	0.0071	18.8	569	—	—
45,000		1	0.666	76	60	0.0064	15.3	518	—	—
40,000		1	0.539	55.7	60	0.00521	10.1	436	—	—
35,000	↓	1	0.431	40.2	60	0.00412	6.4	358	—	—
30,000	10,000	1	0.324	29.3	60	0.00318	3.7	291	—	—
50,000	10,000	2	0.609	92.7	611	0.0287	62.8	2300	88	2300
47,500	↓		0.566	81.2	569	0.0247	50.2	2058	77.3	2058
45,000		2	0.512	72.3	518	0.0212	39.1	1840	68.7	1840
40,000		2	0.414	53.1	436	0.0157	23.4	1449	50.4	1449
35,000	↓	2	0.332	38.3	358	0.0119	14.2	1152	36.4	1152
30,000	10,000	2	0.249	27.9	291	0.00994	8.9	969	26.5	969
50,000	10,000	IC Flow	0.183	92.7	611	—	—	—	90.3	611
47,500	↓		0.171	81.2	569	—	—	—	79.2	569
45,000			0.154	72.3	518	—	—	—	70.5	518
40,000			0.125	53.1	436	—	—	—	51.7	436
35,000	↓		0.090	38.3	358	—	—	—	37.3	358
30,000	10,000	IC Flow	0.075	27.9	291	—	—	—	27.2	291
Inner Combustor Flow (IC) = 20 Percent W _a										
50,000	10,000	1	0.731	97.3	60	0.00777	20.5	611	—	—
47,500	↓		0.679	85.2	60	0.0071	17.3	569	—	—
45,000		1	0.615	76	60	0.0064	14.2	518	—	—
40,000		1	0.497	55.7	60	0.00521	9.3	436	—	—
35,000	↓	1	0.398	40.2	60	0.00412	5.9	358	—	—
30,000	10,000	1	0.299	29.3	60	0.00318	3.4	291	—	—
50,000	10,000	2	0.609	92.7	611	0.0287	62.8	2300	88	2300
47,500	↓		0.566	81.2	569	0.0247	50.2	2058	77.3	2058
45,000		2	0.512	72.3	518	0.0212	39.1	1840	68.7	1840
40,000		2	0.414	53.1	436	0.0157	23.4	1449	50.4	1449
35,000	↓	2	0.332	38.3	358	0.0119	14.2	1152	36.4	1152
30,000	10,000	2	0.249	27.9	291	0.00994	8.9	969	26.5	969
50,000	10,000	IC Flow	0.122	92.7	611	—	—	—	90.3	611
47,500	↓		0.113	81.2	569	—	—	—	79.2	569
45,000			0.103	72.3	518	—	—	—	70.5	518
40,000			0.083	53.1	436	—	—	—	51.7	436
35,000	↓		0.066	38.3	358	—	—	—	37.3	358
30,000	10,000	IC Flow	0.050	27.9	291	—	—	—	27.2	291

cooling airflow rate (IC flow) is not variable during engine running, it is controllable on the hot cascade rig and was varied to bracket the actual engine operating condition of approximately 26 percent of the total airflow.

DISCUSSION OF TEST RESULTS

Hot testing of the cascade section began by setting up the 35,000-rpm (70-percent speed), 30-percent inner combustor flow condition of Table XXVIII. The inner combustor flow was then reduced to the 20-percent flow condition of Table XXVIII, while maintaining the same hot gas flow conditions. These two flow conditions constitute data point readings 1 and 2 respectively.

This test sequence was continued for the 80-, 90-, 95-, and 100-percent speed conditions. Therefore, data point readings 1, 4, 6, 8, and 10 represent the 30-percent inner combustor flow conditions of Table XXVIII, and data point readings 2, 5, 7, 9, and 11 represent the 20-percent inner combustor flow conditions of Table XXVIII. It is to be noted that data point readings 1 and 2, 4 and 5, 6 and 7, 8 and 9, and 10 and 11 represent pairs of data points with the hot gas flow conditions held essentially constant within each pair while the inner combustor (or cooling air) flow was varied.

The vane metal temperatures recorded for each data point have been plotted on schematics of the vane profile to facilitate comparison (Figures 270 through 279).

The test program covered 17.5 hours of hot running, of which 3.5 hours was above 2000°F turbine inlet temperature.

While all data points indicate the effectiveness of the finned internal surface of the vanes, of prime interest are the high temperature readings, data points 10 and 11. These permit comparison with analytical design data.

Since the design analysis was based on a peak gas temperature,

$$\begin{aligned} T_{\text{peak}} &= T_{\text{mean}} + 0.2 (\text{combustor temperature rise}) \\ &= 2300 + 0.2 (2300 - 620) \\ &= 2300 + 336 \\ &= 2636^{\circ}\text{F}, \end{aligned}$$

the test data are reduced to this peak temperature for comparison purposes.

□ INNER SHROUD
 △ CENTERLINE
 ○ OUTER SHROUD

$T_g = 1130^{\circ}\text{F}$
 $T_{\text{ain}} = 346^{\circ}\text{F}$
 $T_{\text{a}}^{\text{out}} = 391^{\circ}\text{F}$
 $T_{\text{a}} = 368^{\circ}\text{F}$
 $W_{\text{ic}} = 0.271 W_g$

○ THERMOCOUPLE LOCATIONS

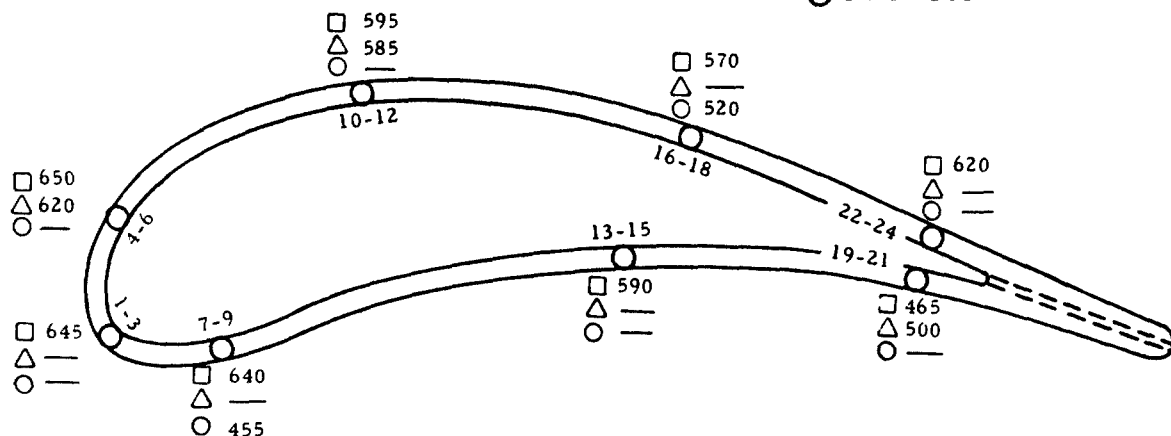


Figure 270. Vane Metal Temperature - Reading No. 1.

□ INNER SHROUD
 △ CENTERLINE
 ○ OUTER SHROUD

$T_g = 1217^{\circ}\text{F}$
 $T_{\text{ain}} = 362^{\circ}\text{F}$
 $T_{\text{a}}^{\text{out}} = 426^{\circ}\text{F}$
 $T_{\text{a}} = 394^{\circ}\text{F}$
 $W_{\text{ic}} = 0.202 W_g$

○ THERMOCOUPLE LOCATIONS

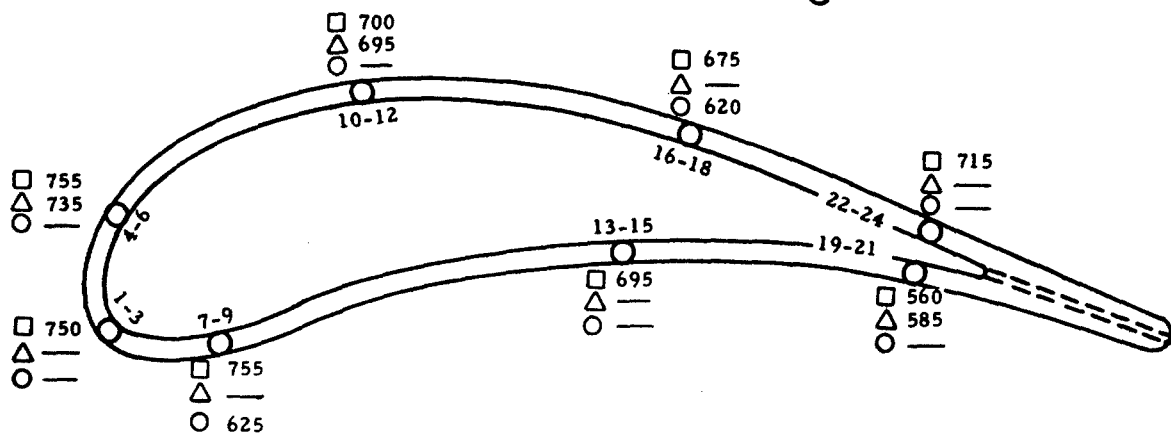


Figure 271. Vane Metal Temperature - Reading No. 2.

- INNER SHROUD
- △ CENTERLINE
- OUTER SHROUD

$T_g = 1423^{\circ}\text{F}$
 $T_{\text{ain}} = 449^{\circ}\text{F}$
 $T_{\text{aout}} = 520^{\circ}\text{F}$
 $T_a = 484^{\circ}\text{F}$
 $W_{\text{ic}} = 0.259 W_g$

○ THERMOCOUPLE LOCATIONS

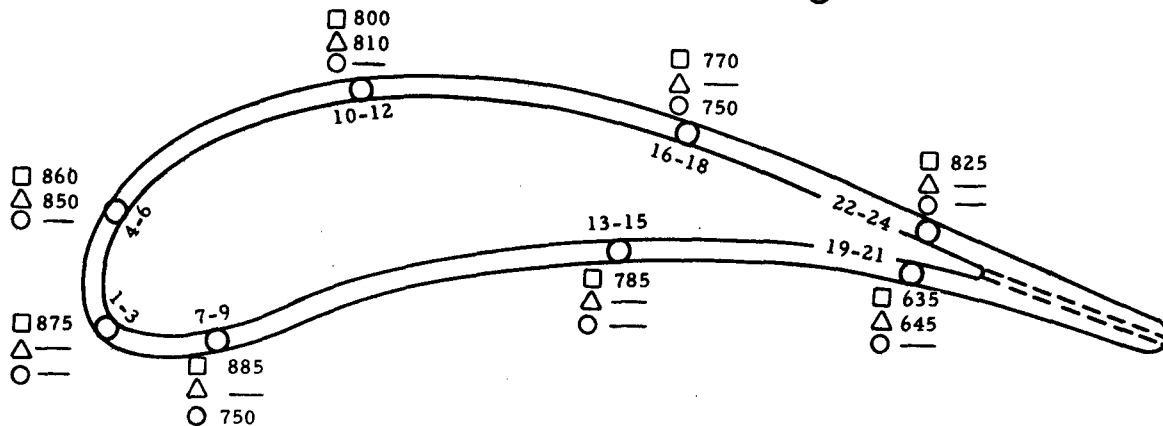


Figure 272. Vane Metal Temperature - Reading No. 4.

- INNER SHROUD
- △ CENTERLINE
- OUTER SHROUD

$T_g = 1484^{\circ}\text{F}$
 $T_{\text{ain}} = 432^{\circ}\text{F}$
 $T_{\text{aout}} = 524^{\circ}\text{F}$
 $T_a = 478^{\circ}\text{F}$
 $W_{\text{ic}} = 0.207 W_g$

○ THERMOCOUPLE LOCATIONS

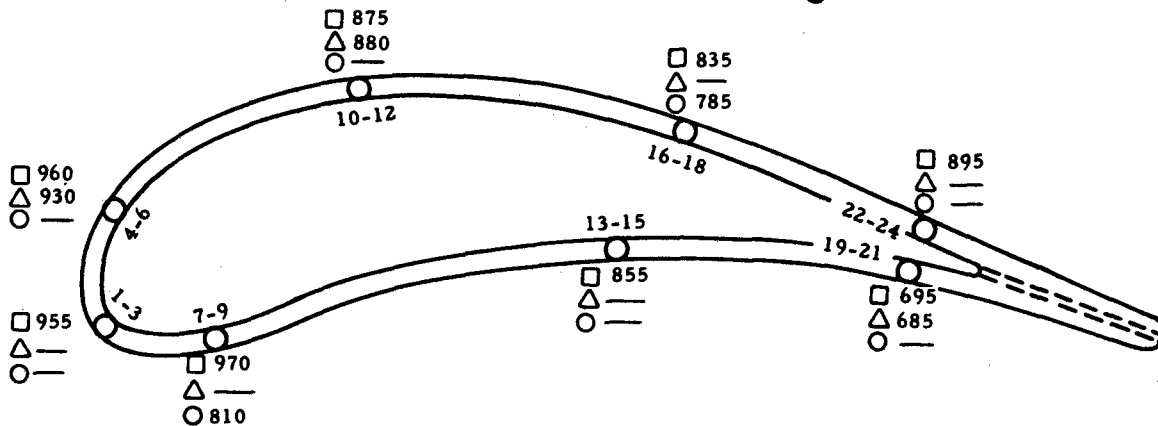


Figure 273. Vane Metal Temperature - Reading No. 5.

- INNER SHROUD
- △ CENTERLINE
- OUTER SHROUD

$T_g = 1832^{\circ}\text{F}$
 $T_{a\text{in}} = 490^{\circ}\text{F}$
 $T_{a\text{out}} = 571^{\circ}\text{F}$
 $T_a = 531^{\circ}\text{F}$
 $W_{ic} = 0.325 W_g$

○ THERMOCOUPLE LOCATIONS

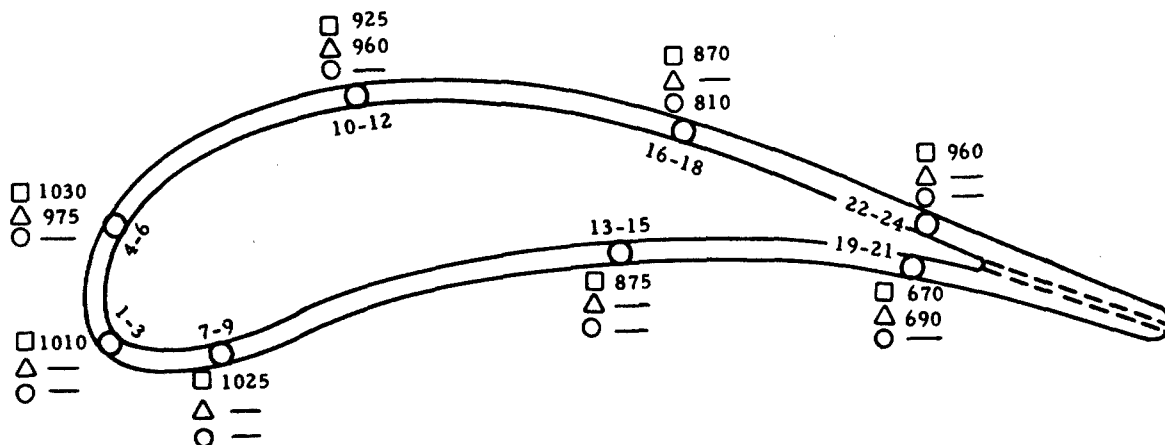


Figure 274. Vane Metal Temperature - Reading No. 6.

- INNER SHROUD
- △ CENTERLINE
- OUTER SHROUD

$T_g = 1838^{\circ}\text{F}$
 $T_{a\text{in}} = 497^{\circ}\text{F}$
 $T_{a\text{out}} = 598^{\circ}\text{F}$
 $T_a = 547^{\circ}\text{F}$
 $W_{ic} = 0.247 W_g$

○ THERMOCOUPLE LOCATIONS

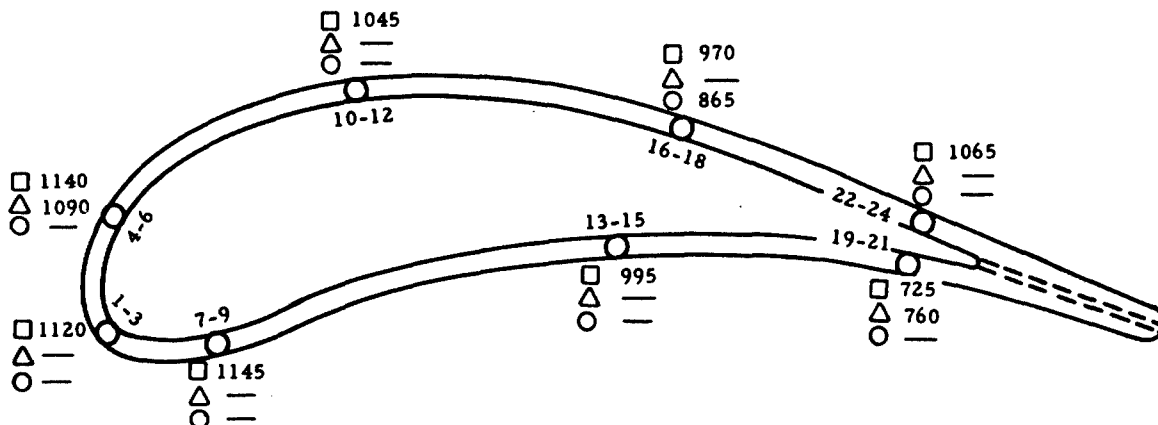


Figure 275. Vane Metal Temperature - Reading No. 7.

- INNER SHROUD
- △ CENTERLINE
- OUTER SHROUD

$T_g = 2120^{\circ}\text{F}$
 $T_{a\text{in}} = 593^{\circ}\text{F}$
 $T_{a\text{out}} = 675^{\circ}\text{F}$
 $T_a = 634^{\circ}\text{F}$
 $W_{ic} = 0.306 \text{ Wg}$

○ THERMOCOUPLE LOCATIONS

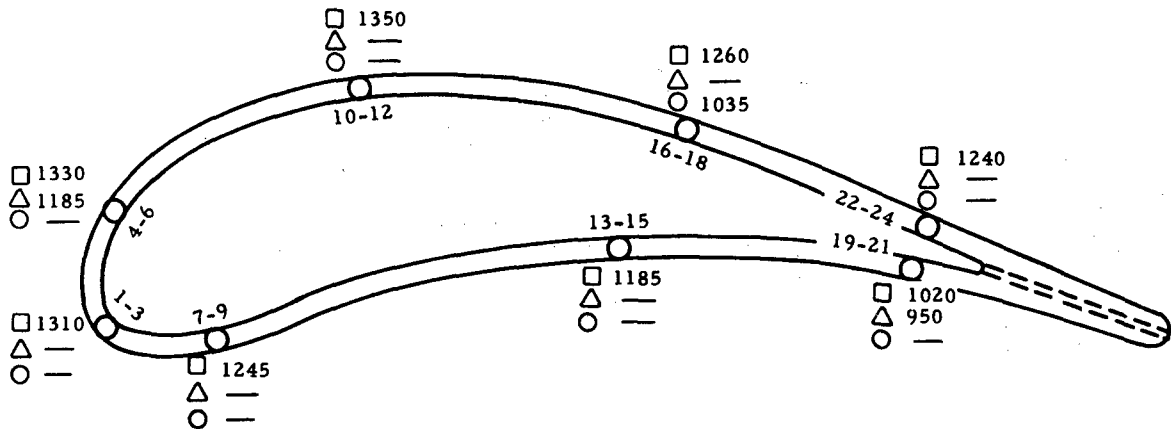


Figure 276. Vane Metal Temperature - Reading No. 8.

- INNER SHROUD
- △ CENTERLINE
- OUTER SHROUD

$T_g = 2074^{\circ}\text{F}$
 $T_{a\text{in}} = 581^{\circ}\text{F}$
 $T_{a\text{out}} = 714^{\circ}\text{F}$
 $T_a = 647^{\circ}\text{F}$
 $W_{ic} = 0.208 \text{ Wg}$

○ THERMOCOUPLE LOCATIONS

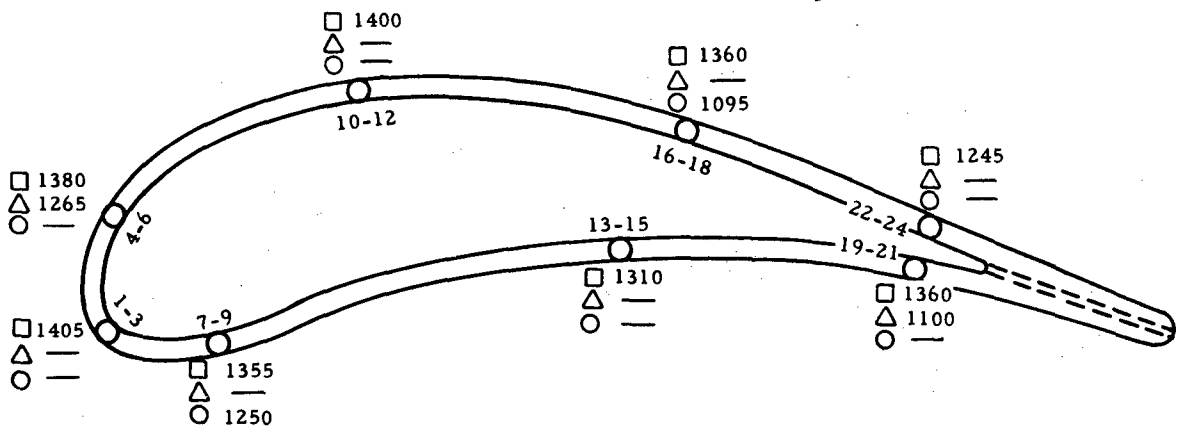


Figure 277. Vane Metal Temperature - Reading No. 9.

- INNER SHROUD
- △ CENTERLINE
- OUTER SHROUD

$T_g = 2374^{\circ}\text{F}$
 $T_{a_{in}} = 608^{\circ}\text{F}$
 $T_{a_{out}} = 713^{\circ}\text{F}$
 $\bar{T}_a = 660^{\circ}\text{F}$
 $W_{ic} = 0.295 W_g$

○ THERMOCOUPLE LOCATIONS

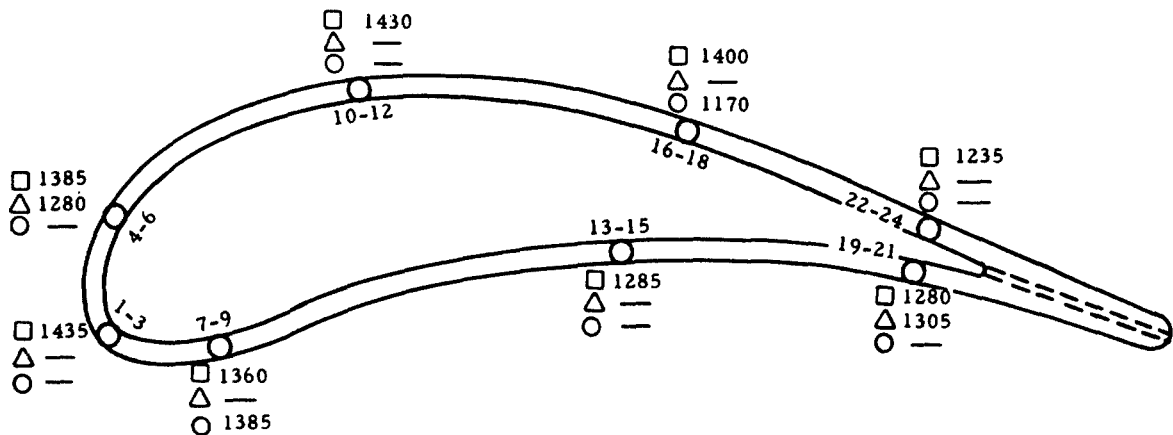


Figure 278. Vane Metal Temperature - Reading No. 10.

- INNER SHROUD
- △ CENTERLINE
- OUTER SHROUD

$T_g = 2403^{\circ}\text{F}$
 $T_{a_{in}} = 615^{\circ}\text{F}$
 $T_{a_{out}} = 765^{\circ}\text{F}$
 $\bar{T}_a = 690^{\circ}\text{F}$
 $W_{ic} = 0.225 W_g$

○ THERMOCOUPLE LOCATIONS

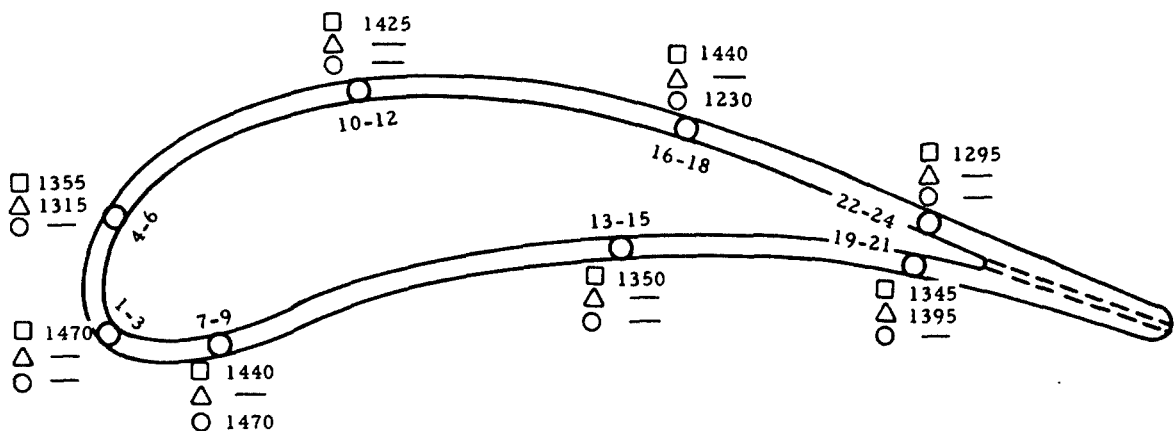


Figure 279. Vane Metal Temperature - Reading No. 11.

Defining an apparent local cooling effectiveness as

(23)

$$\eta_c = \frac{T_g - T_w}{T_g - T_a}$$

where

T_g = Effective gas temperature

T_w = Local wall temperature

T_a = Inlet cooling air temperature,

and assuming that this parameter is constant for each local station (for constant hot gas and cooling airflows), the wall temperatures can be determined that would exist at the peak temperature and a cooling air temperature of 620°F. The vane metal temperatures so derived are plotted on Figure 280.

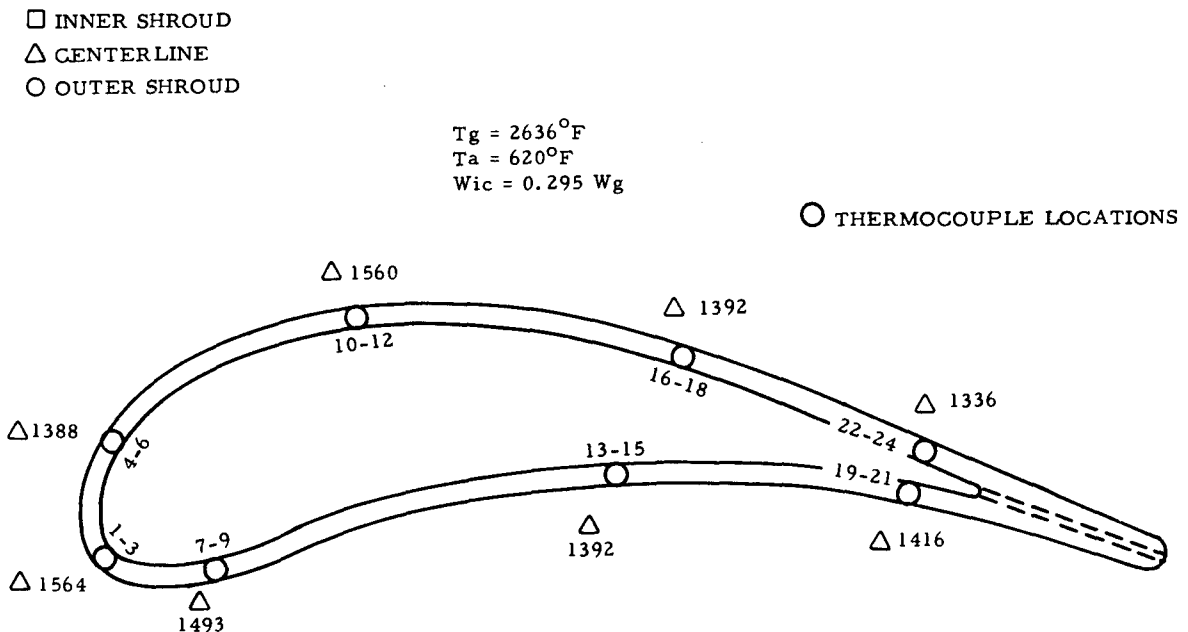


Figure 280. Vane Metal Temperature Reduced to $T_g = 2636^\circ\text{F}$ From $T_g = 2374^\circ\text{F}$ Test Data.

Figure 281 is a comparison of reduced test data and analytical design vane metal temperatures. There is reasonable agreement between the measured and calculated values, but discrepancies exist immediately aft of the leading edge. The differences between the measured and calculated values can be explained by reference to the gas side heat transfer coefficients. The calculated gas side heat transfer coefficients are based on local velocities, pressures, and temperatures derived from an analytically determined critical velocity ratio curve for the appropriate radial station and vane surface.

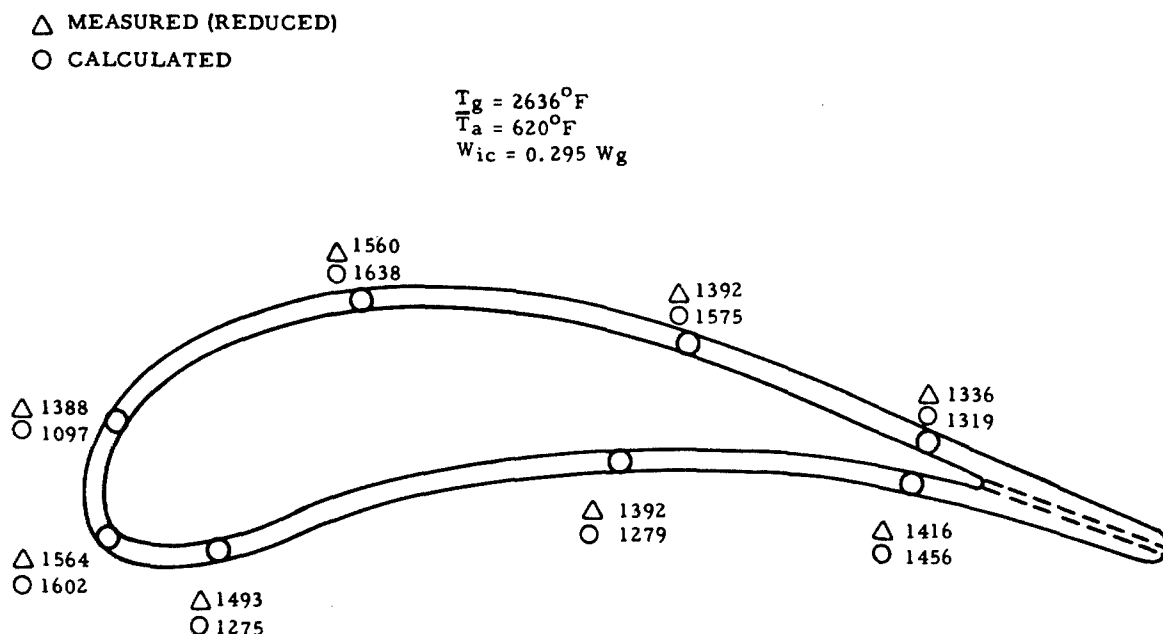


Figure 281. Comparison of Measured (Reduced) and Calculated Temperatures.

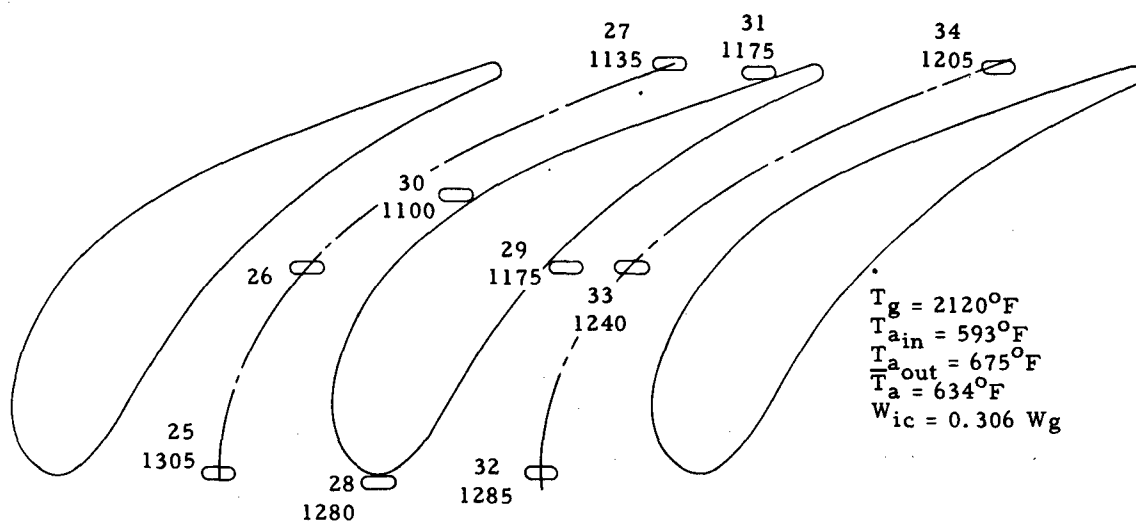
The analysis provides curves over only a portion of the vane surface. For example, at the mean radial section the curve exists from 15- to 65-percent chord for the suction surface and from 25- to 100-percent chord for the pressure surface. For those areas where the curves do not exist, the critical velocity ratios (and hence the local velocities), pressures, and temperatures must be estimated. It is in these areas that the major discrepancies between the measured and calculated values occur.

The analysis predicts lower vane temperatures on the pressure surface and higher vane temperatures on the suction surface than are

indicated by measurement. This might indicate the need for an analytical expression for the gas side heat transfer coefficient that is dependent upon the surface of the vane being considered. This prospect is being pursued toward an empirical modification that best correlates the test data.

The measured turbine inlet nozzle shroud temperatures for data points 8 through 11 are plotted in Figures 282 through 289. Since the nozzle shrouds are to be film cooled in the engine configuration (they were not in this test section), these shroud temperatures are of interest only for correlation of the heat transfer data.

Upon completion of the tests and disassembly and inspection of the test section, it was discovered that the braze fillets between the vane suction surface and outer shroud, the vane pressure surface and inner shroud, and the center vane leading edge and outer shroud had cracked. In addition, the cooling air exit header cracked at the weld joint between the header and the forward, inner shroud flange. These cracks may be seen in Figures 290 and 291.



INNER SHROUD - 25-34

Figure 282. Inner Shroud Metal Temperatures - Reading No. 8.

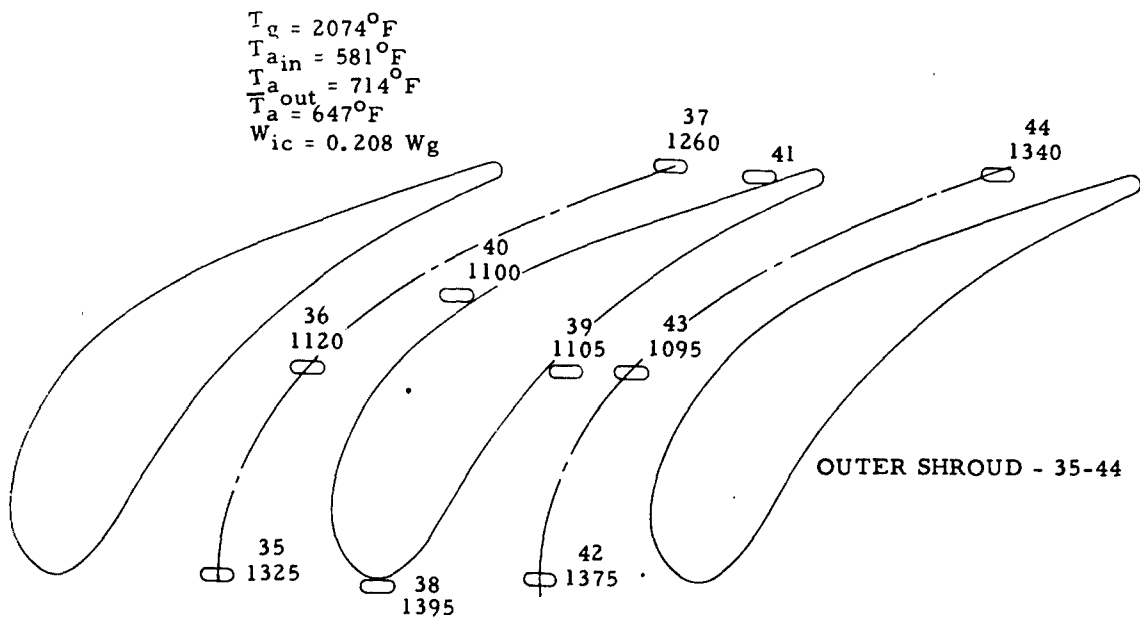


Figure 283. Outer Shroud Metal Temperatures - Reading No. 8.

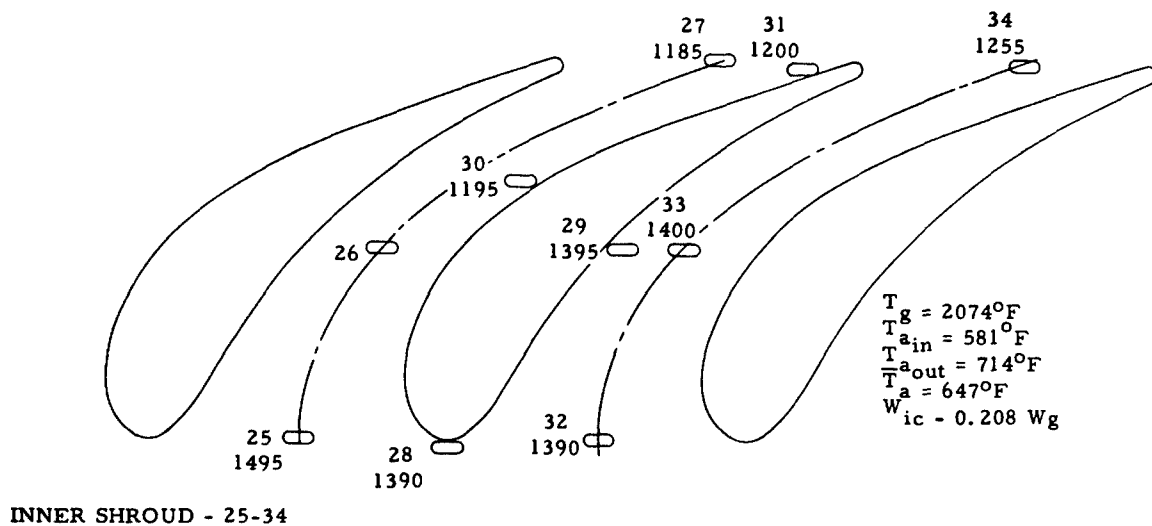


Figure 284. Inner Shroud Metal Temperatures - Reading No. 9.

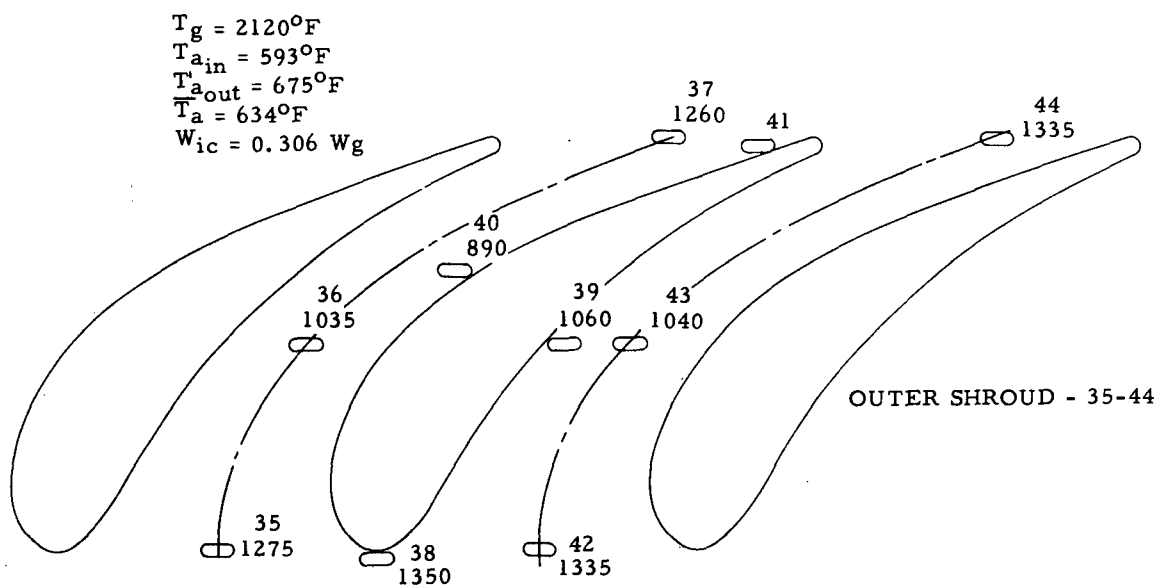


Figure 285. Outer Shroud Metal Temperatures - Reading No. 9.

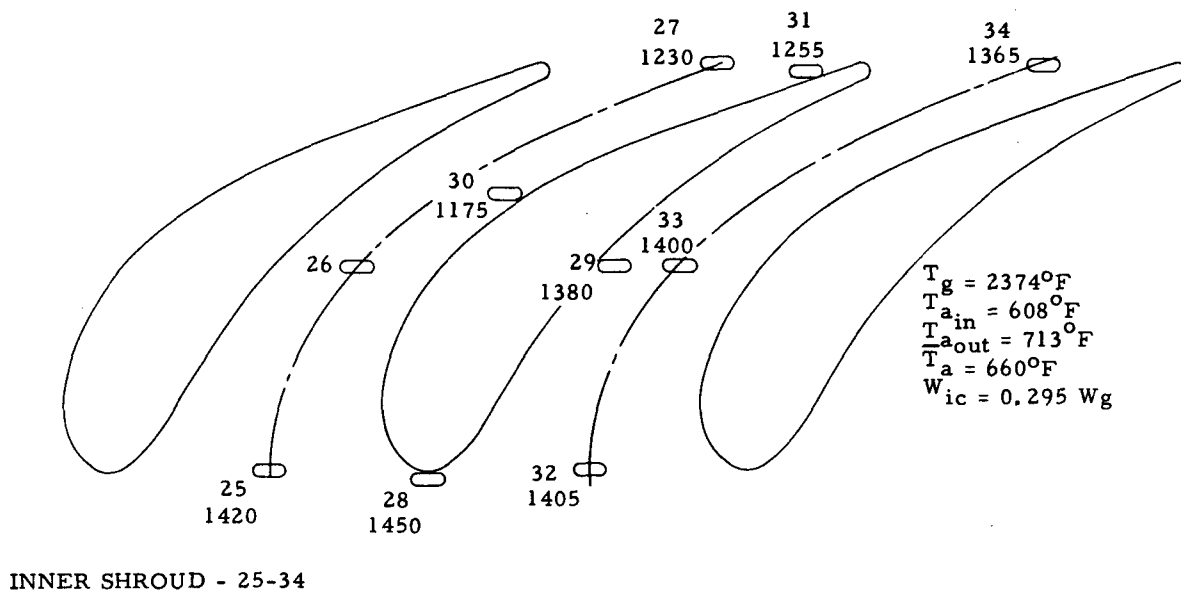


Figure 286. Inner Shroud Metal Temperatures - Reading No. 10.

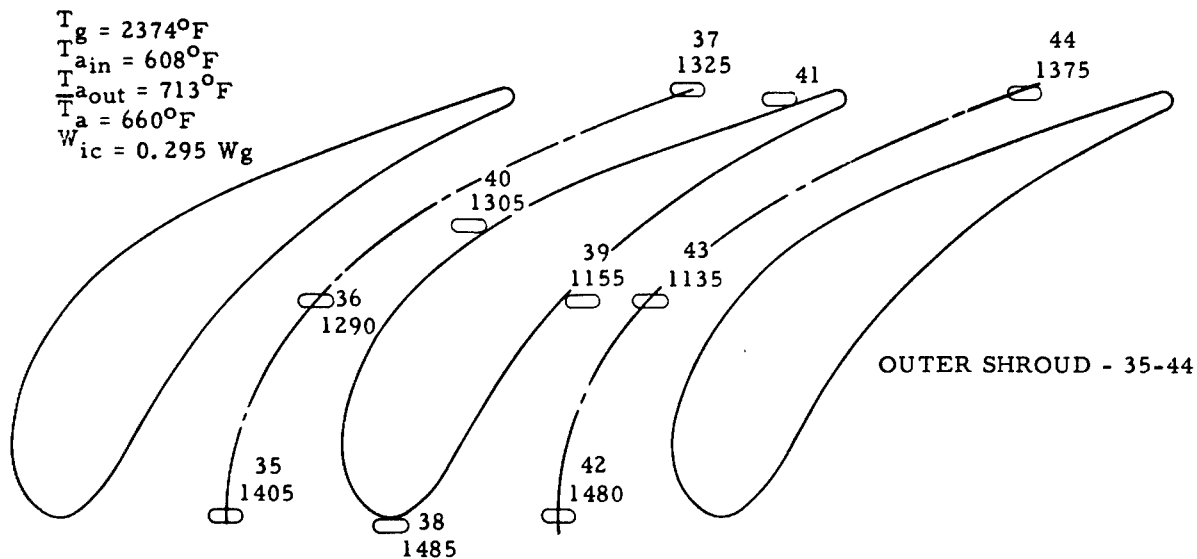


Figure 287. Outer Shroud Metal Temperatures - Reading No. 10.

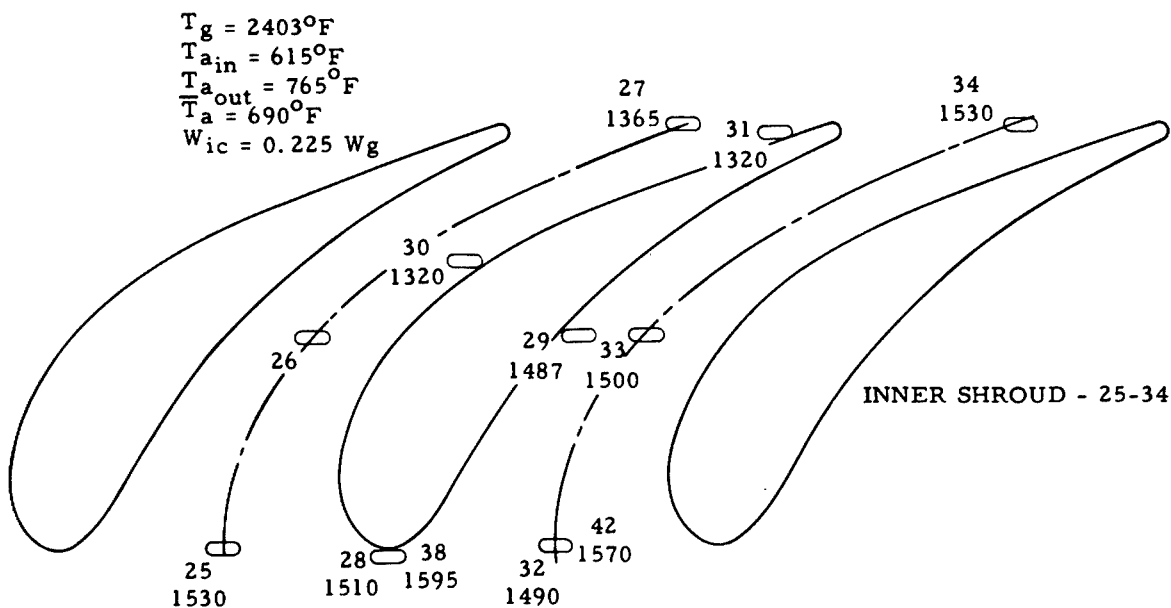


Figure 288. Inner Shroud Metal Temperatures - Reading No. 11.

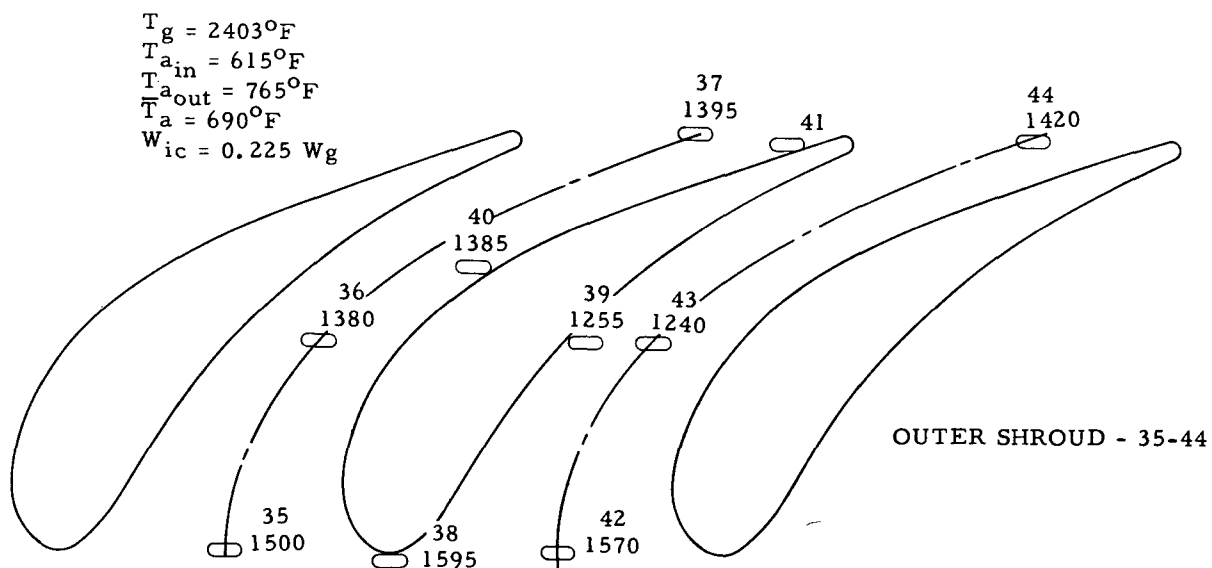


Figure 289. Outer Shroud Metal Temperatures - Reading No. 11.



Figure 290. Turbine Inlet Nozzle Cascade After Test - View of Outer Shroud.



Figure 291. Turbine Inlet Nozzle Cascade After Test - View of Inner Shroud.

Discovery of the cracked vane-to-shroud joints opened a question as to the validity of the test data. Consequently, the test data were scrutinized for an indication of when the cracks had occurred and what effect, if any, they had on the test data.

Various possible effects of the cracks were considered, but no evidence was discovered that would invalidate the test data. Possible effects considered included:

1. Leakage of cooling air through the joint - Leakage of cooling air would have resulted in local, abnormally cool vane temperatures adjacent to the shrouds. None was evident.
2. Leakage of hot gas through the joint - This would have resulted in hot spots on the vanes or shrouds, or possibly an overall increase in metal temperatures. This was not indicated.
3. Loss of thermal contact between the vanes and shrouds - This must certainly have occurred to some degree although the effect would have been small for the temperature differences existing between the shrouds and vanes.

In view of the lack of evidence to the contrary, the cracks are considered to have had no identifiable effects on the test results.

In summary, the results confirm the general level of vane temperatures computed. The highest vane temperature measured was 1470° F at a mean turbine inlet temperature of 2403° F. Measured vane temperature distribution was more uniform than predicted. Measured shroud temperatures were lower than predicted.

The measured vane and shroud temperatures validate the adequacy of the convective cooling system. Measured temperatures were used in the nozzle structural analysis in the preceding section.

INTRODUCTION TO PHASE II

There is a requirement in Army aviation for the advancement of small gas turbine engine component technology to permit the future development of small, lightweight, high-performance turboshaft engines. Since current gas turbine engine component efficiencies have been developed to a high level, major improvement of engine performance is most likely to come from advancing the state of the art for higher turbine inlet temperatures, higher compression ratios, and possibly lightweight, high-effectiveness regenerators. The technology gained from this effort will provide background not only for future aircraft propulsive units but also for future ground vehicle and stationary power units. The fluid-cooled turbine concept, while part of an overall components research program, is for advanced turbine technology only.

The overall contract objective was to advance and demonstrate high turbine inlet temperature technology for small gas turbine engines to a level that would provide the potential for doubling the specific horsepower (horsepower per pound of airflow per second) relative to current small aircraft propulsion engines. A fluid-cooled, single-stage axial flow turbine concept was investigated with the following design point performance goals:

2300° F TIT

85% adiabatic turbine efficiency

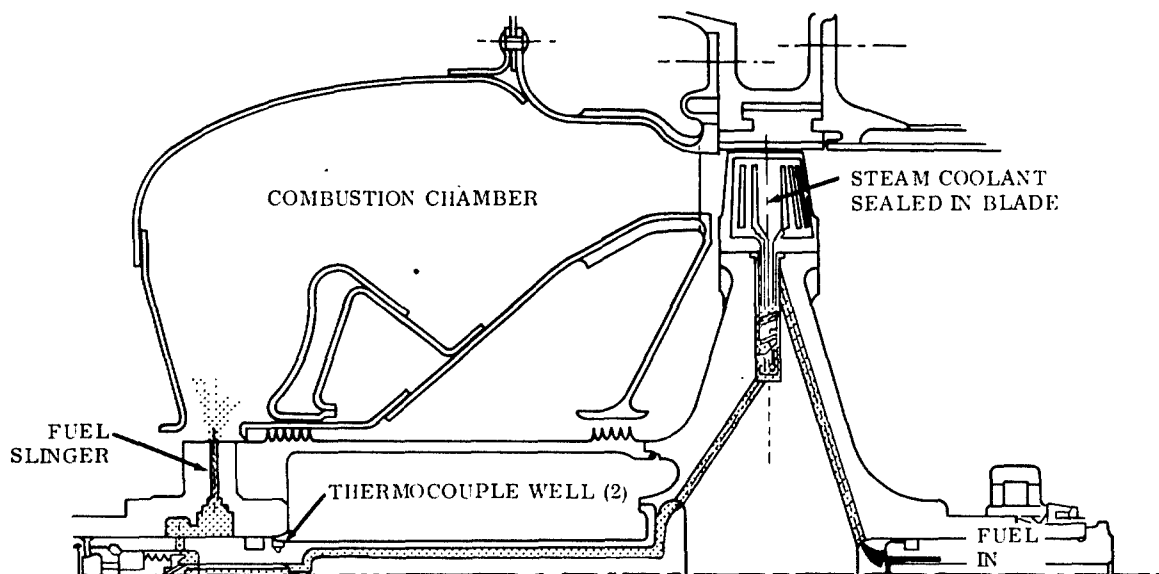
5.0-lb/sec airflow

$$\frac{\Delta H}{\theta_{cr}} = 26.0 \text{ Btu/lb air}$$

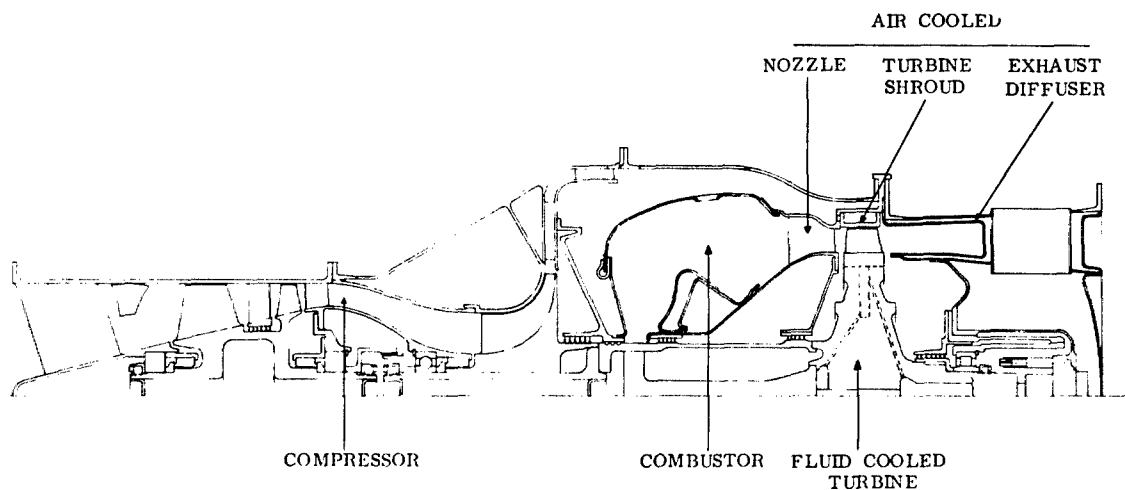
The target of the test phase was to demonstrate the capability of the fluid-cooled turbine in attaining a discharge gas stream specific horsepower of 213 hp/lb/sec. This is based on the assumption that the single-stage gas generator turbine is coupled to a 9.2 pressure ratio, 79.5-percent efficient compressor in a turboshaft engine with 11.5-percent total cycle pressure drop; a power turbine with an efficiency of 92 percent is used. Therefore, the only cycle values necessary to be specified from the turbine testing are efficiency and turbine inlet temperature of the gas generator turbine.

Figure 292a illustrates the combustor nozzle and turbine rotor design utilized to demonstrate the objectives of this contract.

A typical five-pound-per-second turboshaft gas generator incorporating the contract thermodynamic cycle is illustrated in Figure 292b. Using the results of this program, it would be designed for 1000 hp in a 23.5-x-12-inch-diameter envelope, and provide an SFC of 0.50 lb/hp/hr with a two-stage power turbine.



a. Fluid-Cooled Turbine Rotor Assembly.



b. Fluid-Cooled Turbine Gas Generator.

Figure 292. Fluid-Cooled Turbine Rotor Assembly and Gas Generator.

The turbine rotor utilizes a dual-circuit cooling system. The turbine blades are fluid cooled by a closed-loop steam thermosyphon system. The heat absorbed by the cooled cast U-700 blade is transferred to the engine fuel flow, which is used as thermal sink. The secondary steam vapor system operates on the thermosyphon principle, with the heat absorbed by the blade airfoil surface transferred into the steam flowing through the closed-circuit cooling passages inside the turbine blades. In cooling the blade, the steam vapor is heated, becomes less dense, and is forced radially inward by the cooler, more dense, steam coming from the steam-to-fuel heat exchanger. Upon returning to the steam-to-fuel heat exchanger, the steam is again cooled, increases in density, and is forced back to the rotor periphery by the high rotational "g" forces at 45,000 rpm. It is this density gradient, acted upon by the high "g" field, which creates the cooling flow.

Fuel is routed to each blade root by supply tubes in the INCO 718 turbine disc. A single spiral is used on the fuel side of the steam-to-fuel exchanger to control fuel velocity and, therefore, the total heat flow and blade metal temperatures.

Retaining pins made from Udimet 700 and a gold-plated INCO X V-shaped seal under the blade are used to allow for replaceable blading and to permit fuel at 8,000-psi internal pressure to be retained in the fuel circuit.

The Rene'41 nozzle vanes are hollow and convectively cooled. Fins on the internal surface of the vanes provide for an increase of 300 percent in the cooling surface area. Cooling of the vane trailing edge with primary combustor air is accomplished by four slots for bleed air-flow.

The fuel leaves the disc cooling circuit and is piped to a pressurizing valve which maintains the heated fuel at sufficient pressure to prohibit vaporization prior to its being ejected from the slinger into the primary zone of the combustor. Air enters the annular combustor through the front swirl plate, secondary air holes, and the bottom of the primary zone which is fed by air which has passed through the hollow turbine inlet nozzle vanes.

The turbine rotor shroud consists of four air-cooled segments manufactured from HS 25 material. A double-walled, air-cooled exhaust duct is utilized to retain the rear bearing.

The fluid-cooled turbine program was divided into two phases:

Phase I covered the design of the turbine rotor, nozzle assembly, combustor, gearbox, exhaust duct, and the assembling of these components into a test rig. The experimental evaluation of the turbine performance by a cold flow test, and turbine nozzle cooling effectiveness by hot cascade testing, was accomplished. The feasibility of turbine rotor blade fabrication was demonstrated.

Phase II, which is presented in this volume, encompasses the manufacturing and elevated-temperature testing of the fluid-cooled turbine.

The purpose of the fluid-cooled turbine was to provide design data for incorporation of the concept into an advanced 2- to 5-pound-per-second gas generator. To accomplish this end, the specific objective of the turbine rig program was to demonstrate the feasibility of the following items:

- * Fluid thermosyphon cooling system
- * Aerodynamic behavior of the turbine - temperature capability and efficiency
- * Structural-mechanical design concept

Testing was conducted at the Continental Component Laboratory. The test rig, shown in Figure 293, was assembled and instrumented to provide turbine performance, combustor, and heat transfer data on the fluid-cooled turbine.

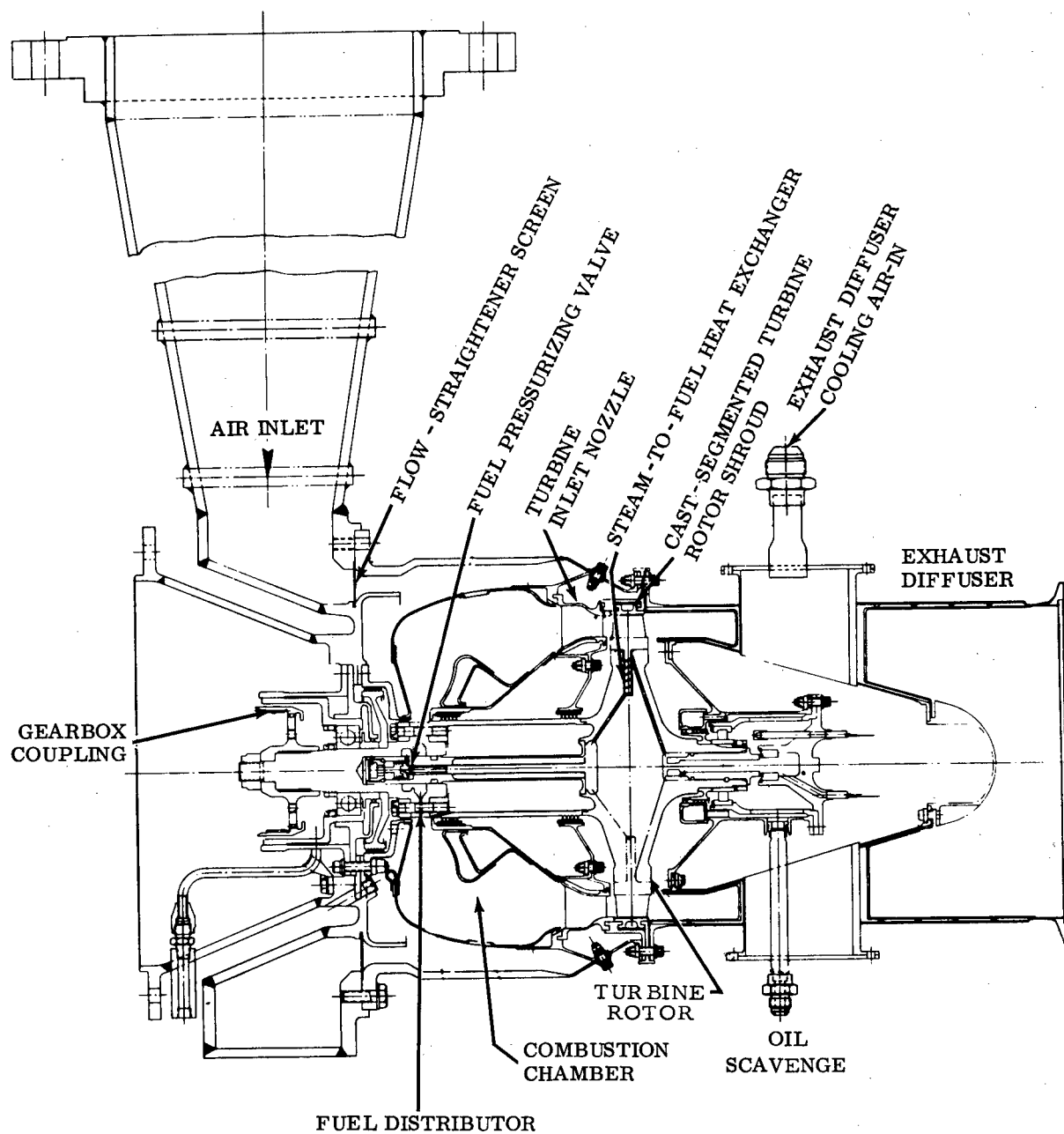


Figure 293. Turbine Test Rig Cross Section.

AEROTHERMODYNAMIC PERFORMANCE

TURBINE

The turbine performance objective was to determine the aerodynamic behavior of the turbine and, consequently, to establish the turbine inlet conditions required to achieve a discharge gas stream with a specific horsepower of 213 hp/lb/sec.

The target efficiency of the fluid-cooled turbine was 85-percent total-to-total adiabatic efficiency. The aerodynamic capability of the first design was established in the Phase I cold flow test series at a maximum of 82 percent, Figure 294. This assembly had 34 rotor blades, 23 nozzle vanes, tight tip clearances, and no cooling flow injections.

Subsequent mechanical design and cooling requirements for hot running allowed only 31 rotor blades with larger clearances and small amounts of air injection for shrouds and nozzle trailing edges. The compromises lowered the theoretical turbine efficiency by an additional three points to 79 percent. This initial configuration was hot tested and resulted in a 74-percent efficient turbine which substantiated the thermosiphon concept and overall structural integrity.

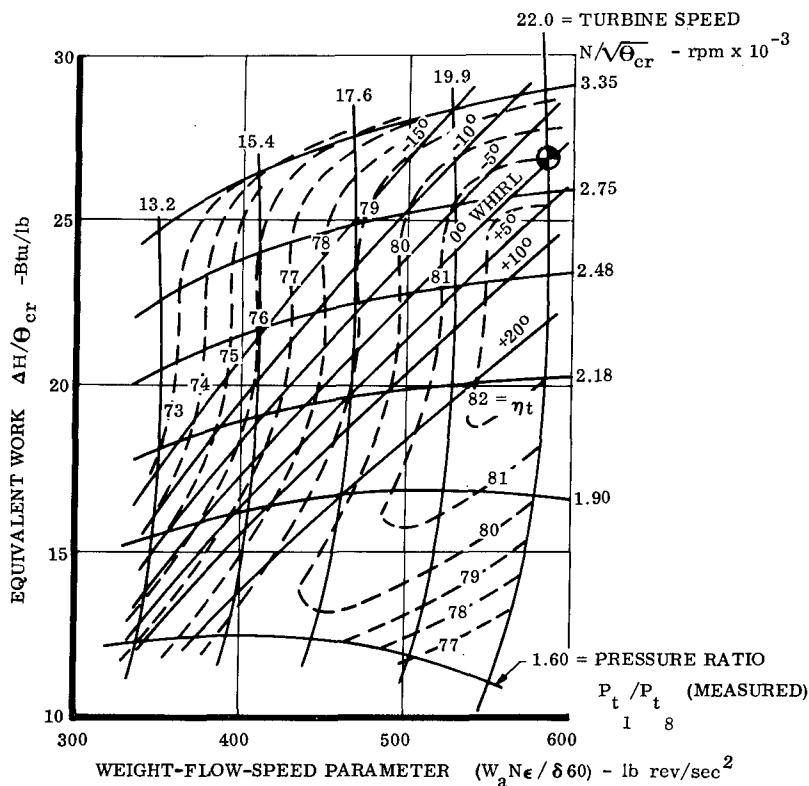
Since the temperature - structure objectives were met and, in some cases, exceeded, some of the aerodynamic compromises in solidity, thickness-chord ratio, and trailing edge could be alleviated in a design for further development to attain the desired program goal efficiency.

The initial contract work scope for the Phase II program included a redesign of the turbine based on Phase I tests, to meet objective efficiency. Inflation in hardware procurement costs and delays in testing of the first configuration were such that the redesign was not contractually possible.

Details of the aerodynamic background for this section will be found in References 43 and 44.

The gas generator turbine performance target was to achieve a turboshaft specific horsepower of 213 with the following set of component assumptions:

1. A power turbine efficiency of 92 percent
2. A total cycle pressure drop of 11.5 percent



● DESIGN WORK $\frac{\Delta H}{\Theta_{cr}} = 26.9 \text{ Btu/lb}$

DESIGN SPEED $N\sqrt{\Theta_{cr}} = 22,040 \text{ rpm}$

CONFIGURATION
 34 ROTOR BLADES, P/N 2490-20-0089
 SET AT NOMINAL STAGGER ANGLE.
 23 TURBINE INLET NOZZLE VANES
 P/N 249020-0086, SET AT $46^\circ 50'$
 DIAL SETTING

Figure 294. Fluid-Cooled Turbine - Test Stand Performance.

3. A gas generator turbine driving a 9.2 pressure ratio compressor with a compressor efficiency of 79.5
4. A combustor efficiency of 98.5 using a fuel with a lower heating value of 18,400 Btu/lb

A specific horsepower of 171 was obtained on test run number 62. This demonstration point was run with a 4.09 turbine pressure ratio and a turbine inlet temperature (TIT) of 2344°F . The escalation running schedule for integrity verification resulted in the turbine's running on run 62 near its limit load at only 84 percent of design referred speed. Design work was exceeded, but speed and limit loading effects caused a 4.5-point falloff of turbine efficiency from design work levels.

To increase the specific horsepower from the attained test value of 171 to the target value of 213, a 42-point shaft horsepower (SHP) increase is required. Twenty-four SHP can be accounted for as follows:

1. Reduction in turbine referred
PR from 4.089 to 3.495 +15 pts
2. Increase in turbine referred speed
from 18,563 to 22,060 rpm + 9 pts
+24 pts

The turbine performance potential under various simulated engine conditions is illustrated in Table XXIX. Column A describes the program objective; Column B, the official performance demonstration test point. As is evident from the recorded turbine loading parameters, the test point was run above design loading conditions (beyond limit loading) and below design referred speed. Therefore, Column C projects the demonstrated temperature to the design work load; Column D, to the design work and speed. A capability of 195 hp/lb/sec is evident. Column E indicates conditions at a maximum test temperature of 2450° F TIT.

The relationship of specific power, gas generator turbine efficiency, and turbine inlet temperature for the cycle assumptions is given in Figure 295.

Forty turbine performance test points were recorded during the high-temperature running of the rig. Another 22 test data points were recorded during combustor development and rig checkout, making a total of 62 data points.

The complete aerodynamic design of the turbine is covered under the Phase I effort of the contract. Several versions of the turbine were cold flow tested to substantiate the design and to evaluate nozzle and rotor solidity and trailing-edge thickness. The hot turbine was designed using airfoil shapes on the nozzle and rotor identical to those on the optimum Phase I cold flow turbine. These airfoils are described in Figures 296 and 297. The cold flow tests showed that the best performance could be obtained with 34 rotor blades and 23 nozzle vanes. Subsequent detailed mechanical design and cooling requirements allowed only 31 rotor blades to be fitted into the disc. Originally, the hot nozzle assembly was designed to be of a split, segmented type. To preserve symmetry, the number of vanes was fixed at 24 instead of 23, which was used for cold flow evaluation. Nozzle and rotor blade stagger angles were reset to maintain the optimum throat ratios obtained in the Phase I testing.

TABLE XXIX

COMPARISON OF PERFORMANCE TESTS TO OBJECTIVE

	A	B	C	D	E
	Objective	Test Point 62	Test Point 62 At Design Work	Equivalent Operation At Design Work & Design Speed	Test Point 60 Max. TIT
TIT					
°R	2760	2804	2804	2804	2911
°F	2300	2344	2344	2344	2450
η_t	0.85	0.67	0.715	0.74	0.618
λ_t	2.78	4.089	3.495	3.396	3.39
ΔH Btu/Lb	26.9	27.56	26.9	26.9	22.57
θ_{cr}					
$N/\sqrt{\theta_{cr}}$	22,060	18,563	18,563	22,060	13,600
Specific Horsepower	213	171	186	195	165
Equivalent Compressor Pressure Ratio	9.2	10.7	9.2	9.2	N. A.
SFC	0.466	0.585	0.550	0.530	N. A.

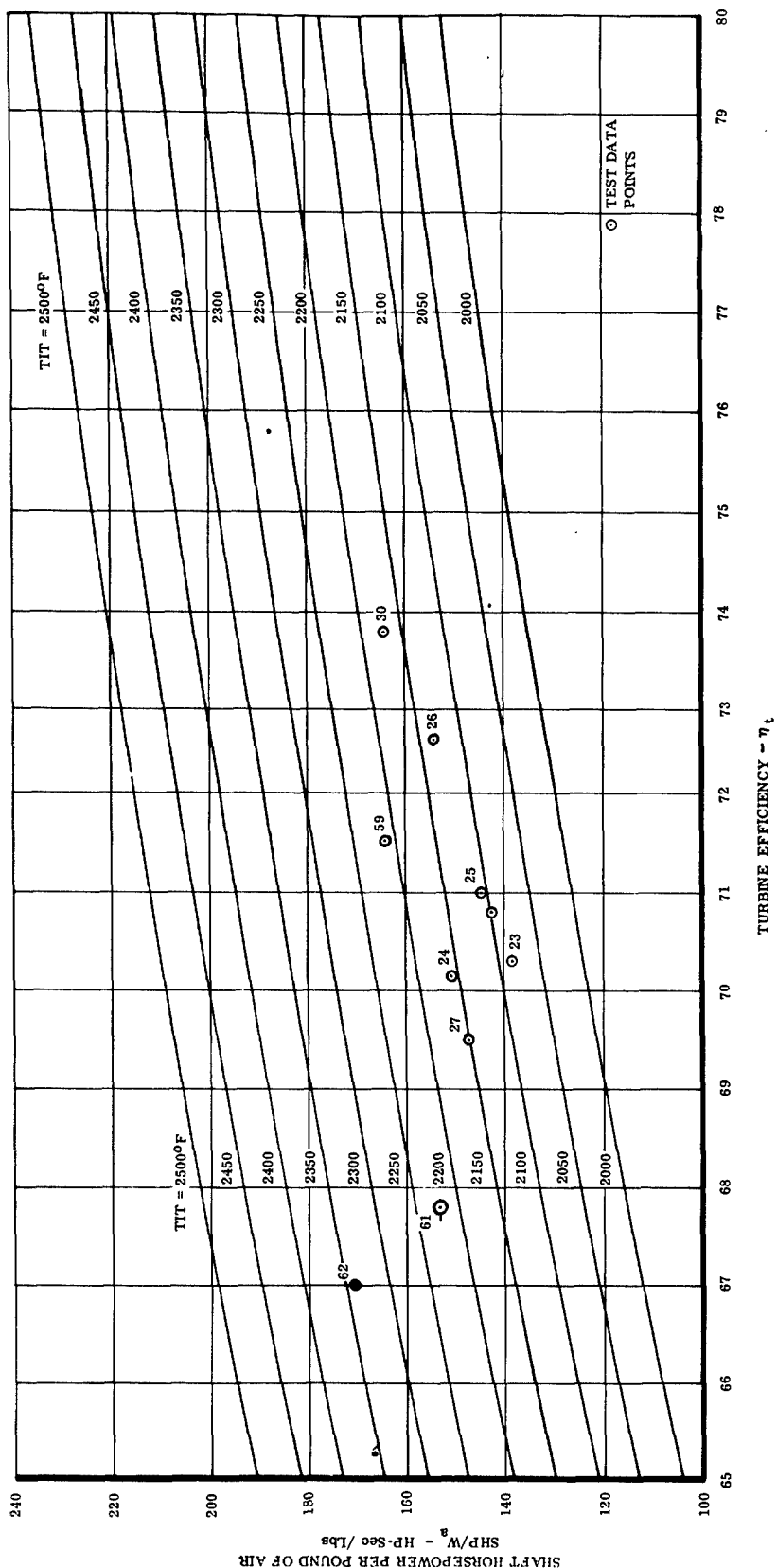


Figure 295. Power Turbine Horsepower at Various Gas Generator Efficiencies.

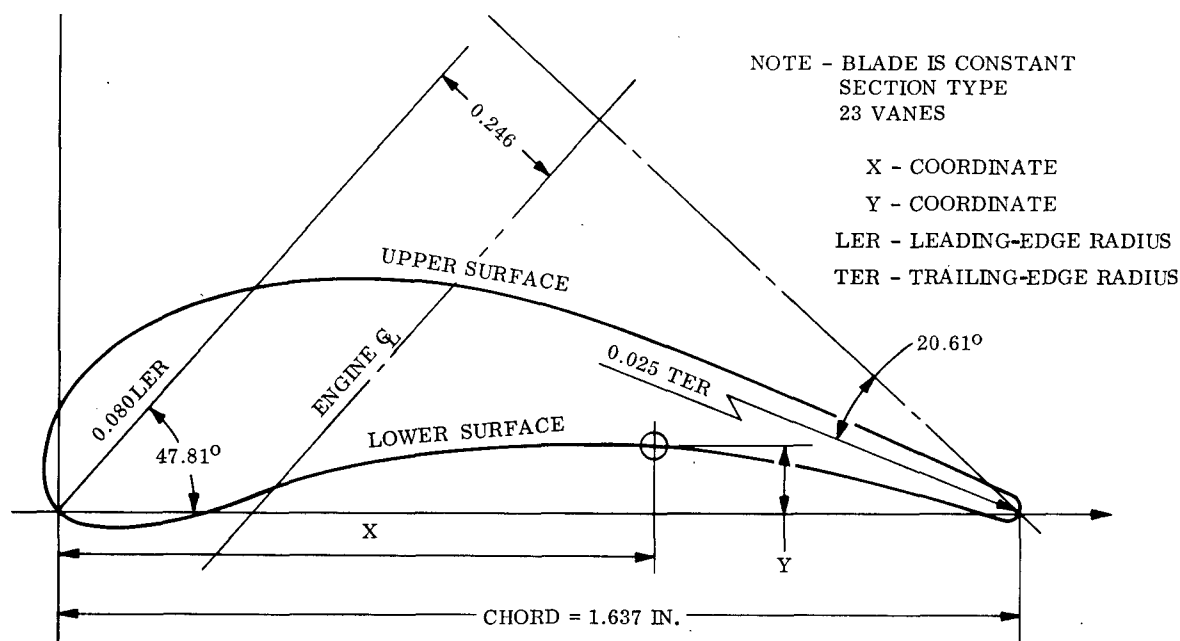


Figure 296. Fluid-Cooled Turbine Nozzle Coordinate Designations.

To maintain aerodynamics between a hot and a cold turbine, compensations were made to allow for thermal and mechanical growths. A comparison of the Phase I cold flow dimensions, the thermal- and stress-compensated dimensions, is given in Figure 298. It shows that under design running conditions, both the hot fluid-cooled turbine and the Phase I cold flow turbine have the same aerodynamic flowpaths.

Correction Factor Analysis

To analyze the test results, it is necessary to reduce the raw test data to a finished condition. Several calibration factors are used in this procedure and are described as follows:

Torque output of the turbine was measured by a Taylor D29S dynamometer, using an 8.0645:1 stepdown gearbox. Performance was based on a free shaft power turbine cycle in which the cooled rotor is directly driving a compressor. The windage, bearing, and gearbox losses must, therefore, be separated from the rig performance.

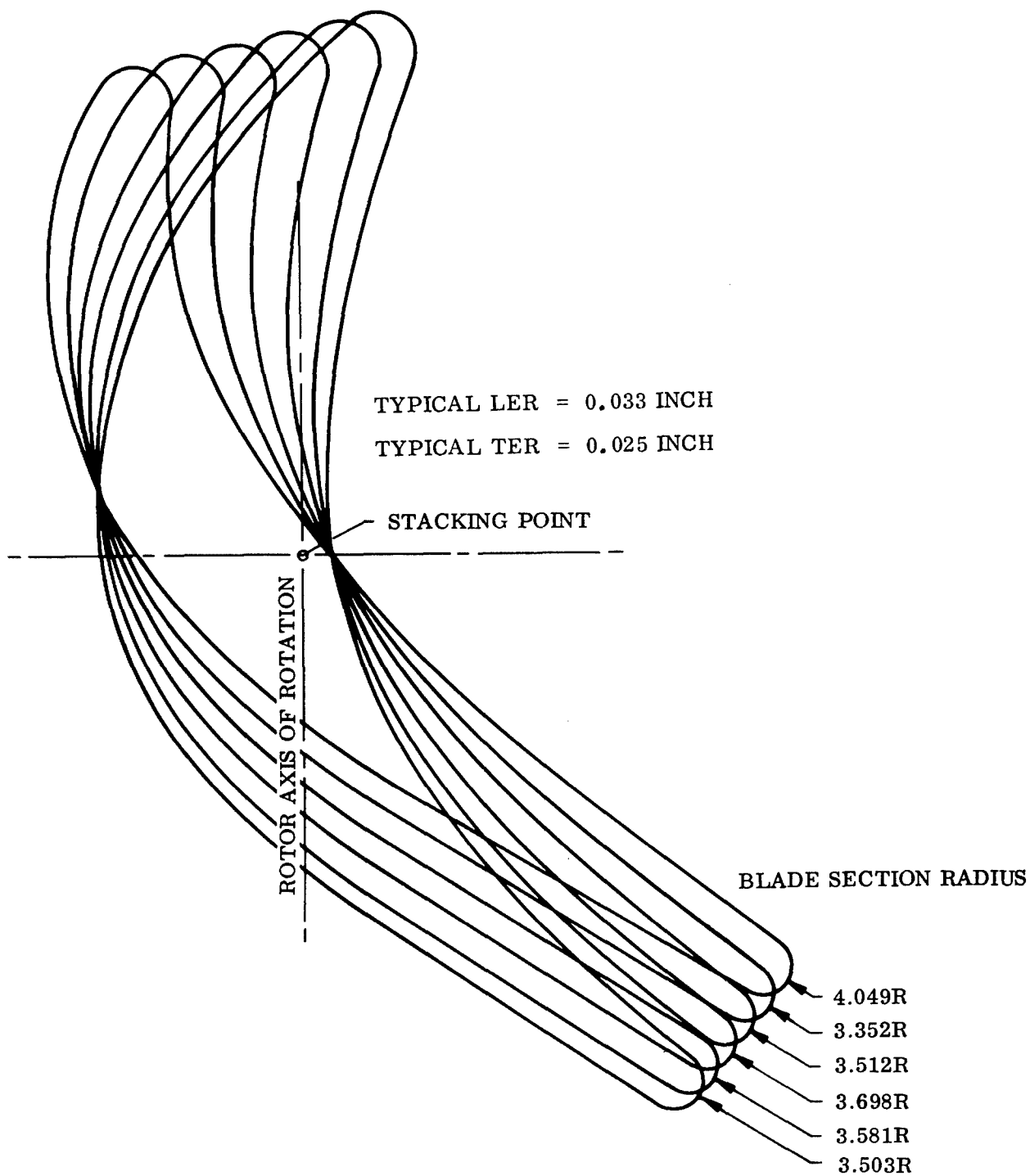


Figure 297. Fluid-Cooled Rotor - 34 Blades.

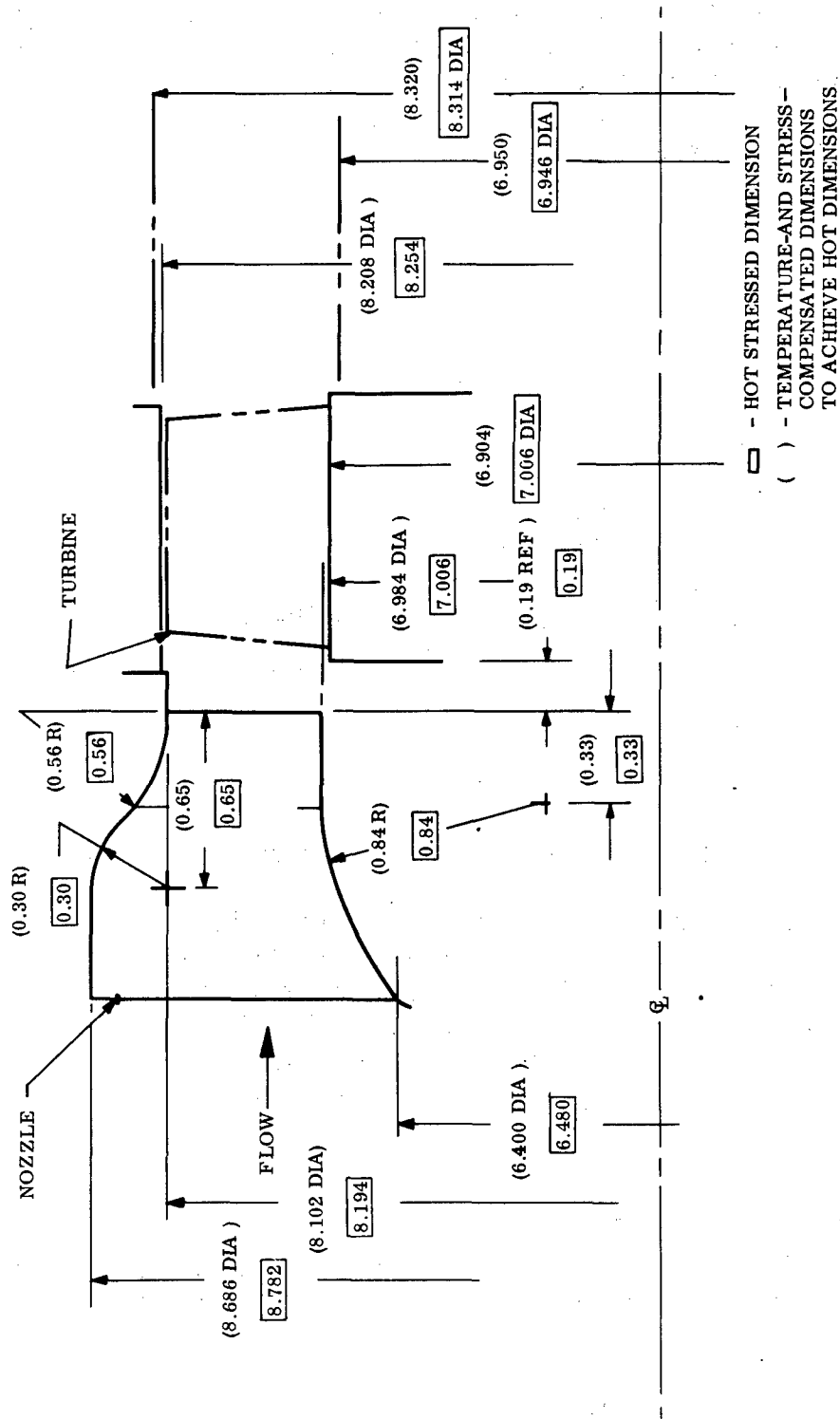


Figure 298. Nozzle/Turbine Dimensional Variation Due to Thermal and Stress Compensation.

To evaluate the losses, a series of coast-down tests was conducted on the gearbox and fuel slinger shaft (no rotor) assembly. The shaft assembly was driven from the low-speed end through a belt and pulley system. Data were obtained at preselected speeds by tensioning undercut pulley belts until failure occurred. Gearbox oil temperatures were maintained at levels representative of full load operation. Figure 299 gives the coast-down rotational speed versus time.

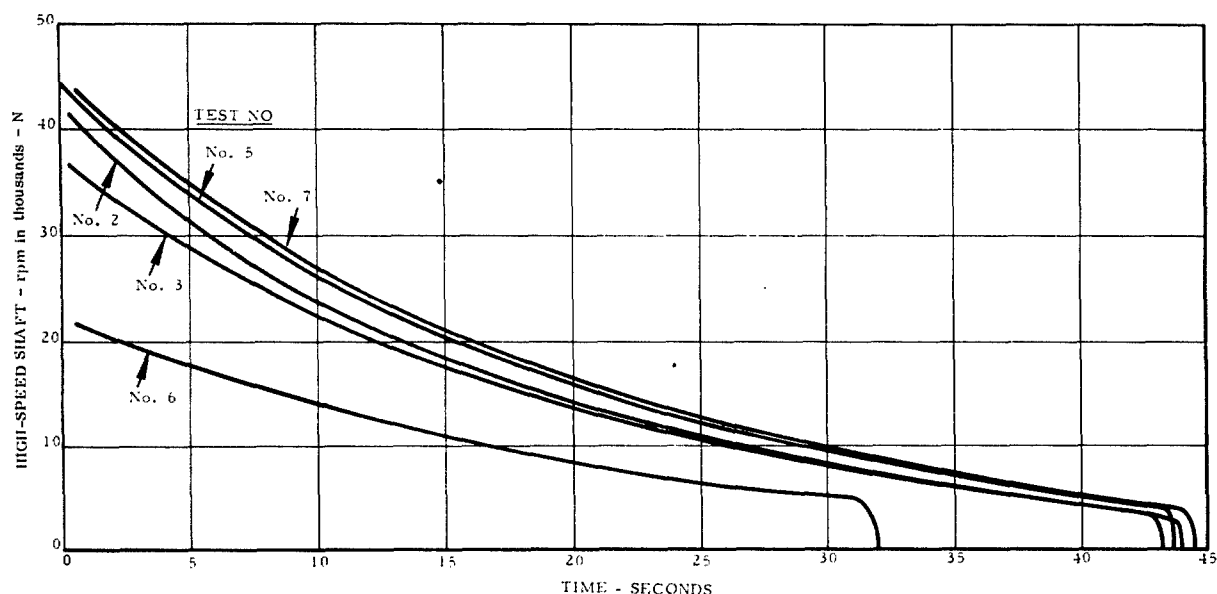


Figure 299. Gearbox Coast-Down Parameter.

By calculating the decrement in speed and knowing the polar moment of inertia of the entire system, the test data can be translated into power loss versus speed. Figure 300 represents this information based on a high-speed polar moment of inertia of $0.1374 \text{ lb/in/sec}^2$. These data show a gearbox efficiency of 97 percent at full load operation at 50,000 rpm. The calibration curve is applied to all performance data of the turbine.

Turbine Analysis

In reducing the measured test data into rigorous aerodynamic performance data, the following list itemizes the corrections which were accounted for:

1. Turbine bypass leakage flow
2. Nozzle trailing-edge ejection flow

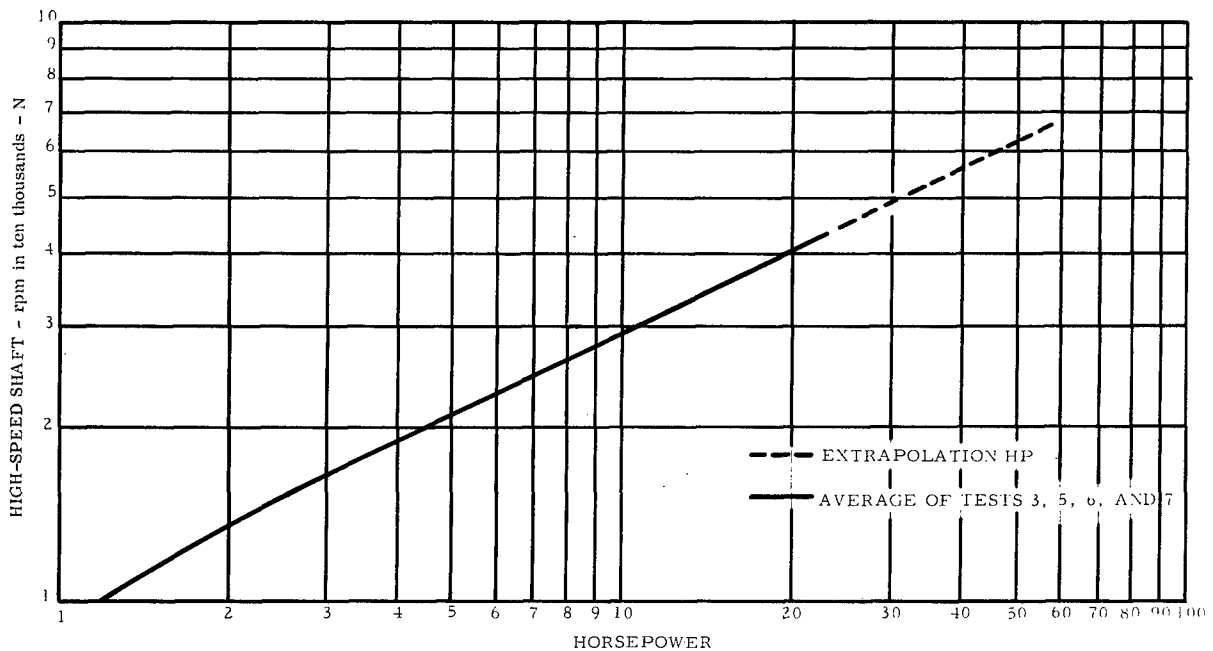


Figure 300. Gearbox and Windage Losses - Horsepower Versus Turbine Shaft Speed.

3. Flow coefficient based on cold flow testing
4. Flowpath thermal growth
5. Nozzle total pressure loss based on cold flow test data
6. Exhaust gas temperature thermocouple radiation and recovery correction
7. Leakage flow rejoining main gas flow

The choked nozzle relation provides a calculated value for turbine inlet temperature, and the dynamometer torque was converted into an equivalent temperature drop per pound of flow. A choking condition at the nozzle discharge was verified by a check on the total-to-static pressure ratio at this plane.

The nozzle exit temperature was reduced on a mass average basis by combining the turbine inlet nozzle flow at throat temperature with the trailing-edge ejection flow at its lower temperature.

The dynamometer torque reading was converted into an equivalent temperature drop per pound of flow. This value was subtracted from the turbine rotor mass average inlet temperature, to provide a turbine exit temperature in the plane of the rotor trailing edge.

Prior to the gas flow's reaching the thermocouple, this temperature was reduced on a mass average basis by injection of the turbine bypass leakage flow back into the main gas stream.

The resulting values of exhaust gas temperature were compared with the thermocouple measurements, corrected for radiation and recovery in accordance with Tables I and II of Reference 2. Figure 301 presents a correlation of the measured exhaust gas temperatures with the calculated temperatures. It can be seen that the correlation is excellent and, therefore, substantiates the method of correction of test data used in data reduction. The method of correction includes seven subcalculations which are discussed in greater detail as follows:

1. Turbine Bypass Leakage Flow - Since this flow completely bypasses the turbine, it produces no useful work. In order to establish a combined value for the shroud cooling and instrumentation fitting leakage flows, cold flow tests were made with the turbine rotor shrouds blanked off.

A calibrated orifice was used to measure the flows shown in Figure 302, and these values were reduced to referred flow conditions in Figure 303.

The curve shown in Figure 303 having been used in conjunction with measured conditions upstream of the combustor, the turbine bypass leakage flow for every test point was known and accounted for in performance evaluation.

2. Nozzle Trailing-Edge Ejection Flow - This was accounted for by assuming that:

- a. The trailing-edge ejection slots are choked (total-to-static pressure ratio is greater than 1.9).
- b. The discharge coefficient of these slots is 0.7.
- c. The pressure and temperature conditions are those of the cooling airflow source.

It should be noted that a 10-percent change in this flow value would affect the turbine nozzle main gas flow value by no more than 0.5 percent, which in the choked nozzle equation would be equivalent to a turbine inlet temperature variation of 1.0 percent.

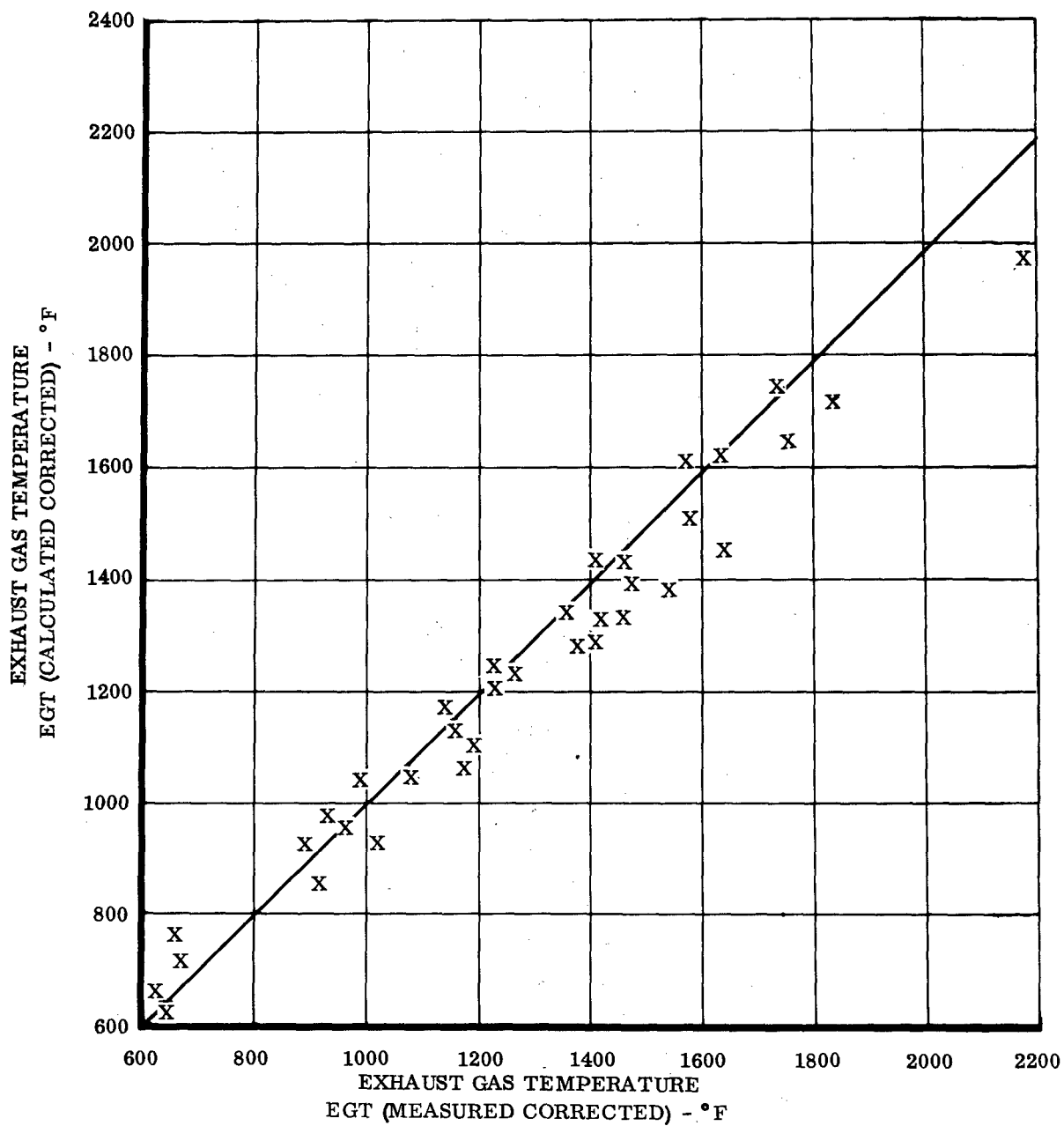


Figure 301. Exhaust Gas Temperature - Corrected.

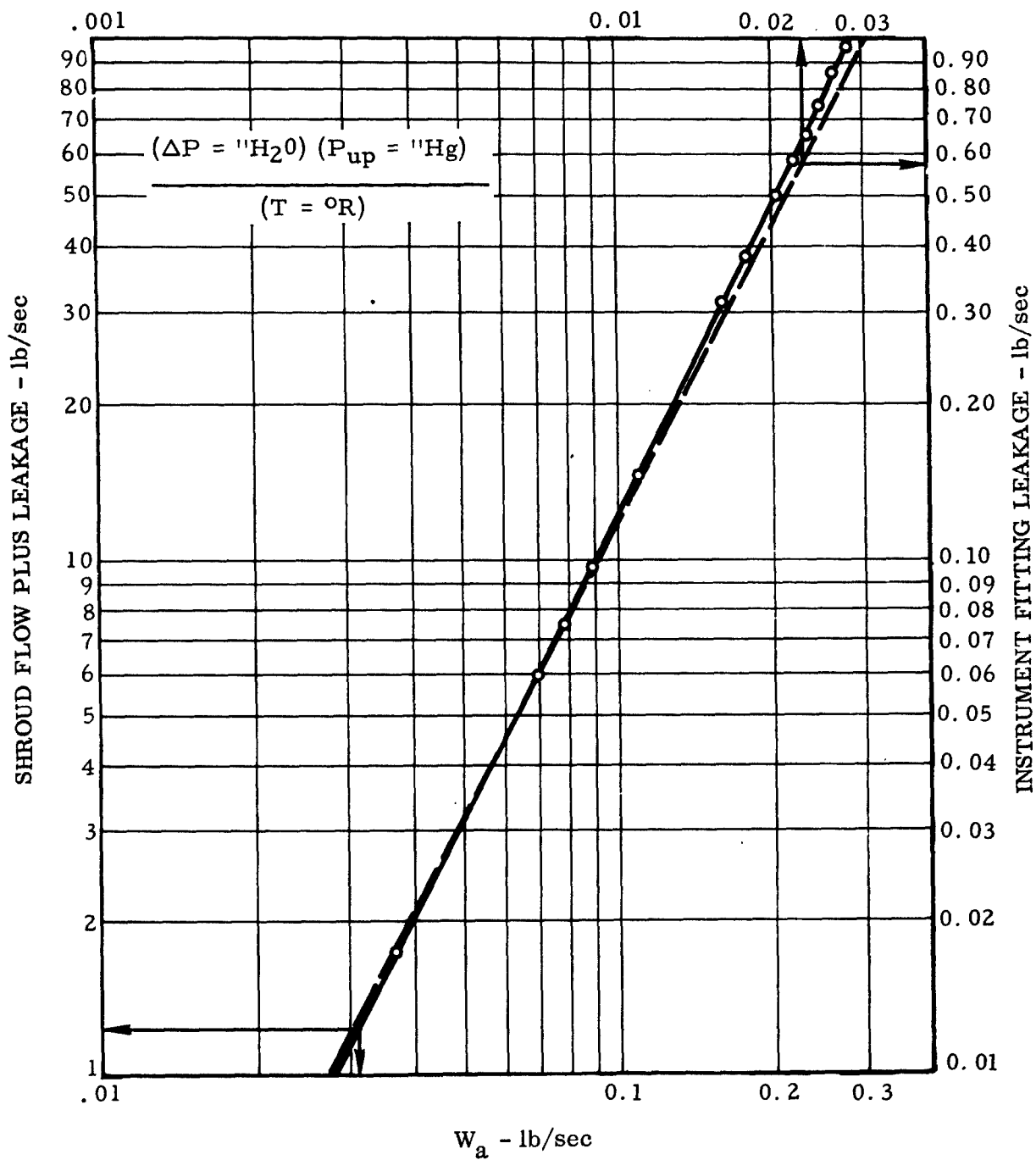


Figure 302. Shroud Cooling Flow and Leakage.

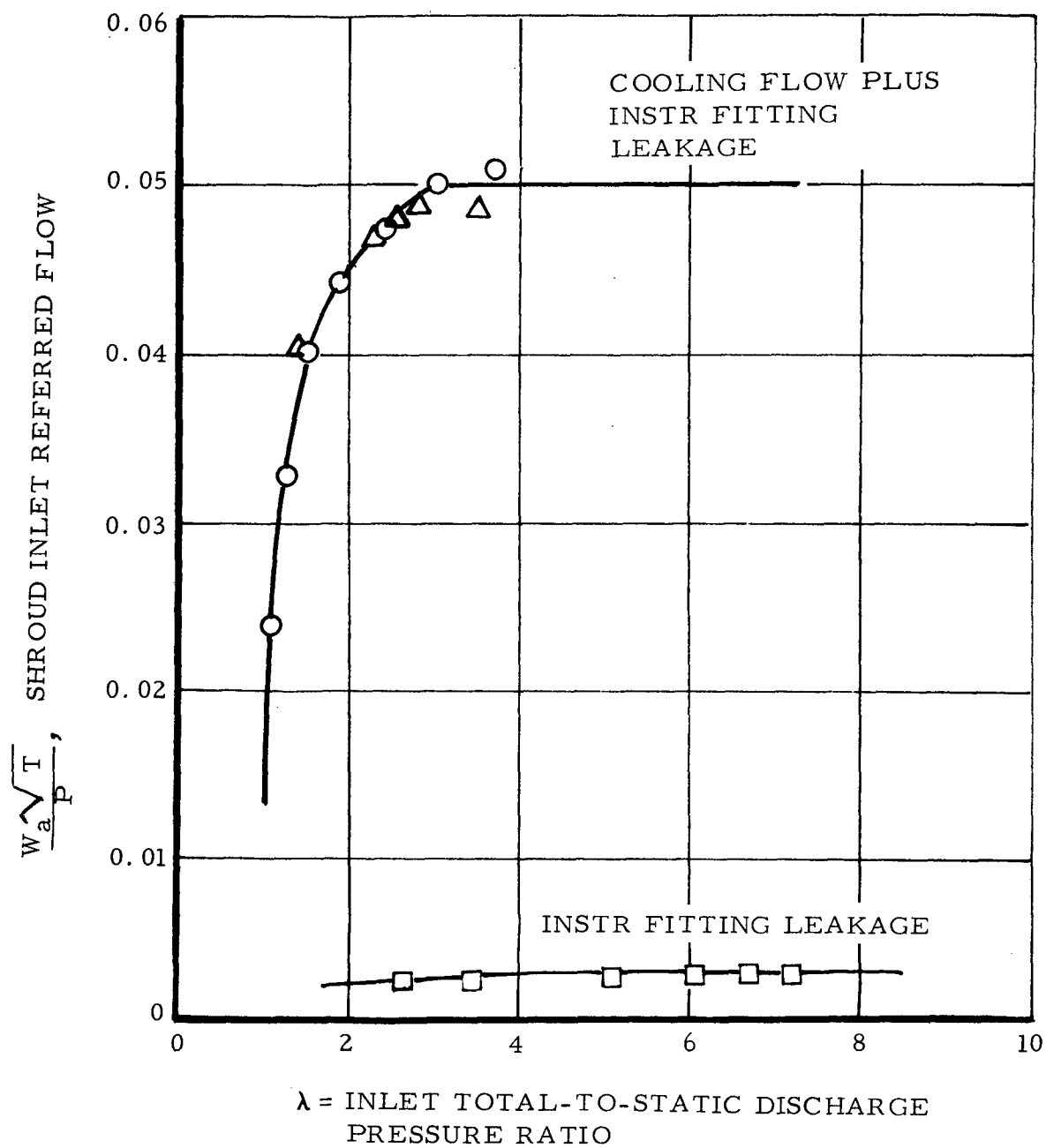


Figure 303. Shroud Inlet Referred Flow Versus Pressure Ratio.

The three assumptions were combined using the continuity equation to calculate the trailing-edge injection flow of 0.5 percent of compressor flow.

3. Nozzle Throat Flow Coefficient Based on Cold Flow Testing - The throat dimensions were measured on a nozzle assembly prior to cold flow testing and were translated into a measured flow area.

This nozzle assembly was then subjected to a cold flow test, with known inlet and exit pressure and temperature, in conjunction with a total pressure loss in being deflected through the nozzle blading, until maximum flow ratio was achieved; the nozzle, therefore, was considered to be choked.

From the choke flow parameter and known gas properties at the throat, the effective flow area was obtained. The ratio of effective-to-physical flow area represents the flow coefficient. Test data showed it to be 0.973, and this coefficient was used for all performance data reduction.

4. Flowpath Thermal Growth - At the operating temperature of the turbine, the hardware dimensions increase from the cold measured values. The influence of stress and temperature was considered at design point conditions, and a 1.6-percent annulus growth was calculated.

For purposes of net effective throat area calculation, this expansion factor was combined with the flow coefficient.

$$\begin{aligned}\text{The resulting combined coefficient} &= 0.973 \times 1.016 \\ &= 0.989\end{aligned}$$

5. Nozzle Total Pressure Loss Based on Aspect Ratio Cold Flow Test Data - The analytical design of the turbine (Volume I) provided an initial estimate of the total pressure loss resulting from passing the gas flow from the nozzle inlet to the throat.

As measurement of this loss was not within the scope of the work of this contract, reference is made to a series of tests conducted in Reference 43, which enable a test value to be assigned to this loss. Since all hot testing of the turbine took place under choked nozzle throat conditions, the cold flow test value of 4-percent total pressure loss was assigned as constant to the calculation of TIT using choked throat computation.

6. Exhaust Gas Temperature Thermocouple Radiation and Recovery Correction - Exhaust gas temperatures were measured with nine thermocouple rakes of four elements each. Each element, or thermocouple junction, approximates the configuration of Probe Number 5. Consequently, radiation and recovery correction factors were taken from Tables I and II, and corrections were made in accordance with Equation 11 of Reference 2. Duct wall temperatures were measured by thermocouples on the outer duct wall adjacent to the exhaust gas temperature rakes.

7. Leakage Flow Rejoining Main Gas Flow - After the turbine shroud is cooled, the bypass flow described under Item 1 reenters the main gas stream through equally spaced ejection holes around the outer annulus, immediately downstream of the turbine rotor.

This cooler flow is added to the rotor exit gas flow. The resultant gas temperature of the two flows was obtained on a mass average basis and is the gas temperature read by the exhaust thermocouples.

Reduction of test data was accomplished by means of a computer program which includes the above itemized corrections. An outline of this program is provided in Appendix V. Appendixes VI and VII show input and output format, respectively.

Test Results

Forty turbine performance points were taken to fulfill two objectives:

1. Determination of design point TIT and turbine efficiency for definition of specific horsepower.
2. As a corollary to combustor development testing, turbine operating data were recorded to establish an approximate turbine map for use as design data in subsequent engine application of the fluid-cooled concept.

Table XXX presents a list of all the reduced data points. Eighty-five percent of these points are within a ± 3 -point agreement in turbine efficiency with the established turbine performance map, Figure 304.

It is of paramount significance to note that the test points which were specifically intended to obtain aerodynamic data at the design referred level of work for both 90-percent and 100-percent referred speed levels produced reduced data within a 1-point efficiency accuracy on the performance map, Figure 304.

TABLE XXX
FLUID-COOLED TURBINE PERFORMANCE

Test Point Run No.	CHOKED NOZZLE CALCULATION				Measured EGT Corr ~ °F	Δ EGT Calc Corr Meas Corr	N Mech RPM	$\frac{N}{\sqrt{\Theta_{cr}}}$ Dyn Ref Speed	P/P Referred Pres Ratio	$\frac{\Delta H}{\Theta_{cr}}$ Btu/lb	$\frac{WN}{\delta 60}$ Dyn Ref Flow
	η_t Turbine Eff	TIT °F	EGT °F	EGT Corr ~ °F							
23	0.703	2084	1675	1615	1599	+16	31,880	14,600	3.378	25.51	347
24	0.820	1781	1341	1298	1393	-95	35,000	17,100	3.508	30.67	404
25	0.710	2108	1674	1610	1540	+70	35,000	16,000	3.577	26.72	379
26	0.727	2137	1697	1633	1687	-54	40,300	18,300	3.527	27.21	434
27	0.695	2151	1783	1719	1778	-59	36,500	16,560	2.926	22.74	392
28	0.631	1817	1453	1399	1443	-56	30,300	14,700	3.814	24.83	348
29	0.647	1868	1503	1447	1596	-149	31,300	15,015	3.619	24.72	355
30	0.738	2168	1800	1734	1691	+43	44,000	19,900	2.737	22.78	472
31	0.732	1800	1386	1334	1432	-98	45,000	21,910	3.815	28.84	518
32	0.649	957	808	768	669	+99	30,600	18,700	1.998	14.30	443
33	0.676	1246	1049	859	915	-56	30,600	17,100	2.163	16.44	406
34	0.686	1477	1256	1108	1172	-64	30,500	16,000	2.184	16.96	381
35	0.663	1754	1521	1318	1398	-80	30,500	15,000	2.151	16.09	358
36	0.688	921	699	663	616	+47	30,500	18,800	2.819	21.74	447
37	0.677	1236	1039	982	934	+48	30,000	16,800	2.173	16.60	399
38	0.675	1460	1240	1166	1139	+27	30,000	15,800	2.216	16.94	376
39	0.709	909	753	714	670	+44	30,000	18,600	1.978	15.48	441
40	0.710	1220	981	956	958	-2	30,250	17,000	2.524	20.44	401
41	0.677	1509	1241	1203	1215	-12	29,968	15,600	2.657	20.41	368
42	0.665	1525	1263	1224	1239	-15	29,909	15,500	2.626	19.83	366

TABLE XXX - Continued

Test Point Run No.	CHOKED NOZZLE CALCULATION				Measured EGT Corr ~ °F	Δ EGT Calc Corr Meas Corr	N Mech RPM	$\frac{N}{\sqrt{\Theta_{cr}}}$ Dyn Ref Speed	P/P Referred Pres Ratio	$\Delta H/\Theta_{cr}$ Btu/lb	$\frac{WN}{\delta 60}$ Dyn Ref Flow
	η_t Turbine Eff	TIT °F	EGT °F	EGT Corr ~ °F							
43	0.663	1615	1339	1289	1363	-14	30,330	15,400	2.694	20.28	364
44	0.700	1156	942	920	891	+29	38,057	21,800	2.391	19.08	515
45	0.687	1403	1178	1060	1151	-91	30,045	16,100	2.278	17.84	382
46	0.733	1184	979	928	1001	-73	39,900	22,700	2.169	18.07	538
47	0.734	1784	1481	1382	1510	-128	40,300	19,800	2.251	18.86	473
48	0.696	1313	1070	1040	994	+46	30,000	16,400	2.516	19.90	388
49	0.716	1557	1274	1231	1229	+2	34,000	17,500	2.592	21.09	413
50	0.706	1787	1478	1425	1388	+37	36,800	18,000	2.648	21.18	425
51	0.667	2087	1687	1532	1641	-109	34,892	16,069	3.620	25.37	381
52	0.744	877	621	614	576	+58	34,995	22,000	3.242	26.23	518
53	0.721	943	681	614	631	-17	31,500	19,300	3.290	25.55	455
54	0.714	1480	1164	1137	1140	-3	36,000	18,900	3.129	24.59	446
55	0.731	1381	1083	1052	1064	-12	40,000	21,500	3.011	24.43	509
56	0.738	1856	1486	1430	1436	-6	45,000	21,600	3.019	25.09	513
57	0.721	1738	1388	1341	1336	+5	40,500	20,000	3.106	24.65	473
58	0.728	1930	1563	1503	1550	-47	42,800	20,250	3.070	24.23	480
59	0.715	2212	1815	1741	1708	+33	45,000	20,200	3.062	24.14	479
60	0.618	2451	2061	1975	2084	-109	31,654	13,600	3.390	22.57	324
61	0.678	2221	1772	1703	1740	-37	42,100	18,880	4.087	27.79	448
62	0.670	2344	1890	1814	1962	-148	42,286	18,563	4.089	27.56	440

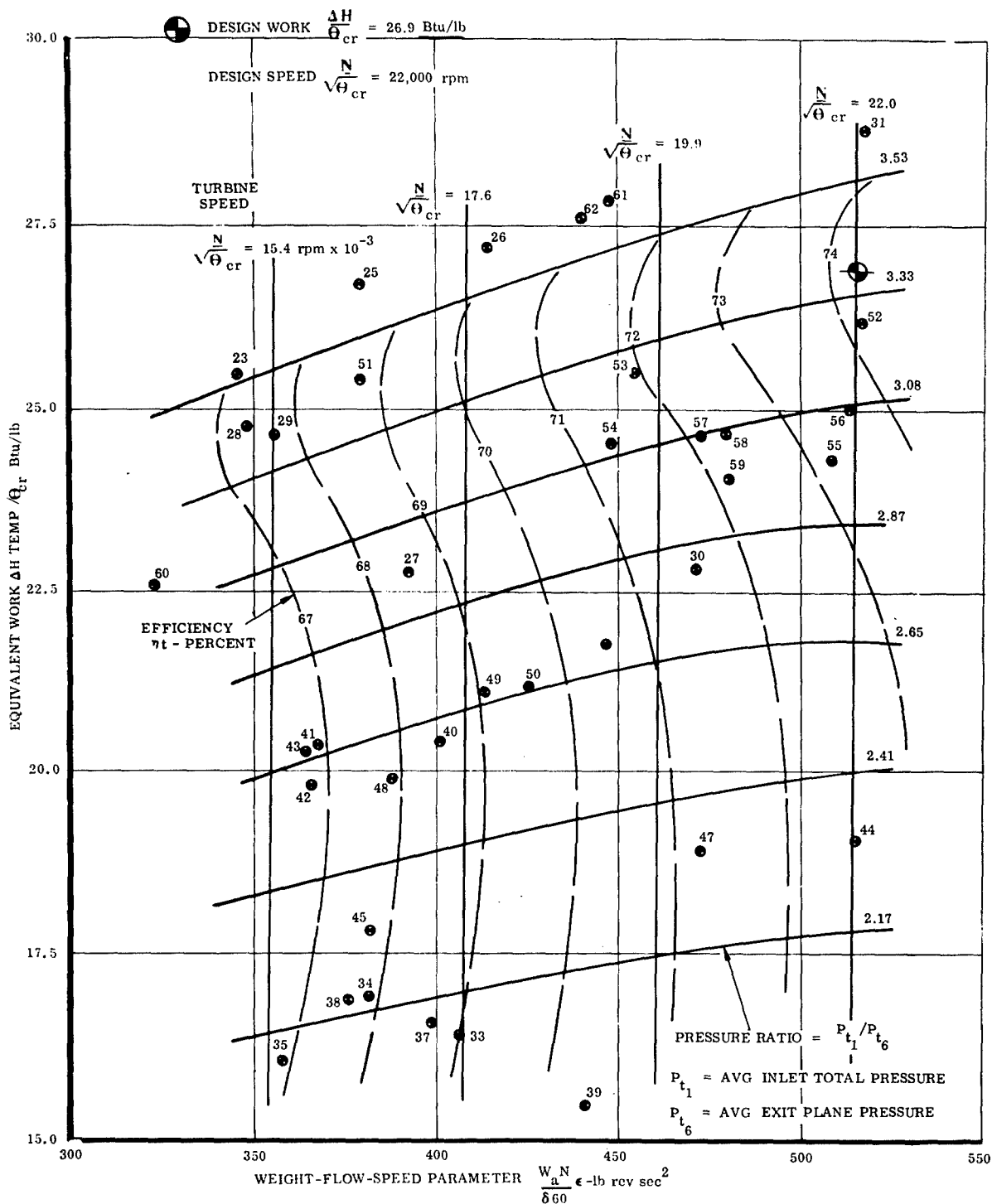


Figure 304. Fluid-Cooled Turbine Performance Map.

At the referred design point, a 74-percent turbine efficiency was obtained.

Cold flow rig data of Phase I showed test design point efficiencies for a 23-nozzle vane and 28-rotor blade version (Figure 305) and a 23-nozzle vane and 34-rotor blade version (Figure 294) of 74.5 percent and 81.0 percent, respectively.

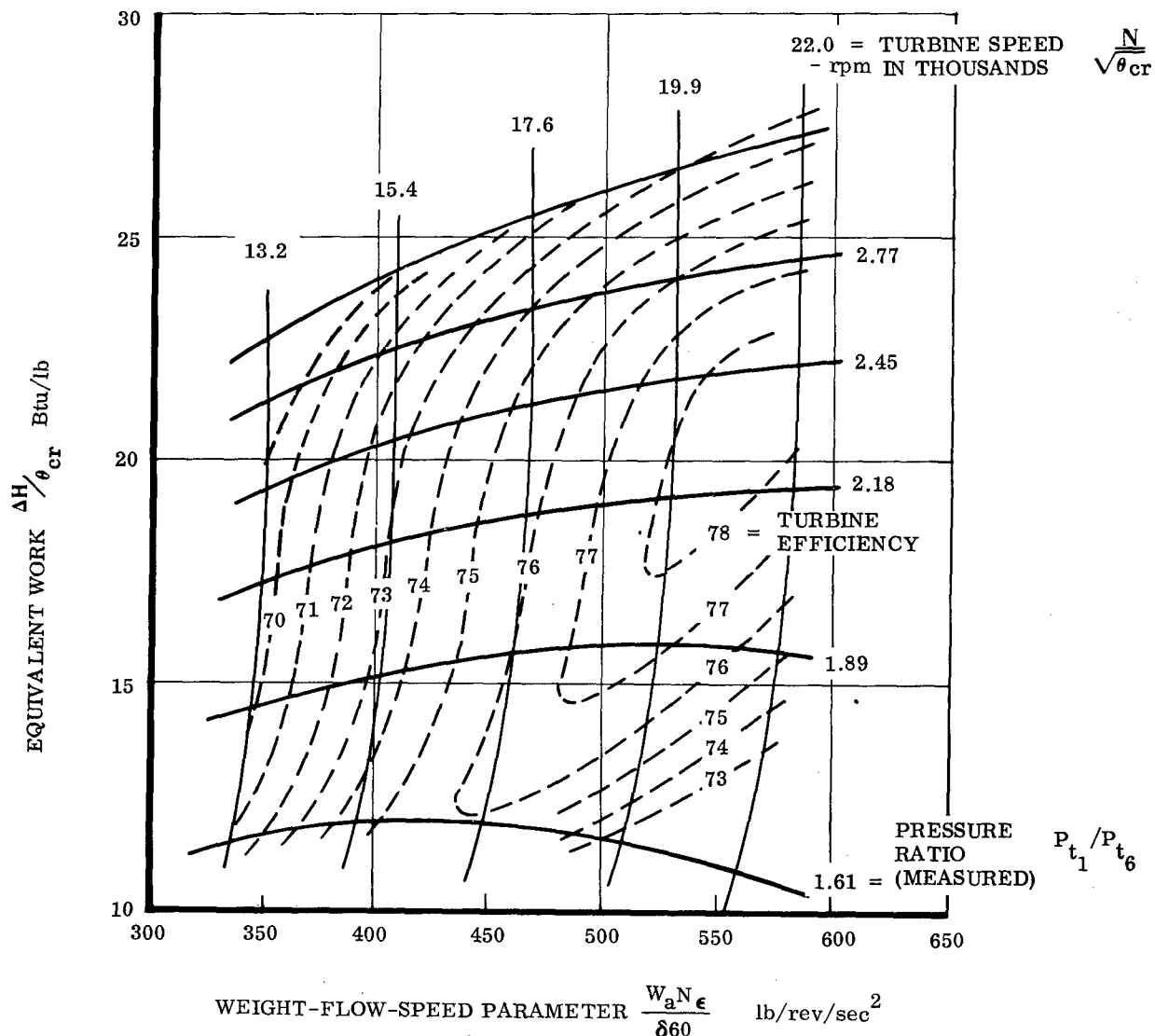


Figure 305. Fluid-Cooled Turbine Performance - 23 Nozzle Vanes and 28 Rotor Blades.

Interpolation between these two provides a design point efficiency of 77.8 percent for the current hot test fluid-cooled turbine, as tested with 31 rotor blades. An efficiency decrement of $77.8 - 74.0 = 3.8$ points between the cold flow test and the subject turbine test can be satisfactorily attributed to the combined effect of the following:

1. Aerodynamic losses due to injection of cooling flow into the main-stream flow.
2. Rotor tip running clearances which for the test rig must be greater for high-temperature operation due to transient clearance requirements.
3. Greater leakage losses due to the higher pressure level of hot rig operation with respect to cold rig operation.

Complementary to the turbine performance map, a curve of the ratio of mean wheel speed/isentropic velocity versus turbine efficiency was plotted for different wheel speeds to confirm that the shapes of these curves for each of the referred speeds were similar and were ascending as the referred speed level was increased, reaching an optimum at, or just beyond, the design value. This was the case, as shown in Figure 306.

COMBUSTOR

The objective of the combustor development program was to provide a combustor capable of supplying hot gases at 2300°F TIT to the fluid-cooled turbine. The combustor, which was designed with a minimum of modifications and additional development, could be incorporated into an engine application.

The combustor efficiency and pressure drop have a significant influence on overall cycle performance objectives. In addition, combustor discharge temperature profiles have a major influence on the structural integrity of any turbine; an improper profile can penalize a cooled turbine design.

In view of the above, and because a means of generating the high turbine inlet temperatures for turbine tests was required, the combustor and turbine were considered to be an integrated subsystem which fulfilled this need and provided additional advanced-technology data.

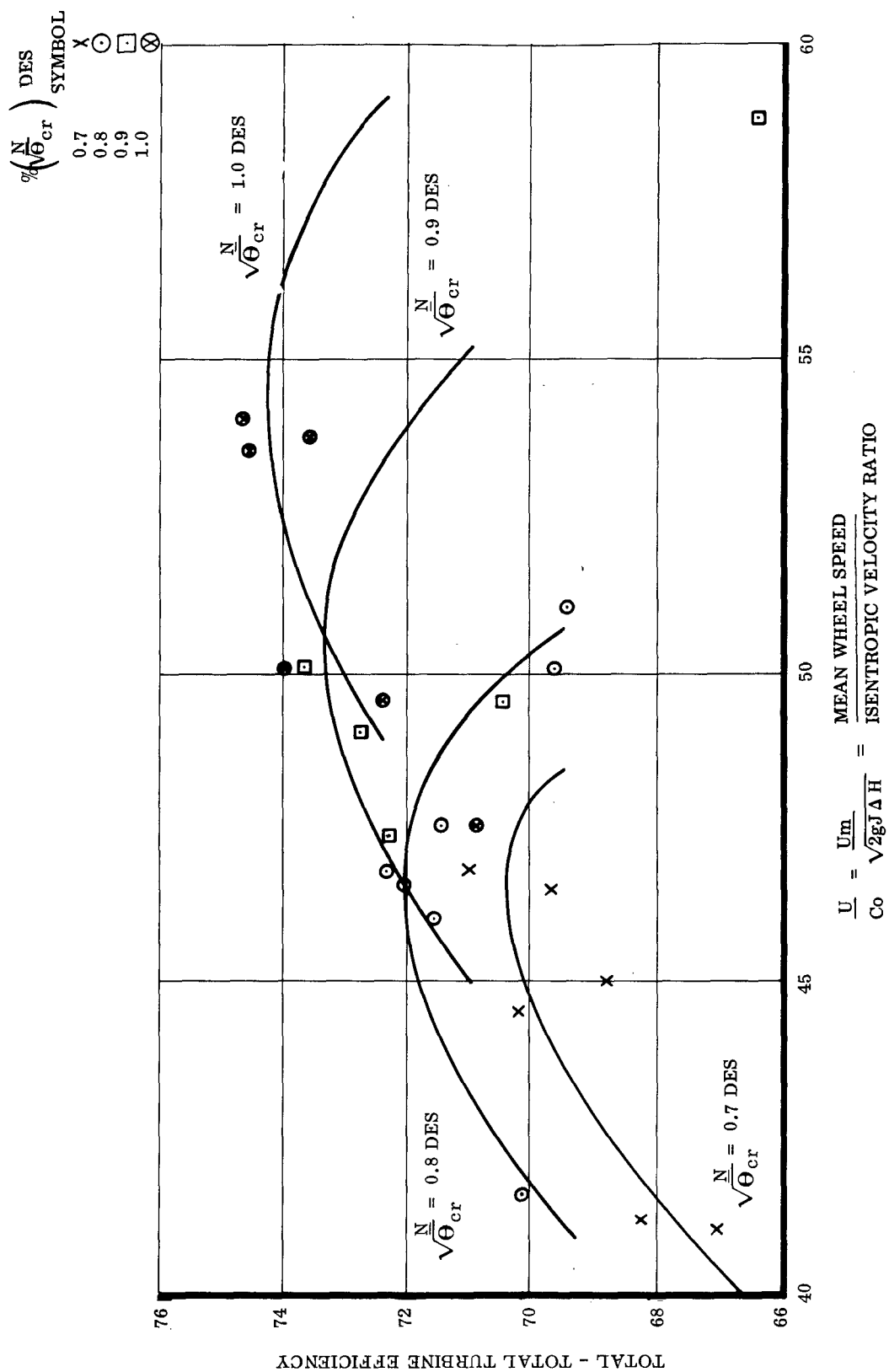


Figure 306. Mean Wheel Speed Versus Turbine Efficiency.

The performance requirements of the combustor were

Temperature Distribution Factor (TDF) 0.20

Circumferential Average Radial Temp Profile . . . $\pm 100^{\circ}\text{F}$ From Mean

Combustion Efficiency 98.5 Percent

Combustor Pressure Loss 4.7 Percent

Design Point Fuel-Air Ratio 0.0274

The combustor development program resulted in a circumferential average radial temperature profile which met the design requirement. However, combustion efficiency is lower and TDF is higher than the design values.

The objectives of the combustor development program are compared in Table XXXI with the test results obtained. Combustion efficiency was low (82 percent) and the TDF was slightly high (0.25 actual against 0.20 goal). The low combustion efficiency may have been the result of fuel leakage. Additional tailoring of these factors would be necessary for an advanced-technology engine cycle. The combustor pressure loss of 4.35 percent is an improvement over the objective of 4.7 percent.

TABLE XXXI
COMBUSTOR PERFORMANCE

	Design Point	
	Objective	Obtained
Rig Airflow, pounds per second	3.5	3.5
Turbine Inlet Temperature, $^{\circ}\text{F}$	2300	2450
Temperature Rise, $^{\circ}\text{F}$	1680	1900
Temperature Distribution Factor (TDF) . .	0.20	0.25
Circumferential Average Radial Temperature Profile, $^{\circ}\text{F}$ from mean	100	90
Combustion Efficiency, percent	98.5	82
Combustor Pressure Loss, percent	4.7	4.35

Combustor Development

The combustor development program consisted of six builds of the combustor rig. The first three builds were tested at low slinger speeds (less than 17,000 rpm) because of the speed limitations placed on the speed-reduction gearbox thrust bearings. This speed limitation was due to the probability of the bearings' skidding at the low-power input required to drive the fuel slinger. This condition was corrected in Build 4, and subsequent testing was conducted at slinger speeds between 30,000 and 35,000 rpm. Figure 307 is a cross section of the combustor with pertinent details identified.

Each build of the combustor rig is presented in chronological order, and the problems encountered, the modifications made, and the combustor performance discussed.

Combustor Build 1 - This was the first assembly of the combustor rig and served as a shakedown run for the reduction gearbox, rig rotating hardware, and initial combustor ignition tests.

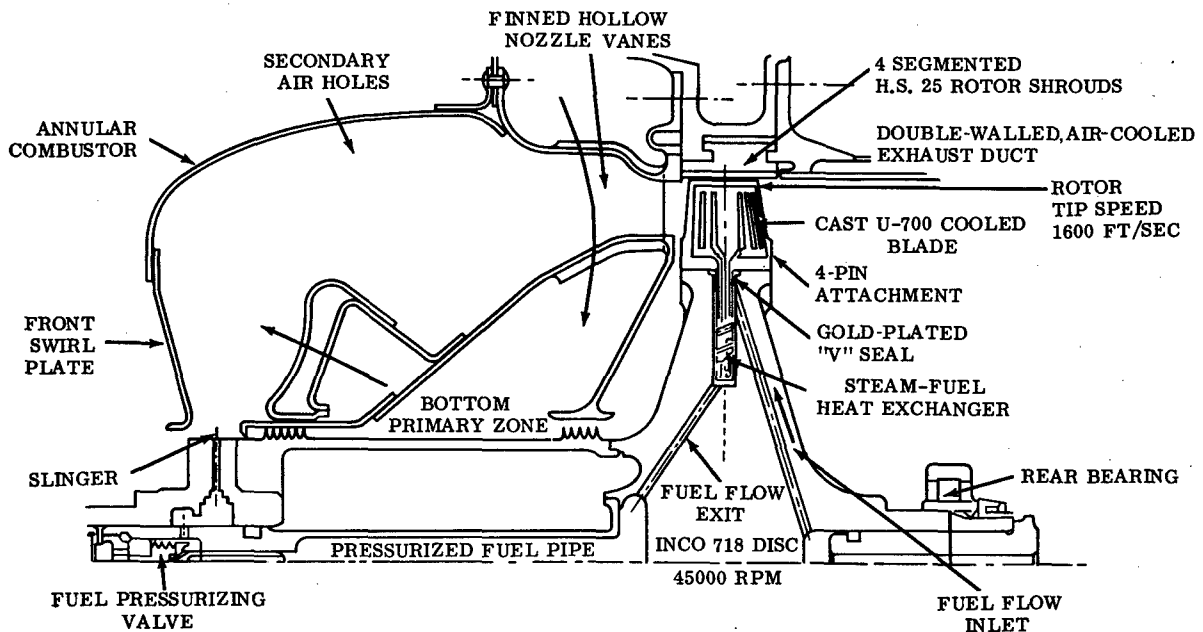


Figure 307. Cooling System and Design Features - Fluid-Cooled Turbine.

Since the thrust bearings in the reduction gearbox limited the speed range of the slinger shaft at low-power inputs, the mechanical shakedown of the rig consisted of low-speed (less than 17,000 rpm) running. The rig slinger shaft passed through its first critical speed between 10,200 and 12,000 rpm with a maximum vibration of 0.60 mil.

Ignition tests conducted at ambient pressure with airflows less than 0.2 pound per second resulted in consistent primer lights. However, at airflows above 0.2 pound per second, primer ignition was not possible.

Modification of the ignitors and primer fuel nozzles to provide more penetration into the recirculation zone below the inlet diffuser resulted in consistent primer lights at airflows approaching 0.6 pound per second. This provided less critical conditions for main fuel ignition.

Main fuel ignition was readily accomplished at all conditions mentioned above at which primer lights were obtained. However, combustion was unstable and was not self-sustaining at fuel-air ratios below approximately 0.017, while fuel-air ratios above 0.017 resulted in aborted starts, due to overtemperature.

In view of the above, and the limited rig instrumentation (two stationary turbine inlet temperature probes in line with the ignitors, and fuel and airflow measurements), this series of tests was concluded.

The unstable combustion which existed during these tests was deduced to be the result of excess air in the primary zone, complicated by maldistribution of air entering the combustor. Modifications were made to alleviate these problems.

Inspection of the combustor hardware during and after disassembly revealed no mechanical or thermal damage.

Combustor Build 2 - To correct the problems found during testing of Build 1, the following combustor modifications were made:

1. The two rows of swirl vane louvers were closed down from a 0.020-inch gap to 0.007 inch on the inner row and 0.012 inch on the outer row. This resulted in a reduction of 18 percent in swirl vane flow area, and about 2.0 percent in primary-zone airflow, Figure 308.
2. A flow-straightener screen of 42-percent blocked area was installed in the combustor inlet to eliminate maldistribution of air entering the combustor.

SWIRL VANE LOUVERS

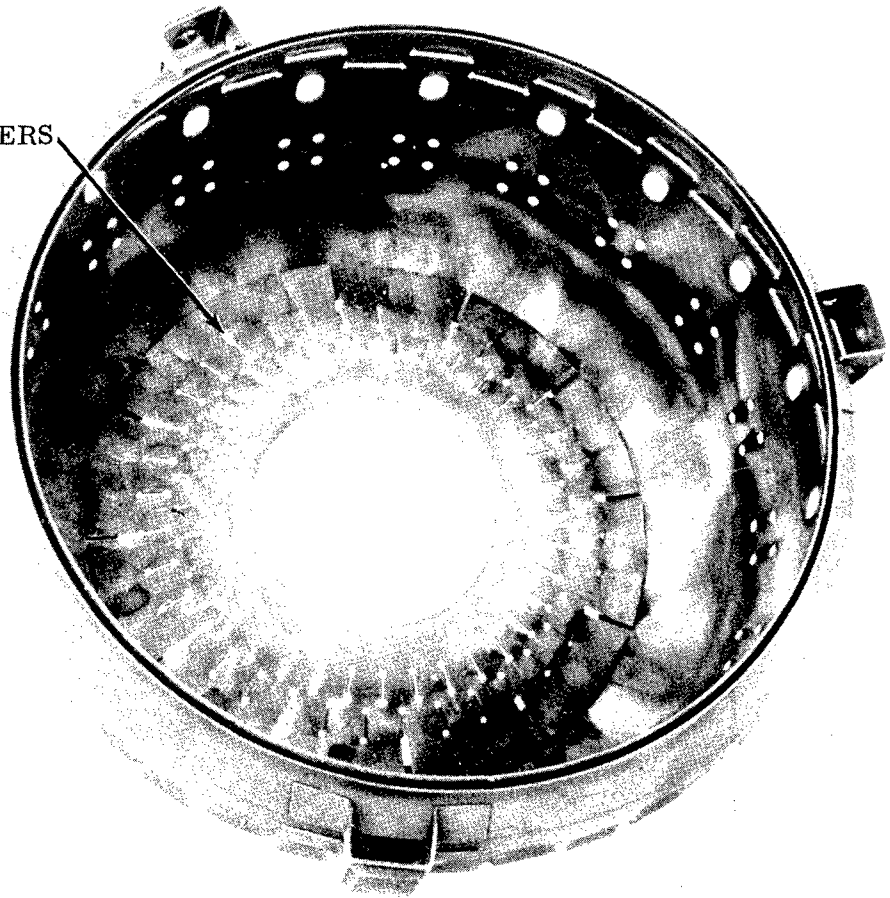


Figure 308. Three-Quarter View of Outer Combustor and Swirl Vane Assembly Showing Swirl Vane Louvers.

In addition, the rig was thoroughly instrumented to measure combustor pressure loss, combustor efficiency, and combustor exit temperature profile. Thermocouples were also installed in the leading edge of two turbine inlet nozzle vanes to monitor metal temperature.

Initial ignition attempts again resulted in aborted starts, due to impending overtemperature at an indicated fuel-air ratio of approximately 0.017. At lesser fuel-air ratios, the combustor blew out when the primers were shut off.

At this point the rig was pressurized, in steps, to approximately one-half atmosphere, gage, to provide a more favorable combustion condition. This reduced the rate of temperature increase on start-up, but did not provide stable combustion.

The rig preheater was then ignited, and the combustor inlet air temperature was increased to 440°F. Main fuel ignition was accomplished with a preset fuel-air ratio of 0.016, and stable combustion was attained.

Subsequently, several data points were taken over a range of fuel-air ratios from 0.012 to 0.021. Figure 309 is a plot of combustor efficiency versus fuel-air ratio and clearly indicates the low combustor efficiency at fuel-air ratios below 0.016.

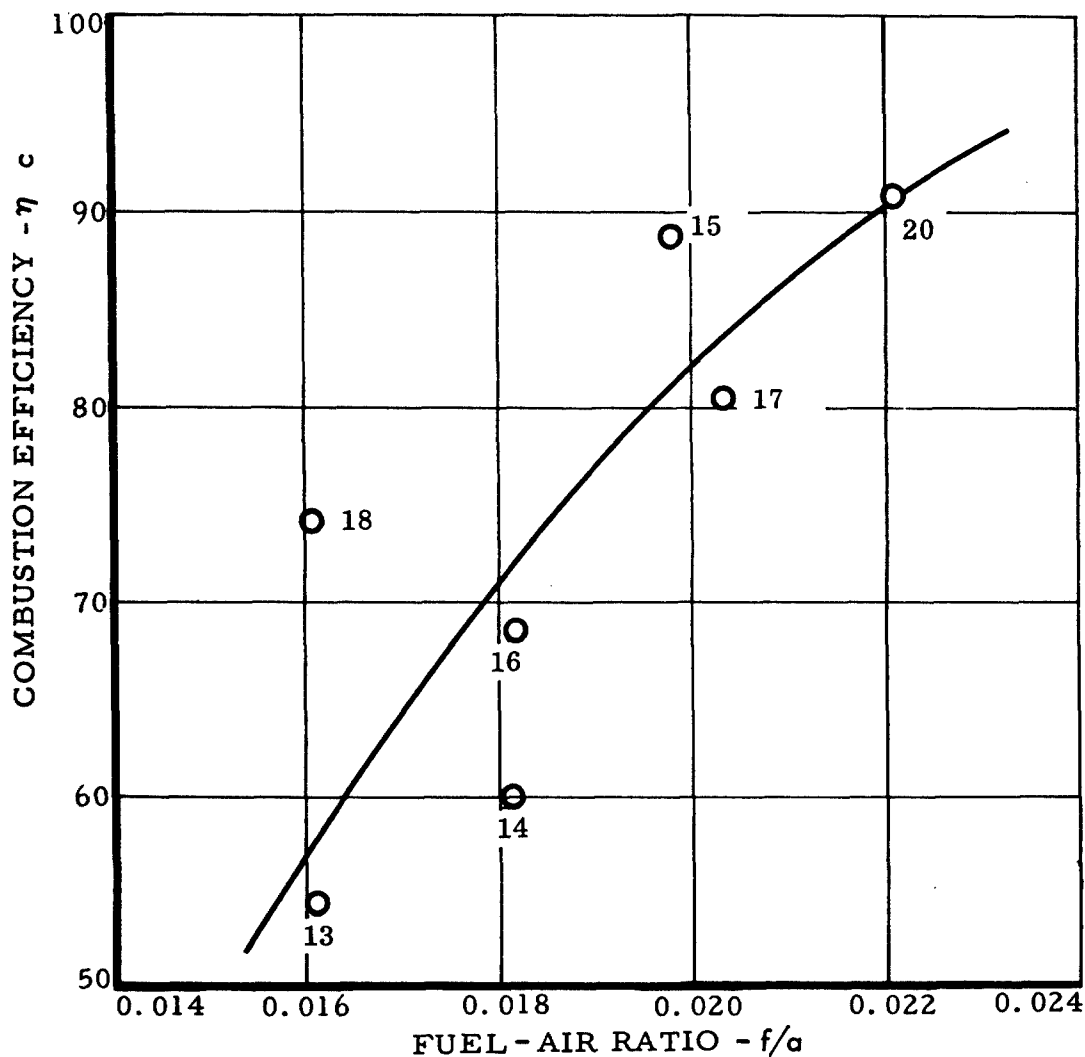


Figure 309. Combustion Efficiency Versus Fuel-Air Ratio - Combustor Build 2.

A plot of TDF versus combustor temperature rise, Figure 310, provides an overall indication of the maximum combustor exit temperature above the mean. The excessively high values of TDF at low combustor temperature rise and the low combustor efficiency at low fuel-air ratios emphasize the condition of excess air in the primary zone.

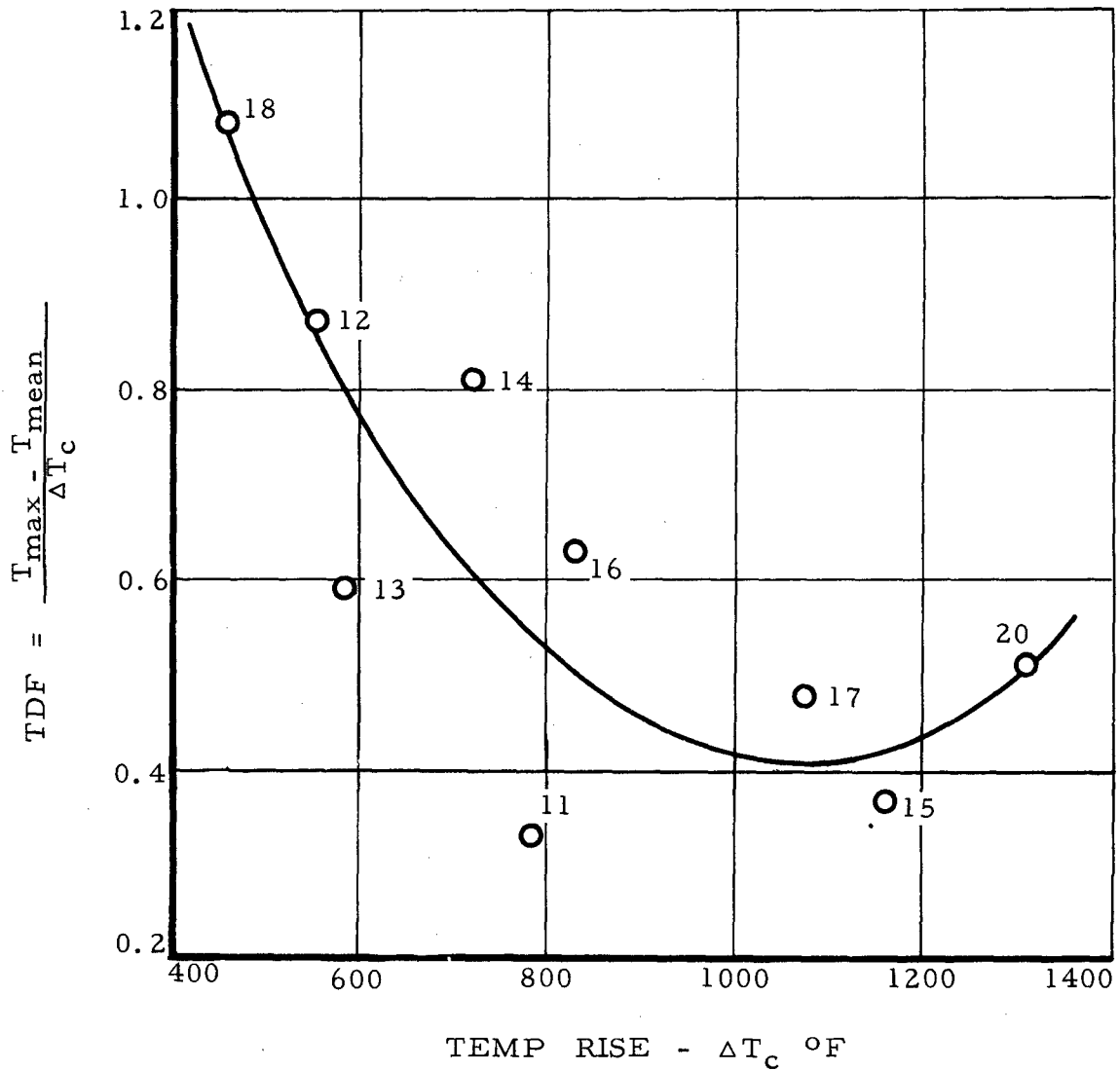


Figure 310. Temperature Distribution Factor Versus Temperature Rise - Combustor Build 2.

The circumferential and radial combustor exit temperature profile is best shown by a plot of temperature versus radius for each circumferential probe location. Figures 311, 312, and 313 are representative of the data taken at low (0.012), mid (0.0172), and high (0.022) fuel-air ratios, respectively. The circumferential gradient as well as the local radial profiles are shown. The circumferential average radial temperature profile is also given and is shown to become more positive with increasing fuel-air ratio.

It is to be noted that at a fuel-air ratio of approximately 0.018, the combustor alternated between a rumble and a screech condition. Introduction of approximately 2 to 3 inches of mercury gage back pressure on the rig eliminated this problem. Consequently, all further tests were conducted with this back pressure.

Combustor pressure drop, corrected to design point flow conditions, was approximately as predicted. Combustor pressure drop was measured during this test series by utilizing two of the actuated, aspirating temperature probes as total pressure probes. This was accomplished by closing off the aspirating circuit during pressure measurement.

It was recognized that this method of measuring combustor pressure loss would introduce errors into the pressure drop calculation. However, it was felt that sufficient accuracy would be retained for these early test runs and that more accurate pressure loss data would be obtained when the rig was fully instrumented later in the development program.

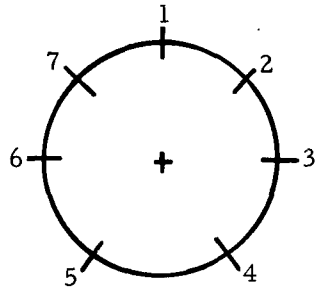
Combustor Build 3 - The combustor was further modified by replacing the swirl plate with a rigimesh swirl plate, Figure 314. This reduced the primary-zone airflow from 43 percent (Build 1) to 34 percent of total combustor airflow, providing a primary-zone, fuel-air ratio of 0.080 for design point flow conditions.

The combustor inlet flow-straightener screen (round wire, 42-percent blocked area) was also replaced with a perforated plate of square-edged orifices with 50-percent blocked area.

Reduction of the primary-zone airflow resulted in less stringent ignition conditions, more stable combustion, and better combustion efficiency at low fuel-air ratios.

Ignition and stable, self-sustaining combustion could now be maintained without preheat of the inlet air. Consequently, testing of Build 3 was accomplished without preheat. Back pressure on the rig was maintained at approximately 2 to 3 inches of mercury gage, and slinger speed was maintained between 16,000 and 17,000 rpm.

DATA POINT 19



$T_3 = 487^{\circ}\text{F}$
 $T_4 = 782^{\circ}\text{F}$
 $\Delta T_c = 295^{\circ}\text{F}$
 $f/a = 0.01225$
 $\eta_c = 0.335$

AFT LOOKING FORWARD

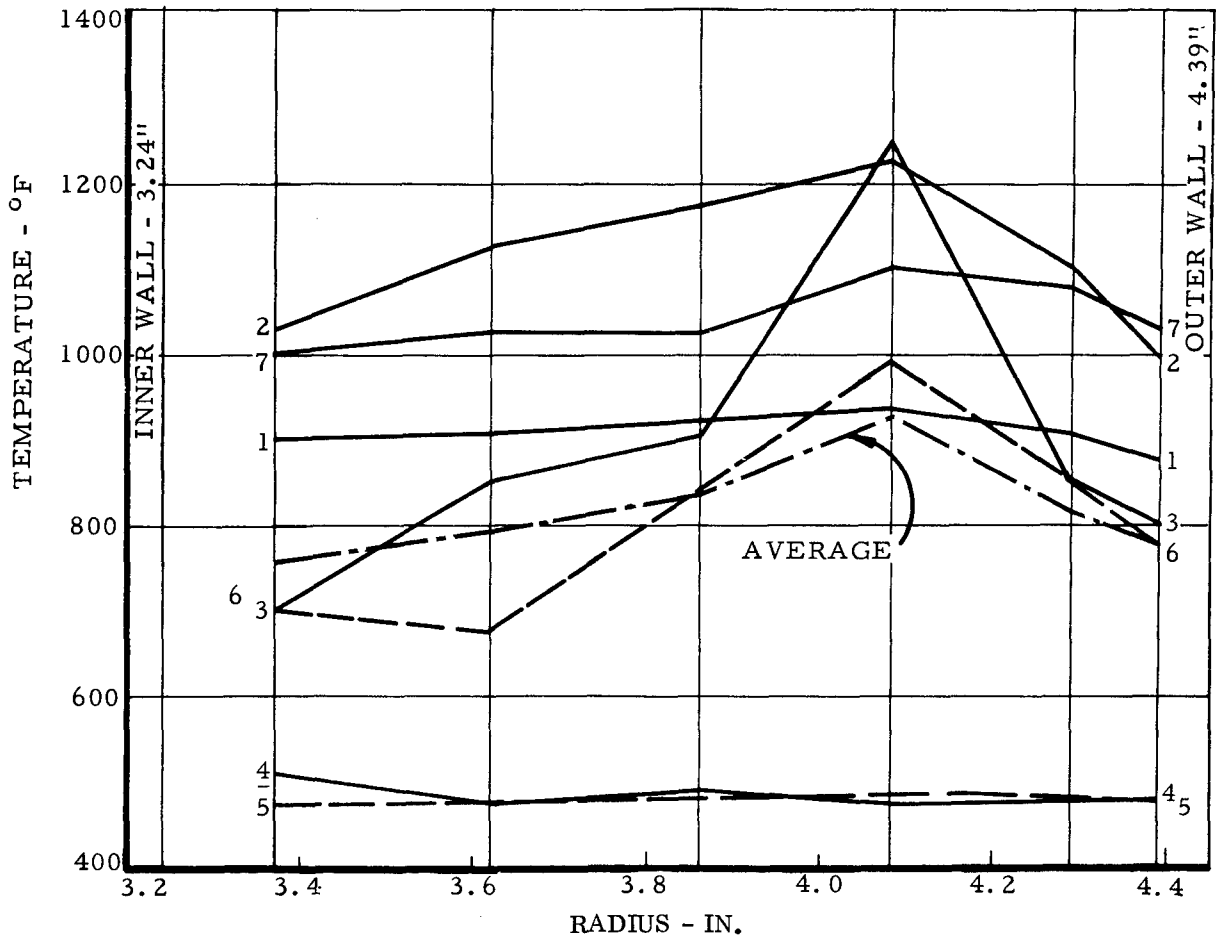


Figure 311. Combustor Exit Radial Temperature Profile.

DATA POINT 12

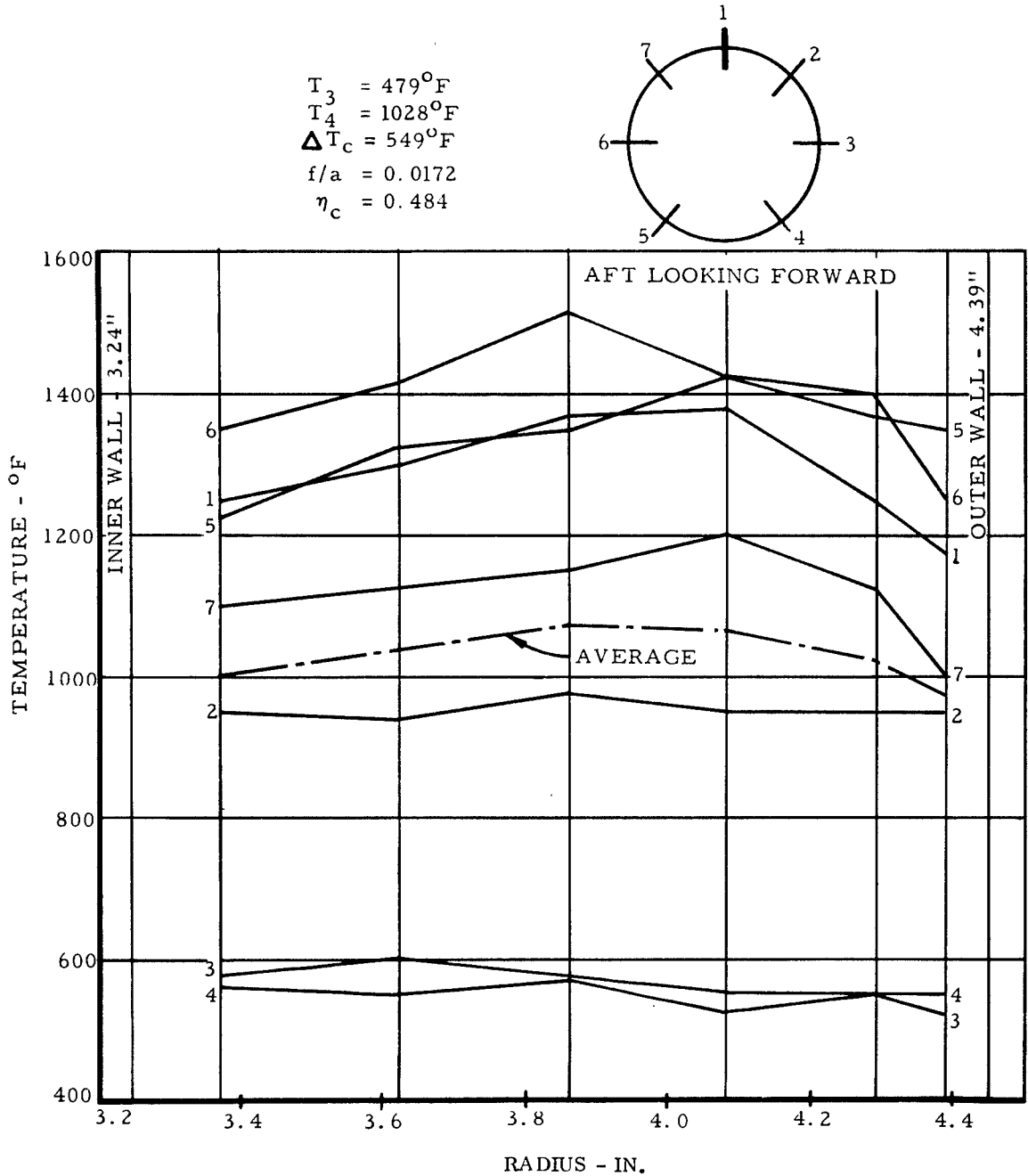


Figure 312. Combustor Exit Radial Temperature Profile.

DATA POINT 20

$T_3 = 471^{\circ}\text{F}$
 $T_4 = 1781^{\circ}\text{F}$
 $\Delta T_c = 1310^{\circ}\text{F}$
 $f/a = 0.0221$
 $\eta_c = 0.908$

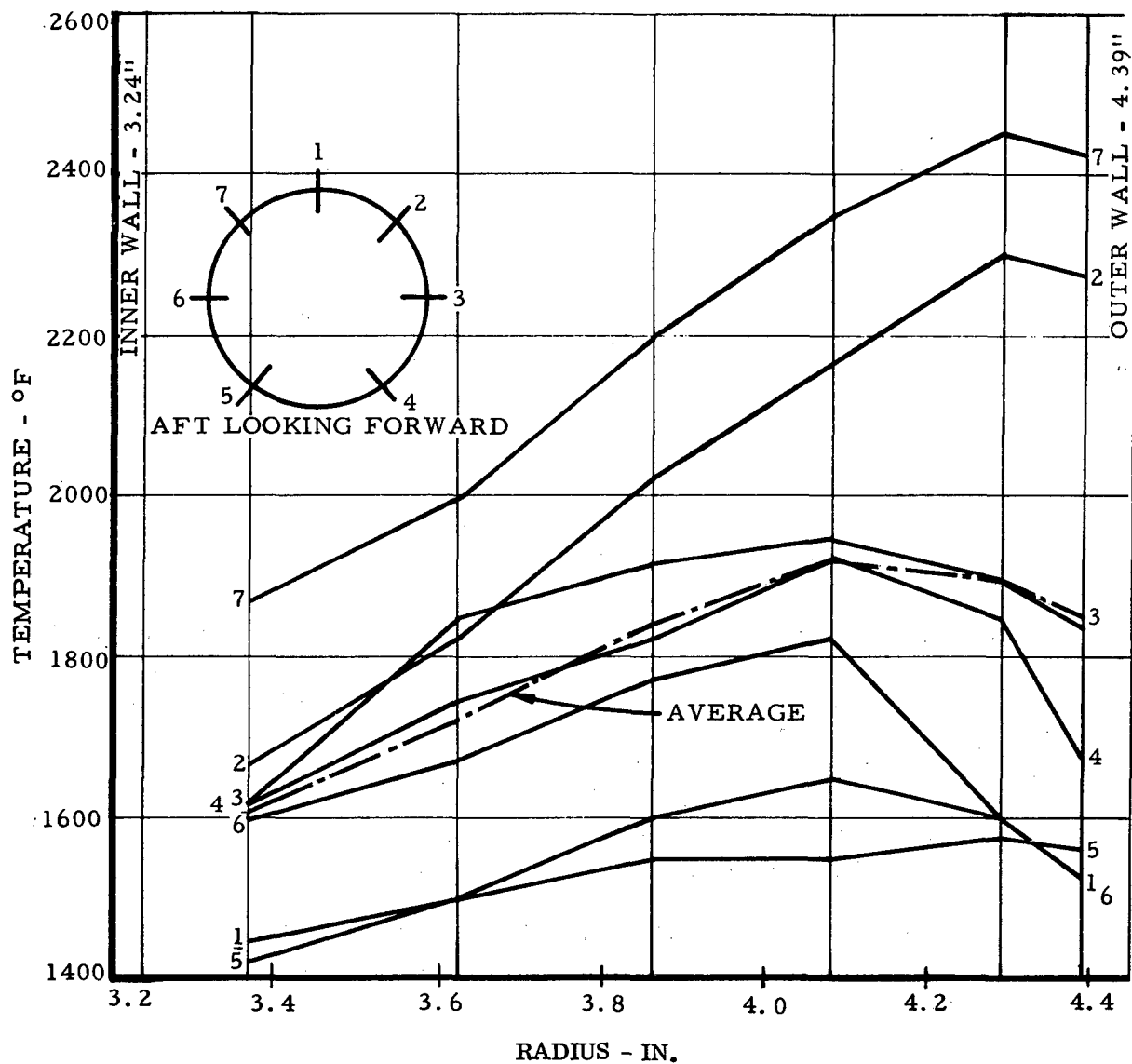


Figure 313. Combustor Exit Radial Temperature Profile.

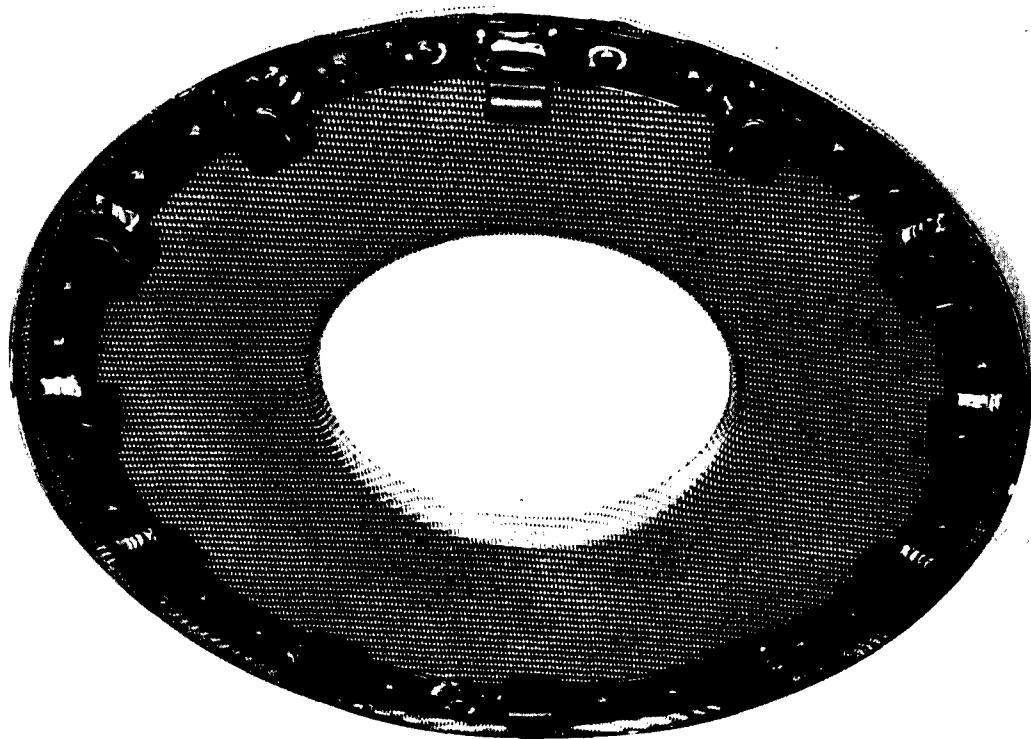


Figure 314. Rigimesh Swirl Plate.

Figure 315, a plot of combustion efficiency versus fuel-air ratio, clearly indicates the improvement of combustion efficiency at low fuel-air ratios, when compared with Figure 309. The indicated combustion efficiency of several data points was above 100 percent. This was attributed to fluctuations in the turbine inlet temperature being transmitted to the TIT readout. This could bias the measurement toward a somewhat higher temperature than actually pertains, because a time average rather than a mass average reading is taken of the fluctuations.

Improvement in the TDF over Build 2, Figure 310, is evident in Figure 316. However, the TDF was still found to be above the design point value of 0.2.

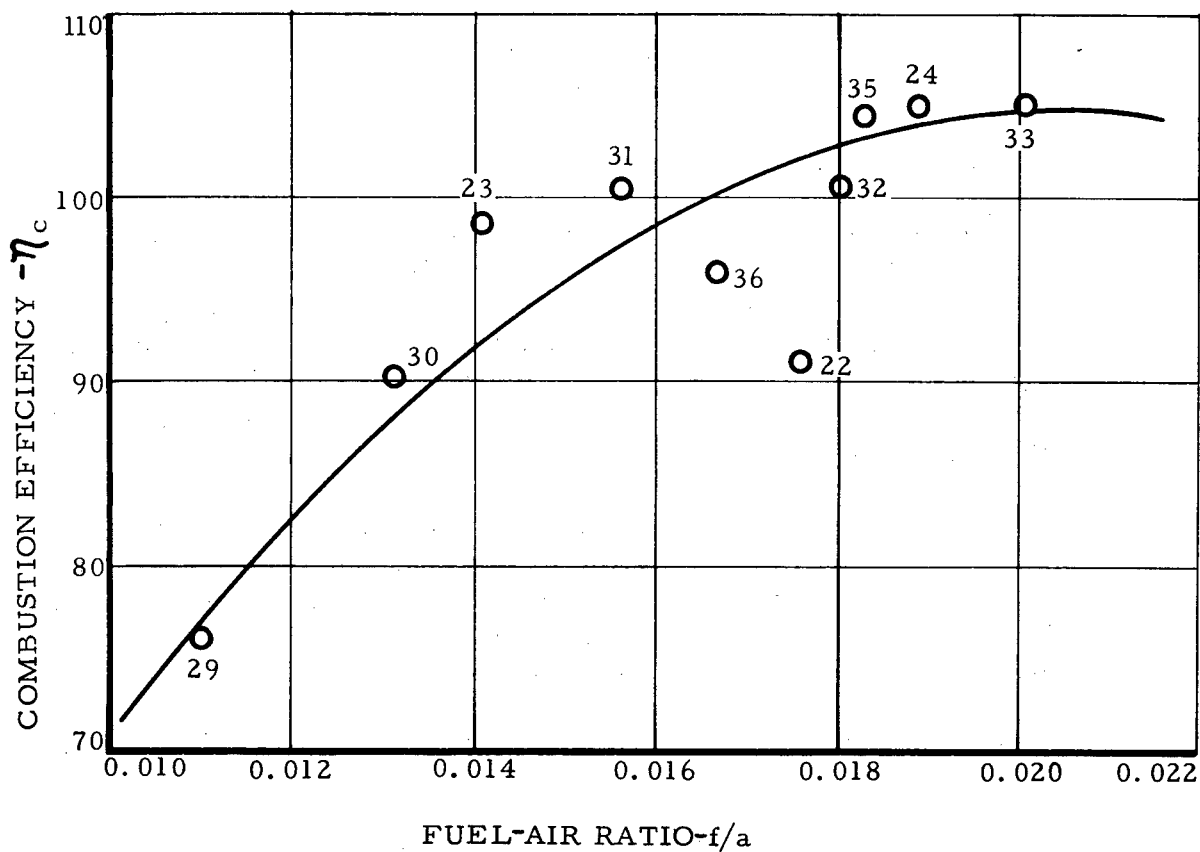


Figure 315. Combustion Efficiency Versus Fuel-Air Ratio.

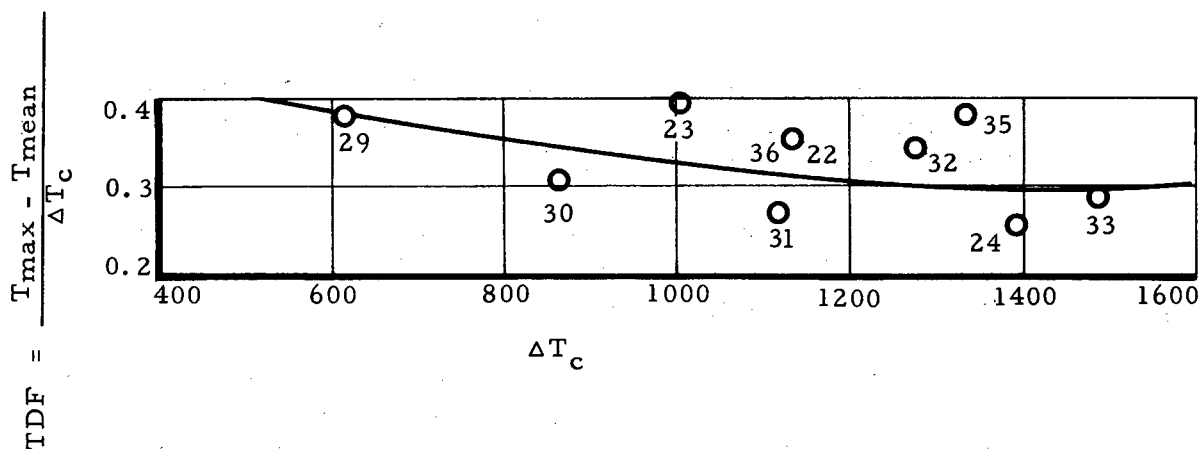


Figure 316. Temperature Distribution Factor Versus Temperature Rise - Combustor Build 3.

Representative plots of the circumferential and radial combustor exit temperature profile are shown in Figures 317, 318, and 319. Some improvement in the circumferential temperature gradient at the lower fuel-air ratios was achieved. However, the circumferential average radial temperature profile becomes increasingly more positive with increasing fuel-air ratio.

It is to be noted, again, that these tests were done at low slinger speeds of 16,000 to 17,000 rpm. Prior to modification of the combustor hardware to eliminate the positive radial temperature gradient, it was desirable to evaluate the combustor performance at higher, near design point, slinger speeds. Higher slinger speeds would result in better atomization and perhaps less penetration of the fuel into the combustor. This could affect the radial temperature profile.

Disassembly and inspection of the rig hardware revealed an over-temperature condition of the outer combustor shell just forward of the secondary air tubes. Metal temperatures in this area reached approximately 1450°F with cold (ambient) inlet air temperatures. Therefore, modifications were made to cool this area.

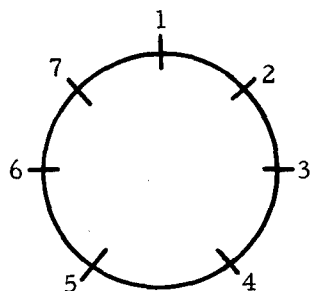
Combustor Build 4 - Modifications to the combustor hardware included

1. Installation of a film cooling strip, to cool the area of the outer combustor shell just forward of the secondary air tubes.
2. Replacement of the dual primers and ignitors with a single glow plug to reduce the circumferential gradient by eliminating the wakes caused by the primers and ignitors.
3. Six total pressure probes were installed in the leading edges of the turbine inlet nozzles to provide combustor pressure drop and turbine inlet pressure information.

To evaluate the effect of increased slinger speed on combustor performance, several data points were run at 16,500 rpm and then repeated at 30,000-rpm slinger speed.

The increased slinger speed and the removal of the ignitors and primer fuel nozzles had little effect on the temperature distribution factor, as indicated in Figure 320. However, there was a marked improvement in combustion efficiency, particularly at the lower fuel-air ratios, Figure 321. Combustion efficiencies in excess of 100 percent can again be accounted for by temperature fluctuations, as discussed in Build 3.

DATA POINT 29



$T_3 = 86^{\circ}\text{F}$
 $T_4 = 704^{\circ}\text{F}$
 $\Delta T_c = 618^{\circ}\text{F}$
 $f/a = 0.011$
 $\eta_c = 0.763$

AFT LOOKING FORWARD

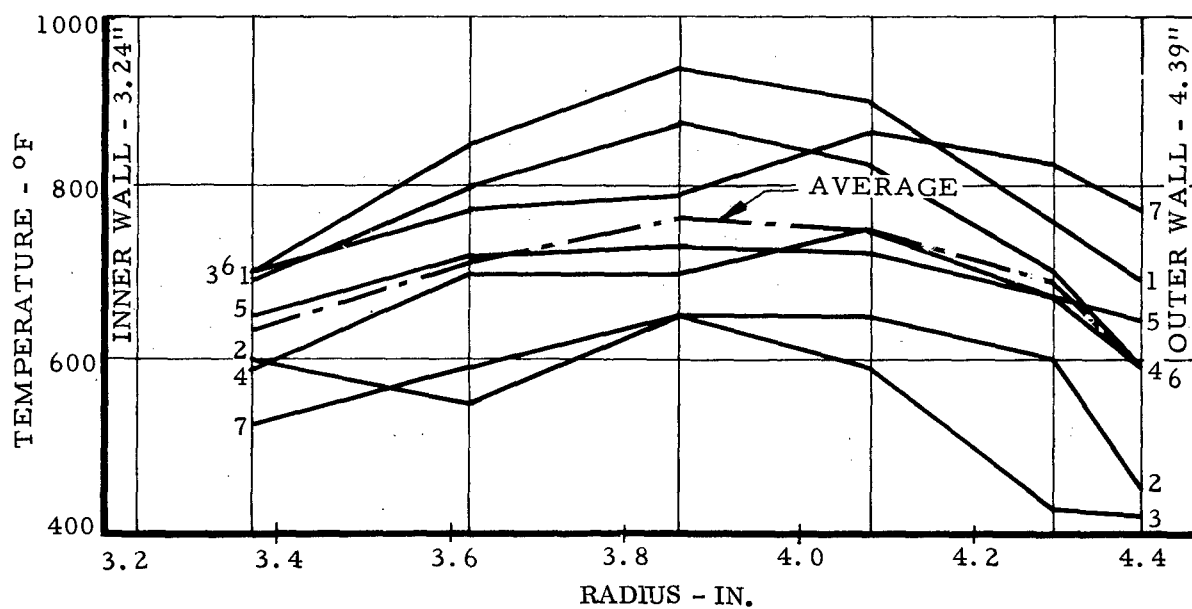
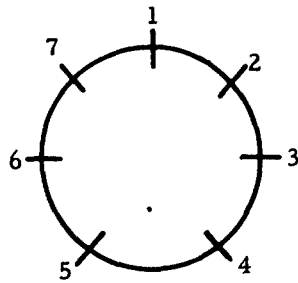


Figure 317. Combustor Exit Radial Temperature Profile.

DATA POINT 31



$T_3 = 99^\circ\text{F}$
 $T_4 = 1220^\circ\text{F}$
 $\Delta T_c = 1121^\circ\text{F}$
 $f/a = 0.0156$
 $\eta_c = 1.005$

AFT LOOKING FORWARD

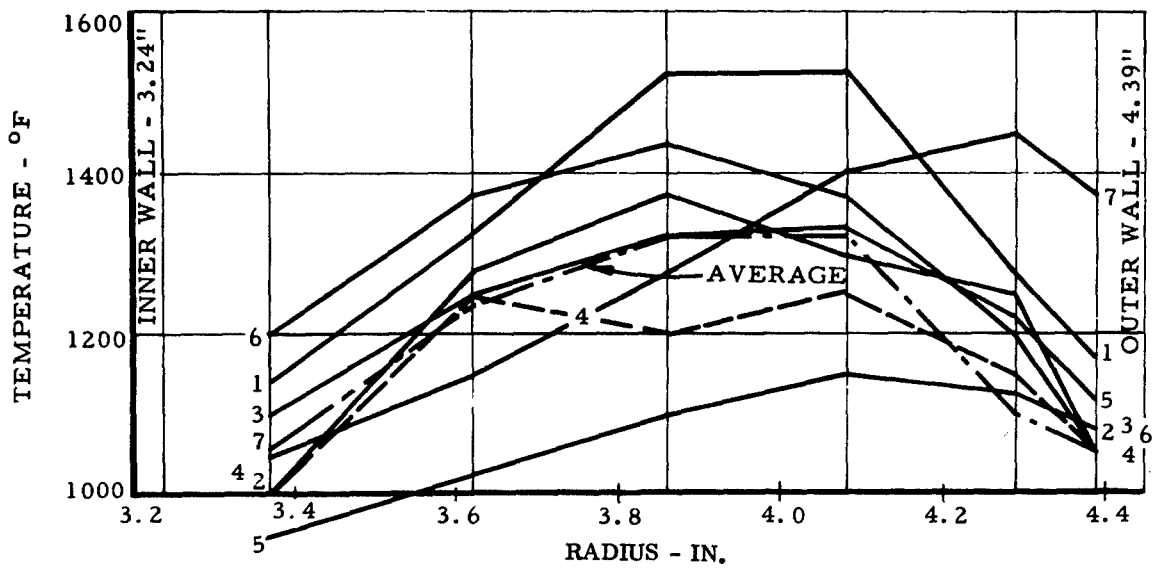


Figure 318. Combustor Exit Radial Temperature Profile.

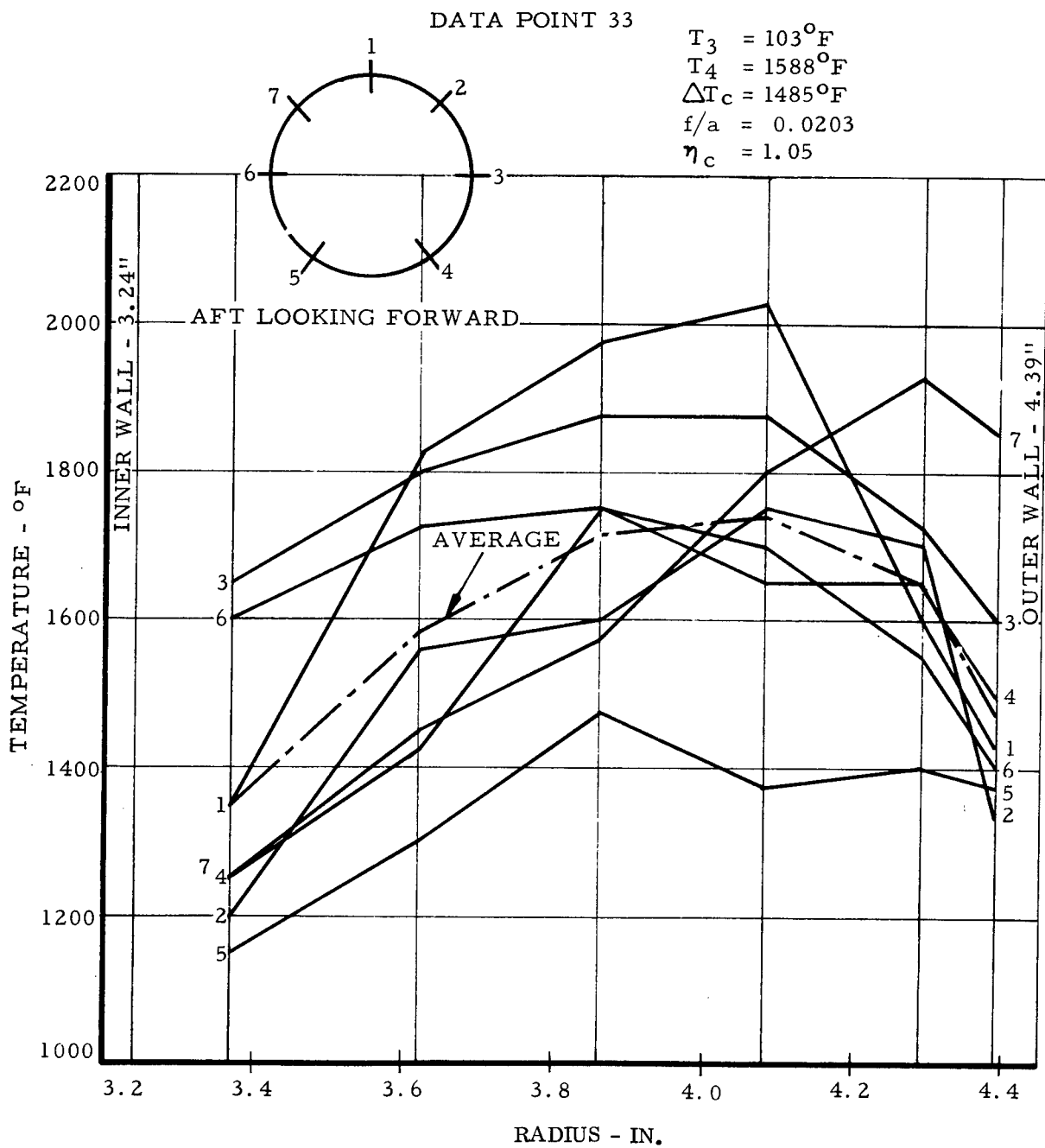


Figure 319. Combustor Exit Radial Temperature Profile.

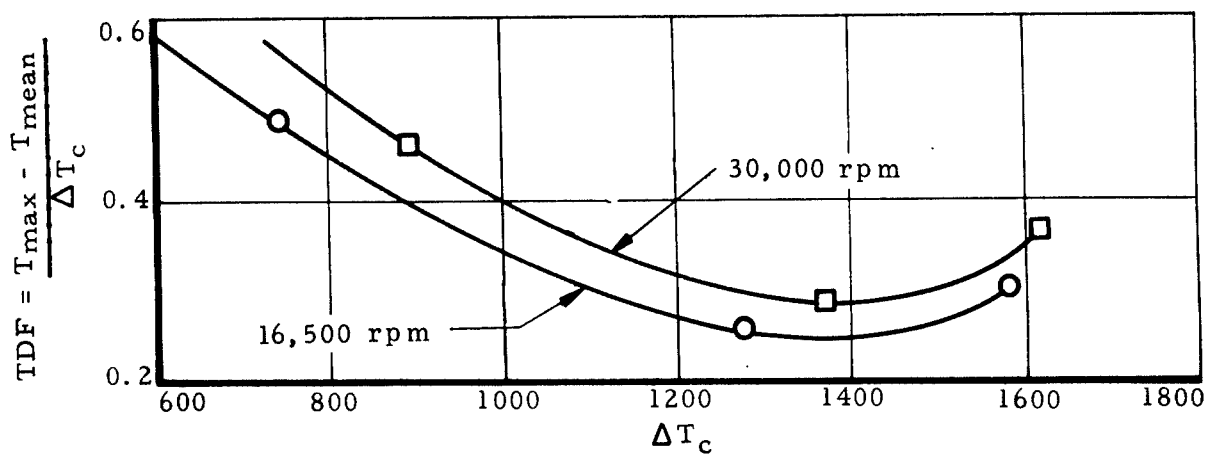


Figure 320. Temperature Distribution Factor Versus Temperature Rise - Combustor Build 4

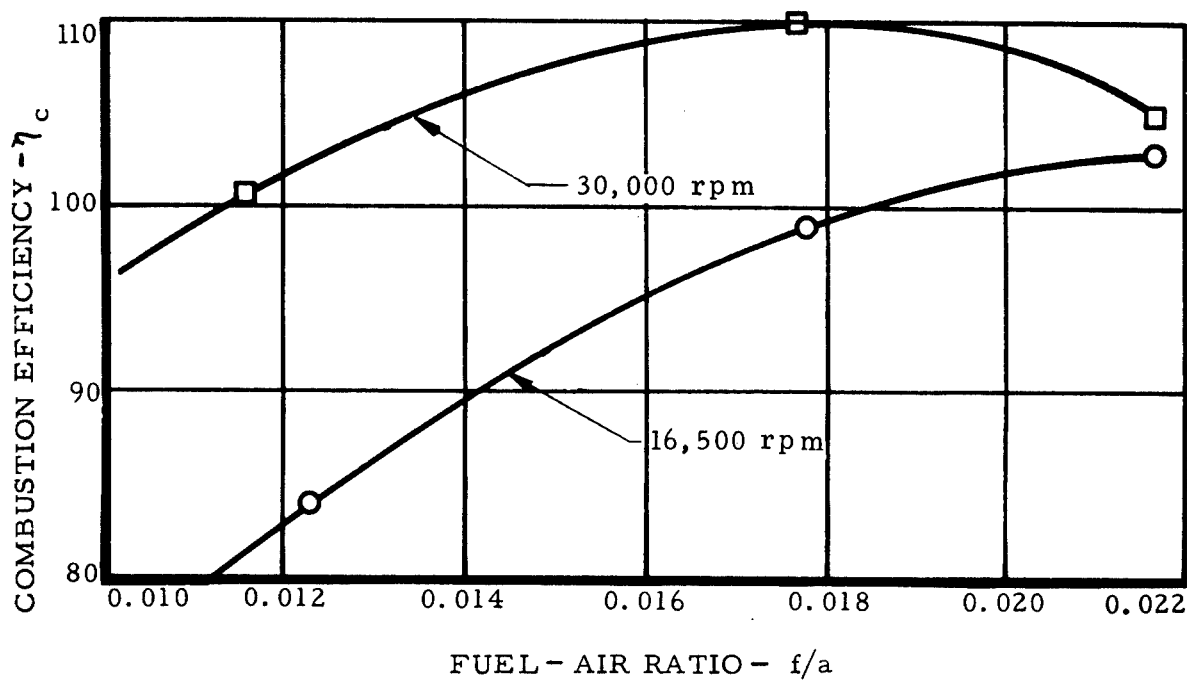


Figure 321. Combustion Efficiency Versus Fuel-Air Ratio - Combustor Build 4

The addition of the film cooling strip effectively cooled the outer combustor shell between the secondary air tubes. However, it also caused the circumferential average radial temperature profile to become slightly more peaked, as may be seen if Figures 322, 323, and 324 are compared to Figures 317, 318, and 319.

Combustor pressure drop, corrected to design conditions, is shown in Figure 325. The combustor pressure loss is slightly lower than the design value of 4.7 percent. This is attributed to an increase in effective flow area of approximately 3 percent provided by the film cooling strip.

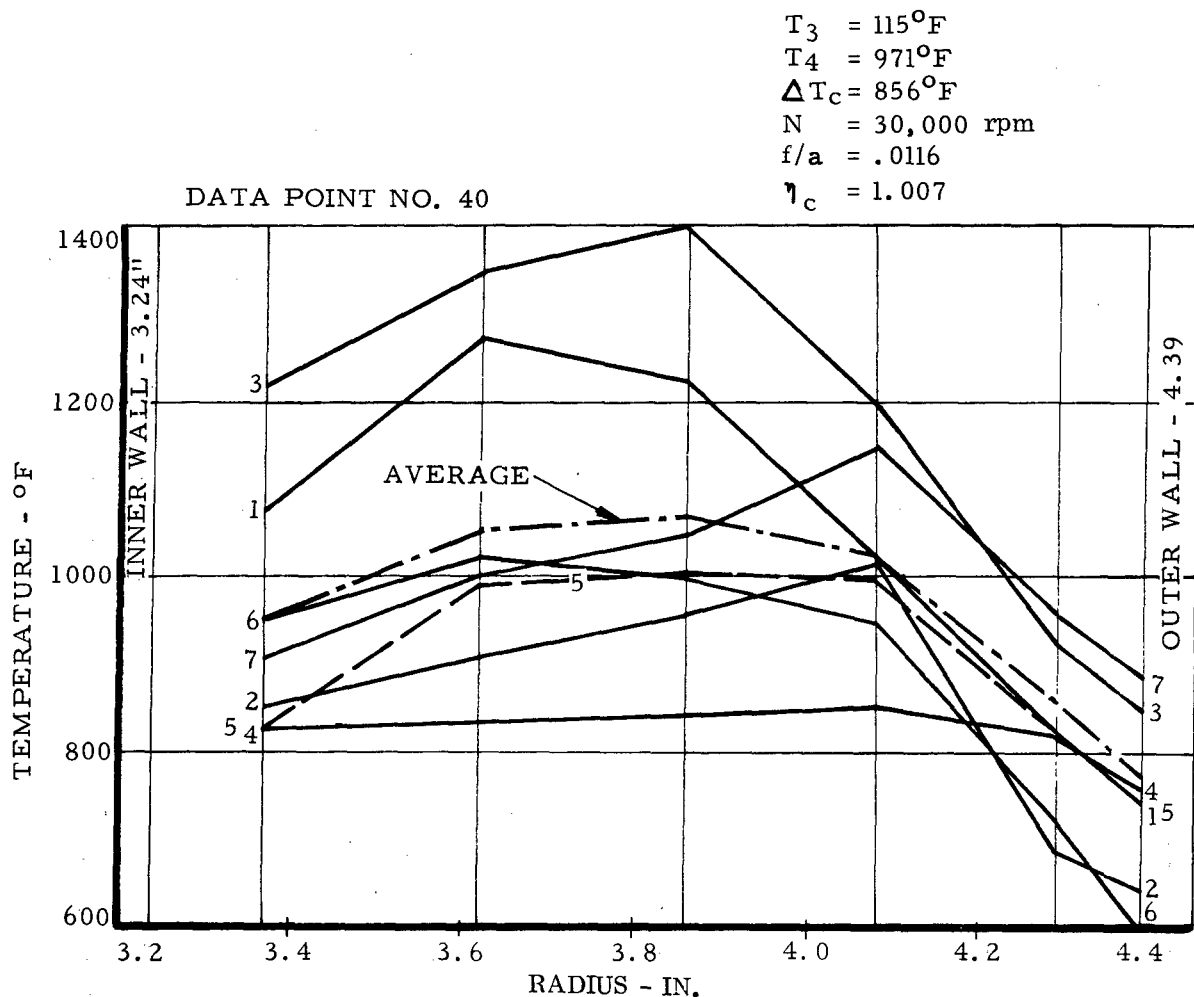


Figure 322. Combustor Exit Radial Temperature Profile.

$T_3 = 122^\circ\text{F}$
 $T_4 = 1489^\circ\text{F}$
 $\Delta T_c = 1367^\circ\text{F}$
 $N = 30,000 \text{ rpm}$
 $f/a = 0.0177$
 $\eta_c = 110\%$

DATA POINT NO. 41

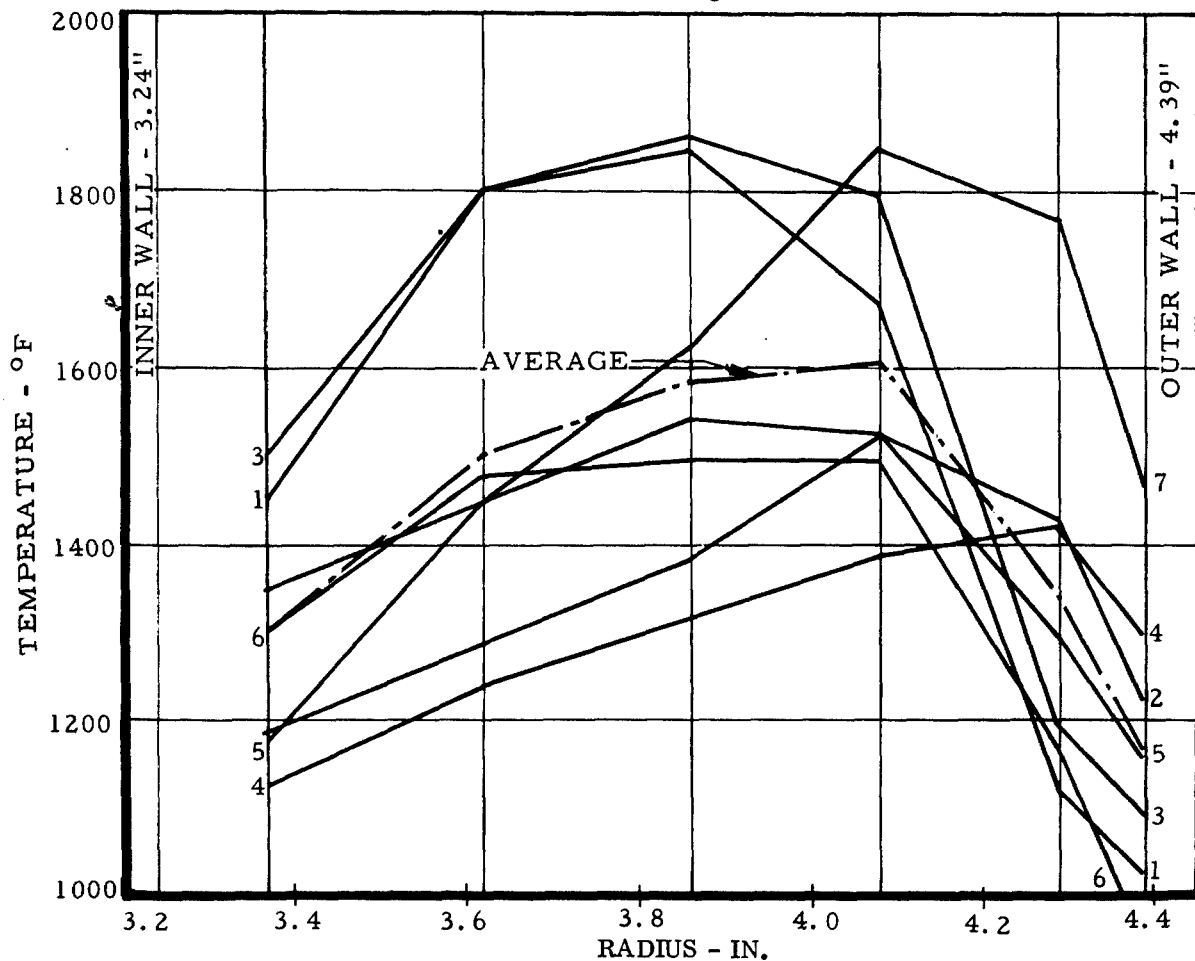


Figure 323. Combustor Exit Radial Temperature Profile.

At high fuel-air ratios (above 0.020), fluctuations of the temperature readout increased and prevented accurate measurement of turbine inlet temperature. Testing was discontinued for hardware evaluation.

The rig was disassembled, and the hardware was visually examined for mechanical or thermal damage which could be the cause of the temperature fluctuations. None were found. It is believed that the fast response of the thermocouples ($P_t 6 \text{ Rh}/P_t 30 \text{ Rh}$) and the readout system was picking up temperature fluctuations caused by mixing action occurring at the combustor exit.

$T_3 = 119^\circ\text{F}$
 $T_4^3 = 1689^\circ\text{F}$
 $\Delta T_c = 1570^\circ\text{F}$
 $N = 30,000 \text{ rpm}$
 $f/a = 0.0217$
 $\eta_c = 1.05$

DATA POINT NO. 42

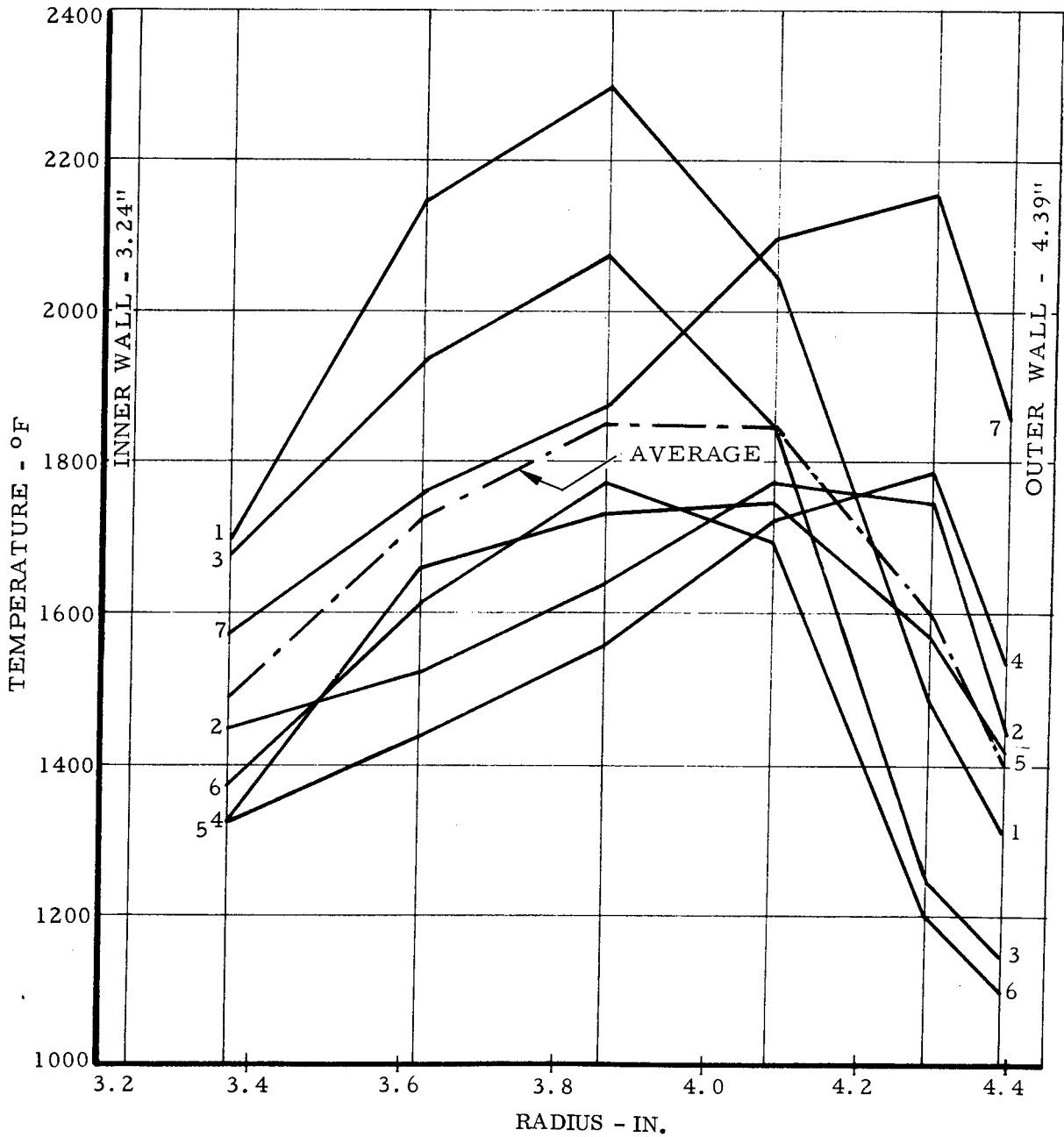


Figure 324. Combustor Exit Radial Temperature Profile.

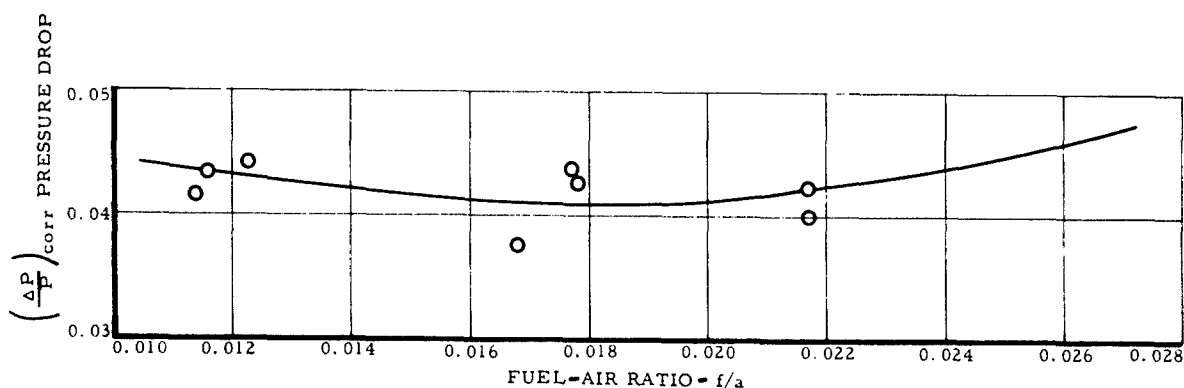


Figure 325. Pressure Drop Corrected Versus Fuel-Air Ratio - Combustor Build 4

Methods of damping out and/or correctly interpreting these temperature fluctuations to obtain an accurate measurement of turbine inlet temperature were considered. No practical method of damping the fluctuations, without introducing possible inaccuracies, was found. Therefore, it was decided to record the turbine inlet temperatures with a strip chart recorder. A correct interpretation of the temperature fluctuations was then made from the recorded data.

Combustor Build 5 - To provide a flatter circumferential average radial temperature profile and to evaluate its effect on the temperature distribution factor, the combustor hardware was modified as follows:

1. The film cooling louvers on the aft portion of the outer combustor shell were mechanically closed and welded shut. Cooling of this area was provided by a film cooling strip using approximately one-half the cooling airflow.
2. The riveted joint between the inner combustor rear cone and the turbine inlet nozzle inner shroud provides a leakage path for cold air along the inner nozzle wall. To evaluate the effect of this leakage, the rivet joint was packed with Sauereisen cement to close off the gap.

The above modifications resulted in a lower, but flatter, combustion efficiency curve, Figure 326. A relatively flat efficiency curve is desirable, since it provides an essentially constant efficiency over a wide operating range of fuel-air ratios. The efficiency level, while somewhat low, was considered to be adequate for this application since specific fuel consumption of the rig was not a design point requirement.

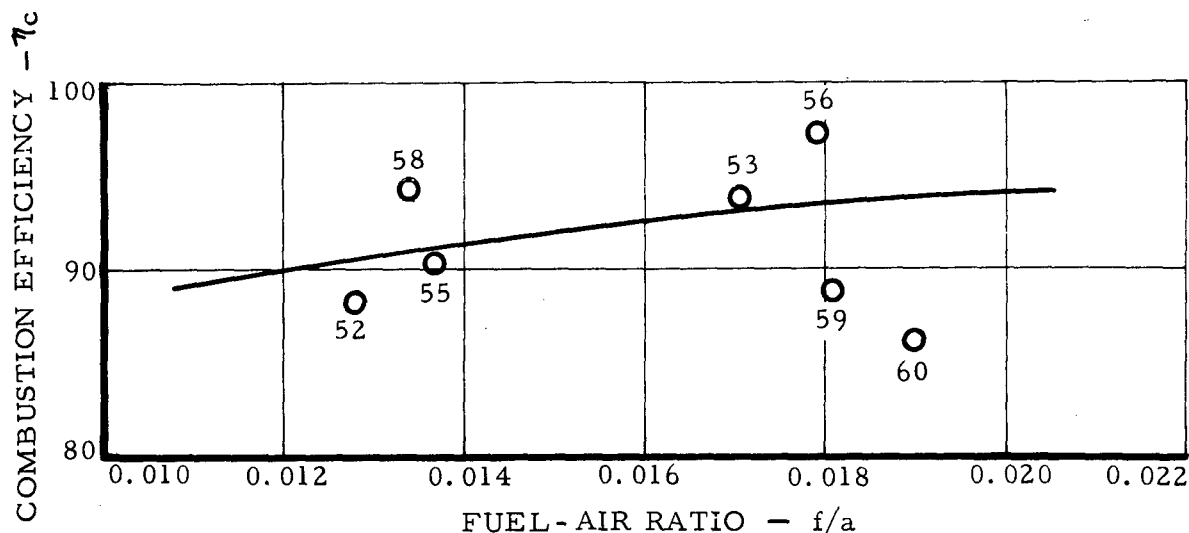


Figure 326. Combustion Efficiency Versus Fuel-Air Ratio - Combustor Build 5.

The TDF factor showed a slight increase, Figure 327, over Build 4 tests, Figure 320. However, the peak in the circumferential average radial temperature profile was reduced and the radial profile then met turbine requirements. Representative plots of the circumferential and radial temperature profiles are shown in Figures 328 and 329.

Combustor performance evaluation at increased airflows and pressures simulating part-speed turbine conditions was initiated. Subsequently, the combustor was operated at simulated 70- and 80-percent turbine speed conditions. These runs are identified as data points 58 and 60 on Figures 326 and 327, respectively. The local and average circumferential radial temperature profiles for these conditions are shown in Figures 330 and 331.

Build 5 testing was halted when the V-belts driving the fuel slinger failed during a 90-percent turbine speed condition. The V-belt failure caused a momentary overtemperature (approaching 3000°F) of the rig. Although the overtemperature condition existed for only a few seconds, it was considered to be advisable to halt testing and to inspect the rig hardware for possible damage. None was found.

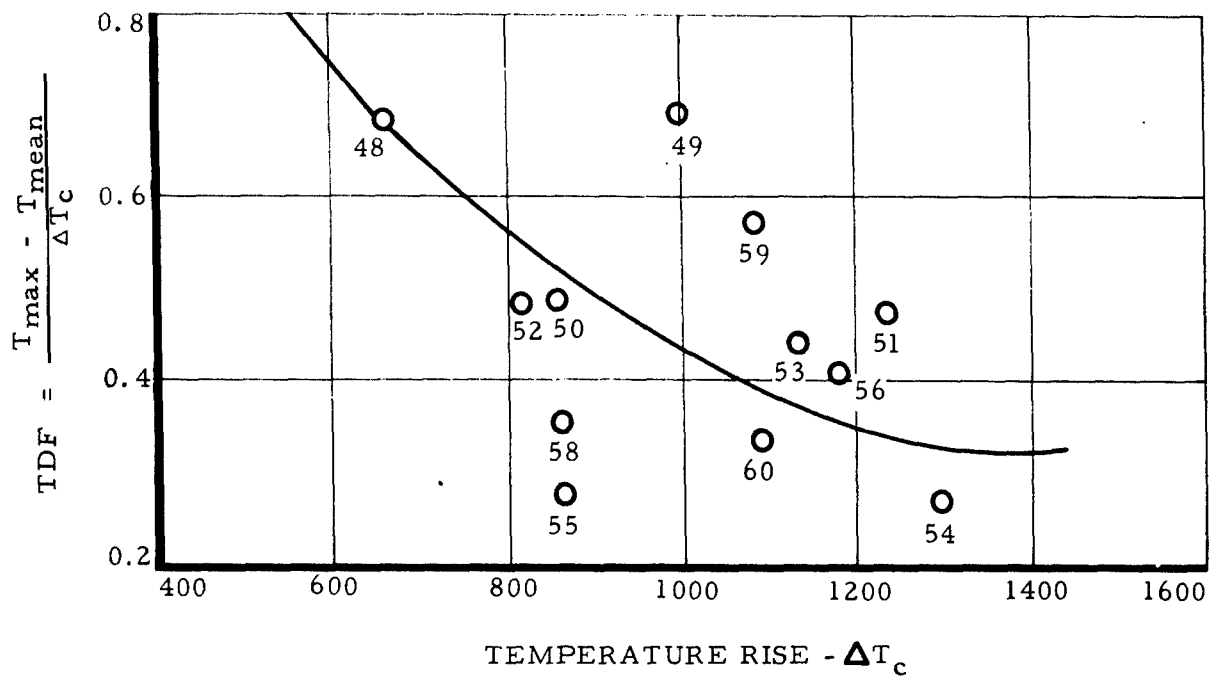


Figure 327. Temperature Distribution Factor Versus Temperature Rise - Combustor Build 5.

$T_3 = 375^\circ\text{F}$
 $T_4 = 1240^\circ\text{F}$
 $\Delta T_c = 865^\circ\text{F}$
 $N = 35,000 \text{ rpm}$
 $f/a = 0.0137$
 $\eta_c = .905$

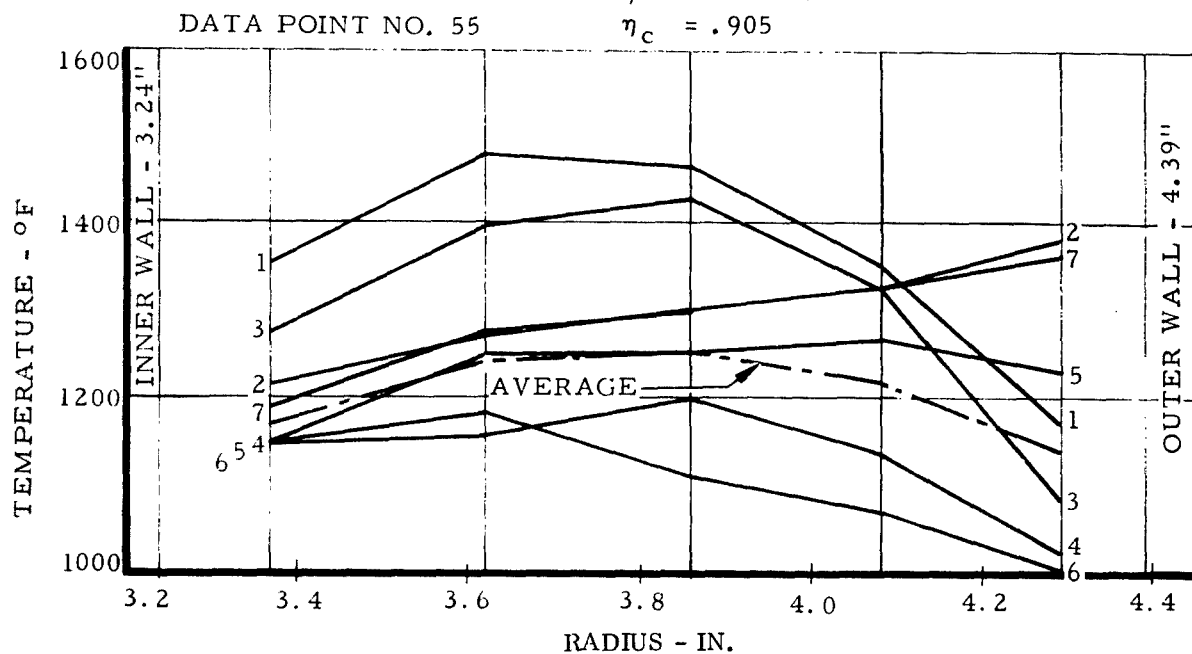


Figure 328. Combustor Exit Radial Temperature Profile.

$T_3 = 397^{\circ}\text{F}$
 $T_4 = 1577^{\circ}\text{F}$
 $\Delta T_c = 1180^{\circ}\text{F}$
 $N = 35,000 \text{ rpm}$
 $f/a = 0.0179$
 $\eta_c = 0.974$

DATA POINT NO. 56

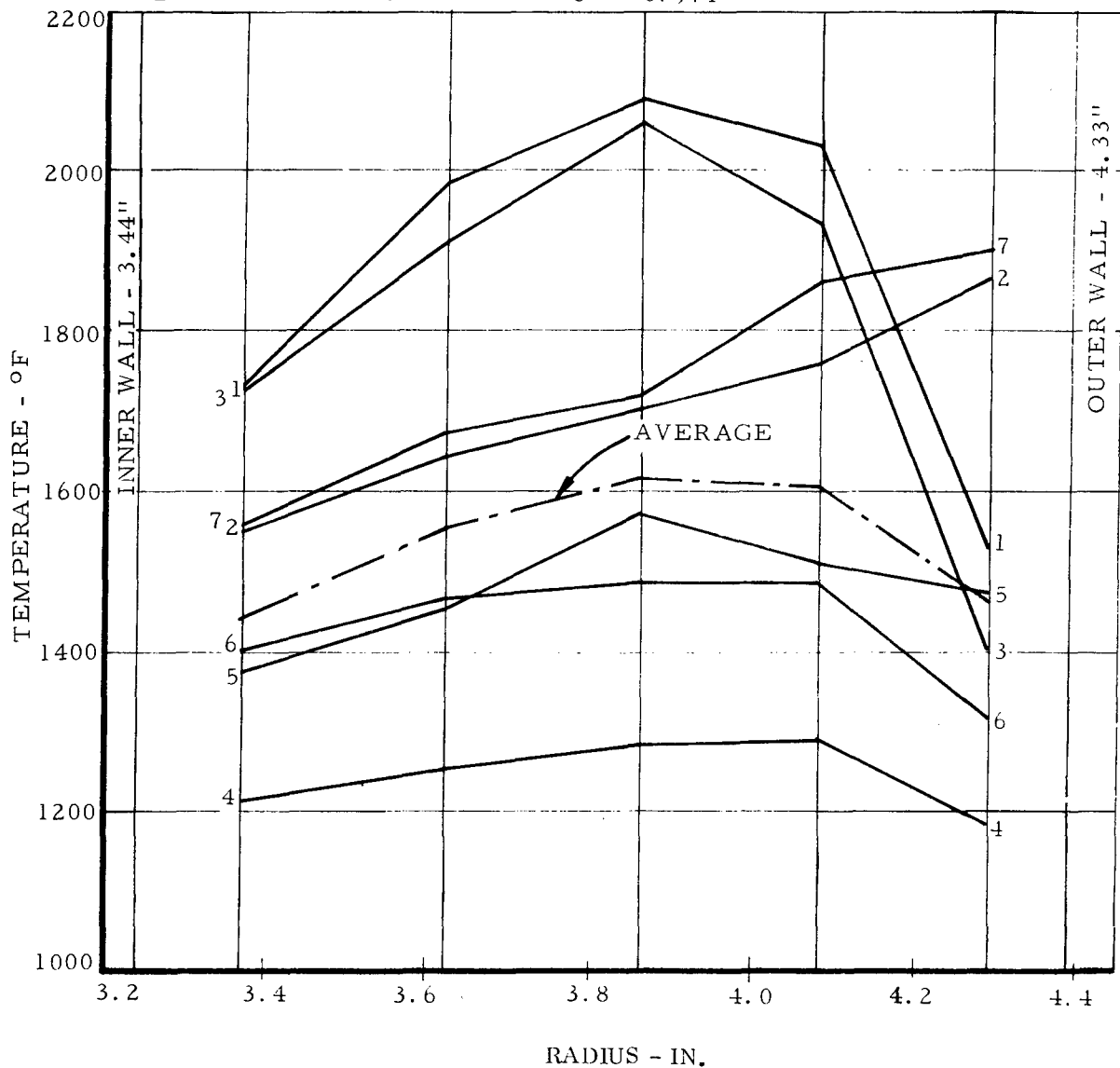


Figure 329. Combustor Exit Radial Temperature Profile.

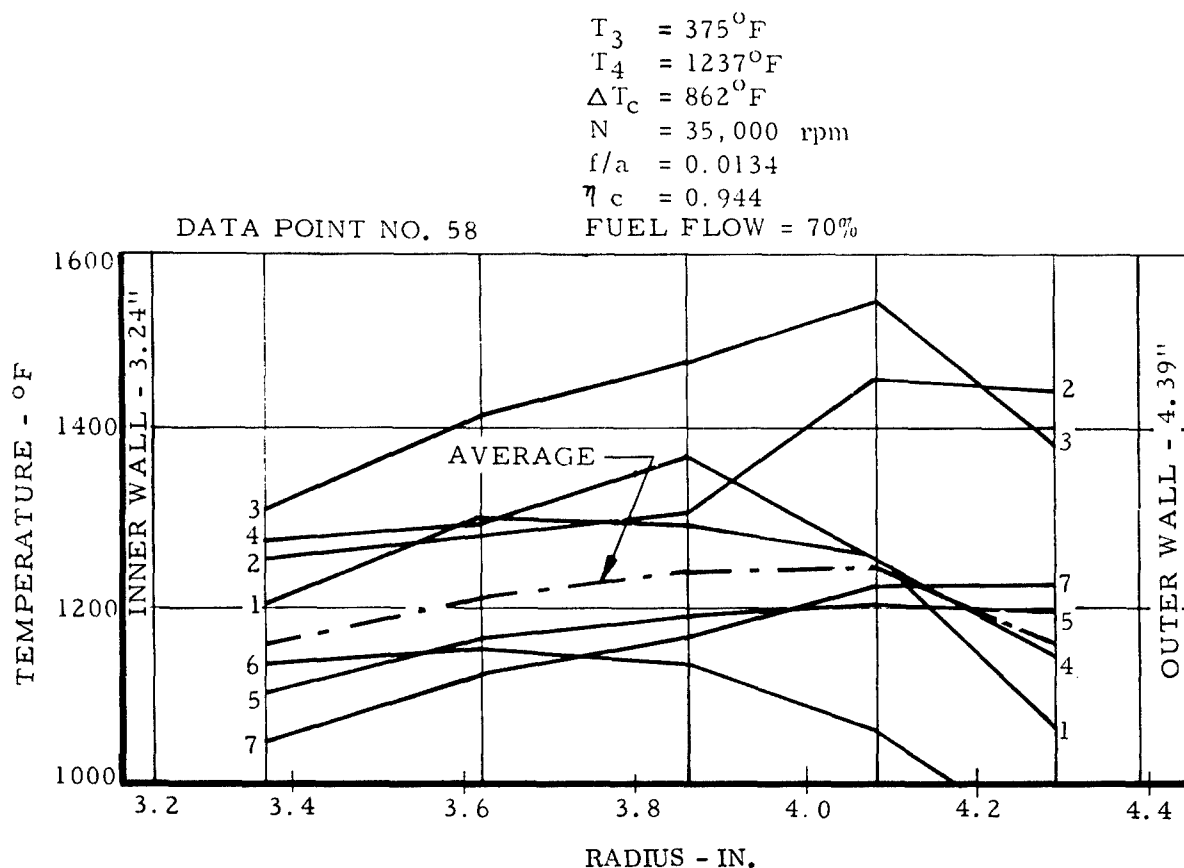


Figure 330. Combustor Exit Radial Temperature Profile.

An investigation into the drive belt failure revealed that extreme turbulence in the rig rear bearing oil sump resulted in a transfer of oil through the interconnected vents to the oil sump serving the rig forward bearing and gearbox. This caused an overfill condition in the forward sump which, in turn, resulted in an excessively high oil level in the gearbox. The excess oil created severe drag on the large driving gear, causing slippage of the drive belts which led to failure. The oil system was subsequently modified to prevent recurrence of this problem.

Combustor Build 6 - The combustor rig was reassembled and combustor testing was resumed without modification to the combustor hardware of Build 5.

Operation of the combustor at simulated part-speed conditions continued. The combustor was subsequently run at approximately the 90- and 100-percent speed conditions. Since Build 6 testing was actually an extension of Build 5, the combustion efficiency and temperature distribution factor data are combined with Build 5 data in Figures 332 and

$T_3 = 455^{\circ}\text{F}$
 $T_4 = 1548^{\circ}\text{F}$
 $\Delta T_c = 1093^{\circ}\text{F}$
 $N = 35,000 \text{ rpm}$
 $f/a = 0.0190$
 $\eta_c = 0.862$
 FUEL FLOW = 80%

DATA POINT NO. 60

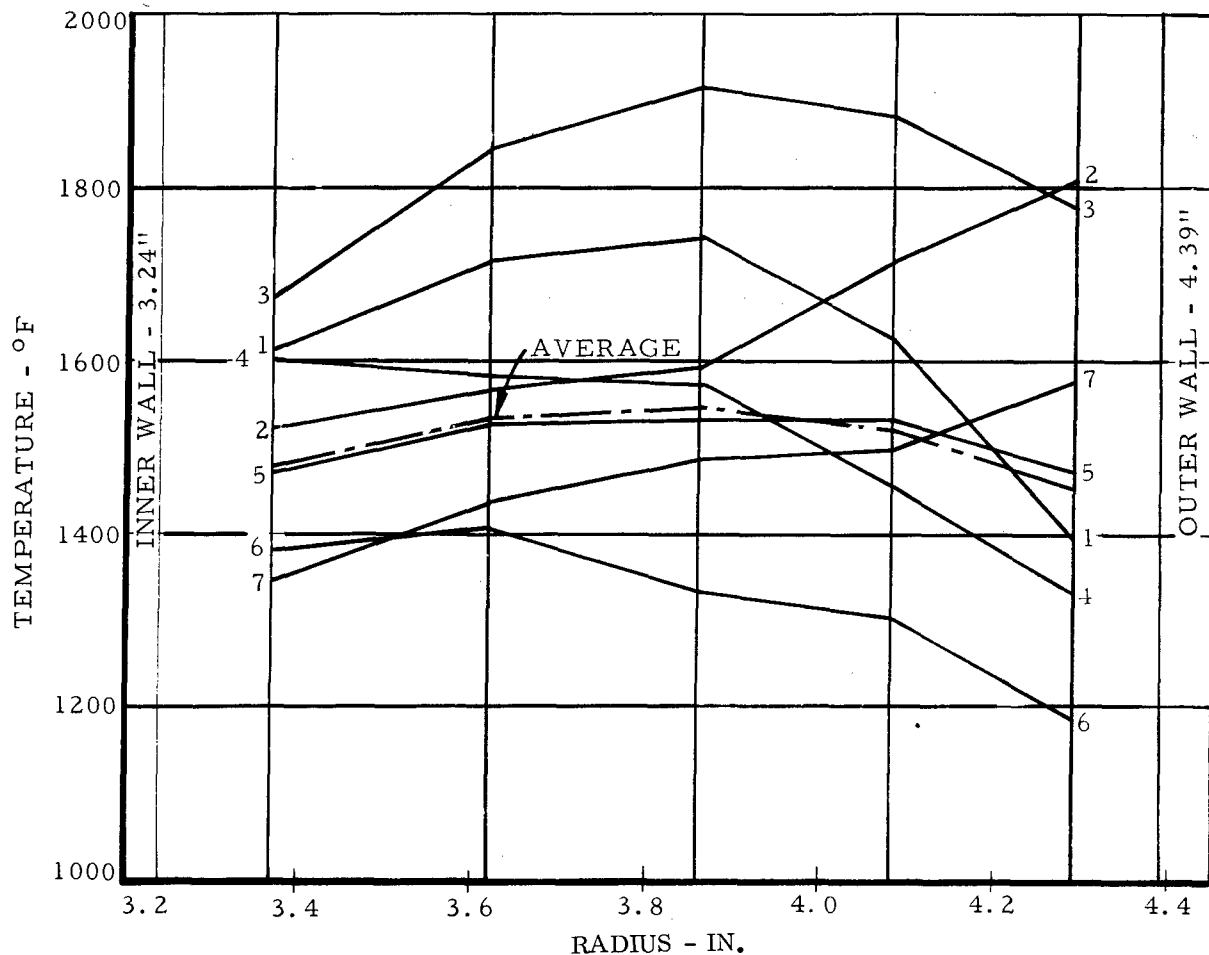


Figure 331. Combustor Exit Radial Temperature Profile.

and 333. Data points 63 and 65 correspond to the 90- and 100-percent simulated turbine speed conditions. Figures 334 and 335 show the radial temperature profiles, and Figures 336 and 337 are plots of the circumferential temperature profiles for these two data points.

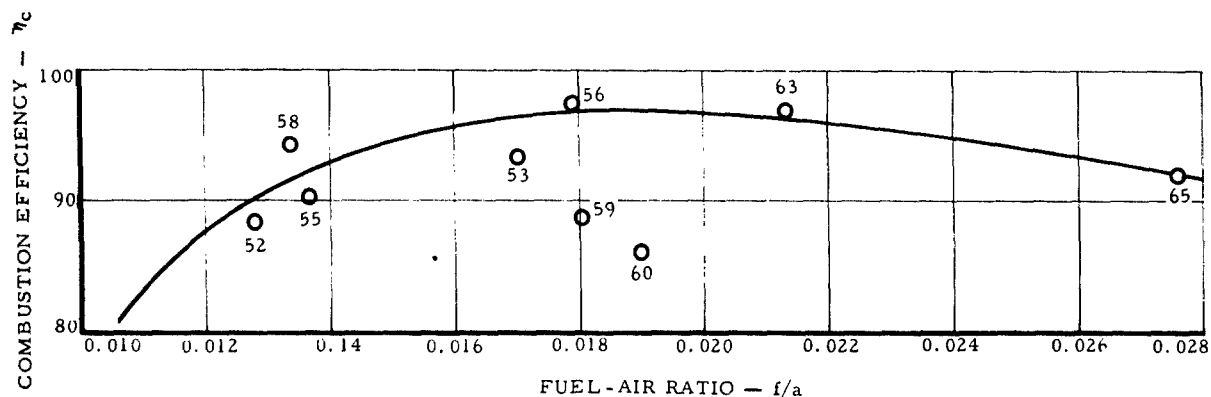


Figure 332. Combustion Efficiency Versus Fuel-Air Ratio - Combustor Builds 5 and 6.

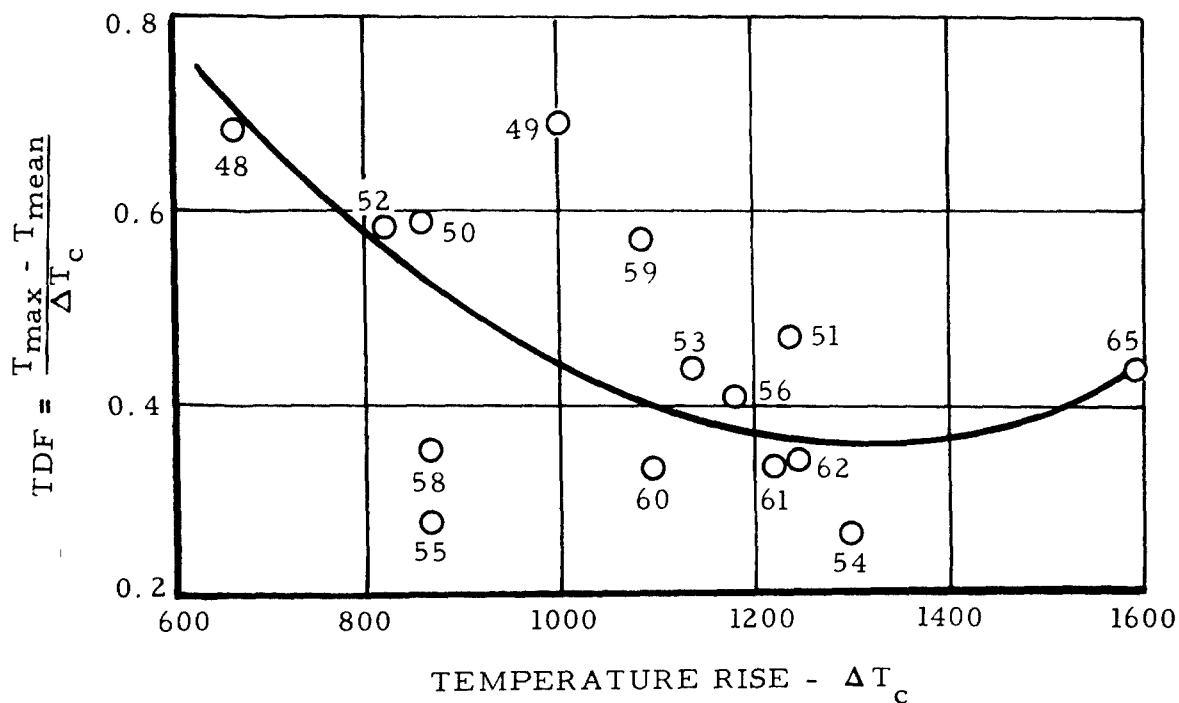


Figure 333. Temperature Distribution Factor Versus Temperature Rise - Combustor Builds 5 and 6.

$T_3 = 478^{\circ}\text{F}$
 $T_4 = 1830^{\circ}\text{F}$
 $\Delta T_c = 1352^{\circ}\text{F}$
 $N = 35,000 \text{ rpm}$
 $f/a = 0.0213$
 $\eta_c = 0.969$

DATA POINT NO. 63

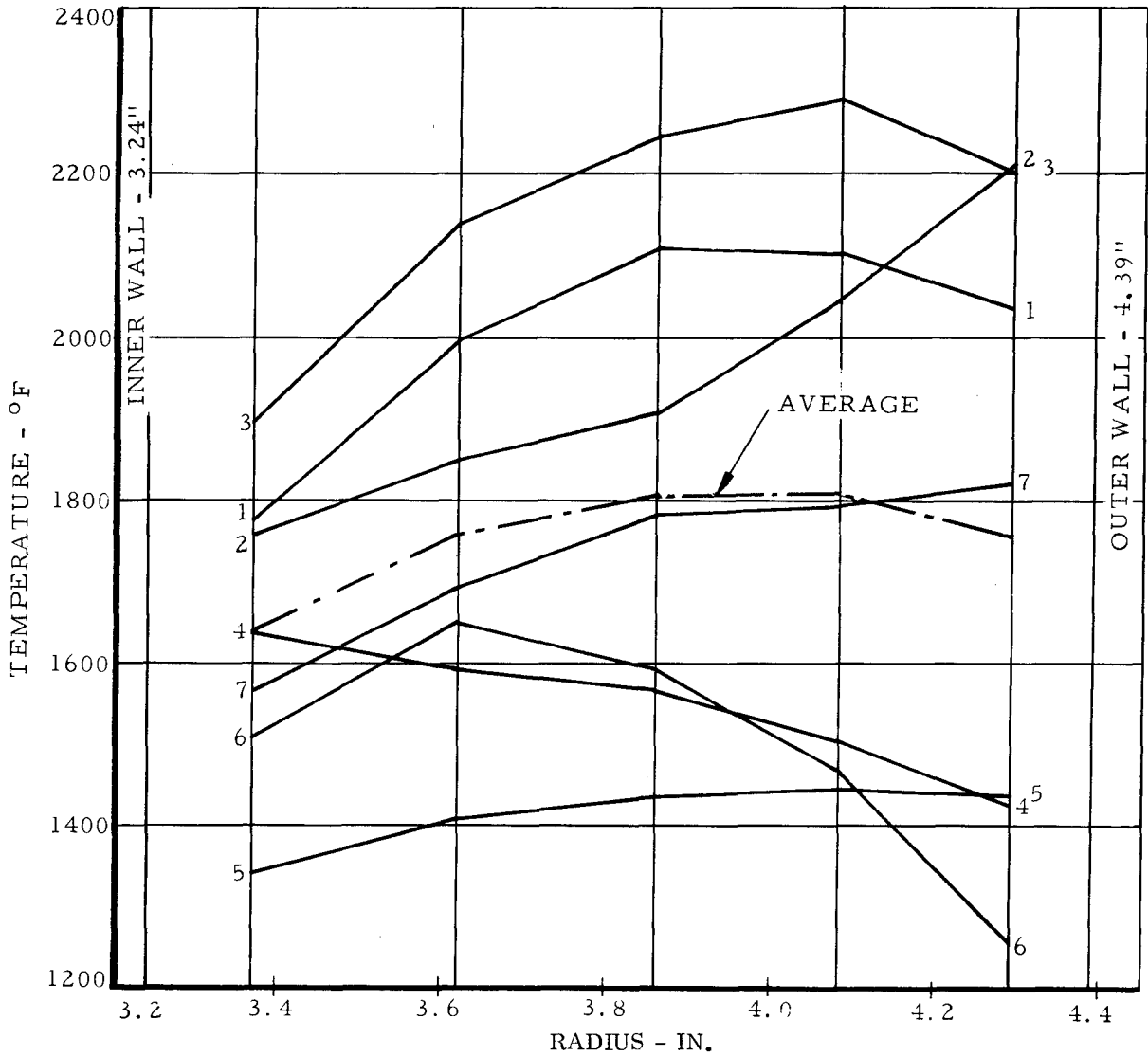


Figure 334. Combustor Exit Radial Temperature Profile Builds 5 and 6.

$T_3 = 627^{\circ}\text{F}$
 $T_4 = 2221^{\circ}\text{F}$
 $\Delta T_c = 1594^{\circ}\text{F}$
 $N = 35,000 \text{ rpm}$
 $f/a = 0.0276$
 $\eta_c = 0.919$

DATA POINT NO. 65

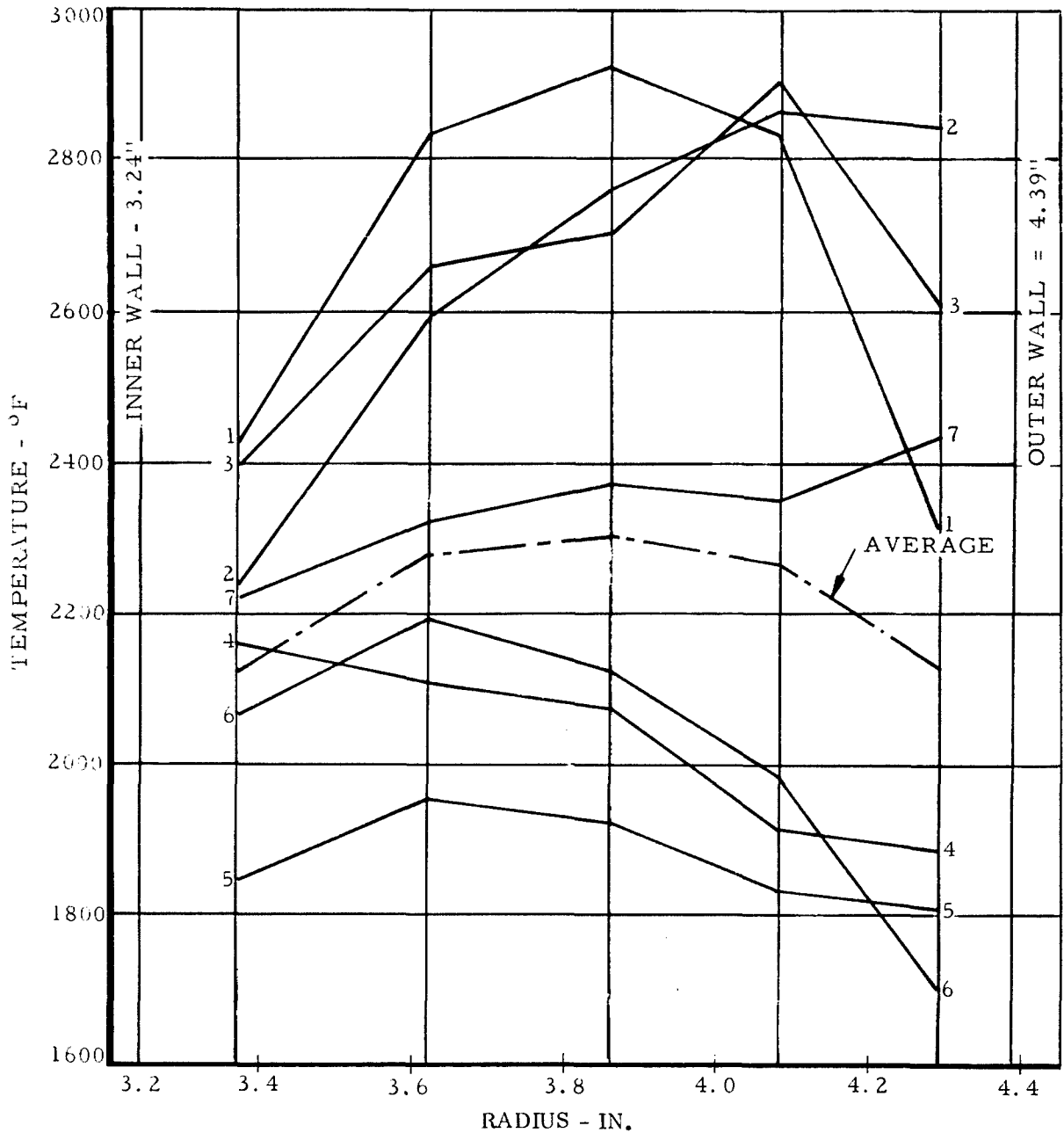


Figure 335. Combustor Exit Radial Temperature Profile.

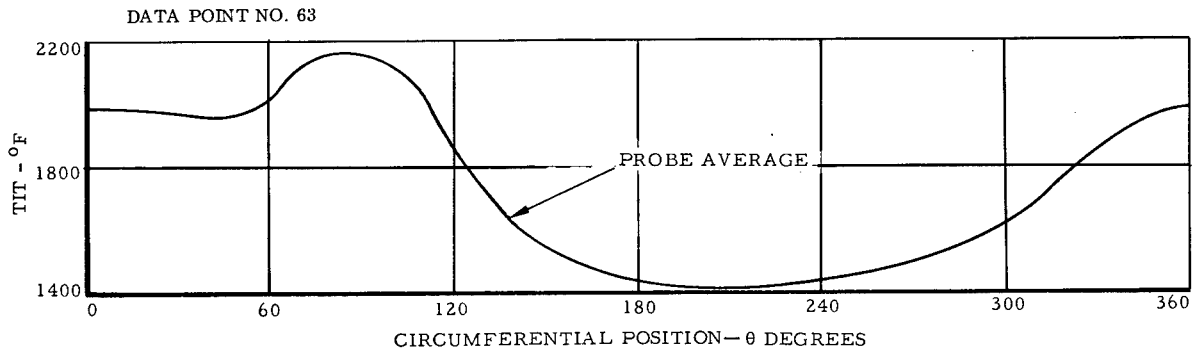
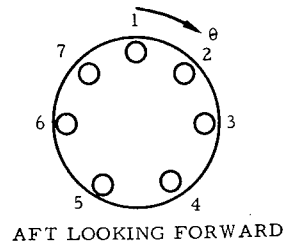


Figure 336. Turbine Inlet Temperature at Various Circumferential Positions.

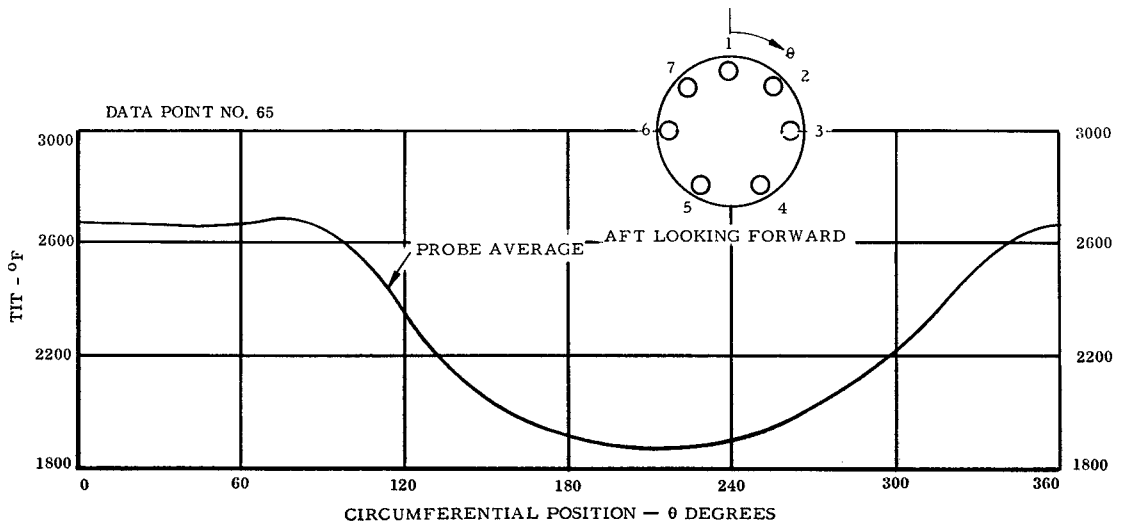


Figure 337. Turbine Inlet Temperature at Various Circumferential Positions.

These figures illustrate that the temperature distribution factor of 0.44 (data point 65) is well above the design value of 0.20. However, TDF primarily affects the turbine inlet nozzle and not the rotor. Therefore, since the nozzles and combustor hardware had shown no evidence of thermal distress, the combustor performance was considered to be adequate for the initiation of rotor testing. Additional tailoring of TDF was done during early rotor tests to meet design objective of 0.20.

Combustor pressure drop data for Builds 5 and 6 are plotted on Figure 338. The combustor pressure loss, up slightly from Build 4 because of a 7-percent decrease in effective flow area (film cooling louvers replaced by a film cooling strip), meets design requirements.

Figures 339 through 343 are views of the combustor hardware after completion of combustor development testing. Figure 339 shows the trailing edges of the nozzle vanes, the turbine shroud, and the inner combustor labyrinth seals and diaphragm. The rough appearance of the nozzle vanes is due to the partial erosion of temperature-indicating paint caused by the scrubbing action of near-sonic hot gases.

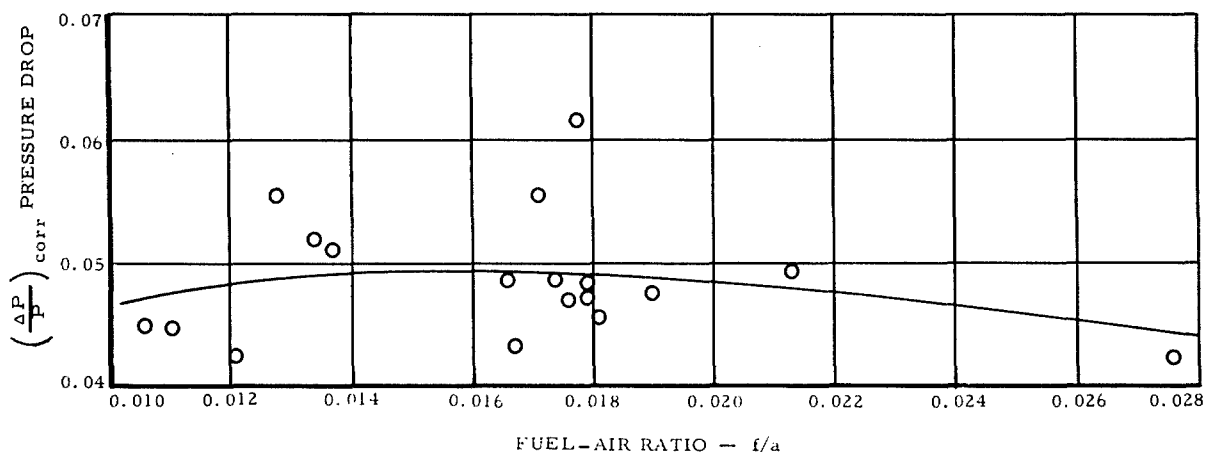


Figure 338. Pressure Drop Corrected Versus Fuel-Air Ratio - Combustor Builds 5 and 6.

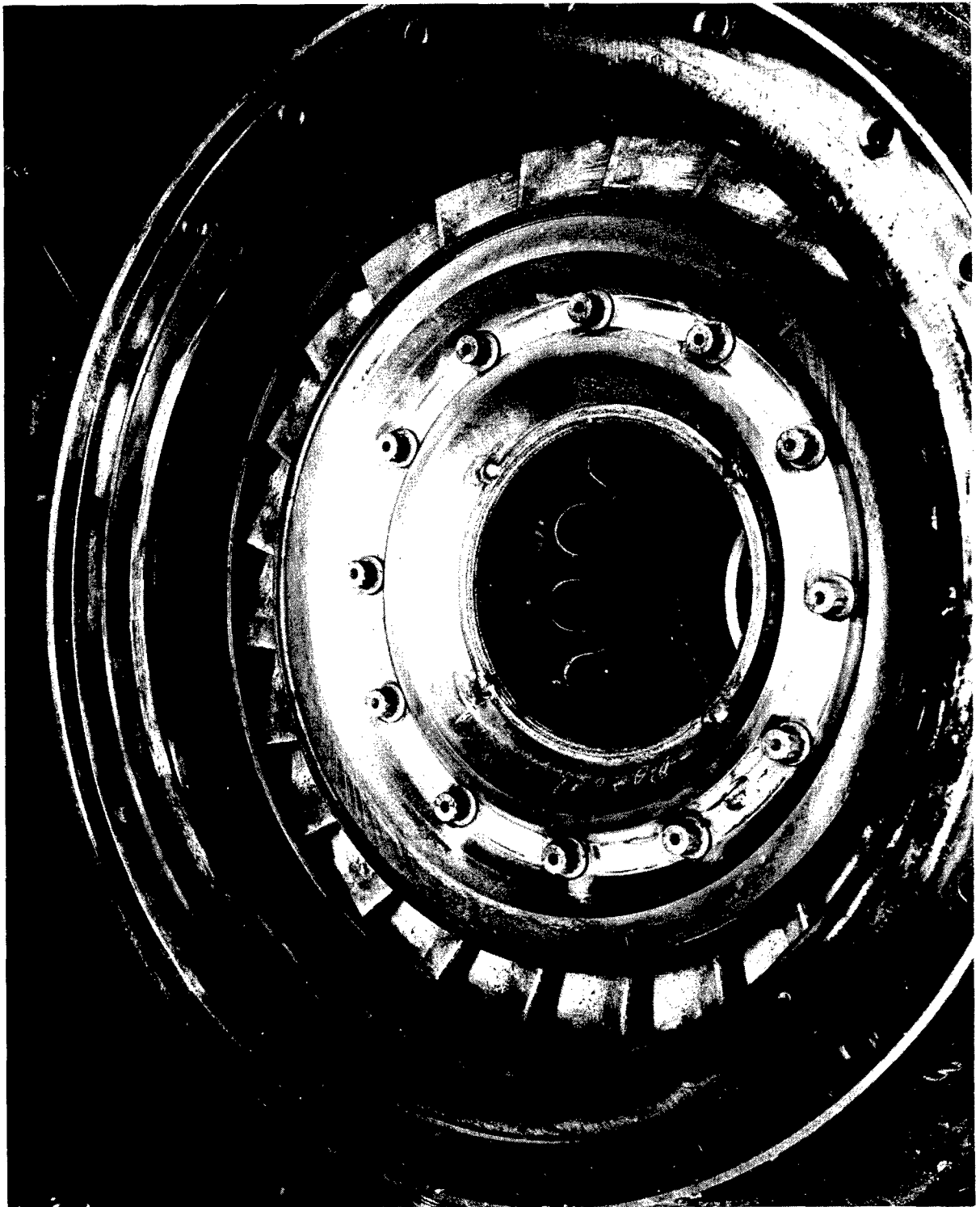


Figure 339. Nozzle Vane Assembly Trailing Edge.

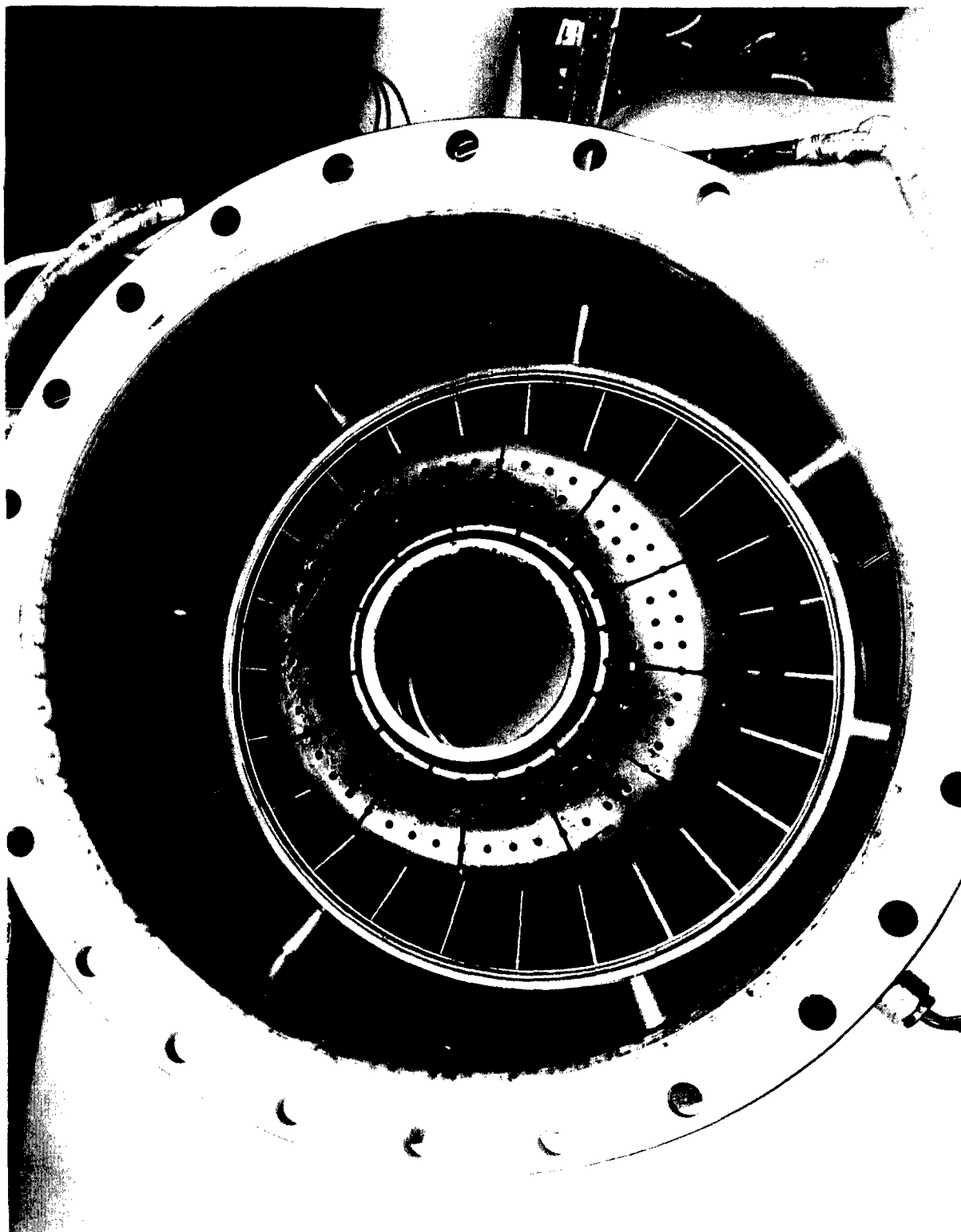


Figure 340. Nozzle Vane Assembly Leading Ledge.

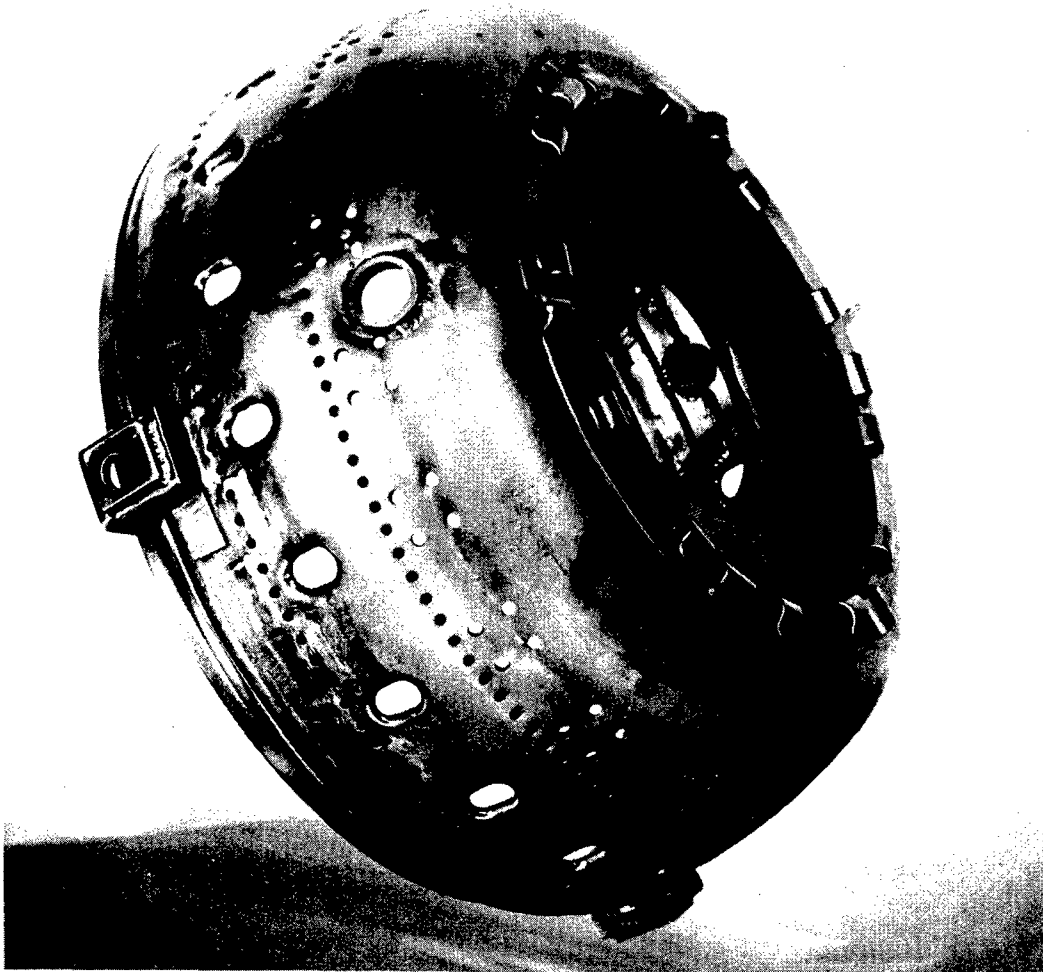


Figure 341. Combustor Assembly.

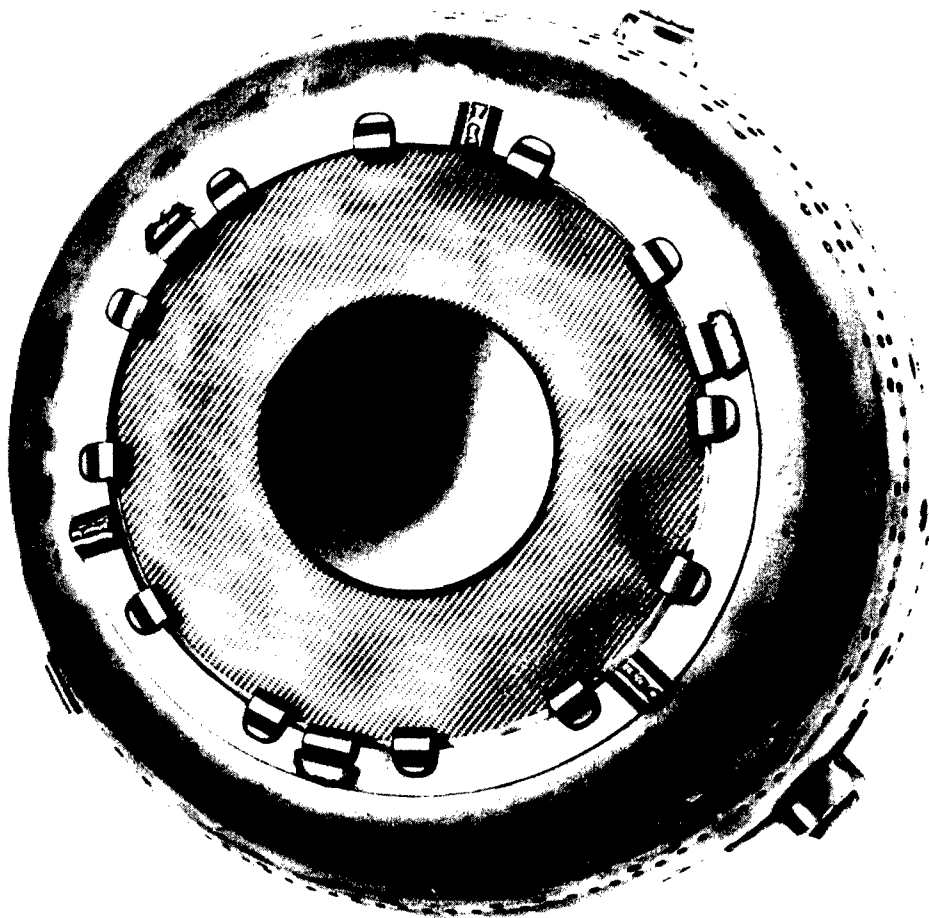


Figure 342. Swirl Plate - Forward.

Figure 340 is a view of the leading edges of the nozzle vanes, the inner combustor face, and the combustor housing. The total pressure probes are visible protruding from the leading edges of the nozzle vanes.

Figures 341 through 343 are several views of the outer combustor and swirl plate assembly. It is evident from these photographs that no thermal or mechanical distress existed. This was further verified by a dimensional check of rig hardware during assembly.

Combustor Development During Rotor Testing

The turbine shaft was assembled into the rig, and turbine testing was initiated. Because of a 0.44 TDF existing at the conclusion of the combustor development program, work on the combustor was continued

during these rotor tests. Modifications were made to the combustor hardware during each build of the turbine rig in an effort to reduce the TDF. This effort successfully reduced the TDF from 0.44 to 0.25.

Turbine Rig Build 1 - The initial modification, rotation of the rigimesh swirl vane 180 degrees about its axis, had no significant effect on the circumferential temperature gradient. However, the combustor experienced a marked drop in combustion efficiency (approximately 10 percentage points) over that recorded during combustor development testing.

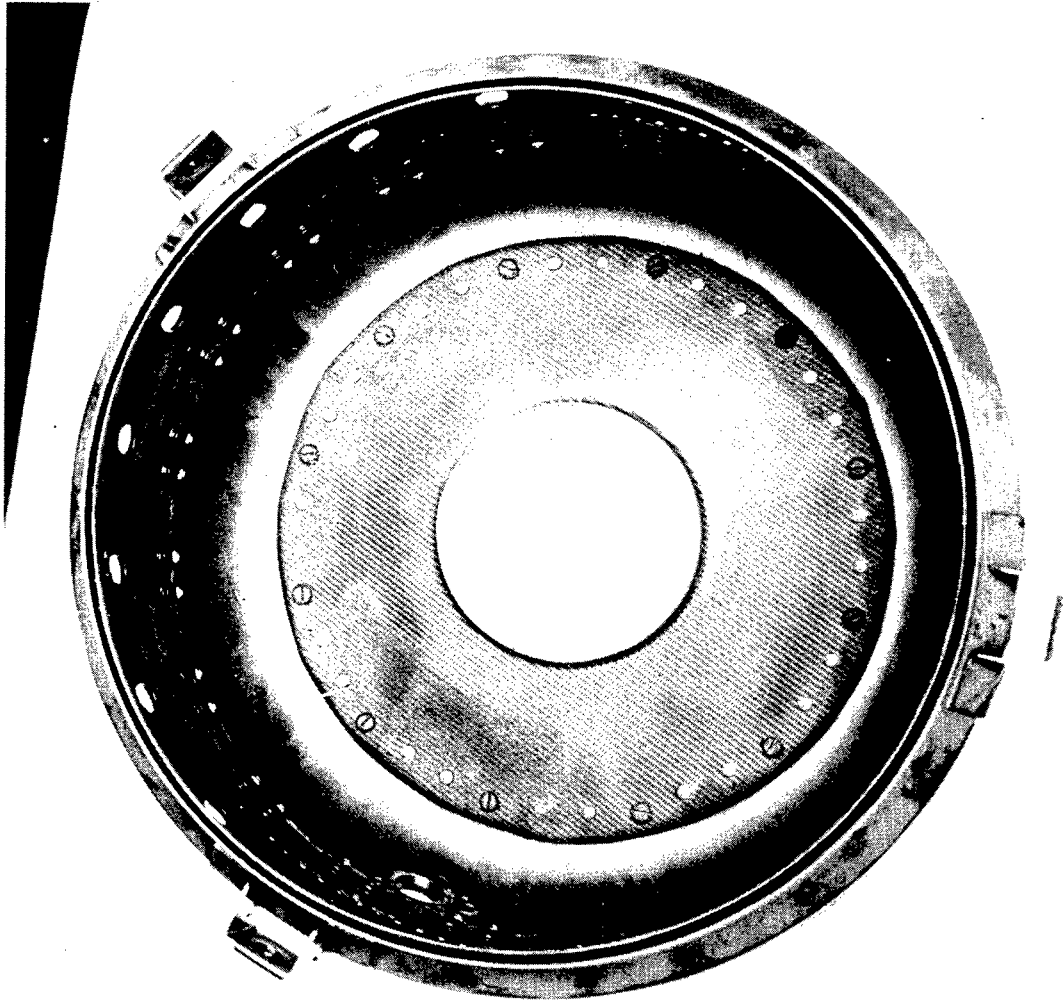


Figure 343. Swirl Plate - Rear.

Figure 344 is a comparison of the combustion efficiency obtained during Builds 5 and 6 of the combustor development program with that obtained during Turbine Rig Build 1 (data points 1-16) of the turbine tests. The reduction in combustion efficiency is evident. Since the addition of the rotor should have had little or no effect on combustor performance, other causes for the low efficiency were investigated. These included instrumentation errors, off-calibration operation of the fuel meters, and fuel leakage. A check of instrumentation revealed no degradation of accuracy. The fuel meters also were found to be accurate.

Two areas of possible fuel leakage exist. Fuel leakage could occur at the rotating shaft carbon face seal or at the blade seals. There was some evidence of minute leakage at the blade seals. However, this leakage was considered to be insignificant and apparently short-lived, as no further evidence of blade seal leakage was found.

Fuel that leaks through the carbon face shaft seal enters the oil sump serving the turbine rig rear bearing. Consequently, leakage of this seal is very difficult to ascertain, particularly at the small leakage rates considered here. Examination of the seal revealed no indication of leakage. A dimensional check of the carbon face seal, the seal housing, and the seal wiper indicated that all parts were to print.

An examination of the combustor hardware revealed that the rigimesh swirl plate was warped, Figure 345. It was consequently replaced during Turbine Rig Build 2 assembly.

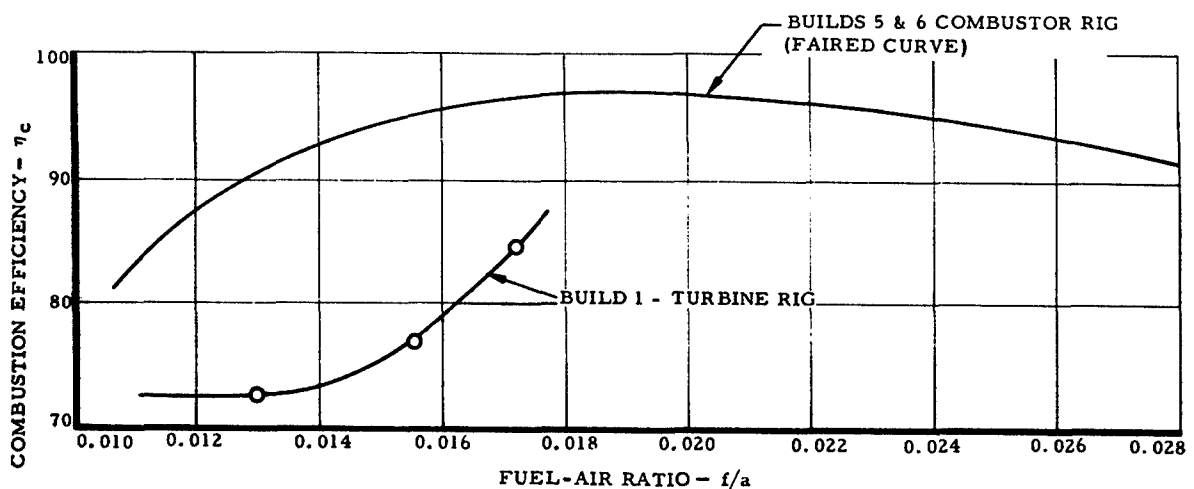


Figure 344. Turbine Rig and Combustor Rig Comparison of Combustion Efficiency Versus Fuel-Air Ratio.

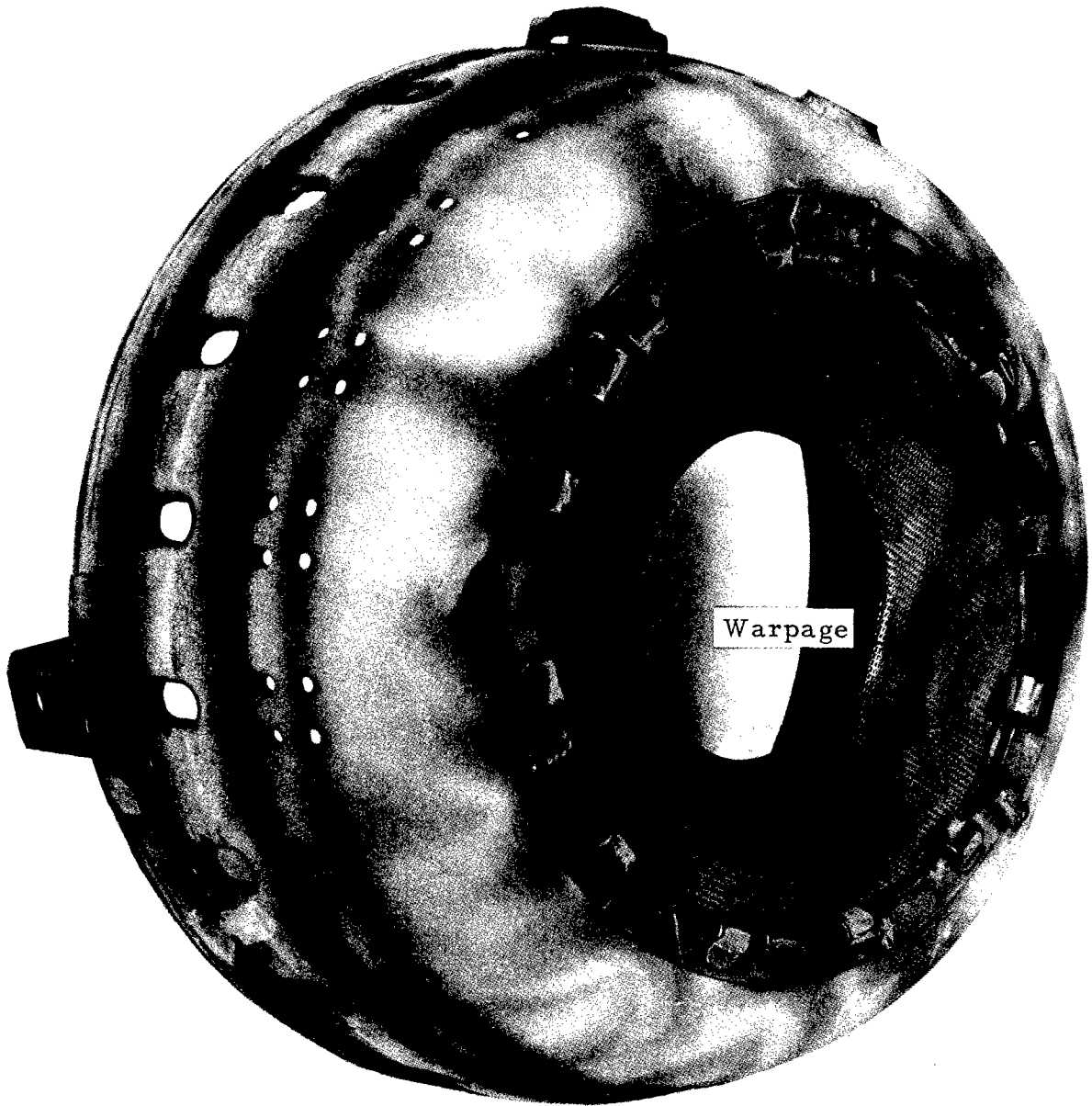


Figure 345. Outer Combustor After Test.

Turbine Rig Build 2 - Combustion efficiency showed no improvement over Turbine Rig Build 1 testing. Figure 346 shows that the trend toward increased combustion efficiency with increasing fuel-air ratio, which was evident in Turbine Rig Build 1 testing, continued in Turbine Rig Build 2 (data points 17-22) testing.

During the above tests, severe fuel leakage at the shaft carbon face fuel seal became apparent, and testing was halted. The cause of the leakage was determined to be loss of the pressure balance which creates the sealing action. The pressure balance was lost when the carbon face insert lifted off its seat in the seal body. When this occurs, excessive seal face pressure and/or seal leakage will result.

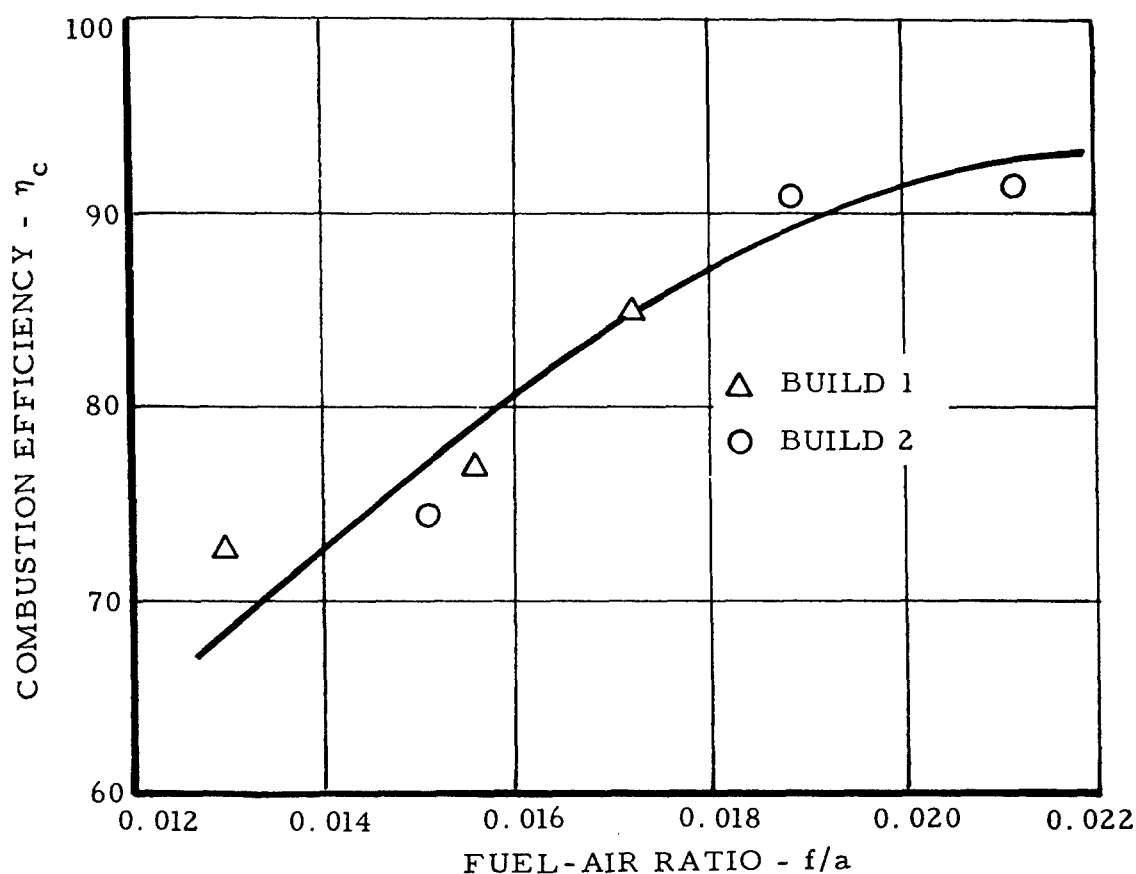


Figure 346. Combustion Efficiency Versus Fuel-Air Ratio, Builds 1 and 2 - Turbine.

Excessive face seal pressure results in overheating of the wiper surface and the carbon face seal insert. Evidence of heating was found on the wiper face and the epoxy which bonds the carbon face insert to the seal body. To alleviate this problem, the fuel tube extending through the carbon face seal was removed to provide better circulation of fuel across the seal surfaces. This proved to be successful, and no further seal problems occurred. However, the low combustion efficiency obtained with the rotor may have resulted from continued leakage at this seal.

An increase in the TDF was accompanied by a shift in the peak temperature approximately 180 degrees circumferentially, Figure 347. The hot streak, occurring at Probe Number 6 position, pegged the temperature readout, indicating that the actual temperature was somewhat higher than the recorded 2400°F. This hot streak carried through the turbine and was recorded by the exhaust gas temperature instrumentation. Because of the limited EGT instrumentation (three evenly spaced, four-element rakes) and its position relative to the hot spot, the full magnitude of the hot streak was not recorded.

However, the objective of this phase of the turbine test program (attainment of 2000°F TIT) had been accomplished. In view of this, and the above-mentioned difficulties in temperature measurement, testing was halted and the rig was disassembled for hardware evaluation.

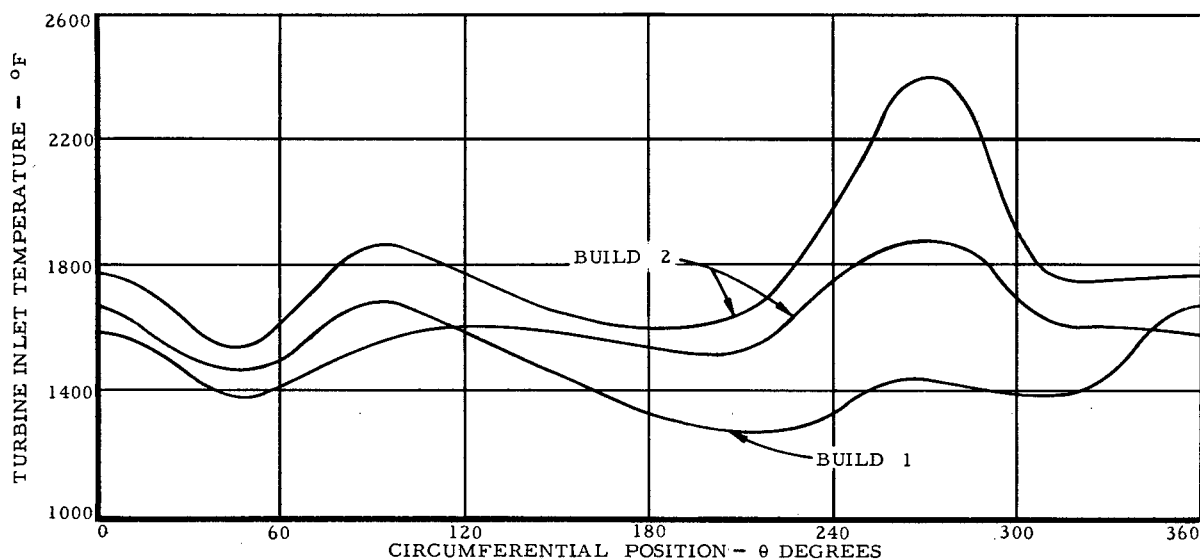


Figure 347. Comparison of Circumferential Temperature Profile - Turbine Build.

During this teardown, a survey of the combustor inlet airflow distribution was accomplished. A three-element pressure probe was fabricated, and a 360-degree circumferential traverse of the combustor inlet was done. Total and static pressure readings were taken at approximately 20-degree intervals. These readings were then correlated according to pressure drop, dynamic head, and position. These local parameters were then related to total airflow and plotted as shown in Figure 348. A variation of approximately 30 percent exists between maximum and minimum local flow points. This degree of maldistribution was not considered to be significant in view of the low Mach number and dynamic head of the flow and the dumping effect at the exit of the axial inlet.

A flow check of the rigimesh swirl vane verified the directional flow properties of the rigimesh, but no significant maldistribution was noted.

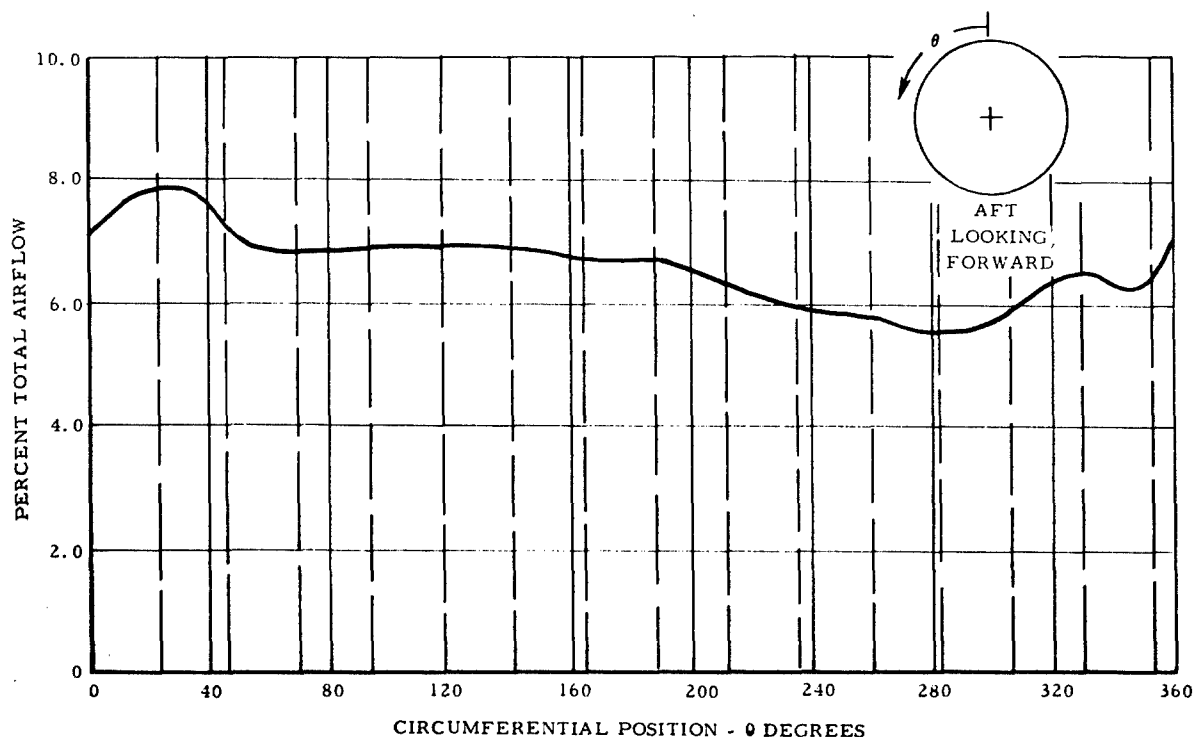


Figure 348. Combustor Circumferential Airflow Distribution Through Axial Inlet.

A complete dimensional check of the rig hardware also revealed no significant changes in seal clearances, concentricities, or axial stack-up dimensions. However, the initial assembly of the inner combustor to the turbine inlet nozzle resulted in the inner combustor front labyrinth seals being approximately 0.035 inch eccentric to the shaft, Figure 349. This required opening up the labyrinth seal shroud to allow assembly of the rotor. Consequently, this assembly was reworked, and concentricity was held to approximately 0.007 inch. During this rework, the inner combustor was also rotated 180 degrees about its axis to determine the effect this might have on combustor performance.

Reduction of the turbine test data indicated a discrepancy between the measured turbine inlet temperature and the calculated turbine inlet temperature based on measured exhaust gas temperature, turbine pressure ratio, and turbine work. Average measured turbine inlet temperatures were consistently higher than those that were calculated. Rig instrumentation was again thoroughly checked out. No discrepancies were found.

The possibility of catalytic action at the probe surfaces was considered. A literature survey subsequently revealed catalysis to be a possible reason for the difference in the measured and calculated temperatures.

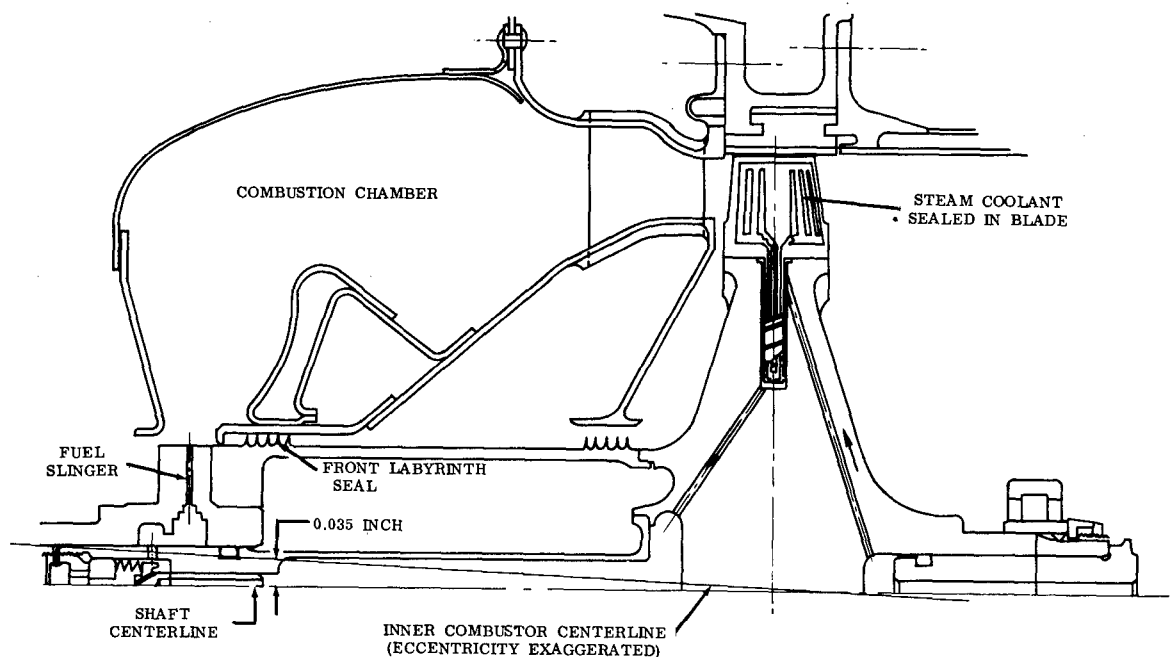


Figure 349. Schematic of Inner Combustor and Shaft Eccentricity.

In the presence of a gas stream containing a suitable fuel-air mixture, platinum and platinum-rhodium alloys may act as catalysts for the oxidation reaction. If this occurs, catalytic heating will cause a thermocouple made of these materials to register a higher temperature than actually exists in the gas stream. The amount of catalytic heating, if any, is not predictable.

Turbine Rig Build 3 - During Turbine Rig Build 3 (data points 23-27) assembly, rig instrumentation was augmented by the addition of six exhaust gas temperature probes, bringing the total to nine 4-element rakes. In addition, the turbine inlet temperature probes were coated with a ceramic cement in an effort to limit catalytic action.

Testing was resumed, and the turbine was subsequently operated at a turbine inlet temperature of approximately 2100°F.

Malfunction of several actuated temperature probes prevented a complete survey of turbine inlet temperatures during these tests, and combustion efficiency was therefore determined from a calculated turbine inlet temperature based on average measured EGT and turbine performance.

This method resulted in a lower combustion efficiency than that obtained with measured turbine inlet temperatures, Figure 350. For comparison, the combustion efficiency of Turbine Rig Builds 1 and 2 was recalculated based on calculated turbine inlet temperatures, Figure 351. The change in combustion efficiency from that of Figure 350 is immediately evident.

Because of the problems encountered with the TIT probes, no comparison of measured and calculated values of combustion efficiency was possible for Turbine Rig Build 3. However, it must be assumed that the trend toward a higher measured combustion efficiency, evident during early testing, continued during Turbine Rig Build 3 testing. It should also be noted, however, that the early test data (Turbine Rig Builds 1 and 2) were obtained with only three 4-element exhaust gas temperature probes, whereas Turbine Rig Build 3 testing used nine 4-element rakes and, consequently, obtained a more accurate measure of exhaust gas temperature.

A direct comparison of temperature distribution factor with previous builds was not possible since a complete survey of turbine inlet temperature was not obtained. However, a qualitative analysis based on EGT indicates a slight increase in TDF accompanied by movement of the hot streak approximately 90 degrees circumferentially.

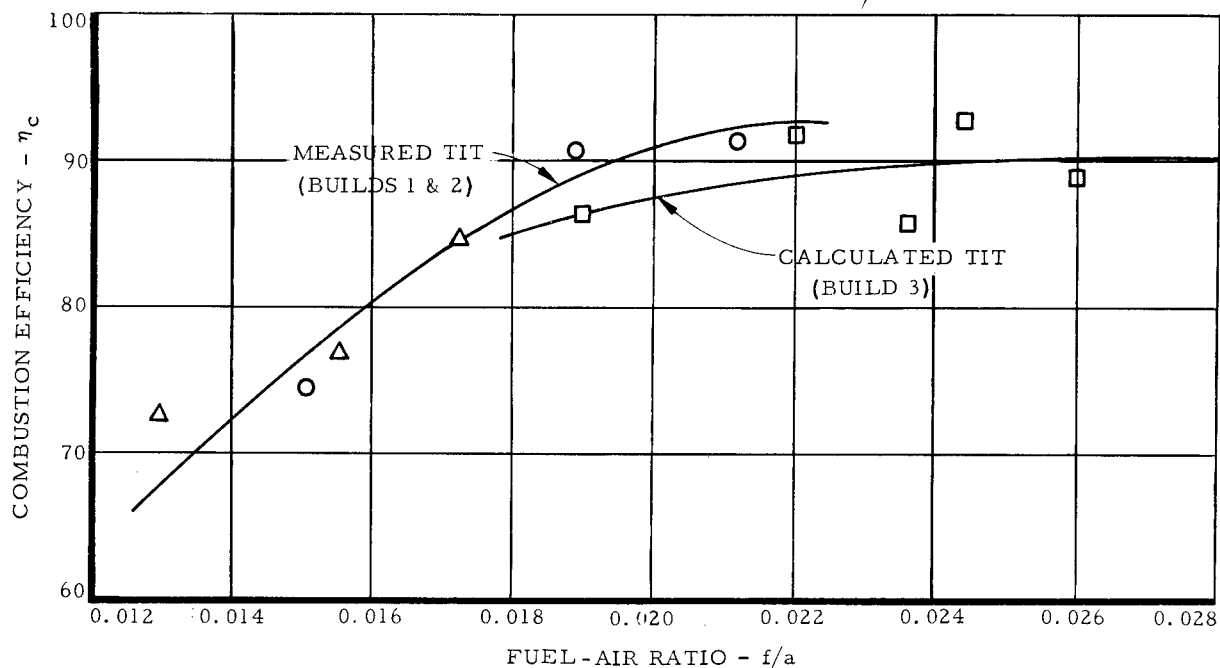


Figure 350. Combustion Efficiency Versus Fuel-Air Ratio - Turbine Rig Build.

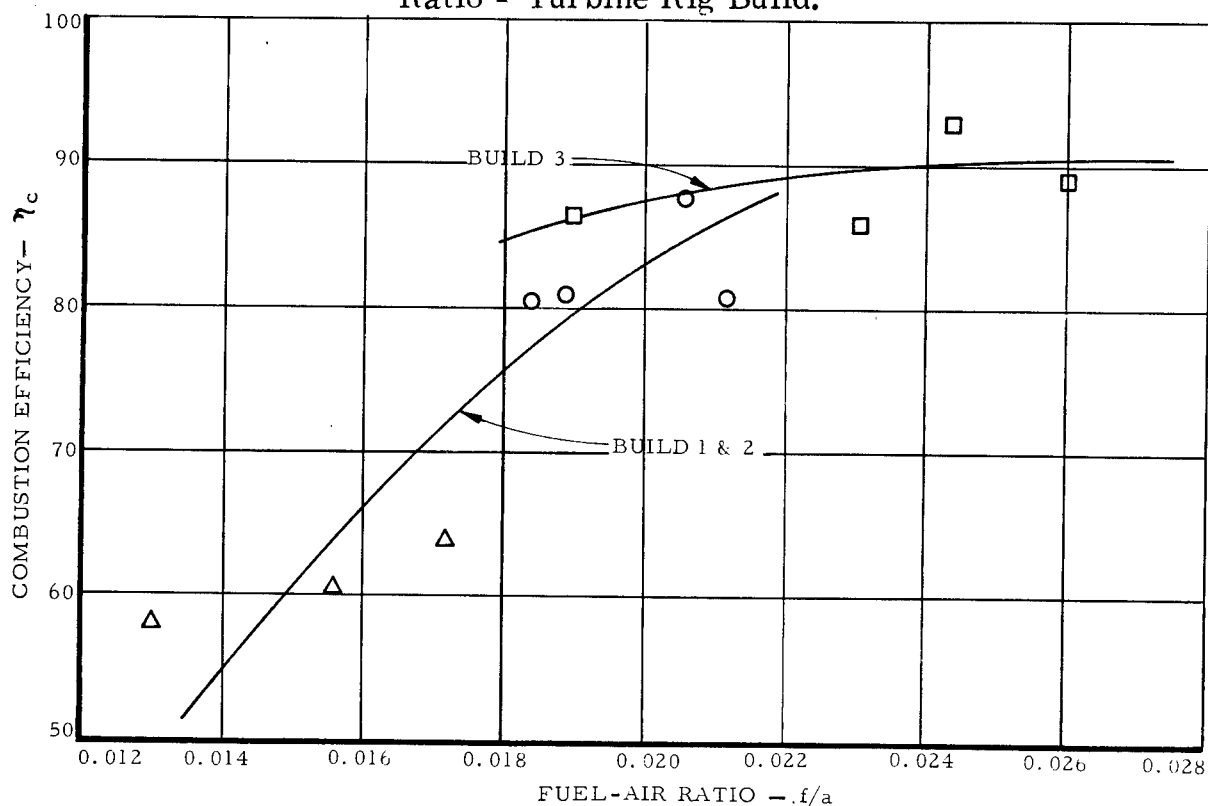


Figure 351. Combustion Efficiency Based on Calculated Turbine Inlet Temperatures - Turbine Rig Build.

Turbine Rig Build 4 - A new rigimesh swirl plate was fabricated of thinner rigimesh material (0.030-inch-thick) and assembled into Turbine Rig Build 4 for testing.

During initial hot running, a severe thermal gradient was accompanied by a rumbling noise apparently originating in the exhaust duct downstream of the turbine rig. Rig disassembly revealed that fuel was leaking past the blade-to-disc seals into the turbine exhaust. Three seals and one blade which had a bad sealing surface were replaced to obtain a positive seal.

An inspection of the combustor hardware during this teardown revealed the new rigimesh swirl plate to be warped and locally oxidized. Consequently, the rigimesh swirl plate used during Turbine Rig Build 3 testing was reinstalled, and assembly for Turbine Rig Build 5 was initiated.

Turbine Rig Build 5 - Hot running during Turbine Rig Build 5 (data points 28-31) resulted in four turbine performance data points at turbine inlet temperatures ranging from 1800°F to approximately 2100°F. Mechanical rotor speeds up to 45,000 rpm were also attained.

Combustor efficiency for these points, based on a turbine inlet temperature calculated from exhaust gas temperature and turbine performance, showed a marked decrease with increasing fuel-air ratio, Figure 352.

The exhaust gas circumferential temperature distribution indicated a severe gradient, as shown in Figure 353. Gradients of this magnitude were not only unfavorable for turbine performance, but also subjected the turbine inlet nozzle to a severe thermal stress environment. Consequently, combustor modifications were made to alleviate the circumferential temperature gradient problem.

The cause of the circumferential gradient was believed to be leakage of air into the primary zone through unsymmetrical gaps about the swirl plate and nonuniform expansion slots in the inner combustor shell. Therefore, the swirl plate was redesigned to provide a circumferentially uniform flow of air into the primary zone. In addition, the hole pattern of the inner combustor shield was modified to permit re-orientation of the shield and inner combustor shell in order to prevent alignment of the shell expansion slots with the holes in the shield.

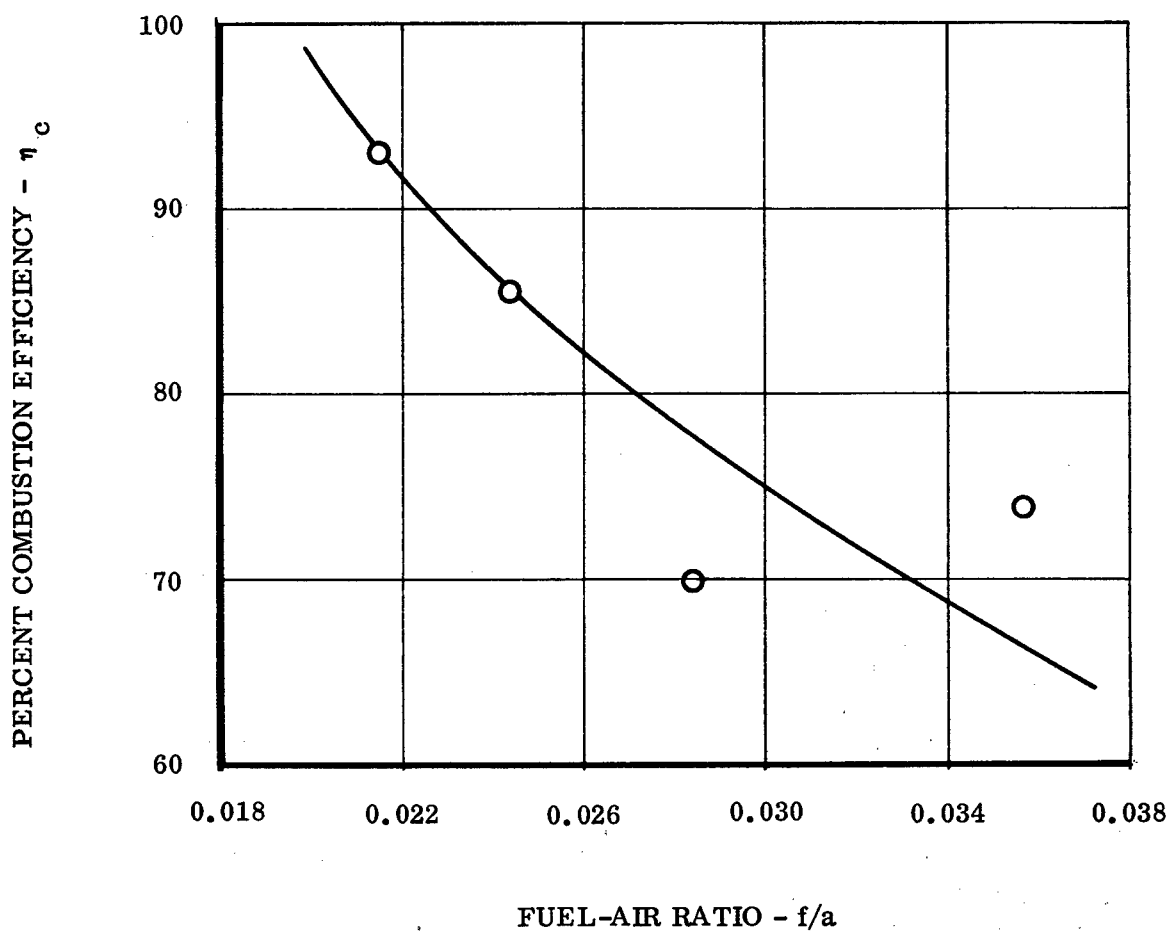


Figure 352. Combustion Efficiency Versus Fuel-Air Ratio, Build 5 - Turbine Rig.

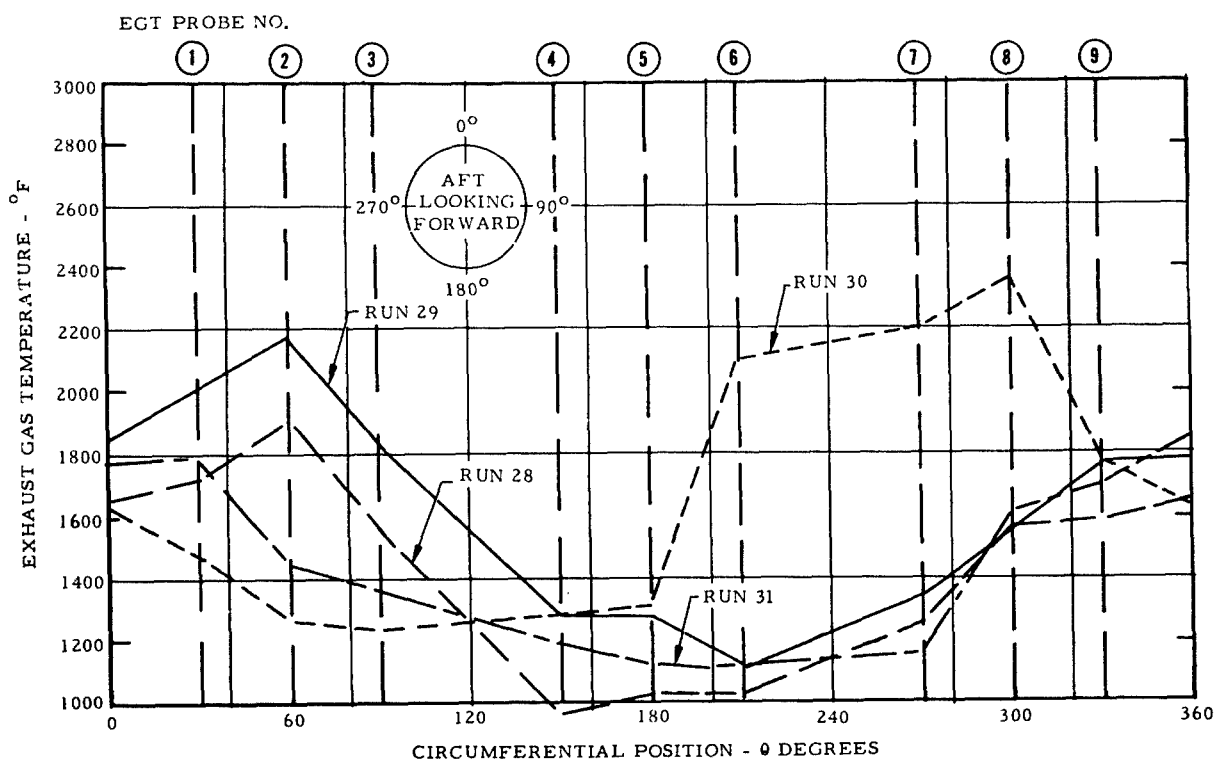


Figure 353. Exhaust Gas Temperature Versus Circumferential Location of Probes - Turbine Rig Build 5.

The redesigned swirl plate, Figure 354, is shown assembled to the outer combustor shell in Figure 355. The small holes, at approximately midradius, supply film cooling for the inner portion of the swirl plate. The larger holes, near the outer edge, provide film cooling for the outer portion of the swirl plate and the crown of the outer combustor shell. The seal ring housing is evident at the inner diameter of the swirl plate.

The reworked inner combustor is shown in Figure 356. Indicated on the figure is the metallic O-ring-type seal between the inner combustor shell and flame shield, and the realignment of the inner combustor shield and shell.

Figure 357 shows the axial holes in the inner lip of the outer combustor labyrinth seal shroud which were added to provide a controlled flow of air across the slinger surface into the primary zone.

A sketch of the combustor assembly, as reworked, is shown in Figure 358.

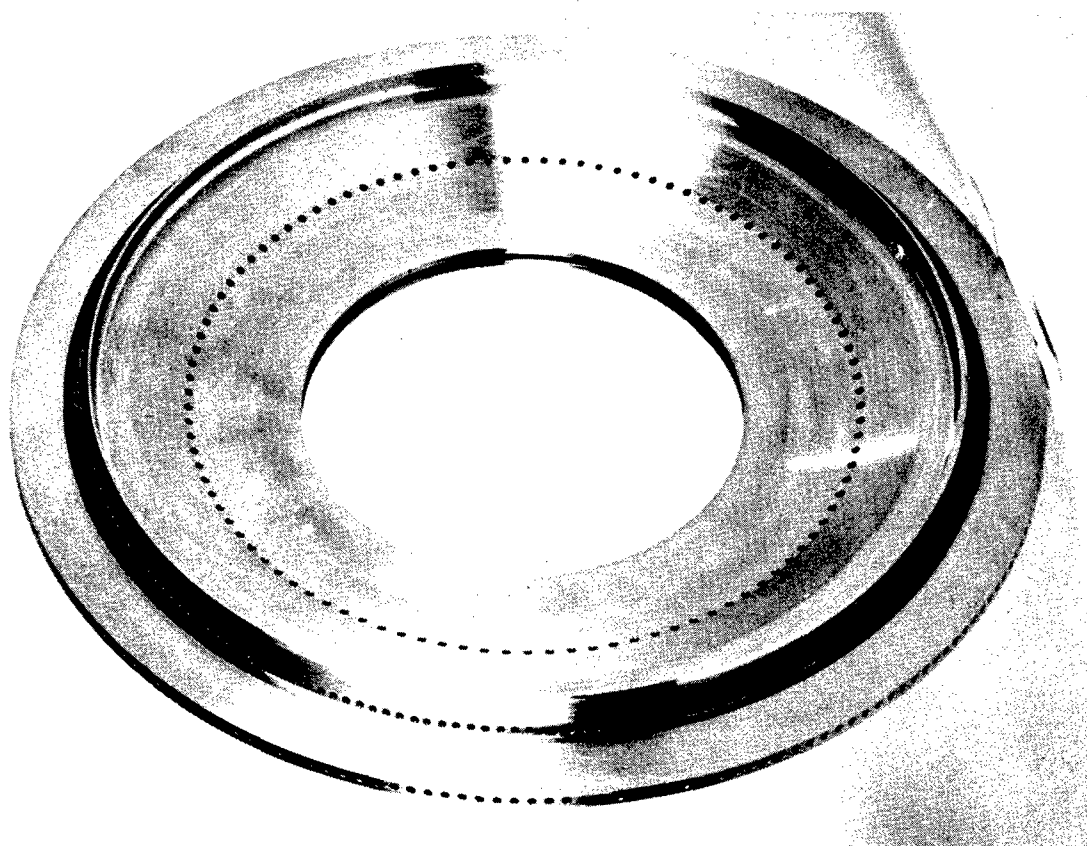
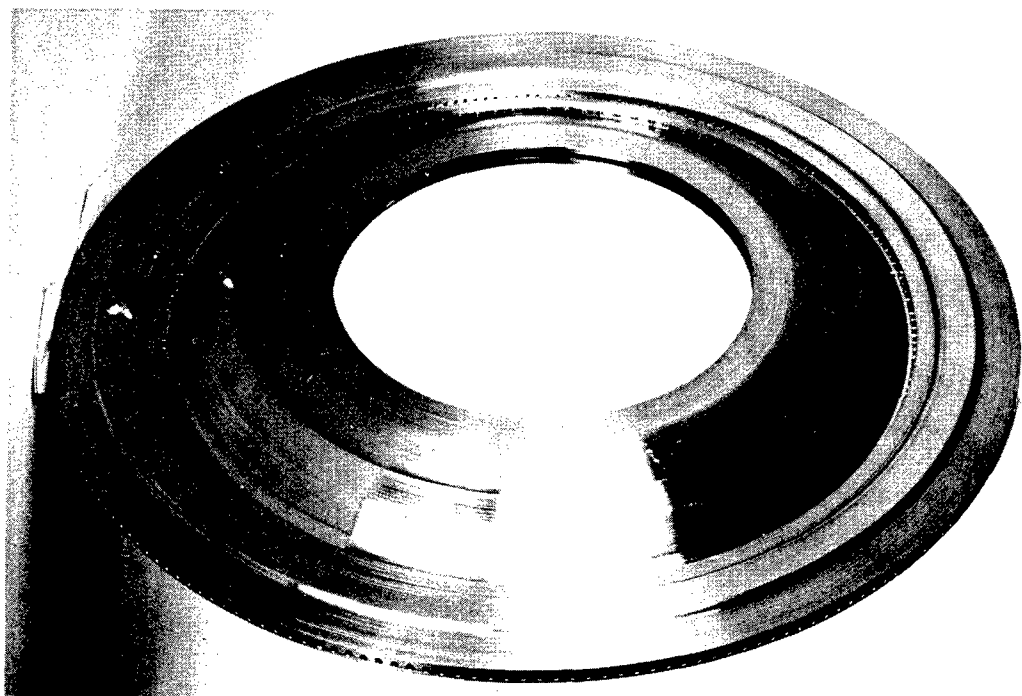


Figure 354. Redesigned Swirl Plate.

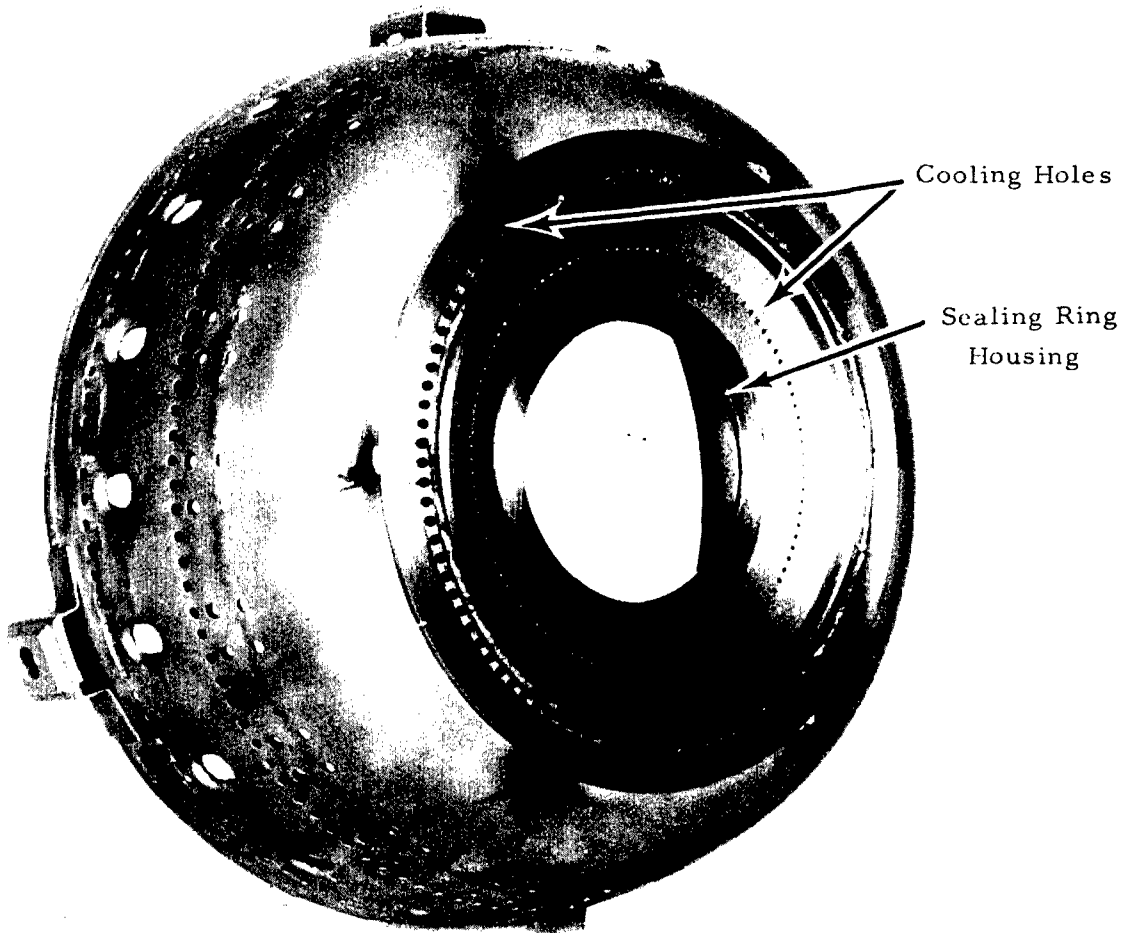


Figure 355. Film-Cooled Swirl Plate Assembled to Outer Combustor Shell.

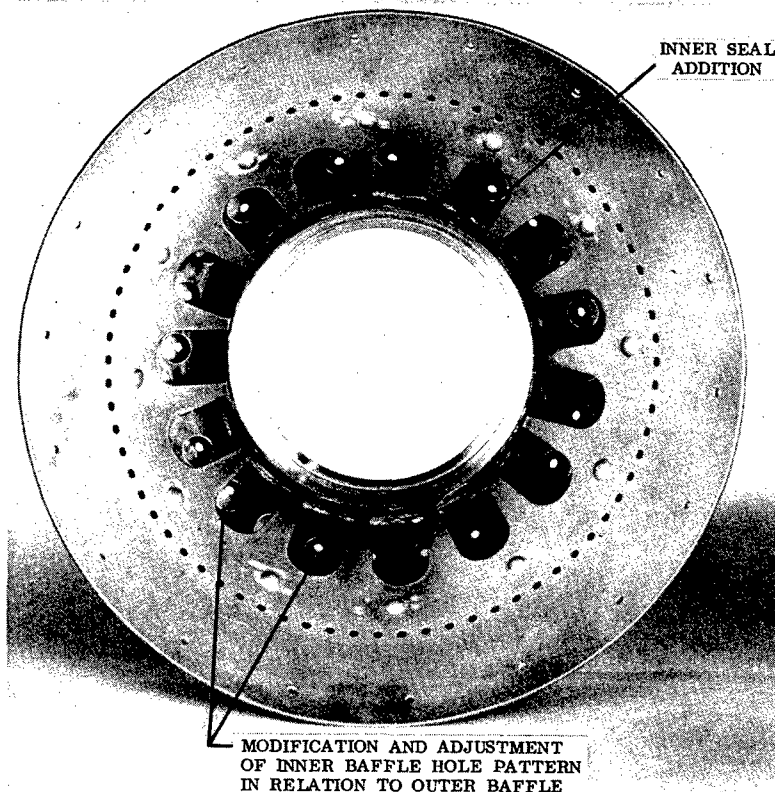
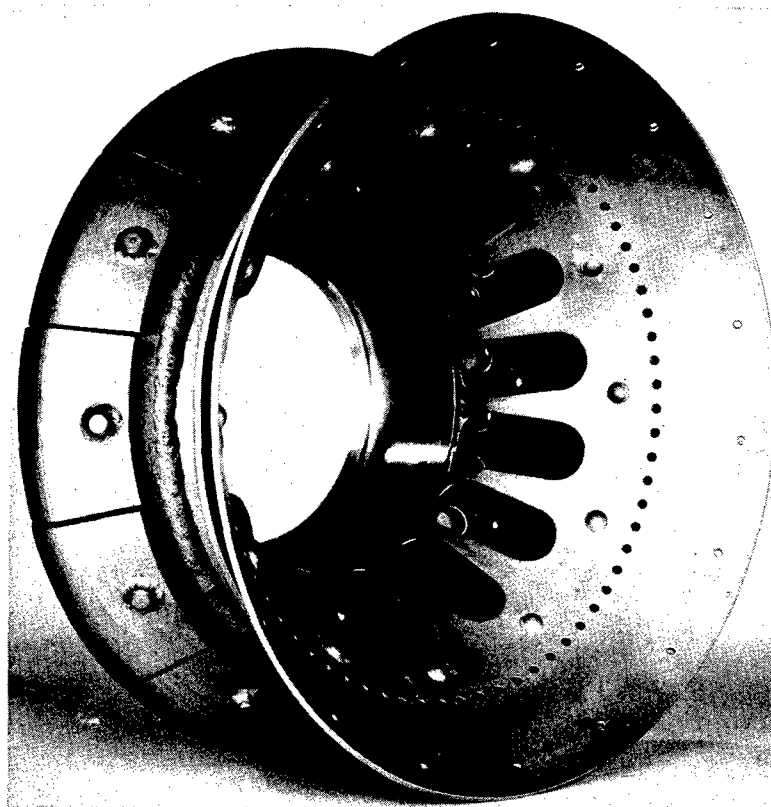


Figure 356. Inner Combustor Modification.

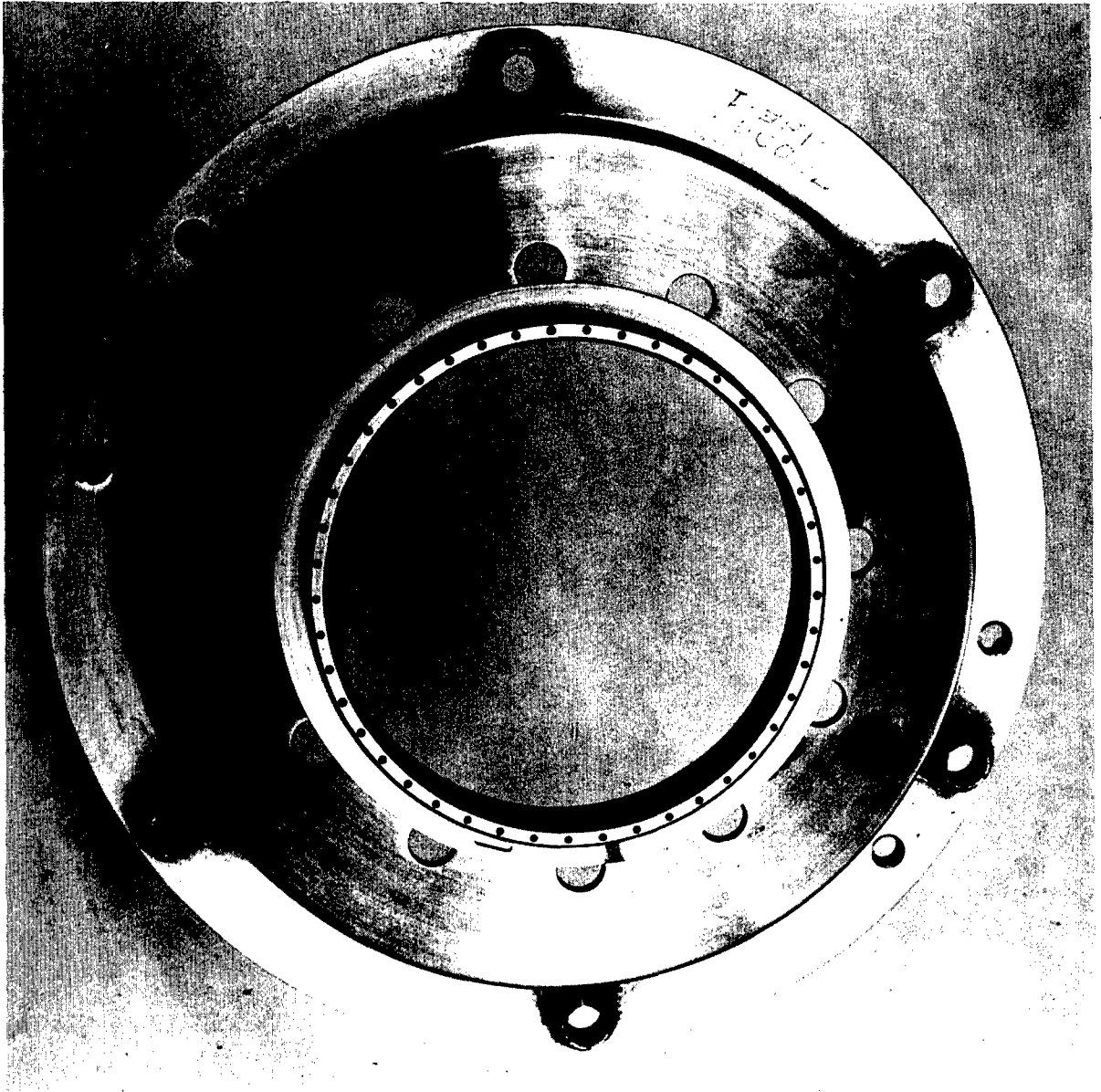


Figure 357. Shroud, Outer Combustor Labyrinth Seal.

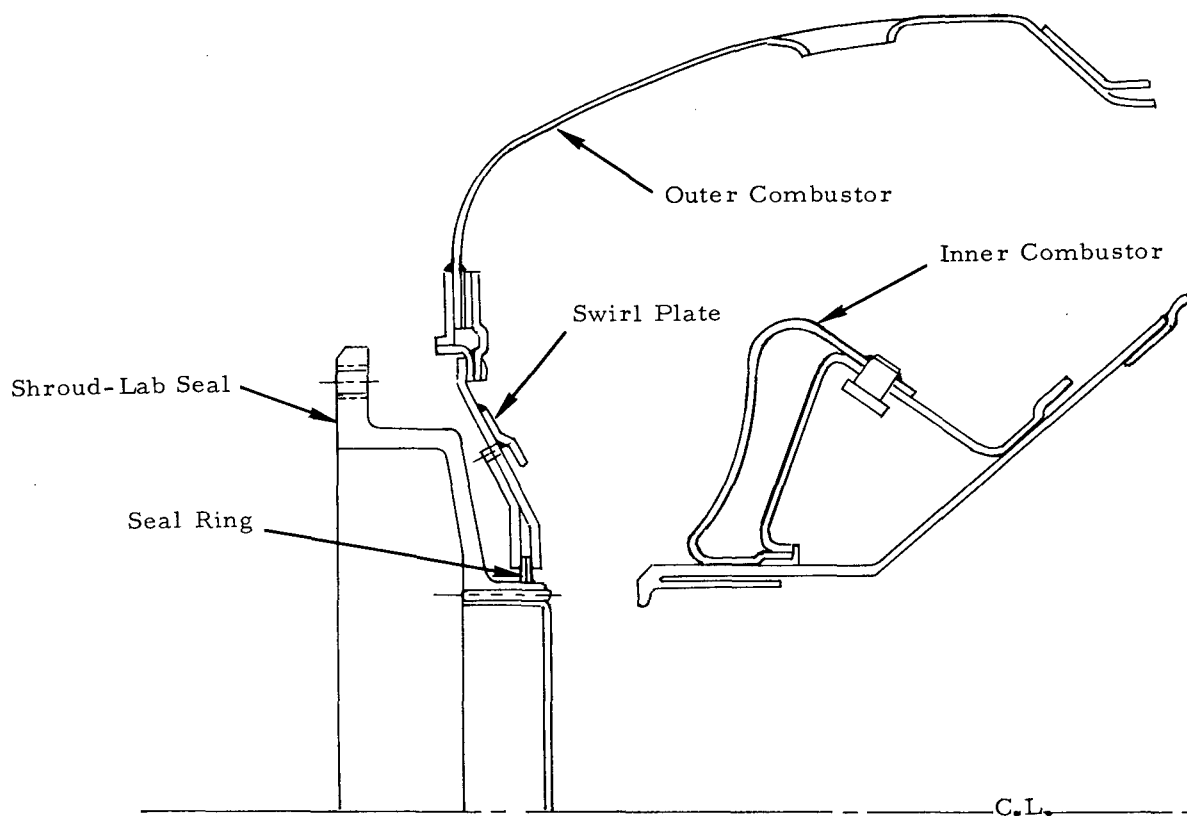


Figure 358. Combustor Assembly.

Turbine Rig Build 6 - Assembly of Turbine Rig Build 6 (data points 32-35) proceeded without difficulty, and a series of combustor evaluation tests was initiated. It was desirable during these tests to operate as near the design point fuel-air ratio as possible, while, at the same time, keeping turbine inlet temperature as low as possible.

It was decided, therefore, to run the initial tests without preheat. Once the combustor performance met acceptable limits, preheated air could be introduced, and the change in performance could be evaluated.

Subsequently, the combustor was operated with ambient temperature inlet air over a range of fuel-air ratios from 0.0117 to 0.0251 at constant airflow.

The improvement in combustor performance was immediately evident, as illustrated in Figures 359 through 361. Figure 359 is a plot of TDF versus combustor temperature rise (ΔTC). The TDF obtained during Turbine Rig Build 5 testing is included for comparison.

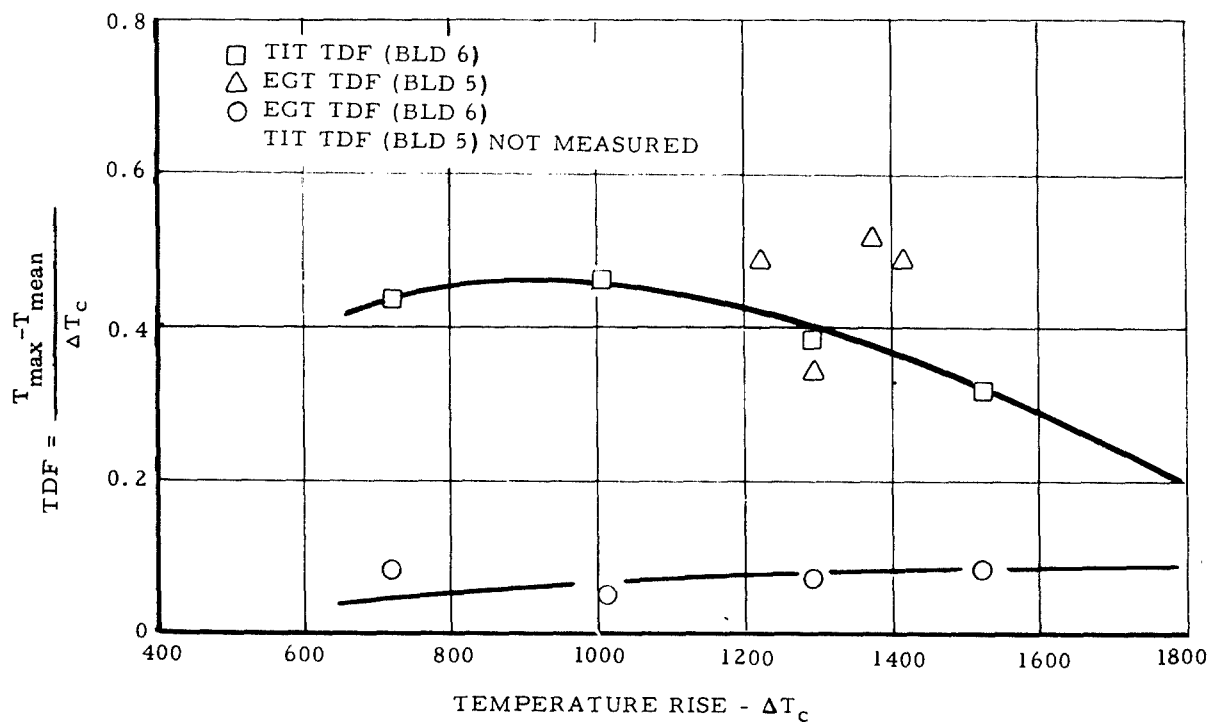


Figure 359. Temperature Distribution Factor, Builds 5 and 6 - Turbine Rig.

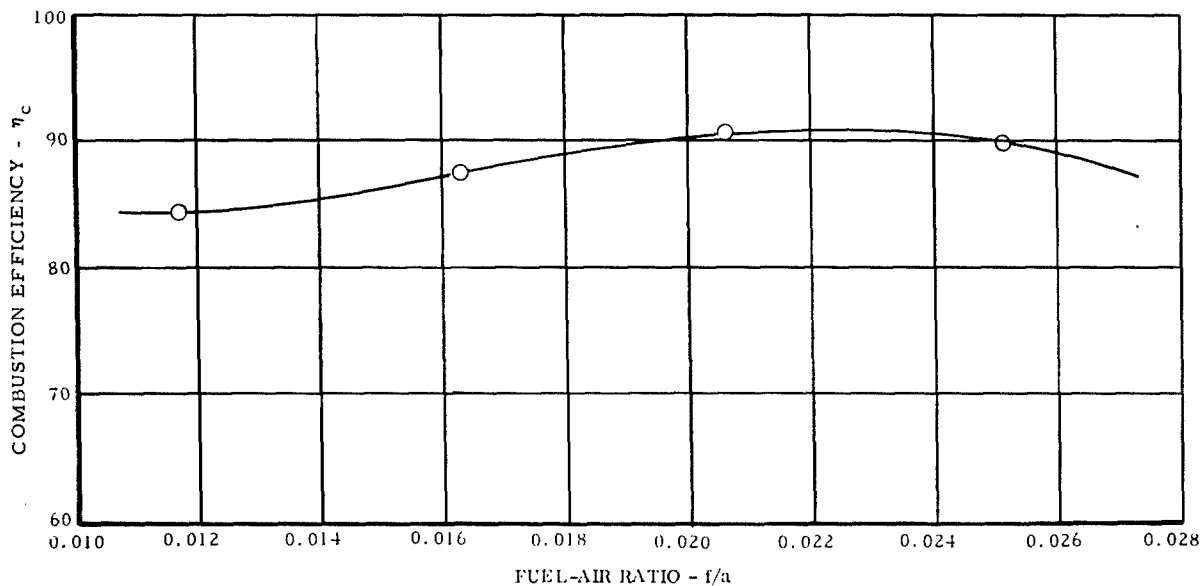


Figure 360. Combustion Efficiency, Build 6 - Turbine Rig.

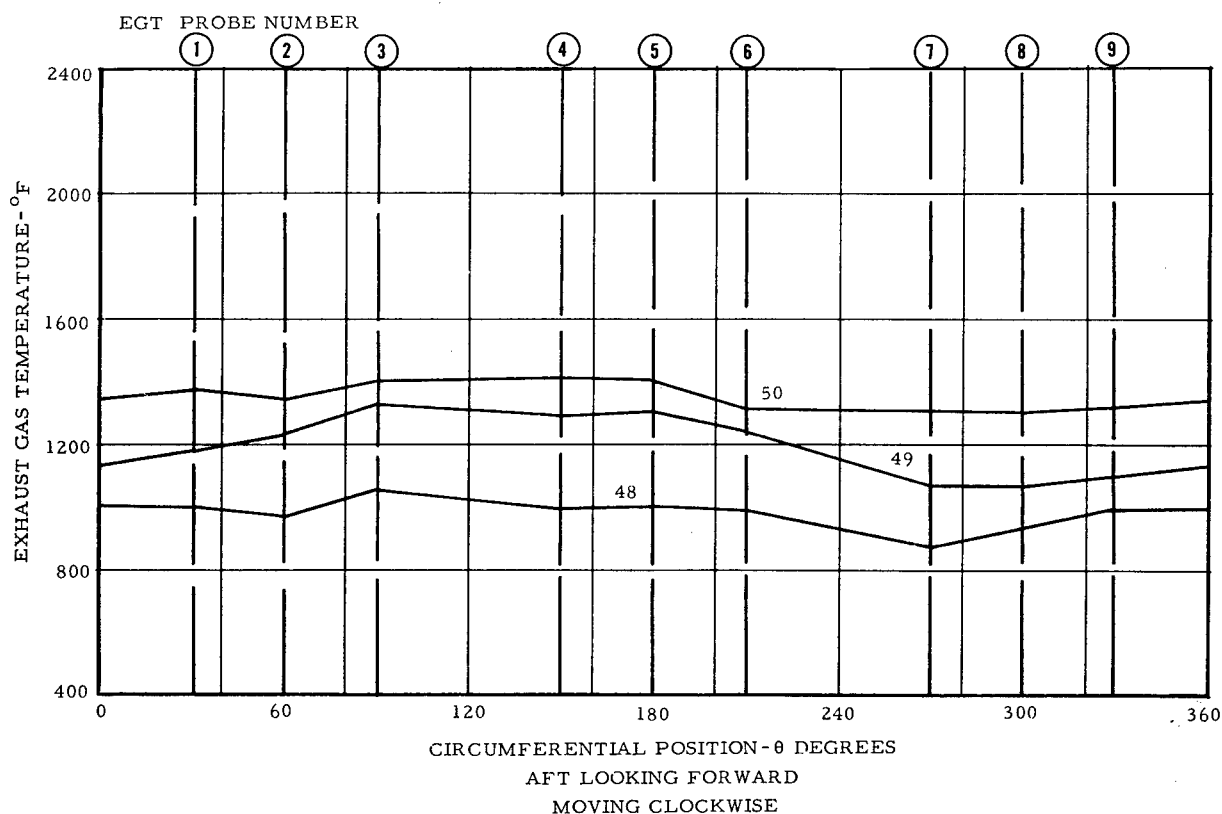


Figure 361. Exhaust Gas Circumferential Temperature Profile - Build 6.

Combustion efficiency, while somewhat lower than desired, Figure 360, is much improved over Turbine Rig Build 5, and does not show the severe dropoff with increasing fuel-air ratio that was experienced during Turbine Rig Build 5.

The improvement in the exhaust gas circumferential temperature profile is evident when Figure 361 is compared with a similar plot obtained during Turbine Rig Build 5 testing (Figure 353).

At the conclusion of the above tests, the rig was disassembled for visual inspection. A buildup of soft carbon was found on the outer portion of the swirl plate, Figure 362. These deposits occur when a locally rich fuel-air mixture is present in the vicinity of a cool structure. It was believed that the film-cooled swirl plate was overly cooled by the ambient combustor inlet air. However, to minimize the buildup of carbon, the inner combustor shell, Figure 363, was reworked, as shown in Figure 364, by adding twelve 0.100- x-0.300-inch slots at the inner portion of the expansion slots. This effectively reduces the local fuel-air ratio adjacent to the outer portion of the swirl plate.

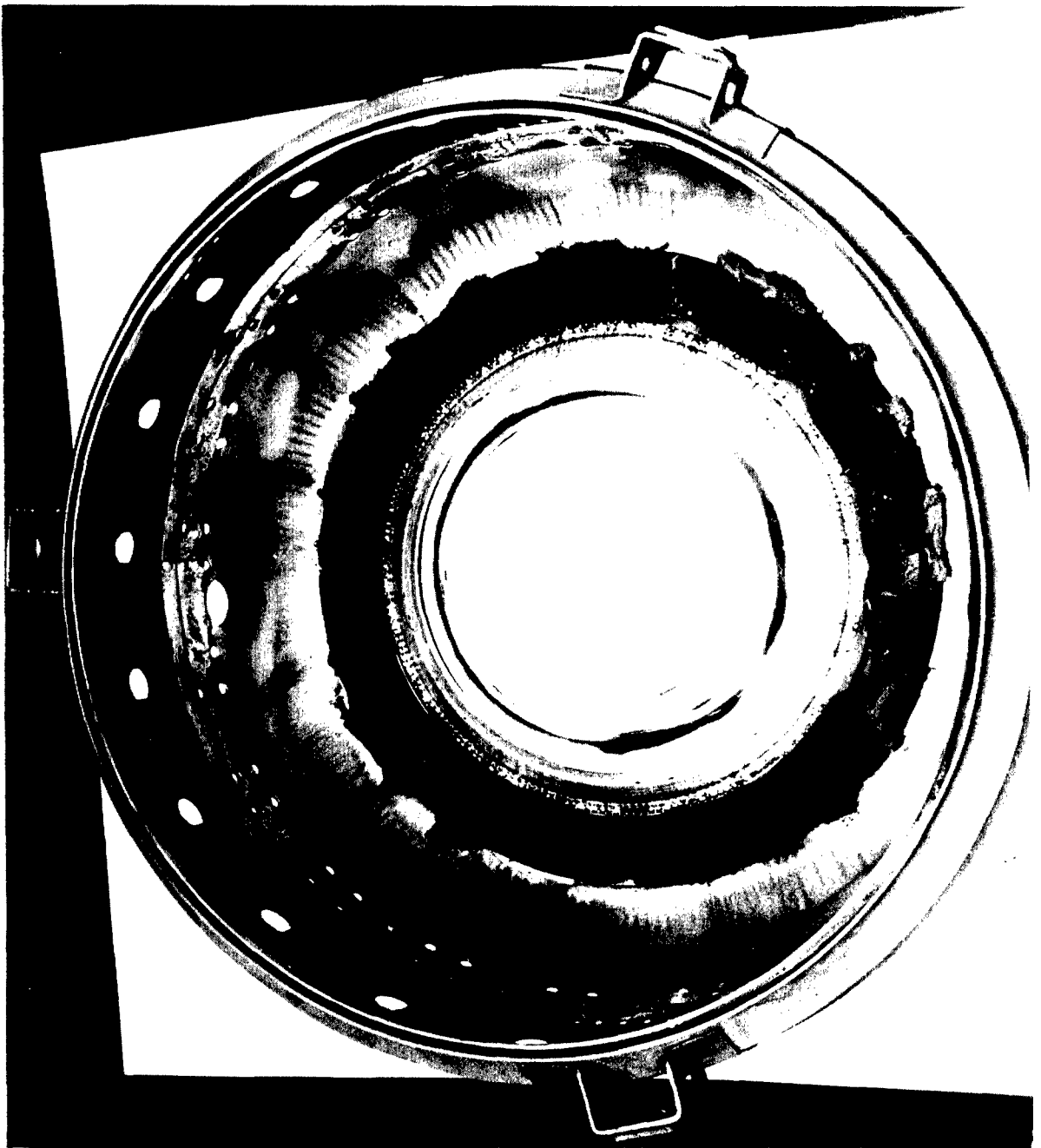


Figure 362. Carbon Buildup on Swirl Plate After Build 6 Testing - Turbine Rig.

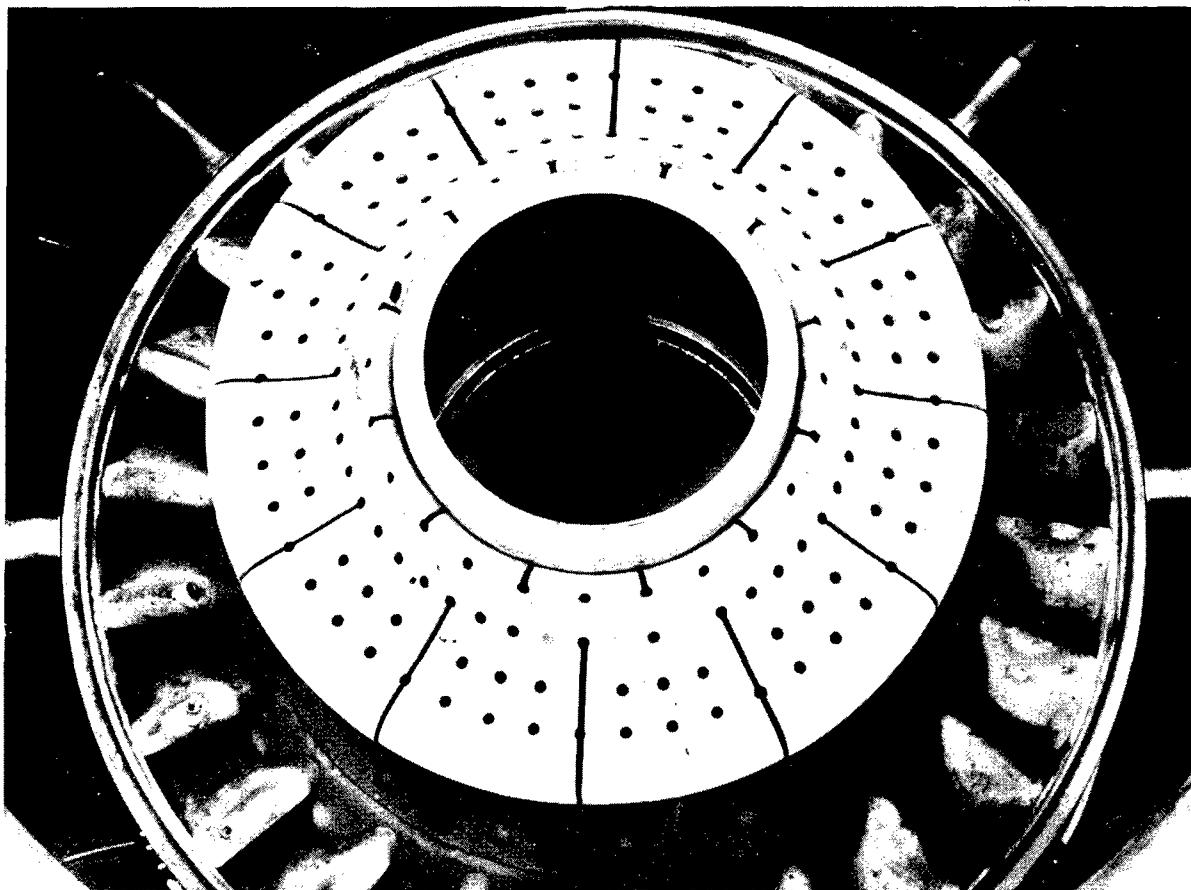


Figure 363. Inner Combustor and Nozzle Assembly After Build 6 Testing - Turbine Rig.

Turbine Rig Build 7 - The turbine rig was subsequently reassembled as Turbine Rig Build 7 (data points 36-50), and combustor evaluation testing was resumed.

Without preheat, there was no significant change in combustion efficiency from that of Turbine Rig Build 6, Figure 365. However, operation of the combustor with preheat resulted in a reduction of combustion efficiency, as shown by curve 2 of Figure 365. The reduction in combustion efficiency is probably due to the vitiation effect of the preheater.

The TDF, with ambient combustor inlet air temperature, showed an initial decrease at low combustor temperature rise, but increased sharply above about 1200°F temperature rise, as shown by curve 1 of Figure 366. The addition of preheat to the combustor inlet air caused an increase in TDF at the low combustor temperature rise, curve 2 of Figure 366.

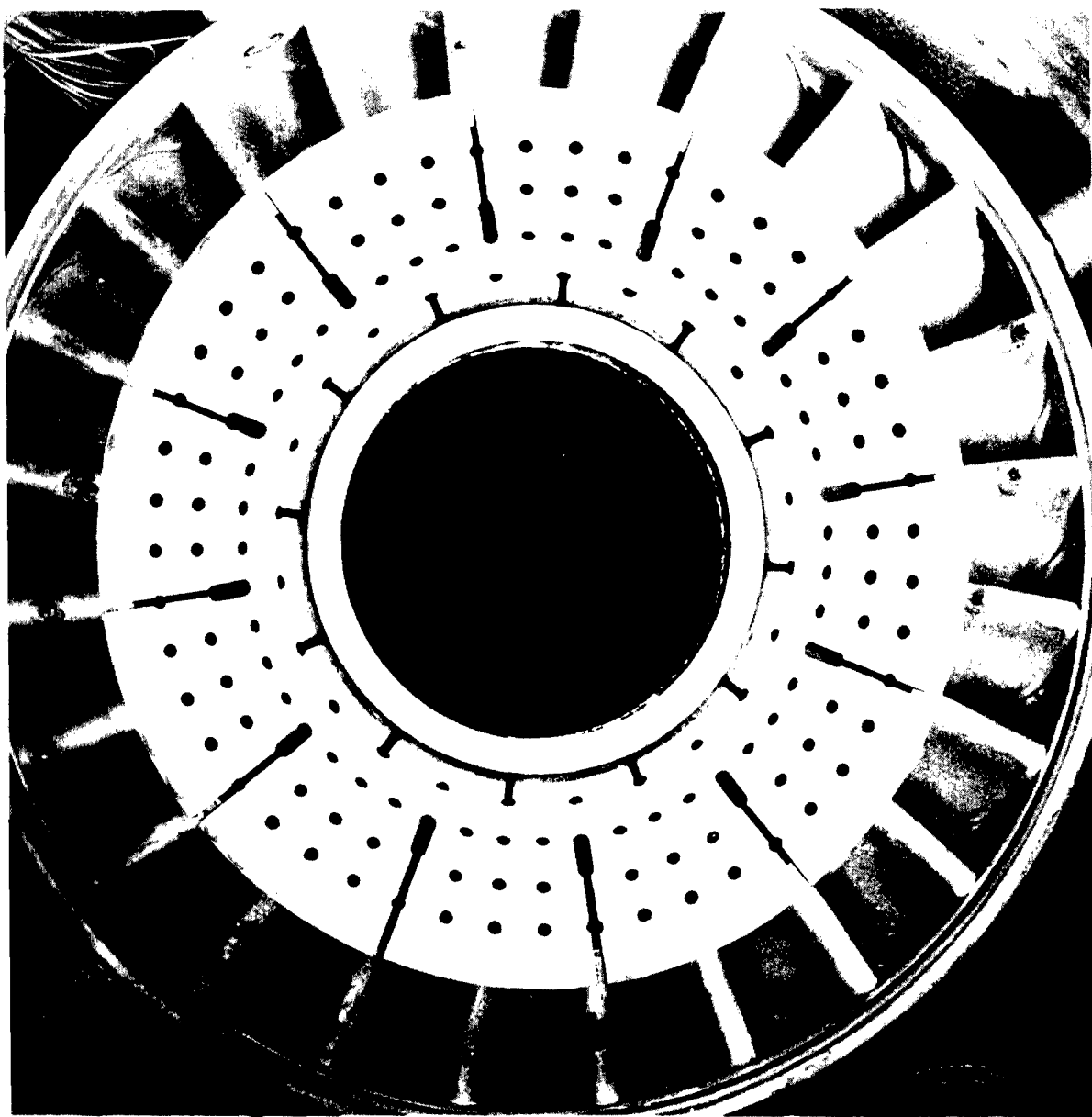


Figure 364. Modified Inner Combustor Shell.

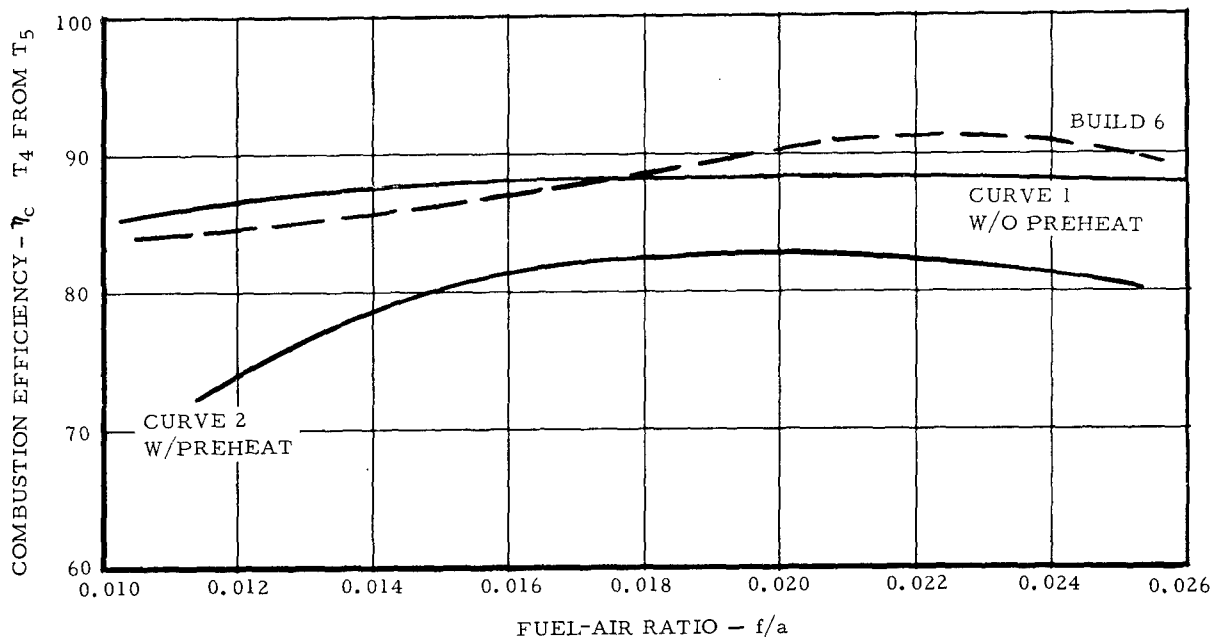


Figure 365. Combustion Efficiency Versus Fuel-Air Ratio, Build 6 - Turbine Rig.

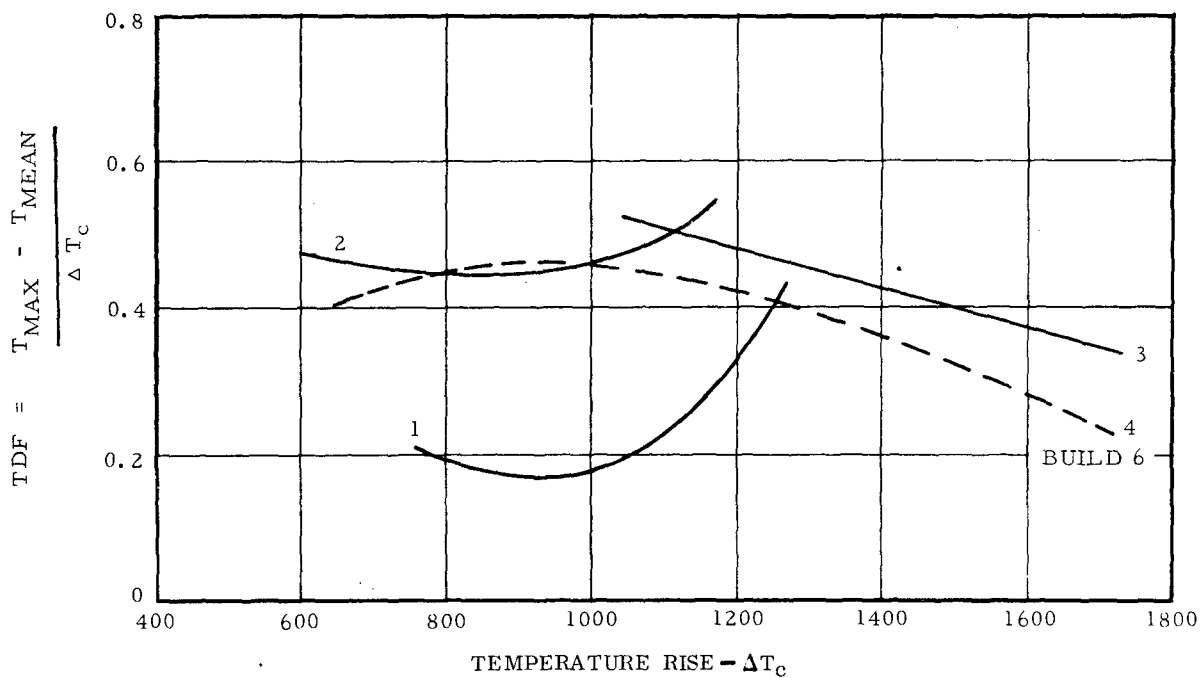


Figure 366. Temperature Distribution Factor Versus Combustor Temperature Rise - Turbine Rig.

Operation of the combustor, without preheat, at various turbine (slinger) speeds between 30,000 and 40,000 rpm resulted in a further variation of TDS, as shown by curve 3 of Figure 366. The TDF curve obtained during Build 6 testing is included on Figure 366 as curve 4 for comparison.

In view of the variation of the TDF curves with and without preheat and with combustor temperature rise, the temperature distribution factor was replotted on a local, probe average basis for the seven circumferential turbine inlet temperature probe positions. These plots are shown in Figures 367 and 368.

The variance in these curves indicates the probability of a shifting airflow distribution into the primary zone as a function of combustor temperature rise and/or preheat temperature. This phenomenon was placed under continuing investigation.

The improvement in the circumferential temperature gradient obtained during Turbine Rig Build 6 testing, Figure 361, was maintained, as evidenced by Figure 369.

At the conclusion of these tests, the turbine rig was disassembled for inspection. Figures 370 and 371 are views of the outer combustor shell and film-cooled swirl plate assembly. The carbon buildup about the outer portion of the swirl plate is the result of a locally rich fuel-air ratio mixture adjacent to a cooled structure, as before. To further alleviate this problem, the area of the axial holes in the outer combustor labyrinth seal shroud (Figure 357) was increased by 35 percent to reduce the local primary-zone fuel-air ratio further. This change was incorporated into Turbine Rig Build 8 testing.

Figure 372 shows the inner combustor and turbine inlet nozzle assembly. The modification to the outer combustor labyrinth seal shroud mentioned above was expected to eliminate the slight carbon buildup which may be seen on the inner combustor shell. However, later testing indicated that this was not the case, and a slight carbon buildup was found at the conclusion of each test series.

Because of the significant improvements in combustor performance obtained during Turbine Rig Builds 6 and 7 testing, it was decided to resume turbine performance running with Turbine Rig Build 8.

Turbine Rig Build 8 - Although the prime purpose of Turbine Rig Build 8 testing (data points 51-59) was turbine performance evaluation, combustor performance was also monitored.

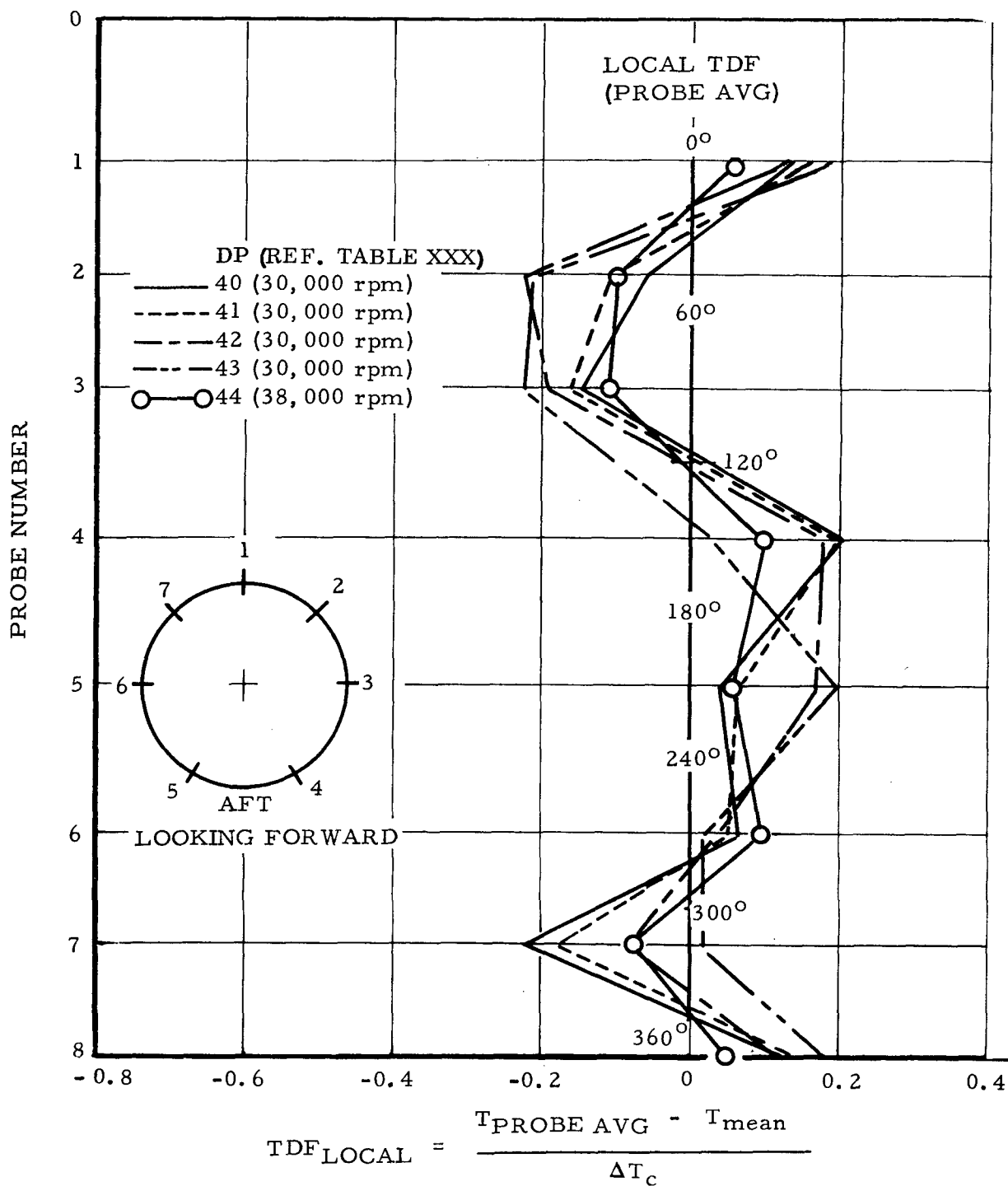


Figure 367. Local Temperature Distribution Factor, Build 7 With Preheat - Turbine Rig.

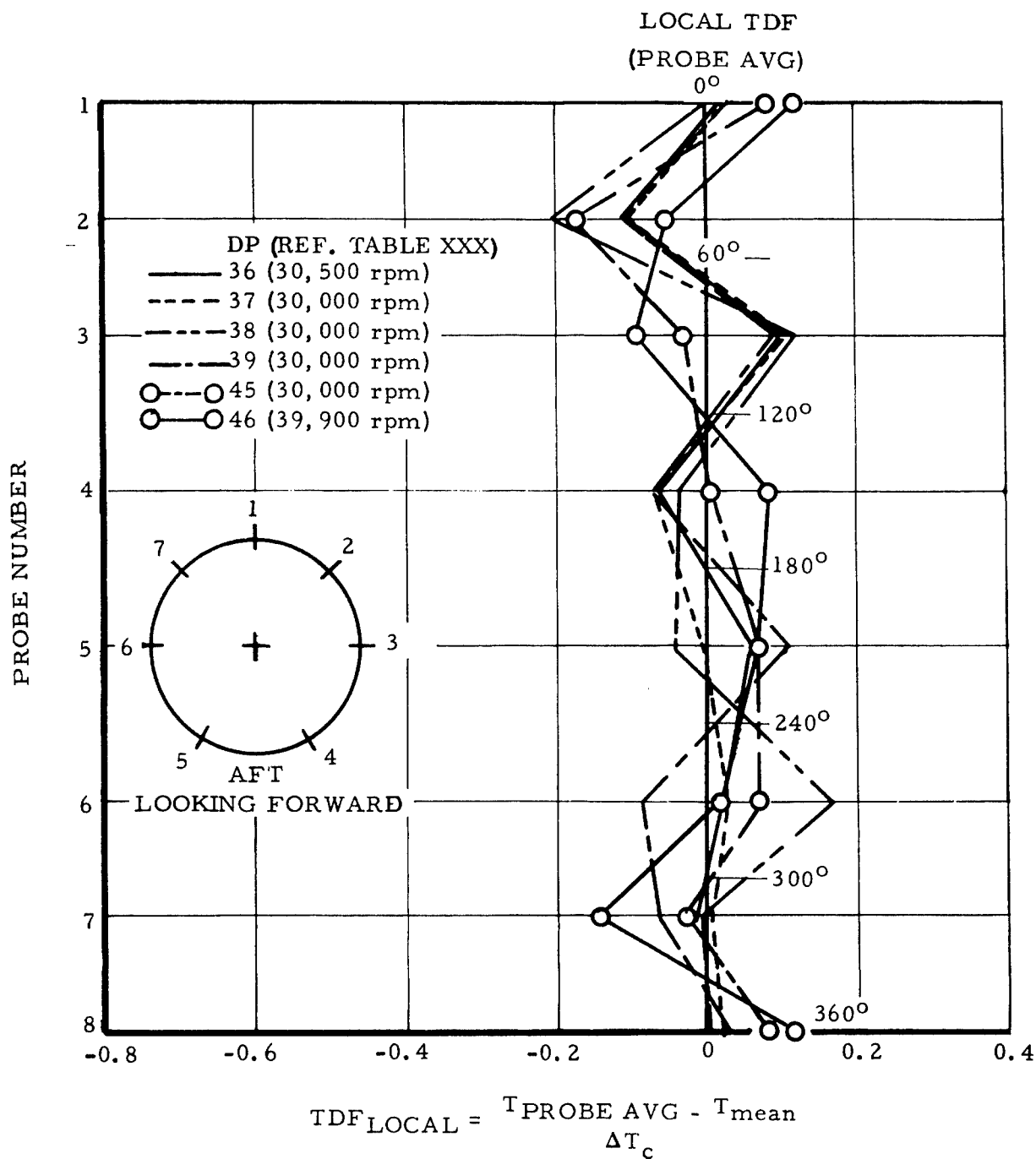


Figure 368. Local Temperature Distribution Factor,
Build 7 Without Preheat - Turbine Rig.

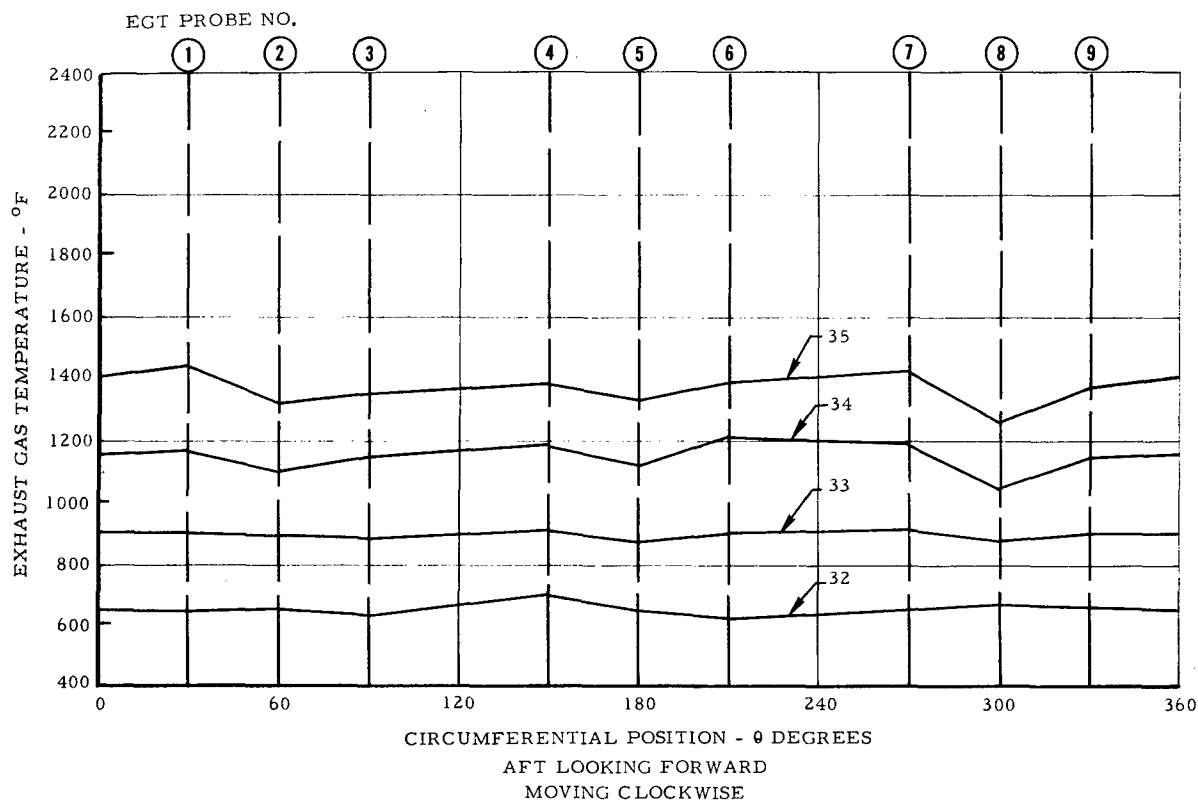


Figure 369. Exhaust Gas Circumferential Temperature Profile, Build 7 - Turbine Rig.

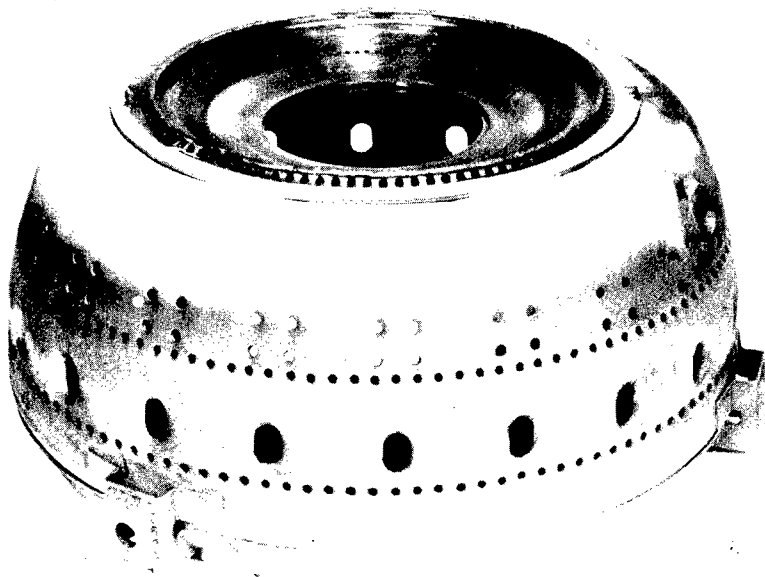


Figure 370. Outer Combustor Shell and Swirl Plate Assembly at Completion of Build 7 Testing - Turbine Rig.

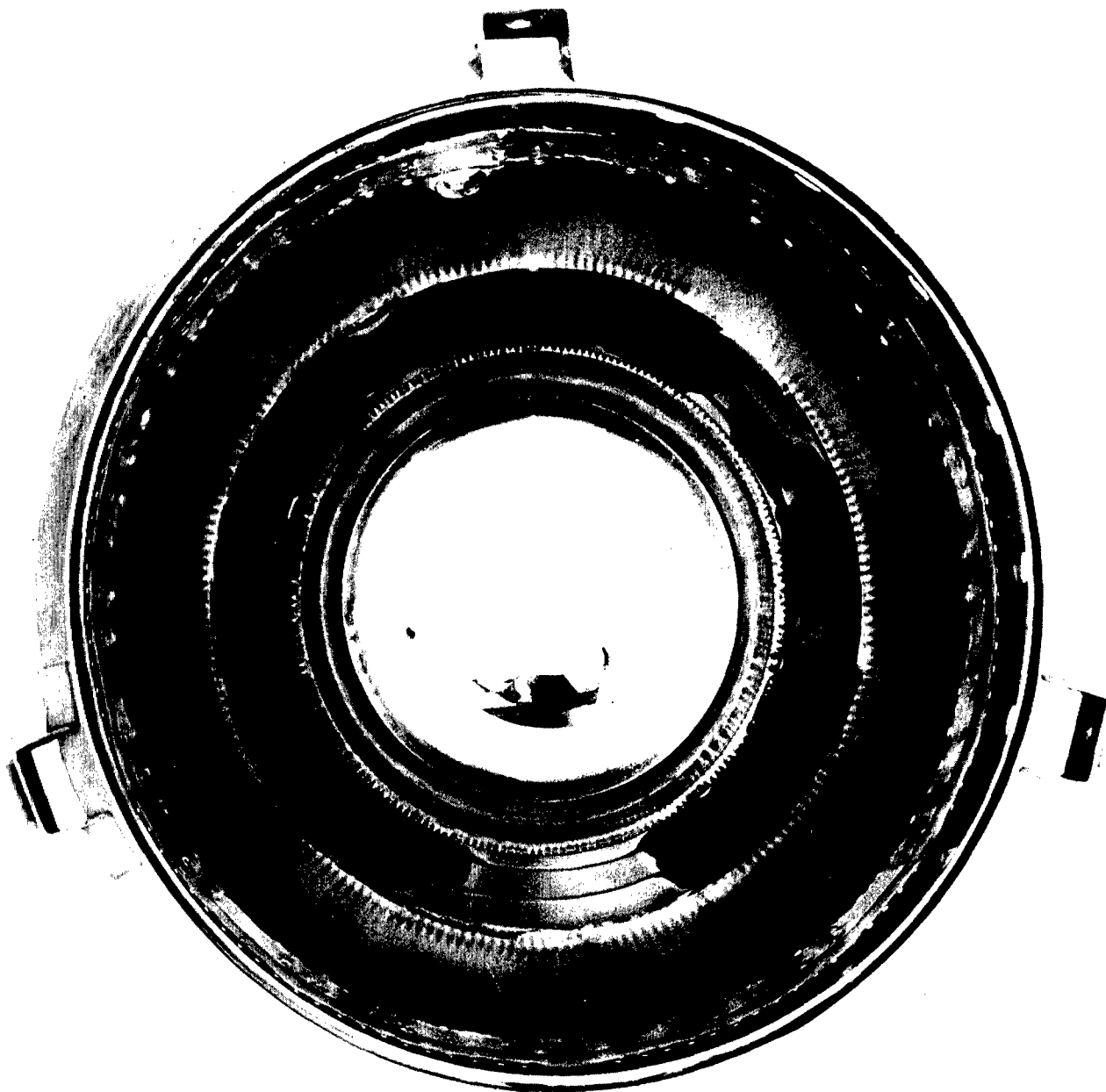


Figure 371. Outer Combustor Shell and Swirl Plate Assembly at Completion of Build 7 Testing - Turbine Rig.



Figure 372. Inner Combustor and Turbine Inlet Nozzle Assembly at Completion of Build 7 Testing - Turbine Rig.

Combustion efficiency showed no significant change from Turbine Rig Build 7 testing. Figure 373 is a plot of combustion efficiency versus fuel-air ratio on which Turbine Rig Build 7 as well as Turbine Rig Build 8 test points are plotted. Although lower than desirable, the efficiency level was sufficient to provide the required combustor temperature rise. Therefore, since low specific fuel consumption was not a prime factor, combustion efficiency was considered to be adequate.

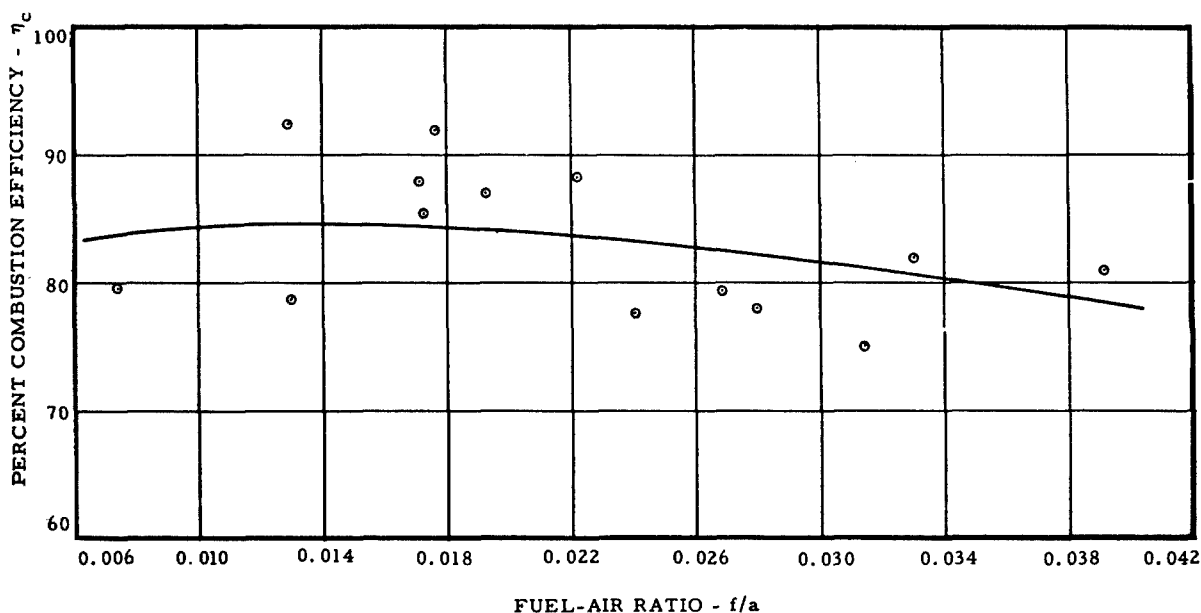


Figure 373. Combustion Efficiency Versus Fuel-Air Ratio - Builds 7 and 8.

The exhaust gas circumferential temperature profile remained at an acceptable level, as shown in Figure 374. This is a plot of the average of four radial locations at each of nine circumferential probe positions for data point 59. This was the highest temperature (TIT of 2212°F) and the highest mechanical speed (45,000 rpm) to which the turbine was subjected during Turbine Rig Build 8 testing. The difference between the maximum and minimum individual EGT readings for this data point was 500°F.

Carbon buildup at the outer edge of the film-cooled swirl plate continued. However, the rate of carbon buildup was slow and was not considered to be a problem during the additional running time anticipated.

All other combustor hardware was in excellent condition and showed no evidence of mechanical or thermal distress.

Turbine Rig Build 9 - Turbine Rig Build 9 testing consisted of a single data point (60) at a turbine inlet temperature of 2450°F and a mechanical speed of 31,650 rpm. There was no significant change in combustor performance from that of Turbine Rig Build 8. The exhaust gas circumferential temperature gradient was essentially unchanged, Figure 374. Also shown on Figure 374 is the circumferential temperature plot of data point 59 for comparison.

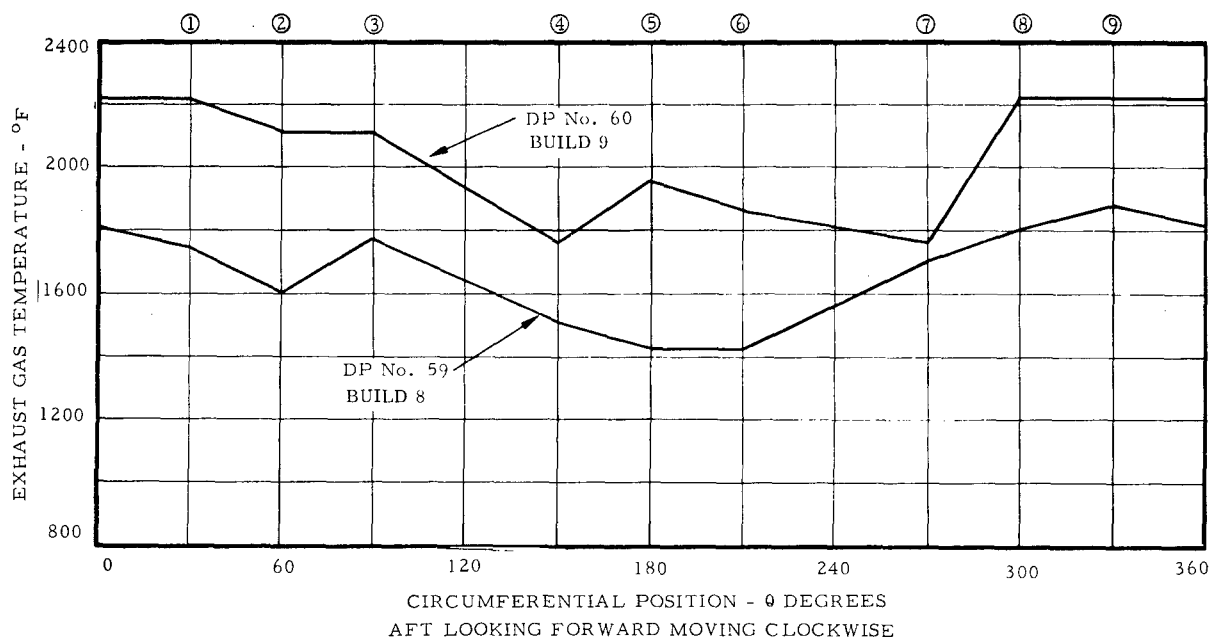


Figure 374. Circumferential Temperature Gradient.

Turbine Rig Builds 10, 11, and 12 - Testing during Turbine Rig Builds 10, 11, and 12 (data points 61-62) of the turbine rig was aimed at operation at design mechanical speed, design turbine inlet temperature, and design power level. The overall performance and structural integrity of the fuel slinger-annular combustor concept has been proven to be satisfactory for utilization with the fluid-cooled turbine.

HEAT TRANSFER

An analysis of turbine rig heat transfer test data has resulted in close agreement between measured and analytically predicted results.

The turbine blade cooling concept, a closed-loop thermosyphon performed essentially as predicted. Operation of the turbine at a turbine inlet temperature of 2450°F (150°F above design) was successfully accomplished.

The cooled turbine test rig included several air-cooled components as well as the fluid-cooled turbine blades. These were 1) the turbine inlet nozzle, 2) the turbine shroud, and 3) the turbine exhaust diffuser. Heat transfer data, obtained on all these components except the turbine shroud, were found to be in close agreement with analytically predicted results.

Visual examination of the turbine shroud during each rig disassembly disclosed no thermal or mechanical distress, indicating that shroud cooling was performing satisfactorily.

While turbine blade metal temperatures were not directly measured, an indication of the degree of blade cooling was achieved through correlation of measured and predicted fuel temperature rise. A more direct indication of blade cooling was obtained at several test data points when the turbine blades were subjected to inertia stresses which, at the metal temperature of an uncooled blade, were well beyond the ultimate strength of the material (see Mechanical-Structural Integrity section).

Measured disc temperatures were also in close agreement with design predictions. At a turbine inlet temperature of 2450°F, the measured disc rim temperature was 1200°F.

The turbine inlet nozzle, the turbine shroud, and the turbine exhaust diffuser were subjected to local gas temperatures approximately 500°F above their respective design temperatures. No thermal distress was noted.

Discussion

Turbine Disc and Blade - The cooling concept utilized in this application is a closed-loop thermosyphon system operating between the turbine blade (the heat source) and the fuel (the heat sink). A secondary heat transfer media (steam) is employed to transport the heat between the source and the sink. A schematic of the cooling circuit is shown in Figure 375.

The closed-loop thermosyphon system establishes a heat balance between the heat absorbed at the blade (Station 2, Figure 375) and the heat rejected to the fuel (Station 9, Figure 375). This heat balance may be expressed as

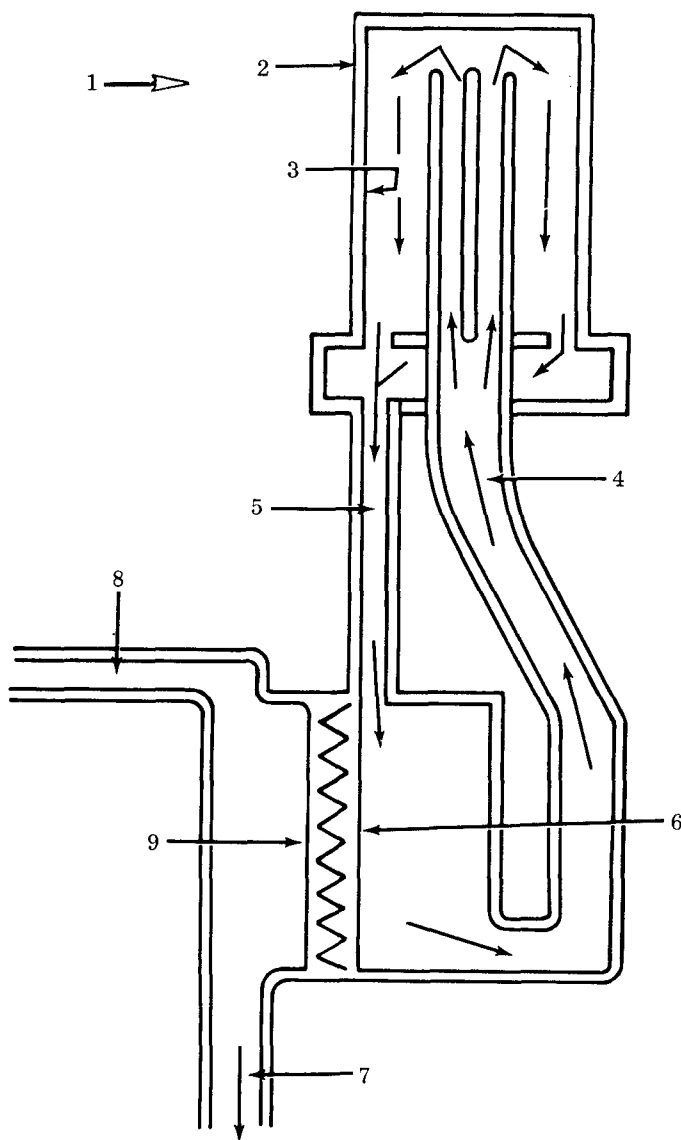
$$q_b = q_s = q_f$$

where

$$q_b = \text{heat input to blade}$$

$$q_s = \text{heat input to steam}$$

and $q_f = \text{heat rejected to fuel.}$



STATION

- 1 Freestream
- 2 Blade Surface - Outside
- 3 Blade Surface - Inside
- 4 Secondary Coolant Inlet Conditions
- 5 Secondary Coolant Exit Conditions
- 6 Heat Exchanger Surface - Hot Side
- 7 Primary Coolant Exit Conditions
- 8 Primary Coolant Inlet Conditions
- 9 Heat Exchanger Surface - Cold Side

Figure 375. Schematic of Closed-Loop Thermosyphon System.

Figure 376 illustrates the fuel circuit which is analyzed in the following pages.

The heat rejected to the fuel is an indirect measure of the blade metal temperature. Fuel temperature is measured as the fuel enters the turbine rig and again immediately upstream of the slinger cavity. The flow path of the fuel through the rotor as well as the thermocouple wells in the fuel valve body may be seen in Figure 376. The rotor inlet and exit fuel temperatures along with the fuel flow rate provide a measure of heat input to the fuel.

Ideally, the only heat rejected to the fuel would come from blade cooling. However, the fuel also picks up heat from sources other than the blade. These heat sources include the disc and friction generated in the rotating fuel seal. The heat input from the seal is small and may be safely neglected; the heat input from the disc may not be neglected.

The relatively cold fuel flowing through the disc cools the disc. This additional heat input to the fuel is reflected in the measured fuel temperature rise, and must be added to the heat rejection to the fuel predicted by the Continental Closed Thermosyphon Computer Program if agreement between measured and predicted values is to be achieved.

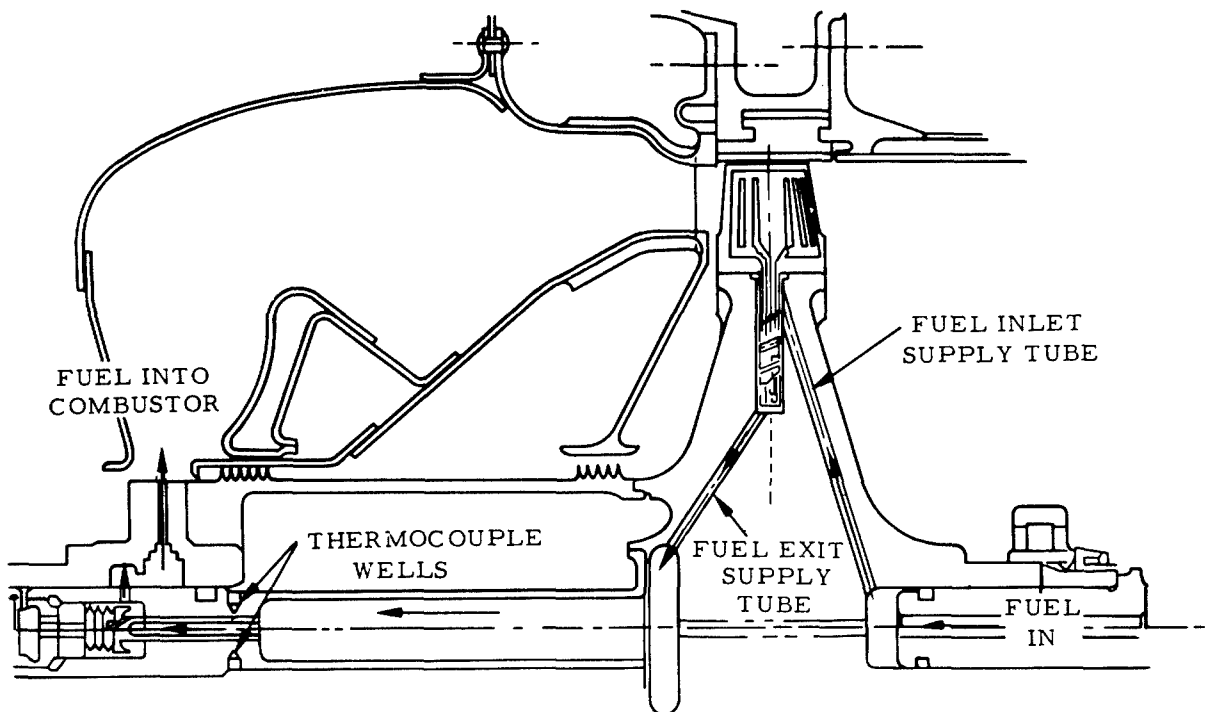


Figure 376. Fuel Flow Through Rotor.

The Continental Closed Thermosyphon Computer Program is an analytical model of the closed-loop thermosyphon cooling circuit and mathematically establishes a heat balance between the heat input to the blade and the heat rejected to the fuel. Originally intended as a design tool (the program was used to establish the blade cooling design parameters), the program was used during this analysis of test data as a part of the data reduction procedure. This was accomplished by inputting measured test rig conditions into the computer program.

Figure 377 is a plot of measured fuel temperature rise versus turbine blade relative gas temperature. Figure 378 is a plot of calculated fuel temperature rise versus relative temperature. As referred to above, computer-derived values of fuel temperature rise were slightly lower than measured values, as may be seen if Figures 377 and 378 are compared. The scatter indicated by the measured data results from the dependency of fuel temperature rise on such parameters as fuel flow rate and rotor speed as well as turbine blade relative gas temperature. It is virtually impossible to run a test rig, holding all of these variables constant for subsequent, easy analytical comparison.

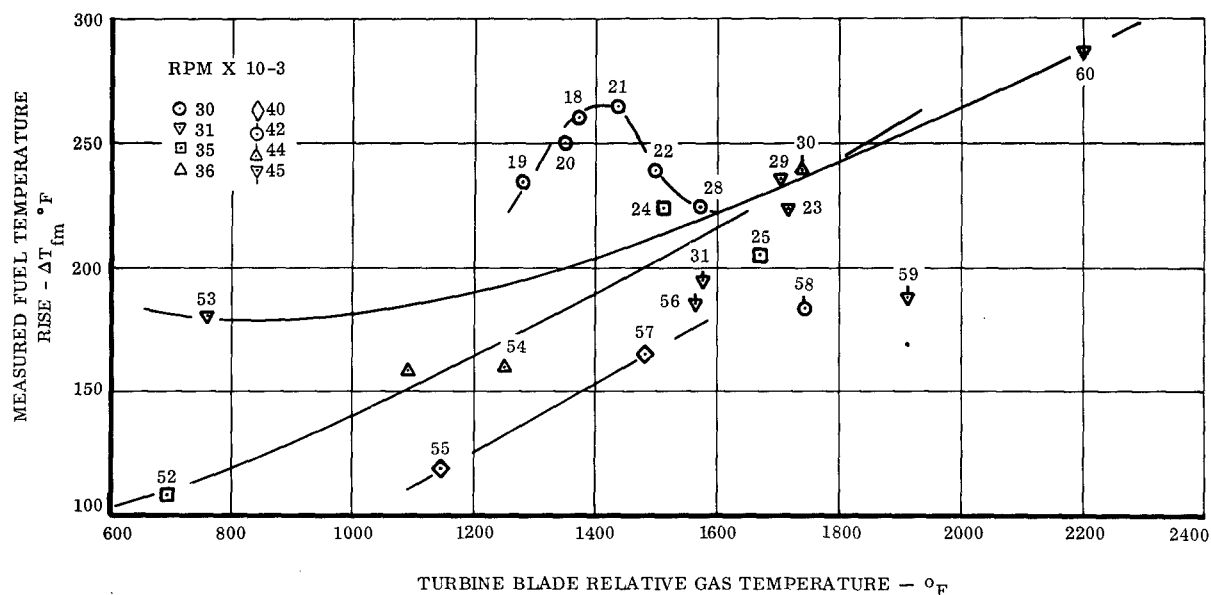


Figure 377. Measured Fuel Temperature Rise Versus Relative Gas Temperature.

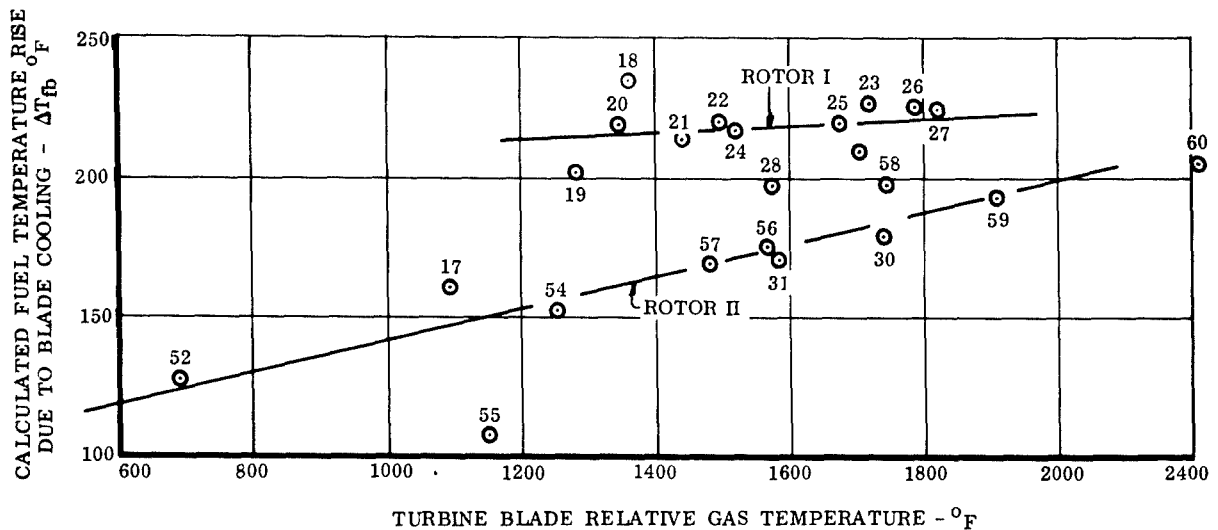


Figure 378. Calculated Fuel Temperature Rise Due to Blade Cooling.

However, since fuel temperature rise is known to be a function of fuel flow and the square of rotor speed, it is possible to normalize the data in a manner similar to the correction of engine performance for standard conditions. The measured data were, therefore, normalized by the following equation:

$$T_f^1 = T_{f_m} \left(\frac{W_{f_m}}{W_{f_{DP}}} \right) \left(\frac{N_m}{N_{DP}} \right)^2 \quad (23)$$

where T_f^1 = normalized fuel temperature rise

T_{f_m} = measured fuel temperature rise

W_{f_m} = measured fuel flow

$W_{f_{DP}}$ = design point fuel flow = 333 lb/hr

N_m = measured mechanical rotor speed

N_{DP} = design point mechanical rotor speed = 45,000 rpm

These normalizing factors were taken at turbine rig design point operating conditions.

The results of this normalization procedure are shown on Figure 379. It is immediately apparent that the scatter evident in Figure 377 has been significantly reduced. However, two rotor assemblies were tested, and there appears to be a tendency for the normalized data to separate into groups associated with a particular turbine assembly. This tendency toward data separation was also noted in the fuel temperature rise due to blade cooling calculated by the computer program, Figure 378, and was carried over in the normalized function, Figure 380.

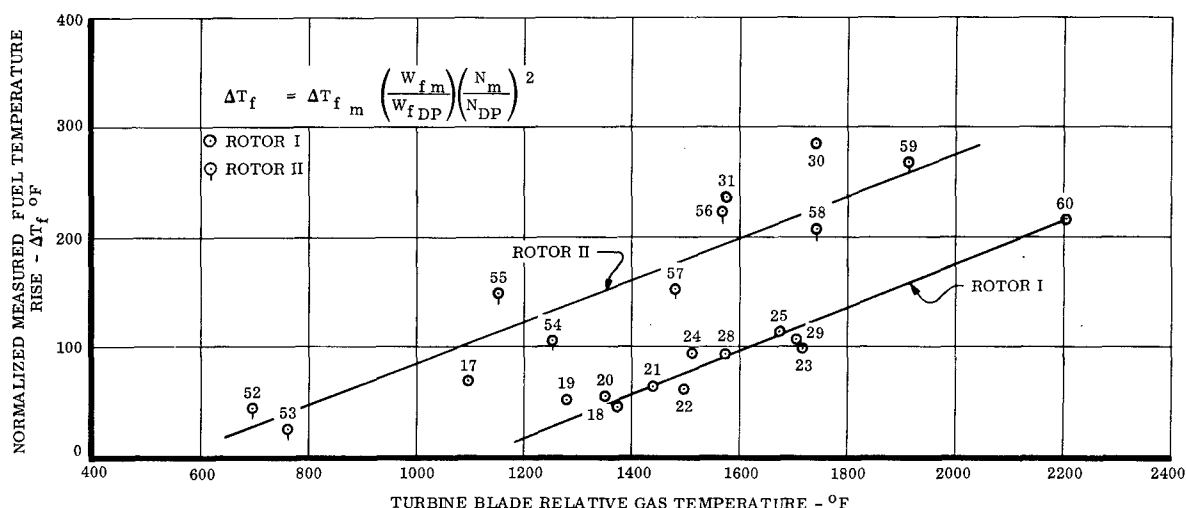


Figure 379. Normalized Measured Fuel Temperature Rise.

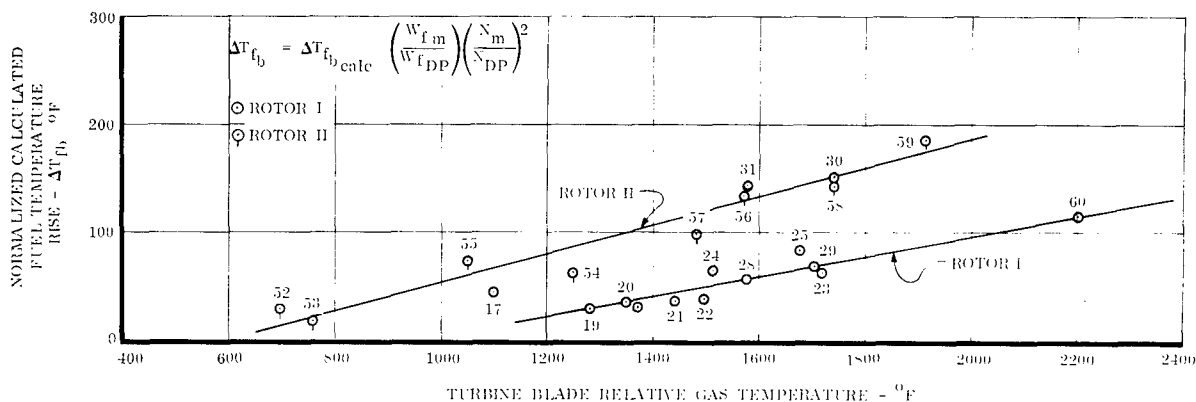


Figure 380. Normalized Calculated Fuel Temperature Rise Due to Blade Cooling.

No significant difference exists between the turbine blades used in the two rotor assemblies. The rotor discs differed only in the size of the fuel inlet supply tube, Figure 376. The fuel inlet tube of turbine rotor II was 0.060-inch diameter for its full length, as shown in Figure 375. However, the fuel inlet tube of turbine rotor I was 0.060-inch diameter for approximately the inner one-third of its length, then opened up to 0.125-inch diameter for the remainder. This was required because of drill breakage due to the large length-to-diameter ratio of the 0.060-inch diameter holes. This difference in the rotor discs affects disc cooling only and, consequently, should have had a relatively small effect on overall fuel temperature rise. Consequently, other causes for the data separation were investigated.

An examination of the data of Figure 377 revealed that, for a given turbine blade relative gas temperature, the fuel temperature rise experienced by rotor I was always greater than that occurring with rotor II. However, when plotted on a heat flow basis, Figure 381, the heat rejected to the fuel in rotor II, again for a constant relative gas temperature, was always greater than that in occurring rotor I. Since heat flow is directly proportional to both fuel flow and fuel temperature rise, this could occur only if the measured fuel flow through rotor II was higher than through rotor I. This had in fact occurred.

Figure 382 is a plot of measured fuel flow versus turbine blade relative gas temperature and shows the significant difference in fuel flow between the two rotor assemblies. It should be noted that this curve does not account for changes in airflow and combustor temperature rise. These factors may be accounted for if combustor temperature rise is plotted against fuel-air ratio, Figure 383. The separation is clearly visible.

The reason for the increased fuel requirement with rotor II has not been definitely identified. It was believed to be the result of 1) fuel leakage at the carbon face shaft fuel seal, 2) leakage at the blade-to-disc fuel seals, or 3) a change in combustor efficiency. There was no way of determining which of the above was at fault. A change in combustor performance was unlikely since no hardware modifications were made nor was any deterioration of hardware noted. Consequently, fuel leakage was believed to be the most probable cause, with the carbon face shaft fuel seal as the prime suspect. This suspicion is somewhat strengthened by the fact that leakage at this seal, at the rate considered here, causes no significant rig problems. However, leakage at the blade-to-disc seals does cause rig handling problems, which did not occur during these runs.

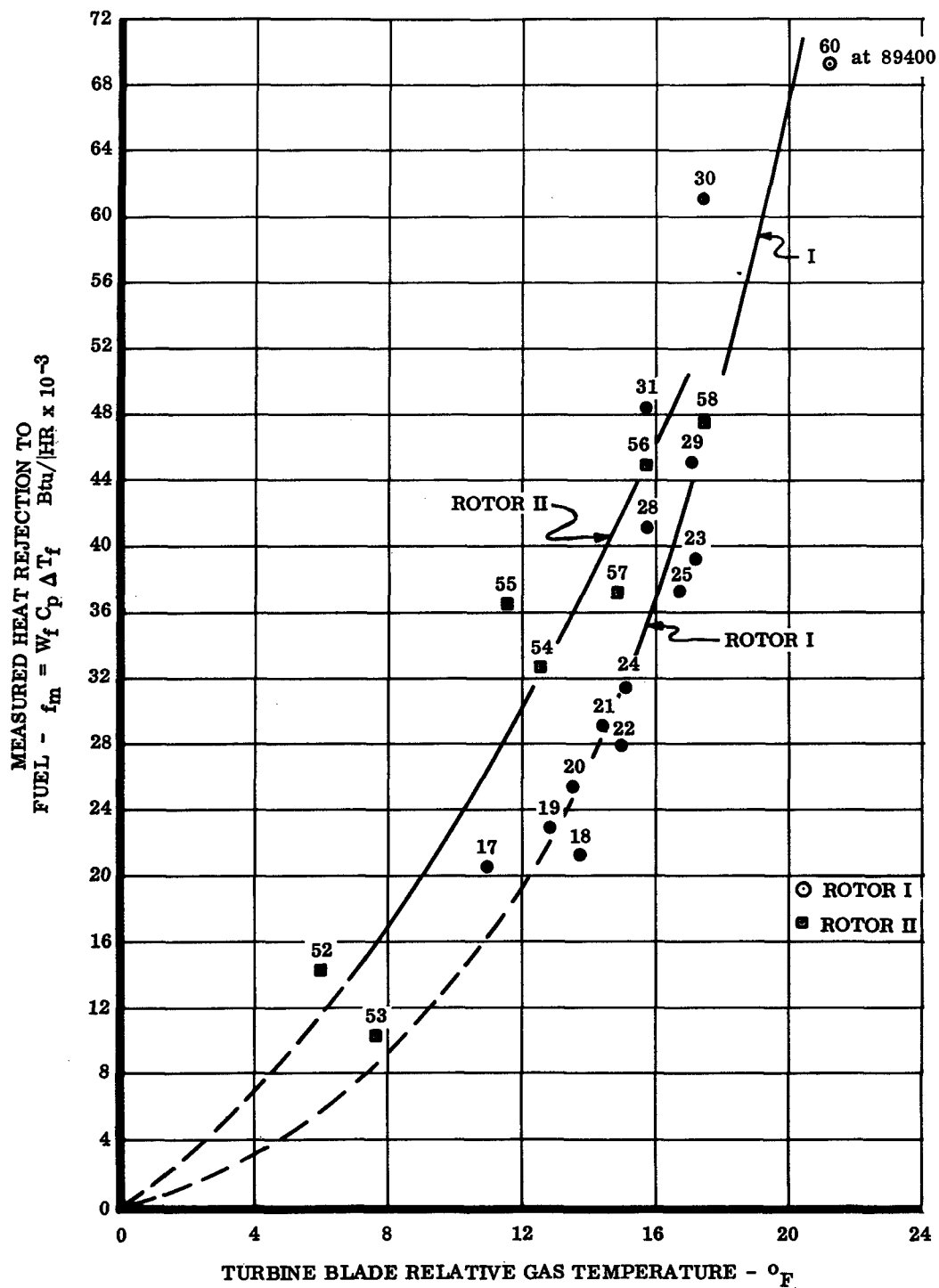


Figure 381. Heat Rejected to Fuel.

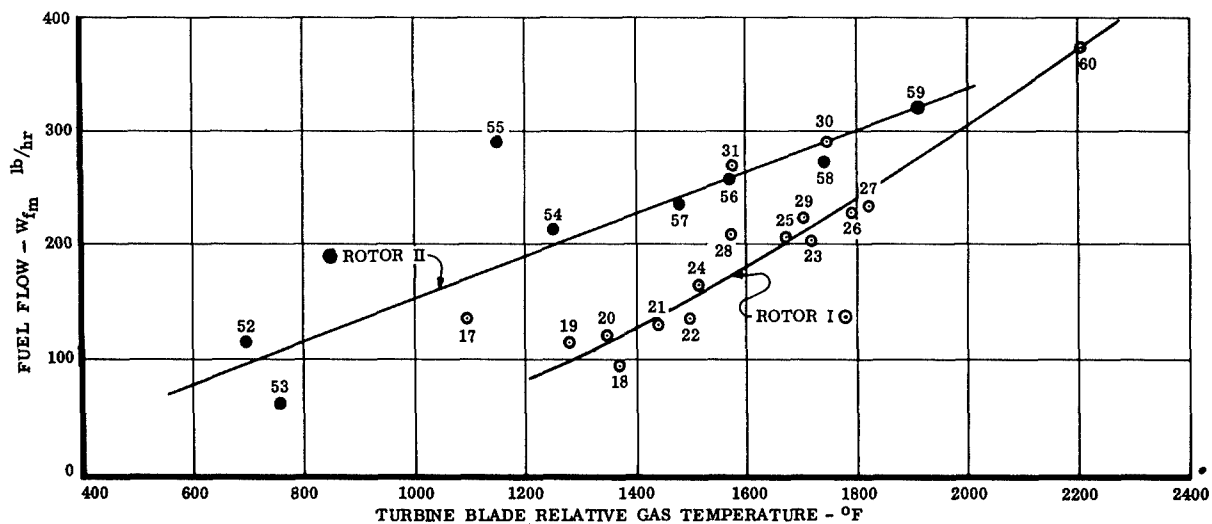


Figure 382. Measured Fuel Flow

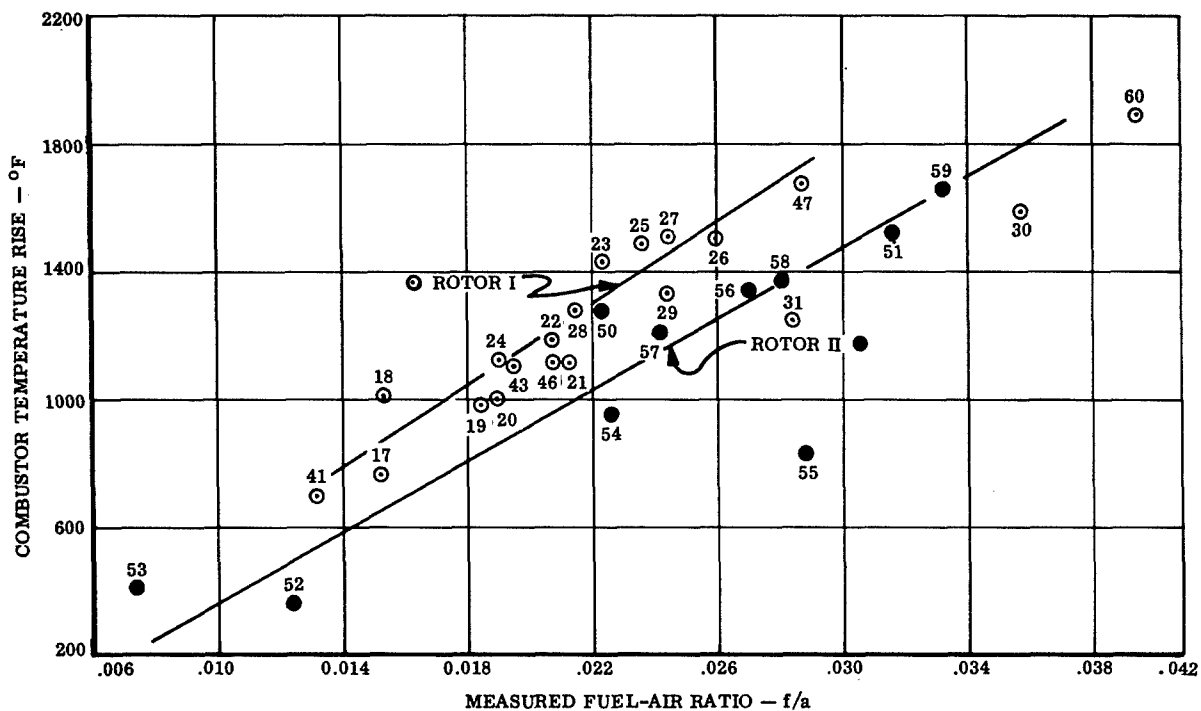


Figure 383. Comparison of Measured Fuel Flow Requirements for Rotors I and II.

The probability of fuel leakage complicates the correlation of measured and calculated fuel temperature rise, as evidenced by Figures 377 through 381 and the above discussion.

Figure 384 is a comparison of calculated fuel temperature rise due to blade cooling (computer program output) and measured fuel temperature rise. The difference between the measured and calculated values is the result of heat input from the disc.

Rotor disc temperatures were measured by thermocouples placed at the dead rim, live rim, and hub, as shown in Figure 385, a view of the instrumented wheel and shaft assembly. Measured disc temperatures are shown in Figure 386. These temperatures provided the means for calculating the heat input to the disc and, subsequently, to the fuel.

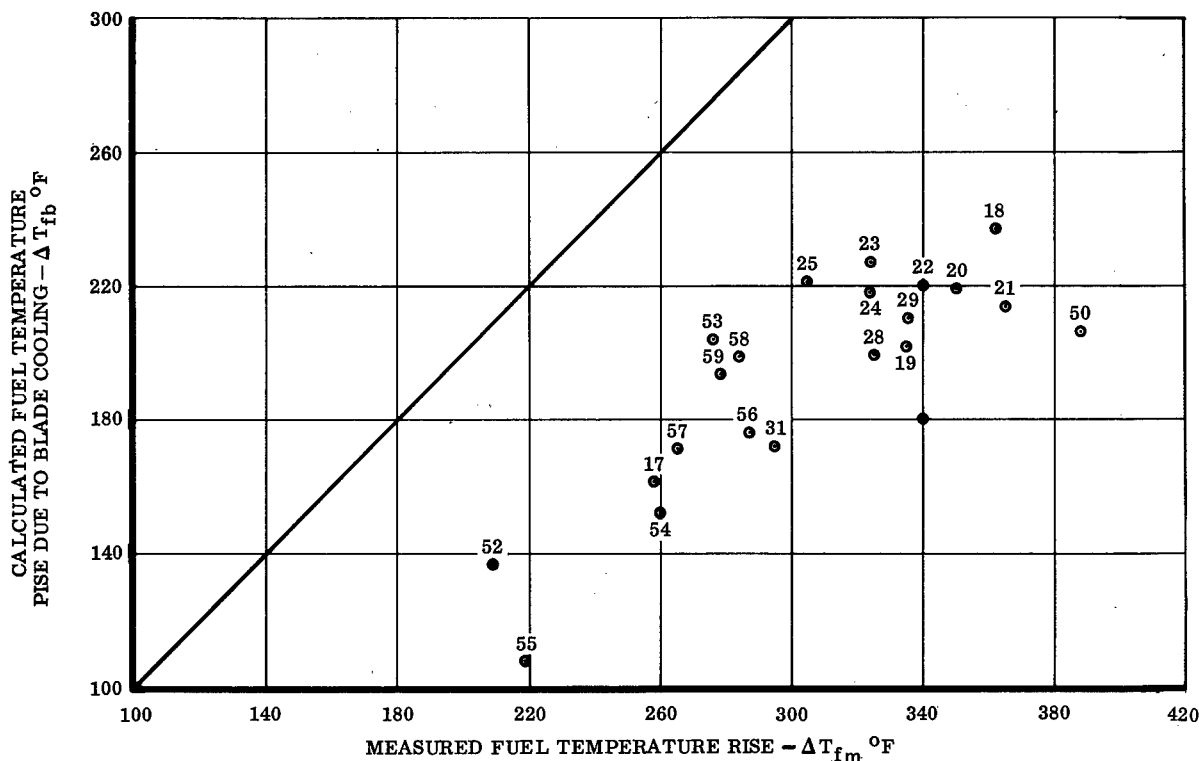


Figure 384. Comparison of Calculated and Measured Fuel Temperature Rise.

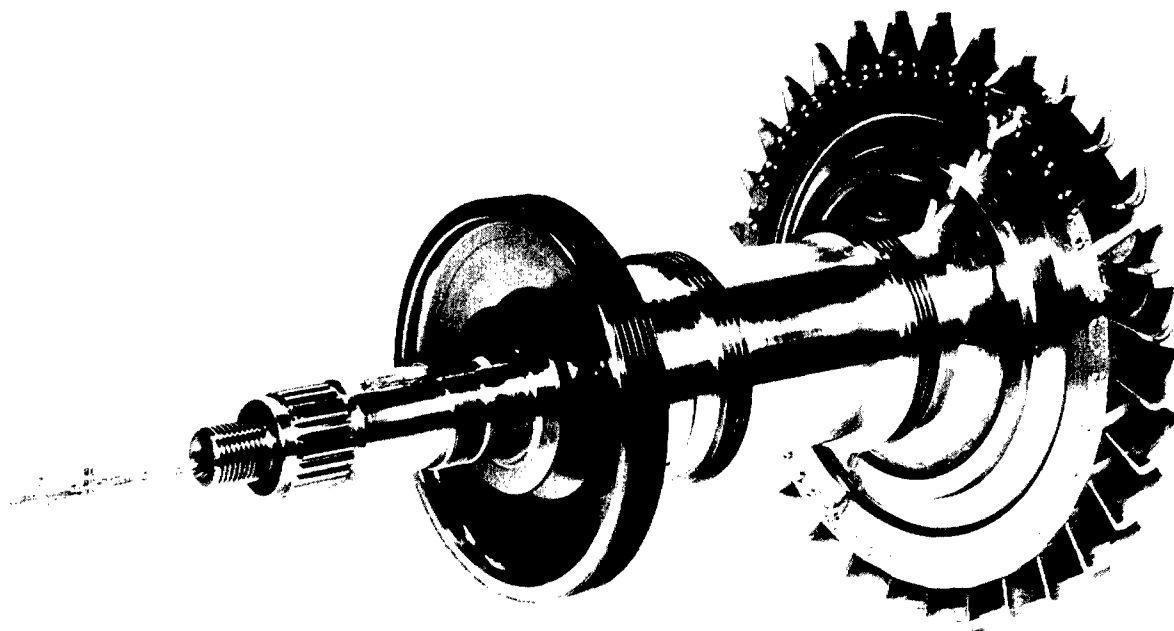


Figure 385. Rotor Disc Temperature Instrumentation.

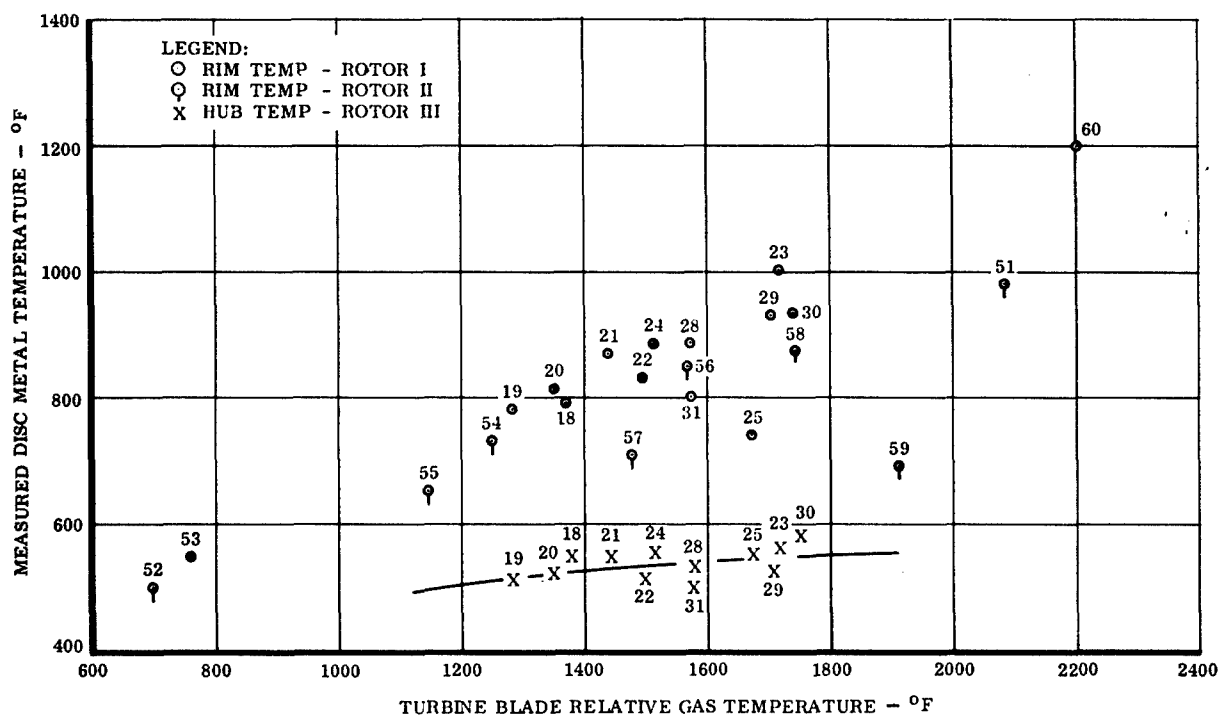


Figure 386. Measured Disc Temperatures.

The heat flow pattern of the disc is shown schematically in Figure 387, along with the applicable heat flow equations. Heat flow into the disc rim was based on the total rim area exposed to the hot gas and the temperature difference between relative gas temperature and measured rim temperature. The rim heat transfer coefficients were calculated from the turbulent flow relation:

$$N_u = \frac{h D}{K} = 0.023 (R_e)^{0.8} (P_r)^{1/3} \quad (24)$$

where

N_u = Nusselt number

h = heat transfer, coefficient, Btu/hr-ft²°F

D = hydraulic diameter, ft

K = thermoconductivity, Btu/hr-ft °F

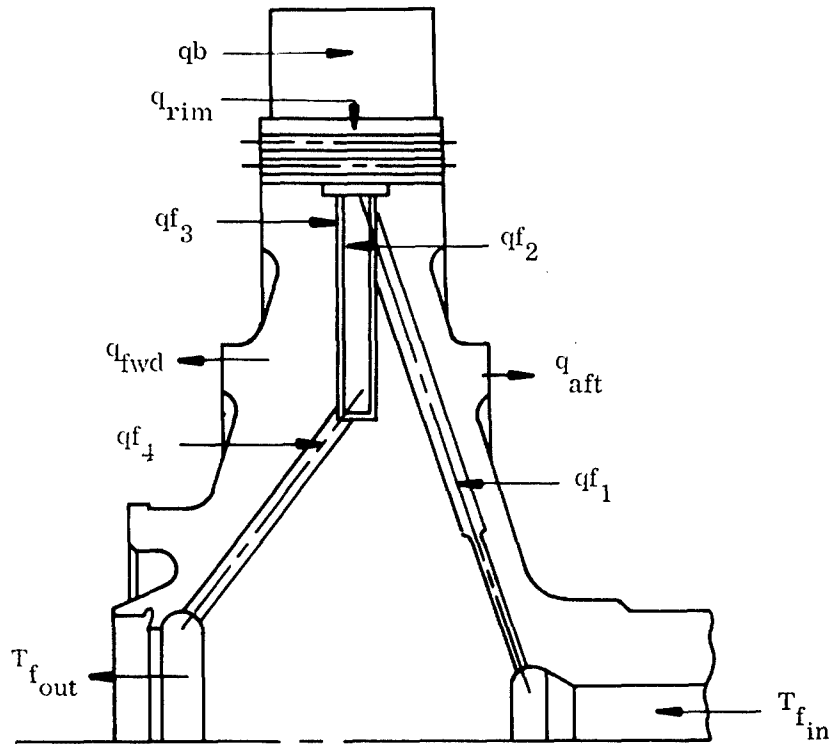
R_e = Reynolds number

P_r = Prandtl number

Fuel side heat transfer coefficients were calculated from

$$N_u = \frac{h D}{K} = 0.0296 (R_e)^{0.8} (P_r)^{1/3} \quad (25)$$

with variables identified as above.



$$\begin{aligned}
 q_f &= W_f C_{pf} (T_{f_{out}} - T_{f_{in}}) \\
 &= q_b + q_{rim} - q_{fwd} - q_{aft} \\
 &= q_{f_1} + q_{f_2} + q_{f_3} + q_{f_4}
 \end{aligned}$$

$$\begin{aligned}
 q_b &= q_{f_{hex}} \\
 q_{rim} &= q_{fwd} + q_{aft} + q_f + q_{f_3} + q_{f_4} \\
 q_{f_{disc}} &= q_{f_1} + q_{f_3} + q_{f_4}
 \end{aligned}$$

where

$$\begin{aligned}
 q_b &= h_b s_b (T_{rel} - T_b) \\
 q_{rim} &= h_{rim} s_{rim} (T_{rel} - T_{rim}) \\
 q_{f_1} &= h_{f_1} s_1 (T_{w_1} - T_{f_1}) \\
 q_{f_2} &= h_{f_2} s_2 (T_{w_2} - T_{f_2}) \\
 q_{f_3} &= h_{f_3} s_{f_3} (T_{w_3} - T_{f_3}) \\
 q_{fwd} &= h_{fwd} s_{fwd} (T_{fwd} - T_{air_{fwd}}) \\
 q_{aft} &= h_{aft} s_{aft} (T_{aft} - T_{air_{aft}})
 \end{aligned}$$

Figure 387. Heat Flow Through the Disc.

Heat flow out of the forward and aft faces of the disc was based on the difference between the cooling air temperature and a mean disc temperature defined as the logarithmic mean between measured hub and rim temperatures. An average heat transfer coefficient was calculated for flow over a rotating disc:

$$\bar{N}_u = \frac{\bar{h} r_o}{K} = 0.015 \frac{(W r_o^2)^{0.8}}{(\gamma)} - 100 \frac{(r_c)^2}{(r_o)^2} \quad (26)$$

where

\bar{N}_u = average Nusselt number from $r = r$ to $r = r_o$

\bar{h} = average heat transfer coefficient between $r = 0$ and $r = r_o$, Btu/hr-ft² °F

K = thermoconductivity, Btu/hr-ft °F

ω = angular velocity of the disc, rad/sec

r_o = outer radius of the disc, ft

γ = kinematic viscosity, ft²/sec

r_c = radius of the transition from laminar to turbulent flow, ft

All heat entering the disc through the rim which is not rejected to the cooling air at the forward and aft disc surfaces must be rejected to the fuel. This occurs through the walls of the heat exchanger well and the inlet and exit supply tubes, Figure 387. Conduction from the disc to the rotor shaft is neglected because of the small conduction areas available.

The heat flow at the rim and the forward disc surface was calculated for several data points. Heat flow at the rear face of the disc, the wall of the heat exchanger well, and the inlet and exit supply tubes cannot be directly calculated because the wall temperatures are not known. Consequently, the heat flow at the rear face of the disc was assumed to be equal to the heat flow at the forward face. The heat rejected to the fuel

from the disc was then determined as the difference between the heat flow into the rim and the heat flow at the forward and rear disc surfaces. From Figure 387,

$$\begin{aligned} q_{\text{rim}} &= h_{\text{rim}} S_{\text{rim}} (T_{\text{rel}} - T_{\text{rim}}) \\ &= q_{\text{fwd}} + q_{\text{aft}} + q_{f_3} + q_{f_4} \end{aligned} \quad (27)$$

then

$$\begin{aligned} q_{\text{rim}} - q_{\text{fwd}} - q_{\text{aft}} &= q_{f_1} + q_{f_3} + q_{f_4} \\ &= q_{f_{\text{disc}}} \\ &= W_f C_{pf} \Delta T_{f_{\text{disc}}} \end{aligned}$$

Therefore, the heat rejected to the fuel from the disc can be converted directly to fuel temperature rise without using the heat flow equations for the inlet and exit fuel supply tubes and the heat exchanger well. This was done for the data points under discussion.

The fuel temperature rise due to disc cooling thus obtained was added to the fuel temperature rise due to blade cooling calculated by the Closed-Loop Thermosyphon Computer Program, and the result was compared to the measured value. This comparison is shown in Figure 388.

Calculated values show an average positive deviation of 11 percent and an average negative deviation of 8 percent from measured values. The maximum deviation obtained was a positive 22 percent. Positive deviation indicates a measured fuel temperature rise greater than the calculated value. Agreement of this order is considered to be well within experimental accuracy.

The above agreement between measured and calculated fuel temperature rise verifies the cooling effectiveness predicted by the Continental Closed-Loop Thermosyphon Computer Program and thus establishes turbine blade metal temperature. This is particularly important since turbine blade temperatures were not directly measured during

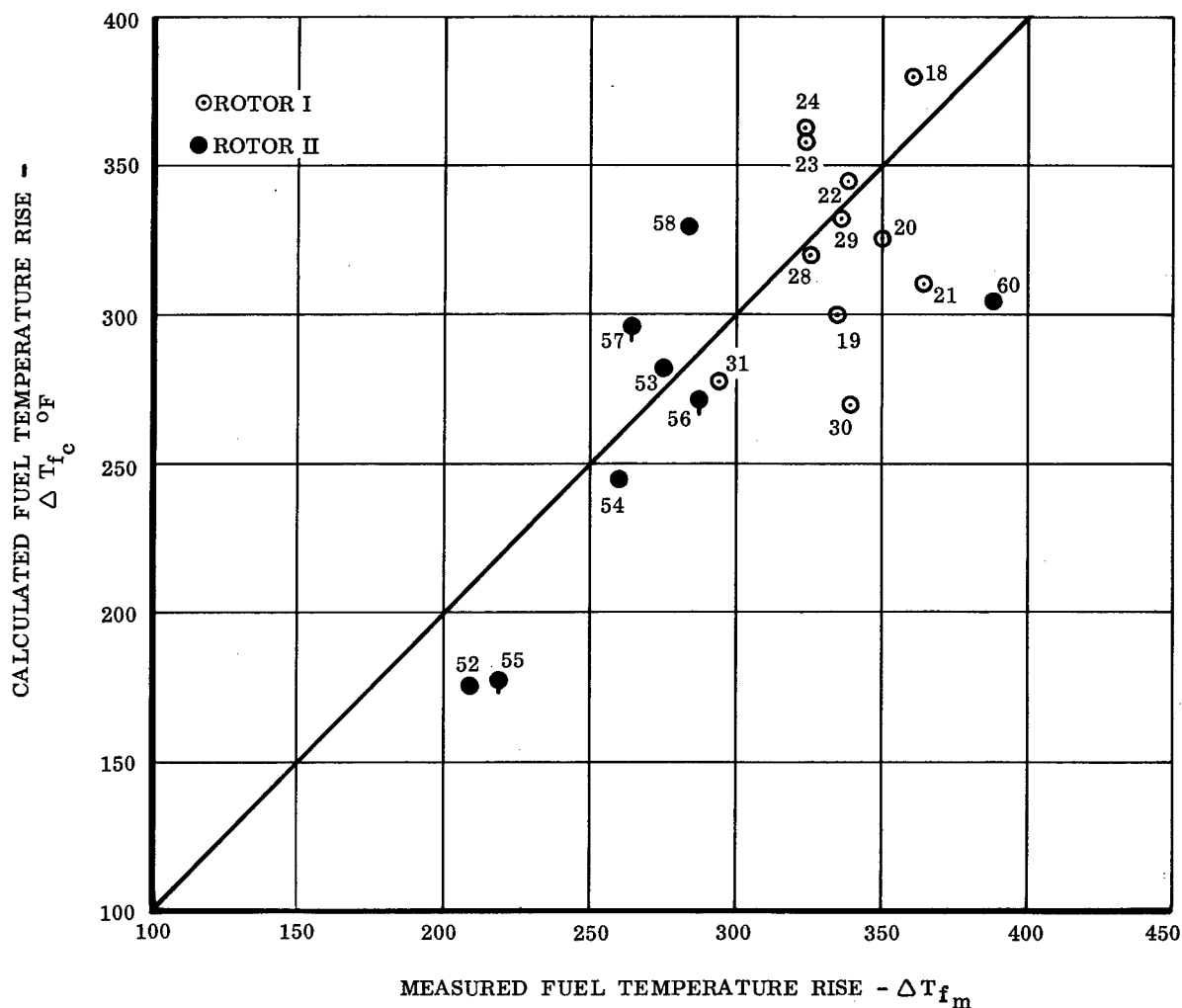


Figure 388. Comparison of Calculated and Measured Fuel Temperature Rise.

these tests, and, consequently, must be determined analytically. Figure 389 is a plot of calculated turbine blade metal temperature (based on actual test conditions) and shows directly the degree of cooling obtained, since relative gas temperature is approximately equal to the temperature that an uncooled blade would attain.

At 2300°F TIT, the blades are cooled to a temperature of 600°F below blade relative gas temperature. Blade cooling increased to 680°F at a TIT of 2450°F. This shows a marked improvement over the 400° to 500°F cooling presently attainable at these turbine inlet temperatures with air cooling. In addition, the air bleeding penalties associated with air cooling are eliminated.

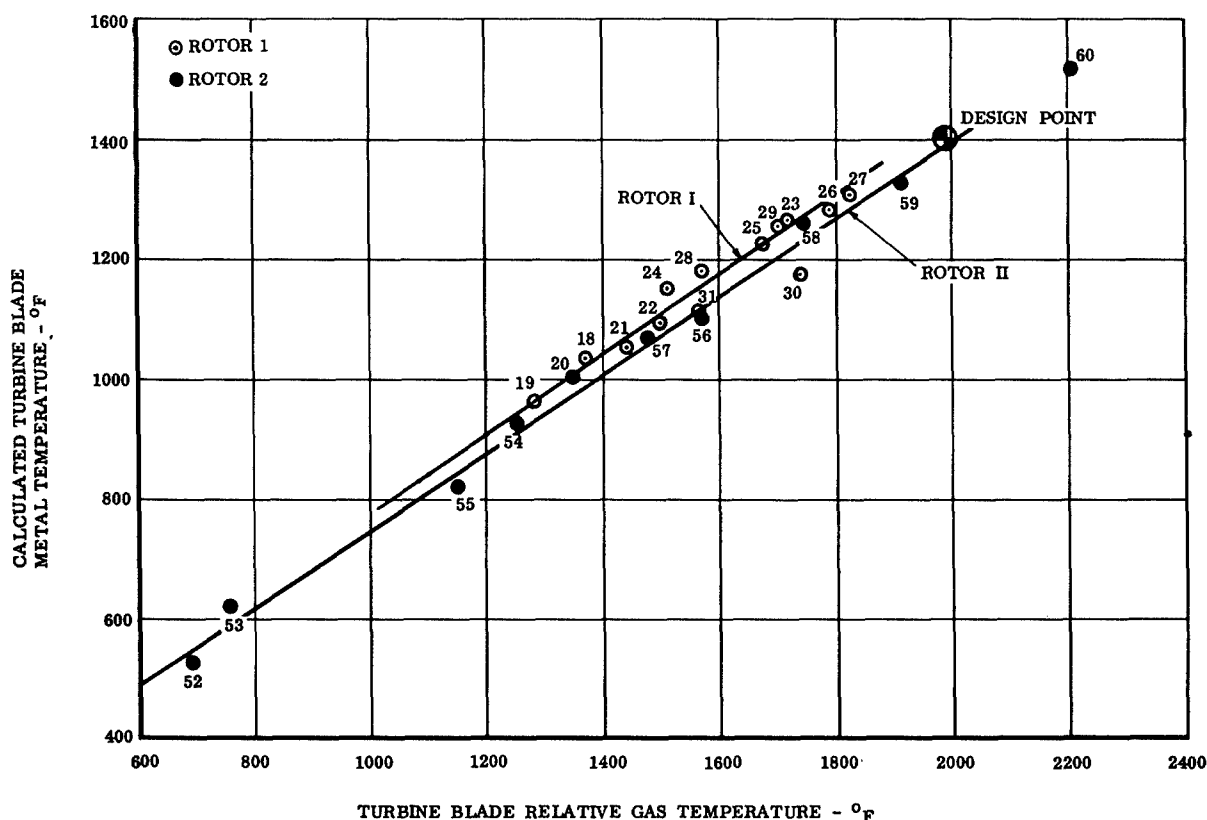


Figure 389. Calculated Turbine Blade Temperature.

Design point conditions are also shown in Figure 389 and fall within the band of the reduced test data.

The apparent separation of the data is, as discussed earlier, the result of a difference in measured fuel flow between the two rotors. To further verify this, several test points were rerun on the computer program with an adjusted fuel flow arbitrarily based on 100-percent combustor efficiency. The result of this adjustment is shown in Figure 390, in which the data separation is eliminated, thus indicating the separation to be a fuel flow phenomenon.

Figures 388 and 389 also emphasize the predictable performance of the turbine blade cooling system at off-design as well as on-design point conditions. This allowed operation of the turbine at a TIT of 2450°F, approximately 150°F above the design point temperature of 2300°F, with reasonable assurance that blade metal temperature would not exceed limits imposed by stress considerations.

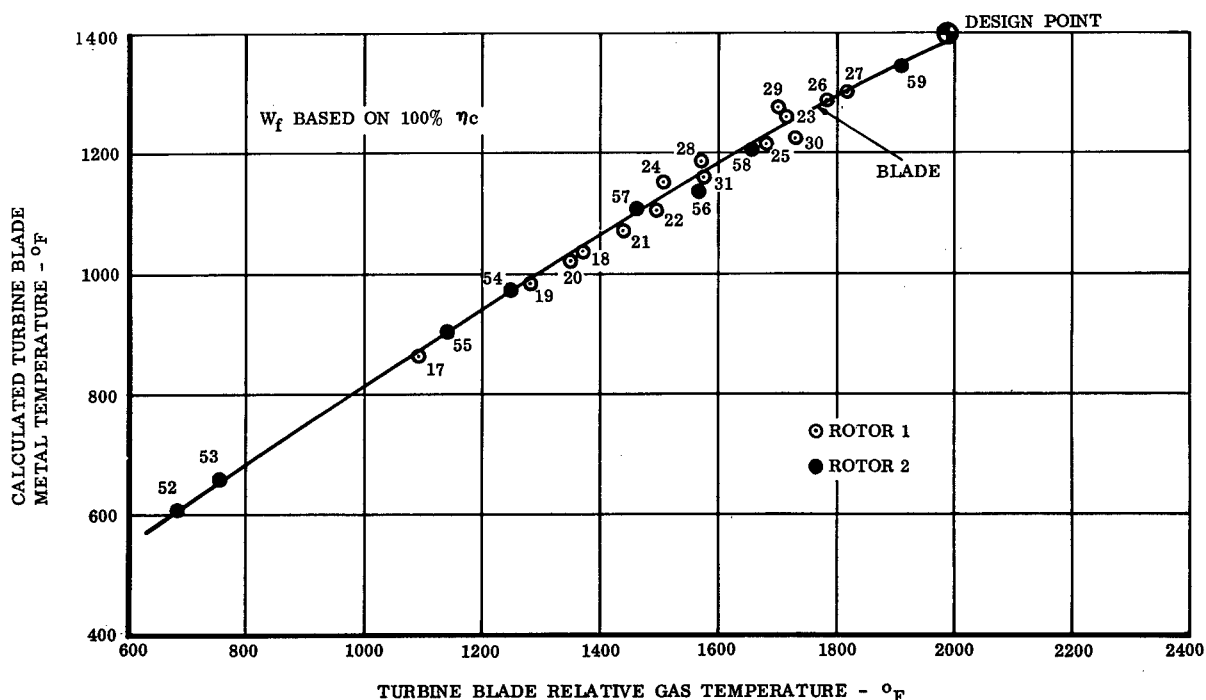


Figure 390. Calculated Turbine Blade Temperature With Adjusted Fuel Flow.

Several test points with stress levels well beyond the ultimate strength of the material at the uncooled blade temperatures were recorded. This is discussed in further detail under Mechanical-Structural Integrity. These test points again emphasize the effectiveness of the cooling system and its successful performance throughout this program.

Turbine Inlet Nozzle - The turbine inlet nozzle is a continuous-ring, air-cooled sheet metal design of welded construction, Figure 391. Cooling is provided by air passing through the hollow, finned nozzle vanes.

The Continental annular combustor requires part of the total airflow (approximately 25 percent) to pass through the hollow nozzle vanes on its way to the primary zone of the combustor. This air can be utilized to cool the vanes with negligible loss to the cycle. Slots in the trailing edge cool this portion of the vane and pass approximately 0.5 percent of the total airflow. The trailing-edge slots are clearly visible in Figure 392.

In order to achieve adequate cooling, without significantly increasing the pressure loss in the nozzle vanes, the internal surface area of the vanes was augmented by the addition of fins, Figure 393. These fins effectively increased the surface area by a factor of approximately three.

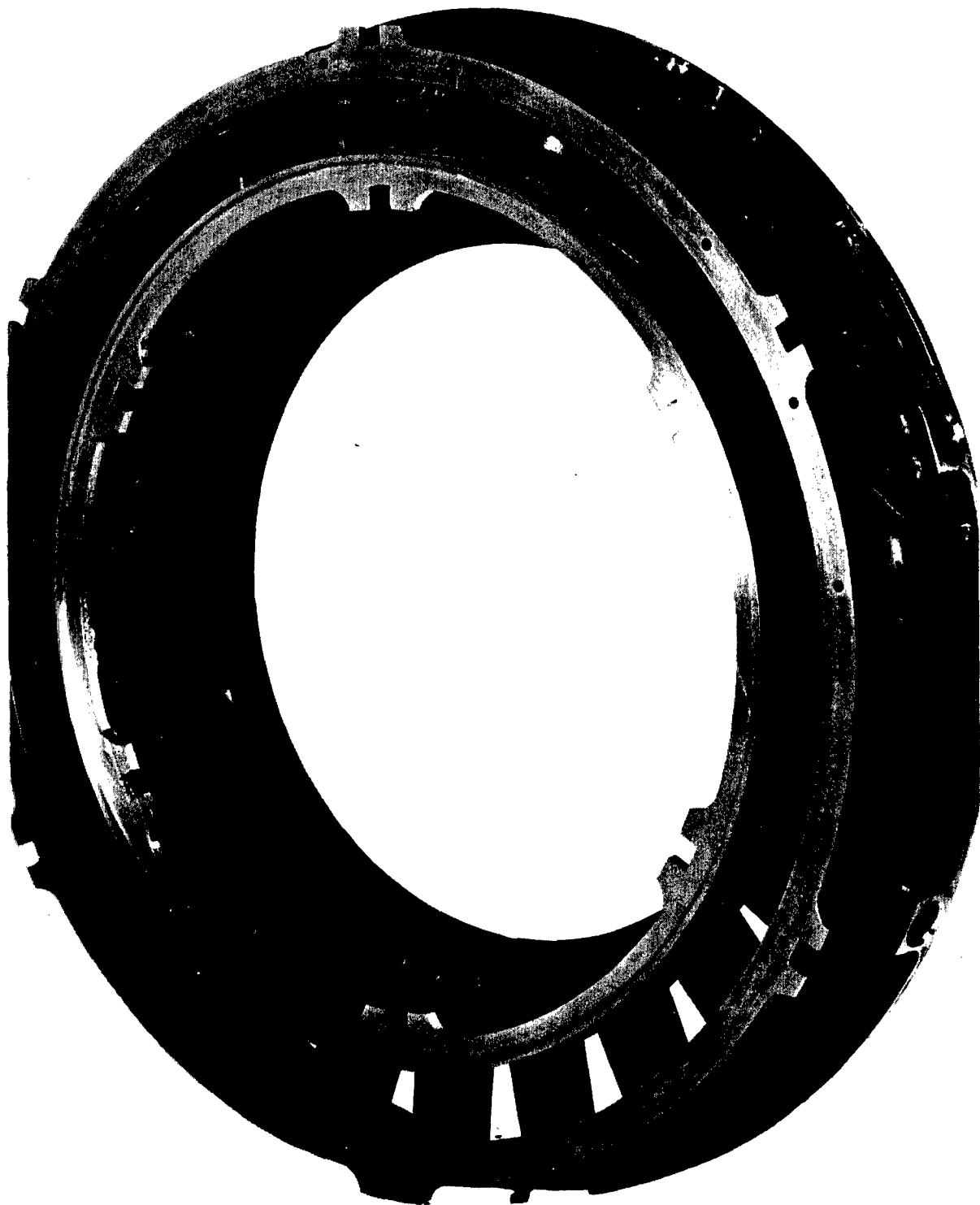


Figure 391. Air-Cooled Nozzle Vane Assembly.

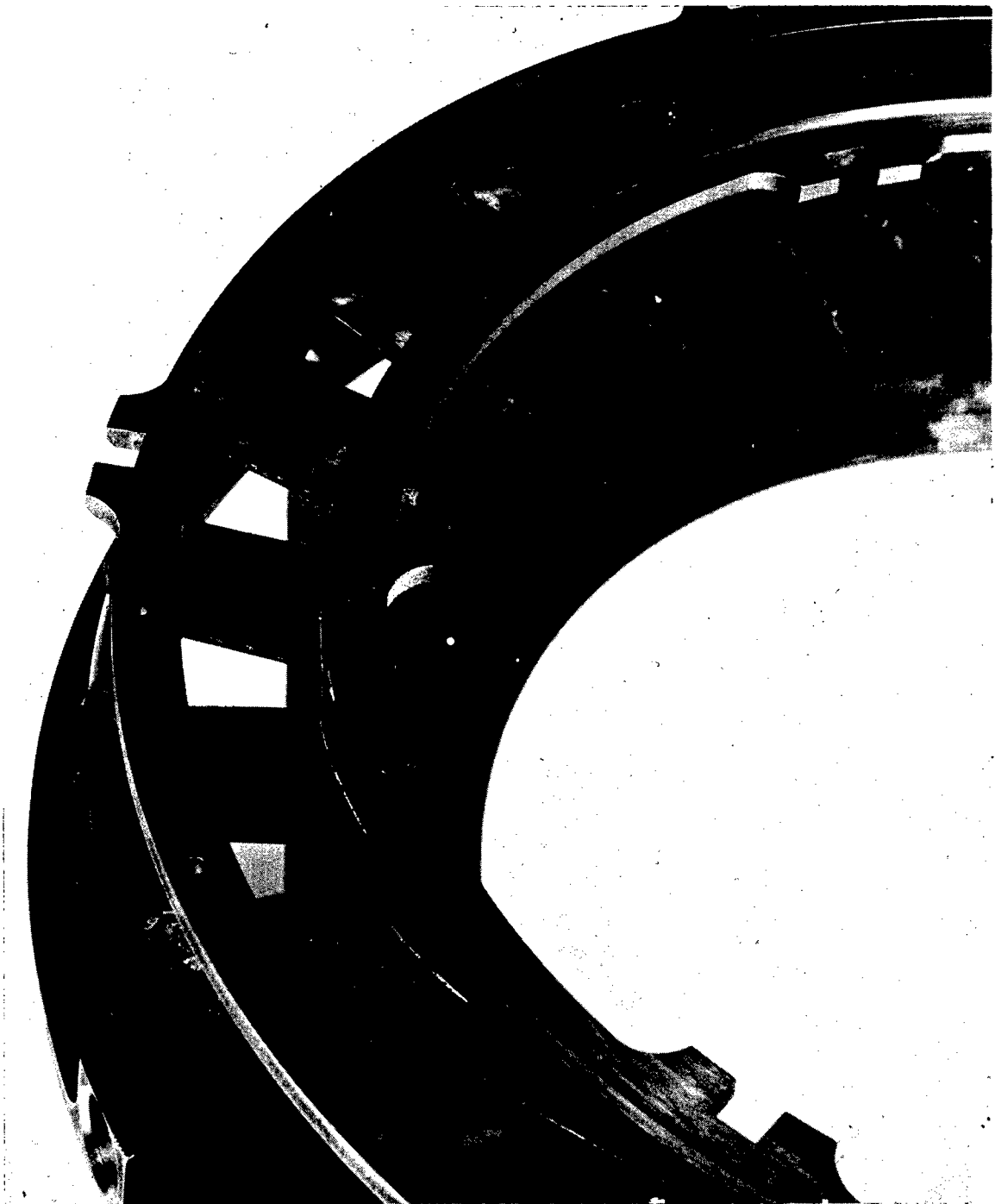


Figure 392. Trailing-Edge Slots, Air-Cooled Nozzle.



Figure 393. Interior Cooling Fins, Air-Cooled Nozzle.

This nozzle vane is identical to the vanes tested in the hot cascade rig with the exception of material and fabrication changes. These changes are tabulated below.

	Cascade Rig	Turbine Inlet Nozzle
MATERIAL	TD - Nickel	Rene'41
FABRICATION	Brazed	Welded

As indicated by the cascade tests, the air-cooled nozzle performed as predicted. Vane metal temperatures were measured during the test program and were compared to the vane temperatures obtained during the cascade tests. This comparison is shown in Figure 394 for the nozzle vane leading edge.

- COMBUSTOR AND TURBINE TESTS (MEASURED DATA)
- × CASCADE TESTS
- ⊗ C AND T TESTS CORRECTED FOR CONDUCTION LOSSES

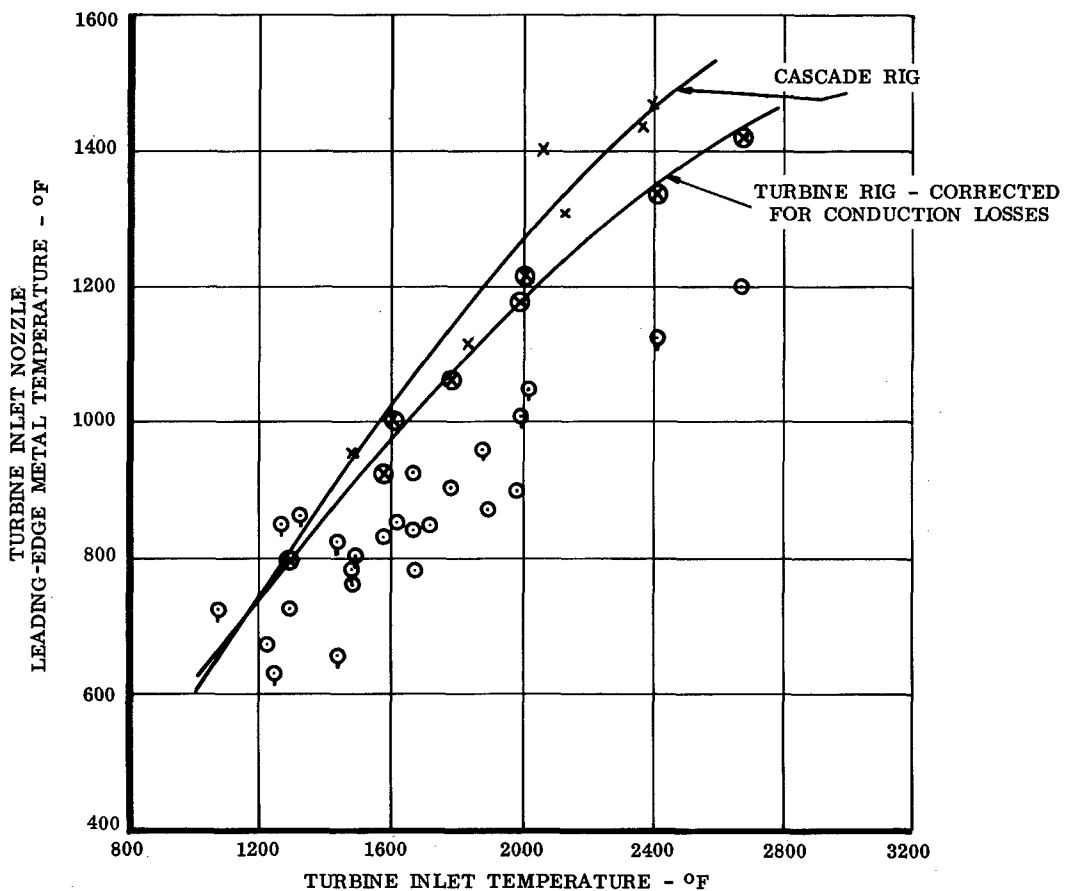


Figure 394. Measured Temperatures Corrected for Conduction Errors.

It is apparent that the metal temperatures measured on the full, round turbine rig are considerably lower than those measured during the cascade tests. As desirable as this appears, these metal temperatures are unreasonably low. An investigation revealed the thermocouples attached to the vanes of the full, round turbine inlet nozzle to be attached in such a manner as to allow a significant conduction error because of the cooling air passing over the thermocouple.

Reference 45 provides a technique for calculating the conduction error in thermocouples by measuring gas temperatures. This technique was adapted to provide an approximation of the conduction error occurring in the measurement of the vane metal temperature by calculating an equivalent immersion depth and a temperature distribution function based on cooling air parameters.

The result of this approximation is also shown in Figure 394. It is difficult to determine thermocouple conduction losses accurately, and, in view of the approximation involved here, the agreement with cascade data was considered to be good.

This agreement verified that the nozzle cooling was performing as predicted analytically and by cascade test data. Consequently, no additional measurements of vane metal temperature were considered to be necessary. Further verification of the turbine inlet nozzle cooling effectiveness was provided by steady-state operation at local gas temperatures near 3000°F with no mechanical or thermal distress.

Total hot operating time of the turbine inlet nozzle was 261 hours. No thermal or mechanical distress was evident.

Exhaust Diffuser - The turbine exhaust diffuser required cooling because of the high mainstream temperatures experienced during rig running. These temperatures were above 2300°F during combustor development testing and above 2000°F during turbine testing.

Cooling of the exhaust diffuser was achieved through the use of a "double-wall" design, shown in Figure 395. This type of construction provided two important advantages:

1. The cooling airflow required was minimized since the air was directed along the parts to be cooled.
2. Structural components were shielded from the hot mainstream. This provided greater strength due to lower temperatures and reduced thermal gradients.

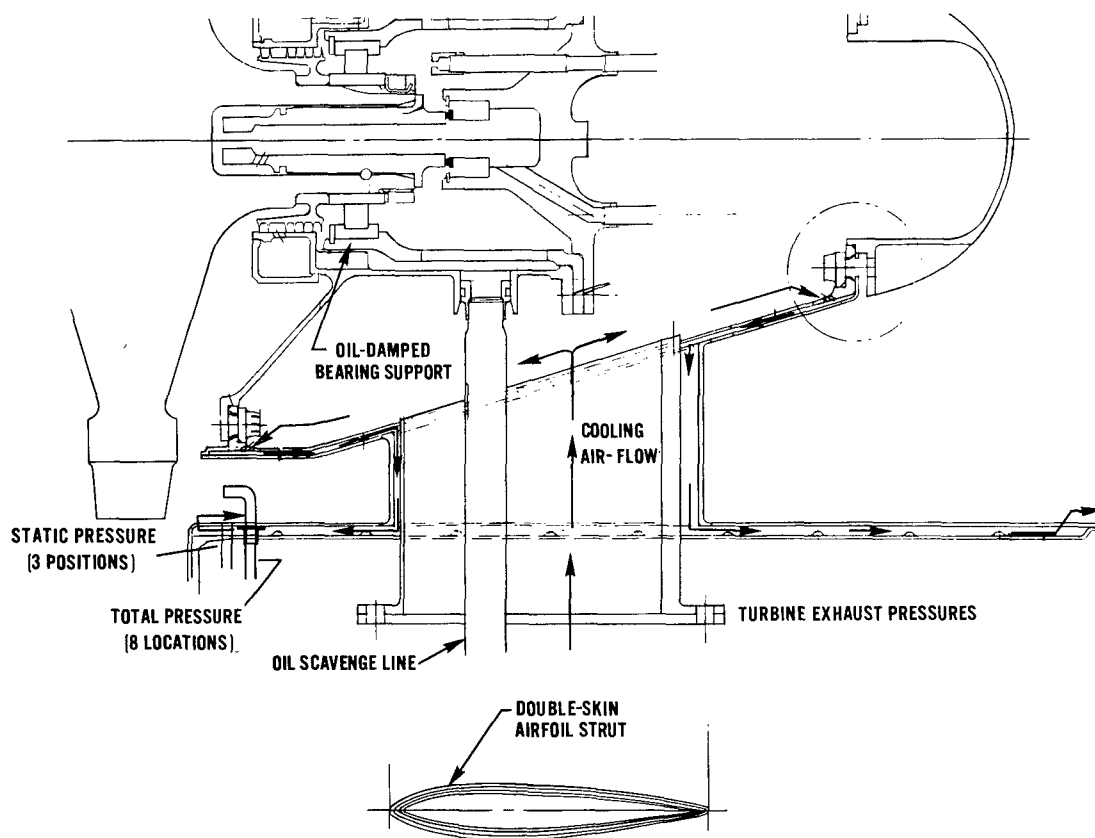


Figure 395. Exhaust Diffuser Cooling.

The cooling airflow path, along with design metal temperatures, is shown in Figure 396. Cooling air bathes the bearing housing before being directed along the inner duct wall, out through the vanes and along the outer duct wall to be dumped into the mainstream at the front and rear through circumferential orifices.

Design point cooling airflow (at compressor discharge temperature) was 0.132 pound per second. To verify the cooling effectiveness, early in the combustor development program the exhaust diffuser was instrumented to provide wall temperatures, and several test points were taken. These were taken at constant mainstream conditions (0.615-lb/sec flow at 1448°F) and at varied cooling airflow rates.

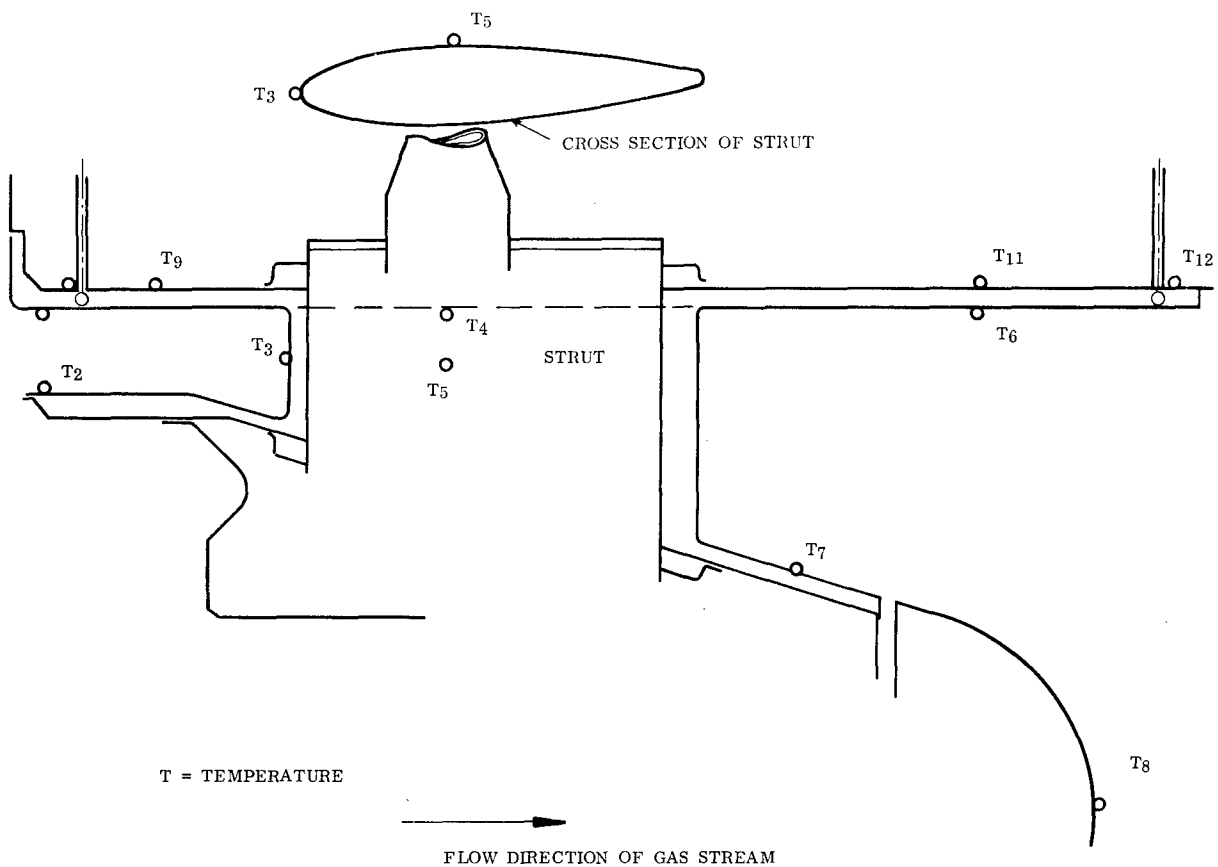


Figure 397. Thermocouple Locations for Exhaust Diffuser Wall.

As can be seen, the maximum temperature recorded was 1100°F at position 4. This gives a cooling effectiveness of 0.252 at this condition. Cooling effectiveness is defined as

$$\frac{T_g - T_w}{T_g - T_c} = E_c \quad (28)$$

where E_c = cooling effectiveness

T_g = gas temperature

T_w = wall temperature

T_c = coolant temperature

MAINSTREAM TEMP TIT - 1448°F
 COOLANT TEMP T_c - 67°F
 MAINSTREAM GAS FLOW - 0.615 lb/sec

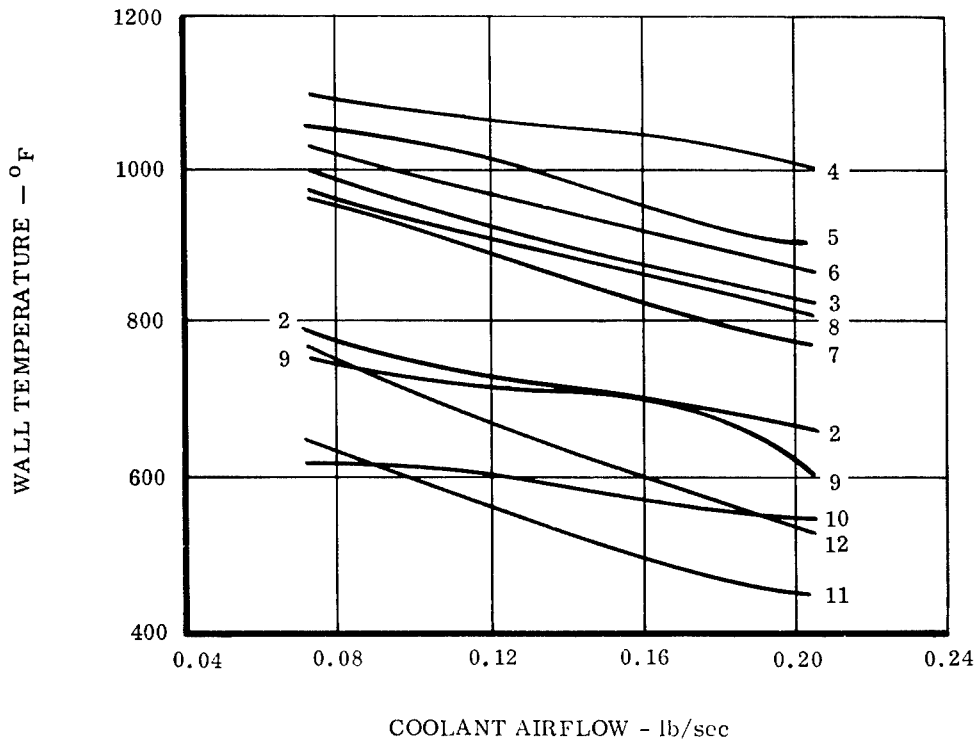


Figure 398. Exhaust Diffuser Wall Temperature for Several Coolant Flow Rates.

Because of the wall temperatures and cooling effectiveness obtained during the above tests, the exhaust diffuser was considered to be adequately cooled, and no further cooling tests were done.

The adequacy of the cooling design was subsequently demonstrated during 261 hours of running time with only minor mechanical or thermal problems, as further described in the Mechanical-Structural Integrity section.

MECHANICAL-STRUCTURAL INTEGRITY

SUMMARY

The fluid-cooled turbine hardware was tested under varying conditions of temperature (to 2450°F TIT), thermal cycling (87 start-stops), and rotor tip speed (1600 ft/sec, 45,000 rpm), to evaluate its capability and endurance characteristics. No catastrophic structural failures occurred during the entire test program.

The total running time of the components is shown in Table XXXII.

TABLE XXXII COMPONENT RUNNING TIME	
Item	Time - Hrs
Gearbox	272
Combustor, Nozzle Assembly, and Rotor Shroud	261
Exhaust Diffuser	261
Turbine Rotor Assembly I	138
Turbine Rotor Assembly II	17

The turbine rotor was subjected to the running times as shown in Table XXXIII for data acquisition at temperatures above 2080°F.

TABLE XXXIII DATA ACQUISITION RUNNING TIME		
Average Turbine Inlet Temperature, °F	Time Hrs Min	
2090 ± 10°F	2	15
2150 ± 10°F	2	30
2210 ± 10°F	1	30
2344	0	20
2450	0	35

The total data point time at temperatures above 2080°F is 7 hours. These times include only actual data points. The time required to establish the rig equilibrium condition at temperature and the time at temperature when a rig malfunction occurred are not included in the time at temperature. A conservative estimate of running time for these items is 14 hours, thus increasing the total time at temperatures above 2080°F to approximately 21 hours.

The hardware status after completion of testing is given in Table XXXIV.

TABLE XXXIV HARDWARE STATUS AFTER TESTING	
Component	Remarks
Combustor	No Failures
Turbine Inlet Nozzle	Minor Cracking One Vane
Turbine Rotor Shroud	Minor Dents From Blade Tip-Cap Failures
Exhaust Duct	Minor Crack at Weld
Gearbox	One Bearing Failure
Turbine Rotor Shafts.	No Failures
Turbine Disc	No Failures
Turbine Blade Attachment and Pins. . . .	No Failures
Turbine Blades:	
Turbine Rotor I 19 Blades (Test Time 138 Hours)	No Failures
Turbine Rotor II 17 Blades. (Test Time 17 Hours)	No Failures
Blade Tip Caps	18 Failed
Blade Airfoil Cracks.	18 Failed
Blade-to-Disc Fuel Seals. (180 Tested)	2 Failed

The prime mechanical problem was failure of tip caps, which was due to the lack of weld penetration at the airfoil tip-cap joint and the manufacturing inconsistencies in the thin blade airfoil wall.

During testing, normal rig vibration was 0.2 mil. Only once, when two adjacent blade tip caps failed, did abnormal rig vibration (0.8 mil) become noticeable.

MECHANICAL ASSEMBLY

Turbine Rotor

The fluid-cooled turbine rotor assembly, Figure 399, consisted of a fuel slinger shaft, a fuel pressurizing valve, a main drive shaft, a disc, blades, blade-to-disc seals, and blade attachment pins. The shaft assemblies were welded to the disc. The assembly techniques were established during assembly of Rotor I.

Rotor I had dimensional deviations at the pin slots, as discussed in Manufacturing Technology. The pin slots of the disc were difficult to machine to print dimensions. This necessitated a selective fit of each pin into an individual pin slot. The pin selection varied from 0.080 to 0.078 inch in diameter in increments of 0.0005 inch. All pins were pressed into position. The pins, once installed, were removed in the opposite direction from which they were inserted. Staking of the pins was not considered to be necessary since the centrifugal force on the blade during running would retain them.

The cast blade consisted of an aerodynamic profile, a platform, and a heat exchanger. The heat exchanger was a stem which was inserted into the disc. On the bottom of the blade platform around the stem, a five-root mean square (RMS) finish was required. The rotor cavity into which the blade heat exchanger stem was inserted also had a five-RMS finish. A gold-plated "V" seal was placed between these two finished surfaces. The function of the seal was to prevent fuel from dissipating out of the rotor. It allowed the fuel to pass over the heat exchanger and into the combustor slinger shaft. The gold plating was soft, which enhanced sealing.

Care was taken during inspection and placement of the seal in the rotor cavity so as not to mar the gold seal surface. Micrometer inspection of each seal height was made. Each seal was then assigned to a specific rotor cavity to assure proper crush. The nominal crush allowed for proper sealing was 0.010 inch. The blade-to-disc gap plus the rotor seal cavity depth determined the proper height of seal needed. Blade-to-disc gaps from 0.002 to 0.005 inch were found to provide the best sealing capabilities.

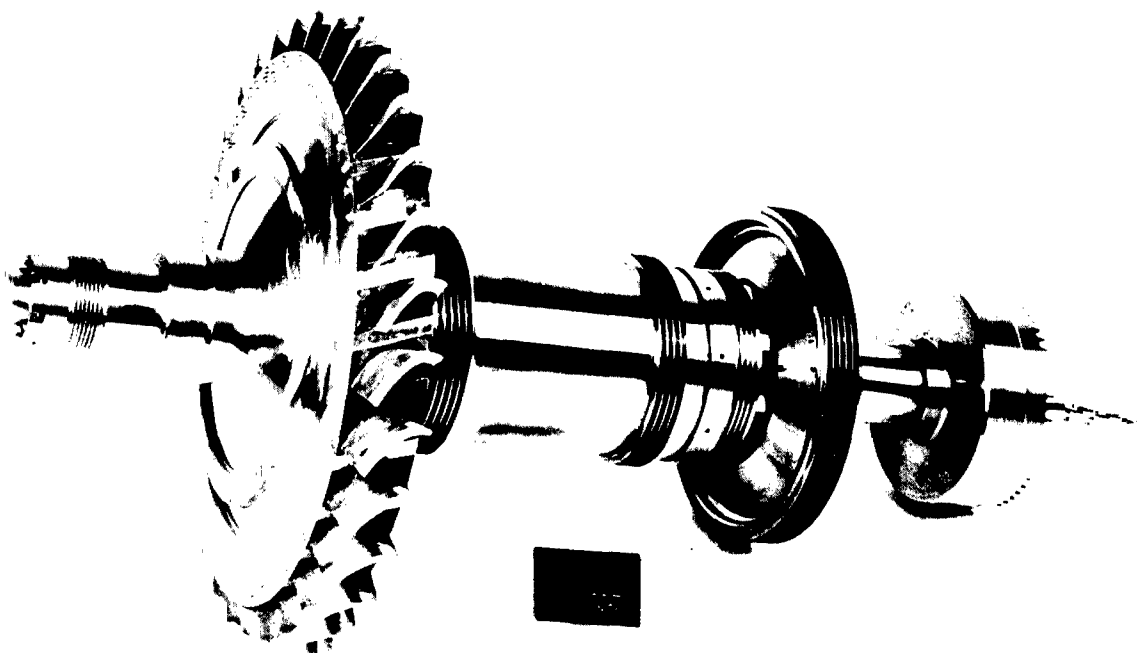


Figure 399. Turbine Rotor Assembly.

Blade-to-disc gaps of 0.010 inch resulted when rotor II blades were assembled into the rotor I disc. The initial set of blades was tailored to disc I slots, while rotor II was fabricated to print dimensions. This was alleviated by plating the blade seal surface. The nickel plating was accomplished by the electrolytic sulfamate process, Figure 400. The plating was then machined to the desired blade-to-disc gap and finish ground.

The plating adherence was evaluated. For 1 hour, the plated blade was heated to 1300°F to check its resistance to spalling. A cross section of the blade was analyzed, Figure 401. The bond of the nickel plated to the Udimet 700 blade was satisfactory and showed no tendency to spall or separate. The blade was assembled into the turbine rotor and pressure checked with satisfactory results.

The blade and disc cavity sealing surfaces were cleaned with acetone prior to installation of the seal.



Figure 400. Nickel Plating of Blade.

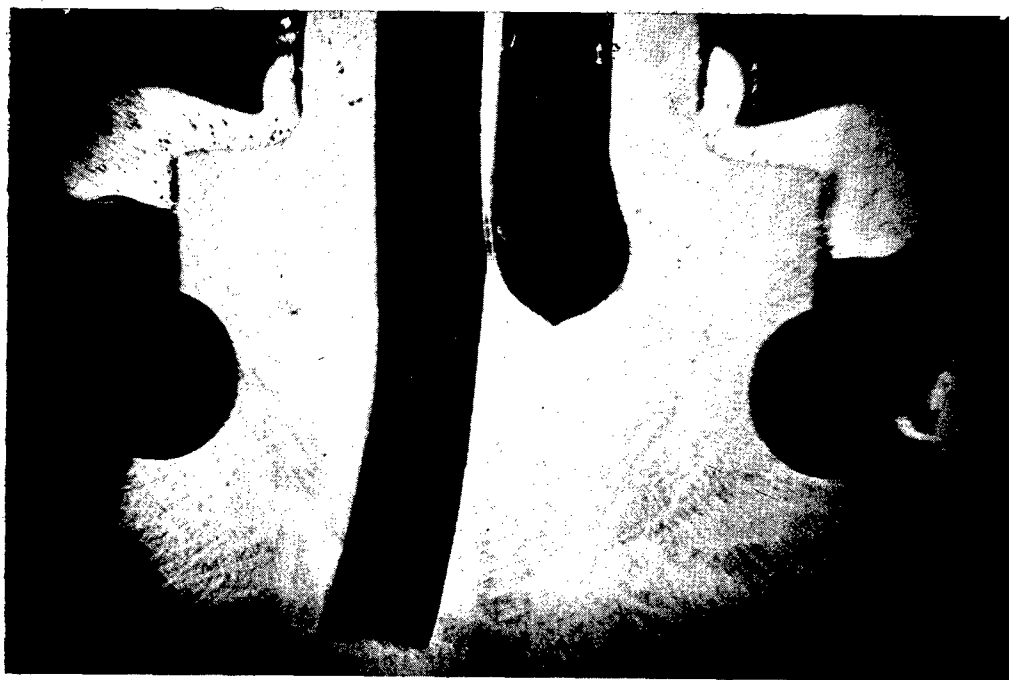


Figure 401. Cross Section of Plating.

After assembly of all the blades, pins, and seals, the rotor was pressure-checked. Shop air, at 100 psig, was applied to the rotor assembly. Each blade seal area was immersed in water to check for seal leakage. Utilizing air at low pressure was considered to be a good leakage check. The seal is required to retain JP-4 fuel at pressures from 1,000 up to 10,000 psi. The higher pressures and fluid density assist in providing a better sealing condition.

The rotor assembly was balanced to 0.005 oz-in. after each assembly. During all tests conducted at various speeds, no evidence of unbalance was noted.

Each blade attachment reassembly required that new "V" seals be installed. The used seals were permanently crushed and were formed to the contour of the initial blade. The seal seat finish, of both blade and disc, was visually inspected at teardown. Imperfections were cleaned with acetone and then polished finely with lapping compound. This method proved to be necessary for good sealing.

Gearbox - Assembly

The gearbox was designed to operate at 52,000 rpm and 1200 hp, with a stepdown gear ratio of 8.06:1. The gearbox hardware consisted of a split cast housing, a pinion gear, and a bull gear plus support bearings, Figures 402, 403, and 404. The design of the assembly is discussed in the Design Section.

The gearbox was positioned in the cell on a 2-inch-thick steel base plate. Anchor bolts fastened the base plate to the cell floor. Oil was pumped to the gearbox and indicated a satisfactory flow at 15 psi. No backlash was detected. The force of the oil impinging on the gear teeth was sufficient to rotate the unit with the face seals removed. A pressure of 35 to 40 psi rotated the bull gear to approximately 30 rpm. Rotation was also sustained at 20 psi.

The gearbox was instrumented. Five thermocouples were installed in the gearbox as follows:

1. Pinion gear thrust (ball) bearing
2. Pinion gear radial (roller) bearing (forward)
3. Pinion gear radial (roller) bearing (aft)
4. Bull gear radial thrust (ball) bearing
5. Bull gear radial (roller) bearing

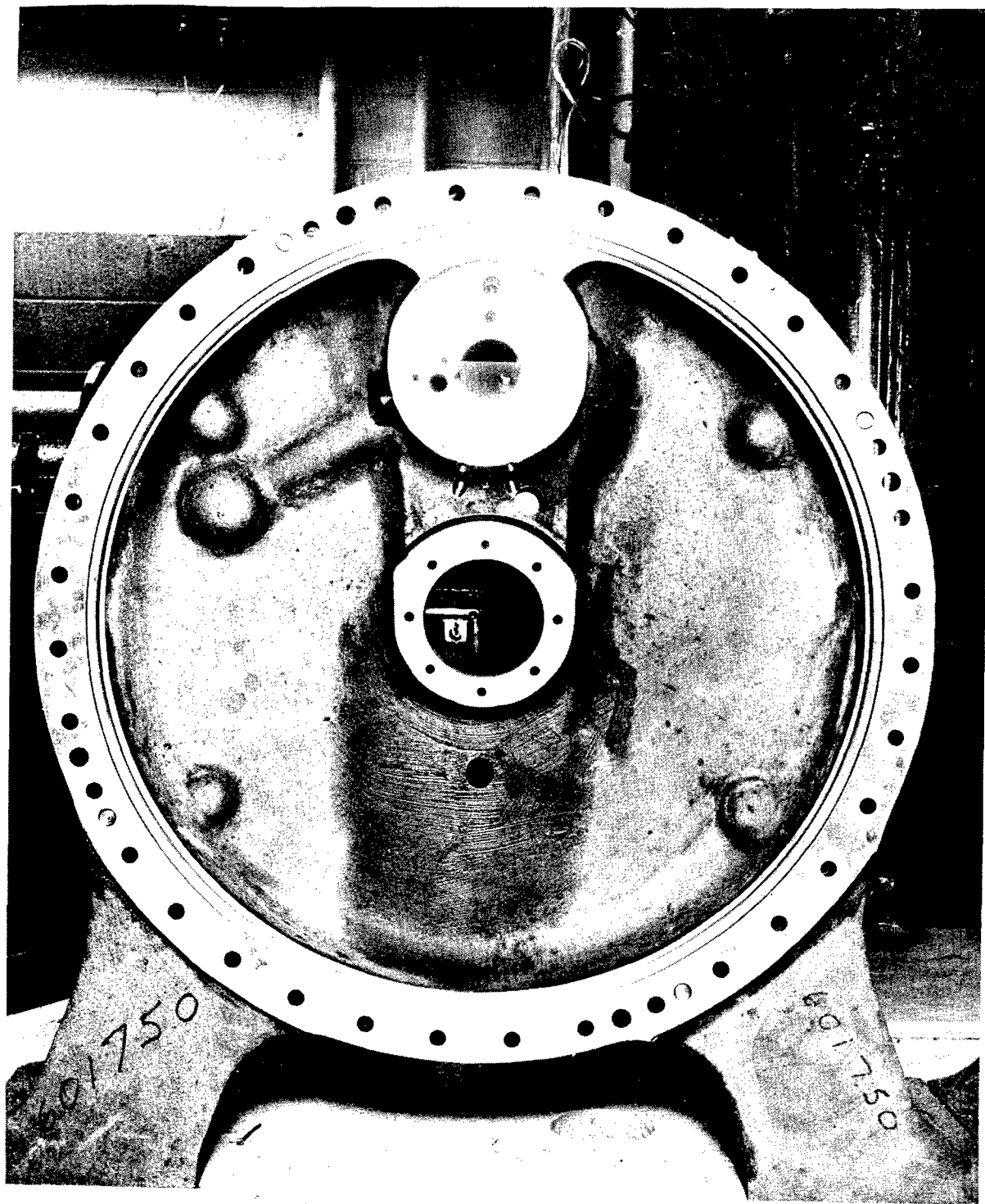


Figure 402. Gearbox Housing - Forward.

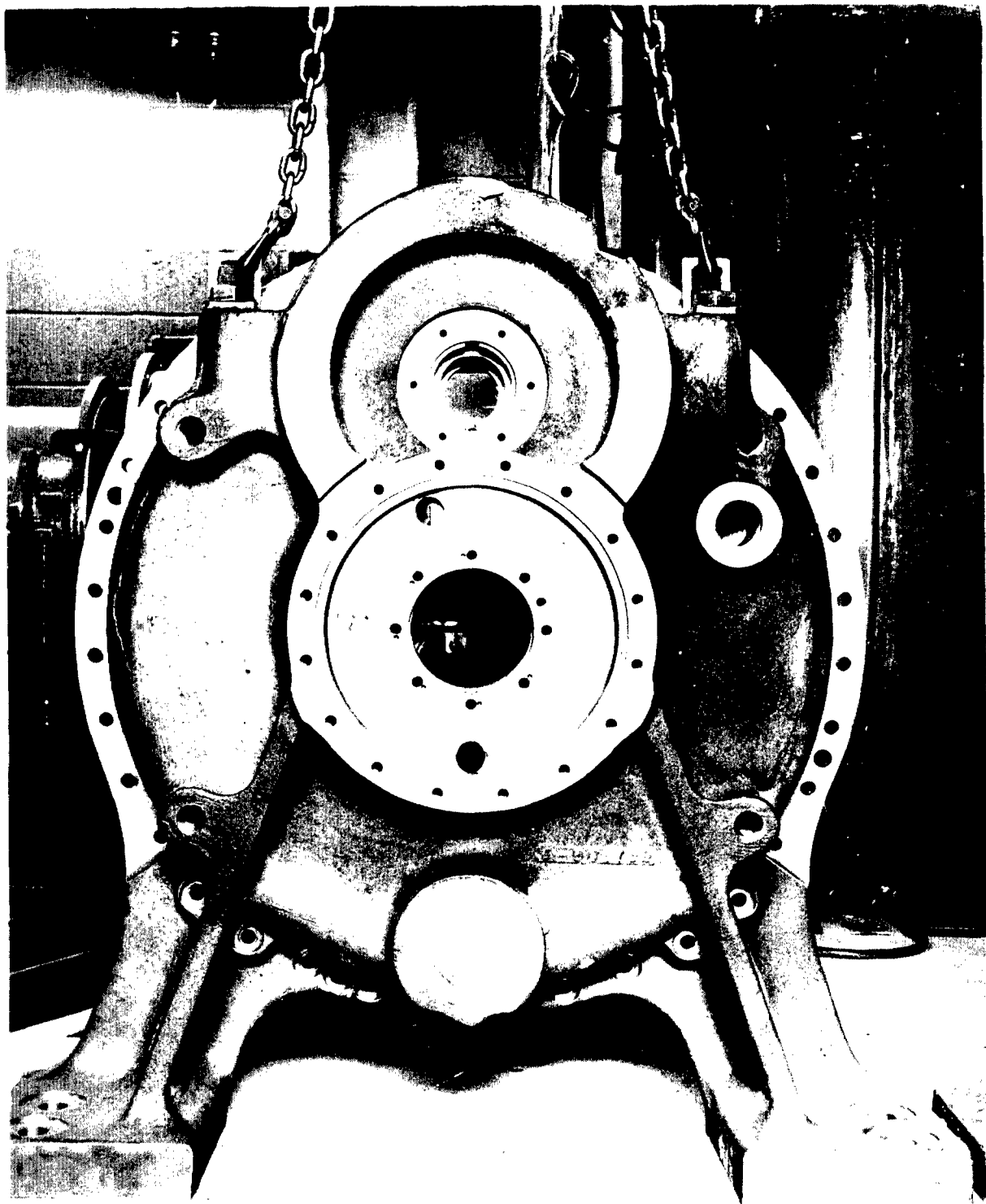


Figure 403. Gearbox Housing - Aft.

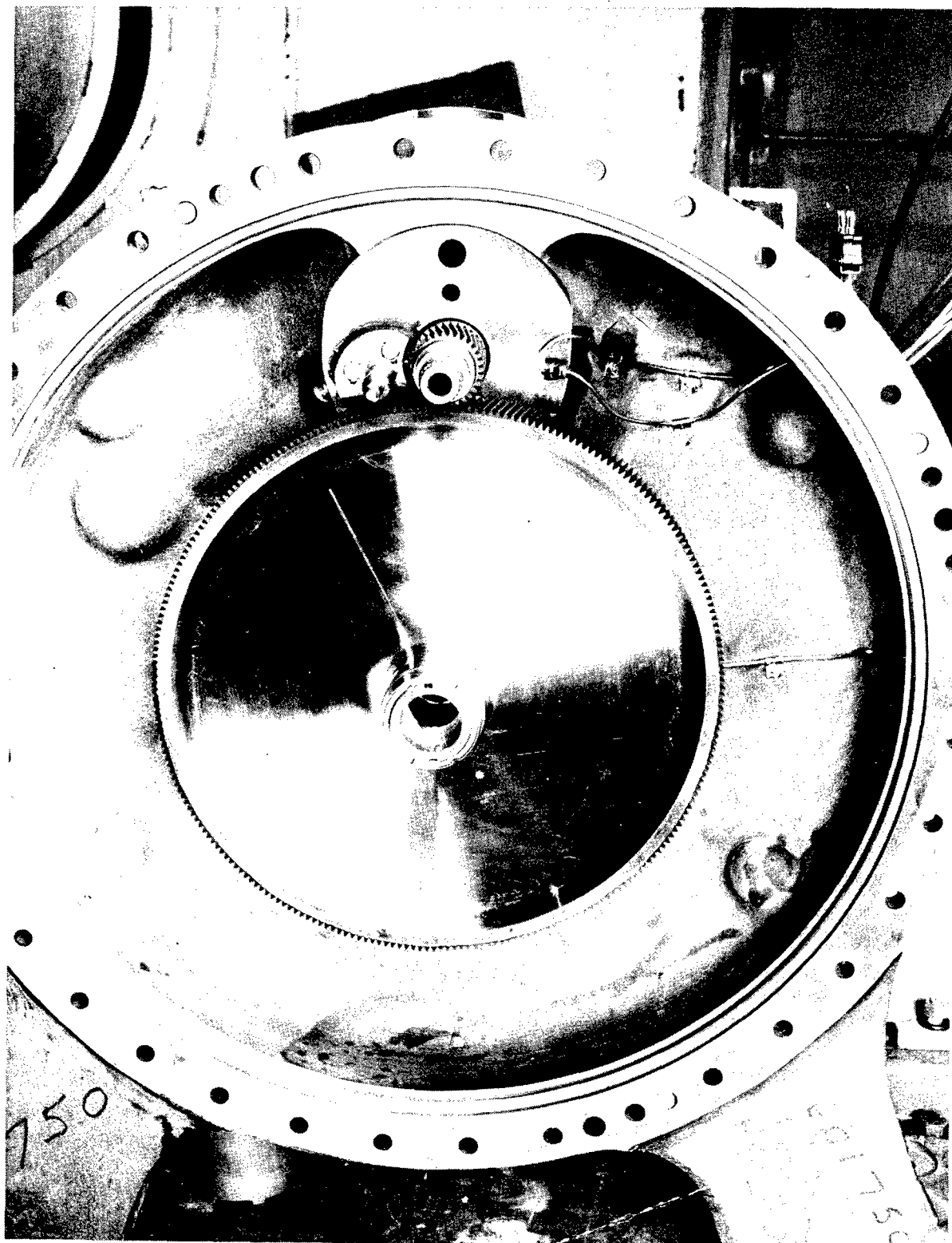


Figure 404. Gearbox Pinion Gear Assembly.

Vibration pickups were also installed in both horizontal and vertical planes.

All oil passages and orifices were flushed to ensure a clean and proper flow. Plexiglas windows were fabricated and installed in each outer end of the pinion and bull gear housings, to observe the oil flow patterns of the lubricated areas.

The gearbox operated satisfactorily throughout all testing. A total of 272 hours of running time was accumulated with no major failures.

TEST AND FAILURE ANALYSIS

Test Plan

Testing was conducted at the Continental Component Laboratory. The test rig installation shown in Figure 405 was assembled and fully instrumented. The instrumentation provided turbine performance and combustor and heat transfer data for the fluid-cooled turbine, Appendix VIII.

The program test plan was:

Test Series I - Preliminary Testing

1. Preliminary rig checkout
Combustor development - with dummy rotor
Cold run - mechanical system with turbine rotor
Preheater run - 600°F
2. Inspection, instrumentation, and rig modification

Test Series II - Initial Power Testing

1. 1300 to 1700°F: thermosyphon - structural
2. Inspection, modification

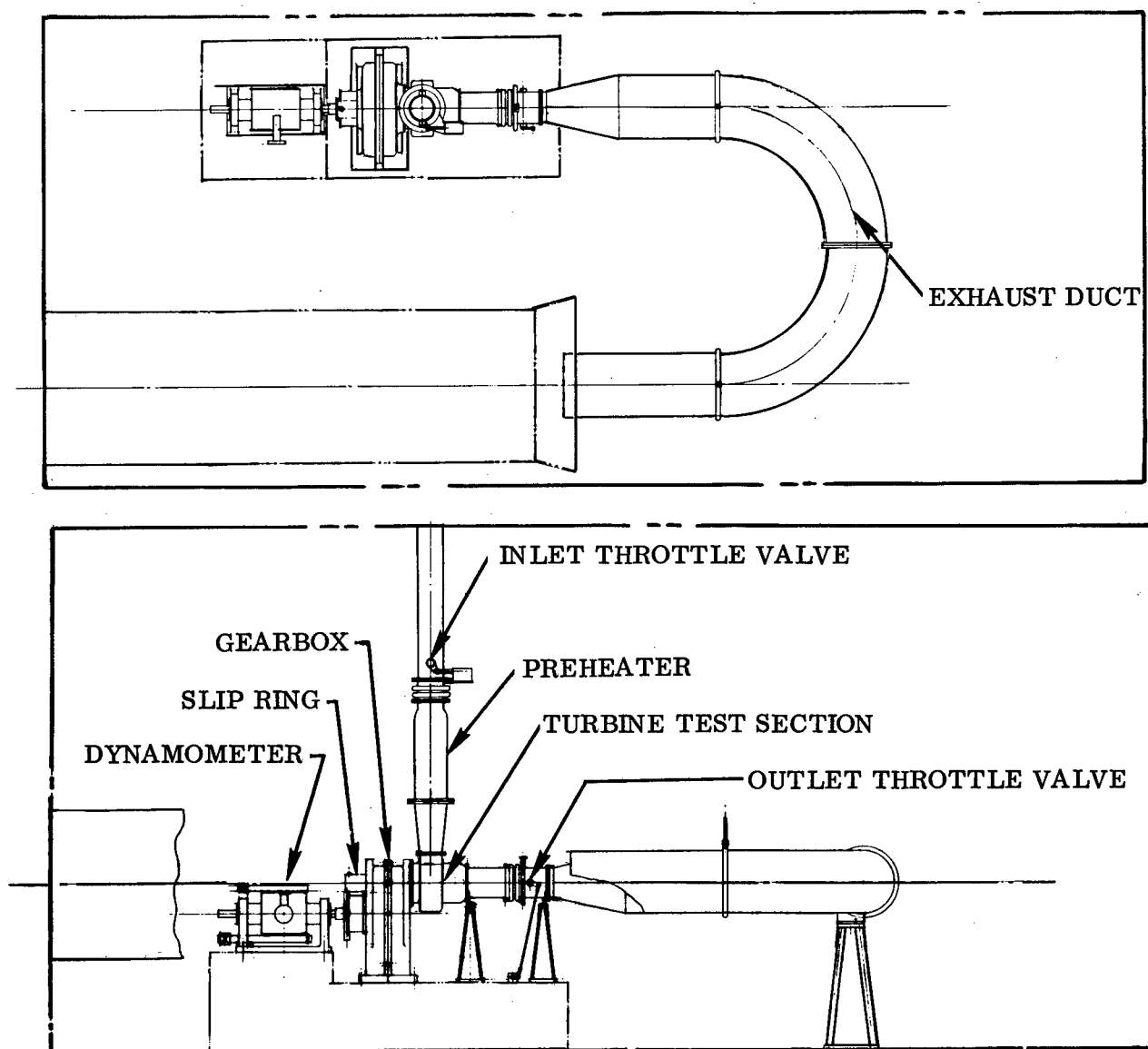


Figure 405. Test Cell Layout.

Test Series III - Qualification Testing

1. 1700 to 2000°F
2. 2000 to 2200°F
3. Qualify at 2300 to 2400°F

The preliminary tests consisted of developing the combustor to provide a turbine inlet temperature of 2300°F. This was done utilizing a dummy rotor (see Figure 406).

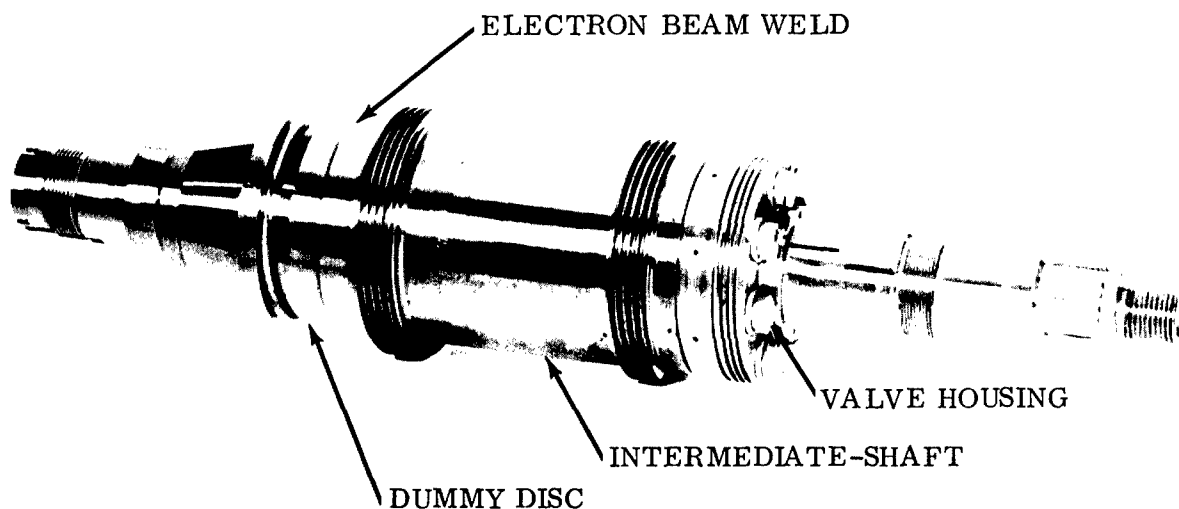


Figure 406. Combustor Development Slinger Shaft.

At the completion of the combustor development (outlined in detail in the Combustor section of this report, page 429), the turbine rotor was installed. The turbine was air motored while checking out the rig mechanical system. Preheater ignition and rig instrumentation were also monitored for functionability.

During the initial power testing, the hardware structural integrity was monitored, and proof of the fluid-cooled thermosyphon concept was obtained. The cooled turbine blade was designed to maintain a structurally acceptable metal temperature below the blade relative temperature of the gas stream. The test was geared toward turbine inlet temperatures of 1700°F so that failure would not occur in case of a blade cooling system deficiency. The cooling effectiveness was established by measuring the fuel inlet and exit temperatures. Thermal-indicating paint was also used to determine approximate metal temperature and, thus, to determine blade cooling.

The qualification testing provided aerodynamic performance and heat transfer data. The turbine rig operated at elevated turbine inlet temperature (to 2450°F) and turbine rotor speeds of 45,000 rpm (1600-ft/sec tip speed). The conditions desired to attain discharge gas stream specific horsepower of 213 were 2300°F and 45,000 rpm with a turbine efficiency of 85 percent.

Sixty-two test data points were recorded. A breakdown of the data points were as follows:

- Performance Data Points 1 through 14 - Combustor Development
- Performance Data Points 15 through 22 - Rig Check-out
- Performance Data Points 23 through 62 - Turbine Performance

Two turbine rotor assemblies were tested. For each turbine assembly, the blades were serialized and assigned to slots in their respective rotors, Figures 407 and 408. The blades maintained their position until replacement was required.

The following discussion reviews the significant events which occurred during the test program.

Test Runs 15-22

The blade thermosyphon cooling system was verified by fuel inlet and exit temperature measurements, and it was supported by thermal paint indications. This is discussed in detail under the Heat Transfer and Structural Verification section, page 238.

In attempts to attain rotor speeds beyond 35,000 rpm, fuel leakage into the oil sump was noted. An investigation revealed that the fuel face seal was leaking, Figure 409. The fuel wiper, Figure 410, was examined. The wiper face, which has a light band surface finish, displayed a jagged and peeled surface at the outer periphery.

The cause of the fuel leakage was attributed to the high pressure used in pumping the fuel. The seal operating specification recommended a maximum pressure of 800 psi at 30,000 rpm. During tests the pressure recorded was 1020 psi at 36,000 rpm. The recommended operating pressure at 50,000 rpm is 20 to 30 psi.

Low operating pressures are required because the disc itself serves as a fuel pump (10,000 psi at 50,000 rpm). This is a result of the fuel density differential between inlet and exit of the disc and the "g" field created by disc rotation.

Details of seal modification are presented in the Combustor section of this report, page 466. This proved to be successful, and no further leakage occurred throughout all testing.

- ① 15-21
- ② 28-31
- ③ 60
- ④ NO DATA
- ⑤ NO DATA
- ⑥ NO DATA
- ⑦ NO DATA
- ⑧ 61-62





Figure 409. Fuel Face Seal.



Figure 410. Fuel Wiper.

The gearbox pinion bearing was running at 285°F at 38,000 rpm and was linearly rising in temperature at the rate of 5°F per 1500-rpm increase. This was considered to be an abnormal operation. An inspection revealed that the drive bearing had failed. Visual inspection of the bearings showed light circumferential scratches on the inner races. The retainers were found noticeably scratched and dented. It was believed that installation, utilizing a sleeve-tool, was the cause of inhibiting, premature failure. This was corrected, and no further problem in the gearbox occurred throughout testing.

After the above modifications, the fluid-cooled turbine rig was considered to be operational to initiate performance testing.

Test Runs 23 Through 27

The maximum conditions run were 40,000-rpm speed and 2100°F average turbine inlet temperature; 62 hours had been accumulated prior to run 27.

During adjustment of airflow, temperature, and speed conditions for a 96-percent speed run, between test run numbers 26 and 27, the forward thrust bearing indicated a sudden, sharp increase in operating temperature. This was accompanied by a slight increase in rig vibration and occurred at approximately 92-percent speed.

Examination of rig instrumentation revealed that the tip of a turbine inlet temperature probe was missing. Further examination of the rotor revealed that three blade tip caps (blades 25, 37, and 51) were also missing. Figure 411 is a view of the rotor after test run 27.

Except for one vane, the turbine inlet nozzle vanes were free from damage. A slot of the trailing edge of the one vane was closed, Figure 412. This vane was located adjacent to the failed TIT measuring probe. Indications were that the missing probe tip impacted the vane, closing the slot.

Loss of blade tip caps resulted in minor impact damage to the rear edge of the turbine shroud, as shown in Figure 413. It is to be noted that the shroud, while damaged, did not prevent continued operation of the turbine. Elevated temperature testing at a turbine inlet temperature of 2100°F was run for approximately half an hour after the blade tip-cap loss.

The forward rig thrust bearing, Figure 414, displayed a cracked outer race cage. The bearing failure was surmised to occur when the rotor tip caps failed.

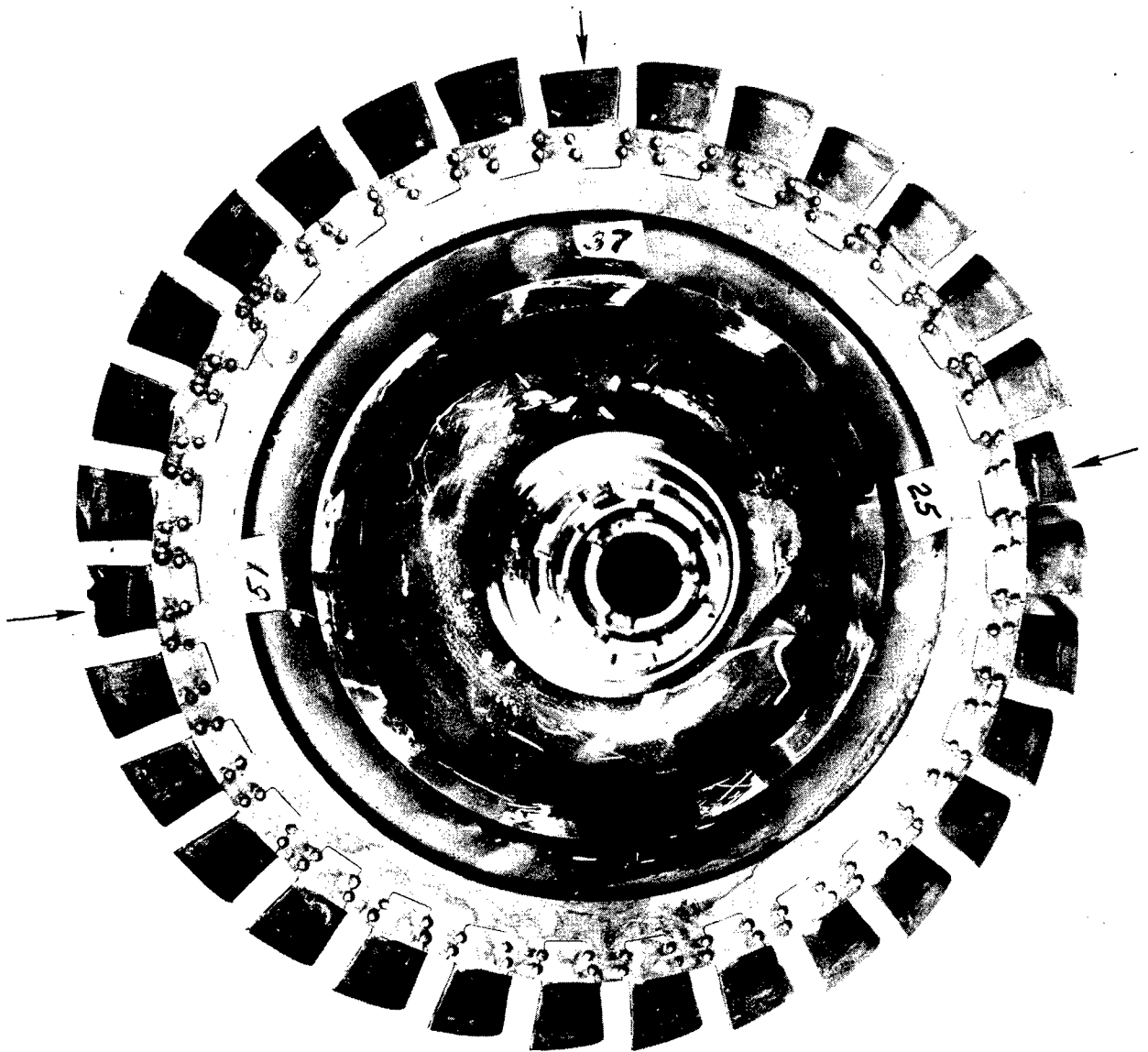


Figure 411. Turbine Rotor Tip-Cap Failures - Nos. 25, 37, and 51.



Figure 412. Nozzle Vane Assembly After Test 27 -
Damaged Vane.

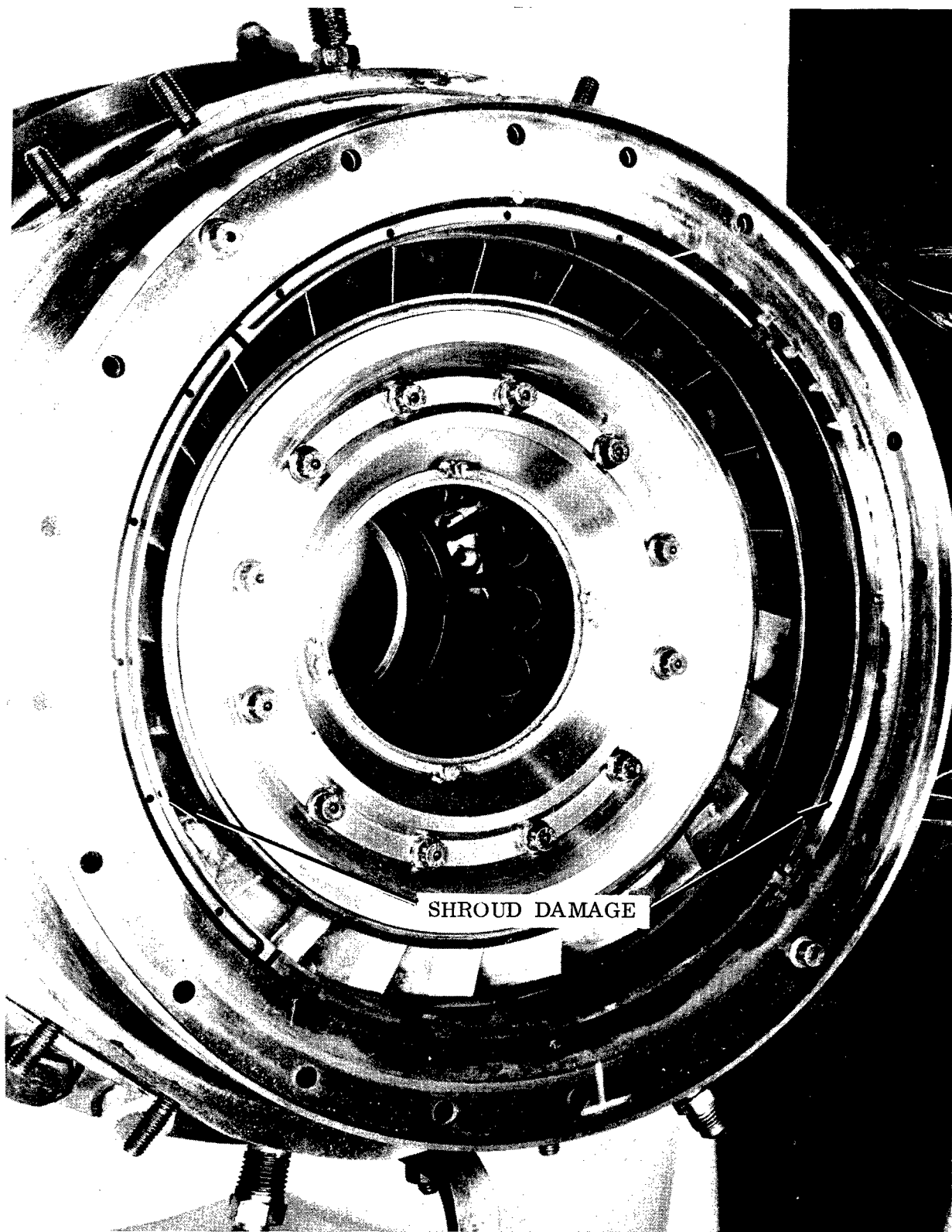


Figure 413. Turbine Shroud and Nozzle Vane Assembly.



Figure 414. Forward Thrust Bearing.

The blades were removed from the rotor, Figures 415 and 416. A reddish black deposit was found on all of the blade heat exchangers. The fuel seals were filled with a loose, flaky deposit. Samples of this deposit along with the test cell fuel (JP-4) were submitted to the Ethyl Corporation for analysis.

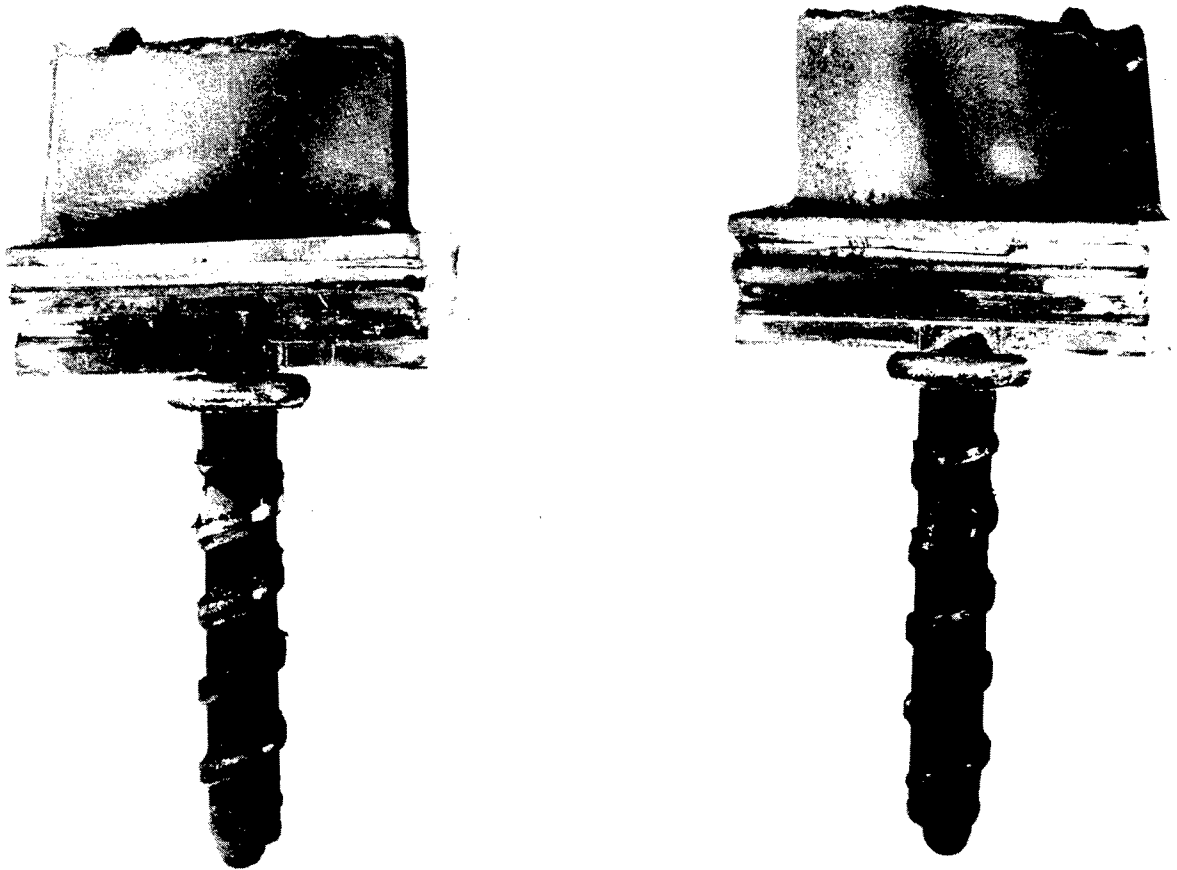


Figure 415. Fluid-Cooled Turbine Blade No. 51.



BLADE 25



BLADE 37

Figure 416. Fluid-Cooled Turbine Blade Nos. 25 and 37.

Analysis of the fuel showed that it was within the MIL-J-5624F specifications. A spectrographic analysis showed the composition of the deposit to be as follows:

Carbon	59.6 Percent
Hydrogen	3.4 Percent
Iron Oxide	10.0 Percent
Copper, Magnesium, Nickel Silicon, Phosphorus, Lead, and Zinc	0.1 to 1.0 Percent Each
Trace Quantities of Al, Ba, Cd, Co, Cr, Mn, Mo, Ti	
Oxygen	Remaining

Thermal stability tests conducted by various oil companies with a fuel coker resulted in a hard, varnish-like deposit on the fuel tube. The deposit adhered strongly to the coker tube. This did not compare with the loose, flaky consistency found at the blade stems. The rig history at which this occurred was as follows:

Fuel Temperature	350°F Steady State
	500°F Transient
Wall Temperature	700° to 850°F
Operating Time	67 Hours
Fuel Pressure	3000 to 5000 psi (Due to high "g" field)

The pressure and temperature combination could not be simulated in the laboratory.

Zyglo inspection of all the blades was inconclusive. Zyglo confirmed cracks known to be present and produced indications along the unblended weld edges of most of the blades. Although the latter indications were reproducible, they were not considered to be due to cracking, since all known cracks occurred at the centers of welds rather than the edges.

The fractures of blades 51 and 25 were irregular and were accompanied by considerable distortion. A large portion of the fracture in the convex wall of blade 37 was very flat and was not visibly associated with any distortion. The fracture appearance was suggestive of fatigue. Visual examination of blade 25 revealed several cracks on the inner surface of its

convex airfoil. The cracks appeared to extend about halfway through the wall and ran parallel to the blade axis to about 0.020 inch from the fracture between airfoil and tip-cap.

Longitudinal metallographic specimens were prepared from blades 37 and 51. It was found that both of the blades broke through the weld in the U-700 airfoil. The U-700 in the area of fracture was probably diluted with Inco 718 from the cap during electron beam (EB) welding. Both the concave and convex walls of blade 51 were "necked down", suggesting ultimate failure by hot tension, Figure 415. Cracks in the airfoil of blade 37 away from the weld were oxidized and also indicated hot tension, Figure 417. However, it exhibited no necking down or other distortion associated with the fracture of its convex wall.

The blades which did not readily display evidence of cracks were pressure-checked in a vessel at 1200 psi with helium. Blades 49, 53, 40, 72, and 27 were found to have cracks.



Figure 417. Blade 37 Fracture.

Hairline cracks of approximately 0.10-inch length were found on blades 49 and 53 at the tip-cap weld area. A metallurgical analysis of blade 49 showed that the blade casting had a crack in its airfoil prior to testing. This crack was probably remelted by the electron beam during initial welding; see Figure 418.

Blades 72, 27, and 40 had pinhole cracks which were not readily visible microscopically. Blade 72 displayed a pinhole at the radius blend between the heat exchanger stem and the blade platform. Blades 40 and 27 revealed pinholes in the concave wall of the blade. Radiographic examination of all three blades showed only the crack in blade 40 as a positive defect.

Several of the failed blades were sectioned parallel to, and about 1/8 inch above, their platform. Each of the blades exhibited its thinnest wall at its concave surface at the two channels closest to the trailing edge. Minimum wall thicknesses were found to be:

<u>Blade Number</u>	<u>Wall Thickness, Mils</u>
51	12 (convex walls)
25	11 (concave wall)
53	8 (concave wall)
49	8 (concave wall)

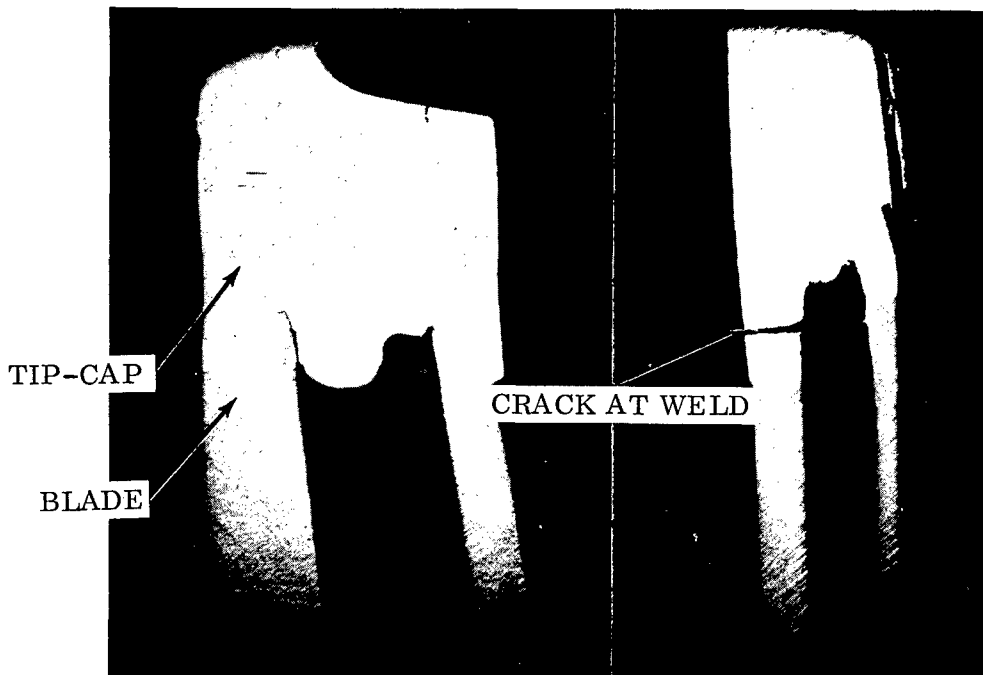


Figure 418. Airfoil Section Between Leading-Edge Blade 49 and Trailing Edge.

R & D Specification No. 51, Appendix I, requires a minimum wall thickness of 10 mils to maintain structural integrity.

The transverse airfoil specimens from failed blades used for wall thickness measurements were studied for alloy depletion. The depth of alloy depletion ranged widely from 0.0003 to 0.0015 inch on both internal and external surfaces. Alloy depletion could have resulted principally from entrapped air or from the coolant (water) or both. The observed alloy depletion might be suggestive of operating temperatures substantially greater than 1200°F or improper heat treatment.

Two blades were EB weld repaired (S/N 27 and 40). The water coolant was reinjected, and the blades were placed back into the rotor for continued testing.

Test Runs 28 Through 31

A turbine inlet temperature of 2168°F at 44,000 rpm was attained, and a turbine rotor speed of 45,000 rpm was attained for test run 31. Because a circumferential temperature gradient of 700°F was experienced, testing was stopped and the rig inspected. It was found that two blade tip caps were missing, numbers 44 and 76.

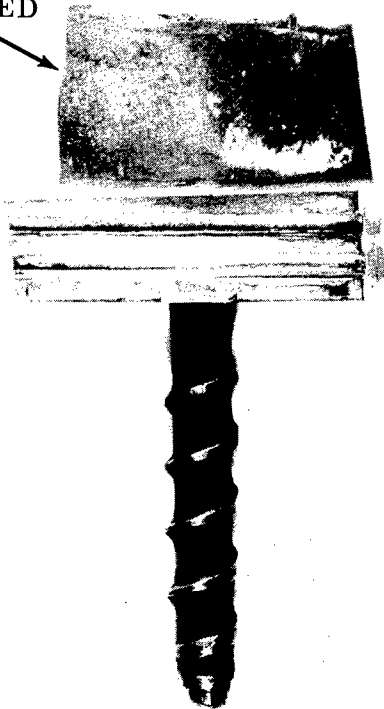
Rig vibration gave no indication of a blade failure. A normal shut-down procedure was followed, and the rig operation was not impaired. The only indication of a malfunction was that an exhaust gas temperature probe was not indicating.

The airfoil of blade 44 was necked down and its concave surface torn. The airfoil of blade 76 was not visibly deformed; see Figure 419.

A review of radiographs of the blades before engine tests failed to show the lack of weld on blade 44. However, the fluid channel nearest the trailing edge of the blade showed an indication of being blocked near the tip of the blade. The cause of the apparent blockage was not visible on the broken blade.

Both blades were sectioned longitudinally to determine the quality of the airfoil-to-tip-cap welds. Blade 44 exhibited shallow penetration of the weld in all of the areas examined. Near the midchord of the airfoil the weld covered only a very slight portion of the joint on the surface and predominantly missed the joint, Figure 420. This resulted in loss of blade coolant and alternate blade failure in hot tension.

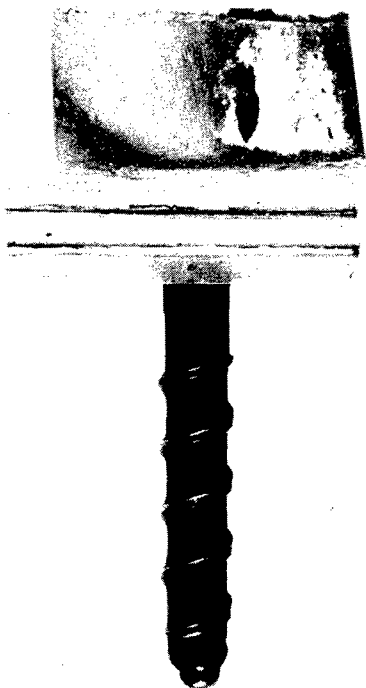
NECKED



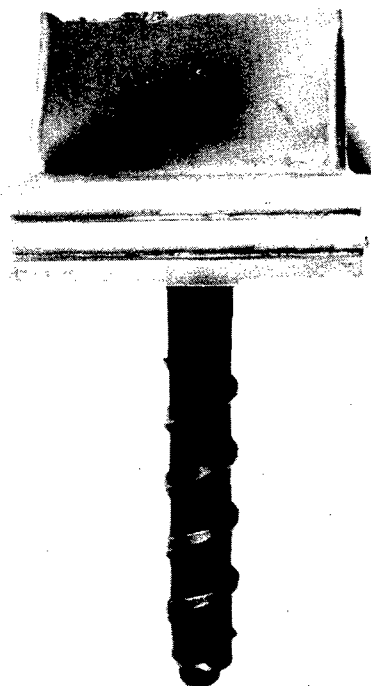
BLADE 44, CONVEX



BLADE 44, CONCAVE



BLADE 76, CONVEX



BLADE 76, CONCAVE

Figure 419. Blades 44 and 76 After Testing.

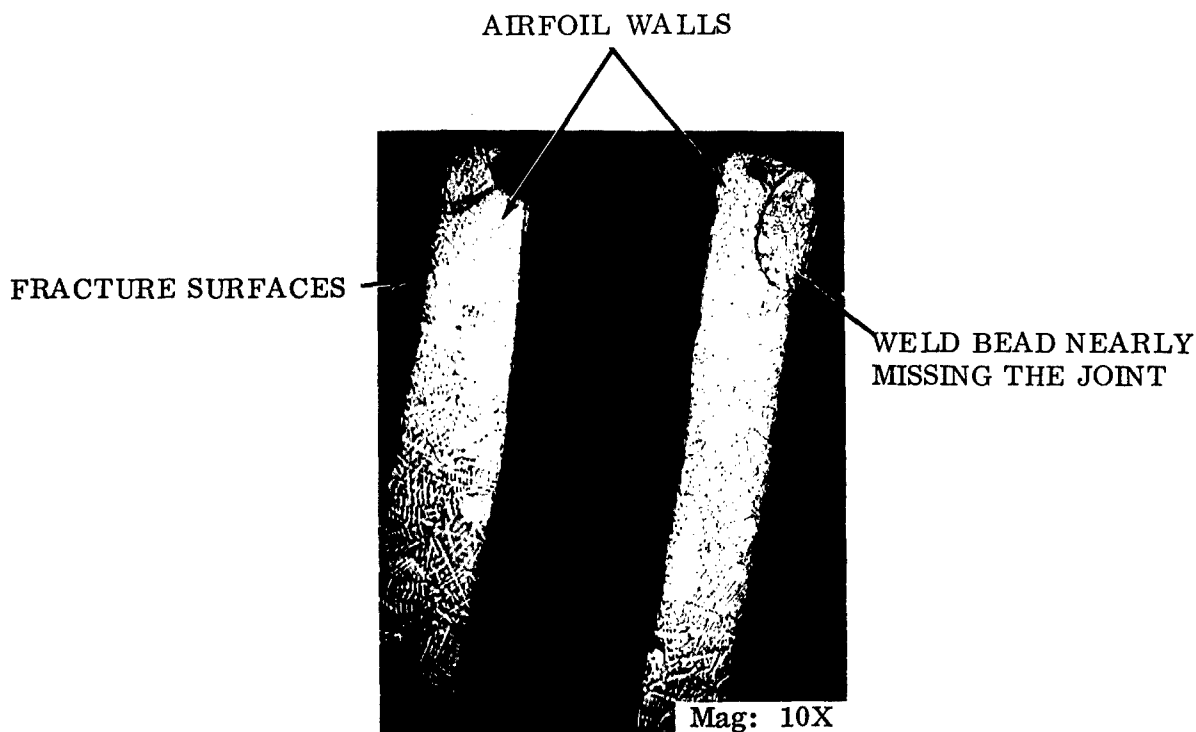


Figure 420. Blade 44 - Welding.

An examination of blade 44 was conducted to evaluate its metallurgical condition to note the effect of temperature on the airfoil.

Longitudinal sections of the blade were metallographically prepared. The sections were alternately ground, polished, and micro-examined to determine the weld quality and microstructures around the blade.

The following items were determined:

1. Gamma prime was absent from the extreme 1/4 inch of the remainder of the broken airfoil, indicating that temperatures about 1900°F were reached in that area.
2. The grain structure of the airfoil had grown through the weld zone so that the only evidence remaining of the weld was a characteristic second phase, Figure 421.
3. Oxidation, alloy depletion, and metal flow near the fracture surface suggested that temperatures approaching the melting point (in excess of 2200°F) were reached in that area.

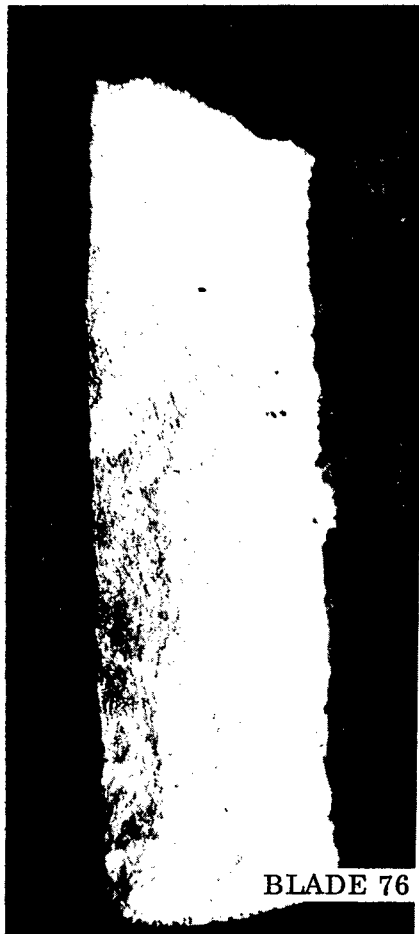


Figure 421. Blades 76 and 44 Microstructural at Weld.

It was concluded that the blade airfoil reached metal temperatures in excess of 1900°F after loss of its coolant.

Results of metallurgical examination of Blade 76 were inconclusive.

Test Runs 32 - 50

By utilizing turbine rotor I, attempts were made to obtain TIT of 2300°F at a rotor speed of 45,000 rpm. In approaching that goal, a rig vibration increase was noted at 42,000 rpm and approximately a TIT of 2300°F. The rig was torn down for evaluation.

Two blade tip caps (S/N 27 and 38) were missing. These blades were adjacent to each other.

Visual examination of blade 27 revealed a repair weldment extending radially from the tip-cap weld. A crack extended down the center of the weldment and through the airfoil wall into the third fluid channel from the trailing edge. There was no evidence of necking in the airfoil wall. There was no evidence of fatigue, Figure 422.

The minimum airfoil wall thickness in each case was 0.014 inch and occurred at the concave side of the fluid channel, closest to the trailing edge. The airfoil walls were the same thickness (0.014 inch) at the tip-cap fracture at a point 1/8 inch above the platform.

Neither airfoil showed diminution of gamma prime phase, indicating that the airfoil temperature reached was less than 1800°F.

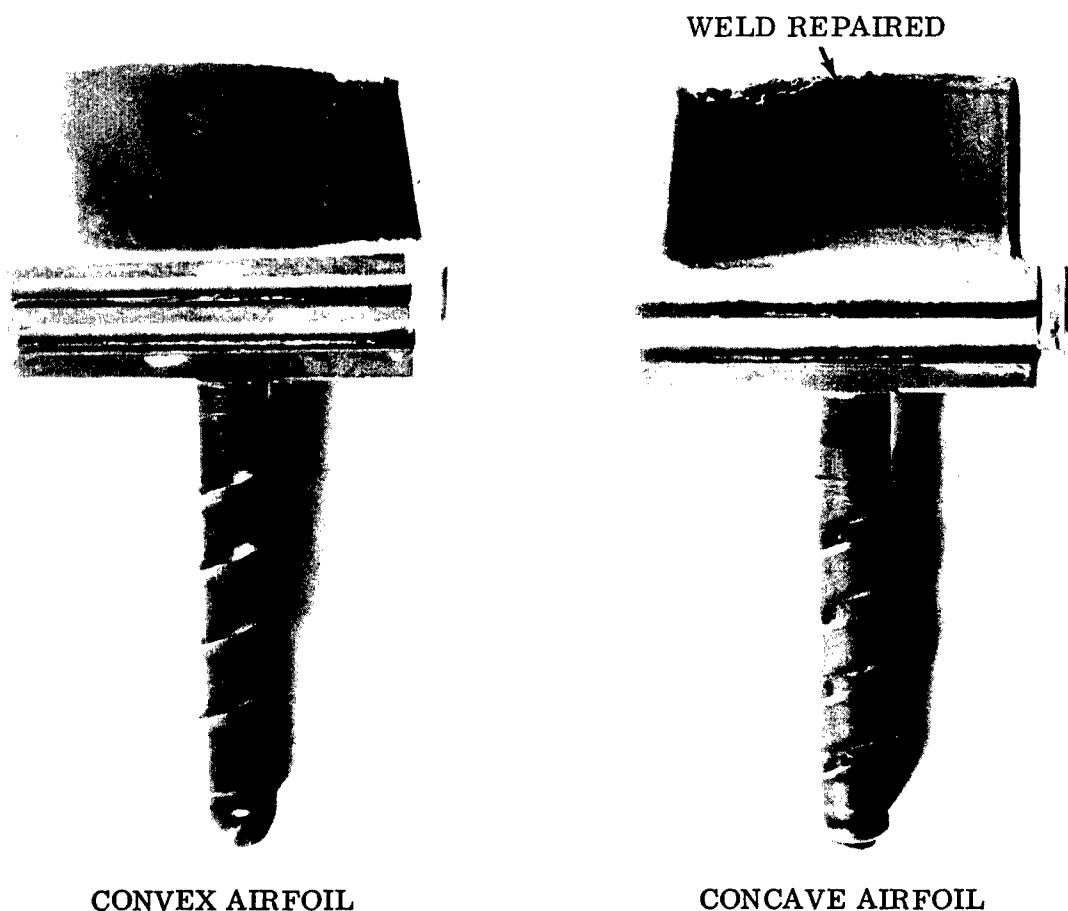


Figure 422. Blade 27.

A second attempt to attain 2300°F TIT and 45,000 rpm was made. At 42,000 rpm and approximately 2100°F TIT, a blade/disc fuel seal burst, causing exhaust gas temperatures to soar in excess of 2300°F. The rig teardown revealed one tip cap to be missing (blade 36) and one blade cracked at the tip-cap weld zone (blade 110). The blade seal that fractured is shown in Figure 423.

Visual examination of the fracture of blade 36 showed no evidence of fatigue. Blade 110 was sectioned and broken open through the crack at its tip-cap-to-airfoil weld. There was no evidence of fatigue on the fracture surface. Wall thicknesses were satisfactory for the 0.010-inch minimum required.

A metal discontinuity was visible to the unaided eye near the thinnest point in the airfoil wall of blade 110 about 1/8 inch above its platform. An intergranular film of oxide was found to be present; it extended entirely through the airfoil wall in several locations, Figure 424.

The electron beam weld missed the airfoil-to-tip-cap joint in blade 110 in the area where the blade cracked. Nearly all of the visible weld zone was below the joint and was very shallow.

Visual examination of the seal indicated that fracture initiated at the edge of the seal near the disc surface. The metal surrounding the rupture point orifice was severely deformed, Figure 425. The seal failure was attributed to a marginal tolerance stackup between the seal cavity in the disc and the bottom of the blade.

The failed seal was metallographically prepared along with two "unfailed" seals. It was found that the failed seal has the finest grain of the three but, otherwise, exhibits a comparable microstructure:

<u>Specimen</u>	<u>Grain Size</u>
Failed seal	ASTM 3-5
Unfailed seal #1	ASTM 0-3
Unfailed seal #42	ASTM 00-1

The hardnesses of the seals were comparable and averaged between Rc 31 and Rc 33. This hardness range is satisfactory for fully heat-treated Inconel X-750 alloy.

The seals were ground and polished, but no material defects were observed which might have contributed to the failure.

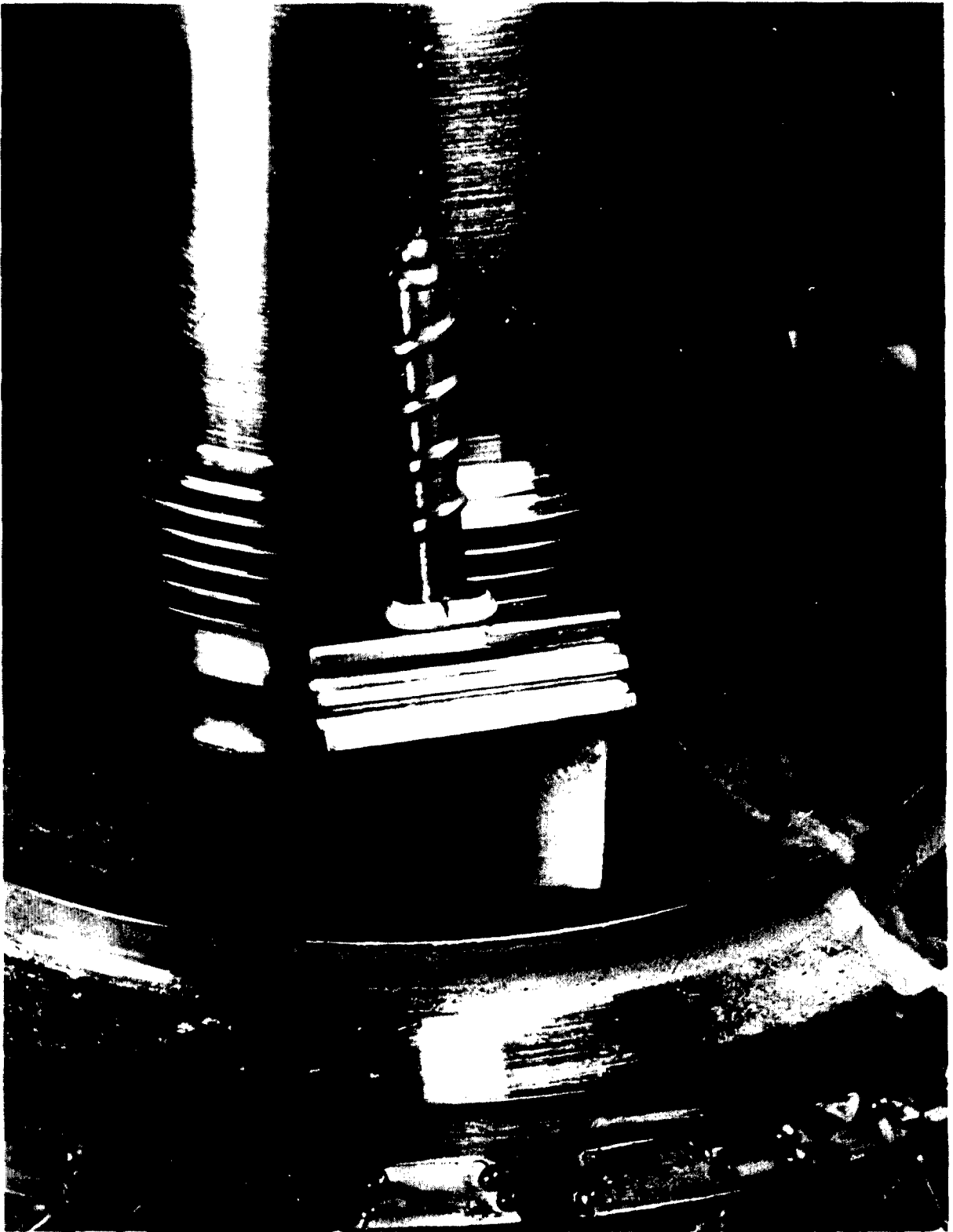
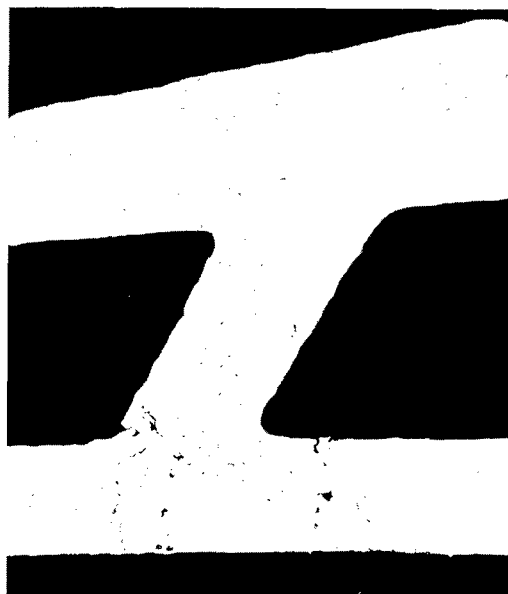


Figure 423. Blade Seal Rupture.



AIRFOIL WALL, MAGNIFICATION 50 X.



Magnification 500 X.

Figure 424. Blade 110 - Oxide Inclusion in Wall.



Mag: 8X

UNDAMAGED SIDE OF FAILED SEAL



Mag: 8X

DAMAGED SIDE OF FAILED SEAL. NOTE THAT THE METAL AROUND THE ORIFICE IS DISTORTED AND PULLED TOWARD THE FRACTURE.



Mag: 8X

THE FRACTURE IN THE FAILED SEAL WAS TYPICAL OF A TENSILE FAILURE.

Figure 425. Blade-to-Disc "V" Seal.

Test Runs 51 - 59

Nine test runs were conducted utilizing turbine rotor II. The turbine blades inserted were fabricated utilizing an alternate technique (see Manufacturing Technology, page 585). Turbine testing was conducted at 100-percent and 90-percent referred design speed. The maximum temperature attained was 2212°F at 45,000-rpm rotor speed.

After all testing was completed, the hardware was evaluated. It was noted that one blade tip-cap was missing, Figure 426. In monitoring rig vibration, again no indication of the turbine rotor imbalance was noted. Fifteen blades were found to have cracks; the remaining 16 blades were pressure-checked and were found to be sound. No set pattern of blade failure on the rotor was noted.

Three blades, 21A, 133, and 230, were broken open through the cracks that extended from their trailing edges about 0.100 inch above their platforms. There was no evidence of fatigue. The cracks were progressing from the concave sides of the blades. Measured at the fractures, blades 21A and 133 both exhibited a minimum airfoil wall thickness of 0.010 inch, and blade 230 exhibited a minimum airfoil wall thickness of 0.014 inch. The minimum thickness in each case was at the fluid channel closest to the trailing edge on the concave side of the blade.

A metallographic specimen was prepared from a longitudinal surface through blade 9A, which lost its tip-cap. There was no evidence of melting or of temperatures sufficiently high to solution the gamma prime phase completely, as occurred in previous failures. The quantity and coarseness of the gamma prime was diminished, which suggested that the airfoil had reached temperatures approaching 1800°F after failing.

The airfoil of blade 9A, Figure 427, was not visibly bent, but the airfoil walls were necked down, indicating that the tip-cap was lost by tensile stresses.

The concave airfoil wall of the fluid channel nearest the trailing edge was only 0.006-inch thick, which was substantially less than the 0.010 inch required. The thin wall would contribute to failure by permitting stresses higher than design stresses to exit.

The rotor was rebuilt for continued testing. The design point turbine inlet temperature of 2300°F was attained with this rotor. In an attempt to reach the design speed of 45,000 rpm, a rig malfunction occurred at a rotor speed of 42,000 rpm. An exhaust gas temperature in excess of 2400°F was recorded.

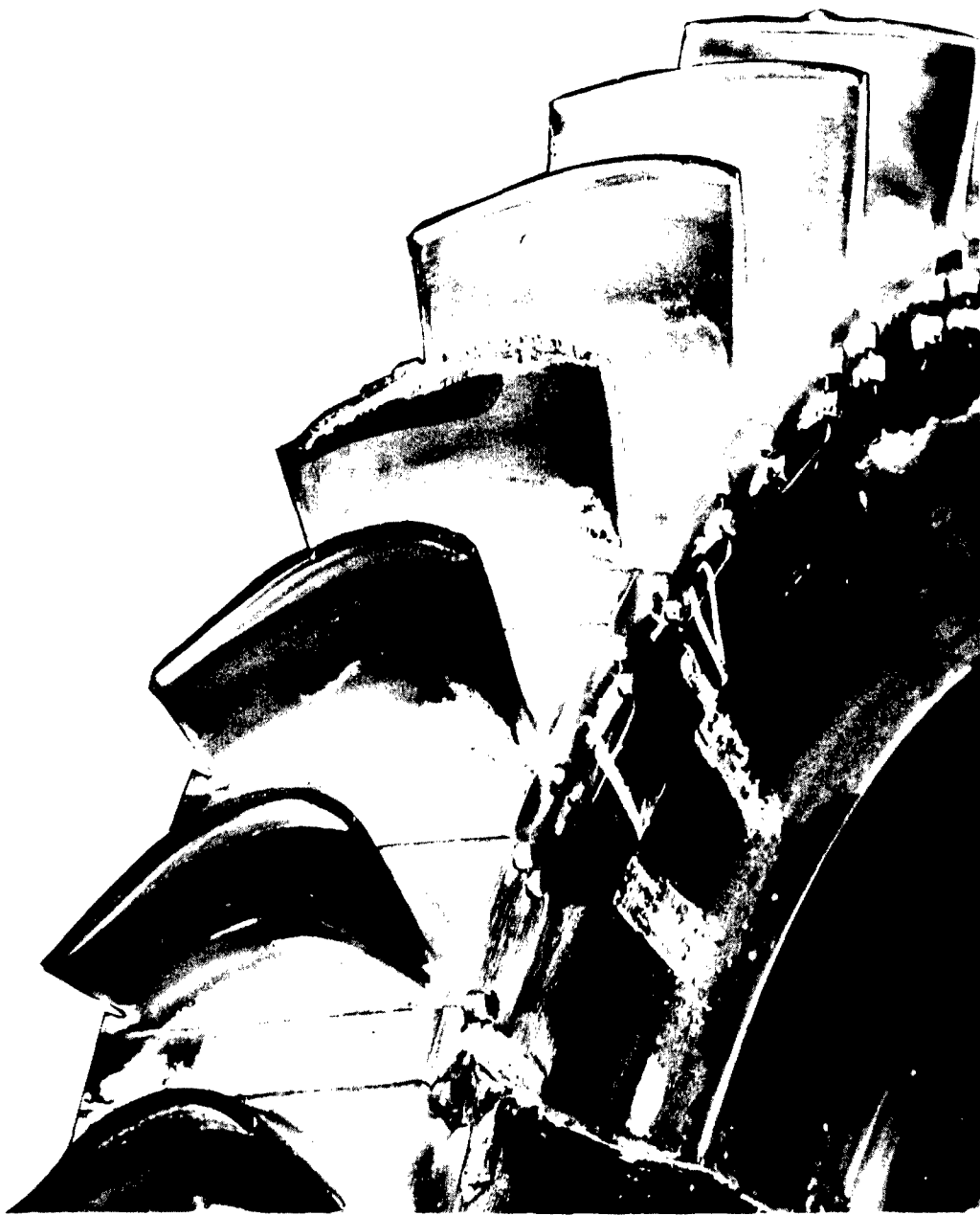


Figure 426. Turbine Rotor II - Tip-Cap Failure.

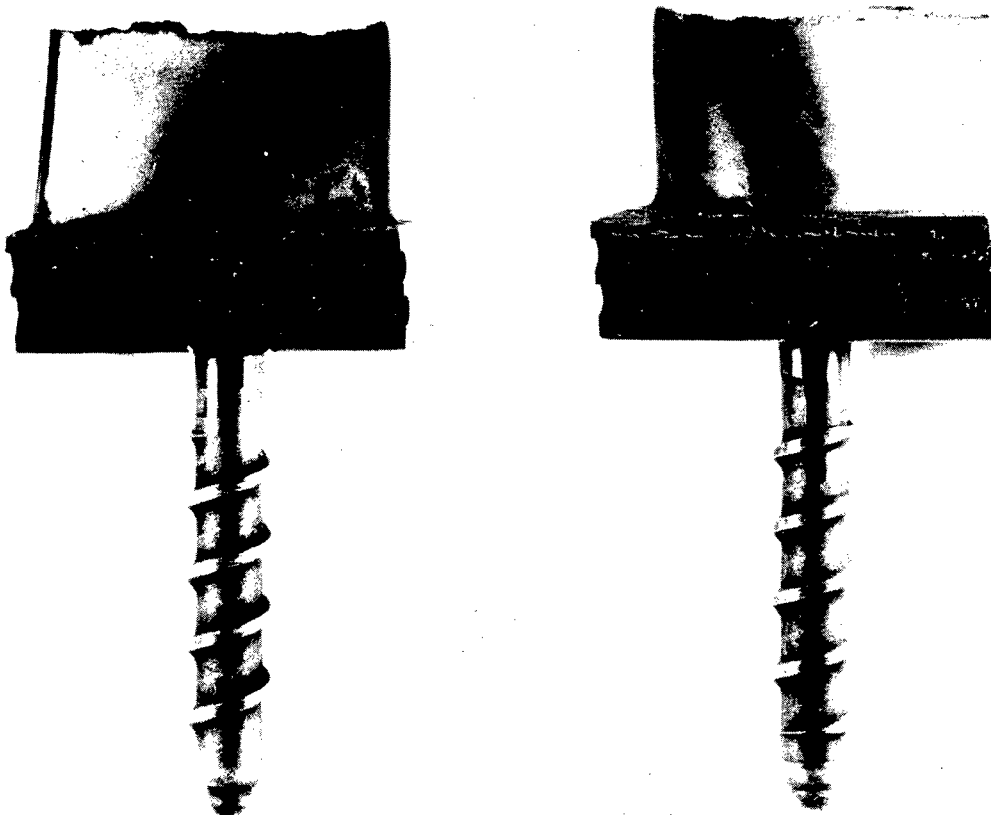


Figure 427. Blade 9A.

A teardown of the rig revealed seven blade tip caps missing, Figures 428 and 429. A fuel seal was found ruptured on blade 6, an unfailed blade. The turbine shroud and some nozzle vane trailing edges had minor damages.

The blade fracture in each case passed close to, or through, the tip-cap-to-airfoil weld. The airfoils of blades 116, 139, and 206 were bent toward their concave sides, suggesting that their tip caps were lost because of impact by fragments from other blades.

Blade 35A was severely necked, Figures 430 and 431. The extreme distortion near its leading edge suggested that the fracture initiated near its trailing edge and progressed toward the leading edge.

None of the blades showed evidences of fatigue.

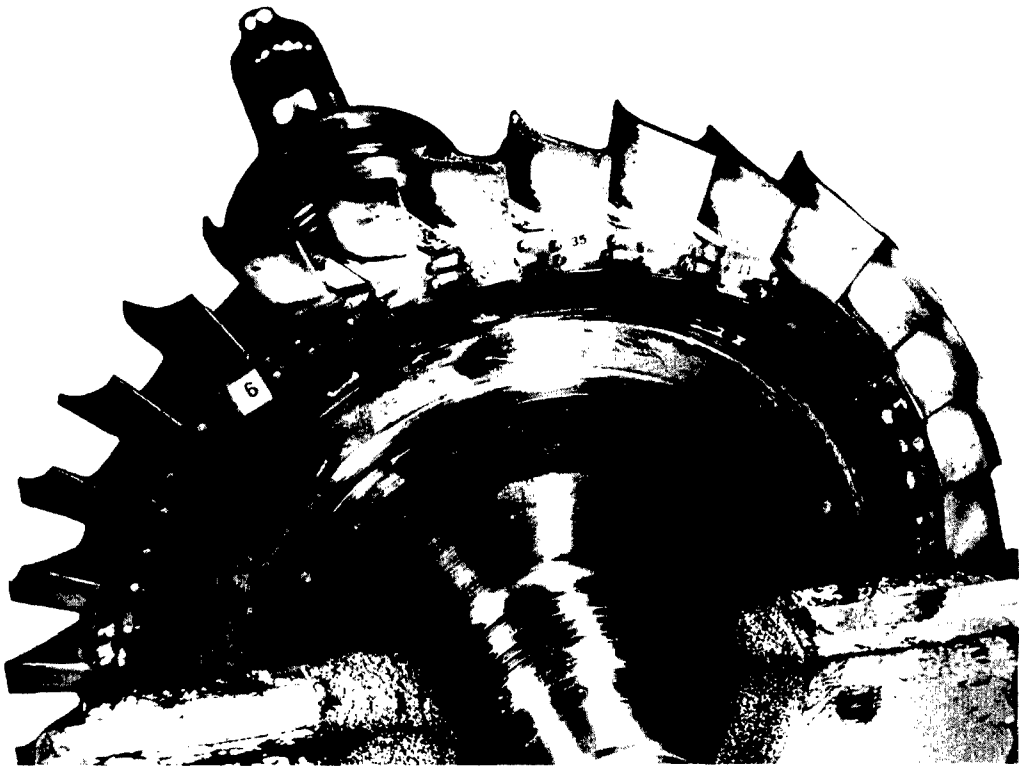


Figure 428. Turbine Rotor II After Testing - Rear View.

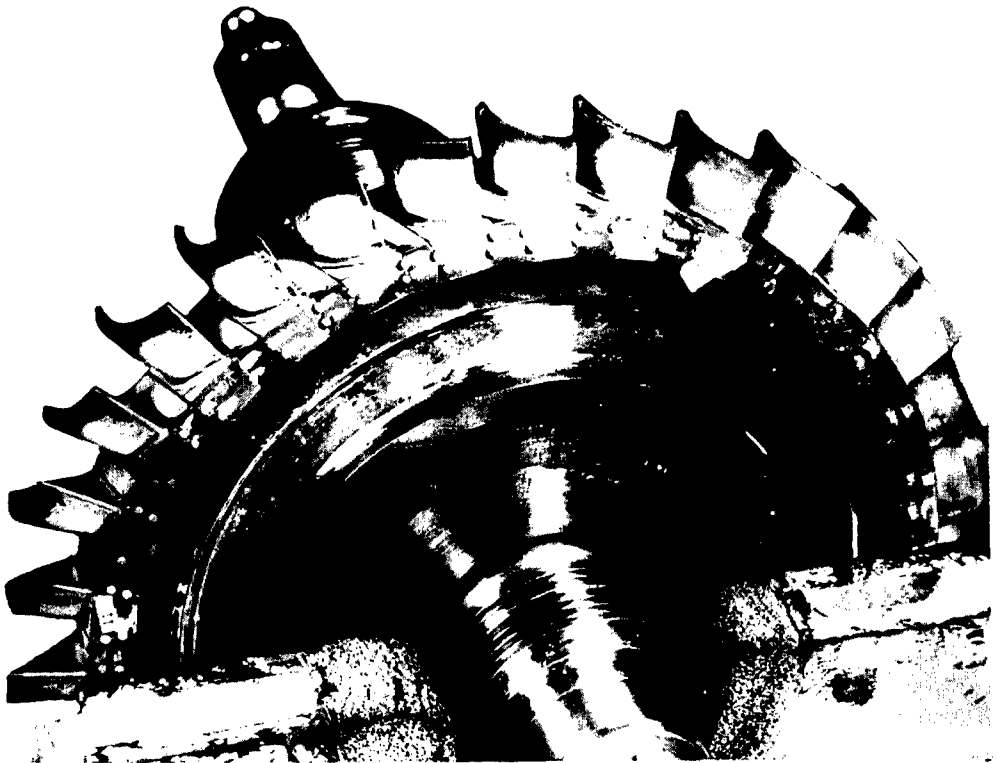
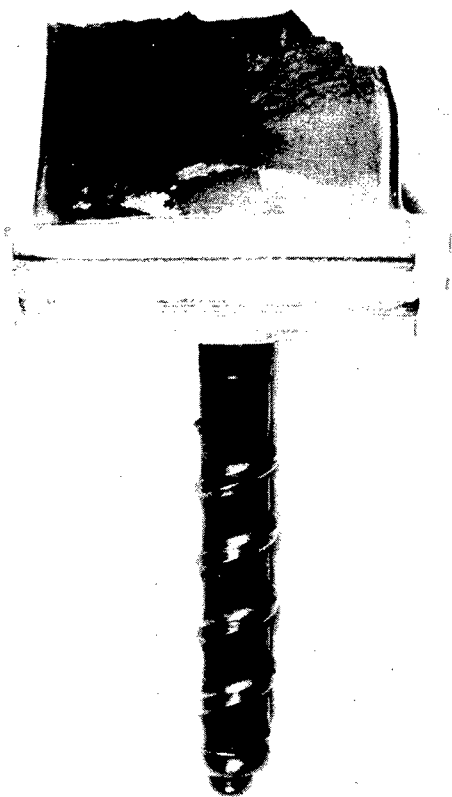
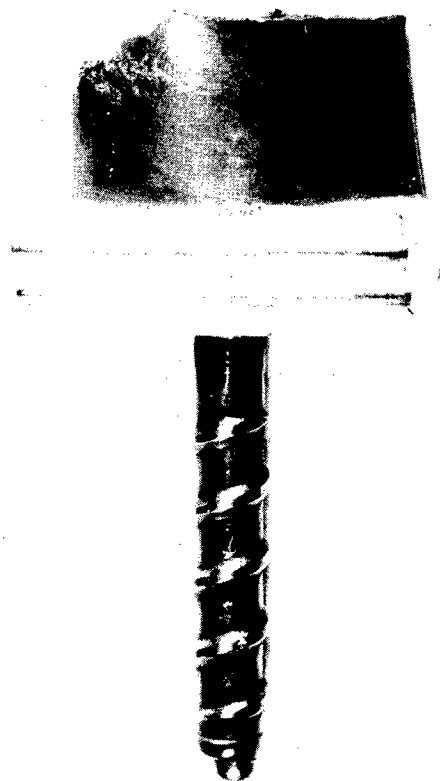


Figure 429. Turbine Rotor II After Testing - Rear View.



Mag: 2X



Mag: 2X

Figure 430. Blade 35A - Airfoil Tearing and Distortion.

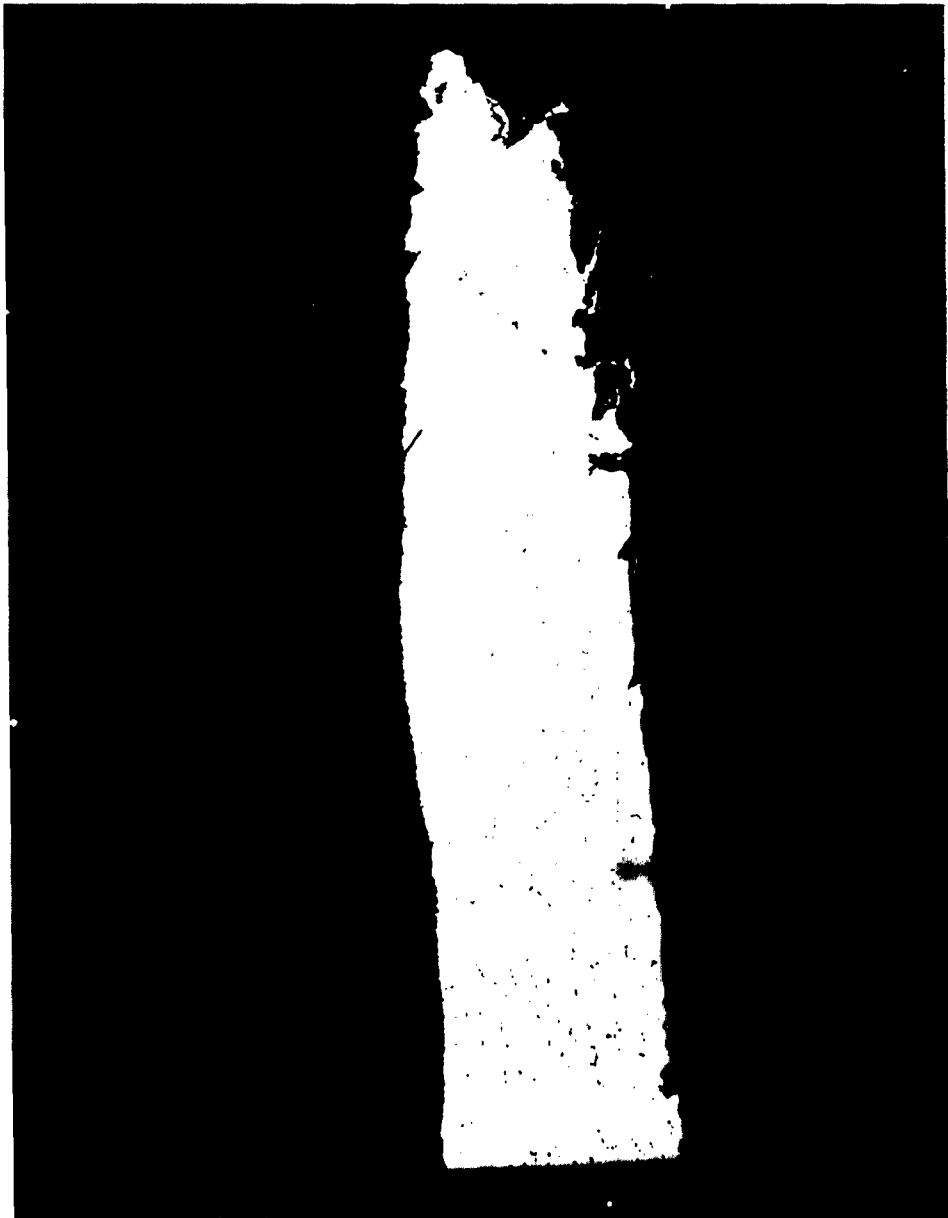


Figure 431. Blade 35A - Airfoil Surface Necking.

The results of a detailed study on the second set of blades relative to wall thickness are described as follows:

The airfoil of each blade was cut off at the platform. The airfoil wall thicknesses were measured at the cut surface (1/8 inch above the platform) and at the tip fracture of each blade. The minimum wall thicknesses measured were:

Blade S/N	Airfoil Wall Thicknesses, Mils		Side of Blade With Thinnest Wall*
	<u>1/8" Above Platform</u>	<u>At Tip Fracture</u>	
HAE 1	7-8	10	Concave
HAE 2	10	12	Convex
13A	4	5	Convex
35A	8	12	Concave
116	15	12	Concave
139	8-9	6	Concave
206	14	11	Concave

* The thinnest airfoil wall always occurred at the fluid channel closest to the trailing edge of the blade.

Except for blades 116 and 206, the blades exhibited airfoil wall thicknesses less than the 0.010-inch minimum value permitted. It should be noted that blades 116 and 206 were bent and failed due to impact or tip rub. This suggests that the failure of the remaining blades might be related to their thin airfoil walls.

Blades 13A and 139 exhibited wall thicknesses substantially less than the required 0.010-inch minimum at their base. Nine base blades were alternately ground, polished, and examined for wall thicknesses at 1/8-inch intervals along their airfoil lengths. The results were as follows:

Blade S/N 13A	<u>Height Above Platform</u>	<u>Minimum Wall Thickness, Mils</u>
	1/8 Inch	4
	5/16 Inch	7
	3/8 Inch	8
	Tip	5

Blade S/N 139	<u>Height Above Platform</u>	<u>Minimum Wall Thickness, Mils</u>
	1/8 Inch	8-9
	7/32 Inch	12
	3/8 Inch	13
	15/32 Inch	7
	Tip	6

These data show that the radial location of the minimum airfoil wall thickness is unpredictable but probably occurs either at the tip or the base of the airfoil.

Longitudinal airfoil sections were metallographically prepared from each blade. The sections were cut from a point midway between the leading and trailing edges. Only the airfoil of blade 35A was significantly "necked", see Figure 431. Several blades, including HAE 1, HAE 2, 116, and 206, showed shallow tip-cap welds. Blades 35A and 139 fractured in their airfoils as well as in their tip-cap welds; the remaining blades failed in their tip-cap welds only.

Blades 13A and 139 both showed diminution of gamma prime in their airfoils, suggesting that they had reached temperatures approaching 1800°F. None of the remaining blades showed any diminution of gamma prime. It was shown above that blade 13A had extremely thin airfoil walls (0.004 inch) and that blade 139 was bent.

As a result of the two rotor failures and the blade wall thickness study, it was concluded that the quality of the second set of turbine blades was insufficient for continued testing. Total test time was 17 hours.

Of the 18 failed blades, 15 blades failed due to this wall condition.

Test Run 60

Turbine rotor I was tested to obtain 2300°F turbine inlet temperature or better. A TIT of 2450°F was attained at 32,000 rpm. The TIT limiting criteria was the rotor rim temperature (1200°F).

One blade tip-cap was missing (blade 8). The rig hardware was intact, and, again, no variation of rig vibration was noted while testing, indicating no blade failure. These blades experienced 97 hours of hot testing.

Blade 14 was selected to determine if the coolant (water) was still present in the blades. The welded tip at the blade stem was ground off to expose the end of its cooling fluid channel. The blade was then centrifuged with its stem in a glass tube. The weights of the blade and tube were measured at 3-minute intervals. It was found that the blade lost weight and that the tube gained weight over a 9-minute period, indicating that water was present in the blade. No water however was visibly evident. The blade was then heated to about 115°C until no further weight changes took place. The blade lost a total of 0.0113 grams during the experiment. This weight matched closely the recorded value of 0.0132 grams for this blade.

Blades 8 and 14 were sectioned and examined for minimum airfoil wall thickness. The thinnest wall in each case was at the concave surface of the fluid channel closest to the trailing edge of the blade. Blade 8 exhibited a minimum wall thickness of 0.013 inch. Blade 14 exhibited a minimum wall thickness of 0.015 inch. These were satisfactory for the 0.010-inch minimum required by Appendix I.

Both blades were sectioned parallel to their axes, as shown in Figure 432. The sections were metallographically prepared and examined. Blade 14 exhibited a uniform gamma prime particle size and distribution. The presence and coarseness of gamma prime in the airfoil of blade 8 was diminished, suggesting that its airfoil temperature had approached 1800°F after its failure. There was no evidence that the airfoil had reached temperatures sufficiently high to cause melting (2220°F) or to solution gamma prime completely (1950°F or greater), as in the case of prior failures.

Test Runs 61 and 62

Turbine rotor I was tested with the intent of obtaining 2300°F TIT at 45,000 rpm. Two test data points were obtained at turbine inlet temperatures of 2220°F and 2340°F. The rotor speed was 43,000 rpm.

The rig was operating smoothly; however, the exhaust gas thermocouples began failing while taking data for run 62. Loss of oil in the lubricating system was also observed. The rig was shut down for evaluation.

Two blade tip caps were found missing, Figure 433. Again, no indication of any rig vibrational change was noted. Further evaluation revealed that the air-cooled exhaust duct displayed a crack at the weld of the oil scavenging port, Figure 434. The rotor was pressure checked, and no blade seal leakage was found.

SECTION CUT IN THIS
DIRECTION FOR
ANALYSIS.

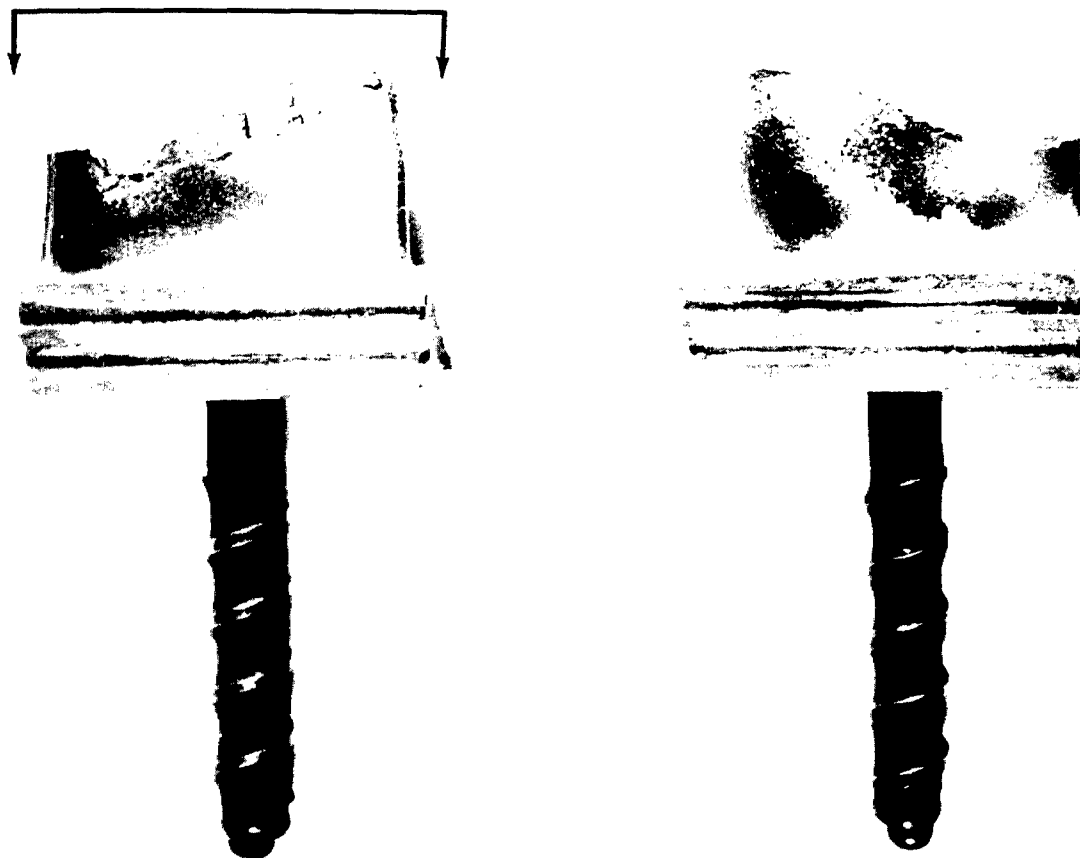


Figure 432. Blade 8 - Break Through Airfoil.

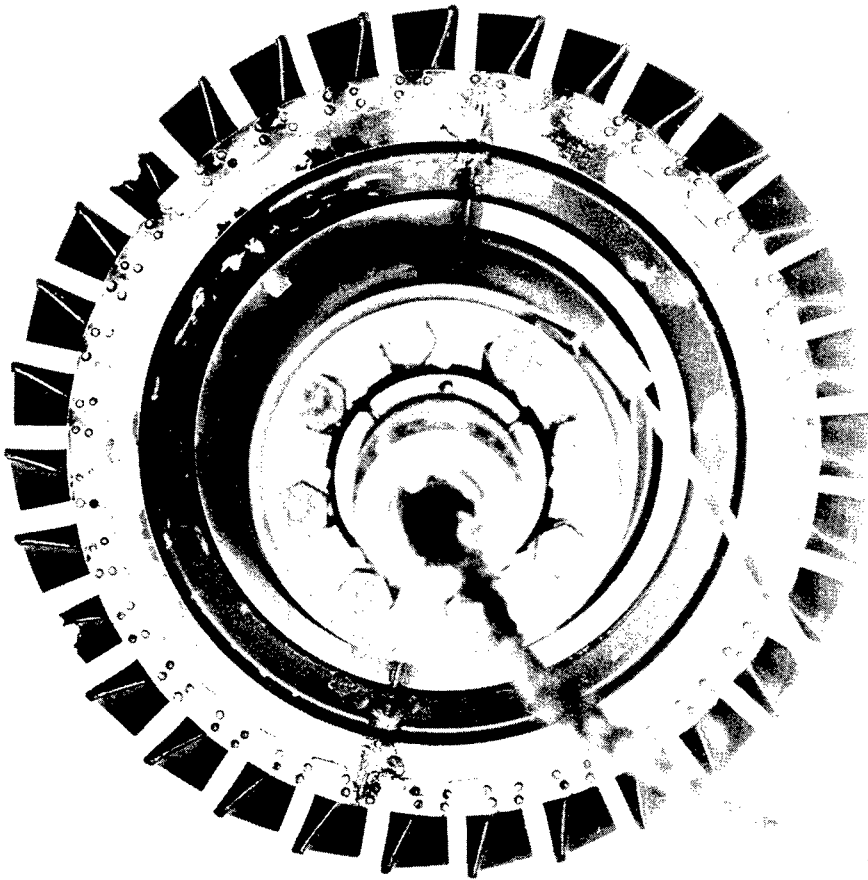


Figure 433. Turbine Rotor Assembly - After Run No. 62.

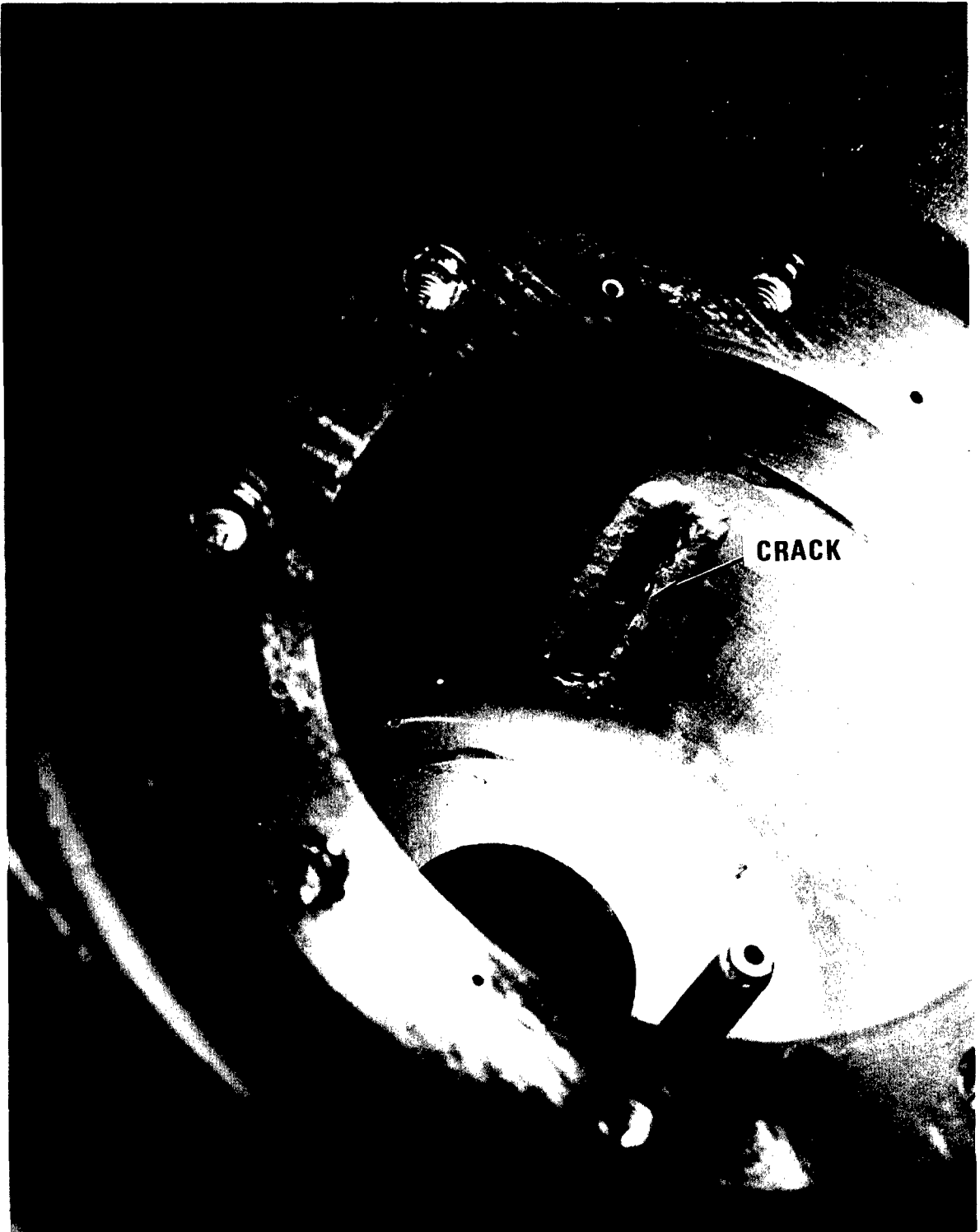


Figure 434. Exhaust Duct Oil Scavenging Port.

Blades 86 and 155 failed. They had experienced 138 hours of service prior to failure.

A defect was noted on the bottom surface of the base of blade 86. The tip of the blade was then dipped in a plastic material which solidified and sealed the blade airfoil. The blade was pressure-tested and was found to be leaking through the defect in the base, Figure 435.

Neither blade exhibited evidences of fatigue.

Both blades were sectioned and metallographically prepared. The microstructures in their attachment areas were satisfactory for Udimet 700 alloy. The microstructures in the extreme 1/4 inch of the remaining airfoils were typical of solution heat-treated Udimet 700 alloy, indicating that these areas had exceeded 1800°F during service. The solutioned areas were severely necked-down and evidenced intergranular oxidation. Both blades had reached temperatures of 2000°F and failed in hot tension. No evidence of melting was found.

Airfoil wall thicknesses were not measurable in most areas because of the extensive necking. The minimum wall thickness at the trailing-edge fluid channel 1/8 inch above the platform was 0.018 inch, which was satisfactory.

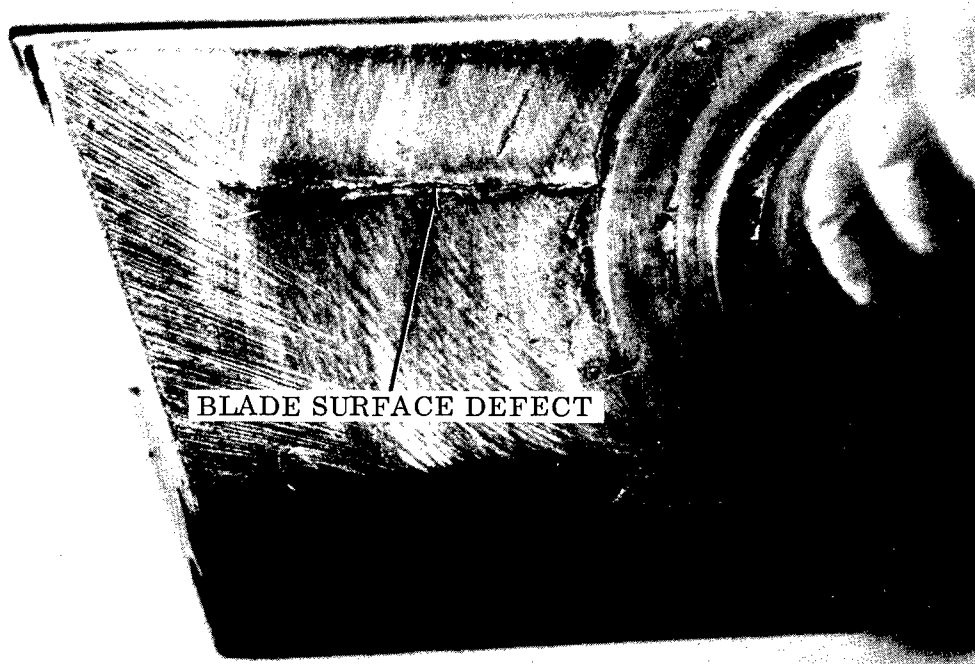


Figure 435. Blade 86 - Fracture.

The defect on the bottom surface of the base of blade 86 was due to breakthrough into a fluid channel, Figure 436. This was concluded to be a fabrication problem.

This concluded the test program. Sufficient hardware exists, that is, turbine blades, disc, nozzle assembly and vanes, and rotor shroud, with the exception of blade-to-disc "V" seals, to rebuild the turbine section.

The basic rig and gearbox are likewise in full operational condition.

Component Testing

The objective of the blade-to-disc pin attachment bench tests was to evaluate the performance of candidate Udimet 700, René 41, and Inconel 718 pin materials and to compare it with the structural design analysis.

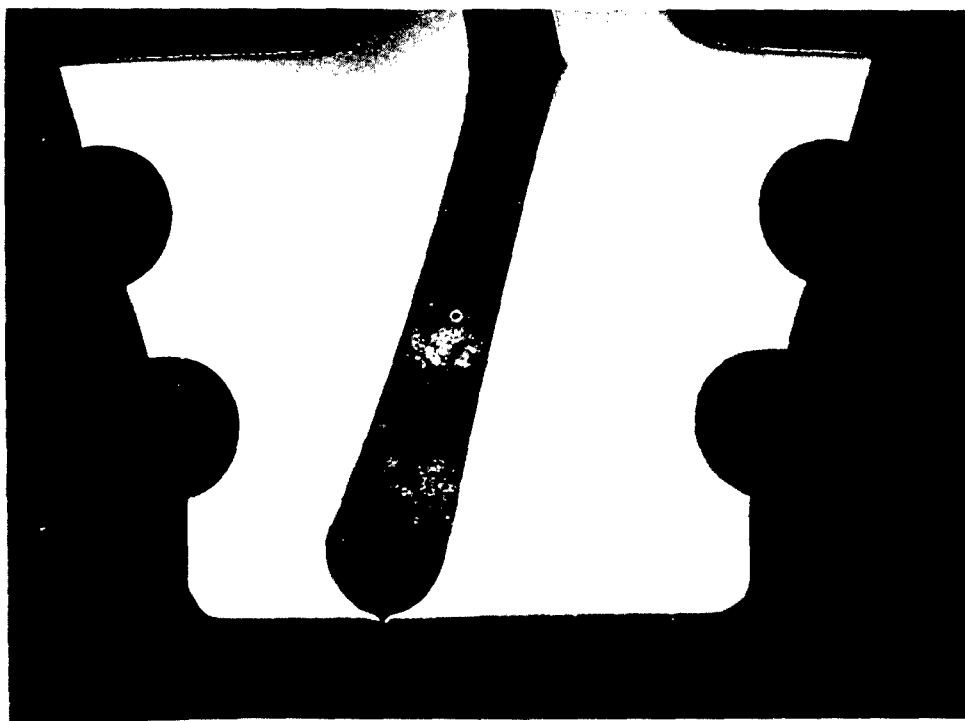


Figure 436. Blade 86 - Cross Section of Fluid Channel.

Three test specimens were machined to simulate the blade/disc pin attachment and material, Figure 437. The disc section was machined from Inconel 718 material. The blade section material was wrought Udimet 700. The actual blades are made of cast Udimet 700, however; lack of cast material availability necessitated this alternate.

The pins were machined from the following materials:

<u>Material</u>	<u>Condition</u>
Udimet 700 (Wrought)	CAE MS 700
Inconel 718 (Drawn Rod)	AMS 5662
René 41 (Drawn Rod)	AMS 5800A

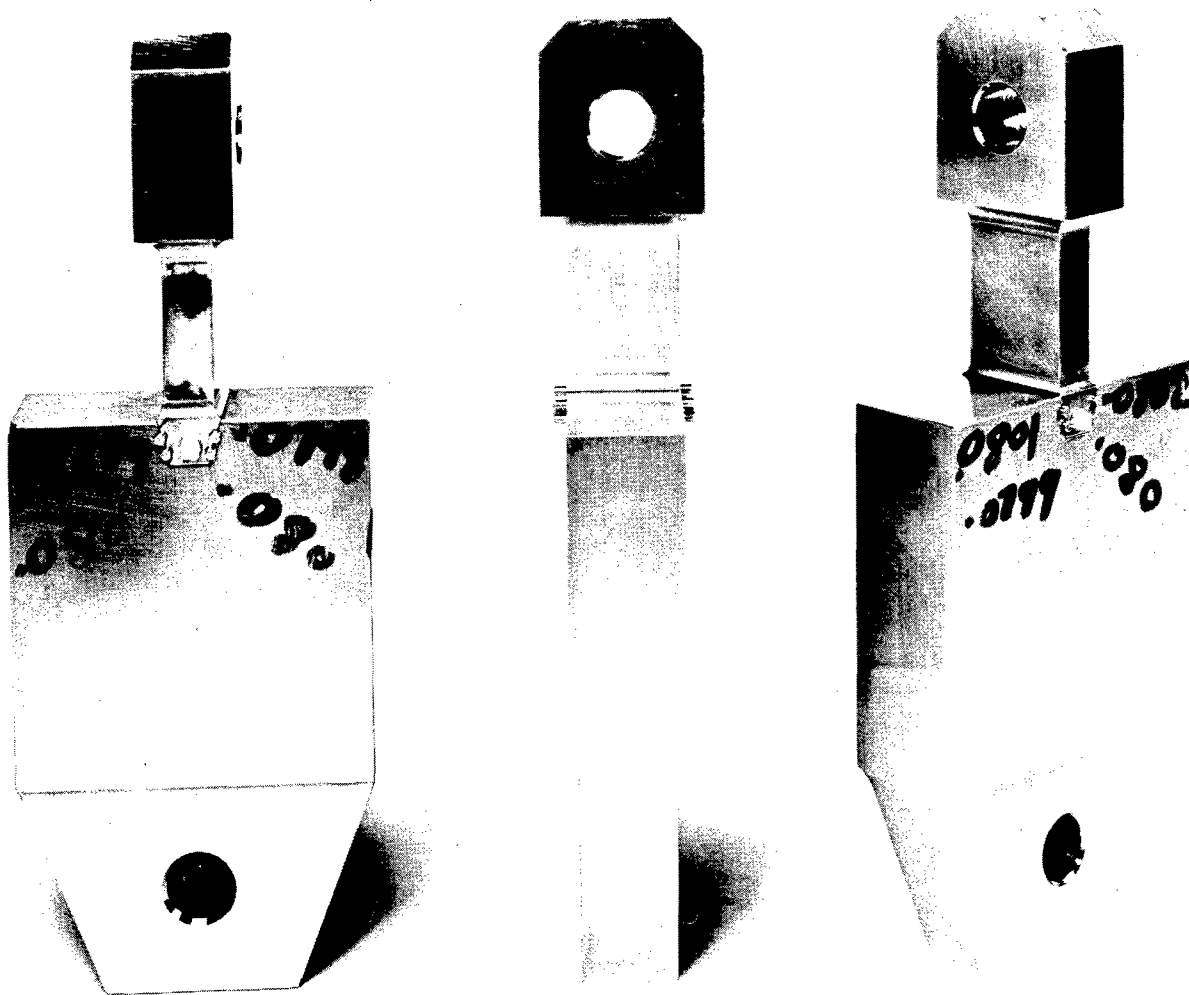


Figure 437. Pinned Blade Attachment Test Specimen.

The maximum design rotor speed was 50,000 rpm. At this speed, analysis indicated that the maximum radial blade load would be 15,000 pounds at a pin temperature of 1100°F.

Test Procedure - Each blade attachment assembly was installed in a tensile testing machine with a radial load applied. The relative radial movement between the blade and disc sections was indicated by dial indicators mounted on the respective sections.

The radial movement between the hub and blade section of the test fixture was recorded at 200-pound increments. This test was repeated four times on each assembly. After this phase of testing, the René 41 test assembly was disassembled for general inspection. The condition of the attachment was satisfactory.

The other two assemblies were not disassembled for inspection. The unit using René 41 pins was reassembled using new pins for continued testing. Each assembly was mounted on the Tinius Olsen testing machine with a recording extensometer. The test specimens were loaded slowly to 13,000 pounds, in increments of 1,000 pounds, and held for 30 seconds at each increment to stabilize the elongation measurements.

Discussion - Under room-temperature conditions, yielding of the test pieces, Figures 438, 439, and 440, occurred at the following loads:

<u>Pin Material</u>	<u>Load (Pounds) at Which Yielding Started (Room Temperatures)</u>
Udimet 700	17,000
Inconel 718	20,000
René 41	21,000

At 1100°F temperature, as compared to room temperature, the yield points of the materials used in the test fixtures will decrease approximately 10 percent. The above-mentioned loads at which yielding occurs at room temperature were adjusted to be applicable at 1100°F as follows:

<u>Pin Material</u>	<u>Load (Pounds) at Which Yielding Starts (1100°F)</u>
Udimet 700	15,300
Inconel 718	18,000
René 41	18,900

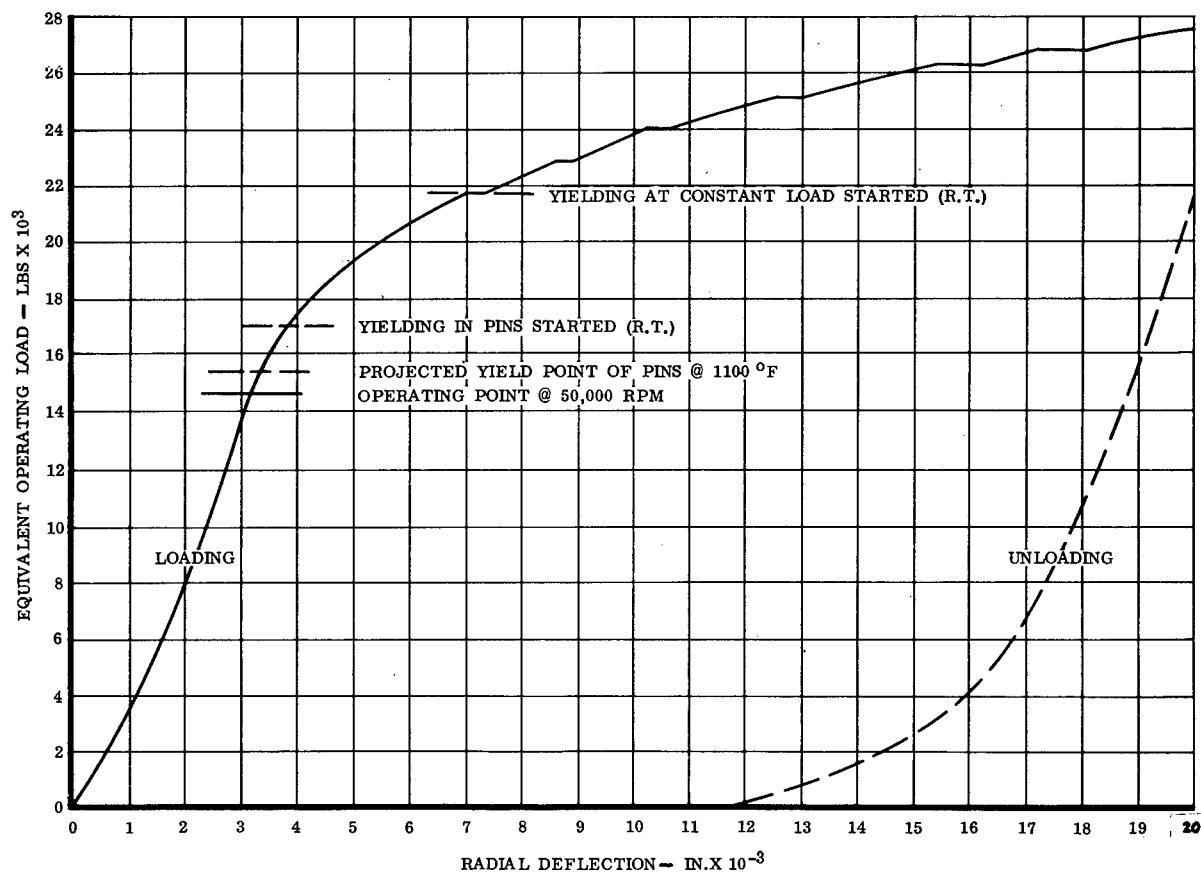


Figure 438. Load Versus Deflection Udimet 700 Pins (4).

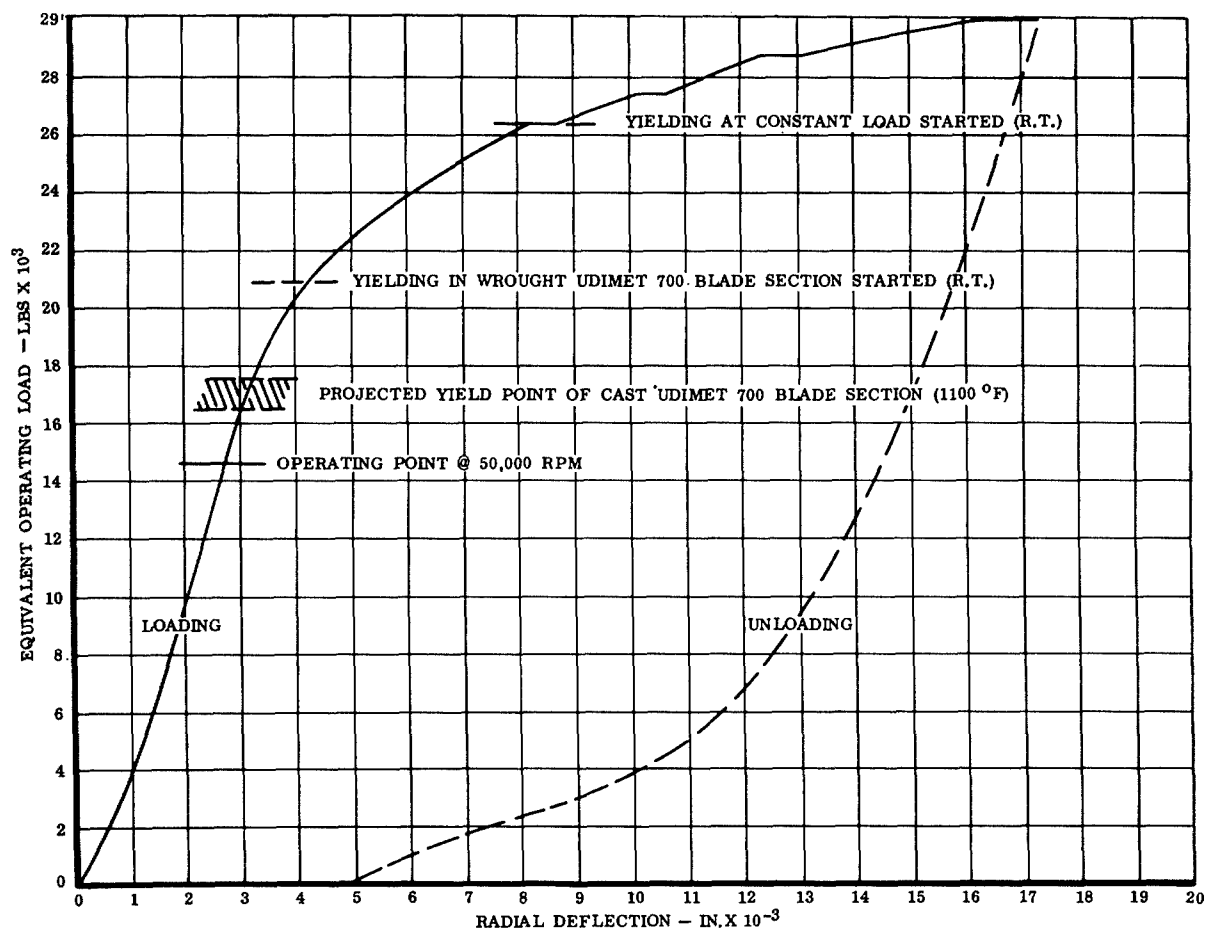


Figure 439. Load Versus Deflection Inconel 718 Pins.

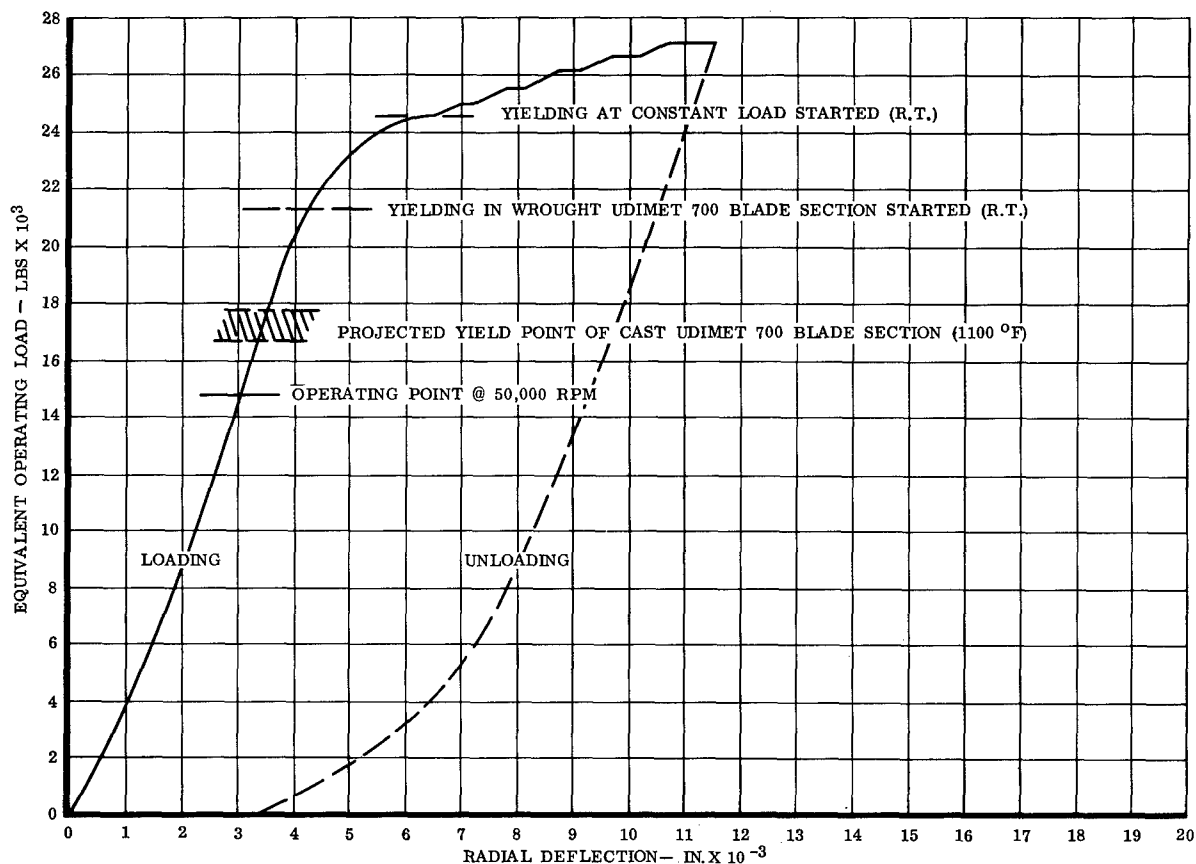


Figure 440. Load Versus Deflection René 41 Pins

The measurable yielding in the pins and in the assembly was as follows:

Pins	Yielding in Pins In.	Yielding in Assembly In.	Max Load Lbs
Udimet 700	0.004	0.010 - 0.011	27,500
Inconel 718	0.0005	0.004 - 0.005	29,800
René 41	0.0005	0.003 - 0.004	27,000

In the Inconel 718 and René 41 pin materials, nearly all of the yielding occurred in the blade section of the attachment rather than the pins. Figure 441 shows little pin deformation occurring. Inspection of



Figure 441. Pin Deformation.

the test pieces reveals that the majority of the deformation was in the blade section, Figures 442 and 443. Therefore, it can be concluded that the points of yielding on Figures 438 and 439 are those of the wrought Udimet 700 blade section. This occurs at a 20,000- to 21,000-pound load at room temperature and at an 18,000- to 18,900-pound load at 1100°F. The lower yield point of the assembly with the Udimet 700 pins is considered to be the yield point of the pins, which was reached before that of the blade section.

When the load which caused yielding of the wrought Udimet 700 blade section is known, the yield point of the same part made with cast Udimet 700 (material used for actual blades) can be predicted. The yield strength of cast Udimet 700 at 1100°F is 8 percent less than that of the wrought Udimet 700 used in the blade section of the test specimens (established by comparing published data for cast Udimet 700 with data received from a tensile test bar cut from the wrought Udimet 700 section of one of the test specimens). It therefore follows that the load which will induce yielding in the actual cast blades (attachment area) at 1100°F is 16,500 to 17,500 pounds.

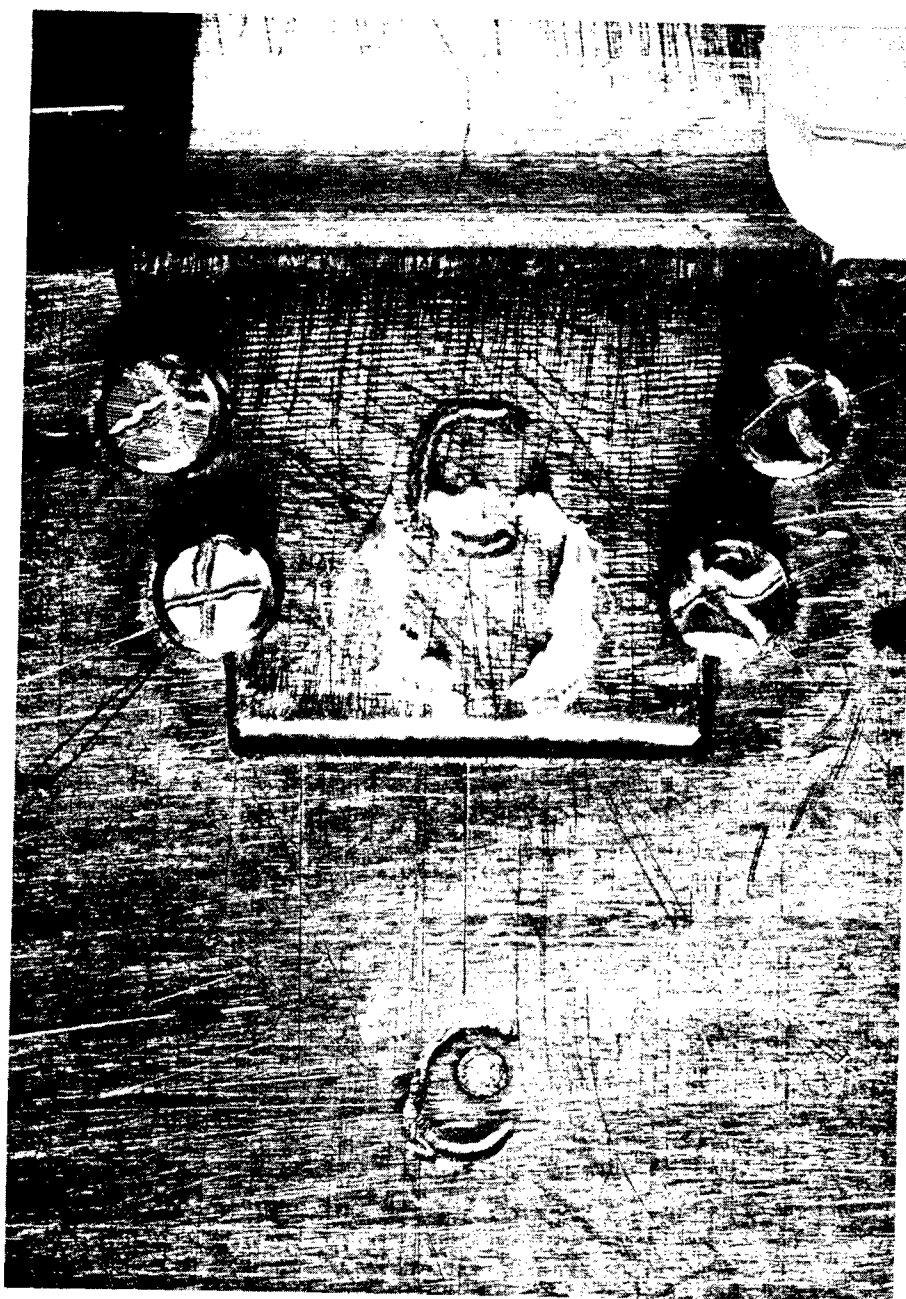


Figure 442. Blade/Disc Pin Attachment.

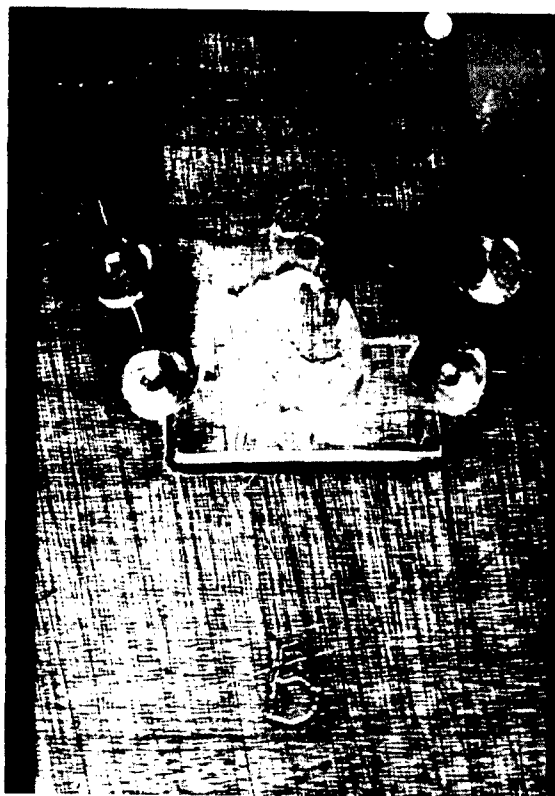
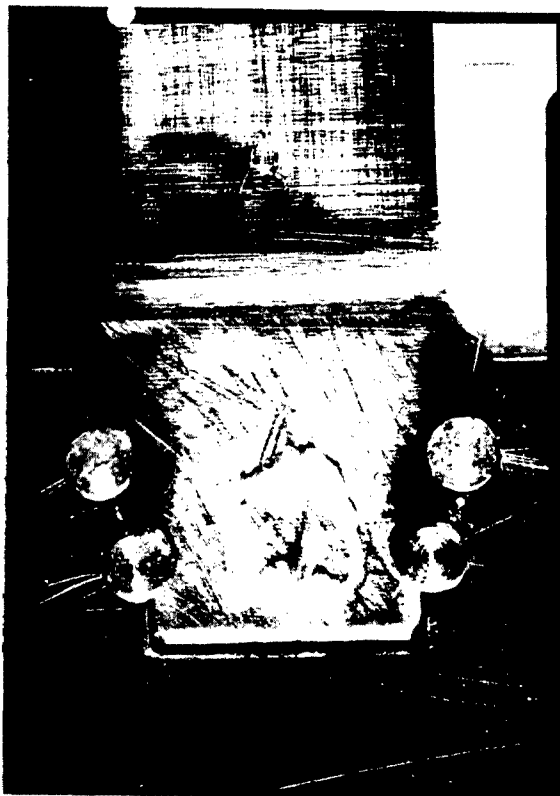


Figure 443. Blade/Disc Pin Attachment Yield Comparison.

Test results gave no apparent indications of the disc section of the attachments being a marginal area. Virtually no deformation was noted on the disc sections of the test specimens after they were subjected to loads of 30,000 pounds. Temperatures in the area of the disc tang are relatively lower than those in the blade section and pins. Comparison of the calculated stresses in the disc tang area with the Inconel 718 material properties presents an acceptable safety margin.

The following was concluded from the tests conducted:

1. Inconel 718 or René 41 material pins display greater strength than the blade section of the attachment assembly. Yielding will occur at loads from 16,500 to 17,500 pounds. At design speed and temperature, the blade section will be utilizing 85 percent of its yield strength.

2. Udimet 700 material pins yield before the blade section and are the weakest part in the attachment assembly. Yielding in the pins will occur at a load of approximately 15,300 pounds. At design conditions, the pins would be utilizing 95 percent of their yield strength.

It should be noted that any design speed running at attachment area temperatures in excess of 1100°F would lower the yield strength of the attachment to a level where yielding would be likely to occur.

It was recommended that both speed and temperature be limited during testing to 45,000 rpm and 1100°F maximum temperature of the attachment.

The tests revealed that if the maximum pin temperature is limited to 1100°F, any of the three pin materials tested could provide satisfactory performance with respect to material strengths. However, until the cooling concept was proven to be satisfactory, it was recommended that the wrought Udimet 700 pins, although they appear to be of slightly lesser strength than the others, be used due to superior mechanical properties at higher temperatures.

The "V" seal design was experimentally confirmed through sub-component testing. The design allowable expansion of the blade/disc "V" seal is 0.008 inch. The attachment elongation measurements obtained during the pull tests indicated that the maximum separation at design load is 0.0035 inch, Figures 438, 439, and 440. Therefore, separation between the seal and the blade-to-disc will not occur, resulting in proper sealing.

VERIFICATION OF DESIGN

The following discussion summarizes specific items relative to mechanical-structural integrity. In some cases, conclusions are drawn by deduction, rather than by comparison of measurement with design analysis. Sufficient go/no-go observations are available to substantiate Phase I analysis, and recommendations have been made for research into direct measurement techniques which will supply desired data.

Turbine Blades

The turbine blades which hermetically seal their coolant (water) were evaluated after testing. This was done by observing the thermal-indicating paint coloration change on the blade profile.

A blade metal temperature of approximately 1350°F was predicted while operating at a TIT of 2090°F and a rotor speed of 35,000 rpm. The thermal-indicating paint indicated the blade metal temperature to be between 1070° and 1470°F.

In order to confirm the presence of blade coolant, one of the blades, which was tested for 97 hours, was opened at its stem. The blade was centrifuged to drive out the coolant. From the blade weight change observed, it was determined that the coolant was present and that the thermal paint evaluation was valid.

The prime cause of blade failure was loss of the coolant. Loss of the coolant resulted from blade cracks which were caused by wall thickness inconsistencies and the lack of tip-cap weld penetration. This is discussed in greater detail under the Test and Failure Analysis section. The lack of nondestructive test procedures to assure manufacturing soundness caused these conditions to prevail.

Airfoil Stress Analysis

At the design point, a combined loading radial stress of 56,000 (presented in detail in Phase I) was predicted at the airfoil midspan, midchord location for a blade metal temperature of 1500°F. This would result in a stress rupture life of slightly greater than 100 hours. Nineteen turbine blades were subjected to 138 hours in such an environment with no indication of apparent failure. Therefore, stress levels experienced in the test program are within predicted limits.

The structural analysis of the blade airfoil concluded that low-cycle thermal fatigue could result under the following conditions:

<u>Stress (psi)</u>	<u>Location</u>	<u>Temperature</u>
66,500 - Compression	Trailing Edge	1700°F
33,900 - Tension	Midchord	1500°F

Due to the lack of this type of failure, it can be surmised that the thermal stresses were counterbalanced by the inertia and steam pressure (1500 psi) stresses successfully.

An elevated-temperature portion of a stress-versus-temperature plot for Udimet 700 (the blade material) is shown in Figure 444. Superimposed upon this plot are the calculated blade metal temperatures for several test points. Stress levels plotted are calculated inertia plus internal pressure stresses only. Thermal stresses will add to these stresses in some portions of the blade and will subtract in others.

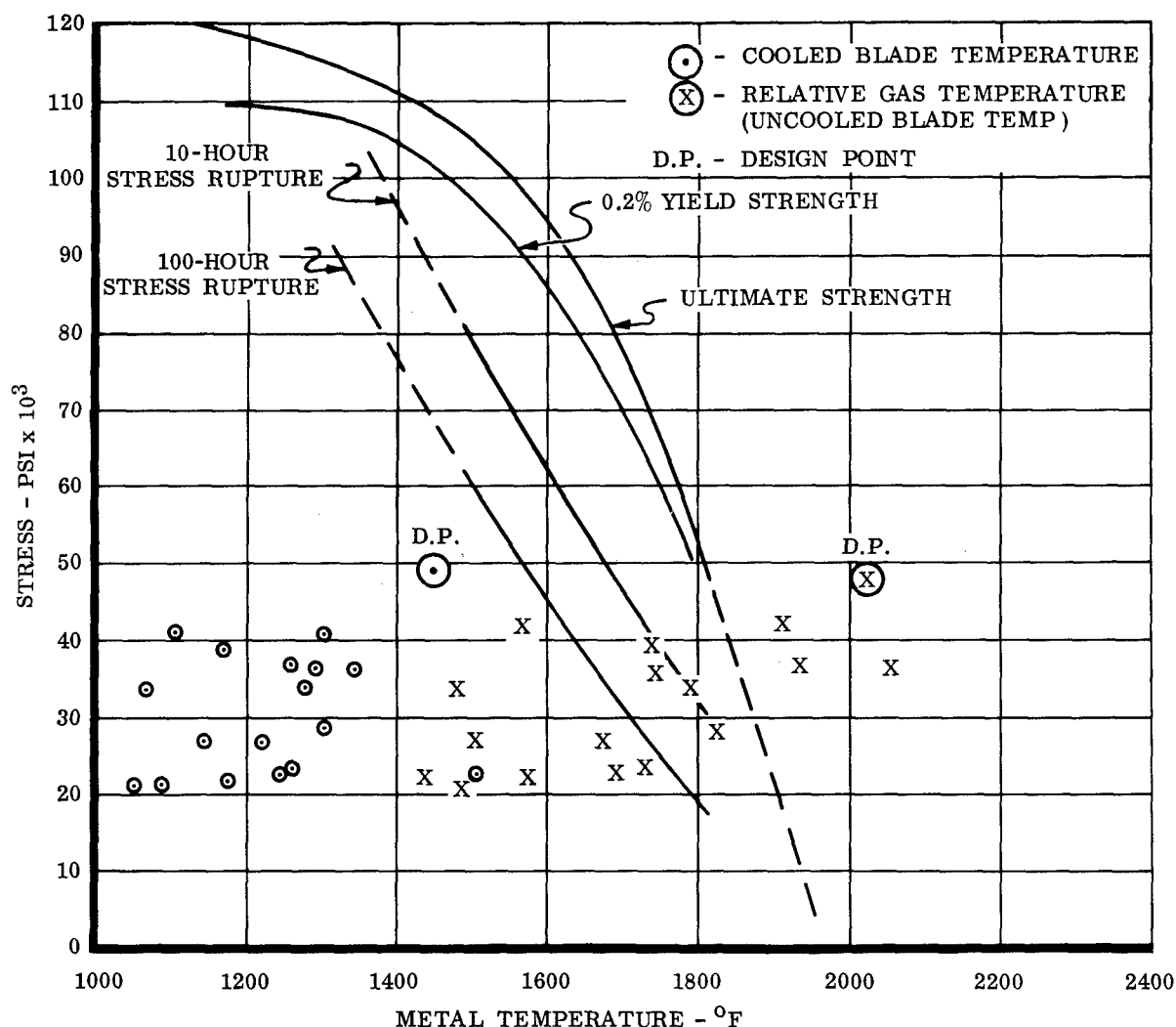


Figure 444. Stress-Temperature Relationship of Udimet 700.

Also plotted in Figure 444 are the relative gas temperatures (which are approximately equal to the uncooled blade metal temperature) for these test points. Several test points illustrate stress levels well beyond the ultimate strength of the material at the uncooled blade temperature. These test points outline the structural strength and the effectiveness of the cooling system in successfully maintaining blade integrity.

Blade-to-Disc Pin Attachment

The design concept of retaining the blade to the disc with four shear pins was successfully demonstrated. The pins were designed to operate at an average shear stress of 48,000 psi at 1100°F. Therefore, stress levels experienced in the test program were within predicted limits.

The disc pinholes in the blade attachment slot were undercut. This was done to permit the blade portion of the attachment to expand radially in the disc slot during elevated-temperature testing. This concept was successfully demonstrated. No pin or attachment failures occurred throughout all testing.

Blade-to-Disc Seal

A gold-plated Inconel X mechanical V-shaped seal was used between the turbine rotor disc and turbine blades. The purpose of the seal was to contain the fuel which passes through the disc and around the blade heat exchanger in the fuel circuit. It was designed to seal a 10,000-psi internal pressure with an expansion and contraction flexibility of 0.008 inch.

One hundred and eighty seals were rig-tested and provided good sealing capabilities. Two seals ruptured during tests; however, this did not result in a blade failure, Figure 423. The seal failures were attributed to a marginal tolerance stackup between the seal cavity in the disc and the bottom of the blade.

Disc Stress Analysis

The forged Inconel 718 turbine disc operated successfully at rim temperatures of 1200°F and 42,000 rpm. (Design operating conditions are described in detail under Structural Analysis - Turbine Disc, Phase I.) No indications of cracking are apparent in the disc where the various heat exchanger holes intersect the fuel circuit holes or where the fuel circuit holes intersect, in close proximity, at the fuel inlet and exit shafts. Therefore, the close proximity of these holes did not cause a stress concentration sufficient to propagate a crack, as had been feared in the design.

The design principle of enlarging the blade attachment slot at the disc rim by 0.003 inch per slot successfully permitted the disc to expand during reverse thermal gradient condition on shutdown without crushing the hollow blade manifold section between the attachment pins.

Fuel Circuit

Turbine Shaft-Fuel Seal - Fuel leakage was initially observed in the first series of tests between the stationary fuel inlet pipe and the turbine rotor stub shaft. This was attributed to a wiper face seal failure, Figure 410. Evaluation of the seal face revealed that an overtemperature condition caused the carbon wiper face surface to become unbonded and to crack. Removal of the fuel tube stem allowed better fuel circulation in this area, which reduced the wiper face temperature. No further problems in this area were noted throughout testing.

Fuel Deposits

After the initial 67 hours of turbine rotor testing, the turbine blades were removed for inspection. Deposits on the heat exchanger stem ranging from slight discoloration to a 0.003-inch-thick reddish black deposit were found, Figure 416. The deposit became powdery when the fuel evaporated. The substance was 90-percent organic and 10-percent iron oxide. The iron oxide was probably caused by fuel line deposits. This type of buildup had never been observed by Ethyl Corporation under laboratory test conditions on fuel coking; hence, they could not substantiate its cause. No malfunction of the rig operation during the entire test program was attributed to this condition. The phenomenon was kept under constant surveillance during remaining test series.

The passing of fuel over the blade-stem heat exchanger provided sufficient cooling to maintain the structural integrity of the blade attachment after tip-cap failure. The turbine blades, although failed, did not endanger the continued running of the rig.

Bearings

Two bearing failures occurred throughout all testing, one in the rig and the other in the gearbox. The gearbox pinion bearing failed during a run at 38,000 rpm. An inspection of the bearing revealed scratches on the bearing retainer. The failure was attributed to improper installation, causing premature failure.

The rig forward thrust bearing displayed a crack at the outer race cage. The bearing manufacturer reevaluated the bearing selection and found it not suitable for the test conditions required. This bearing was replaced with a different series bearing. No further problems were encountered.

Turbine Shroud

The turbine rotor shroud was designed in four segments to permit circumferential expansion during elevated-temperature testing, thus preventing the shroud from buckling. The shroud operated successfully at TIT to 2450°F. Minor damage in the form of dents occurred during several blade tip-cap failures, but did not prevent continued rig operation.

Exhaust Duct

Throughout all testing, the air-cooled duct operated successfully. After 261 hours of testing, only a minor crack in the oil scavenge area of the weld was found.

Turbine Nozzle and Combustor Assemblies

The air-cooled turbine inlet nozzle was in excellent condition throughout all testing (261 hours), as expected from Phase I cascade data analysis. The nozzle was exposed to local gas temperatures of 500°F above the design temperature with only one minor vane crack. A circumferential gradient of 1000°F was prevalent during early combustor development, and no thermal distress on the assembly was noted. The vane cooling concept utilizing internal fins was proven to be satisfactory.

The vane trailing edges displayed minor damage when the debris of the blade tip caps and a failed turbine inlet temperature probe impinged on their surfaces. This damage was minor and did not interfere with continued operation.

No failures in either the inner or the outer combustor assemblies were experienced. The outer and inner combustor shells were tested for 261 hours.

Thus, it has been established that the design techniques for the stationary structure are adequate for utilization on an advanced gas generator engine.

MANUFACTURING TECHNOLOGY

BACKGROUND:

The development of the prototype blade for the advanced fluid-cooled turbine is described in this report. Briefly, the manufacturing techniques investigated in developing this prototype were:

1. Electron beam welding of cored plates
2. Diffusion bonding of cored plates
3. Precision casting of hollow blades

Precision casting was chosen as the preferred method.

Section II documented the tooling, casting, and inspection techniques to cast the cored fluid-cooled turbine blade. Also included in this report was the development of a blade tip-cap, produced by using the cast blade as an EDM electrode to sink a cavity in the tip-cap to produce an intimate fit with the cast airfoil. This is shown in Figure 445.

Techniques were developed in Phase I to electron beam weld this square-cap configuration to the cast blade and to electron beam weld the heat exchanger plug to the cast blade. Also described in Phase I was the filling and sealing of the blade with water. An electron beam-welded turbine blade prior to finish machining is shown in Figure 446.

The results of mechanical thermal shock tests of the welded blades and of the tests performed to verify the presence of liquid in a finished blade concluded the Phase I section of this report.

The discussion below presents techniques, problems, and solutions encountered in providing hardware for full-scale Phase II testing.

DISCUSSION

Turbine Disc

Disc Process I - The material selected for the turbine rotor disc was Inconel 718, based on stress, weldability, and availability. The properties of the forging are shown in Table XXXV.

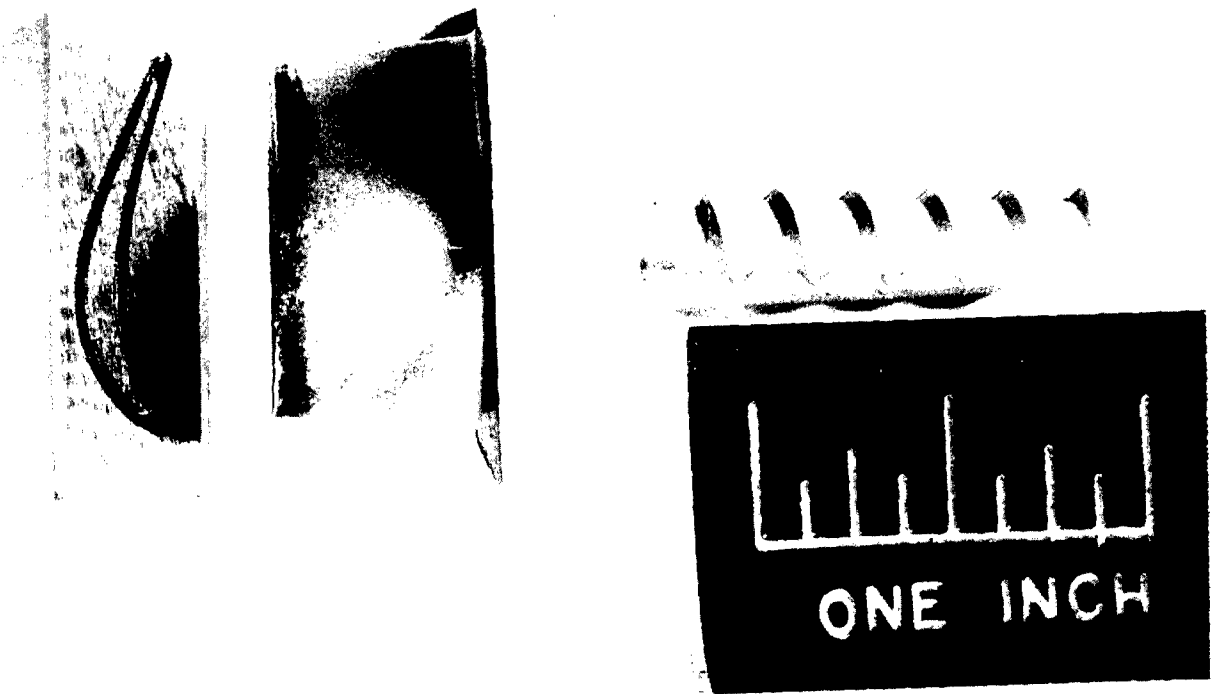


Figure 445. Turbine Blade Fabrication - Tip-Cap Grooved by EDM, Using Blade as a Tool.

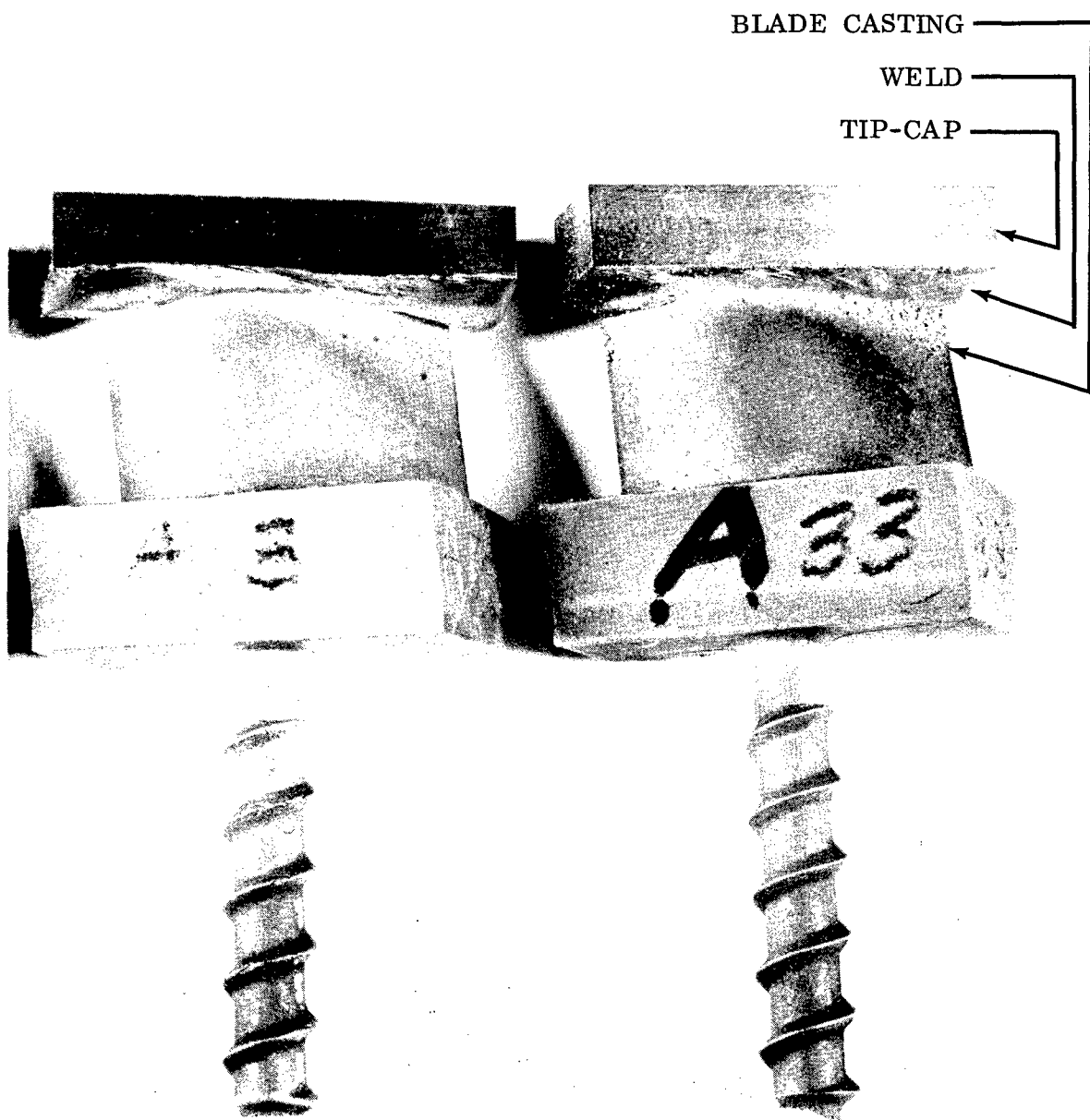


Figure 446. Experimental Manufacturing of Joining Methods for Tip-Caps.

Table XXXV
COMPONENT MATERIALS AND SPECIFICATIONS

MECHANICAL PROPERTIES	Specification CAE HS-718	Certified Result
TURBINE DISC - ALLOY INCONEL 718		
Room Temp Tensile (psi min)	140, 000	167, 000
Room Temp Yield (psi min)	125, 000	150, 000
Room Temp Elongation (percent)	10	17
Room Temp Hardness (psi min)	R _c 35	R _c 41
Stress Rupture (hrs min) @ 1200°F + 100, 000 psi	25	70

Two areas were considered to be difficult to machine because of the accuracy required: 1) blade/disc attachment, pinholes, and 2) fuel cooling passages. Sample specimens were processed to establish the optimum method of machining the disc pinholes for the blade attachment prior to machining the disc.

Several fabrication techniques for the blade/disc attachment were evaluated. The first method was an EDM operation for roughing the hole underside with the blade assembled in the disc slot. Difficulties with chips fouling the EDM tool were encountered, Figure 447. Some of the holes were successfully machined but lacked repeatability.

A second method, conventional drilling with cobalt drills, was tried on the assembled pieces. Due to the differences in machinability between the Inconel 718 (disc) and Udimet 700 (blade) materials, the drill wandered, Figure 448. Drill breakage also presented a problem.

A third method was developed using carbide cutters contoured for cutting the semicircular grooves in the disc slot. This method produced the best pinhole fabrication results. The relief in the disc pinholes was not as accurate as desired but was acceptable due to lack of good machining techniques at this time. The rapid wear of the 0.315-inch-diameter cutters for producing the pinholes was the cause of the inconsistencies. This was the best available method and was used for the blade/disc attachment.

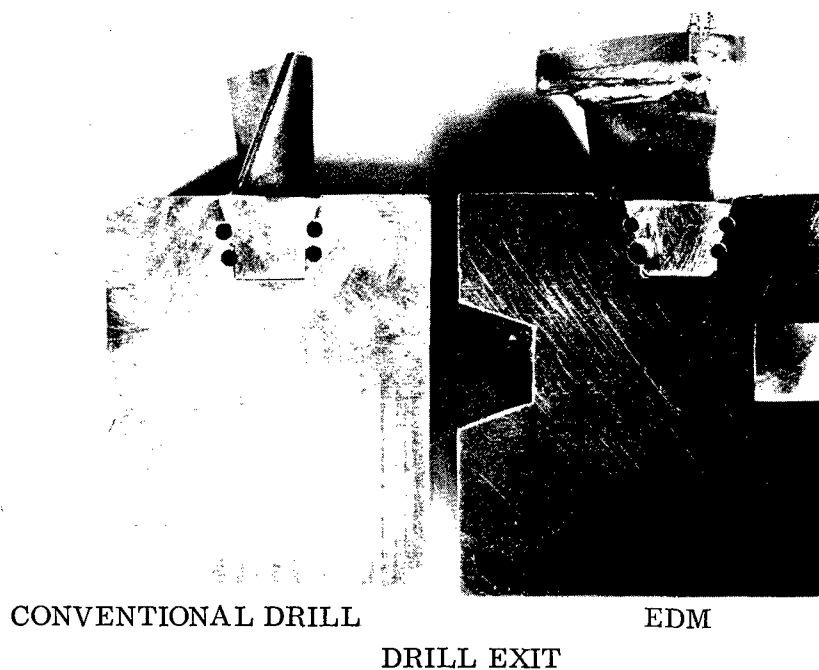
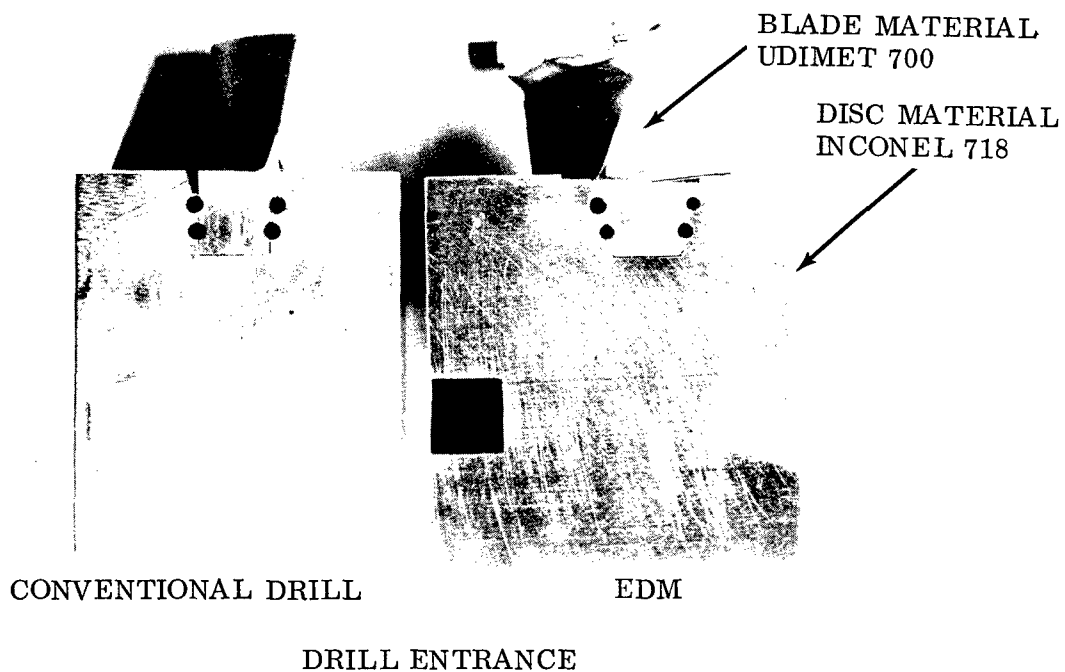


Figure 447. Sample EDM Drilling of Blade-to-Disc Materials.

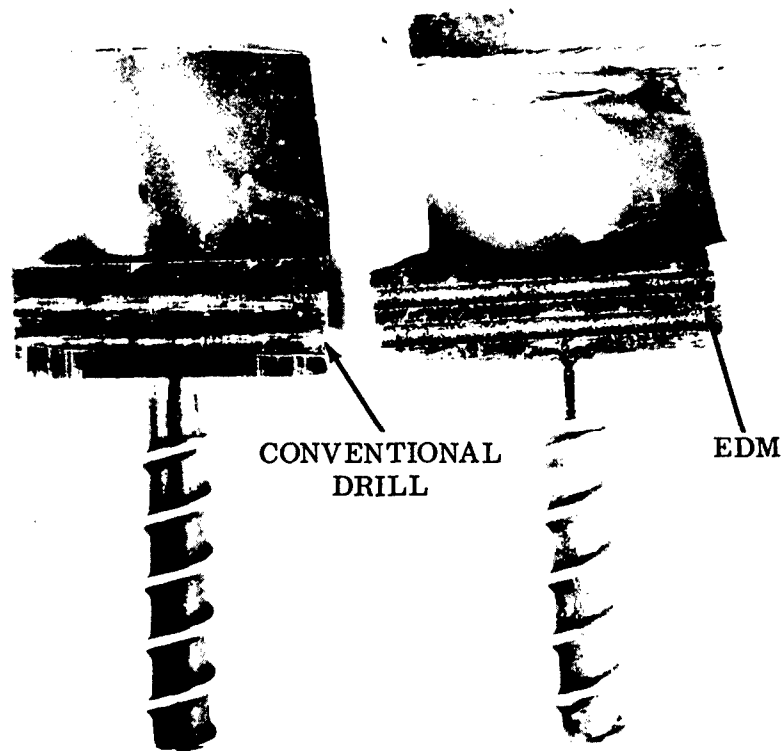


Figure 448. Blade Root Machining of Pinholes.

For each of the 31 blade slots, two fuel passages were required, Figure 449. A long (3.0 inches), thin (0.061 inch diameter) cobalt drill was required for the fabrication of these passages. The feed was slow and tedious, resulting in excessive drill breakage.

In order to alleviate this problem, the passages were opened to 0.125 inch in diameter. The fuel inlet passage at the center of the disc was maintained at a 0.061 inch diameter, Figure 449. This was done to prevent the passages, which merged at the center of the disc, from forming sharp edges which could cause high stress concentration factors.

Disc Process II - Turbine Disc I manufacturing history revealed that the process used for making accurate pin slots was difficult. Therefore, a grinding, roughing, and finishing operation sequence was developed to replace the cutter operation.

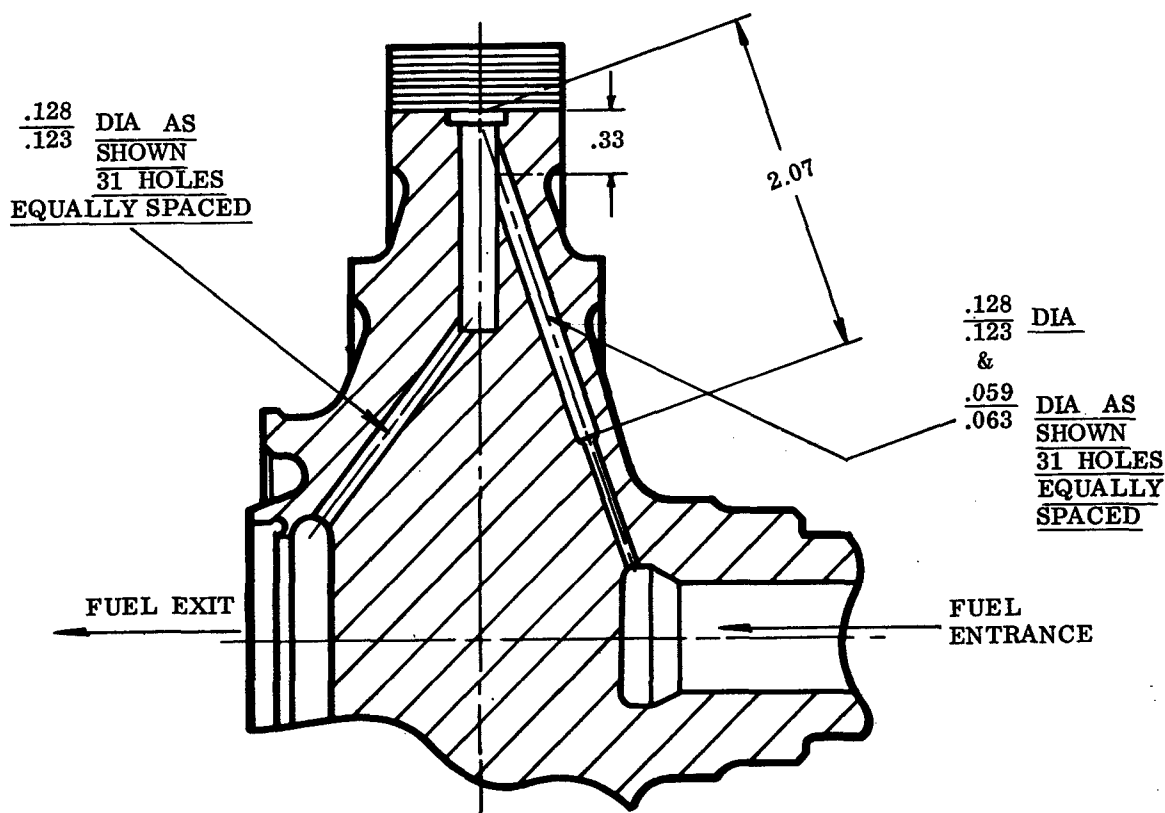


Figure 449. Disc - Fuel Passage.

The rough machining of the pinhole was performed by grinding a 0.075-inch-diameter relief cut first, using a 6-inch-diameter grinding wheel. This removed a major portion of the material, Figure 450. The cavity parallelism of the four pinholes along the length of the slot was found to be 0.0002 inch to the blade base platform. This roughing operation was used on the four pinholes of each disc slot.

The finish operation on the upper pair of pinholes was performed with a wheel grinder, Figure 451. The grinder followed the track made by the rough machining. The misalignment along the length of the hole (from end to end) was found to be 0.0005 inch. This was considered to be an improvement over the cutter tool method used on the first disc, and was therefore used on the outer pinholes of the second disc. However, the lower pinholes were not accessible with this tooling due to the required diameter of the grinding wheel. Therefore, another approach to the finish machining process was evaluated for the lower pinholes.

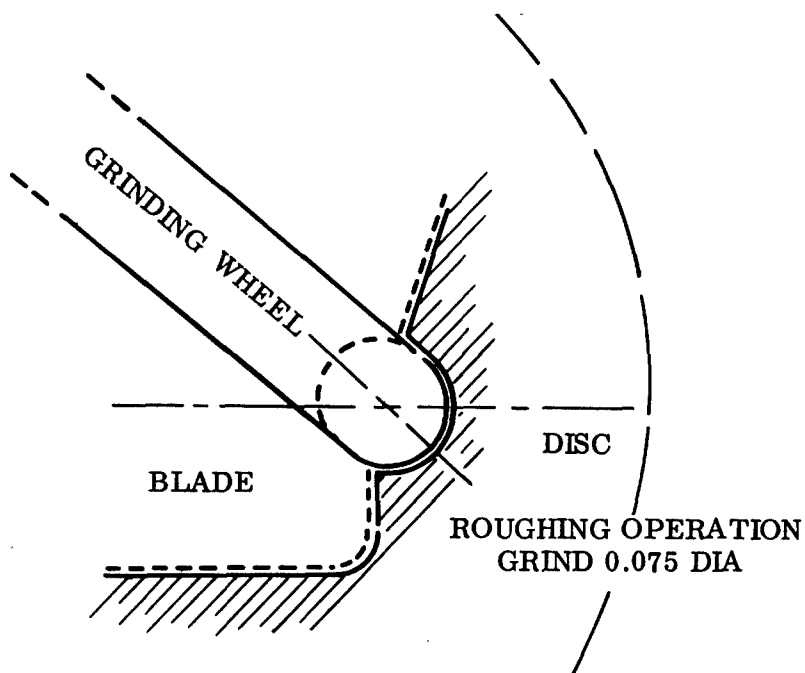


Figure 450. Turbine Disc and Blade Pin Attachment - Rough Machining.

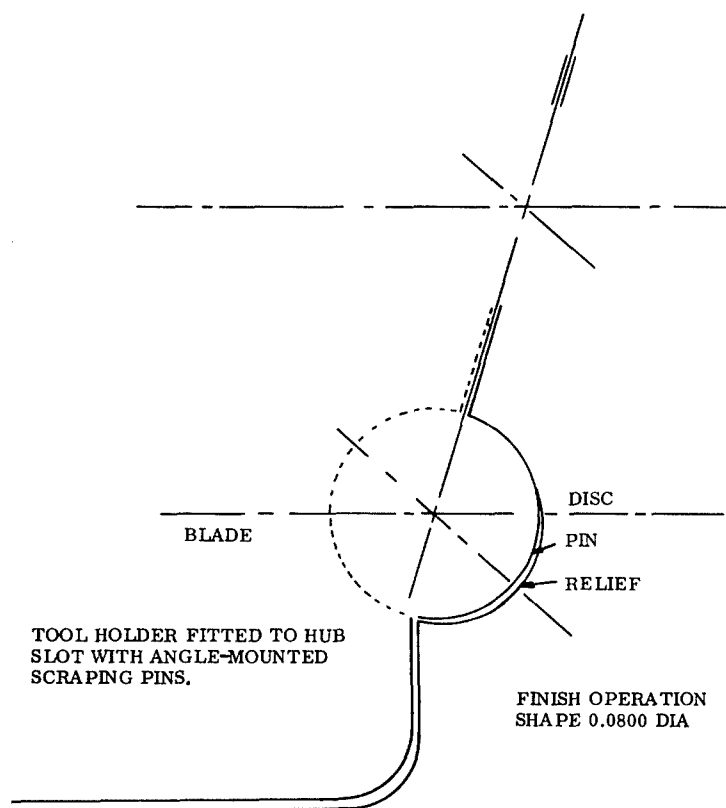


Figure 451. Turbine Disc and Blade Pin Attachment - Finish Machining.

A guide tool was made to fit the disc slot. Two tool steel pins were mounted in the guide tool, Figures 452 and 453. These pins acted as scrapers to finish excess material left by the initial rough grind. The scraper pins were adjusted in increments for the depth of cut desired. The process is similar to a shaper or broach-type operation. This method produced the dimensional accuracy (± 0.0002 inch) and repeatability.

The two fuel passages required per slot were electro-discharge machined. This proved to be an improved method over the drilling method used on Disc I. A hole diameter of 0.061 inch was made in the longest leg of the fuel passage. The shorter length hole diameter remained at 0.125 inch.

Turbine Blade

Blade Process I - The material selected for the turbine blades was cast Udimet 700 alloy. The properties are given in Table XXXVI and were within the Continental specification requirements.

The casting of these blades was outlined in Phase I.

A two-pass welding method for the contoured tip-cap was evaluated on sample blades. This process consisted of welding a wrought cap, contoured to an oversize envelope approximately 0.025 inch, containing an EDM cavity of 0.030-inch depth in the blade. The EB welding of the blade and cap assembly was done by passing the assembly linearly under the electron beam, over the contour of the blade-to-cap joint. A typical blade welded by this technique is shown in Figure 454.

Sample caps were tried, utilizing a 0.030-inch-deep EDM cavity in the contoured tip-cap. It was found that, by shifting to a Hamilton Standard-type electron beam gun using a fine focused beam, the depth of the EDM cavity could be reduced in this contoured tip-cap. An EDM cavity of 0.015-inch depth was used in the final fabrication of the welded tip caps. This joint had the advantage of 1) accurately locating the cap with reference to the blade, and 2) compensating the blade wall thickness variation with the minimum input of welding energy.

The blade was fitted with a heat exchanger plug which was electron-beam-welded to the heat exchanger. This plug was designed with a fill spout, Figure 454.

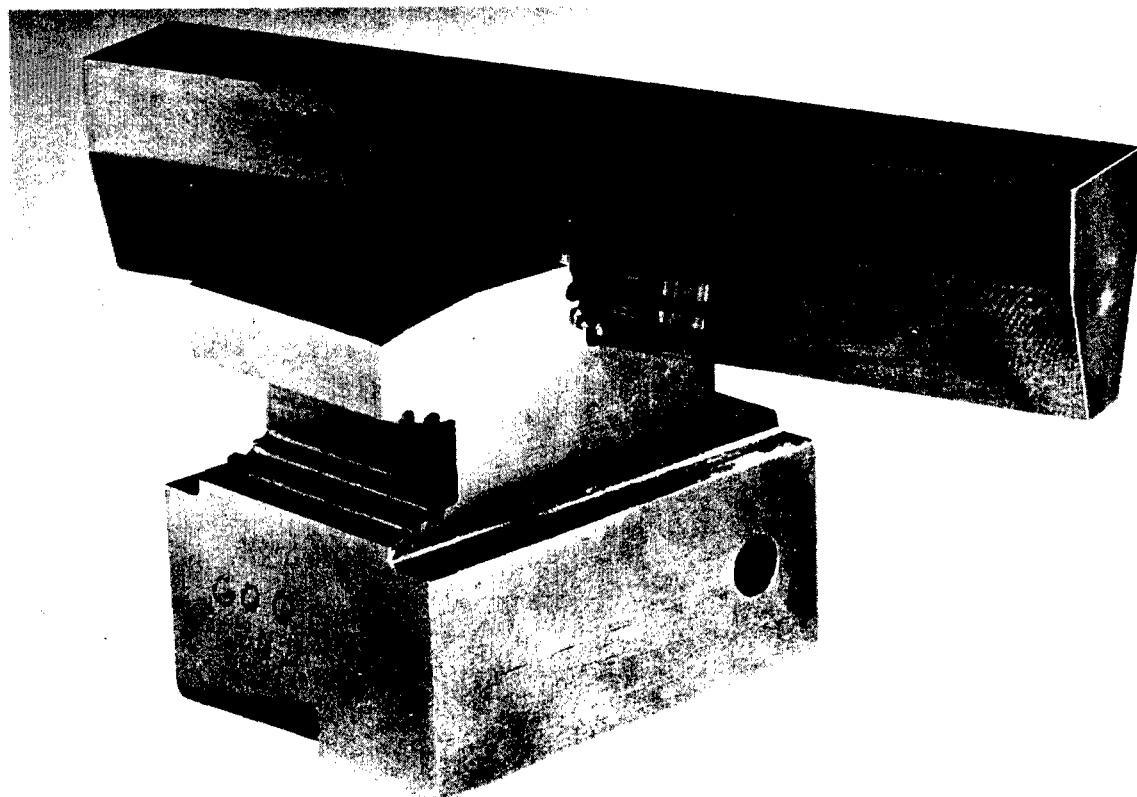
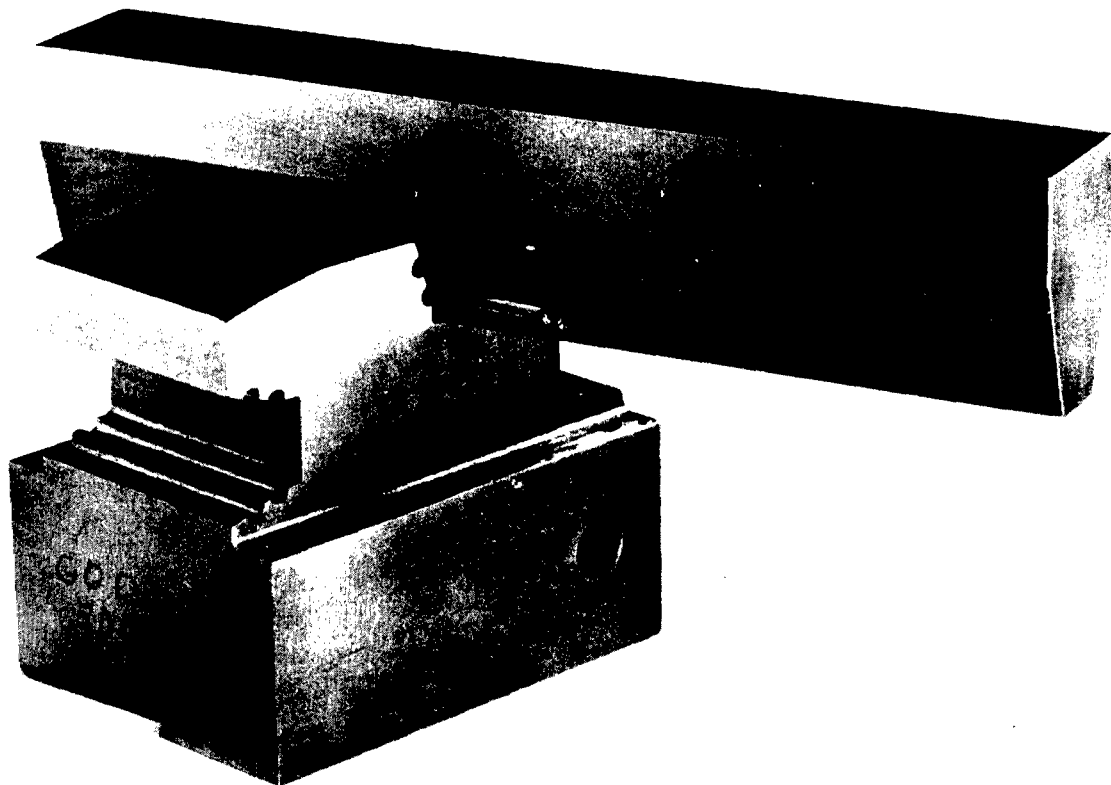


Figure 452. Rotor Pinhole Blade Attachment Sample, Fluid-Cooled Turbine.

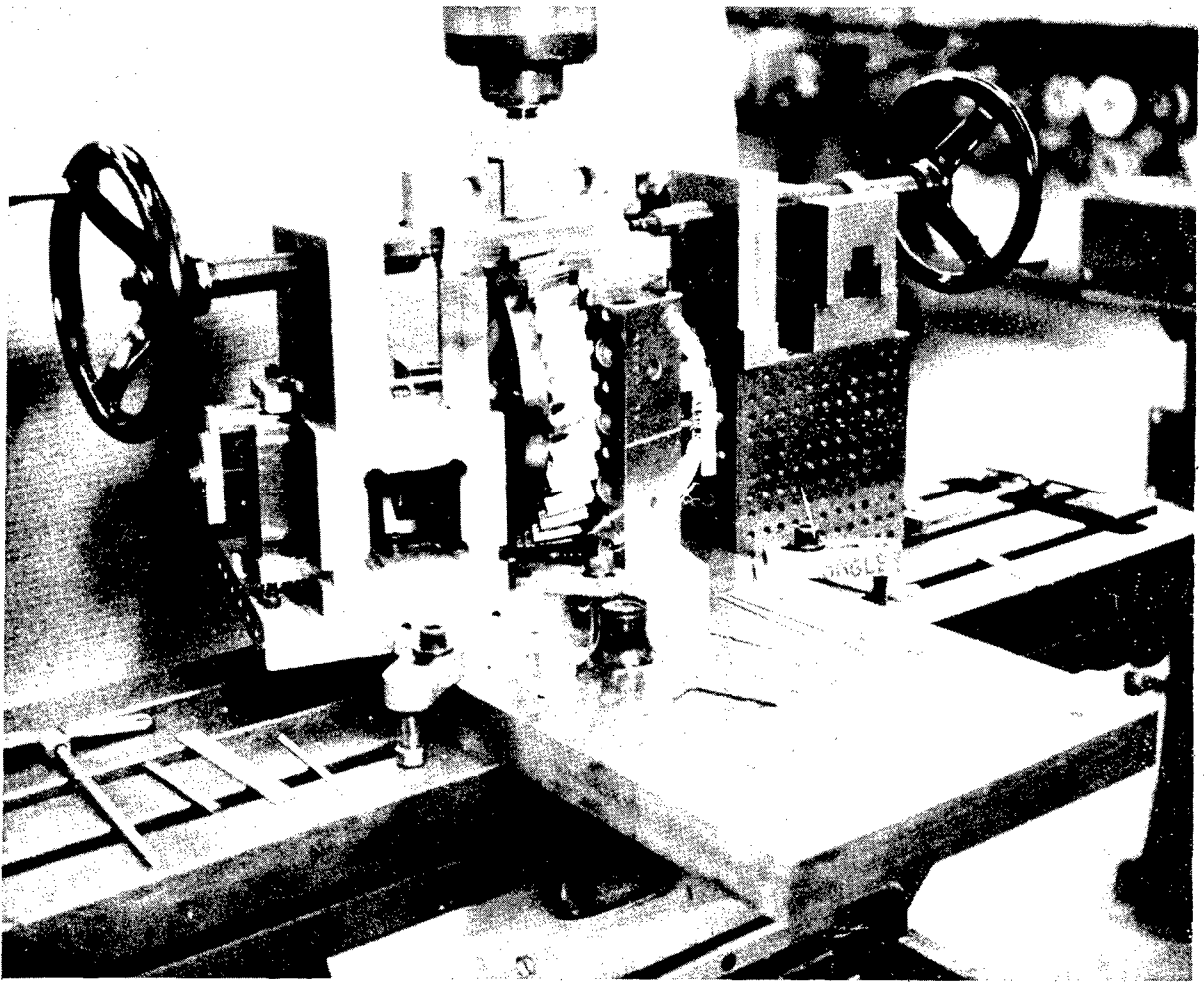


Figure 453. Pinhole Broaching Setup - Fluid-Cooled Turbine.

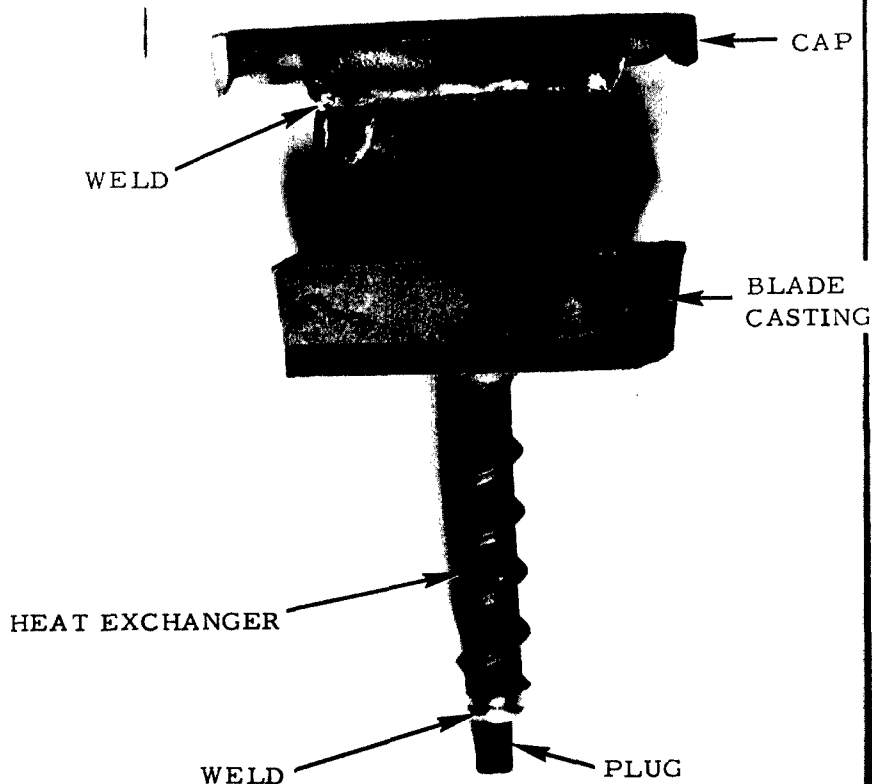


Figure 454. Fluid-Cooled Blade, Welded Assembly.

Table XXXVI
COMPONENT MATERIALS AND SPECIFICATIONS

MECHANICAL PROPERTIES	Specification Nominal	Certified Result
TURBINE BLADE - ALLOY UDIMET 700		
Room Temp Tensile (psi min).	160, 000	163, 000
Room Temp Yield (psi min)	125, 000	126, 000
Room Temp Elongation (percent).	10	11
Stress Rupture (hrs min) @ 1000°F + 22, 000 psi	25	49

After welding the tip-cap and the heat exchanger plug, the intermediate machining operations (Appendix I) were performed. This was then followed by pressure checking to assure the integrity of the weld. The blades were then held in a shuttle, and the platform area was rough machined. The heat exchanger stem was ground to produce the correct fin height, and the blade tip area was finish ground. Following this operation, the blades were filled with fluid. A micrometer hypodermic syringe was calibrated for the insertion of the water coolant to the blades. The blades were filled with 0.0133 cc of water (2 percent by volume of the core), sealed by welding, and re-pressure checked with helium in a container for 5 minutes at 1200 psi. The blades were then placed in a container filled with acetone and were observed for any evidence of bubbles caused by leakage.

After the final weld, the blade attachment area was machined to provide the required gap in the disc slots. The blade pinholes were machined to coincide with the location of the disc pinholes. The blades were identified and assigned to corresponding disc slots. The finished blade is shown in Figure 455. The complete blade processing is shown in Appendix IX.

The blade casting method used in Process I yielded 75 acceptable castings out of approximately 700 cores, which yielded 41 finished blades for testing.

Blade Process II - Due to casting difficulties encountered, a review of the fabrication was made with the precision casting source. The problems were associated with the cores. They were summarized as 1) core breakage at all core-making operations, including core molding, core baking, slot cavitation, core assembly, and core waxing, and 2) core breakage during casting.

The low yield of blades, principally due to core breakage, did not improve even with close surveillance and checking of all operations. Process changes were made to rectify the problem as follows:

1. Core material was changed to a higher strength mix.
2. The injection molding procedure was replaced by transfer molding.
3. The core was reinforced by a cross piece at the top of the forked core, Figure 456.
4. The core tooling was modified to include the forming of the slots; this eliminated the Cavitron machining operation.

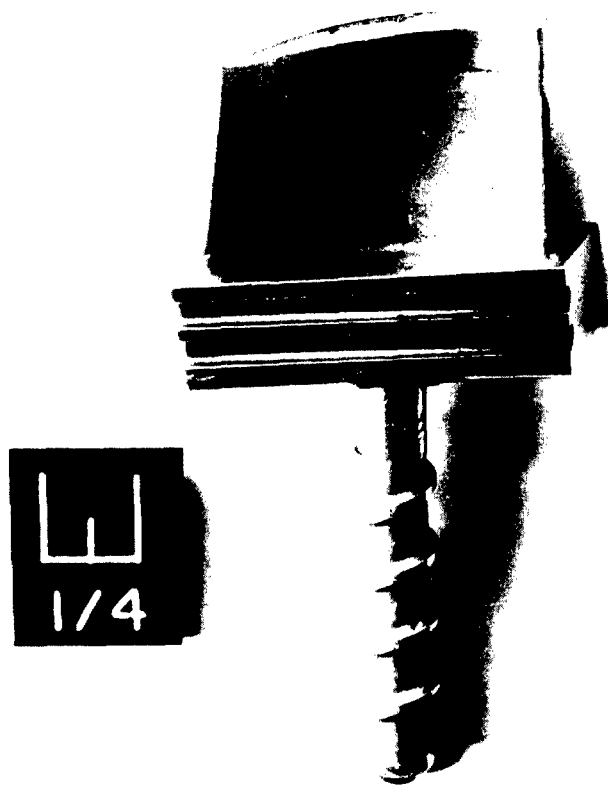


Figure 455. Finish Machined Blade.

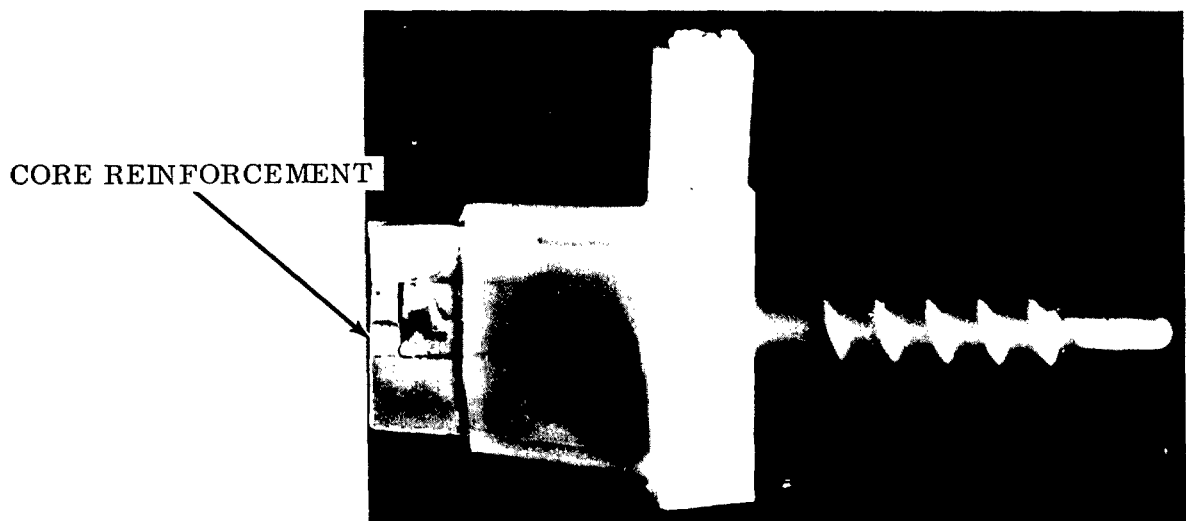


Figure 456. Wax Pattern and Core for Blade.

Sample castings were evaluated (see Appendix I). Metallurgical evaluation of accepted castings revealed sound metal throughout the airfoil, attachment area, and heat exchanger (free from porosity, shrink, and gas holes). However, radiographic inspection revealed internal oxide inclusions in some of the castings. Verification was made microscopically, Figure 457, and the parts were rejected.

The tip station was accessible, and the wall thickness was checked 100 percent. A typical undersize tip thickness is shown in Figure 458 and was caused by a core mismatch. The midspan thickness could only be spot checked, because spot checking had to be done by destructive tests. A tip minimum thickness check was made and certified by the casting vendor on all blade castings.



Figure 457. Photograph of Blade Microscopic Showing Area of Oxide Inclusions and Shrinkage.



Figure 458. Blade Showing Thin Wall at Trailing Edge Caused by Core Mismatch.

A surface condition, which appeared to be either alloy depletion or oxidation, was found on several of these castings. The depth of this surface condition measured from 0.0005 inch to 0.001 inch, Figure 459. The cause of surface depletion was thought to be either a mold/core reaction with the metal or a side effect of the core removal process. This condition could not be readily remedied; however, the depth of the defect was not considered to be detrimental, and the blades were accepted.

The tooling modifications were completed, incorporating the process changes, and the blade castings were produced. This process yielded 88 acceptable castings out of 100 cores, which yielded 55 finished blades for testing.

As indicated in the Mechanical-Structural Integrity section, a 100-percent tip thickness check did not ensure that the blade midspan wall was of adequate thickness to meet structural specifications. In fact, 15 blades manufactured from Process II cracked in the lower airfoil area due to wall thicknesses below specified design level.

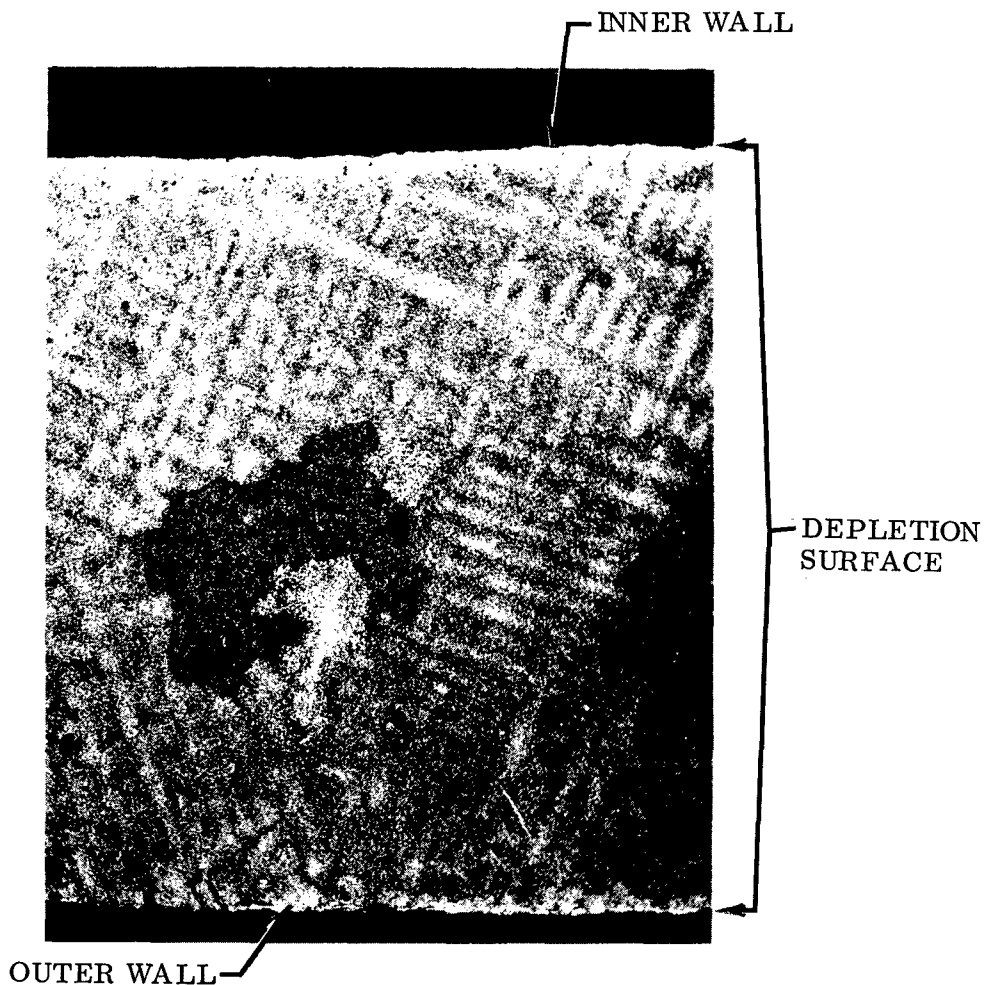


Figure 459. Surface Condition Found on Castings.

This again emphasizes the need for methods specifically developed for NDT of small turbine blades.

The preparations prior to machining were: 1) casting each airfoil into soft metal holding shuttles, and 2) aligning the heat exchanger shanks with respect to the airfoil, as required to meet print specifications.

The tooling and templates used in the machining operations of the blade are shown in Figures 460 and 461. A shuttle fixture was used for positioning the cast blade in the holding fixtures prior to imbedding with a soft metal matrix, Figure 461.

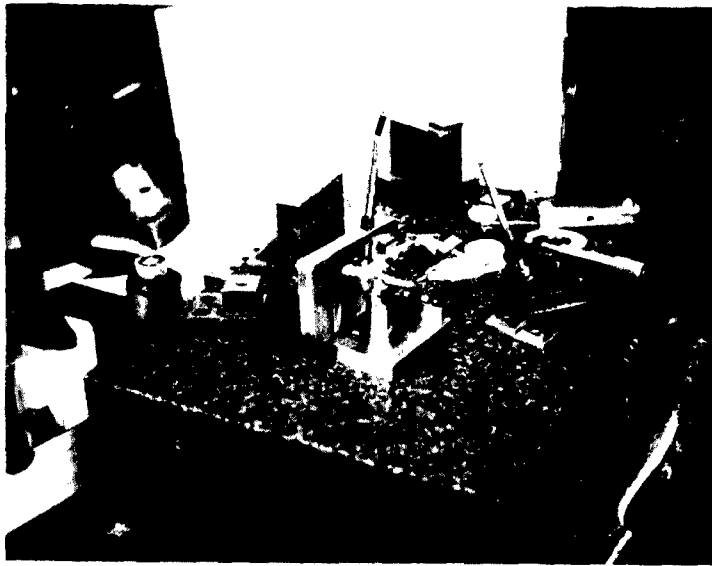


Figure 460. Blade - Shuttle Fixture for Locating Prior to Machining.



Figure 461. Blade - Grinding Wheels and Dressing Templates.

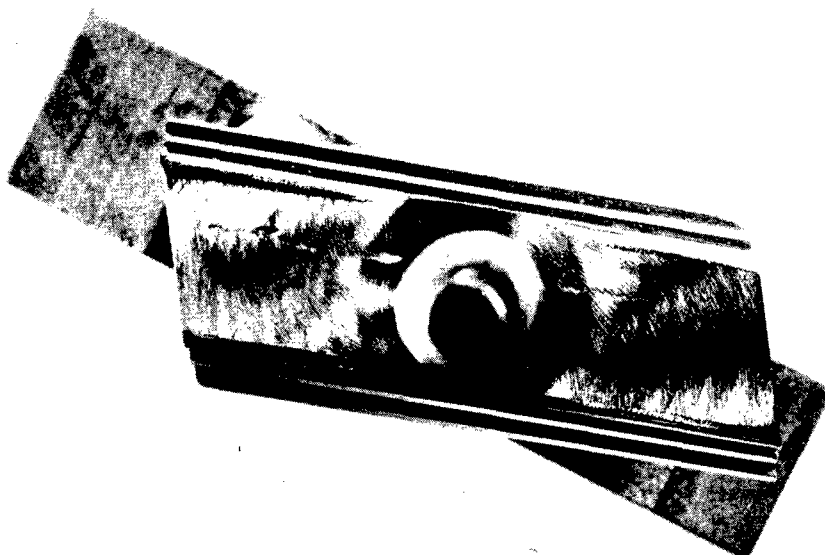


Figure 464. Turbine Blade Platform.

Additional nondestructive tests were surveyed, and preliminary tests were conducted to improve the integrity of the blades in the following areas: 1) wall thickness, and 2) soundness of the electron-beam-welded tip caps.

Wall thickness measurements using radioactive probes were investigated. Satisfactory wall thickness measurements of the fluid-cooled blade were not practical at this time, due to current NDT limitations (the available probes were too large for these blades). Thickness measurements utilizing ultrasonic techniques such as those used to measure foil thickness were also found to be unsatisfactory. Two difficulties were encountered with this technique: 1) unavailability of transducers with a spot size small enough to delineate the core passage only, and 2) complexity of fixtures necessary to maintain the ultrasonic beam normal to the airfoil at all times.

The soundness of the electron-beam-welded tip caps was determined principally by an internal pressure test at several stages of manufacture, and by an external pressure test after final machining and blade sealing. These tests were supplemented by a careful examination at Continental using radiographs of the finished blades.

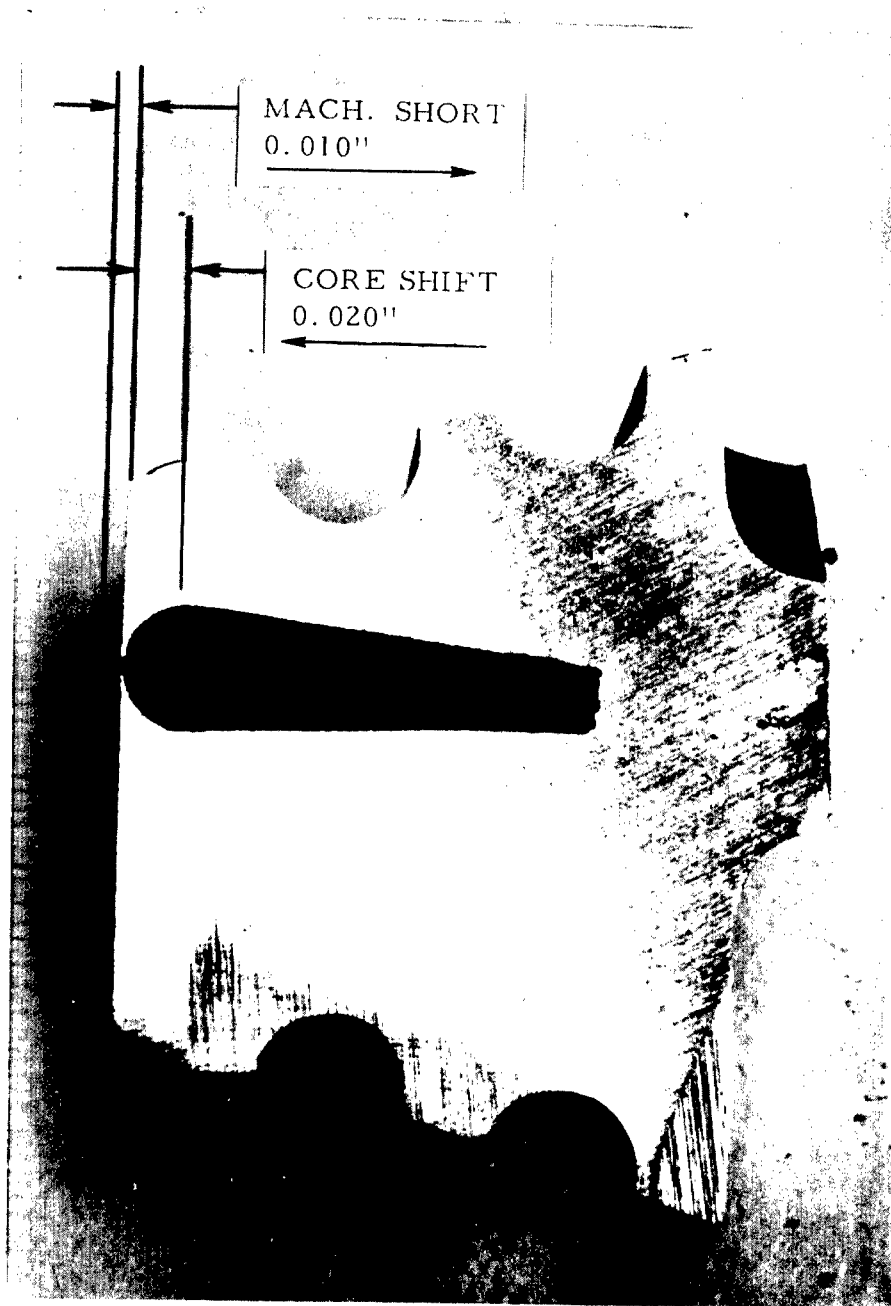


Figure 465. Turbine Blade Platform.

Ultrasonic tests to determine weld discontinuities were conducted and found to be impractical for this application, due to the short blade length and thin wall thickness, which would require transducers having a smaller spot size than those currently being manufactured.

Turbine Shaft Assembly

Three shaft assemblies were fabricated. A fuel slinger shaft assembly was used for the combustor development test program. This assembly consisted of a fuel shaft housing, a dummy disc-shaft, and an intermediate shaft, Figure 466. The fuel valve housing was electron beam welded to the dummy disc and pressure checked.

Turbine rotor I shaft assembly, Figure 467, was assembled basically in the following manner:

1. Weld fuel valve housing to disc and pressure check.
2. Assemble the complete shaft, and weld intermediate shaft to the rotor.
3. Disassemble the front shaft, and stress relieve the weldments.
4. Reassemble the complete shaft assembly, and finish grind the front and rear bearing journals.

After the welding of the fuel valve housing to the disc, an eccentricity of 0.012 inch was observed. This was improved by burnishing the valve stem. After finish welding the intermediate shaft, the runout was 0.004-inch total indicated reading (TIR), which was considered to be acceptable for final grinding of bearing races.

The welding fixture for rotor II was modified by including a spring-loaded-type live center and heating it to improve alignment of components during welding. The runout of the fuel valve after welding was improved by this technique (0.005-inch TIR).

After welding and heat straightening, the intermediate shaft was found to be within 0.004-inch TIR. The shaft assembly was stress-relieved and ground between centers. All bearing surfaces checked were concentric within 0.0015-inch TIR. A detailed operation sequence is found in Appendix X.

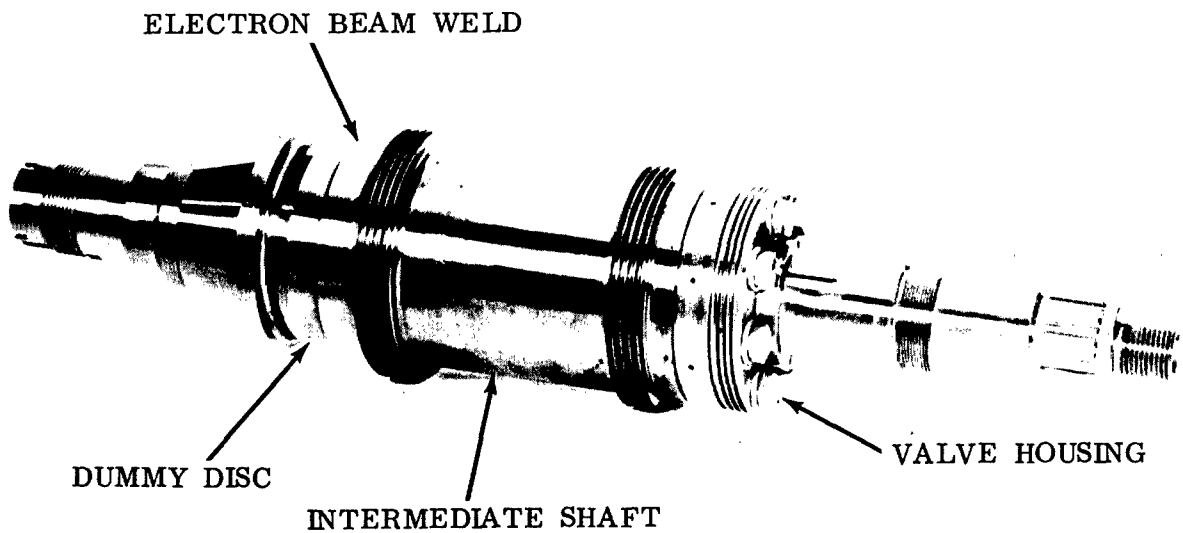


Figure 466. Combustor Development Slinger Shaft.

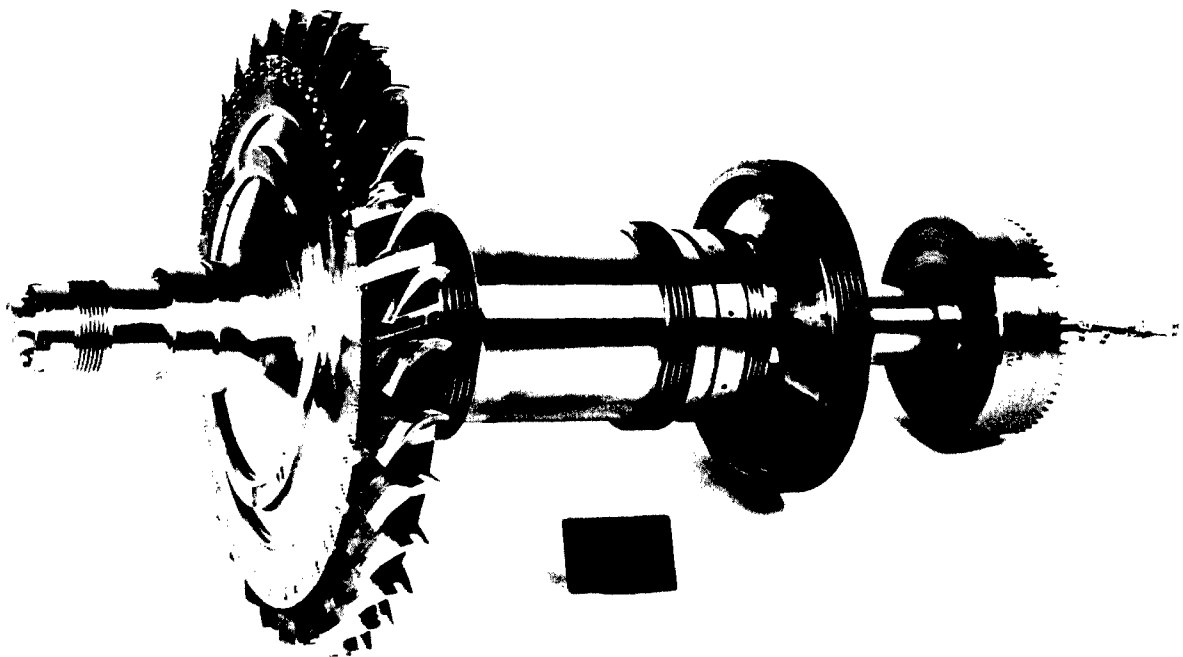


Figure 467. Turbine Rotor I Shaft Assembly.

Pin

The blades are attached to the rotor by four pins approximately 1 inch in length and 0.080 inch in diameter. The pins for both turbine rotors were roughed out of heat-treated forging stock by EDM and finish ground to final dimensions, Figure 468. This was done because of the commercial unavailability of small-diameter Udimet-700 material. Metallurgical analysis during processing was made to determine the depth of the EDM surface effect, which is considered to be detrimental to the strength properties of the pins. Adequate stock was provided; therefore, this surface condition was removed during final grinding, Figure 469.

The nozzle vane assembly consisted of 24 vanes and an inner and outer shroud, Figure 470. No manufacturing difficulties were encountered. At inspection, the nozzle throat area was found to be out of print, resulting in an undersize throat area by approximately 10 percent. The nozzle assembly was accepted under these conditions to avoid further delays in the test schedule.

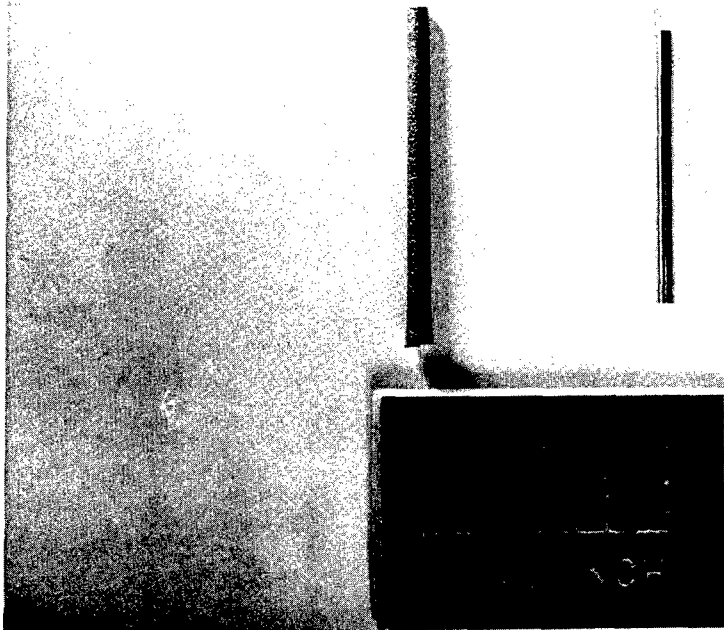


Figure 468. Pins - Blade-to-Disc Attachment.

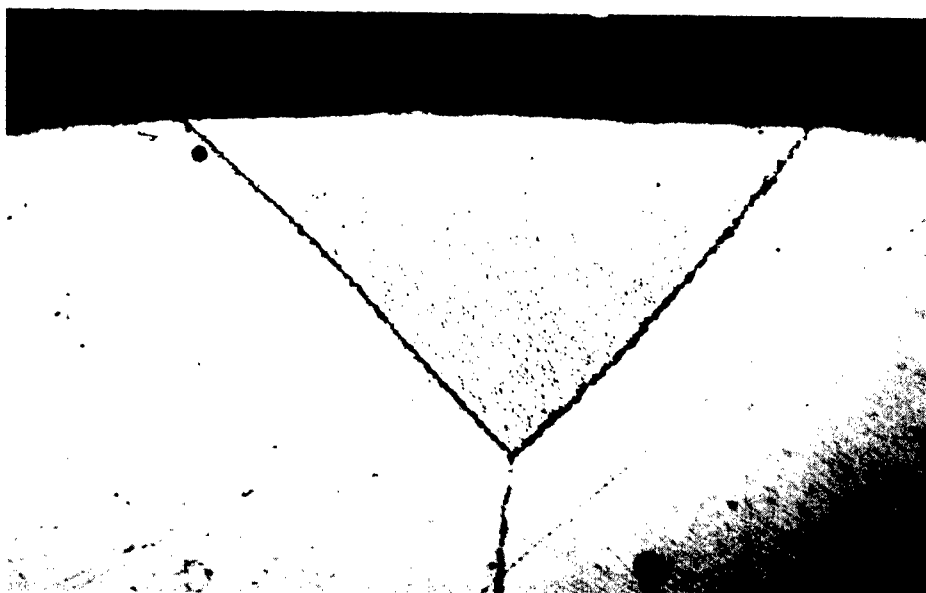
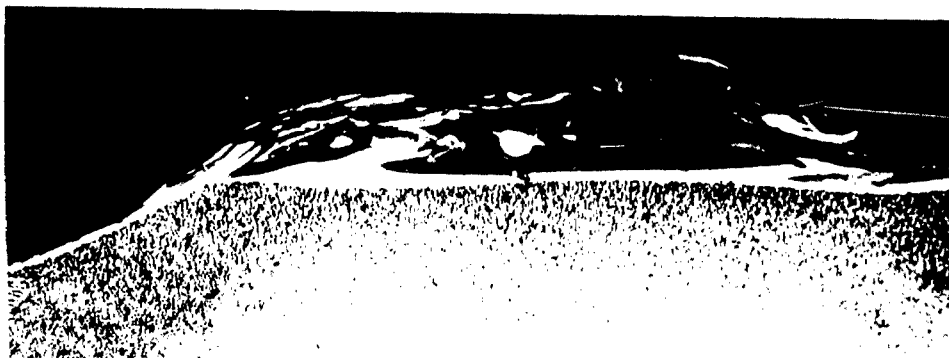


Figure 469. Microstructure - Attachment Pin Surfaces.

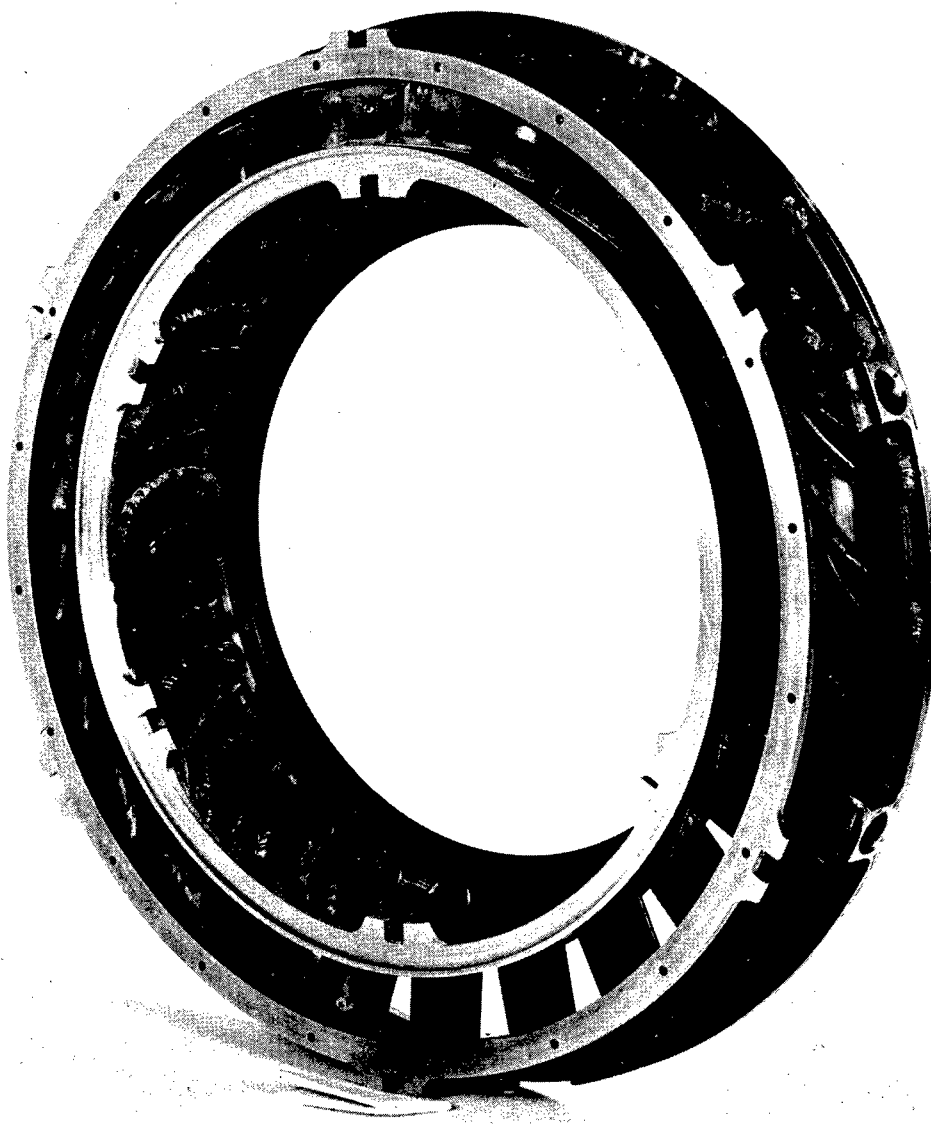


Figure 470. Air-Cooled Turbine Inlet Nozzle.

Subcomponents

The following rig hardware assemblies were also fabricated and procured:

<u>Item</u>	<u>Quantity</u>
Nozzle Vane	2
Turbine Shroud	2
Combustor	1
Exhaust Duct	1
Gearbox	1

The turbine shroud was made from a circular section and was segmented into four equal pieces, Figure 471. Its assembly into the rig is shown in Figure 472. Fabrication of the segments, however, did provide some difficulty. The ring was made as a unit in a fixture. After all machining was completed, the ring was cut into segments, which were slightly warped. At assembly the shroud was oval in contour, causing the blade tip clearance to vary from 0.020 to 0.030 inch.

The combustor is similar in size to the Continental T65 engine combustor and was procured, Figure 473, without fabrication problems.

The exhaust diffuser assembly was fabricated from L-605 material, Figures 474 and 475. No fabrication difficulties were encountered for this assembly.

The gearbox assembly was composed of two housing castings, a pinion gear and a bull gear (Figures 402, 403, and 404). The gearbox housing displayed a large amount of porosity. These areas were repaired and provided satisfactory for operation.

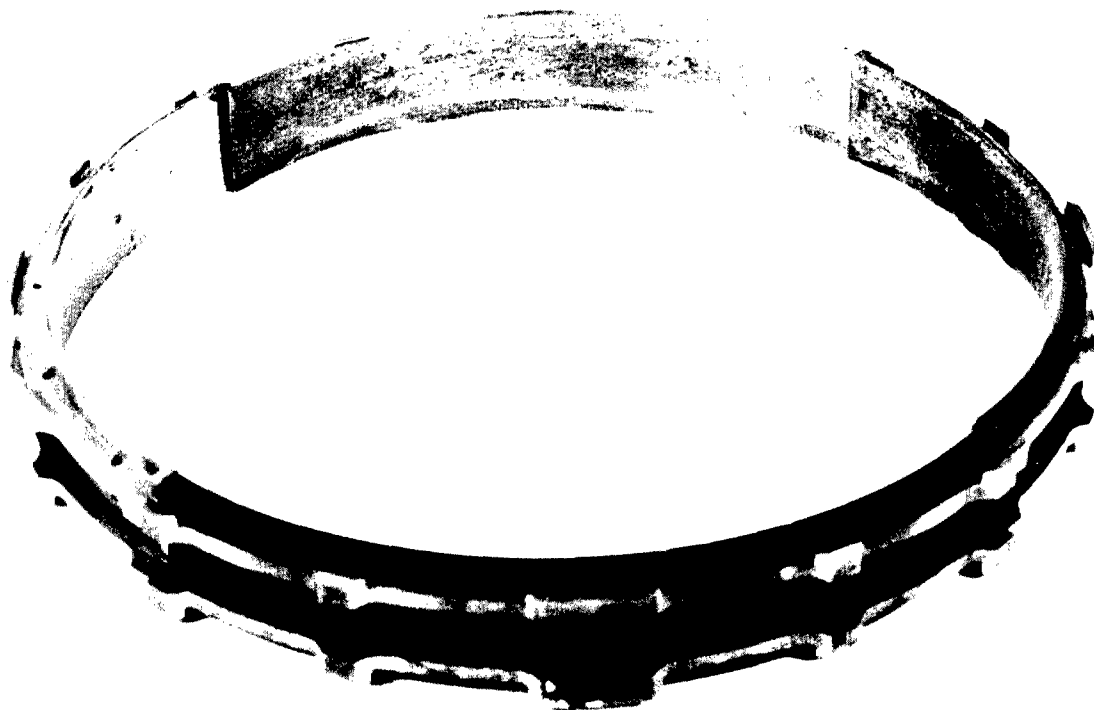


Figure 471. Air-Cooled Turbine Shroud.

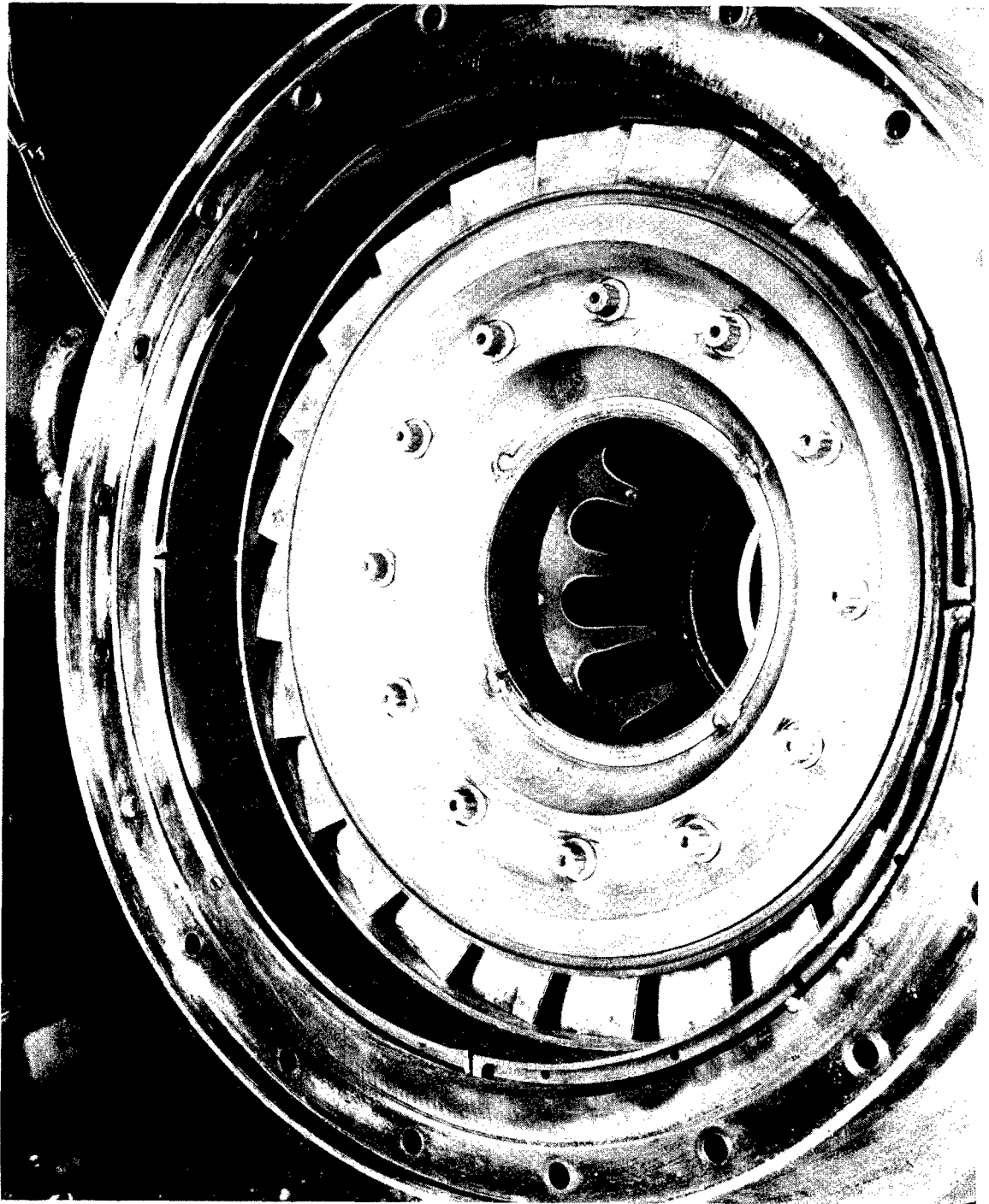


Figure 472. Nozzle - Shroud Assembly.

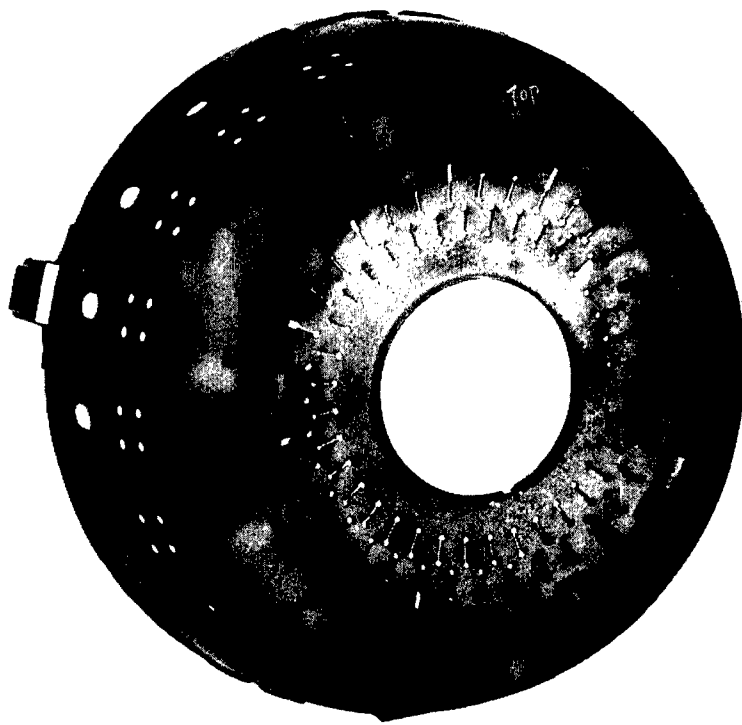


Figure 473. Outer Combustor Assembly.

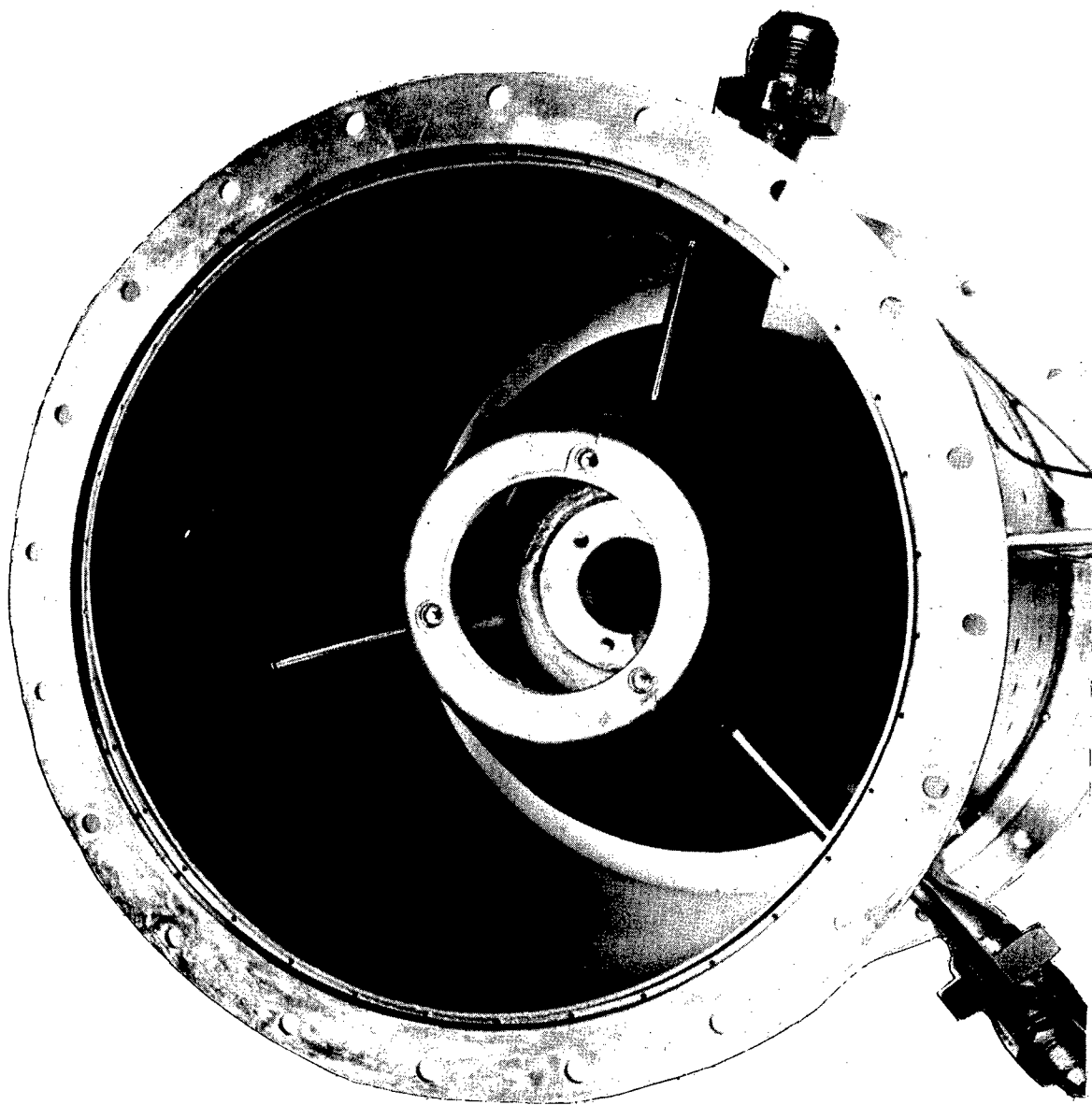


Figure 474. Exhaust Diffuser Assembly - Aft.

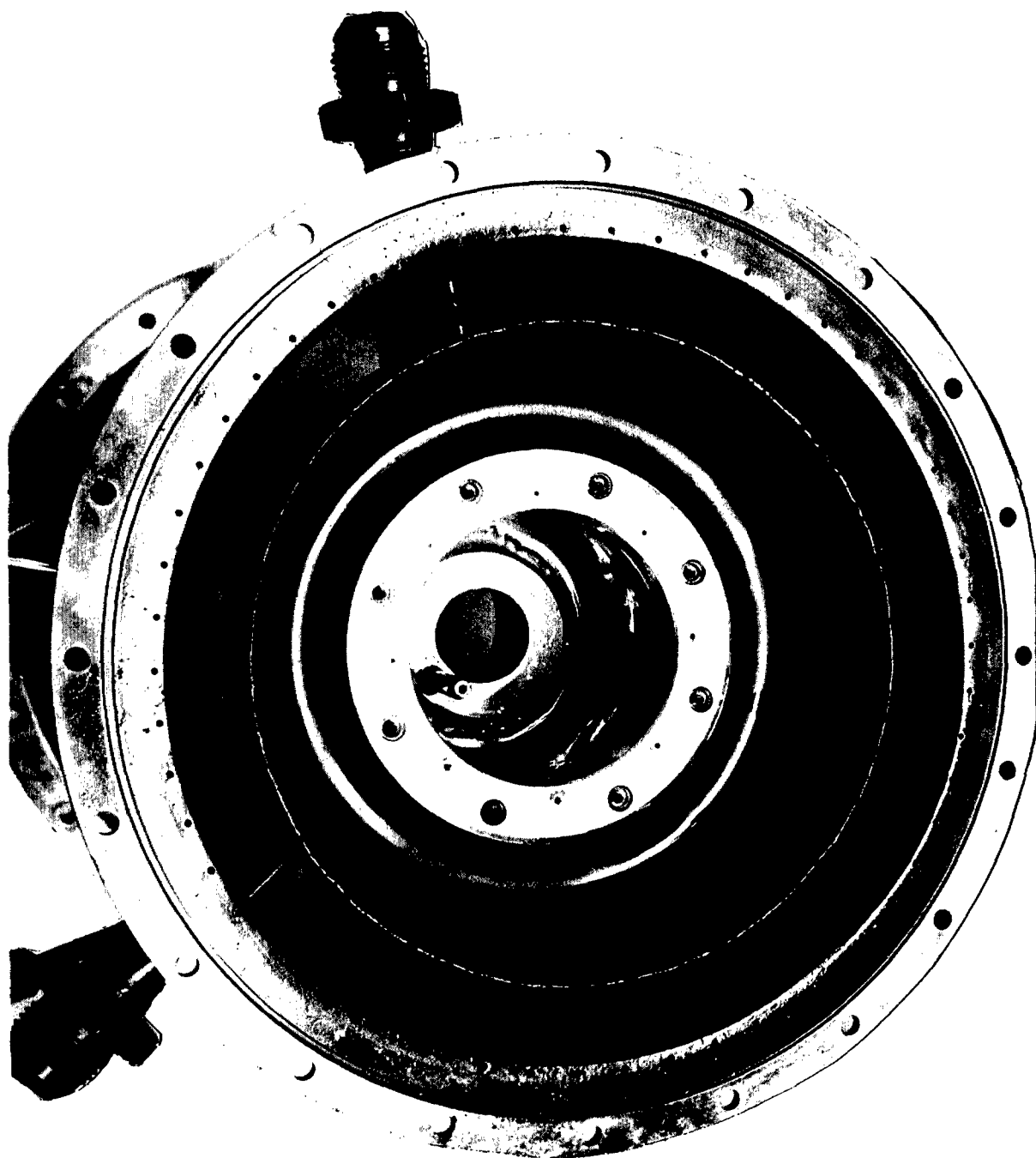


Figure 475. Exhaust Diffuser Assembly - Forward.

CONCLUSIONS AND RESULTS

The conclusions and results of the experimental investigation are summarized as follows:

1. A specific horsepower of 171-hp/lb/sec air was demonstrated; a capability of 195, also at a turbine inlet temperature of 2344° F, was shown. The objective of 213-hp/lb/sec air can be achieved with a turbine inlet temperature of 2454° F and the efficiencies run in this program. This temperature has been demonstrated at an off design speed and efficiency.
2. The thermosyphon system demonstrated effective cooling to turbine inlet temperatures of 2450° F.
3. Hot testing of the turbine showed a peak efficiency of 74 percent. The turbine assembly was not aerodynamically optimized. Cold flow testing with optimum solidities and blade tip clearances demonstrated an efficiency of 82 percent. It was noted that the short, thick turbine blading and low aspect ratios used cause high secondary losses which deteriorated performance severely. The objective efficiency of 85 percent was not demonstrated with the present conventional geometry blading.
4. The turbine blades operated at turbine inlet temperatures of 2450° and 2200° F at speeds of 32,000 and 45,000 rpm, respectively.
5. The blade-disc pin attachment provided the required blade retention under predicted loading conditions.
6. The blade-disc fuel seal functioned properly under design pressures, temperature, and loads when assembled within design tolerances.
7. The air-cooled exhaust duct, turbine shroud, and turbine inlet nozzle assemblies displayed no structural distress and demonstrated their cooling effectiveness.
8. The gearbox hardware functioned, throughout all testing, without any major malfunction.
9. The turbine rig operated smoothly with a minimum of vibration throughout all testing.

10. Vapor-tight blading can be produced within the state of the art.
11. The precision casting technique must be optimized; core integrity was low, resulting in high scrap rates.
12. The measurement of the blade cooling fluid, filling of the blades and sealing of the heat exchanger section by welding with a filler plug, was successfully accomplished.
13. Inspection of the finished blades by pressure testing, in a helium chamber, was the best method of accurately detecting blade coolant sealing at room temperature.
14. No adequate Nondestructive Testing techniques could be found that would insure the structural integrity of the blade after the assembly was welded.
15. The assessment of organic and iron oxide deposits on the blade stems after testing was inconclusive, in that the blades operated successfully in this condition. The rig was subjected to high-temperature starting and running conditions that were higher than those that would be experienced during actual engine operation.

RECOMMENDATIONS

1. A redesign of the turbine assembly to provide spacing for 34 blades is required to improve program turbine efficiencies.
2. Three-dimensional surveys should be made on the nozzle and the rotor with several wall constriction shapes to determine an optimum geometry. The effect of change in radial distribution of reaction caused by tilting nozzle vanes with respect to a radial line normal to the wheel axis should be investigated.
3. The aspect ratio investigation results (Reference 43) suggest a trade-off of reaction for blade height. This concept should be incorporated with the results obtained from Items 1 and 2. Structural integrity verification allows a relaxation on blade thicknesses and chordal requirements. A combination of all these factors makes the efficiency of 85 percent in a single stage a realistic goal in a redesign effort.
4. A redesign and/or elimination of the turbine blade welded tip-cap is required. Alternatives for fabrication investigation are
 - a. Diffusion bonding of two blade halves.
 - b. Casting of tip section with basic airfoil.
5. Methods should be developed for instrumentation to measure directly blade metal temperature in a hot gas stream environment (2500°F).
6. Methods should be developed for a technique to establish the presence of coolant in the blade after it is hermetically sealed.
7. Casting dimensional control must be improved, particularly in the cored sections of the blade, including the heat exchanger.
8. Nondestructive Testing methods such as 1) radioactive probe, 2) magnetic probe, and 3) impulse decay method must be developed for utilization on small turbine blades to verify the integrity of the blade. These methods were not sufficiently developed at the time of the second blade procurement to result in an increase in hardware quality.

REFERENCES

- 1 Fluid Meters, Their Theory and Application, a report of the ASME Research Committee on Fluid Meters, fifth edition, 1959.
- 2 Radiation and Recovery Corrections and Time Constants of Several Chrome Alumel Thermocouple Probes in High Temperature, High Velocity Gas Streams by G. E. Glawe, F. S. Simmons and T. M. Stickney. NACA TN 3766.
- 3 Wind Tunnel Investigation of a Number of Total Pressure Tubes at High Angles of Attack Supersonic Speeds by W. Gracey, D. E. Coletti and W. R. Russel. NACA TN 2261.
- 4 Wind Tunnel Investigation of a Number of Total Pressure Tubes at High Angles of Attack Supersonic Speeds by W. Gracey, W. Letko, and W. R. Russel. NACA TN 2331.
- 5 Aerodynamic Measurements, Published by the M.I.T. Press - by R. C. Dean, Jr., Massachusetts Institute of Technology, 1953.
- 6 Instrument Society of America Report Thermocouples and Thermocouple Extension Wires. RP 1.1-7.
- 7 High Temperature Strain Gage Adhesives by H. C. Rechter and Y. Harada. Instrument Society of America Paper 3.2.62.1.
- 8 Zweifel, O.; "The Spacing of Turbomachine Blading Especially With Large Angular Deflection", The Brown Boveri Review, Vol. 32, 12 November 1945.
- 9 Huppert, M. C., and MacGregor, Charles; "Comparison Between Predicted and Observed Performance of Gas Turbine Stator Designed for Free-Vortex Flow", NACA TN 1810, 1949.
- 10 Steward, W. L., Whitney, W. J., and Miser, J. W.; "Use of Effective Momentum Thickness in Describing Turbine Rotor-Blade Losses", NACA Report No. RME56B29, 14 May 1956.
- 11 Method of Increasing the Efficiency of Turbine Stages with Short Blades, Translation No. 2816. Associated Electrical Industries (Manchester) Limited, 29 April 1960.

- 12 Stewart, W. L.; "A Study of Axial-Flow Turbine Efficiency Characteristics in Terms of Velocity Diagram Parameters"; American Society of Mechanical Engineers Paper No. 61-WA-37, 1961.
- 13 Ainley, D. G., and Mathieson, G. C. R.; "A Method of Performance Estimation for Axial-Flow Turbines"; Aeronautical Research Council, R. and M. 2974 (1957).
- 14 Barringer, C. M.; "Stability of Jet Fuels at High Temperatures"; SAE pp 55-526, 1955. A study of deposits and residue formation in JP-4 fuels.
- 15 Rogers, J. D., Jr.; "Turbine Fuel Thermal Stability - CFR Coker and Flight Evaluations"; SAE pp 59-103T, 1959. Determination of threshold temperature of JP-4 fuels with correlation to flight tests.
- 16 Crampton, A. B., et al; "Thermal Stability - A New Frontier for Jet Fuels"; SAE pp 55-525, 1955. Comparison of fuel coker and full-scale mockup data plus methods of improving thermal stability.
- 17 Minor, H. B., Nixon, A. C., and Thorpe, R. E.; "Stability of Jet Turbine Fuels"; WADC Tech. Rpt. 53-63, Parts 2, 3, 4, 5, and 6. A study of the mechanism of instability and inhibitor action on various grades of JP-4 fuels. Includes thermal and oxidative stability and effects of nuclear radiation.
- 18 Barnett, H. C., and Hibbard, R. R.; "Properties of Aircraft Fuels"; NACA TN 3276, August 1956. Physical properties and specifications of aircraft fuels.
- 19 Lusebrink, T. R.; "Thermal Stability of Experimental High Temperature Fuels"; WADC - ASD Tech. Rpt. 61-687, April 1962. Determination of high temperature stability of seven pure hydrocarbon fuels.
20. Fabuss, B. M., Borsanyi, A. S., et al; "Evaluation of Materials as Endothermic Aviation Fuels"; WADD Tech. Rpt. 60-841, Part I, Feb. 1961. Investigation of cetane (n - hexadecane), a pure hydrocarbon as an endothermic fuel.
- 21 Smith, J. O., Fabuss, B. M., et al; "Evaluation of Materials as Endothermic Aviation Fuels"; WADD Tech. Rpt. 60-841, Part II, December 1961. Investigation of seven pure hydrocarbons as potential endothermic fuels.

- 22 Smith, J. O., Fabuss, B. M., et al; "Research on Materials for Use as Endothermic Fuels"; WADD TR 60-841, Part III, October 1962. Evaluation of six CRC fuels (including JP-6) as endothermic fuels.
- 23 Fabuss, B. M., Kafesjian, R., et al; "Research on the Mechanism of Thermal Decomposition of Hydrocarbon Fuels"; WADD-ASD-TDR-63-102, Part I, January 1963. Rates of decomposition and particle formation for naphthenic and paraffinic hydrocarbons at 800°F.
- 24 Editorial Panel of Thermal Stability Group of Aviation Fuels Division; "Investigation of Thermal Stability of Aviation Turbine Fuels With CFR Fuel Coker"; CRC Project No. CFA-2-54, April 1957. Development and operation of CFR Fuel Coker and results on ten test fuels representative of JP-4 type fuels.
- 25 Kittredge, G. D.; "Thermal Stability of Hydrocarbon Fuels"; WADD-ASD-TR 61-238, Part II, July 1962. Storage stability and thermal stability determination with bench scale test procedure (JP-6).
- 26 Kittredge, G. D.; "Thermal Stability of Hydrocarbon Fuels"; WADD-ASD-TR 61-238, Part III, July 1963. Study of possible accelerated storage tests on JP-6 fuels.
- 27 Smith, J. O., Fabuss, M. A., et al; "Evaluation of Hydrocarbons for High Temperature Fuels. Part II - Fuel Evaluation and Property Correlation. Volume I - Correlation Studies, Thermal Stability, and Contaminant Effects"; WADC TR 59-327, Part II, Vol. I, February 1962. Determination of chemical and physical properties of pure hydrocarbons. Test procedure and discussion of results.
- 28 Smith, J. O., Fabuss, M. A., et al; "Evaluation of Hydrocarbons for High Temperature Jet Fuels. Part II - Fuel Evaluation and Property Correlation. Volume II - Hydrocarbon Properties"; WADC TR 59-327, Part II, Vol. II, February 1962. Tabulation of chemical and physical properties of pure hydrocarbons.
- 29 Kutzko, G. G.; "Effect of Hydrocarbon Fuels on the Operation of Vapor Phase Fuel Systems"; WADD-ASD-TDR 62-920, Parts I and II, October 1962. Measurement of heat transfer coefficients, fuel enthalpy, and amount and kind of decomposition products.

- 30 Bialy, J. J., Norris, T. A., and Frascati, F. P.; "Research on Thermal Effects on Fuels Attributable to Storage"; APL TDR 64-83, July 1964.
- 31 Kittredge, G. D.; "Thermal Stability of Hydrocarbon Fuels"; WADD-ASD-TDR 61-238, Part I, July 1961.
- 32 Bialy, J. J., Frost, R. A., and Dilley, K. L.; "An Investigation of the Thermal Stability of Potential Supersonic Jet Fuels"; WADD-ASD-TDR 62-852, September 1962.
- 33 Bialy, J. J., Norris, T. A., and Frascati, F. P.; "An Investigation of the Thermal Stability of Potential Supersonic Jet Fuels"; WADD-ASD-TDR 62-852, Part II, May 1963.
- 34 Grandey, M. F., and Wehner, E. H.; "Thermal Stability of Clean and Contaminated JP-6 Fuels"; SAE pp 61-431A, October 1961.
- 35 Petrick, Ernest N., and Smith, Richard D.; "Experimental Cooling of Radial Flow Turbines"; ASME Paper No. 54A245.
- 36 Kestin, J., and Maeder, P. F.; "Influence of Turbulence on Transfer of Heat From Cylinders"; NACA TN 4018.
- 37 Manson, S. S.; "The Determination of Elastic Stresses in Gas Turbine Disks"; NACA TN 1279.
- 38 Aero Space Structural Metals Handbook, Volume II-A Non-Ferrous Alloys.
- 39 Mendelson, A., and Hirschberg, M.; "Analysis of Elastic Thermal Stresses in Thin Plate With Spanwise and Chordwise Variations of Temperature and Thickness".
- 40 Eckert and Livingood; "Comparison of Convection, Transpiration and Film Cooling Methods"; NACA Report No. 1182.
- 41 Hatch, J. E., and Papell, S. S.; "Use of a Theoretical Flow Model to Correlate Data for Film Cooling or Heating an Adiabatic Wall by Tangential Injection of Gases of Different Fluid Properties"; NACA TN D-130, November 1959.

- 42 Glawe, G. E., Simmons, F. S., and Stickney, T. M.; "Radiation and Recovery Corrections and Time Constants of Several Chromel-Alumel Thermocouple Probes in High Temperature, High Velocity Gas Streams"; NACA TN 3766, October 1956.
- 43 Marshall, R., and Rogo, C.; "Experimental Investigation of Low Aspect Ratio and Tip Clearance on Turbine Performance and Aerodynamic Design"; Continental Report No. 1043, February 1968.
- 44 Rogo, C.; "Experimental Aspect Ratio and Tip Clearance Investigation on Small Turbines"; Society of Automotive Engineer's (SAE) Paper 680-448, 1968.
- 45 Scadron, M. D., and Warehowski, I.; "Experimental Determination of Time Constants and Musselt Numbers for Bare Wire Thermocouples in High Velocity Air Streams and Analytic Approximation of Conduction and Radiation Errors"; NACA TN 2599.
- 46 Stepka, F. S.; "Comparison of Calculated and Experimental Temperatures and Coolant Pressure Losses for a Cascade of Small Air-Cooled Turbine Rotor Blades, NACA TN E58E20, 17 July 1962.

APPENDIX I

RESEARCH AND DEVELOPMENT QUALITY CONTROL SPECIFICATION NO. 51 BLADE CASTING AND MACHINING

BLADE CASTING PROCESS

Process:

Vacuum-melted, precision cast, internally cooled turbine rotors.

Scope:

This standard is to establish acceptable quality and dimensional levels for the cast, internally cooled, turbine rotor blades.

Dimensions:

Airfoil contour, on one side, to be within +0.005 inch to -0.003 inch.

Envelope, surrounding the air-foil, 0.008 inch.

Wall thickness tolerance - (0.010-inch min Part No. 709627; 0.015-inch min Part No. 712903).

Surface finish - 64-RMS max outer diameter and inner diameter.

Quality:

Core breakage and removal - Cause for rejection if shown by X ray or off dimensional.

Grain size - Surface, 1/8-inch diameter, maximum 1/16-inch or less average, mostly equalized, some columnar grain allowed: Use fine grain practice; etch all blades. (Tentative Only).

Leak testing - Continental responsible for leak testing. Vendor to replace any casting with leaks due to foundry defects.

*Microporosity (Internal) - To be determined by sectioning a final rigging sample plus one additional casting per mold. Core print areas or others, specified as weld areas. No micro-shrinkage allowed.

General:

- a. Defects in areas to be subsequently machined are not limited, provided quality requirements are met after machining.
- b. The removal of raised defects is not limited. The removal of other defects is limited to the dimensional limits on the applicable drawing.
- c. Combinations of defects materially affecting strength or performance are not allowed.
- d. Plugging of defects by welding is not allowed.
- *e. Fabricating vendor must ensure that internal passages are not blocked.

Visual Inspection Standards:

- a. Cast surfaces shall be nonmetallic blast cleaned to 64 RMS or better.
- b. Tightly adherent raised defects shall be ground smooth.
- c. Parting line evidence and pattern mismatch shall not exceed 0.005 inch.
- *d. Smooth bottom-type negative defects are allowed up to 0.005-inch diameter. When separated, not less than 1/16 inch is allowed in all areas except Area I (see Figure 476). Area I welding area - no defects allowed. Area II has a 0.030-inch diameter (see Figure 476) and is 0.005 inch deep when separated by not less than 1/4 inch and limited to five defects per side. Area III (see Figure 476) - any defects over the passages will be subject to review; otherwise, same as Area II.
- e. Nonfilled areas on blade leading and trailing edges are not allowed if they fall out of print tolerance.

*Designates Changes

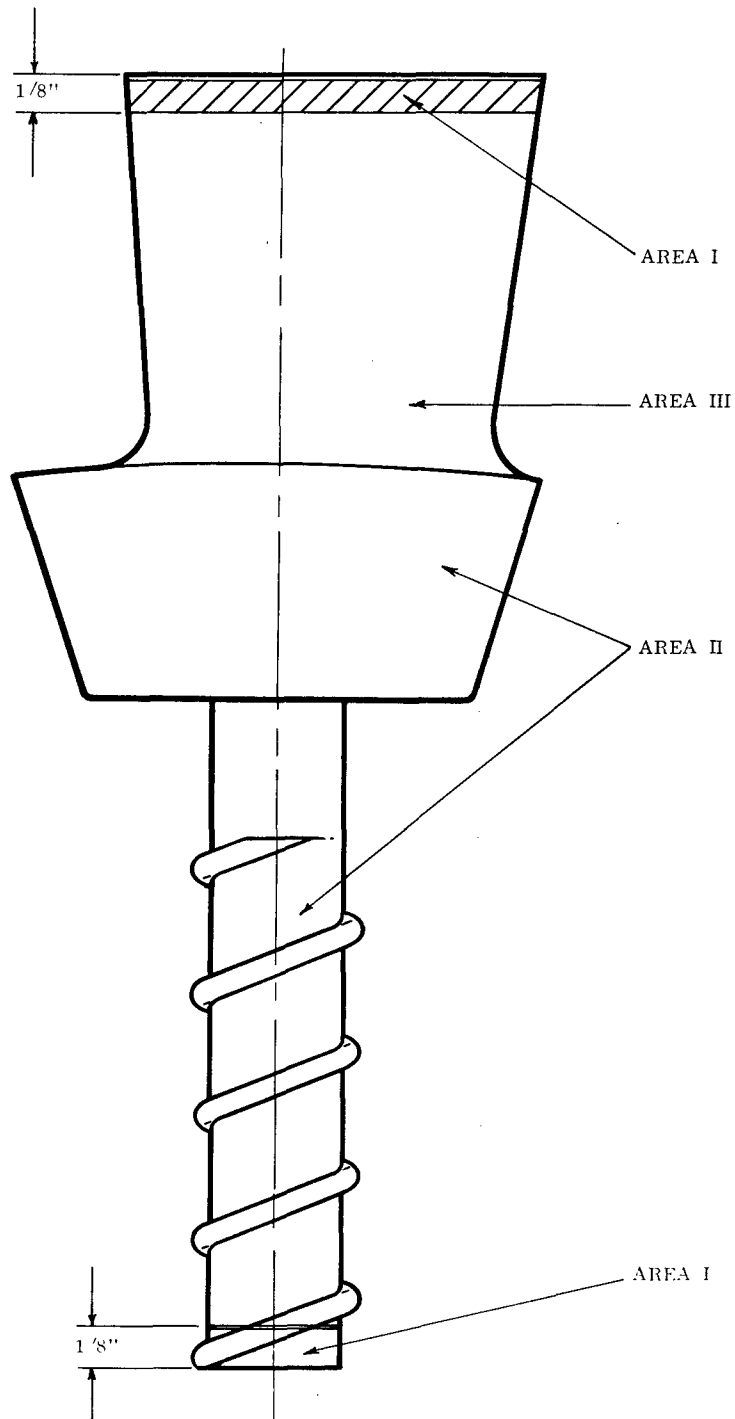


Figure 476. Turbine Blade - Cast,

Penetrant Inspection Standards (Using ZL22 Penetrant):

- a. Cracks, aligned porosity (line-type defects), cold shuts, and through porosity are not allowed.
- *b. Well-scattered pin point indications are allowed using the visual standards above.

*Fluorescent Penetrant Inspection:

This procedure shall be 100 percent and shall be preceded by etch and thermal shock tests to determine the presence of cracks in IN-100 alloy only (Part No. 712903) and unmachined castings only, as follows:

- a. Remove riser and inspect blade visually.
- b. Remove cores, finish airfoil, sandblast.
- c. Vapor degrease 160° to 185° F.
- d. Zyglo.
 - 1) Penetrant, ZL 22, 30 minutes minimum
 - 2) Emulsifier, ZE 4A or ZE 2, 1-1/2 minutes maximum
 - 3) Developer, ZP 4 (4A) dry, or ZP 5 wet
- *e. Thermal test. 1975° F, argon atmosphere, 10 minutes, air cool. (1600° F, 12 hours, argon, A.C. cycle to be included in the final Zyglo test on the finished parts.)
- f. Sand or vapor blast.
- g. Chemical etch.
 - 1) Hydrochloric acid (HCl)
 - 2) Hydrogen peroxide (H₂O₂), 30-percent concentration
 - 3) Add one part H₂O₂ to nine parts HCl by volume
 - 4) Immerse blade 1-1/2 minutes in etchant at room temperature, water wash

*Designates Changes

5) Intergranular attack shall not exceed 0.0008 inch (Tentative)

h. Zyglo. Same as 1), 2), and 3), above.

i. X-ray.

j. Ship to Continental in etched condition.

*X-ray Inspection Standards (Use Mercury Technique):

a. Cracks, line-type defects, and aligned porosity are not allowed.

*b. Other defects, provided they are not aligned or clustered, are allowed, as noted in Table XXXVII.

c. Blockage of internal passages, as shown by fins or excess metal, to be evaluated by flow check, destructive tests, or testing, etc.

TABLE XXXVII

X-RAY QUALITY STANDARDS
(See Figure 476)

Defects	Area I	Area II - III
Gas Hole	None allowed	0.005-inch diameter when separated by not less than 1/8 inch and limited to five defects per blade.
Shrinkage Porosity	None allowed	Sponge and dendritic porosity allowed to density of Film Std No. 1 for sponge porosity.
Foreign Material	None allowed	Include in gas hole standard for size, distribution, and quantity.
Fins, excess metal in Internal Passages	To be evaluated for passage restriction.	To be evaluated for passage restriction.

*Designates Changes

BLADE MACHINING PROCESS

<u>OPERATION NO.</u>	<u>DESCRIPTION</u>	<u>REMARKS</u>
1	Receive cast blades.	Figure 477.
2	Check cast blades for serial numbers on ends of platforms.	Be sure serial number is legible, and vibro-etch if necessary, Figure 477.
3	Inspect airfoil contour at two specified stations (STA 3.581 and 4.049) for proper angle and contour.	If the pattern equipment has not been changed, it is safe to assume that the blade base bears the proper angular relationship to the airfoil section nearest the base. Inspection is necessary because on some blades, airfoils have been collapsed, the cord length has shrunk, and the camber has been increased. Airfoils have also been bowed in a spanwise direction, resulting in an apparent offset of the tip section, Figure 477.
4	Hold the airfoil in a metal matrix block or guillotine gage, and bend the shank so that the shank centerline is parallel to the airfoil centerline.	Zyglo all straightened blades for cracks at stem/base radius, Figure 477.
5	Inspect for stud offset from true position (0.005 inch acceptable).	If the airfoil chord is short, the stud moves forward or backward on the base. A spanwise curved airfoil tends to move the stud sidewise on the base, Figure 477.

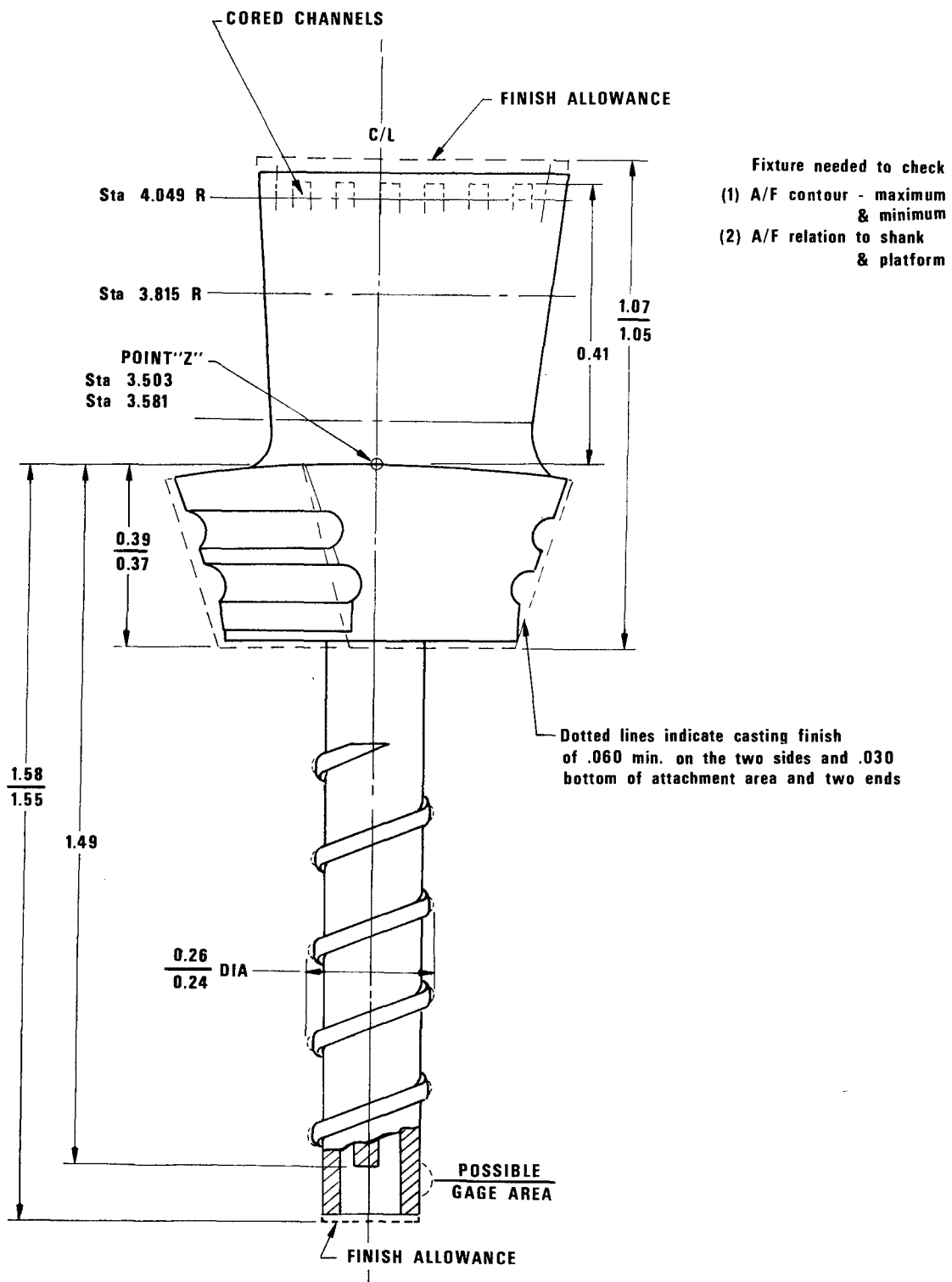


Figure 477. Blade Machining Operations 1 Through 5.

<u>OPERATION NO.</u>	<u>DESCRIPTION</u>	<u>REMARKS</u>
6	Grip the stud and machine to length, machine counter-bore, remove the short lengths of spiral fin, and cut back the cross channel inside the stem to print dimension.	See Figure 478.
7	Cut blades to length for EDM operation. Clean out fins.	Clean out fins to top of channels, Figure 479.
8	Prepare plugs for stem.	See Figure 480.
9	Prepare rectangular tip cap blanks.	See Figure 481.
10	Contour tip-cap blanks to airfoil shape at least 0.080 inch deep.	See Figure 482.
11	EDM tip-cap groove 0.015 inch deep, using blade as electrode.	See Figure 483.
12	<u>Welding and Heat Treat</u> Degrease and airblast inside. Wire brush EDM surfaces on blade tip-caps prior to welding.	
13	Electron beam weld tip-cap.	See Figure 484.
14	Insert plug in counterbore in stud at proper angle to blade base, and EB weld in place.	See Figure 485.
15	Pressure test per Continental Operation Sheet No. 15.	See Figure 484.

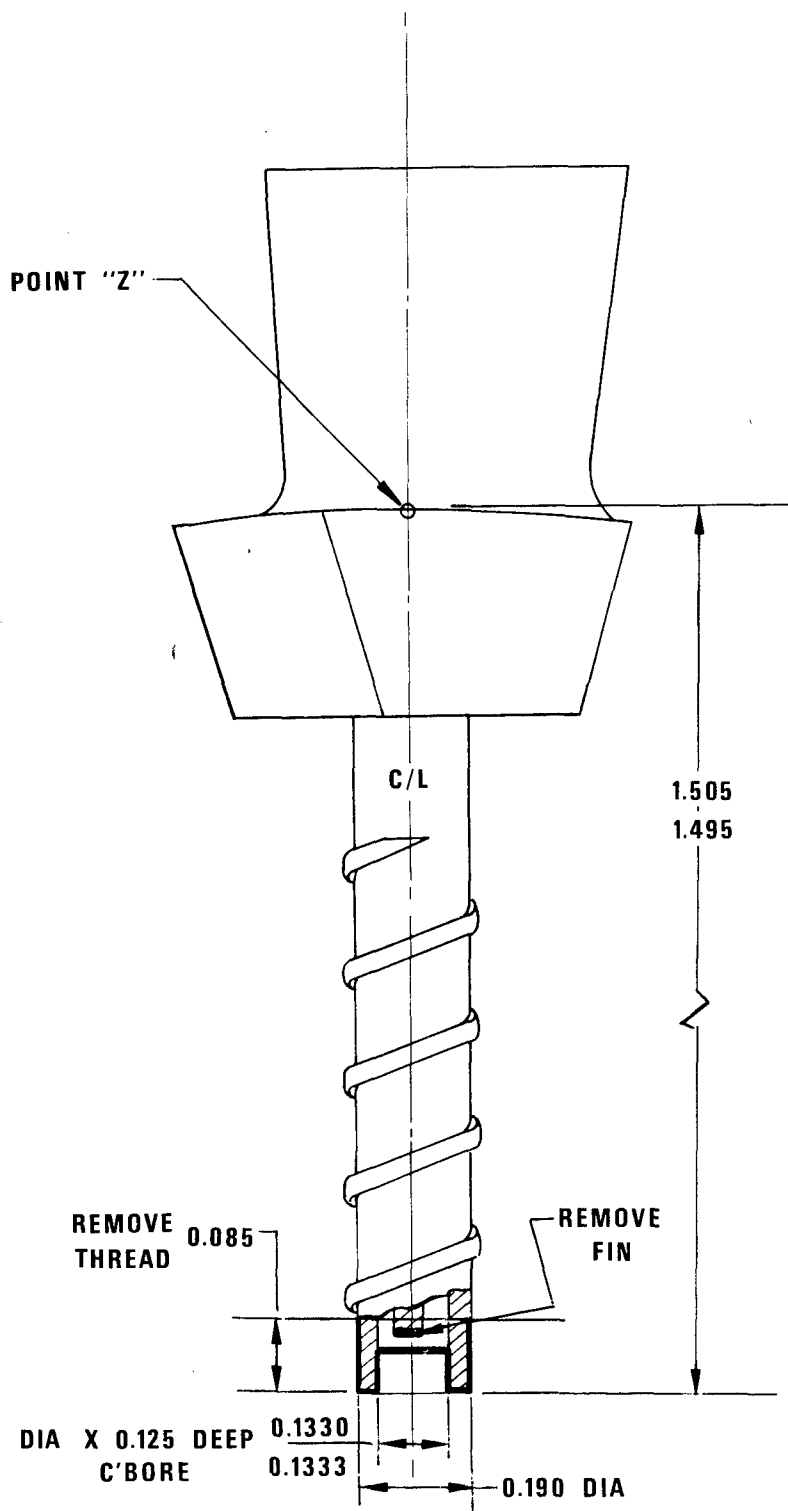


Figure 478. Blade Machining Operation 6.

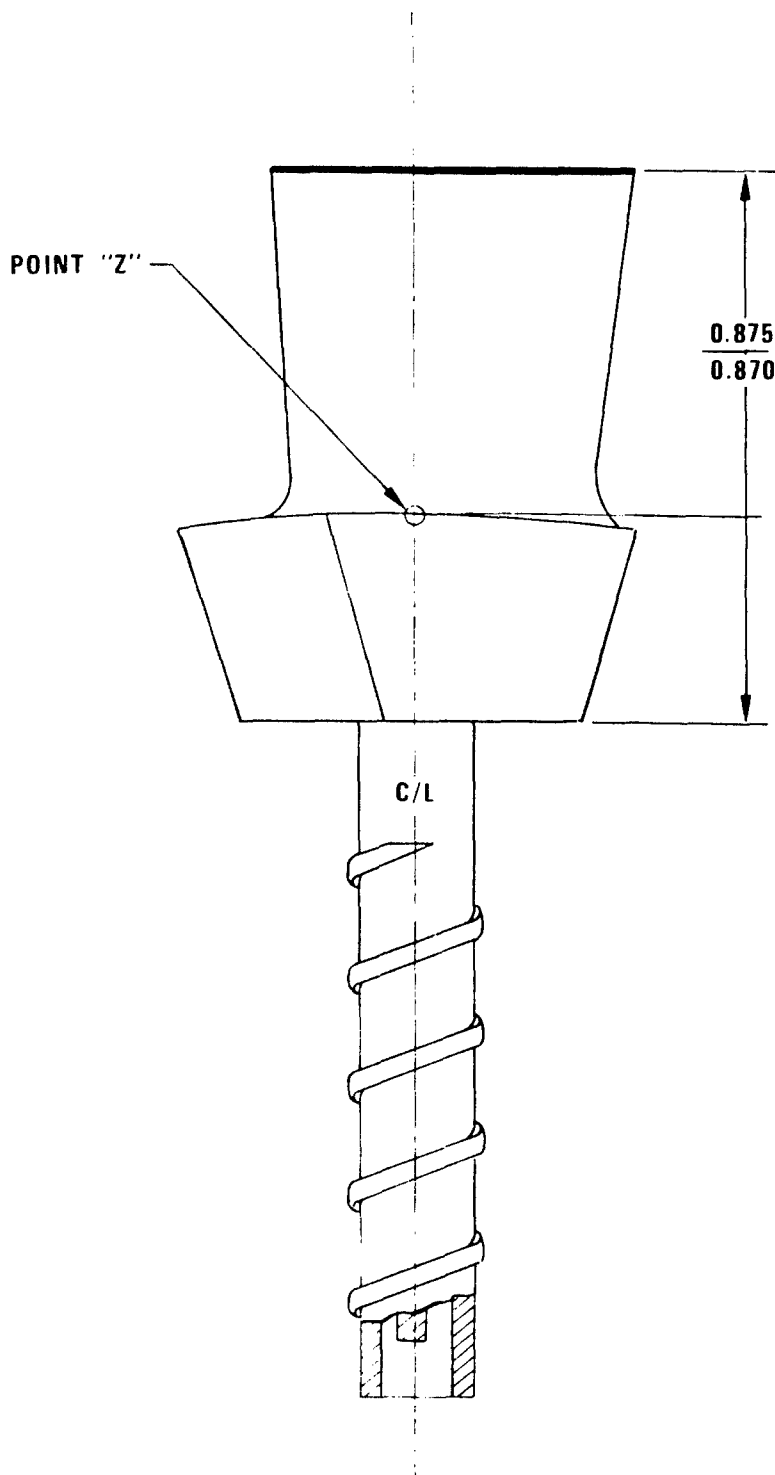


Figure 479. Blade Machining Operation 7.

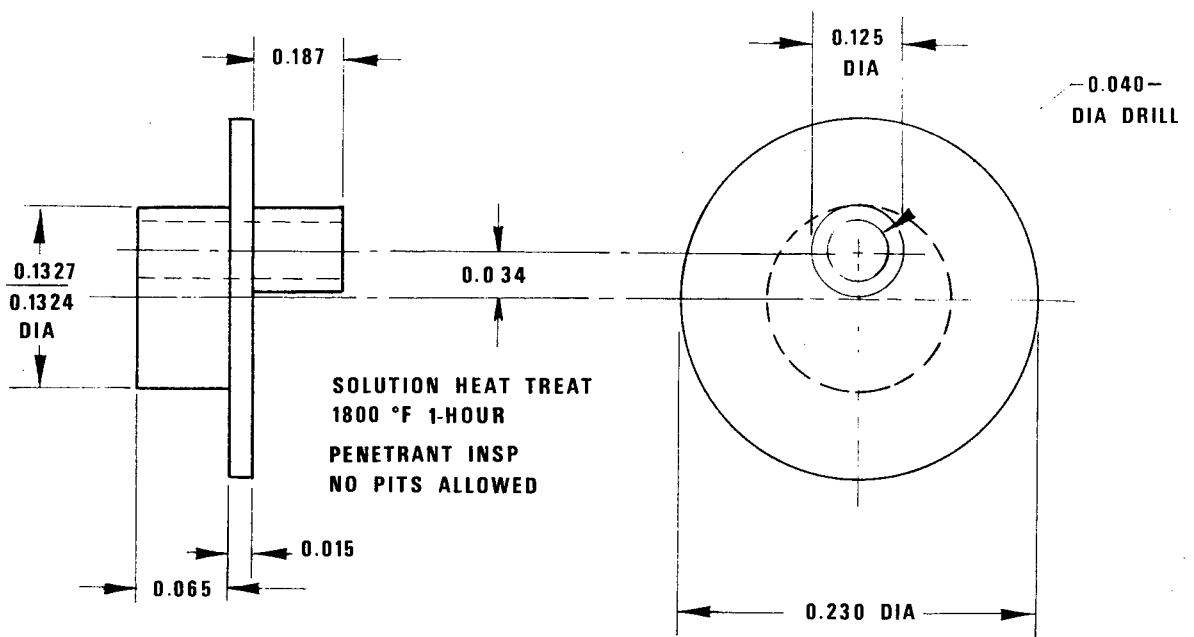
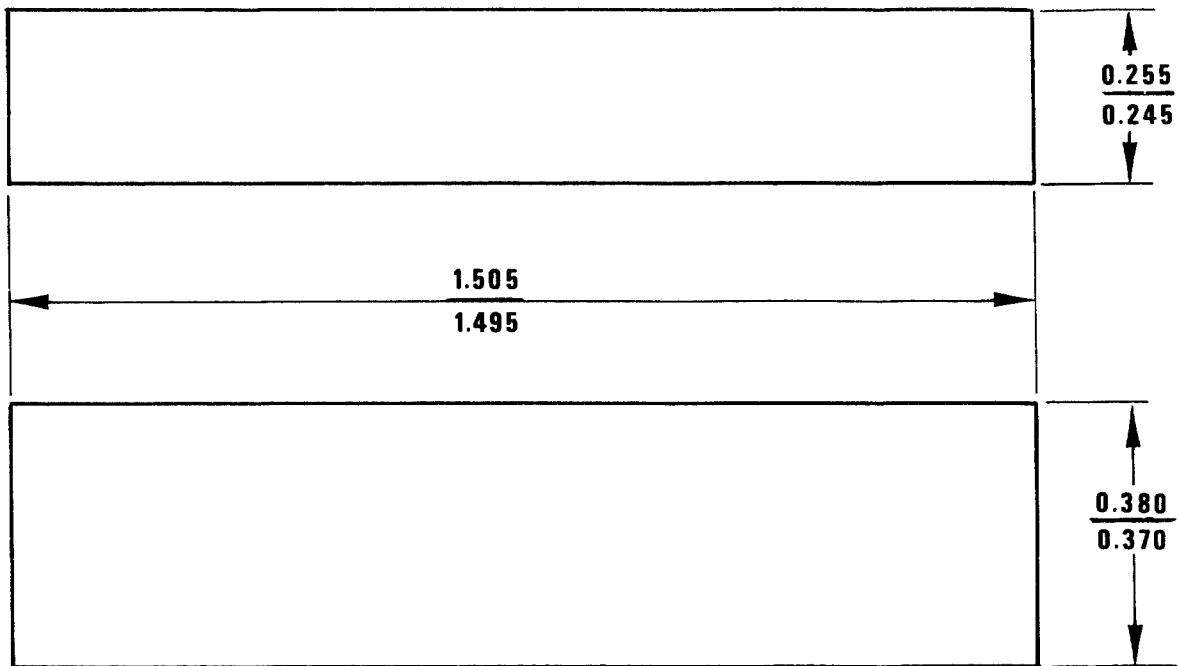


Figure 480. Blade Machining Operation 8 - Plug.



MATERIAL 718 WROUGHT

HEAT TREAT - SOLUTION, 1800 °F - 1 HOUR

Figure 481. Tip-Cap Machining Operation 9.

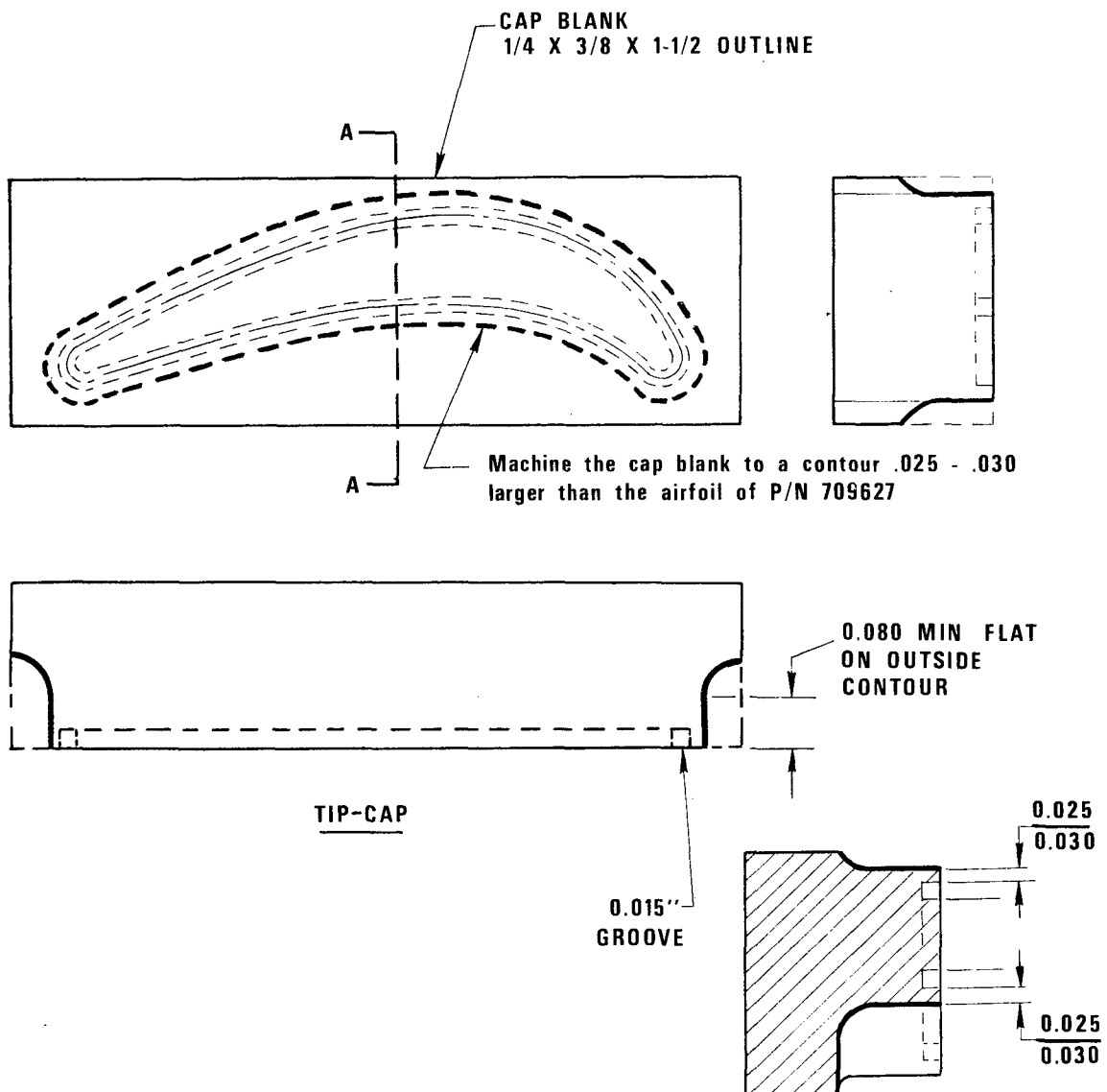


Figure 482. Tip-Cap Machining Operation 10.

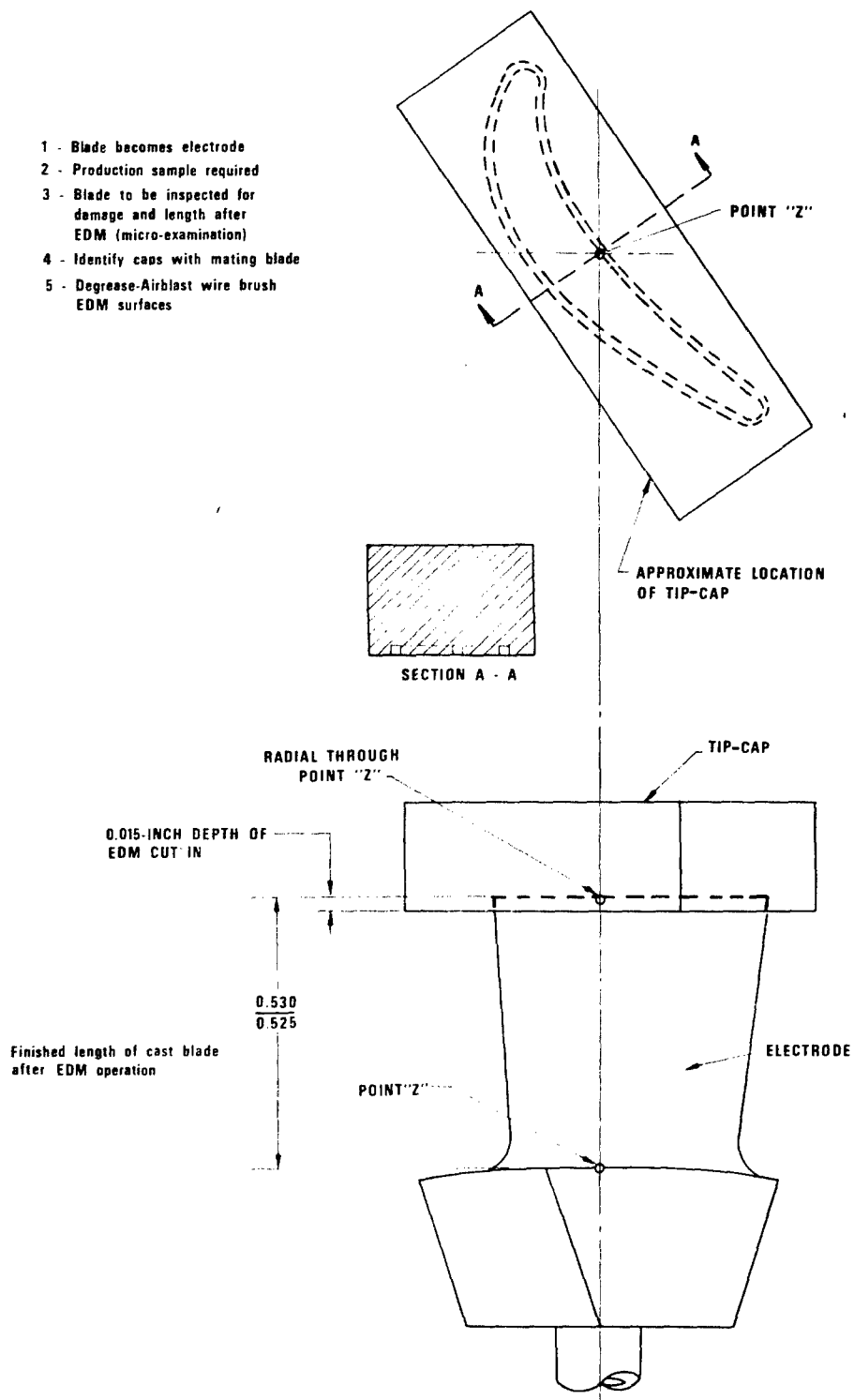


Figure 483. Tip-Cap Machining Operation 11.

Operation 13 EB weld tip-cap
 Operation 15 1200 psig helium
 (internal) pressure test
 Operation 16 heat treat EB weld

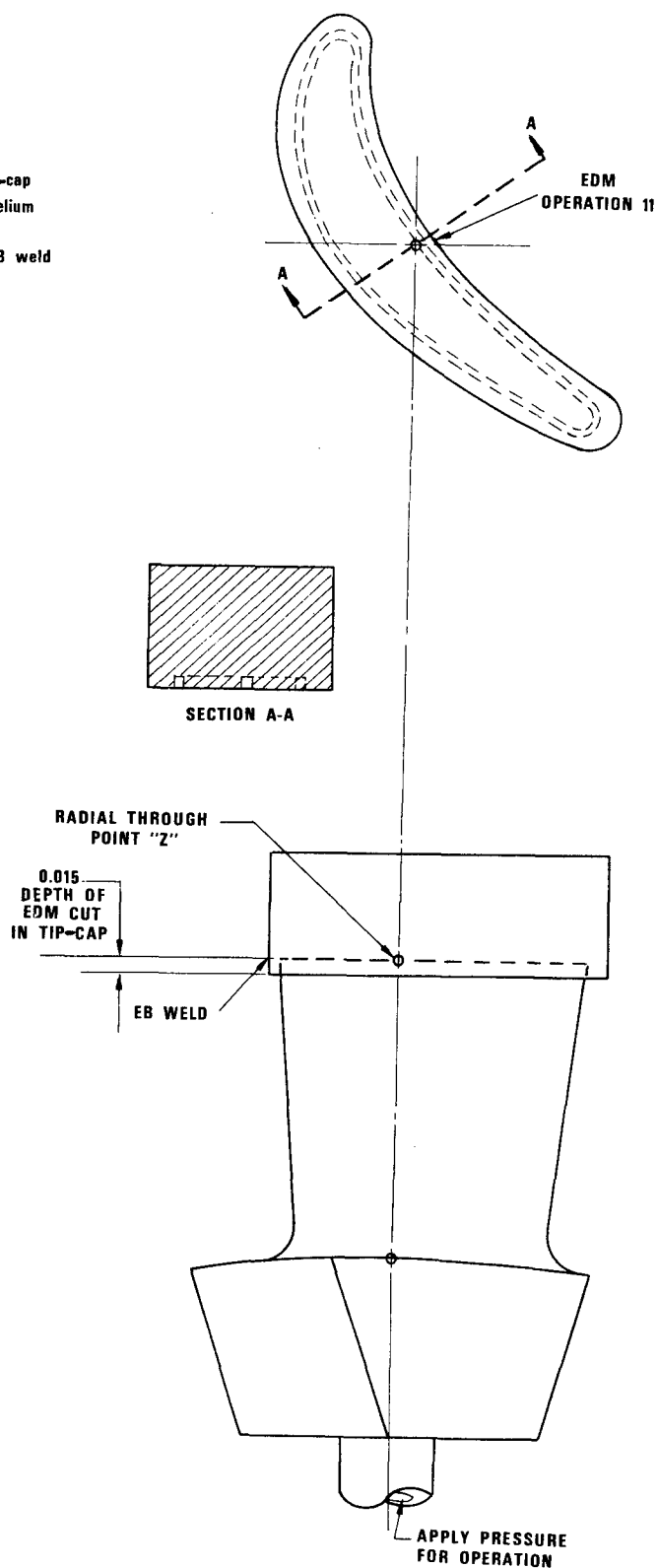


Figure 484. Tip-Cap Operations 13, 15, and 16.

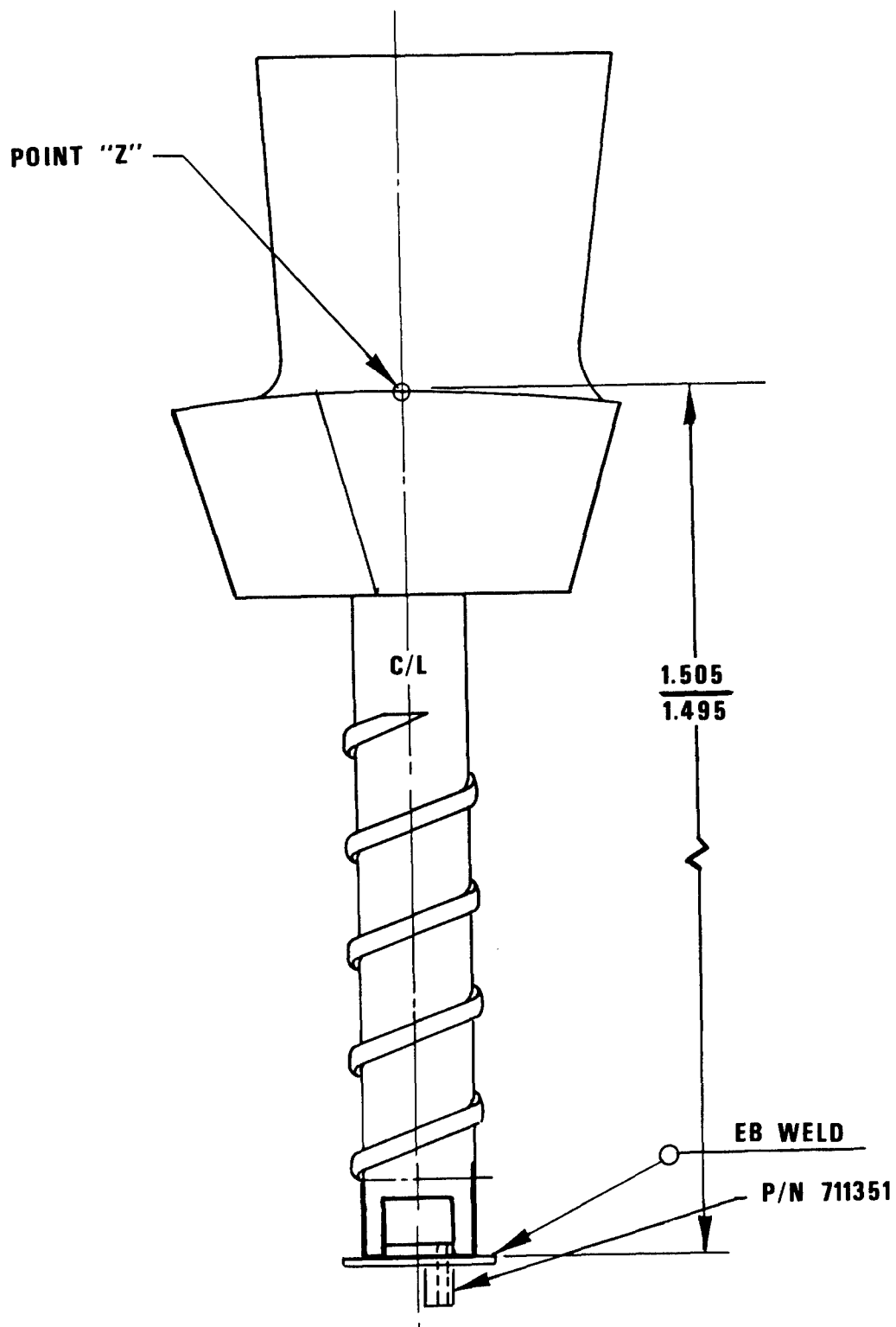


Figure 485. Plug Weld - Operation 14.

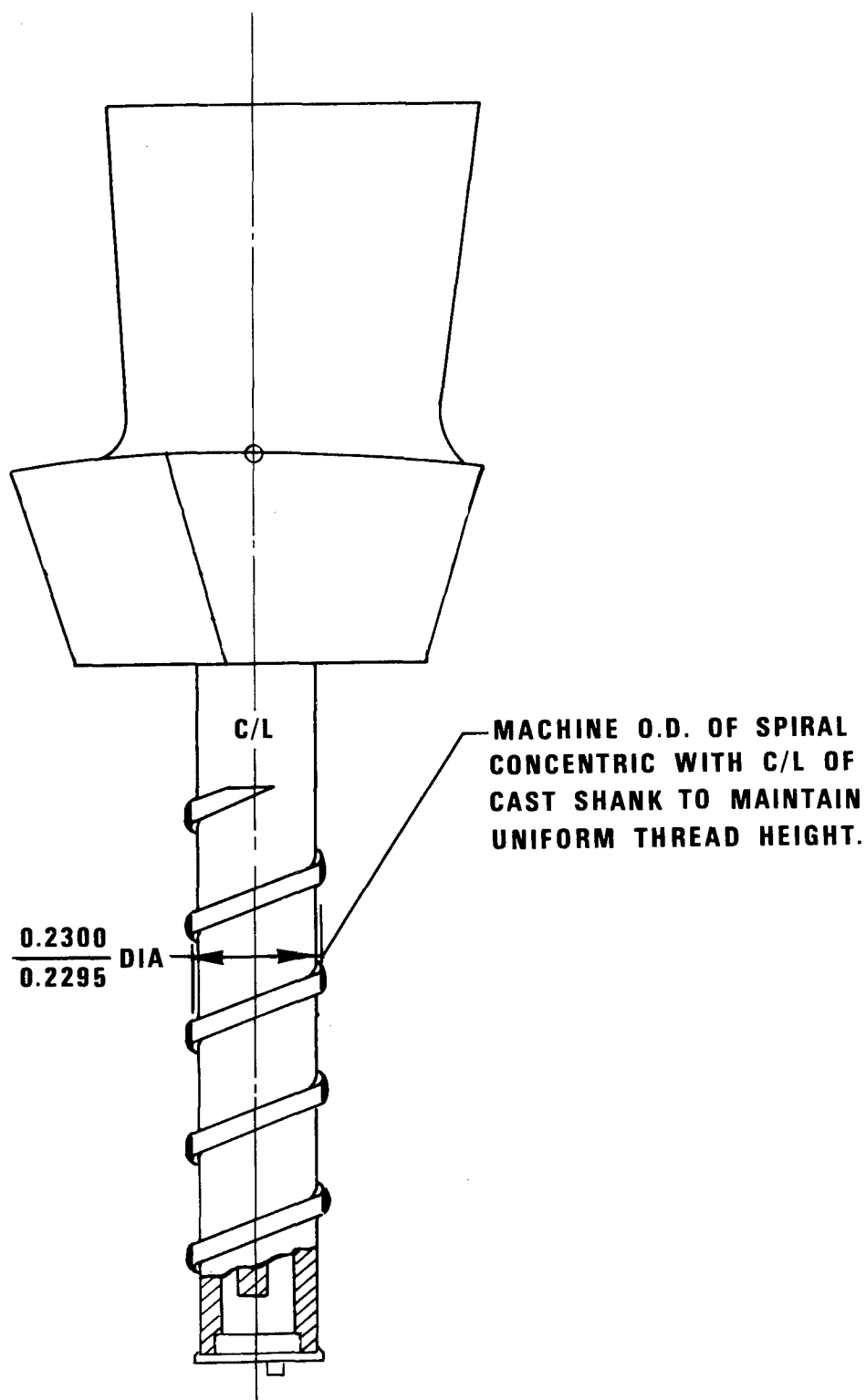


Figure 486. Heat Exchanger Machining Operation 19.

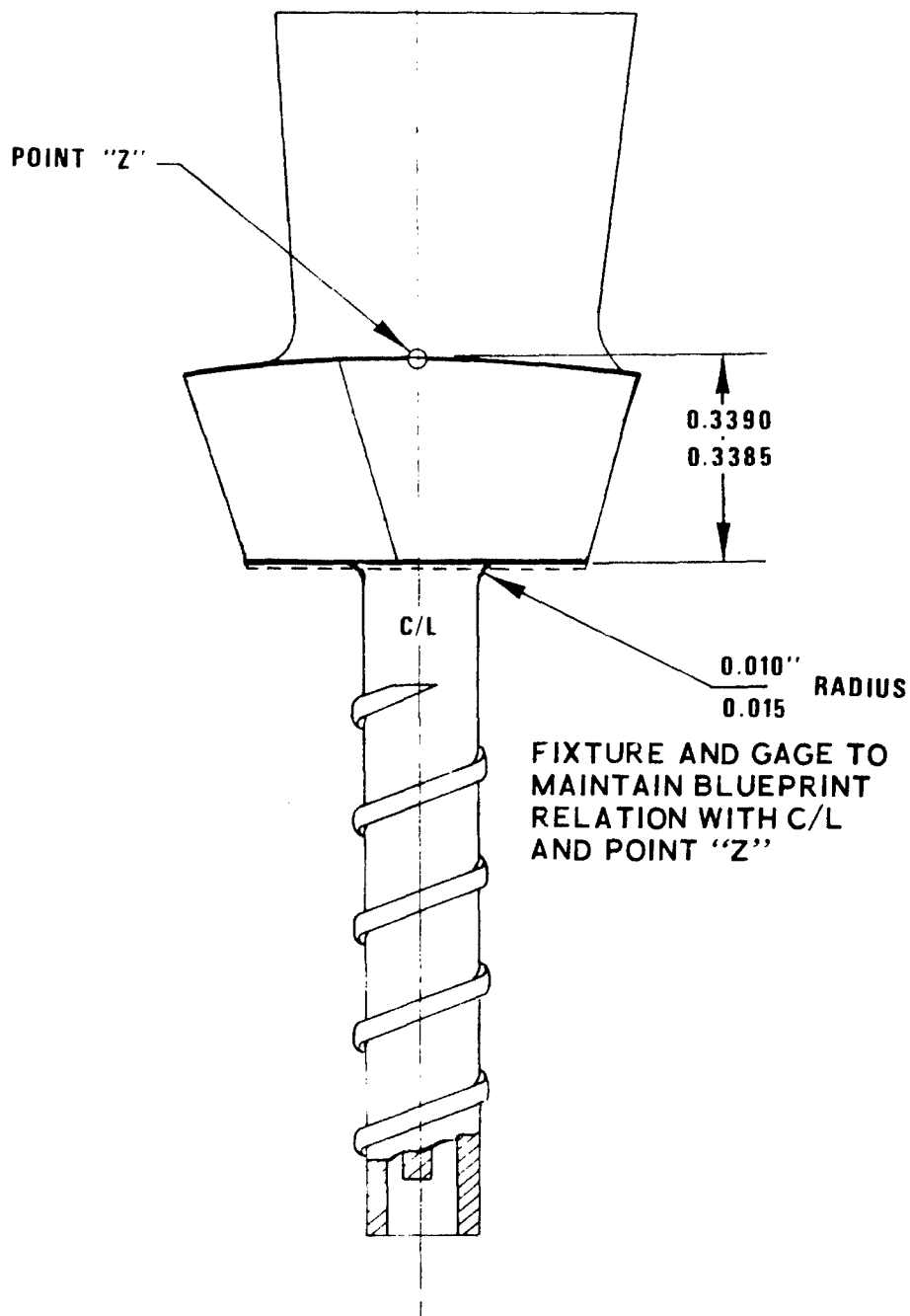


Figure 487. Heat Exchanger Machining Operation 20.

<u>OPERATION NO.</u>	<u>DESCRIPTION</u>	<u>REMARKS</u>
16	Heat treat.	See Figure 484.
17	Repressure test. OP. 15.	If leaks are found, resolve, repair, and repeat 15, 16, and 17.
<u>Postweld Machining</u>		
18a	In a suitable fixture, locating from the outer diameter of the shank and one mylar station, cast the blade into a shuttle.	Experience shows that air-foil does not coincide with shank C/L. Do not locate entirely off A/F.
18b	Restraighten stud.	Hold stud in shuttle fixture or shuttle. Bend neck of stud as required. Zyglo for cracks.
19	Grind the tips of the spiral fin. (0.2300 diameter) (0.2295 diameter)	Maintain concentricity with cast (1.190 diameter) shank to provide uniform thread height, Figure 486.
20	Grind the bottom of the blade base and radius at the stem.	Approximately 0.030-inch grind stock is provided on the bottom and 0.060 inch on each side. This grinding operation should provide clearance for the inside diameter of the seal. It is probable that the full tolerance cannot be used in the radius between the shank and the bottom of the blade base. Do not undercut the as-cast shank to provide clearance for the seal, Figure 487.

<u>OPERATION NO.</u>	<u>DESCRIPTION</u>	<u>REMARKS</u>
21	Grind two flats and two ends of platform, concentric with shank diameter.	Fixture must establish 15-degree angle of platform with airfoil station and must locate the parallel surfaces an equivalent distance from the ground thread diameter, Figure 488.
22	Grind two angular sides of platform.	Fixture to locate off of flats and bottom of platform. Machine to template 712457, Figure 489.
23	Grind four pin holes.	Template 712457, Figure 490.
24	Lap the eight-RMS circular lay.	See Figure 491.
25	Break bottom edges of platform.	See Figure 491.
26	Swing the blade tip radius.	Blade length must be established in this operation from ground surfaces of platform, not from cast top surface, Figure 492.
27	Hand blend tip-cap to airfoil contour.	Leave the cap about 0.003 inch larger than the airfoil, all around, to minimize stock removal on the cast airfoil during roughing. Finish grind cap contour to 0.001/0.000 larger than cast airfoil, Figure 492.
28	EDM the squealer (tip groove).	See Figure 492.
29	Cut the stem to length.	See Figure 493.

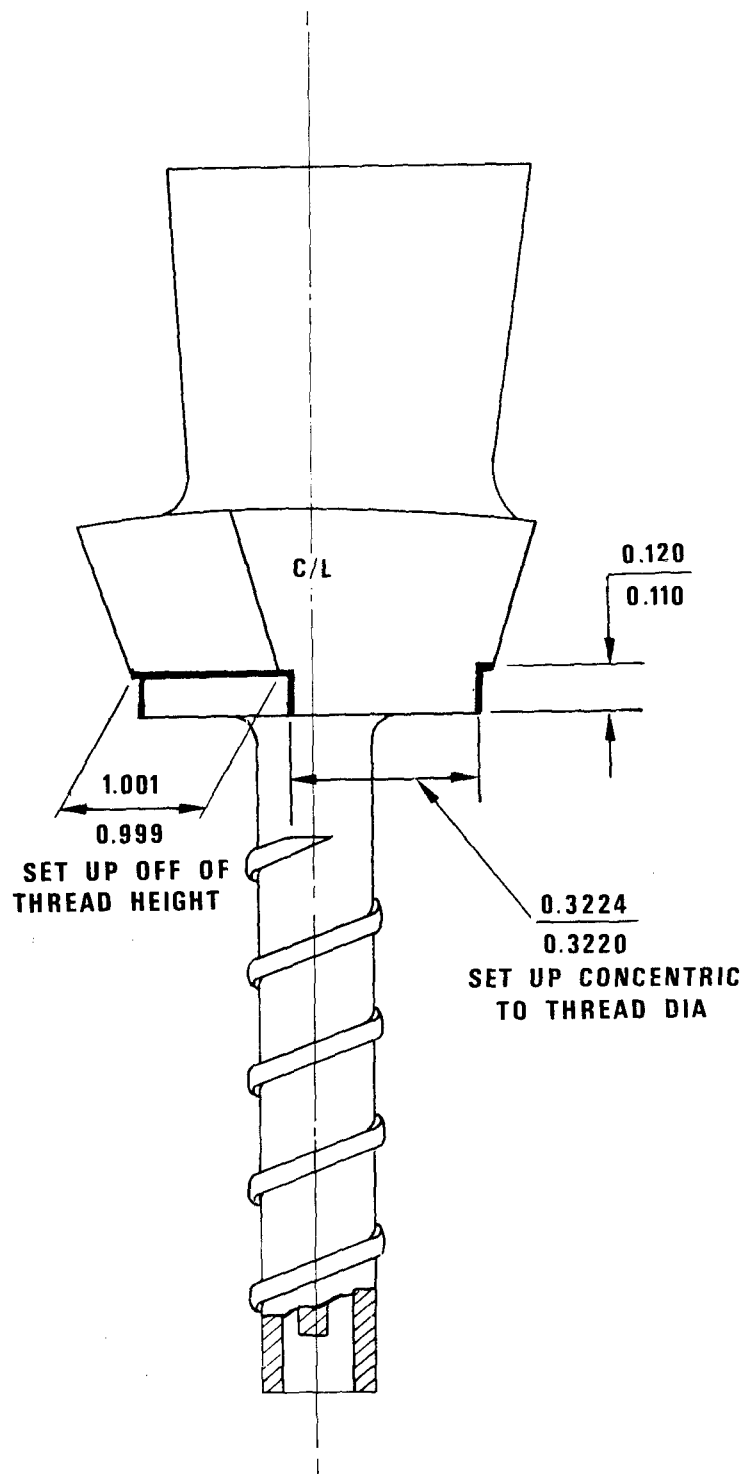
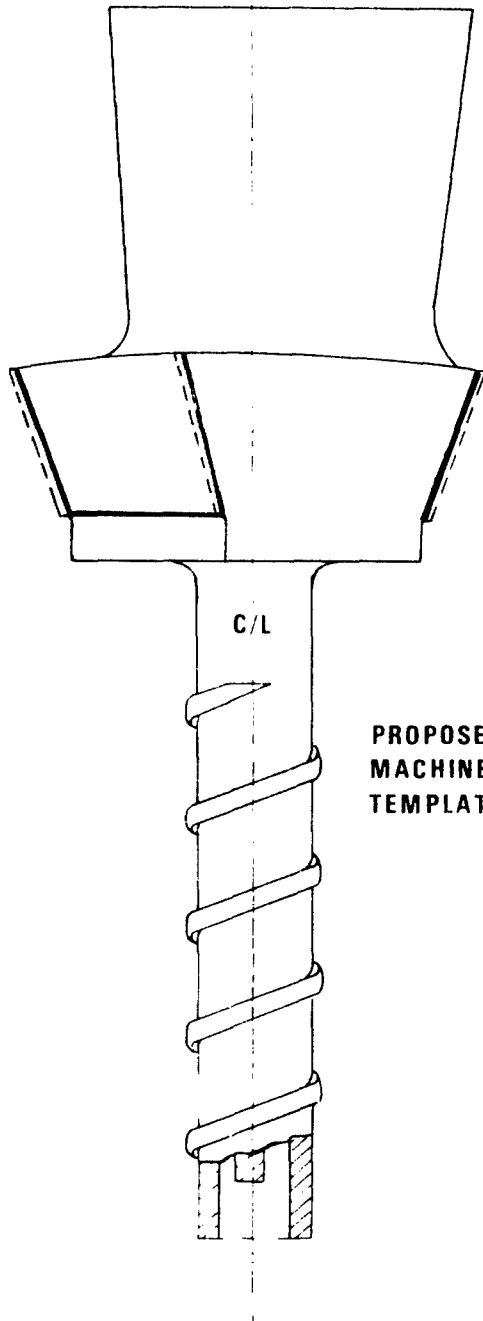


Figure 488. Blade Platform Machining - Operation 21.



PROPOSED OPERATION NO. 22
MACHINE PLATFORM SIDES TO
TEMPLATE DRAWING 712457

Figure 489. Blade Platform Machining - Operation 22.

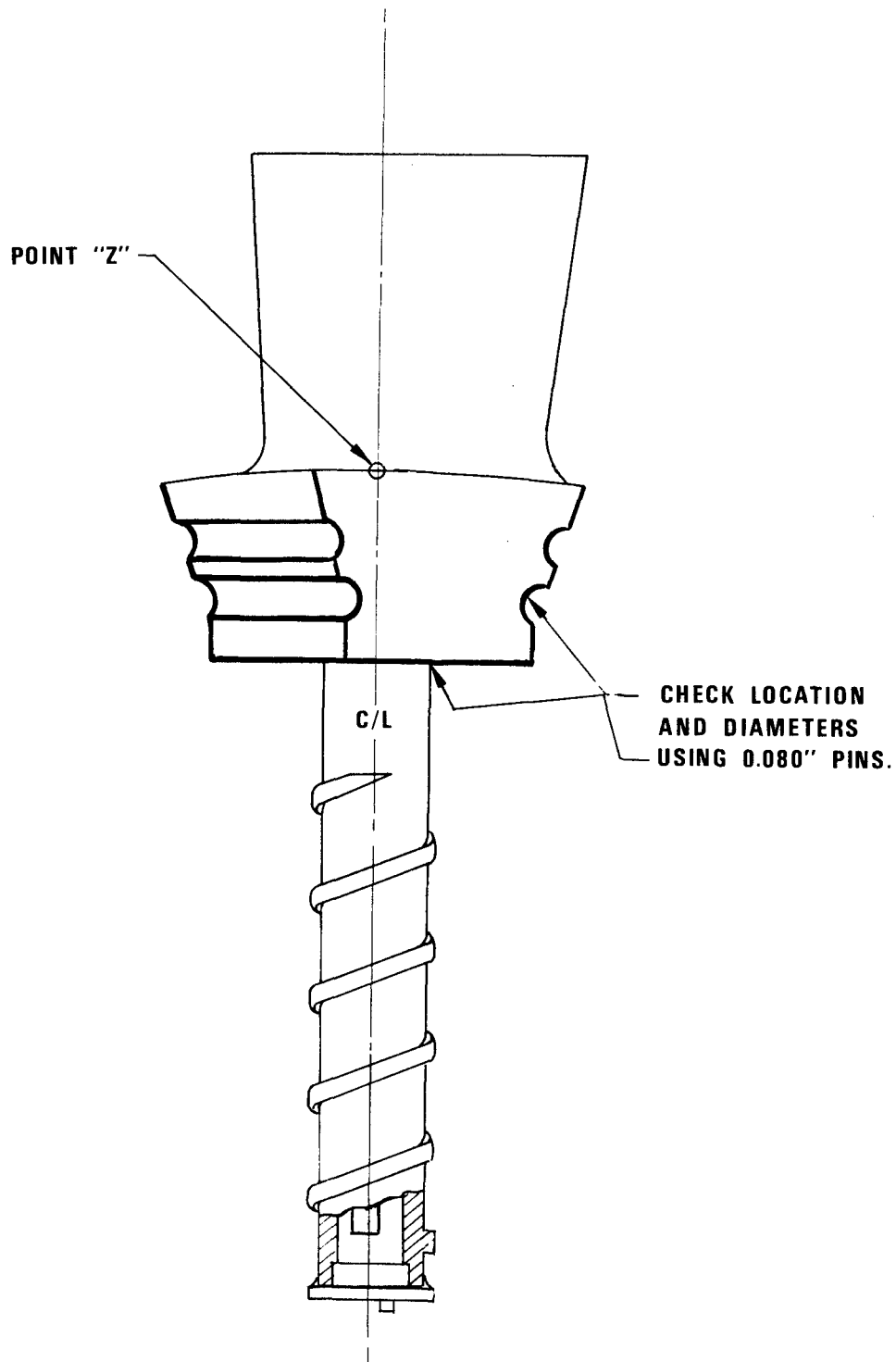


Figure 490. Blade Platform Machining - Operation 23.

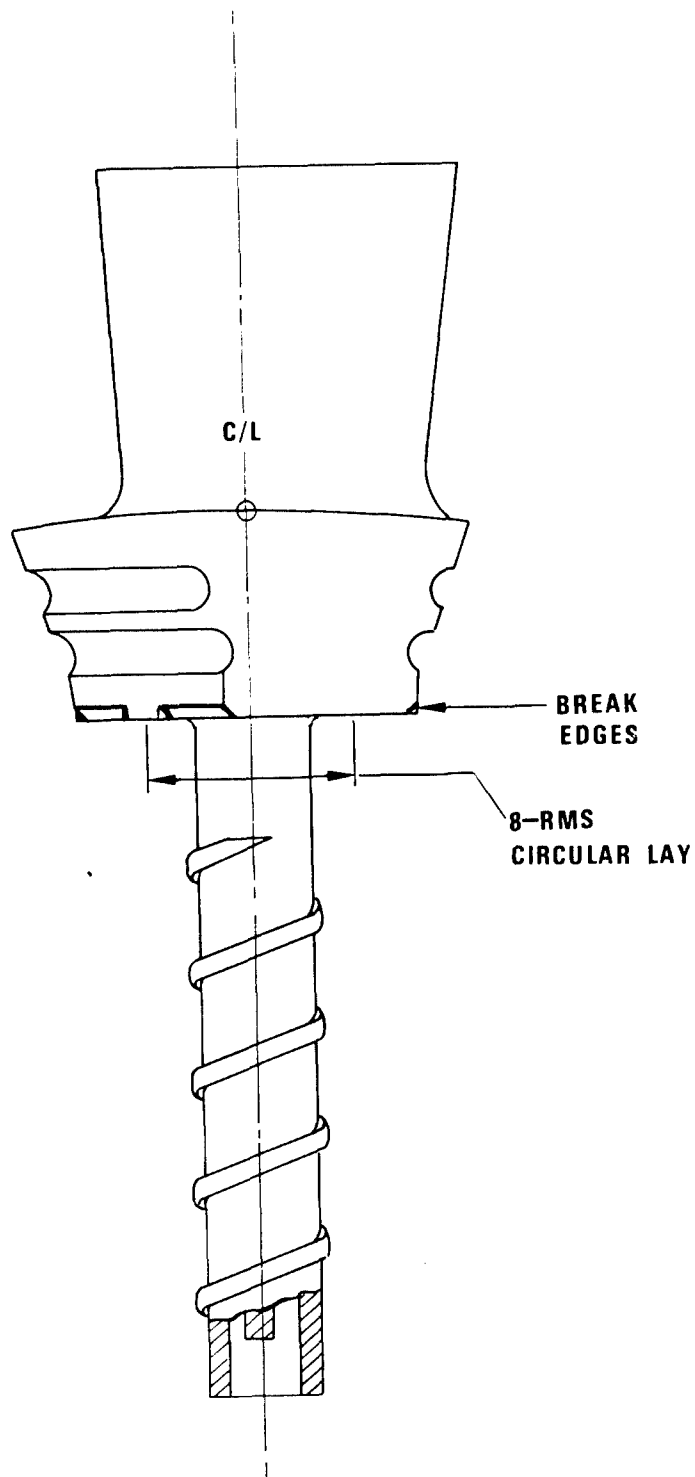


Figure 491. Blade Platform Machining - Operations 24 and 25.

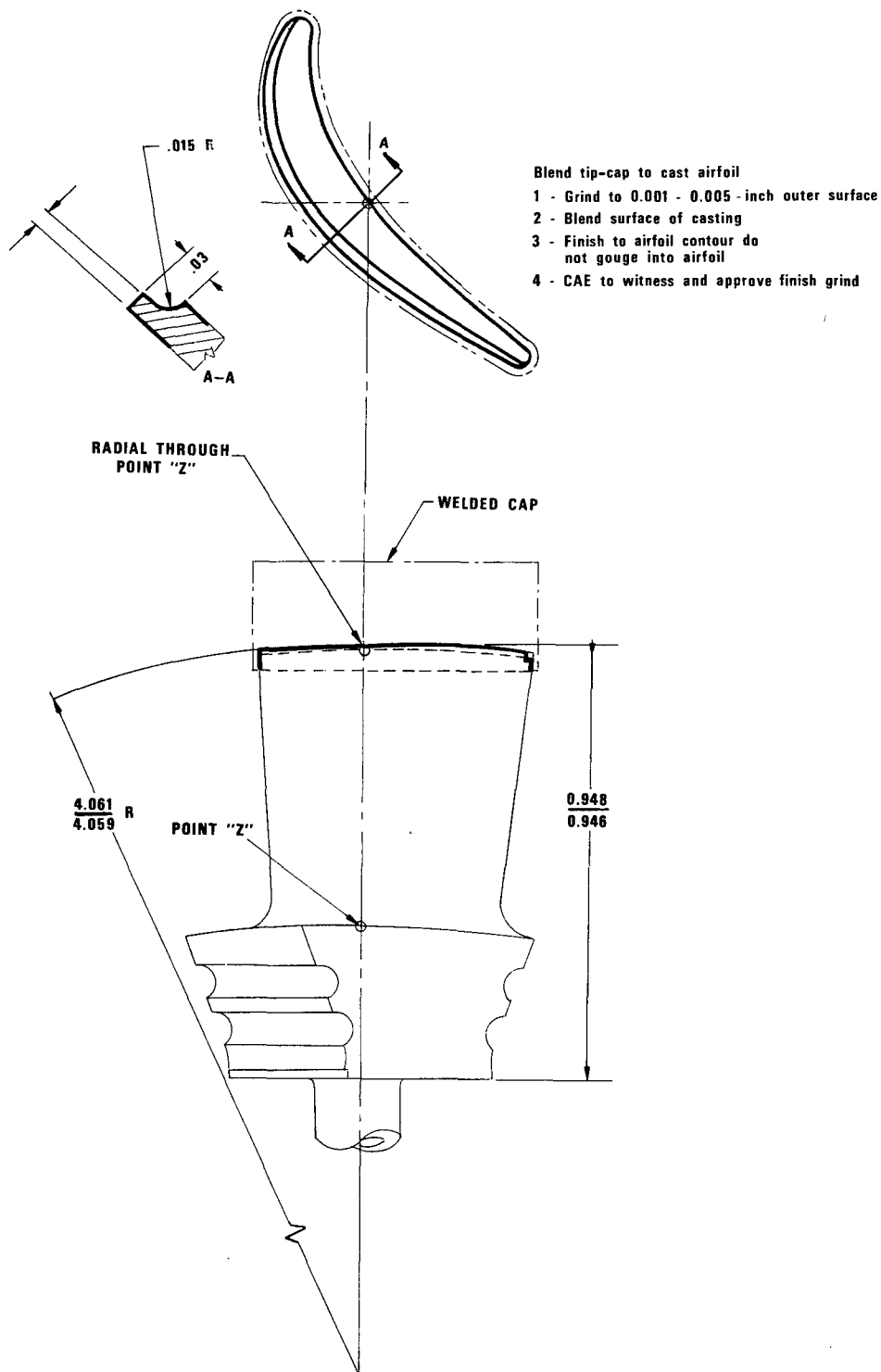


Figure 492. Final Machine Tip-Cap - Operations 26, 27, and 28.

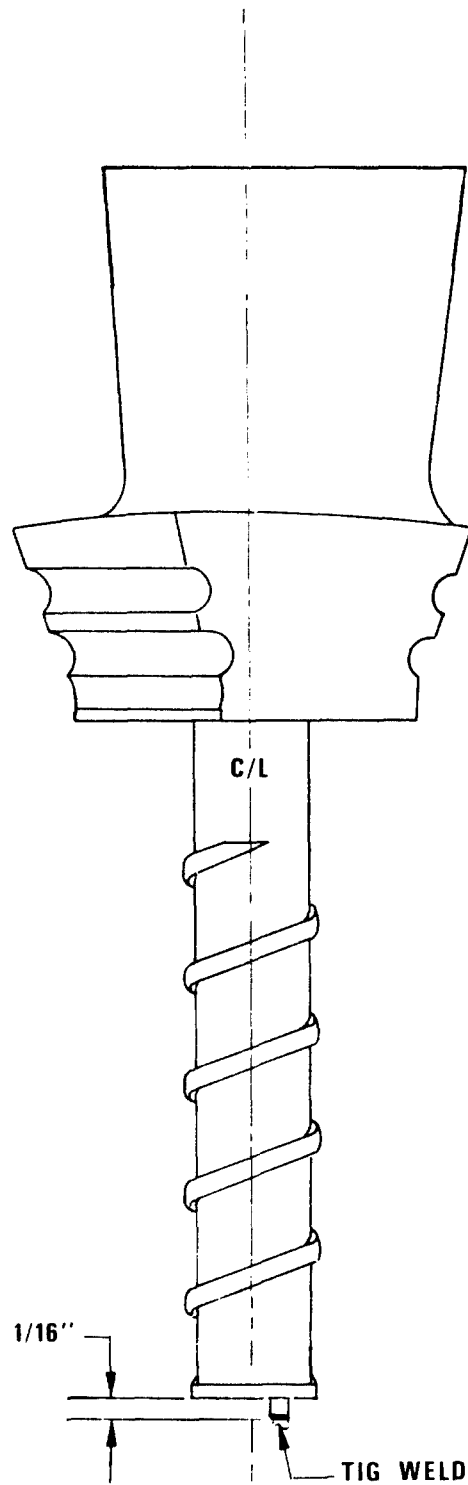


Figure 493. Sealing Heat Exchanger - Operations 29, 30, 31, 32, and 33.

<u>OPERATION NO.</u>	<u>DESCRIPTION</u>	<u>REMARKS</u>
30	Clean blade thoroughly, inside and out.	See Figure 493.
31	Dry blade in oven.	This is a time-consuming operation. The blades must be alternately heated and specimen blades weighted until a constant weight is achieved, to be sure that all volatile residue has been re- moved, Figure 493.
32	Fill blades with 0.012 to 0.016 cc of water.	See Figure 493.
33	Seal blade by tungsten inert gas (TIG) welding.	See Figure 493.
34	External pressure test in bomb. Hold for 5 minutes in 1,500-psig helium. Place in acetone and ob- serve bubbles for 5 minutes.	

APPENDIX II

HEAT TRANSFER IN A COOLED TURBINE BLADE CONTINENTAL IBM PROGRAM 25-007

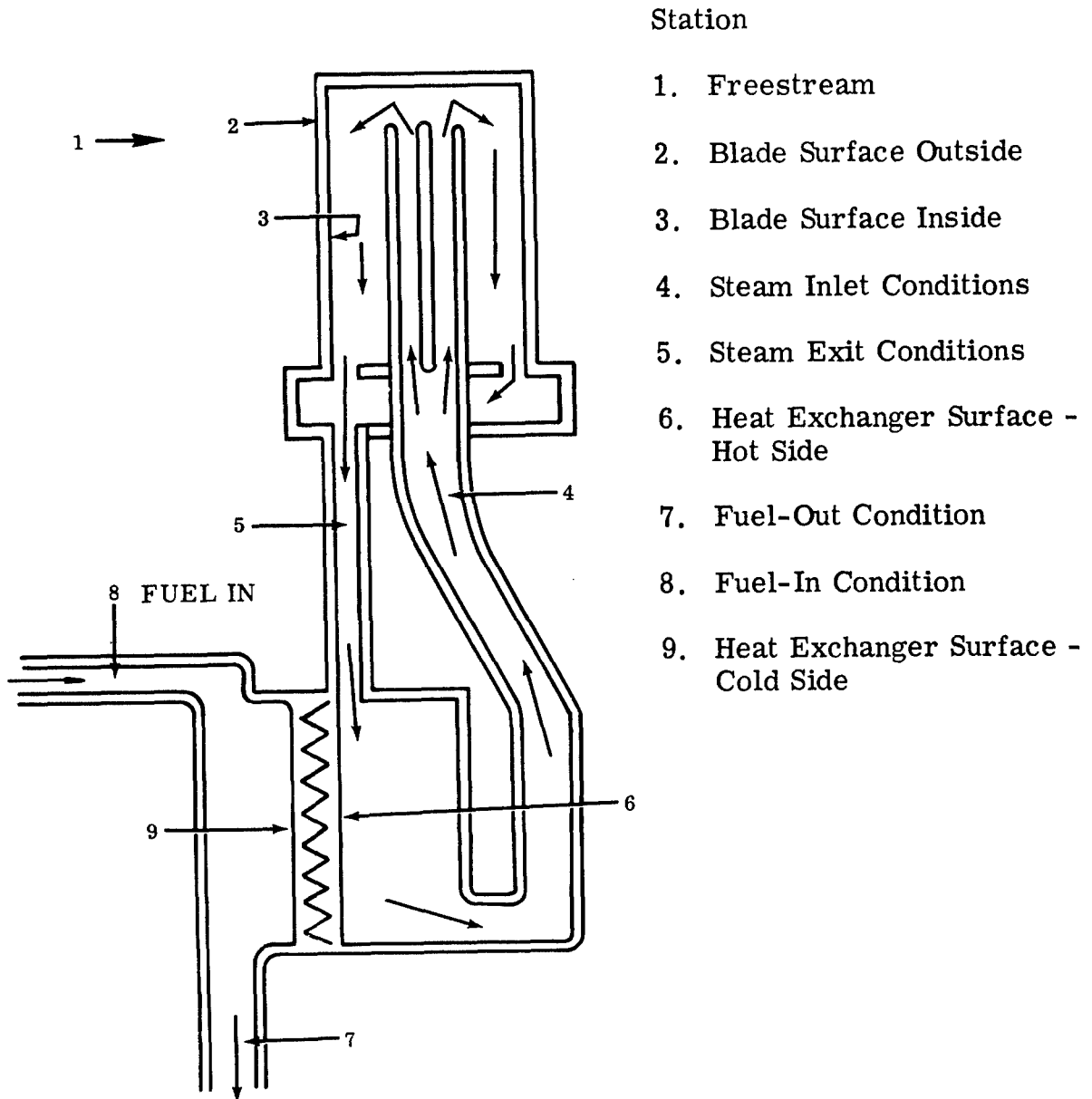


Figure 494. Schematic of Closed-Loop Thermosyphon System.

Input

1	A_2	A_3	A_6	A_9	a_4	a_6
2	D_{H1}	D_{H4}	D_{H6}	D_{H9}	t_{2-3}	t_{6-9}
3	N_{GG}	T_{tl}	T_c	P_{tl}	W_f	f/a
4	θ	r_t	r_n	D	L_c	N_{4-5}
5	4-5	$Vol._c$	$k(Cp)$	a_9	R_s	C_2
6	H_2	H_{4-5}	H_6	H_a	ξ	
7	T_8	F	Z	ΔT_{g-b}	ϵ	

Output

1	V_{r1}	U	V_{4-5}	V_6	V_9	P_{4-5}
2	T_r	T_2	T_3	T_{4-5}	T_4	T_5
3	T_6	T_7	T_8	T_9	T_f	T_{fl}
4	h_2	h_3	h_6	h_9	ΔP	Force
5	N_{u2}	N_{u4-5}	N_{u6}	N_{u9}	ΔT_{4-5}	X
6	P_{r2}	P_{r4-5}	P_{r6}	P_{r9}	ω	$\omega^2 r$
7	k_2	k_{2-3}	k_{4-5}	k_6	k_{6-9}	k_9
8	R_{e2}	R_{e4-5}	R_{e6}	R_{e9}	P_m	q
9	2^μ	μ_{4-5}	U_6	U_9	R_s	Q

Purpose: To calculate heat distribution and related nondimensional groupings for a cooled turbine using a secondary cooling fluid (steam).

Input

A	=	Surface areas - sq. ft.
a	=	Cross-sectional areas - sq. ft.
D _H	=	Hydraulic diameters - ft.
t	=	Metal thickness - in.
NGG	=	Engine speed - rpm
T	=	Temperature - °R
P _t	=	Total pressure at turbine inlet
Q	=	Nozzle exit angle - deg.
W _f	=	Fuel flow - lb./hr.
f/a	=	Fuel-air ratio
r	=	Radii - ft.
\overline{D}	=	Mean diameter - ft.
L _c	=	Coolant path length - ft.
N ₄₋₅	=	Coolant passage pressure drop factor
ρ	=	Density
Vol _c	=	Volume of coolant system
K(C _p)	=	Steam C _p scale factor
R _s	=	Steam gas constant
C ₂	=	Iteration punch, if = 0 will punch after each loop
H	=	Input heat transfer coefficients - Btu/hr. ft. ² °F
F	=	Constant for gas-side heat transfer equation
Z	=	Power to which R _e must be raised in gas-side equation

Output

V	=	Velocity-ft./sec.
h	=	Calculated heat transfer coefficient-Btu/hr. ft. ² °F
ΔP	=	Pressure drop across coolant system
F	=	Force available in coolant system
N_u	=	Nusselt number
ΔT_{4-5}	=	Temperature rise of steam
X	=	Power to which pressure is missed as a result of thermosyphon action
$P_{r\omega}$	=	Prandtl number
$\omega^2 r$	=	Mean angular acceleration-ft./sec. ²
K	=	Thermal conductivity-Btu ft./hr. sq. ft. °F all except K_{2-3} and K_{6-9} which are Btu in./hr. sq. ft. °F
R_e	=	Reynolds number
P_m	=	Mean pressure of coolant system - psia
U	=	Viscosity: lb./sec. ft. all except u_a = lb./hr. ft.
q	=	Heat flow - Btu/sec.
Q	=	Heat flow - Btu/hr.

Calculations

$$\text{Set } C_1, T_{b2}, C_2, \text{ and } C_3 = 0$$

$$T_{sl} = \frac{T_{tl}}{1.165} V_{abs.} = 44.27 \sqrt{T_{tl}}$$

$$V_a = V_{abs.} \sin \theta \quad V_{wl} = V_{abs.} \cos \theta$$

$$U = \frac{\pi \bar{D} N_{GG}}{60}$$

$$V_{w2} = V_{wl} - U$$

$$V_{rl} = \sqrt{(V_a)^2 + (V_{w2})^2}$$

$$T_R = T_{tl} - \frac{(V_{abs.})^2 - (V_{rl})^2}{50,103 C_{pl}} \quad \& \ C_{pl} = f(T_{tl} \ \& \ f/a)$$

$$P_{sl} = P_{tl} \left(\frac{T_{sl}}{T_{tl}} \right)^{\frac{\gamma_1}{\gamma_1 - 1}}$$

$$T_2 = T_r - \Delta T_{g-b}$$

Entry A

$$\rho_2 = \frac{P_{sl} \times 144}{53.35 T_2}$$

$$\mu_2 = 0.1711 (T_2)^{0.632} \times 10^{-6}$$

$$Re_2 = \frac{144 \times P_{tl} \times D_{H1}}{\sqrt{T_r} \times \mu_2}$$

$$C_{p2} = f (T_2^e - f/a)$$

$$k_2 = 0.690 (T_2)^{0.858} \times 10^{-4}$$

$$P_{r2} = \frac{C_{p2} \mu_2}{k_2} \times 3600$$

$$N_{u2} = F (R_{e2})^Z (P_{r2})^{1/3}$$

$$\text{is } H_2 = 0 \left\{ \begin{array}{l} \text{Yes: Continue.} \\ \text{No: Store } H_2 \text{ in } h_2 \text{ and go to entry B.} \end{array} \right.$$

$$h_2 = \frac{N_{u2} k_2}{D_{H1}}$$

$$Q = h_2 A_2 (T_r - T_2) \quad \text{Entry B}$$

$$\text{Assume } T_3 = T_2 \quad \text{Entry C}$$

$$K_{2-3} = 0.053 \left[\frac{T_3 + T_2}{2} \right] + 40.5$$

$$\Delta T_{2-3} = \frac{(Q)(t_{2-3})}{k_{2-3}} \times \frac{2}{A_2 + A_3}$$

$$T_3' = T_2 - \Delta T_{2-3}$$

$$\text{is } H_3 = 0 \left\{ \begin{array}{l} \text{Yes: Continue.} \\ \text{No: Store } H_3 \text{ in } h_3 \text{ and go to entry D.} \end{array} \right.$$

$$\text{Assume } h_3 = 1000$$

$$T_{4-5} = T_3 - \frac{Q}{h_3 A_3} \quad \text{Entry D}$$

$$W_c = Vol_c \times \rho_{4-5}$$

$$C_{p4-5} = 0.0568 (T_{4-5})^{0.303} \times k (C_p)$$

$$q = \rho \frac{Q}{3600}$$

$$A = \frac{q L_c}{W_c C_{p4-5}}$$

$$B = \frac{N_{4-5} \rho_{4-5}}{2g}$$

$$\frac{\omega^2 r}{2} = \frac{\omega^2}{2} \left(\frac{r_h + r_t}{2} \right) \quad \omega = \frac{2 \pi N_{GG}}{60}$$

$$C = \frac{\rho_{4-5} \omega^2 r}{(T_{4-5}) (2 g)}$$

$$\Delta T_{4-5} = \frac{3 \sqrt{(A)^2 \times B}}{C}$$

$$\text{Force} = C \times \Delta T_{4-5}$$

$$T_4 = T_{4-5} - \frac{\Delta T_{4-5}}{2}$$

$$T_5 = T_{4-5} + \frac{\Delta T_{4-5}}{2}$$

$$\mu_{4-5} = 0.019 (T_{4-5})^{0.946} \times 10^{-6}$$

$$V_{4-5} = \frac{A}{\Delta T_{4-5}} \quad \Delta P = B \times V_{4-5}^2$$

$$R_{e4-5} = \frac{\rho_{4-5} V_{4-5} D_{H4}}{\mu_{4-5}}$$

$$P_{r4-5} = 1.63 (T_{4-5})^{-0.0798}$$

$$N_{\mu_{4-5}} = 0.023 (R_{e4-5})^{0.8} (P_{r4-5})^{1/3}$$

$$k_{4-5} = 0.353 \times (T_{4-5})^{1.275} \times 10^{-5}$$

$$\text{is } H_3 = 0 \quad \begin{cases} \text{Yes: Continue.} \\ \text{No: Go to entry E.} \end{cases}$$

$$h_3 = \frac{N_{\mu_{4-5}} k_{4-5}}{D_{H4}}$$

$$\text{Check is } h'_3/h_3 - 1 \leq \pm 0.005$$

$$\begin{cases} \text{No: Return to entry D and store } h'_3 \text{ in } h_3. \\ \text{Yes: Store } h'_3 \text{ in } h_3 \text{ and continue.} \end{cases}$$

$$P_{4-5} = \frac{\rho_{4-5} R_s T_{4-5}}{144} \quad \text{Entry E}$$

$$\bar{r} = \frac{r_h + r_t}{2}$$

$$\chi = \frac{\omega^2 r}{5377.4} T_{4-5}$$

$$P_m = e^{\chi} P_{4-5}$$

$$R_s = -1.045 \times 10^{-3} P_m + 85$$

Loop once to entry E and recalculate P_m with R_s

$$V_6 = V_{4-5} \frac{a_4}{2 \times a_6}$$

$$\text{is } H_6 = 0 \quad \begin{cases} \text{Yes: Continue.} \\ \text{No: Store } H_6 \text{ in } h_6 \text{ and go to entry F.} \end{cases}$$

$$\text{Assume } h_6 = h_3$$

$$T_6 = T_{4-5} - \frac{Q}{h_6 A_6} \quad \text{Entry F}$$

$$T_f = \frac{T_6 + T_{4-5}}{2}$$

$$\mu_6 = 0.019 (T_f)^{0.946} \times 10^{-6}$$

$$R_{e6} = \frac{\rho_{4-5} V_6 D_{H6}}{6}$$

$$P_{r6} = 1.63 (T_f)^{-0.0798}$$

$$N\mu_6 = 0.023 (R_{e6})^{0.8} (P_{r6})^{1/3}$$

$$k_6 = 0.353 (T_f)^{1.275} \times 10^{-5}$$

$$\text{is } H_6 = 0 \quad \begin{cases} \text{Yes: Continue.} \\ \text{No: Store } H_6 \text{ in } h_6 \text{ and go to entry G.} \end{cases}$$

$$h'_6 = \frac{N\mu_6 k_6}{D_{H6}}$$

$$\text{is } h'_6 - 1 \leq \pm 0.005$$

{ No: Store h'_6 in h_6 and return to entry F.
 { Yes: Store h'_6 in h_6 and continue.

ENTRY G

$$\text{Assume } T_6 = T_9$$

ENTRY H

$$k_{6-9} = 0.056 \left[\frac{T_6 + T_9}{2} \right] + 75.1$$

$$T'_9 = T_6 - \frac{[Q][T_{6-9}]}{k_{6-9}} \times \frac{2}{A_6 + A_9}$$

$$\text{is } \frac{T'_9}{T_9} - 1 \leq \pm 0.001$$

{ No: Store T'_9 in T_9 and return to entry H.
 { Yes: Store T'_9 in T_9 and continue.

$$T_{f1} = T_8 + 200$$

Entry J

$$\text{Log } C_{p9} = 0.36 \times 10^{-3} (T_{f1}) - 0.479$$

$$T_7 = T_8 + \frac{Q}{W_f C_{p9}}$$

$$T'_{f1} = \frac{T_8 + T_7}{2}$$

$$\text{is } T'_{f1}/T_{f1} - 1 \leq \pm 0.002$$

{ Yes: Store T'_{f1} in T_{f1} and continue.
 { No: Store T_{f1} in T_{f1} and go to entry J.

$$\text{Log } \rho_9 = -0.336 \times 10^{-3} (T_{f1}) + 1.868$$

$$V_9 = \frac{W_f}{\rho_9 a_9}$$

$$\text{Log } P_{r9} = -1.685 \times 10^{-3} (T_{f1}) + 2.235$$

is $T_{f1} \leq 660$: - Yes

$$\text{Log } \mu_9 = -2.46 \times 10^{-3} (T_{f1}) + 1.59$$

$$\text{No: Log } \mu_9 = 1.707 \times 10^{-3} (T_{f1}) + 1.092$$

$$R_{e9} = \frac{\rho_9 V_9 D_{H9}}{\mu_9}$$

$$\text{is } C_3 = 0$$

{ Yes: $C_3 = C_3 + 1$. Store $6T_9$ in T_{f2} and go to entry K.
 { No: is $T_{f2} \leq 0.6 T_9$.

{ Yes: Store $6 T_9$ in T_{f2} go to entry K.
 { No: Go to entry K.

ENTRY K

$$N_{\mu 9} = 0.02 (R_{e9})^{0.8} (P_{r9})^{1/3} (T_{f2}/T_9)^{.15}$$

$$\text{Log } \mu_{k9} = -0.181 \times 10^{-3} (T_{f1}) - 0.9957$$

$$\text{is } H_9 = 0$$

{ Yes: Continue.
 { No: Store H_9 in h_9 and go to entry L.

$$h_9 = \frac{N_{u9} k_9}{D_{H9}}$$

ENTRY L

$$T_{f2} = T_9 - \frac{Q}{h_9 A_9}$$

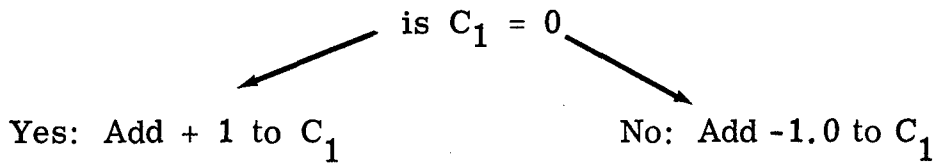
$$\text{is } T_{f2}/T_{f1} - 1 \leq \pm 0.002$$

Yes: Punch output.

No: is $C_2 = 0$

Yes: Punch output and continue.

No: Continue without punching.



$$\text{is } T_{b2} = 0$$

Yes store T_{f1} in T_{b1}

T_{f2} in T_{b3}

T_2 in T_{2A}

add + 100 to T_2 and
return to entry A.

No Store T_{f1} in T_{b1}

T_{f2} in T_{b3}

T_2 in T_{2A}

and calculate T'_2

Store T_{f1} in T_{b2}

T_{f2} in T_{b4}

T_2 in T_{2b}

and calculate T_2

$$T'_2 = \left\{ \frac{(T_{b3} - T_{b1})(T_{2A} - T_{2b})}{T_{b1} - T_{b2} - T_{b3} + T_{b4}} \right\} + T_{2A}$$

$$\text{is } \frac{T_2'}{T_2} - 1 \leq \pm 0.0005$$

{ Yes: Punch output.
 { No: Store T_2' in T_2 and return to entry A.

APPENDIX III

DESIGN OF FLUID-COOLED TURBINE FUEL-TO-STEAM HEAT EXCHANGER

Two basic configurations of the fuel-steam heat exchanger were analyzed:

1. Independently sealed cooling system in each blade with a coolant to fuel heat exchanger in the blade root.
2. A common secondary coolant circuit to all blades with a single coolant to fuel heat exchanger in the engine shaft.

The engine operating conditions at design point, regenerated, are:

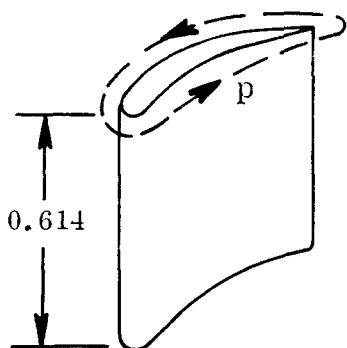
Turbine inlet pressure	-	P_{t1}	-	126.8 psia
Turbine inlet temperature	-	TIT	-	2300°F
Airflow	-	W	-	5 lb./sec.
Fuel flow (regenerative)	-	W_f	-	343 lb./hr. (11.1/blade)
Compressor delivery temperature	-	T_c	-	600°F
Turbine rpm	-	N_{gg}	-	50,000 rpm
Fuel-air ratio	-	f/a	-	0.0191

The above data were the result of cycle and aerodynamic analyses. These design parameters are dictated by the required specific horsepower and specific fuel consumption of the Request for Proposal.

Calculation of Heat Transfer for Computer Program (02007)

Configuration 1 (on a per-blade basis for 31 blades)

A_2 = Blade wetted area



$$= \text{perimeter} \times 0.614$$

$$= 2.46 \times 0.614 \dots = 1.51 \text{ sq. in.}$$

$$= 0.0105 \text{ sq. ft.}$$

Blade Surface Area (Internal)

$P_1 = .17 \text{ In.}$	ΣP	= 1.69 In.	$P_2 = .24 \text{ In.}$	$\text{Area} = \Sigma P \times L + \text{Area of Top Manifold}$
$P_3 = .28 \text{ In.}$			$\text{Area} = .978 \text{ In.}^2$	
$P_4 = .52 \text{ In.}$			$P_5 = .26 \text{ In.}$	$= 1.69 \times .484 + \text{per of Manifold} \times .08''$
$P_6 = .22 \text{ In.}$				$.818 + .16$
				$= .679 \times 10^{-2} \text{ Ft.}^2$

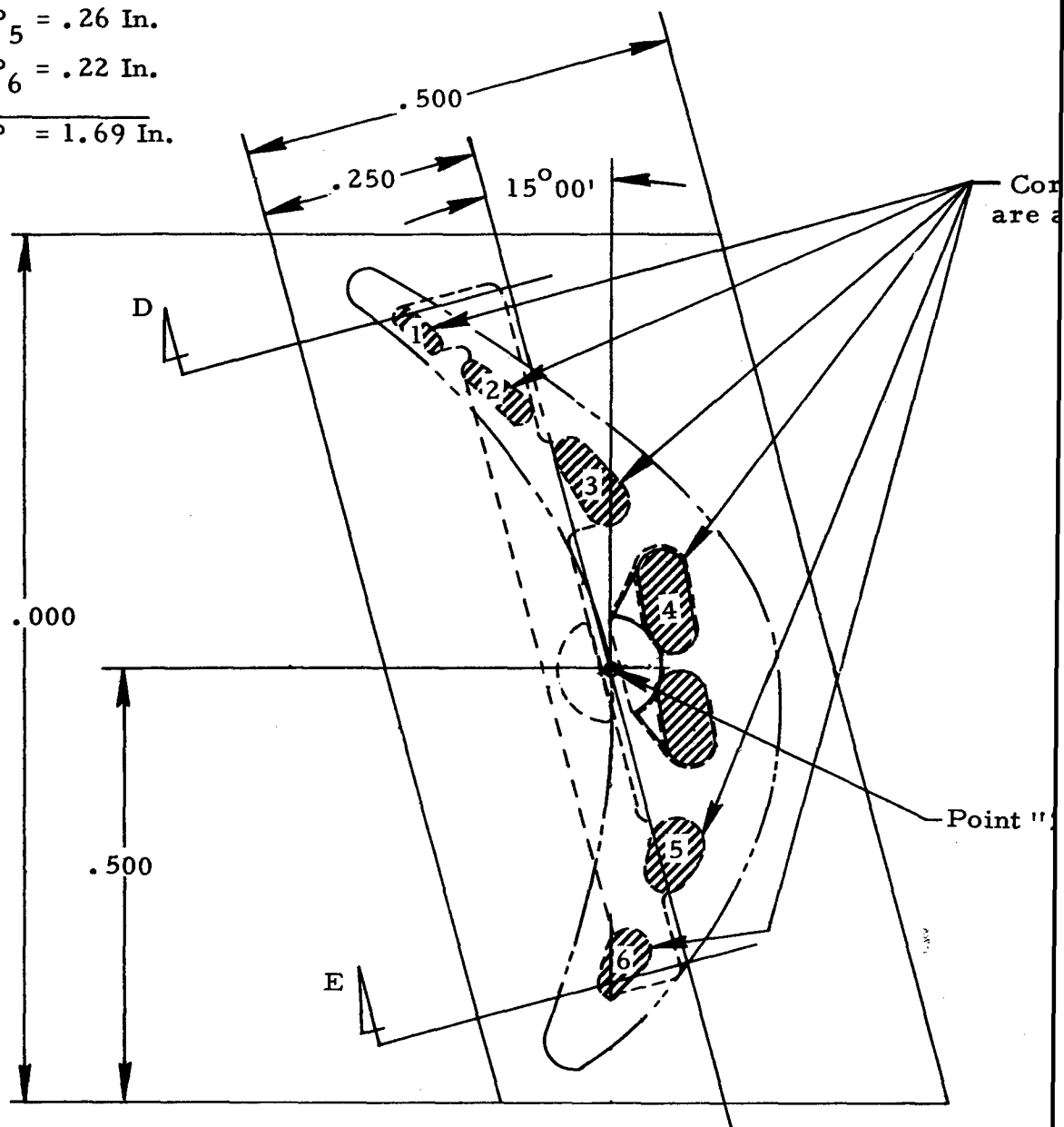


Figure 495. Fluid-Cooled Turbine Blade Flow Areas

Blade Cooling Hole Cross-Sectional Area

$$A_1 = .001941 \text{ In.}^2$$

$$A_2 = .00291 \text{ In.}^2$$

$$A_3 = .00458 \text{ In.}^2$$

$$A_4 = .0165 \text{ In.}^2$$

$$A_5 = .005095 \text{ In.}^2$$

$$A_6 = .00291 \text{ In.}^2$$

$$\Sigma A = .034206 \text{ In.}^2$$

$$\Sigma A = .2379 \times 10^{-3} \text{ Ft.}^2$$

es Shown
t 3.503 R

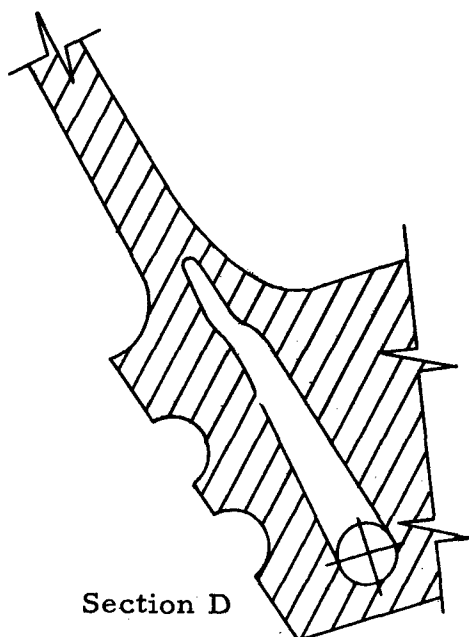
$$\text{Average } D_H = 4. \quad \Sigma A/P$$

Volume of

$$= 4 \left[\frac{A_1 + A_2 + \dots}{P_1 + P_2} \right]$$

$$= .0702 \text{ In.}$$

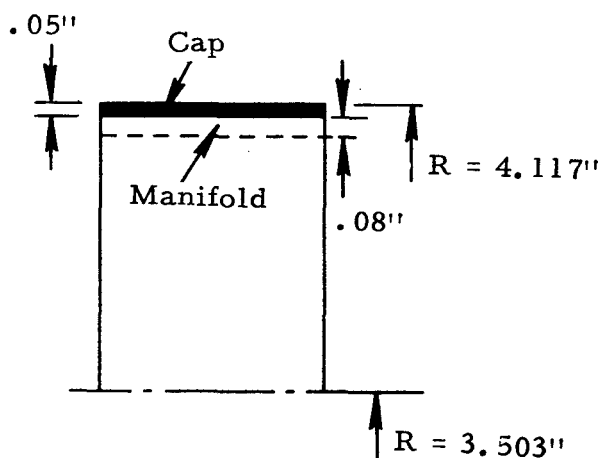
$$D_{H_4} = .00585 \text{ Ft.}$$



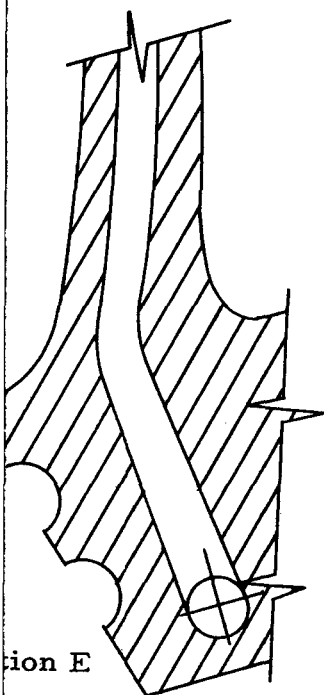
Section D

Sec

Blade Cooling Volume



$$\begin{aligned} \text{Vol. of Blade} &= \Sigma A \times L + \text{Vol. of Manifold} \\ &= .034206 \times .484 + .08 \times .9 \times .06 \\ \text{Volume} &= .02089 \text{ In.}^3 \\ \text{Vol. Blade} &= .121 \times 10^{-4} \text{ Cu. Ft.} \end{aligned}$$



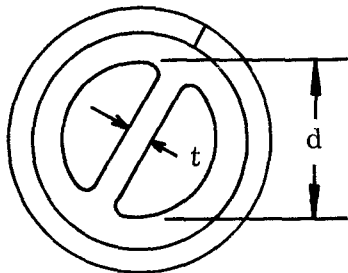
A_3 = Blade internal wetted area

From Figure 495,

$$A_3 = 0.978 \text{ in.}^2 \text{ or } 0.679 \times 10^{-2} \text{ sq. ft.}$$

A_6 = Heat exchanger steam wetted area

A_6 = Wetted perimeter x length of heat exchanger



$$(\pi d - 2t + 2d) L_{Hex}$$

$$(\pi \times 0.13 - 2 \times 0.02 + 0.26) \times 1.15 =$$

$$(0.408 + 0.22) 1.15 = 0.723 \text{ sq. in. or } 0.502 \times 10^{-2} \text{ ft.}^2$$

$$A_6 = 0.502 \times 10^{-2} \text{ ft.}^2$$

A_9 = Heat exchanger fuel wetted area (Ref. Figure 496)

This comprises a tube 1.14 inches long and 0.190 inch in diameter, plus a spiral fin.

$$\underline{A_{\text{Tube}}} = \pi \times 0.19 \times 1.14 = 0.68 \text{ sq. in.}$$

$A_{\text{effective of spiral}} = A_{\text{spiral}}$

$A_{\text{spiral}} = \text{Length of spiral} \times 2 \times \text{fin height}$

$A_{\text{spiral}} = S \times 2 \times h_f$

$$S = n \sqrt{(2\pi r)^2 + p^2}$$

n = number of turns = 5

$$r = \text{radius, assumed} = r = \frac{0.19 + 0.23}{4} = 0.105 \text{ in.}$$

p = pitch = 0.18 in.

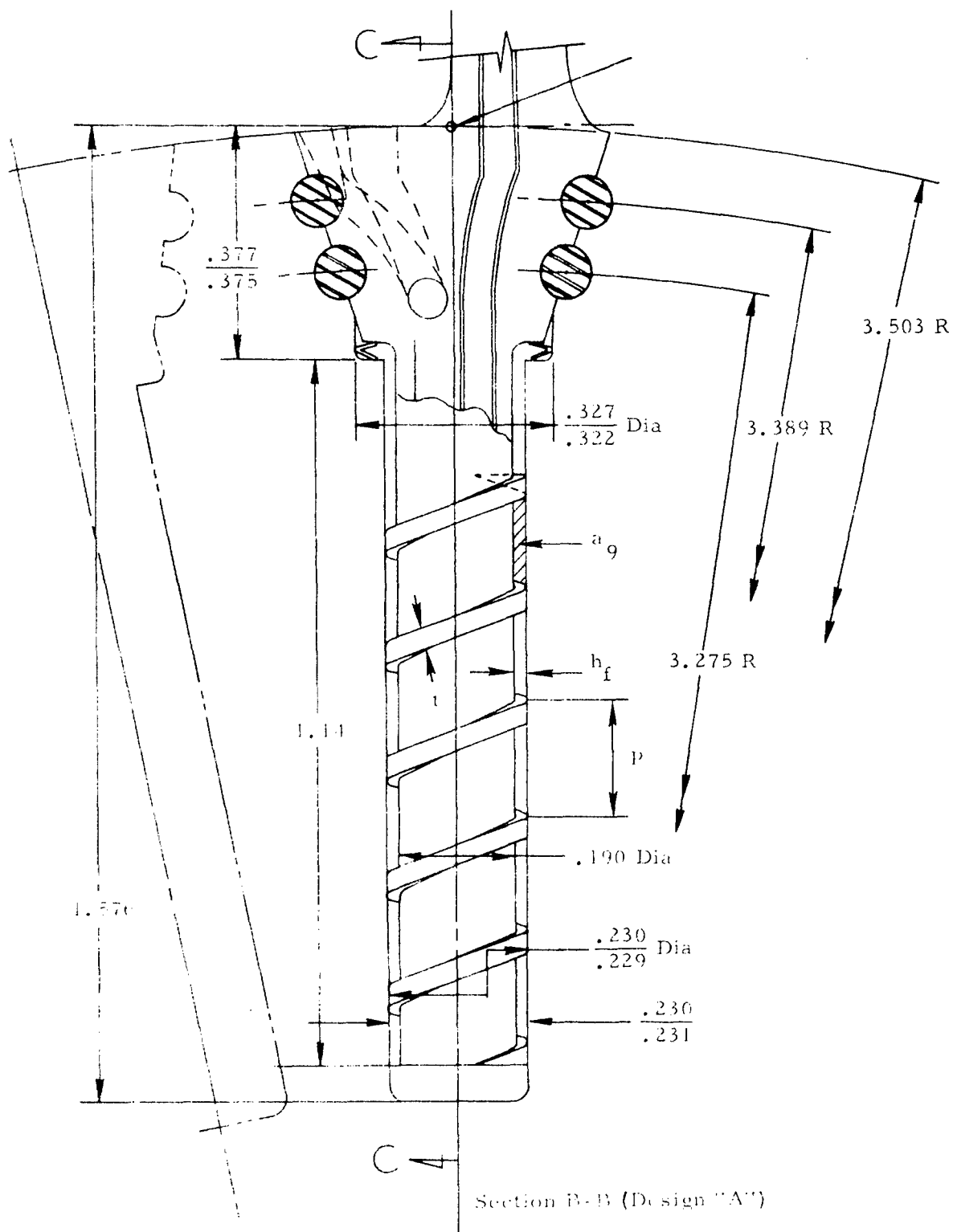


Figure 496. Heat Exchanger Fuel Wetted Area.

$$S = 5 \sqrt{(2 \pi r)^2 + 0.18^2} = 5 \sqrt{0.4355 + 0.0324}$$

$$5 \times \sqrt{0.4679} = 5 \times 0.684 = 3.42 \text{ in.}$$

$$S = 3.42 \text{ in.}$$

$$A_{\text{spiral}} = 3.42 \times 2 \times h_f = 3.42 \times 0.04 \text{ in.}$$

$$A_{\text{spiral}} = 0.1368 \text{ sq. in.}$$

Area covered by fins

$$= \text{length of fin} \times t$$

$$= \left(5 \sqrt{\left(2 \pi \frac{0.19}{2} \right)^2 + (0.18^2)} \right) \times 0.03 =$$

$$\left(5 \times \sqrt{0.3565 + 0.0324} \right) \times 0.03$$

$$\underline{A_{\text{fins}}} = 0.15 \times 0.624 = 0.09355 \text{ in.}^2$$

$$\therefore = A_g = A_{\text{tube}} - A_{\text{fins}} + A_{\text{spiral}}$$

$$= 0.68 - 0.09355 + 0.1368 = 0.7232 \text{ sq. in.}$$

$$A_g = 0.7232 \text{ sq. in.} = 0.502 \times 10^{-2} \text{ sq. ft.}$$

$$\underline{a_4} = \text{Blade cross-sectional flow area (steam)}$$

From Figure 495,

$$a_4 = 0.034256 \text{ in.}^2 \text{ or } 0.2379 \times 10^{-3} \text{ ft.}^2$$

a_6 = Heat exchanger cross-sectional flow area (steam)

$$= \frac{\pi d^2}{4 \times 2} - \frac{d \times t}{2}$$

$$= \frac{\pi \times 0.13^2}{4 \times 2} - \frac{0.13 \times 0.02}{2} = \frac{\pi}{4 \times 2} \times 0.0169 - \frac{0.0026}{2}$$

$$0.00664 - 0.0013$$

$$a_6 = 0.00534 \text{ sq. in.} = 0.3708 \times 10^{-4} \text{ sq. ft.}$$

D_{H1} = Hydraulic diameter of gas side of blade

$$D_{H1} = \frac{\text{blade parameter}}{\pi} \quad (\text{Reference 46})$$

$$= \frac{2.46 \text{ in.}}{\pi} = 0.7835 \text{ in.}$$

$$D_{H1} = 0.0652 \text{ ft.}$$

D_{H4} = Blade internal hydraulic diameter

From Figure 495,

$$D_{H4} = 4 \left(\frac{A_1}{P_1} + \frac{A_2}{P_2} + A_3/P_3 \dots \right)$$

$$= 0.0702 \text{ in.}$$

$$D_{H1} = 0.00585 \text{ ft.}$$

D_{H6} = Hydraulic diameter on stream side of heat exchanger

$$D_{H6} = \frac{4 \times a_6}{\text{Per.}} = \frac{4 \times 0.00534}{0.628 \times 0.5} = 0.068 \text{ in.}$$

$$D_{H6} = 0.567 \times 10^{-2} \text{ ft.}$$

D_{H9} = Hydraulic diameter on the fuel side

$$D_{H9} = \frac{4 \times a_9}{P_9}$$

$$P_9 = 0.02 + 0.15 + 0.02 + 0.15 = 0.34 \text{ in.}$$

$$\text{so } D_{H9} = \frac{4 \times 0.003}{0.34} = 0.0353 \text{ in.}$$

$$D_{H9} = 0.002985 \text{ ft.}$$

t_{2-3} = Blade wall thickness

$$t \text{ average value for } t_{2-3} = 0.04 \text{ in.}$$

t_{6-9} = Heat exchanger wall thickness

$$t_{6-9} = 0.03 \text{ in.}$$

θ = Turbine nozzle exit angle

From aerodynamic design this is equal to

$$\theta = 21^\circ$$

r_t = Turbine rotor tip radius

$$r_t = 4.117 \text{ in.} = 0.343 \text{ ft.}$$

$$\underline{r_h} = \text{Turbine hub radius} = 3.503 \text{ in.}$$

$$r_h = 3.503 \text{ in.} = 0.292 \text{ ft.}$$

$$\underline{\bar{D}} = \text{Mean blade diameter}$$

$$\bar{D} = r_t + r_h = 4.117 + 3.503$$

$$\bar{D} = 7.620 \text{ in.} = 0.635 \text{ ft.}$$

$$\underline{L_c} = \text{Length of cooling path}$$

$$\text{Approx.} = 2 \times \text{blade height} + \text{length of blade tip manifold} + 2 \times \text{length of heat exchanger} + 2 \times \text{length of rim manifold.}$$

$$L_c = 2 \times 0.614 + 0.9 + 2 \times 1.15 + 2 \times 0.375$$

$$1.228 + 0.9 + 2.30 + 0.75 = 5.378 \text{ in.}$$

$$L_c = 5.378 \text{ in. or } 0.447 \text{ ft.}$$

$$\underline{N_{4-5}} \text{ is the number of bends in the cooling system}$$

$$N_{4-5} = 7.0$$

$$\underline{\rho_{4-5}} \text{ is the density of the steam}$$

$$\rho_{4-5} = 1.4 \text{ lb./cu. ft.}$$

$$\underline{\text{Vol. } c} = \text{Volume of cooling system (Ref. Figures 495 and 497)}$$

$$\text{Vol. } c = 0.2598 \times 10^{-4} \text{ cu. ft.}$$

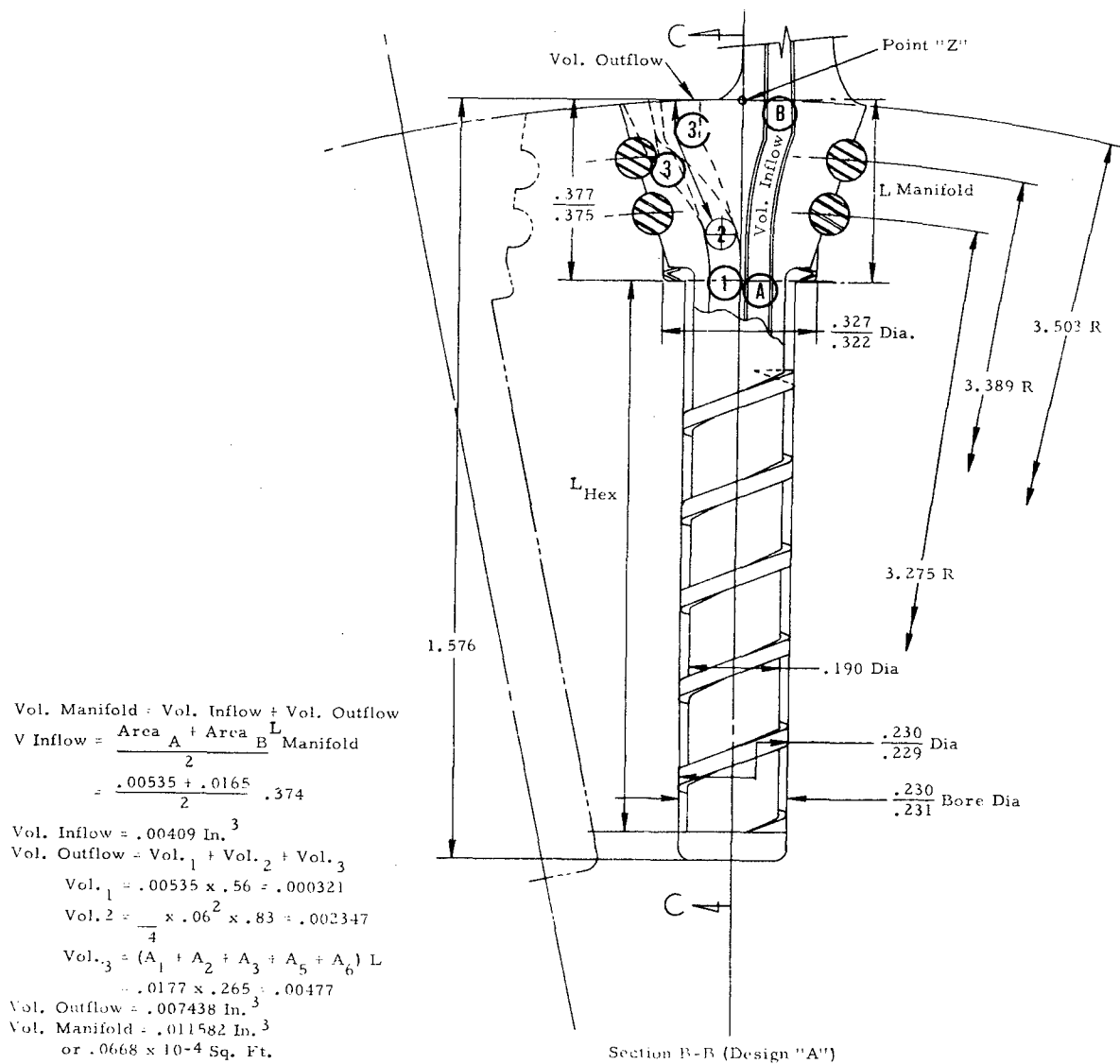
$$\underline{k (c_p)} = \text{Scale factor on specific heat of steam}$$

$$\text{usually assumed equal to 1.0 except at temperatures less than } 1000^\circ \text{ F.}$$

$$a_g = \text{Fuel throughflow area}$$

$$= 0.02 \times 0.15 \text{ sq. in.} = 0.003 \text{ sq. in.}$$

$$a_g = 0.003 \text{ sq. in. or } 0.2085 \times 10^{-4} \text{ sq. ft.}$$



Total Cooling Volume = V_{Tot}

V_{Tot} = V_{Blade} + V_{Manifold} + V_{Hex}

$= .02089 + .011528 + .012461$

V_{Tot} = .044879 Cu. In.

$= .2598 \times 10^{-4}$

Figure 497. Cooling Volume of Heat Exchanger Manifold.

R_s = Gas constant for steam

R_s assumed = 83.5 for first guess, is calculated in the program as a temperature dependent variable.

C_2 is an iteration check: If put equal to 1.0, program will punch data at completion of each individual calculation. If entered as 0, program will punch data after each complete loop.

H_2 , H_{4-5} , H_6 , H_9 are heat transfer coefficients of the blade, gas side, blade steam side, heat exchanger steam side, and heat exchanger fuel side respectively. If entered as 0, program will calculate these film coefficients. If entered as a positive value, program will override calculated values and use input values.

ξ is a mean flow function describing the flow through the turbine nozzle;

$$\text{that is, } \xi \times \sqrt{\frac{T_r}{P_{t1}}} = \frac{W}{R}$$

is a function of M , $\xi = 0.261$ for these rotors.

T_8 = Fuel inlet temperature

$T_8 = 100^\circ\text{F}$ (an assumed conservative value)

F and Z are constants on the gas side heat transfer equations which is of the form

$$N_u = F (R_e)^Z (P_r)^{1/3}$$

F and Z are 0.092 and 0.7 respectively

Reference 46, Page 3

Configuration 2 (total engine basis, 31 blades)

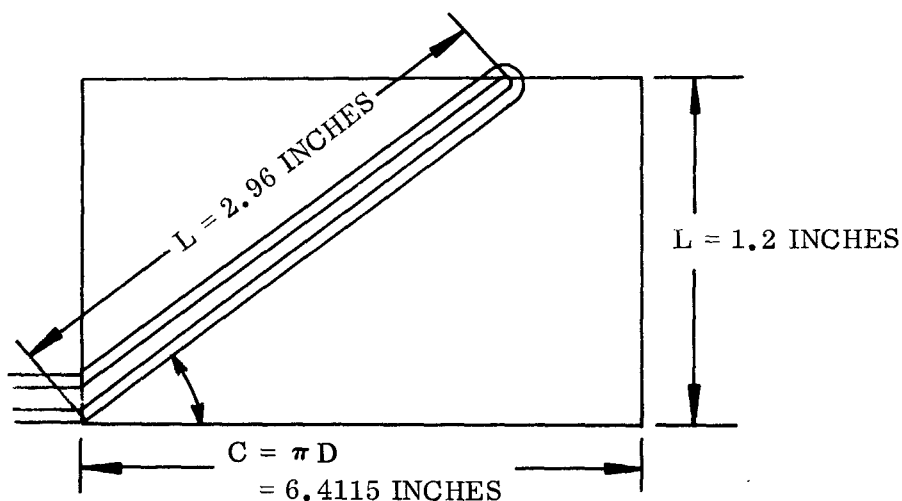
All input items are unchanged with the exception of the following:

A_2 = Blade wetted area
= 0.0105 sq. ft./blade x 31 blades = 0.3255 sq. ft.

$$A_3 = \text{Blade internal wetted area} \\ = 0.679 \times 10^{-2} \text{ sq. ft./blade} \times 31 \text{ blades} = 0.21049 \text{ ft.}^2$$

$$A_6 = \text{Heat exchanger steam wetted area}$$

Fuel flows through seven "U" tubes (0.125 in. OD) which spiral 260 degrees in the axial direction. A development sketch of the outer heat exchanger cylinder is shown with one "U" tube attached.



Therefore,

$$A_6 = (\text{tube O.D. circum.}) (\text{tube length}) (2 \times \text{number of tubes})$$

+ effective fin area of shaft O.D. and I.D. wall

$$= \frac{\pi}{8} (2.96) (2 \times 7) + 6.77$$

$$= 16.27 + 6.77 = 23.04 \text{ sq. in.}$$

$$= 0.16 \text{ sq. ft.}$$

$$A_9 = \text{Heat exchanger fuel wetted area}$$

$$= (\text{tube I.D. circumference}) (\text{tube length}) (2 \times \text{number of tubes})$$

$$= (0.069 \pi) (2.96) (2 \times 7) = 8.983 \text{ sq. in.} = 0.0623 \text{ sq. ft.}$$

$$a_4 = \text{Blade cross-sectional flow area (steam)}$$

$$= 0.2379 \times 10^{-3} \text{ sq. ft.} \times 31 \text{ blades} = 7.375 \times 10^{-3} \text{ sq. ft.}$$

a_6 = Heat exchanger cross-sectional flow area (steam)

$$= \frac{\pi}{4} \left[(\text{O.D. Hex})^2 - (\text{I.D. Hex})^2 \right] \sin \alpha - \frac{\pi}{4} (\text{tube O.D.})^2$$

x (Number of tubes)

$$= 0.1656 \text{ sq. in.} = 1.15 \times 10^{-3} \text{ sq. ft.}$$

D_{H6} = Hydraulic diameter on steam side of hex.

$$= 4 \frac{\text{flow area}}{\text{wetted perimeter}}$$

$$\text{flow area} = a_6 = 0.1656 \text{ sq. in.}$$

$$\begin{aligned} \text{wetted perimeter} &= 2(1.07 + 0.9) + 14 \left(\frac{\pi}{8} \right) \\ &= 9.552 \text{ inches} \end{aligned}$$

Therefore,

$$D_{H6} = 4 \left(\frac{0.1656}{9.552} \right) = 0.06934 \text{ inch} = 5.7 \times 10^{-3} \text{ ft.}$$

D_{H9} = Hydraulic diameter on fuel side
 = inside diameter of fuel tube
 = 0.069 in. = 0.00575 ft.

t_{6-9} = Fuel tube wall thickness
 = 0.028 inch

L_c = Length of cooling path
 = 2 (blade length) + (chord length) + 2 (hub radius - hex. radius)
 + 2 (hex. length)
 = 13.934 in. = 1.16117 ft.

$$\begin{aligned}
 V_c &= \text{Volume of cooling system} \\
 &= 31 (\text{blade volume}) + 31 (\text{supply tube volume}) + (\text{volume of hex}) \\
 &= 31 (.02089) + 31 (\pi / 4) (.0036) (2.503 - 2.903) + 2.491 \\
 &= .64759 + 0.47383 + 2.491 \\
 &= 3.612 \text{ cu. in.} \\
 &= 2.09 \times 10^{-3} \text{ cu. ft.}
 \end{aligned}$$

$$\begin{aligned}
 a_g &= 7 \left(\frac{\pi}{4} \right) (.069)^2 \\
 &= 0.02617 \text{ sq. in.} \\
 &= 0.1817 \times 10^{-3} \text{ sq. ft.}
 \end{aligned}$$

I	R	J	N	O	R	T	O	N	7	-	2	6	-	6	5		5	4	9	3	9	4		
I	A	M	L	F	L	U	I	D	C	O	O	L	E	O	T	U	R	B	I	N	E			
I	C	O	N	F	I	G	U	R	A	T	I	O	N	I	I	S	H	A	F	T	H	E	X	
I	S	E	A	-	L	E	V	E	L	R	E	G	E	N	E	R	A	T	E	O	3	1	B	D

I.D.	VAR - 1	VAR - 2	VAR - 3	VAR - 4	VAR - 5	VAR - 6	CTL
1000	0.3255	0.2105	0.16	0.623	4.4857	1.15	1
2000	0.0652	0.585	5.7	0.575	0.04	0.03	1
3000	50.0	2760.	1640.	126.8	343.0	0.0191	1
4000	21.0	0.343	0.292	0.635	1.1612	18.0	1
5000	1.4	2.09	1.0	0.1817	83.5	1.0	1
6000	0.0	0.0	0.0	0.0	5.0	0.0	1
7000	560.	0.092	0.7	500.	0.0005	0.0	1
8000	2247.	31.6	60.0	0.0907	0.0	0.0	2

I	R	J	N	O	R	T	O	N	7	-	2	6	-	6	5	5	4								
I	A	M	L	F	L	U	I	D	C	O	O	L	E	O	T	U	R	B	I	N	E				
I	C	O	N	F	I	G	U	R	A	T	I	O	N	I	I	S	P	I	R	A	L	-	F	I	N
I	S	E	A	-	L	E	V	E	L	R	E	G	E	N	E	R	A	T	E	D	3	1	B	D	

I.D.	VAR - 1	VAR - 2	VAR - 3	VAR - 4	VAR - 5	VAR - 6	CTL
1000	0.0105	0.679	0.502	0.502	0.1447	0.3708	1
2000	0.0652	0.585	0.567	0.2985	0.04	0.03	1
3000	50.0	2760.	1640.	126.8	11.1	0.0191	1
4000	21.0	0.343	0.292	0.635	0.447	7.0	1
5000	1.4	0.26	1.0	0.2085	83.5	1.0	1
6000	0.0	0.0	0.0	0.0	5.0	0.0	1
7000	560.	0.092	0.7	500.0	0.0005	0.0	1
8000	2247.	31.6	60.	0.0907	0.0	0.0	2

JOB 5
 XEQS
 I R J NORTON 7-26-65 SQ 25.0
 I AML FLUID COOLED TURBINE
 I CONFIGURATION I SPIRAL-FIN
 I SEA LEVEL REGENERATED 31B U

ID	VR1	U	V4-5	V6	V9	P4-5
100	9.1536E+02	1.6624E+03	1.3475E+02	2.6293E+02	1.2228E+04	1.3171E+03
	TR	T2	T3	T4-5	T4	T5
200	2.4804E+03	1.9130E+03	1.8614E+03	1.6300E+03	1.5925E+03	1.6675E+03
	T6	T7	T8	T9	TF	TF1
300	1.4424E+03	8.0397E+02	5.6000E+02	1.3810E+03	1.5362E+03	6.8198E+02
	H2	H3	H6	H9	DP	F1
400	2.6568E+02	1.0080E+03	1.6817E+03	4.5109E+02	2.7656E+03	2.7674E+03
	NU2	NU4-5	NU6	NU9	DT4-5	X
500	3.8375E+02	1.3405E+02	2.3379E+02	1.7715E+01	7.5022E+01	3.1529E-01
	PR2	PR4-5	PR6	PR9	W	W2R
600	6.7085E-01	9.0334E-01	9.0762E-01	1.2185E+01	5.2360E+03	2.7637E+06
	K2	K2-3	K4-5	K6	K6-9	K9
700	4.5140E-02	1.4052E+02	4.3988E-02	4.0786E-02	1.5417E+02	7.6008E-02
	RE2	RE4-5	RE6	RE9	PM	QQ
800	1.7962E+05	5.3129E+04	1.0627E+05	1.8763E+03	1.8054E+03	4.3973E-01
	MU2	MU4-5	MU6	MU9	RS	Q
900	2.9606E-05	2.0773E-05	1.9640E-05	8.4693E-01	8.3113E+01	1.5830E+03
	TF2	A	B	C		
1000	6.8202E+02	1.0109E+04	1.5229E-01	3.6888E+01		

JULY 26, 1965

JOB 5
XEROX

JULY 27, 1985

1 R J MORTON 7-28-85 090304
1 AMI FLUID COOLED TOWER
1 CONFEIGURATION II SHAFER KEY
1 SEA-LEVEL REGENERATED 31 RD

10	V61	V4-5	V6	V9	V4-5
100	0.1546E+02	1.6624E+03	1.8565E+02	4.3050E+04	1.3274E+03
	TR	TR	T4-5	T4	TF
200	2.4904E+02	1.9672E+03	1.6429E+03	1.5944E+03	1.6914E+03
	TR	TR	T9	TF	TF1
300	1.4110E+03	5.6000E+02	1.3425E+03	1.5324E+03	6.7272E+02
	TR	HA	H9	OP	SI
400	7.5665E+02	1.2701E+03	1.0748E+03	3.5486E+03	3.5510E+03
	MU2	MU6	MU9	DT4-5	X
500	3.7464E+02	1.7306E+02	8.0996E+01	9.7025E+01	3.1282E-01
	PR2	PR6	PR9	W	W2
600	6.7077E-01	9.0780E-01	1.2631E+01	5.2360E+03	2.7637E+04
	K1	K4-5	K6	K6-9	K9
700	4.6235E-02	4.4431E-02	4.0658E-02	1.5254E+02	7.6302E-02
	RF2	RE6	RE9	PM	00
800	1.7623E+05	3.7252E+04	1.2358E+04	1.8149E+03	1.2460E+01
	MU2	MU6	MU9	RS	Q
900	3.0176E-05	2.0928E-05	8.7831E-01	8.3103E+01	4.4857E+04
	TF2	A	C		
1000	6.7274E+02	9.2360E+03	3.6599E+01		

APPENDIX IV

GENERAL THREE-DIMENSIONAL TRANSIENT TEMPERATURE DISTRIBUTION

SUMMARY

Continental's IBM Program 25.012 provides an evaluation of transient and steady-state temperature distributions considering the flow of heat in one, two, or three dimensions. Any size or shape model may be examined at up to 100 points with all three modes of heat transfer affecting each temperature. Polymetallic models may be studied.

DISCUSSION

This program provides the thermal examination of up to 100 elements as selected within a model to be evaluated. In elements whose shape resembles a plate, cylinder, or sphere, the error introduced by assuming the temperature at any instant to be uniform throughout the element is less than 5 percent if the Biot number (hl/k) for that element is less than 0.1. If a large model with marked thermal gradients is considered to be divided into small elements with individual Biot numbers less than 0.1, the small elements (nodes) may be treated as point masses and heat transfer equations written around them.

For each node, the general finite-difference heat transfer equation is written

$$\frac{Q_{\text{net}}}{\Delta \theta} = \sum q_{\text{conduction}} + \sum q_{\text{radiation}} + \sum q_{\text{convection}}$$

where for

conduction between nodes m and n (note, i.f. refers to interface),

$$q_{m-n} = \frac{k_m A_{m-n}}{l_m - \text{i.f.}} (T_m - T_{\text{i.f.}}) = \frac{k_n A_{m-n}}{l_{\text{i.f.}} - n} (T_{\text{i.f.}} - T_n)$$

so

$$q_{m-n} = \frac{(T_m - T_n)}{\frac{l_m - i.f.}{k_m A_{m-n}} + \frac{l_{i.f.} - n}{k_n A_{m-n}}}$$

radiation between nodes m and j:

$$q_{m-j} = (0.1713) \left(\frac{A_{m-j} F_{m-j} + A_{j-m} F_{j-m}}{2} \right) \left(\frac{\epsilon_m}{\epsilon_m + \epsilon_j} \right)$$

$$\left[\left(\frac{T_m + 460}{100} \right)^4 - \left(\frac{T_j + 460}{100} \right)^4 \right]$$

radiation between node m and source (s):

$$q_{m-s} = (0.01713) (A_{m-s} F_{m-s}) (\epsilon_m) \left[\left(\frac{T_m + 460}{100} \right)^4 - \left(\frac{T_s + 460}{100} \right)^4 \right]$$

convection between node m and gas (g_1):

$$q_{m-g_1} = h_{g_1} A_{m-g_1} (T_m - T_{g_1})$$

Note: + Q = heat flow out
- Q = heat flow in

Program storage allows the establishment of up to six conduction equations, up to two radiation equations, and up to two convection equations for each node. With the input of significant nodal constants (conductivity, areas, emissivities, convective coefficients, and so forth), thermal parameters are calculated and heat flow during a small finite time becomes a function of temperature difference alone. Note that since nodal constants are distinct inputs for each node, they may vary from node to node.

During time interval $\Delta \theta$, nodal temperatures are assumed to be constant at T_θ and nodal heat flows are calculated for this time interval. Node temperature may now be calculated at time $\theta + \Delta \theta$ for node m by

$$T_m \Big|_{\theta + \Delta \theta} = T_m \Big|_{\theta} - \frac{Q_{m \text{ Net}}}{\rho_m V_m C_m} \Big|_{\theta} + \Delta \theta$$

and similarly for all other nodes. Node temperatures are not reset at

$$T_m \Big|_{\theta + \Delta \theta} \text{ and temperatures at } \theta + 2 \Delta \theta \text{ calculated.}$$

The selection of a proper $\Delta \theta$ is essential to the stability, accuracy, and computer time of a particular program run. In order to establish the maximum stable limit of $\Delta \theta$ for a particular node,

$$\text{Let } \Delta T_{\text{Effective}} = \frac{\epsilon q_{\text{conduction}} + \epsilon q_{\text{radiation}} + \epsilon q_{\text{convection}}}{\epsilon \frac{KA}{L} + \epsilon \sigma F A \epsilon + \epsilon hA}$$

$$\begin{aligned} \text{Now } Q_{\text{Net}} &= \Delta \theta (\epsilon q_{\text{cond.}} + \epsilon q_{\text{rad.}} + \epsilon q_{\text{conv.}}) \\ &= (\Delta \theta) (\Delta T_{\text{eff.}}) \left(\epsilon \frac{KA}{L} + \epsilon \sigma F A \epsilon + \epsilon hA \right) \end{aligned}$$

$$\text{also } Q_{\text{Net}} = \rho V C \Delta T \Big|_{\theta}^{\theta + \Delta \theta}$$

so that

$$\Delta \theta = \frac{\Delta T \Big|_{\theta}^{\theta + \Delta \theta}}{\Delta T_{\text{effective}}} \times \left(\frac{\rho V C}{\epsilon \frac{KA}{L} + \epsilon \sigma F A \epsilon + \epsilon hA} \right)$$

define

$$\text{Critical Factor, } f_c = \frac{\Delta T \left| \frac{\theta + \Delta \theta}{\theta} \right|}{\Delta T_{\text{eff.}}}$$

so

$$\Delta \theta_{\text{Critical}} = f_c \frac{\rho V C}{\left(\epsilon \frac{KA}{L} + \epsilon \sigma A F + \epsilon h A \right)}$$

It can be shown that if $0 < f_c \leq 0.5$, the possible error will be bounded and the program will always remain stable. For $f_c > 0.5$, stability is not guaranteed.

The program calculates $\Delta \theta_c$ for each node and scans to select the smallest one. It then checks the required print-out time interval ($\Delta \theta$ on input sheet No. 1) to see if

$$\Delta \theta_{\text{Print}} \leq \Delta \theta_{\text{Critical}}$$

If not, it divides by the positive integer "N" ($N = 2, 3, 4---$) until

$$\frac{\Delta \theta_{\text{Print}}}{N} \leq \Delta \theta_{\text{Critical}}$$

Program calculations are then made at time intervals of $\frac{\Delta \theta_{\text{Print}}}{N}$

and the program prints every N^{th} calculation until it reaches the inputted final θ . Steady-state temperatures are approached as θ_{final} is increased.

APPENDIX V

TURBINE PERFORMANCE DATA REDUCTION PROGRAM - 08.079

DESCRIPTION

This is the data reduction program utilized for the fluid-cooled turbine. The program accepts turbine rig test data and calculates turbine parameter.

INPUT

N	Engine Speed - rpm
M	Torque - percent if table is used - actual torque if table is not used
ΔP	Pressure Loss Across Inlet Orifice Valve - Inches Mercury
T_{UP}	Upstream Temperature - °F
P_{UP}	Upstream Pressure - Inches Mercury
$(CPS)_E$	Engine Fuel Meter - cycles per second
$(CPS)_P$	Preheater Fuel Meter - cycles per second
P_{BAR}	Barometric Pressure - Inches Mercury
Torque Cont	- 0. if Torque Curve is used 1. if Torque Curve is not used
N_{P1}	Number of P_1 Readings
P_1	All Inlet Pressures - Inches Mercury
N_{P9}	Number of P_9 Readings
P_9	All Exit Pressures - Inches Mercury
N_{T9}	Number of T_9 Readings

INPUT (Cont'd)

T_9	All Exit Temperature - °F
A_7	Rotor Throat Area - In ²
A_3	Nozzle Throat Area - In ²
$\left(\frac{W\sqrt{T}}{P}\right)_L$	Leakage Flow Parameter
A_B	Nozzle T.E. Cooling Area - In ²
$\Delta p/P_3$	Nozzle Total Pressure Loss
	Nozzle Override constant

OUTPUT

Gearbox Horsepower
Engine Fuel Flow - Lb/Hr
Fuel-Air Ratio
Dynamometer Efficiency
Dynamometer Referred Speed - rpm
Dynamometer Turbine Inlet Temperature - °F
Airflow - Lb/Sec
Preheater Fuel Flow - Lb/Hr
Dynamometer Work - Btu/Lb
Dynamometer Referred Flow - Lb-Rev/Sec²
Dynamometer Referred Pressure Ratio
Exhaust Gas Temperature - °F
Messages on Nozzle: Choked or Unchoked or Override Test
Dynamometer Efficiency - *_{DYN}
Exhaust Temperature - T_9^* - °R (Rankine)

TABLE

Meter Reading versus Torque

The table is changed occasionally when the rig is recalibrated.

PROGRAM CALCULATIONS:

Read Table and Input Data

Is TORQUE CONTROL = 0. ?

YES: $T = TLU$ at M Table 1

Go to 1

NO: $T = M$

Go to 1

GEARBOX HORSEPOWER

$$HP_{GB} = \left(\frac{N}{9935} \right)^{2.126}$$

Entry 1

$$\frac{(\Delta P) P_{UP}}{T_{UP}} = \frac{(\Delta P) P_{UP}}{T_{UP} + 459.688}$$

$$W_a = 0.488 \left[\frac{(\Delta P) P_{UP}}{T_{UP}} \right]^{-0.6544}$$

AIRFLOW - Lb/Sec

$$W_a = e W_a$$

ENG. FUEL FLOW - PPH (pounds per hour)

$$W_{fe} = 0.3427 (CPS)_E$$

PREHEATER FUEL FLOW - PPH

$$W_{fp} = 1.17 (\text{CPS})_p + 3.0$$

$$P_1 = \frac{\sum_{i=1}^{N_{pi}} P_i}{N_{Pi}} + \left(\frac{P_{BAR}}{29.92} \right) \quad 14.7$$

$$P_9 = \frac{\sum_{i=1}^{N_{pq}} P_q}{N_{P_q}} + \left(\frac{P_{BAR}}{29.92} \right) \quad 14.7$$

$$W_L = \left(\frac{W\sqrt{T}}{P} \right)_L \sqrt{\frac{P_1}{T_{UP} + 459.688 + \left(\frac{18.5 W_{fp}}{W_a} \right)}}$$

$$W_g = W_a + \left(\frac{W_{fe} + W_{fp}}{3600} \right) - W_L$$

FUEL-AIR RATIO

$$f/a = \frac{W_{fe} + W_{fp}}{3600 W_a}$$

$$\lambda = \frac{P_1}{P_q}$$

$$T_9 = \frac{\sum_{i=1}^{N_{T9}} T_9}{N_{T9}} + 459.688$$

$$HP_{DYN} = \frac{T \times N}{42355.706}$$

$$HP_{TOT} = HP_{DYN} + HP_{GB}$$

$$\Delta H_{DYN} = \frac{HP_{TOT}}{1.41454 \times W_g}$$

$$\gamma_9 = \text{TLU at } f/a \text{ and } T_9$$

$$T_1' = \left[\frac{\Delta H_{DYN} (\gamma_9 - 1.0)}{\gamma_9} \right] \times 14.602681 + T_9$$

$$\gamma_1' = \text{TLU at } f/a \text{ and } T_1'$$

$$1\gamma_9' = \frac{\gamma_1' + \gamma_9}{2.}$$

$$T_{1DYN} = \left[\frac{\Delta H_{DYN} (1\gamma_9' - 1.)}{1\gamma_9'} \right] \times 14.602681 + T_9$$

$$\gamma_1 = \text{TLU at } f/a \text{ and } T_{1DYN}$$

$$\Theta_{CRDYN} = \frac{1 \times T_{1DYN}}{(\gamma_1 + 1.) \times 302.568}$$

DYNAMOMETER WORK

$$\frac{\Delta H}{\Theta_{CRDYN}} + \frac{\Delta H_{DYN}}{\Theta_{CRDYN}}$$

$$\epsilon = \frac{.73959}{\gamma_1} \left(\frac{\gamma_1 + 1}{2} \right) \frac{\gamma_1}{\gamma_1 - 1}$$

$$1\gamma_9 = \frac{\gamma_1 + \gamma_9}{2}$$

$$T_9' = T_{1DYN} \left(\frac{P_9}{P_1} \right)^{\frac{1.79 - 1}{1.79}}$$

DYNAMOMETER EFFICIENCY

$$\eta_{DYN} = \frac{T_{1DYN} - T_9}{T_{1DYN} - T_9'}$$

DYNAMOMETER REF. FLOW

$$\frac{WN}{860} \epsilon = \frac{W_g \times N \times \epsilon}{4.0823 \times P_1}$$

DYNAMOMETER REF. SPEED

$$\frac{N}{\sqrt{\theta_{CRDYN}}} = \frac{N}{\sqrt{\theta_{CRDYN}}}$$

$$\lambda_T = \frac{1.}{\left\{ 1 - 0.16701 \left(\frac{\gamma_1 + 1}{\gamma_1 - 1} \right) \left[1 - \left(\frac{P_9}{P_1} \right)^{\frac{\gamma_1 - 1}{\gamma_1}} \right] \right\}^{3.49376}}$$

CHOKED NOZZLE OPTION

$$P_3 = \left[1 - \left(\frac{\Delta P_3}{P_1} \right) \right] P_1$$

$$T_{UP} = t_{UP} + 459.688 + \frac{18.5 W_{fp}}{W_a}$$

$$\gamma_{UP} = \text{TLU at } T_{UP}$$

$$T_B = \sqrt{\frac{g \gamma_{UP}}{R} \left(\frac{2}{\gamma_{UP} + 1} \right)^{\frac{\gamma_{UP} + 1}{\gamma_{UP} - 1}}}$$

$$\omega_B = \frac{T_B A_B P_3}{\sqrt{T_{UP}}}$$

$$W_3 = W_g - \omega_B$$

$$T_3 = \sqrt{\frac{g \gamma_1}{R} \left(\frac{2}{\gamma_1 + 1} \right)^{\frac{\gamma_1 + 1}{\gamma_1 - 1}}}$$

$$(T_3)_{DYN} = \frac{W_3 \sqrt{(T_1)_{DYN}}}{A_3 P_3}$$

If (OVERRIDE)

= 1, Print OVERRIDE NOZZLE CHOKE TEST

Continue

= 0, If $((T_3)_{DYN} - T_3) =$

0, positive, Print Nozzle Choked

Continue

Negative, Print Nozzle Unchoked

Stop Calculations Here

$$T_3 = \left[\frac{T_3 A_3 P_3}{W_3} \right]^2$$

Return to γ_1 Calculation With $(T_1)_{DYN}$ Replaced by T_3

Print Output Using T_3

$$T_9^* = T_3 - \frac{(\Delta H)_{DYN} J (1 \gamma_9 - 1)}{R_1 \gamma_9'}$$

$$T_9' = T_3 \left(\frac{P_9}{P_1} \right)^{\frac{1 \gamma_9 - 1}{1 \gamma_9}}$$

$$\eta_{DYN}^* = \frac{T_3 - T_9^*}{T_3 - T_9'^*}$$

PRINT

$$T_9^* = T_9^* - 459.688$$

PRINT

TURBINE PERFORMANCE DATA REDUCTION PROGRAM - INPUT
COMPUTER PROGRAM 08.079 TURBINE TEST 62

D	A	T	E										N	A	M	E								S	Q		
I																											
I			F	L	U	I	D		C	O	L	E	D		T	U	R	B	I	N	E						
I			T	E	S	T		P	O	I	N	T		N	O	.	6	2									

Card		Sort		Engine		M								
No.		No.		N (RPM)		(Torque in %)		P		(T) UP		(P) UP		(CPS) E
± 1		± 6		± 11		± 21		± 31		± 41		± 51		± 61
+0001		+0001		42286		575.0		92.0		56.0		190.7		1325

Card No.	Sort No.	(CPS)	P	(P) BAR	Torque Control *
+0002	+0001	72.0		29.34	1.0

Card No.	Sort No.	A ₇	A ₃	LKG Flow	A _B	P/P ₃	Noz. Cont.**
+0003	+0001	0	4.211	0.050	0.065	0.04	1.0

Card No.	Sort No.	No. of Pl
00004	00001	7.0

Card No.	Sort No.	$P_1(I)$	$P_1(I+1)$	$P_1(I+2)$	$P_1(I+3)$	$P_1(I+4)$	$P_1(I+5)$
+0005	+0001	59.0		59.0	58.5	59.0	58.0
+0005	+0007	58.5					
+0005	+0013						

* Torque control = 0, if M is entered as a percent and the torque curve is used.
Torque control = 1, if M is entered as a torque value and the torque curve is used.

Torque control = 1. if M is entered as the actual torque.

**** Nozzle control = 1, override nozzle test.**

Nozzle control = 0, perform nozzle test.

Card No.	Sort No.	No. of P9
±1	±6	±11
+0005	+0001	4.0

Card No.	I	P9 (I)	P9 (I + 1)	P9 (I + 2)	P9 (I + 3)	P9 (I + 4)	P9 (I + 5)
±1	±6	±11	±21	±31	±41	±51	±61
+0006	+0001	6.0	6.0	6.0	7.2	6.0	5.7
+0006	+0007	6.0	6.5	9.0	6.2	5.0	6.6
+0006	+0013	5.0	4.2				
+0006	+0019						

Card No.	Sort No.	No. of T9
±1	±6	±11
+0007	+0001	29.0

Card No.	I	T9 (I)	(T9 (I + 1)	T9 (I + 2)	T9 (I + 3)	T9 (I + 4)	T9 (I + 5)
±1	±6	±11	±21	±31	±41	±51	±61
+0008	+0001	1985.0	2025.0	1960.0	1960.0	2000.0	2050.0
	07	2100.0	2050.0	2110.0	2110.0	2160.0	2120.0
	13	1625.0	1660.0	1600.0	1600.0	1900.0	1723.0
	19	1750.0	1800.0	1900.0	1700.0	1925.0	1800.0
	25	1750.0	1700.0	2120.0	2100.0	2140.0	
	31						

APPENDIX VII

TURBINE PERFORMANCE DATA REDUCTION PROGRAM - READOUT COMPUTER PROGRAM 08.079

TURBINE TEST 62

INPUT -

N	M	DELTA P	(T)UP	(P)UP	(CPS)E
42286.000	575.000	92.000	56.000	190.700	1325.000
(CPS)P	P-BAR	TOR. CONT.			
72.000	29.340	1.000			
A7	A3	LKG. FLOW	AB	DP/P3	NOZ. CONT.
0.000	4.211	0.050	0.065	0.040	1.000

OUTPUT -

Gearbox HP	= 0.21742776E+02	Airflow	= 0.29059783E+01
Engine WF PPH	= 0.45407750E+03	Preheater WF	= 0.87240000E+02
Fuel-Air Ratio	= 0.51743670E-01	Dynamometer Wrk.	= 0.27332977E+02
Dyn. Efficiency	= 0.66496840E+00	Dyn. Ref. Flow	= 0.44013837E+03
Dyn. Ref. Speed	= 0.18484758E+05	Dyn. Ref. P Ratio	= 0.40914958E+01
Dyn. T.I.T. Deg. F	= 0.23677817E+04	Ex. Temp. Deg. F	= 0.19139655E+04
Override Nozzle Choke Test			

Output Using T3 Calculated

Dynamometer Wrk.	= 0.27563916E+02	Dyn. Ref. Flow	= 0.44005284E+03
Dyn. Ref. Speed	= 0.18562683E+05	Dyn. Ref. P Ratio	= 0.40892931E+01
Dyn. T.I.T. Deg. F	= 0.23436744E+04	Ex. Temp. Deg. F	= 0.19139655E+04
Dyn. Efficiency	= 0.67033303E+00	Ex. Temp. Deg. F	= 0.18898582E+04

APPENDIX VIII

TURBINE RIG INSTRUMENTATION

The prime objective of the program was to measure the turbine performance and to verify heat transfer analyses as applied to fluid cooling of the turbine rotor and air cooling of the turbine inlet nozzle vanes, turbine shroud, and exhaust diffuser.

The following list of instrumentation represents the total instrumentation utilized.

Turbine Inlet and Turbine Inlet Nozzle

	Quantity
Actuated TTT Probes	7
Total Pressure Probes	8
Static Pressure Taps at Turbine Inlet Nozzle Throat	6

Inlet Housing (Combustor Inlet)

Inlet Total Temperature Probes (I/C)	6
Inlet Static Pressure Taps	4

Combustor Housing

Static Pressure Taps	3
--------------------------------	---

Turbine Exhaust and Exhaust Diffuser

Four-Element EGT Rakes (C/A)	9
Four-Element EG Total Pressure Probes	6
Actuated Yaw Probes - Total Pressure and Angle	2
Cooling Air Inlet Static Pressure	1
Cooling Air Exit Static Pressure	2
Cooling Air Upstream Orifice Pressure	1

Quantity

Rotor and Shaft (Slip Ring Readout)

Disc Temperature (C/A)	6
Fuel Exit Temperature (C/A)	2

Supply Air Metering Station

Upstream Orifice Pressure	1
Downstream Orifice Pressure	1
Orifice Pressure Drop - Inches Water With Switchover to Inches Hg	1
Upstream Orifice Temperature (I/C)	1
Downstream Orifice Temperature (I/C)	1

Exhaust Duct (Water Injection)

EGT Upstream of Water Injection (C/A)	1
EGT Downstream of Water Injection (C/A)	1
Exhaust Duct Static Pressure	1

Fuel System

Inlet Fuel Temperature to Turbine (I/C)	1
Recirculating Fuel Temperature Turbine Rig (I/C)	1
Inlet Fuel Temperature to Preheater (I/C)	1
Recirculating Fuel Temperature - Preheater (I/C)	1
Fuel Pressure Into Turbine	1
Fuel Pressure Upstream of Flow Control Valve (Pump Discharge Pressure)	1
Fuel Pressure to Preheater Nozzle	1
Fuel Flow Rate to Turbine Rig	1
Fuel Flow Rate to Preheater	1

Dynamometer

Torque Measurement	1
Water Exit Temperature (I/C)	1
Bearing Temperatures	1

Miscellaneous Rig Instrumentation

Vibration Pickups	4
Slip Ring Temperature (I/C)	2
Rig and Gearbox Bearing Temperature (I/C)	7
Lubricating Oil Temperature (I/C)	5
Lubricating Oil Pressure	2
Rotor Speed	2
Optical Pyrometer Temperature (I/C)	1

The instrumentation location on the test rig is shown in Figures 498, 499, and 500.

Turbine blade cooling was monitored utilizing a temperature-sensitive point, Thermidex (OG 6). This point provided satisfactory evaluation of approximate blade metal temperature which correlated well with the predicted values.

TEST CELL - INSTRUMENTATION

The test cell provided the air supply system, cooling system, lubricating system, fuel supply system, and instrumentation.

The air was passed through a calibrated orifice by ram compressors. The air passed into a can-type preheater. The preheated air then entered through a plenum into the combustor, Figure 501. Cooling air was supplied to the exhaust ducting. It too was passed through a calibrated orifice.

The lubricating system supplied oil to the gearbox and turbine rig assemblies, Figures 502 and 503. The fuel was supplied from storage tanks at 250 psi and pumped into the turbine rig, Figure 504.

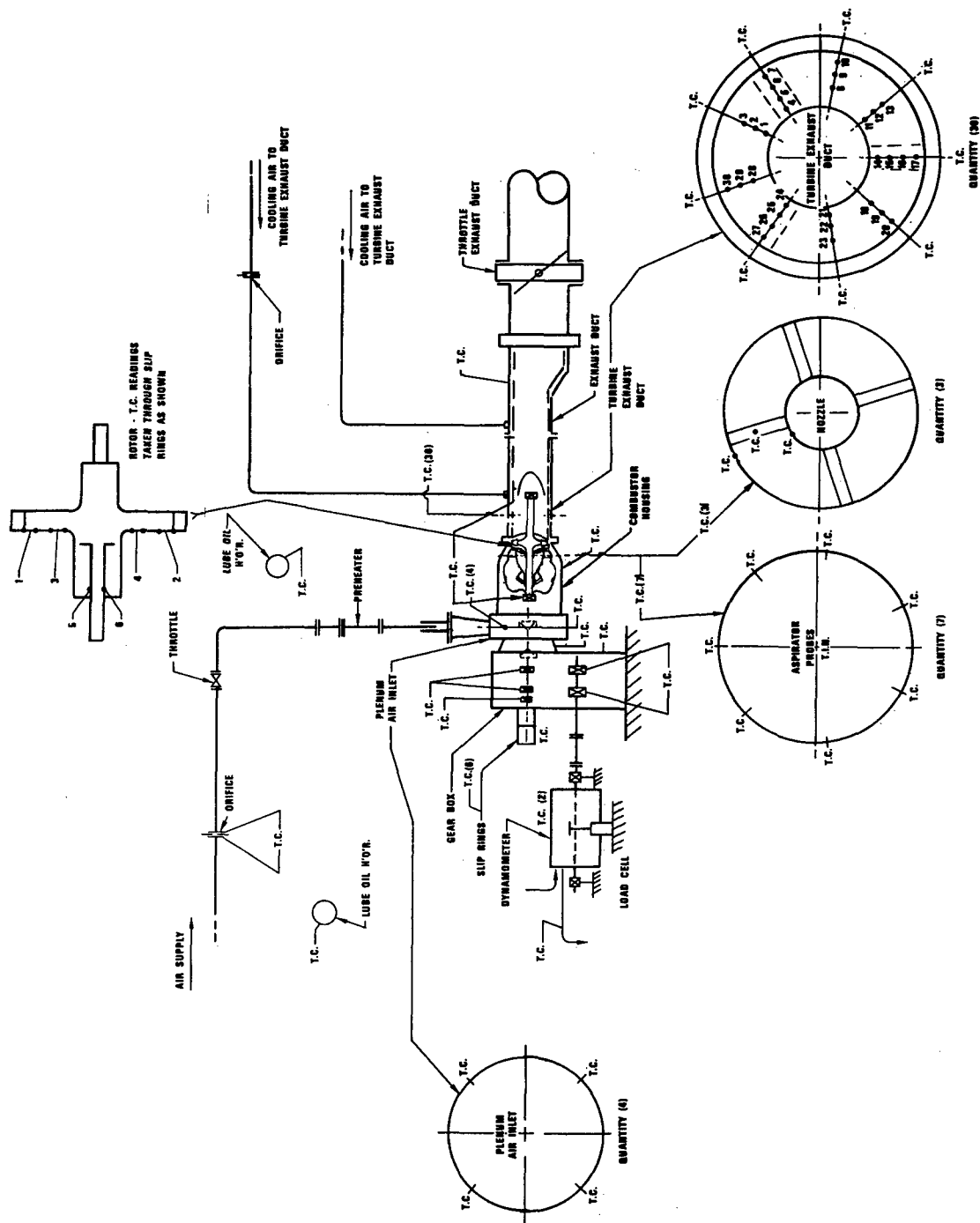


Figure 498. Instrumentation Schematic Test Rig Fluid-Cooled Turbine Thermocouple Locations.

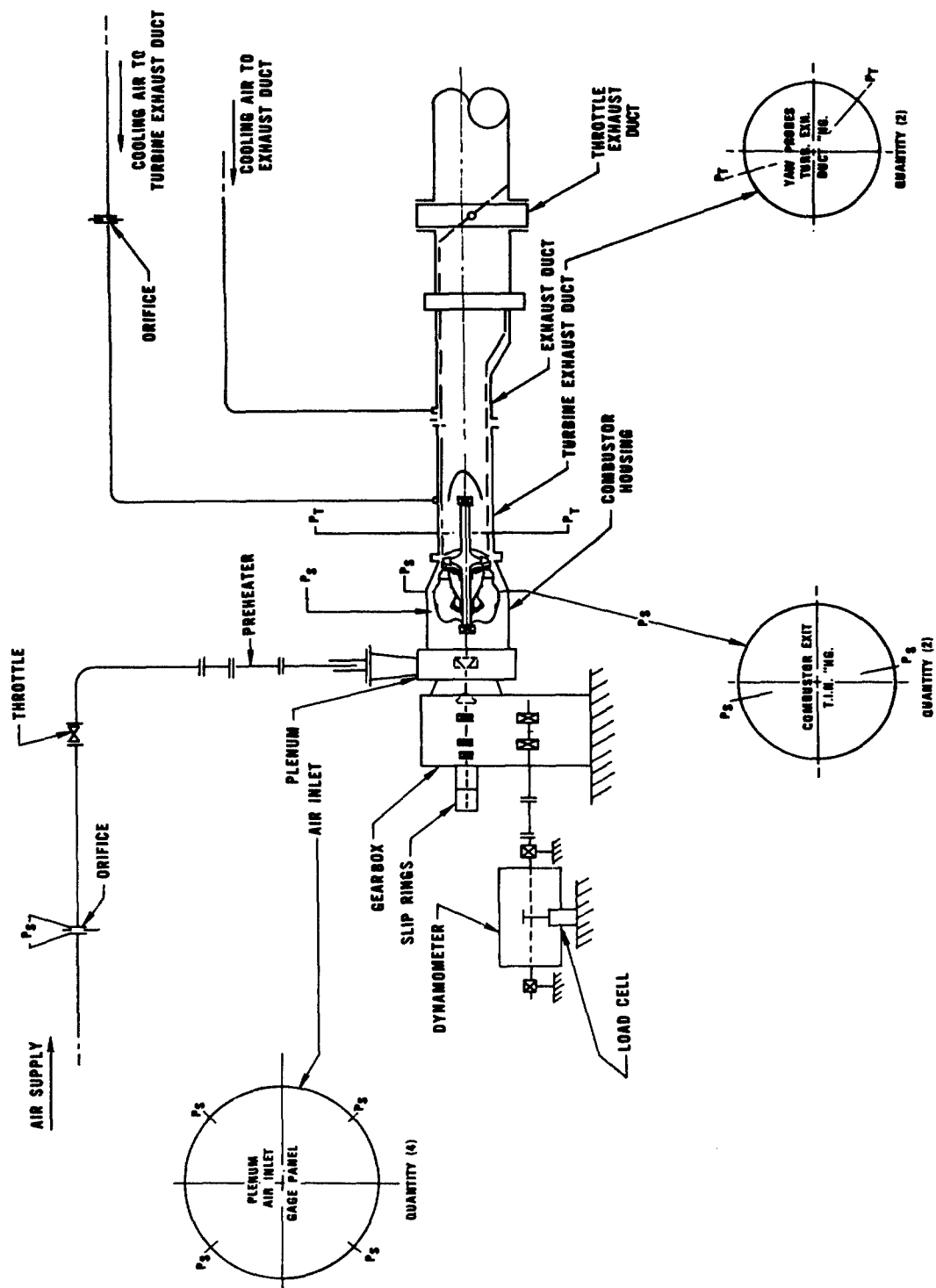


Figure 499. Instrumentation Schematic Test Rig Fluid-Cooled Turbine Thermocouple Locations.

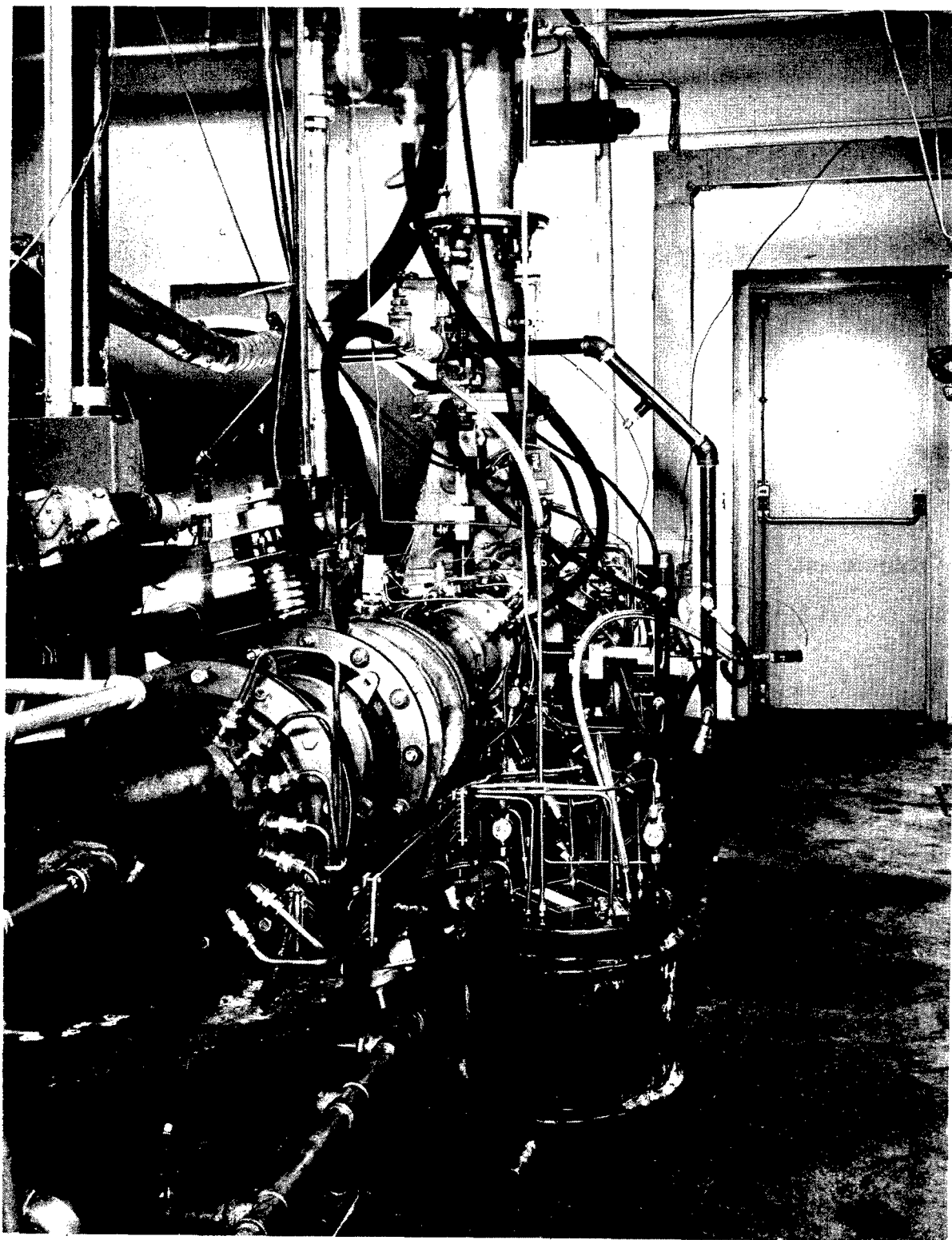


Figure 500. Test Rig Instrumentation.

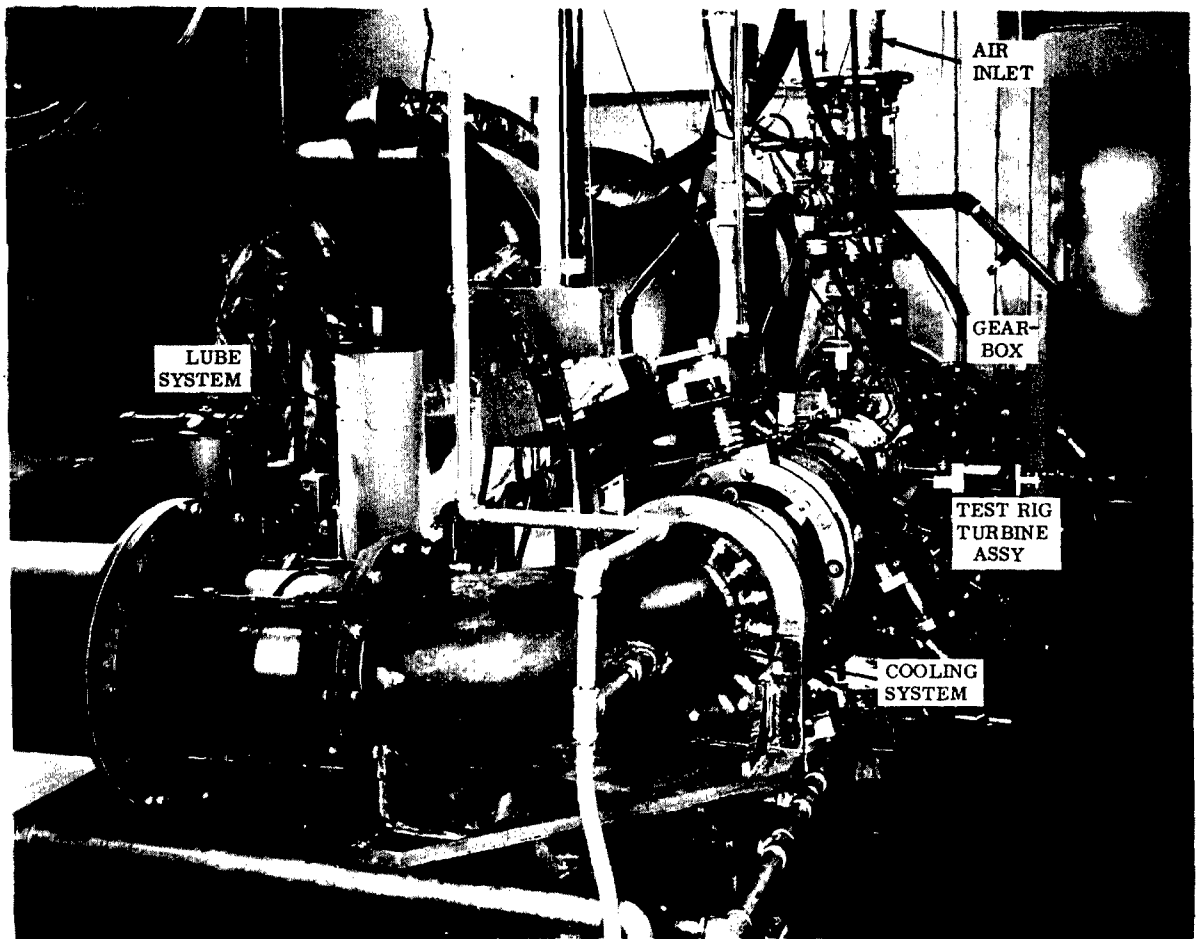


Figure 501. Test Rig Assembly.

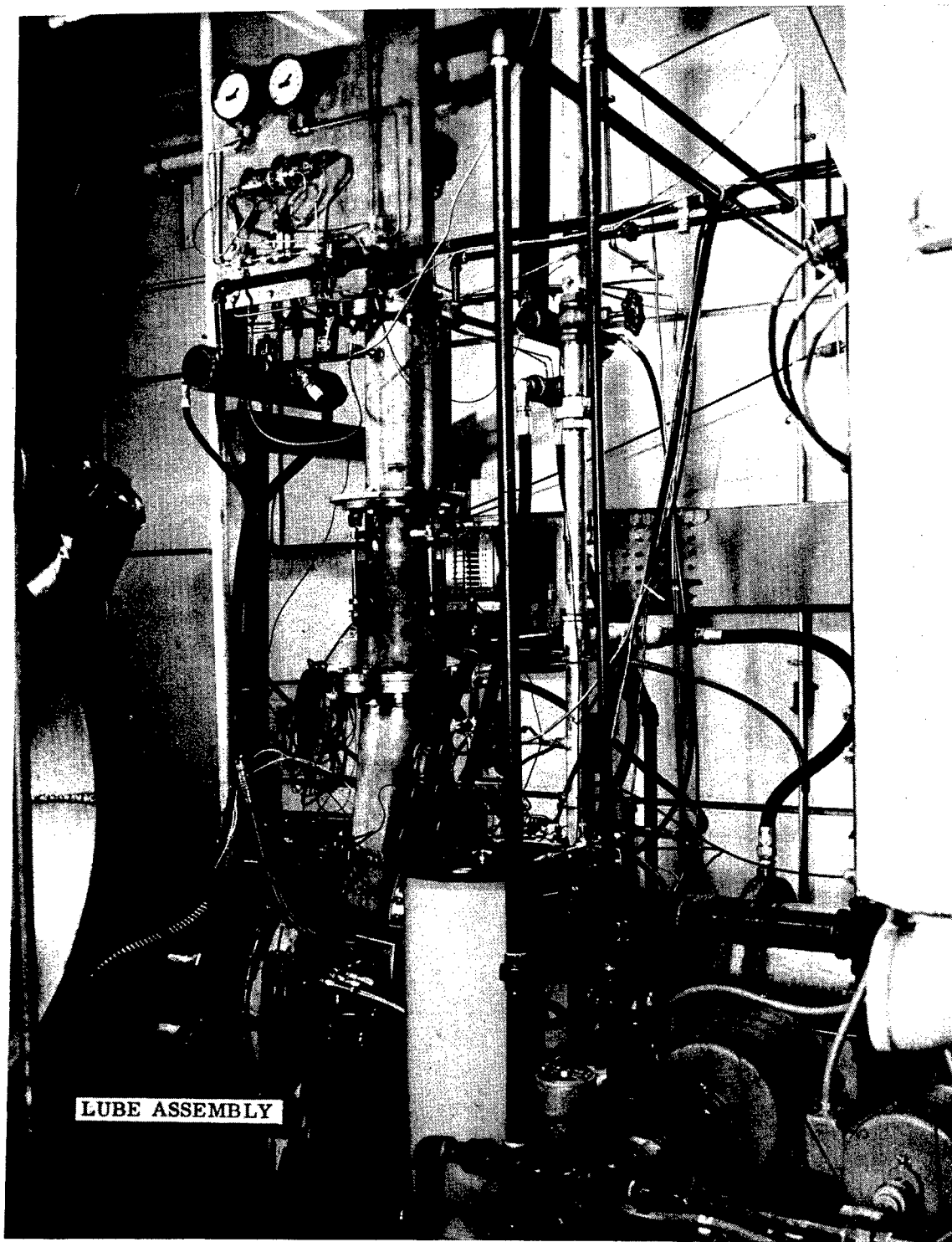


Figure 502. Rig Lubricating Assembly.

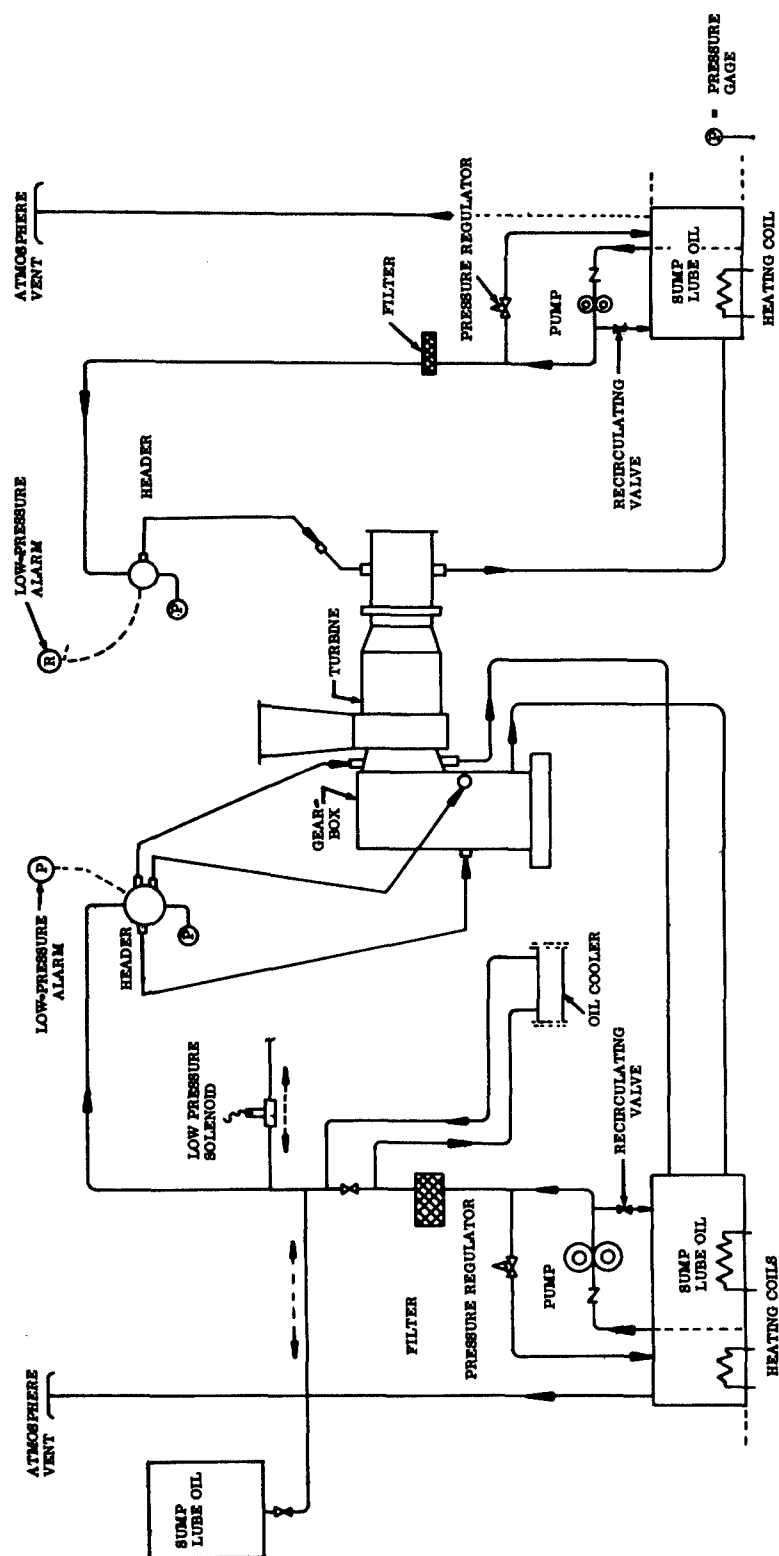


Figure 503. Lube Oil System.

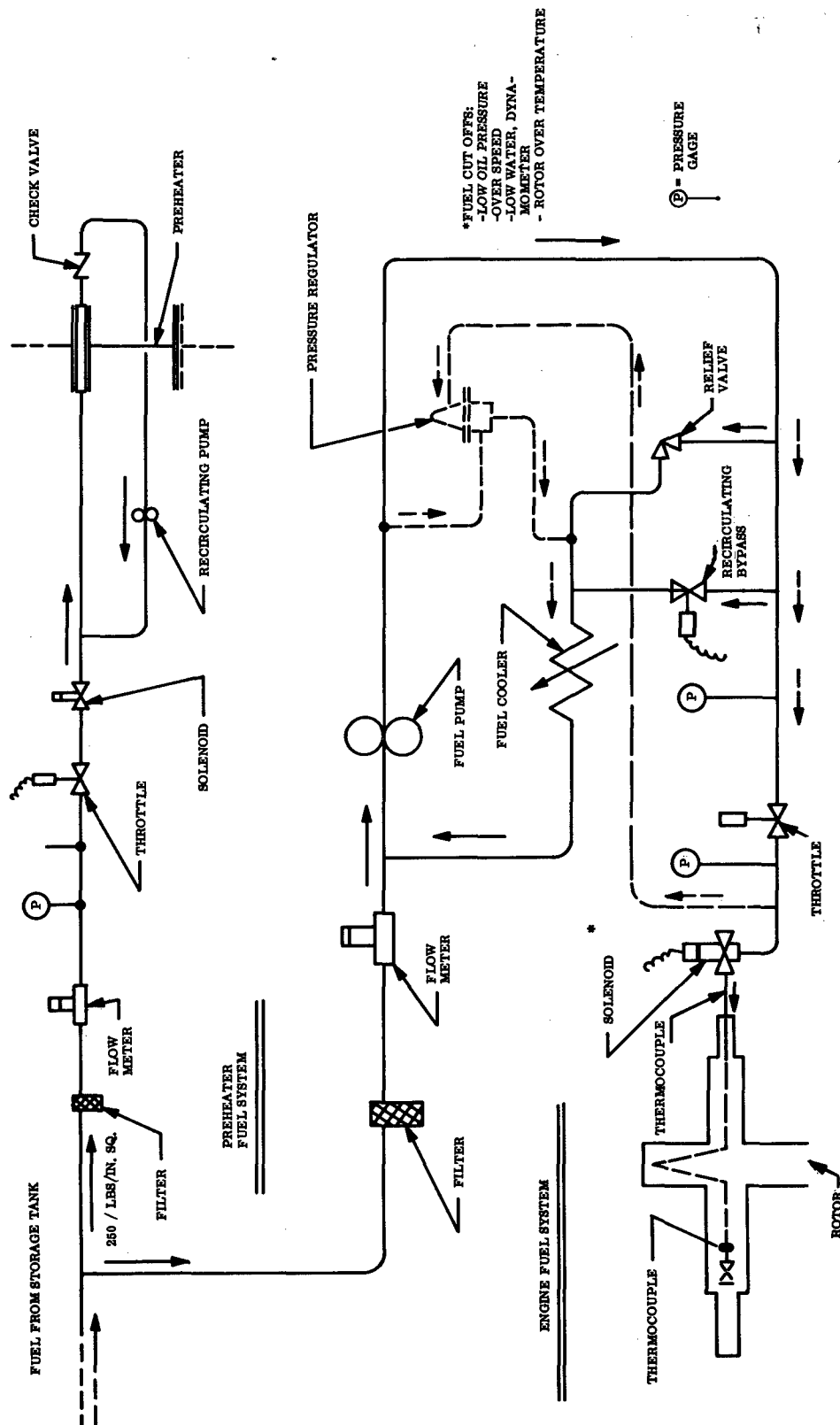


Figure 504. Fuel System.

The instrumentation for safety cutouts were supplied as follows:

- * Rig fuel, in cutout, energized by low-level warning on dynamometer water reservoir.
- * Rig fuel, in cutout, and maximum dynamometer water flow energized by rotor.
- * Rig fuel, in cutout, energized by turbine exit temperature in excess of 2380°F.
- * Lube system short-circuit provision - energized solenoid to connect gearbox lube pump discharge and rig lube pump discharge.
- * Annunciation for loss of rig oil pressure.
- * Annunciators and "Emergency" light for loss of gearbox oil pressure.

The cell was equipped with a strip recorder for a platinum rhodium thermocouple trace of TIT (0 to 3000°F). A visicorder for transient traces of speed, fuel flow, torque, turbine exit temperature, fuel exit temperature, and disc temperature versus time was also supplied.

APPENDIX IX

ELECTRON BEAM WELDING AND SEALING FLUID- COOLED BLADE, PART NO. 709627

CONTINENTAL PROCESS 402

SCOPE

This supplement establishes the detailed requirements for electron beam welding of Part No. 709627, fluid-cooled turbine blade, not included in the general specification CAE-PS 402. Requirements for preparation, fixturing, welding procedures, parameters, and stress relief are included.

This supplement is a part of electron beam welding specification CAE-PS 402.

MANUFACTURER'S PREPARATION

Machining

The blade cap shall be prepared as an oversize contour (0.030 inch per side approximately) in weld area.

This blade cap shall have an airfoil contoured cavity 0.015 inch deep, produced by using the casting as an EDM electrode.

The heat exchanger plug shall be machined in accordance with Continental drawing number 711487.

Cleanliness

The blade, blade cap, and plug assemblies shall be free of contamination. All chips and/or grinding dust shall be removed from between the fins, and the assemblies shall be ultrasonically cleaned to remove all grease, oil, and other contaminating substances before welding.

FIXTURING

A rotating fixture used to position and hold the assemblies while welding shall be furnished by the manufacturer. It shall incorporate those features that will maintain the alignment requirements set forth in the following sections.

WELDING PARAMETERS

The following welding parameters were established for welding the tip-cap using high-voltage-type equipment. Should other equipment be used, new parameters must be established and certified by Continental or outlined in paragraph 4.1 of the general welding specification CAE-PS 402.

Gun-To-Work Distance (inches)	4.0
Beam Current (Milliamps) (MA)	7.0
Voltage (Kilovolts) (KV)	100.0
Travel Speed (Inches Per Minute) (IPM)	30.0

The following welding parameters were developed for welding the heat exchange plug using high-voltage-type equipment.

Gun-To-Work Distance (inches)	4.0
Beam Current (MA)	2.5
Voltage (KV)	80.0
Rotational Speed (rpm)	25.0

WELDING PROCEDURES

Prior to welding components, the established parameters shall be verified by making the required cap and plug welds on a test blade for assurance of the following:

Weld penetration through cap shall be 0.018 inch to 0.020 inch past the casting wall.

Weld penetration of stem plug shall be approximately 0.010 inch. Hole in plug shall not be blocked by welding.

Above requirements shall be verified by microexamination.

WELDING OF TIP-CAP

Scribe reference lines on cap 0.015 inch from EDM surface.

Clean welding surfaces in accordance with paragraph 4.2 of CAE-PS 402.

Assemble parts in fixture for welding.

Tack weld on two places, each concave and convex side.

Line up visually through microscope on reference line, and adjust runout to ± 0.001 inch.

Check travel of work under microscope, and adjust speed to conform to parameter established in paragraph 4.1 of CAE-PS 402.

Weld cap to blade using weld parameters previously established in paragraph 4.1 of CAE-PS 402, welding concave side first, then convex side.

WELDING OF HEAT EXCHANGE PLUG

Clean welding surfaces in accordance with paragraph 4.2 of CAE-PS 402.

Assemble parts in fixture, and adjust runout to ± 0.001 inch.

Locate heat exchanger plug such that the offset stem is in line with the convex passage in blade.

Check welding speed.

Weld per energy settings established in paragraph 4.2 of CAE-PS 402.

Fluorescent penetrant inspect for evidence of cracks.

Submit welded assembly to an internal pressure test of 1200-psig helium. Pressure must be held for 5 minutes.

Heat treat at 1325°F for 8 hours; furnace cool to 1150°F followed by air cooling.

After heat treatment, submit to fluorescent penetrant and internal pressure tests or testing described above.

SEAL WELDING

Clean surfaces in accordance with paragraph 4.2 of CAE-PS 402.

Insert 0.013-cc water through hole in plug using a microliter hypodermic syringe.

Seal hole using inert-gas tungsten arc process. No filler wire required.

Place completed assembly in a bomb fixture, and pressurize to 2000-psi helium. Hold for 5 minutes.

Remove from bomb, immediately immerse assembly in glass container filled with acetone, and observe for 5 minutes for bubbles originating in welds or other areas of casting.

QUALITY CONTROL

During production welding, each fifth blade will be weighed as follows to verify the quantity of water inserted.

1. Prior to filling with water
2. After insertion of water and immediately prior to welding
3. Immediately following welding
4. Weight change shall not exceed ± 0.015 gram

WELD REPAIR

A written repair welding request shall be prepared and submitted to Continental for approval prior to any weld repairs.

APPENDIX X

WELDING OF TURBINE SHAFT (FUEL VALVE HOUSING, PART NO. 711008)

The following is the welding procedure utilized for the fluid-cooled turbine shafts.

WELDING OF PART NO. 711008

1. Establish welding parameters (speed, current, and technique) for flat joints.
2. Assemble fuel valve housing (711008) to rotor disc (711423) by shrink fit.
3. Assemble into welding fixture with rear shaft mounted in combination collet and four-jaw chuck.
4. Adjust fixture to have disc run true.
5. Assemble spring, loaded dead center, into fuel valve housing.
6. Check runout of entire assembly.
7. Insert into chamber and check alignment, including total indicated reading (TIR) and speed and tracking of joint.
8. Tack weld joint and check joint tracking.
9. Weld joint, and remove fixture from chamber.
10. Indicate the runout in the fixture.
11. Remove from fixture and inspect run on all critical diameters.
12. Replace in fixture and recheck runout.
13. Straighten fuel valve housing by rewelding joint on high spot.
14. Repeat inspection per steps 12, 13, and 14 until joint runs true.

15. Waiver was obtained by phone to accept 0.006-inch TIR at end of fuel valve housing and to omit machining of 0.020-inch excess weld metal.
16. Pressure test electron beam weld joint fuel valve housing to disc.

WELDING OF INTERMEDIATE SHAFT PART NO. 711010

1. Establish welding parameters (speed, current, and technique) using simulated flats.
2. Assemble intermediate shaft (711010) to rotor disc (711423) by shrink fit.
3. Assemble into welding fixture with rear shaft mounted in combination collet and four-jaw chuck.
4. Adjust fixture to have disc run true.
5. Assemble prepared plug into front of intermediate shaft in combination with spring, loaded dead center.
6. Check runout of entire assembly.
7. Insert into chamber and check alignment, tracking of joint, and speed.
8. Tack weld and check joint tracking.
9. Weld joint, and remove from chamber.
10. Indicate the runout in the fixture.
11. Remove from fixture and inspect runout of all critical dimensions.
12. Replace in fixture and recheck runout.
13. Straighten intermediate shaft assembly by rewelding high spot.
14. Repeat inspection per steps 12, 13, and 14 until joint runs true.
15. Waiver obtained by phone to accept 0.004-inch TIR at weld joint.
16. Heat treat per print instructions.

17. After heat treating, assemble front shaft and check runout.
18. Obtained waiver by phone to square up 0.002 inch out of parallel discovered after heat treatment.
19. Reassemble front shaft and check runout prior to grind.
20. Grind bearing surface with assembly mounted between centers.
21. After grinding, recheck runout must fall within blueprint specifications.

DISTRIBUTION

US Army Materiel Command	5
US Army Aviation Systems Command	5
Chief of R&D, DA	2
US Army R&D Group (Europe)	2
US Army Aviation Materiel Laboratories	18
US Army Mobility Equipment R&D Center	1
US Army Limited War Laboratory	1
US Army Human Engineering Laboratories	1
US Army Ballistic Research Laboratories	2
Army Aeronautical Research Laboratory, Ames Research Center	1
US Army Research Office-Durham	1
US Army Test and Evaluation Command	1
US Army Combat Developments Command, Fort Belvoir	2
US Army Combat Developments Command Experimentation Command	1
US Army Combat Developments Command Transportation Agency	1
US Army Aviation School	1
US Army Tank-Automotive Command	3
US Army Armor and Engineer Board	1
US Army Aviation Test Board	2
US Army Aviation Test Activity, Edwards AFB	2
Air Force Flight Test Center, Edwards AFB	1
US Army Field Office, AFSC, Andrews AFB	1
Air Force Aero Propulsion Laboratory, Wright-Patterson AFB	1
Air Force Materials Laboratory, Wright-Patterson AFB	2
Air Force Flight Dynamics Laboratory, Wright-Patterson AFB	1
Systems Engineering Group, Wright-Patterson AFB	2
Naval Air Systems Command, DN	16
Office of Naval Research	2
Commandant of the Marine Corps	1
Marine Corps Liaison Officer, US Army Transportation School	1
Lewis Research Center, NASA	1
Ames Research Center, NASA	2
NASA Scientific and Technical Information Facility	2
NAFEC Library (FAA)	2
US Army Board for Aviation Accident Research	1
Bureau of Aviation Safety, National Transportation Safety Board	2
Federal Aviation Administration, Washington, DC	2
US Government Printing Office	1
Defense Documentation Center	20

Unclassified

Security Classification

DOCUMENT CONTROL DATA - R & D

(Security classification of title, body of abstract and indexing annotation must be entered when the overall report is classified)

1. ORIGINATING ACTIVITY (Corporate author) Continental Aviation and Engineering Corporation Detroit, Michigan		2a. REPORT SECURITY CLASSIFICATION Unclassified	
		2b. GROUP	
3. REPORT TITLE ADVANCEMENT OF HIGH-TEMPERATURE TURBINE TECHNOLOGY FOR SMALL GAS TURBINE ENGINES - FLUID-COOLED AXIAL FLOW TURBINE			
4. DESCRIPTIVE NOTES (Type of report and inclusive dates) Final Report			
5. AUTHOR(S) (First name, middle initial, last name) Ronald M. Gabel Arthur J. Tabbey			
6. REPORT DATE January 1969		7a. TOTAL NO. OF PAGES 765	7b. NO. OF REFS 46
8a. CONTRACT OR GRANT NO. DA 44-177-AMC 184 (T)		9a. ORIGINATOR'S REPORT NUMBER(S) USAAVLABS Technical Report 68-65	
b. PROJECT NO. 1G121401D14413		9b. OTHER REPORT NO(S) (Any other numbers that may be assigned this report)	
c.			
d.			
10. DISTRIBUTION STATEMENT This document has been approved for public release and sale; its distribution is unlimited.			
11. SUPPLEMENTARY NOTES		12. SPONSORING MILITARY ACTIVITY U. S. Army Aviation Materiel Laboratories Fort Eustis, Virginia	
13. ABSTRACT <p>This report presents the results of an investigation directed toward the design and demonstration of a fluid-cooled turbine for an advanced small gas turbine. The primary objective was to advance and demonstrate high turbine inlet temperature technology for small gas turbine engines to the level that would provide a potential for doubling the specific horsepower relative to current small aircraft propulsion engines.</p> <p>While all major goals were met, proving the fluid-cooled turbine concept using a thermosiphon system to be valid, difficulty was encountered while attempting to provide 213 horsepower per pound of air for a free turbine.</p>			

DD FORM 1473
1 NOV 65

REPLACES DD FORM 1473, 1 JAN 64, WHICH IS
OBSOLETE FOR ARMY USE.

Unclassified

Security Classification

14. KEY WORDS	LINK A		LINK B		LINK C	
	ROLE	WT	ROLE	WT	ROLE	WT
Fluid-Cooled Turbine Component Technology Small Gas Turbine						